JOHANNES GUTENBERG UNIVERSITÄT MAINZ

Evaluation of functionalized nanoparticles for cellular uptake and their induction of antigen-specific immune responses

Dissertation

zur Erlangung des Grades

„Doctor rerum naturalium“

(Dr. rer. nat.)

Fachbereich Biologie

an der Johannes-Gutenberg-Universität Mainz

Grey Carolina Medina Montaño

geboren am 17. Februar 1988

in Riohacha-Kolumbien

Mainz, Januar 2024

This doctoral thesis was carried out in the period from December 2019 to December 2023 at the Department of Dermatology at the University Medical Center of the University of Mainz, Germany

Dean: [redacted]

Reviewer 1: [redacted]

Reviewer 2: [redacted]

Date of oral examination: ____.____.2024

VERSICHERUNG

Name: Grey Carolina Medina Montaño

Hiermit versichere ich gemäß § 12, (2) der Promotionsordnung vom 01.04.2018:

(zutreffendes ist angekreuzt.)

□ Ich habe die heute als Dissertation vorgelegte Arbeit selbst angefertigt und ausschließlich die angegebenen Quellen und Hilfsmittel verwendet.

□ Ich habe oder hatte die jetzt als Dissertation vorgelegte Arbeit noch an keiner anderen deutschen oder ausländischen Hochschule oder vergleichbaren Einrichtung zur Erlangung eines akademischen Grades eingereicht.

□ Ich habe noch kein Promotions-, PhD- oder ein vergleichbares Graduierungsverfahren im Promotionsfach erfolglos beendet.

□ Ich habe noch kein Promotions-, PhD- oder ein vergleichbares Graduierungsverfahren im Promotionsfach erfolgreich beendet.

Für die Anfertigung der vorgelegten Arbeit wurde keine entgeltliche Hilfe Dritter, insbesondere eine Promotionsberatung oder –vermittlung in Anspruch genommen.

Mainz, den _____ _____

(Unterschrift)

Acknowledgments

For privacy reasons, the acknowledgments have been removed from the electronic version of this dissertation.

Content

Abbreviations 8

List of figures 11

List of tables 12

Abstract 13

1. Effect of properties of NPs on cellular uptake (and on cellular responses) 14

1.1 Size 15
1.2 Shape 17
1.3 Surface charge 21
1.4 Surface modification 22
1.5 Elasticity 24
1.6 Hydrophobicity and hydrophilicity 26
1.7 Protein corona 26

2. Active and passive nano-vaccination 28

2.1. Tumor vaccination 28
2.2. Non-targeting NPs (Passive) 30
2.2.1. Blood cells and protein-corona interaction with the non-targeting NPs 30
2.2.2. Non-targeting NPs and their interaction with the MPS 31
2.3. Targeting NPs (Active) 32
2.3.1. mRNA NPs 32
2.3.2. B cells-based NPs 33

3. NPs mediated targeting for immunotherapy 34

3.1. Specific binding (Receptor-mediated targeting) 34
3.1.1. Mannose receptors (MR) 34
3.1.2. Antibodies 35
3.1.3. Toll-like receptors (TLR) ligands 36
3.2. Recognition of NPs via phagocytic receptors 39
3.2.1. Fc receptors 39
3.2.2. Complement receptors 40
3.2.3. Scavenger receptors 41

4. NPs and their role in the liver 42

4.1. The liver as a NP-binding organ for NP-mediated induction of immune responses 42
4.2. Liver inflammation 43

5. Material and methods 46
5.1. Antibodies 46
5.2. Isolation and culture of immune cells 47
5.3. Biological evaluation of NPs *in vitro* 50
5.4. Biological evaluation of NPs *in vivo* 56

6. Summary and future outlook 59

7. Zusammenfassung 61

8. Curriculum vitae 63

9. References 65

10. Appendix 78
10.1. Publication 1 78
10.2. Publication 2 104
10.3. Publication 3 134
10.4. Publication 4 198
10.5. Publication 5. 241
10.6. Publication 6 318
10.7. Publication 7 359
10.8. Publication 8 379
10.9. Publication 9 434
10.10. Publication 10 457
10.11. Publication 11 (submitted) 485

Abbreviations

APC	antigen presenting cell
CD	cluster of differentiation
cDC	conventional DC
CLR	c-type lectin receptors
CR	complement receptor
CRC	collaborative research center
CTL	cytotoxic T lymphocyte
DC	dendritic cell
DC-SIGN	dendritic cell-specific ICAM-grabbing non-integrin
DEC205 (CD205)	cluster of differentiation 205
DNA	deoxyribonucleic acid
DXM	dexamethasone
EPR	enhanced permeability and retention effect
Fc	fragment crystallizable
fDC	follicular dendritic cell
IFN	interferon
IMDQ	imidazoquinoline
KC	kupffer cell
LNP	lipid nanoparticle

LSEC	liver sinusoidal endothelial cell
L-SIGN	liver/lymph node-specific ICAM-3-grabbing integrin
MAC	macrophage
MHC	major histocompatibility complex
MR	mannose receptor
mRNA	messenger ribonucleic acid
MPS	mononuclear phagocyte system
NK	natural killer cell
NLC	nanostructured lipid carrier
NP	nanoparticle
NPC	liver non-parenchymal cell
OVA	ovalbumin
PAMP	pathogen-associated molecular pattern
PB	peptobrush
pDC	plasmacytoid dendritic cell
PEG	Polyethylenglycol
PMN	polymorphonuclear neutrophil
PRR	pattern recognition receptor
RNA	ribonucleic acid
ScR	scavenger receptor

TLR	Toll-like receptor
Treg	regulatory T cell
TierSchG	Tierschutzgesetz (German Protection of Animals Act)
WHO	world health organization

List of figures

Figure 1: Schema of the physical properties of NPs including size, shape, surface charge, material composition, and stiffness used for immunotherapies 14

Figure 2: Cellular uptake of several NP with different size ranges but same surface charge (neutral). 16

Figure 3: Biodistribution of different NPs in vivo and ex vivo in different organs after 24 hr. intravenous injection. 20

Figure 4: Effect of shape on NP–cell membrane interaction/uptake (Salatin and Yari Khosroushahi 2017). 20

Figure 5: Passive and active tissue targeting (Pearce and O'Reilly 2019) 29

Figure 6: Liver non-parenchymal cells (Created by Biorender) 33

Figure 7: Overview of the important PRR subfamily of Toll-like receptors (TLRs) and their respective ligands/agonists. 37

Figure 8: Schema of liver non-parenchymal cell (NPC) enrichment by liver perfusion (LP) and liver dissociation (LD) (Medina-Montano, Cacicedo et al. 2022). 49

Figure 9: Gating strategy of spleen cells 51

Figure 10: Gating strategy of liver NPC 52

Figure 11: Gating strategy of BMDCs-GM CSF 52

Figure 12: Gating strategy of BMDCs-FT3L 53

Figure 13: Graphical summary of NP-based vaccine research categories dealt with in this thesis. 59

List of tables

Table 1: Overview of the different organic and inorganic NP formats biologically evaluated in this project within the framework of the Collaborative Research Center 1066, and also in collaboration with other groups outside of the Collaborative Research Center 1066. 19

Table 2: Overview of the different antibodies dealt with in this thesis. 46

Table 3: Overview of the different cytokines included in this thesis. 54

Table 4: Reference values for female C57BL/6 and BALB/c mice. 57

Abstract

Nanotechnology has emerged as a promising avenue for vaccine development, offering precise control of antigen delivery, and then induction and modulation of immune responses. The work that is subject to this thesis focused on the evaluation of functionalized nanoparticles (NP) designed for optimal uptake by antigen presenting cells (APCs) and subsequent induction of antigen-specific immune responses. The NPs were engineered with surface modifications to enhance their interactions with target cells. In this study, we conducted a systematic assessment of the efficacy of NPs, beginning with an exploration of their physicochemical properties and stability. Subsequently, their ability to enter immune cells was investigated, with a focus on their cellular uptake and intracellular trafficking. The studies dealt with in this thesis aimed to elucidate the impact of surface functionalizations on the ability of NPs to engage APCs, thereby influencing the efficiency of antigen presentation. For this purpose, different NPs were synthesized and functionalized by various collaborators with different biological components, such as i) antibodies to address specific immune cells, ii) antigens to be processed by APCs for presentation to T cells, and iii) adjuvants recognized through pattern recognition receptors (PRRs) that are required to stimulate APCs to induce T effector cells. In this case, NPs need to facilitate the co-delivery of antibodies, adjuvants, and antigens since all three components are required for a successful vaccination.

Furthermore, the immunogenicity of the NPs was evaluated by a series of *in vitro* and *in vivo* experiments regarding their biodistribution, their ability to target APC and their capacity to induce antigen-specific T cell immune responses. These results highlight the potential of functionalized NPs to optimize vaccine design, with implications for the development of effective and targeted immunization approaches.

In conclusion, this thesis provides valuable insights into the design and evaluation of functionalized NPs, shedding light on their cellular uptake mechanisms and their ability to elicit antigen-specific immune responses. These findings hold promise for improvement of vaccine development, offering innovative solutions for combating infectious diseases, and promoting a more targeted and robust immune response as for example in the context of tumor therapy.

Keywords: Nanomedicine, nanoparticles, uptake, properties, cancer, adjuvant, antigen.

1. Effect of properties of NPs on cellular uptake (and on cellular responses)

Nanomedicine is the application of nanotechnology in medicine. It involves the engineering of tiny machines to achieve innovation in healthcare for the diagnosis, treatment, and prevention of diseases (Greish, Mathur et al. 2018, Soares, Sousa et al. 2018, Weissig, Elbayoumi et al. 2021). It uses properties developed by a material at a nanometric scale of 10^{-9} m which often differ in terms of physics, chemistry or biology from the same material at a larger scale (Bayda, Adeel et al. 2019). Nanotechnology can be used to diagnose and treat diseases such as cancer, because their nanometric sizes are similar in size to biological molecules and should be able to gain or allow NPs to cross natural barriers, to access new sites of delivery or entry into different cellular and tissue compartments to interact with DNA or small proteins at different levels, in the blood or within organs or cells (Blanco, Shen et al. 2015).

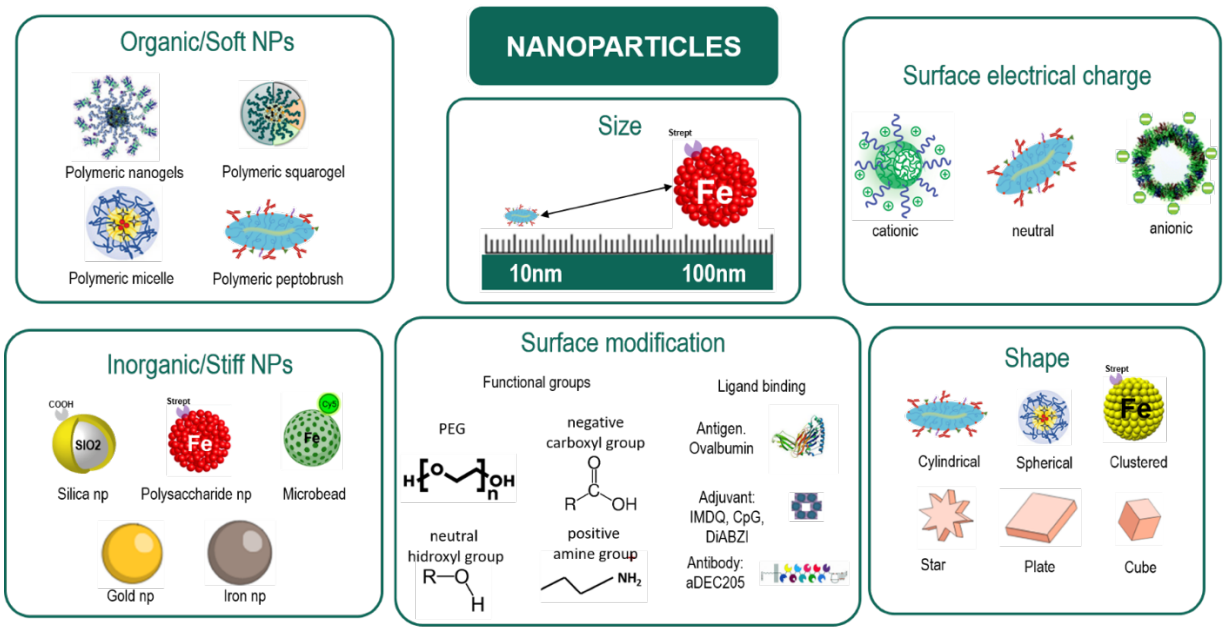

Figure 1: Schema of the physical properties of NPs including size, shape, surface charge, material composition, and stiffness used for immunotherapies

Nanoparticles (NPs) have unique properties, such as a high surface area-to-volume ratio and the ability to cross biological barriers, making them promising candidates for targeted delivery, imaging, and sensing. Using this technology, it is possible to program their physicochemical properties (size, surface charge, shape, composition, etc.) allowing precise management of cellular functions and influencing NP uptake into cells (Chan 2017, Najahi-Missaoui, Arnold et al. 2020, Selmani, Kovačević et al. 2022). (Fig.1)

An overview of the physicochemical properties of NPs and their impact on cell internalization is described below:

1.1 Size

One of the most important aspects to consider when designing NPs passing through the cell membrane is their size (Table 1). NPs enter the cell via passive or active pathways, but their size can influence the internalization mechanisms, cargo delivery and immune responses (Sabourian, Yazdani et al. 2020). Small NPs with a size range of 30∼100 nm enter the cells via pino- or micropinocytosis. On the other hand, NPs with a size range of 120∼150 nm are internalized via clathrin- or caveolin-mediated endocytosis (Foroozandeh and Aziz 2018). The smaller the NP size, the easier they can be internalized by cells as smaller NPs have a larger surface area than same mass of larger NPs, allowing them more contact with the biological membranes (Hoshyar, Gray et al. 2016, Salatin and Yari Khosroushahi 2017). Several non-phagocytic cells -as lymphocytes, epithelial cells, endothelial cells and fibroblasts- favored the uptake of smaller NPs instead phagocytic cell lines -as macrophages (MAC), monocytes and dendritic cells (DCs)- favored the uptake of larger NPs (Kettler, Veltman et al. 2014).

Emphasizing this aspect, in this thesis, NPs of different sizes (organic and inorganic) were tested and compared (Table 1). Organic small NPs such as peptobrushes and polymeric nanogels with a size range of 10∼25 nm can be taken up by non-parenchymal cells (NPC) as liver sinusoidal endothelial cells (LSEC), macrophages (MAC), and dendritic cells (DC) after intravenous injection *in vivo*. Further analysis of the single liver NPC population revealed that small NPs were largely taken up by LSEC. For other liver APCs, liver MACs and DCs could also internalize small NPs to a lesser extent. In the spleen, the internalization of organic small NPs into various APC subpopulations has been demonstrated to a variable extent *in vivo* (Kappel, **Medina-Montano et al. 2021**, Stickdorn, **Medina-Montano et al. 2022**). On the other hand, inorganic carbohydrate-coated larger NPs ∼100 nm could also be internalized in all myeloid cell types, including neutrophils (PMN, polymorphonuclear granulocytes), MACs and DCs, as well as in lymphoid cells such as NK cells and B cells, to a greater extent *in vitro* (Bednarczyk, **Medina-Montano et al. 2021**) (Fig.2). However, beyond size surface coatings and protein adsorption processes may also influence these mechanisms, tremendously.

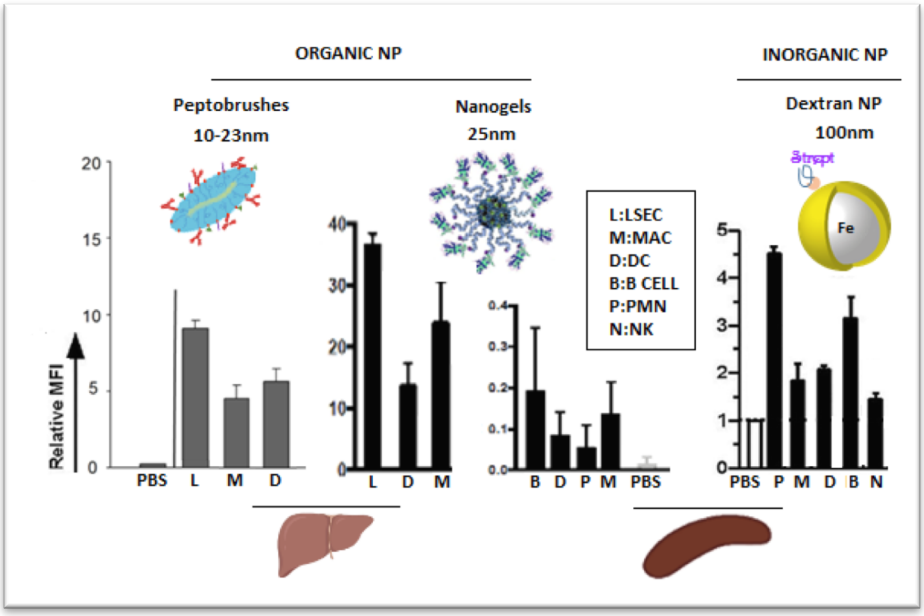

Figure 2: Cellular uptake of several NP with different size ranges but same surface charge (neutral).

NP size also affects APCs and their cellular responses. Intradermally or subcutaneously applied NPs traffic to the draining lymph nodes in a size-dependent manner. Large particles (500~2.000 nm) can independently penetrate through tissues via the lymphatic flow and accumulate in draining lymph nodes where they are taken up by peripheral APCs at the injection site, whereas small NPs (20~200 nm) are internalized by DCs and MACs residing in lymph nodes. Smaller NPs can ever deeper diffuse across the interstitium and penetrate the lymphatic system, whereas delayed transport of larger NPs to lymph nodes supports the requirement for cell-based transport. NPs 40~50 nm in size have been shown to elicit stronger T cell responses (Park, Lee et al. 2013). The covalent conjugation of antigens, including ovalbumin (OVA), to NPs reportedly allows for antibody and CD8+T cell immunity and provides protective immunity against exposure to OVA. In the analysis of antibody secretion and OVA-specific T cell generation, our organic small NPs, TLR7/8-OVA polymeric nanogels with a size of ~25 nm, revealed increased secretion of OVA-specific IgG2a antibodies and, more importantly, an increase in OVA-specific CD8+T cells. These findings provide evidence for the induction of cellular immune responses (Park, Lee et al. 2013, Stickdorn, **Medina-Montano et al. 2022**). In addition, the interferon-gamma (IFN-γ) secretory Th1 response is greater for OVA presented on particles 40~50 nm in size than for other sizes (Park, Lee et al. 2013). Th1-mediated immune responses could also be reported using organic smaller TLR7/8-OVA nanogels with a size of ~25 nm, which trigger high secretion levels of pro-inflammatory cytokines, such as TNF-α, IFN-γ, IL-6, IL-12, and type I interferon

(Stickdorn, **Medina-Montano et al. 2022**). In contrast, IL-4 secretory Th2 responses are the greatest when OVA is presented using NPs 93~123 nm in size (Park, Lee et al. 2013). In addition, the sizes usually refer to NPs after synthesis, but changes might occur during the experiments because of aggregation or attachment of serum components (Kettler, Veltman et al. 2014). This aspect is discussed in more detail below regarding the protein corona formation.

1.2 Shape

In addition, the shape of the NPs, including spherical and non-spherical (rod-like, cylindrical, elongated, discoid, clubbed, ellipsoid) geometries, can also play a pivotal role in the uptake pathway and targeted delivery. Likewise, shape has been found to significantly modulate biodistribution and blood residence time (Salatin and Yari Khosroushahi 2017, Foroozandeh and Aziz 2018). NPs with higher aspect ratio show greater affinity to enter cells by either active or passive transports. Studies have shown that all cell morphologies are taken up via clathrin-mediated endocytosis. Spherical NPs were retained in the cytoplasm, whereas non-spherical NPs moved towards the nucleus by microtubules (Xu, Niebert et al. 2008). Several studies have shown certain differences according to the internalization of NPs. It has been demonstrated that spherical NPs are internalized by several cell lines at a higher rate (five-fold higher uptake) than non-spherical NPs (Chithrani and Chan 2007).

Due to their high uptake rate, we included mainly spherical NPs in this thesis (Table 1). Spherical NPs have numerous advantages over non-spherical NPs, apart from the fact that spherical NPs are better studied than non-spherical NPs. Spherical NPs have not only a higher cellular internalization rate but also a longer blood-circulation time (pharmacokinetics after intravenous administration), good biocompatibility and improved tumor penetration (Yating Zhao 2017). By studying the biodistribution of different spherical NPs after intravenous administration, we demonstrated the biodistribution of NPs in major organs 24h after intravenous injection, and we found that all NPs tended to accumulate in the liver and kidney after intravenous exposure compared with other organs (Fig.3). This indicates that the liver and kidney were the major sites of NP accumulation for this type of materials after intravenous administration. Spherical NPs were also present in the spleen to a lesser degree. These results indicated that after 24h, it was more difficult to remove the spherical NPs from the reticuloendothelial system (RES) organs, and that they were protected from MACs, resulting in longer blood circulation (Kappel, **Medina-Montano et al. 2021**, Stickdorn,

Medina-Montano et al. 2022). Previous papers have reported that non-spherical NPs had a longer circulation half-life *in vivo* compared with spherical NPs after intravenous injection (Geng, Dalhaimer et al. 2007, von Maltzahn, Park et al. 2009).

Biocompatibility is also an important aspect when foreign substances such as NPs are introduced into cells. In our study, we showed that there were no significant changes in cells exposed to NPs compared to control cells that were not exposed to NPs, indicating that the spherical NPs used in this study were non-toxic or had very low cell toxicity. As the dose increased, the cell viability remained nearly constant, even at a higher concentration (1000 µg/ml). Such good compatibility can be attributed to several factors, such as their stable physicochemical properties and good biodegradability (data not shown) (**Medina-Montano**, Rivero Berti et al. 2022). In general, spherical NPs possess high stability, excluding their aggregation and non-specific binding to the membrane. Clearly, spherical NPs play a key role in their properties; therefore, they are used as a bridge between NPs and the cell membrane (Arno, Inam et al. 2020).

On the other hand, Venkataraman et al. reported that non-spherical NPs possess drug-loading capacities and biological behaviors that frequently deviate from their historically well-studied spherical counterparts, which have been shown to be advantageous for improving blood circulation time and organ distribution and avoiding premature clearance by phagocytosis in various situations (Venkataraman, Hedrick et al. 2011). Non-spherical NPs are taken up by cells more avidly than spherical NPs, with a negative correlation evident between aspect ratio and uptake rate.

Nanoparticle Type		Organic nanoparticles												Inorganic nanoparticles				
		Peptobrushes	Nanocapsule		Cationic Nanogels	Squarogels	Soluble Polymers	Micelles			Nanogels			Nanostructured Lipid Carriers	Colloidal	Polysaccharide nanoparticles			Microbead
Material		Polylysine backbone Polysarcosine (PSar) side chains	Azide-functionalized ovalbumin linked to a dialkin (hexanediol dipropiolate) through the metal-free azide-alkyne click reaction to the OVA capsules.		Nanogels from micelles consisting of (mPEG)113-b-(MTC-PFP)26 block copolymer.	Hydrophilic, core-crosslinked nanogels based on polymethacrylamide mPEG113-b-poly(MA-SQ)40	Polymethacrylamide backbone Polydimethylmaleicanhydride-PEG sidechains and Cholesterol Endgroup	Amphiphile Polyethylenglykol-Polycarbonat Blockcopolymere mPEG113-b-poly(MTC-OBn)15	Polyethylenglykol-Polycarbonat Blockcopolymere: $mPEG_{113}$-b-poly(TMC-SSBn)$_{15}$	mPEG-b-Poly carbonat, ketal side chains	Hydrophilic, core-crosslinked nanogels based on polycarbonate mPEG113-b-poly(MTC-NHX)	Polymethacrylate backbone; side chains: Poly(methoxy triethylene glycol methacrylate) P(mTEGMA), Poly(pentafluorophenyl methacrylate) P(PFPMA) bzw. Polyhydroxyethylmethacrylate P(HEMA)	Surface functionalized hydrophilic core crosslinked nanogels based on polycarbonate azide-PEG113-b-poly(MTC-NHX).	Myristyl myristate (Crodamol TM, MM) and the oil (Crodamol TM GTCC-LQ), Poloxamer 188 (Pluronic® F68) and Dexamethasone (DXM)	Green fluorescent silica particles	Cross-linked dextran-iron oxide composite particles	Cross-linked hydroxyethyl starch-iron oxide composite particles	Green fluorescent particles from cross-linked bovine serum albumin	Ferromagnetic core with a Dextran coating
Size (ϕ)		10-23 nm	250 nm		20-40 nm	45 nm	>10nm	25 nm	28-32 nm	20-30 nm	25 nm	40-90 nm	30 nm	145 nm	100nm	100nm	100nm	250nm	63nm
Surface electric charge		neutral (-3,-6 mV)	anionic (-30 mV)		cationic (+30 mV)	neutral	neutral	neutral	neutral	neutral	neutral	neutral	neutral	neutral (-9 mV)					anionic (-13 mV)
Shape		cylindrical	spherical		spherical	spherical	spherical	spherical	spherical	spherical	spherical	spherical	spherical	spherical	spherical	clustered	clustered	spherical	
Synthese		SPAAC (strain promoted azide-alkyne coupling)	Metall-free azide-alkyne click crosslinking in inverse miniemulsion		Micelle: self-assembly ultrasound, nanogel: reactive ester chemistry - core crosslinking with spermine.	Controlled radical polymerization (RAFT) to reactive block copolymers. Assembly into micelles and postpolymerization modification under covalent linkage of IMDQ and hydrophilic core crosslinking.	RAFT Polymerization and Modification via anhydride groups, Cholesterol mediates binding to albumin/ cell membranes	Ring opening polymerization (ROP) assembly to CL075-loaded micelles by solvent evaporation.	Organo-catalytic ring opening polymerization (ROP). Formulation of polymeic micelles by solvent evaporation.	ROP (ring opening polymerization)	ROP to reactive block copolymers. Assembly into micelles and postpolymerization modification under covalent linkage of IMDQ and hydrophilic core crosslinking.	SPAAC (strain promoted azide-alkyne coupling)	Analogous to IMDQ polycarbonate nanogels starting from azide-PEG113-OH, followed by surface decoration with DBCO-modified peptides using SPAAC.	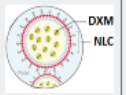 Hot-homogenization and ultra-sonication method	Core-Shell-Process	Core-Shell-Process	Core-Shell-Process	Core-Shell-Process	
Surface modification	Address Struktur	aDEC205																	
	Adjuvant		Poly I:C (TLR3)	IMDQ (TLR7/8)	Poly I:C (TLR3) CpG ODN (TLR9)	IMDQ (TLR7/8)	Me-IMDQ (TLR7/8)	CL075 (TLR7/8)	diABZI (STING)	IMDQ (TLR7/8)	IMDQ (TLR7/8)	IMDQ (TLR7/8)	IMDQ (TLR7/8)						
	Model Antigen		TRP2-Peptid									Ovalbumin	SIINFEKL Grey peptid						
Another cargo														Dexamethasone	Sicastar®-greenF	BNF-Dextran-redF	BNF-Starch-redF	Albumin-greenF	
In cooperation with		Matthias Barz	Katharina Landfester		Lutz Nuhn									Stephan Gehring					Meike Roskamp
University of Cooperation		Biotherapeutic Delivery, Leiden Academic Center for Drug Research (LACDR)	Max Planck Institute for Polymer Research of the Johannes-Gutenberg-University Mainz.		Macromolecular chemistry, Institute of Functional Material and Biofabrication, Faculty of Chemistry and Pharmacy, Julius-Maximilians-University Würzburg									Pediatric Immunology and Infectious Diseases; Clinic and Polyclinic for Pediatric and Adolescent Medicine of the University Medical Center of the Johannes-Gutenberg-University Mainz.			Micromod®				Miltenyi-Biotec
PhD Student		Christine Seidl	Natkritta Hüppe		Alexander Fuchs	Anne Huppertsberg	Alina Heck	Christian Czysch	Patric Komforth	Adrian Hauck	Christian Czysch	Judith Stickdorn	Judith Stickdorn/Christian Czysch	Maximiliano Cacicedo (PostDoc)					
References		Kappel, C., C. Seidl, C. Medina-Montano. ACS Nano, 2021				Huppertsberg, A., L. Kaps,..., Medina-Montano. J Am Chem Soc, 2021		Czysch, C., C. Medina-Montano. Macromol Rapid Commun, 2022			Czysch, C., C. Medina-Montano. Advanced Functional Materials, 2022	Stickdorn, J., L. Stein, C. Medina-Montano. ACS Nano, 2022		Medina-Montano, C. Pharmaceutics, 2022		Bednarczyk, M., C. Medina-Montano. Int J Mol Sci, 2022			

Table 1: Overview of the different organic and inorganic NP formats biologically evaluated in this project within the framework of the Collaborative Research Center 1066, and also in collaboration with other groups outside of the Collaborative Research Center 1066.

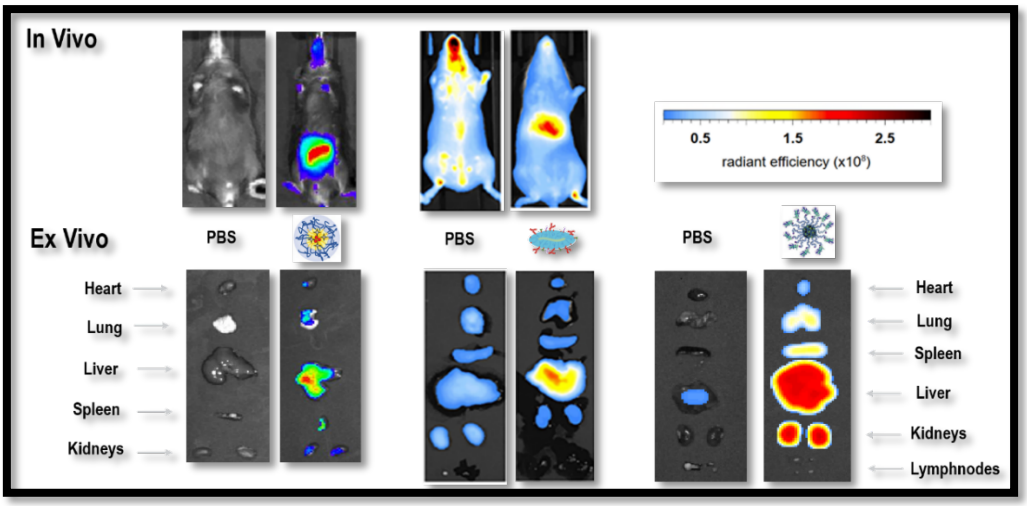

Figure 3: Biodistribution of different NPs *in vivo* and *ex vivo* in different organs after 24 hr. of intravenous injection.

This was attributed to the larger average curvature radius of the adsorbed non-spherical NPs experienced by the cells (Florez, Herrmann et al. 2012). Gratton et al. found that non-spherical NPs had the highest internalization rates compared to spheres, cylinders, and cubes (Gratton, Ropp et al. 2008). Elongated, non-spherical NPs have been reported to yield a higher efficiency in adhering to the cells as compared to spherical NPs, especially after surface modification, having a higher surface area and the ability to interact more efficiently with the cell surface membrane with respect to their shape (Fig.4) (Salatin and Yari Khosroushahi 2017)

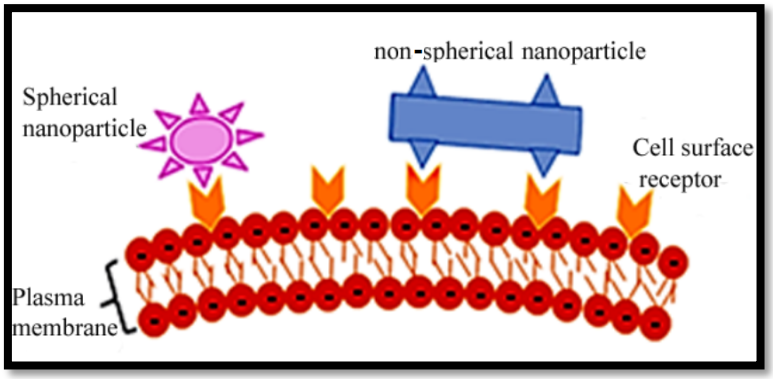

Figure 4: Effect of shape on NP–cell membrane interaction/uptake (Salatin and Yari Khosroushahi 2017).

In this work, it reports the synthesis of non-spherical NPs based on cylindrical brush polymers. Branched or dendritic side chains were introduce as “dendronized polymers,” leading to similar cylindrical conformations. Because the main chain and side chain lengths of cylindrical brushes can be controlled independently, their size and shape (aspect ratio)

may be continuously varied from spherical to cylindrical to rod- or wormlike brushes (**Seidl, Medina-Montano et al. in preparation)**. These non-spherical NPs, or cylindrical brushes, are interesting candidates for studying the effect of shape on cell uptake and blood circulation, as shown by (Kappel, **Medina-Montano et al. 2021**). These cylindrical brushes were well tolerated by cells, did not cause aggregation in concentrated blood serum, and showed extended circulation in the bloodstream of mice (70% remaining brushes after 24h) after intravenous injection, independent of size and shape. In addition, a high level of NP uptake in relevant immunological liver non-parenchymal cells has been reported **(**Kappel**, Medina-Montano et al. 2021)**

1.3 Surface charge

Another critical factor that influences the cellular uptake of NPs is the surface charge. Because the electrical charge of the cell membrane is negative, positively charged NPs are more easily attracted to the cellular membrane than neutral and negatively charged NPs. A positive surface charge has been shown to increase NP uptake in phagocytes and non-phagocytic cells. Positive surface charges increase the cell surface affinity and uptake of NPs in both cell types (Kettler, Veltman et al. 2014). Additionally, cationic charged NPs can enhance DC uptake compared with negatively charged NPs (Park, Lee et al. 2013). One example is the use of cationic liposomes composed of the cationic lipid 1,2-dioleoyl-3-trimethylammonium-propane (DOTAP), which leads to activation of mouse bone marrow DCs (BMDCs) (Park, Lee et al. 2013). Yan et al. reported that DOTAP stimulates in a concentration-dependent manner the generation of reactive oxygen species (ROS) in BMDCs, which in turn lead to activation of extracellular signal-regulated kinase (ERK) and p38, cytokine/chemokine production, and expression of the B7 costimulatory molecules CD80 and CD86 (Yan, Chen et al. 2008). The same effect was observed in liver MACs, which were also stimulated with cationic liposomes (DOTAP), showing an increase in the expression of co-stimulators CD80 and CD86 in response to DOTAP (**Medina-Montano**, Cacicedo et al. 2022). However, the uptake of positively charged NPs may disrupt the integrity of the cell membrane, leading to an increase in cell toxicity. In general, positively charged NPs induce cell death (Foroozandeh and Aziz 2018, Sabourian, Yazdani et al. 2020). Interestingly, neutrally charged NPs showed lower cellular uptake than negatively charged NPs did. The internalization of negatively charged NPs leads to gelation of membranes, while positively charged NPs cause fluidity in the cell membrane (Wang, Zhang

et al. 2008, Arvizo, Miranda et al. 2010). In most studies, an increase in the positive or negative surface charge leads to increased NP uptake compared to less charged or uncharged NPs. Zero surface charges, either by neutral surface groups (e.g., hydroxyl groups) or zwitterionic ligands, have been shown to lead to low cellular uptake compared to charged particles. This can be explained by the low affinity of NPs toward the negatively charged cell membrane. Zero surface charges hinder nonspecific protein adsorption, and a strong hydration layer may be formed via electrostatic interactions (Kettler, Veltman et al. 2014). Most of the NPs included in this thesis possess a neutral surface charge (Table 1). Thus, the aim is to avoid general cellular uptake by all cells, but only in immune cells, especially phagocytic APCs (Fig.2). Kappel et al. and Stickdorn et al. showed that APCs could internalize neutral NPs to a greater extent than other unwanted cells **(**Kappel**, Medina-Montano et al. 2021,** Stickdorn**, Medina-Montano et al. 2022**). In addition to the uptake rate of NPs, surface charges also affect the uptake mechanisms. More specifically, positively charged NPs are mainly internalized by the cell via macropinocytosis, whereas clathrin-/caveolae-independent endocytosis is the mechanism for the uptake of negatively charged NPs (Foroozandeh and Aziz 2018).

1.4 Surface modification

Surface modification of NPs by cell-specific targeting molecules has been reported to be a powerful tool for increasing cell-specific uptake, for example, modification of different functional groups and/or the addition of ligands to improve targeted drug/gene delivery. Using the last, a specific ligand depends on several different parameters including the nature of the target cell, the material used in the formulation of NPs and the chemistry available for conjugating ligands to the NP surface (Salatin and Yari Khosroushahi 2017, Sabourian, Yazdani et al. 2020).

Functional groups

Surface functionalization of NPs mostly comprises polyethylene glycol (PEG), alternatively negative carboxyl (-COOH) groups, neutral functional groups such as hydroxyl (-OH) groups, or positive amines (-NH2) which lead to an enhanced positive surface charge and, hence, increased uptake of NPs into cells. Similarly,–COOH functional groups increase the negative charge of NPs and accordingly enhance their uptake in certain cases (Kettler, Veltman et al. 2014, Foroozandeh and Aziz 2018). Stickdorn et al. have designed a PEGylated-NP platform.

They reported that functionalized NPs have better targeting efficacy compared to non-functionalized NPs, indicating higher cellular uptake rates for functionalized NPs, which translates into enhanced therapeutic effects **(**Stickdorn**, Medina-Montano et al. 2022)**.

Ligand binding

Surface modification of NPs can be used to increase circulation time in the bloodstream, enhance cell uptake, reduce non-specific biodistribution, increase target-selective delivery, and reduce cytotoxicity (Chen, Wang et al. 2010). One of the obstacles for NPs to reach the targeted site is clearance by the immune system. Blood clearance of NPs is a natural function of the kidney, liver, and immune system, and it removes excess amounts of drugs and drug-loaded NPs from the blood (Barua and Mitragotri 2014). To increase circulation time and therapeutic efficacy, NPs were functionalized with certain ligands or biological components (Table 1). Ligands chemically or physically attached to the surface of NPs inhibit biological proteins from adhering to their surfaces and prevent the immune system and liver from clearance and opsonization of NPs (Sabourian, Yazdani et al. 2020). This can be achieved by using NPs containing specific peptides, antibodies, polysaccharides, lectins, membranes derived from blood cells, and also by the addition of serum proteins to drugs (Hong, Choi et al. 2020). Some ligands use the characteristics of the mononuclear phagocyte system and phagocytic innate processes to trigger an immune response (Gustafson, Holt-Casper et al. 2015). For example, NPs can provide direct intracellular access, facilitating engagement of endosomal toll-like receptors (TLR) 3, 7, 8, and 9 by their ligands, improving their efficacy as vaccine adjuvants (Park, Lee et al. 2013, Nuhn, Vanparijs et al. 2016). Stickdorn et al. designed NPs focus on the target of TLR 7/8. For this, a model antigen (ovalbumin) and an immune adjuvant (Imidazoquinoline-type TLR7/8 agonist) were attached to the same NP system. These NPs showed good cell uptake involving immune cell subsets (phagocytic and non-phagocytic cells) such as B cells, MACs, DCs and neutrophils. Moreover, they have been demonstrated to trigger high levels of pro-inflammatory cytokines, such as TNF-α, IFN-γ, IL-6, and IL-12, resulting in Th1-mediated immune responses. They also showed specific biodistribution and did not display any cytotoxicity **(**Stickdorn**, Medina-Montano et al. 2022**). In another study by Kappel et al., NPs were designed and tested, which could efficiently target DCs using an antibody against an endocytic receptor expressed at high levels in DCs, the aDEC205 protein. These NPs displayed an enhanced half-life, minimal entrapment in the liver, and effective binding to their target cells (Kappel, **Medina-Montano et al. 2021**).

Targeting specific cell populations with NPs has been described as either passive or active delivery (Fig. 5). Passive targeting is influenced by intrinsic particle properties, including size, charge, and stiffness. Physiological factors that influence particle trafficking and tissue-specific accumulation include lymphatic and hemodynamic forces, diffusive mechanisms, and epithelial/endothelial permeability. On the other hand, active targeting involves the addition of ligands to, or the surface modification of the NP exterior to direct cellular interactions by ligand-receptor binding (Peer 2014). In summary, binding NPs to various ligands can significantly affect their behavior, biodistribution, and therapeutic efficacy. NPs could bind to different ligands for 1. specific binding or receptor-mediated targeting such as mannose receptors, antibodies, Toll-Like Receptors (TLRs) and 2. non-specific binding through phagocytic receptors (Fc receptors and complement receptors) and scavenger receptors. This topic is explained in detail in Chapter 3.

1.5 Elasticity

Another factor that plays an important role in NP internalization by cells is elasticity. The elasticity of NP can affect their biodistribution, targeted delivery, and cellular uptake in a physiological environment (Sabourian, Yazdani et al. 2020). The elasticity can be explained by its resistance to changes when forces are applied. Stiffness, hardness, and rigidity are terms that are synonymous in describing the elasticity of NPs. Quantifying the effect of NP elasticity on cellular uptake is challenging because of the experimental difficulties in measuring the micro- and nanoscale (Eshaghi, Alsharif et al. 2020). One of the problems in the study of the effects of elasticity on NP endocytosis is that many physiochemical properties of NPs are strongly related to each other. This makes it difficult to synthesize NPs with exclusive parameters (Chen, Li et al. 2018).

The measurement index used to gauge the elasticity of the NPs is “Young’s modulus” and the unit of measurement is Pascal (Pa). Based on this measurement, a higher Young’s modulus value denotes higher NP elasticity, and vice versa (Donahue, Acar et al. 2019). NPs that have higher elastic values are called hard NPs (as Au NPs, quantum dots, magnetic NPs). NPs with low elastic values are called soft NPs (hydrogels, liposomes, and biodegradable polymers). Numerous studies that have focused on this parameter with respect to cellular uptake have reported the preference of cells to internalize stiffer NPs more efficiently than softer NPs because of their easier membrane penetration and larger surface area to interact with the cell membrane (Yi, Shi et al. 2011, Anselmo, Zhang et al. 2015). This

observation is attributed to the lower overall energy expenditure by membranes when wrapping stiffer NPs compared to softer NPs, even though the deformational energy required to wrap the NPs varies throughout the internalization process (Sun, Zhang et al. 2015). However, other studies have reported that softer NPs were internalized more efficiently than stiffer NPs, and intermediate elastic NPs were internalized more efficiently than either stiff or soft NPs (Tang, Ye et al. 2015).

In this thesis, we included both types of elastic NPs: stiff and soft (Table 1). Most NPs included in this study were PEG-based NPs with tunable elasticity, while keeping all other parameters (size, shape, and charge) constant. Soft-PEG-based NPs such as peptobrushes exhibited long circulation times, likely due to the presence of PEG, which grants resistance to both opsonization and reticuloendothelial system clearance **(**Kappel**, Medina-Montano et al. 2021**). Softer NPs circulate longer than stiff NPs at short time points, likely because softer particles avoid permanent clearance by macrophage-hosting reticuloendothelial organs. One possible reason for this enhanced binding and uptake of harder NPs and longer circulation of softer NPs is that the forces exerted by phagocytic cells, such as MACs, on particles during phagocytosis may be sufficiently strong to deform the particles. Depending on how the particle deforms, the particle may deform in such a way that its radius of curvature changes in the direction normal to the cell membrane. One possibility is that the extent of phagocytosis can be decreased if the shape of the NPs becomes elongated or stretched (Anselmo, Zhang et al. 2015). Regarding cellular uptake, some differences were observed between the two types of NPs. Stiff NPs (dextran NPs) could be taken up more efficiently by polymorphonuclear neutrophils such as granulocytes as well as by lymphocytic cells as B cells as compared to soft NPs (peptobrushes or polymeric nanogels) (Fig.2). Biodistribution studies showed increased accumulation of soft NPs in certain organs after 24 h (Fig.3). Interestingly, the liver showed a high concentration of soft NPs after 24 h, suggesting that the liver is responsible for the clearance of soft NPs. Unfortunately, in this study, stiff NPs were not tested in biodistribution studies.

Anselmo et al. demonstrated that the modulation of NPs elasticity offers a promising strategy for altering the circulation time, biodistribution, and cellular internalization of NPs (Anselmo, Zhang et al. 2015). For this reason, tuning the elasticity of NPs for a higher extent of cellular internalization could be better investigated as a valuable tool in biomedical applications such as cell targeting and/or drug delivery.

1.6 Hydrophobicity and hydrophilicity

Hydrophobicity/Hydrophilicity of NPs has a remarkable effect on NPs and their interaction with the cell membrane. Several studies have suggested that the surface hydrophobicity of NPs affects not only cell uptake, but also their opsonization and biodistribution (Sabourian, Yazdani et al. 2020). Hydrophobic NPs were included in the cell membrane, whereas hydrophilic NPs were found to adsorb onto the cell membrane and their selective uptake by specific cell types (Zhu, Nie et al. 2013, Kranz, Diken et al. 2016, Foroozandeh and Aziz 2018). Polyethylene glycol (PEG) is a highly hydrophilic molecule. The PEG and/or polysarcosine layer on the NPs creates a steric barrier surrounding the nanocarriers, which prevents NP opsonization and prolongs retention time in the body. PEG NPs show suitable physicochemical properties, excellent biocompatibility and enhanced serum stability. An increase in hydrophilicity leads to a decrease in particle uptake by MACs. The PEG chains hinder the binding of opsonins to the particles. Amphipathic polymers showed very similar effects as PEG. Their hydrophobic properties allow adsorption on the NP surface, while their hydrophilic part points toward the aqueous solution and hinders the adsorption of plasma proteins, leading to increased longevity of the NPs (Kettler, Veltman et al. 2014).

1.7 Protein corona

If the NP surface is not well stabilized, NPs can accumulate serum factors on their surface. Interactions between NPs and serum factor proteins are governed by the characteristics of the corona. The features of NPs, such as size, surface chemistry, and charge, are critical factors influencing the composition of the protein corona. “Protein corona” plays a crucial role in NP-cell interactions and cell uptake, since it changes the nature and chemistry of the NP surface. Cellular uptake of NPs can differ in the presence or absence of corona proteins (Francia, Yang et al. 2019). On one hand, the adsorbed proteins might affect the fate and biological activity of NPs, and the formed protein corona can mask their targeting functions, preventing them from reaching their intended goal (Shen, Tenzer et al. 2018, Kopac 2021). In contrast, NP-adsorbed serum factors may engage receptors expressed by non-target cells, resulting in unwanted uptake. An example of this was shown by Mortimer et al., where proteins adsorbed onto silica-based NPs altered their conformation, resulting in a recognition by class A scavenger receptors on MACs (Mortimer, Butcher et al. 2014). To limit unwanted binding, many strategies have been developed to minimize protein adsorption by functionalization of NP surfaces with various polymers such as dextran, polyvinylpyrrolidone,

and most prominently polyethylene glycol. Such a strategy can increase the circulating half-life of NPs, but modifications using hydrophilic stealth polymers can still interfere with the targeting functionalities (Kopac 2021). This strategy was also applied by Bednarczyk et al., who demonstrated that dextran-coated NPs may trigger the complement pathway, resulting in the activation of complement C3 fragments engaging polymorphonuclear neutrophils (Bednarczyk**, Medina-Montano et al. 2021)**. Serum shows different effects on particle uptake by phagocytes which can be explained by the type of proteins present in the medium, protein corona composition and particle opsonization. After the addition of serum, NP uptake by phagocytes has been reported to be indifferent, to increase or decrease, depending on the type of protein present. These contradictory effects can be explained, as mentioned before, by the presence of various proteins in the medium by a change in the protein corona composition over time because of protein abundance and affinity, and by NP opsonization (Kettler, Veltman et al. 2014).

2. Active and passive nano-vaccination

According to the World Health Organization (WHO), cancer is a generic term for a large group of diseases that can start in almost any organ or tissue of the body when cells mutation-dependently grow uncontrollably, go beyond their usual boundaries to invade adjoining parts of the body, and/or spread to other organs. The latter process is called metastasis and is a major cause of cancer-related death (WHO 2022). Cancer is a leading cause of death worldwide, accounting for nearly 10 million deaths in 2020 (Ferlay J 2020, Garcia-Fernandez, Saz et al. 2021). Accurate cancer diagnosis is essential for appropriate and effective treatment because every cancer type requires a specific treatment regimen. Treatment usually includes surgery, radiotherapy, and/or systemic therapies such as chemotherapy, hormonal treatments, and tumor vaccination (Riley, June et al. 2019, Cacicedo, **Medina-Montano et al. 2020**, Garcia-Fernandez, Saz et al. 2021). The last is a type of cancer treatment that supports the immune system to fight cancer. The immune system is essential for the body to fight infections and other diseases. It is composed of white blood cells, primary lymphoid organs as thymus and the bone marrow and secondary lymphoid organs including lymph nodes, the spleen, the tonsils and certain tissues of the lymph system (Yang 2015, Abbott and Ustoyev 2019).

2.1. Tumor vaccination

Cancer vaccines are composed of selected tumor antigens combined with adjuvants that activate DCs. Therapeutic cancer vaccines aim to stimulate the patient's adaptive immune system against specific tumor antigens to regain control over tumor growth, induce regression of established tumors, and eradicate residual cells. The basic principles needed for successful therapeutic vaccination against tumors include the delivery of large amounts of tumor-associated or -specific antigen to DCs, optimal DC activation, DC-induced stimulation of antigen-specific $CD4^+$ T helper cell and cytotoxic T lymphocytes (CTL), infiltration of the tumor immune microenvironment by CTL and CTL-mediated tumor cell killing (Garcia-Fernandez, Saz et al. 2021, Saxena, van der Burg et al. 2021). Research on cancer immunotherapy has made significant progress over the last 20 years. Cancer vaccines are considered a promising therapeutic strategy in the immunotherapy of solid tumors because they stimulate anti-tumor immunity against tumor antigens, which can be delivered in the form of whole cells, peptides, nucleic acids, etc., using NPs **(**Cacicedo, **Medina-Montano et al. 2020,** Bednarczyk**, Medina-Montano et al. 2021,** Mainini, De Santis et al. 2021). Thus, an

intelligent and precise NP formulation design needs to allow for selective delivery to the cell population or environment of interest, reduce side effects, increase the efficiency of the treatment, and temporally control immunomodulation (Mitchell, Billingsley et al. 2021). Ideal cancer nano-vaccines can overcome immune suppression in tumors and induce both humoral and cellular immunity (Liu, Fu et al. 2022). The number of NPs is increasing. A well example in which NPs is having a key role, is in the development of vaccines against different types of cancer. Thus, Fornaguera et al. proposed the encapsulation of mRNA in lipid and polymeric NPs to deliver mRNA encoding tumor antigens and/or adjuvants to DCs and thus activating the immune response (Fornaguera, Guerra-Rebollo et al. 2018). Also, Stickdorn et al. proposed the combination of a model antigen (ovalbumin) with an immune adjuvant (Imidazoquinoline-type TLR7/8 agonist) on the same nanocarrier system **(**Stickdorn, **Medina-Montano et al. 2022)**. This system could elicit antigen-specific T and B cell responses, prevented tumor growth in prophylactic tumor models and attenuated tumor growth in therapeutic studies in an antigen-specific manner.

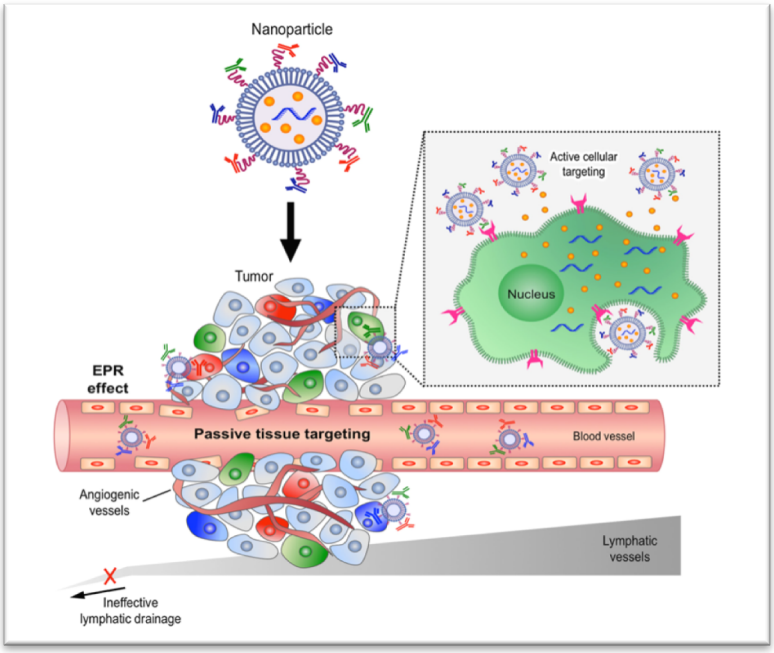

Figure 5: Passive and active tissue targeting (Pearce and O'Reilly 2019)

Passive tissue targeting is achieved by extravasation of NPs through increased permeability of the tumor vasculature and ineffective lymphatic drainage (enhanced permeability and retention: EPR effect). Active cellular targeting (inset) can be achieved by decorating the surface of NPs with multiple targeting moieties that promote cell-specific recognition and

binding. (Peer 2014). NPs can target in two ways: passive and active, respectively. Passive targeting allows for the efficient localization of NPs within the tumor microenvironment. Active targeting facilitates the uptake of NPs by tumor cells (Bazak, Houri et al. 2015, Pearce and O'Reilly 2019) Fig. 5.

2.2. Non-targeting NPs (Passive)

Non-targeting nanovaccines can enhance the intracellular concentration of drugs and other cargo in cancer cells while avoiding unwarranted toxicity towards healthy cells. Malignant tumors release angiogenic growth factor proteins that stimulate new blood vessels or confer rerouting of existing vessels to supply oxygen and nutrients (Carmeliet and Jain 2000). Tumor tissue is characterized by a highly disorganized vascular architecture, irregular blood flow, reduced lymphatic drainage, and vessel leakage. Because of reduced lymphatic drainage, the permeating nanocarriers are not removed efficiently and are thus retained in the tumor tissue (Maeda 2001). These features provide an enhanced permeability and retention (EPR) effect, which constitutes an important mechanism for passive targeting and selective accumulation of NP in the tumor and surrounding tissue (Yu, Park et al. 2012, Pearce and O'Reilly 2019). The work that is subject to this thesis focused on the importance of how non-targeting NP can interact with blood cells, the protein corona, MPS, and their recognition and activation through PRRs for an effective immune response.

2.2.1. Blood cells and protein-corona interaction with the non-targeting NPs

Systematically administered non-targeting NPs are often recognized by the innate immune system as potential pathogens (such as viruses and bacteria), and thereby trigger processes and mechanisms that protect the host organism against foreign agents (Digiacomo, Pozzi et al. 2020). Intravenously injected NPs interact with several blood components. NPs in the bloodstream could be engulfed by circulating blood cells, such as monocytes and PMNs. Additionally, serum proteins and other biomolecules within the bloodstream are adsorbed onto the NP surface. This protein adsorption leads to the formation of a protein corona, which is an energetically favorable biochemical process (Narum, Le et al. 2020). The protein corona represents a biological interface that mediates interactions between nanomaterials and the immune system (Digiacomo, Pozzi et al. 2020). The protein corona may significantly affect cellular interactions, leading to their non-specific uptake into healthy tissues (Nguyen and Lee 2017). Bednarczyk et al. showed that NPs coated with carbohydrates such as dextran

trigger the lectin complement pathway, resulting in the deposition of active complement C3 fragments. C3-opsonized dextran-coated NPs could engage blood neutrophils (polymorphonuclear granulocytes) via engagement of the complement receptor (CR)3 and also may address B cells (B-1, B-2) and follicular dendritic cells (fDC) via CR1/2 and conventional DCs (cDC) via CR3 (Shen, Tenzer et al. 2018, Bednarczyk, **Medina-Montano et al. 2021**). In addition, Kappel et al. used a type of linear, peptide-based NP, termed peptobrushes (PBs) that were functionalized with antibodies, showing that PBs with a higher antibody number display a more pronounced protein corona, and its constituents may engage various cellular receptors. Functionalization of PBs with high numbers of antibodies resulted in the formation of a protein corona, which may contribute to the observed off-target accumulation and does not depend on specific Fc or Fab recognition **(**Kappel, **Medina-Montano et al. 2021)**. As mentioned before, protein absorption can affect NP stability, promote NP disintegration, and compromise the delivery of cargo to the intended tissue (Nguyen and Lee 2017, Francia, Yang et al. 2019). To overcome these issues, for example, surface chemistry modifications, (such as PEGylation, polysarcosine-coating) are required to prevent serum protein absorption onto NP and to try to dismiss their non-specific uptake into healthy tissues (Shreffler, Pullan et al. 2019). Another approach to minimize non-specific clearance of NP is to coat them with a biomimetic coating consisting of cell membranes derived from erythrocytes or leukocytes in an effort to promote self-recognition of the NP construct (Jimenez-Jimenez, Manzano et al. 2020). This self-recognition strategy relies on interactions of antiphagocytic ligands; one of which is mediated through CD47–SIRPα (signal-regulatory protein alpha), to generate ‘don’t eat me’ signals (Chao, Weissman et al. 2012, Bros, Nuhn et al. 2018, Qu, Li et al. 2022).

2.2.2. Non-targeting NPs and their interaction with the MPS

The body itself has a large network of mononuclear phagocyte system (MPS) organs and immune cells that effectively remove foreign nanomaterials from the bloodstream (Narum, Le et al. 2020). These organs include the spleen (B cells, MAC, T cells, PMN), bone marrow (conventional dendritic cells Typ 1/2, plasmacytoid dendritic cells), the liver (containing immune cells known as NPCs: DCs, KC and LSEC) (Fig.6), and other organs with resident phagocytic MACs (Song, Petschauer et al. 2014). Biodistribution analyses have shown that the accumulation of NPs in MPS organs and cells is a universal phenomenon, which has been observed for different types of materials such as micelles, polymeric NPs, liposomes,

carbon nanotubes, quantum dots, and gold NPs (Narum, Le et al. 2020). This off-target NP accumulation in MPS organs is a significant challenge for the development and clinical translation of NPs because it impedes the efficient delivery of NPs to desired sites (Narum, Le et al. 2020). Thus, Kappel et al. performed comparative studies on the biodistribution of antibody-decorated NPs, mainly focusing on NP accumulation in distinct organs and on target cell type-specific binding. We used peptobrushes conjugated with distinct average numbers of antibodies (2, 6, and 12) targeting the surface receptor DEC205 (CD205), a type I cell surface protein predominantly expressed by DCs (Castenmiller, Keumatio-Doungtsop et al. 2021). Peptobrushes with low antibody numbers (2) exhibited only limited liver accumulation, whereas an intermediate antibody density (6) was sufficient to confer massive deposition of peptobrush-based NPs in the liver. At the cellular level, peptobrushes-antibody (6, 12) conjugates predominantly engaged NPCs, such as LSECs and MACs (Fig.2) **(**Kappel, **Medina-Montano et al. 2021).** Parallel studies, performed by Stickdorn et al., corroborated the interaction of other types of NPs, TLR7/8 agonist-conjugated nanogels, with immune cells belonging to the MPS **(**Stickdorn, **Medina-Montano et al. 2022)**. Murine splenocytes were used as heterogeneous primary immune cell populations and placed in contact with the nanogels, which showed nanogels uptake by various immune cell subsets, especially by B cells, MACs, DCs, and PMNs (Fig.2). In addition, in biodistribution studies, we showed that the majority of NPs were found in the liver, a typical non-specific sink for systemically administered NPs (Fig.3) **(**Stickdorn, **Medina-Montano et al. 2022).** Nonetheless, a significant amount was also detected in the spleen as a relevant lymphatic organ to induce antigen-specific immune responses (Zhao, Liu et al. 2015, Aliyu, Zohora et al. 2021). In addition, accumulation of NPs in the MPS may cause severe toxicity-related side effects, particularly in organs such as the liver and spleen (Bahadar, Maqbool et al. 2016). However, Stickdorn et al. demonstrated that systemic application of TLR7/8 agonist-conjugated nanogels in vivo can be safely administered so that these NPs yielded no toxicity-associated changes at the blood serum, organ, and tissue levels **(**Stickdorn, **Medina-Montano et al. 2022).**

2.3. Targeting NPs (Active)

2.3.1. mRNA NPs

Encapsulation of genetic material, such as mRNA, is gaining special attention for cancer immunotherapy (Garcia-Fernandez, Saz et al. 2021). Thus, Fornaguera et al. proposed the

use of lipid NPs to deliver mRNA in DCs, selectively introducing genetic material encoding tumor antigens and thus activating the immune response (Fornaguera, Guerra-Rebollo et al. 2018). Since 2020, with the beginning of the Corona pandemic, this type of NP has become more important in clinical studies, as described by Meyer et al. in their review. They also explained that the most successful materials used to mediate the successful intracellular delivery of mRNA are lipids. Lipid NPs, composed of at least three lipids with distinct chemical features, possess many material properties that are desirable for gene delivery. Such a formulation has been utilized in the mRNA-based COVID-19 vaccine (Walsh, Frenck et al. 2020, Schoenmaker, Witzigmann et al. 2021, Meyer, Neshat et al. 2022).

2.3.2. B cells-based NPs

Most nanovaccines are target-oriented to address DCs because of their ability to present the processed antigen on MHC complexes to T cells. In contrast, the initiation of an adaptive humoral immune response requires the encountering of protein antigens by B cells. In addition to the antigen in its natural conformation, B cells may also require signals from T helper cells (Zilker, Kozlova et al. 2017). For this reason, Zilker et al. reported the possibility of inducing a T-independent antibody response, not requiring help from $CD4^+$T cells, by using NP i) to efficiently reach draining lymph nodes and deliver the protein in its native conformation to the B-cell area and ii) to be efficiently taken up by DCs following activation of T-helper cells. In addition, the incorporation of TLR ligands (CpG, PolyI:C, R848, Flagellin) into the NPs may be a promising strategy to modulate signals by enhanced DC maturation and T-cell activation, and/or directly modulate antigen-specific immune responses in targeted B cells *in vivo* (Zilker, Kozlova et al. 2017).

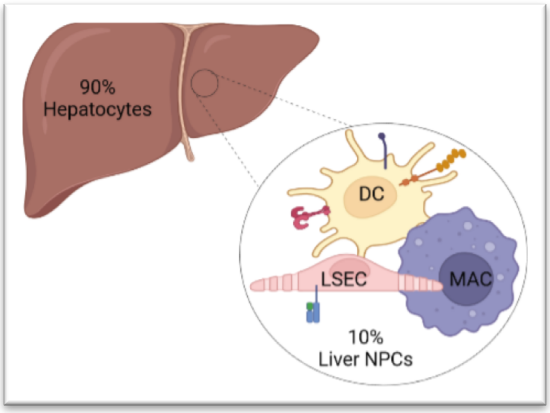

Figure 6: Liver non-parenchymal cells (Created by Biorender)

3. NPs mediated targeting for immunotherapy

One major challenge in nanomedicine is the selective delivery of NPs to desired tissues and cells. To overcome this issue, NPs can be functionalized with specific ligands to interact with target molecules or cells in a highly specific manner (Friedman, Claypool et al. 2013). The concept behind ligand-binding NPs is to enhance the selectivity and efficiency of interactions between NPs and their intended targets (Mitchell, Billingsley et al. 2021). This reduces off-target effects and enhances the therapeutic potential of the NPs (Yang, Zhai et al. 2022). This chapter illustrates several ligand-NP functionalization processes including small molecules, peptides, antibodies, and engineered proteins. The binding of NPs to different types of ligands for specific and nonspecific binding is explained below.

3.1. Specific binding (Receptor-mediated targeting)

Receptors on the surface of cells can specifically recognize certain targeting structures on the NP surface, leading to specific binding and uptake (Yu, Tai et al. 2010). Examples include:

3.1.1. Mannose receptors (MR)

MR also termed CD206, is a member of the C-type lectin family. MR (CD206) is the member of the MR family of proteins that in mammals also includes the urokinase-type plasminogen activator receptor-associated protein Endo180 (CD280), the M-Typ-Phospholipase A2-Rezeptor (M-type PLA2R), and DEC205 (CD205) (Martinez-Pomares 2012). Members of this family contain C-type lectin domains, which play an important function in ligand recognition to be recognized by NP. MR are primarily present on the surface of MAC, immature DCs and LSECs (van der Zande, Nitsche et al. 2021). Utilizing antigens targeting mannose receptors (MR) shows great promise for the development of novel immunotherapeutic treatments involving antigen presentation on antigen-presenting cells (APCs). In these instances, proteins or peptides capable of immune system activation are either encapsulated or conjugated with a moiety that facilitates binding and subsequent uptake through MR-mediated endocytosis in APCs to achieve effective immunization (Dalle Vedove, Costabile et al. 2018). C-type lectin receptors (CLRs) are attractive targets, as DC subsets are known to express different CLRs, which are involved in the recognition and capture of many glycosylated antigens (van Dinther, Stolk et al. 2017, da Costa and Freire 2022). For example, studies in animals targeting antigens to CLRs (Clec9a, DEC205) have shown effective generation of T cell responses. Targeting antigen to Clec9a in animal models

induced cellular and humoral immune responses, which is essential for effective vaccination (Sabado, Balan et al. 2017, Simon, Fichter et al. 2022).

3.1.2. Antibodies

Active targeting of NPs is widely used to improve their selectivity towards the cell or tissue of interest. For example, antibodies are commonly conjugated to NPs to promote selective targeting (Woythe, Madhikar et al. 2022). DC-focused targeting approaches include antibodies that are specific for CLRs or agonistic antibodies (e.g., anti-DEC205, anti-CD40, anti-Clec9a) that are conjugated with the antigen of interest (Matsuo, Yoshie et al. 2021). DEC205 is a C-type lectin receptor and its expression in mice is abundant on $CD8\alpha^{+}$DCs, which have a superior capacity for cross-presentation (Gutiérrez-Martínez, Planès et al. 2015). Although other receptors on DCs can also be targeted, DEC205 is the only CLR receptor observed on numerous DCs types within the T-cell areas of human lymphoid organs. Targeting the DEC205 receptor leads to efficient endocytosis of antigens into endocytic vesicles containing major histocompatibility complex (MHC) class II molecules. This results in antigen uptake and in case of sufficient DC stimulation induces T cell stimulation yielding profound anti-tumor antigen specific responses (Wang, Zaidi et al. 2012). DEC-205 has a fondness for apoptotic or necrotic cell particles and a liking for CpG oligos. In the realm of ODN binding, DEC-205 plays favorites—forming a robust connection with B class ODN, establishing a moderate bond with C class ODN, offering a minimal embrace to P class ODN, and maintaining a polite distance from A class ODN. It's quite the discerning receptor, navigating its interactions with a touch of selectivity (Li, Panetta et al. 2021). In this thesis, we concentrated on utilizing an antibody designed to target active dendritic cells through DEC205 (anti-DEC205). The pivotal steps of antigen recognition by dendritic cells, subsequent maturation, and activation of antigen-specific T effector cells are crucial for eliciting a robust adaptive immune response. The precise delivery of antigens and cargo to these cells is of significant importance in the design of NPs (von Roemeling, Jiang et al. 2017). DCs are the most potent APCs capable of inducing both effective and memory immune responses. DCs have a superior capacity to acquire and process antigens for presentation to T cells, and at activated state express high levels of costimulatory and coinhibitory molecules that determine immune activation versus anergy, respectively (Sabado, Balan et al. 2017, Hilligan and Ronchese 2020). Due to these properties, DCs are the primary aim of nano-vaccination approaches. However, current approaches in immunotherapy using DC-

based vaccination are mainly based on antigen loading on *in vitro*-generated DCs and activating them with TLR ligands and/or cytokine combinations (Matsuo, Yoshie et al. 2021). Accordingly, further experiments were performed by Kappel et al. to assess the efficiency of DC targeting via DEC205. We used antibody-conjugated peptobrushes with antibodies specific for DEC205. *In vitro* studies using bone marrow-derived DCs confirmed that peptobrush antibody-conjugates engaged DCs at comparable extent, irrespective of their antibody density. We found that peptobrushes coated with an average of 2-αDEC205 antibodies per brush primarily bound to cells in lymphatic organs via specific interactions between the αDEC205 antibody and the DEC205 receptor **(**Kappel, **Medina-Montano et al. 2021)**. In the spleen, DEC205^{+}DCs co-express CD8α^{+} (Bonifaz, Bonnyay et al. 2004). Thus, within the total DC population, CD8α^{+} but not CD8α^{-} DCs were specifically addressed by the αDEC205-coated NP *in vivo*. Notably, more than 8% of the CD8α^{+} DCs, compared to less than 1% of CD8α^{-} DCs, in the spleen contained detectable numbers of NP coated with an average of 2-αDEC205 antibodies per brush, thus proving a high efficacy and selectivity of DC targeting with antibody-decorated NP as presented in this work. Owed to the observed stealth-like nature of peptobrushes, we consider them an ideal platform for molecular vaccines. Therefore, these novel peptobrushes were selected for further modification with antibodies for DC targeting (aDEC-205 specific antibodies), antigens (ovalbumin), and immune activators (CpG). Preliminary *in vitro* T cell proliferation assays showed that peptobrushes alone induced efficient immune responses and indicated differences due to their size and shape. After subcutaneous injection of OVA-coupled peptobrush, conjugates were found in the draining lymph nodes and spleen, yielding OT-I and OT-II T cell proliferation, indicating T cell immunity. These peptobrushes inhibited tumor growth and induced tumor regression in a B16-melanoma model (**Seidl, Medina-Montano et al. in preparation)**.

3.1.3. Toll-like receptors (TLR) ligands

Pattern recognition receptors (PRRs) are proteins of immune cells, notably in myeloid cells (MACs, DCs, and granulocytes), as well as in lymphocytic cells, such as T and B cells, which are able to recognize Pathogen-Associated Molecular Patterns (PAMPs) often found in pathogens (Shekarian, Valsesia-Wittmann et al. 2017). PAMPs thereby strongly stimulate immune cells via the activation of PRRs, and the triggered intracellular pathways result in proinflammatory responses (Li and Wu 2021). NP-based immune activation can be achieved

using adjuvants. Adjuvants trigger the stimulatory capacity of PRRs. The most widely introduced TLR immunoadjuvants for DC stimulation and maturation include lipopolysaccharides (LPS, TLR4), CpG oligonucleotides (ssDNA, TLR9), imiquimod (R837 and resiquimod (R848) (both are TLR-7/8 agonists), and poly (I:C) (dsRNA, TLR3) (Banstola, Jeong et al. 2020, Owen, Fults et al. 2021). These immunoadjuvants are a good strategy to modulate the immune system and can be used in nanovaccines (Coffman, Sher et al. 2010, Abbasi and Uchida 2021). For example, NP systems, such as lipid NPs, employ the double-stranded RNA poly(I:C), which is capable of activating both endosomal (TLR3) and cytosolic receptors (STING) and is one of the strongest type I Interferon (IFN) inducers, elevating both humoral- and cell-mediated responses to specific antigens (Hafner, Corthésy et al. 2013).

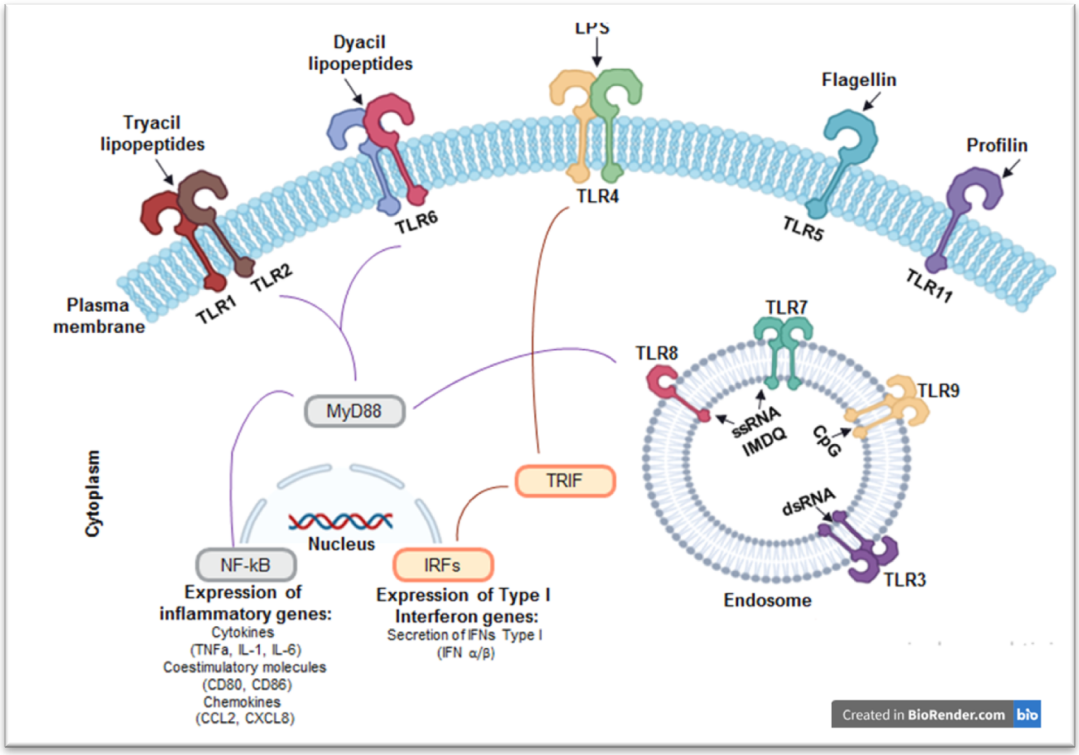

Figure 7: Overview of the important PRR subfamily of Toll-like receptors (TLRs) and their respective ligands/agonists**.**

Stimulation of PRRs by pathogen-associated molecular patterns (PAMPs) or damage-associated molecular patterns (DAMPs) results in type I IFN expression in target cells and the release of proinflammatory cytokines.

Unfortunately, TLR ligands that contain nucleic acid derivatives are susceptible to degradation by nucleases, rendering it difficult to target specific cell populations or tissues within the body with these agents (Zhu, Zhu et al. 2022). For successful application, it is also necessary to avoid systemic distribution of free adjuvants. This concept has been explored

further by Nuhn and colleagues working with imidazoquinolines, which are analogs of DNA/RNA oligonucleotides (Nuhn, De Koker et al. 2018). Imiquimod and its analog IMDQ are among the best-established TLR7/8 ligands. These agonists stimulate DCs and MACs to produce cytokines like IFN-α, IL-6, IL-8, and IL-12, which resulted in the induction of Th1 cell-mediated immunity (Huang, Ge et al. 2022, **Medina-Montano**, Cacicedo et al. 2022). To avoid systemic degradation of IMDQ NP, Nuhn and colleagues introduced polymerizable squaric ester amides as novel functionable tools to fabricate pH-responsive nanogels, serving as a versatile nanocarrier platform for delivery of the highly potent immunomodulator IMDQ after intravenous administration (Huppertsberg, **Medina-Montano et al. 2021**). Stickdorn et al. could also develop a nanogel platform as an antitumor vaccine that proved safe for intravenous application and could elicit robust immune responses *in vitro and in vivo.* The underlying chemical design allowed for covalent attachment of a model antigen (ovalbumin) and an adjuvant (Imidazoloquinoline-type TLR7/8 agonist) onto the same nanocarrier system. This NP platform elicited antigen-specific T and B cell responses that outperformed mixtures of the individual components. These nanovaccines yielded an antigen-specific growth reduction of different tumors expressing ovalbumin intracellularly or on their surface in prophylactic and therapeutic tumor studies **(**Stickdorn**, Medina-Montano et al. 2022).** These pH-degradable nanogels are promising platforms for the intravenous administration of small-molecule TLR7/8 agonists, and thus offer the opportunity to explore their adjuvant potency for systemic vaccination or cancer immunotherapy **(**Huppertsberg**, Medina-Montano et al. 2021,** Stickdorn, **Medina-Montano et al. 2022).** Despite the promising results of the pH-degradable nanogel platforms mentioned above, these have some disadvantages, as a large fraction of particles does not reach the desired target, and the NPs remain intact and accumulate at undesired sites such as the liver, lungs or kidneys (Baetke, Lammers et al. 2015). For this reason, new chemically modified NPs continue to be tested, but all of them have the same purpose: to enhance the pharmacokinetics of immunostimulatory drugs and to guarantee their delivery into APCs. This approach was also investigated by Nuhn et al., and aliphatic polycarbonates were shown to be promising due to their degradability and biocompatibility **(**Czysch, **Medina-Montano et al. 2022**). Using again the immunoadjuvant IMDQ as a TLR7/8 agonist, this NP formulation triggered localized activation of APCs. They focused on the delivery of NPs to the lymph nodes, to favor a transient immune stimulation behavior and initiating a spatially controlled maturation of APCs (Czysch**, Medina-Montano et al. 2022)**.

As an alternative to imidazoquinolines and imiquimod, synthetic thiazoloquinolone immunostimulatory agonist-containing NPs were tested (compound CL075) **(**Czysch, **Medina-Montano et al. 2022**). These NPs are based on core-cross-linked block copolymers by encapsulation of the Toll-like receptor 7/8 (TLR7/8) agonist CL075. These immunostimulatory polymeric micelles are internalized by various DCs and promote their maturation (Spranger, Javotovic et al. 2009, Dowling, Scott et al. 2017, Czysch, **Medina-Montano et al. 2022**).

In summary, the aim of this interdisciplinary project was to evaluate the efficacy of different types of functionalized NPs for vaccination to generate an immune response. The different NPs that have been provided by the collaboration partners are listed in Table 1.

3.2. Recognition of NPs via phagocytic receptors

Phagocytosis is a cellular process by which cells internalize solid particles such as bacteria, cell debris, and NPs. Various types of cells, including immune cells, such as MACs and DCs, are capable of phagocytosis (Foroozandeh and Aziz 2018). This process is mediated by specific receptors that recognize and bind to particles, triggering cellular engulfment. For NPs, the specific receptors involved in their phagocytosis can vary depending on the type of cells and the characteristics of the NPs themselves (Behzadi, Serpooshan et al. 2017). Some of the known phagocytic receptors involved in NP-mediated cellular uptake are as follows:

3.2.1. Fc receptors

Fc Receptors are a class of cell-surface molecules that bind to the Fc region of antibodies and facilitate efficient antibody–antigen interactions. Fc receptors are found on the surface of various immune cells including MACs, DCs and natural killer cells (Junker, Gordon et al. 2020). Receptors of the Fc region of IgGs are FcγRs and are involved in immune responses such as cell activation and inhibition, phagocytosis, antibody-dependent cell-mediated toxicity (ADCC), cytokine release, and B cell proliferation. The FcγRs are divided into three classes: FcγRI (CD64), FcγRII (CD32), and FcγRIII (CD16) (Kim, Galloway et al. 2014). The Fc region of the antibodies, which is found at the tail end of the Y-shaped antibody structure, is recognized by Fc receptors. The Fc region is accessible for interaction with Fc receptors on the immune cells (Chan, Ong et al. 2015). The binding of NPs to Fc receptors can activate immune cells, leading to the release of cytokines and other signaling molecules that

coordinate immune responses. This activation can influence the adaptive immune system by recruiting other immune cells to the NP exposure sites (Liu, Hardie et al. 2017). Researchers have also explored the use of NPs conjugated with specific antibodies to target specific cells or tissues. By exploiting the interaction between antibodies on NPs and Fc receptors on immune cells, they aimed to enhance the delivery of therapeutic agents to specific locations (Friedman, Claypool et al. 2013, Mitchell, Billingsley et al. 2021). It is important to note that the recognition of NPs through Fc receptors is highly context-dependent and can vary based on factors such as the type of NPs, type of antibodies used, specific Fc receptor subtype involved, and the immune cell population present (Gustafson, Holt-Casper et al. 2015). As in the case of MACs and DCs that express Fc receptors can engulf and process NPs that are opsonized with antibodies (Panico, Capolla et al. 2022).

3.2.2. Complement receptors

The complement system is a complex cascade of proteins that plays a critical role in immune defense, inflammation, and the clearance of pathogens and foreign particles, including NPs (Ostrycharz and Hukowska-Szematowicz 2022). Complement receptors are key components of the innate immune response and are responsible for binding complement fragments that opsonize non-self surfaces (Rus, Cudrici et al. 2005). When NPs are exposed to complement receptors, several processes can occur. One of them, NPs opsonized by complement factors can bind to complement receptors on MACs, DCs, B cells and LSECs leading to engulfment (Shen, Tenzer et al. 2018, Bednarczyk, **Medina-Montano et al. 2021**, Kappel, **Medina-Montano et al. 2021**). NP-mediated complement activation depends on the physicochemical properties of NPs, including their surface chemistry, charge, size, and shape (Ilinskaya, Shah et al. 2019). Depending on their composition, NPs may induce complement activation through classical, mannose-binding lectin, or alternative pathways. Complement activation triggered by NPs results in both the liberation of proinflammatory mediators, such as anaphylatoxins, and the opsonization of NPs with C3b, which interacts with phagocytes. Anaphylatoxins (C3a, C4a, and C5a) stimulate the release of additional inflammatory mediators (e.g., histamine) by immune cells (La-Beck, Islam et al. 2020). Surface modifications of NPs with polyethylene glycol (“PEGylation”) can cause significant differences in the degree of complement activation as used to reduce protein adsorption and complement/phagocytic activity, resulting in improve stability in plasma, and prolong circulation time of several NPs, which are all important for effective targeting (Gustafson, Holt-Casper et al. 2015).

3.2.3. Scavenger receptors

Scavenger receptors (ScRs) are primarily expressed by MACs, DCs and other cells such as KCs and high endothelial venules (Alquraini and El Khoury 2020). This group of receptors is classified into three types based on their structure: Class A, Class B, and Class C. The ligand specificity of ScRs, varies based on their types. ScRs are a diverse group involved in recognizing and clearing various molecules, often playing a role in immune response and homeostasis. For example: Class A ScRs often have affinity for modified lipoproteins, Class B ScRs might interact with oxidized low-density lipoproteins, Class C ScRs could be involved in pathogen recognition (Mukhopadhyay and Gordon 2004, Cheng, Zheng et al. 2021). To date, research has identified the roles of Class A and Class B ScRs in the removal and cellular responses to NPs (Shannahan, Bai et al. 2015). ScRs have broad ligand specificity and can recognize various ligands, including modified lipids and carbohydrates, present on the surface of NP (Yu, Guo et al. 2015). Previous studies have shown that oligonucleotides on the NPs lead to the adsorption of serum proteins and facilitate cellular uptake. Patel et al. showed that serum proteins generally inhibit cellular uptake of DNA-Au NPs (Patel, Giljohann et al. 2010). Biochemical analyses indicated that these NPs were taken up by a process involving receptor-mediated endocytosis, primarily mediated by ScRs. NPs functionalized with siRNA have been shown to enter through the same pathway (Refsnes, Skuland et al. 2021). Thus, ScRs are required for cellular uptake of polyvalent oligonucleotide functionalized NPs (Patel, Giljohann et al. 2010). Other studies have shown that NPs combined with dextran sulfate can target class A scavenger receptors (SR-A) for the diagnosis and treatment of atherosclerotic vulnerable plaques (Ye, Zhou et al. 2019).

4. NPs and their role in the liver

The liver is a solid organ comprising mainly hepatocytes and less abundant cells known as liver non-parenchymal cells (NPCs) (Fig.6). Briefly, liver NPCs include Kupffer cells (KCs, 20%), dendritic cells (DCs, 25%), liver sinusoidal endothelial cells (LSECs, approximately 50% of NPCs), stellate cells, and other cell types (Sun, Kang et al. 2021, **Medina-Montano**, Cacicedo et al. 2022).

4.1. The liver as a NP-binding organ for NP-mediated induction of immune responses

It is known that when blood enters liver sinusoids, its fluid velocity decreases compared with blood velocities in arteries and veins in systemic circulation (approx. 1000-fold). Reduction in blood velocity within the liver sinusoid is responsible for increased NP uptake by phagocytic cells. NPs that escape blood clearance pass through the liver, return to the systemic circulation and may return to the liver. This process can be repeated until the NP clearance from the bloodstream is complete. It functions as a closed circuit (Tsoi, MacParland et al. 2016). During this process, liver immune cells, such as KCs, recognize opsonins within the NP protein corona via ScRs. This molecular recognition may lead to liver accumulation of opsonized NPs as a result of phagocytic cell uptake (Wang, Wu et al. 2012, Narum, Le et al. 2020). As shown in our experiments, liver KCs, DCs, and LSECs bound complement-opsonized NPs to an increased extent. However, similar results have been obtained using serum devoid of complement activity, suggesting the involvement of other receptors (Bednarczyk, **Medina-Montano et al. 2021**). DCs process pathogen-derived antigens and present them to T cells as a necessary step to induce antigen-specific T cell responses for the induction of immunity or tolerance (Fucikova, Palova-Jelinkova et al. 2019). Therefore, to understand this NP-cell interaction, we designed NPs to target DCs and minimize unwanted binding/uptake in other liver immune cells. For this purpose, we chose a specific surface receptor in DCs, DEC205 using antibody-conjugated NPs with 2, 6, and 12 antibodies per peptobrush. We observed that NP antibody conjugates were trapped in the liver, and that the extent of liver accumulation strongly increased with the number of attached antibodies (Kappel, **Medina-Montano et al. 2021**). Most studies have focused on KCs because they have been described as the main NP-binding cell population in the liver. They can internalize NPs through different mechanisms, including macropinocytosis and clathrin- and caveolin-mediated endocytosis (Cacicedo, **Medina-Montano et al. 2020**). As previously described,

there are two cell type targeting strategies: passive and active targeting. KCs can be targeted using both of these strategies. Using these strategies and the plasticity properties of KCs, these cells can be repolarized into classically activated (M1) and alternatively activated (M2) MACs (Wang, Ma et al. 2021). The classification into M1/M2 MACs describes the two major and opposing activities of MACs. M1 activity inhibits cell proliferation and causes tissue damage while M2 activity promotes cell proliferation and tissue repair (Mills 2012). It has been shown that regulatory MACs (M2 type) exhibit more than 40% higher NP uptake than proinflammatory MACs (M1 type) (Hoppstadter, Seif et al. 2015). Based on this fact, therapeutic strategies are being followed to induce a shift between the pro-inflammatory and tolerogenic phenotypes. This effect has also been reported using nanostructured lipid carriers (NLC) that induce the release of TNF-α and IL-6. Thus, the ability of NPs to reprogram hepatic KCs has been demonstrated (Cacicedo**, Medina-Montano et al. 2020, Medina-Montano,** Rivero Berti et al. 2022)**.** However, the contribution of LSECs in this regard (targeting and NP uptake) remains to be elucidated. Targeted drug delivery to LSECs using NPs necessitates precise interaction with specific endocytic surface receptors, such as CD206, which are prominently present in this particular cell type. It is worth noting that CD206 is also found in KCs, MACs, and conventional DCs in various locations in the body. In contrast to this, the C-type lectin receptor (CLR) known as L-SIGN has been documented as being selectively expressed solely on LSECs (Knolle and Wohlleber 2016, Cacicedo, **Medina-Montano et al. 2020**). Surprisingly, in our study, LSECs exerted a stronger NP antibody-conjugate binding capacity than KCs and DCs (Kappel, **Medina-Montano et al. 2021**). LSECs internalize NPs mostly via FcγRIIB (Mousavi, Sporstøl et al. 2007). They express FcR and have been reported to facilitate the uptake of IgG immune complexes via FcγRIIB (Ganesan, Kim et al. 2012). To elucidate the importance of FcR for LSEC-mediated NP uptake, Kappel et al. performed experiments in which FcγRIIB was blocked. The findings revealed that systemic blockade of Fc receptors reduced the accumulation of NP antibody-conjugates in the liver and abrogated the binding of applied NP antibody-conjugates to LSECs, indicating that FcγRIIB is responsible for binding of NP antibody-conjugates (Kappel, **Medina-Montano et al. 2021**).

4.2. Liver inflammation

Due to its pivotal role in lipid and glucose metabolism, liver inflammation holds a significant connection with metabolic disorders like non-alcoholic fatty liver disease (NAFLD), a

condition impacting as much as 40% of adults in Western societies (Koyama and Brenner 2017). NAFLD encompasses a range of conditions extending from hepatic steatosis alone to non-alcoholic steatohepatitis (NASH), an advancing stage marked by inflammation, cellular damage, and fibrosis. NASH is closely linked to factors such as obesity, type 2 diabetes, hyperlipidemia, and insulin resistance, and its progression can lead to cirrhosis (Benedict and Zhang 2017, Godoy-Matos, Silva Junior et al. 2020). During liver inflammation, NPCs interact with hepatocytes, and the extracellular matrix to coordinate immune responses and tissue repair (Cheng, Yang et al. 2021). Dysregulation of these interactions can lead to chronic inflammation, fibrosis, and ultimately liver dysfunction (Koyama and Brenner 2017). Understanding the roles of non-parenchymal cells in liver inflammation is important for developing strategies, such as using NPs to manage liver diseases.

Dexamethasone (DXM) is a potent corticosteroid medication widely used for its anti-inflammatory and immunosuppressive properties (Noreen, Maqbool et al. 2021). In the context of liver inflammation, DXM can play a crucial role in mitigating the inflammatory response. It functions by suppressing the immune system's activity and reducing the release of pro-inflammatory molecules, such as cytokines and chemokines. This can help alleviate the symptoms of liver inflammation and potentially prevent further damage to the liver tissue (Li, Jiang et al. 2021). DXM's ability to modulate the immune response makes it valuable in treating various liver conditions characterized by inflammation, such as hepatitis, autoimmune liver diseases, and certain cases of drug-induced liver injury (Ye, Li et al. 2022). It's important to note that while DXM can be effective in reducing inflammation, it also has potential side effects, especially with prolonged use or at high doses (Noreen, Maqbool et al. 2021). In this work, we examined DXM-loaded nanostructured lipid carriers (DXM-NLCs). NLCs were internalized by the NPCs in a dose-dependent manner. NLCs -alone- have intrinsic tolerance-inducing properties. DXM released from NLCs showed pharmacological activity, as evidenced by the decreased levels of inflammatory cytokines (IL-6 and TNF-α) in LPS-stimulated NPCs. Another indication of anti-inflammatory effects is that both soluble DXM and NLCs-DXM decreased the levels of the activation marker CD86 in stimulated LSECs and DCs (Cacicedo, **Medina-Montano et al. 2020**, **Medina-Montano**, Rivero Berti et al. 2022). In addition to DXM-NLCs, there are strategies that directly introduce antigens into tolerogenic environments in the liver, where antigen presentation promotes tolerance to self-or foreign antigens. LSECs play an important role in this process (Dou, Ono et al. 2018, Zheng and Tian 2019). Liu et al. used PLGA-OVA NPs decorated with ligands for specialized

targets to tolerogenic LSECs, which are capable of generating regulatory T-cells (Tregs) (Liu, Liu et al. 2022). OVA NPs induce the differentiation of Foxp3+ Treg cells, together with abundant TGF-β, IL-4, and IL-10 production and suppression of anti-OVA IgE responses (Liu, Wang et al. 2021, Liu, Liu et al. 2022).

In summary, this study utilizing DXM-NLCs provides valuable insights into the potential of NP-based therapies of liver inflammation. The use of NLCs to encapsulate and deliver DXM shows that nanotechnology can contribute to improving the specificity and efficacy of anti-inflammatory interventions while minimizing side effects. Further studies and clinical trials could help to validate and translate these findings into clinical practice, offering new avenues for treating liver inflammatory disorders.

5. Material and methods

5.1. Antibodies

Cell population	Cell type	Target protein	Fluorochrome	Antibody clone
Spleen cells	T cell	CD3	V500	500A2
	cytotoxic T cell	CD8a	PE	53-6.7
	myeloid cell	CD11b	SB600	M1/70
	DC	CD11c	BV421	N418
	B cell	CD19	SB702, AF488	1D3
	PMN	Ly6G	eFl610	1AB
	NK cell	NK1.1	PE-Cy7	PK136
Liver NPCs	leukocyte	CD45	BV711	30-F11
	MAC	F4/80	eFl506, eFluor450	BM8
	EC	CD31	PE	390
	LSEC	CD146	APC	ME9FI
	LSEC	CD32b	APC, PE	AT130-2
	DC	CD11c	BV421, PE-Cy7	N418
BMDC GM-CSF	DC	CD11c	PE-Cy7, BV421	N418
BMDC FTL3	DC	CD11c	PE-Cy7, BV421	N418
	cDC2	CD11b	SB600	M1/70
	pDC	B220/CD45R	V500	RA3-6B2
	cDC1	XCR1	BV421, AF467	ZET
Miscellaneous				
Activation		CD80	PE, PerCP-eFl780	16-10A1
		CD86	FITC	GL1
		MHCII	PE-eFl610, eFl450	2G9
		CD40	PE	1C10
Fc Block		CD16/32	na	2.4G2
Live/Dead		Fixable Viability Dye	eFl450, eFl781	na
		Annexin V	AF647	na
		Sytox	na	na
		7AAD	na	na

na: not applied

Table 2: Overview of the different antibodies dealt with in this thesis.

5.2. Isolation and culture of immune cells

BMDC (Bone marrow-derived dendritic cells) culture

Bone marrow (BM) cells were isolated from femurs and tibiae of C57BL/6 mice, and were resuspended in IMDM medium containing 5% FBS, 2 mM L-glutamine, 100 IU/ml penicillin, 100 µg/ml streptomycin and 50 µM β-Mercaptoethanol (all reagents from Sigma-Aldrich, Deisenhofen, Germany), termed test media in the following, and supplemented with 10 ng/ml recombinant murine GM-CSF (R&D Systems, Wiesbaden, Germany). BM cells were seeded in 12 well suspension cell culture cluster plates ($2x10^5$/ml). On day 3 and day 6, respectively, culture media were replenished. On days 7-8, the different NP formulations were applied to the differentiated cells. On the following day, samples were harvested and were subjected to flow cytometric analysis. All experiments were performed at least in triplicates. For BMDCs-FLT3L (Bone marrow-derived dendritic cells – recombinant FMS-related tyrosine kinase 3 ligand) culture, a similar procedure was followed with a modification. The BM cells were resuspended in IMDM-based culture medium supplemented with 250ng/ml FLT3 ligand (FLT3L) from BioLegend WSan Diego, USA). Cells were seeded in 12-well suspension cell culture cluster plates at a concentration of 10^6 cells/ml and incubated for one week before being treated with various compounds. The harvested samples were subjected to flow cytometric analysis on the following day, and the experiments were performed in triplicate. Notably, in some experiments, FLT3L was used instead of GM-CSF.

Spleen cells culture

Spleens were mashed using a sterile syringe plunger on a 40 µm cell strainer (EASYstrainer™; Sarstedt, Nümbrecht, Germany) pre-soaked with PBS. Mashed spleen tissue was washed through the strainer using 10 mL of PBS/2 mM EDTA buffer, and cells were pelleted by centrifugation (1,200 rpm, 10 min, 4 °C). Lysis buffer was added, and cells were pelleted again by centrifugation (1,200 rpm, 10 min, 4 °C). Cells were resuspended in test media and subjected to experiments.

Enrichment of liver non-parenchymal cells (NPCs)

In some experiments, Liver NPCs of female C57/Bl6 and BALB/c mice were isolated by liver perfusion: (Fig.8, left panel). In short, mice were anesthetized with a Ketamine/Xylazine

mixture (Ketamine 120 mg/Kg; Xylasin 16 mg/kg) and the abdominal cavity was opened. See Figure 8, left panel (**Medina-Montano**, Cacicedo et al. 2022). The vena portae was cannulated and flushed with 20 mL of HBSS (Hank's Balanced Salt Solution; ThermoFisher, Waltham, MA, USA) containing 100 U/mL of collagenase A (Sigma-Aldrich, St. Louis, MO, USA) and 10 µg/mL of DNase I (Sigma-Aldrich, St. Louis, MO, USA). Then, the liver was retrieved, cut into pieces, and incubated for 15 min at 37 °C in a 50 mL tube with PBS containing 100 U/mL of collagenase A and 10 µg/mL of DNase I. Afterwards, the liver tissue was mashed through a 70 µm nylon cell strainer and medium (DMEM (Dulbecco's Modified Eagle Medium)/F-12 GlutaMAX™, ThermoFisher Scientific) was applied. The cell suspension was subjected to density centrifugation using 30% Histodenz- HBSS (both from Sigma-Aldrich, St. Louis, MO, USA) as described. The obtained liver NPCs were then either cultured in medium (DMEM/ F-12, GlutaMAX, ThermoFisher Scientific) or subjected to antibody staining for subsequent flow cytometry analysis. Alternatively, NPCs were enriched by liver dissociation. For this, mice were killed by cervical dislocation and the liver was retrieved. See Fig.8, right panel (**Medina-Montano**, Cacicedo et al. 2022). An enzyme-dependent dissociation mixture of proprietary composition (Liver dissociation kit; Miltenyi Biotec, Bergisch-Gladbach, Germany) was preincubated for 15 min in C tubes (Miltenyi Biotec). Then, liver tissues were cut into little pieces and transferred into the prepared C tubes. The latter were placed into a gentleMACS Dissociator and the tissue was minced (two times program *m_liver _03*). Afterwards, the cell suspension was incubated for 30 min at 37 °C under continuous shaking, followed by another round of gentleMACS-mediated disintegration (two times program *m_liver_04*). The samples were cleared using a Cell Strainer (100µm; Sarstedt). Erythrocytes were lysed using a hypotonic buffer. Then, the liver NPCs were enriched by density centrifugation as described above. Following density centrifugation, NPCs were counted using Trypan blue. Cells were rinsed on ice and transferred to flow cytometry tubes for staining.

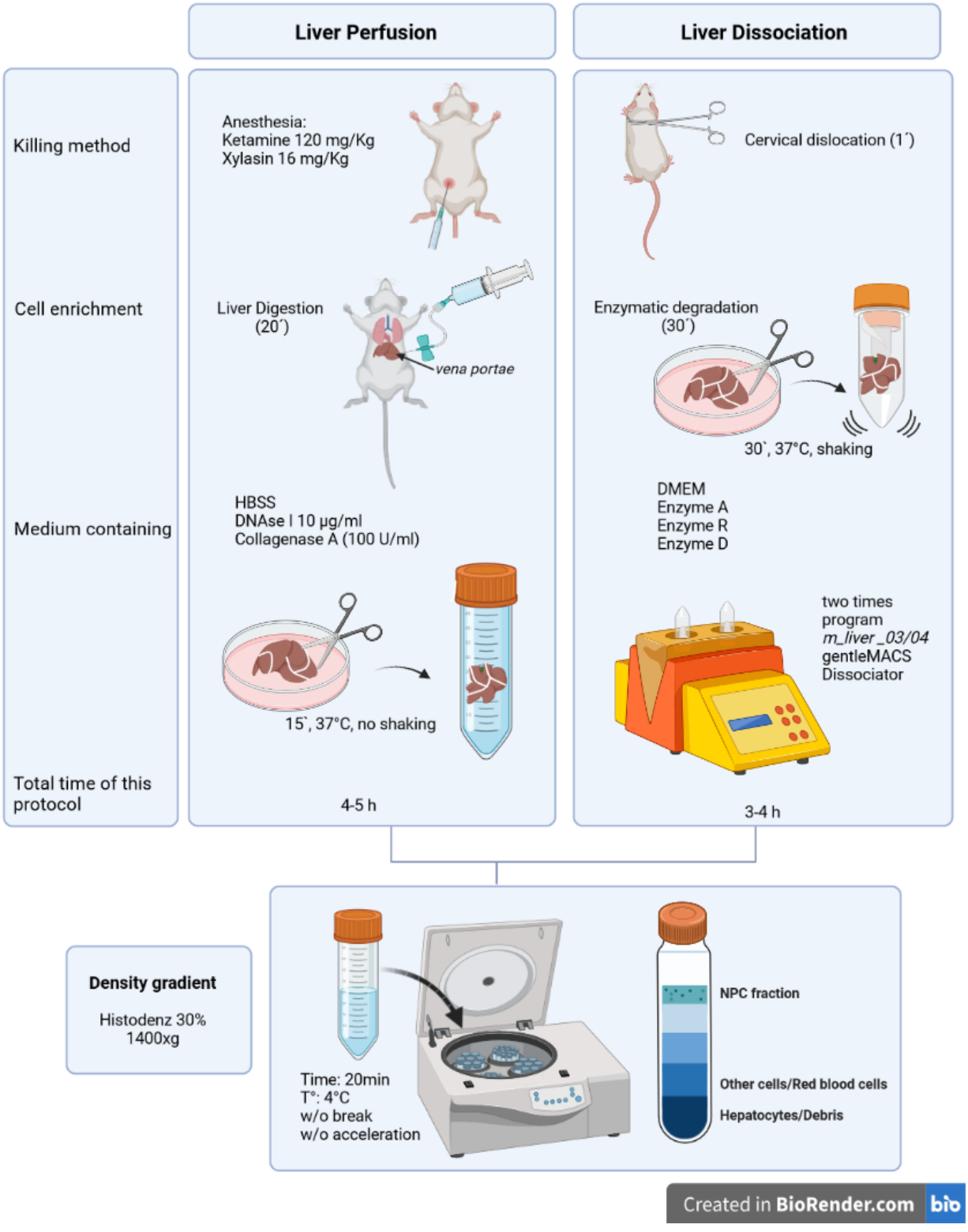

Figure 8: Schema of liver non-parenchymal cell (NPC) enrichment by liver perfusion (LP) and liver dissociation (LD) (**Medina-Montano**, Cacicedo et al. 2022).

RAW-Blue™ cell culture:

RAW-Blue™ cells were cultured in DMEM supplemented with 10% fetal bovine serum, 2 mM L-glutamine, 1 mM sodium pyruvate, and 0.01% Zeocin (200 µg/ml) at 37 °C with 5% CO_2 saturation.

5.3. Biological evaluation of NPs *in vitro*

NP Binding Studies

Aliquots of the different NPs were pre-incubated in parallel with equal volumes of native or heat-inactivated mouse serum for 1 h at 37 °C in low protein binding 0.5mL reaction tubes (Greiner Bio-One). Afterwards, untreated and differentially pretreated NPs were applied at different concentrations (evaluated in corresponding pre-experiments) to BMDC differentiated in 12-well cell cluster plates and to spleen cells and liver NPCs kept in sterile FACS tubes (each $2x10^6$/500 µL), respectively. Three hours after the onset of incubation, samples were harvested and subjected to flow cytometric analysis. In some cases, cells were incubated over-night with LPS (100 ng/mL; Sigma-Aldrich). Supernatant was stored for CBA assays at -20°C. Samples were harvested and subjected to flow cytometric analysis

Flow cytometry

After incubation, cells were harvested and transferred to FACS tubes. Samples were incubated with a rat anti-mouse CD16/CD32 antibody (15 min, 4 °C) to prevent Fc-mediated binding of subsequently applied antibodies (clone 2.4G2; 15 min, room temperature). Afterward, samples were incubated (20 min, 4 °C) with distinct sets of fluorescence-labeled antibodies as indicated in Table 2. Samples left untreated, incubated with the according formulations alone or with either antibody alone served as controls. Subsequently, samples were incubated with FVD as recommended by the manufacturer to delineate dead cells. Antibodies were purchased from BD Biosciences, Thermo Fisher or BioLegend. FVD was obtained from Thermo Fisher. After incubation with FVD, samples were fixed (4 % paraformaldehyde, 2mM EDTA) and analyzed in an Attune NxT flow cytometer (Thermo Fisher). The resulting data were processed by Attune Nxt Software v3.1.1. following the gating strategy (Fig. 9, 10, 11, 12).

Gating strategy of spleen cells

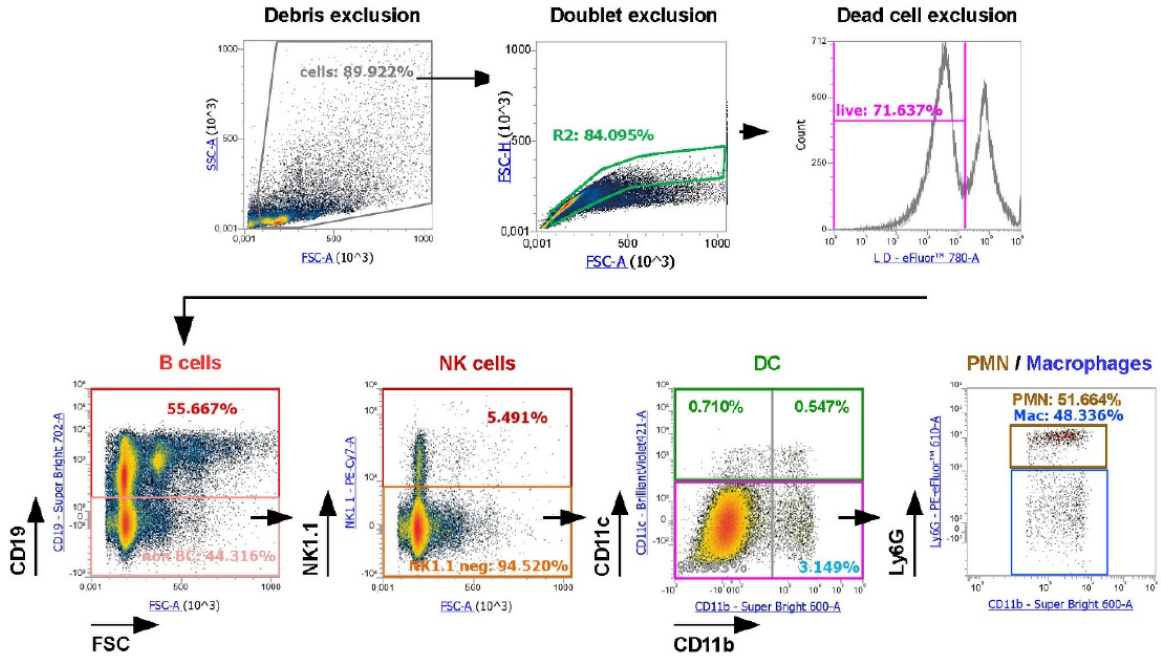

Figure 9: Gating strategy of spleen cells

After exclusion of debris, doublets and dead cells, spleen cell populations were identified sequentially according to lineage marker expression, B cells (CD19+), NK cells (CD19-NK1.1+), DCs (CD19-NK1.1-CD11c+), PMNs (CD19-NK1.1-CD11c-CD11b+Ly6G+) and MACs (CD19-NK1.1-CD11c-CD11b+Ly6G-).

Gating strategy of liver NPCs

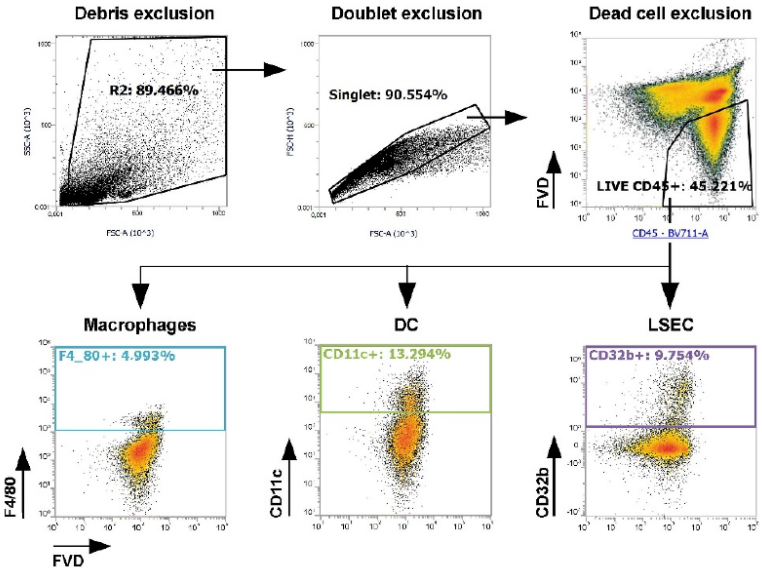

Figure 10: Gating strategy of liver NPCs

After exclusion of debris, doublets and dead cells (fixable viability dye [FVD]-), CD45+ cells were differentiated according to expression of F4/80 (MACs), CD11c (DCs), and CD32b (LSECs).

Gating strategy of BMDCs differentiated using GM-CSF

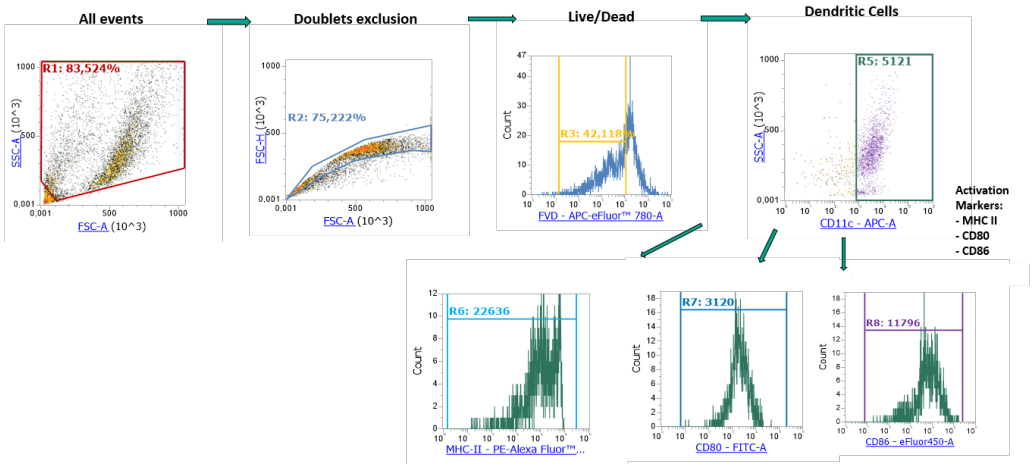

Figure 11: Gating strategy of BMDCs-GM CSF

After exclusion of debris, doublets and dead cells (fixable viability dye [FVD]-), CD11c+ cells were characterized. From this population also different activation markers as MHC-II, CD80 and CD86 could be measured.

Gating strategy of BMDCs differentiated using FLT3L

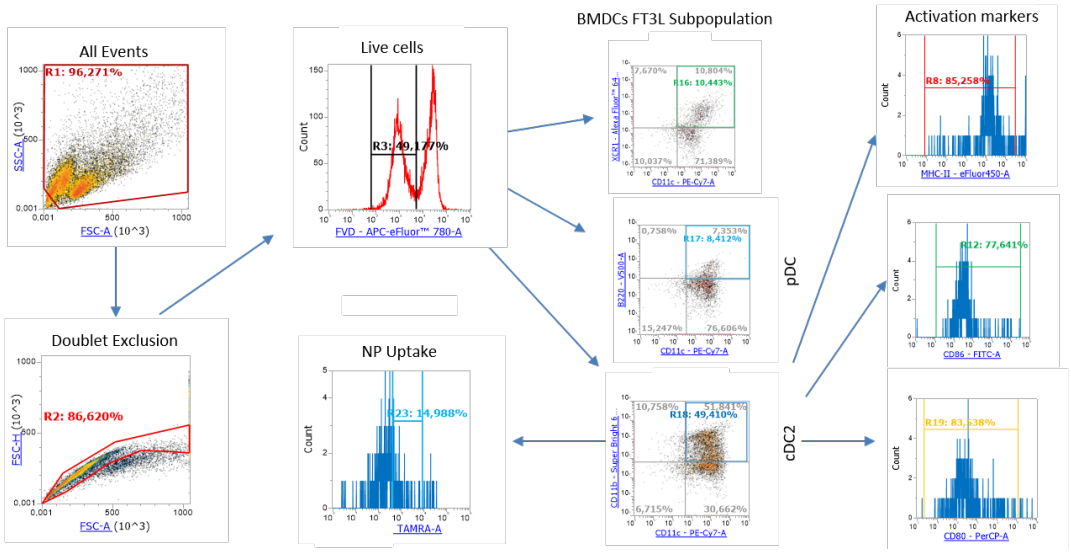

Figure 12: Gating strategy of BMDCs-FT3L

After exclusion of debris, doublets and dead cells, spleen cell populations were identified sequentially according to lineage marker expression, cDC2 (CD45+, CD11b), pDC (CD45+, B220/CD45R), cDC1 (CD45+, XCR1). From each cell population, it is also possible to check cell uptake and maturation.

Flow cytometry data analysis

Data were analyzed using GraphPad PRISM v5 and v9 software, resp. (GraphPad Software Inc., San Diego, CA, USA). Data are given as mean ± SEM for the indicated number of independent experiments. Statistical differences were determined by unpaired Student's t-tests when comparing two groups, one-way ANOVA followed by post-hoc Tukey`s test when comparing multiple groups monitored at a given time point, and two-way ANOVA/Tukey tests when comparing multiple groups assessed at different time points, assuming significant differences at $p < 0.05$ in either case.

Fluorescence measurements

Immune cells left untreated or incubated overnight with NPs were lysed in Passive Lysis Buffer (PLB; Promega, Madison, WI). Cell lysates and NPs were serially diluted in PLB in a black 96 well plate with clear bottom (each 100 µL). AF647 fluorescence intensities were

recorded (Excitation: 638 nm, bandwidth 10nm; Emission: 677 nm, bandwidth: 10 nm; integration time 40 µs) in a microplate reader (Spark; Tecan, Männedorf, Switzerland).

T-cell proliferation in vitro

Differentially pretreated BMDCs were harvested, reseeded in triplicates into 96-well plates (10^5/mL; 100 µL/well) and were serially diluted. OVA peptide-specific splenic $CD8^+$ T cells from OT-I mice and $CD4^+$ T cells from OTII mice were isolated by negative immunomagnetic enrichment (Barnden, Allison et al. 1998, Clarke, Barnden et al. 2000). Isolated T cells ($5x10^5$/mL; each 100 µL) were added to diluted BMDCs. Aliquots of cell culture supernatants were taken on day 1, 2 and 3 and stored at -20 °C. On day 3, ^{3}H-thymidine (0.5 µCi/well) was added for the last 16-18 h of coculture. Afterwards, cells were harvested onto glass fiber filters, and retained radioactivity was quantified in a microplate scintillation counter (1450 MicroBeta Trilux; Perkin Elmer, Waltham, MA). All samples were run in triplicate.

Cytometric Bead Assay

Supernatants of cell cultures or blood sera (diluted 1:2) were retrieved and stored at −20 °C for subsequent analysis. Pro-inflammatory and anti-inflammatory cytokines were quantified using a Cytometric Bead Assay (CBA; BD Biosciences) as recommended by the manufacturer. IFNs type I were measured using Legendplex reagents as recommended (Table 3). In any case, the kit used a bead-based multiplex assay, comprising fluorescence–encoded beads that were conjugated with cytokine-specific capture antibodies. Samples were mixed with capture beads, subsequently incubated with detection antibodies and then with PE-conjugated detection antibodies (all at room temperature in the dark under shaking), and subjected to flow cytometric analysis. Results were analyzed using FCAP Array Analysis Software v.1.0.1 (BD Biosciences) and Qognit Legendplex Analysis Software (BioLegend).

BD Biosciences		**BioLegend**
Pro-inflammatory	Anti-inflammatory	Typ I IFNs
TNF-α, IL-6	IL-10	IFN-α
IL-1ß, IFN-γ	IL-12, IL-23	IFN- β

Table 3: Overview of the different cytokines included in this thesis.

Stimulation of liver NPCs

Liver NPCs were seeded into wells of 96-well plates (10^5/100 µL) and were treated overnight in parallel settings with LPS (100 ng/m; Kenilworth, NJ, USA), R848 (1 µg/m, Invivogen, San Diego, CA, USA), Ovalbumine-encoding mRNA (1 µg/mL; Tri-Link, San Diego, CA, USA), DOTAP (6,4 µL/mL; Roth, Weiden, Germany), and DOTAP/mRNA complexes, which were formed by mixing both components at the mentioned amounts as recommended by the manufacturer (Roth).

Detection of Nuclear Factor 'Kappa-Light-Chain-Enhancer' of Activated B-Cells (NF-kB) in a Raw-Blue™ Reporter Cell Line (Quanti Blue Assay)

The MAC reporter subline RAW-Blue™ (InvivoGen, San Diego, CA, USA) was used to determine NF-κB activity. RAW-Blue™ cells express secreted embryonic alkaline phosphatase (SEAP), which is inducible by active NF-κβ. RAW-Blue™ cells were incubated with 1,000 µg/mL of Dexamethason (DXM) and equimolar amounts of nanostructured lipid carrier (NLC)-encapsulated DXM as indicated and stimulated with LPS applied 45 min later. Supernatants (20 µL) were collected 6h and 24h after LPS stimulation. All samples were treated in parallel with Quanti Blue solution (180 µL; InvivoGen) serving as SEAP substrate according to the vendor. Finally, NF-κβ activity was determined as substrate turnover by colorimetric analysis in a spectrophotometer (EMax® Pus Microplate Reader; Molecular Devises, San José, CA, USA) at 620–655 nm. All experiments were performed in quadruplicates.

Cellular metabolic activity

Cellular metabolic activity as general indicator of cell viability, proliferation and cytotoxicity was determined after incubation of immune cells with the different NPs using a colorimetric 3-(4,5-dimethylthiazol-2-yl)-2,5-diphenyltetrazolium bromide (MTT) assay. Each well containing immune cells was treated with different NP formulations at the given concentrations. After 24 h, 25 µL of (MTT, 2 mg/mL in PBS) was added, respectively, and the samples were incubated at 37 °C for 1.5 h. To dissolve the formed formazan crystals, 100 µL of 10% SDS (m/v)/0.01 M HCL was added to each well followed by incubation at 37 °C overnight. Cellular metabolic activity was determined in relation to positive (PBS blank,

100% activity) and negative (10% DMSO, 0% activity) control samples based on absorbance measurements at 570 nm. Experiments were performed in quadruplicates.

5.4. Biological evaluation of NPs *in vivo*

Mice

Female C57BL/6 mice (6-8 weeks old, body weight approximately 20–25 g) were bred and housed in the Translational Animal Research Center (TARC) of Johannes Gutenberg-University Mainz under specific pathogen-free conditions, following the guidelines of the regional animal care committee. Additionally, female BALB/*c* mice of the same age and body weight were sourced from Charles River (Sulzfeld, Germany) and maintained in accordance with the institute and local government guidelines, including 12-hour light-dark cycles at 25 °C, 40–60% humidity, and humane care, with access to regular chow and water *ad libitum*.

The guide for the care and use of laboratory animals as well as the 3R principles in laboratory animal experiments were followed. Mice were sacrificed at an age of between 12–16 weeks for organ retrieval according to § 8 TierSchG. The conducted animal study followed an approval by the local ethics committee on animal care (G20-1-123 DACH TVA, Government of Rhineland Palatinate, Germany). All mice were housed at the animal facility of the Johannes Gutenberg-University Mainz. Animal experiments were performed following institutional guidelines and with permission of the State Rhineland Palatinate.

Biodistribution imaging of NPs

To investigate the biodistribution of the NPs, formulations were injected intravenously into C57BL/6J or BALB/c mice (n=3, two mice treated with PBS served as control at least 3 times). Prior to injection mice were anesthetized with isoflurane gas and treated *via* tail vein injection with the NP. After 24 h, mice were again anesthetized with isoflurane gas and transferred into an IVIS (*in vivo* imaging spectrum) system (Caliper Life Sciences, Hopkinton, MA, USA) for *in vivo* dye-fluorescence imaging. Picture integration time of the fluorescence source was set to 4 s. Recording parameters were set for excitation at 745 nm and emission at 800 nm to visualize the dye-labeled NPs. Afterwards, mice were sacrificed, and organs were harvested and put again into the imaging chamber for *ex vivo* signal quantification using Live Image software from PerkinElmer (Waltham, MA, USA). Organs were carefully bordered by

region-of-interests (ROIs), and then their fluorescence was quantified as the average of area-normalized radiant efficiency.

Liver enzyme activity

Blood retrieved by heart puncture was used to determine serum contents of aspartate aminotransferase (AST), alanine aminotransferase (ALT), alkaline phosphatase (ALP), L-lactate dehydrogenase (LDH) and blood urea by nitrogen content (BUN) according to reference values as stated in Table 4 (Bailey, Stearman et al. 1963, Porras 2002, Zur 2005, River 2023). These parameters were measured by the central diagnostic laboratory of the University Medical Center Mainz.

Liver Enzymes		**Reference values**
AST	Aspartate aminotransferase	67-381 U/L
ALT	Alanine aminotransferase	40-170 U/L
ALP	Alkaline Phosphatase	108-367 U/L
LDH	L-Lactatdehydrogenase	271-321 U/L
BUN	Blood urea nitrogen	7-31 mg/dL
BIL	Bilirubin	0,2-0,7mg/dL
GGT	Gamma-Glutamyl Transpeptidase	8,8-23,2 U/L
CREA	Creatinine	0,2-0,5 U/L
GLDH	Glutamat-Dehydrogenase	<9 U/L
CK	Creatin-Kinase	3-2300 IU/L

Table 4: Reference values for female C57BL/6 and BALB/c mice.

Histopathological analysis by hematoxylin & eosin (H&E) staining

Mice were injected with 100 ul of NP (3µg IMDQ-NP; 10µg OVA), intravenous in the tail vain. For histopathological analysis inner organs (namely: heart, lungs, liver, spleen and kidneys) were retrieved after 24 h, paraffin-embedded blocks were prepared, and derived tissue sections (3 µm) were stained with hematoxylin & eosin (H&E) to assess inflammatory responses and tissue injury. To this end, H&E-stained tissue sections were examined by microscopy in a blinded fashion by an independent pathologist using a scoring system that quantified the degree of tissue inflammation or tissue injury (0–3). In general, three randomly

selected areas on each slide were analyzed with an Axioscope 5 equipped with an Axiocam 208 (Zeiss, Jena, Germany).

T cell proliferation in vivo

Single cell suspensions of spleens of OT-I and OT-II mice were labelled with the fluorescent cell division dyes carboxyfluorescein succinimidyl ester (CFSE, 5µM) and cell trace violet (CTV, 5µM), respectively. C57BL/6J mice were intraperitoneally injected with each $2x10^6$ labelled OT-I and OT-II cells (each 150µl), respectively. After 1 h, the recipient animals were injected subcutaneously on their right flank with either empty or functionalized peptobrushes, (each 150µl, respectively). Five days later the spleen, blood and skin-draining lymph nodes of injected and non-injected skin lymph nodes were analyzed by flow cytometry.

6. Summary and future outlook

The studies treatised in this thesis evaluated functionalized NPs, a cutting-edge approach in vaccine development. The focus was on optimizing cellular uptake and triggering antigen-specific immune responses. NPs crafted with precise surface modifications were evaluated regarding their physicochemical properties, stability, and ability to enter immune cells. Notably, their interaction with APCs, as a requirement for antigen presentation and T cell stimulation, was explored. Preliminary findings revealed that such functionalized NPs surpassed corresponding conventional formulations in terms of cellular uptake. Moreover, the induced immune responses exhibited specificity toward the targeted antigen. This underscores the potential of NPs as a revolutionary strategy for vaccine design and as promising, more effective, and targeted immunization approaches.

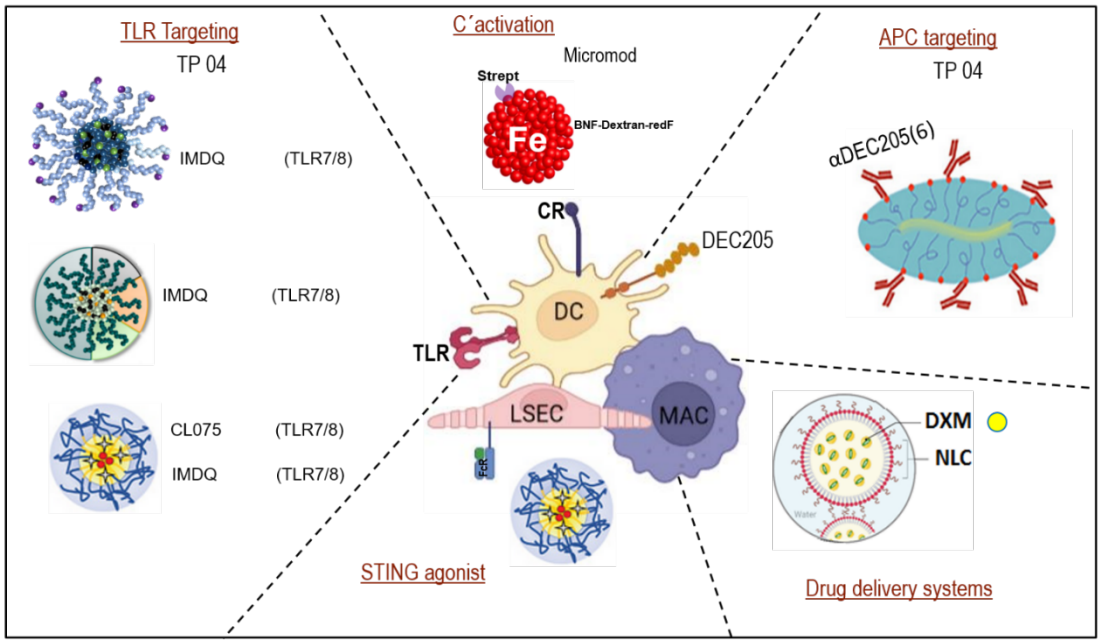

Figure 13: Graphical summary of NP-based vaccine research categories dealt with in this thesis.

In this thesis, peptobrushes, polycarbonate nanogels, micelles, and lipid NPs were used as multifunctional nanocarrier systems (Fig.13). NPs showed favorable physicochemical properties and exhibited significant potential for the targeting, activation, and delivery of payloads, such as DXM. Cellular uptake studies underscored the efficient uptake of NPs by target cells, demonstrating the successful targeting of NPs to crucial APC such as DCs and B cells both *in vitro* and *in vivo*. By concurrently delivering antigens and adjuvants, we not only activated these cells but also enhanced antigen presentation, ultimately promoting the differentiation of effector T cells. Although the presented NPs have shown a consistent effect,

certain challenges persist, necessitating further research. For instance, issues related to nanoparticle stability and the potential for immune system recognition pose significant hurdles that require further investigation. Testing alternative targeting ligands (aDEC205), antigens (OVA), and adjuvants (IMDQ), either individually or in synergistic combinations, is crucial to develop a promising tool in mice that may be tested in humans. The success of functionalized NPs in enhancing cellular uptake and eliciting specific immune responses suggests a paradigm shift in this field. Further research could delve into optimizing surface modifications, exploring diverse antigens, and fine-tuning NP designs, as in our Collaborative Research Center (CRC)1066, to optimize the use of NPs in tumor immunotherapy and, furthermore, for a broader spectrum of infectious diseases. Additionally, the potential for memory cell generation opens new avenues for long-term immunity studies. The scalability and manufacturability of the NPs should be addressed for practical applications considering regulatory and translational aspects. In summary, our outlook involves refining and expanding the application of functionalized NPs, propelling us toward a new era of precision immunization strategies with the potential to revolutionize global healthcare.

7. Zusammenfassung

In dieser Studie wurden funktionalisierte Nanopartikel (NP) als ein innovativer Ansatz in der Impfstoffentwicklung evaluiert. Der Fokus lag auf der Optimierung der zellulären Aufnahme und der Auslösung antigenspezifischer Immunantworten. NP mit reproduzierbaren Oberflächenmodifikationen wurden auf ihre physikalisch-chemischen Eigenschaften, ihre Stabilität und ihre Fähigkeit, von Immunzellen internalisiert zu werden, untersucht. Insbesondere wurde ihre Interaktion mit Antigen-präsentierenden Zellen untersucht, die für die Induktion antigenspezifischer Immunantworten essentiell sind. Vorläufige Ergebnisse zeigten, dass funktionalisierte NP die herkömmlichen Formulierungen hinsichtlich der Zellaufnahme übertrafen. Die induzierten Immunantworten wiesen eine Spezifität gegenüber dem Zielantigen auf. Dies unterstreicht das Potenzial dieser Nanoimpfstoffe für die Impfstoffentwicklung.

In dieser Arbeit wurden Peptobürsten, Polycarbonat-Nanogele, Mizellen und Lipid-NP als multifunktionalisierte Nanoträgersysteme verwendet (Abb. 13). Einige Nanopartikel zeigten vorteilhafte physikalisch-chemische Eigenschaften und wiesen ein bedeutendes Potenzial für die präzise Ausrichtung, Aktivierung und Lieferung von Wirkstoffen wie Dexamethason (DXM) auf. Untersuchungen zur zellulären Aufnahme betonten die effiziente Internalisierung der Nanoträger durch Zielzellen und demonstrierten die erfolgreiche gezielte Ausrichtung von Nanoimpfstoffen auf entscheidende Immunzellen wie dendritische Zellen (DCs) und B-Zellen sowohl *in vitro* als auch *in vivo*. Durch die gleichzeitige Applikation von Antigenen und Adjuvantien haben wir diese Zellen nicht nur aktiviert, sondern auch die Antigenpräsentation verbessert und letztendlich die Differenzierung von Effektor-T-Zellen gefördert. Obwohl die vorgestellten NPs eine konsistente Wirkung gezeigt haben, bestehen bestimmte Herausforderungen, die weitere Forschung erfordern. Beispielsweise stellen Probleme im Zusammenhang mit der Stabilität von Nanopartikeln und der Erkennung durch das Immunsystem bedeutende Hürden dar, die weitere Untersuchungen erfordern. Das Testen alternativer Targeting-Liganden (aDEC205), Antigene (OVA) und Adjuvantien (IMDQ), entweder einzeln oder in synergistischen Kombinationen, ist entscheidend, um ein vielversprechendes Werkzeug bei Mäusen zu entwickeln, dass in Menschen getestet werden kann. Der Erfolg funktionalisierter NPs bei der Verbesserung der zellulären Aufnahme und der Auslösung spezifischer Immunantworten deutet auf einen Paradigmenwechsel in diesem Bereich hin. Weitere Forschung könnte sich darauf konzentrieren, Oberflächenmodifikationen zu optimieren, verschiedene Antigene zu erforschen und das

Design von NPs, wie im Rahmen der Arbeit unseres Sonderforschungsbereichs (SFB)1066 gezeigt, für die Tumor-Immuntherapie und darüber hinaus eine breitere Palette von Infektionskrankheiten zu optimieren.

Des Weiteren eröffnet das Potenzial zur Generierung von Gedächtniszellen neue Perspektiven für Langzeitimmunitätsstudien. Die Skalierbarkeit und Herstellbarkeit der NP sollten für die praktische Anwendung unter Berücksichtigung regulatorischer und translationaler Aspekte verbessert werden. Zusammenfassend betrachtet umfasst unser Ausblick das Verfeinern und Erweitern der Anwendung funktionalisierter NPs, was uns in eine neue Ära präziser Immunisierungsstrategien führen könnte, mit dem Potenzial, die globale Gesundheitsversorgung zu revolutionieren.

8. Curriculum vitae

For privacy reasons, the CV has been removed from the electronic version of this dissertation.

9. References

Abbasi, S. and S. Uchida (2021). "Multifunctional Immunoadjuvants for Use in Minimalist Nucleic Acid Vaccines." Pharmaceutics **13**(5).

Abbott, M. and Y. Ustoyev (2019). "Cancer and the Immune System: The History and Background of Immunotherapy." Semin Oncol Nurs **35**(5): 150923.

Aliyu, M., F. Zohora and A. A. Saboor-Yaraghi (2021). "Spleen in innate and adaptive immunity regulation." AIMS Allergy and Immunology **5**(1): 1-17.

Alquraini, A. and J. El Khoury (2020). "Scavenger receptors." Curr Biol **30**(14): R790-R795.

Anselmo, A. C., M. Zhang, S. Kumar, D. R. Vogus, S. Menegatti, M. E. Helgeson and S. Mitragotri (2015). "Elasticity of nanoparticles influences their blood circulation, phagocytosis, endocytosis, and targeting." ACS Nano **9**(3): 3169-3177.

Arno, M. C., M. Inam, A. C. Weems, Z. Li, A. L. A. Binch, C. I. Platt, S. M. Richardson, J. A. Hoyland, A. P. Dove and R. K. O'Reilly (2020). "Exploiting the role of nanoparticle shape in enhancing hydrogel adhesive and mechanical properties." Nat Commun **11**(1): 1420.

Arvizo, R. R., O. R. Miranda, M. A. Thompson, C. M. Pabelick, R. Bhattacharya, J. D. Robertson, V. M. Rotello, Y. S. Prakash and P. Mukherjee (2010). "Effect of nanoparticle surface charge at the plasma membrane and beyond." Nano Lett **10**(7): 2543-2548.

Baetke, S. C., T. Lammers and F. Kiessling (2015). "Applications of nanoparticles for diagnosis and therapy of cancer." Br J Radiol **88**(1054): 20150207.

Bahadar, H., F. Maqbool, K. Niaz and M. Abdollahi (2016). "Toxicity of Nanoparticles and an Overview of Current Experimental Models." Iran Biomed J **20**(1): 1-11.

Bailey, J. M., M. Stearman and J. Clough (1963). "Ldh Levels in Blood and Tissues of Mice Infected with an Ldh Agent." Proc Soc Exp Biol Med **114**: 148-153.

Banstola, A., J.-H. Jeong and S. Yook (2020). "Immunoadjuvants for cancer immunotherapy: A review of recent developments." Acta Biomaterialia **114**: 16-30.

Barnden, M. J., J. Allison, W. R. Heath and F. R. Carbone (1998). "Defective TCR expression in transgenic mice constructed using cDNA-based alpha- and beta-chain genes under the control of heterologous regulatory elements." Immunol Cell Biol **76**(1): 34-40.

Barua, S. and S. Mitragotri (2014). "Challenges associated with Penetration of Nanoparticles across Cell and Tissue Barriers: A Review of Current Status and Future Prospects." Nano Today **9**(2): 223-243.

Bayda, S., M. Adeel, T. Tuccinardi, M. Cordani and F. Rizzolio (2019). "The History of Nanoscience and Nanotechnology: From Chemical-Physical Applications to Nanomedicine." Molecules **25**(1).

Bazak, R., M. Houri, S. El Achy, S. Kamel and T. Refaat (2015). "Cancer active targeting by nanoparticles: a comprehensive review of literature." J Cancer Res Clin Oncol **141**(5): 769-784.

Bednarczyk, M., C. Medina-Montano, F. J. Fittler, H. Stege, M. Roskamp, M. Kuske, C. Langer, M. Vahldieck, E. Montermann, I. Tubbe, N. Rohrig, A. Dzionek, S. Grabbe and M. Bros (2021). "Complement-Opsonized Nano-Carriers Are Bound by Dendritic Cells (DC) via Complement Receptor (CR)3, and by B Cell Subpopulations via CR-1/2, and Affect the Activation of DC and B-1 Cells." Int J Mol Sci **22**(6).

Behzadi, S., V. Serpooshan, W. Tao, M. A. Hamaly, M. Y. Alkawareek, E. C. Dreaden, D. Brown, A. M. Alkilany, O. C. Farokhzad and M. Mahmoudi (2017). "Cellular uptake of nanoparticles: journey inside the cell." Chem Soc Rev **46**(14): 4218-4244.

Benedict, M. and X. Zhang (2017). "Non-alcoholic fatty liver disease: An expanded review." World J Hepatol **9**(16): 715-732.

Blanco, E., H. Shen and M. Ferrari (2015). "Principles of nanoparticle design for overcoming biological barriers to drug delivery." Nat Biotechnol **33**(9): 941-951.

Bonifaz, L. C., D. P. Bonnyay, A. Charalambous, D. I. Darguste, S. Fujii, H. Soares, M. K. Brimnes, B. Moltedo, T. M. Moran and R. M. Steinman (2004). "In vivo targeting of antigens to maturing dendritic cells via the DEC-205 receptor improves T cell vaccination." J Exp Med **199**(6): 815-824.

Bros, M., L. Nuhn, J. Simon, L. Moll, V. Mailander, K. Landfester and S. Grabbe (2018). "The Protein Corona as a Confounding Variable of Nanoparticle-Mediated Targeted Vaccine Delivery." Front Immunol **9**: 1760.

Cacicedo, M. L., C. Medina-Montano, L. Kaps, C. Kappel, S. Gehring and M. Bros (2020). "Role of Liver-Mediated Tolerance in Nanoparticle-Based Tumor Therapy." Cells **9**(9).

Carmeliet, P. and R. K. Jain (2000). "Angiogenesis in cancer and other diseases." Nature **407**(6801): 249-257.

Castenmiller, C., B. C. Keumatio-Doungtsop, R. van Ree, E. C. de Jong and Y. van Kooyk (2021). "Tolerogenic Immunotherapy: Targeting DC Surface Receptors to Induce Antigen-Specific Tolerance." Front Immunol **12**: 643240.

Chan, K. R., E. Z. Ong, D. Z. Mok and E. E. Ooi (2015). "Fc receptors and their influence on efficacy of therapeutic antibodies for treatment of viral diseases." Expert Rev Anti Infect Ther **13**(11): 1351-1360.

Chan, W. C. W. (2017). "Nanomedicine 2.0." Acc Chem Res **50**(3): 627-632.

Chao, M. P., I. L. Weissman and R. Majeti (2012). "The CD47-SIRPalpha pathway in cancer immune evasion and potential therapeutic implications." Curr Opin Immunol **24**(2): 225-232.

Chen, H., L. Wang, J. Yeh, X. Wu, Z. Cao, Y. A. Wang, M. Zhang, L. Yang and H. Mao (2010). "Reducing non-specific binding and uptake of nanoparticles and improving cell targeting with an antifouling PEO-b-PgammaMPS copolymer coating." Biomaterials **31**(20): 5397-5407.

Chen, L., X. Li, Y. Zhang, T. Chen, S. Xiao and H. Liang (2018). "Morphological and mechanical determinants of cellular uptake of deformable nanoparticles." Nanoscale **10**(25): 11969-11979.

Cheng, C., E. Zheng, B. Yu, Z. Zhang, Y. Wang, Y. Liu and Y. He (2021). "Recognition of lipoproteins by scavenger receptor class A members." J Biol Chem **297**(2): 100948.

Cheng, Q. N., X. Yang, J. F. Wu, W. B. Ai and Y. R. Ni (2021). "Interaction of non-parenchymal hepatocytes in the process of hepatic fibrosis (Review)." Mol Med Rep **23**(5).

Chithrani, B. D. and W. C. Chan (2007). "Elucidating the mechanism of cellular uptake and removal of protein-coated gold nanoparticles of different sizes and shapes." Nano Lett **7**(6): 1542-1550.

Clarke, S. R., M. Barnden, C. Kurts, F. R. Carbone, J. F. Miller and W. R. Heath (2000). "Characterization of the ovalbumin-specific TCR transgenic line OT-I: MHC elements for positive and negative selection." Immunol Cell Biol **78**(2): 110-117.

Coffman, R. L., A. Sher and R. A. Seder (2010). "Vaccine adjuvants: putting innate immunity to work." Immunity **33**(4): 492-503.

Czysch, C., C. Medina-Montano, N. K. Dal, T. Dinh, Y. Froder, P. Winterwerber, K. Maxeiner, H. J. Rader, D. Schuppan, H. Schild, M. Bros, B. Biersack, F. Feranoli, S. Grabbe and L. Nuhn (2022). "End Group Dye-Labeled Polycarbonate Block Copolymers for Micellar (Immuno-)Drug Delivery." Macromol Rapid Commun **43**(12): e2200095.

Czysch, C., C. Medina-Montano, Z. Zhong, A. Fuchs, J. Stickdorn, P. Winterwerber, S. Schmitt, K. Deswarte, M. Raabe, M. Scherger, F. Combes, J. De Vrieze, S. Kasmi, N. N. Sandners, S. Lienenklaus, K. Koynov, H.-J. Räder, B. N. Lambrecht, S. A. David, M. Bros, H. Schild, S. Grabbe, B. G. De Geest and L. Nuhn (2022). "Transient Lymph Node Immune Activation by Hydrolysable Polycarbonate Nanogels." Advanced Functional Materials **32**(35): 2203490.

da Costa, V. and T. Freire (2022). "Advances in the Immunomodulatory Properties of Glycoantigens in Cancer." Cancers (Basel) **14**(8).

Dalle Vedove, E., G. Costabile and O. M. Merkel (2018). "Mannose and Mannose-6-Phosphate Receptor-Targeted Drug Delivery Systems and Their Application in Cancer Therapy." Adv Healthc Mater **7**(14): e1701398.

Digiacomo, L., D. Pozzi, S. Palchetti, A. Zingoni and G. Caracciolo (2020). "Impact of the protein corona on nanomaterial immune response and targeting ability." Wiley Interdiscip Rev Nanomed Nanobiotechnol **12**(4): e1615.

Donahue, N. D., H. Acar and S. Wilhelm (2019). "Concepts of nanoparticle cellular uptake, intracellular trafficking, and kinetics in nanomedicine." Adv Drug Deliv Rev **143**: 68-96.

Dou, L., Y. Ono, Y. F. Chen, A. W. Thomson and X. P. Chen (2018). "Hepatic Dendritic Cells, the Tolerogenic Liver Environment, and Liver Disease." Semin Liver Dis **38**(2): 170-180.

Dowling, D. J., E. A. Scott, A. Scheid, I. Bergelson, S. Joshi, C. Pietrasanta, S. Brightman, G. Sanchez-Schmitz, S. D. Van Haren, J. Ninković, D. Kats, C. Guiducci, A. de Titta, D. K. Bonner, S. Hirosue, M. A. Swartz, J. A. Hubbell and O. Levy (2017). "Toll-like receptor 8 agonist nanoparticles mimic immunomodulating effects of the live BCG vaccine and enhance neonatal innate and adaptive immune responses." Journal of Allergy and Clinical Immunology **140**(5): 1339-1350.

Eshaghi, B., N. Alsharif, X. An, H. Akiyama, K. A. Brown, S. Gummuluru and B. M. Reinhard (2020). "Stiffness of HIV-1 Mimicking Polymer Nanoparticles Modulates Ganglioside-Mediated Cellular Uptake and Trafficking." Adv Sci (Weinh) **7**(18): 2000649.

Ferlay J, e. a. (2020). Global Cancer Observatory: Cancer Today. Lyon, International Agency for Research on Cancer**:** https://gco.iarc.fr/today/home.

Florez, L., C. Herrmann, J. M. Cramer, C. P. Hauser, K. Koynov, K. Landfester, D. Crespy and V. Mailander (2012). "How shape influences uptake: interactions of anisotropic polymer nanoparticles and human mesenchymal stem cells." Small **8**(14): 2222-2230.

Fornaguera, C., M. Guerra-Rebollo, M. Angel Lazaro, C. Castells-Sala, O. Meca-Cortes, V. Ramos-Perez, A. Cascante, N. Rubio, J. Blanco and S. Borros (2018). "mRNA Delivery System for Targeting Antigen-Presenting Cells In Vivo." Adv Healthc Mater **7**(17): e1800335.

Foroozandeh, P. and A. A. Aziz (2018). "Insight into Cellular Uptake and Intracellular Trafficking of Nanoparticles." Nanoscale Res Lett **13**(1): 339.

Francia, V., K. Yang, S. Deville, C. Reker-Smit, I. Nelissen and A. Salvati (2019). "Corona Composition Can Affect the Mechanisms Cells Use to Internalize Nanoparticles." ACS Nano **13**(10): 11107-11121.

Friedman, A. D., S. E. Claypool and R. Liu (2013). "The smart targeting of nanoparticles." Curr Pharm Des **19**(35): 6315-6329.

Fucikova, J., L. Palova-Jelinkova, J. Bartunkova and R. Spisek (2019). "Induction of Tolerance and Immunity by Dendritic Cells: Mechanisms and Clinical Applications." Front Immunol **10**: 2393.

Ganesan, L. P., J. Kim, Y. Wu, S. Mohanty, G. S. Phillips, D. J. Birmingham, J. M. Robinson and C. L. Anderson (2012). "FcγRIIb on liver sinusoidal endothelium clears small immune complexes." J Immunol **189**(10): 4981-4988.

Garcia-Fernandez, C., A. Saz, C. Fornaguera and S. Borros (2021). "Cancer immunotherapies revisited: state of the art of conventional treatments and next-generation nanomedicines." Cancer Gene Ther **28**(9): 935-946.

Geng, Y., P. Dalhaimer, S. Cai, R. Tsai, M. Tewari, T. Minko and D. E. Discher (2007). "Shape effects of filaments versus spherical particles in flow and drug delivery." Nat Nanotechnol **2**(4): 249-255.

Godoy-Matos, A. F., W. S. Silva Junior and C. M. Valerio (2020). "NAFLD as a continuum: from obesity to metabolic syndrome and diabetes." Diabetol Metab Syndr **12**: 60.

Gratton, S. E., P. A. Ropp, P. D. Pohlhaus, J. C. Luft, V. J. Madden, M. E. Napier and J. M. DeSimone (2008). "The effect of particle design on cellular internalization pathways." Proc Natl Acad Sci U S A **105**(33): 11613-11618.

Greish, K., A. Mathur, M. Bakhiet and S. Taurin (2018). "Nanomedicine: is it lost in translation?" Ther Deliv **9**(4): 269-285.

Gustafson, H. H., D. Holt-Casper, D. W. Grainger and H. Ghandehari (2015). "Nanoparticle uptake: The phagocyte problem." Nano Today **10**(4): 487-510.

Gutiérrez-Martínez, E., R. Planès, G. Anselmi, M. Reynolds, S. Menezes, A. C. Adiko, L. Saveanu and P. Guermonprez (2015). "Cross-Presentation of Cell-Associated Antigens by MHC Class I in Dendritic Cell Subsets." Frontiers in Immunology **6**.

Hafner, A. M., B. Corthésy and H. P. Merkle (2013). "Particulate formulations for the delivery of poly(I:C) as vaccine adjuvant." Advanced Drug Delivery Reviews **65**(10): 1386-1399.

Hilligan, K. L. and F. Ronchese (2020). "Antigen presentation by dendritic cells and their instruction of CD4+ T helper cell responses." Cell Mol Immunol **17**(6): 587-599.

Hong, S., D. W. Choi, H. N. Kim, C. G. Park, W. Lee and H. H. Park (2020). "Protein-Based Nanoparticles as Drug Delivery Systems." Pharmaceutics **12**(7).

Hoppstadter, J., M. Seif, A. Dembek, C. Cavelius, H. Huwer, A. Kraegeloh and A. K. Kiemer (2015). "M2 polarization enhances silica nanoparticle uptake by macrophages." Front Pharmacol **6**: 55.

Hoshyar, N., S. Gray, H. Han and G. Bao (2016). "The effect of nanoparticle size on in vivo pharmacokinetics and cellular interaction." Nanomedicine (Lond) **11**(6): 673-692.

Huang, L., X. Ge, Y. Liu, H. Li and Z. Zhang (2022). "The Role of Toll-like Receptor Agonists and Their Nanomedicines for Tumor Immunotherapy." Pharmaceutics **14**(6): 1228.

Huppertsberg, A., C. Medina-Montano, L. Kaps, Z. Zhong, S. Schmitt, J. Stickdorn, K. Deswarte, F. Combes, C. Czysch, J. De Vrieze, S. Kasmi, N. Choteschovsky, A. Klefenz, C. Medina-Montano, P. Winterwerber, C. Chen, M. Bros, S. Lienenklaus, N. N. Sanders, K. Koynov, D. Schuppan, B. N. Lambrecht, S. A. David, B. G. De Geest and L. Nuhn (2021). "Squaric Ester-Based, pH-Degradable Nanogels: Modular Nanocarriers for Safe, Systemic Administration of Toll-like Receptor 7/8 Agonistic Immune Modulators." J Am Chem Soc **143**(26): 9872-9883.

Ilinskaya, A. N., A. Shah, A. E. Enciso, K. C. Chan, J. A. Kaczmarczyk, J. Blonder, E. E. Simanek and M. A. Dobrovolskaia (2019). "Nanoparticle physicochemical properties determine the activation of intracellular complement." Nanomedicine **17**: 266-275.

Jimenez-Jimenez, C., M. Manzano and M. Vallet-Regi (2020). "Nanoparticles Coated with Cell Membranes for Biomedical Applications." Biology (Basel) **9**(11).

Junker, F., J. Gordon and O. Qureshi (2020). "Fc Gamma Receptors and Their Role in Antigen Uptake, Presentation, and T Cell Activation." Front Immunol **11**: 1393.

Kappel, C., C. Medina-Montano, C. Seidl, M. Schinnerer, I. Alberg, C. Leps, J. Sohl, A. K. Hartmann, M. Fichter, M. Kuske, J. Schunke, G. Kuhn, I. Tubbe, D. Passlick, D. Hobernik, R. Bent, K. Haas, E. Montermann, K. Walzer, M. Diken, M. Schmidt, R. Zentel, L. Nuhn, H. Schild, S. Tenzer, V. Mailander, M. Barz, M. Bros and S. Grabbe (2021). "Density of Conjugated Antibody Determines the Extent of Fc Receptor Dependent Capture of Nanoparticles by Liver Sinusoidal Endothelial Cells." ACS Nano **15**(9): 15191-15209.

Kettler, K., K. Veltman, D. van de Meent, A. van Wezel and A. J. Hendriks (2014). "Cellular uptake of nanoparticles as determined by particle properties, experimental conditions, and cell type." Environ Toxicol Chem **33**(3): 481-492.

Kim, C., J. F. Galloway, K. H. Lee and P. C. Searson (2014). "Universal antibody conjugation to nanoparticles using the Fcgamma receptor I (FcgammaRI): quantitative profiling of membrane biomarkers." Bioconjug Chem **25**(10): 1893-1901.

Knolle, P. A. and D. Wohlleber (2016). "Immunological functions of liver sinusoidal endothelial cells." Cell Mol Immunol **13**(3): 347-353.

Kopac, T. (2021). "Protein corona, understanding the nanoparticle-protein interactions and future perspectives: A critical review." Int J Biol Macromol **169**: 290-301.

Koyama, Y. and D. A. Brenner (2017). "Liver inflammation and fibrosis." J Clin Invest **127**(1): 55-64.

Kranz, L. M., M. Diken, H. Haas, S. Kreiter, C. Loquai, K. C. Reuter, M. Meng, D. Fritz, F. Vascotto, H. Hefesha, C. Grunwitz, M. Vormehr, Y. Husemann, A. Selmi, A. N. Kuhn, J. Buck, E. Derhovanessian, R. Rae, S. Attig, J. Diekmann, R. A. Jabulowsky, S. Heesch, J. Hassel, P. Langguth, S. Grabbe, C. Huber, O. Tureci and U. Sahin (2016). "Systemic RNA delivery to dendritic cells exploits antiviral defence for cancer immunotherapy." Nature **534**(7607): 396-401.

La-Beck, N. M., M. R. Islam and M. M. Markiewski (2020). "Nanoparticle-Induced Complement Activation: Implications for Cancer Nanomedicine." Front Immunol **11**: 603039.

Li, D. and M. Wu (2021). "Pattern recognition receptors in health and diseases." Signal Transduction and Targeted Therapy **6**(1): 291.

Li, J., F. Panetta, M. O'Keeffe, I. M. Leal Rojas, K. J. Radford, J. G. Zhang, D. Fernandez-Ruiz, G. M. Davey, B. S. Gully, K. M. Tullett, J. Rossjohn, R. Berry, C. N. Lee, M. H. Lahoud, W. R. Heath and I. Caminschi (2021). "Elucidating the Motif for CpG Oligonucleotide Binding to the Dendritic Cell Receptor DEC-205 Leads to Improved Adjuvants for Liver-Resident Memory." J Immunol **207**(7): 1836-1847.

Li, M., S. Jiang, A. Haller, S. Wirsching, M. Fichter, J. Simon, M. Wagner, V. Mailander, S. Gehring, D. Crespy and K. Landfester (2021). "Encapsulation of polyprodrugs enables an efficient and controlled release of dexamethasone." Nanoscale Horiz **6**(10): 791-800.

Liu, J., M. Fu, M. Wang, D. Wan, Y. Wei and X. Wei (2022). "Cancer vaccines as promising immuno-therapeutics: platforms and current progress." J Hematol Oncol **15**(1): 28.

Liu, J., Z. Liu, Y. Pang and H. Zhou (2022). "The interaction between nanoparticles and immune system: application in the treatment of inflammatory diseases." Journal of nanobiotechnology **20**(1): 127-127.

Liu, Q., X. Wang, X. Liu, Y. P. Liao, C. H. Chang, K. C. Mei, J. Jiang, S. Tseng, G. Gochman, M. Huang, Z. Thatcher, J. Li, S. D. Allen, L. Lucido, T. Xia and A. E. Nel (2021). "Antigen- and Epitope-Delivering Nanoparticles Targeting Liver Induce Comparable Immunotolerance in Allergic Airway Disease and Anaphylaxis as Nanoparticle-Delivering Pharmaceuticals." ACS Nano **15**(1): 1608-1626.

Liu, Y., J. Hardie, X. Zhang and V. M. Rotello (2017). "Effects of engineered nanoparticles on the innate immune system." Semin Immunol **34**: 25-32.

Maeda, H. (2001). "The enhanced permeability and retention (EPR) effect in tumor vasculature: the key role of tumor-selective macromolecular drug targeting." Adv Enzyme Regul **41**: 189-207.

Mainini, F., F. De Santis, G. Fuca, M. Di Nicola, L. Rivoltini and M. Eccles (2021). "Nanobiotechnology and Immunotherapy: Two Powerful and Cooperative Allies against Cancer." Cancers (Basel) **13**(15).

Martinez-Pomares, L. (2012). "The mannose receptor." J Leukoc Biol **92**(6): 1177-1186.

Matsuo, K., O. Yoshie, K. Kitahata, M. Kamei, Y. Hara and T. Nakayama (2021). "Recent Progress in Dendritic Cell-Based Cancer Immunotherapy." Cancers **13**(10): 2495.

Medina-Montano, C., M. L. Cacicedo, M. Svensson, M. J. Limeres, Y. Zeyn, J. E. Chaves-Giraldo, N. Rohrig, S. Grabbe, S. Gehring and M. Bros (2022). "Enrichment Methods for Murine Liver Non-Parenchymal Cells Differentially Affect Their Immunophenotype and Responsiveness towards Stimulation." Int J Mol Sci **23**(12).

Medina-Montano, C., I. Rivero Berti, R. C. Gambaro, M. J. Limeres, M. Svensson, G. Padula, C. Y. Chain, J. S. Cisneros, G. R. Castro, S. Grabbe, M. Bros, S. Gehring, G. A. Islan and M. L. Cacicedo (2022). "Nanostructured Lipid Carriers Loaded with Dexamethasone Prevent Inflammatory Responses in Primary Non-Parenchymal Liver Cells." Pharmaceutics **14**(8).

Meyer, R. A., S. Y. Neshat, J. J. Green, J. L. Santos and A. D. Tuesca (2022). "Targeting strategies for mRNA delivery." Materials Today Advances **14**: 100240.

Mills, C. D. (2012). "M1 and M2 Macrophages: Oracles of Health and Disease." Crit Rev Immunol **32**(6): 463-488.

Mitchell, M. J., M. M. Billingsley, R. M. Haley, M. E. Wechsler, N. A. Peppas and R. Langer (2021). "Engineering precision nanoparticles for drug delivery." Nat Rev Drug Discov **20**(2): 101-124.

Mortimer, G. M., N. J. Butcher, A. W. Musumeci, Z. J. Deng, D. J. Martin and R. F. Minchin (2014). "Cryptic epitopes of albumin determine mononuclear phagocyte system clearance of nanomaterials." ACS Nano **8**(4): 3357-3366.

Mousavi, S., M. Sporstøl, C. Fladeby, R. Kjeken, N. Barois and T. Berg (2007). "Receptor-mediated endocytosis of immune complexes in rat liver sinusoidal endothelial cells is mediated by FcγRIIb2." Hepatology (Baltimore, Md.) **46**: 871-884.

Mukhopadhyay, S. and S. Gordon (2004). "The role of scavenger receptors in pathogen recognition and innate immunity." Immunobiology **209**(1-2): 39-49.

Najahi-Missaoui, W., R. D. Arnold and B. S. Cummings (2020). "Safe Nanoparticles: Are We There Yet?" Int J Mol Sci **22**(1).

Narum, S. M., T. Le, D. P. Le, J. C. Lee, N. D. Donahue, W. Yang and S. Wilhelm (2020). Chapter 4 - Passive targeting in nanomedicine: fundamental concepts, body interactions, and clinical potential. Nanoparticles for Biomedical Applications. E. J. Chung, L. Leon and C. Rinaldi, Elsevier**:** 37-53.

Nguyen, V. H. and B. J. Lee (2017). "Protein corona: a new approach for nanomedicine design." International Journal of Nanomedicine **12**: 3137-3151.

Noreen, S., I. Maqbool and A. Madni (2021). "Dexamethasone: Therapeutic potential, risks, and future projection during COVID-19 pandemic." Eur J Pharmacol **894**: 173854.

Nuhn, L., S. De Koker, S. Van Lint, Z. Zhong, J. P. Catani, F. Combes, K. Deswarte, Y. Li, B. N. Lambrecht, S. Lienenklaus, N. N. Sanders, S. A. David, J. Tavernier and B. G. De Geest (2018). "Nanoparticle-Conjugate TLR7/8 Agonist Localized

Immunotherapy Provokes Safe Antitumoral Responses." Advanced Materials **30**(45): 1803397.

Nuhn, L., N. Vanparijs, A. De Beuckelaer, L. Lybaert, G. Verstraete, K. Deswarte, S. Lienenklaus, N. M. Shukla, A. C. Salyer, B. N. Lambrecht, J. Grooten, S. A. David, S. De Koker and B. G. De Geest (2016). "pH-degradable imidazoquinoline-ligated nanogels for lymph node-focused immune activation." Proc Natl Acad Sci U S A **113**(29): 8098-8103.

Ostrycharz, E. and B. Hukowska-Szematowicz (2022). "New Insights into the Role of the Complement System in Human Viral Diseases." Biomolecules **12**(2).

Owen, A. M., J. B. Fults, N. K. Patil, A. Hernandez and J. K. Bohannon (2021). "TLR Agonists as Mediators of Trained Immunity: Mechanistic Insight and Immunotherapeutic Potential to Combat Infection." Frontiers in Immunology **11**.

Panico, S., S. Capolla, S. Bozzer, G. Toffoli, M. Dal Bo and P. Macor (2022). "Biological Features of Nanoparticles: Protein Corona Formation and Interaction with the Immune System." Pharmaceutics **14**(12).

Park, Y. M., S. J. Lee, Y. S. Kim, M. H. Lee, G. S. Cha, I. D. Jung, T. H. Kang and H. D. Han (2013). "Nanoparticle-based vaccine delivery for cancer immunotherapy." Immune Netw **13**(5): 177-183.

Patel, P. C., D. A. Giljohann, W. L. Daniel, D. Zheng, A. E. Prigodich and C. A. Mirkin (2010). "Scavenger receptors mediate cellular uptake of polyvalent oligonucleotide-functionalized gold nanoparticles." Bioconjug Chem **21**(12): 2250-2256.

Pearce, A. K. and R. K. O'Reilly (2019). "Insights into Active Targeting of Nanoparticles in Drug Delivery: Advances in Clinical Studies and Design Considerations for Cancer Nanomedicine." Bioconjug Chem **30**(9): 2300-2311.

Peer, D. (2014). "Harnessing RNAi nanomedicine for precision therapy." Mol Cell Ther **2**: 5.

Porras, N., Zeidán, Q, Strauss, M, & Anselmi, G (2002). "Valores Séricos de Marcadores Hepáticos en Ratas: Aporte de un Patrón de Referencia." AVFT [online] **21**.

Qu, T., B. Li and Y. Wang (2022). "Targeting CD47/SIRPα as a therapeutic strategy, where we are and where we are headed." Biomarker Research **10**(1): 20.

Refsnes, M., T. Skuland, J. Ovrevik and M. Lag (2021). "Role of scavenger receptors in silica nanoparticle-induced cytokine responses in bronchial epithelial cells." Toxicol Lett **353**: 100-106.

Riley, R. S., C. H. June, R. Langer and M. J. Mitchell (2019). "Delivery technologies for cancer immunotherapy." Nat Rev Drug Discov **18**(3): 175-196.

River, C. (2023). "Clinical Pathology Data for BALB/c Mouse Colonies in North America for January 2008 - December 2012." Retrieved 06.07.2023, 2023, from https://www.criver.com/products-services/find-model/balbc-mouse?region=23.

Rus, H., C. Cudrici and F. Niculescu (2005). "The role of the complement system in innate immunity." Immunol Res **33**(2): 103-112.

Sabado, R. L., S. Balan and N. Bhardwaj (2017). "Dendritic cell-based immunotherapy." Cell Res **27**(1): 74-95.

Sabourian, P., G. Yazdani, S. S. Ashraf, M. Frounchi, S. Mashayekhan, S. Kiani and A. Kakkar (2020). "Effect of Physico-Chemical Properties of Nanoparticles on Their Intracellular Uptake." Int J Mol Sci **21**(21).

Salatin, S. and A. Yari Khosroushahi (2017). "Overviews on the cellular uptake mechanism of polysaccharide colloidal nanoparticles." J Cell Mol Med **21**(9): 1668-1686.

Saxena, M., S. H. van der Burg, C. J. M. Melief and N. Bhardwaj (2021). "Therapeutic cancer vaccines." Nat Rev Cancer **21**(6): 360-378.

Schoenmaker, L., D. Witzigmann, J. A. Kulkarni, R. Verbeke, G. Kersten, W. Jiskoot and D. J. A. Crommelin (2021). "mRNA-lipid nanoparticle COVID-19 vaccines: Structure and stability." International Journal of Pharmaceutics **601**: 120586.

Selmani, A., D. Kovačević and K. Bohinc (2022). "Nanoparticles: From synthesis to applications and beyond." Adv Colloid Interface Sci **303**: 102640.

Shannahan, J. H., W. Bai and J. M. Brown (2015). "Implications of scavenger receptors in the safe development of nanotherapeutics." Receptors Clin Investig **2**(3): e811.

Shekarian, T., S. Valsesia-Wittmann, J. Brody, M. C. Michallet, S. Depil, C. Caux and A. Marabelle (2017). "Pattern recognition receptors: immune targets to enhance cancer immunotherapy." Annals of Oncology **28**(8): 1756-1766.

Shen, L., S. Tenzer, W. Storck, D. Hobernik, V. K. Raker, K. Fischer, S. Decker, A. Dzionek, S. Krauthauser, M. Diken, A. Nikolaev, J. Maxeiner, P. Schuster, C. Kappel, A. Verschoor, H. Schild, S. Grabbe and M. Bros (2018). "Protein corona-mediated targeting of nanocarriers to B cells allows redirection of allergic immune responses." J Allergy Clin Immunol **142**(5): 1558-1570.

Shreffler, J. W., J. E. Pullan, K. M. Dailey, S. Mallik and A. E. Brooks (2019). "Overcoming Hurdles in Nanoparticle Clinical Translation: The Influence of Experimental Design and Surface Modification." International Journal of Molecular Sciences **20**(23): 6056.

Simon, J., M. Fichter, G. Kuhn, M. Brückner, C. Kappel, J. Schunke, T. Klaus, S. Grabbe, K. Landfester and V. Mailänder (2022). "Achieving dendritic cell subset-specific targeting in vivo by site-directed conjugation of targeting antibodies to nanocarriers." Nano Today **43**: 101375.

Soares, S., J. Sousa, A. Pais and C. Vitorino (2018). "Nanomedicine: Principles, Properties, and Regulatory Issues." Frontiers in Chemistry **6**.

Song, G., J. S. Petschauer, A. J. Madden and W. C. Zamboni (2014). "Nanoparticles and the mononuclear phagocyte system: pharmacokinetics and applications for inflammatory diseases." Curr Rheumatol Rev **10**(1): 22-34.

Spranger, S., M. Javotovic, M. Bürdek, S. Wilde, S. Tippmer, I. Bigalke, C. Geiger, B. Frankenberger and D. Schendel (2009). The Synthetic Thiazoloquinolone Immunostimulatory Compound CL075 Serves as a Toll-like Receptor 7/8 Agonist and Substitutes for R848 to Produce Mature Human Monocyte-derived Dendritic Cells With the Capacity to Secrete High Amounts of Interleukin-12(P70) Cytokine.

Stickdorn, J., C. Medina-Montano, L. Stein, D. Arnold-Schild, J. Hahlbrock, C. Medina-Montano, J. Bartneck, T. Ziss, E. Montermann, C. Kappel, D. Hobernik, M. Haist, H. Yurugi, M. Raabe, A. Best, K. Rajalingam, M. P. Radsak, S. A. David, K. Koynov, M. Bros, S. Grabbe, H. Schild and L. Nuhn (2022). "Systemically Administered TLR7/8 Agonist and Antigen-Conjugated Nanogels Govern Immune Responses against Tumors." ACS Nano **16**(3): 4426-4443.

Sun, J., L. Zhang, J. Wang, Q. Feng, D. Liu, Q. Yin, D. Xu, Y. Wei, B. Ding, X. Shi and X. Jiang (2015). "Tunable rigidity of (polymeric core)-(lipid shell) nanoparticles for regulated cellular uptake." Adv Mater **27**(8): 1402-1407.

Sun, T., Y. Kang, J. Liu, Y. Zhang, L. Ou, X. Liu, R. Lai and L. Shao (2021). "Nanomaterials and hepatic disease: toxicokinetics, disease types, intrinsic mechanisms, liver susceptibility, and influencing factors." Journal of Nanobiotechnology **19**(1): 108.

Tang, H., H. Ye, H. Zhang and Y. Zheng (2015). "Wrapping of nanoparticles by the cell membrane: the role of interactions between the nanoparticles." Soft Matter **11**(44): 8674-8683.

Tsoi, K. M., S. A. MacParland, X. Z. Ma, V. N. Spetzler, J. Echeverri, B. Ouyang, S. M. Fadel, E. A. Sykes, N. Goldaracena, J. M. Kaths, J. B. Conneely, B. A. Alman, M. Selzner, M. A. Ostrowski, O. A. Adeyi, A. Zilman, I. D. McGilvray and W. C. Chan (2016). "Mechanism of hard-nanomaterial clearance by the liver." Nat Mater **15**(11): 1212-1221.

van der Zande, H. J. P., D. Nitsche, L. Schlautmann, B. Guigas and S. Burgdorf (2021). "The Mannose Receptor: From Endocytic Receptor and Biomarker to Regulator of (Meta)Inflammation." Front Immunol **12**: 765034.

van Dinther, D., D. A. Stolk, R. van de Ven, Y. van Kooyk, T. D. de Gruijl and J. M. M. den Haan (2017). "Targeting C-type lectin receptors: a high-carbohydrate diet for dendritic cells to improve cancer vaccines." Journal of leukocyte biology **102**(4): 1017-1034.

Venkataraman, S., J. L. Hedrick, Z. Y. Ong, C. Yang, P. L. Ee, P. T. Hammond and Y. Y. Yang (2011). "The effects of polymeric nanostructure shape on drug delivery." Adv Drug Deliv Rev **63**(14-15): 1228-1246.

von Maltzahn, G., J. H. Park, A. Agrawal, N. K. Bandaru, S. K. Das, M. J. Sailor and S. N. Bhatia (2009). "Computationally guided photothermal tumor therapy using long-circulating gold nanorod antennas." Cancer Res **69**(9): 3892-3900.

von Roemeling, C., W. Jiang, C. K. Chan, I. L. Weissman and B. Y. S. Kim (2017). "Breaking Down the Barriers to Precision Cancer Nanomedicine." Trends Biotechnol **35**(2): 159-171.

Walsh, E. E., R. Frenck, A. R. Falsey, N. Kitchin, J. Absalon, A. Gurtman, S. Lockhart, K. Neuzil, M. J. Mulligan, R. Bailey, K. A. Swanson, P. Li, K. Koury, W. Kalina, D. Cooper, C. Fontes-Garfias, P. Y. Shi, O. Tureci, K. R. Thompkins, K. E. Lyke, V. Raabe, P. R. Dormitzer, K. U. Jansen, U. Sahin and W. C. Gruber (2020). "RNA-Based COVID-19 Vaccine BNT162b2 Selected for a Pivotal Efficacy Study." medRxiv.

Wang, B., N. Zaidi, L.-Z. He, L. Zhang, J. M. Y. Kuroiwa, T. Keler and R. M. Steinman (2012). "Targeting of the non-mutated tumor antigen HER2/neu to mature dendritic cells induces an integrated immune response that protects against breast cancer in mice." Breast cancer research : BCR **14**(2): R39-R39.

Wang, B., L. Zhang, S. C. Bae and S. Granick (2008). "Nanoparticle-induced surface reconstruction of phospholipid membranes." Proc Natl Acad Sci U S A **105**(47): 18171-18175.

Wang, C., C. Ma, L. Gong, Y. Guo, K. Fu, Y. Zhang, H. Zhou and Y. Li (2021). "Macrophage Polarization and Its Role in Liver Disease." Front Immunol **12**: 803037.

Wang, H., L. Wu and B. M. Reinhard (2012). "Scavenger receptor mediated endocytosis of silver nanoparticles into J774A.1 macrophages is heterogeneous." ACS nano **6**(8): 7122-7132.

Weissig, V., T. Elbayoumi, B. Flühmann and A. Barton (2021). "The Growing Field of Nanomedicine and Its Relevance to Pharmacy Curricula." American journal of pharmaceutical education **85**(8): 8331-8331.

WHO (2022). Cancer**:** https://www.who.int/news-room/fact-sheets/detail/cancer.

Woythe, L., P. Madhikar, N. Feiner-Gracia, C. Storm and L. Albertazzi (2022). "A Single-Molecule View at Nanoparticle Targeting Selectivity: Correlating Ligand Functionality and Cell Receptor Density." ACS Nano **16**(3): 3785-3796.

Xu, Z. P., M. Niebert, K. Porazik, T. L. Walker, H. M. Cooper, A. P. Middelberg, P. P. Gray, P. F. Bartlett and G. Q. Lu (2008). "Subcellular compartment targeting of layered double hydroxide nanoparticles." J Control Release **130**(1): 86-94.

Yan, W., W. Chen and L. Huang (2008). "Reactive oxygen species play a central role in the activity of cationic liposome based cancer vaccine." J Control Release **130**(1): 22-28.

Yang, T., J. Zhai, D. Hu, R. Yang, G. Wang, Y. Li and G. Liang (2022). ""Targeting Design" of Nanoparticles in Tumor Therapy." Pharmaceutics **14**(9).

Yang, Y. (2015). "Cancer immunotherapy: harnessing the immune system to battle cancer." J Clin Invest **125**(9): 3335-3337.

Yating Zhao, Y. W., Fu Ran, Yu Cui, Chang Liu, Qinfu Zhao, Yikun Gao, Da Wang and Siling Wang (2017). "A comparison between sphere and rod nanoparticles regarding their in vivo biological behavior and pharmacokinetics." Scientific Reports **7**.

Ye, C., W. Li, L. Li and K. Zhang (2022). "Glucocorticoid Treatment Strategies in Liver Failure." Front Immunol **13**: 846091.

Ye, M., J. Zhou, Y. Zhong, J. Xu, J. Hou, X. Wang, Z. Wang and D. Guo (2019). "SR-A-Targeted Phase-Transition Nanoparticles for the Detection and Treatment of Atherosclerotic Vulnerable Plaques." ACS Appl Mater Interfaces **11**(10): 9702-9715.

Yi, X., X. Shi and H. Gao (2011). "Cellular uptake of elastic nanoparticles." Phys Rev Lett **107**(9): 098101.

Yu, B., H. C. Tai, W. Xue, L. J. Lee and R. J. Lee (2010). "Receptor-targeted nanocarriers for therapeutic delivery to cancer." Mol Membr Biol **27**(7): 286-298.

Yu, M. K., J. Park and S. Jon (2012). "Targeting strategies for multifunctional nanoparticles in cancer imaging and therapy." Theranostics **2**(1): 3-44.

Yu, X., C. Guo, P. B. Fisher, J. R. Subjeck and X. Y. Wang (2015). "Scavenger Receptors: Emerging Roles in Cancer Biology and Immunology." Adv Cancer Res **128**: 309-364.

Zhao, L., L. Liu, B. Guo and B. Zhu (2015). "Regulation of adaptive immune responses by guiding cell movements in the spleen." Frontiers in Microbiology **6**.

Zheng, M. and Z. Tian (2019). "Liver-Mediated Adaptive Immune Tolerance." Frontiers in Immunology **10**.

Zhu, M., G. Nie, H. Meng, T. Xia, A. Nel and Y. Zhao (2013). "Physicochemical properties determine nanomaterial cellular uptake, transport, and fate." Acc Chem Res **46**(3): 622-631.

Zhu, Y., L. Zhu, X. Wang and H. Jin (2022). "RNA-based therapeutics: an overview and prospectus." Cell Death Dis **13**(7): 644.

Zilker, C., D. Kozlova, V. Sokolova, H. Yan, M. Epple, K. Überla and V. Temchura (2017). "Nanoparticle-based B-cell targeting vaccines: Tailoring of humoral immune responses by functionalization with different TLR-ligands." Nanomedicine **13**(1): 173-182.

Zur, B. (2005). Laborchemische Referenzbereiche für Wistarratten und C57BL/6-Mäuse. Doktor der Medizin, Heinrich-Heine-Universität Düsseldorf.

10. Appendix

10.1. Publication 1

"Role of liver-mediated tolerance in NP-based tumor therapy"

This review has been published in MDPI (Cells). This review aimed to summarize the current knowledge on the use of NPs for immunotherapy of liver diseases with a focus on the role of liver NPCs. Several studies have shown that NPs accumulate strongly in the liver after systemic application. Starting at this point, me, as a shared-first author, carried out literature research and preparation of the review together with the co-authors. We focused on the importance of liver non-parenchymal cells (NPCs), Kupffer cells (KCs), liver sinusoidal endothelial cells (LSECs), and hepatic stellate cells (HSCs), and their potential role in the immunological outcome of systemic nano-vaccination approaches for tumor therapy in the liver and in other organs.

DOI: 10.3390/cells9091985

Published in: *Cells* **2020**, *9*(9), 1985.

Reprinted with permission under creative commons attribution 4.0 (CC BY-NC) from Cacicedo*, M.L.; **Medina-Montano*, C**.; Kaps, L.; Kappel, C.; Gehring, S.; Bros, M. Role of Liver-Mediated Tolerance in NP-Based Tumor Therapy. *Cells* **2020**, *9*, 1985. doi: 10.3390/cells9091985.

***** Authors contributed equally

cells

MDPI

Review

Role of Liver-Mediated Tolerance in Nanoparticle-Based Tumor Therapy

Maximiliano L. Cacicedo [1,†], Carolina Medina-Montano [2,†], Leonard Kaps [3], Cinja Kappel [2], Stephan Gehring [1] and Matthias Bros [2,*]

1 Children's Hospital, University Medical Center, Langenbeckstrasse 1, 55131 Mainz, Germany; mcaciced@uni-mainz.de (M.L.C.); Stephan.Gehring@uni-mainz.de (S.G.)
2 Department of Dermatology, University Medical Center Mainz, Langenbeckstrasse 1, 55131 Mainz, Germany; gmedinam@students.uni-mainz.de (C.M.-M.); cinkappe@uni-mainz.de (C.K.)
3 Department of Medicine, University Medical Center Mainz, I. Langenbeckstrasse 1, 55131 Mainz, Germany; lenardkaps@googlemail.com
* Correspondence: mbros@uni-mainz.de; Tel.: +49-6131-17-9846
† These authors contributed equally to this work.

Received: 4 August 2020; Accepted: 26 August 2020; Published: 28 August 2020

Abstract: In the last decades, the use of nanocarriers for immunotherapeutic purposes has gained a lot of attention, especially in the field of tumor therapy. However, most types of nanocarriers accumulate strongly in the liver after systemic application. Due to the default tolerance-promoting role of liver non-parenchymal cells (NPCs), Kupffer cells (KCs), liver sinusoidal endothelial cells (LSECs), and hepatic stellate cells (HSCs), their potential role on the immunological outcome of systemic nano-vaccination approaches for therapy of tumors in the liver and in other organs needs to be considered. Concerning immunological functions, KCs have been the focus until now, but recent studies have elucidated an important role of LSECs and HSCs as well. Therefore, this review aims to summarize current knowledge on the employment of nanocarriers for immunotherapeutic therapy of liver diseases and the overall role of liver NPCs in the context of nano-vaccination approaches. With regard to the latter, we discuss strategies on how to address liver NPCs, aiming to exploit and modulate their immunological properties, and alternatively how to avoid unwanted engagement of nano-vaccines by liver NPCs for tumor therapy.

Keywords: nano-vaccine; immunotherapy; tumor therapy; liver sinusoidal endothelial cells; Kupffer cells; hepatic stellate cells; tumor-associated macrophages

1. Introduction

During the last decades, the development of nanoparticles (NPs) that deliver drugs and biologicals in a cell type-specific manner has received growing interest as a new therapeutic strategy in cancer therapy [1]. Targeting may be an intrinsic property of the NP due to its size and surface properties [2] or can be conferred by conjugated moieties that bind target cell surface receptors, including antibodies, derivatives of natural ligands, and aptamers [3,4].

In case of tumor therapy, NPs may be designed to target tumor cells directly and to deliver cytotoxic drugs or biologicals [5]. More recently, direct targeting of regulatory immune cell types within the tumor microenvironment (TME), comprising tumor-associated macrophages (TAM), myeloid-derived suppressor cells (MDSCs), and regulatory T cells (Treg) that inhibit other immune cells both within the TME and in the periphery, has proven to be an interesting approach [6]. In that case, nano-vaccines may contain a payload, which either acts in a cytotoxic manner or serves to reprogram a regulatory immune cell to counteract tumor tolerance, e.g., by inhibiting the activity of transcription factor STAT

(signal transducer and activator of transcription) 3 that promotes expression of protolerogenic proteins like IL-10 [7]. Nano-vaccines aim to exert tumor-specific immune responses by co-delivery of a tumor antigen and an adjuvant to antigen-presenting cells (APCs) like dendritic cells (DCs), which constitute the most important APC population [8,9].

Topical nano-vaccination delivery, e.g., via the skin, may induce predominantly skin-targeting T effector cells. Hence, systemic delivery of a nano-vaccine may be preferable for therapy of metastatic tumors in order to induce T effector cells that may home any organ [10]. However, so far, virtually all types of functionalized NPs have been reported to accumulate in the liver for considerable extent after systemic application [11]. Therefore, unless the liver is the intended target organ of functionalized NP, for example in the case of treatment of liver fibrosis [12] or hepatocellular carcinoma (HCC) [13], the role of the liver as an obstacle in nano-vaccination needs to be elucidated.

This review aims to summarize knowledge on the immunoregulatory activity of liver non-parenchymal cells (NPCs) with a focus on liver sinusoidal endothelial cells (LSECs) and Kupffer cells (KCs) and on their interaction with systemically applied NP. In case of nano-vaccines that are employed to induce, e.g., antitumor responses, unwanted engagement by liver NPCs may result in tolerance-promoting effects. However, NP-based immunotherapeutic strategies may also aim to exploit the default tolerogenic function of liver NPCs for therapy of autoimmune diseases and allergies. Moreover, functionalized NPs have been used to reprogram liver macrophages with regulatory functions towards a proinflammatory state for tumor therapy.

2. NPC Populations of the Liver Contribute to its Tolerogenic Activity

The liver constitutes an important tolerance-promoting organ which is conferred by the concerted activity of non-parenchymal liver cell populations [14]. Antigen-specific tolerance in the liver is largely mediated by KCs that constitute the liver-resident macrophage population and by LSECs. Liver DCs have been ascribed an overall tolerogenic role as well, nicely reviewed by Dou et al. [15]. So far, it is well established that NPs engage KCs [16]. However, the role of LSECs in this regard and the consequences of antigen delivery to KCs and LSECs concerning their effect on immune responses have scarcely been addressed yet. Further, hepatic stellate cells (HSC), which also exert important immune-relevant functions, were shown to engage NPs as well [17].

2.1. Immunological Role of LSECs

LSECs represent about 60% of liver NPCs and are strategically placed lining the hepatic sinusoid [18]. Therefore, LSECs are the first liver cell type that may engage pathogens, immune complexes, and circulating lymphocytes. LSECs possess fenestrations acting as a sieve, which allow the exchange of fluid, solutes, and particles between the blood and the space of Disse [19] (Figure 1). LSECs act as scavengers to clear (potentially dangerous) macromolecules from blood. In addition, as described below, LSECs possess both innate and adaptive immune functions and are highly acknowledged as an important player in liver immunity, including HCC development and progression [18]. Most importantly, under homeostatic conditions, antigen presentation by LSEC leads to tolerance induction in $CD8^+$ cells and to the induction of immunosuppressive $CD4^+$ regulatory T cells (Treg) [20].

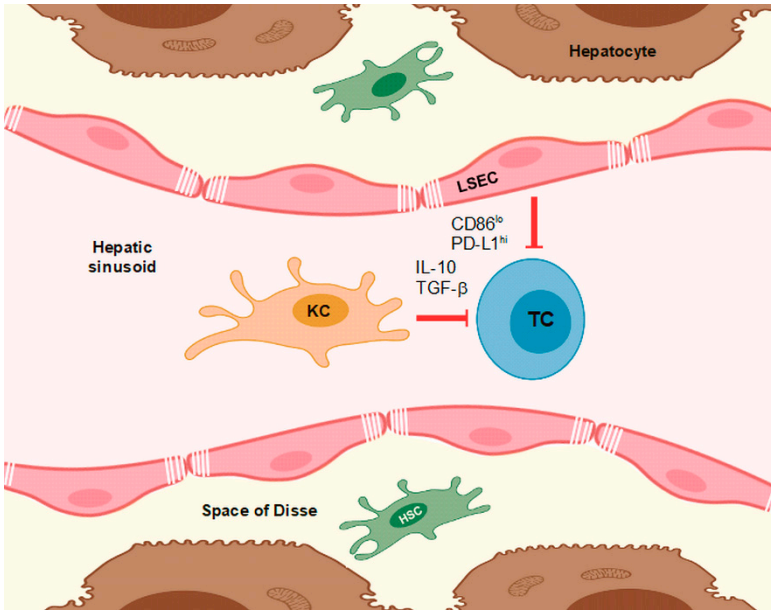

Figure 1. Kupffer cells (KCs) and liver sinusoidal endothelial cells (LSECs) by default confer T cell tolerance by presenting antigens in a non-stimulatory context, characterized by low expression of costimulatory receptors like CD86 but high expression of PD-L1 and by the release of anti-inflammatory cytokines like interleukin (IL)-10 and tumor growth factor (TGF)-β.

2.2. Immune-Relevant Properties of LSEC

2.2.1. Phenotype

Phenotypic characterization of LSEC requires combined detection of several surface receptors. LSECs are the only liver-resident cell population that expresses FcγRIIb2 (CD32b) [21], and besides, KCs express the mannose receptor CD206 at high levels [22]. CD45 is highly expressed on periportal LSECs, lowly expressed on midlobular LSECs, and is not apparent on centrilobular LSECs [23,24]. Therefore, differential expression of CD45 in LSECs allows for delineation of their localization within the liver. CD31 serves as a panendothelial cell marker [25]. In addition, LSECs were shown to express von-Willebrand-Factor (VWF), the scavenger receptors Stabilin-1 and -2, vascular endothelial growth factor receptors (VEGFR) 2 and 3, the CD44 homolog lymphatic vessel endothelial receptor (LYVE) 1, and the adhesion receptor CD146 [18,20,23,26]. Accordingly, LSECs can be phenotypically described as $CD31^{+}CD146^{+}$ $CD32b^{+}$.

2.2.2. Endocytic Capacity

LSECs have the highest endocytotic capacity of all human cell types [18]. Their clathrin-dependent endocytic machinery confers efficient uptake of foreign and physiological (waste) products, like connective tissue macromolecules, heparin, lysosomal enzymes, modified proteins and lipoproteins, and soluble IgG complexes [27]. LSECs are equipped with various endocytosis receptors, including scavenger receptors class A (SCARA1-5), B (SCARB1-3), E (SCARE1-2), and H (stabilin-12) [18,23,28]. As mentioned above, LSECs also express different C-type lectin receptors (CLRs). These receptors are predominantly expressed by professional APCs in a population-specific manner [29] and in a CLR-type-specific manner recognizing pathogen-specific glycoproteins [30], endogenous damage-associated molecular patterns derived from dead cells [31], and proteins with a tumor-dependently altered glycosylation pattern [32]. As shown for APCs, both the type of CLR engaged as well as concomitant triggering of other types of receptors, like TLR (Toll-like receptor), determine whether CLR engagement yields stimulatory or inhibitory signaling [33].

LSECs express the CLR CD206, which is also apparent on monocytes/macrophages and conventional DCs [34], and L-SIGN (liver/lymph node-specific intercellular adhesion molecule (ICAM)-3 grabbing non-integrin), also known as DC-SIGNR (DC-SIGN-related protein; CD209L), and LSECtin [35]. DC-SIGNR/L-SIGN is a homolog of DC-SIGN (CD209) which is expressed predominantly by cDC and by some macrophage populations [36]. Besides LSECs, macrophages [37], including KC [38] were reported to express LSECtin too. So far, L-SIGN and DC-SIGN were demonstrated to bind largely the same pathogen-associated glycoproteins [39,40], whereas LSECtin was shown to engage only a subset of viruses that bind DC-SIGN/DC-SIGNR [35].

LSECs recognize and endocytose IgG-containing immune complexes via FcγRIIb2 [18,20,23,28]. FcγRIIb is the only Fc receptor that induces inhibitory cell signaling upon engagement [21]. As described by Tanikagi and collegues, stimulation of activating FcγR in endothelial cells, vascular smooth muscle cells, and monocytes/macrophages causes a variety of cellular responses that may contribute to vascular disease pathogenesis [41].

2.2.3. Immune Functions

LSECs express various PRR (pathogen-associated recognition receptors), including TLR2-4, TLR6, TLR8, and TLR9 [42] as well as NOD (nucleotide binding oligomerization domain containing) 1/2 receptors [43], and produce innate cytokines in response to stimulation (e.g., tumor necrosis factor (TNF) α, IL-6, and IL-1β). LSECs exert APC activity during immune surveillance and liver inflammation and predominantly contribute to peripheral immune tolerance [44]. The APC activity of LSECs has been attributed to the constitutive and inducible expression of several surface markers and costimulatory molecules associated with professional APCs, such as major histocompatibility complex (MHC) I and II [45], ICAM (intercellular adhesion molecule) 1 [46], vascular cell adhesion protein (VCAM) 1 [47], CD40, CD80, CD86 [48], L-SIGN, and vascular adhesion protein (VAP) 1 [23]. Of note, LSECs can present antigens of exogenous origin via MHCII to $CD4^+$ T cells [49] and via MHCI to $CD8^+$ T cells [50], termed cross-presentation. Cross-presentation has also been reported to enable LSECs to present antigens derived from internalized apoptotic tumor cells to $CD8^+$ cells leading to T cell tolerance [50]. LSECs express the lectin galectin-1, which is known to bind and to induce apoptosis in activated T cells, resulting in immunological tolerance as well [19]. Of note, besides LSECs, only subpopulations of DCs are capable of cross-presenting antigens derived from internalized material [51]. In the case of LSECs, their tolerogenic phenotype as characterized by programmed death-ligand 1 $(PD\text{-}L1)^{high}$ $CD80/CD86^{low}$ expression by default supports induction of $CD8^+$ T cell tolerance [52]. Further, lipopolysaccharide-activated LSEC can induce naïve $CD4^+$ T cells to produce interferon (IFN)-γ, interleukin (IL)-4, interleukin (IL)-10, and tumor growth factor (TGF)-β but do not induce a stable T helper cell type (Th)1 or Th2 phenotype [53]. Besides, LSECs were reported to diminish the functional activity of Th1 and Th17 via PD-L1 and IL-10 [54]. Moreover, LSECs were shown to induce expression of the anti-inflammatory cytokine IL-10 in Th1 without affecting their IFN-γ production [55]. Thereby, LSECs also contribute to impairing autoreactive $CD4^+$ T cells in the periphery. Moreover, as compared to KCs, LSECs are more efficient at inducing differentiation of naïve $CD4^+$ T cells to $CD25^+Foxp3^+$ Treg due to their ability to secrete TGF-α and to tether exogenous TGF-β [49,52]. However, stimulation of LSECs with TLR1/2 ligands resulted in a profound increase in their T cell stimulatory activity, accompanied by upregulation of APC surface markers and a release of IL-12 promoting Th1 and cytotoxic T lymphocyte (CTL) induction [56].

2.2.4. Targeting of LSEC with Nanocarriers

Nano-vaccines can be used for treatment of allergies or autoimmune diseases aiming either to promote antigen-specific immune tolerance or to redirect an adaptive immune response. Concerning the former strategy, targeting of LSECs (and KCs) which promote antigen-specific tolerance to self- or foreign antigens by default is an attractive option [57]. Due to inhibitory signaling evoked by triggering FcγRIIb on LSECs, a nano-vaccine designed to induce tolerance may not necessarily require

co-delivery of an anti-inflammatory moiety. However, the latter may be necessary to override any potential activating signal induced by addressing a given receptor [58].

The potential of LSECs as a target for immunotherapy has scarcely been issued yet. Finding a way to adjust the NP surface for LSEC targeting is a universal approach to improve the efficacy of NP targeting and drug delivery to endothelial cell types in the liver [4]. LSECs are specialized in the uptake of soluble material and of immune complexes which have a mean diameter of about 40 nm, at a range from 20–150 nm [21]. KCs endocytose material as well but, due to Fc-receptor (FcR) and complement receptor (CR) expression, are also equipped to phagocytose pathogens, including bacteria and fungi [59]. Therefore, nano-vaccines intended to target LSECs should be of a smaller size (≤150 nm) [21].

LSEC-focused NP delivery may require targeting of endocytic surface receptors expressed by this cell population at high density, for example, CD206 [22]. However, this receptor is also expressed by KCs, other macrophages, and conventional DC populations throughout the body [59]. On the contrary, so far, the CLR L-SIGN has been reported as expressed by LSEC only [49]. Nonetheless, since DC-SIGN is homologous to L-SIGN, receptor ligands to be used as LSEC-targeting moieties may also address DCs and macrophages [35]. Engagement of CD206 promotes cross-presentation of derived antigens and may evoke stimulatory cellular signals that enhance APC activity [40]. So far, signaling consequences of triggering CD206 on LSECs as well as L-SIGN have not been studied. LSECs also express FcγRIIb at high extents to internalize immune complexes [60]. This Fc receptor is the only one which transmits an inhibitory signal upon engagement and, therefore, may contribute to the default tolerance-promoting state of LSECs [21]. The potential of LSEC-focused nano-vaccination to reestablish tolerance as required for effective treatment of autoimmune diseases and allergies has also been scarcely analyzed. So far, only one study has been published describing the use of an LSEC-targeting nano-vaccine with therapeutic efficacy in a model of ovalbumine-induced asthma [57].

It has been demonstrated that the default protolerogenic state of LSECs can be overcome by treatment with different stimuli, including TLR ligands. At an activated state, LSECs induce T effector cells [49]. This property might be of general interest with regard to the development of immunotherapeutic strategies for treatment of (liver) cancer, including tumor metastasis in the liver, as well as for treatment of (chronic) infections in this organ [57].

2.3. Liver Macrophages Maintain Tolerance under Homeostatic Conditions

2.3.1. KCs Are the Main Macrophage Population under Homeostatic Conditions

KCs have been described as the biggest macrophage population residing in the liver. These resident macrophages are a fundamental pillar for intrahepatic and general innate immunity. Actually, KCs represent around 80% of all tissue macrophages in the body [61]. KCs are mostly located in the liver sinusoids, an ideal place to display their role as sentinels of the immune system. However, recently, it has been described that KCs extend their cell body to the space of Disse where they can interact with HSC and hepatocytes [62]. This kind of interaction is important from a functional point of view as KCs are responsible, e.g., for the transfer of iron from apoptotic red blood cells to hepatocytes [63]. Very recently, a study using single-cell RNA sequencing analyzed the differences between intrahepatic monocyte/macrophage populations [64]. It is well-recognized by now that nonmigratory macrophages derived from embryogenic roots constitute KCs.

Following injury, there is an influx of monocyte-derived macrophages (MoMFs) into the liver (Figure 2). These macrophages then acquire the KC-specific genetic program [62]. It remains under discussion whether monocyte-derived macrophages in the liver need to be considered as a KC subpopulation [64,65]. MoMFs display pro-inflammatory functions and can be identified by their distinct phenotypic marker profile (HLA-DR$^+$CD25$^+$CD86$^+$) in human liver tissue. MoMFs remove protein complexes and particulate material and apoptotic cells from the blood by phagocytosis [66]. Their function complements LSECs, generating an efficient barrier to avoid penetration by pathogens

inside the liver through the portal vein [67]. In comparison, KCs confer immunomodulatory functions and can be identified by markers like CD163, CD206, and CD209 [6]. Besides, KC expresses MARCO (macrophage receptor with collagenous structure) [68]. The expression of MARCO in the tumor microenvironment (TEM) has been related to poor prognosis in different cancers [64].

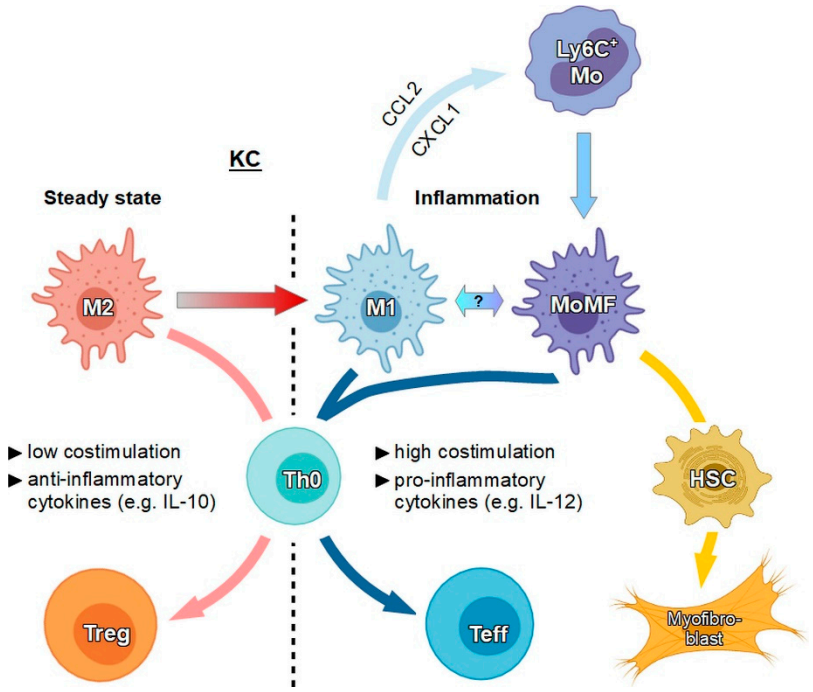

Figure 2. Under steady state conditions, KCs exhibit a protolerogenic M2-like immunophenotype and convert T cells, as shown for naïve CD4+ T cells (Th0), towards Treg due to low co-stimulation and secretion of anti-inflammatory cytokines. In response to stimulation, KCs may acquire an immunogenic M1-like state and may attract Ly6$^+$ monocytes (Mo), which then differentiate to monocyte-derived macrophages (MoMFs). The exact relation between KCs and MoMFs is unclear yet. Both immunogenic M1-like KCs and MoMFs induce T effector cells (Teff) since they express costimulatory receptors and pro-inflammatory cytokines at high extents. Furthermore, MoMFs induce trans-differentiation of hepatic stellate cells (HSCs) towards myofibroblasts.

Although the findings on liver function and immunity in mice usually fit well with human liver, those markers used to identify macrophage populations are different. Hepatic macrophage markers, for example, are commonly CD45$^+$F4/80$^+$. Of these, MoMFs express markers like CD16, CD32, and CD11c, while KCs express CD206 and CD209 [69–71].

2.3.2. KCs Promote Tolerance by Default but Exert Pro-Inflammatory Activity in Case of Liver Inflammation

Macrophages are equipped with various types of danger receptors that enable sensing and recognition of pathogens, such as scavenger receptors, TLR, retinoic acid-inducible gene (RIG)-like receptors (RLR), NOD-like receptors (NLR), and CLR [66]. KCs are equipped with TLR1-9 [72], complement receptors (CR1, CR3, and CR4) [73], and scavenger receptors including class AI/II [74].

Under steady state conditions, KCs are of a M2-like phenotype [75], characterized by low expression levels of MHCII, CD80, CD86, and CD40 and by generation of anti-inflammatory IL-10 at considerable extents [76] (see Figure 2). Antigen presentation by KC leads to CD4$^+$ T cell arrest and Treg expansion [77] as well as inhibition of antigen-specific T effector cells that have been induced by other APCs [69]. Furthermore, KCs also produce immunomodulatory mediators, such as IL-10, TGF-β, galectin-9, PD-L1, and PD-L2 during hepatitis infection, which suppress antiviral T cell

responses [69,78]. In summary, all of these effects elicit tolerogenic immunity [79]. IL-10 release also reduces the production of TNF-α, IL-6, and other cytokines contributing to tolerance [80]. Altogether, KCs are self-renewing, resident, and principally nonmigratory macrophages that serve as sentinels in the liver [65] and serve to promote tolerance by default [81]. Thus, immune responses against harmless antigens like those derived from the diet or from gut microbiota can be avoided [82]. However, under conditions like liver inflammation and fibrosis, KCs may repolarize towards a M1-like proinflammatory phenotype [77]. Above, activation of KC by stimulation of TLR also leads to an increase in CCL2 and chemokine (C-X-C motif) ligand (CXCL) 1 levels, attracting MoMFs [65]. In the case of MoMFs, once a foreign macromolecule is recognized by a danger receptor, a set of inflammatory cytokines like TNF-α, IL-1β, IL-6, IL-12, IL-15, and IL-18 and chemokines like chemokine (C-C motif) ligand (CCL)2–5 [77,83] are released. As a consequence, these mediators induce recruitment of several immune cells to the liver, like neutrophils, natural killer T (NKT) cells, and MoMFs, starting a cascade of immunological responses.

In addition, when KCs are depleted in the course of disease or liver injury, MoMFs have the capacity to regenerate liver macrophages by differentiating to KCs [84]. However, this regenerative situation may lead also to uncontrollable inflammation, which increases the probability of inducing liver damage. Meanwhile, KCs can promote tissue repair but may also induce aberrant tissue repair, resulting in fibrosis and cancer [65,69].

2.3.3. Targeting Hepatic Macrophage Populations with Nanocarriers for Immunotherapy

Liver macrophages work as a sink for all particulate material that circulates within blood. As an immediate consequence, targeting a specific macrophage population within the liver can be a difficult task. In general, NP internalization by hepatic macrophages was shown to be driven by different mechanisms including macropinocytosis, clathrin- as well as caveolin-mediated endocytosis, and additional endocytotic pathways [85]. There are two major cell type-targeting strategies: passive and active targeting. Passive targeting includes the modulation of NP properties, for example, size and surface charge, to increase its probability to reach the specific target cell.

Passive Targeting

The uptake of non-functionalized NPs by macrophages has been demonstrated to depend mainly on NP size and on macrophage phenotype. In a recent study, human-derived monocytes were differentiated in vitro towards macrophages using different cytokine cocktails, inducing so-called M1- and M2-like phenotypes, respectively [86]. Regardless of the macrophage phenotype, uptake of gold NP was much higher for NPs with a larger diameter (100 nm) than smaller NPs (15 nm and 60 nm). Notably, for each given type of NP, a big difference in uptake between differentially polarized macrophages was observed: those with a regulatory phenotype (M2 type) showed more than 40% higher uptake than proinflammatory macrophages (M1 type). In agreement, KCs were found to internalize relatively large NPs (>200 nm Ø) in vivo [85]. An interesting approach to assessing the intrinsic targeting properties of NP in a systemic manner, being mainly performed with liposomes, is the creation of formulation libraries in which several structural changes of NP are tested comparatively, such as changes in the type of phospholipids being used. Cell distribution studies allowed for identification of formulations that preferably accumulate in KC [87]. The preference in NP accumulation by regulatory macrophages has been exploited to induce tolerance against autoimmune diseases. In this regard, NPs loaded with self-antigen were directed to KCs, which in turn presented the antigen and induced T cell tolerance [88,89].

Active Targeting

NP functionalized with the sugar moiety mannose intending to target the main mannose binding receptor CD206 (also) expressed by KCs resulted in significantly increased binding to that cell population [78,90,91]. Dual targeting using two different oligosaccharides as ligands for mannose/fucose

receptors has proven to induce an accumulation of NPs in murine KCs. Attachment of these ligands, named 4-aminophenyl-α-D-mannopyranoside (APM) and 4-aminophenyl-β-L-fucopyranoside (APF), to liposomes has been used to study the contribution of KC to the accelerated blood clearance phenomenon and for specific depletion of KC [92,93]. However, as mentioned above, CD206 is also expressed by DCs and LSECs, and folate can bind to receptors on normal epithelial cells and tumor cells [94], suggesting that targeting of either receptor may not yield macrophage-specific NP uptake. As an alternative approach, novel synthetic peptides have been developed to target regulatory macrophages in a more exclusive manner. To this end, a peptide library selection approach was followed which allowed identification of a unique targeting ligand for murine M2-type macrophages, named M2pep. M2-type tumor associated macrophages (TAM) have been targeted using M2pep-modified liposomes to deplete them from melanoma [95]. Another study using HCC cells has studied M2pep binding also to TAMs, showing selectivity for M2-type macrophages. The authors also reported about M2pep binding to KCs, though binding to TAM was higher in comparison [96]. In summary, specific targeting to liver macrophage populations has been proven to be very challenging though extremely necessary to achieve different therapeutic objectives such as NP accumulation for specific drug delivery to induce or avoid immune responses or to modulate M1/M2 macrophage balance.

Reprogramming of Liver Macrophages

Macrophage plasticity is still a challenging field of study and is of huge interest for therapeutic purposes. Macrophages present in different tissues can modulate their phenotype with dependency on the surrounding environment [97]. Based on this fact, therapeutic strategies are followed, aiming to induce a shift between pro-inflammatory and tolerogenic phenotypes. Concerning the capability of NPs to reprogram hepatic macrophages, silica NPs have been reported to induce the release of TNF-α and IL-1β [98]. In another study, peptide-functionalized gold NPs have been the cause of liver macrophage polarization [99]. In that study, the bioactive tripeptides RGD and GLF were attached to the NP surface. RGD-NP induced a downregulation of both M1 and M2 surface markers. In contrast, GLF-NP upregulated M1 and M2 markers. Other strategies aim to deliver compounds that can activate/inhibit inflammatory pathways or can induce macrophage polarization. Although there is still quite the uncertainty about different molecular interactions involved in the complexity of macrophage functions, some progress has raised interest in this regard. For instance, peroxisome proliferator-activated receptor (PPAR-)γ has emerged as a master regulator for macrophage polarization [100]. Recent studies reported that upregulation of PPAR-γ shifts macrophages polarization from a M1- to a M2-like phenotype. A switch in macrophage polarization was associated with the interaction between PPAR-γ and nuclear factor kappa B (NF-κB) p65 signaling pathways [101]. This report showed that manipulation of PPAR-γ activity can modulate M1/M2 macrophage polarization, having the potential to prevent development of nonalcoholic fatty liver disease (NAFLD). Understanding of these immunomodulatory functions in liver macrophages can lead to the development of novel therapeutic strategies based on macrophage polarization.

Strategies involved in adapting macrophages to acquire a more inflammatory phenotype could be valuable for further development of immunotherapeutic cancer approaches.

2.4. Immunorelevant Functions of HSC

HSCs are mesenchymal cells and compromise about 5–8% of all liver cells [102]. HSCs fulfill a variety of tasks depending on their state as either activated or so-called quiescent HSC. Normally, HSCs are in a quiescent state and constitute the major storage site of vitamin A, secrete extracellular matrix components, and play a role in intercellular communication [103,104]. After their activation, as induced by liver injuries, HSCs transdifferentiate into myofibroblasts [105]. As such, they produce a lot of collagen, which explains their implication in the pathogenesis of liver fibrosis [106]. Besides, activated HSCs also influence the formation and the progression of HCC [107]. In addition, due to

their localization near KCs and LSECs in the perisinusoidal space (see Figure 1), HSCs play a role in hepatic immune responses, which qualifies them as a target for immunotherapy.

2.4.1. Immune Functions

Under homeostatic conditions, HSCs primarily contribute to the livers' immune tolerance, similar to other cell types found within the liver [108]. However, it is known that HSCs also express several TLRs which, when triggered, can induce the release of pro-inflammatory cytokines shaping the livers' response to injury or infection [109–111]. Besides a direct innate immune reaction by HSCs [112,113], this cell population also constitutes an important modulator of immune responses by interacting with immune cells like neutrophils [114], macrophages [115], DCs [112], and LSECs [116] via pro-inflammatory or inhibitory cytokines and trogocytosis, a process in which molecules are exchanged between cells [112]. Furthermore, it has been shown that activated HSCs can act as nonconventional APCs. In this regard, Winau and colleagues demonstrated that HSCs not only are capable of activating $CD4^+$ T cells [117,118] but also showed cross-priming capability, resulting in activation of $CD8^+$ T cells [119]. These various properties of HSCs to shape the livers' immune response offer new therapeutic opportunities for liver diseases.

2.4.2. HSC as a Target for Nanocarriers for Immunotherapy

The liver is the main organ in which systemically applied NPs accumulate and are cleared from the body. As outlined above, KCs and LSECs are considered the key players in this regard, but HSCs have also been reported to engulf NPs, albeit to a lesser extent, partly because their location hardly allows any contact with blood-borne particles before these would reach KCs or LSECs [17]. However, active targeting of HSCs by NPs conjugated with moieties that address surface receptors expressed at high density by this cell type may be an effective approach. Popular surface receptors for active targeting of HSCs are the mannose-6-phosphat (M6P) receptor [120], the retinol binding protein (RBP) receptor [121], the platelet-derived growth factor (PDGF) receptor [122], and the collagen type VI receptor [123]. All of these receptors have been targeted successfully in vivo and/or in vitro mainly with liposomal NPs sized between 15 and 400 nm (Ø), aimed to decrease the fibrotic activities of HSCs. Most of the published results about HSCs targeted in the context of NP-mediated immunotherapy are about the improvement of therapy for liver fibrosis, and several nanoparticular systems are already tested in clinical trials [12,124,125]. Although studies about nanocarriers targeting HSCs for the treatment of HCC are missing, by now, this could be a future approach. The potential of HSCs to act as APCs and their ability to cross-talk with other immune cells might open up new possibilities when it comes to the initiation or modulation of an immune response. Depending on the intention, the right type of actively targeted nanocarrier combined with a suitable drug, antigen, and/or adjuvant could vastly improve the therapy of liver fibrosis and presumably the treatment of HCC as well. The antifibrotic or antitumor effects of such types of nanomedicine could even be amplified if several liver cell types, interfering with each other, are targeted at the same time, leading to an effective multi-faceted approach.

Altogether, besides KCs and LSECs, HSCs have also become a target for NP-based (immuno)therapeutic approaches because of their implication in the onset and progression of liver fibrosis and HCC combined with their various immunological functions.

3. HCC—Risk Factors and Current Treatment

The liver can be considered an organ with high physical resilience as it possesses a remarkable capacity to regenerate from acute conditions, e.g., hepatectomy or drug-induced-liver injury [126]. Under chronic conditions, its regenerative capacity becomes a two-sided sword. It consists of parenchymal and non-parenchymal cells, while hepatocytes are the most abundant (>80%) and functionally active cells [127]. Albeit debates are still ongoing, there is mounting evidence that HCC derives primarily from transformed hepatic progenitor cells and hepatocytes as a consequence of accumulating genetic mutations and epigenetic alterations [128].

3.1. Risk Factors for HCC

The chronic component in the development of HCC is underlined by the fact that HCC occurs almost always (approximately 90%) in cirrhotic livers [129]. Cirrhosis can be considered a precancerous condition and represents the most important risk factor of HCC. Accordingly, cirrhotic patients run a yearly risk of approximately 5% for the development of HCC. Cirrhosis is characterized by an excessive accumulation of scare tissue, primarily collagen, in the liver. This severe distortion of the parenchymal and vascular structure represents the end-stage of every chronic liver disease. Other HCC-promoting risk factors are viral hepatitis B (and C), which together account globally for 80% of HCC cases [130,131].

Furthermore, metabolic liver disease has become the most common liver disease in developed countries and an increasing major risk factor for HCC [132,133]. Nonalcoholic fatty liver disease (NAFLD) had the highest population-attributable fraction of 37% for HCC [134]. In contrast to other underlying diseases, HCC occurs frequently in the absence of cirrhosis in NAFLD. A US population-based study of 1500 patients with HCC demonstrated that non-cirrhotic patients with NAFLD-associated HCC had a fivefold risk of having HCC compared to non-cirrhotic patients with hepatitis C virus (HCV)-associated HCC [135]. Diabetes, which displays an increasing incidence in the Western World, is an independent risk factor (2–3-fold) for HCC [136]. Insulin resistance with exacerbated production of reactive oxygen species lead to subclinical chronic hepatic inflammation, being a driver of hepatocarcinogenesis [137,138]. In addition, primary biliary cholangitis, a rare autoimmune disease, has been shown to predispose for HCC development [139]. Further, hemochromatosis, which causes accumulation of iron in inner organs and thereby their dysfunction has been identified as a risk factor for HCC [140]. Alcohol consumption is a common risk factor of HCC in the Western world [141]. Further risk factors are biotoxins such as aflatoxins, which play a minor role in industrialized countries [142].

3.2. Current Treatment Options for HCC

Altogether, HCC is the most frequent malignant form of primary liver cancer (annual incidence 7/100,000) and is the second leading cause of cancer-related deaths worldwide, accounting for more than 45,000 deaths per year only in Europe [143]. Management of HCC is complex and depends on the tumor extent, patient's comorbidities, and the remaining liver function as most treatments risk exacerbating the underlying disease. HCC treatment includes a multidisciplinary team, consisting of hepatologists, visceral surgeons, and interventional radiologists to achieve the best outcomes. Surgical resection is recommended as a curative treatment in HCC patients with respectable disease in an early stage [144,145]. Liver transplantation represents the most definite treatment option when patients meet the Milan criteria [146]. The Milan criteria describe the extent of the disease and take into account quantity, size, gross vascular invasion, and extrahepatic manifestations of the tumors [147]. Percutaneous local ablation by radiofrequency [148] or microwaves as well as transarterial chemoembolization [149] and proton beam are treatment options at an early or intermediate advanced state [148]. However, at advanced stages, systemic treatment remains the last therapeutic option. Sorafenib is a small-molecule multikinase inhibitor that inhibits VEGFR1-3, PDGF receptor-β, and Raf family kinases [150]. It was the first approved drug for first-line systemic treatment, prolonging the median survival of 10.7 months in the sorafenib group vs. 7.9 months in the placebo group [151]. Recently, the multikinase inhibitors levantinib [152] and regorafenib [153] were approved as first- and second-line therapy options after sorafenib treatment, respectively. In 2017 and 2018, the immune checkpoint inhibitors nivolumab [154] and pembrolizumab [155], both PD1-inhibitors, have emerged as second-line therapy, respectively. Recently, ramucirumab, an antiangiogenic VEGFR2 antagonist, expanded the field of second-line therapies and was approved for patients with high serums levels of α-fetoprotein (≥400 ng/mL) and previous treatment with sorafenib [156]. Despite significant progress having been made in systemic therapy of HCC, prognosis is still limited (median survival < 1 year) [130].

Thus, novel therapeutic approaches which are synergistic to established regimes are urgently needed to improve outcomes.

3.3. Macrophages Are Key Players in HCC Progression

The tumor biology of HCC can only be fully conceived when considering also the tumor surrounding tissue: the TME [157]. The extracellular matrix represents the non-cellular component of the TME. It contains polysaccharides (e.g., glycosaminoglycan hyaluronic acid) and proteoglycans which are found at high levels in the TME of HCC [158]. Beside the tumor cells, the cellular component of the TME consists of a variety of parenchymal and non-parenchymal cells, including tumor-associated fibroblasts, endothelial cells, adipocytes, and cells of the immune system. The sum of immune cells inside the TME build the tumor immune microenvironment (TIME). There is mounting evidence that the TME and especially the TIME play crucial roles in the development and progression of HCC [157].

KCs and MoMFs play pivotal roles in the development and growth of HCC in the TIME [78]. KCs are liver-resident macrophages, self-renewing, and non-migratory phagocytes and serve as sentinels for liver homeostasis [159]. Upon liver injury, they become activated and excrete inflammatory cytokines (e.g., TNF-α) and chemokines (e.g., CCL2), attracting numerous pro-inflammatory Ly-6C$^+$ monocytes from the bone marrow [78]. These inflammatory MoMFs activate HSCs and drive their trans-differentiation into activated myofibroblasts [160]. The latter are the major collagen-producing cells, and a main source of both profibrotic and proangiogenic cytokines (e.g., TGF-β1 and PDGF) in liver fibrogenesis [161].

Since both KCs and MoMFs possess high plasticity, TAMs are thought to derive from these two distinct macrophage populations [78]. As high numbers of TAMs are regularly observed in resections or explants of patients with HCC, they are supposed to promote development and progress of HCC [162]. This assumption is further supported by the fact that TAM numbers correlate with HCC progression and poor survival [163]. TAMs were also found to express PD-L1, which suppresses anti-tumoral CTL responses [164,165] (Figure 3). Furthermore, TAMs provide soluble factors that favor tumor cell proliferation, inhibit apoptosis of cancer cells and promote angiogenesis [157], and induce the conversion of fibroblasts towards cancer-associated fibroblasts (CAFs) [166], which in turn via modulation of the ECM and the production of numerous immunomodulatory soluble mediators shape the TME [167]. TAMs retain their plasticity and can switch their phenotype towards "antifibrotic" and putatively "anti-tumor" macrophages [168]. This phenotype is characterized by low expression of Ly-6C in mice and high expression of anti-inflammatory mediators (e.g., HGF and IL-10) and matrix (degrading) metalloproteinases (e.g., MMP-9, MMP-12, and MMP-13) [169]. Thus, a drug-induced phenotypic switch towards "good-natured" macrophages is an appealing concept and has gained increasing attention in basic and drug translational research in the last decade.

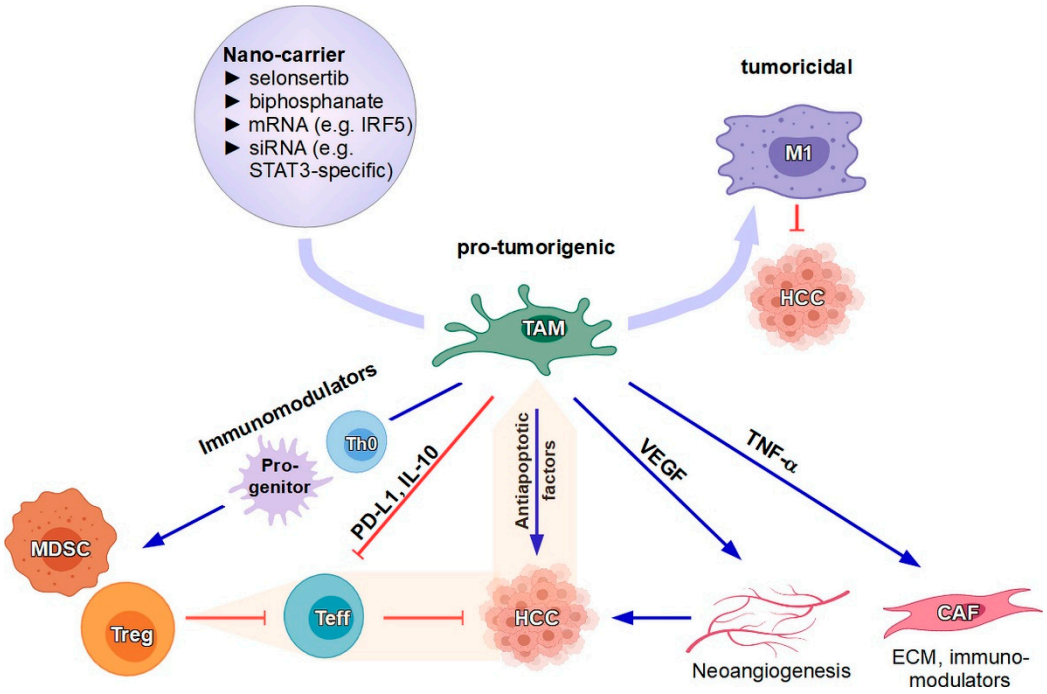

Figure 3. Hepatocellular carcinoma (HCC) generates numerous immunomodulatory soluble factors which govern the differentiation of infiltrating macrophages towards M2-like tumor-associated macrophages (TAMs) and the induction/expansion of myeloid-derived suppressor cells (MDSCs) and Treg and inhibit T effector cells (Teff). TAMs exert overall pro-tumorigenic effects by producing soluble mediators which support tumor progression directly and indirectly via VEGF-dependent neoangiogenesis, and induction of cancer-associated fibroblasts (CAFs) that also shape the tumor microenvironment (TME). Similar to HCC, TAMs also inhibit infiltrating Teff and promote MDSCs as well as Treg that also inhibit antitumor responses. Due to their crucial role, reprogramming of TAMs towards M1-like macrophages with tumoricidal activity has been evaluated using nanocarriers that deliver nucleic acid-based therapeutics. Moreover, drugs like selonsertib and bisphosphonate, previously shown to repolarize TAMs, are suitable payloads for TAM-targeting nanocarriers, thereby minimizing cytotoxicity.

3.4. Targeting of TAMs with NPs for Tumor Therapy

TAMs express rather a tolerogenic phenotype and thus provoke tumor progression and metastasis [170]. In this sense, it has been of great interest to induce TAM polarization towards a proinflammatory state that can elicit immune responses and tumor regression. TAMs can be targeted by nanoparticle-based drug delivery [13]. Nanocarriers are ideal for this purpose for three reasons. First, TAMs as phagocytes have a high scavenging capacity and efficiently engulf foreign particles, including NPs, by passive targeting [171]. Second, after intravenous injection in mice, the majority of nanocarriers like nanohydrogel particles (approximately 50 nm Ø) [172,173], hard-shell microbubbles (approximately 2 nm Ø), liposomes (approximately 2 nm Ø), and polymers (approximately 10 nm Ø) [90] accumulate efficiently in the liver and arrive in close proximity to liver macrophages. Third, cell-specific active targeting of NP may enhance their uptake by TAMs. TAMs express CD206, which efficiently binds mannose residues at high extents [174]. Mannose-functionalized nanohydrogel particles (ManNPs) loaded with colony stimulating factor (CSF)-1 receptor small interfering RNA (siRNA) demonstrated a robust knockdown of CSF-1 in CD206 overexpressing primary macrophages in vitro, while CD206-negative macrophages were not affected [173]. Thus, ManNPs represent a promising platform for cell type-specific delivery of siRNA to profibrotic macrophages which share characteristics with TAMs.

A recent study reported the use of polymeric NPs engineered to deliver mRNA-encoded modulatory proteins. Delivery of mRNA species that encoded interferon regulatory factor (IRF) 5 and IκB kinase (IKK)β, which activates IRF5 [175], was intended to cause a shift of TAMs towards a pro-inflammatory and cytotoxic M1-like phenotype [176]. In line, in in vivo models of advanced-stage ovarian cancer, metastatic melanoma, and glioblastoma, a reduced density of TAM in tumor lesions and concomitantly a marked increase in inflammatory myeloid cells with M1-type transcriptional profiles was observed. Even though this approach has not been tested for hepatic macrophages, the efficacy of this strategy proves that NP may be employed, e.g., for tumor therapy to repolarize macrophages with regulatory function to exert pro-inflammatory effects.

siRNA are double-stranded noncoding RNA oligos (20–25 base pairs) that sequence-specifically hybridize with their target mRNA to induce its degradation and to thereby diminish its half-life and translation [177]. RNA inference by siRNA allows transient silencing of virtually any gene, offering a huge value for therapeutic applications. It can be envisioned that NPs loaded with siRNA which target relevant pathways of TAMs may induce a phenotype switch or apoptosis of TAMs [178]. Cell type-specific delivery of therapeutic siRNA with functionalized carriers (e.g., ManNPs) to TAMs could improve efficacy and could avoid off-target effects in non-targeted cell types. For example, in a human tumor xenograft model, lipid NP loaded with siRNA specific for the M2-promoting transcription factor STAT (signal transducer and activator of transcription) 3 repolarized TAMs towards a M1-like immunophenotype and therefore reverted their pro-tumoral effects [179].

Hepatic macrophages and hepatocytes share a set of intracellular inflammatory signaling pathways (e.g., NF-κB, apoptosis signal-regulating kinase 1 (ASK-1), c-Jun N-terminal kinase, and p38) [180]. It is conceivable that specific inhibitors of inflammatory signaling like the ASK-1 inhibitor selonsertib have effects not only on hepatocyte metabolism but also on macrophage activation [78,181]. Encapsulation of this small-molecule drug in NPs could enhance the effect on TAMs. Further, bisphosphonates are anti-resorptive agents used in the clinic for osteoporosis [182] and complications of bone metastasis [183]. There is evidence that bisphosphonates also have an effect on the phenotype of macrophages, shifting it from pro-tumoral to tumoricidal [184]. Since bisphosphonates are largely excreted by the urinary tract und rapidly bind to bones upon intravenous administration, their encapsulation by biocompatible carriers could be of interest to target TAMs.

Altogether, TAMs are immunosuppressive cells in the TIME of HCC and were identified as a crucial cell population to fuel tumor development and growth. Therapeutic targeting of TAMs seems promising and might be achieved either by small-molecule or siRNA-based drugs encapsulated in NPs.

4. Conclusions

Liver NPCs are equipped with numerous receptors to internalize material and, by default, to confer tolerance [76]. Consequently, liver NPCs also strongly bind systemically applied NPs which, on the one hand, can be exploited for direct targeting of KCs or LSECs, e.g., to induce antigen-specific tolerance [57], but, on the other hand, constitutes an unwanted outcome in the case of NPs applied to evoke immune responses in secondary lymphoid organs. With regard to the latter, it is not clear yet whether LSECs and KCs that internalize nano-vaccines aimed to induce antitumor T cell responses may promote tumor antigen-specific tolerance as depicted in Figure 4 and therefore to counteract vaccine-induced adaptive immune reactions. As a perspective, nano-vaccines may be designed to co-deliver adjuvants that activate not only APCs in secondary lymphoid organs but also LSECs [185] and KCs [186] to promote the establishment of effector T cell responses throughout the body. However, it needs to be taken into account that hyperactivated liver NPCs, for example, M1-type KCs, may also cause inflammation and tissue damage [101,187]. Alternatively, nano-vaccines aimed to induce adaptive immune responses in secondary lymphoid organs may be generated in such a manner that unwanted binding and uptake by liver NPC is largely avoided. For this, nano-vaccines should not be decorated with APC-targeting moieties that are also recognized by surface receptors expressed by either liver immune cell population (e.g., CD206 [34]). In general, cellular interaction of NPs and NP-induced

alterations of the cellular immunophenotype should be assessed first in vitro, e.g., by using in parallel assays murine liver NPCs and spleen cells, also taking into account that a serum-dependently formed protein corona may strongly alter the targeting properties of NPs [188].

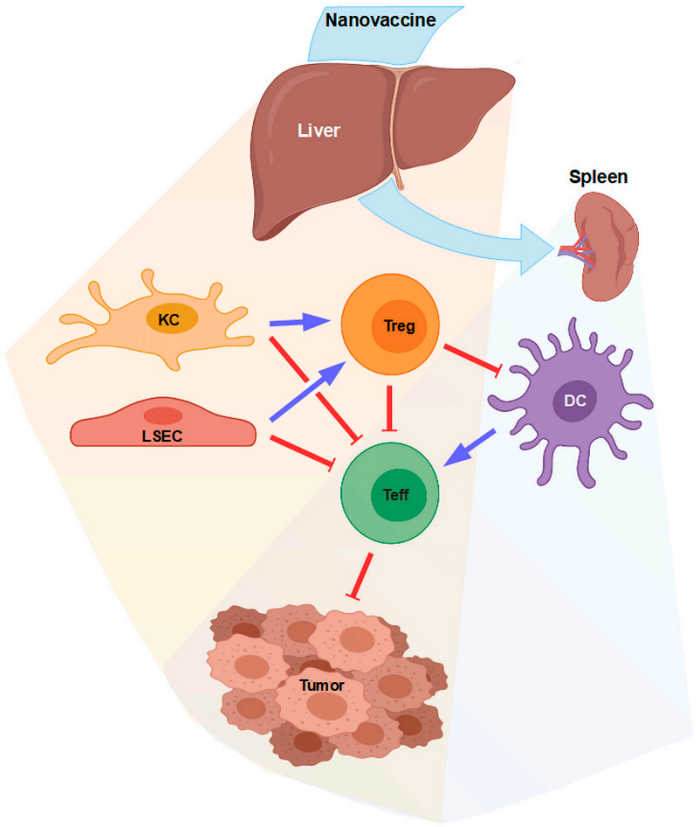

Figure 4. Systemically applied nano-vaccines often accumulate in the liver and reach secondary lymphoid organs only at low extents. In liver, nano-vaccines may be internalized largely by KCs and LSECs, which at default state promote Treg induction and could inhibit tumor-specific T effector cells induced by dendritic cells (DCs) in lymphoid organs. To avoid this outcome, nano-vaccines may either be designed to contain adjuvants that activate KCs/LSECs or to avoid unwanted uptake by liver non-parenchymal cells (NPCs).

Author Contributions: Each author has substantially contributed to drafting this review. M.L.C., S.G. and M.B. conceptualized the review topic. M.L.C., C.M.-M., L.K., C.K., and M.B. wrote the manuscript draft and M.B. revised it. All authors have read and agreed to the published version of the manuscript.

Funding: This work was funded by the Deutsche Forschungsgemeinschaft grant number SFB1066.

Conflicts of Interest: The authors declare no conflict of interest.

Abbreviations

APC	antigen presenting cell
APF	4-aminophenyl-β-L-fucopyranoside
APM	4-aminophenyl-α-D-mannopyranoside
ASK-1	apoptosis signal-regulating kinase 1
CAF	cancer-associated fibroblasts
CLR	C-type lectin receptor
CCL	chemokine (C-C motif) ligand
CLR	C-type lectin receptor

CR	complement receptor
CSF-1	colony stimulating factor 1
CTL	cytotoxic T lymphocyte
CXCL	chemokine (C-X-C motif) ligand
DC	dendritic cell
DC-SIGNR	DC-SIGN-related protein
FcR	Fc receptor
HCC	hepatocellular carcinoma
HSC	hepatic stellate cell
ICAM	intercellular adhesion molecule
IFN	interferon
IL	interleukin
IRF	interferon regulatory factor
KC	Kupffer cell
L-SIGN	liver/lymph node-specific intercellular adhesion molecule [ICAM]-3 grabbing non-integrin
LSEC	liver sinusoidal endothelial cells
LYVE-1	lymphatic vessel endothelial receptor 1
M6P	mannose-6-phosphat
ManNP	mannose-functionalized nanohydrogel particles
MARCO	macrophage receptor with collagenous structure
MDSC	myeloid-derived suppressor cell
MHC	major histocompatibility complex
MMP	matrix metalloproteinase
MoMF	monocyte-derived macrophages
NAFLD	non-alcoholic fatty liver disease
NF-κB	nuclear factor kappa B
NKT	natural killer T cell
NOD	nucleotide binding oligomerization domain containing
NPC	non-parenchymal cell
NP	nanoparticle
PDGF	platelet-derived growth factor
PD-L1	programmed death-ligand 1
PPAR	peroxisome proliferator activated receptor
RBP	retinol binding protein
PRR	pathogen-associated molecular pattern
RIG	retinoic acid-inducible gene
RLR	RIG-like receptor
SCAR	scavenger receptor
siRNA	small interfering RNA
STAT	signal transducer and activator of transcription
TAM	tumor-associated macrophage
TEM	tumor microenvironment
TIME	tumor immune microenvironment
TGF	tumor growth factor
Th	T helper cell
TLR	Toll-like receptor
Treg	regulatory T cell
VAP	vascular adhesion protein
VCAM	vascular cell adhesion protein
VEGFR	vascular endothelial growth factor
VWF	von-Willebrand-Factor

References

1. Lungu, I.I.; Grumezescu, A.M.; Volceanov, A.; Andronescu, E. Nanobiomaterials Used in Cancer Therapy: An Up-To-Date Overview. *Molecules* **2019**, *24*, 3547. [CrossRef] [PubMed]
2. Kranz, L.M.; Diken, M.; Haas, H.; Kreiter, S.; Loquai, C.; Reuter, K.C.; Meng, M.; Fritz, D.; Vascotto, F.; Hefesha, H.; et al. Systemic RNA delivery to dendritic cells exploits antiviral defence for cancer immunotherapy. *Nature* **2016**, *534*, 396–401. [CrossRef] [PubMed]
3. Baetke, S.C.; Lammers, T.; Kiessling, F. Applications of nanoparticles for diagnosis and therapy of cancer. *Br. J. Radiol.* **2015**, *88*, 20150207. [CrossRef] [PubMed]
4. Lee, A.R.; Nam, K.; Lee, B.J.; Lee, S.W.; Baek, S.M.; Bang, J.S.; Choi, S.K.; Park, S.J.; Kim, T.H.; Jeong, K.S.; et al. Hepatic Cellular Distribution of Silica Nanoparticles by Surface Energy Modification. *Int. J. Mol. Sci.* **2019**, *20*, 3812. [CrossRef] [PubMed]
5. Vijayan, V.; Mohapatra, A.; Uthaman, S.; Park, I.K. Recent Advances in Nanovaccines Using Biomimetic Immunomodulatory Materials. *Pharmaceutics* **2019**, *11*, 534. [CrossRef] [PubMed]
6. Li, S.Y.; Liu, Y.; Xu, C.F.; Shen, S.; Sun, R.; Du, X.J.; Xia, J.X.; Zhu, Y.H.; Wang, J. Restoring anti-tumor functions of T cells via nanoparticle-mediated immune checkpoint modulation. *J. Control. Release* **2016**, *231*, 17–28. [CrossRef]
7. Schmetterer, K.G.; Pickl, W.F. The IL-10/STAT3 axis: Contributions to immune tolerance by thymus and peripherally derived regulatory T-cells. *Eur. J. Immunol.* **2017**, *47*, 1256–1265. [CrossRef]
8. Paulis, L.E.; Mandal, S.; Kreutz, M.; Figdor, C.G. Dendritic cell-based nanovaccines for cancer immunotherapy. *Curr. Opin. Immunol.* **2013**, *25*, 389–395. [CrossRef]
9. Liu, J.; Wang, J.; Zhu, Q.; Yu, C.; Yin, J.; Zheng, L.; Li, A. Mannosylated PEGylated-Polyethyleneimine as Efficient CpG Oligodeoxynucleotide Carriers for Efficient Dendritic Cell Targeting Delivery and Activation. *J. Biomed. Nanotechnol.* **2019**, *15*, 1454–1467. [CrossRef]
10. Souto, E.B.; Ribeiro, A.F.; Ferreira, M.I.; Teixeira, M.C.; Shimojo, A.A.M.; Soriano, J.L.; Naveros, B.C.; Durazzo, A.; Lucarini, M.; Souto, S.B.; et al. New Nanotechnologies for the Treatment and Repair of Skin Burns Infections. *Int. J. Mol. Sci.* **2020**, *21*, 393. [CrossRef]
11. Meng, H.; Leong, W.; Leong, K.W.; Chen, C.; Zhao, Y. Walking the line: The fate of nanomaterials at biological barriers. *Biomaterials* **2018**, *174*, 41–53. [CrossRef] [PubMed]
12. Surendran, S.P.; Thomas, R.G.; Moon, M.J.; Jeong, Y.Y. Nanoparticles for the treatment of liver fibrosis. *Int. J. Nanomed.* **2017**, *12*, 6997–7006. [CrossRef] [PubMed]
13. Yong, S.B.; Chung, J.Y.; Song, Y.; Kim, J.; Ra, S.; Kim, Y.H. Non-viral nano-immunotherapeutics targeting tumor microenvironmental immune cells. *Biomaterials* **2019**, *219*, 119401. [CrossRef] [PubMed]
14. Zheng, M.; Tian, Z. Liver-Mediated Adaptive Immune Tolerance. *Front. Immunol.* **2019**, *10*, 2525. [CrossRef] [PubMed]
15. Dou, L.; Ono, Y.; Chen, Y.F.; Thomson, A.W.; Chen, X.P. Hepatic Dendritic Cells, the Tolerogenic Liver Environment, and Liver Disease. *Semin. Liver Dis.* **2018**, *38*, 170–180. [CrossRef] [PubMed]
16. Samuelsson, E.; Shen, H.; Blanco, E.; Ferrari, M.; Wolfram, J. Contribution of Kupffer cells to liposome accumulation in the liver. *Colloids Surf. B Biointerfaces* **2017**, *158*, 356–362. [CrossRef] [PubMed]
17. Park, J.K.; Utsumi, T.; Seo, Y.E.; Deng, Y.; Satoh, A.; Saltzman, W.M.; Iwakiri, Y. Cellular distribution of injected PLGA-nanoparticles in the liver. *Nanomed. Nanotechnol. Biol. Med.* **2016**, *12*, 1365–1374. [CrossRef]
18. Poisson, J.; Lemoinne, S.; Boulanger, C.; Durand, F.; Moreau, R.; Valla, D.; Rautou, P.E. Liver sinusoidal endothelial cells: Physiology and role in liver diseases. *J. Hepatol.* **2017**, *66*, 212–227. [CrossRef]
19. Karrar, A.; Broome, U.; Uzunel, M.; Qureshi, A.R.; Sumitran-Holgersson, S. Human liver sinusoidal endothelial cells induce apoptosis in activated T cells: A role in tolerance induction. *Gut* **2007**, *56*, 243–252. [CrossRef]
20. Sorensen, K.K.; Simon-Santamaria, J.; McCuskey, R.S.; Smedsrod, B. Liver Sinusoidal Endothelial Cells. *Compr. Physiol.* **2015**, *5*, 1751–1774. [CrossRef]
21. Ganesan, L.P.; Kim, J.; Wu, Y.; Mohanty, S.; Phillips, G.S.; Birmingham, D.J.; Robinson, J.M.; Anderson, C.L. FcgammaRIIb on liver sinusoidal endothelium clears small immune complexes. *J. Immunol.* **2012**, *189*, 4981–4988. [CrossRef] [PubMed]

22. Elvevold, K.; Simon-Santamaria, J.; Hasvold, H.; McCourt, P.; Smedsrod, B.; Sorensen, K.K. Liver sinusoidal endothelial cells depend on mannose receptor-mediated recruitment of lysosomal enzymes for normal degradation capacity. *Hepatology* **2008**, *48*, 2007–2015. [CrossRef] [PubMed]
23. DeLeve, L.D.; Maretti-Mira, A.C. Liver Sinusoidal Endothelial Cell: An Update. *Semin. Liver Dis.* **2017**, *37*, 377–387. [CrossRef] [PubMed]
24. Xie, G.; Wang, L.; Wang, X.; Wang, L.; DeLeve, L.D. Isolation of periportal, midlobular, and centrilobular rat liver sinusoidal endothelial cells enables study of zonated drug toxicity. *Am. J. Physiol. Gastrointest. Liver Physiol.* **2010**, *299*, G1204–G1210. [CrossRef] [PubMed]
25. Lertkiatmongkol, P.; Liao, D.; Mei, H.; Hu, Y.; Newman, P.J. Endothelial functions of platelet/endothelial cell adhesion molecule-1 (CD31). *Curr. Opin. Hematol.* **2016**, *23*, 253–259. [CrossRef]
26. Dingle, A.M.; Yap, K.K.; Gerrand, Y.W.; Taylor, C.J.; Keramidaris, E.; Lokmic, Z.; Kong, A.M.; Peters, H.L.; Morrison, W.A.; Mitchell, G.M. Characterization of isolated liver sinusoidal endothelial cells for liver bioengineering. *Angiogenesis* **2018**, *21*, 581–597. [CrossRef]
27. Simon-Santamaria, J.; Malovic, I.; Warren, A.; Oteiza, A.; Le Couteur, D.; Smedsrod, B.; McCourt, P.; Sorensen, K.K. Age-related changes in scavenger receptor-mediated endocytosis in rat liver sinusoidal endothelial cells. *J. Gerontol. A Biol. Sci. Med. Sci.* **2010**, *65*, 951–960. [CrossRef]
28. Meyer, J.; Gonelle-Gispert, C.; Morel, P.; Buhler, L. Methods for Isolation and Purification of Murine Liver Sinusoidal Endothelial Cells: A Systematic Review. *PLoS ONE* **2016**, *11*, e0151945. [CrossRef]
29. Busold, S.; Nagy, N.A.; Tas, S.W.; van Ree, R.; de Jong, E.C.; Geijtenbeek, T.B.H. Various Tastes of Sugar: The Potential of Glycosylation in Targeting and Modulating Human Immunity via C-Type Lectin Receptors. *Front. Immunol.* **2020**, *11*, 134. [CrossRef]
30. Mnich, M.E.; van Dalen, R.; van Sorge, N.M. C-Type Lectin Receptors in Host Defense Against Bacterial Pathogens. *Front. Cell Infect. Microbiol.* **2020**, *10*, 309. [CrossRef]
31. Drouin, M.; Saenz, J.; Chiffoleau, E. C-Type Lectin-Like Receptors: Head or Tail in Cell Death Immunity. *Front. Immunol.* **2020**, *11*, 251. [CrossRef] [PubMed]
32. Nonaka, M.; Ma, B.Y.; Murai, R.; Nakamura, N.; Baba, M.; Kawasaki, N.; Hodohara, K.; Asano, S.; Kawasaki, T. Glycosylation-dependent interactions of C-type lectin DC-SIGN with colorectal tumor-associated Lewis glycans impair the function and differentiation of monocyte-derived dendritic cells. *J. Immunol.* **2008**, *180*, 3347–3356. [CrossRef] [PubMed]
33. Del Fresno, C.; Iborra, S.; Saz-Leal, P.; Martínez-López, M.; Sancho, D. Flexible Signaling of Myeloid C-Type Lectin Receptors in Immunity and Inflammation. *Front. Immunol.* **2018**, *9*, 804. [CrossRef] [PubMed]
34. Pustylnikov, S.; Sagar, D.; Jain, P.; Khan, Z.K. Targeting the C-type lectins-mediated host-pathogen interactions with dextran. *J. Pharm. Pharm. Sci.* **2014**, *17*, 371–392. [CrossRef]
35. Zhang, F.; Ren, S.; Zuo, Y. DC-SIGN, DC-SIGNR and LSECtin: C-type lectins for infection. *Int. Rev. Immunol.* **2014**, *33*, 54–66. [CrossRef]
36. Van den Berg, L.M.; Gringhuis, S.I.; Geijtenbeek, T.B. An evolutionary perspective on C-type lectins in infection and immunity. *Ann. N. Y. Acad. Sci.* **2012**, *1253*, 149–158. [CrossRef]
37. Yang, Z.; Li, Q.; Wang, X.; Jiang, X.; Zhao, D.; Lin, X.; He, F.; Tang, L. C-type lectin receptor LSECtin-mediated apoptotic cell clearance by macrophages directs intestinal repair in experimental colitis. *Proc. Natl. Acad. Sci. USA* **2018**, *115*, 11054–11059. [CrossRef]
38. Domínguez-Soto, A.; Aragoneses-Fenoll, L.; Gómez-Aguado, F.; Corcuera, M.T.; Clária, J.; García-Monzón, C.; Bustos, M.; Corbí, A.L. The pathogen receptor liver and lymph node sinusoidal endotelial cell C-type lectin is expressed in human Kupffer cells and regulated by PU.1. *Hepatology* **2009**, *49*, 287–296. [CrossRef]
39. Malovic, I.; Sorensen, K.K.; Elvevold, K.H.; Nedredal, G.I.; Paulsen, S.; Erofeev, A.V.; Smedsrod, B.H.; McCourt, P.A. The mannose receptor on murine liver sinusoidal endothelial cells is the main denatured collagen clearance receptor. *Hepatology* **2007**, *45*, 1454–1461. [CrossRef]
40. Cormier, E.G.; Durso, R.J.; Tsamis, F.; Boussemart, L.; Manix, C.; Olson, W.C.; Gardner, J.P.; Dragic, T. L-SIGN (CD209L) and DC-SIGN (CD209) mediate transinfection of liver cells by hepatitis C virus. *Proc. Natl. Acad. Sci. USA* **2004**, *101*, 14067–14072. [CrossRef]
41. Tanigaki, K.; Sundgren, N.; Khera, A.; Vongpatanasin, W.; Mineo, C.; Shaul, P.W. Fcgamma receptors and ligands and cardiovascular disease. *Circ. Res.* **2015**, *116*, 368–384. [CrossRef] [PubMed]

42. Wu, J.; Meng, Z.; Jiang, M.; Zhang, E.; Trippler, M.; Broering, R.; Bucchi, A.; Krux, F.; Dittmer, U.; Yang, D.; et al. Toll-like receptor-induced innate immune responses in non-parenchymal liver cells are cell type-specific. *Immunology* **2010**, *129*, 363–374. [CrossRef] [PubMed]
43. Huang, S.; Wu, J.; Gao, X.; Zou, S.; Chen, L.; Yang, X.; Sun, C.; Du, Y.; Zhu, B.; Li, J.; et al. LSECs express functional NOD1 receptors: A role for NOD1 in LSEC maturation-induced T cell immunity in vitro. *Mol. Immunol.* **2018**, *101*, 167–175. [CrossRef] [PubMed]
44. Kruse, N.; Neumann, K.; Schrage, A.; Derkow, K.; Schott, E.; Erben, U.; Kuhl, A.; Loddenkemper, C.; Zeitz, M.; Hamann, A.; et al. Priming of CD4+ T cells by liver sinusoidal endothelial cells induces CD25low forkhead box protein 3- regulatory T cells suppressing autoimmune hepatitis. *Hepatology* **2009**, *50*, 1904–1913. [CrossRef] [PubMed]
45. Rubinstein, D.; Roska, A.K.; Lipsky, P.E. Liver sinusoidal lining cells express class II major histocompatibility antigens but are poor stimulators of fresh allogeneic T lymphocytes. *J. Immunol.* **1986**, *137*, 1803–1810.
46. Damle, N.K.; Aruffo, A. Vascular cell adhesion molecule 1 induces T-cell antigen receptor-dependent activation of CD4+T lymphocytes. *Proc. Natl. Acad. Sci. USA* **1991**, *88*, 6403–6407. [CrossRef]
47. Lalor, P.F.; Edwards, S.; McNab, G.; Salmi, M.; Jalkanen, S.; Adams, D.H. Vascular adhesion protein-1 mediates adhesion and transmigration of lymphocytes on human hepatic endothelial cells. *J. Immunol.* **2002**, *169*, 983–992. [CrossRef]
48. Slawek, A.; Maj, T.; Chelmonska-Soyta, A. CD40, CD80, and CD86 costimulatory molecules are differentially expressed on murine splenic antigen-presenting cells during the pre-implantation period of pregnancy, and they modulate regulatory T-cell abundance, peripheral cytokine response, and pregnancy outcome. *Am. J. Reprod. Immunol.* **2013**, *70*, 116–126. [CrossRef]
49. Knolle, P.A.; Wohlleber, D. Immunological functions of liver sinusoidal endothelial cells. *Cell. Mol. Immunol.* **2016**, *13*, 347–353. [CrossRef]
50. Berg, M.; Wingender, G.; Djandji, D.; Hegenbarth, S.; Momburg, F.; Hammerling, G.; Limmer, A.; Knolle, P. Cross-presentation of antigens from apoptotic tumor cells by liver sinusoidal endothelial cells leads to tumor-specific CD8+ T cell tolerance. *Eur. J. Immunol.* **2006**, *36*, 2960–2970. [CrossRef]
51. Blander, J.M. Regulation of the Cell Biology of Antigen Cross-Presentation. *Annu. Rev. Immunol.* **2018**, *36*, 717–753. [CrossRef]
52. Diehl, L.; Schurich, A.; Grochtmann, R.; Hegenbarth, S.; Chen, L.; Knolle, P.A. Tolerogenic maturation of liver sinusoidal endothelial cells promotes B7-homolog 1-dependent CD8+ T cell tolerance. *Hepatology* **2008**, *47*, 296–305. [CrossRef] [PubMed]
53. Knolle, P.A.; Germann, T.; Treichel, U.; Uhrig, A.; Schmitt, E.; Hegenbarth, S.; Lohse, A.W.; Gerken, G. Endotoxin down-regulates T cell activation by antigen-presenting liver sinusoidal endothelial cells. *J. Immunol.* **1999**, *162*, 1401–1407. [PubMed]
54. Carambia, A.; Frenzel, C.; Bruns, O.T.; Schwinge, D.; Reimer, R.; Hohenberg, H.; Huber, S.; Tiegs, G.; Schramm, C.; Lohse, A.W.; et al. Inhibition of inflammatory CD4 T cell activity by murine liver sinusoidal endothelial cells. *J. Hepatol.* **2013**, *58*, 112–118. [CrossRef] [PubMed]
55. Neumann, K.; Rudolph, C.; Neumann, C.; Janke, M.; Amsen, D.; Scheffold, A. Liver sinusoidal endothelial cells induce immunosuppressive IL-10-producing Th1 cells via the Notch pathway. *Eur. J. Immunol.* **2015**, *45*, 2008–2016. [CrossRef]
56. Liu, J.; Jiang, M.; Ma, Z.; Dietze, K.K.; Zelinskyy, G.; Yang, D.; Dittmer, U.; Schlaak, J.F.; Roggendorf, M.; Lu, M. TLR1/2 ligand-stimulated mouse liver endothelial cells secrete IL-12 and trigger CD8+ T cell immunity in vitro. *J. Immunol.* **2013**, *191*, 6178–6190. [CrossRef]
57. Liu, Q.; Wang, X.; Liu, X.; Kumar, S.; Gochman, G.; Ji, Y.; Liao, Y.P.; Chang, C.H.; Situ, W.; Lu, J.; et al. Use of Polymeric Nanoparticle Platform Targeting the Liver To Induce Treg-Mediated Antigen-Specific Immune Tolerance in a Pulmonary Allergen Sensitization Model. *ACS Nano* **2019**, *13*, 4778–4794. [CrossRef]
58. Arosio, D.; Chiodo, F.; Reina, J.J.; Marelli, M.; Penades, S.; van Kooyk, Y.; Garcia-Vallejo, J.J.; Bernardi, A. Effective targeting of DC-SIGN by alpha-fucosylamide functionalized gold nanoparticles. *Bioconjug. Chem.* **2014**, *25*, 2244–2251. [CrossRef]
59. Toth, C.A.; Thomas, P. Liver endocytosis and Kupffer cells. *Hepatology* **1992**, *16*, 255–266. [CrossRef]
60. Ishikawa, T.; Yokoyama, H.; Matsuura, T.; Fujiwara, Y. Fc gamma RIIb expression levels in human liver sinusoidal endothelial cells during progression of non-alcoholic fatty liver disease. *PLoS ONE* **2019**, *14*, e0211543. [CrossRef]

61. Jenne, C.N.; Kubes, P. Immune surveillance by the liver. *Nat. Immunol.* **2013**, *14*, 996–1006. [CrossRef]
62. Bonnardel, J.; T'Jonck, W.; Gaublomme, D.; Browaeys, R.; Scott, C.L.; Martens, L.; Vanneste, B.; De Prijck, S.; Nedospasov, S.A.; Kremer, A.; et al. Stellate Cells, Hepatocytes, and Endothelial Cells Imprint the Kupffer Cell Identity on Monocytes Colonizing the Liver Macrophage Niche. *Immunity* **2019**, *51*, 638–654.e639. [CrossRef] [PubMed]
63. Bilzer, M.; Roggel, F.; Gerbes, A.L. Role of Kupffer cells in host defense and liver disease. *Liver Int.* **2006**, *26*, 1175–1186. [CrossRef] [PubMed]
64. MacParland, S.A.; Liu, J.C.; Ma, X.Z.; Innes, B.T.; Bartczak, A.M.; Gage, B.K.; Manuel, J.; Khuu, N.; Echeverri, J.; Linares, I.; et al. Single cell RNA sequencing of human liver reveals distinct intrahepatic macrophage populations. *Nat. Commun.* **2018**, *9*, 4383. [CrossRef]
65. Guillot, A.; Tacke, F. Liver Macrophages: Old Dogmas and New Insights. *Hepatol. Commun.* **2019**, *3*, 730–743. [CrossRef] [PubMed]
66. Boltjes, A.; Movita, D.; Boonstra, A.; Woltman, A.M. The role of Kupffer cells in hepatitis B and hepatitis C virus infections. *J. Hepatol.* **2014**, *61*, 660–671. [CrossRef]
67. Vollmar, B.; Menger, M.D. The hepatic microcirculation: Mechanistic contributions and therapeutic targets in liver injury and repair. *Physiol. Rev.* **2009**, *89*, 1269–1339. [CrossRef]
68. Movita, D.; Kreefft, K.; Biesta, P.; van Oudenaren, A.; Leenen, P.J.; Janssen, H.L.; Boonstra, A. Kupffer cells express a unique combination of phenotypic and functional characteristics compared with splenic and peritoneal macrophages. *J. Leukoc. Biol.* **2012**, *92*, 723–733. [CrossRef]
69. Van der Heide, D.; Weiskirchen, R.; Bansal, R. Therapeutic Targeting of Hepatic Macrophages for the Treatment of Liver Diseases. *Front. Immunol.* **2019**, *10*, 2852. [CrossRef]
70. Chen, G.; Ni, Y.; Nagata, N.; Xu, L.; Zhuge, F.; Nagashimada, M.; Kaneko, S.; Ota, T. Pirfenidone prevents and reverses hepatic insulin resistance and steatohepatitis by polarizing M2 macrophages. *Lab. Investig.* **2019**, *99*, 1335–1348. [CrossRef]
71. Huang, H.; Zhang, X.; Zhang, C.; Chen, H.; Ling, Q.; Zheng, S. The time-dependent shift in the hepatic graft and recipient macrophage pool following liver transplantation. *Cell. Mol. Immunol.* **2020**, *17*, 412–414. [CrossRef] [PubMed]
72. Su, G.L.; Klein, R.D.; Aminlari, A.; Zhang, H.Y.; Steinstraesser, L.; Alarcon, W.H.; Remick, D.G.; Wang, S.C. Kupffer cell activation by lipopolysaccharide in rats: Role for lipopolysaccharide binding protein and toll-like receptor 4. *Hepatology* **2000**, *31*, 932–936. [CrossRef] [PubMed]
73. Hinglais, N.; Kazatchkine, M.D.; Mandet, C.; Appay, M.D.; Bariety, J. Human liver Kupffer cells express CR1, CR3, and CR4 complement receptor antigens. An immunohistochemical study. *Lab. Investig.* **1989**, *61*, 509–514. [PubMed]
74. Hughes, D.A.; Fraser, I.P.; Gordon, S. Murine macrophage scavenger receptor: In vivo expression and function as receptor for macrophage adhesion in lymphoid and non-lymphoid organs. *Eur. J. Immunol.* **1995**, *25*, 466–473. [CrossRef]
75. Dey, A.; Allen, J.; Hankey-Giblin, P.A. Ontogeny and polarization of macrophages in inflammation: Blood monocytes versus tissue macrophages. *Front. Immunol.* **2014**, *5*, 683. [CrossRef] [PubMed]
76. Karimi, M.H.; Geramizadeh, B.; Malek-Hosseini, S.A. Tolerance Induction in Liver. *Int. J. Organ Transpl. Med.* **2015**, *6*, 45–54.
77. Heymann, F.; Peusquens, J.; Ludwig-Portugall, I.; Kohlhepp, M.; Ergen, C.; Niemietz, P.; Martin, C.; van Rooijen, N.; Ochando, J.C.; Randolph, G.J.; et al. Liver Inflammation Abrogates Immunological Tolerance Induced by Kupffer Cells. *Hepatology* **2015**, *62*, 279–291. [CrossRef]
78. Tacke, F. Targeting hepatic macrophages to treat liver diseases. *J. Hepatol.* **2017**, *66*, 1300–1312. [CrossRef]
79. Abdullah, Z.; Knolle, P.A. Liver macrophages in healthy and diseased liver. *Pflug. Arch. Eur. J. Physiol.* **2017**, *469*, 553–560. [CrossRef]
80. Knolle, P.; Schlaak, J.; Uhrig, A.; Kempf, P.; Gerken, G.; Btischenfelde, M. Human Kupffer cells secrete IL-10 in response to lipopolysaccharide (LPS) challenge. *J. Hepatol.* **1995**, *22*, 226–229. [CrossRef]
81. Doherty, D.G. Immunity, tolerance and autoimmunity in the liver: A comprehensive review. *J. Autoimmun.* **2016**, *66*, 60–75. [CrossRef]
82. Doherty, D.G. Antigen-specific immune tolerance in the liver. *Nat. Biomed. Eng.* **2019**, *3*, 763–765. [CrossRef] [PubMed]

83. Jager, J.; Aparicio-Vergara, M.; Aouadi, M. Liver innate immune cells and insulin resistance: The multiple facets of Kupffer cells. *J. Intern. Med.* **2016**, *280*, 209–220. [CrossRef] [PubMed]
84. Scott, C.L.; Zheng, F.; De Baetselier, P.; Martens, L.; Saeys, Y.; De Prijck, S.; Lippens, S.; Abels, C.; Schoonooghe, S.; Raes, G.; et al. Bone marrow-derived monocytes give rise to self-renewing and fully differentiated Kupffer cells. *Nat. Commun.* **2016**, *7*, 10321. [CrossRef] [PubMed]
85. Colino, C.I.; Lanao, J.M.; Gutierrez-Millan, C. Targeting of Hepatic Macrophages by Therapeutic Nanoparticles. *Front. Immunol.* **2020**, *11*, 218. [CrossRef]
86. MacParland, S.A.; Tsoi, K.M.; Ouyang, B.; Ma, X.Z.; Manuel, J.; Fawaz, A.; Ostrowski, M.A.; Alman, B.A.; Zilman, A.; Chan, W.C.W.; et al. Phenotype Determines Nanoparticle Uptake by Human Macrophages from Liver and Blood. *ACS Nano* **2017**, *11*, 2428–2443. [CrossRef]
87. Gan, Z.; Lokugamage, M.P.; Hatit, M.Z.C.; Loughrey, D.; Paunovska, K.; Sato, M.; Cristian, A.; Dahlman, J.E. Nanoparticles containing constrained phospholipids deliver mRNA to liver immune cells in vivo without targeting ligands. *Bioeng. Transl. Med.* **2020**. [CrossRef]
88. Saito, E.; Kuo, R.; Kramer, K.R.; Gohel, N.; Giles, D.A.; Moore, B.B.; Miller, S.D.; Shea, L.D. Design of biodegradable nanoparticles to modulate phenotypes of antigen-presenting cells for antigen-specific treatment of autoimmune disease. *Biomaterials* **2019**, *222*, 119432. [CrossRef]
89. Hunter, Z.; McCarthy, D.P.; Yap, W.T.; Harp, C.T.; Getts, D.R.; Shea, L.D.; Miller, S.D. A biodegradable nanoparticle platform for the induction of antigen-specific immune tolerance for treatment of autoimmune disease. *ACS Nano* **2014**, *8*, 2148–2160. [CrossRef]
90. Ergen, C.; Heymann, F.; Al Rawashdeh, W.; Gremse, F.; Bartneck, M.; Panzer, U.; Pola, R.; Pechar, M.; Storm, G.; Mohr, N.; et al. Targeting distinct myeloid cell populations in vivo using polymers, liposomes and microbubbles. *Biomaterials* **2017**, *114*, 106–120. [CrossRef]
91. Melgert, B.N.; Olinga, P.; Van Der Laan, J.M.; Weert, B.; Cho, J.; Schuppan, D.; Groothuis, G.M.; Meijer, D.K.; Poelstra, K. Targeting dexamethasone to Kupffer cells: Effects on liver inflammation and fibrosis in rats. *Hepatology* **2001**, *34*, 719–728. [CrossRef] [PubMed]
92. Lai, C.; Li, C.; Luo, X.; Liu, M.; Liu, X.; Hu, L.; Kang, L.; Qiu, Q.; Deng, Y.; Song, Y. Use of Dual-Ligand Modification in Kupffer Cell-Targeted Liposomes to Examine the Contribution of Kupffer Cells to Accelerated Blood Clearance Phenomenon. *Mol. Pharm.* **2018**, *15*, 2548–2558. [CrossRef] [PubMed]
93. Lai, C.; Li, C.; Liu, M.; Qiu, Q.; Luo, X.; Liu, X.; Hu, L.; Deng, Y.; Song, Y. Effect of Kupffer cells depletion on ABC phenomenon induced by Kupffer cells-targeted liposomes. *Asian J. Pharm. Sci.* **2019**, *14*, 455–464. [CrossRef] [PubMed]
94. Cieslewicz, M.; Tang, J.; Yu, J.L.; Cao, H.; Zaèaljeèski, M.; Motoyama, K.; Lieber, A.; Raines, E.W.; Pun, S.H. Targeted delièery of proapoptotic peptides to tumor-associated macrophages improèes surèièal. *Proc. Natl. Acad. Sci. USA* **2013**, *110*, 15919–15924. [CrossRef]
95. Qian, Y.; Qiao, S.; Dai, Y.; Xu, G.; Dai, B.; Lu, L.; Yu, X.; Luo, Q.; Zhang, Z. Molecular-Targeted Immunotherapeutic Strategy for Melanoma via Dual-Targeting Nanoparticles Delivering Small Interfering RNA to Tumor-Associated Macrophages. *ACS Nano* **2017**, *11*, 9536–9549. [CrossRef]
96. Kakoschky, B.; Pleli, T.; Schmithals, C.; Zeuzem, S.; Brüne, B.; Vogl, T.J.; Korf, H.W.; Weigert, A.; Piiper, A. Selective targeting of tumor associated macrophages in different tumor models. *PLoS ONE* **2018**, *13*, e0193015. [CrossRef]
97. Ju, C.; Tacke, F. Hepatic macrophages in homeostasis and liver diseases: From pathogenesis to novel therapeutic strategies. *Cell. Mol. Immunol.* **2016**, *13*, 316–327. [CrossRef]
98. Liu, T.; Li, L.; Fu, C.; Liu, H.; Chen, D.; Tang, F. Pathological mechanisms of liver injury caused by continuous intraperitoneal injection of silica nanoparticles. *Biomaterials* **2012**, *33*, 2399–2407. [CrossRef]
99. Bartneck, M.; Ritz, T.; Keul, H.A.; Wambach, M.; Gbureck, U.; Ehling, J.; Lammers, T.; Heymann, F.; Gassler, N.; Lu, T.; et al. Peptide-Functionalized Gold Nanorods Increase Liver Injury in Hepatitis. *ACS Nano* **2012**, *6*, 8767–8777. [CrossRef]
100. Yao, Q.; Liu, J.; Zhang, Z.; Li, F.; Zhang, C.; Lai, B.; Xiao, L.; Wang, N. Peroxisome proliferator-activated receptor γ (PPARγ) induces the gene expression of integrin α(V)β(5) to promote macrophage M2 polarization. *J. Biol. Chem.* **2018**, *293*, 16572–16582. [CrossRef]
101. Luo, W.; Xu, Q.; Wang, Q.; Wu, H.; Hua, J. Effect of modulation of PPAR- γ activity on Kupffer cells M1/M2 polarization in the development of non-alcoholic fatty liver disease. *Sci. Rep.* **2017**, *7*, 44612. [CrossRef] [PubMed]

102. Wake, K. "Sternzellen" in the liver: Perisinusoidal cells with special reference to storage of vitamin A. *Am. J. Anat.* **1971**, *132*, 429–461. [CrossRef]
103. Wells, R.G. Cellular Sources of Extracellular Matrix in Hepatic Fibrosis. *Clin. Liver Dis.* **2008**, *12*, 759–768. [CrossRef]
104. Devhare, P.B.; Sasaki, R.; Shrivastava, S.; Di Bisceglie, A.M.; Ray, R.; Ray, B. Exosome-Mediated Intercellular Communication between Hepatitis C Virus-Infected Hepatocytes and Hepatic Stellate Cells. *J. Virol.* **2017**, *91*. [CrossRef] [PubMed]
105. Puche, J.E.; Saiman, Y.; Friedman, S.L. Hepatic Stellate Cells and Liver Fibrosis. *Arch. Patol. Lab. Med.* **2013**, *3*, 1473–1492. [CrossRef]
106. Gandhi, C.R. Hepatic stellate cell activation and pro-fibrogenic signals. *J. Hepatol.* **2017**, *67*, 1104–1105. [CrossRef]
107. Mikula, M.; Proell, V.; Fischer, A.N.M.; Mikulits, W. Activated hepatic stellate cells induce tumor progression of neoplastic hepatocytes in a TGF-β dependent fashion. *J. Cell. Physiol.* **2006**, *209*, 560–567. [CrossRef]
108. Gandhi, C.R. Chapter 14—Stellate Cells in Hepatic Immunological Tolerance. In *Stellate Cells in Health and Disease*; Academic Press: Cambridge, MA, USA, 2015; pp. 227–250. [CrossRef]
109. Wang, B.; Trippler, M.; Pei, R.; Lu, M.; Broering, R.; Gerken, G.; Schlaak, J.F. Toll-like receptor activated human and murine hepatic stellate cells are potent regulators of hepatitis C virus replication. *J. Hepatol.* **2009**, *51*, 1037–1045. [CrossRef] [PubMed]
110. Watanabe, A.; Hashmi, A.; Gomes, D.A.; Town, T.; Badou, A.; Flavell, R.A.; Mehal, W.Z. Apoptotic hepatocyte DNA inhibits hepatic stellate cell chemotaxis via toll-like receptor 9. *Hepatology* **2007**, *46*, 1509–1518. [CrossRef] [PubMed]
111. Bigorgne, A.E.; John, B.; Ebrahimkhani, M.R.; Shimizu-Albergine, M.; Campbell, J.S.; Crispe, I.N. TLR4-dependent secretion by hepatic stellate cells of the neutrophil-chemoattractant CXCL1 mediates liver response to gut microbiota. *PLoS ONE* **2016**, *11*, e0151063. [CrossRef] [PubMed]
112. Weiskirchen, R.; Tacke, F. Cellular and molecular functions of hepatic stellate cells in inflammatory responses and liver immunology. *Hepatobil Surg. Nutr.* **2014**, *3*, 344–363. [CrossRef]
113. Yu, M.C.; Chen, C.H.; Liang, X.; Wang, L.; Gandhi, C.R.; Fung, J.J.; Lu, L.; Qian, S. Inhibition of T-cell responses by hepatic stellate cells via B7-H1-mediated T-cell apoptosis in mice. *Hepatology* **2004**, *40*, 1312–1321. [CrossRef] [PubMed]
114. Zhou, Z.; Xu, M.J.; Cai, Y.; Wang, W.; Jiang, J.X.; Varga, Z.V.; Feng, D.; Pacher, P.; Kunos, G.; Torok, N.J.; et al. Neutrophil-Hepatic Stellate Cell Interactions Promote Fibrosis in Experimental Steatohepatitis. *Cell. Mol. Gastroenterol. Hepatol.* **2018**, *5*, 399–413. [CrossRef] [PubMed]
115. Cai, X.; Li, Z.; Zhang, Q.; Qu, Y.; Xu, M.; Wan, X.; Lu, L. CXCL6-EGFR-induced Kupffer cells secrete TGF-β1 promoting hepatic stellate cell activation via the SMAD2/BRD4/C-MYC/EZH2 pathway in liver fibrosis. *J. Cell. Mol. Med.* **2018**, *22*, 5050–5061. [CrossRef]
116. Benedicto, A.; Herrero, A.; Romayor, I.; Marquez, J.; Smedsrød, B.; Olaso, B.; Arteta, B. Liver sinusoidal endothelial cell ICAM-1 mediated tumor/endothelial crosstalk drives the development of liver metastasis by initiating inflammatory and angiogenic responses. *Sci. Rep.* **2019**, *9*, 1–12. [CrossRef]
117. Viñas, O.; Bataller, R.; Sancho-Bru, P.; Ginès, P.; Berenguer, C.; Enrich, C.; Ercilla, G.; Vives, J.; Gallart, T.; Arroyo, V.; et al. Human hepatic stellate cells show features of antigen-presenting cells and stimulate lymphocyte proliferation. *Hepatology* **2003**, *38*, 919–929. [CrossRef] [PubMed]
118. Alisi, A.; Romania, P.; Nobili, V.; Locatelli, F.; Fruci, D. Human hepatic stellate cells are liver-resident antigen-presenting cells. *Hepatology* **2011**, *54*, 1107. [CrossRef]
119. Winau, F.; Hegasy, G.; Weiskirchen, R.; Weber, S.; Cassan, C.; Sieling, P.A.; Modlin, R.L.; Liblau, R.S.; Gressner, A.M.; Kaufmann, S.H.E. Ito Cells Are Liver-Resident Antigen-Presenting Cells for Activating T Cell Responses. *Immunity* **2007**, *26*, 117–129. [CrossRef]
120. Luk, J.M.; Zhang, Q.-S.; Lee, N.P.; Wo, J.Y.; Leung, P.P.; Liu, L.-X.; Hu, M.-Y.; Cheung, K.-F.; Hui, C.-K.; Lau, G.-K.; et al. Hepatic stellate cell-targeted delivery of M6P-HSA-glycyrrhetinic acid attenuates hepatic fibrogenesis in a bile duct ligation rat model. *Liver Int.* **2007**, *27*, 548–557. [CrossRef]
121. Sato, Y.; Murase, K.; Kato, J.; Kobune, M.; Sato, T.; Kawano, I.; Takimoto, R.; Takada, K.; Miyanishi, K.; Matsunaga, T.; et al. Resolution of liver cirrhosis using vitamin A-coupled liposomes to deliver siRNA against a collagen-specific chaperone. *Nat. Biotechnol.* **2008**, *26*, 431–442. [CrossRef]

122. Beljaars, L.; Weert, B.; Geerts, A.; Meijer, D.K.F.; Poelstra, K. The preferential homing of a platelet derived growth factor receptor-recognizing macromolecule to fibroblast-like cells in fibrotic tissue. *Biochem. Pharmacol.* **2003**, *66*, 1307–1317. [CrossRef]
123. Beljaars, L.; Molema, G.; Schuppan, D.; Geerts, A.; De Bleser, P.J.; Weert, B.; Meijer, D.K.F.; Poelstra, K. Successful targeting to rat hepatic stellate cells using albumin modified with cyclic peptides that recognize the collagen type VI receptor. *J. Biol. Chem.* **2000**, *275*, 12743–12751. [CrossRef] [PubMed]
124. Adrian, J.E.; Kamps, J.A.A.M.; Poelstra, K.; Scherphof, G.L.; Meijer, D.K.F.; Kaneda, I. Delivery of viral vectors to hepatic stellate cells in fibrotic livers using HVJ envelopes fused with targeted liposomes. *J. Drug Target.* **2007**, *15*, 75–82. [CrossRef]
125. Hu, Q.; Lee, J.-Y.; Luo, Y. Nanoparticles Targeting Hepatic Stellate Cells for the Treatment of Liver Fibrosis. *Eng. Sci.* **2019**, *6*, 12–21. [CrossRef]
126. Michalopoulos, G.K.; Bhushan, B. Liver regeneration: Biological and pathological mechanisms and implications. *Nat. Rev. Gastroenterol. Hepatol.* **2020**. [CrossRef] [PubMed]
127. Kitade, M.; Kaji, K.; Yoshiji, H. Relationship between hepatic progenitor cell-mediated liver regeneration and non-parenchymal cells. *Hepatol. Res.* **2016**, *46*, 1187–1193. [CrossRef] [PubMed]
128. Tummala, K.S.; Brandt, M.; Teijeiro, A.; Graña, O.; Schwabe, R.F.; Perna, C.; Djouder, N. Hepatocellular Carcinomas Originate Predominantly from Hepatocytes and Benign Lesions from Hepatic Progenitor Cells. *Cell Rep.* **2017**, *19*, 584–600. [CrossRef]
129. Alqahtani, A.; Khan, Z.; Alloghbi, A.; Said Ahmed, T.S.; Ashraf, M.; Hammouda, D.M. Hepatocellular Carcinoma: Molecular Mechanisms and Targeted Therapies. *Medicina* **2019**, *55*, 526. [CrossRef]
130. Yang, J.D.; Hainaut, P.; Gores, G.J.; Amadou, A.; Plymoth, A.; Roberts, L.R. A global view of hepatocellular carcinoma: Trends, risk, prevention and management. *Nat. Rev. Gastroenterol. Hepatol.* **2019**, *16*, 589–604. [CrossRef]
131. El-Serag, H.B. Epidemiology of viral hepatitis and hepatocellular carcinoma. *Gastroenterology* **2012**, *142*, 1264–1273.e1261. [CrossRef]
132. Younossi, Z.M.; Ratziu, V.; Loomba, R.; Rinella, M.; Anstee, Q.M.; Goodman, Z.; Bedossa, P.; Geier, A.; Beckebaum, S.; Newsome, P.N.; et al. Obeticholic acid for the treatment of non-alcoholic steatohepatitis: Interim analysis from a multicentre, randomised, placebo-controlled phase 3 trial. *Lancet* **2019**, *394*, 2184–2196. [CrossRef]
133. Lazarus, J.V.; Colombo, M.; Cortez-Pinto, H.; Huang, T.T.; Miller, V.; Ninburg, M.; Schattenberg, J.M.; Seim, L.; Wong, V.W.S.; Zelber-Sagi, S. NAFLD–sounding the alarm on a silent epidemic. *Nat. Rev. Gastroenterol. Hepatol.* **2020**, *17*, 377–379. [CrossRef] [PubMed]
134. Welzel, T.M.; Graubard, B.I.; Quraishi, S.; Zeuzem, S.; Davila, J.A.; El-Serag, H.B.; McGlynn, K.A. Population-attributable fractions of risk factors for hepatocellular carcinoma in the United States. *Am. J. Gastroenterol.* **2013**, *108*, 1314–1321. [CrossRef] [PubMed]
135. Mittal, S.; El-Serag, H.B.; Sada, Y.H.; Kanwal, F.; Duan, Z.; Temple, S.; May, S.B.; Kramer, J.R.; Richardson, P.A.; Davila, J.A. Hepatocellular Carcinoma in the Absence of Cirrhosis in United States Veterans is Associated With Nonalcoholic Fatty Liver Disease. *Clin. Gastroenterol. Hepatol.* **2016**, *14*, 124–131.e121. [CrossRef] [PubMed]
136. Li, T.C.; Li, C.I.; Liu, C.S.; Lin, W.Y.; Lin, C.H.; Yang, S.Y.; Lin, C.C. Risk score system for the prediction of hepatocellular carcinoma in patients with type 2 diabetes: Taiwan Diabetes Study. *Semin. Oncol.* **2018**, *45*, 264–274. [CrossRef] [PubMed]
137. Hirosumi, J.; Tuncman, G.; Chang, L.; Görgün, C.Z.; Uysal, K.T.; Maeda, K.; Karin, M.; Hotamisligil, G.S. A central role for JNK in obesity and insulin resistance. *Nature* **2002**, *420*, 333–336. [CrossRef]
138. Balkwill, F.; Mantovani, A. Inflammation and cancer: Back to Virchow? *Lancet* **2001**, *357*, 539–545. [CrossRef]
139. Lleo, A.; de Boer, Y.S.; Liberal, R.; Colombo, M. The risk of liver cancer in autoimmune liver diseases. *Adv. Med. Oncol.* **2019**, *11*, 1758835919861914. [CrossRef]
140. Nowak, A.; Giger, R.S.; Krayenbuehl, P.A. Higher age at diagnosis of hemochromatosis is the strongest predictor of the occurrence of hepatocellular carcinoma in the Swiss hemochromatosis cohort: A prospective longitudinal observational study. *Medicine* **2018**, *97*, e12886. [CrossRef]
141. Ramadori, P.; Cubero, F.J.; Liedtke, C.; Trautwein, C.; Nevzorova, Y.A. Alcohol and Hepatocellular Carcinoma: Adding Fuel to the Flame. *Cancers* **2017**, *9*, 130. [CrossRef]

142. Gouas, D.; Shi, H.; Hainaut, P. The aflatoxin-induced TP53 mutation at codon 249 (R249S): Biomarker of exposure, early detection and target for therapy. *Cancer Lett.* **2009**, *286*, 29–37. [CrossRef] [PubMed]
143. Golabi, P.; Fazel, S.; Otgonsuren, M.; Sayiner, M.; Locklear, C.T.; Younossi, Z.M. Mortality assessment of patients with hepatocellular carcinoma according to underlying disease and treatment modalities. *Medicine* **2017**, *96*, e5904. [CrossRef] [PubMed]
144. Berzigotti, A.; Reig, M.; Abraldes, J.G.; Bosch, J.; Bruix, J. Portal hypertension and the outcome of surgery for hepatocellular carcinoma in compensated cirrhosis: A systematic review and meta-analysis. *Hepatology* **2015**, *61*, 526–536. [CrossRef] [PubMed]
145. Teh, S.H.; Christein, J.; Donohue, J.; Que, F.; Kendrick, M.; Farnell, M.; Cha, S.; Kamath, P.; Kim, R.; Nagorney, D.M. Hepatic resection of hepatocellular carcinoma in patients with cirrhosis: Model of End-Stage Liver Disease (MELD) score predicts perioperative mortality. *J. Gastrointest. Surg.* **2005**, *9*, 1207–1215; discussion 1215. [CrossRef] [PubMed]
146. Sapisochin, G.; Bruix, J. Liver transplantation for hepatocellular carcinoma: Outcomes and novel surgical approaches. *Nat. Rev. Gastroenterol. Hepatol.* **2017**, *14*, 203–217. [CrossRef] [PubMed]
147. Xu, X.; Chen, J.; Wei, Q.; Liu, Z.-H.; Yang, Z.; Zhang, M.; Wang, G.-U.; Gao, J.; Yang, Z.; Guo, W.-E.; et al. EASL Clinical Practice Guidelines: Liver transplantation. *J. Hepatol.* **2016**, *64*, 433–485. [CrossRef]
148. Shiina, S.; Sato, K.; Tateishi, R.; Shimizu, M.; Ohama, H.; Hatanaka, T.; Takawa, M.; Nagamatsu, H.; Imai, Y. Percutaneous Ablation for Hepatocellular Carcinoma: Comparison of Various Ablation Techniques and Surgery. *Can. J. Gastroenterol. Hepatol.* **2018**, *2018*, 4756147. [CrossRef]
149. Lencioni, R.; de Baere, T.; Soulen, M.C.; Rilling, W.S.; Geschwind, J.F. Lipiodol transarterial chemoembolization for hepatocellular carcinoma: A systematic review of efficacy and safety data. *Hepatology* **2016**, *64*, 106–116. [CrossRef]
150. Keating, G.M. Sorafenib: A Review in Hepatocellular Carcinoma. *Target. Oncol.* **2017**, *12*, 243–253. [CrossRef]
151. Llovet, J.M.; Ricci, S.; Mazzaferro, V.; Hilgard, P.; Gane, E.; Blanc, J.-F.; de Oliveira, A.C.; Santoro, A.; Raoul, J.-L.; Forner, A.; et al. Sorafenib in Advanced Hepatocellular Carcinoma. *N. Engl. J. Med.* **2008**, *359*, 378–390. [CrossRef]
152. Al-Salama, Z.T.; Syed, Y.Y.; Scott, L.J. Lenvatinib: A Review in Hepatocellular Carcinoma. *Drugs* **2019**, *79*, 665–674. [CrossRef] [PubMed]
153. Bruix, J.; Qin, S.; Merle, P.; Granito, A.; Huang, Y.H.; Bodoky, G.; Pracht, M.; Yokosuka, O.; Rosmorduc, O.; Breder, V.; et al. Regorafenib for patients with hepatocellular carcinoma who progressed on sorafenib treatment (RESORCE): A randomised, double-blind, placebo-controlled, phase 3 trial. *Lancet* **2017**, *389*, 56–66. [CrossRef]
154. Finkelmeier, F.; Waidmann, O.; Trojan, J. Nivolumab for the treatment of hepatocellular carcinoma. *Expert Rev. Anticancer* **2018**, *18*, 1169–1175. [CrossRef] [PubMed]
155. Zhu, A.X.; Finn, R.S.; Edeline, J.; Cattan, S.; Ogasawara, S.; Palmer, D.; Verslype, C.; Zagonel, V.; Fartoux, L.; Vogel, A.; et al. Pembrolizumab in patients with advanced hepatocellular carcinoma previously treated with sorafenib (KEYNOTE-224): A non-randomised, open-label phase 2 trial. *Lancet Oncol.* **2018**, *19*, 940–952. [CrossRef]
156. Zhu, A.X.; Kang, Y.K.; Yen, C.J.; Finn, R.S.; Galle, P.R.; Llovet, J.M.; Assenat, E.; Brandi, G.; Pracht, M.; Lim, H.Y.; et al. Ramucirumab after sorafenib in patients with advanced hepatocellular carcinoma and increased α-fetoprotein concentrations (REACH-2): A randomised, double-blind, placebo-controlled, phase 3 trial. *Lancet Oncol.* **2019**, *20*, 282–296. [CrossRef]
157. Sevic, I.; Spinelli, F.M.; Cantero, M.J.; Reszegi, A.; Kovalszky, I.; García, M.G.; Alaniz, L. The Role of the Tumor Microenvironment in the Development and Progression of Hepatocellular Carcinoma. In *Hepatocellular Carcinoma*; Tirnitz-Parker, J.E.E., Ed.; Codon Publications: Brisbane, QLD, Australia, 2019. [CrossRef]
158. Tanaka, Y.; Tateishi, R.; Koike, K. Proteoglycans Are Attractive Biomarkers and Therapeutic Targets in Hepatocellular Carcinoma. *Int. J. Mol. Sci.* **2018**, *19*, 3070. [CrossRef]
159. Ritz, T.; Krenkel, O.; Tacke, F. Dynamic plasticity of macrophage functions in diseased liver. *Cell. Immunol.* **2018**, *330*, 175–182. [CrossRef]
160. Higashi, T.; Friedman, S.L.; Hoshida, Y. Hepatic stellate cells as key target in liver fibrosis. *Adv. Drug Deliv. Rev.* **2017**, *121*, 27–42. [CrossRef]

161. Mattyasovszky, S.G.; Wollstädter, J.; Martin, A.; Ritz, U.; Baranowski, A.; Ossendorf, C.; Rommens, P.M.; Hofmann, A. Inhibition of Contractile Function in Human Joint Capsule Myofibroblasts by Targeting the TGF-β1 and PDGF Pathways. *PLoS ONE* **2016**, *11*, e0145948. [CrossRef]
162. Degroote, H.; Van Dierendonck, A.; Geerts, A.; Van Vlierberghe, H.; Devisscher, L. Preclinical and Clinical Therapeutic Strategies Affecting Tumor-Associated Macrophages in Hepatocellular Carcinoma. *J. Immunol. Res.* **2018**, *2018*, 7819520. [CrossRef]
163. Yeung, O.W.; Lo, C.M.; Ling, C.C.; Qi, X.; Geng, W.; Li, C.X.; Ng, K.T.; Forbes, S.J.; Guan, X.Y.; Poon, R.T.; et al. Alternatively activated (M2) macrophages promote tumour growth and invasiveness in hepatocellular carcinoma. *J. Hepatol.* **2015**, *62*, 607–616. [CrossRef] [PubMed]
164. Kuang, D.M.; Zhao, Q.; Peng, C.; Xu, J.; Zhang, J.P.; Wu, C.; Zheng, L. Activated monocytes in peritumoral stroma of hepatocellular carcinoma foster immune privilege and disease progression through PD-L1. *J. Exp. Med.* **2009**, *206*, 1327–1337. [CrossRef] [PubMed]
165. Wu, K.; Kryczek, I.; Chen, L.; Zou, W.; Welling, T.H. Kupffer cell suppression of CD8+ T cells in human hepatocellular carcinoma is mediated by B7-H1/programmed death-1 interactions. *Cancer Res.* **2009**, *69*, 8067–8075. [CrossRef] [PubMed]
166. Mueller, L.; Goumas, F.A.; Affeldt, M.; Sandtner, S.; Gehling, U.M.; Brilloff, S.; Walter, J.; Karnatz, N.; Lamszus, K.; Rogiers, X.; et al. Stromal fibroblasts in colorectal liver metastases originate from resident fibroblasts and generate an inflammatory microenvironment. *Am. J. Pathol.* **2007**, *171*, 1608–1618. [CrossRef] [PubMed]
167. Cirri, P.; Chiarugi, P. Cancer-associated-fibroblasts and tumour cells: A diabolic liaison driving cancer progression. *Cancer Metastasis Rev.* **2012**, *31*, 195–208. [CrossRef] [PubMed]
168. Ramachandran, P.; Pellicoro, A.; Vernon, M.A.; Boulter, L.; Aucott, R.L.; Ali, A.; Hartland, S.N.; Snowdon, V.K.; Cappon, A.; Gordon-Walker, T.T.; et al. Differential Ly-6C expression identifies the recruited macrophage phenotype, which orchestrates the regression of murine liver fibrosis. *Proc. Natl. Acad. Sci. USA* **2012**, *109*, E3186–E3195. [CrossRef]
169. Baeck, C.; Wei, X.; Bartneck, M.; Fech, V.; Heymann, F.; Gassler, N.; Hittatiya, K.; Eulberg, D.; Luedde, T.; Trautwein, C.; et al. Pharmacological inhibition of the chemokine C-C motif chemokine ligand 2 (monocyte chemoattractant protein 1) accelerates liver fibrosis regression by suppressing Ly-6C(+) macrophage infiltration in mice. *Hepatology* **2014**, *59*, 1060–1072. [CrossRef]
170. Chen, Y.; Zhang, S.; Wang, Q.; Zhang, X. Tumor-recruited M2 macrophages promote gastric and breast cancer metastasis via M2 macrophage-secreted CHI3L1 protein. *J. Hematol. Oncol.* **2017**, *10*, 1–13. [CrossRef]
171. Das, R.P.; Gandhi, V.V.; Singh, B.G.; Kunwar, A. Passive and Active Drug Targeting: Role of Nanocarriers in Rational Design of Anticancer Formulations. *Curr. Pharm. Des.* **2019**, *25*, 3034–3056. [CrossRef]
172. Kaps, L.; Nuhn, L.; Aslam, M.; Brose, A.; Foerster, F.; Rosigkeit, S.; Renz, P.; Heck, R.; Kim, Y.O.; Lieberwirth, I.; et al. In Vivo Gene-Silencing in Fibrotic Liver by siRNA-Loaded Cationic Nanohydrogel Particles. *Adv. Healthc. Mater.* **2015**, *4*, 2809–2815. [CrossRef]
173. Leber, N.; Kaps, L.; Yang, A.; Aslam, M.; Giardino, M.; Klefenz, A.; Choteschovsky, N.; Rosigkeit, S.; Mostafa, A.; Nuhn, L.; et al. α-Mannosyl-Functionalized Cationic Nanohydrogel Particles for Targeted Gene Knockdown in Immunosuppressive Macrophages. *Macromol. Biosci.* **2019**, *19*, e1900162. [CrossRef] [PubMed]
174. Scodeller, P.; Simón-Gracia, L.; Kopanchuk, S.; Tobi, A.; Kilk, K.; Säälik, P.; Kurm, K.; Squadrito, M.L.; Kotamraju, V.R.; Rinken, A.; et al. Precision Targeting of Tumor Macrophages with a CD206 Binding Peptide. *Sci. Rep.* **2017**, *7*, 14655. [CrossRef] [PubMed]
175. Lopez-Pelaez, M.; Lamont, D.J.; Peggie, M.; Shpiro, N.; Gray, N.S.; Cohen, P. Protein kinase IKKβ-catalyzed phosphorylation of IRF5 at Ser462 induces its dimerization and nuclear translocation in myeloid cells. *Proc. Natl. Acad. Sci. USA* **2014**, *111*, 17432–17437. [CrossRef] [PubMed]
176. Zhang, F.; Parayath, N.N.; Ene, C.I.; Stephan, S.B.; Koehne, A.L.; Coon, M.E.; Holland, E.C.; Stephan, M.T. Genetic programming of macrophages to perform anti-tumor functions using targeted mRNA nanocarriers. *Nat. Commun.* **2019**, *10*, 3974. [CrossRef] [PubMed]
177. Bobbin, M.L.; Rossi, J.J. RNA Interference (RNAi)-Based Therapeutics: Delivering on the Promise? *Annu. Rev. Pharm. Toxicol.* **2016**, *56*, 103–122. [CrossRef] [PubMed]
178. Zins, K.; Abraham, D. Cancer Immunotherapy: Targeting Tumor-Associated Macrophages by Gene Silencing. *Methods Mol. Biol.* **2020**, *2115*, 289–325. [CrossRef]

179. Shobaki, N.; Sato, Y.; Suzuki, Y.; Okabe, N.; Harashima, H. Manipulating the function of tumor-associated macrophages by siRNA-loaded lipid nanoparticles for cancer immunotherapy. *J. Control. Release* **2020**, *325*, 235–248. [CrossRef]
180. McNelis, J.C.; Olefsky, J.M. Macrophages, immunity, and metabolic disease. *Immunity* **2014**, *41*, 36–48. [CrossRef]
181. Loomba, R.; Lawitz, E.; Mantry, P.S.; Jayakumar, S.; Caldwell, S.H.; Arnold, H.; Diehl, A.M.; Djedjos, C.S.; Han, L.; Myers, R.P.; et al. The ASK1 inhibitor selonsertib in patients with nonalcoholic steatohepatitis: A randomized, phase 2 trial. *Hepatology* **2018**, *67*, 549–559. [CrossRef]
182. Tu, K.N.; Lie, J.D.; Wan, C.K.V.; Cameron, M.; Austel, A.G.; Nguyen, J.K.; Van, K.; Hyun, D. Osteoporosis: A Review of Treatment Options. *Pharm. Ther.* **2018**, *43*, 92–104.
183. Menshawy, A.; Mattar, O.; Abdulkarim, A.; Kasem, S.; Nasreldin, N.; Menshawy, E.; Mohammed, S.; Abdel-Maboud, M.; Gadelkarim, M.; El Ashal, G.G.; et al. Denosumab versus bisphosphonates in patients with advanced cancers-related bone metastasis: Systematic review and meta-analysis of randomized controlled trials. *Support Care Cancer* **2018**, *26*, 1029–1038. [CrossRef] [PubMed]
184. Van Acker, H.H.; Anguille, S.; Willemen, Y.; Smits, E.L.; Van Tendeloo, V.F. Bisphosphonates for cancer treatment: Mechanisms of action and lessons from clinical trials. *Pharmathera* **2016**, *158*, 24–40. [CrossRef] [PubMed]
185. Yu, X.; Chen, L.; Liu, J.; Dai, B.; Xu, G.; Shen, G.; Luo, Q.; Zhang, Z. Immune modulation of liver sinusoidal endothelial cells by melittin nanoparticles suppresses liver metastasis. *Nat. Commun.* **2019**, *10*, 574. [CrossRef] [PubMed]
186. Tang, T.; Sui, Y.; Lian, M.; Li, Z.; Hua, J. Pro-inflammatory activated Kupffer cells by lipids induce hepatic NKT cells deficiency through activation-induced cell death. *PLoS ONE* **2013**, *8*, e81949. [CrossRef] [PubMed]
187. Zhang, J.; Li, N.; Yang, L.; Xie, H.; Yang, Y.; Wang, H.; Wu, C.; Shen, T.; Zhu, Q. Bradykinin contributes to immune liver injury via B2R receptor-mediated pathways in trichloroethylene sensitized mice: A role in Kupffer cell activation. *Toxicology* **2019**, *415*, 37–48. [CrossRef]
188. Bros, M.; Nuhn, L.; Simon, J.; Moll, L.; Mailander, V.; Landfester, K.; Grabbe, S. The Protein Corona as a Confounding Variable of Nanoparticle-Mediated Targeted Vaccine Delivery. *Front. Immunol.* **2018**, *9*, 1760. [CrossRef]

© 2020 by the authors. Licensee MDPI, Basel, Switzerland. This article is an open access article distributed under the terms and conditions of the Creative Commons Attribution (CC BY) license (http://creativecommons.org/licenses/by/4.0/).

10.2. Publication 2

"Complement-opsonized nano-carriers are bound by dendritic cells (DC) via complement receptor (CR)3, and by B cell subpopulations via CR-1/2, and affect the activation of DC and B-1 cells"

This chapter has been published in MDPI (International Journal of Molecular Sciences). As co-author, I was responsible for the performance and evaluation of several *in vitro* experiments. This study describes how NPs can accumulate serum factors on their surface (protein corona), which may affect their cellular binding. In previous studies, we have shown that carbohydrate-coated NPs can trigger the lectin-dependent complement pathway, resulting in enhanced binding of the NPs to B cells via the complement receptor (CR)1/2. We also showed that these NPs engaged all types of splenic leukocytes known to express CR3 at a high rate when NPs were pre-incubated with native mouse serum, resulting in complement opsonization. By focusing on DCs as an important antigen-presenting cell type, we showed that CR3 is essential for the binding/uptake of complement-opsonized NPs. These findings may have important implications for the design of nanovaccines. NPs functionalized with carbohydrates to trigger complement activation *in vivo* or with complement receptor-binding ligands may result in concomitant targeting of DCs and B cells and thereby may strongly enhance the extent of dual cellular/humoral immune responses.

DOI: 10.3390/ijms22062869

Published in: *International Journal of Molecular Sciences.* **2021**, *22*(6), 2869

Reprinted with permission under creative commons attribution 4.0 (CC BY-NC) from Bednarczyk M, **Medina-Montano C**, Fittler FJ, Stege H, Roskamp M, Kuske M, Langer C, Vahldieck M, Montermann E, Tubbe I, Röhrig N, Dzionek A, Grabbe S, Bros M. Complement-Opsonized Nano-Carriers Are Bound by Dendritic Cells (DC) via Complement Receptor (CR)3, and by B Cell Subpopulations via CR-1/2, and Affect the Activation of DC and B-1 Cells. Int J Mol Sci. 2021 Mar 11;22(6):2869. doi: 10.3390/ijms22062869. PMID: 33799879; PMCID: PMC8001596.

International Journal of
Molecular Sciences

MDPI

Article

Complement-Opsonized Nano-Carriers are Bound by Dendritic Cells (DC) via Complement Receptor (CR)3, and by B Cell Subpopulations via CR-1/2, and Affect the Activation of DC and B-1 Cells

Monika Bednarczyk [1], Carolina Medina-Montano [1], Frederic Julien Fittler [1,†], Henner Stege [1,†], Meike Roskamp [2], Michael Kuske [1], Christian Langer [2], Marco Vahldieck [2], Evelyn Montermann [1], Ingrid Tubbe [1], Nadine Röhrig [1], Andrzej Dzionek [2], Stephan Grabbe [1] and Matthias Bros [1,*]

[1] Department of Dermatology, University Medical Center Mainz, Langenbeckstraße 1, 55131 Mainz, Germany; m.bednarczyk.09@aberdeen.ac.uk (M.B.); gmedinam@students.uni-mainz.de (C.M.-M.); ffittler@students.uni-mainz.de (F.J.F.); Henner.Stege@unimedizin-mainz.de (H.S.); mikuske@uni-mainz.de (M.K.); monterma@uni-mainz.de (E.M.); tubbe@uni-mainz.de (I.T.); n.roehrig@uni-mainz.de (N.R.); stephan.grabbe@unimedizin-mainz.de (S.G.); mbros@uni-mainz.de (M.B.)

[2] Miltenyi Biotec GmbH, Friedrich-Ebert-Strasse 68, 51429 Bergisch Gladbach, Germany; meiker@miltenyi.com (M.R.); christianlan@miltenyi.com (C.L.); MarcoV@miltenyi.com (M.V.); Andreasd@miltenyibiotec.de (A.D.)

* Correspondence: mbros@uni-mainz.de; Tel.: +49-6131-17-9846

† These authors contributed equally to this work.

Citation: Bednarczyk, M.; Medina-Montano, C.; Fittler, F.J.; Stege, H.; Roskamp, M.; Kuske, M.; Langer, C.; Vahldieck, M.; Montermann, E.; Tubbe, I.; et al. Complement-Opsonized Nano-Carriers are Bound by Dendritic Cells (DC) via Complement Receptor (CR)3, and by B Cell Subpopulations via CR-1/2, and Affect the Activation of DC and B-1 Cells. *Int. J. Mol. Sci.* **2021**, *22*, 2869. https://doi.org/10.3390/ijms22062869

Academic Editor: Aurelia Tubaro

Received: 27 January 2021
Accepted: 9 March 2021
Published: 11 March 2021

Publisher's Note: MDPI stays neutral with regard to jurisdictional claims in published maps and institutional affiliations.

Copyright: © 2021 by the authors. Licensee MDPI, Basel, Switzerland. This article is an open access article distributed under the terms and conditions of the Creative Commons Attribution (CC BY) license (http://creativecommons.org/licenses/by/4.0/).

Abstract: The development of nanocarriers (NC) for biomedical applications has gained large interest due to their potential to co-deliver drugs in a cell-type-targeting manner. However, depending on their surface characteristics, NC accumulate serum factors, termed protein corona, which may affect their cellular binding. We have previously shown that NC coated with carbohydrates to enable biocompatibility triggered the lectin-dependent complement pathway, resulting in enhanced binding to B cells via complement receptor (CR)1/2. Here we show that such NC also engaged all types of splenic leukocytes known to express CR3 at a high rate when NC were pre-incubated with native mouse serum resulting in complement opsonization. By focusing on dendritic cells (DC) as an important antigen-presenting cell type, we show that CR3 was essential for binding/uptake of complement-opsonized NC, whereas CR4, which in mouse is specifically expressed by DC, played no role. Further, a minor B cell subpopulation (B-1), which is important for first-line pathogen responses, and co-expressed CR1/2 and CR3, in general, engaged NC to a much higher extent than normal B cells. Here, we identified CR-1/2 as necessary for binding of complement-opsonized NC, whereas CR3 was dispensable. Interestingly, the binding of complement-opsonized NC to both DC and B-1 cells affected the expression of activation markers. Our findings may have important implications for the design of nano-vaccines against infectious diseases, which codeliver pathogen-specific protein antigen and adjuvant, aimed to induce a broad adaptive cellular and humoral immune response by inducing cytotoxic T lymphocytes that kill infected cells and pathogen-neutralizing antibodies, respectively. Decoration of nano-vaccines either with carbohydrates to trigger complement activation in vivo or with active complement may result in concomitant targeting of DC and B cells and thereby may strongly enhance the extent of dual cellular/humoral immune responses.

Keywords: nanocarrier; carbohydrate surface; complement activation; complement receptor 3; complement receptor 4; dendritic cell; B-1; B-2

1. Introduction

In the field of biomedical applications, nanocarriers (NC) have gained increasing interest based on their capacity to codeliver different drugs and biologicals in a targeting manner to distinct cell types [1]. Targeted delivery may reduce the overall amount of payload required for therapeutic applications as well as adverse effects caused by effects of drugs on non-target cells. However, NC most often accumulate serum factors on their surface, termed protein corona [2]. On one hand, the protein corona may shield targeting moieties and thereby attenuate intended target cell binding. On the other hand, NC-adsorbed serum factors may engage receptors expressed by non-target cells resulting in unwanted uptake. In this regard, Zhang and coworkers first identified constituents of the protein corona of gold nanoparticles [3]. Then, these NC were incubated with serum deficient of single constituents to elucidate their individual role for the overall composition of the protein corona and corona-dependent NC binding to macrophages. By this approach, antithrombin III, fibronectin and other factors of the protein corona were shown to bind IgG. This, in turn, resulted in elevated binding of the antibody-opsonized NC to Fc receptors on macrophages. The cellular interaction of NC may also be affected in case NC surface properties affect the conformational state of adsorbed proteins. For example, Mortimer and coworkers demonstrated that albumin that adsorbed onto silicate-based NC altered its conformation, which resulted in its recognition by class A scavenger receptors (SR-A) on macrophages. To limit the unwanted binding of NC, especially to myeloid cells, NC have been decorated with polyethyleneglycol (PEG) and dysopsonic proteins, which serve to minimize the formation of a protein corona [2,4] [5,6]. Moreover, We [7] and others [8] have demonstrated that solid core NC coated with the carbohydrate dextran (DEX) to ensure biocompatibility may trigger the carbohydrate complement pathway in vivo resulting in the deposition of active complement C3 fragments. C3-opsonized DEX-coated NC were reported to engage blood neutrophils (polymorphonuclear granulocytes; PMN) via engagement of the complement receptor (CR)3, a heterodimer composed of CD11b and CD18 [9]. However, in other studies, DEX-coated NC were demonstrated to bind SR-A, but not CR3 [10–13]. We showed that in the spleen, complement-opsonized NC preferably targeted splenic B cells [7] by engagement of CR1/2 [14].

CR3 is commonly expressed by myeloid cells, comprising monocytes/macrophages (MAC), PMN and conventional dendritic cells type 2 (cDC2), enabling efficient binding and internalization of complement-opsonized pathogens as well as of immune complexes [9]. Interestingly, CR3 is also apparent on natural killer (NK) cells [15] and a minor B cell subpopulation, termed B-1 [16], known to contribute to pathogen clearance by phagocytosis, production of IgM, and to confer T cell activation [17].

CR3 also binds numerous serum factors [9], has also been implicated in Toll-like receptor (TLR)/MyD88 signaling processes, and triggering of CR3 was shown to result in inhibitory cell signaling [18,19]. In mice, CR4 (CD11c/CD18) [20] constitutes a pan-DC marker [21], and therefore, is frequently used to identify this important population of antigen-presenting cells (APC) [22]. In contrast to CR3, CR4 has not been reported to display broad substrate affinities and signaling effects when triggered.

Given the important role of DC for the initiation and shaping of immune responses, we wanted to delineate the relative importance of CR3, as expressed by cDC2 only, and of CR4 as expressed by all (murine) DC, for the binding/uptake of complement-opsonized NC. Furthermore, due to the general finding of strong accumulation of most types of NC in the liver, including DEX-coated NC [7,23], we asked for the role of complement factors in this regard.

We show here that within liver DC, MAC and liver sinusoidal endothelial cells (LSEC) bound complement-opsonized NC to an increased extent. However, similar results were obtained using serum devoid of complement activity, suggesting the involvement of other receptors. SR-A, which have been frequently discussed in this regard [10,12,13], did not contribute to NC engagement. In the spleen, all CR1/2- and CR3-expressing types of leukocytes engaged NC at a much stronger extent only when these were

complement-opsonized. In general, we observed no functional role of SR-A. Furthermore, by using both CD11b$^{-/-}$ DC as well as CD11b-blocking antibodies, we show that CR3, but not CR4 was critical for binding/uptake of complement-opsonized NC. Finally, within B cells, we identified the B-1 subpopulation as highly active in NC binding, with CR-1/2 playing a major role. In the case of DC and B-1 cells, NC engagement attenuated the expression of activation markers after subsequent LPS-mediated stimulation. Our results suggest that nano-vaccines, which codeliver antigen and native protein adjuvant and address DC and B cells in a complement-dependent manner, may be capable of inducing profound cellular and humoral immune responses.

2. Results

To delineate the role of activated complement as a constituent of the protein corona of an NC for its binding to immune cells, we comparatively assessed the binding characteristics of fluorescence-labeled NC coated with the carbohydrates dextran (DEX), solid iron oxide core (FeO-DEX) and bionized nanoferrite (BNF-DEX) and starch (BNF-starch), and included albumin-based NC as an internal control (Table S1).

2.1. B cells and CR3-Expressing Immune Cell Types in Spleen Bind Complement-Opsonized NC at High Extent

All myeloid cell types, comprising neutrophils (PMN, polymorphonuclear granulocytes), macrophages, and (conventional) DC, as well as NK cells and B cells, engaged carbohydrate-coated NC to a higher extent when these were pretreated with native mouse serum to enable adsorption of active complement on the NC surface (Figure 1). This effect was largely observed both with regard to the frequencies of NC-binding cells (Figure 1, upper panel) and the mean fluorescence intensities (MFI) of cell-bound NC (Figure 1, lower panel). This effect was largely abrogated when heat-inactivated (h.i.) serum, devoid of complement activity, was used for NC pretreatment. Blocking studies using dextran sulfate as a well-established inhibitor of SR-A, and the corresponding control agent chondroitin sulfate, ruled out the involvement of SR-A (Figure S2).

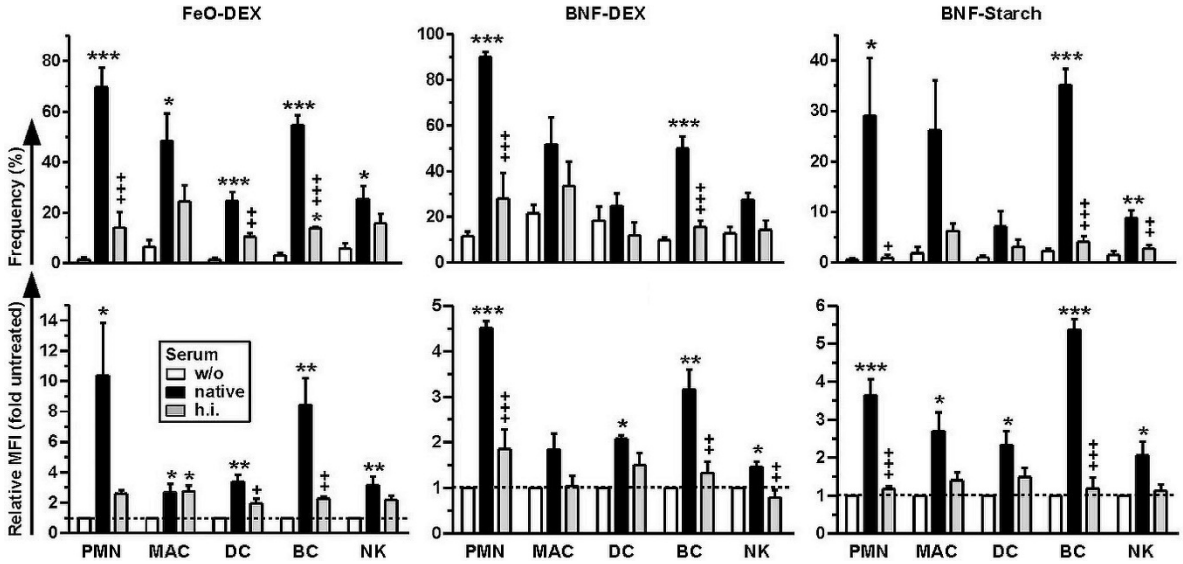

Figure 1. Carbohydrate-coated nanocarriers (NC), when pre-incubated with native serum, engage complement receptor-expressing splenic cell populations at a high extent. Spleen cells were incubated for 3 h with differentially pretreated (left untreated (w/o), pretreated with native or heat-inactivated (h.i.) serum) types of carbohydrate-coated NC. NC binding to neutrophils (PMN), macrophages (MAC), DC, B cells (BC) and natural killer cells (NK) was assessed by FACS analysis. Details on the gating strategy are given in Figure S1. Graphs denote the frequencies of NC-positive cells (upper panel) and NC-dependent MFI (lower panel) of various splenic leukocyte populations (mean ± SEM of 3–4 experiments). Statistical differences versus *w/o serum and $^{+}$native serum are indicated (one-way ANOVA, Tukey's test). $^{*,+}$ $p < 0.05$, $^{**,++}$ $p < 0.01$, $^{***,+++}$ $p < 0.001$.

In the case of albumin NC, only B cells displayed considerably higher binding in the case of pretreatment with native serum (Figure S3). All splenic immune cell types assessed showed attenuated binding of albumin NC pretreated with hi. Serum as compared to non-treated NC. These observations rule out the involvement of CR for the binding of albumin NC. Altogether, our observations indicate that specifically carbohydrate-coated NC, when pre-incubated with native serum, engage complement receptor-expressing splenic cell populations to a higher extent as compared to NC applied w/o pretreatment or pre-incubated with h.i. serum. These findings suggest an important role of complement opsonization of NC for subsequent binding by splenic leukocytes.

For numerous types of NC, considerable accumulation in the liver has been noted [24]. Besides Kupffer cells, which constitute the major liver-resident MAC population, also DC and LSEC, which exert immune functions as well, were reported to internalize NC [24]. To delineate the potential of these cell types to bind NC in a complement-dependent manner, liver NPC (nonparenchymal cells) that comprise the aforementioned liver cell types were isolated and incubated with differentially pretreated NC. Then, engagement of NP liver macrophages, DC and LSEC was assessed (Figure S4).

As shown in Figure S5A, LSEC and DC displayed stronger binding of BNF-DEX and BNF-Starch pre-incubated with native as well as h.i. mouse serum. These findings suggest that other types of receptors than CR may be involved in NC binding. Blocking studies suggested that SR-A did not contribute to the binding of differentially pretreated FeO-DEX (Figure S5B). The protein corona formed around albumin NC by incubation with native or h.i. serum had no effect on binding by liver NPC. Taken together, these observations suggest that MAC and DC in the liver bind complement-opsonized NC by additional/other receptors than the corresponding cell type in the spleen (see Figure 1).

DC constitute the most potent type of APC, and DC in secondary lymphoid organs are frequently addressed in NC-based vaccination approaches. Our finding of complement-mediated binding of carbohydrate-coated NC to this cell type prompted us to perform an in-depth analysis of receptors involved in NC engagement by this cell type. In mice, DC are identified as $CD11c^+$ cells, which thereby express CR4 (CD11c/CD18). Splenic DC largely comprise CD11b-positive cDC2, which co-express CR3 and CR4, and CD11b-negative DC that constitute either cDC1 or plasmacytoid (p) DC. As exemplified for FeO-DEX, cDC2 engaged this type of NC to a higher extent than cDC1/pDC at either condition (Figure S6). This finding may indicate DC subpopulation-specific differences in the capacity to engage NC, but may also suggest a role of CR3 in this regard.

2.2. Concomitant Expression of CR4 Does not Increase Binding of Serum-Pretreated NC to DC

To delineate specifically the relative contribution of CR3 and CR4 for the binding and uptake of complement-opsonized NC by DC, we set up cultures in which bone marrow (BM) progenitor cells were differentiated using GM-CSF [25]. After one week, differentiated cells commonly express CR3 (CD11b/CD18) (Figure S7, upper panel), and a high-frequency co-expresses CR4 (CD11c/CD18), termed (inflammatory) BMDC ($CD11b^+CD11c^+$). The minor fraction of $CD11b^+CD11c^-$ ($CR3^+$) cells is considered as MAC.

As observed for splenic cells, $CD11c^+$ BMDC, which thereby co-express CR3 and CR4, bind all types of carbohydrate-coated NC to a higher extent when these were complement-opsonized due to pre-incubation with native mouse serum as compared to NC left untreated or pre-incubated with h.i. serum (Figure 2). Complement-dependent binding of DC was most pronounced in the case of FeO-DEX. Macrophages ($CD11b^+CD11c^-$) within the same cultures displayed similar binding patterns (Figure S8A). Albumin NC engaged DC and non-DC at the highest level when pre-incubated with h.i. serum (Figure S8B). These observations confirm that BMDC are a suitable model to study complement-dependent NC binding.

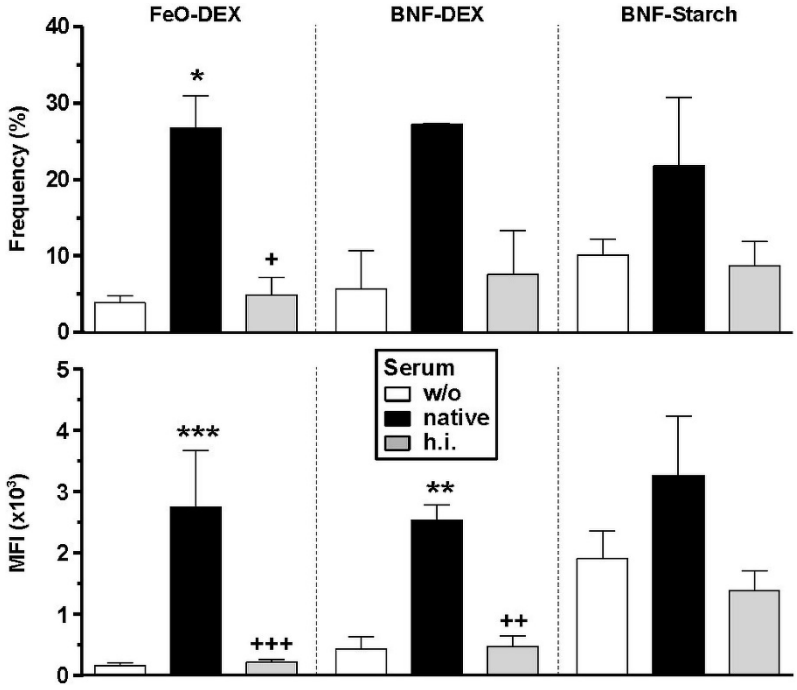

Figure 2. BMDC that express CR3 and CR4 engage carbohydrate-coated NC to a higher extent when pre-incubated with native serum. BMDC were incubated for 3 h with differentially pretreated (left untreated (w/o), pretreated with native or heat-inactivated (h.i.) serum) carbohydrate-coated types of NC. NC binding to $CD11c^+$ DC was assessed by flow cytometry and is given as MFI (mean ± SEM of 3 experiments). Details on the gating strategy are given in Figure S7. Statistical differences versus * w/o serum and $^+$native serum are indicated (one-way ANOVA, Tukey's test). $^{*,+}$ $p < 0.05$, $^{**,++}$ $p < 0.01$, $^{***,+++}$ $p < 0.001$.

2.3. CR3, But not CR4 is Required for Binding and Uptake of Complement-Opsonized NC by DC

To elucidate the importance of CR3 on BMDC for the engagement of complement-opsonized NC further, we employed BMDC derived from $CD11b^{-/-}$ mice, which thereby express CR4 only. Since all types of NC that were coated with carbohydrates yielded similar results, with FeO-DEX displaying the most significant differences, we used only this type of NC throughout the following experiments.

Untreated FeO-DEX applied to BMDC kept in fetal calf serum (FCS) free culture medium or in normal culture medium displayed only minor cell binding (Figure 3A), which indicates that the presence of FCS in culture media has no effect on the binding of FeO-DEX in this regard. However, when FeO-DEX were pre-incubated with native mouse serum, only WT, but not CR3-deficient BMDC engaged FeO-DEX to a higher extent. As expected, pretreatment of FeO-DEX with h.i. serum did not result in significantly enhanced binding to either BMDC population. Complement-dependent binding of FeO-DEX to BMDC via CR3 was evaluated by mixing WT and CR3-deficient BMDC, followed by incubation with differentially pretreated FeO-DEX. In subsequent flow cytometric assays, BMDC were differentiated according to the dual expression of CR3 and CR4 (WT) versus CR4 only ($CD11b^{-/-}$). Interestingly, $CD11b^{-/-}$ DC displayed lower FeO-DEX engagement not only in the case of NC pretreatment with native but also h.i. serum, which may suggest the involvement of CR3 in binding of FeO-DEX with a complement-deficient protein corona (Figure 3B). To rule out indirect effects of CR3 on FeO-DEX binding, e.g., due to differential expression of other endocytic surface receptors by $CD11b^{-/-}$ as compared to WT BMDC, the latter were incubated with a CD11b (and thereby CR3) blocking antibody. Blockade of CD11b, but not the application of a corresponding isotype control antibody, significantly reduced binding of FeO-DEX pretreated with a native mouse (Figure 3C). Heparin has been demonstrated to inhibit the function of various complement factors [26].

Therefore, as an alternative approach to inhibit complement activity in serum, instead of mild heat treatment, serum was pretreated with a clinically applied heparin formulation (Innohep) prior to the addition of FeO-DEX for protein corona formation. Subsequent binding assays showed decreased binding of FeO-DEX pre-incubated with Innohep-pretreated serum to BMDC in a dose-dependent manner (Figure 3D). This finding confirmed the role of carbohydrate-dependent complement activation on the surface of FeO-DEX as a prerequisite for CR3 engagement.

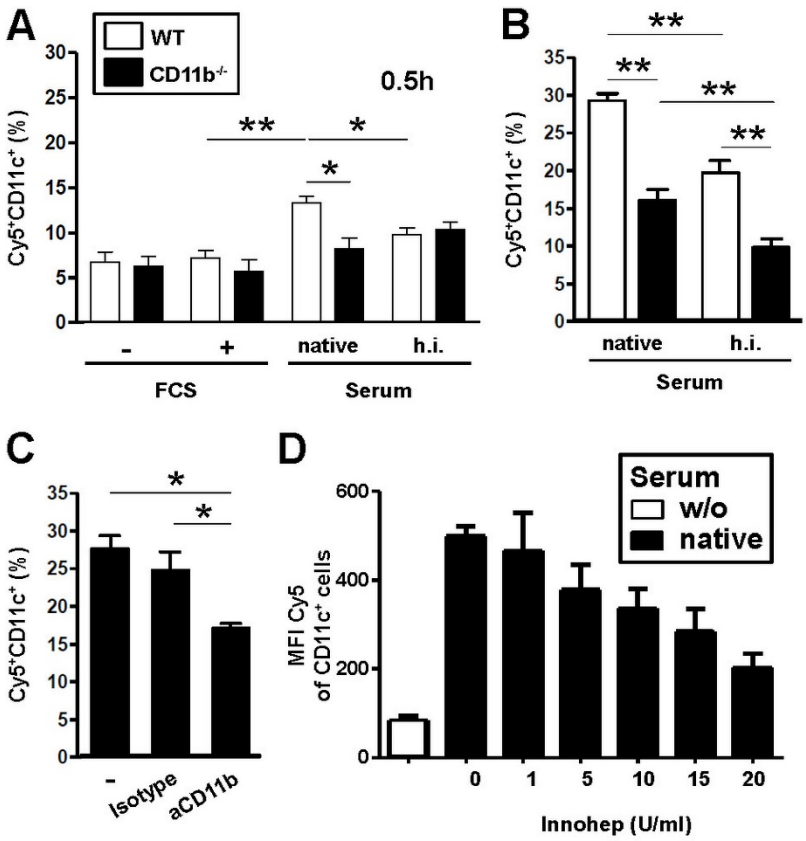

Figure 3. Binding of native serum-pre-incubated solid iron oxide core (FeO-DEX) to BMDC depends on complement activation and CR3 engagement. (**A**,**B**) BMDC differentiated from bone marrow progenitors derive from wild type (WT), and CD11b$^{-/-}$ mice were incubated with differentially pretreated (left untreated (w/o), pretreated with native or heat-inactivated (h.i.) serum) FeO-DEX as indicated. (**A**) BMDC were incubated with non-pretreated FeO-DEX (BMDC kept in parallel in fetal calf serum (FCS) free (−) or standard culture medium (+) and with native and h.i. serum-pre-incubated FeO-DEX (BMDC kept in FCS-containing media) as indicated. After 0.5 h, frequencies of Cy5$^+$ BMDC (CD11c$^+$ cells) were assessed by FACS analysis (mean ± SEM of 3 experiments). (**B**) WT and CD11b$^{-/-}$ BMDC were mixed and incubated for 4 h with FeO-DEX pre-incubated with native or h.i. serum. Frequencies of Cy5$^+$ BMDC were assessed by FACS analysis (mean ± SEM of 3 experiments). (**C**) WT BMDC were pretreated in parallel with blocking anti-CD11b and a corresponding isotype control antibody, followed by incubation with native serum-pre-incubated FeO-DEX applied 45 min later. Frequencies of Cy5$^+$ BMDC were assessed after 3 h by FACS analysis. (**D**) Native serum was pre-incubated in parallel with increasing doses of complement blocking heparin (Innohep) for 10 min. FeO-DEX were added, and samples were incubated for 1 h. Pretreated FeO-DEX were applied to WT BMDC, and after 4 h, Cy5 MFI of DC (CD11c$^+$) were monitored (mean ± SEM of 3 experiments). (**A**–**C**) Statistical differences between groups are indicated (one-way ANOVA, Tukey's test). * $p < 0.05$, ** $p < 0.01$.

Confocal laser scanning microscopy (CLSM) confirmed that complement-opsonized FeO-DEX were internalized to a higher extent by WT than by CD11b$^{-/-}$ BMDC (Figure 4). When h.i. serum was used for FeO-DEX pretreatment, NC were scarcely internalized by

either BMDC population. Altogether, these observations show that the enhanced binding/uptake of FeO-DEX that were pre-incubated with native mouse serum by BMDC depends on complement activation and CR3 expression.

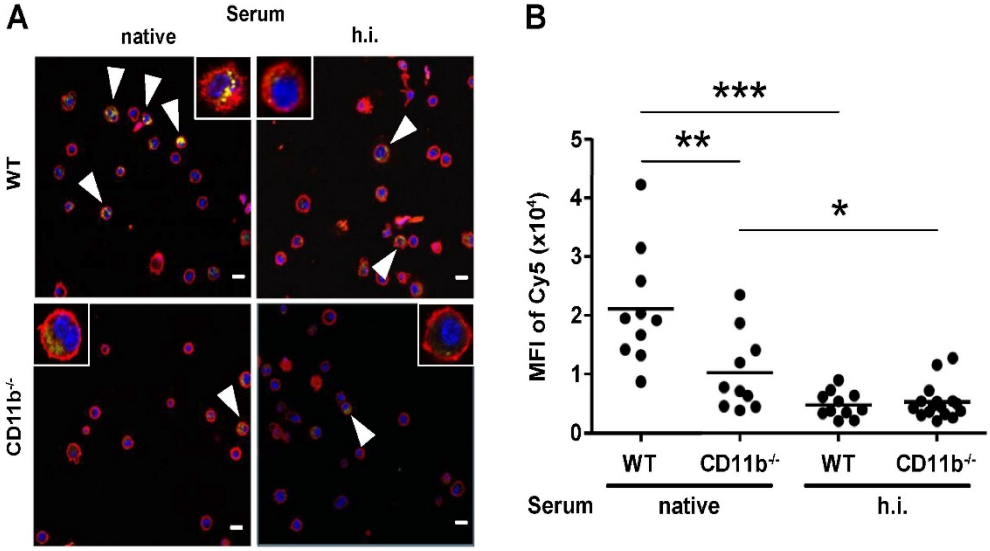

Figure 4. Complement activity and CR3 expression are required for uptake of FeO-DEX by BMDC. In parallel assays, WT and CD11b$^{-/-}$ BMDC were incubated with FeO-DEX pretreated with native and h.i. serum, respectively. After 3 h, samples were cytospun, incubated with anti-CD11c antibody (red), and DAPI for nuclear staining (blue). Samples were assessed by confocal laser scanning microscopy (CLSM). Cy5 fluorescence of FeO-DEX is given in yellow. (**A**) Representative CLSM pictures. Inlets: single-cells. Arrowheads indicate Cy5-positive cells. Bar length: 10 µm. (**B**) Quantification of intracellular Cy5 intensities of Cy5^{+} BMDC (mean ± SEM of each 10 CD11c^{+} BMDC). Statistical differences between groups are indicated (one-way ANOVA, Tukey's test). * $p < 0.05$, ** $p < 0.01$, *** $p < 0.001$.

2.4. Binding of Complement-Coated NC Interferes with DC Activation

Engagement of DC by immune complexes via CR3 has been shown to affect their activation state [27]. To delineate the potential effects of complement-opsonized FeO-DEX in this regard, BMDC were incubated with native serum-pretreated FeO-DEX. In parallel settings BMDC were stimulated with LPS after NC application. On the next day, the expression of activation markers was assessed. As depicted in Figure 5, FeO-DEX-positive BMDC were characterized by a somewhat lower expression of MHCII and the costimulator CD86 as compared to untreated BMDC. Further, the application of LPS as a genuine TLR4 ligand resulted in profound upregulation of either activation marker in BMDC. This effect was markedly attenuated in the case of samples incubated with complement-opsonized FeO-DEX. This result shows that engagement of CR3 on BMDC by serum-opsonized FeO-DEX diminished their responsiveness towards stimulation.

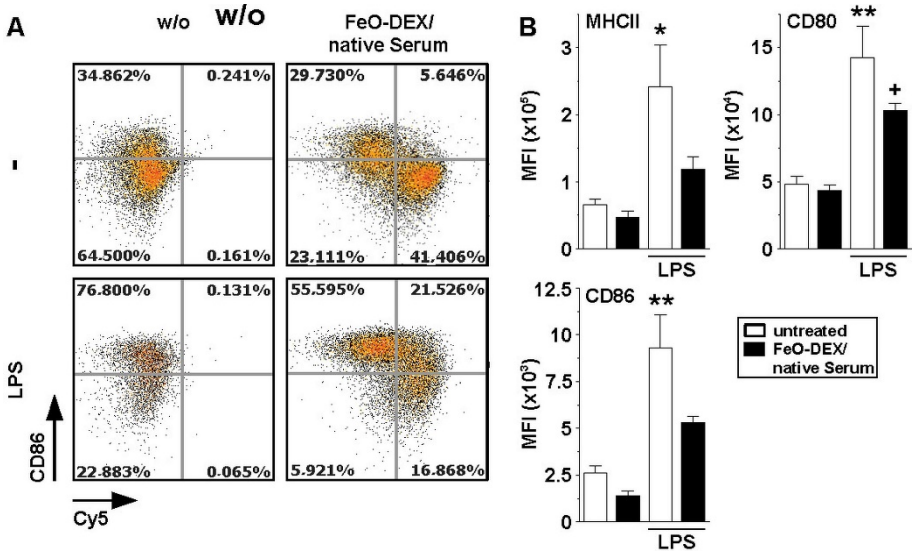

Figure 5. Engagement of CR3 by serum-opsonized FeO-DEX attenuates upregulation of activation markers in response to stimulation. BMDC were incubated with native serum-pre-incubated FeO-DEX. Aliquots were treated with LPS (100 ng/m) applied 1 h later. On the next day, the expression of DC activation markers (MHCII, CD80, CD86) was assessed by FACS analysis. (**A**) Representative FACS plots showing CD86 expression (gating strategy described in Figure S6). (**B**) Quantification of activation marker expression (MFI) of $CD11c^+$ BMDC (mean ± SEM of 3 experiments). Statistical differences versus *untreated and $^+$FeO-DEX/native serum are indicated (one-way ANOVA, Tukey's test). $^{*,+}$ $p < 0.05$, ** $p < 0.01$.

2.5. Among B Cells, FeO-DEX are Highly Engaged by B-1 Cells

We have previously demonstrated that complement-opsonized FeO-DEX bound splenic B cells via CR1/2 [7]. B-1 cells comprise a minor B cell population, which, besides CR1/2, also expresses CR3 [28]. Therefore, we asked whether B-1 cells, due to co-expression of both complement receptors, would bind FeO-DEX to a higher extent as compared to conventional B-2 cells. To this end, murine spleen cells were incubated with differentially pretreated FeO-DEX, and their binding to B cell subpopulations was assessed by flow cytometry. In our experiment, up to 8% of splenic $CD19^+$ B cells constituted B-1 as deduced from co-expression of CR3 (Figure 6A, left panel). B-1 cells are phenotypically subdivided into $CD5^+$ B-1a and $CD5^-$ B-1b cells. Both B-1 subpopulations readily engaged FeO-DEX as assessed after over-night incubation (right panel). B-1 cells bound directly applied FeO-DEX at a much higher extent than B-2 cells, both in terms of frequency (Figure 6B, left panel) and overall MFI (Figure 6B, right panel). Pretreatment of FeO-DEX with native serum enhanced their binding to either B cell population. This effect was abolished when FeO-DEX were pretreated with h.i. serum. Similar results were also obtained after 3 h incubations (Figure S9).

Due to our findings of an inhibitory effect of FeO-DEX engagement of DC with regard to their response towards subsequent stimulation, we asked for corresponding effects in the case of B cells. After incubation with native-serum-pretreated FeO-DEX, FeO-DEX-binding B-1 and B-2 cells displayed no alterations in the case of costimulator CD86 (Figure 6C) expression. Both B cell subpopulations were characterized by elevated CD86 expression after LPS stimulation. B-2 cells stimulated with LPS after the onset of incubation with serum-pretreated FeO-DEX displayed comparable CD86 expression levels as non-incubated samples. In contrast, FeO-DEX-positive B-1 cells were characterized by diminished upregulation of CD86 in response to subsequent stimulation with LPS. Therefore, binding of serum-pretreated FeO-DEX may exert inhibitory effects on activation marker expression by B-1 cells. Taken together, these findings show that B-1 cells, in general, engage FeO-DEX to a higher extent than B-2 cells and that binding of complement-opsonized FeO-DEX affected their activation state, which was not observed for B-2 cells.

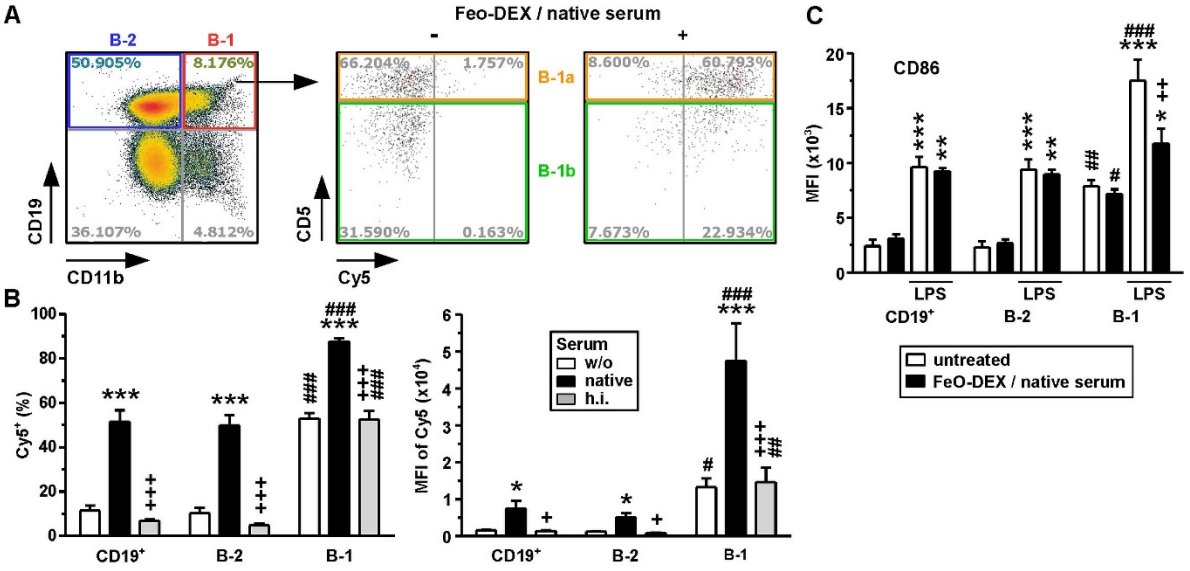

Figure 6. B-1 cells engage FeO-DEX to a higher extent than B-2 cells but are affected in their activation state. Spleen cells were incubated over-night with differentially pretreated (left untreated (w/o), pretreated with native or heat-inactivated (h.i.) serum) FeO-DEX. (**A**) FACS plot identifying splenic B-1 cells that co-express CD19 and CD11b (left panel) and delineating $CD5^+$ B-1-a and CD5- B-1b cells, which engage native serum-pre-incubated FeO-DEX (right panel). Plots are representative of 4 experiments. (**B**) Frequencies of $Cy5^+$ (left panel) and MFI of Cy5 (right panel) of B cell populations (total B cells ($CD19^+$), B-2 cells ($CD11b^-CD19^+$) and B-1 cells ($CD11b^+CD19^+$)). Data denote the mean ± SEM of 3 experiments. Statistical differences versus *w/o, +native serum, #B-1 versus B-2 (corresponding group) are indicated (one-way ANOVA, Tukey's test). (**C**) Quantification of CD86 activation marker expression (MFI) of B cell populations (see above) after over-night incubation with native serum-pretreated FeO-DEX (mean ± SEM of 3 experiments). Statistical differences versus *according to the group at unstimulated state, $^{\#}$B-1 versus B-2 (corresponding group) and $^{+}$LPS-stimulated are indicated (one-way ANOVA, Tukey's test). (**B**,**C**) $^{*,+,\#}p<0.05$, $^{**,++,\#\#}p<0.01$, $^{***,+++,\#\#\#}p<0.001$.

Finally, we asked for the relative importance of CR1/2 and CR3 as expressed by B-1 cells for the binding of differentially pretreated FeO-DEX. To this end, spleen cells were pretreated with antagonist antibodies for either CR, followed by incubation with differentially pretreated FeO-DEX for 3 h. In contrast, binding of FeO-DEX left untreated or pretreated with h.i. serum to B-2 and B-1 cells was not affected by either antagonistic antibody, binding of serum-pretreated FeO-DEX to either B cell subpopulation in the case of CR1/2 blockade (Figure 7). Similar observations were made after over-night incubation (Figure S10A). Interestingly, blockade of CR3 yielded no such effect on B-1 and B-2 cells but strongly reduced Cy5 intensities of CD11b-expressing non-B cells (Figure S10B). These observations suggest that the elevated capacity of B-1 cells to bind (complement-opsonized) FeO-DEX does not depend on CR3 but CR1/2 only.

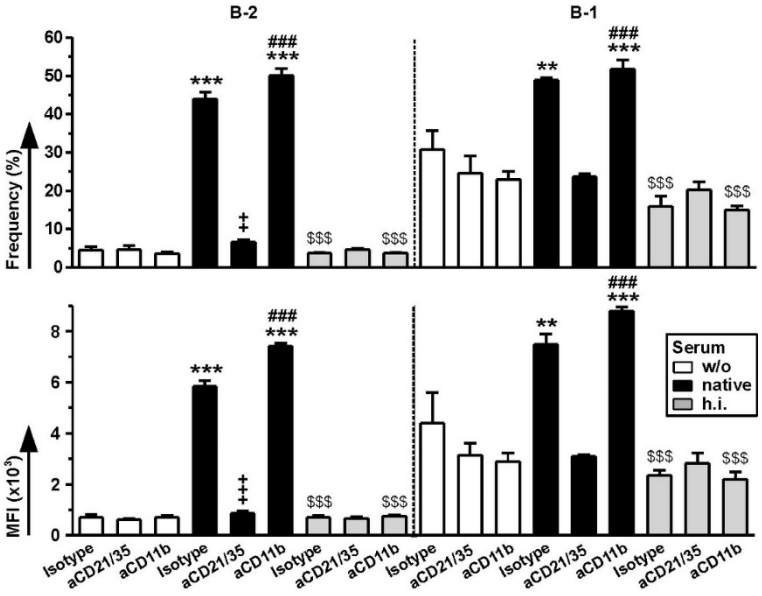

Figure 7. B-1 cells engage complement-opsonized FeO-DEX via CR1/2, but not CR3. Spleen cells were pretreated in parallel with antagonistic anti-CD21/CD35 (CR1/2), anti-CD11b (CR3) and an according isotype control antibody (each 5 μg/mL), followed by incubation with differentially pretreated FeO-DEX (left untreated (w/o), pretreated with native or heat-inactivated (h.i.) serum) applied 45 min later. Frequencies of $Cy5^+$ cells (upper panel) and MFI of Cy5 (lower panel) of B-2 (left panel) and B-1 (right panel) cells, identified as $CD11b^-CD19^+$ (B-2 cells) and $CD11b^+CD19^+$ (B-1 cells) were assessed 3 h after the onset of incubation with FeO-DEX (mean ± SEM of 3 experiments). Statistical differences * versus w/o and $ versus native serum group (treated with the same antibody), + versus isotype and # versus aCD21/35 (within same group) are indicated (one-way ANOVA, Tukey's test). $*,+,\#$ $p < 0.05$, $**,++,\#\#$ $p < 0.01$, $***,+++,\#\#\#,\$\$\$$ $p < 0.001$.

3. Discussion

It is well established by now that in vivo, a protein corona may be formed around NC, which may significantly affect cellular interaction, and thereby its targeting and drug delivery properties. Aside from "passive" protein adsorption onto the NC surface [2], surface structures of the NC may also be recognized by the innate immune system, as shown by us and others for carbohydrate-coated NC, which triggered the lectin-dependent complement pathway [7].

Here we show that CR3-expressing cell types within the spleen, including myeloid cell types [9], engaged complement-opsonized NC to a higher extent as compared to NC applied directly or after pretreatment with h.i. serum lacking complement activity. We further showed that CR3 is necessary for binding and uptake of complement-opsonized NC by BMDC, whereas CR4, which in mouse constitutes a pan-DC lineage marker [29], is dispensable. It is conceivable that in the case of cDC2, CR3 may largely contribute to the binding of (complement-opsonized) NC. However, in the case of cDC1 and pDC, which lack CR3, other receptors may play a role in NC binding. Additional studies are necessary to identify contributing receptors.

Besides DEX and starch also other carbohydrates like chitosan [30] were reported to trigger complement activation, which is of considerable importance given the ongoing interest in chitosan-based and–coated NC for biomedical applications [31]. Aside from carbohydrates also other surface properties may trigger complement activation as reported for positively charged poly(lactic-co-glycolic) acid (PLGA) based NC [32], another type of NC frequently used in preclinical [33] and clinical [34] studies. Therefore, in vivo complement opsonization of NC may contribute to their biodistribution in numerous cases.

CR3 may play an important role in the binding and uptake of complement-opsonized NC in the case of myeloid cells and NK cells. CR3 may also facilitate the binding of NC

via other constituents of their protein corona due to its rather broad substrate affinities, including numerous serum factors [9]. In agreement, polystyrene microparticles coated with bovine serum albumin, fibronectin or fibrinogen showed stronger uptake by WT as compared to $CD11b^{-/-}$ MAC [35]. Above, adsorption of fibrinogen onto negatively charged poly(acrylic acid)-conjugated gold NC resulted in its unfolding, which in turn enhanced its binding to MAC via CR3 [36]. Superparamagnetic iron oxide nanoparticles, which are clinically employed for resonance imaging of atherosclerotic plaques [37], when tested in vitro, engaged CR3 as delineated using CD11b-blocking antibodies [38]. However, it remains unclear whether, under these circumstances, constituents of the protein corona, which is inevitably formed by contact with FCS in cell culture media [39], may have served as CR3 ligand(s).

Anyway, that study also highlighted that the activation state of CR3 might contribute to the extent of NC engagement. In this regard, it is noteworthy that CR3 can exhibit different conformation states, which in turn may affect its binding affinity for substrates [20]. The conformation state of CR3 is dynamically regulated by distinct mediators and signaling pathways as well as ligands [40,41] in a cell type-specific manner [42]. Insofar, both the cellular microenvironment and the character of the CR3 engaging ligand may contribute to the extent of its binding to CR3-expressing cells.

In general, CR3 may also serve as an inhibitor of DC activation since DC deficient for CD11b [43] and CD18 [19] displayed hyper-activation in response to stimulation with TLR ligands. Similar observations were made for MAC [19,44]. We observed that BMDC, which bound complement-opsonized FeO-DEX were characterized by diminished upregulation of activation markers in response to subsequently applied LPS. This result corroborates with previous studies that reported inhibitory effects of CR3 triggering on DC, e.g., by complement-opsonized apoptotic cells, shown to promote self-tolerance [45,46]. In the case of infection, however, opsonized pathogens, which are frequently recognized and internalized by CR3, yield activation of DC (and other types of APC) due to co-delivered pathogen-derived molecular patterns that act as danger signals [47] and thereby override the inherent inhibitory effect of CR3 triggering.

Danger signals, as exemplified, e.g., for LPS, were reported to increase CR3 surface expression [48,49]. Therefore, it is conceivable that NC intrinsically exerts adjuvant activity, as, for example, poly (lactic-co-glycolic acid) (PLGA) [50], and/or deliver a danger signal intended to serve as an adjuvant (e.g., immunostimulatory TLR ligands like unmethylated CpG motifs [51]) into a myeloid cell may in the course of cell activation also mediate the acquisition of a high-affinity state of CR3 and overall elevated CR3 expression. By these mechanisms, CR3-dependent binding and uptake of applied NC may be increased. However, at later time points after the onset of activation, in the case of professional APC like cDC, internalization of the material may cease as a consequence of the functional switch of the activated APC to emigrate towards secondary lymphoid organs to present (pathogen-) derived antigen to T cells [52].

Our studies also showed that within the splenic B cell population, especially B-1 cells, characterized by CR3 expression, engaged FeO-DEX at a stronger extent than "conventional" B-2 cells. This difference was apparent both in the case of non-pretreated FeO-DEX as well as NC pretreated with native or h.i. serum. Somewhat surprisingly, our blocking studies, on one hand, suggest that CR3 plays no role in the engagement of either type of differentially pretreated FeO-DEX, which could be explained by a low-affinity conformation state of CR3 [40,41]. On the other hand, CR1/2 was essential for binding of serum-pretreated FeO-DEX, both in the case of B-1 as well as B-2 cells, which corroborates our previous findings [7]. Similar to BMDC, engagement of complement-opsonized FeO-DEX affected surface expression of CD86 of B-1 cells. Although CR3 played no role in the binding of FeO-DEX, we cannot rule out a contribution of CR3 as a signaling adaptor to inhibit the state of activation of B-1 cells after contact with FeO-DEX. Further studies are required to delineate which signaling adaptors are important in this regard.

B-1 cells reside predominantly in the peritoneum and pleural cavities [53]. As an early response to infection, B-1 cells via interferon I-induced activation of CR3 migrate towards lymphatic organs [54] and are activated further by pathogen-derived stimuli [17]. Deficiency of CD11b (and thereby CR3) was reported to result in hyper-activation and prolonged survival of B-1 cells [55], as also has been observed for myeloid cell types [43,44]. B-1 cells comprise two subpopulations, which are phenotypically differentiated according to co-expression of CD5 ($CD5^+$: B-1a, $CD5^-$: B-1-b) and display a different ontogeny [16]. In our studies, B-1a and B-1b engaged FeO-DEX at comparable levels. Both B-1 subpopulations exert primarily innate immune functions to eradicate pathogens by producing (natural) IgM antibodies [56] and exert phagocytosis [17] but also serve as APC that induces (primary) T cell responses [28,57]. Altogether, B-1 cells, due to their innate-like functional properties, significantly contribute to early immune responses in viral [58] and parasite [17] infections. Consequently, B-1 cells have been ascribed strong therapeutic potential, as confirmed in a number of adoptive transfer studies [59].

Conventional antigen-specific B-2 cells play an important role in the later course of infection by producing antibodies that opsonize pathogens [60] and bind infected cells, which de novo express pathogen-specific proteins on their surface, resulting in antibody-dependent cellular cytotoxicity, cell phagocytosis and complement-dependent cytotoxicity [61]. The same mechanisms are exploited by numerous clinically applied monoclonal antibodies designed to label malignant cells [62]. We exploited the intrinsic, complement-mediated binding of FeO-DEX to splenic B cells to shift T helper cell type 2 (Th2)-biased humoral responses towards Th1 [7] using CpG ODN as an adjuvant [63]. In therapeutic settings, vaccination of mice with FeO-DEX conjugated with ovalbumin (OVA) as a model antigen and CpG ODN prevented allergic reactions by inhibiting IgE production [7]. It is conceivable that by this approach, besides B-2 cells, also B-1 cells, as well as myeloid cells, may have been addressed.

To date, most NC-focused immunotherapeutic strategies aimed to induce adaptive immune responses to target DC [64], which at an activated state constitute the most potent APC population, able to induce primary T cell responses [22]. In contrast, only a few studies have issued active B cell targeting [65]. To the best of our knowledge, the engagement of B-1 cells by NC has not been described before. In light of the important role of B-1 cells for innate as well as adaptive immunity, further studies should also take into account the potential interaction of this cell type with NC and the consequences concerning the state of activation of NC-binding B-1 cells.

Altogether, our results confirm that the design of NC for biomedical purposes needs to take into account the possibility of recognition of surface structures like carbohydrates by the complement system, resulting in complement opsonization and predominant interaction with CR-expressing leukocytes. Above, in some cases, an NC may trigger the alternative complement pathway due to its "foreign" surface as recently demonstrated for silica particles [66], and the classical complement pathway in the case (natural) antibodies that bind NC surface structures, resulting in recognizable exposed Fc ends [67]. Of note, activation of the classical complement pathway also has been demonstrated for NC coated with poly(2-methyl-2-oxazoline) (PMOXA), actually intended to prevent serum protein adsorption [68].

Aside from complement activation also other constituents of the protein corona may yield targeting, e.g., of CR3, like denatured fibrinogen [36], and of SR-A [69]. With regard to the latter, we observed no contribution of SR-A to cellular binding of differentially pretreated carbohydrate-coated types of NC as demonstrated for FeO-DEX. It remains a pressing issue, which factors governed binding, especially of (h.i.) serum-pretreated carbohydrate-coated NC to liver NPC. It is tempting to speculate that besides the involvement of CR3 and CR4, respectively, other receptors may contribute to NC engagement. The latter holds true also for LSEC since this cell type is not known to express any CR [24] but showed elevated binding of carbohydrate-coated NC pretreated with native/h.i. serum. Since we observed no involvement of SR-A in this regard, and due to the fact that

most types of NC after systemic application strongly accumulate in the liver, further studies are paramount to identify the contributing receptors. By now, a number of strategies have been developed to minimize unwanted cellular interaction of NC, including the use of PEG [70] and dysopsonic proteins [4] to minimize protein adsorption [4,70], and conjugation with CD47 serving as a "do not eat me" signal to reduce uptake by myeloid cell types [71].

In general, our study confirms the necessity to include serum in in vitro studies on cellular interaction of NC to mimic somewhat more closely the behavior of NC in vivo on a cellular level, as shown by us [7] and others [72], and to use primary (immune) cells for testing. More specifically, most in vitro studies on NC binding properties, which are performed as a prerequisite for subsequent in vivo testing, are performed using cell lines or primary immune cells that are rather easily accessible, like peripheral blood mononuclear cells (human) or splenic immune cells (mouse). However, in light of the frequent finding of strong NC accumulation in the liver in vivo, it may be of advantage to include liver NPC as well [24].

With regard to a translational perspective, our results suggest that complement-opsonized NC could be a suitable vaccine platform to induce a broad cellular and humoral immune response, similar to pathogens that are recognized by the complement system [73]. As depicted in Figure 8, such nano-vaccines, co-delivering pathogen- or tumor-specific antigen and adjuvant, may address on one hand especially cDC2 via CR3, which at activated state stimulate antigen-specific $CD4^+$ Th [74] and $CD8^+$ T cells [75]. The latter yield cytotoxic T lymphocytes that recognize and kill infected or malignant somatic cells [76]. On the other hand, corresponding nano-vaccines may target as well B cells via CR1/2, as shown previously by us [7]. In the case of B-2 cells, antigen specificity may be achieved in the case the nano-vaccine is decorated with a native protein antigen, which allows for concomitant binding of the B cell receptor (BCR). In fact, it has been demonstrated that the presence [77] and triggering [78] of CR1/2 on B cells is required to mount sustained antigen-specific antibody production. In the case of a pathogen-specific nano-vaccine, the candidate antigen would be a pathogen-specific surface protein in order to induce neutralizing antibodies [79]. Alternatively (or in addition), a pathogen-derived protein, which would be apparent on the surface of infected cells [80], would be a suitable antigen, inducing the production of antibodies that recognize infected cells, and trigger classical complement activation [81] or antibody-dependent cytotoxicity [82]. A nano-vaccine applied for tumor therapy should be decorated with a tumor-associated/specific surface protein in order to obtain antibodies that recognize malignant cells and confer antibody-mediated cytotoxic effects [83,84]. Targeting of B-1 cells by a nano-vaccine via CR1/2 may result in a profound generation of IgM antibodies [56]. In addition, B-1 cells [17,28] and myeloid cells [85], which are targeted via CR-3, may exert on one hand elevated innate responses, like phagocytosis, and on the other hand, acquire APC activity, and thereby contribute to the overall induction of cellular immune responses. DC [86] and B cells [87] that engage the nano-vaccine will also induce Th cells, which in turn activate $CD8^+$ T cells [88] and B cells [89].

Follicular dendritic cells (FDC) contribute to affinity maturation and memory B cell induction and survival [90] by long-term storage of complement-opsonized immune complexes [90] that are internalized via CR1/2 [91]. We previously observed binding and uptake of FeO-DEX by FDC in vivo [7], suggesting the involvement of CR1/2. It remains to be shown whether direct addressing of FDC by a complement-opsonized nano-vaccine may yield beneficial effects concerning B cell affinity maturation and B cell memory.

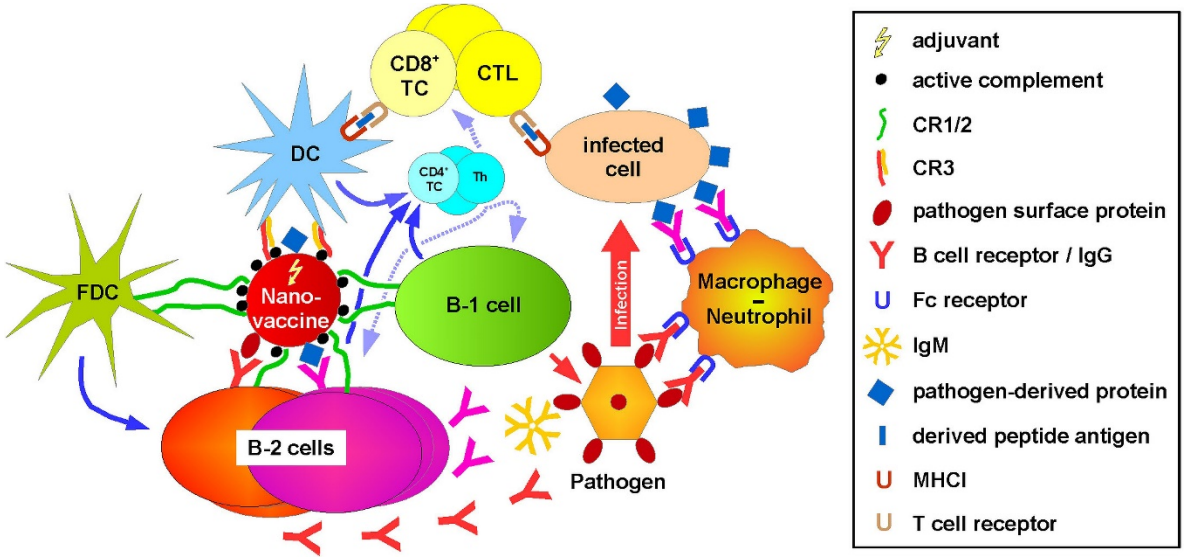

Figure 8. Nano-vaccines coated with active complement may concomitantly induce cellular and humoral immune responses. A nano-vaccine decorated with active complement may address B cells (B-1, B-2) and follicular dendritic cells (FDC) via CR1/2 and (conventional) DC via CR3. In the case of B-2 cells, antigen-specific internalization may be achieved by decoration with a pathogen-specific protein binding the B cell receptor. Codelivery of an adjuvant will result in the production of antigen-specific antibodies (B-2), which opsonize either the pathogen or the infected cells. Exposed Fc parts can trigger the classical complement pathway and directly bind Fc receptors. Antibody and/or complement-opsonized pathogens and infected cells are phagocytosed by myeloid cell types. Uptake of the nano-vaccine by B-1 cells may result in enhanced production of IgM and phagocytosis of pathogens via yet unknown receptors. Stimulated DC activates antigen-specific $CD8^+$ T cells, yielding cytotoxic T lymphocytes (CTL). CTL, in turn, kills infected cells that present the corresponding antigen. Full activation of $CD8^+$ T cells and B-2 cells requires help by activated $CD4^+$ T cells, called T helper cells (Th). These are stimulated by activated antigen-presenting cells, namely DC and B cells (B-1, B-2). FDC facilitates sustained B cell responses.

4. Materials and Methods

4.1. Materials

Fluorescent-labeled types of NP were obtained from micromod (Rostock, Germany) or from Miltenyi Biotech (Bergisch Gladbach, Germany). The characteristics of the various types of NP are listed in Table S1. Mouse serum was purified from whole blood (C57BL/6) by centrifugation using Z Serum Sep columns (Greiner Bio-One, Frickenhausen, Germany) and was quantified in a NanoDrop 2000 (Thermo Fisher, Waltham, MA, USA). Protein contents were about 30 mg/mL (Nanodrop 2000; Thermo Fisher). Aliquots of native mouse serum were heat-inactivated (56 °C, 30 min). Fucoidan, dextran sulfate, chondroitin sulfate, polyinosinic acid and polycytidylic acid (all from Sigma-Aldrich, Deisenhofen, Germany) were used to assess the contribution of SR-A for FeO-DEX binding. The heparin formulation Innohep (Leo Pharma, Neu-Isenburg, Germany) was used to inhibit the complement activity of mouse serum. Antibodies used for FACS analysis are listed in Table S2. PE/Cy7-labeled anti-CD11c antibody (clone N418) and DAPI (nuclear staining) used for CLSM analysis were purchased from Thermo Fisher. To assess the role of distinct CR for NC binding, samples were incubated with antibodies that block CR1/2 (anti-CD21/CD35; clone 7G6; BD Biosciences, Franklin Lakes, NJ, USA) and CR3 (anti-CD11b; clone M1/70; BioLegend, San Diego, CA, USA), respectively. In parallel, a corresponding isotype control antibody (Thermo Fisher) was employed.

4.2. Mice

C57BL/6 mice and $CD11b^{-/-}$ mice on a C57BL/6 background (B6.129S4-Itgam^{tm1Myd}/J) were bred and maintained in the Central Animal Facility of the Johannes Gutenberg-University Mainz under specific pathogen-free conditions on a standard diet according to the guidelines of the regional animal care committee. Female mice (6–12 weeks) were used

throughout all experiments. The "Principles of Laboratory Animal Care" (NIH publication no. 85-23, revised 1985) were followed. Mice were sacrificed for organ retrieval according to § 4(3) TierSchG.

4.3. Immune Cells

Liver nonparenchymal cells (NPC) were isolated using a liver dissociation kit and the gentle MACS dissociator (both Miltenyi Biotec) as recommended by the manufacturer with some modifications. In brief, after liver dissociation, cells were resuspended in 1 mL cold HBSS buffer (w/o Ca^{2+} and Mg^{2+}). The cell suspension was mixed with a double volume of freshly prepared 30% HistoDenZ (Sigma-Aldrich) and overlaid with 1 mL of cold HBSS buffer. After centrifugation (1500× *g*, 4 °C, w/o break), the cell containing interphase was retrieved and washed. Erythrocytes were lysed using a hypotonic buffer.

Spleen cells were isolated using a 40 μM cell strainer (Greiner Bio-One) to obtain a single-cell suspension. In parallel settings, spleen cells were resuspended in medium (IMDM, 2 mM L-glutamine, 100 U/mL penicillin, 100 μg/mL streptomycin (all from Sigma-Aldrich, Deisenhofen, Germany), and 50 μM ß-mercaptoethanol (Roth, Karlsruhe, Germany)) containing 5% FCS (PAN).

Bone marrow cells (2×10^5/mL) were seeded in 12-well cell cluster plates (Greiner Bio-One) in an IMDM-based culture medium (see above) supplemented with 10 ng/mL recombinant murine GM-CSF (R&D Systems, Wiesbaden, Germany). Culture media was replenished on days 3 and 6 of culture.

4.4. NP Binding Studies

Aliquots of the different NP were pre-incubated in parallel with equal volumes of native or heat-inactivated mouse serum for 1 h at 37 °C in low protein binding 0.5 mL reaction tubes (Greiner Bio-One). Afterward, untreated and differentially pretreated NP were applied at concentrations evaluated in corresponding pre-experiments (see Table S1) to BMDC differentiated in 12-well cell cluster plates and to the spleen cells and liver NPC kept in sterile FACS tubes (each 2×10^6/500 μL). Three hours after the onset of incubation, samples were harvested and subjected to flow cytometric analysis. In some cases, cells were harvested after over-night incubation. In some cases, samples were stimulated overnight with LPS (100 ng/mL; Sigma-Aldrich). The relevance of distinct CR for NC binding was assessed using CR-blocking antibodies and a corresponding isotype control antibody (each 5 μg/mL; see 4.1. Materials) applied 45 min prior to administration of NC.

The contribution of class A scavenger receptors for binding of FeO-DEX was tested using various pharmacological inhibitors. To this end, cells were pre-incubated with fucoidan (25 μg/mL), dextran sulfate and chondroitin sulfate (each 25 μg/mL), and polyinosinic acid and polycytidylic acid (each 12.5 μg/mL) for 1 h prior to application of differentially pretreated FeO-DEX.

4.5. Flow Cytometry

After incubation with NP, cells were washed in staining buffer (PBS/2% FCS), and Fcγ receptors were blocked by applying rat anti-mouse CD16/CD32 antibody (clone 2.4G2; 15 min, room temperature). Afterward, samples were incubated (20 min, 4 °C) with distinct sets of fluorescence-labeled antibodies as indicated in Table S2. Subsequently, samples were incubated with FVD (eFl450 or eFl780) to delineate dead cells. Antibodies were purchased from BD Biosciences, Thermo Fisher or BioLegend. FVD was obtained from Thermo Fisher. Samples were analyzed on an Attune NxT flow cytometer (Thermo Fisher). Data were analyzed using FlowJo software (FLOWJO, Ashland, OR, USA).

4.6. CLSM

BMDC (d8 of culture) were incubated with FeO-DEX as indicated, washed with FACS buffer (PBS, 1% FCS, 0.5 mM EDTA), and transferred onto chamber slides (IBIDI, Martinsried, Germany). Cells were incubated with anti-CD11c-PE/Cy7 antibody and DAPI for nuclear staining. Confocal microscope: LSM510-UV (Zeiss, Jena, Germany).

4.7. Statistical Analysis

Statistical analysis was performed using GraphPad Prism Software v5.0 (GraphPad Software Inc., San Diego, CA, USA). Results were expressed as mean ± standard error of the mean (SEM). Differences among groups were tested by one-way ANOVA, followed by post hoc Tukey's test, assuming significance at $p < 0.05$.

Supplementary Materials: Supplementary Materials can be found at www.mdpi.com/1422-0067/22/6/2869/s1.

Author Contributions: Conceptualization, S.G., M.B. (Matthias Bros); methodology, M.B. (Monika Bednarczyk), C.M.-M., F.J.F., H.S., M.R., M.K.; software, M.B. (Monika Bednarczyk), M.B. (Matthias Bros); validation, M.B. (Monika Bednarczyk), M.B. (Matthias Bros); formal analysis, M.B. (Monika Bednarczyk), C.M.-M., F.J.F., H.S., M.K.; investigation, M.B. (Monika Bednarczyk), C.M.-M., F.J.F., H.S., M.K., E.M., I.T., N.R.; resources, M.R., A.D., C.L., M.V.; data curation, M.B. (Monika Bednarczyk), C.M.-M., F.J.F., H.S., M.K.; writing—original draft preparation, M.B. (Matthias Bros); writing—review and editing, S.G., M.R.; visualization, M.B. (Monika Bednarczyk), C.M.-M., F.J.F., H.S., M.K., M.B. (Matthias Bros); supervision, M.R., S.G., M.B. (Matthias Bros); project administration, M.R., S.G., M.B. (Matthias Bros); funding acquisition, S.G., M.B. (Matthias Bros). All authors have read and agreed to the published version of the manuscript.

Funding: This research was supported by SFB-1066, grant numbers B04 (S.G.) and B05 (M.B. (Matthias Bros)). Further, M.B. (Matthias Bros) was supported by the intramural funding program of the University Medical Center of Johannes Gutenberg University Mainz.

Institutional Review Board Statement: Ethical review and approval were waived for this study due to exclusive use of isolated mouse cells derived from mice sacrificed for organ retrieval according to § 4(3) TierSchG.

Informed Consent Statement: Not applicable.

Data Availability Statement: All relevant data are included within the manuscript.

Conflicts of Interest: The authors declare no conflicts of interest.

Abbreviations

APC Antigen-presenting cell
BM Bone marrow
CR Complement receptor
cDC Conventional dendritic cell
CLSM Confocal laser scanning microscopy
DC Dendritic cell
FCS Fetal calf serum
FDC Follicular dendritic cells
LSEC Liver sinusoidal endothelial cell
MAC Macrophage
NC Nanocarrier
NPC Nonparenchymal cell
NK Natural killer cell
ODN Oligodeoxynucleotides
OVA Ovalbumin
pDC Plasmacytoid DC
PMN Polymorphonuclear cell
SPION Superparamagnetic iron oxide nanoparticles
SR-A Scavenger receptor class A

Th	T helper cell
TLR	Toll-like receptor
WT	Wild type

References

1. Du, G.; Sun, X. Engineering nanoparticulate vaccines for enhancing antigen cross-presentation. *Curr. Opin. Biotechnol.* **2020**, *66*, 113–122, doi:10.1016/j.copbio.2020.06.015.
2. Bros, M.; Nuhn, L.; Simon, J.; Moll, L.; Mailänder, V.; Landfester, K.; Grabbe, S. The Protein Corona as a Confounding Variable of Nanoparticle-Mediated Targeted Vaccine Delivery. *Front. Immunol.* **2018**, *9*, 1760, doi:10.3389/fimmu.2018.01760.
3. Zhang, Y.; Wu, J.L.Y.; Lazarovits, J.; Chan, W.C.W. An Analysis of the Binding Function and Structural Organization of the Protein Corona. *J. Am. Chem. Soc.* **2020**, *142*, 8827–8836, doi:10.1021/jacs.0c01853.
4. Takeuchi, T.; Kitayama, Y.; Sasao, R.; Yamada, T.; Toh, K.; Matsumoto, Y.; Kataoka, K. Molecularly Imprinted Nanogels Acquire Stealth In Situ by Cloaking Themselves with Native Dysopsonic Proteins. *Angew. Chem. Int. Ed. Engl.* **2017**, *56*, 7088–7092, doi:10.1002/anie.201700647.
5. Mortimer, G.M.; Butcher, N.J.; Musumeci, A.W.; Deng, Z.J.; Martin, D.J.; Minchin, R.F. Cryptic epitopes of albumin determine mononuclear phagocyte system clearance of nanomaterials. *ACS Nano* **2014**, *8*, 3357–3366, doi:10.1021/nn405830g.
6. Vincent, M.P.; Bobbala, S.; Karabin, N.B.; Frey, M.; Liu, Y.; Navidzadeh, J.O.; Stack, T.; Scott, E.A. Surface chemistry-mediated modulation of adsorbed albumin folding state specifies nanocarrier clearance by distinct macrophage subsets. *Nat. Commun.* **2021**, *12*, 648, doi:10.1038/s41467-020-20886-7.
7. Shen, L.; Tenzer, S.; Storck, W.; Hobernik, D.; Raker, V.K.; Fischer, K.; Decker, S.; Dzionek, A.; Krauthäuser, S.; Diken, M.; et al. Protein corona-mediated targeting of nanocarriers to B cells allows redirection of allergic immune responses. *J. Allergy Clin. Immunol.* **2018**, *142*, 1558–1570, doi:10.1016/j.jaci.2017.08.049.
8. Wang, G.; Griffin, J.I.; Inturi, S.; Brenneman, B.; Banda, N.K.; Holers, V.M.; Moghimi, S.M.; Simberg, D. In Vitro and In Vivo Differences in Murine Third Complement Component (C3) Opsonization and Macrophage/Leukocyte Responses to Antibody-Functionalized Iron Oxide Nanoworms. *Front. Immunol.* **2017**, *8*, 151, doi:10.3389/fimmu.2017.00151.
9. Bednarczyk, M.; Stege, H.; Grabbe, S.; Bros, M. β2 Integrins-Multi-Functional Leukocyte Receptors in Health and Disease. *Int. J. Mol. Sci.* **2020**, *21*, doi:10.3390/ijms21041402.
10. Chao, Y.; Karmali, P.P.; Simberg, D. Role of carbohydrate receptors in the macrophage uptake of dextran-coated iron oxide nanoparticles. *Adv. Exp. Med. Biol.* **2012**, *733*, 115–123, doi:10.1007/978-94-007-2555-3_11.
11. Chao, Y.; Makale, M.; Karmali, P.P.; Sharikov, Y.; Tsigelny, I.; Merkulov, S.; Kesari, S.; Wrasidlo, W.; Ruoslahti, E.; Simberg, D. Recognition of dextran-superparamagnetic iron oxide nanoparticle conjugates (Feridex) via macrophage scavenger receptor charged domains. *Bioconjug. Chem.* **2012**, *23*, 1003–1009, doi:10.1021/bc200685a.
12. Chao, Y.; Karmali, P.P.; Mukthavaram, R.; Kesari, S.; Kouznetsova, V.L.; Tsigelny, I.F.; Simberg, D. Direct recognition of superparamagnetic nanocrystals by macrophage scavenger receptor SR-AI. *ACS Nano* **2013**, *7*, 4289–4298, doi:10.1021/nn400769e.
13. Wang, G.; Serkova, N.J.; Groman, E.V.; Scheinman, R.I.; Simberg, D. Feraheme (Ferumoxytol) Is Recognized by Proinflammatory and Anti-inflammatory Macrophages via Scavenger Receptor Type AI/II. *Mol. Pharm.* **2019**, *16*, 4274–4281, doi:10.1021/acs.molpharmaceut.9b00632.
14. Erdei, A.; Isaák, A.; Török, K.; Sándor, N.; Kremlitzka, M.; Prechl, J.; Bajtay, Z. Expression and role of CR1 and CR2 on B and T lymphocytes under physiological and autoimmune conditions. *Mol. Immunol.* **2009**, *46*, 2767–2773, doi:10.1016/j.molimm.2009.05.181.
15. Ross, G.D.; Větvicka, V. CR3 (CD11b, CD18): A phagocyte and NK cell membrane receptor with multiple ligand specificities and functions. *Clin. Exp. Immunol.* **1993**, *92*, 181–184, doi:10.1111/j.1365-2249.1993.tb03377.x.
16. Yoshimoto, M. The ontogeny of murine B-1a cells. *Int. J. Hematol.* **2020**, *111*, 622–627, doi:10.1007/s12185-019-02787-8.
17. Novaes, E.B.R.R.; Dos Santos Toledo, M.; Labussiere, G.M.; Dupin, T.V.; de Campos Reis, N.F.; Perez, E.C.; Xander, P. B-1 cell response in immunity against parasites. *Parasitol. Res.* **2019**, *118*, 1343–1352, doi:10.1007/s00436-019-06211-2.
18. Reed, J.H.; Jain, M.; Lee, K.; Kandimalla, E.R.; Faridi, M.H.; Buyon, J.P.; Gupta, V.; Clancy, R.M. Complement receptor 3 influences toll-like receptor 7/8-dependent inflammation: Implications for autoimmune diseases characterized by antibody reactivity to ribonucleoproteins. *J. Biol. Chem.* **2013**, *288*, 9077–9083, doi:10.1074/jbc.M112.403303.
19. Yee, N.K.; Hamerman, J.A. β(2) integrins inhibit TLR responses by regulating NF-κB pathway and p38 MAPK activation. *Eur. J. Immunol.* **2013**, *43*, 779–792, doi:10.1002/eji.201242550.
20. Vorup-Jensen, T.; Jensen, R.K. Structural Immunology of Complement Receptors 3 and 4. *Front. Immunol.* **2018**, *9*, 2716, doi:10.3389/fimmu.2018.02716.
21. Zhu, X.J.; Yang, Z.F.; Chen, Y.; Wang, J.; Rosmarin, A.G. PU.1 is essential for CD11c expression in CD8(+)/CD8(-) lymphoid and monocyte-derived dendritic cells during GM-CSF or FLT3L-induced differentiation. *PLoS ONE* **2012**, *7*, e52141, doi:10.1371/journal.pone.0052141.
22. Wang, Y.; Xiang, Y.; Xin, V.W.; Wang, X.W.; Peng, X.C.; Liu, X.Q.; Wang, D.; Li, N.; Cheng, J.T.; Lyv, Y.N.; et al. Dendritic cell biology and its role in tumor immunotherapy. *J. Hematol. Oncol.* **2020**, *13*, 107, doi:10.1186/s13045-020-00939-6.

23. Shen, L.; Krauthauser, S.; Fischer, K.; Hobernik, D.; Abassi, Y.; Dzionek, A.; Nikolaev, A.; Voltz, N.; Diken, M.; Krummen, M.; et al. Vaccination with trifunctional nanoparticles that address CD8(+) dendritic cells inhibits growth of established melanoma. *Nanomedicine* **2016**, *11*, 2647–2662, doi:10.2217/nnm-2016-0174.
24. Cacicedo, M.L.; Medina-Montano, C.; Kaps, L.; Kappel, C.; Gehring, S.; Bros, M. Role of Liver-Mediated Tolerance in Nanoparticle-Based Tumor Therapy. *Cells* **2020**, *9*, doi:10.3390/cells9091985.
25. Na, Y.R.; Jung, D.; Gu, G.J.; Seok, S.H. GM-CSF Grown Bone Marrow Derived Cells Are Composed of Phenotypically Different Dendritic Cells and Macrophages. *Mol. Cells* **2016**, *39*, 734–741, doi:10.14348/molcells.2016.0160.
26. Ludwig, R.J. Therapeutic use of heparin beyond anticoagulation. *Curr. Drug Discov. Technol.* **2009**, *6*, 281–289, doi:10.2174/157016309789869001.
27. Schmidt, J.; Klempp, C.; Büchler, M.W.; Märten, A. Release of iC3b from apoptotic tumor cells induces tolerance by binding to immature dendritic cells in vitro and in vivo. *Cancer Immunol. Immunother.* **2006**, *55*, 31–38, doi:10.1007/s00262-005-0690-5.
28. Margry, B.; Wieland, W.H.; van Kooten, P.J.; van Eden, W.; Broere, F. Peritoneal cavity B-1a cells promote peripheral CD4+ T-cell activation. *Eur. J. Immunol.* **2013**, *43*, 2317–2326, doi:10.1002/eji.201343418.
29. Metlay, J.P.; Witmer-Pack, M.D.; Agger, R.; Crowley, M.T.; Lawless, D.; Steinman, R.M. The distinct leukocyte integrins of mouse spleen dendritic cells as identified with new hamster monoclonal antibodies. *J. Exp. Med.* **1990**, *171*, 1753–1771, doi:10.1084/jem.171.5.1753.
30. Bertholon, I.; Vauthier, C.; Labarre, D. Complement activation by core-shell poly(isobutylcyanoacrylate)-polysaccharide nanoparticles: Influences of surface morphology, length, and type of polysaccharide. *Pharm. Res.* **2006**, *23*, 1313–1323, doi:10.1007/s11095-006-0069-0.
31. Torres, F.G.; Troncoso, O.P.; Pisani, A.; Gatto, F.; Bardi, G. Natural Polysaccharide Nanomaterials: An Overview of Their Immunological Properties. *Int. J. Mol. Sci.* **2019**, *20*, doi:10.3390/ijms20205092.
32. Fornaguera, C.; Calderó, G.; Mitjans, M.; Vinardell, M.P.; Solans, C.; Vauthier, C. Interactions of PLGA nanoparticles with blood components: Protein adsorption, coagulation, activation of the complement system and hemolysis studies. *Nanoscale* **2015**, *7*, 6045–6058, doi:10.1039/c5nr00733j.
33. Kokate, R.A.; Chaudhary, P.; Sun, X.; Thamake, S.I.; Maji, S.; Chib, R.; Vishwanatha, J.K.; Jones, H.P. Rationalizing the use of functionalized poly-lactic-co-glycolic acid nanoparticles for dendritic cell-based targeted anticancer therapy. *Nanomedicine* **2016**, *11*, 479–494, doi:10.2217/nnm.15.213.
34. El-Maghawry, E.; Tadros, M.I.; Elkheshen, S.A.; Abd-Elbary, A. Eudragit(®)-S100 Coated PLGA Nanoparticles for Colon Targeting of Etoricoxib: Optimization and Pharmacokinetic Assessments in Healthy Human Volunteers. *Int. J. Nanomed.* **2020**, *15*, 3965–3980, doi:10.2147/ijn.S244124.
35. Zaveri, T.D.; Dolgova, N.V.; Lewis, J.S.; Hamaker, K.; Clare-Salzler, M.J.; Keselowsky, B.G. Macrophage integrins modulate response to ultra-high molecular weight polyethylene particles and direct particle-induced osteolysis. *Biomaterials* **2017**, *115*, 128–140, doi:10.1016/j.biomaterials.2016.10.038.
36. Deng, Z.J.; Liang, M.; Monteiro, M.; Toth, I.; Minchin, R.F. Nanoparticle-induced unfolding of fibrinogen promotes Mac-1 receptor activation and inflammation. *Nat. Nanotechnol.* **2011**, *6*, 39–44, doi:10.1038/nnano.2010.250.
37. Neuwelt, A.; Sidhu, N.; Hu, C.A.; Mlady, G.; Eberhardt, S.C.; Sillerud, L.O. Iron-based superparamagnetic nanoparticle contrast agents for MRI of infection and inflammation. *AJR Am. J. Roentgenol.* **2015**, *204*, W302–W313, doi:10.2214/ajr.14.12733.
38. Von Zur Muhlen, C.; von Elverfeldt, D.; Bassler, N.; Neudorfer, I.; Steitz, B.; Petri-Fink, A.; Hofmann, H.; Bode, C.; Peter, K. Superparamagnetic iron oxide binding and uptake as imaged by magnetic resonance is mediated by the integrin receptor Mac-1 (CD11b/CD18): Implications on imaging of atherosclerotic plaques. *Atherosclerosis* **2007**, *193*, 102–111, doi:10.1016/j.atherosclerosis.2006.08.048.
39. Gan, N.; Sun, Q.; Zhao, L.; Tang, P.; Suo, Z.; Zhang, S.; Zhang, Y.; Zhang, M.; Wang, W.; Li, H. Protein corona of metal-organic framework nanoparticals: Study on the adsorption behavior of protein and cell interaction. *Int. J. Biol. Macromol.* **2019**, *140*, 709–718, doi:10.1016/j.ijbiomac.2019.08.183.
40. O'Brien, X.M.; Heflin, K.E.; Lavigne, L.M.; Yu, K.; Kim, M.; Salomon, A.R.; Reichner, J.S. Lectin site ligation of CR3 induces conformational changes and signaling. *J. Biol. Chem.* **2012**, *287*, 3337–3348, doi:10.1074/jbc.M111.298307.
41. Zhang, Y.; Hayenga, H.N.; Sarantos, M.R.; Simon, S.I.; Neelamegham, S. Differential regulation of neutrophil CD18 integrin function by di- and tri-valent cations: Manganese vs. gadolinium. *Ann. Biomed. Eng.* **2008**, *36*, 647–660, doi:10.1007/s10439-008-9446-7.
42. Varga, G.; Balkow, S.; Wild, M.K.; Stadtbaeumer, A.; Krummen, M.; Rothoeft, T.; Higuchi, T.; Beissert, S.; Wethmar, K.; Scharffetter-Kochanek, K.; et al. Active MAC-1 (CD11b/CD18) on DCs inhibits full T-cell activation. *Blood* **2007**, *109*, 661–669, doi:10.1182/blood-2005-12-023044.
43. Stevanin, M.; Busso, N.; Chobaz, V.; Pigni, M.; Ghassem-Zadeh, S.; Zhang, L.; Acha-Orbea, H.; Ehirchiou, D. CD11b regulates the Treg/Th17 balance in murine arthritis via IL-6. *Eur. J. Immunol.* **2017**, *47*, 637–645, doi:10.1002/eji.201646565.
44. Han, C.; Jin, J.; Xu, S.; Liu, H.; Li, N.; Cao, X. Integrin CD11b negatively regulates TLR-triggered inflammatory responses by activating Syk and promoting degradation of MyD88 and TRIF via Cbl-b. *Nat. Immunol.* **2010**, *11*, 734–742, doi:10.1038/ni.1908.
45. Behrens, E.M.; Sriram, U.; Shivers, D.K.; Gallucci, M.; Ma, Z.; Finkel, T.H.; Gallucci, S. Complement receptor 3 ligation of dendritic cells suppresses their stimulatory capacity. *J. Immunol.* **2007**, *178*, 6268–6279, doi:10.4049/jimmunol.178.10.6268.

46. Morelli, A.E.; Larregina, A.T.; Shufesky, W.J.; Zahorchak, A.F.; Logar, A.J.; Papworth, G.D.; Wang, Z.; Watkins, S.C.; Falo, L.D., Jr.; Thomson, A.W. Internalization of circulating apoptotic cells by splenic marginal zone dendritic cells: Dependence on complement receptors and effect on cytokine production. *Blood* **2003**, *101*, 611–620, doi:10.1182/blood-2002-06-1769.
47. Macri, C.; Fancke, B.; Radford, K.J.; O'Keeffe, M. Monitoring Dendritic Cell Activation and Maturation. *Methods Mol. Biol.* **2019**, *1988*, 403–418, doi:10.1007/978-1-4939-9450-2_28.
48. Lynn, W.A.; Raetz, C.R.; Qureshi, N.; Golenbock, D.T. Lipopolysaccharide-induced stimulation of CD11b/CD18 expression on neutrophils. Evidence of specific receptor-based response and inhibition by lipid A-based antagonists. *J. Immunol.* **1991**, *147*, 3072–3079.
49. Ammon, C.; Meyer, S.P.; Schwarzfischer, L.; Krause, S.W.; Andreesen, R.; Kreutz, M. Comparative analysis of integrin expression on monocyte-derived macrophages and monocyte-derived dendritic cells. *Immunology* **2000**, *100*, 364–369, doi:10.1046/j.1365-2567.2000.00056.x.
50. Barillet, S.; Fattal, E.; Mura, S.; Tsapis, N.; Pallardy, M.; Hillaireau, H.; Kerdine-Römer, S. Immunotoxicity of poly (lactic-co-glycolic acid) nanoparticles: Influence of surface properties on dendritic cell activation. *Nanotoxicology* **2019**, *13*, 606–622, doi:10.1080/17435390.2018.1564078.
51. Hanagata, N. CpG oligodeoxynucleotide nanomedicines for the prophylaxis or treatment of cancers, infectious diseases, and allergies. *Int. J. Nanomed.* **2017**, *12*, 515–531, doi:10.2147/ijn.S114477.
52. De Winde, C.M.; Munday, C.; Acton, S.E. Molecular mechanisms of dendritic cell migration in immunity and cancer. *Med. Microbiol. Immunol.* **2020**, *209*, 515–529, doi:10.1007/s00430-020-00680-4.
53. Morris, G.; Puri, B.K.; Olive, L.; Carvalho, A.F.; Berk, M.; Maes, M. Emerging role of innate B1 cells in the pathophysiology of autoimmune and neuroimmune diseases: Association with inflammation, oxidative and nitrosative stress and autoimmune responses. *Pharmacol. Res.* **2019**, *148*, 104408, doi:10.1016/j.phrs.2019.104408.
54. Waffarn, E.E.; Hastey, C.J.; Dixit, N.; Soo Choi, Y.; Cherry, S.; Kalinke, U.; Simon, S.I.; Baumgarth, N. Infection-induced type I interferons activate CD11b on B-1 cells for subsequent lymph node accumulation. *Nat. Commun.* **2015**, *6*, 8991, doi:10.1038/ncomms9991.
55. Ding, C.; Ma, Y.; Chen, X.; Liu, M.; Cai, Y.; Hu, X.; Xiang, D.; Nath, S.; Zhang, H.G.; Ye, H.; et al. Integrin CD11b negatively regulates BCR signalling to maintain autoreactive B cell tolerance. *Nat. Commun.* **2013**, *4*, 2813, doi:10.1038/ncomms3813.
56. Aziz, M.; Holodick, N.E.; Rothstein, T.L.; Wang, P. The role of B-1 cells in inflammation. *Immunol. Res.* **2015**, *63*, 153–166, doi:10.1007/s12026-015-8708-3.
57. Griffin, D.O.; Rothstein, T.L. A small CD11b(+) human B1 cell subpopulation stimulates T cells and is expanded in lupus. *J. Exp. Med.* **2011**, *208*, 2591–2598, doi:10.1084/jem.20110978.
58. Aziz, M.; Brenner, M.; Wang, P. Therapeutic Potential of B-1a Cells in COVID-19. *Shock* **2020**, *54*, 586–594, doi:10.1097/shk.0000000000001610.
59. Schoenlaub, L.; Elliott, A.; Freches, D.; Mitchell, W.J.; Zhang, G. Role of B cells in host defense against primary Coxiella burnetii infection. *Infect. Immun.* **2015**, *83*, 4826–4836, doi:10.1128/iai.01073-15.
60. Lam, J.H.; Baumgarth, N. The Multifaceted B Cell Response to Influenza Virus. *J. Immunol.* **2019**, *202*, 351–359, doi:10.4049/jimmunol.1801208.
61. Lewis, G.K.; Pazgier, M.; Evans, D.T.; Ferrari, G.; Bournazos, S.; Parsons, M.S.; Bernard, N.F.; Finzi, A. Beyond Viral Neutralization. *AIDS Res. Hum. Retrovir.* **2017**, *33*, 760–764, doi:10.1089/aid.2016.0299.
62. Chen, W.; Yuan, Y.; Jiang, X. Antibody and antibody fragments for cancer immunotherapy. *J. Control. Release* **2020**, *328*, 395–406, doi:10.1016/j.jconrel.2020.08.021.
63. Adamus, T.; Kortylewski, M. The revival of CpG oligonucleotide-based cancer immunotherapies. *Contemp. Oncol.* **2018**, *22*, 56–60, doi:10.5114/wo.2018.73887.
64. Macri, C.; Dumont, C.; Johnston, A.P.; Mintern, J.D. Targeting dendritic cells: A promising strategy to improve vaccine effectiveness. *Clin. Transl. Immunol.* **2016**, *5*, e66, doi:10.1038/cti.2016.6.
65. Glass, J.J.; Yuen, D.; Rae, J.; Johnston, A.P.; Parton, R.G.; Kent, S.J.; De Rose, R. Human immune cell targeting of protein nanoparticles–caveospheres. *Nanoscale* **2016**, *8*, 8255–8265, doi:10.1039/c6nr00506c.
66. Park, J.H.; Jackman, J.A.; Ferhan, A.R.; Belling, J.N.; Mokrzecka, N.; Weiss, P.S.; Cho, N.J. Cloaking Silica Nanoparticles with Functional Protein Coatings for Reduced Complement Activation and Cellular Uptake. *ACS Nano* **2020**, *14*, 11950–11961, doi:10.1021/acsnano.0c05097.
67. Janco, E.W.; Hulander, M.; Andersson, M. Curvature-dependent effects of nanotopography on classical immune complement activation. *Acta Biomater.* **2018**, *74*, 112–120, doi:10.1016/j.actbio.2018.04.053.
68. Tavano, R.; Gabrielli, L.; Lubian, E.; Fedeli, C.; Visentin, S.; Polverino De Laureto, P.; Arrigoni, G.; Geffner-Smith, A.; Chen, F.; Simberg, D.; et al. C1q-Mediated Complement Activation and C3 Opsonization Trigger Recognition of Stealth Poly(2-methyl-2-oxazoline)-Coated Silica Nanoparticles by Human Phagocytes. *ACS Nano* **2018**, *12*, 5834–5847, doi:10.1021/acsnano.8b01806.
69. Lara, S.; Perez-Potti, A.; Herda, L.M.; Adumeau, L.; Dawson, K.A.; Yan, Y. Differential Recognition of Nanoparticle Protein Corona and Modified Low-Density Lipoprotein by Macrophage Receptor with Collagenous Structure. *ACS Nano* **2018**, *12*, 4930–4937, doi:10.1021/acsnano.8b02014.
70. Zou, Y.; Ito, S.; Yoshino, F.; Suzuki, Y.; Zhao, L.; Komatsu, N. Polyglycerol Grafting Shields Nanoparticles from Protein Corona Formation to Avoid Macrophage Uptake. *ACS Nano* **2020**, *14*, 7216–7226, doi:10.1021/acsnano.0c02289.

71. Hayat, S.M.G.; Jaafari, M.R.; Hatamipour, M.; Penson, P.E.; Sahebkar, A. Liposome Circulation Time is Prolonged by CD47 Coating. *Protein Pept. Lett.* **2020**, *27*, 1029–1037, doi:10.2174/0929866527666200413100120.
72. Partikel, K.; Korte, R.; Mulac, D.; Humpf, H.U.; Langer, K. Serum type and concentration both affect the protein-corona composition of PLGA nanoparticles. *Beilstein J. Nanotechnol.* **2019**, *10*, 1002–1015, doi:10.3762/bjnano.10.101.
73. Lukácsi, S.; Mácsik-Valent, B.; Nagy-Baló, Z.; Kovács, K.G.; Kliment, K.; Bajtay, Z.; Erdei, A. Utilization of complement receptors in immune cell-microbe interaction. *FEBS Lett.* **2020**, *594*, 2695–2713, doi:10.1002/1873-3468.13743.
74. Noubade, R.; Majri-Morrison, S.; Tarbell, K.V. Beyond cDC1: Emerging Roles of DC Crosstalk in Cancer Immunity. *Front. Immunol.* **2019**, *10*, 1014, doi:10.3389/fimmu.2019.01014.
75. Bosteels, C.; Fierens, K.; De Prijck, S.; Van Moorleghem, J.; Vanheerswynghels, M.; De Wolf, C.; Chalon, A.; Collignon, C.; Hammad, H.; Didierlaurent, A.M.; et al. CCR2- and Flt3-Dependent Inflammatory Conventional Type 2 Dendritic Cells Are Necessary for the Induction of Adaptive Immunity by the Human Vaccine Adjuvant System AS01. *Front. Immunol.* **2020**, *11*, 606805, doi:10.3389/fimmu.2020.606805.
76. Halle, S.; Halle, O.; Förster, R. Mechanisms and Dynamics of T Cell-Mediated Cytotoxicity In Vivo. *Trends Immunol.* **2017**, *38*, 432–443, doi:10.1016/j.it.2017.04.002.
77. Croix, D.A.; Ahearn, J.M.; Rosengard, A.M.; Han, S.; Kelsoe, G.; Ma, M.; Carroll, M.C. Antibody response to a T-dependent antigen requires B cell expression of complement receptors. *J. Exp. Med.* **1996**, *183*, 1857–1864, doi:10.1084/jem.183.4.1857.
78. Luxembourg, A.T.; Cooper, N.R. Modulation of signaling via the B cell antigen receptor by CD21, the receptor for C3dg and EBV. *J. Immunol.* **1994**, *153*, 4448–4457.
79. Ali, M.G.; Zhang, Z.; Gao, Q.; Pan, M.; Rowan, E.G.; Zhang, J. Recent advances in therapeutic applications of neutralizing antibodies for virus infections: An overview. *Immunol. Res.* **2020**, *68*, 325–339, doi:10.1007/s12026-020-09159-z.
80. Webb, N.E.; Bernshtein, B.; Alter, G. Tissues: The unexplored frontier of antibody mediated immunity. *Curr. Opin. Virol.* **2021**, *47*, 52–67, doi:10.1016/j.coviro.2021.01.001.
81. Merle, N.S.; Noe, R.; Halbwachs-Mecarelli, L.; Fremeaux-Bacchi, V.; Roumenina, L.T. Complement System Part II: Role in Immunity. *Front. Immunol.* **2015**, *6*, 257, doi:10.3389/fimmu.2015.00257.
82. Chenoweth, A.M.; Wines, B.D.; Anania, J.C.; Mark Hogarth, P. Harnessing the immune system via FcγR function in immune therapy: A pathway to next-gen mAbs. *Immunol. Cell Biol.* **2020**, *98*, 287–304, doi:10.1111/imcb.12326.
83. Golay, J.; Taylor, R.P. The Role of Complement in the Mechanism of Action of Therapeutic Anti-Cancer mAbs. *Antibodies* **2020**, *9*, doi:10.3390/antib9040058.
84. Van der Horst, H.J.; Nijhof, I.S.; Mutis, T.; Chamuleau, M.E.D. Fc-Engineered Antibodies with Enhanced Fc-Effector Function for the Treatment of B-Cell Malignancies. *Cancers* **2020**, *12*, doi:10.3390/cancers12103041.
85. Germic, N.; Frangez, Z.; Yousefi, S.; Simon, H.U. Regulation of the innate immune system by autophagy: Monocytes, macrophages, dendritic cells and antigen presentation. *Cell Death Differ.* **2019**, *26*, 715–727, doi:10.1038/s41418-019-0297-6.
86. Amon, L.; Hatscher, L.; Heger, L.; Dudziak, D.; Lehmann, C.H.K. Harnessing the Complete Repertoire of Conventional Dendritic Cell Functions for Cancer Immunotherapy. *Pharmaceutics* **2020**, *12*, doi:10.3390/pharmaceutics12070663.
87. Hua, Z.; Hou, B. The role of B cell antigen presentation in the initiation of CD4+ T cell response. *Immunol. Rev.* **2020**, *296*, 24–35, doi:10.1111/imr.12859.
88. Bedoui, S.; Heath, W.R.; Mueller, S.N. CD4(+) T-cell help amplifies innate signals for primary CD8(+) T-cell immunity. *Immunol. Rev.* **2016**, *272*, 52–64, doi:10.1111/imr.12426.
89. Aloulou, M.; Fazilleau, N. Regulation of B cell responses by distinct populations of CD4 T cells. *Biomed. J.* **2019**, *42*, 243–251, doi:10.1016/j.bj.2019.06.002.
90. Heesters, B.A.; Myers, R.C.; Carroll, M.C. Follicular dendritic cells: Dynamic antigen libraries. *Nat. Rev. Immunol.* **2014**, *14*, 495–504, doi:10.1038/nri3689.
91. Roozendaal, R.; Carroll, M.C. Complement receptors CD21 and CD35 in humoral immunity. *Immunol. Rev.* **2007**, *219*, 157–166, doi:10.1111/j.1600-065X.2007.00556.x.

International Journal of
Molecular Sciences

MDPI

Supplemental Materials

Complement-Opsonized Nano-Carriers are Bound by Dendritic Cells (DC) via Complement Receptor (CR)3, and by B Cell Subpopulations via CR-1/2, and Affect the Activation of DC and B-1 Cells

Monika Bednarczyk[1], Carolina Medina-Montano[1], Frederic Julien Fittler[1,†], Henner Stege[1,†], Meike Roskamp[2], Michael Kuske[1], Christian Langer[2], Marco Vahldieck[2], Evelyn Montermann[1], Ingrid Tubbe[1], Nadine Röhrig[1], Andrzej Dzionek[2], Stephan Grabbe[1] and Matthias Bros[1,*]

[1] Department of Dermatology, University Medical Center Mainz, Langenbeckstraße 1, 55131 Mainz, Germany; m.bednarczyk.09@aberdeen.ac.uk (M.B.); gmedinam@students.uni-mainz.de (C.M.-M.); ffittler@students.uni-mainz.de (F.J.F.); Henner.Stege@unimedizin-mainz.de (H.S.); mikuske@uni-mainz.de (M.K.); monterma@uni-mainz.de (E.M.); tubbe@uni-mainz.de (I.T.); n.roehrig@uni-mainz.de (N.R.); stephan.grabbe@unimedizin-mainz.de (S.G.); mbros@uni-mainz.de (M.B.)

[2] Miltenyi Biotec GmbH, Friedrich-Ebert-Strasse 68, 51429 Bergisch Gladbach, Germany; meiker@miltenyi.com (M.R.); christianlan@miltenyi.com (C.L.); MarcoV@miltenyi.com (M.V.); Andreasd@miltenyibiotec.de (A.D.)

* Correspondence: mbros@uni-mainz.de; Tel.: +49-6131-17-9846

† These authors contributed equally to this work.

Supplemental tables

Table S1. NC properties

	NC			
Properties	BNF-STA	BNF-DEX	FeO-DEX	Albumin
Composition	Cross-linked iron oxide-starch composite	Cross-linked iron oxide-dextran composite	Iron-dextran composite	cross-linked bovine serum albumin
Diameter (nm)	100	100	63	250
Fluorescent dye[1]	RedF	RedF	Cy5	GreenF
Final concentration (μg/ml)[3]				
Liver NPC	5	50	1.25	2.5
Spleen cells	5	50	1.25	2.5
BMDC	25	10	1.25	1

[1]RedF: Excitation: 552 nm, Emission 580 nm; GreenF: 485 nm, 510 nm; Cy5: 649 nm, 666 nm; [2]assessed in pre-experiments using BMDC; [3]determined based on dose kinetic experiments using spleen cells, liver NPC and BMDC.

Table S2. Antibodies

Antibody	Fluorochrome	Clone	Marker
Spleen cells			
CD3	V500	500A2	T cell
CD5	PerCP	03.07.53	B-1a
CD11b	SB600	M1/70	Myeloid cell
CD11c	BV421	N418	DC
CD19	SB702	1D3	B cell
Ly6G	eFl610	1AB	PMN
NK1.1	PE-Cy7	PK136	NK cell
Liver NPC			
CD11c	BV421, PE-Cy7	N418	DC
CD32b	APC, PE	AT130-2	LSEC
CD45	BV711	30-F11	Leukocyte
F4/80	eFl506	BM8	Macrophage
BMDC			
CD11b	SB600	M1/70	Myeloid cells
CD11c	PE-Cy7 / BV421	N418	DC
CD80	PE	16-10A1	Activation

CD86	FITC	GL1	Activation
MHCII	PE-eFl610	M5/114-15.2	Activation

Supplemental figures

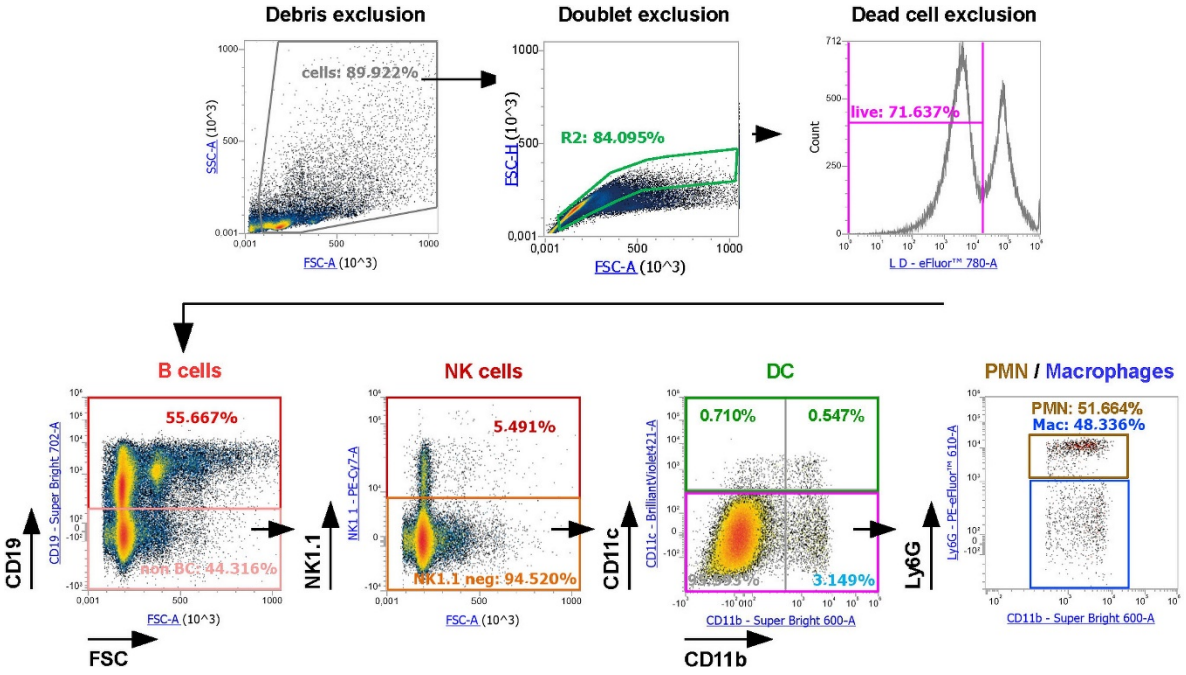

Figure S1. Gating strategy of spleen cells. After exclusion of debris, doublets and dead cells, spleen cell populations were identified sequentially according to lineage marker expression, B cells ($CD19^+$), NK cells ($CD19^-NK1.1^+$), DC ($CD19^-NK1.1^-CD11c^+$), PMN ($CD19^-NK1.1^-CD11c^-CD11b^+Ly6G^+$) and MAC ($CD19^-NK1.1^-CD11c^-CD11b^+Ly6G^-$).

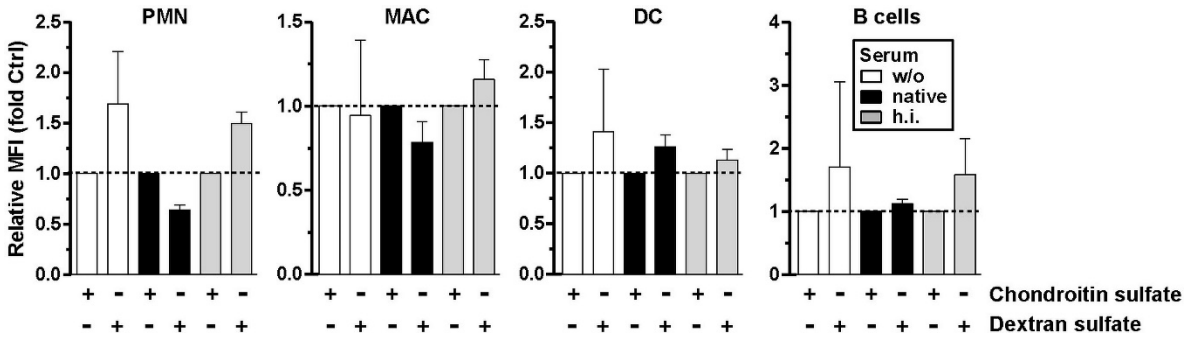

Figure S2. Scavenger receptors type A (SR-A) are not involved in binding of FeO-DEX. Spleen cells were pre-incubated in parallel with a SR-A inhibitor (dextran sulfate) and the according control agent (chondroitin sulfate, Ctrl) for 45 min. Then, samples were incubated for 3h with differentially pretreated (left untreated [w/o], pretreated with native or heat-inactivated [h.i.] serum) Cy5-labeled FeO-DEX and assayed by flow cytometry (see figure S1). Graphs denote the relative MFI of Cy5 in various splenic cell populations (mean±SD of 2 experiments).

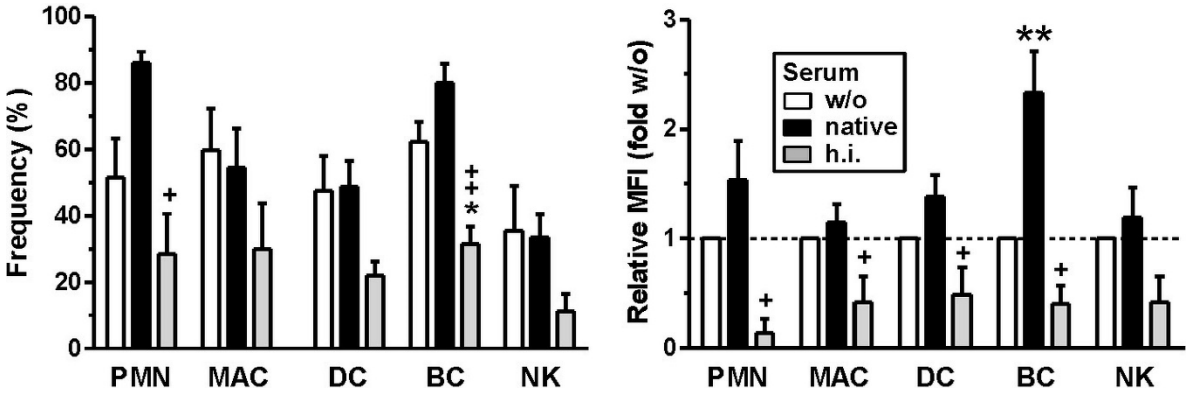

Figure S3. Albumin NC pre-incubated with h.i. serum bind most spleen cell populations at reduced extent. Differentially pretreated (left untreated [w/o], pretreated with native or heat-inactivated [h.i.] serum) GreenF-labeled albumin NC were incubated for 3h with spleen cells. The extent of NC binding to the various spleen cell populations was assessed by flow cytometry (see figures 1, S1). Graphs denote the frequencies of GreenF-positive cells (left panel) and the relative MFI of either spleen cell type (right panel) (mean±SEM of 3-4 experiments). PMN: neutrophils, MAC: macrophages, DC: dendritic cells, BC: B cells, NK: natural killer cells. Statistical differences: versus *w/o serum and $^{+}$native serum (one way ANOVA, Tukey test). $^{*,+}p<0.05$, $^{**,++}p<0.01$.

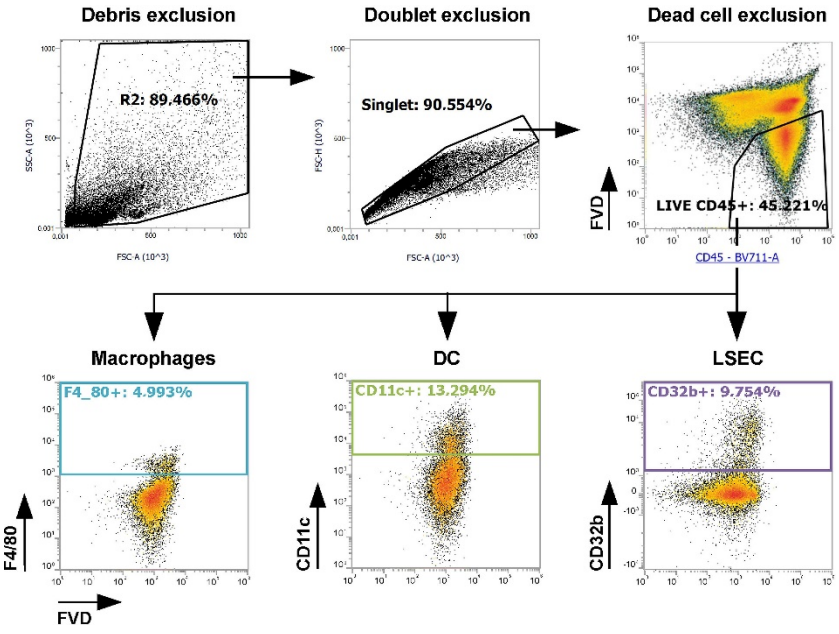

Figure S4. Gating strategy of liver NPC. After exclusion of debris, doublets and dead cells (fixable viability dye [FVD]$^{-}$), CD45^{+} cells were differentiated according to expression of F4/80 (macrophages), CD11c (DC), and CD32b (LSEC; liver sinusoidal endothelial cells).

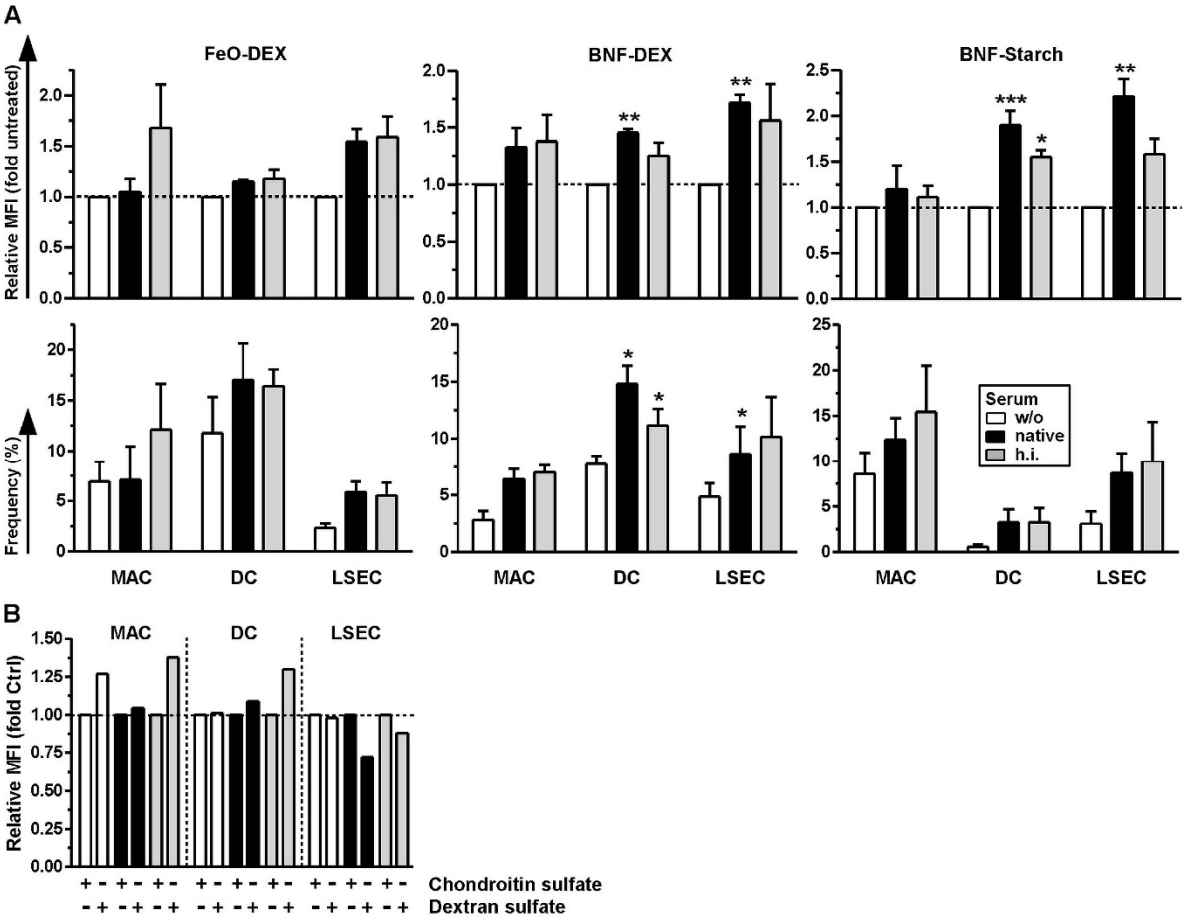

Figure S5. Binding of lectin-coated types of NC to liver non-parenchymal cells (NPC) is influenced by their protein corona. (**A**) Liver NPC were incubated with differentially pretreated (left untreated [w/o], pretreated with native or heat-inactivated [h.i.] serum) fluorescence-labeled types of NC for 3h. The extent of NC binding to macrophages (MAC), dendritic cells (DC) and liver sinusoidal endothelial cells (LSEC) was assessed by flow cytometry (see figure S4). Data denote the frequencies of NC-positive liver NPC (upper panel) and relative MFI of NC-specific fluorescence of either liver NPC population (lower panel) (mean±SEM of 3-4 independent experiments). MAC: macrophages. Statistical differences: versus *w/o serum and $^{+}$native serum (one way ANOVA, Tukey test). *p<0.05, **p<0.01, ***p<0.001. (**B**) Liver NPC were pre-incubated in parallel with a SR-A inhibitor (dextran sulfate) and the according control agent (chondroitin sulfate, Ctrl) for 45 min. Then, samples were incubated for 3h with differentially pretreated Cy5-labeled FeO-DEX and assayed by FACS analysis (see figure S1). The graph denotes the relative MFI of Cy5 in liver NPC populations and is representative for 2 experiments.

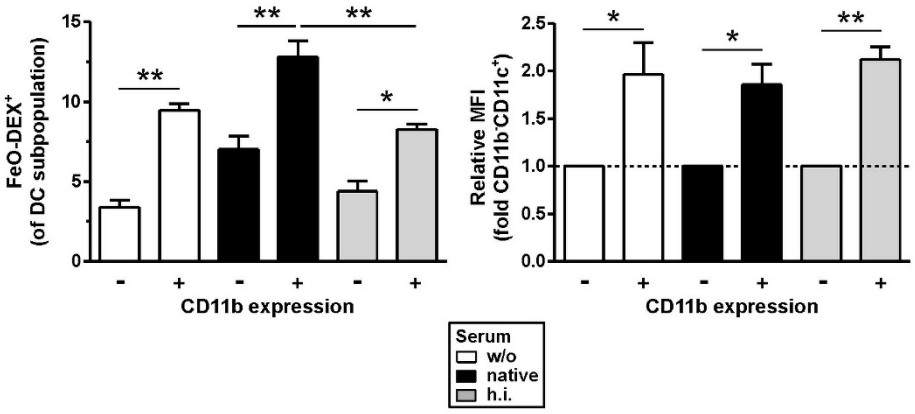

Figure S6. CD11b⁺ splenic DC bind FeO-DEX at higher extent. Spleen cell were incubated for 3h with differentially pretreated (left untreated [w/o], pretreated with native or heat-inactivated [h.i.] serum) FeO-DEX. The extent of FeO-DEX binding was assessed by FACS analysis (see figure S1). Data denote the frequencies of Cy5⁺ cells (left panel) and the relative MFI of Cy5 (right panel) of CD11b-deficient (-) and CD11b-expressing (+) splenic DC (mean±SEM of 3 experiments). Statistical differences between groups are indicated (one way ANOVA, Tukey test). *p<0.05, **p<0.01.

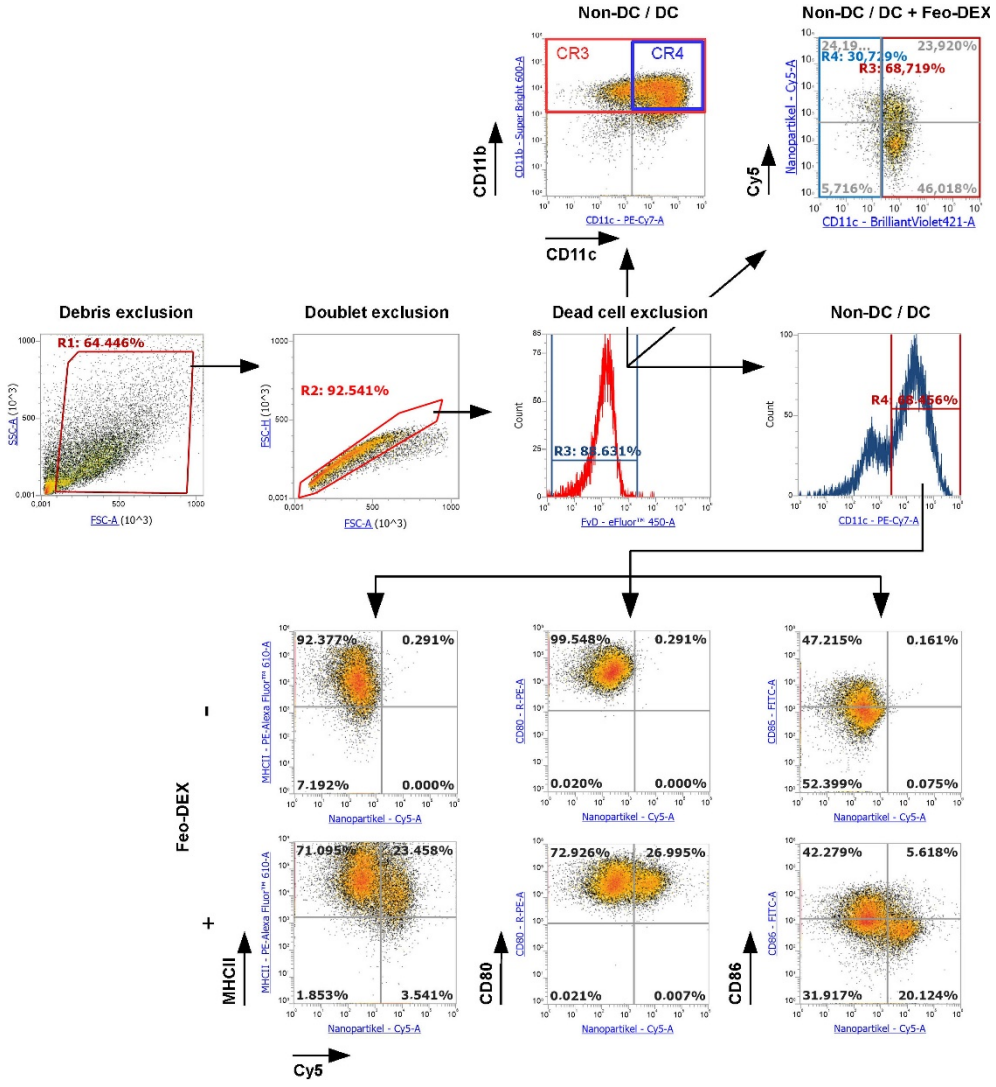

Figure S7. Gating strategy of BMDC. Middle panel: Debris, doublets and dead cells were excluded. Upper panel: Within the BMDC culture, non-DC and DC commonly express CD11b (CD11b/CD18, CR3), whereas only DC express CD11c (CD11c/CD18, CR4) (left plot). Both cell types engage carbohydrate-coated NC as shown for native serum-pretreated Cy5-labeled FeO-DEX (right plot). Lower panel: Assessment of DC activation markers (MHCII, CD80, CD86) in $CD11c^+$ DC left untreated and after over-night incubation with native serum-pretreated FeO-DEX is shown.

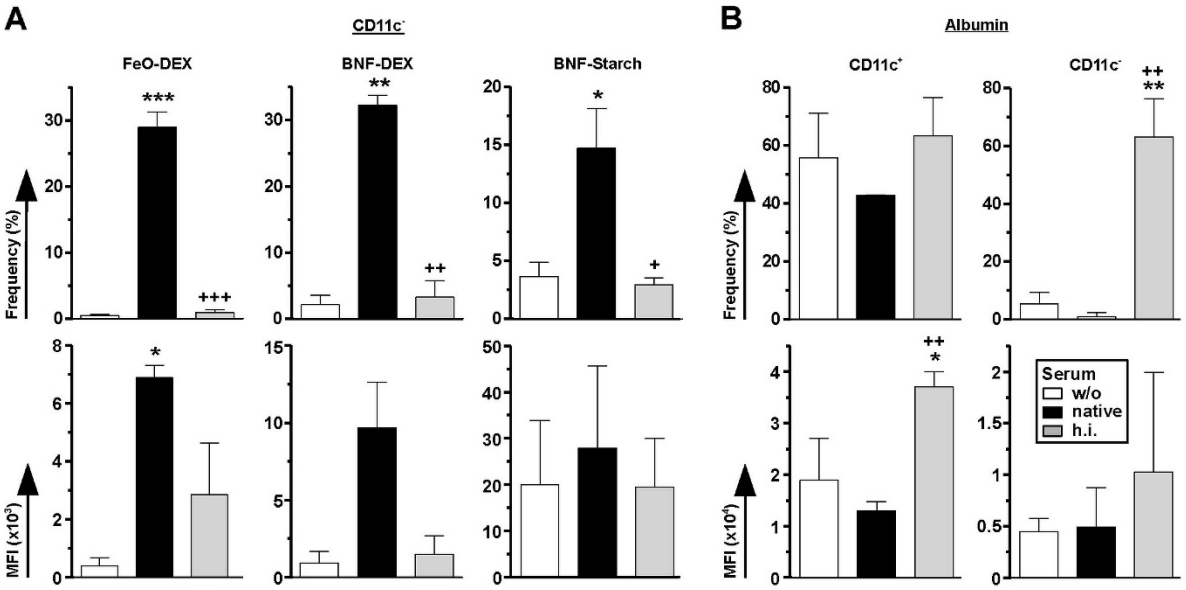

Figure S8. Macrophages ($CD11b^+CD11c^-$) within BMDC cultures engage complement-opsonized NC at higher extent. BMDC cultures were incubated for 3h with differentially pretreated (left untreated [w/o], pretreated with native or heat-inactivated [h.i.] serum) types of fluorescence-labeled (A) carbohydrate-coated and (B) albumin NC. The extent of NC binding was assessed by flow cytometry (see figure S7). Data denote the frequencies (upper panel) of NC-positive $CD11c^-$ non-DC (A) and both DC and non-DC (B), and the relative MFI of NC-specific fluorescence (lower panel) of non-DC (A) and non-DC/DC (B) (mean±SEM of 3-4 independent experiments). Statistical differences versus *w/o serum and $^+$native serum are indicated (one way ANOVA, Tukey test). $^{*,+}p<0.05$, $^{**,++}p<0.01$, $^{***,+++}p<0.001$.

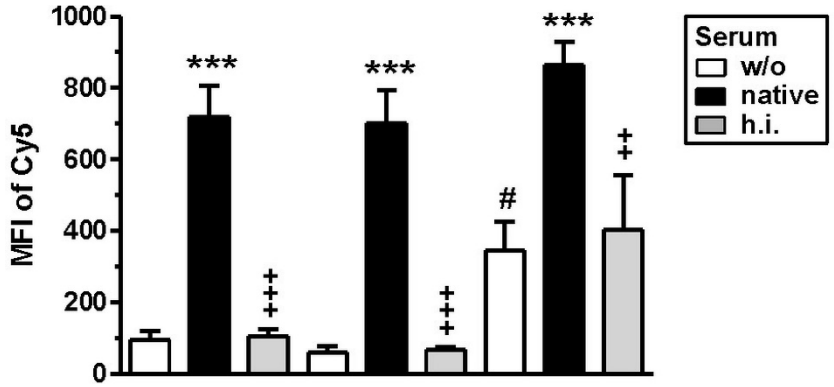

Figure S9. B-1 cells bind FeO-DEX at higher extent than B-2 cells. Spleen cells were incubated for 3h with differentially pretreated (left untreated [w/o], pretreated with native or heat-inactivated [h.i.]

serum) FeO-DEX. Data denote the Cy5 intensity (MFI) of total B cells ($CD19^+$), B-2 cells ($CD11b^-CD19^+$) and B-1 cells ($CD11b^+CD19^+$), given as the mean±SEM of 3 experiments. Statistical differences *versus w/o, $^+$versus native serum (same B cell population), $^\#$B-1 versus B-2 (according group) are indicated (one way ANOVA, Tukey test). $^\#p<0.05$, $^{++}p<0.01$, $^{***,+++}p<0.001$.

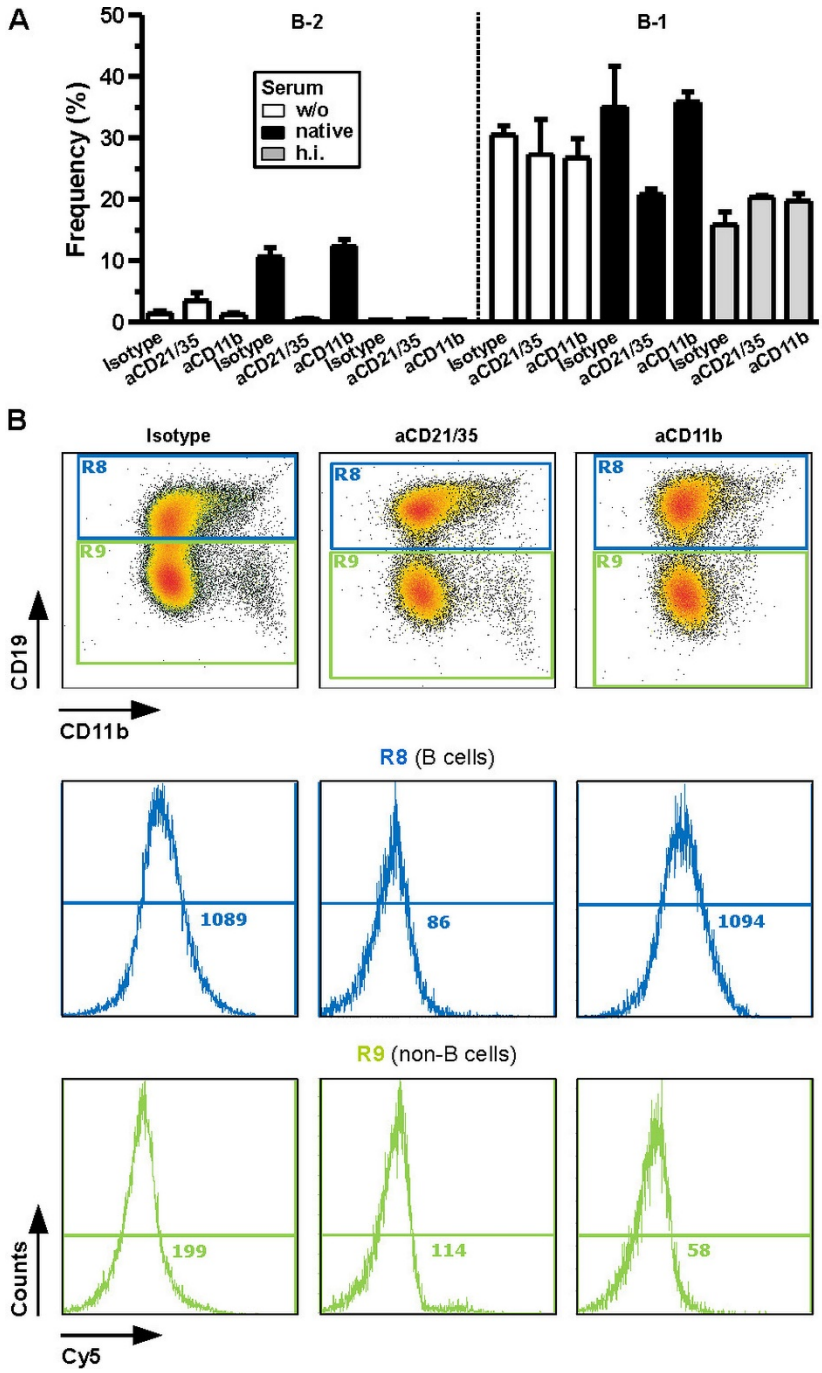

Figure S10. B cells bind complement-opsonized FeO-DEX via CR1/2. Spleen cells were pretreated in parallel with anti-CD21/CD35 (CR1/2) and anti-CD11b (CR3) blocking antibody, and an according isotype control antibody (each 5 µg/ml). Differentially pretreated FeO-DEX (left untreated [w/o], pretreated with native or heat-inactivated [h.i.] serum) were added after 45 min, and samples were incubated over-night. (**A**) The frequencies of $Cy5^+$ B-2 (left panel) and B-1 (right panel) cells (see figure

6) were assessed by FACS analysis (mean±SD of 2 experiments). (**B**) Histograms denote for $CD19^+$ B cells (R8) and $CD19^-$ non-B cells (R9) (upper panel) Cy5 intensities (MFI) (lower panel).

10.3. Publication 3

"Squaric ester-based, pH-degradable nanogels: modular nanocarriers for safe, systemic administration of Toll-like receptor 7/8 agonistic immune modulators"

The following chapter has been published by the American Chemical Society. As co-autor, I contributed by performing *in vitro* cell experiments to test Imidazoquinolines (IMDQ) loaded Squarogels, in terms of small-molecular Toll-like receptor 7/8 (TLR7/8) agonists. The latter hold promise as immune modulators for a variety of immune therapeutic purposes including cancer therapy. However, due to their rapid systemic distribution, which causes unwanted widespread inflammatory effects, their application is particular systemically. To address this problem, Dr. Huppertsberg designed pH-responsive nanogels intended to serve as immunodrug nanocarriers for the delivery of TLR7/8-stimulating IMDQ after intravenous administration. For this, squaric ester-based, pH-degradable nanogels were used with profound stability in human plasma but stimuli-responsive degradation upon exposure to endolysosomal pH conditions. These findings underline the potential of squaric ester-based, pH-degradable nanogels as a promising platform to permit intravenous administration of small-molecular TLR7/8 agonists and, thus, the opportunity to explore their adjuvant potency for systemic vaccination and cancer immunotherapy purposes.

DOI: 10.1021/jacs.1c03772

Published in: *Journal of the American Chemical Society*. **2021**, 143, 26, 9872–9883

Reprinted with permission from [Anne Huppertsberg, Leonard Kaps, Zifu Zhong, Sascha Schmitt, Judith Stickdorn, Kim Deswarte, Francis Combes, Christian Czysch, Jana De Vrieze, Sabah Kasmi, Niklas Choteschovsky, Adrian Klefenz, **Carolina Medina-Montano**, Pia Winterwerber, Chaojian Chen, Matthias Bros, Stefan Lienenklaus, Niek N. Sanders, Kaloian Koynov, Detlef Schuppan, Bart N. Lambrecht, Sunil A. David, Bruno G. De Geest, and Lutz Nuhn. *Journal of the American Chemical Society* **2021** *143* (26), 9872-9883]. Copyright [2023] American Chemical Society.

JACS
JOURNAL OF THE AMERICAN CHEMICAL SOCIETY
pubs.acs.org/JACS
Article

Squaric Ester-Based, pH-Degradable Nanogels: Modular Nanocarriers for Safe, Systemic Administration of Toll-like Receptor 7/8 Agonistic Immune Modulators

Anne Huppertsberg, Leonard Kaps, Zifu Zhong, Sascha Schmitt, Judith Stickdorn, Kim Deswarte, Francis Combes, Christian Czysch, Jana De Vrieze, Sabah Kasmi, Niklas Choteschovsky, Adrian Klefenz, Carolina Medina-Montano, Pia Winterwerber, Chaojian Chen, Matthias Bros, Stefan Lienenklaus, Niek N. Sanders, Kaloian Koynov, Detlef Schuppan, Bart N. Lambrecht, Sunil A. David, Bruno G. De Geest, and Lutz Nuhn*

Cite This: https://doi.org/10.1021/jacs.1c03772

Read Online

ACCESS | Metrics & More | Article Recommendations | Supporting Information

ABSTRACT: Small-molecular Toll-like receptor 7/8 (TLR7/8) agonists hold promise as immune modulators for a variety of immune therapeutic purposes including cancer therapy or vaccination. However, due to their rapid systemic distribution causing difficult-to-control inflammatory off-target effects, their application is still problematic, in particular systemically. To address this problem, we designed and robustly fabricated pH-responsive nanogels serving as versatile immunodrug nanocarriers for safe delivery of TLR7/8-stimulating imidazoquinolines after intravenous administration. To this aim, a primary amine-reactive methacrylamide monomer bearing a pendant squaric ester amide is introduced, which is polymerized under controlled RAFT polymerization conditions. Corresponding PEG-derived squaric ester amide block copolymers self-assemble into precursor micelles in polar protic solvents. Their cores are amine-reactive and can sequentially be transformed by acid-sensitive cross-linkers, dyes, and imidazoquinolines. Remaining squaric ester amides are hydrophilized affording fully hydrophilic nanogels with profound stability in human plasma but stimuli-responsive degradation upon exposure to endolysosomal pH conditions. The immunomodulatory behavior of the imidazoquinolines alone or conjugated to the nanogels was demonstrated by macrophages *in vitro*. *In vivo*, however, we observed a remarkable impact of the nanogel: After intravenous injection, a spatially controlled immunostimulatory activity was evident in the spleen, whereas systemic off-target inflammatory responses triggered by the small-molecular imidazoquinoline analogue were absent. These findings underline the potential of squaric ester-based, pH-degradable nanogels as a promising platform to permit intravenous administration routes of small-molecular TLR7/8 agonists and, thus, the opportunity to explore their adjuvant potency for systemic vaccination or cancer immunotherapy purposes.

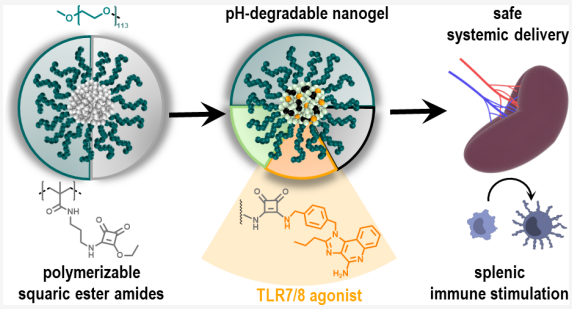

INTRODUCTION

Nanosized drug carriers can improve the pharmacokinetics of potent but systemically toxic small-molecular drugs; however, key challenges remain to establish robust fabrication processes, prevent premature drug release, and guarantee sufficient carrier integrity under physiological conditions. Moreover, opportunities toward on-demand drug release and carrier degradation would be desired.[1−4] Polymer-based nanocarriers can be designed to address these challenges chemically, especially for applications in immunotherapy.[5,6] A spatiotemporal control over recently identified, highly potent immunomodulators is crucial, since their drug leakage can cause uncontrolled systemic immune responses combined with immense off-target toxicity.[7,8] Covalent conjugation of immunomodulators to polymer-based nanocarriers that control the drug's pharmacokinetic profile can pave the way to safer systemic applications in cancer immunotherapy or as adjuvants during vaccination.[9−11]

One promising class of immunomodulators are agonists of Toll-like receptor 7/8 (TLR7/8) that usually sense viral single-stranded RNA and raise an immediate cellular innate immune response.[12] Imidazoquinolines, a class of synthetic TLR7/8 agonists, are particularly powerful in stimulating these receptors.

Received: April 9, 2021

Downloaded via UNIV MAINZ on June 25, 2021 at 07:39:33 (UTC).
See https://pubs.acs.org/sharingguidelines for options on how to legitimately share published articles.

ACS Publications
© XXXX The Authors. Published by American Chemical Society

https://doi.org/10.1021/jacs.1c03772
J. Am. Chem. Soc. XXXX, XXX, XXX−XXX

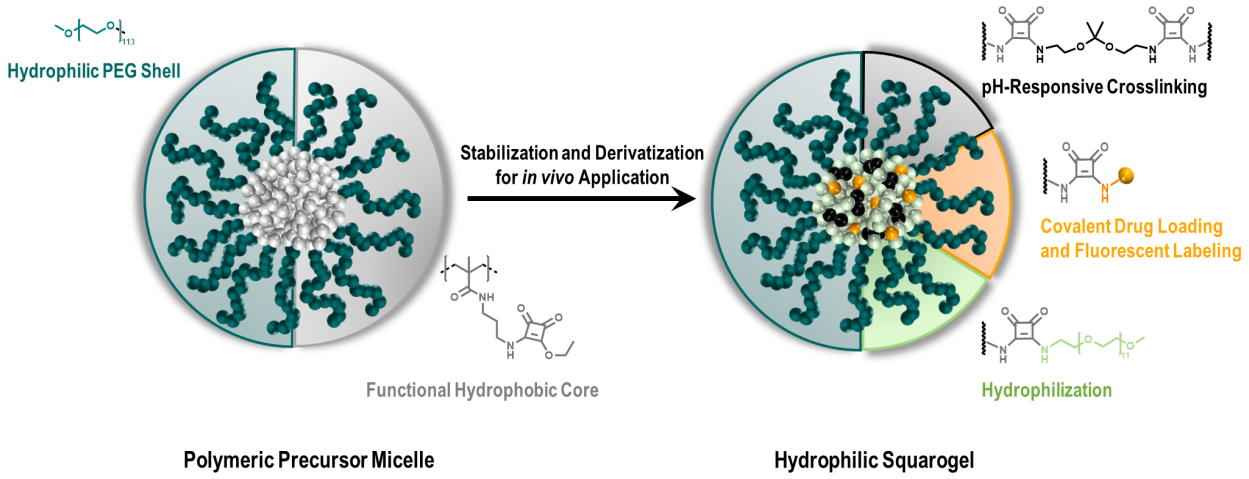

Figure 1. Squaric ester-based nanogels derived from polymeric precursor micelles formed by self-assembly of squaric ester amide-containing amphiphilic block copolymers. Subsequent transformation for *in vivo* application is achieved by amidation of pendant squaric ester amide groups inside the amine-reactive, hydrophobic core including pH-responsive cross-linking, covalent drug or dye loading, and hydrophilization, affording fully hydrophilic drug-loaded nanogels.

They can induce the maturation of antigen-presenting cells and the release of cytokines that promote cellular immune responses, especially via activation of T helper 1 (Th1) and cytotoxic T cells.[13,14] The latter play a key role in combating cancer and intracellular pathogens.[15,16] As TLR7/8 are located at the endosomal membrane of phagocytosing innate immune cells, they can be preferentially targeted by nanocarriers equipped with imidazoquinoline-derived TLR7/8 agonists.[17]

Previous studies demonstrated that undesired systemic inflammation by the highly potent small-molecular TLR7/8 agonist 1-(4-(aminomethyl)benzyl)-2-butyl-1*H*-imidazo[4,5-*c*]quinolin-4-amine (IMDQ)[18] can be circumvented through its covalent conjugation to different types of nanocarriers. Thereby, its activity upon subcutaneous administration can be restricted to the site of injection and the draining lymph nodes. A variety of nanocarriers has been investigated for this objective including lipids,[19,20] polysaccharides,[21] synthetic polymers,[22] micelles,[23] and nanogels.[24,25] These nanocarrier formulations have generally been injected subcutaneously and provided a local TLR7/8 activation by lymph node trafficking. However, a few findings revealed that intravenous injections would result in even improved immune responses.[26−29] Especially during intravenous nanoparticle vaccination, more stem-like antigen-specific $CD8^+$ T cells are generated that lead to superior antitumor responses, especially during immune checkpoint inhibition therapy.[30] Yet, systemic treatments set new requirements for safety and allow for new targeting strategies as compared to local administration. Thus, new efforts have to be made in the design of novel blood-stable nanocarriers enabling intravenous and organ-targeted TLR7/8 agonist administration.

A straightforward way to covalently load IMDQ into nanocarriers is self-assembled reactive ester block copolymers that are converted by amidation reactions into pH-degradable nanogels.[24,25,31] Via controlled radical polymerization processes we have previously generated poly(triethylene glycol monomethyl ether methacrylate)-*block*-poly(pentafluorophenyl methacrylate) as precursor polymers for which the pentafluorophenyl esters trigger both micellar self-assembly in polar aprotic solvents such as DMSO and selective reactivity toward primary amines.[32,33] This could also be applied for conjugation of IMDQ and subsequent transformation into fully hydrophilic nanogels. However, for this approach the hydrophilic triethylene glycol monomethyl ether methacrylate block renders a lower critical solution temperature in water,[34] which can impair the required shielding properties after exposure to biological media. Additionally, the applied pentafluorophenyl ester exhibits only limited hydrolytic resistance. Already slight traces of water can risk its hydrolysis into methacrylic acid[35] and, thus, impede access to the nanogel formation process. In addition, during amidation toxic pentafluorophenol is released,[36] which requires careful purification prior to applications *in vitro* or *in vivo*.

Consequently, alternative amine-reactive groups with higher hydrolytic stability and nontoxic byproducts are needed. Tietze et al. reported on squaric alkyl esters for selective amine coupling reactions with high functional group tolerance as well as excellent yields, even under mild conditions in aqueous media.[37] Due to their homo-bifunctionality squaric alkyl esters can consecutively be aminolyzed by two different amines, whereby an enhanced aromatic stability after first amidation is obtained, providing reduced reactivity for another amidation. Thus, it assures a controlled sequential squaric bisamide formation.[38] Compared to other reactive esters (including pentafluorophenyl) this alternative linking chemistry allows conjugation in biocompatible solvents (e.g., water, ethanol) while releasing alcohols as nontoxic byproducts.[39]

In this study, we therefore introduce polymerizable squaric ester amides for a more robust and hydrolysis-resistant postpolymerization modification of pH-degradable, immuno-drug-loaded nanogels. Methacrylamides with pendant squaric ester amides are grafted under controlled radical polymerization conditions onto linear hydrophilic PEG chains and serve as solvophobic groups for spontaneous micellar self-assembly now also in polar protic solvents (Figure 1).

By sequential functionalization with primary amines, they can be converted into a modular pH-responsive nanogel platform. This process supports covalent conjugation of both hydrophobic and hydrophilic drugs into the core of these nanogels, e.g., the amine-functionalized TLR7/8 agonist IMDQ. Due to its high degree of PEGylation, this system features excellent stability in blood that permits intravenous administration and local maturation of antigen-presenting immune cells inside the spleen, while circumventing systemic inflammatory responses

https://doi.org/10.1021/jacs.1c03772
J. Am. Chem. Soc. XXXX, XXX, XXX−XXX

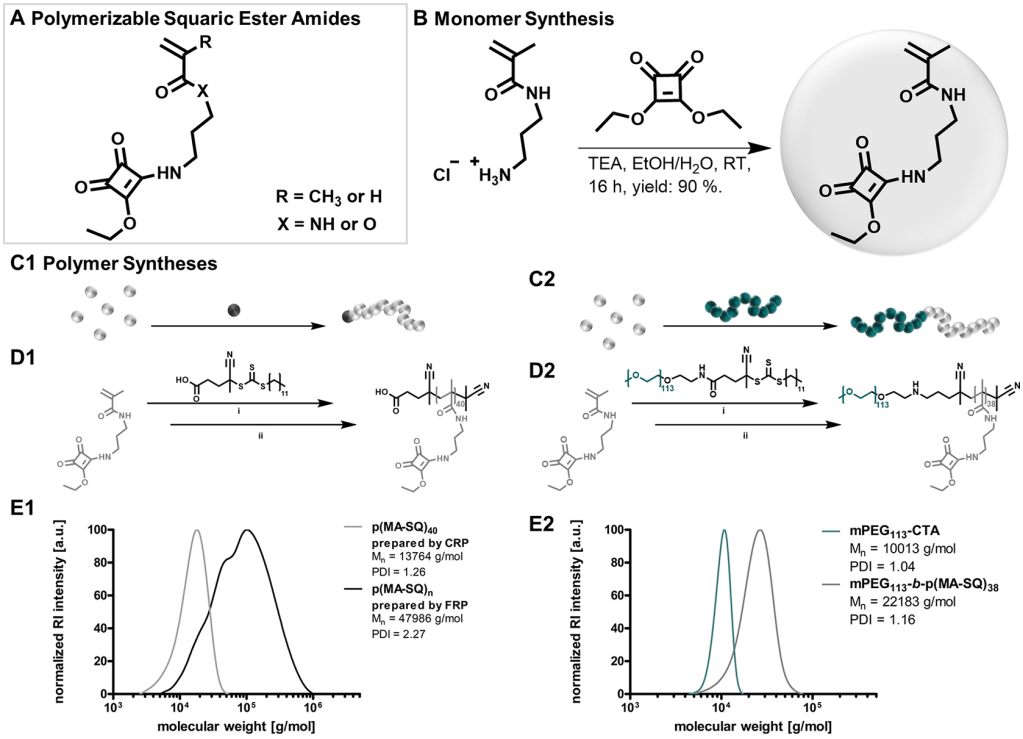

Figure 2. Synthesis of polymerizable squaric ester amides. (A) General chemical structure of synthesized monomers with a pendant squaric ester amide group. (B) Synthesis route toward the most suitable monomer squaric ester amide methacrylamide (MA-SQ). (C) Schematic illustrations and (D) synthesis schemes of RAFT homopolymerization of MA-SQ with a small molecular trithiocarbonate chain transfer agent (TTC-CTA) (C1 and D1) and block copolymerization with macro-chain-transfer agent PEG-TTC-CTA (C2 and D2) (reaction conditions: (i) DMF, 70 °C, 0.2 equiv AIBN per 1.0 equiv TTC-CTA, and (ii) DMF, 70 °C, 50 equiv AIBN (to remove the TTC end group)). (E) Molecular weight distributions of polymers obtained by radical polymerization: (E1) RAFT-derived homopolymer compared to the homopolymer obtained by FRP; (E2) RAFT-derived block copolymer compared to PEG-TTC-CTA as macro-chain-transfer agent.

caused by the unbound TLR7/8 agonist. Altogether, these observations demonstrate the broad versatility of amine-reactive squaric ester-based precursor polymers and how they provide access to a modular pH-degradable nanogel platform for safe systemic administration of immune modulators.

RESULTS AND DISCUSSION

We first aimed to synthesize a polymerizable squaric ester amide monomer that can be polymerized under controlled conditions into well-defined homo- and block copolymers using reversible addition−fragmentation chain transfer (RAFT) agents. While squaric ester amides have already been studied as amine-reactive groups for atom transfer radical polymerization (ATRP)[40] or RAFT[41] chain transfer agents, to the best of our knowledge, the use of squaric esters as functional side groups of monomers and corresponding polymers has not been introduced before. They provide access to a new class of hydrolysis-resistant, amine-reactive precursor polymers for multiple postpolymerization purposes.[39] We investigated the polymer's reactivity toward different types of amines and observed a self-assembly behavior of corresponding block copolymers in water or ethanol. The core of the resulting micelles can be used to ligate fluorescent dyes or IMDQ followed by core-cross-linking and hydrophilization affording pH-degradable nanogels. Subsequent *in vitro* and *in vivo* characterization revealed long blood circulation and maturation of antigen-presenting cells in the spleen while omitting inflammatory off-target effects.

Monomer and Polymer Syntheses. Initially, polymerizable squaric ester amide monomers with acrylate, acrylamide, or methacrylamide groups were synthesized (Figure 2A). Direct (meth-)acryloylation of 2-aminoethanol-functionalized squaric ester amides failed due to occurring bisacryloyl derivatives and autopolymerization. For instance, we carefully treated 3-ethoxy-4-((2-hydroxyethyl)amino)cyclobut-3-ene-1,2-dione with acryloyl chloride but obtained besides the desired squaric ester amide acrylate product 2-((2-ethoxy-3,4-dioxocyclobut-1-en-1-yl)amino) ethyl acrylate (At-SQ) also a bisacrylated species (At-SQ-At) at similar yields, as documented in the Supporting Information (Figures S14−S23). We therefore opted for (meth-)acrylamides by controlled monoamidation of squaric acid diethyl ester with amine-functionalized (meth-) acrylamides. Unfortunately, due to their aza-Michael reactivity, amino-functionalized (meth-)acrylamides are only stable as protonated salt species. While the corresponding methacrylamide-based monomer was commercially available, we synthesized the TFA salt of *N*-(3-aminopropyl)acrylamide as corresponding acrylamide derivative (Supporting Information Figure S7). It was converted with squaric acid diethyl ester catalyzed by triethylamine in ethanol and water and provided the desired acrylamide monomer at acceptable yields (64%, A-SQ, NMR characterization in Supporting Information Figures S10−S13). However, several attempts to polymerize it, even under free radical polymerization (FRP) conditions, failed or yielded only conversions below 30%. Fortunately, synthesis and polymerization of the methacrylamide analogue was more promising.

https://doi.org/10.1021/jacs.1c03772
J. Am. Chem. Soc. XXXX, XXX, XXX−XXX

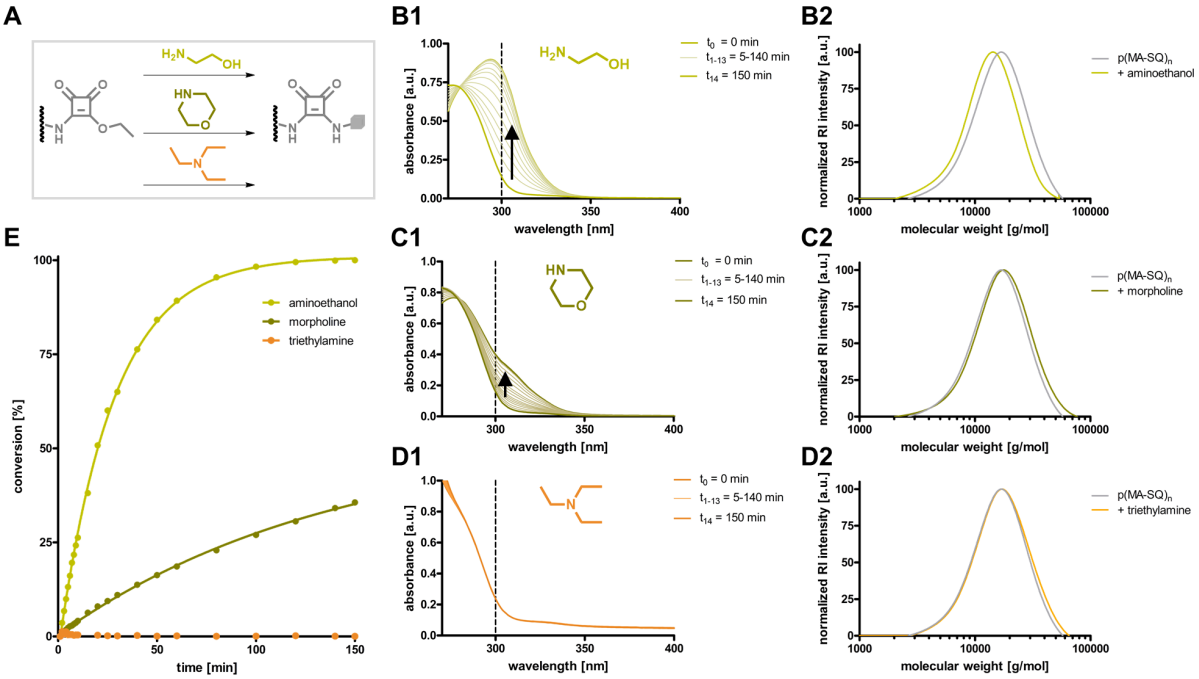

Figure 3. Amine selectivity of pendant squaric amide groups of p(MA-SQ)$_{40}$. (A) Scheme for the conversion of polymeric squaric ester amides to squaric bisamides by amidation with aminoethanol, morpholine, or triethylamine. UV/vis spectra during conversion with (B1) aminoethanol, (C1) morpholine, or (D1) triethylamine and the corresponding molecular weight distributions of p(MA-SQ)$_{40}$ before and after conversion with (B2) aminoethanol, (C2) morpholine, or (D2) triethylamine. (E) Corresponding conversions estimated by UV absorbance over time.

Monoamidation of squaric acid diethyl ester with the commercially available *N*-(3-aminopropyl)methacrylamide hydrochloride was again conducted in ethanol and water catalyzed by triethylamine. It afforded a squaric ester amide methacrylamide monomer (MA-SQ) with a high yield of 90% (Figure 2B, NMR and MS characterization in Supporting Information, Figures S1−S6).

MA-SQ could afterward be polymerized under FRP conditions at 70 °C using AIBN as radical source with quantitative conversion. Consequently, it was an ideal candidate for RAFT polymerization. We chose a trithiocarbonate as chain transfer agent (TTC-CTA) and polymerized MA-SQ with either a small-molecular TTC-CTA or a PEG-functionalized macro-TTC-CTA (Supporting Information Figure S24−S26; note that instead of commercially available macro-TTC-CTAs bearing an ester group between PEG and the CTA group, we preferred to apply an amide derivative to avoid possible ester aminolysis and cleavage during amidation). At a monomer to CTA ratio of 50:1, conversions of 75−80% were found affording p(MA-SQ)$_{40}$ as homopolymer and PEG$_{113}$-*b*-p(MA-SQ)$_{38}$ as block copolymer (Figure 2C/D).

Consistent with earlier reports, NMR analysis validated that squaric ester amide moieties withstood radical polymerization conditions and remained intact (Figures S28 and S32).[40,41] Molecular weight distributions of p(MA-SQ)$_{40}$ obtained by size-exclusion chromatography (SEC) revealed well-defined homopolymers with a number-average molar mass (M_n) of 13 800 g/mol and polydispersity index (PDI) of 1.26 (Figure 2E1). In stark contrast to the FRP, the RAFT homopolymers of MA-SQ confirmed controlled polymerization conditions. Via NMR spectroscopy, monomer conversion over time demonstrated first-order kinetics for the polymer formation (Figures S34 and S35). Similar conditions were applied during block copolymerization and provided polymers with a narrow PDI of 1.16 and M_n of 22 200 g/mol (Figure 2E2). The molecular weight shift of the block copolymer (PEG$_{113}$-*b*-p(MA-SQ)$_{38}$) compared to PEG-TTC-CTA clearly attested full MA-SQ monomer grafting onto the macro-CTA. Additionally, DOSY NMR analysis confirmed successful block copolymer formation by providing identical diffusion coefficients of both blocks (Figure S29). To avoid interference with the trithiocarbonate (TTC) end group during subsequent amidation of the squaric ester amides, both homo- and block copolymer were further treated with an excess of AIBN for end group removal. This additional step did not impair the composition or distribution of the polymers (compare Supporting Information Figures S30 and S33).

Amine-Selective Conversion. In order to verify amine reactivity, the homopolymer p(MA-SQ)$_{40}$ was first reacted with an excess of primary, secondary, or tertiary amine. As model compounds aminoethanol, morpholine, and triethylamine were selected (Figure 3A, note that these reactions were conducted in DMSO to ensure complete solubility of the homopolymer). Interestingly, the formed squaric bisamides provide an absorption maximum around 300 nm compared to the squaric ester amide educts. Therefore, their aminolysis can easily be monitored over time by UV/vis absorbance spectroscopy.[39] A strong and fast increase in absorbance at 300 nm revealed rapid and quantitative conversion of the squaric ester amides by the primary amine aminoethanol. The secondary amine morpholine could only convert about 25% after 2 h, while no conversion was observed with triethylamine as tertiary amine (Figure 3B1−D1, Figure 3E, and Supporting Information Figure S37). The respective homopolymers were isolated by precipitation in diethyl ether. Recorded molecular weight distributions by SEC demonstrated no significant change in M_n and PDI for p(MA-

https://doi.org/10.1021/jacs.1c03772
J. Am. Chem. Soc. XXXX, XXX, XXX−XXX

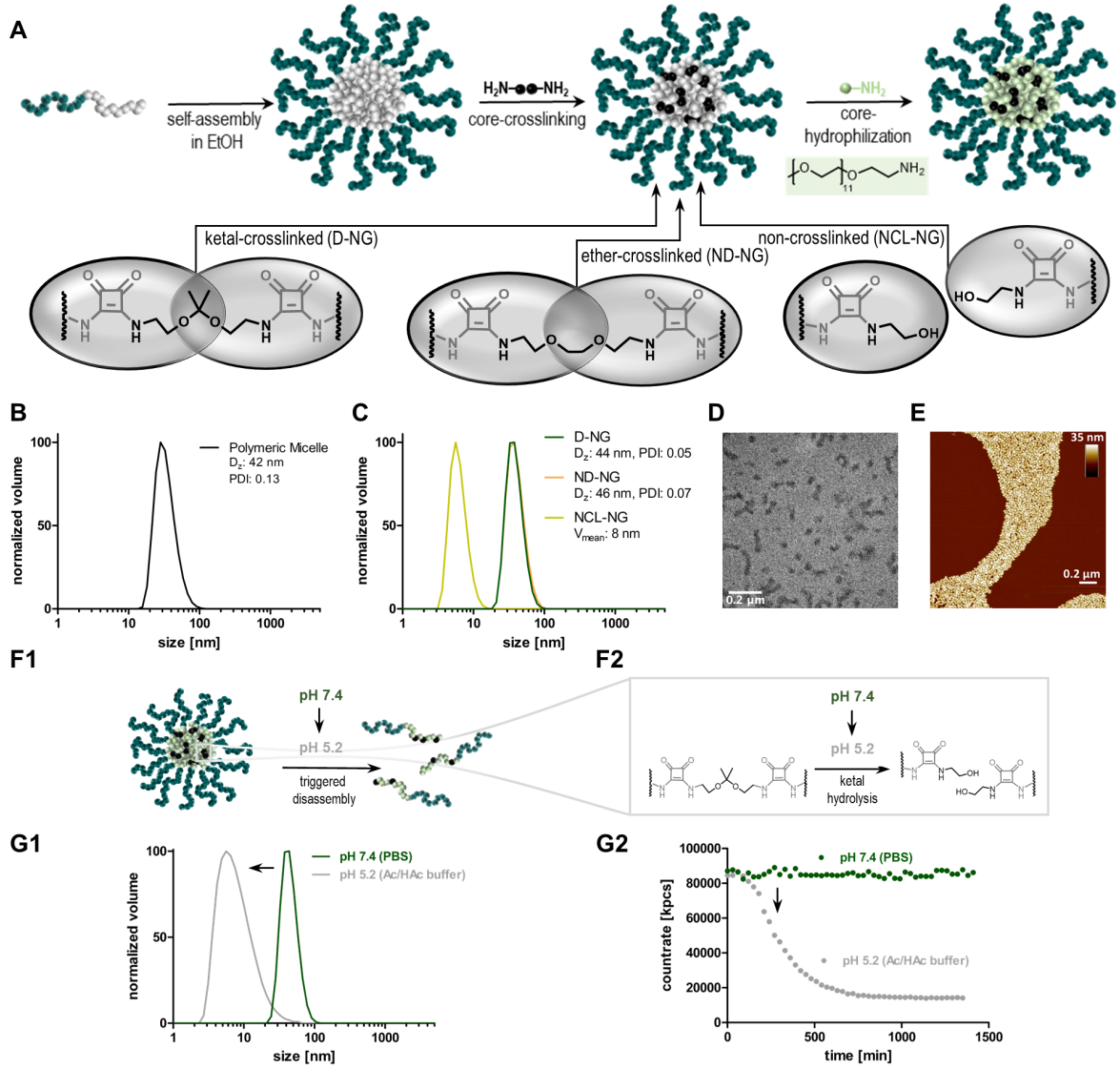

Figure 4. Nanogel fabrication process. (A) Scheme of sequential nanogel formation from squaric ester amide-derived, self-assembling precursor polymers. Based on the cross-linking strategy, degradable nanogels (D-NG) as well as nondegradable or non-cross-linked control samples (ND-NG, NCL-NG) can be obtained. (B) DLS size distribution of self-assembled micelles in ethanol and (C) fully fabricated nanogels D-NG, ND-NG, and NCL-NG in PBS. (D) TEM image of D-NG. (E) AFM image of D-NG. (F1 and F2) Scheme of ketal-hydrolysis in acidic media resulting in D-NGs' disassembly into soluble unimers (NCL-NG). (G) DLS study of D-NG at neutral pH in PBS compared to mildly acidic pH in HAc/Ac buffer by (G1) size distribution and (G2) DLS count rate over time.

$SQ)_{40}$ treated with triethylamine, while a complete peak shift to smaller molecular weights was found after conversion with aminoethanol (Figure 3B2−D2). The squaric ester amide polymers treated with morpholine showed only a minimal peak shift reflecting their incomplete conversion. These observations were confirmed by NMR analysis (Figures S38 and S39). Further studies indicated that full conversion by secondary amine morpholine can still be achieved at elevated temperature and extended reaction time (Figure S40, e.g., after 22 h at 70 °C complete squaric ester amide aminolysis was demonstrated; compare Figures S41 and S42). These results highlight the suitability of squaric ester amides as reactive polymer side groups for quantitative postpolymerization modification with preferentially fast conversion of primary amines.

Nanogel Fabrication and Characterization. Polymeric squaric ester amides can be used as precursors to introduce new functionalities by amidation reactions. Following the design concept of Figure 4A, we were interested in whether this postpolymerization modification can also be combined with self-assembly to sequentially access nanogels (by micelle formation, covalent core-cross-linking, and transformation of the core from hydrophobic to hydrophilic). The well-defined amphiphilic block copolymer PEG_{113}-*b*-p(MA-$SQ)_{38}$ was suspended in ethanol and treated with ultrasound, yielding narrowly dispersed micelles. By dynamic light scattering (DLS) their sizes were analyzed, revealing a *z*-average diameter (D_Z) of 44 nm and a narrow PDI of 0.13 (Figure 4B). Next, the polarity of the core was switched chemically by exploiting its reactivity toward hydrophilic amines. After addition of 5.0 equiv of PEG_{11}-amine the micelles disassembled within 30 min and provided fully soluble polymers (Supporting Information Figures S43 and S44; note that amines like aminoethanol did not increase the polarity

https://doi.org/10.1021/jacs.1c03772
J. Am. Chem. Soc. XXXX, XXX, XXX−XXX

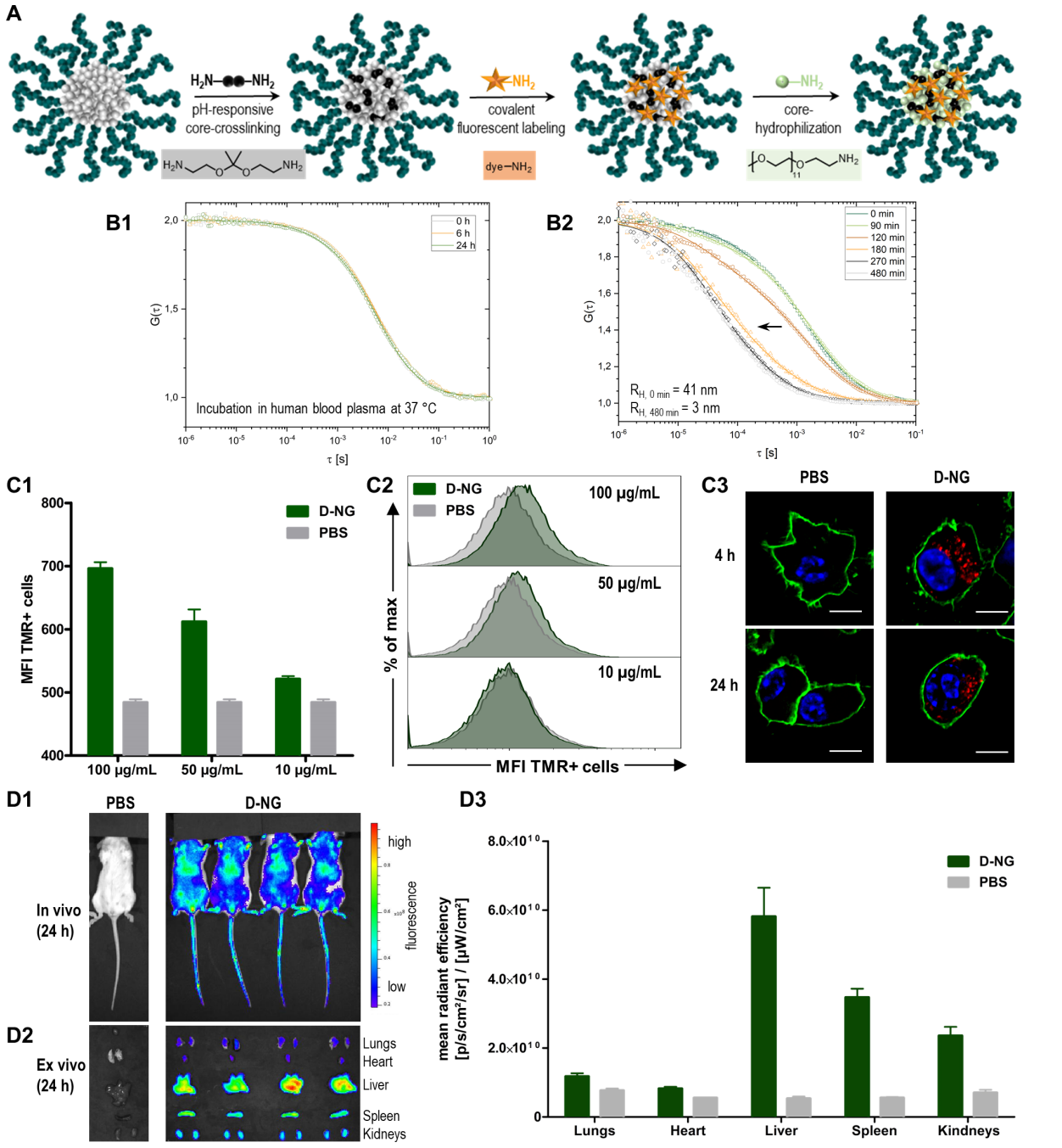

Figure 5. Fluorescently labeled nanogels provide sufficient particle integrity for safe *in vivo* administration. (A) Scheme of sequential nanogel fabrication with *in situ* installed fluorescent dye-labeling. (B) Oregon Green cadaverine (OG)-labeled nanogels (D-NG) investigated by fluorescence correlation spectroscopy toward stability in plasma and the ability to disassemble upon exposure to endolysosomal pH values: (B1) normalized autocorrelation curves (dots) and corresponding fits (solid line) of OG-labeled D-NG incubated in human blood plasma for 0, 6, and 24 h; (B2) normalized autocorrelation curves (dots) and corresponding fits (solid line) of OG-labeled D-NG incubated in acidic buffer (pH 5.2) over time. (C) Tetramethylrhodamine cadaverine (TMR)-labeled nanogels (D-NG) investigated for the *in vitro* uptake behavior in RAW murine macrophages using flow cytometry and confocal microscopy imaging (n = 3): (C1) cellular mean fluorescence intensities (MFI) of RAW macrophages incubated with TMR-labeled D-NG at 100, 50, and 10 μg/mL for 24 h; (C2) corresponding histograms of RAW macrophages incubated with TMR-labeled D-NG at 100, 50, and 10 μg/mL for 24 h (n = 3) or PBS (control). (C3) Confocal microscopy images of RAW macrophages incubated with TMR-labeled D-NG at 100 μg/mL for 4 and 24 h (blue: nuclei stained with Hoechst 33258; green: cell membrane stained with cholera toxin B (CTB)-AF488; red: TMR-labeled D-NG, scale bar 10 μm). (D) Near infrared dye 800RS cadaverine (NIR)-labeled nanogels (NIR-labeled D-NG) investigated for their biodistribution after systemic application to BALB/c mice via tail vein injection using an *in vivo* NIR-imaging system (IVIS): (D1) whole body fluorescence imaging 24 h after intravenous injection of 100 μL of NIR-labeled D-NG dispersion (2 mg/mL); (D2) *ex vivo* organ distribution imaging and (D3) semiquantitative analysis (n = 4).

https://doi.org/10.1021/jacs.1c03772
J. Am. Chem. Soc. XXXX, XXX, XXX−XXX

to unfold the micelles). Thus, core hydrophilization is possible to fabricate fully hydrophilic nanogels.

Next, polymeric micelles were modified by pH-responsive cross-links prior to hydrophilization (note that the following process is possible in both pure ethanol and buffered water; compare Supporting Information Figure S50). In relation to 1.0 equiv of pendant squaric ester amide moieties, 0.15 equiv of the ketal-containing bisamine 2,2′-bis(aminoethoxy)propane was added. Its ketal unit renders the nanocarriers' sensitivity to endosomal acidic pH. As shown in previous reports, it can effectively hydrolyze at pH 5, resulting in a disassembly of nanogels into soluble polymer chains.[33,42,43] In order to provide a nondegradable nanogel version, the core of the micelles was conjugated with 0.15 equiv of an ether-containing bisamine (1,2-(bis(aminoethoxy)ethane). Additionally, a non-cross-linked soluble polymer representing the ketal-cross-linked nanogel after hydrolysis was obtained by aminolysis with 0.3 equiv of 2-aminoethanol. For each species, all remaining squaric ester amide moieties were finally converted with 3.0 equiv of PEG_{11}-amine, resulting in fully hydrophilic nanogel or soluble polymer species (Figure 4A). All samples were purified by dialysis against water containing 0.1 wt % ammonia to prevent premature ketal-hydrolysis. Subsequent lyophilization afforded the nanogels as dry powders, which could be easily redispersed in PBS buffer.

UV/vis absorbance spectroscopy could again be used to monitor the conversion of the squaric esters inside the self-assembled micelles/core-cross-linked nanogels by following the increase of the absorption maximum around 300 nm related to the formed squaric bisamides (compare Supporting Information Figures S46−S48). Sequential addition of primary amines for functionalization, cross-linking, and final conversion of the remaining squaric ester amide moieties with PEG_{11}-amine yielded a stepwise increase of the absorbance. Note that no difference between the absorption after addition of 3.0 equiv of PEG_{11}-amine and the purified nanogel after extensive dialysis against water with 0.1 wt % ammonia could be found, confirming quantitative squaric ester conversion inside the nanogels during the fabrication process (compare Supporting Information Figures S46−S48).

As shown by DLS analysis, the ketal-cross-linked, degradable nanogel (D-NG) showed a very narrow monomodal distribution and a D_z of 44 nm, which was similar to the size of the precursor micelle. The same was found for the nondegradable nanogel (ND-NG, D_z = 46 nm), while for the non-cross-linked version (NCL-NG) a significantly lower count rate was detected indicating the absence of particular scattering. The average volume diameter of the NCL-NG was 8 nm (Figure 4C). The ketal-cross-linked nanogels were imaged by transmission electron microscopy (TEM) and atomic force microscopy (AFM). The dried particles could be recorded as spherical and some slightly elongated morphologies with narrow dispersities (Figure 4D and E; Supporting Information Figure S49). To prove that the ketal-cross-linked nanogels fully disassemble into soluble unimers under endolysosomal pH conditions (Figure 4F1,F2), several DLS stability studies at pH 7.4 or 5.2 were performed. D-NG was exposed to acidic pH in acetate buffer at 10 mg/mL and subsequently monitored over time by DLS. A gradual decline in count rate within 600 min was observed, while a decrease of the particles' size distribution demonstrated complete nanogel disassembly into single polymer chains (Figure 4G1,G2). In contrast, no change in count rate or size was observed at neutral pH for D-NG in PBS (Figure 4G1,G2). This was also the case for ND-NG and NCL-NG at both pH levels over time (Supporting Information (Figure S54). Thus, ketal-cross-linked nanogels represent ideal candidates for drug delivery due to their transient supramolecular architecture that unfolds into secretable smaller entities upon exposure to endolysosomal pH values.

Nanogel Functionalization. To further investigate the nanogels' covalent drug delivery function, their squaric ester amides were first used to introduce fluorescent labels. Prior to the described cross-linking and core-hydrophilization, 0.01 equiv of amine-bearing fluorescent dyes (e.g., Oregon Green cadaverine (OG), tetramethylrhodamine cadaverine (TMR), or the near-infrared dye 800RS cadaverine (NIR)) was conjugated to the core (Figure 5A). Covalent dye conjugation did not affect the nanogel fabrication process. To ensure the absence of free dye, nanogels were extensively spin-filtrated (MWCO: 10 000 g/mol) using a mixture of 0.1 wt % ammonia in water/EtOH (v/v, 1:2) in addition to the described purification methods. Dye labeling enables analyses of the nanocarriers' behavior in complex biological environment and, thus, provides key features to evaluate their applicability for immunomodulating drug delivery.

We first investigated the dye-labeled nanogel's stability in human blood plasma as complex biological medium relevant for *in vitro* and *in vivo* application. Selective monitoring of nanogel integrity over time was facilitated by fluorescence correlation spectroscopy (FCS). It provides information about the nanocarrier's size in solution by autocorrelation analysis of fluorescence intensity fluctuations that result from diffusional motions of fluorescent species (e.g., labeled nanocarriers) through a confocal volume.[44] After incubation of pH-degradable nanogels (OG-labeled D-NG) in human blood plasma for 0, 6, and 24 h at 37 °C, FCS analysis confirmed that the nanogel's autocorrelation curve and the corresponding hydrodynamic radius remained identical (Figure 5B1). Consequently, the carriers are profoundly stable under these biologically relevant conditions: Neither an increase of the nanogel's size, which would reflect aggregation with serum components nor its decrease was observed, which would imply nanogel degradation. The latter could only be observed by FCS when the ketal-cross-linked OG-labeled D-NG was again exposed to pH 5.2 using acetate buffer. As evident from the shift of the autocorrelation curves, one can perfectly observe a sequential disassembly of the nanogels into single unimers (Figure 5B2).

Next, cellular nanogel interaction was studied for TMR-labeled D-NG using flow cytometry as well as confocal microscopy. RAW macrophages were selected as model for phagocytosing cells of the reticuloendothelial system that usually rapidly engulf nanocarriers after systemic administration. However, only a minor uptake of D-NG was observed after dosing from 10 to 100 μg/mL. A weak increase in mean fluorescence intensity from 500 (basal autofluorescence) to 700 could be recorded by flow cytometry (Figure 5C1), and the resulting histogram provided only a minor but homogeneous shift of all cells to increased fluorescence (Figure 5C2). These observations were independent from the type of nanogel, as similar low mean fluorescence intensities and low TMR-positive cells were found for all species (D-NG, ND-NG, and NCL-NG; compare Supporting Information Figure S56). These results were further supported by confocal microscopy images of RAW macrophages incubated at 100 μg/mL for both 4 and 24 h (Figure 5C3 and Supporting Information Figure S55). All cells provided a homogeneous intracellular localization of some

https://doi.org/10.1021/jacs.1c03772
J. Am. Chem. Soc. XXXX, XXX, XXX−XXX

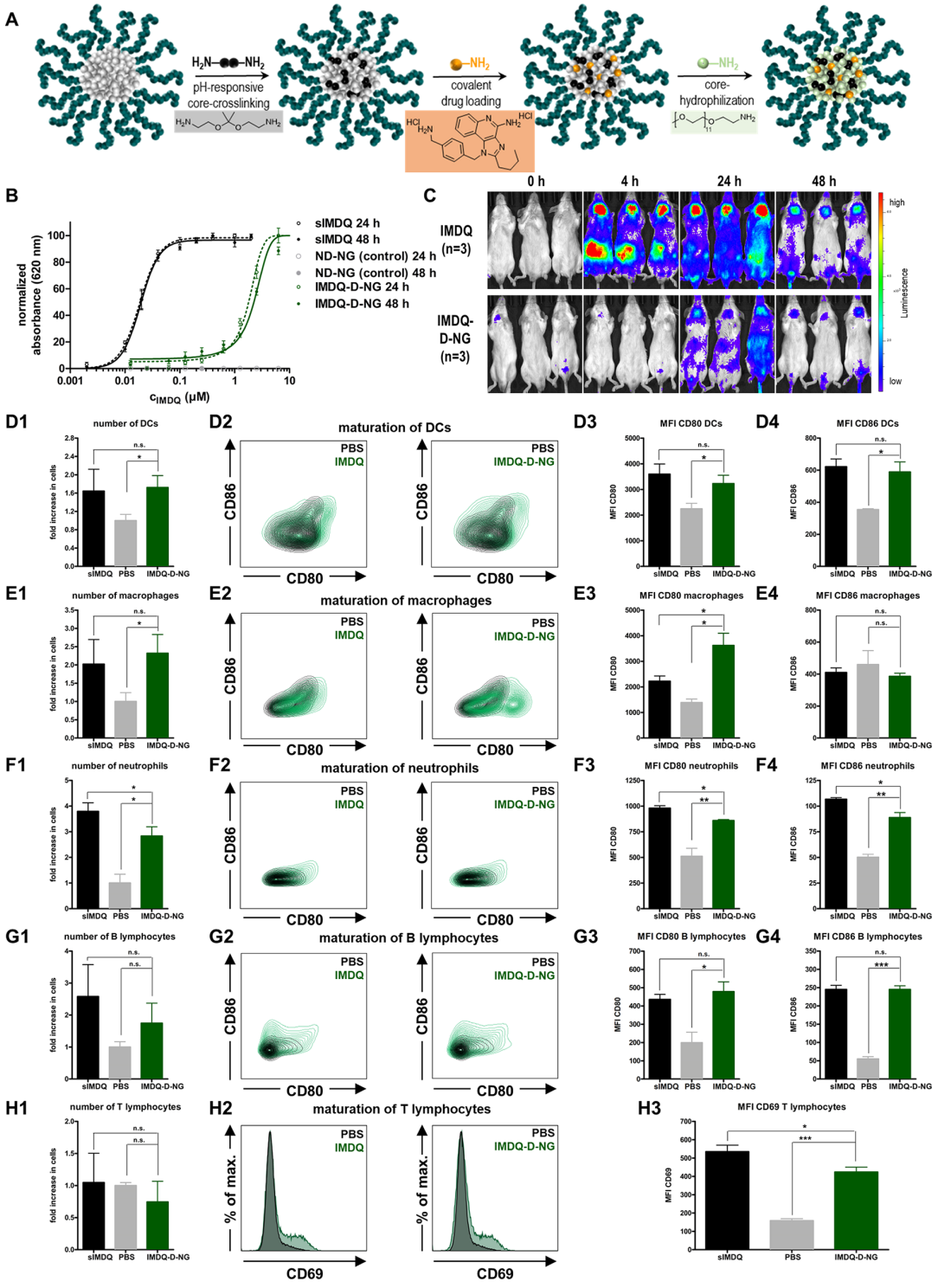

Figure 6. Squaric ester amide-based nanogels with covalently attached TLR7/8 agonist IMDQ. (A) Scheme of sequential nanogel fabrication with integral *in situ* conjugation of IMDQ. (B) TLR agonistic activity of soluble IMDQ (sIMDQ) and covalently attached IMDQ to degradable nanogels (IMDQ-D-NG) measured by NF-κB activation of RAW Blue cells after 24 and 48 h via a Quanti-Blue reporter assay (n = 4). (C) Bioluminescence images of heterozygous IFN-β (IFN-$\beta^{+/\Delta\beta\text{-luc}}$) reporter mice intravenously injected with sIMDQ and covalently attached IMDQ-D-NG (5 μg of IMDQ soluble or bound to nanogel in 100 μL of PBS); images were recorded before (0 h) as well as 4, 24, and 48 h after tail vein injection (n = 3). (D–H) Results of flow cytometric analysis of isolated splenocytes (compare Figure S60 for the applied gating procedure) after systemic administration of soluble IMDQ vs nanogel-conjugated IMDQ (1: fold increase of cells in the spleen in relation to PBS treated mice; 2: maturation plots by CD86 and CD80 or CD69 for T cells; 3: corresponding MFI values). (D) Dendritic cells (DCs), (E) macrophages, (F) neutrophils, (G) B lymphocytes, and (H) T lymphocytes.

https://doi.org/10.1021/jacs.1c03772
J. Am. Chem. Soc. XXXX, XXX, XXX−XXX

nanogels presumably inside vesicular compartments. Due to the fact that particle uptake was only observed upon high particle dosing at 100 μg/mL, these *in vitro* studies suggested the potentially useful property of these nanogel carriers to withstand rapid phagocytosis, making them applicable for systemic *in vivo* applications.

We therefore intravenously injected NIR-labeled D-NG into mice's tail veins and observed after 24 h still a strong fluorescent signal distributed all over the body by the *in vivo* NIR imaging system (IVIS) (Figure 5D1). These findings confirmed that the nanogels remained in the blood circulation long enough to address multiple organs. Subsequently, major organs were harvested and imaged *ex vivo* to better quantitate the NIR signals (Figure 5D2). Semiquantitative analysis confirmed that nanogels were sequestrated not only in the liver, a typical nonspecific sink for systemically administered nanocarriers, and kidneys (probably due to the renal clearance properties of the soluble polymers after hydrolysis of ketal-cross-linked nanogels), but also in the spleen. The spleen is a central organ of the lymphatic system, being highly relevant for immunodrug delivery because it harbors many antigen-presenting cells (Figure 5D3). We, therefore, opted for a strategy to systemically deliver a TLR7/8 agonist into this organ and induce a local immune modulation.

Effective and Safe TLR7/8 Agonist Delivery for Intravenous Routes of Administration. The highly potent small-molecular TLR7/8 agonist IMDQ[18] was selected as an immune modulatory compound to trigger maturation of splenic antigen-presenting cells. This compound has been demonstrated to activate TLR7/8 even when it is bound to macromolecular nanocarriers.[24,45,46] Due to its primary benzylic amine, IMDQ can straightforwardly be conjugated to pendant squaric ester amide groups and, therefore, directly be incorporated into the nanogel fabrication process (Figure 6A). IMDQ conjugation did not affect the nanogel fabrication, as cross-linked nanogels (IMDQ-D-NG and IMDQ-ND-NG) were of similar size and the non-cross-linked species (IMDQ-NCL-NG) was again completely soluble (compare Supporting Information Figure S51). Quantification of the covalently attached IMDQ was conducted by ^{1}H NMR spectroscopy. For the soluble NCL-NG species, a drug load of 2.7 wt % was found (compare Supporting Information Figure S52) being covalently attached to the polymer (confirmed by DOSY NMR, Figure S53).

For demonstrating TLR7/8 stimulation activity, we used a RAW-Blue macrophage reporter cell line that is genetically engineered to secrete embryonic alkaline phosphatase (SEAP) in response to TLR activation and downstream signaling via the NF-κB pathway. SEAP expression itself can readily be detected from the cell culture supernatant via UV/vis spectrophotometry after addition of a coloring substrate (Quanti-Blue assay). RAW Blue macrophages were pulsed with increasing doses of either soluble IMDQ (sIMDQ) or IMDQ-D-NG (empty nanogel D-NG served as a control). A strong TLR activation was found for sIMDQ already at sub-micromolar concentrations, while nonligated control nanogels did not induce any significant activation (Figure 6B). IMDQ-D-NG led to a dose-dependent activation, albeit less potent than sIMDQ, but still active in the micromolar concentration range. Similar activities were found after 24 as well as 48 h and could be confirmed for both IMDQ-ND-NG and IMDQ-NCL-NG (Figure S58), which may corroborate the weak cellular internalization. In parallel, RAW Blue cellular viability was monitored by an MTT assay. No significant influence on metabolic activity was found for all nanogel samples in the tested experimental window (Figure S57).

We then investigated the nanogel's *in vivo* immune stimulatory activity with a special focus on the activation of antigen-presenting cells in the spleen while avoiding systemic off-target effects. The latter can be visualized by bioluminescence imaging of heterozygous BALB/c IFN-β (IFN-$\beta^{+/\Delta\beta\text{-luc}}$) reporter mice,[47] in which luciferase as reporter gene is genetically linked to the expression of type I interferon IFN-β, a cytokine that is induced upon TLR7/8 stimulation. Mice were intravenously injected into the tail vein, and bioluminescence was monitored after 4, 24, and 48 h (Figure 6C and Supporting Information Figure S59). For sIMDQ, a strong signal was observed all over the body, reflecting a systemic inflammatory response in those mice. A prominent IFN-β expression occurred in the neck and abdomen and remained high up to 48 h postinjection. The nanogel-conjugated IMDQ, however, did not cause such a severe global immune activation all over the body. After 4 h no severe systemic inflammation was recorded. Only after 24 h a mild activity was observed with some expression in the abdomen and neck region, but with reduced gain compared to sIMDQ (Figure 6C and Supporting Information Figure S59). These observations clearly underline that severe systemic inflammatory responses are absent for the nanogel carrier system.

To further corroborate the absence of soluble IMDQ's acute toxicity, we also monitored the systemic inflammatory cytokines in sera of mice treated with soluble IMDQ vs nanogel-conjugated IMDQ. The results are provided in the Supporting Information Figure S62−S64 and confirm the observations of the IFN-β reporter mice: After 4 h, increasing serum cytokine levels of TNF-α, IL-6, and INF-γ are found in mice treated with soluble IMDQ. They are significantly elevated compared to mice treated with PBS, while mice treated with nanogel-bound IMDQ only provide slightly increased but not significant TNF-α, IL-6, and INF-γ levels (Supporting Information Figure S62).

After 24 h, those cytokines are again decreased to levels of PBS-treated mice. The elevated cytokine levels for soluble IMDQ-treated mice caused further liver toxicities by increased ALT, AST, and GLDH enzyme serum activities (Supporting Information Figure S63). Additionally, further influence on pancreas toxicity by high lipase serum activity as well as kidney toxicity by elevated blood urea nitrogen (BUN) can be observed (Supporting Information Figure S64). These data underline again the improved safety profile for the IMDQ-loaded nanogels to circumvent these acute toxicities but focus the immune stimulatory potential of the TLR7/8 agonist to the spleen.

One may speculate that such reduced systemic off-target effects for the nanogel-conjugated IMDQ might simply be caused by the minor receptor activation potency or reduced bioavailability. However, when it comes to immune intervention strategies (e.g., vaccination or cancer immunotherapy), site-specific immune activation (i.e., spleen specific, rather than systemic) is of important relevance and the major goal of this study.

Previous biodistribution analysis confirmed that a sufficient amount of nanogels was found inside the spleen after systemic activation (Figure 5D). To further validate that IMDQ-loaded nanogels still activate spleen-resident immune cells, we isolated splenocytes from the mice 48 h after injection and performed quantitative flow cytometric analyses (for further details on the gating procedure compare Supporting Information Figure S60). Both sIMDQ and IMDQ-D-NG comparably increased the

https://doi.org/10.1021/jacs.1c03772
J. Am. Chem. Soc. XXXX, XXX, XXX−XXX

number of myeloid cells with no influence on B and T lymphocytes (Figure 6D−H1). Dendritic cells (DCs), macrophages, and neutrophils are known to express and respond to TLR7/8 activation effectively. Their numbers are therefore increased to a similar extent for both sIMDQ and IMDQ-D-NG (Figure 6D1−F1).

We then checked for maturation markers on those cells and found again that IMDQ-D-NG triggered their expression to a similar level as sIMDQ while omitting systemic inflammations (Figure 6D2−H2 and Supporting Information Figure S61). For DCs and neutrophils (Figure 6D3/4 and F3/4) the expression levels of CD80 and CD86 were significantly enhanced by IMDQ-D-NG as well as sIMDQ. They were also upregulated on B lymphocytes that in contrast to T lymphocytes have antigen presenting ability (Figure 6G3/4). Also, the T lymphocyte activation marker CD69 was induced, again comparably, by IMDQ-D-NG and sIMDQ treatment, indicating further downstream T lymphocyte activation (Figure 6H3).

Most interestingly, for macrophages no difference in the expression of CD86 was observed (Figure 6E4), as CD86 upregulation is more typical for DCs. However, CD80 expression was more significantly triggered by IMDQ-D-NG and even exceeded the expression levels of sIMDQ (Figure 6E3). Apparently, nanogel-bound IMDQ seems to have a preferential stimulation potential in those highly phagocytotic immune cells inside the spleen. These properties outperform the treatment with sIMDQ and make the nanogels highly interesting for further therapeutic immune interventions.

Altogether, these observations confirm the hypothesis that our nanocarrier can deliver the TLR7/8 agonist into the spleen and maintain its immune stimulatory activity inside that organ. It prevents massive systemic immune activations and subsequent severe inflammatory off-target effects but conserves organ-specific immune stimulation inside the spleen, especially to resident macrophages. Since this organ is highly relevant for further immune intervention strategies including cancer immunotherapy or vaccination,[48,49] we consider squaric ester-based, pH-degradable nanogels as a relevant platform to exploit further systemic immunologic adjuvant strategies.

CONCLUSIONS

In this study, we have introduced polymerizable squaric ester amides as novel functionable tool to robustly fabricate pH-responsive nanogels serving as a versatile nanocarrier platform for safe delivery of the highly potent immunomodulator IMDQ after intravenous administration. To the best of our knowledge, the synthesis of methacrylamide monomers with a functional pendant squaric ester amide moiety has not been reported before. Its subsequent controlled RAFT block copolymerization as well as its self-assembling behavior in polar protic solvents provides access to precursor micelles with amine-reactive cores. Through their sequential amidation, covalent dye or drug loading, acid-sensitive cross-linking, and core-transformation from hydrophobic to hydrophilic polarity can be performed, affording fully hydrophilic nanogels with profound stability in plasma and the bloodstream, with modest uptake by phagocytic cells and with an inherently triggered degradation upon exposure to mildly endolysosomal pH conditions. The carriers' potential to covalently conjugate IMDQ as a highly potent immunomodulator enables the drug's safe and efficient delivery by preventing systemic off-target inflammation but retaining its spatial activity in the spleen. These findings underline the potential of this carrier platform to access intravenous administrations routes for small-molecular TLR7/8 agonists (and other relevant immune modulators) and, thus, provide novel opportunities to explore their superior adjuvant potency for systemic vaccination or cancer immunotherapy purposes.

ASSOCIATED CONTENT

Supporting Information

The Supporting Information is available free of charge at https://pubs.acs.org/doi/10.1021/jacs.1c03772.

Experimental details including materials, instrumentation, monomer and polymer syntheses, and characterization, nanogel fabrication and characterization, IMDQ ligation and quantification, *in vitro* and *in vivo* evaluation (PDF)

AUTHOR INFORMATION

Corresponding Author

Lutz Nuhn − *Max Planck Institute for Polymer Research, 55128 Mainz, Germany*; orcid.org/0000-0003-0761-1106; Phone: +49 (0) 6131-379-311; Email: lutz.nuhn@mpip-mainz.mpg.de

Authors

Anne Huppertsberg − *Max Planck Institute for Polymer Research, 55128 Mainz, Germany*

Leonard Kaps − *Institute for Translational Immunology and Research Center for Immune Therapy, University Medical Center, Johannes Gutenberg-University Mainz, 55131 Mainz, Germany; Department of Internal Medicine I, University Medical Center of the Johannes Gutenberg-University Mainz, 55131 Mainz, Germany*

Zifu Zhong − *Department of Pharmaceutics and Cancer Research Institute Ghent (CRIG), Ghent University, Ghent 9000, Belgium*

Sascha Schmitt − *Max Planck Institute for Polymer Research, 55128 Mainz, Germany*

Judith Stickdorn − *Max Planck Institute for Polymer Research, 55128 Mainz, Germany*

Kim Deswarte − *Department of Internal Medicine and Pediatrics, Ghent University, VIB Center for Inflammation Research, Ghent 9052, Belgium*

Francis Combes − *Laboratory of Gene Therapy, Department of Nutrition, Genetics and Ethology, Ghent University, Merelbeke 9820, Belgium*

Christian Czysch − *Max Planck Institute for Polymer Research, 55128 Mainz, Germany*

Jana De Vrieze − *Department of Pharmaceutics and Cancer Research Institute Ghent (CRIG), Ghent University, Ghent 9000, Belgium*

Sabah Kasmi − *Department of Pharmaceutics and Cancer Research Institute Ghent (CRIG), Ghent University, Ghent 9000, Belgium*

Niklas Choteschovsky − *Institute for Translational Immunology and Research Center for Immune Therapy, University Medical Center, Johannes Gutenberg-University Mainz, 55131 Mainz, Germany*

Adrian Klefenz − *Institute for Translational Immunology and Research Center for Immune Therapy, University Medical Center, Johannes Gutenberg-University Mainz, 55131 Mainz, Germany*

Carolina Medina-Montano − *Department of Dermatology, University Medical Center of Johannes Gutenberg-University Mainz, 55131 Mainz, Germany*

https://doi.org/10.1021/jacs.1c03772
J. Am. Chem. Soc. XXXX, XXX, XXX−XXX

Pia Winterwerber − *Max Planck Institute for Polymer Research, 55128 Mainz, Germany*
Chaojian Chen − *Max Planck Institute for Polymer Research, 55128 Mainz, Germany;* orcid.org/0000-0002-2588-2447
Matthias Bros − *Department of Dermatology, University Medical Center of Johannes Gutenberg-University Mainz, 55131 Mainz, Germany*
Stefan Lienenklaus − *Institute for Laboratory Animal Science and Institute of Immunology, Hannover Medical School, 30625 Hannover, Germany*
Niek N. Sanders − *Laboratory of Gene Therapy, Department of Nutrition, Genetics and Ethology, Ghent University, Merelbeke 9820, Belgium;* orcid.org/0000-0003-4585-0343
Kaloian Koynov − *Max Planck Institute for Polymer Research, 55128 Mainz, Germany;* orcid.org/0000-0002-4062-8834
Detlef Schuppan − *Institute for Translational Immunology and Research Center for Immune Therapy, University Medical Center, Johannes Gutenberg-University Mainz, 55131 Mainz, Germany; Division of Gastroenterology, Beth Israel Deaconess Medical Center, Harvard Medical School, Boston, Massachusetts 02215, United States*
Bart N. Lambrecht − *Department of Internal Medicine and Pediatrics, Ghent University, VIB Center for Inflammation Research, Ghent 9052, Belgium; Department of Pulmonary Medicine, Erasmus University Medical Center, Rotterdam 3015, Netherlands*
Sunil A. David − *ViroVax, LLC, Lawrence, Kansas 66047, United States;* orcid.org/0000-0003-1655-4641
Bruno G. De Geest − *Department of Pharmaceutics and Cancer Research Institute Ghent (CRIG), Ghent University, Ghent 9000, Belgium;* orcid.org/0000-0001-9826-6170

Complete contact information is available at: https://pubs.acs.org/10.1021/jacs.1c03772

Author Contributions

The manuscript was written through contributions of all authors. All authors have given approval to the final version of the manuscript.

Notes

The authors declare no competing financial interest.

■ ACKNOWLEDGMENTS

A.H. and L.N. acknowledge support by the Max Planck Graduate Center with the Johannes Gutenberg-Universität Mainz (MPGC). Moreover, L.N. kindly acknowledges financial support by the DFG through the Emmy Noether program as well as the SFB 1066 projects Q02, B03, and B04. Both A.H. and L.N. would also like to thank Tanja Weil for providing access to excellent laboratory facilities.

■ REFERENCES

(1) Singh, R.; Lillard, J. W. Nanoparticle-Based Targeted Drug Delivery. *Exp. Mol. Pathol.* **2009**, *86* (3), 215−223.
(2) Mitchell, M. J.; Billingsley, M. M.; Haley, R. M.; Wechsler, M. E.; Peppas, N. A.; Langer, R. Engineering Precision Nanoparticles for Drug Delivery. *Nat. Rev. Drug Discovery* **2021**, *20* (2), 101−124.
(3) Talelli, M.; Barz, M.; Rijcken, C. J. F.; Kiessling, F.; Hennink, W. E.; Lammers, T. Core-Crosslinked Polymeric Micelles: Principles, Preparation, Biomedical Applications and Clinical Translation. *Nano Today* **2015**, *10* (1), 93−117.
(4) Crommelin, D. J. A.; Florence, A. T. Towards More Effective Advanced Drug Delivery Systems. *Int. J. Pharm.* **2013**, *454* (1), 496−511.
(5) Banik, B. L.; Fattahi, P.; Brown, J. L. Polymeric Nanoparticles: The Future of Nanomedicine. *Wiley Interdiscip. Rev. Nanomedicine Nanobiotechnology* **2016**, *8* (2), 271−299.
(6) Tong, R.; Tang, L.; Ma, L.; Tu, C.; Baumgartner, R.; Cheng, J. Smart Chemistry in Polymeric Nanomedicine. *Chem. Soc. Rev.* **2014**, *43* (20), 6982−7012.
(7) Harrison, L. I.; Astry, C.; Kumar, S.; Yunis, C. Pharmacokinetics of 852A, an Imidazoquinoline Toll-Like Receptor 7-Specific Agonist, Following Intravenous, Subcutaneous, and Oral Administrations in Humans. *J. Clin. Pharmacol.* **2007**, *47* (8), 962−969.
(8) Gunzer, M.; Riemann, H.; Basoglu, Y.; Hillmer, A.; Weishaupt, C.; Balkow, S.; Benninghoff, B.; Ernst, B.; Steinert, M.; Scholzen, T.; Sunderkötter, C.; Grabbe, S. Systemic Administration of a TLR7 Ligand Leads to Transient Immune Incompetence Due to Peripheral-Blood Leukocyte Depletion. *Blood* **2005**, *106* (7), 2424−2432.
(9) Stickdorn, J.; Nuhn, L. Reactive-Ester Derived Polymer Nanogels for Cancer Immunotherapy. *Eur. Polym. J.* **2020**, *124*, 109481.
(10) Lybaert, L.; Vermaelen, K.; De Geest, B. G.; Nuhn, L. Immunoengineering through Cancer Vaccines − A Personalized and Multi-Step Vaccine Approach towards Precise Cancer Immunity. *J. Controlled Release* **2018**, *289*, 125−145.
(11) Milling, L.; Zhang, Y.; Irvine, D. J. Delivering Safer Immunotherapies for Cancer. *Adv. Drug Delivery Rev.* **2017**, *114*, 79−101.
(12) O'Neill, L. A. J.; Golenbock, D.; Bowie, A. G. The History of Toll-like Receptors-Redefining Innate Immunity. *Nat. Rev. Immunol.* **2013**, *13* (6), 453−460.
(13) Mancini, R. J.; Stutts, L.; Ryu, K. A.; Tom, J. K.; Esser-Kahn, A. P. Directing the Immune System with Chemical Compounds. *ACS Chem. Biol.* **2014**, *9* (5), 1075−1085.
(14) Iwasaki, A.; Medzhitov, R. Control of Adaptive Immunity by the Innate Immune System. *Nat. Immunol.* **2015**, *16* (4), 343−353.
(15) Schön, M. P.; Schön, M. TLR7 and TLR8 as Targets in Cancer Therapy. *Oncogene* **2008**, *27* (2), 190−199.
(16) Baldridge, J. R.; McGowan, P.; Evans, J. T.; Cluff, C.; Mossman, S.; Johnson, D.; Persing, D. Taking a Toll on Human Disease: Toll-like Receptor 4 Agonists as Vaccine Adjuvants and Monotherapeutic Agents. *Expert Opin. Biol. Ther.* **2004**, *4* (7), 1129−1138.
(17) Kawai, T.; Akira, S. The Role of Pattern-Recognition Receptors in Innate Immunity: Update on Toll-like Receptors. *Nat. Immunol.* **2010**, *11* (5), 373−384.
(18) Beesu, M.; Salyer, A. C. D.; Brush, M. J. H.; Trautman, K. L.; Hill, J. K.; David, S. A. Identification of High-Potency Human TLR8 and Dual TLR7/TLR8 Agonists in Pyrimidine-2,4-Diamines. *J. Med. Chem.* **2017**, *60* (5), 2084−2098.
(19) Van Hoeven, N.; Fox, C. B.; Granger, B.; Evers, T.; Joshi, S. W.; Nana, G. I.; Evans, S. C.; Lin, S.; Liang, H.; Liang, L.; Nakajima, R.; Felgner, P. L.; Bowen, R. A.; Marlenee, N.; Hartwig, A.; Baldwin, S. L.; Coler, R. N.; Tomai, M.; Elvecrog, J.; Reed, S. G.; Carter, D. A Formulated TLR7/8 Agonist Is a Flexible, Highly Potent and Effective Adjuvant for Pandemic Influenza Vaccines. *Sci. Rep.* **2017**, *7* (1), 1−15.
(20) De Vrieze, J.; Louage, B.; Deswarte, K.; Zhong, Z.; De Coen, R.; Van Herck, S.; Nuhn, L.; Kaas Frich, C.; Zelikin, A. N.; Lienenklaus, S.; Sanders, N. N.; Lambrecht, B. N.; David, S. A.; De Geest, B. G. Potent Lymphatic Translocation and Spatial Control Over Innate Immune Activation by Polymer−Lipid Amphiphile Conjugates of Small-Molecule TLR7/8 Agonists. *Angew. Chem., Int. Ed.* **2019**, *58* (43), 15390−15395.
(21) Yoo, E.; Salyer, A. C. D.; Brush, M. J. H.; Li, Y.; Trautman, K. L.; Shukla, N. M.; De Beuckelaer, A.; Lienenklaus, S.; Deswarte, K.; Lambrecht, B. N.; De Geest, B. G.; David, S. A. Hyaluronic Acid Conjugates of TLR7/8 Agonists for Targeted Delivery to Secondary Lymphoid Tissue. *Bioconjugate Chem.* **2018**, *29* (8), 2741−2754.
(22) Lynn, G. M.; Chytil, P.; Francica, J. R.; Lagová, A.; Kueberuwa, G.; Ishizuka, A. S.; Zaidi, N.; Ramirez-Valdez, R. A.; Blobel, N. J.; Baharom, F.; Leal, J.; Wang, A. Q.; Gerner, M. Y.; Etrych, T.; Ulbrich,

https://doi.org/10.1021/jacs.1c03772
J. Am. Chem. Soc. XXXX, XXX, XXX−XXX

K.; Seymour, L. W.; Seder, R. A.; Laga, R. Impact of Polymer-TLR-7/8 Agonist (Adjuvant) Morphology on the Potency and Mechanism of CD8 T Cell Induction. *Biomacromolecules* **2019**, *20* (2), 854−870.
(23) Van Herck, S.; Deswarte, K.; Nuhn, L.; Zhong, Z.; Portela Catani, J. P.; Li, Y.; Sanders, N. N.; Lienenklaus, S.; De Koker, S.; Lambrecht, B. N.; David, S. A.; De Geest, B. G. Lymph-Node-Targeted Immune Activation by Engineered Block Copolymer Amphiphiles-TLR7/8 Agonist Conjugates. *J. Am. Chem. Soc.* **2018**, *140*, 14300−14307.
(24) Nuhn, L.; De Koker, S.; Van Lint, S.; Zhong, Z.; Catani, J. P.; Combes, F.; Deswarte, K.; Li, Y.; Lambrecht, B. N.; Lienenklaus, S.; Sanders, N. N.; David, S. A.; Tavernier, J.; De Geest, B. G. Nanoparticle-Conjugate TLR7/8 Agonist Localized Immunotherapy Provokes Safe Antitumoral Responses. *Adv. Mater.* **2018**, *30* (45), 1−9.
(25) Nuhn, L.; Van Hoecke, L.; Deswarte, K.; Schepens, B.; Li, Y.; Lambrecht, B. N.; De Koker, S.; David, S. A.; Saelens, X.; De Geest, B. G. Potent Anti-Viral Vaccine Adjuvant Based on PH-Degradable Nanogels with Covalently Linked Small Molecule Imidazoquinoline TLR7/8 Agonist. *Biomaterials* **2018**, *178*, 643−651.
(26) Lynn, G. M.; Sedlik, C.; Baharom, F.; Zhu, Y.; Ramirez-Valdez, R. A.; Coble, V. L.; Tobin, K.; Nichols, S. R.; Itzkowitz, Y.; Zaidi, N.; Gammon, J. M.; Blobel, N. J.; Denizeau, J.; de la Rochere, P.; Francica, B. J.; Decker, B.; Maciejewski, M.; Cheung, J.; Yamane, H.; Smelkinson, M. G.; Francica, J. R.; Laga, R.; Bernstock, J. D.; Seymour, L. W.; Drake, C. G.; Jewell, C. M.; Lantz, O.; Piaggio, E.; Ishizuka, A. S.; Seder, R. A. Peptide−TLR-7/8a Conjugate Vaccines Chemically Programmed for Nanoparticle Self-Assembly Enhance CD8 T-Cell Immunity to Tumor Antigens. *Nat. Biotechnol.* **2020**, *38* (3), 320−332.
(27) Van Lysebetten, D.; Malfanti, A.; Deswarte, K.; Koynov, K.; Golba, B.; Ye, T.; Zhong, Z.; Kasmi, S.; Lamoot, A.; Chen, Y.; Van Herck, S.; Lambrecht, B. N.; Sanders, N. N.; Lienenklaus, S.; David, S. A.; Vicent, M. J.; De Koker, S.; De Geest, B. G. Lipid-Polyglutamate Nanoparticle Vaccine Platform. *ACS Appl. Mater. Interfaces* **2021**, *13* (5), 6011−6022.
(28) Cho, H.; Il; Barrios, K.; Lee, Y. R.; Linowski, A. K.; Celis, E. BiVax: A Peptide/Poly-IC Subunit Vaccine That Mimics an Acute Infection Elicits Vast and Effective Anti-Tumor CD8 T-Cell Responses. *Cancer Immunol. Immunother.* **2013**, *62* (4), 787−799.
(29) Seder, R. A.; Chang, L. J.; Enama, M. E.; Zephir, K. L.; Sarwar, U. N.; Gordon, I. J.; Holman, L. S. A.; James, E. R.; Billingsley, P. F.; Gunasekera, A.; Richman, A.; Chakravarty, S.; Manoj, A.; Velmurugan, S.; Li, M. L.; Ruben, A. J.; Li, T.; Eappen, A. G.; Stafford, R. E.; Plummer, S. H.; Hendel, C. S.; Novik, L.; Costner, P. J. M.; Mendoza, F. H.; Saunders, J. G.; Nason, M. C.; Richardson, J. H.; Murphy, J.; Davidson, S. A.; Richie, T. L.; Sedegah, M.; Sutamihardja, A.; Fahle, G. A.; Lyke, K. E.; Laurens, M. B.; Roederer, M.; Tewari, K.; Epstein, J. E.; Sim, B. K. L.; Ledgerwood, J. E.; Graham, B. S.; Hoffman, S. L. Protection against Malaria by Intravenous Immunization with a Nonreplicating Sporozoite Vaccine. *Science (Washington, DC, U. S.)* **2013**, *341* (6152), 1359−1365.
(30) Baharom, F.; Ramirez-Valdez, R. A.; Tobin, K. K. S.; Yamane, H.; Dutertre, C. A.; Khalilnezhad, A.; Reynoso, G. V.; Coble, V. L.; Lynn, G. M.; Mulè, M. P.; Martins, A. J.; Finnigan, J. P.; Zhang, X. M.; Hamerman, J. A.; Bhardwaj, N.; Tsang, J. S.; Hickman, H. D.; Ginhoux, F.; Ishizuka, A. S.; Seder, R. A. Intravenous Nanoparticle Vaccination Generates Stem-like TCF1+ Neoantigen-Specific CD8+ T Cells. *Nat. Immunol.* **2021**, *22* (1), 41−52.
(31) Nuhn, L.; Vanparijs, N.; De Beuckelaer, A.; Lybaert, L.; Verstraete, G.; Deswarte, K.; Lienenklaus, S.; Shukla, N. M.; Salyer, A. C. D.; Lambrecht, B. N.; Grooten, J.; David, S. A.; De Koker, S.; De Geest, B. G. PH-Degradable Imidazoquinoline-Ligated Nanogels for Lymph Node-Focused Immune Activation. *Proc. Natl. Acad. Sci. U. S. A.* **2016**, *113* (29), 8098−8103.
(32) Nuhn, L.; Hirsch, M.; Krieg, B.; Koynov, K.; Fischer, K.; Schmidt, M.; Helm, M.; Zentel, R. Cationic Nanohydrogel Particles as Potential SiRNA Carriers for Cellular Delivery. *ACS Nano* **2012**, *6* (3), 2198−2214.
(33) Nuhn, L.; Van Herck, S.; Best, A.; Deswarte, K.; Kokkinopoulou, M.; Lieberwirth, I.; Koynov, K.; Lambrecht, B. N.; De Geest, B. G. FRET Monitoring of Intracellular Ketal Hydrolysis in Synthetic Nanoparticles. *Angew. Chem., Int. Ed.* **2018**, *57* (33), 10760−10764.
(34) Bebis, K.; Jones, M. W.; Haddleton, D. M.; Gibson, M. I. Thermoresponsive Behaviour of Poly[(Oligo(Ethyleneglycol Methacrylate)]s and Their Protein Conjugates: Importance of Concentration and Solvent System. *Polym. Chem.* **2011**, *2* (4), 975−982.
(35) Mohr, N.; Barz, M.; Forst, R.; Zentel, R. A Deeper Insight into the Postpolymerization Modification of Polypenta Fluorophenyl Methacrylates to Poly(N-(2-Hydroxypropyl) Methacrylamide). *Macromol. Rapid Commun.* **2014**, *35* (17), 1522−1527.
(36) Jones, K. Pentafluorophenol. In *Encyclopedia of Reagents for Organic Synthesis*; American Cancer Society, 2001.
(37) Tietze, L. F.; Arlt, M.; Beller, M.; Gliisenkampb, K.-H.; Jahdeb, E.; Rajewskyb, M. F. Squaric Acid Diethyl Ester: A New Coupling Reagent for the Formation of Drug Biopolymer Conjugates. Synthesis of Squaric Acid Ester Amides and Diamides. *Chem. Ber.* **1991**, *124*, 1215−1221.
(38) Quiñonero, D.; Frontera, A.; Ballester, P.; Deyà, P. M. A Theoretical Study of Aromaticity in Squaramide and Oxocarbons. *Tetrahedron Lett.* **2000**, *41* (12), 2001−2005.
(39) Wurm, F. R.; Klok, H. A. Be Squared: Expanding the Horizon of Squaric Acid-Mediated Conjugations. *Chem. Soc. Rev.* **2013**, *42* (21), 8220−8236.
(40) Steinbach, T.; Wurm, F.; Klok, H. A. Squaric Acid Mediated Bioconjugation Expanded to Polymers Prepared by ATRP. *Polym. Chem.* **2014**, *5* (13), 4039−4047.
(41) Zhang, Z.; Vanparijs, N.; Vandewalle, S.; Du Prez, F. E.; Nuhn, L.; De Geest, B. G. Squaric Ester Amides as Hydrolysis-Resistant Functional Groups for Protein-Conjugation of RAFT-Derived Polymers. *Polym. Chem.* **2016**, *7* (47), 7242−7248.
(42) Kockelmann, J.; Stickdorn, J.; Kasmi, S.; De Vrieze, J.; Pieszka, M.; Ng, D. Y. W.; David, S. A.; De Geest, B. G.; Nuhn, L. Control over Imidazoquinoline Immune Stimulation by PH-Degradable Poly-(Norbornene) Nanogels. *Biomacromolecules* **2020**, *21* (6), 2246−2257.
(43) Leber, N.; Kaps, L.; Aslam, M.; Schupp, J.; Brose, A.; Schäffel, D.; Fischer, K.; Diken, M.; Strand, D.; Koynov, K.; Tuettenberg, A.; Nuhn, L.; Zentel, R.; Schuppan, D. SiRNA-Mediated in Vivo Gene Knockdown by Acid-Degradable Cationic Nanohydrogel Particles. *J. Controlled Release* **2017**, *248*, 10−23.
(44) Koynov, K.; Butt, H. J. Fluorescence Correlation Spectroscopy in Colloid and Interface Science. *Curr. Opin. Colloid Interface Sci.* **2012**, *17* (6), 377−387.
(45) Shukla, N. M.; Malladi, S. S.; Mutz, C. A.; Balakrishna, R.; David, S. A. Structure-Activity Relationships in Human Toll-like Receptor 7-Active Imidazoquinoline Analogues. *J. Med. Chem.* **2010**, *53* (11), 4450−4465.
(46) Kim, W. G.; Choi, B.; Yang, H. J.; Han, J. A.; Jung, H.; Cho, H.; Kang, S.; Hong, S. Y. Covalent Conjugation of Small-Molecule Adjuvants to Nanoparticles Induces Robust Cytotoxic T Cell Responses via DC Activation. *Bioconjugate Chem.* **2016**, *27* (9), 2007−2013.
(47) Lienenklaus, S.; Cornitescu, M.; Ziętara, N.; Łyszkiewicz, M.; Gekara, N.; Jabłońska, J.; Edenhofer, F.; Rajewsky, K.; Bruder, D.; Hafner, M.; Staeheli, P.; Weiss, S. Novel Reporter Mouse Reveals Constitutive and Inflammatory Expression of IFN-β In Vivo. *J. Immunol.* **2009**, *183* (5), 3229−3236.
(48) Steenbrugge, J.; De Jaeghere, E. A.; Meyer, E.; Denys, H.; De Wever, O. Splenic Hematopoietic and Stromal Cells in Cancer Progression. *Cancer Res.* **2020**, *81*, 27−34.
(49) Bronte, V.; Pittet, M. J. The Spleen in Local and Systemic Regulation of Immunity. *Immunity* **2013**, *39* (5), 806−818.

https://doi.org/10.1021/jacs.1c03772
J. Am. Chem. Soc. XXXX, XXX, XXX−XXX

Supporting Information

Squaric Ester-Based, pH-Degradable Nanogels: Modular Nanocarriers for Safe, Systemic Administration of Toll-Like Receptor 7/8 Agonistic Immune Modulators

Anne Huppertsberg[‖], Leonard Kaps[‡,Π], Zifu Zhong[†], Sascha Schmitt[‖], Judith Stickdorn[‖], Kim Deswarte[Δ], Francis Combes[§], Christian Czysch[‖], Jana De Vrieze[†], Sabah Kasmi[†], Niklas Choteschovsky[‡], Adrian Klefenz[‡], Carolina Medina-Montano[º], Pia Winterwerber[‖], Chaojian Chen[‖], Matthias Bros[º], Stefan Lienenklaus[$], Niek N. Sanders[§], Kaloian Koynov[‖], Detlef Schuppan[‡,∇], Bart N. Lambrecht[Δ,⊥], Sunil A. David[#], Bruno G. De Geest[†], and Lutz Nuhn[‖,*]

[‖] Max Planck Institute for Polymer Research, 55128 Mainz, Germany;
[‡] Institute for Translational Immunology and Research Center for Immune Therapy, University Medical Center, Johannes Gutenberg-University Mainz, 55131 Mainz, Germany;
[Π] Department of Internal Medicine I, University Medical Centre of the Johannes Gutenberg-University Mainz, 55131 Mainz, Germany;

[†] Department of Pharmaceutics and Cancer Research Institute Ghent (CRIG), Ghent University, Ghent 9000, Belgium;

[Δ] Department of Internal Medicine and Pediatrics, Ghent University, VIB Center for Inflammation Research, Ghent 9000, Belgium;
[§] Laboratory of Gene Therapy, Department of Nutrition, Genetics and Ethology, Ghent University, Merelbeke 9820, Belgium;
[º] Department of Dermatology, University Medical Center of Johannes Gutenberg-University Mainz, 55131 Mainz, Germany;
[$] Institute for Laboratory Animal Science and Institute of Immunology, Hannover Medical School, 30625 Hannover, Germany;
[∇] Division of Gastroenterology, Beth Israel Deaconess Medical Center, Harvard Medical School, Boston, MA 02215, United States;

[⊥] Department of Pulmonary Medicine, Erasmus University Medical Center, Rotterdam 3015, Netherlands;

[#] ViroVax, LLC, Lawrence, Kansas 66047, United States.

Table of Content

1. Chemicals and Solvents **3**

2. Instrumentation **4**

2.1 Nuclear Magnetic Resonance (NMR) Spectroscopy 4

2.2 Electrospray-Ionization mass spectrometry (ESI-MS) 4

2.3 Ultraviolet-Visible Spectroscopy (UV-Vis) 4

2.4 Size-Exclusion Chromatography (SEC) 4

2.5 Dynamic Light Scattering (DLS) 4

2.6 Fluorescence Correlation Spectroscopy (FCS) 5

2.7 Atomic Force Microscopy (AFM) 5

2.8 Transmission Electron Microscopy (TEM) 6

3. Syntheses **7**

3.1 Monomers 7

3.2 Synthesis of macro-trithiocarbonate-chain transfer agent (macro-TTC-CTA) 23

3.3 Block copolymerization of MA-SQ with PEG-TTC-CTA 26

3.4 Homopolymerization of MA-SQ with TTC-CTA 29

3.5 Reaction kinetics of RAFT homopolymerization 31

3.6 Polymer-analogous reaction of homopolymer by amidation with primary, secondary, or tertiary amines 32

3.7 Block copolymer-analogous reaction of self-assembled micelles by amidation with primary amines 36

4. Nanogel Fabrication **37**

4.1 Preparation of nanogels 37

4.2 IMDQ quantification via ^{1}H NMR analysis 41

4.3 Degradation/hydrolysis study of ketal-crosslinked nanogels 42

5. *In Vitro* Experiments **43**

5.1 Cell culturing 43

5.2 Cell uptake experiment in RAW Blue-macrophages using confocal fluorescence microscopy 43

5.3 Flow cytometry (FACS) 44

5.4 Cellular metabolic activity of RAW-Blue macrophages using MTT assay 44

5.5 RAW-Blue macrophage TLR reporter assay 45

6. *In Vivo* Experiments **46**

6.1 Biodistribution imaging of 800RS-labeled nanogels 46

6.2 Bioactivity imaging of IMDQ-loaded nanogels 46

6.3 Flow cytometry analysis of splenic innate immune activation 47

6.4 Acute toxicity studies 50

7. Statistical analysis **51**

1. Chemicals and Solvents

Unless otherwise stated, all chemicals were obtained from commercial sources, such as Sigma Aldrich (Taufkirchen, Germany), TCI Chemicals (Tokyo, Japan) or Rapp Polymere (Tübingen, Germany) and used as received. Fluorescent dyes Oregon Green 488 cadaverine and tetramethylrhodamine cadaverine were obtained from Thermo Fisher Scientific (Waltham, MA, USA) and 800RS-amine was purchased from Li-Cor Biosciences (Lincoln, NE, USA).

Azobisisobutyronitrile (AIBN) was recrystallized from ethanol twice, prior to use. TLR 7/8 agonist 1-(4-(aminomethyl)benzyl)-2-butyl-1-H-imidazo[4,5-c]quinolin-4-amine (IMDQ) could be provided following an earlier report.[1]

Solvents (HPLC grade) were purchased from Acros Organics (Geel, Belgium) and Thermo Fisher Scientific. Deuterated solvents were obtained from Sigma Aldrich. Millipore water was prepared using a MILLI-Q® Reference A+ System. Silica gel chromatography was performed using silica obtained from Machery-Nagel (particle size: 0.063–0.2 mm). For dialysis Spectra/Por7™ dialysis membranes with a molecular weight cut-off of 1000 g/mol were used.

Cell culture medium and supplements as well as Dulbecco's PBS were obtained from Thermo Fisher Scientific. The RAW-Blue reporter cell line (264.7) and QUANTI-Blue™ substrate was purchased from InvivoGen (San Diego, CA, USA). RAW-Blue macrophages were cultured in DMEM-GlutaMAX™ medium, which was supplemented with 10% fetal bovine serum, 1% penicillin/streptomycin, 0.02 % normocin, and 0.01% zeocin at 37°C with 5% CO_2 saturation.

[1] Shukla, N. M.; Malladi, S. S.; Mutz, C. A.; Balakrishna, R.; David, S. A. Structure-Activity Relationships in Human Toll-like Receptor 7-Active Imidazoquinoline Analogues. *J. Med. Chem.* **2010**, 53 (11), 4450–4465.

2. Instrumentation

2.1 Nuclear Magnetic Resonance (NMR) Spectroscopy

^{1}H, and ^{13}C NMR spectra were recorded at room temperature (RT) on a Bruker Avance III 300 MHz, Bruker Avance III 400 MHz or Bruker Avance III 500 MHz spectrometer. The chemical shifts (δ) are given in parts per million (ppm) relative to TMS. NMR spectra were processed with the software MestReNova 11.0.4 by Mestrelab Research. Samples were prepared in deuterated solvents and their corresponding signals referenced to residual non-deuterated solvent signals.

2.2 Electrospray-Ionization mass spectrometry (ESI-MS)

ESI mass spectra were recorded by an Agilent 6545 QTOF-MS (Santa Clara, CA, USA). Samples were prepared at 0.1 mg/mL in methanol.

2.3 Ultraviolet-Visible Spectroscopy (UV-Vis)

UV/Vis spectra of the polymer-analogous reaction of homopolymer with amines were recorded on a V-630 spectrophotometer equipped with a Peltier thermostatted ETC-717 single cell holder purchased from JASCO (Pfungstadt, Germany). Measurement conditions of 20 °C were guaranteed by a V50 water thermostat from Krüss Optronic (Hamburg, Germany).

RAW-Blue and MTT assay analysis were performed using a Spark 20M Multimode Microplate Reader from Tecan Trading AG (Mannedorf, Switzerland).

2.4 Size-Exclusion Chromatography (SEC)

SEC was performed using 20A system equipped with a 20A ISO-pump and a 20A refractive index (RI) detector purchased from Shimadzu (Tokyo, Japan). N,N-dimethylacetamide (DMAc) containing 50 mM lithium bromide was used as eluent at a flow rate of 0.7 mL/min and a column temperature of 50 °C. PLgel 5 µm MIXED-D columns were obtained from Agilent Technologies (Santa Clara, CA, USA) and calibrated using poly(methyl methacrylate) (PMMA) standards obtained from PSS (Mainz, Germany).

As internal standard toluene was added to the samples. Samples were prepared at 1 mg/mL and filtered through GHP syringe filters (0.2 µm pore size, Acrodisc) prior to injection. The data was processed with the software PSS WINGPC UniChrom.

2.5 Dynamic Light Scattering (DLS)

Single-angle DLS measurements were performed at 25 °C using a Malvern ZetaSizer Nano S purchased from Malvern Instruments Ltd. (Malvern, Great Britain) with a He/Ne Laser (λ = 633 nm) at a fixed scattering angle of 173°. All measurements were performed in triplicate. The obtained data was processed by cumulant fitting for D_z and PDI, or by CONTIN fitting for intensity-, volume-, and number-weighted particle size distribution. Samples were prepared at 0.1 mg/mL. Dust was removed prior to each measurement by filtration through GHP syringe filters (0.2 µm pore size, Acrodisc).

2.6 Fluorescence Correlation Spectroscopy (FCS)

Prior to FCS measurements fluorescently Oregon Green-labeled nanogels were purified from remaining unbound dye by spin-filtration. Thus, 2 mg of the respective nanogel type was re-dispersed in 1 mL PBS using sonification, before unbound Oregon Green cadaverine dye was removed by spin-filtration of the nanogel dispersion using centrifugal filter units (regenerated cellulose, MWCO: 10,000 g/mol). After centrifugation 0.8 mL PBS was added and centrifuged again. This procedure was repeated until complete disappearance of Oregon Green-derived absorbance in the filtrate was monitored by UV-Vis measurements.

To monitor degradation of pH-responsive nanogels under acidic conditions 10 µL of nanogel dispersion (2 mg/mL in PBS) was diluted with 90 µL Ac/HAc buffer (pH 5.2). FCS measurements were performed after 0, 90, 120, 180, 270, and 480 min.

To investigate the nanogels plasma stability 10 µL of nanogel dispersion (2 mg/mL in PBS) was incubated with 90 µL of human plasma at 37 °C under vigorous shaking. FCS data were recorded after 0, 6, and 24 h.

FCS measurements were performed using a commercial LSM880 setup (Carl Zeiss, Jena, Germany) equipped with a C-Apochromat 40x/1.2 W water immersion objective. For excitation of Oregon Green an argon laser (488 nm) was used. The fluorescence light was collected with the same objective and after passing a pinhole directed to a spectral detection unit (Quasar, Carl Zeiss). There the fluorescence light is separated spectrally by a grating element on a 32 channel array of GaAsP detectors operating in a single photon counting mode. The emission for Oregon Green was collected in the spectral range of 508-606 nm.

All measurements were performed in eight-well polystyrene-chambered coverglass (Laboratory-Tek, Nalge Nunc International, Penfield, NY, USA). The obtained FCS autocorrelation curves were fitted with the theoretical model function for an ensemble of either one or two types of freely diffusing fluorescence species. The fits yielded the diffusion coefficients (D) of the studied species. Finally, the hydrodynamic radii (R_H) were calculated using the Stokes-Einstein relation: $R_H = \frac{k_B T}{6\pi\eta D}$, where k_B is the Boltzmann constant, T is the temperature, and η is the viscosity of the solvent.

2.7 Atomic Force Microscopy (AFM)

AFM measurements were performed with a Bruker Dimension FastScan Bio® atomic force microscope, which was operated in PeakForce mode. AFM probes with a nominal spring constant of 0.25 N/m (FastScan-D, Bruker) were applied. For sample preparation 30 µL of nanogel dispersion (0.5 mg/mL in Millipore water) was dropcasted onto a freshly cleaved mica substrate (circular, 15 mm). Samples were scanned with scan rates of 0.994 Hz and data was processed using NanoScope Analysis 1.8.

2.8 Transmission Electron Microscopy (TEM)

For preparation of TEM images 5 μL of nanogel dispersion (0.5 mg/mL in Millipore water containing 0.1 wt% ammonia) was added onto a carbon-coated copper grid. After air-drying TEM measurements were performed using a JEOL JEM-1400 TEM operating at an accelerating voltage of 120 kV.

3. Syntheses

3.1 Monomers

3.1.1 N-(3-(2-ethoxy-3,4-dioxocyclobut-1-en-1-yl)amino)propyl)methacrylamide, Squaric ester amide methacrylamide (MA-SQ)

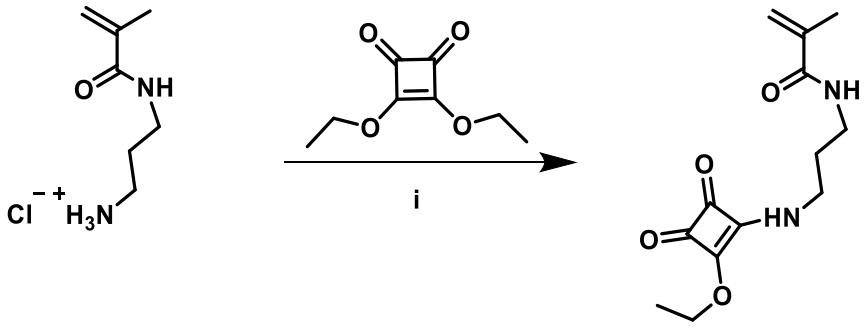

Figure S 1: Synthesis of MA-SQ, i) TEA, EtOH/H_2O, RT, 16 h, yield: 90 %.

In a round bottom flask, squaric acid diethyl ester (7.86 g, 46 mmol, 1.1 eq.) and triethylamine (TEA) (6.37 g, 63 mmol, 1.5 eq.) were diluted in ethanol (70 mL). To this solution N-(3-aminopropyl)methacrylamide hydrochloride (APMA) dissolved in mixture of water (30 mL) and ethanol (30 mL) was slowly added *via* dropping funnel over 2 h. The reaction mixture was allowed to stir for 16 h at RT. After a negative Ninhydrin test indicated complete conversion of the primary amine APMA, toluene (2 x 250 mL) was added to the reaction mixture to remove ethanol and water by azeotropic evaporation *in vacuo*. To remove MEHQ inhibitor the resulting crude product was dissolved in a mixture of ethyl acetate (15 mL) and ethanol (30 mL) and purified by passing over a short column of activated basic alumina. Again, toluene (2 x 50 mL) was added to remove the solvents by azeotropic evaporation *in vacuo*. Further purification of the product was achieved by silica gel chromatography using ethyl acetate as eluent. The product was obtained as white solid (10.10 g, 90 %).

^{1}H-NMR (300 MHz, DMSO-d_6): δ (ppm) = 8.73 (s, 0.5H, **a**)[a)] 8.54(s, 0.5H, **a**)[a)], 7.90 (s, 1H, **b**), 5.63 (s, 1H, **c**), 5.32 (s, 1H, **d**), 4.64 (m, 2H, **e**), 3.48[a)] (m, 1H, **f**), 3.29[a)] (m,1H, **f**) 3.13 (m, 2H, **g**) 1.84 (s, 3H, **h**)1.69 (m, 2H, **i**), 1.35 (m, 3H, **j**). [a)] due to rotamers a splitting of the signals is observed.

^{13}C-NMR (75 MHz, DMSO-d_6): δ (ppm) = 189.39 (**a**)[a)], 189.30 (**a**)[a)], 182.12(**b**)[a)], 181.92 (**b**)[a)], 177.00 (**c**)[a)], 176.54 (**c**)[a)], 172.58 (**d**)[a)], 172.22 (**d**)[a)], 167.55 (**e**)[a)], 167.52(**e**)[a)], 139.94 (**f**), 118.95 (**g**), 68.80 (**h**), 41.67 (**i**), 41.33 (**i**), 36.00, (**j**) 30.24 (**k**), 29.76 (**l**), 18.63 (**m**), 15.65 (**n**). [a)] due to rotamers a splitting of the signals is observed.

ESI-MS: [m/z] = 267.17 $[M+H]^+$ calc. 267.13), 289.19 $[M+Na]^+$ (calc. 289.12), 555.57 $[2M+Na]^+$ (calc. 555.24).

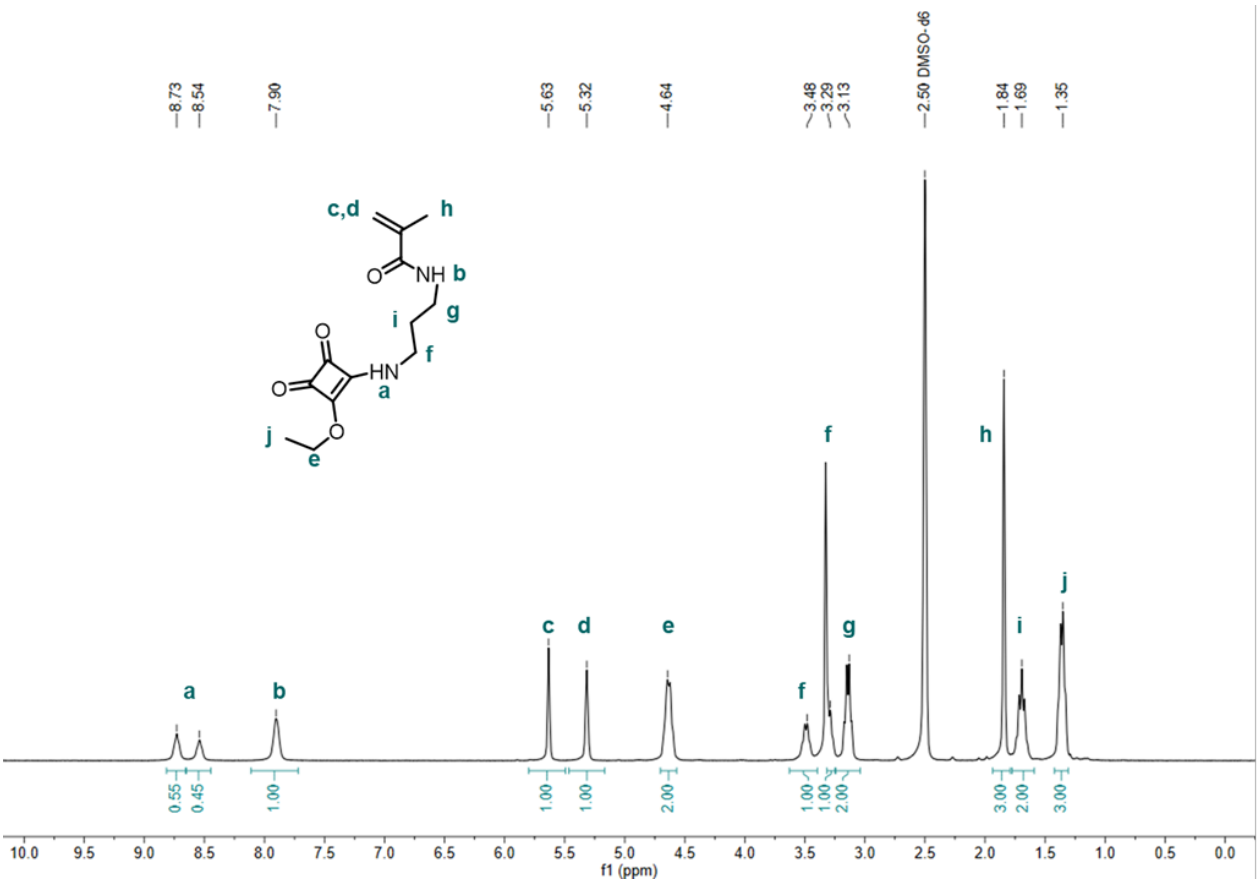

Figure S 2: [1]H-NMR spectrum (300 MHz) of MA-SQ in DMSO-d6.

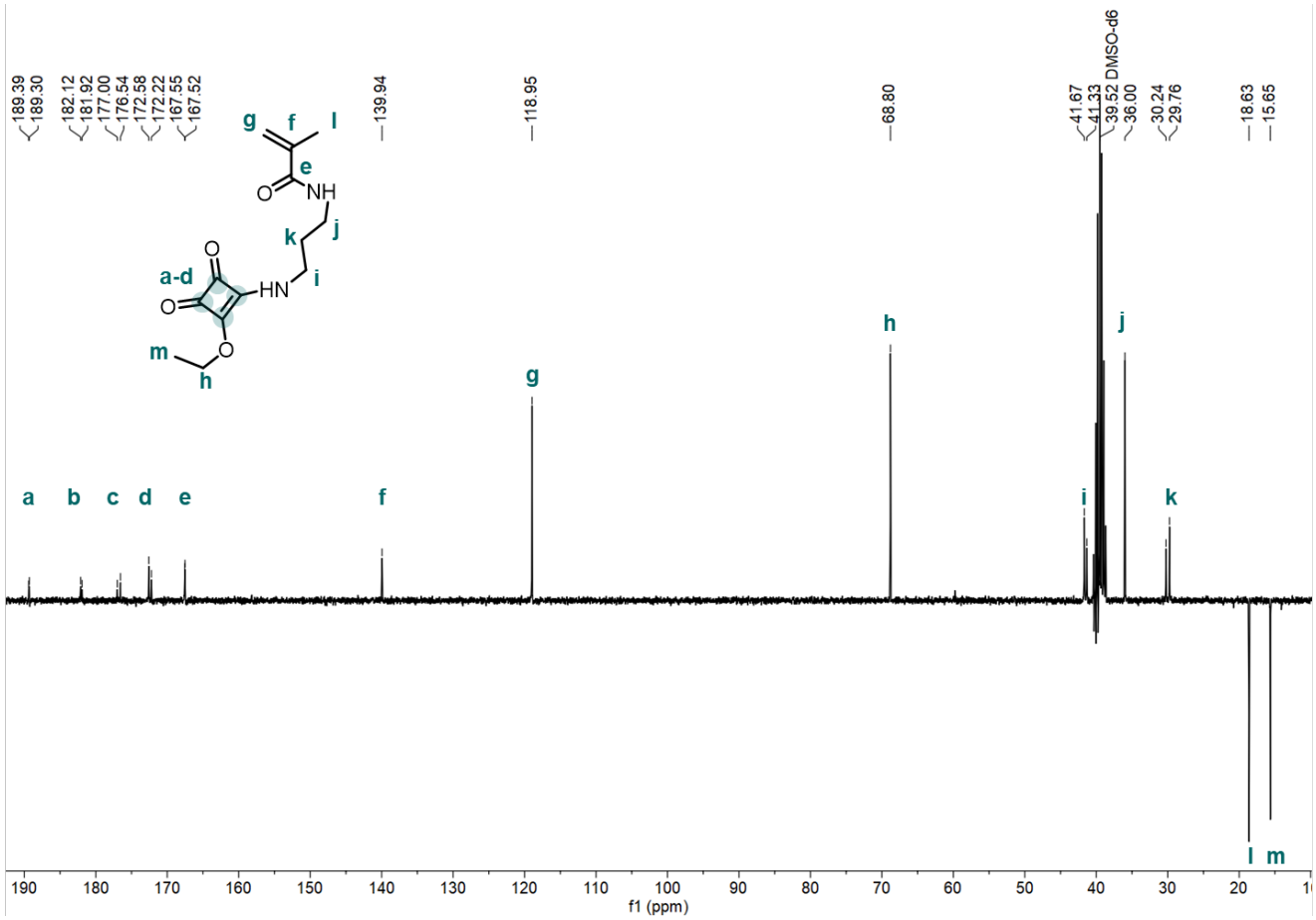

Figure S 3: APT [13]C NMR spectrum (75 MHz) of MA-SQ in DMSO-d6.

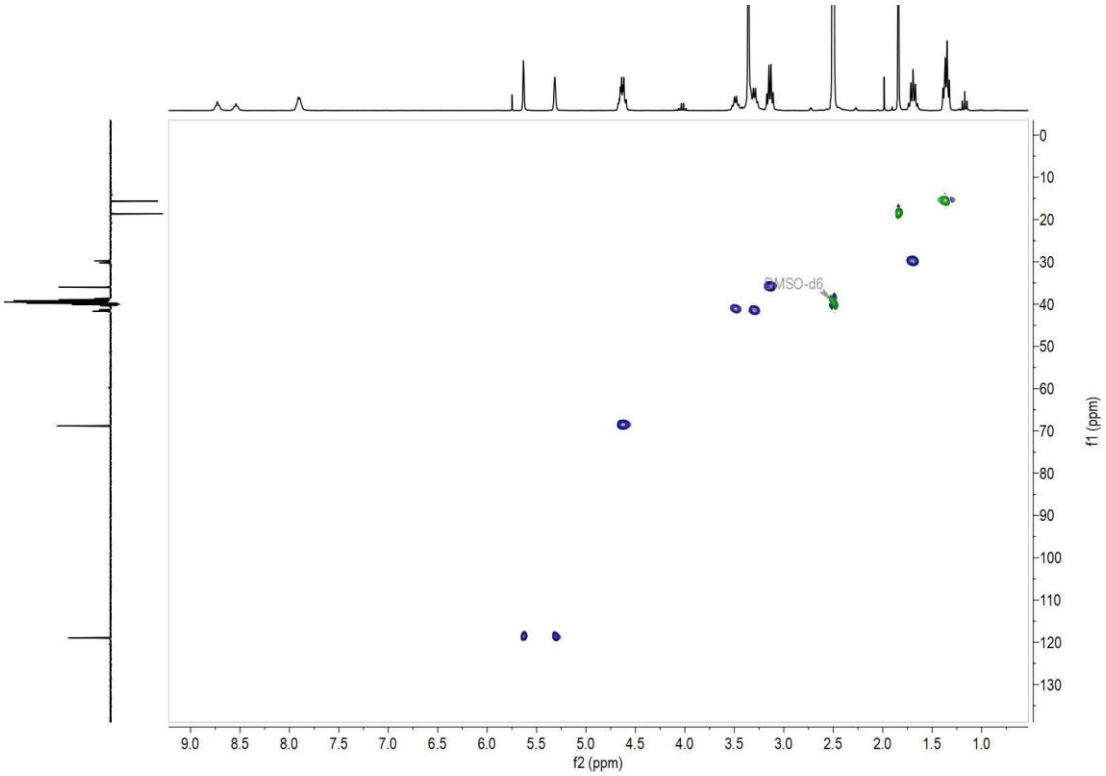

Figure S 4: 2D HSQC NMR spectrum of MA-SQ in DMSO-d_6.

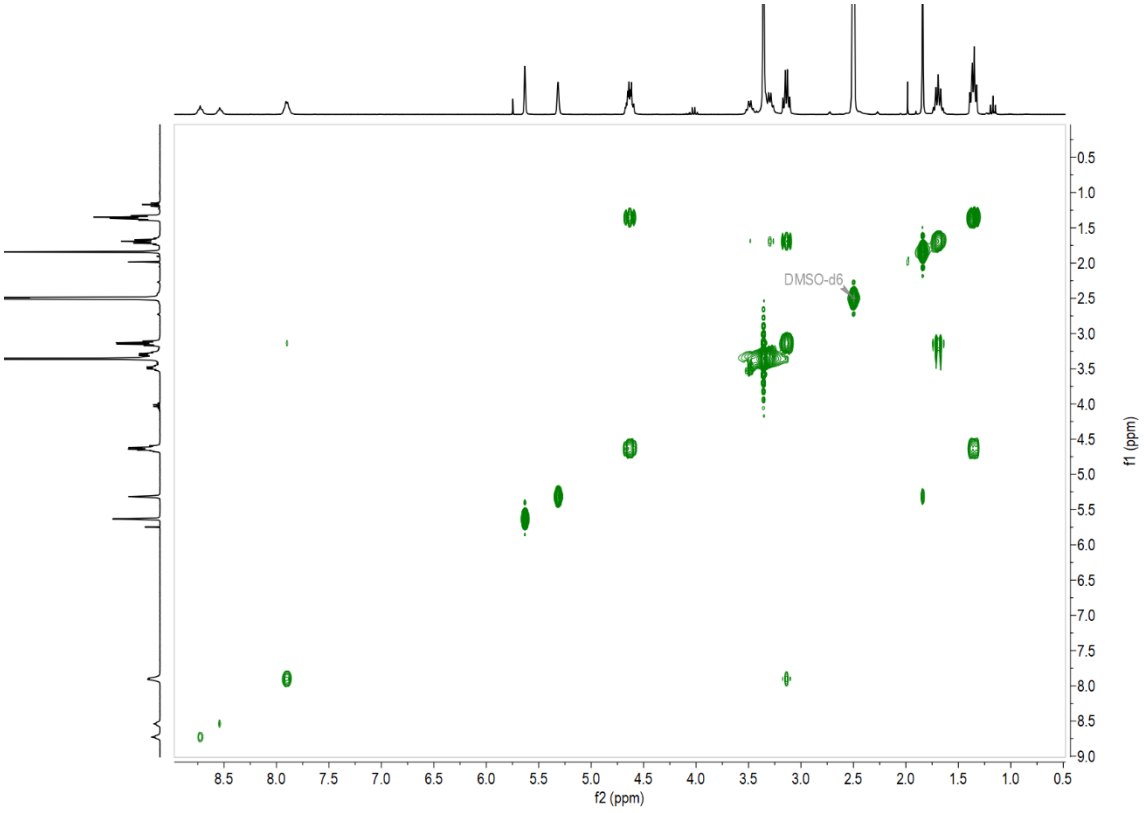

Figure S 5: 2D COSY NMR spectrum of MA-SQ in DMSO-d_6.

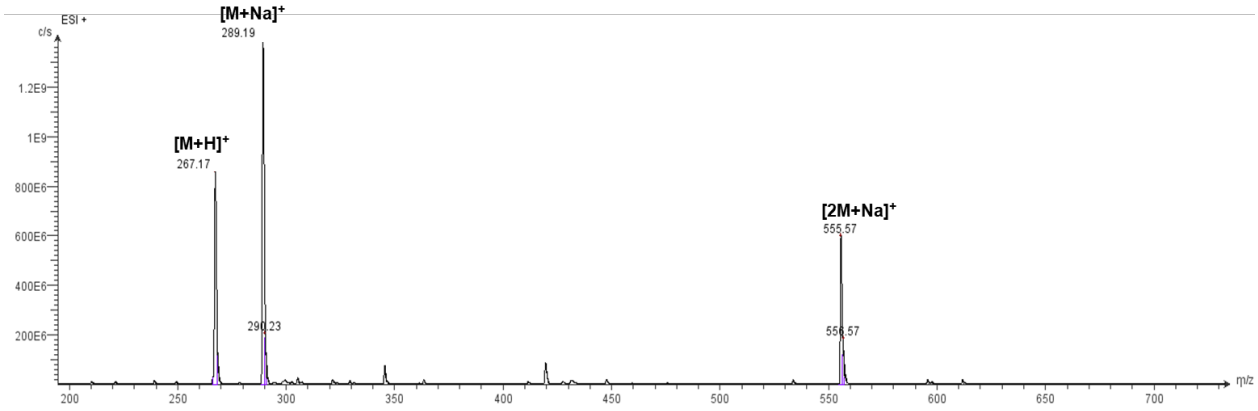

Figure S 6: ESI-MS spectrum of MA-SQ (positive ion mode).

3.1.2 N-(3-((2-ethoxy-3,4-dioxocyclobut-1-en-1-yl)amino)propyl)acrylamide, Squaric ester amide acrylamide (A-SQ)

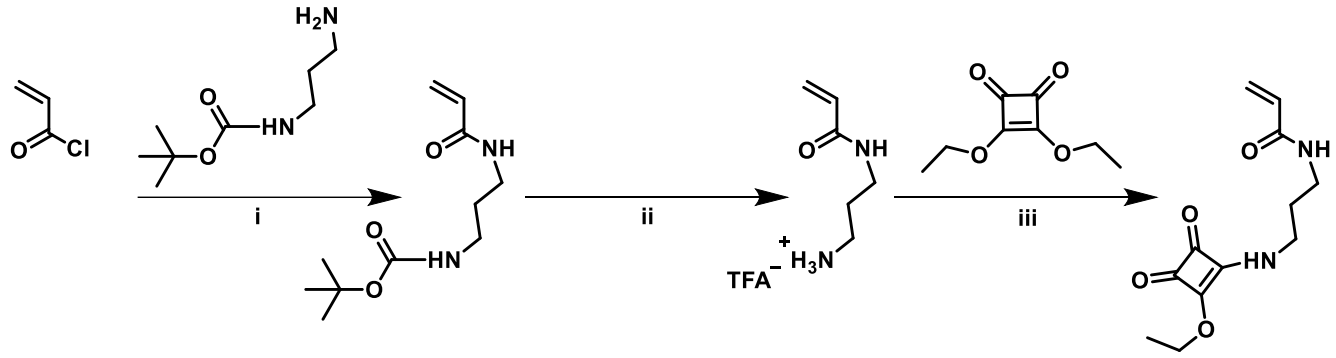

Figure S 7: Synthesis of A-SQ: i) TEA, DCM, 0 °C, 16 h, yield: 32 %, ii) TFA, DCM, RT, 4 h, yield: quantitative, and iii) TEA, EtOH, RT, yield: 64 %.

Synthesis of N-(Boc-3-aminopropyl)acrylamide (i)

In an oven-dried round-bottom flask, acryloyl chloride (6.89 mmol, 0.56 mL, 1.2 eq.) was dissolved under Argon atmosphere in anhydrous DCM (100 mL). The solution was cooled for 30 min using an ice bath, before a mixture of N-Boc-1,3-propanediamine (5.74 mmol, 1.00 g, 1 eq.) and TEA (37.31 mmol, 5.3 mL, 6.5 eq.) dissolved in anhydrous DCM (100 mL) was added dropwise *via* dropping funnel over 3 h. The reaction mixture was allowed to stir overnight on ice melting to water, before being extracted with brine (3x 200 mL). The combined organic layers were dried over Na_2SO_4, filtered, and concentrated *in vacuo*. Further purification of the product was achieved by silica gel chromatography using a mixed eluent of ethyl acetate and n-hexane (2:1). The product was obtained as yellow oil (0.41 g, 32%).

^{1}H-NMR (300 MHz, DMSO-d_6): δ (ppm) = 8.05 (t, *J* = 5.4 Hz, 1H, **a**), 6.78 (t, *J* = 5.7 Hz, 2H, **b**), 6.19 (dd, *J* = 17.1, 9.9 Hz, 1H, **c**), 6.05 (dd, *J* = 17.1, 2.5 Hz, 1H, **d**), 5.56 (dd, *J* = 9.9, 2.5 Hz, 1H, **e**), 3.11 (q, *J* = 6.9 Hz, 2H, **f**), 2.92 (q, *J* = 6.8 Hz, 2H, **g**), 1.53 (p, *J* = 7.1 Hz, 2H, **h**), 1.37 (s, 9H, **i**).

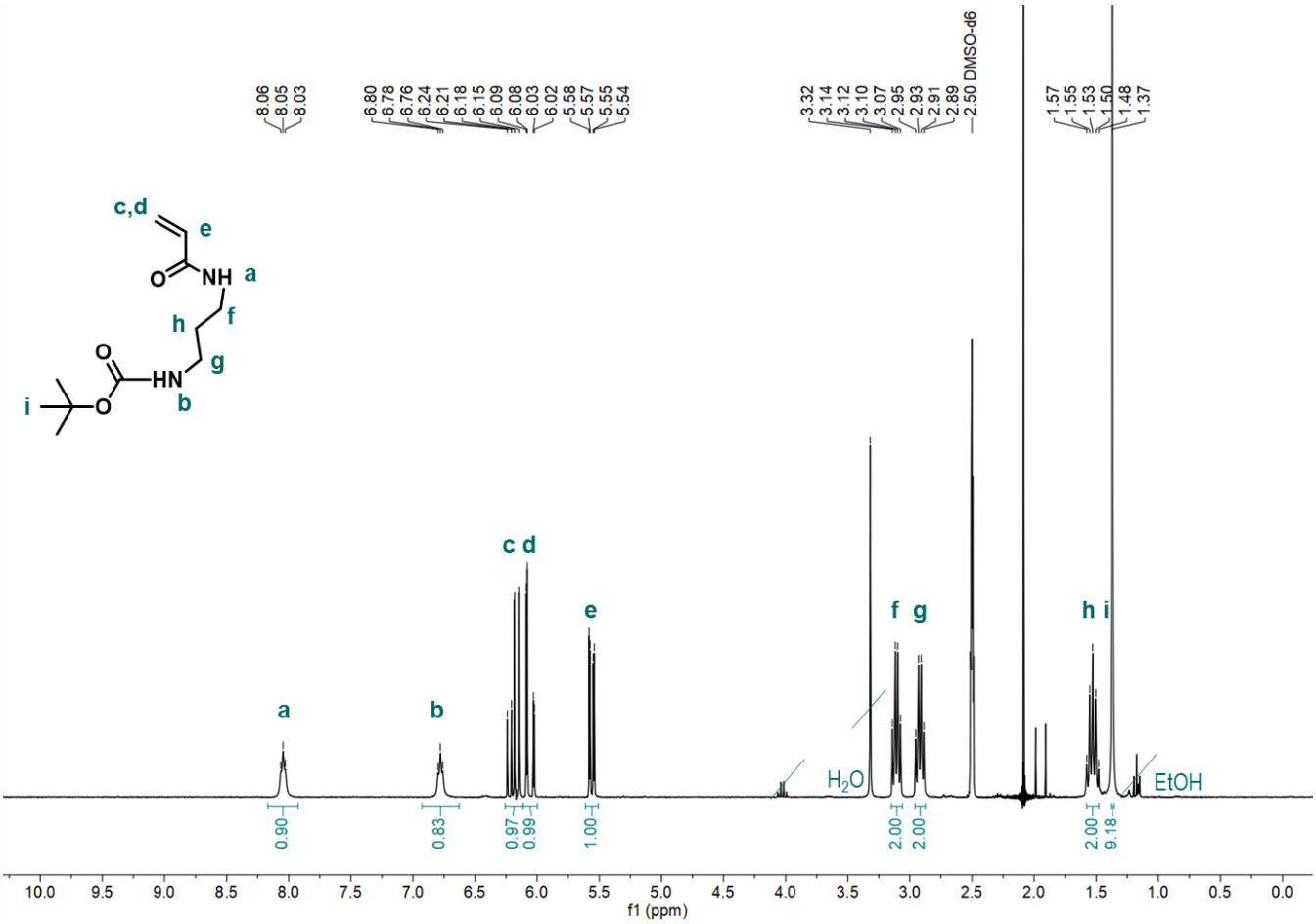

Figure S 8: [1]H-NMR spectrum (300 MHz) of N-(Boc-3-aminopropyl)acrylamide in DMSO-d_6.

Synthesis of N-(3-aminopropyl)acrylamide TFA salt (ii)

In an oven-dried round bottom flask, N-(Boc-3-aminopropyl)acrylamide (400 mg, 1.75 mmol, 1 eq.) was dissolved under Argon atmosphere in anhydrous DCM (10 mL). This solution was treated with a mixture of TFA and anhydrous DCM (10 mL, v:v, 1:1). The reaction mixture was allowed to stir for 4 h at RT, before toluene (2x 100 mL) was added to remove TFA by azeotropic evaporation *in vacuo*. The remaining oily crude product was dissolved in ethanol (25 mL), filtered, and concentrated *in vacuo* affording the product as amber oil (425 mg, quantitative).

[1]H-NMR (400 MHz, DMSO-d_6): δ (ppm) = 8.28 (t, J = 5.9 Hz, 1H, **a**), 7.81 (s, 3H, **b**), 6.21 (dd, J = 17.1, 10.0 Hz, 1H, **c**), 6.08 (dd, J = 17.1, 2.3 Hz, 1H, **d**), 5.60 (dd, J = 10.0, 2.3 Hz, 1H, **e**), 3.19 (q, J = 6.7 Hz, 2H, **f**), 2.86 – 2.71 (m, 2H, **g**), 1.71 (p, J = 14.3, 6.8 Hz, 2H, **h**).

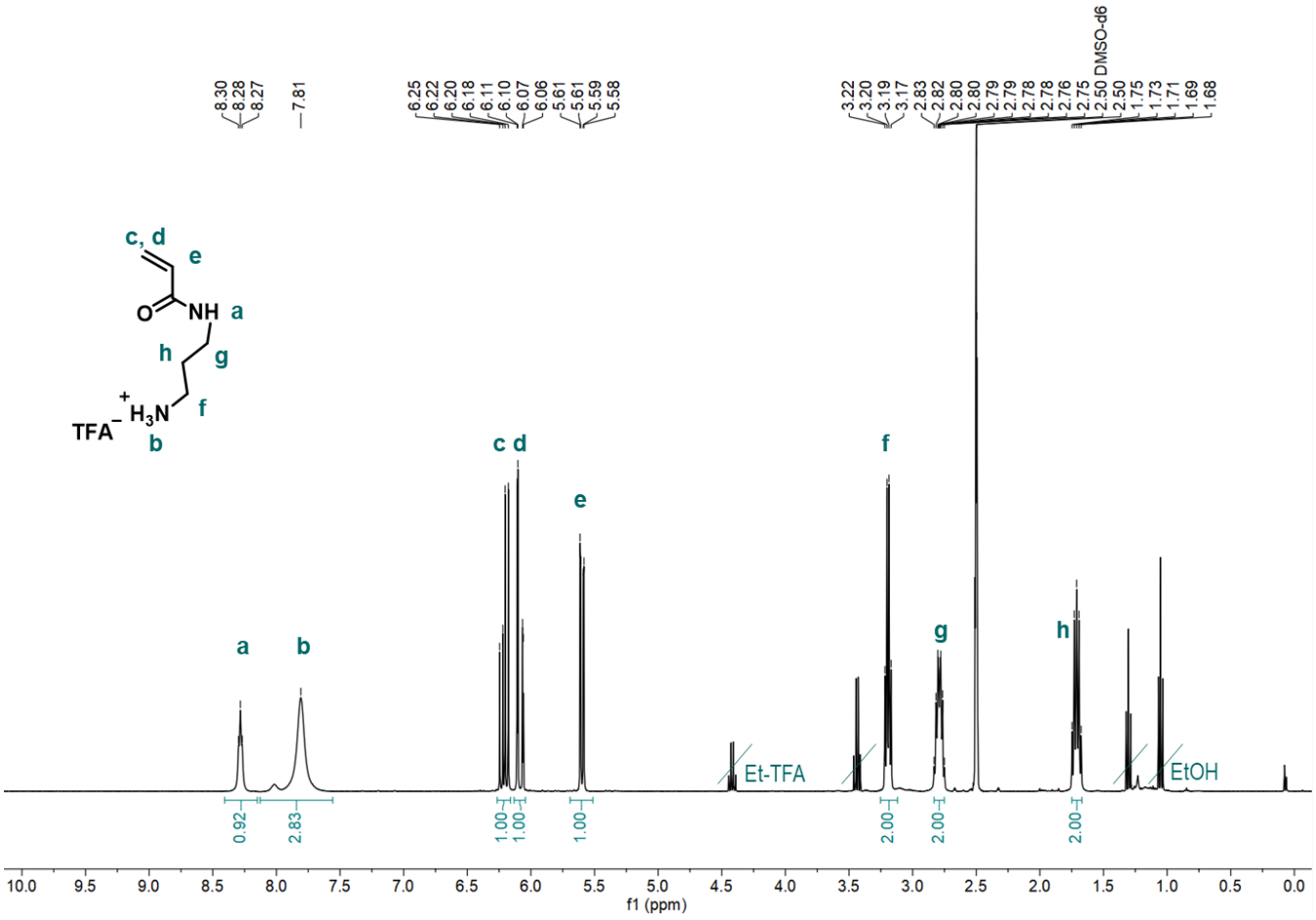

Figure S 9: ^{1}H-NMR spectrum (400 MHz) of N-(3-aminopropyl)acrylamide TFA salt in DMSO-d_6.

Synthesis of N-(3-((2-ethoxy-3,4-dioxocyclobut-1-en-1-yl)amino)propyl)acrylamide, Squaric ester amide acrylamide (A-SQ)

In a round bottom flask, squaric acid diethyl ester (326.6 mg, 1.92 mmol, 1.1 eq.) and TEA (264.8 mg, 2.62 mmol, 1.5 eq.) were diluted in ethanol (20 mL). To this solution N-(3-aminopropyl)acrylamide TFA salt (423.0 mg, 1.75 mmol, 1 eq.) dissolved in ethanol (5 mL) was slowly added *via* dropping funnel over 1 h, whereby the product formed a white precipitate. After a reaction time of 6 h, the reaction mixture was concentrated *in vacuo*. Further purification of the crude product was achieved by silica gel chromatography using ethyl acetate as eluent. The product was obtained as white crystalline powder (282.1 mg, 64 %).

^{1}H-NMR (400 MHz, DMSO-d_6): δ (ppm) = 8.74 (t, 6.0 Hz, 0.5H, **a**) [a)], 8.56 (t, 6.0 Hz, 0.5H, **a**) [a)], 8.09 (t, *J* = 5.6 Hz, 1H, **b**), 6.19 (dd, *J* = 17.0, 10.0 Hz, 1H, **c**), 6.06 (dd, *J* = 17.1, 2.2 Hz, 2H, **d**), 5.57 (dd, *J* = 10.0, 2.3 Hz, 1H, **e**), 4.64 (qd, *J* = 6.9 Hz, 2H, **f**), 3.49 (q, *J* = 6.1 Hz, 1H, **g**) [a)], 3.30 (q, *J* = 6.1 Hz, 1H, **g**) [a)], 3.16 (q, *J* = 6.9, 5.7 Hz, 2H, **h**), 1.69 (p, *J* = 7.0 Hz, 2H, **i**), 1.36 (td, *J* = 7.3 Hz, 3H, **j**). [a)] due to rotamers a splitting of the signals is observed.

^{13}C-NMR (101 MHz, DMSO-d_6): δ (ppm) = 189.28 (**a**)[a)], 182.03 (**b**)[a], 176.77 (**c**)[a)], 172.38 (**d**)[a)], 164.62 (**e**), 131.71 (**f**), 124.97 (**g**), 68.76 (**h**), 41.49 (**i**) [a)], 35.75 (**j**) [a)], 30.02 (**k**), 15.62 (**l**). [a)] due to rotamers a splitting of the signals is observed.

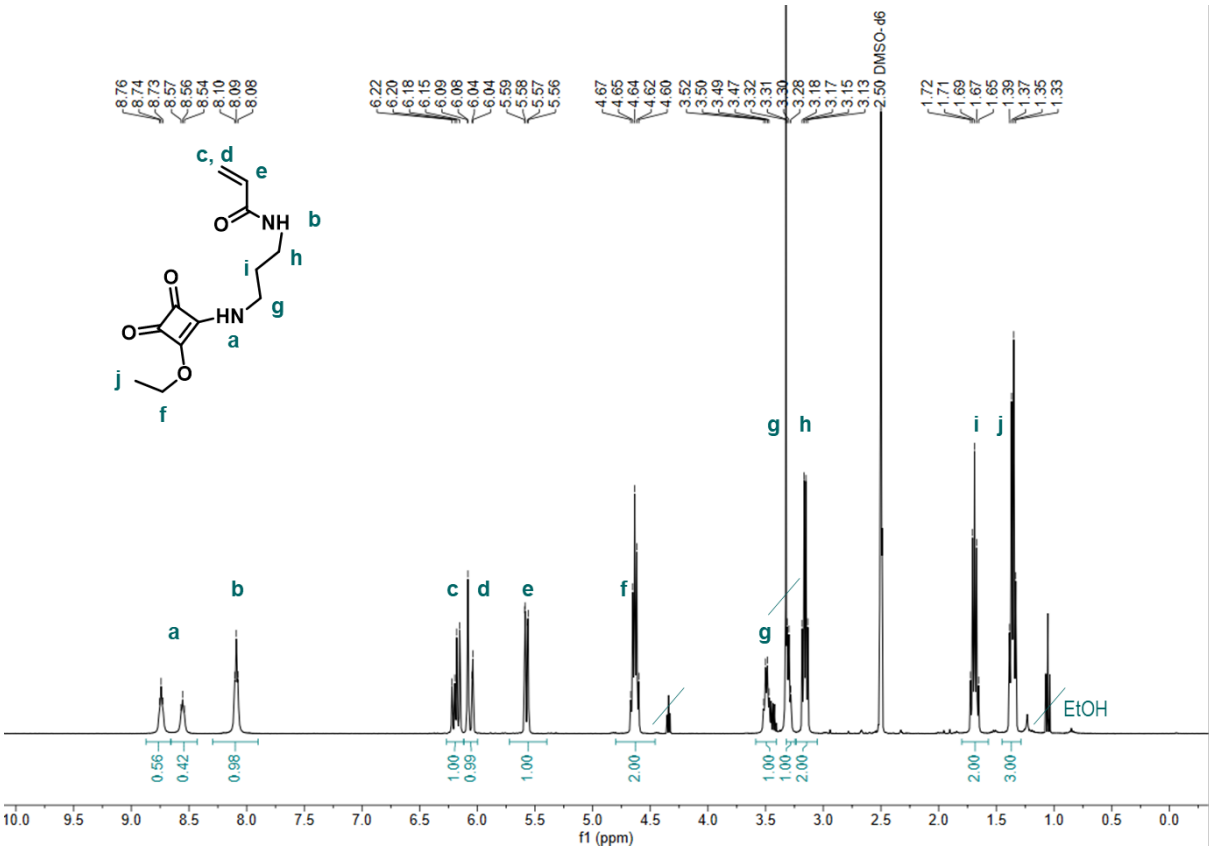

Figure S 10: [1]H-NMR spectrum (400 MHz) of A-SQ in DMSO-d6.

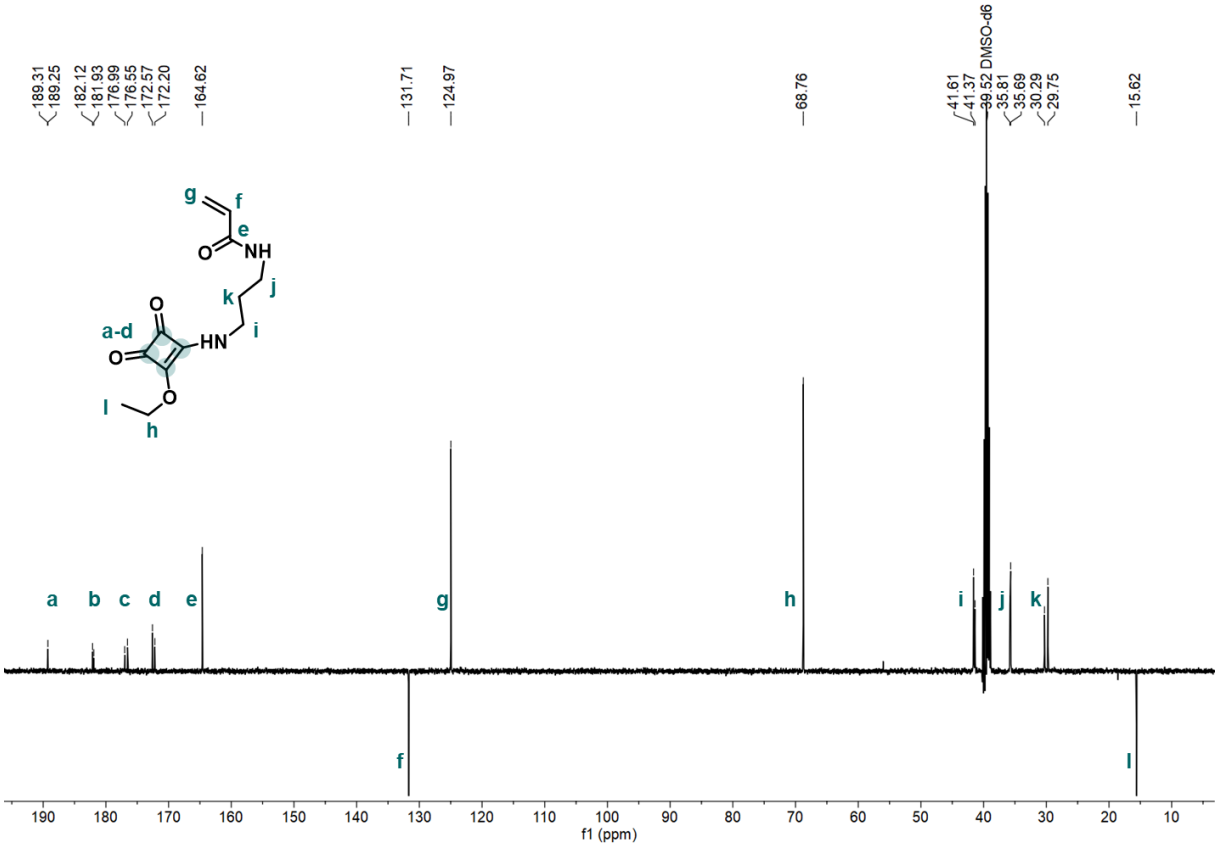

Figure S 11: APT [13]C NMR spectrum (101 MHz) of A-SQ in DMSO-d6.

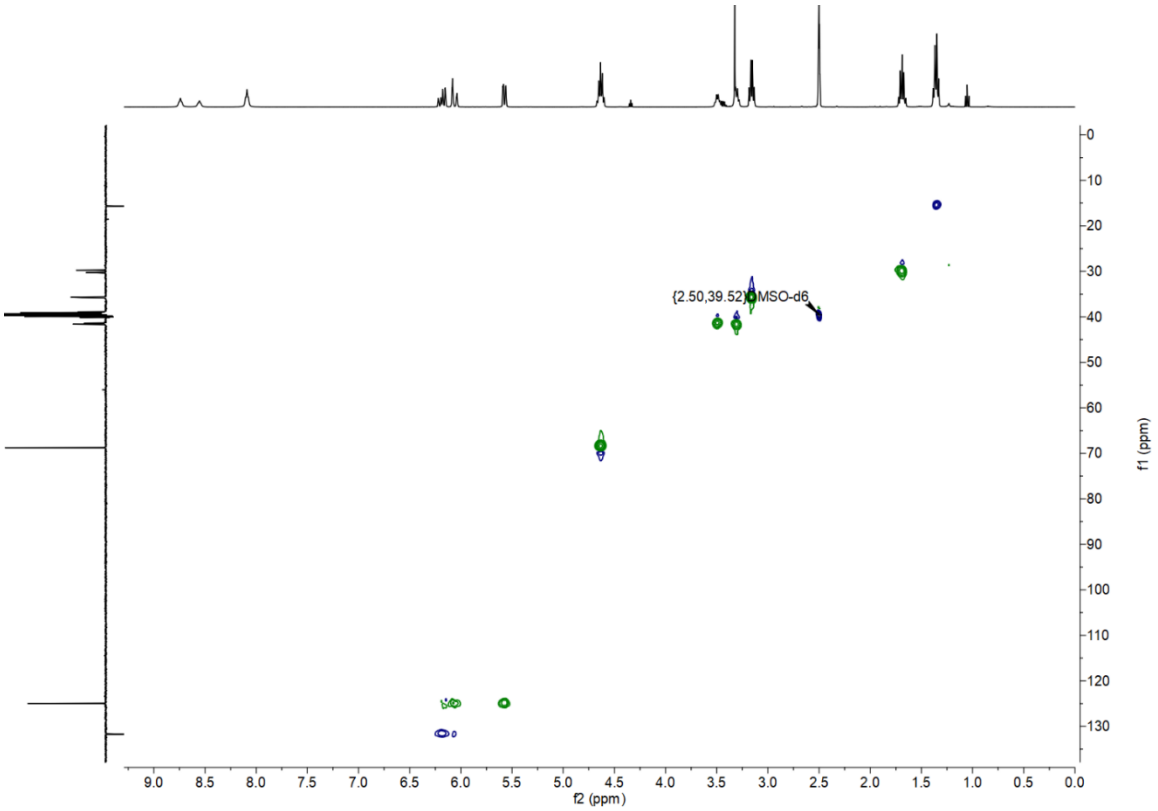

Figure S 12: 2D HSQC NMR spectrum of A-SQ in DMSO-d6.

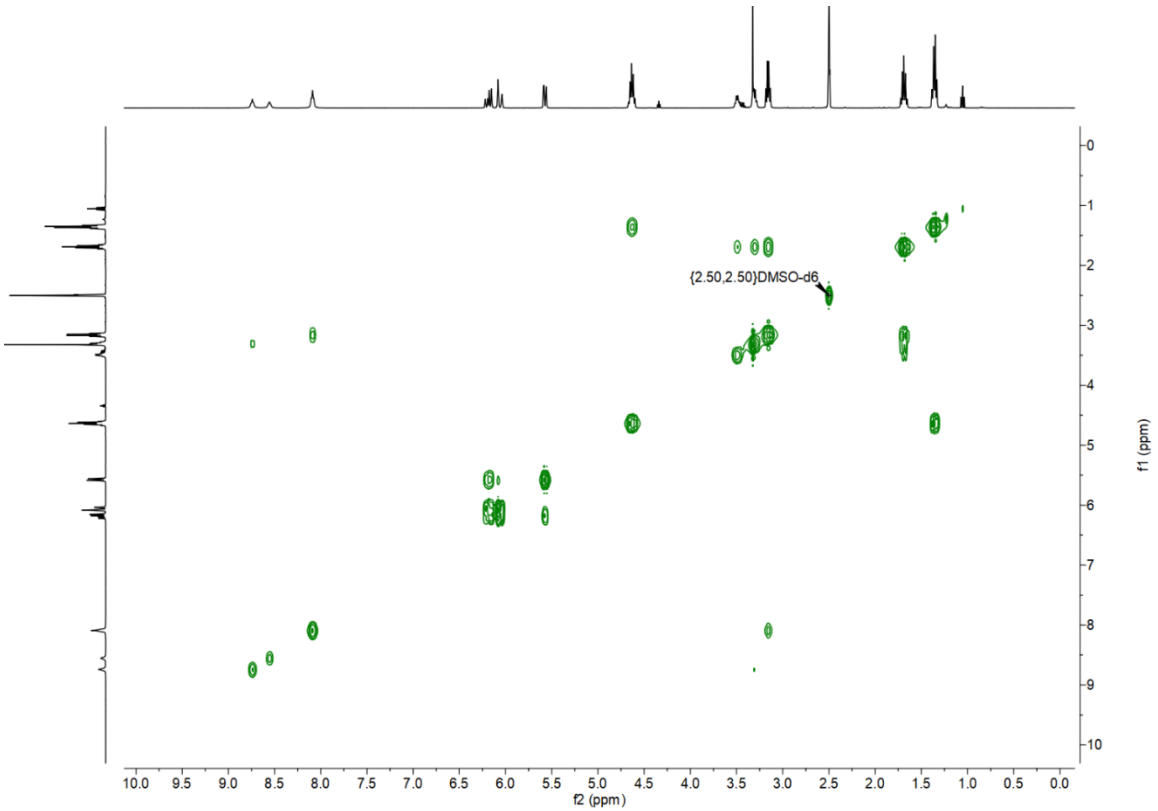

Figure S 13: 2D COSY NMR spectrum (400 MHz) of A-SQ in DMSO-d6.

3.1.3 2-((2-ethoxy-3,4-dioxocyclobut-1-en-1-yl)amino)ethyl acrylate, Squaric ester amide acrylate (At-SQ)

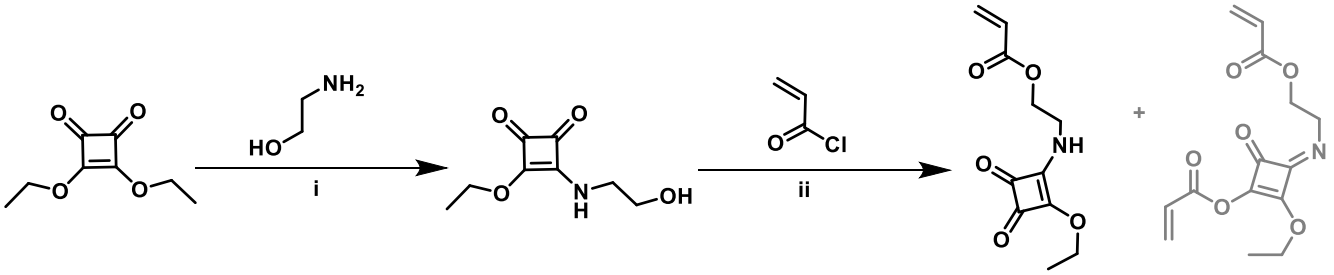

Figure S 14: Synthesis of At-SQ: i) EtOH, RT, 16 h, yield: 78 %, and ii) TEA, DCM, 0 °C, yield: 21 %.

Synthesis of 3-ethoxy-4-((2-hydroxyethyl)amino)cyclobut-3-ene-1,2-dione

In a round bottom flask, squaric acid diethyl ester (2.00 g, 1.74 mL, 11.75 mmol, 1.0 eq.) was dissolved in ethanol (50 mL). 2-Aminoethanol (0.72 g, 0.70 mL, 11.75 mmol, 1.0 eq.) was slowly added dropwise and the reaction mixture stirred for 16 h at RT. Afterwards the reaction mixture was concentrated *in vacuo* to half of its volume, poured into ice cold diethyl ether and placed overnight at -20 ºC. A colorless precipitate was formed that could be filtered off and dried *in vacuo* to yield the product as white powder (1.70 g, 78 %).

^{1}H-NMR (300 MHz, DMSO-d_6): δ (ppm) = 8.72 (br, 0.5H, **a**)[a)],8.56 (br, 0.5H, **a**)[a)], 4.64 (q, J =7.1 Hz, 2H, **b**), 3.49 (br, 3H,**c+d**)[a)], 3.33 (m, 1H, **d**)[a)], 1.36 (t, J = 7.1 Hz, 3H, **e**). [a)] due to rotamers a splitting of the signals is observed.

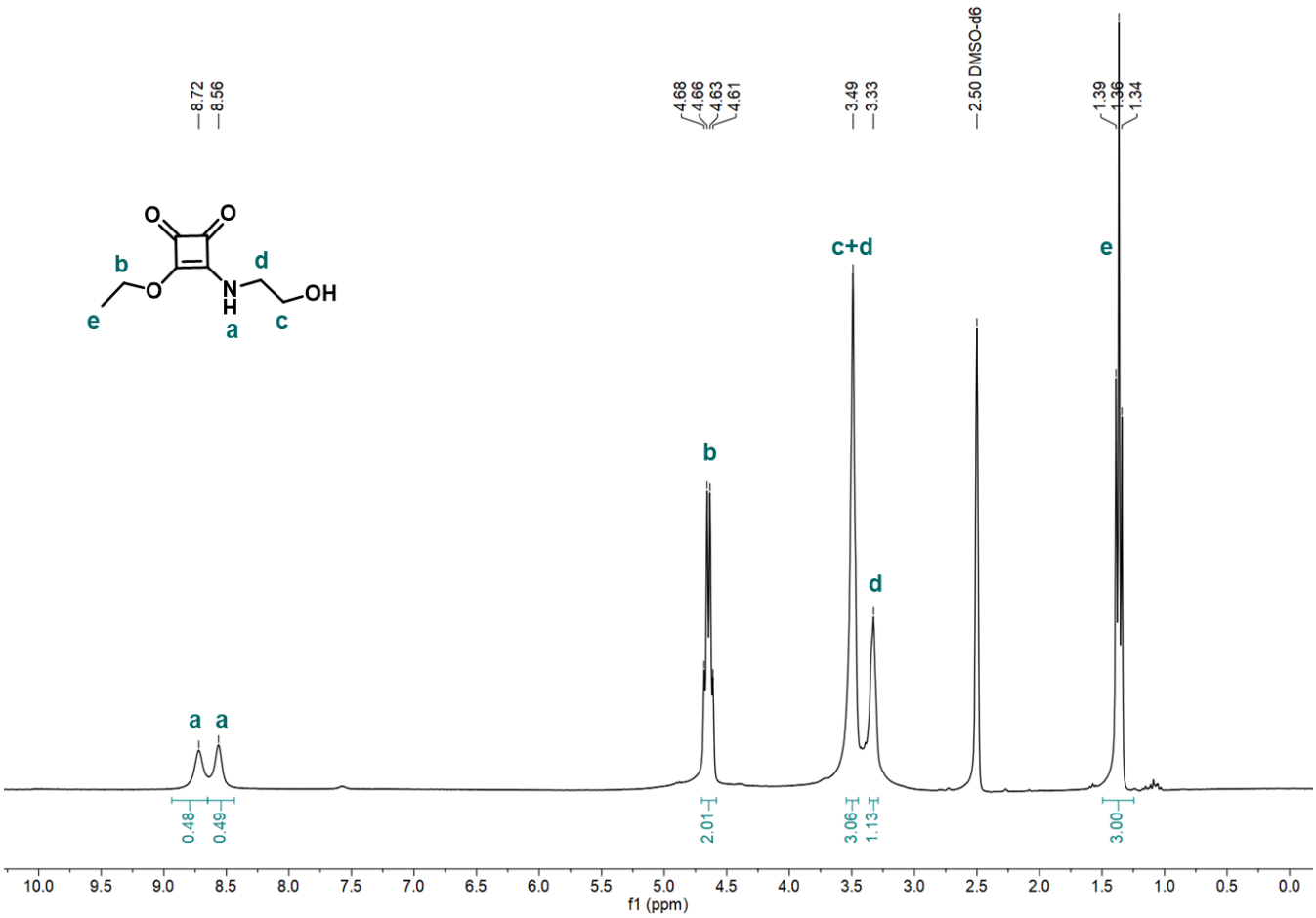

Figure S 15: ^{1}H NMR spectrum of 3-ethoxy-4-((2-hydroxyethyl)amino)cyclobut-3-ene-1,2-dione (300 MHz) in DMSO-d_6.

Synthesis of 2-((2-ethoxy-3,4-dioxocyclobut-1-en-1-yl)amino)ethyl acrylate, Squaric ester amide acrylate (At-SQ)

In an oven-dried round-bottom flask 3-ethoxy-4-((2-hydroxyethyl)amino)cyclobut-3-ene-1,2-dione (1.0 g, 5.4 mmol, 1.0 eq.) was dispersed under Argon atmosphere in anhydrous DCM (10 mL). After addition of TEA (0.83 mL, 5.9 mmol, 1.1 eq.) the solution became more clear. It was cooled for 30 min using an ice bath, before acryloyl chloride was added dropwise (0.48 mL, 5.0 mmol, 1.1 eq.). The reaction mixture was allowed to stir overnight on ice melting to water, before it was poured into water (100 mL) and the product was extracted with DCM (3x 20 mL). The combined organic layers were dried over Na_2SO_4, filtered, and concentrated *in vacuo*. Further purification of the product was achieved by silica gel chromatography using a mixed eluent of ethyl acetate and n-hexane (v:v, 1:3 to 1:1). The desired product At-SQ was obtained as colorless crystals (0.27 g, 1.14 mmol, 21%). In addition, the by-product 2-((3-(acryloyloxy)-2-ethoxy-4-oxocyclobut-2-en-1-ylidene)amino)ethyl acrylate (At-SQ-At), which was eluting faster, was afforded as yellow oil (0.39 g, 24%).

At-SQ:

^{1}H-NMR (300 MHz, Chloroform-*d*)): δ (ppm) = 7.00 (s, 0.7H, **a**)[a)] 6.43 (dd, *J* = 17.3, 1.4 Hz, 1H, **b**), 6.11 (dd, *J* = 17.3, 10.4 Hz, 1H, **c**), 5.88 (dd, *J* = 10.4, 1.4 Hz, 1H, **d**), 5.82 (s, 0.3H, **a**)[a)], 4.75 (q, *J* = 7.1 Hz, 2H, **e**), 4.39 – 4.29 (m, 2H, **f**), 3.86 (m, 2H, **g**), 1.45 (t, *J* = 7.1 Hz, 3H, **h**). [a)] due to mesomeric structures a splitting of the signals is observed.

^{13}C-NMR (75 MHz, Chloroform-*d*): δ (ppm) = 177.95 (**a**), 172.80 (**b**), 165.88 (**c**), 132.02 (**d**), 127.80 (**e**), 70.07 (**f**), 63.39 (**g**), 43.88 (**h**), 15.94 (**i**).

At-SQ-At:

^{1}H-NMR (300 MHz, Chloroform-*d*)): δ (ppm) = 6.70 (dd, J = 16.5, 10.1 Hz, 1H, **a**), 6.53 (dd, J = 16.6, 1.7 Hz, 1H, **b**), 6.32 (dd, J = 17.2, 1.5 Hz, 1H, **c**), 6.01 (dd, J = 17.2, 10.4 Hz, 1H, **d**), 5.93 (dd, J = 10.1, 1.8 Hz, 1H, **e**), 5.83 (dd, J = 10.4, 1.5 Hz, 1H, **f**), 4.85 (q, J = 7.1 Hz, 2H, **g**), 4.40 (t, J = 5.2 Hz, 2H, **h**), 4.28 (t, J = 5.2 Hz, 2H, **i**), 1.48 (t, J = 7.1 Hz, 3H, **j**).

^{13}C-NMR (75 MHz, Chloroform-*d*): δ (ppm) = 188.26 (**a**), 186.55 (**b**), 183.74 (**c**), 171.91(**d**), 165.55(**e**), 164.77(**f**), 132.59 (**g**), 131.87 (**h**), 127.78 (**i**), 127.77 (**j**), 71.70 (**k**), 62.45(**l**), 45.23 (**m**), 15.84(**n**).

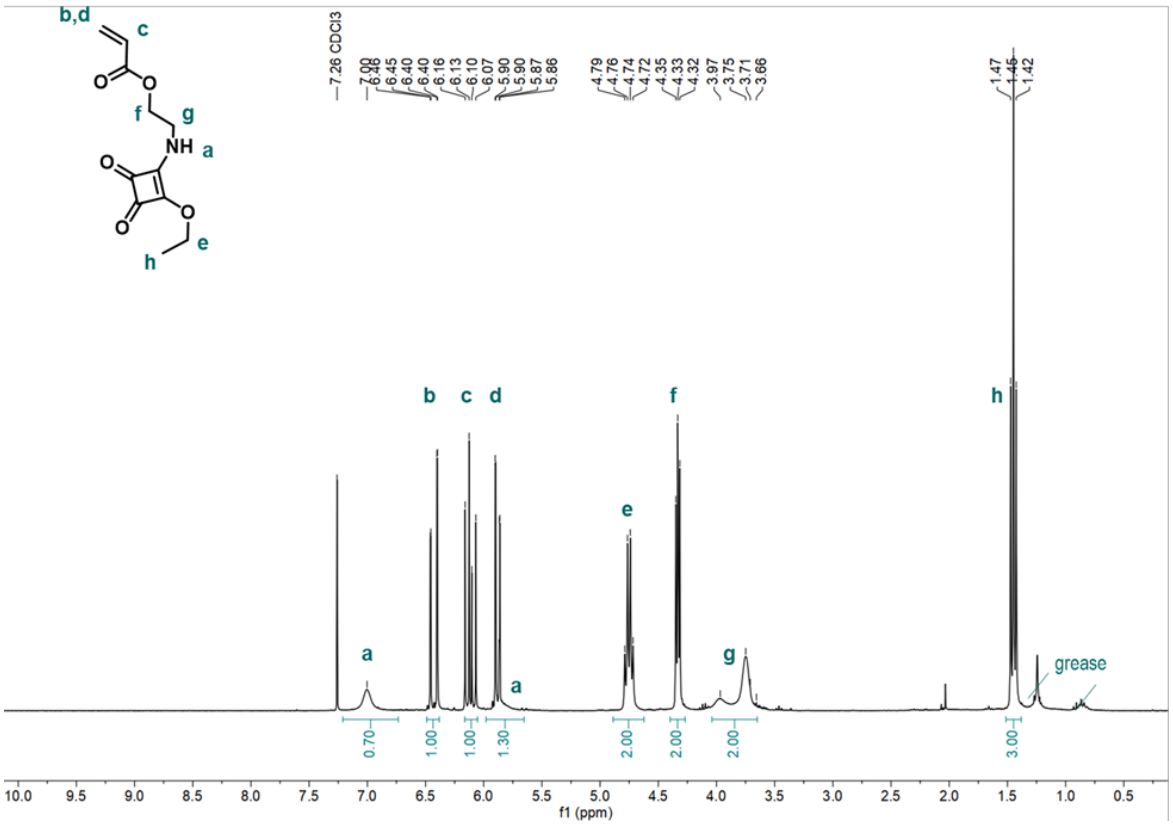

Figure S 16: ^{1}H NMR spectrum of At-SQ (300 MHz) in $CDCl_3$.

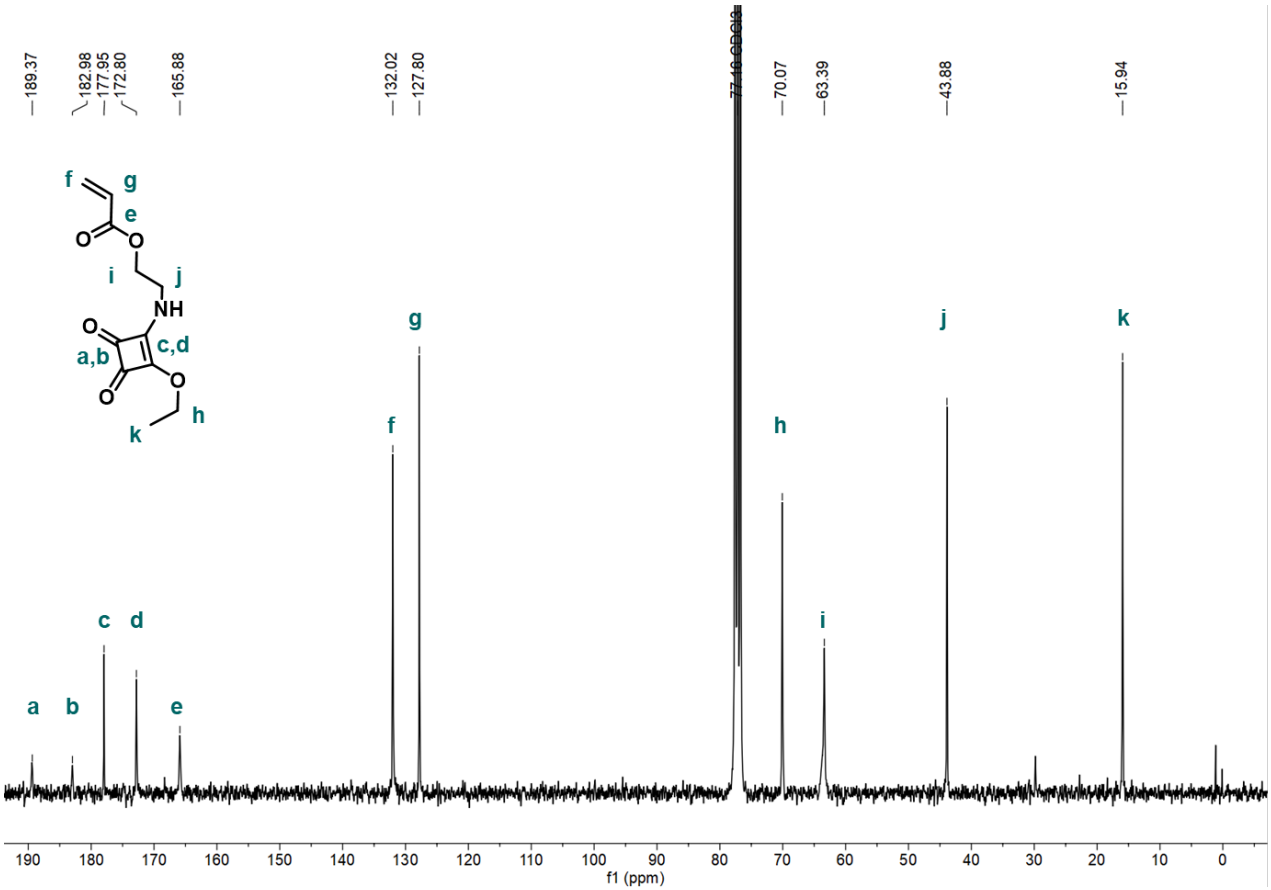

Figure S 17: ^{13}C NMR spectrum of At-SQ (75 MHz) in $CDCl_3$.

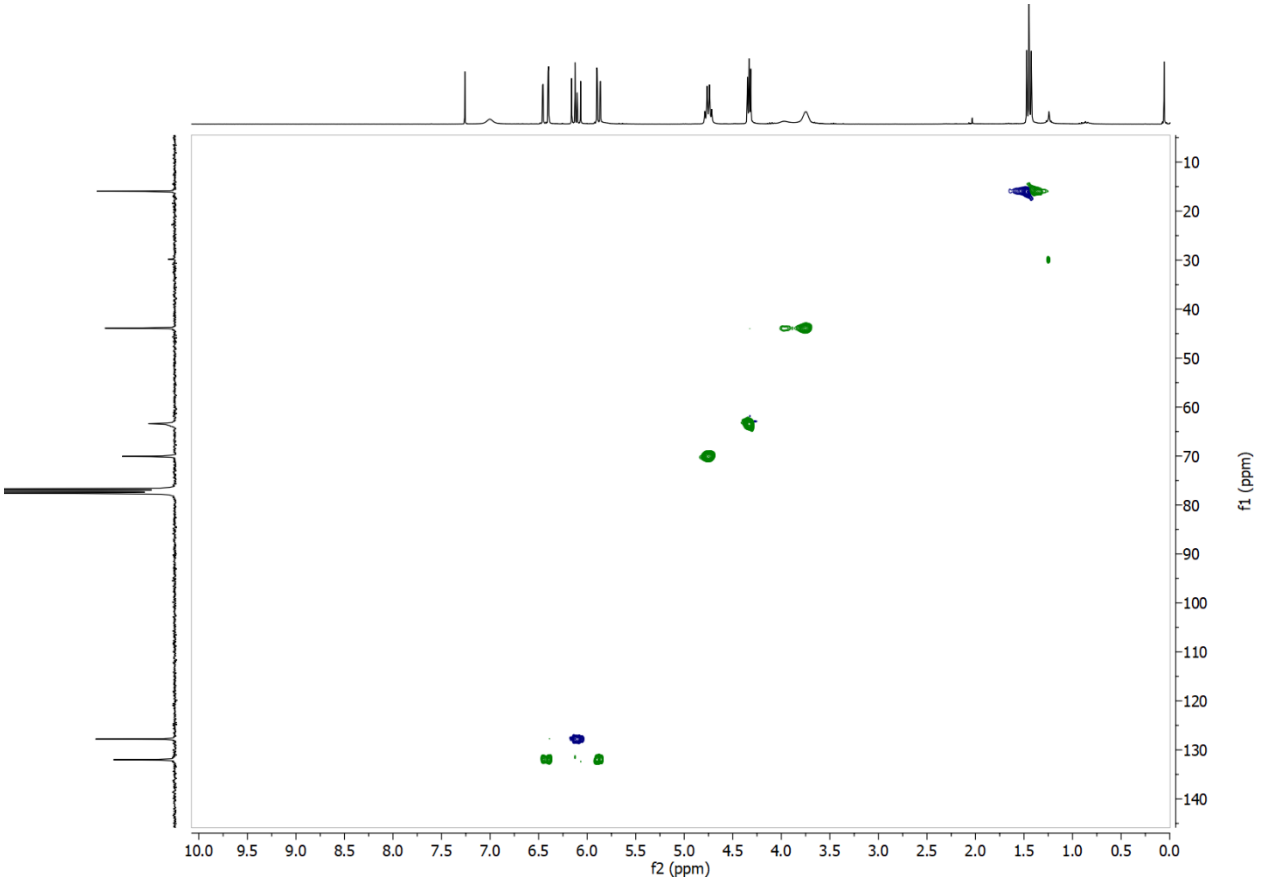

Figure S 18: 2D HSQC NMR spectrum of At-SQ in $CDCl_3$.

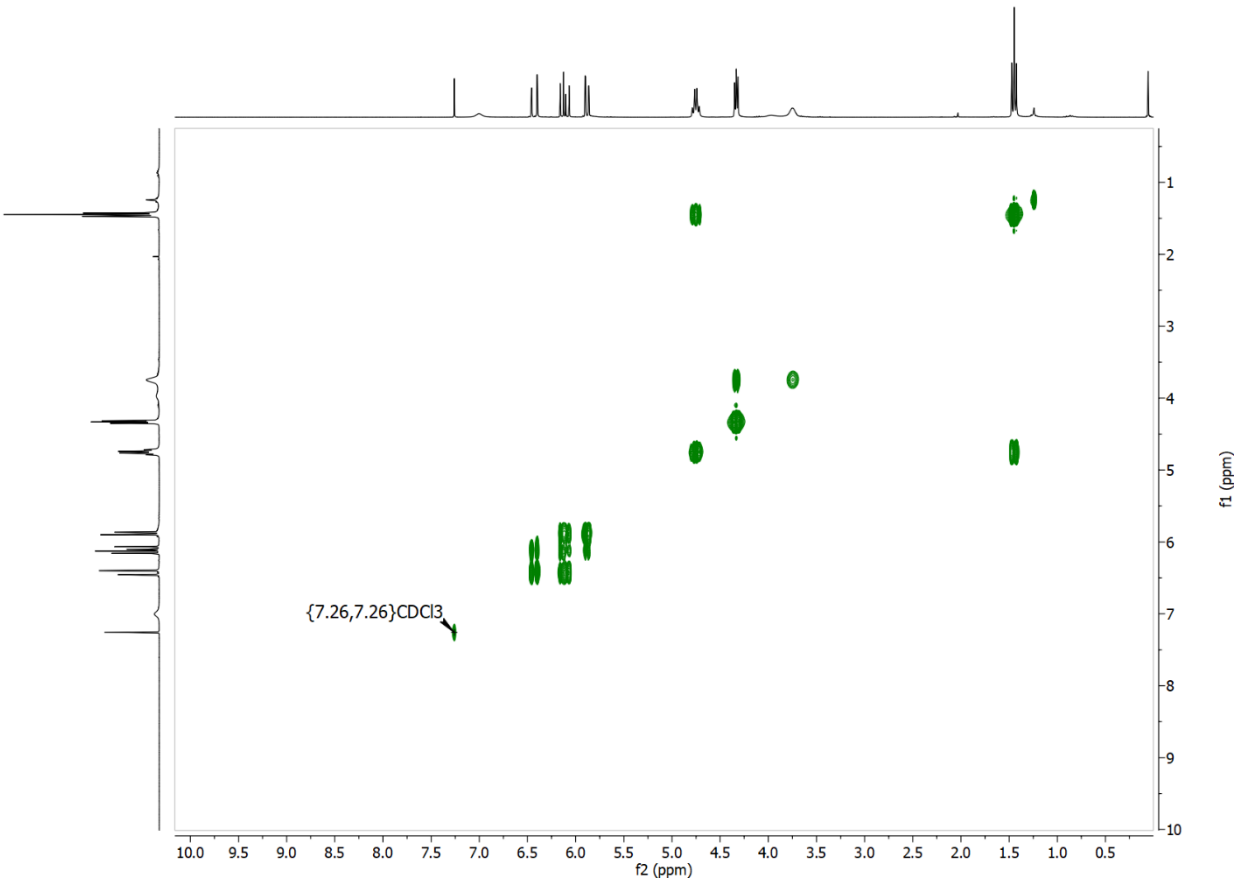

Figure S 19: 2D COSY NMR spectrum (300 MHz) of SQ-At in $CDCl_3$.

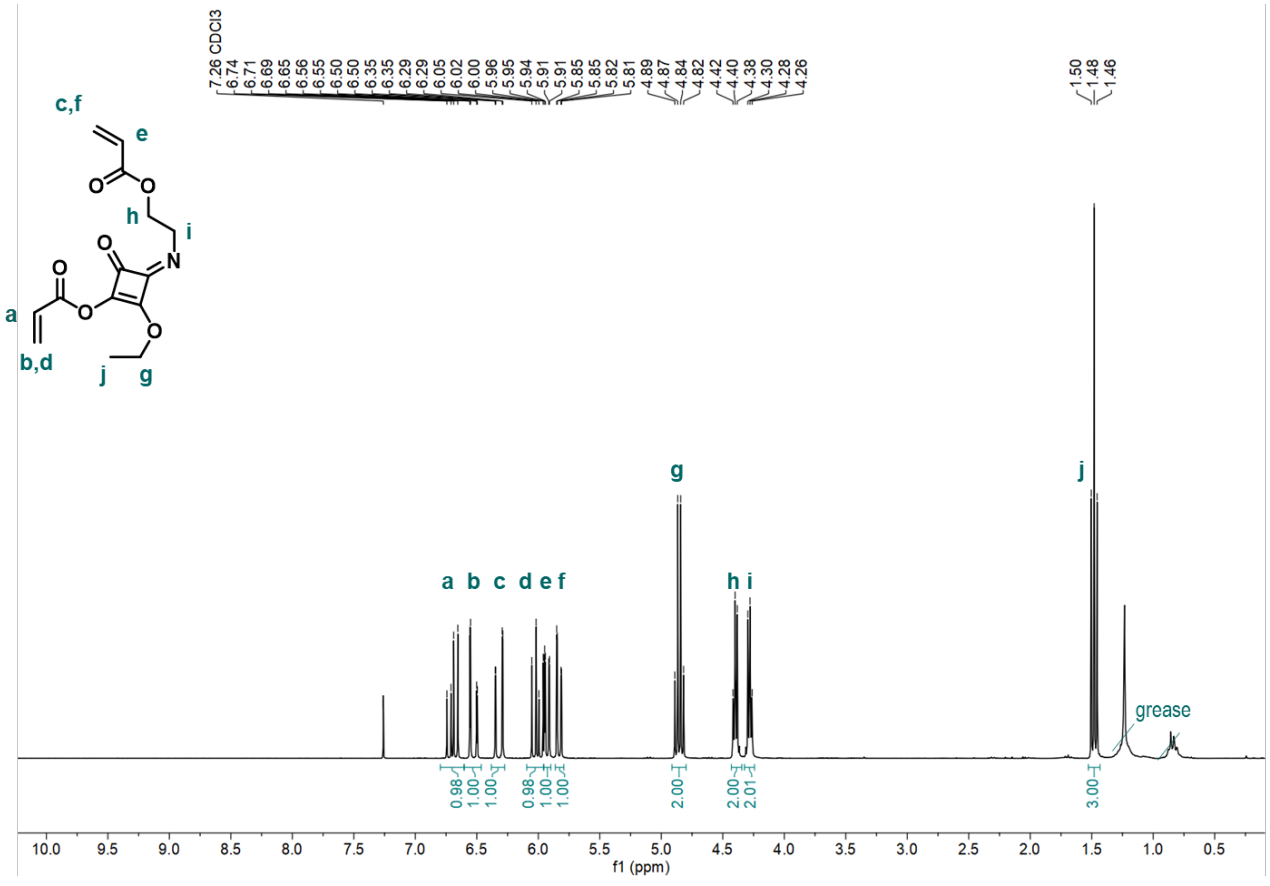

Figure S 20: ^1H NMR spectrum of At-SQ-At (by-product) (300 MHz) in $CDCl_3$.

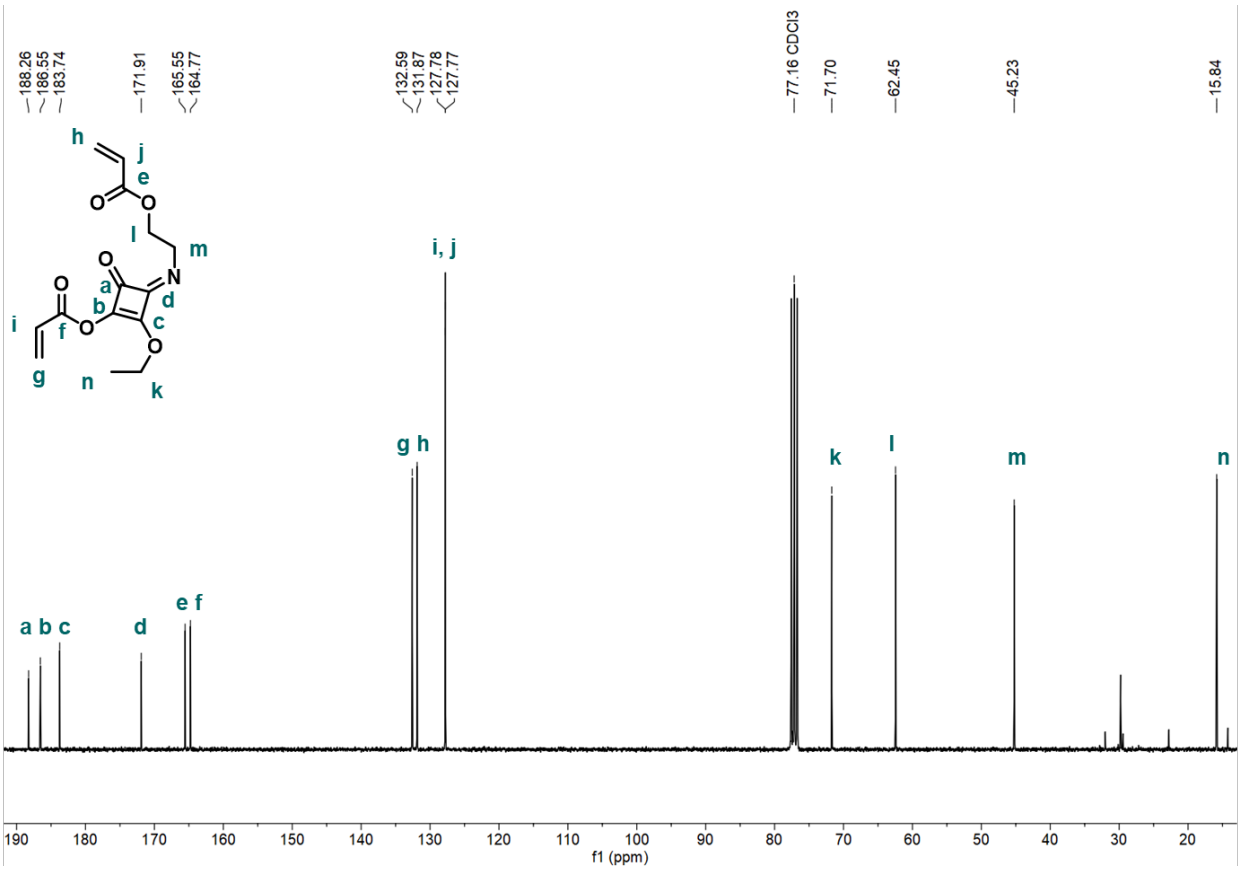

Figure S 21: ^{13}C NMR spectrum of At-SQ-At (by-product) (75 MHz) in $CDCl_3$.

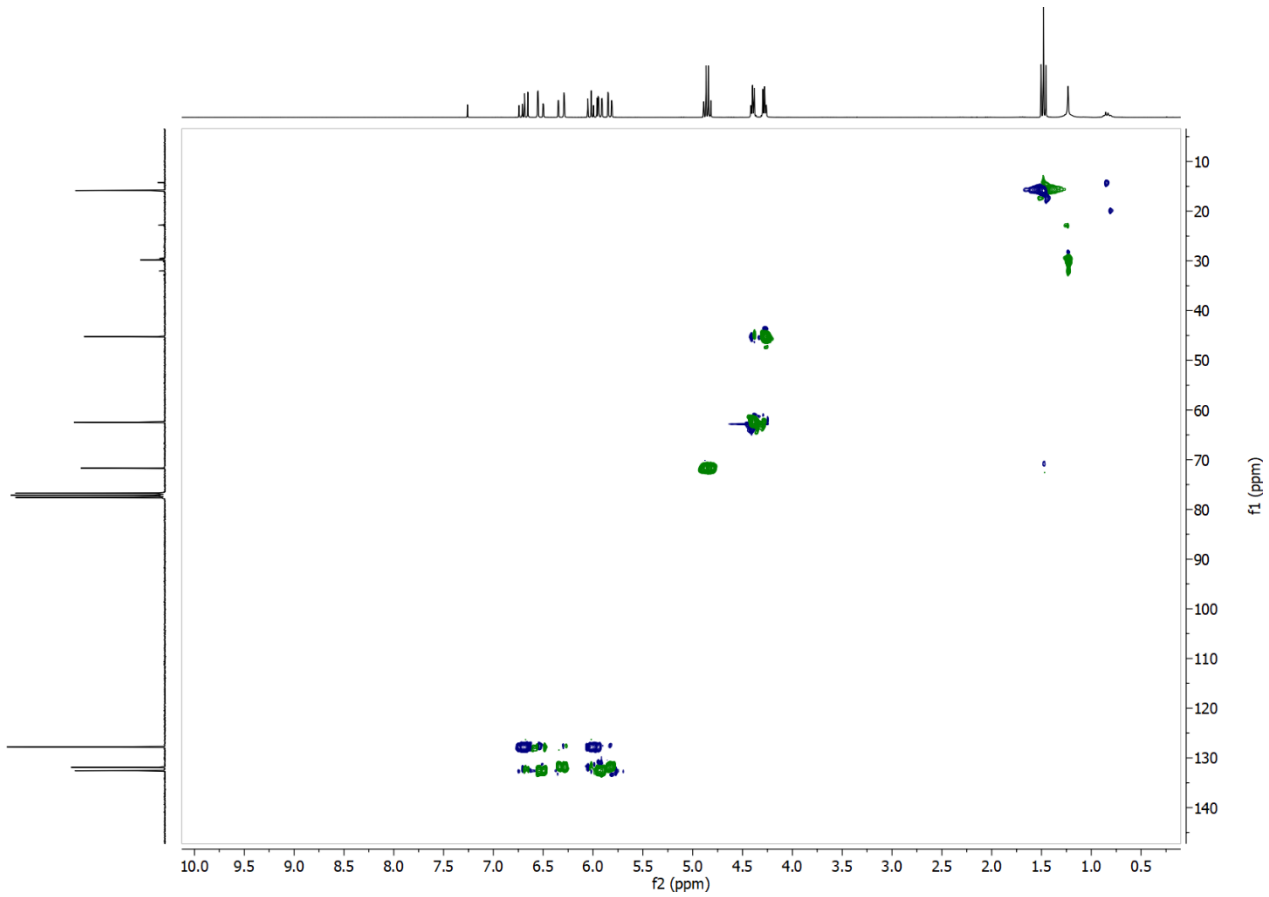

Figure S 22: 2D HSQC NMR spectrum of At-SQ-At (by-product) in $CDCl_3$.

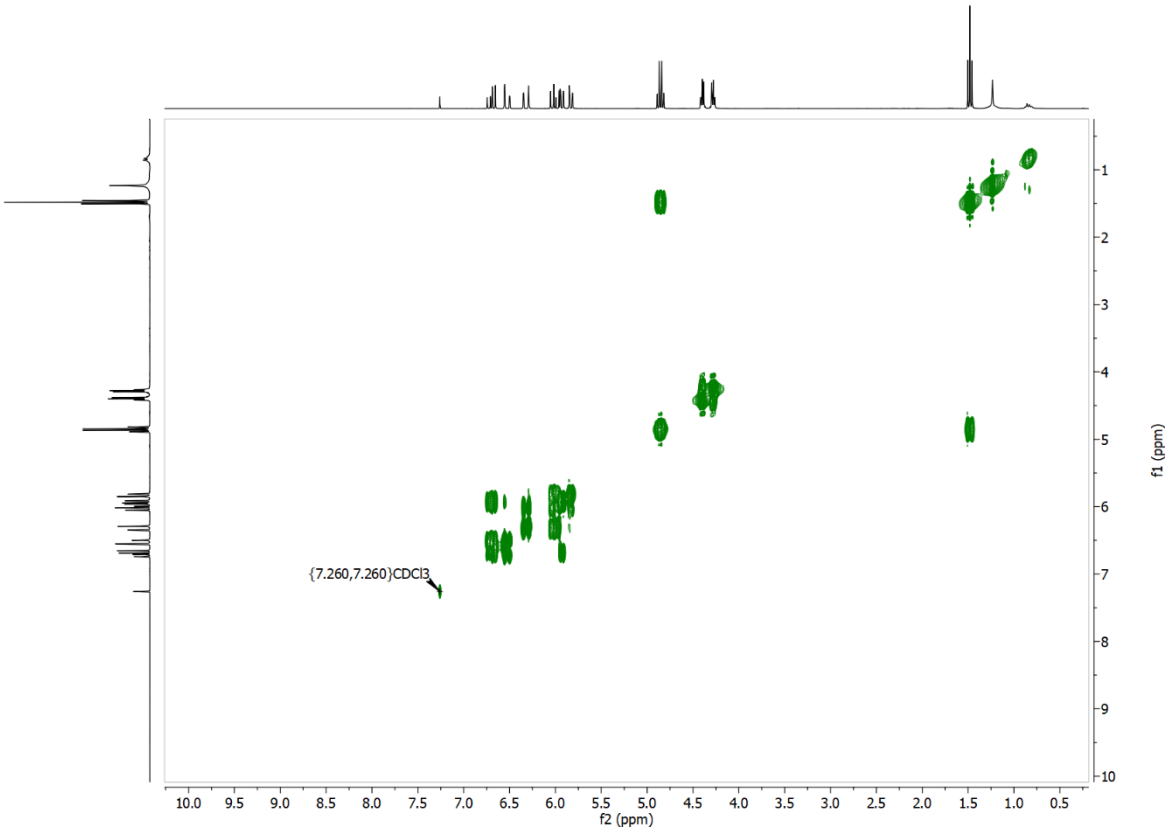

Figure S 23: 2D COSY NMR spectrum of At-SQ-At (by-product) in $CDCl_3$.

3.2 Synthesis of macro-trithiocarbonate-chain transfer agent (macro-TTC-CTA)

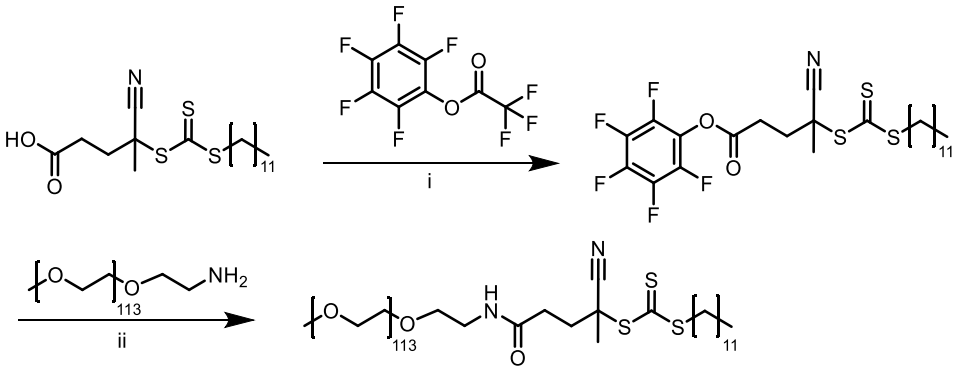

Figure S 24: Synthesis of poly(ethylene glycol)-trithiocarbonate-CTA, i) TEA, DCM, 0 °C, 3 h, yield: 77 %, ii) TEA, DCM, 0 °C, 16 h, yield: 95 %.

Synthesis of pentafluorophenyl-trithiocarbonate chain transfer agent (PFP-TTC-CTA) (i)

In an oven-dried round bottom flask 4-cyano-4-[(dodecylsulfanylthiocarbonyl)sulfanyl]pentanoic acid (TTC-CTA, 1.00 g, 2.5 mmol, 1 eq.) was dissolved under Argon atmosphere in anhydrous DCM (25 mL) and TEA (0.75 mg, 7.4 mmol, 2.5 eq.). The solution was cooled for 30 min using an ice bath and under protection from light, before pentafluorophenyl trifluoroacetate (1.74 g, 8.2 mmol, 2.5 eq.) was added dropwise *via* syringe over 45 min. The reaction mixture was allowed to stir for another 3 h on ice, before the reaction mixture was diluted with DCM (10 mL) washed with water (25 mL). The obtained aqueous layer was extracted with DCM (30 mL). The combined organic layers were dried over $MgSO_4$, filtered, and concentrated *in vacuo*. Further purification of the product was achieved by silica gel chromatography using a mixed eluent of petroleum ether and ethyl acetate (15:1). The product PFP-TTC-CTA was obtained as orange oil (1.10 g, 77 %).

^{1}H-NMR (300 MHz, Chloroform-*d*): δ (ppm) = 3.34 (t, 2H, **a**), 3.06-2.99 (m, 2H, **b**), 2.71-2.64 (m, 1H, **c**), 2.55-2.48 (m,1H, **d**), 1.93 (s, 3H, **e**), 1.72 – 1.68 (m, 2H, **f**), 1.43 – 1.38 (m, 2H, **g**), 1.30-1.26 (m, 16H, **h**), 0.88 (s, 3H, **i**).

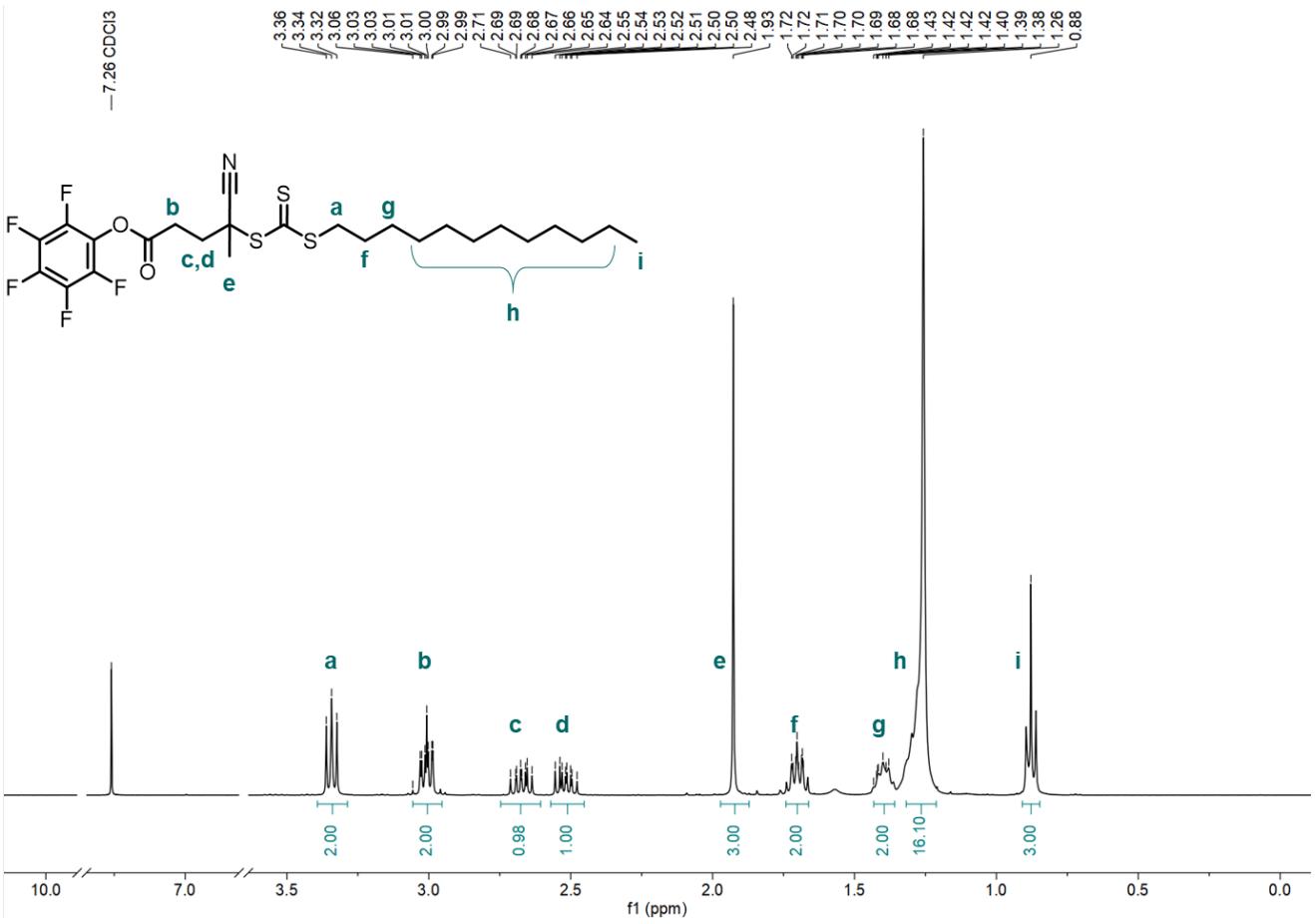

Figure S 25: ^{1}H-NMR spectrum (300 MHz) of PFP-TTC-CTA in $CDCl_3$.

Synthesis of Poly(ethylene glycol)-Trithiocarbonate-CTA, PEG-TTC-CTA (ii)

PFP-TTC-CTA (0.57 g, 1.0 mmol, 5 eq.) was dissolved in an oven-dried round bottom flask under Argon atmosphere in anhydrous DCM (5 mL). This solution was stirred for 15 min using an ice bath and under protection from light, before methoxypoly(ethylene glycol)amine (mPEG-NH_2, M_n: 5 kDa) (1.00 g, 0.20 mmol, 1 eq.) dissolved in anhydrous DCM (10 mL) and TEA (0.10 g, 1.00 mmol, 5 eq.) was added over 70 min forming an intense orange solution. The mixture was stirred for 16 h on ice melting to water. The reaction mixture was concentrated *in vacuo* to 7 mL, before being precipitated three times in cold diethyl ether (- 20 °C). To remove remaining pentafluorophenyl-TEA salts the precipitated PEG-TTC-CTA was dissolved in millipore water (40 mL) and dialyzed for 24 h against Millipore water. Finally, the PEG-TTC-CTA was isolated by lyophilization as yellowish powder (1.03 g, 95 %).

^{1}H-NMR (400 MHz, Chloroform-*d*): δ (ppm) = 6.42-6.40 (m, 1H, **a**), 3.82 – 3.79 (m, 2H, **b**), 3.66-3.61 (m, 497H, **c**), 3.47 – 3.42 (m, 2H, **d**), 3.37 (s, 3H, **e**), 3.33 – 3.29 (m, 2H, **f**), 2.51 – 2.34 (m, 4H, **g**), 1.88 (s, 3H, **h**), 1.71-1.64 (m, 2H, **i**), 1.38-1.35 (m, 2H, **j**), 1.25-1.24 (m, 16H, **k**), 0.88-0.85 (m, 3H, **l**).

SEC (DMAc, PMMA-Std.) M_n = 10,013 g/mol, M_w = 10,384 g/mol, PDI = 1.04.

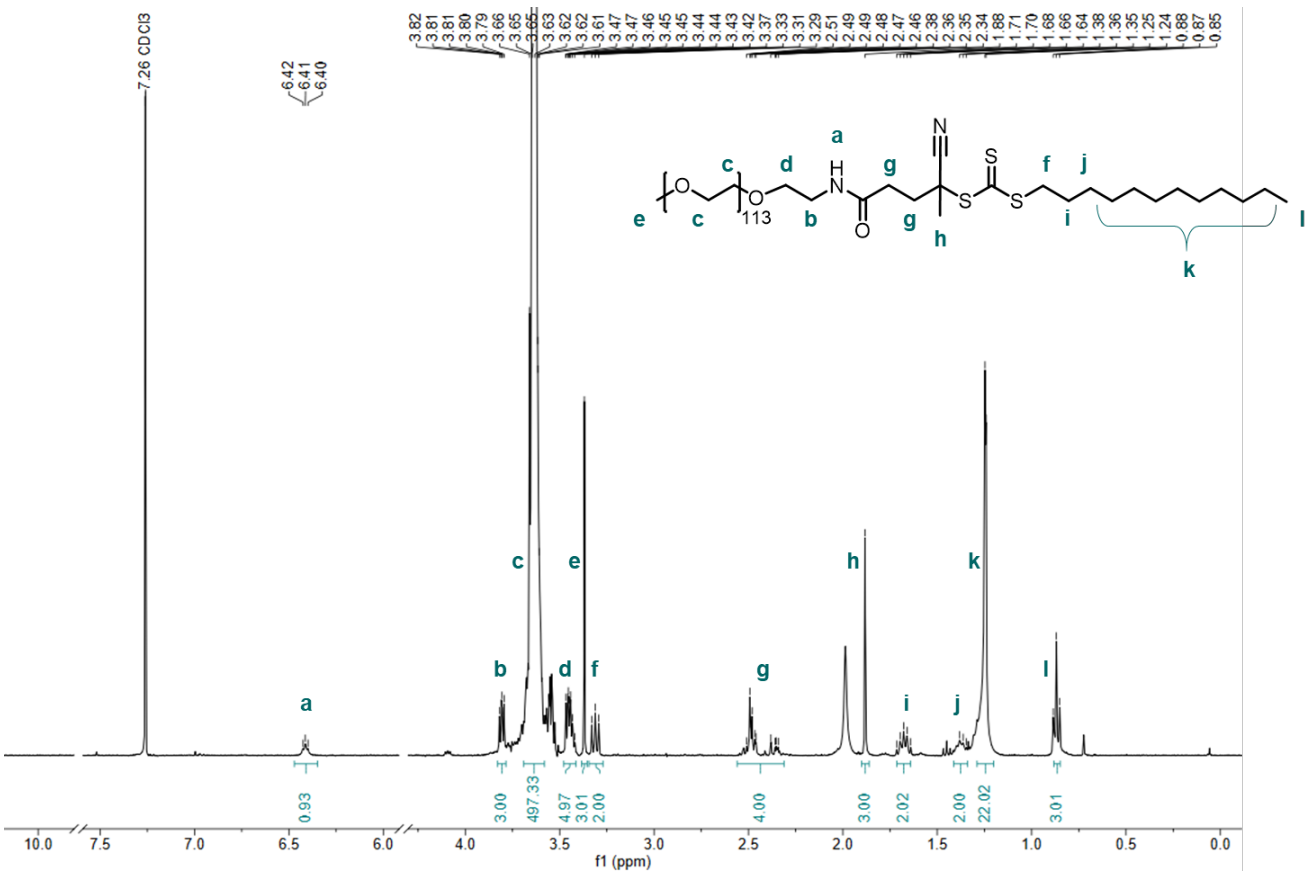

Figure S 26: ^{1}H-NMR spectrum (300 MHz) of PEG-TTC-CTA in $CDCl_3$.

3.3 Block copolymerization of MA-SQ with PEG-TTC-CTA

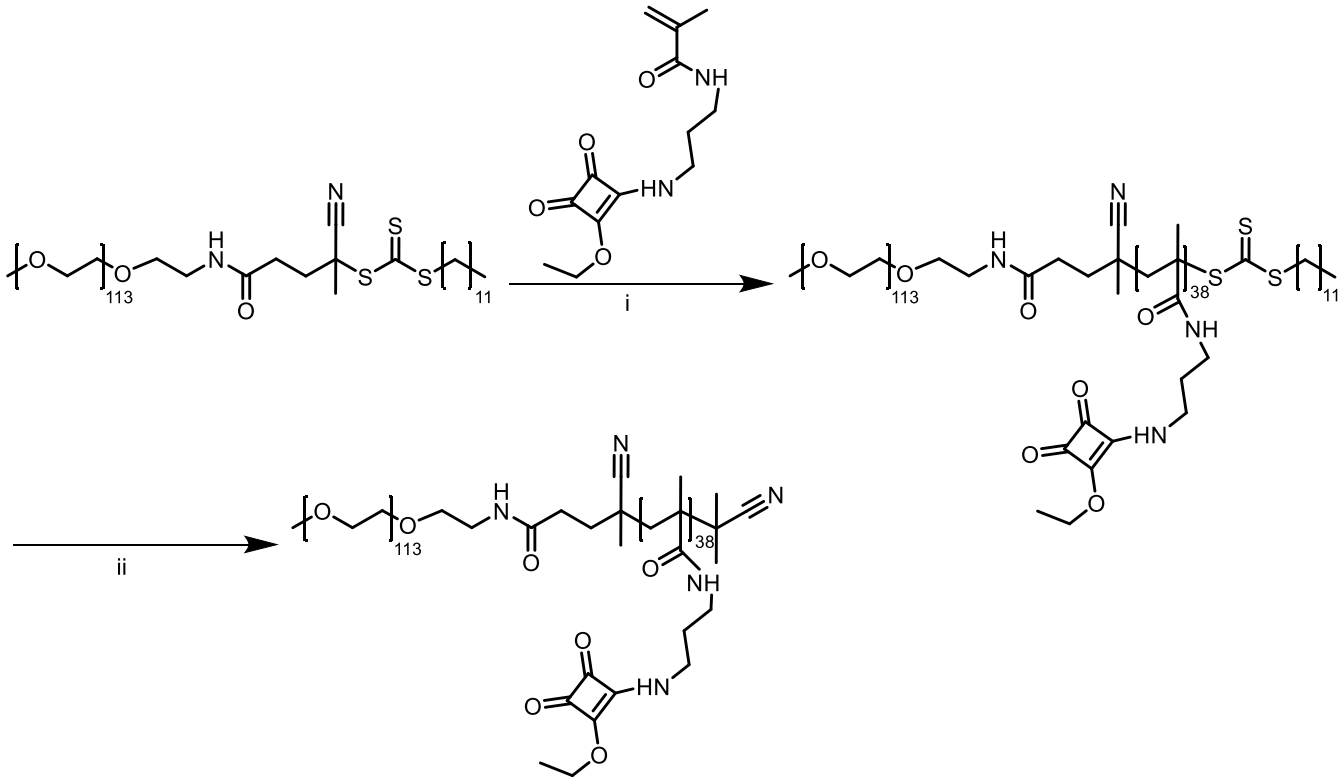

Figure S 27: Synthesis of block copolymer $mPEG_{113}$-b-$p(MA\text{-}SQ)_{38}$ with macro-PEG-TTC-CTA, i) AIBN, DMF, 70 °C, 45 h, yield: quantitative, ii) excess AIBN, DMF, 70 °C, 12 h, yield: 97%.

Block copolymerization (i)

A typical block copolymerization of MA-SQ with a theoretical degree of polymerization (DP) of 50 was performed using the macro-CTA in a Schlenk tube equipped with a stir bar. The reaction vessel was loaded with AIBN (1.0 mg, 7.0 µmol, 0.2 eq.), macro-CTA (180.0 mg, 33.0 µmol, 1.0 eq.), and MA-SQ (443.8 mg, 1.67 mmol, 50 eq.), which were subsequently dissolved in anhydrous pre-degassed DMF (1.7 mL). After three freeze-pump-thaw cycles the tube, while being in its evacuated state, was immersed in an oil bath at 70 °C for 45 h. After the reaction time, ^{1}H-NMR indicated a monomer conversion of 78 %. The block copolymer was precipitated three times in cold diethyl ether (-20 °C), isolated by subsequent centrifugation, and dried under high vacuum for 14 h affording $mPEG_{113}$-*b*-$p(SQ\text{-}MA)_{38}$-CTA (526.2 mg, quantitative) as yellow solid.

SEC (DMAc, PMMA-Std.): M_n = 22,183 g/mol, M_w = 25,830 g/mol, PDI = 1.16.

Removal of trithiocarbonate end group (ii)

In a Schlenk tube equipped with a stir bar $mPEG_{113}$-$p(SQ\text{-}MA)_{38}$-CTA (526.2 mg, 33.3 µmol, 1 eq.) and AIBN (274.4 mg ,1.670 mmol, 50 eq.) were dissolved under argon atmosphere in pre-degassed DMF (2.5 mL). The tube was immersed in an oil bath at 70 °C for 12 h. The resulting polymer was isolated by threefold precipitation into cold diethyl ether (-20 °C) and centrifugation. Finally, the polymer was dried under high vacuum for 13 h affording $mPEG_{113}$-*b*-$p(SQ\text{-}MA)_{38}$ (491.2 mg, 32.0 µmol, 97 %) as yellow solid.

^{1}H-NMR (400 MHz, DMSO-d_6): δ (ppm) = 8.72 (s, 0.5H, **a**)[a)] 8.56 (s, 0.5H, **a**)[a)], 7.30 (s, 1H, **b**), 4.65 (s, 2H, **c**), 3.51 (s, 14H, **d**), 3.46-3.40 (m, 1H, **e**)[a)], 3.32-3.26 (m, 1H, **e**)[a)],2.99 (m, 2H (1.7+0.2H), **f**), 1.62-0.78 (m, 10H, **g**). [a)] due to rotamers a splitting of the signals is observed.

SEC (DMAc, PMMA-Std.): M_n = 20,207 g/mol, M_w = 25,951 g/mol, PDI = 1.28.

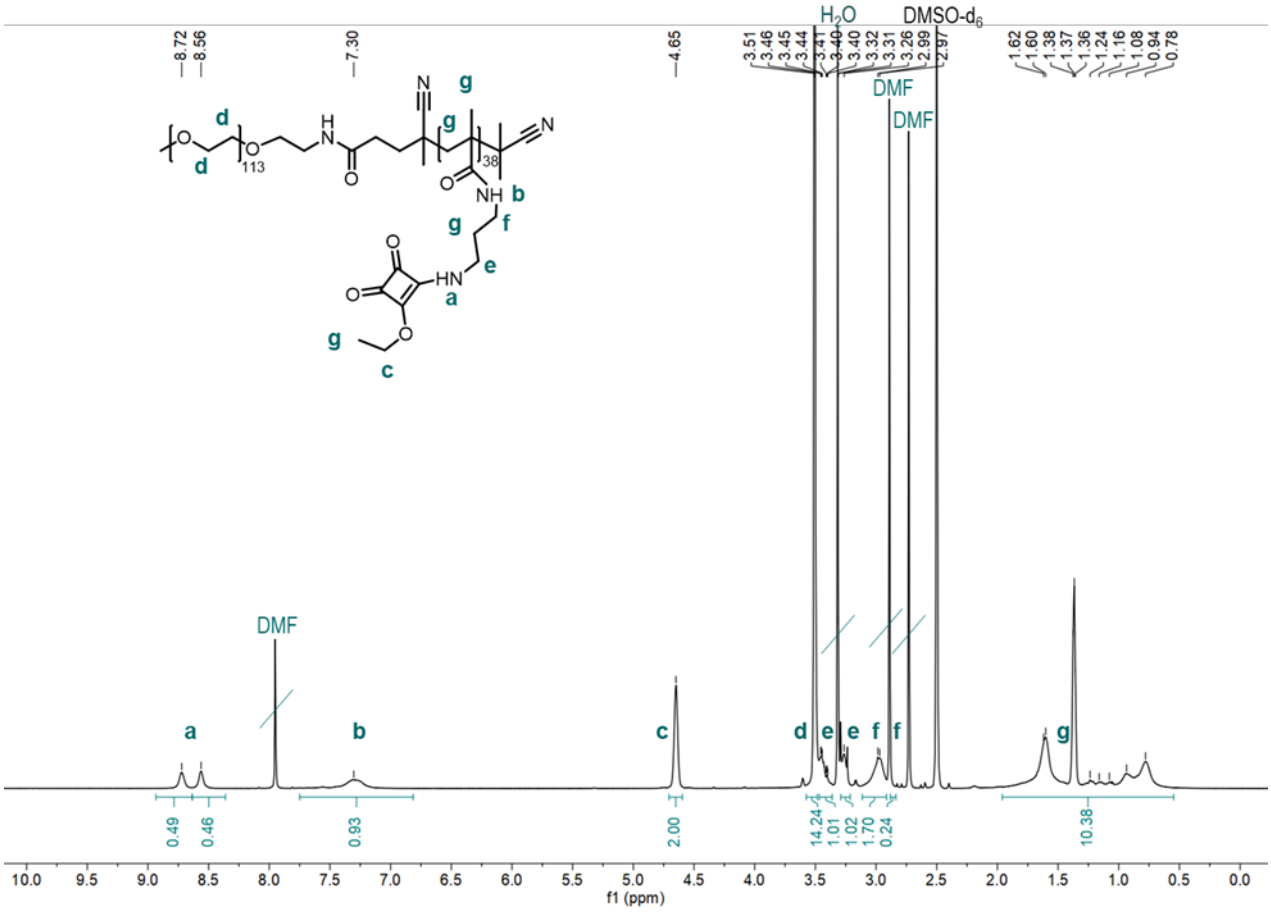

Figure S 28: ^{1}H-NMR (300 MHz) spectrum of mPEG$_{113}$-b-p(MA-SQ)$_{38}$ in DMSO-d$_6$.

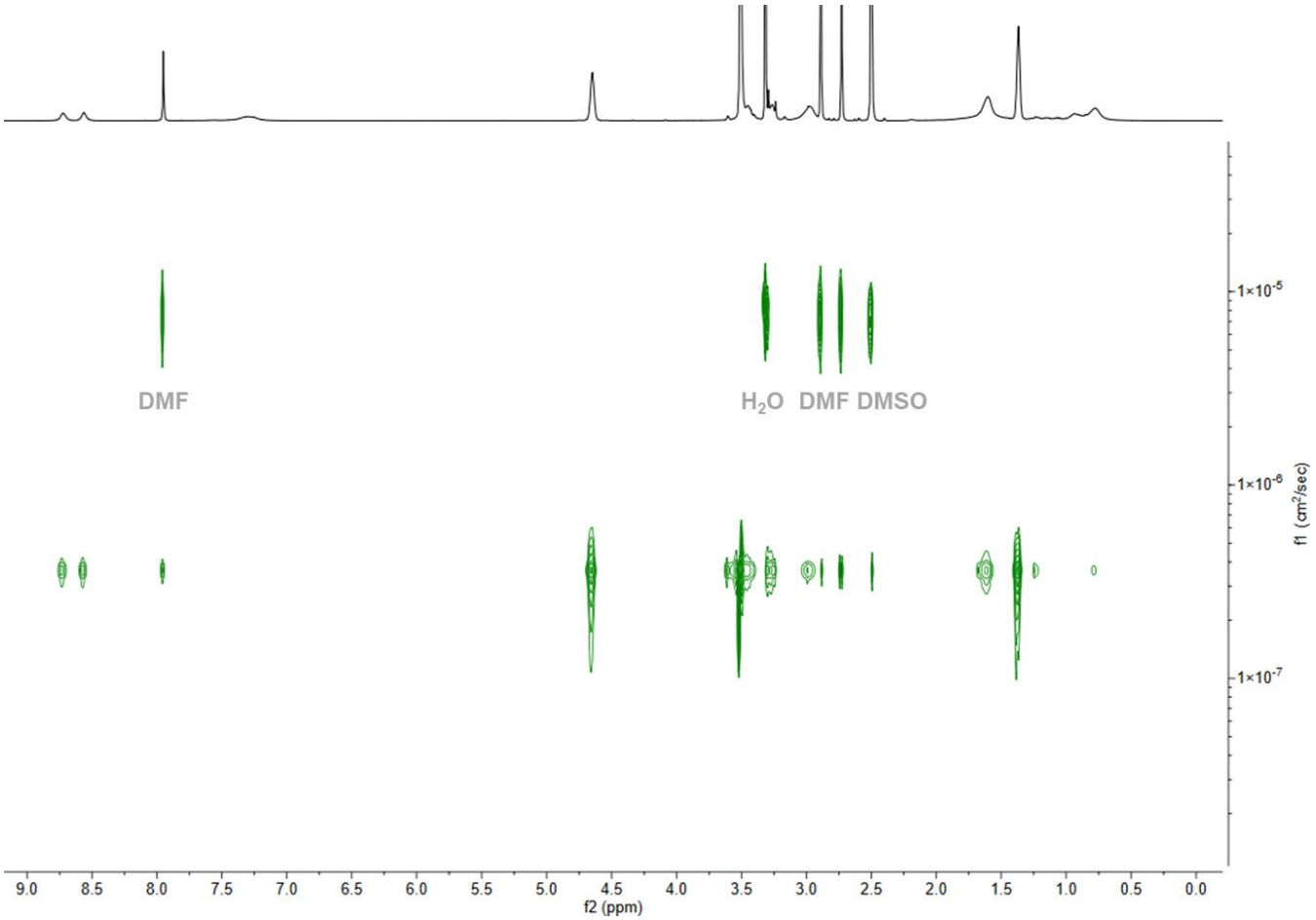

Figure S 29: DOSY spectrum of mPEG$_{113}$-b-p(MA-SQ)$_{38}$ in DMSO-d$_6$.

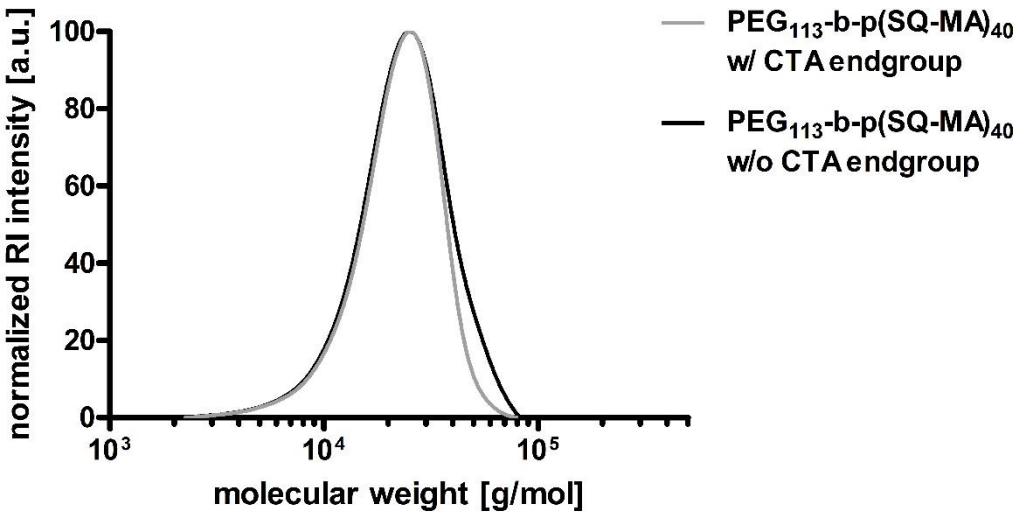

Figure S 30: Molecular weight distributions of block copolymer mPEG$_{113}$-p(SQ-MA)$_{38}$ before (grey) and after RAFT end group removal (black) determined by SEC ((DMAc, PMMA-Std).

3.4 Homopolymerization of MA-SQ with TTC-CTA

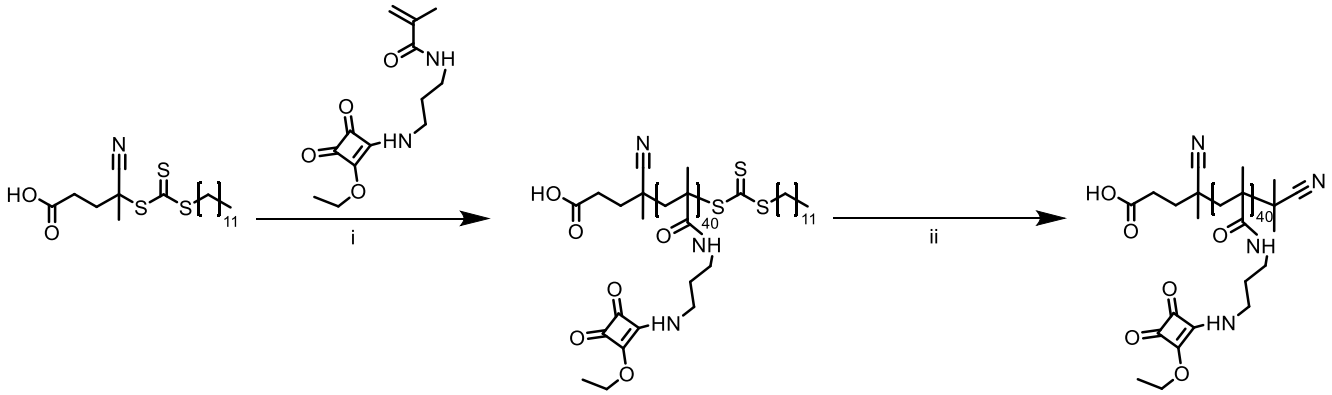

Figure S 31: Synthesis of homopolymer p(MA-SQ)$_{40}$ with TTC-CTA i) AIBN, DMF, 70 °C, 18 h, yield: quantitative, ii) excess AIBN, DMF, 70 °C, 12 h, yield: 97 %.

For a typical homopolymerization with a DP of 50, MA-SQ (533.0 mg, 2.0 mmol, 50 eq.), TTC-CTA (16.1 mg, 40.0 µmol, 1.0 eq.), and AIBN (1.3 mg, 8 µmol, 0.2 eq.) were dissolved in 2 mL anhydrous pre-degassed DMF. The solution was degassed by three freeze-pump-thaw cycles, before it was immersed in an oil bath at 70 °C for 37 h, while being in its evacuated state. After the reaction time, ^{1}H-NMR analysis indicated a monomer conversion of 79 %. The homopolymer was precipitated three times in cold diethyl ether (-20 °C), isolated by subsequent centrifugation, and dried under high vacuum for 16 h affording p(SQ-MA)$_{40}$-CTA (440.2 mg, 40.2 µmol, quantitative) as yellow solid.

SEC (DMAc, PMMA-Std.): M_n =13,764 g/mol, M_w = 17,296 g/mol, PDI = 1.26.

For free radical polymerization conditions, the homopolymerization was proceeded analogously without TTC-CTA and with increased equivalents of the radical initiator AIBN (5.7 mg, 40 µmol, 1 eq.).

SEC (DMAc, PMMA-Std.): M_n = 47,986 g/mol, M_w = 108,804 g/mol, PDI = 2.27.

Removal of trithiocarbonate end group:

Analogously to the previously described end group removal, the homopolymer p(SQ-MA)$_{40}$-CTA (440.2 mg, 40.2 µmol, 1 eq.) and AIBN (331.0 mg, 2.02 mmol, 50 eq.) were dissolved under argon atmosphere in pre-degassed DMF (1.5 mL). The tube was immersed in an oil bath at 70 °C for 12 h. The resulting polymer was isolated by threefold precipitation into cold diethyl ether (-20 °C) and centrifugation. After the polymer was dried under high vacuum for 14 h, p(SQ-MA)$_{40}$ (425.3 mg, 39.2 µmol, 97 %) was obtained as yellow solid.

^{1}H-NMR (300 MHz, DMSO-d_6): δ (ppm) = 8.73 (s, 0.5H, **a**)[a)], 8.57 (s, 0.5H, **a**)[a)], 7.31 (s, 1H, **b**), 4.66-4.64 (m, 2H, **c**), 3.45 (m, 1H, **d**)[a)], 3.27 (m, 1H, **d**)[a)], 3.01-2.71 (m, 2H, **e**), 1.62-0.78 (m, 10H, **f**). [a)]due to rotamers a splitting of the signals is observed.

SEC (DMAc, PMMA-Std.): M_n =13,757 g/mol, M_w = 17,892 g/mol, PDI = 1.30.

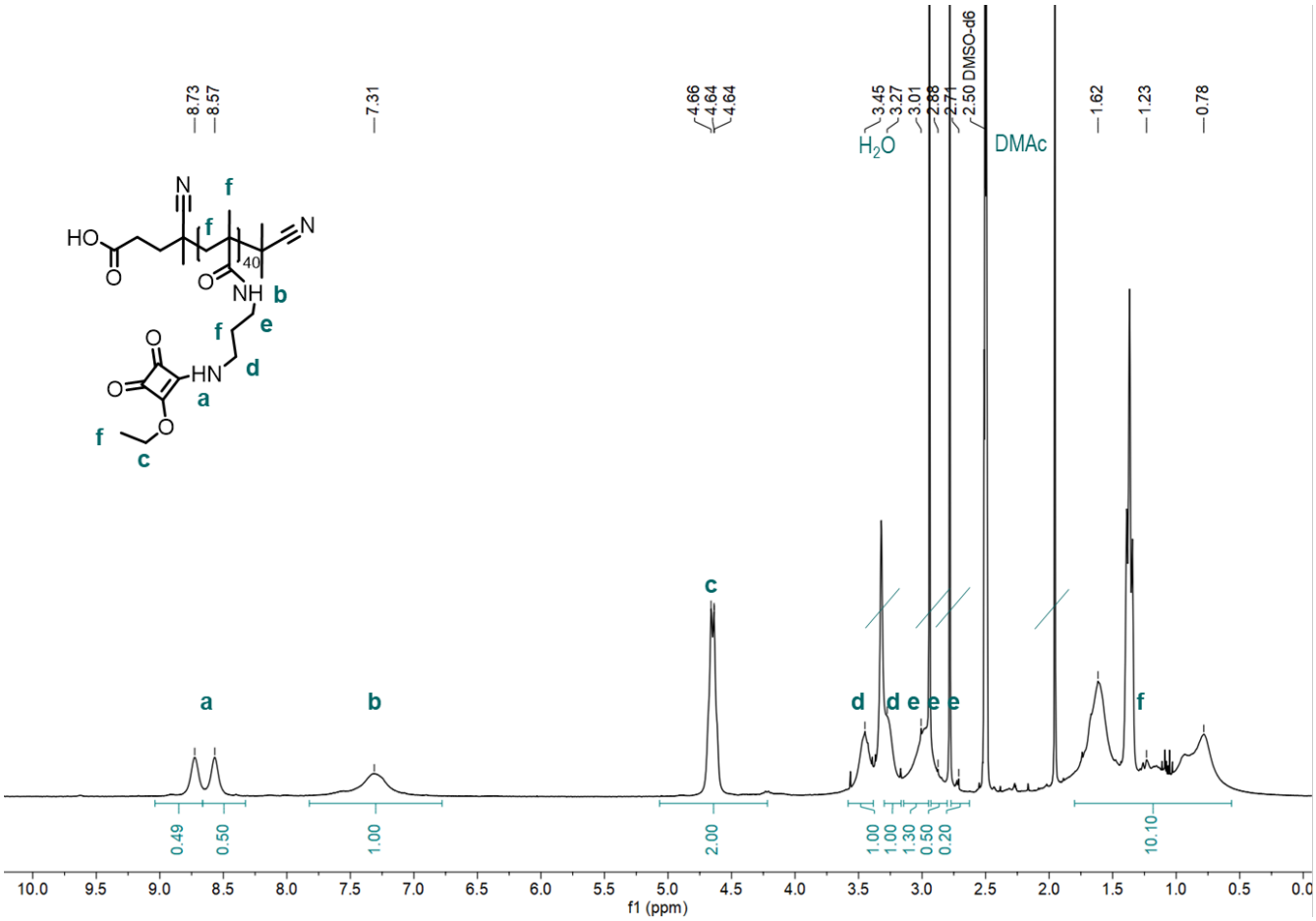

Figure S 32: ^{1}H-NMR (300 MHz) spectrum of p(MA-SQ)$_{38}$ in DMSO-d$_6$.

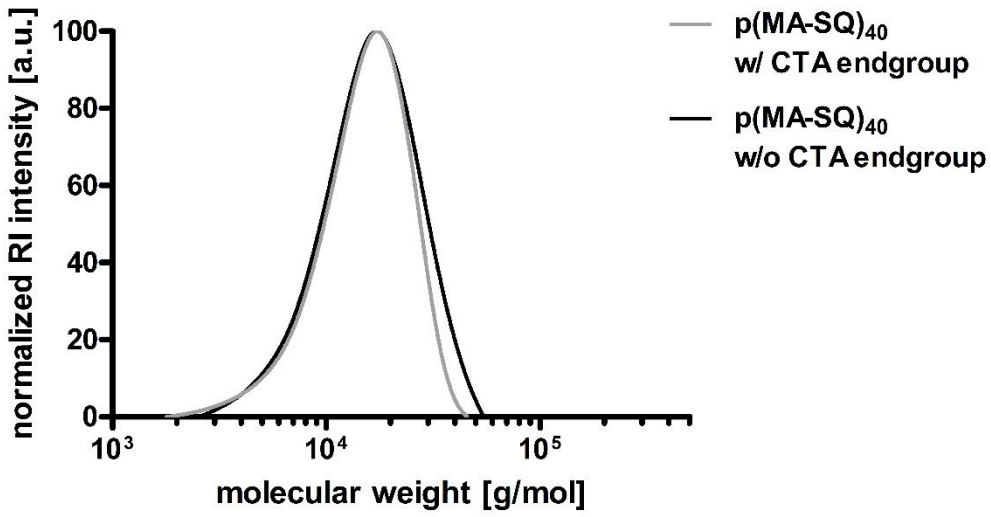

Figure S 33: Molecular weight distributions of homopolymer p(SQ-MA)$_{40}$ before and after RAFT end group removal determined by SEC (DMAc, PMMA-Std).

3.5 Reaction kinetics of RAFT homopolymerization

To investigate the kinetics of the RAFT homopolymerization of MA-SQ, samples of the reaction mixture were taken at different time points. After 0, 90, 180, and 320 min 15 µL reaction mixture was taken, while the reaction mixture stayed under inert Argon atmosphere. Samples were diluted immediately with DMSO-d_6 and exposed to air, before ^{1}H NMR measurements were performed. Monomer conversion was determined by the ratio between the integrals of the polymer (CH_2-*NH*-C- at 8.7 and 8.6 ppm; -O-*CH_2*-CH_3 at 4.7 ppm, grey) to integrals of the monomer (*CH_2*=C- at 5.6 and 5.3 ppm, orange).

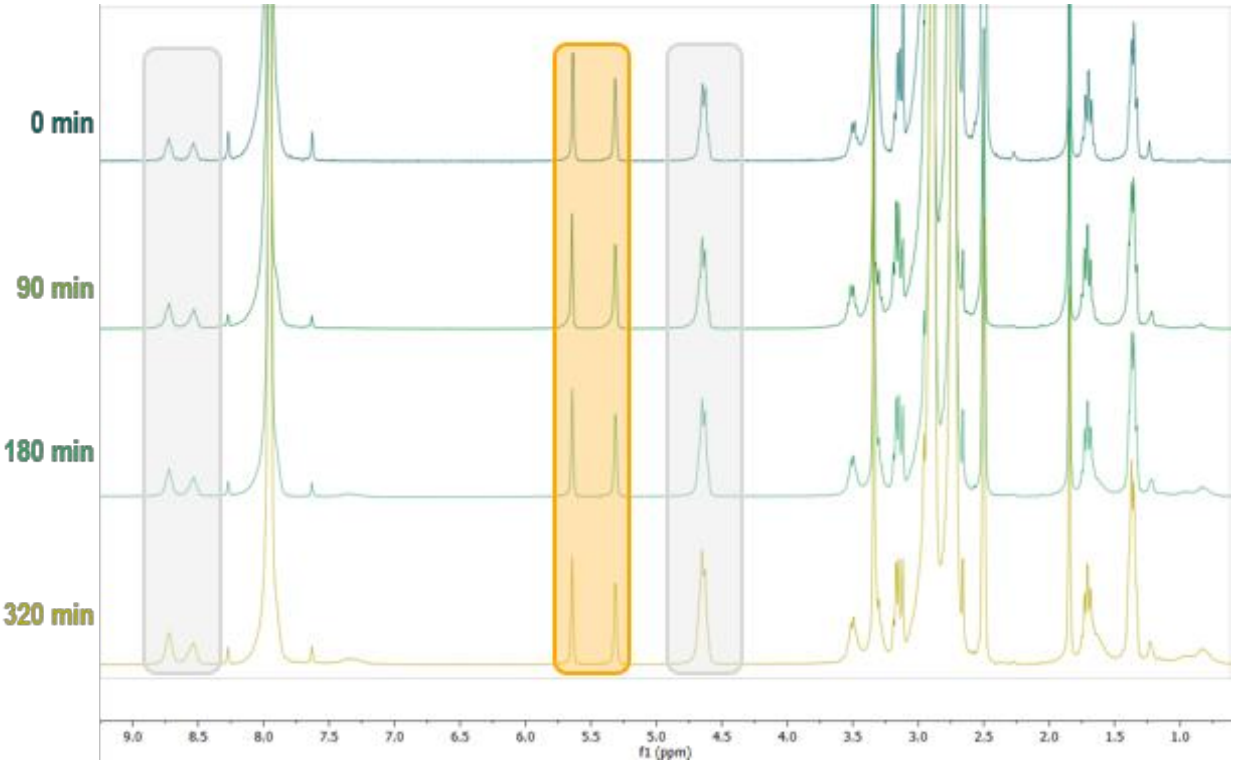

Figure S 34: ^{1}H NMR spectra (300 MHz) of reaction mixture of p(MA-SQ) after 0, 90, 180, and 320 min in DMSO-d_6.

A

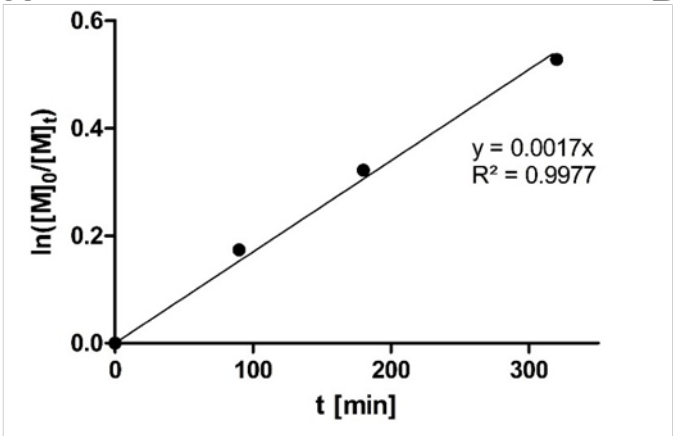

B

t [min]	conv. [%]	[M]	$\ln([M]_0/[M]_t)$
0	0	0.744	0
90	16	0.625	0.174
180	27,5	0.539	0.322
320	41	0.439	0.528

Figure S 35: (A) Monomer conversion ($\ln([M]_0/[M]_t)$) over reaction time, (B) Corresponding monomer conversion (conv.), monomer concentration ([M]), and ($\ln([M]_0/[M]_t)$) over time.

3.6 Polymer-analogous reaction of homopolymer by amidation with primary, secondary, or tertiary amines

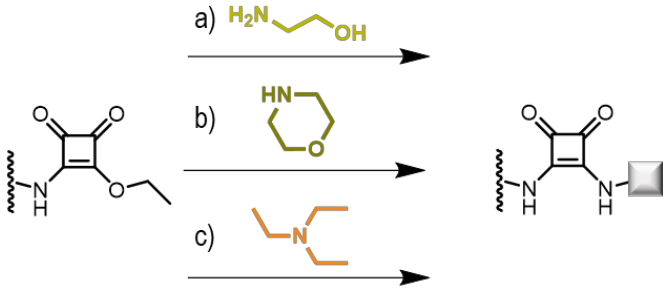

Figure S 36: Schematic reaction of pendant squaric ester amide moieties of homopolymer p(MA-SQ)$_{40}$ with a) aminoethanol, b) morpholine or c) triethylamine (TEA).

The reaction kinetics of the pendant squaric ester amide moieties of p(MA-SQ)$_{40}$ with primary, secondary, or tertiary amines were monitored by UV/Vis absorbance. Therefore, 25 µg homopolymer (25 µL of a 1.00 mg/mL stock solution in DMSO, 0.09 µmol, 1 eq.) was diluted with 1975 µL DMSO (v:v, 1:80) yielding a final concentration of 12.5 µg/mL. To this solution an excess of aminoethanol (5.4 µL, 90.00 µmol, 1000 eq.), morpholine (7.8 µL, 90.00 µmol, 1000 eq.), or TEA (12.6 µL, 90.00 µmol, 1000 eq.) was added, respectively. UV/Vis spectra were recorded regularly over 2.5 h.

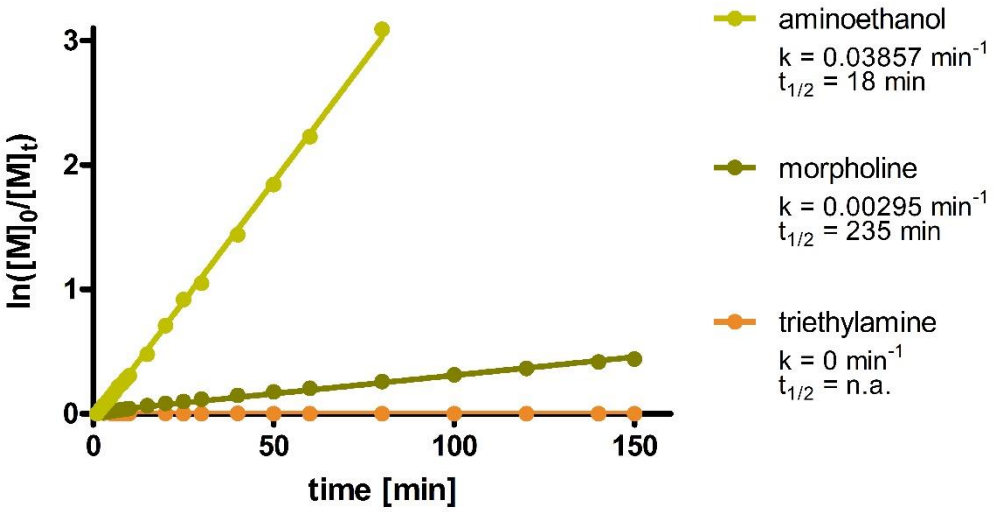

Figure S 37: ln ([M]$_0$/([M]$_t$) over time. Under the assumption the reaction followed - due to the vast excess of amine - first order kinetics, the reaction half time ($t_{½}$, time needed for half of the squaric ester amides to react with the amines) and the reaction rate constant k are given.

The same reaction could also be conducted on preparative scale using 20 mg homopolymer (72.6 µmol, 1 eq.) and only a slight excess of aminoethanol (21.7 µL, 0.36 mmol, 5.0 eq), morpholine (31.6 µL, 0.36 mmol, 5.0 eq), or TEA (50.5 µL, 0.36 mmol, 5.0 eq) was added. The reaction was conducted in 0.7 mL of DMSO-d_6 to record ^{1}H-NMR spectra before and after addition of the amines. After the reaction time the modified homopolymers were isolated by three-fold precipitation in cold diethyl ether (-20 °C) and dried under high vacuum. Subsequently, ^{1}H NMR and SEC analysis of the purified samples were performed.

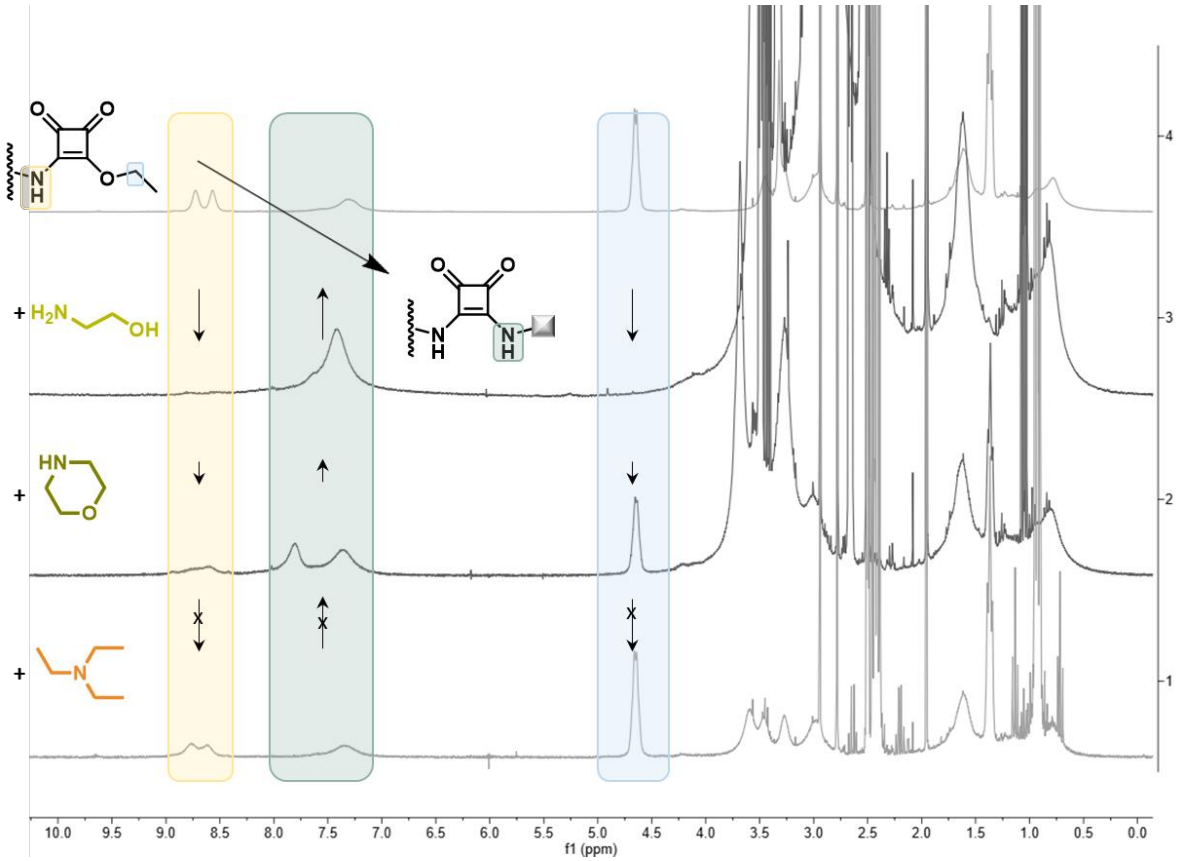

Figure S 38: ^{1}H NMR spectra of p(MA-SQ)$_{40}$ in DMSO-d$_6$ and the corresponding reaction mixtures 2.5 h after addition of primary amine aminoethanol, secondary amine morpholine, or tertiary amine TEA.

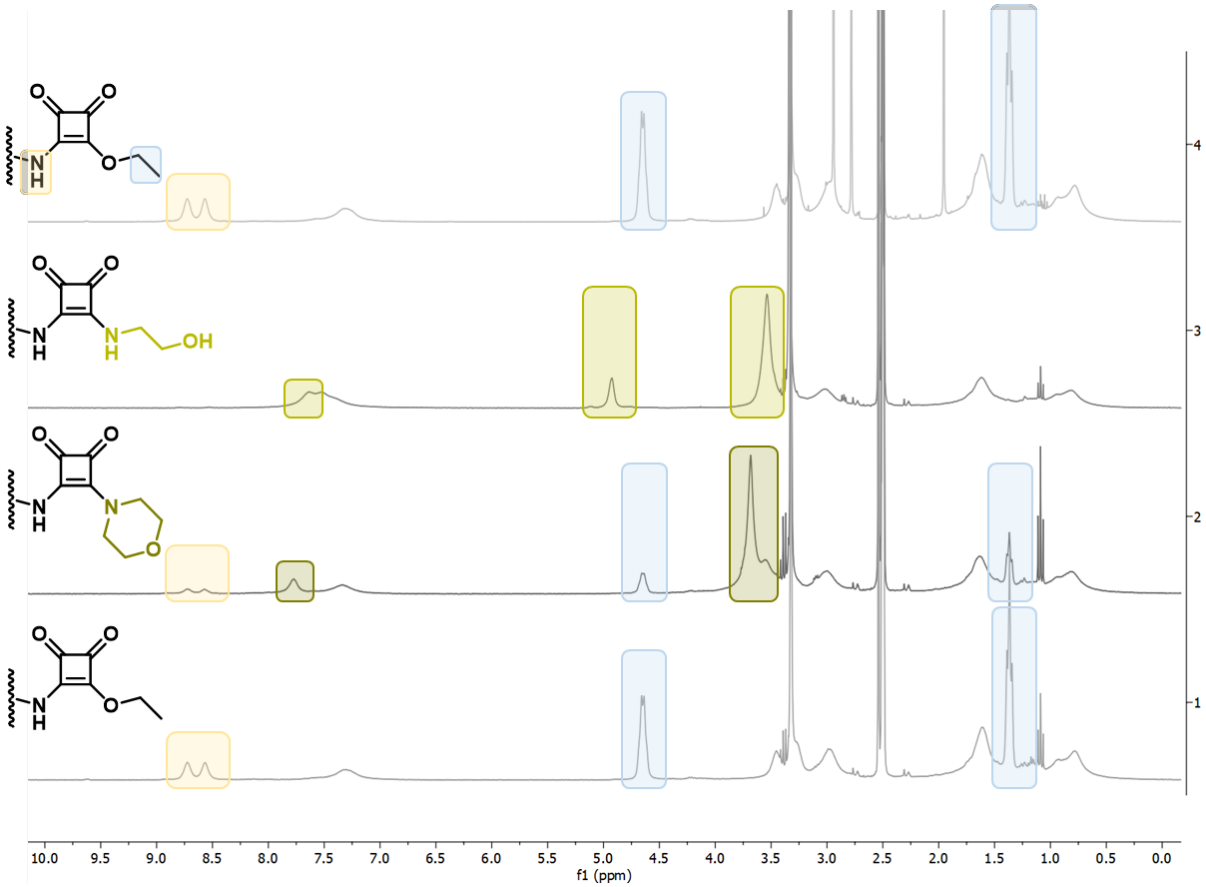

Figure S 39: ^{1}H NMR spectra of p(MA-SQ)$_{40}$ in DMSO-d$_6$ and purified p(MA-SQ)$_{40}$ after modification with primary amine aminoethanol, secondary amine morpholine, or tertiary amine TEA.

To investigate whether the reaction with the secondary amine morpholine could reach full conversion the polymer-analogous reaction of the homopolymer with morpholine was repeated with an increased reaction time of 22 h at an elevated temperature of 70 °C.

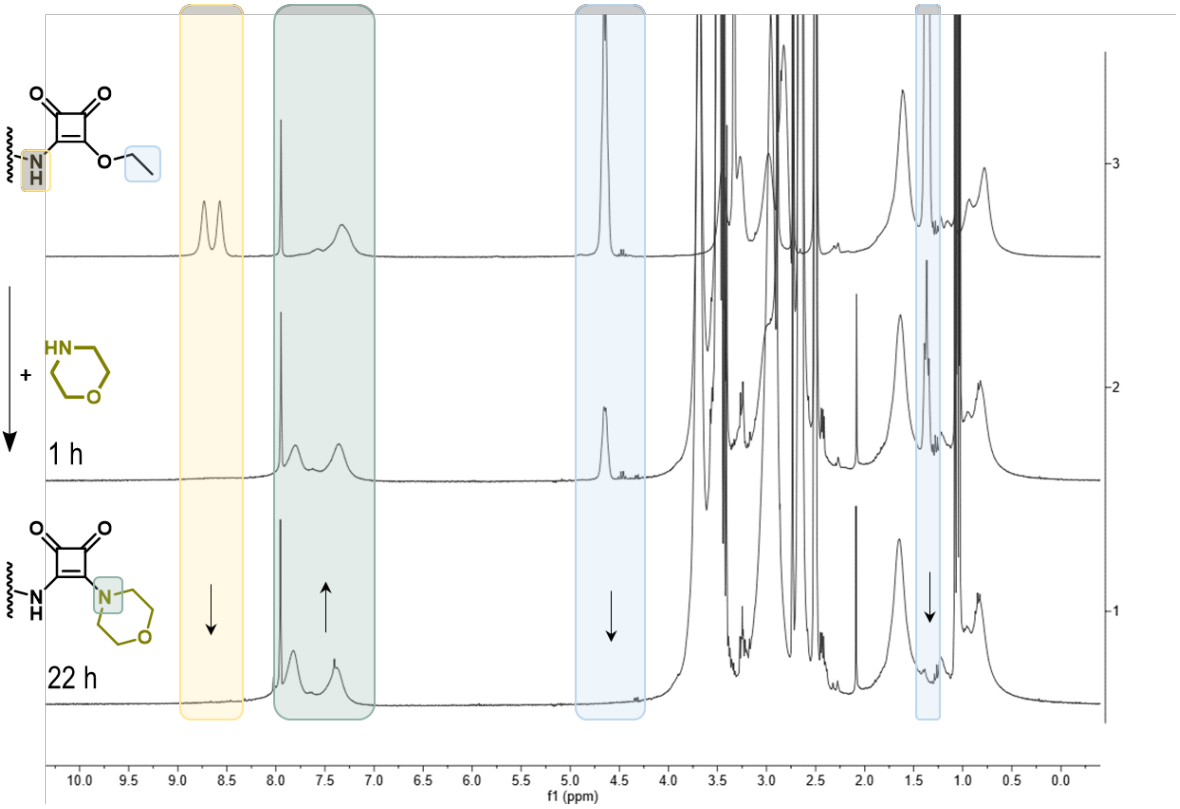

Figure S 40: ^{1}H NMR spectra of p(MA-SQ)$_{25}$ in DMSO-d$_6$ and the corresponding reaction mixtures 1 and 22 h after addition of the secondary amine morpholine at 70 °C.

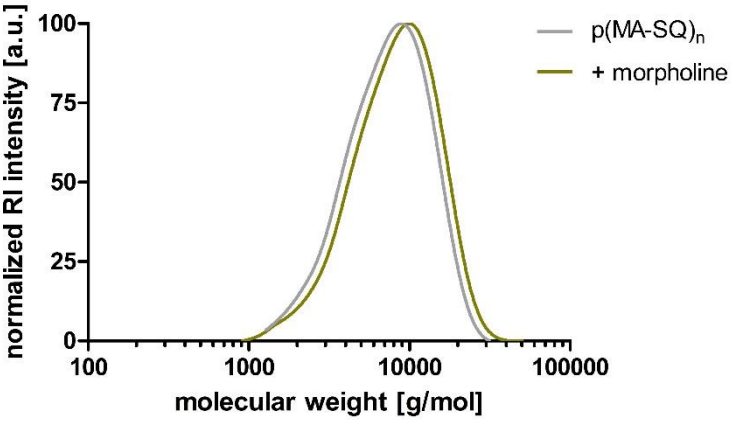

Figure S 41: SEC molecular weight distribution of p(MA-SQ)$_{25}$ before and after conversion with morpholine.

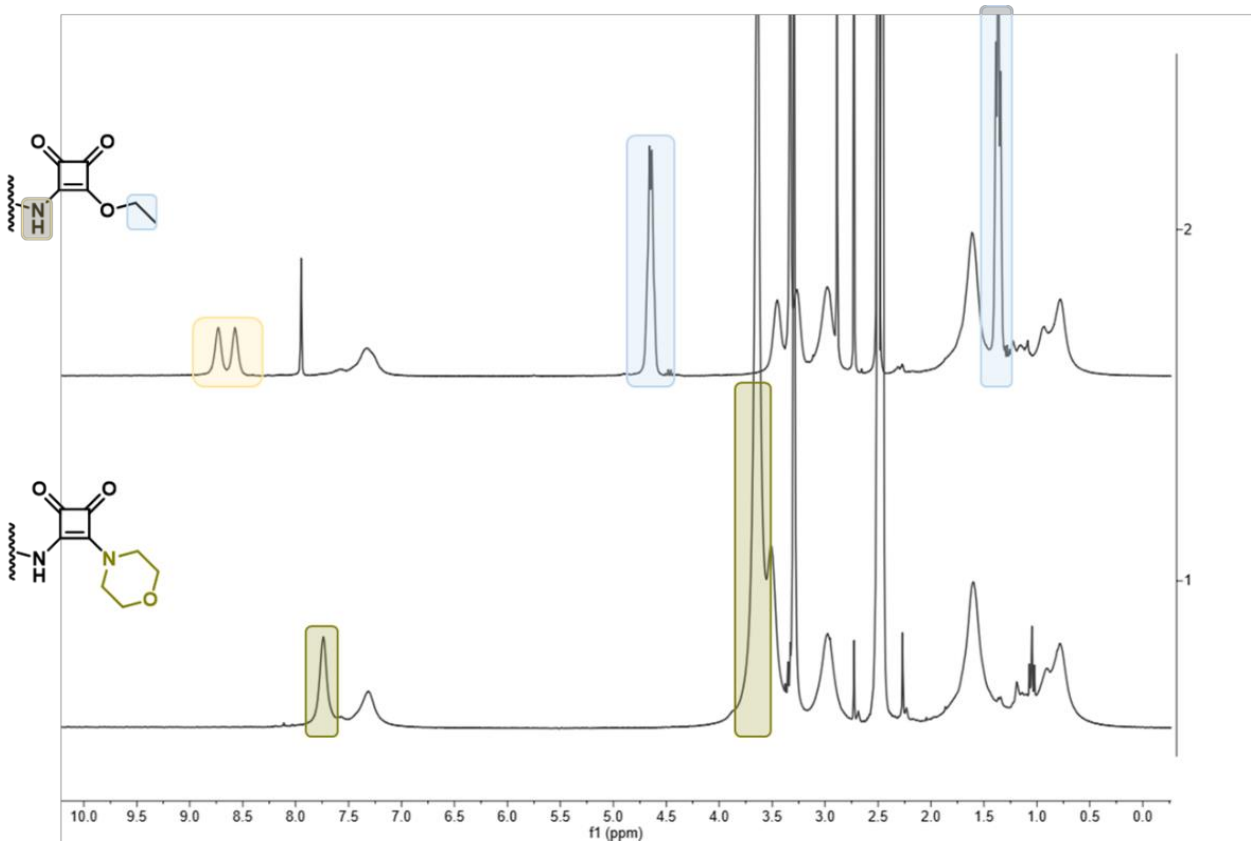

Figure S 42 ^{1}H NMR spectra of p(MA-SQ)$_{25}$ in DMSO-d$_6$ and purified p(MA-SQ)$_{25}$ after modification with secondary amine morpholine.

3.7 Block copolymer-analogous reaction of self-assembled micelles by amidation with primary amines

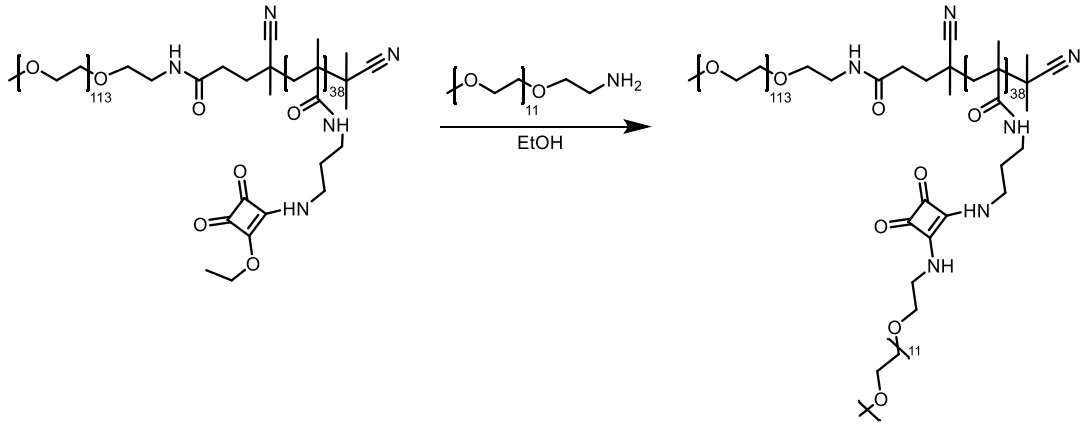

Figure S 43: Schematic reaction of self-assembled squaric ester amide block copolymer micelles mPEG$_{113}$-b-p(MA-SQ)$_{38}$ with PEG$_{11}$-amine.

In a DLS cuvette 1 mg of micelles mPEG$_{113}$-b-p(MA-SQ)$_{38}$ dispersed in 200 µL of ethanol (5.0 mg/mL, 2.56 µmol amine reactive units, 1.0 eq.) were treated with PEG$_{11}$-amine (9.6 mg, 12.8 µmol, 5.0 eq.) and monitored over time by repeated DLS measurements. A gradual particle unfolding and micelle disassembly could be observed both by mean volume mean as well as scattering count rate, and after 30 min all micelles disappeared.

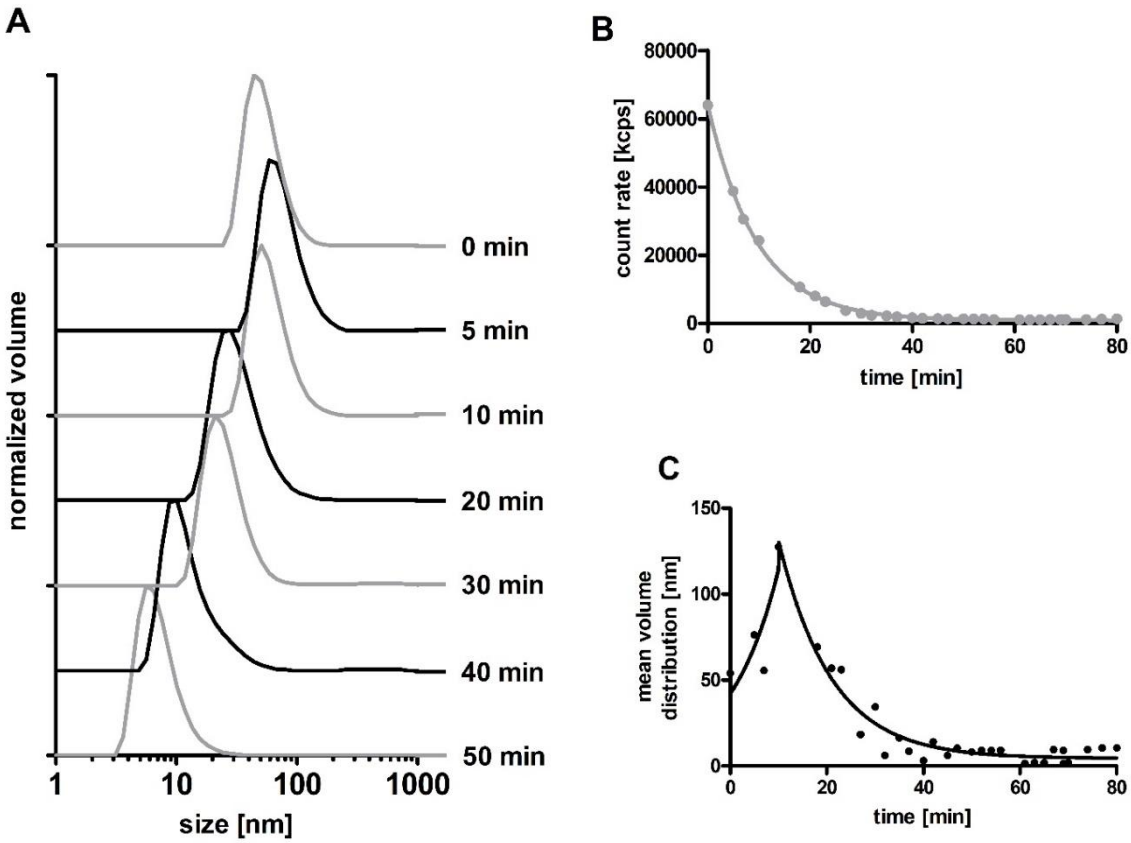

Figure S 44:DLS analysis of the aminolysis and micelle unfolding of the self-assembled squaric ester amide block copolymer micelles mPEG$_{113}$-b-p(MA-SQ)$_{38}$ with PEG$_{11}$-amine. (A) Particle size distribution, (B) scattering count rate, and (C) mean volume distribution

4. Nanogel Fabrication

4.1 Preparation of nanogels

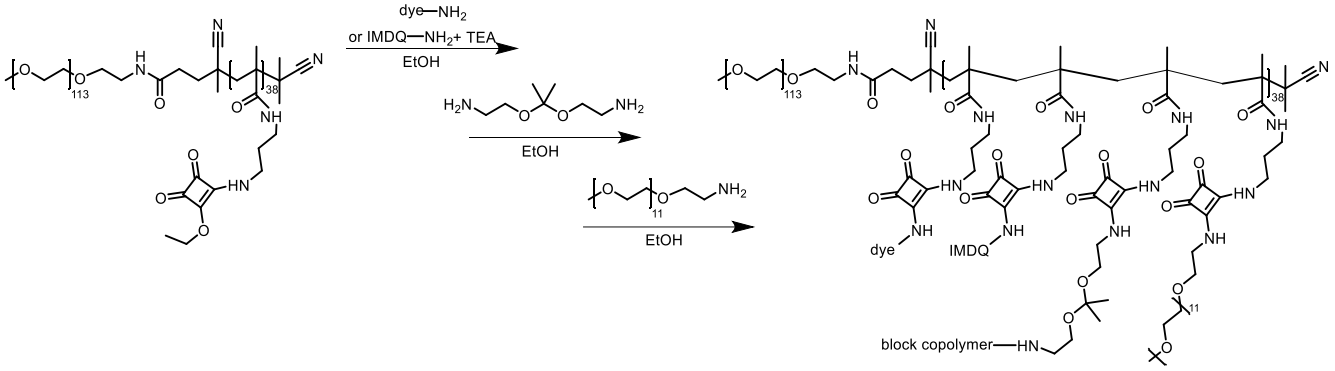

Figure S 45: Scheme of sequential preparation of nanogels

The block copolymer $mPEG_{113}$-$p(SQ\text{-}MA)_{38}$ (47.0 mg, 2.98 µmol polymer, 113.11 µmol reactive squaric ester amide units) was dispersed in ethanol (4.7 mL, 10 mg/mL). Ultrasonication of this dispersion for 1 h resulted in the self-assembly of polymeric micelles, which was verified by subsequent DLS measurements. For fluorescent labeling of the nanogels 113 µL Oregon Green (OG) or 117 µL tetramethylrhodamine (TMR) stock solution (2.5 mg/mL in DMSO, 0.57 µmol, 0.005 eq.) or 433 µL 800RS stock solution (2.5 mg/mL in DMSO, 1.14 µmol, 0.01 eq.) was added to the clear micellar dispersion and stirred for two days. For covalent drug loading of the nanogels with the immune modulator IMDQ, 489.1 µL of IMDQ stock solution (10 mg/mL in ethanol, 11.31 µmol, 0.10 eq.) was added to the micellar dispersion as well. After addition of 47.3 µL TEA (339.33 µmol, 3.00 eq.), the reaction mixture was allowed to stir at RT for 2 days.

The obtained dye-labeled IMDQ-conjugated or native dispersion was used to prepare three different kinds of nanogels (ketal-crosslinked, ether-crosslinked, and non-crosslinked). Thus, the dispersion was divided into three, wherefore 1.5 mL (15.0 mg, 0.95 µmol polymer, 36.2 µmol reactive squaric ester amide units) each was transferred into a Schlenk tube equipped with stirring bar. The different crosslinkers were added to the dispersions, whereby the added equivalents were adjusted in reference to the amine-reactive squaric ester amide units. 2,2,bis(aminoethoxy)propane (0.9 µL 5.4 µmol, 0.15 eq.) and 1,2-bis(aminoethoxy)ethane (0.8 µL 5.4 µmol, 0.15 eq.) were added as ketal- or ether-crosslinker. For the formulation of non-crosslinked nanogels 2-aminoethanol (0.7 µL 10.8 µmol, 0.30 eq.) was added. The reaction mixtures were allowed to stir at RT for one day. For complete conversion of the reactive squaric ester amide moiety, an excess of mPEG-NH_2 (M_n 0.75 kDa) (814 µL of 100 mg/mL in DMSO, 108.6 µmol, 3 eq.) was added to each reaction mixture, before they were allowed to stir for another five days. Complete conversion of the reactive ester units was confirmed by UV-Vis absorbance measurements. Subsequently, the reaction mixtures were dialyzed (MWCO: 1 kDa) against Millipore water containing 0.1 wt% NH_3 (1 L) for five days with water exchange twice per day. After lyophilization the nanogels were obtained as voluminous, yellowish powder (3x 21 mg, 63%), which could be easily re-dispersed in aqueous buffer at given concentrations.

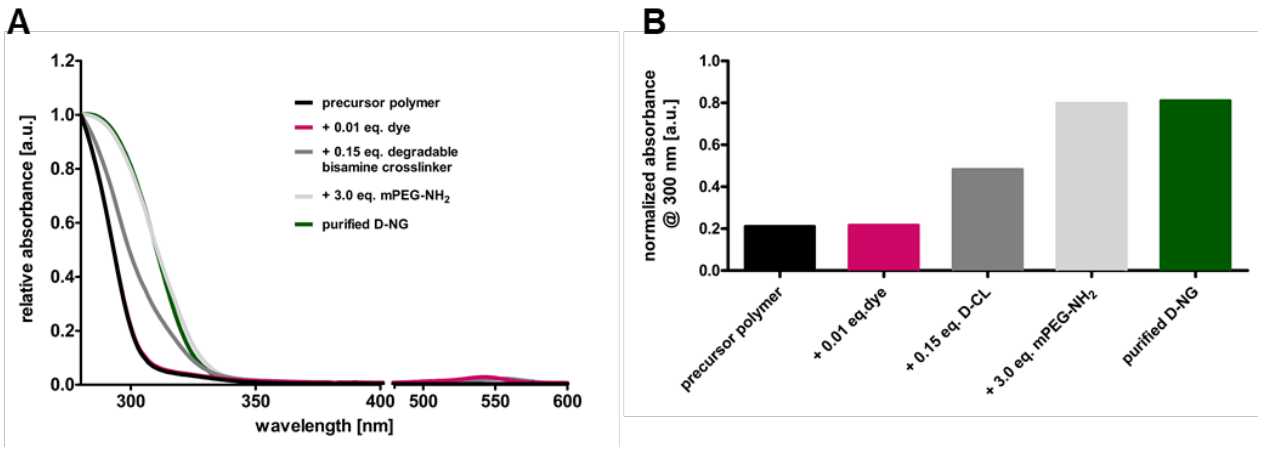

Figure S 46: Conversion of polymeric squaric ester amides to squaric bisamides during preparation of D-NG monitored by UV absorbance. (A) UV-Vis spectra of precursor polymer after step-wise nanogel preparation in ethanol compared to fully fabricated D-NG in PBS after purification, and (B) their corresponding absorbance at 300 nm.

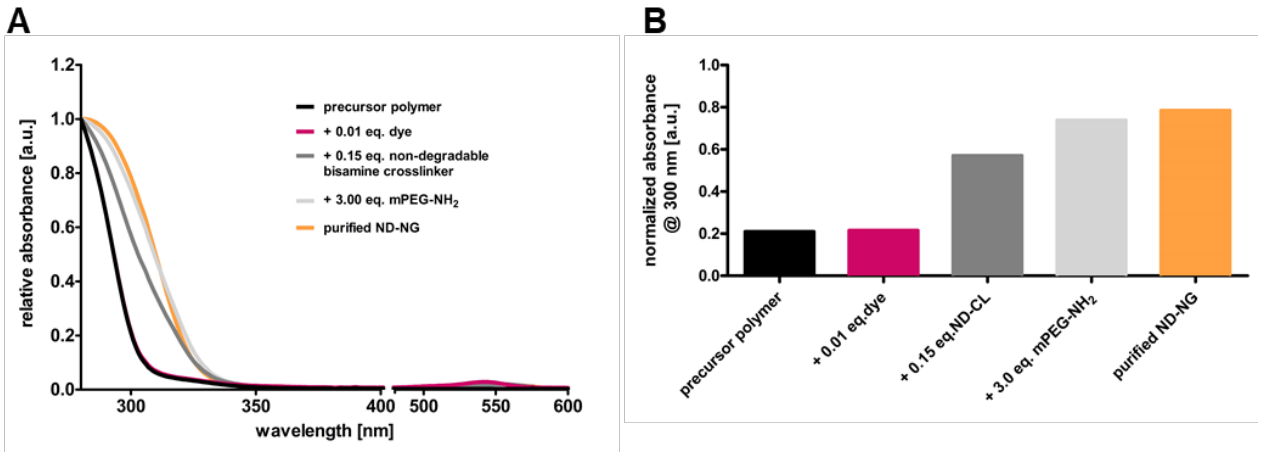

Figure S 47: Conversion of polymeric squaric ester amides to squaric bisamides during preparation of ND-NG monitored by UV absorbance. (A) UV-Vis spectra of precursor polymer after step-wise nanogel preparation in ethanol compared to fully fabricated ND-NG in PBS after purification, and (B) their corresponding absorbance at 300 nm.

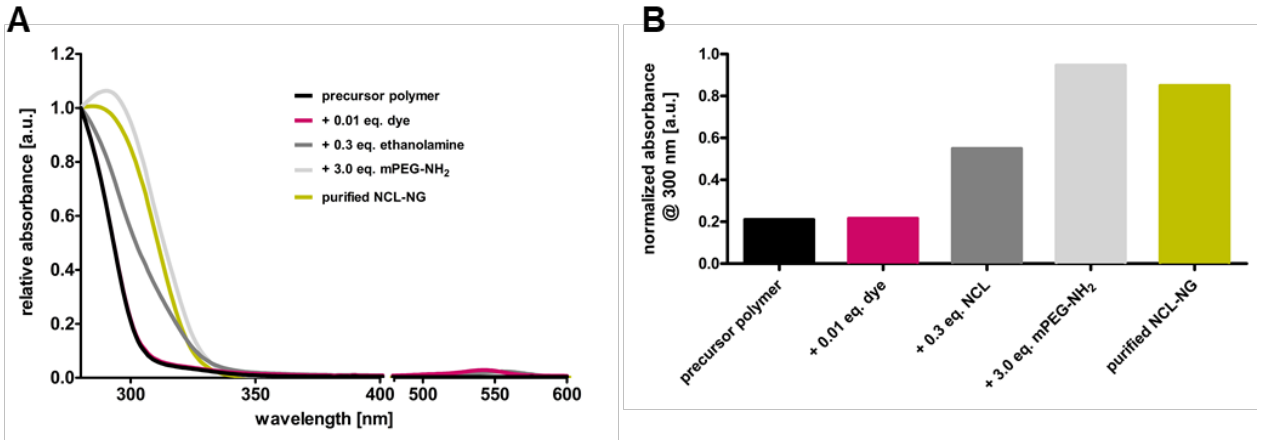

Figure S 48: Conversion of polymeric squaric ester amides to squaric bisamides during preparation of NCL-NG monitored by UV absorbance. (A) UV-Vis spectra of precursor polymer after step-wise nanogel preparation in ethanol compared to fully fabricated NCL-NG in PBS after purification, and (B) their corresponding absorbance at 300 nm.

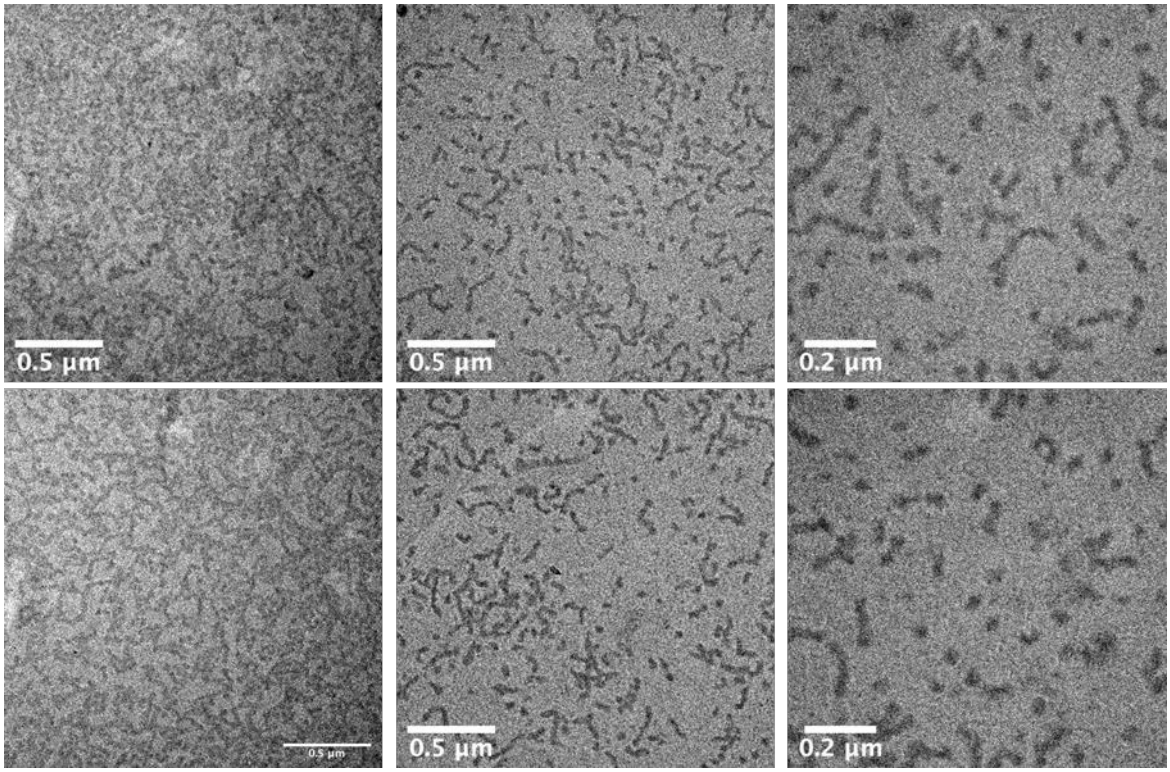

Figure S 49: TEM images of D-NG.

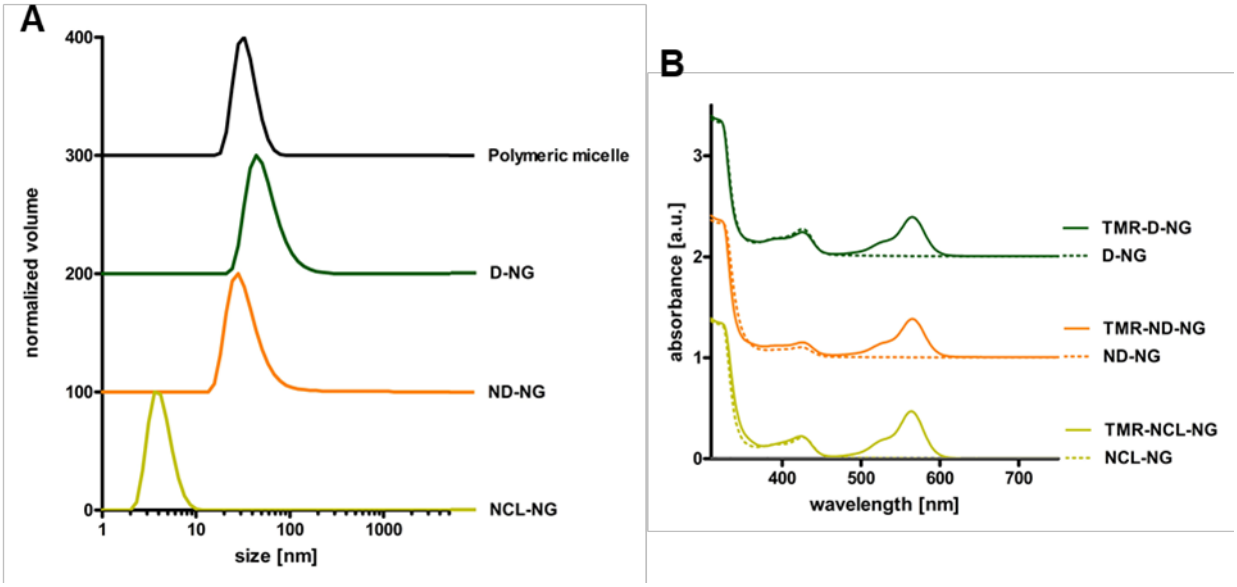

Figure S 50: Nanogel preparation in aqueous solution using sodium borate buffer. (A) DLS size distribution of polymeric precursor micelle, as well as of the corresponding fully fabricated and purified D-NG, ND-NG, and NCL-NG in aqueous solution. (B) UV Vis spectra of D-NG, ND-NG, and NCL-NG without and with fluorescent TMR-labeling indicating effective dye conjugation under aqueous conditions.

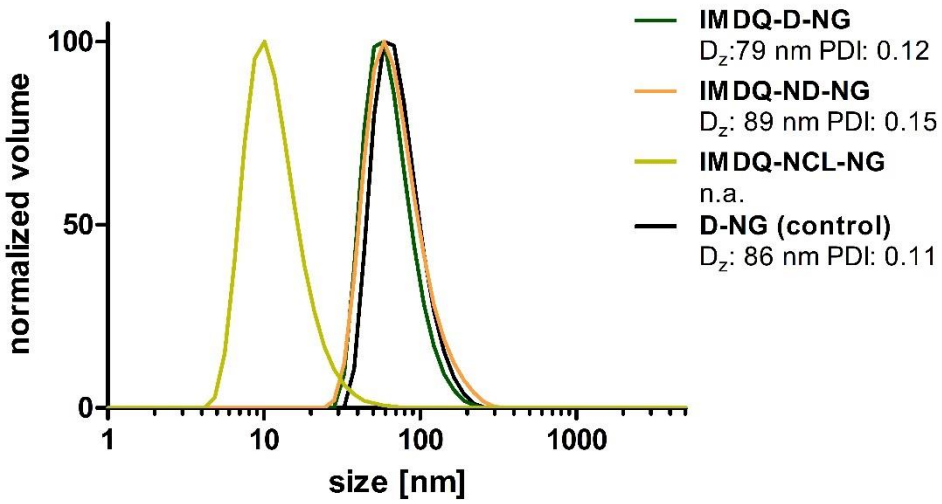

Figure S 51: DLS size distribution of fully fabricated nanogels IMDQ-D-NG, IMDQ-ND-NG, IMDQ-NCL-NG as well as empty ND-NG (control) in PBS. Note that NCL-NG disassemble upon preparation into fully soluble unimers.

4.2 IMDQ quantification via ^{1}H NMR analysis

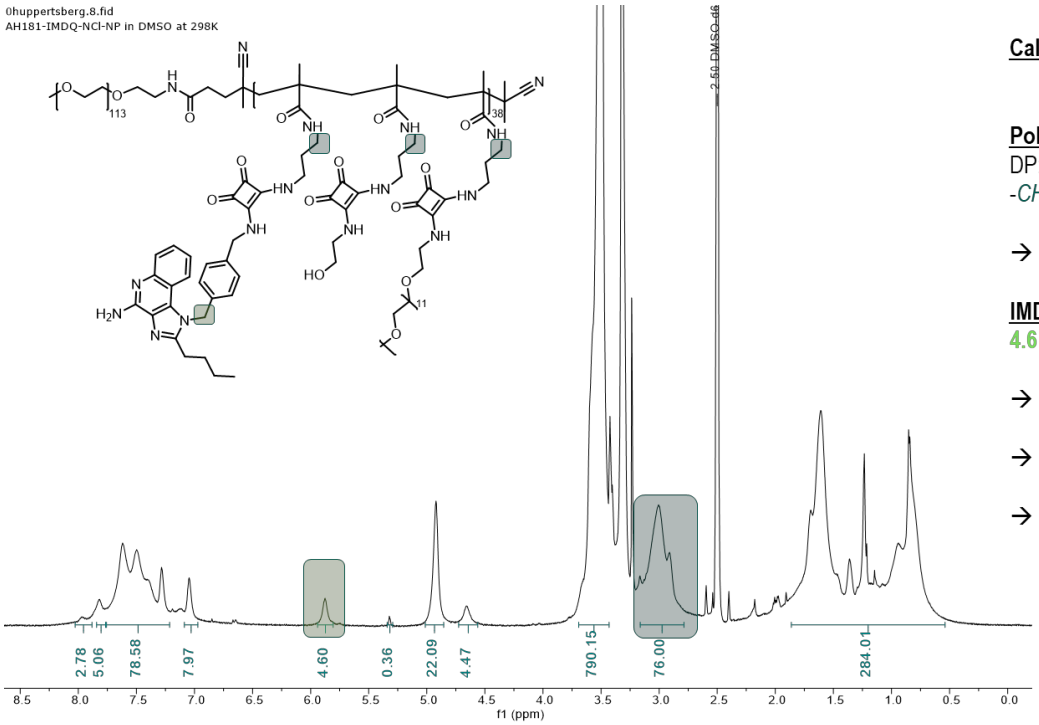

Calculation:

Polymer:
DP: 38
-CH_2-NH-CO-C-: 2 H

→ 2H * 38 = **76 H**

IMDQ:
4.6 H ≙ 2 H of -Bn-CH_2-N-

→ 2.3 IMDQ / polymer

→ (2.3 * 359 g/mol) / 30.400 g/mol

→ = **2.7 w%**

Figure S 52: ^{1}H NMR spectrum of IMDQ-NCL-NG in DMSO-d_6.

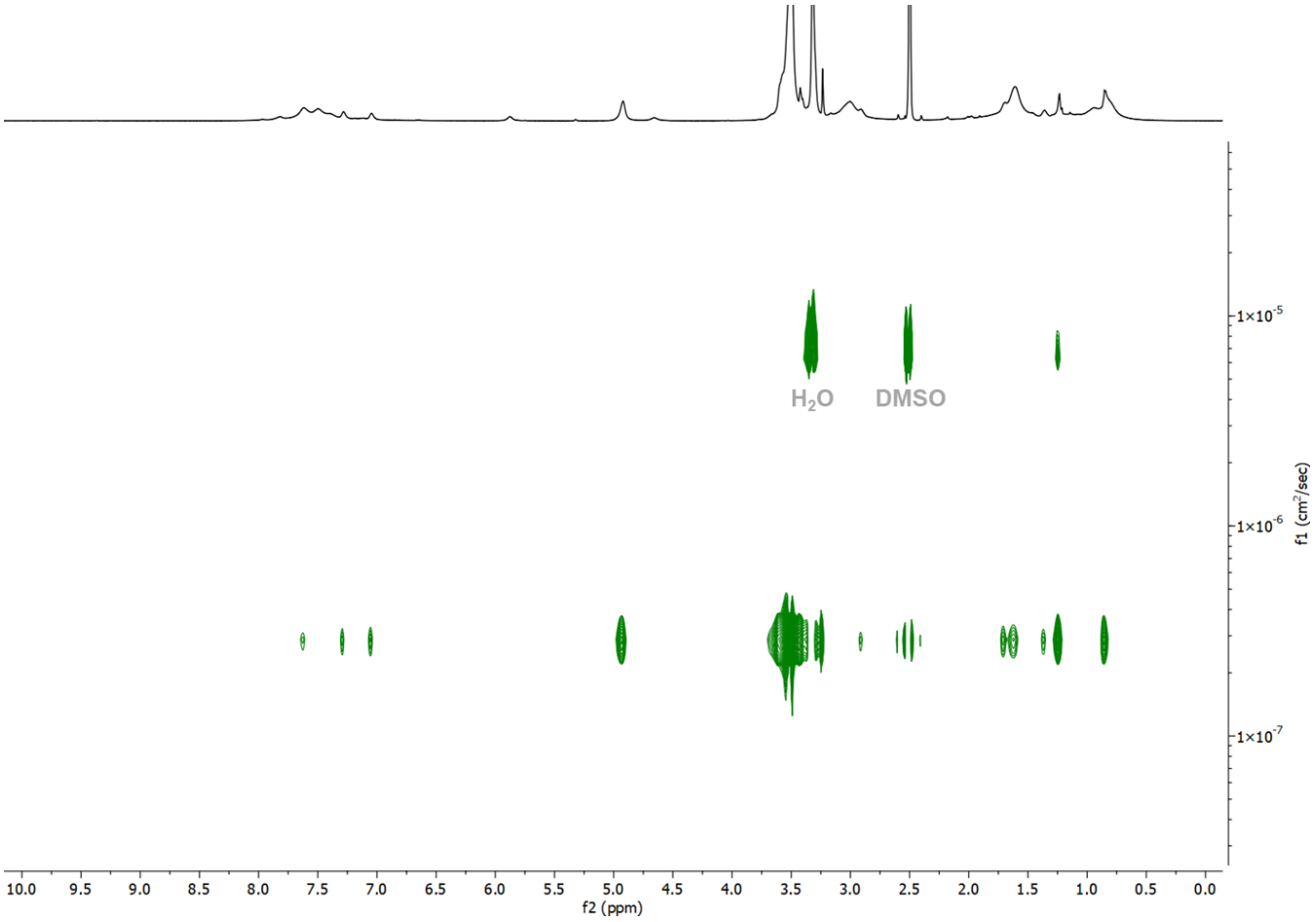

Figure S 53: DOSY spectrum of IMDQ-NCL-NG in DMSO-d_6.

4.3 Degradation/hydrolysis study of ketal-crosslinked nanogels

To investigate the degradability of the nanogels 50 mM acetate buffer (pH 5.2) was used. The lyophilized nanogels were re-dispersed directly in acetate buffer at 10.0 mg/mL followed by 5 min ultrasonication, subsequently DLS measurements were performed at 25 °C every 30 min for 24 h. To further evaluate stability at neutral pH nanogels were also re-dispersed in PBS and DLS measurements were conducted analogously.

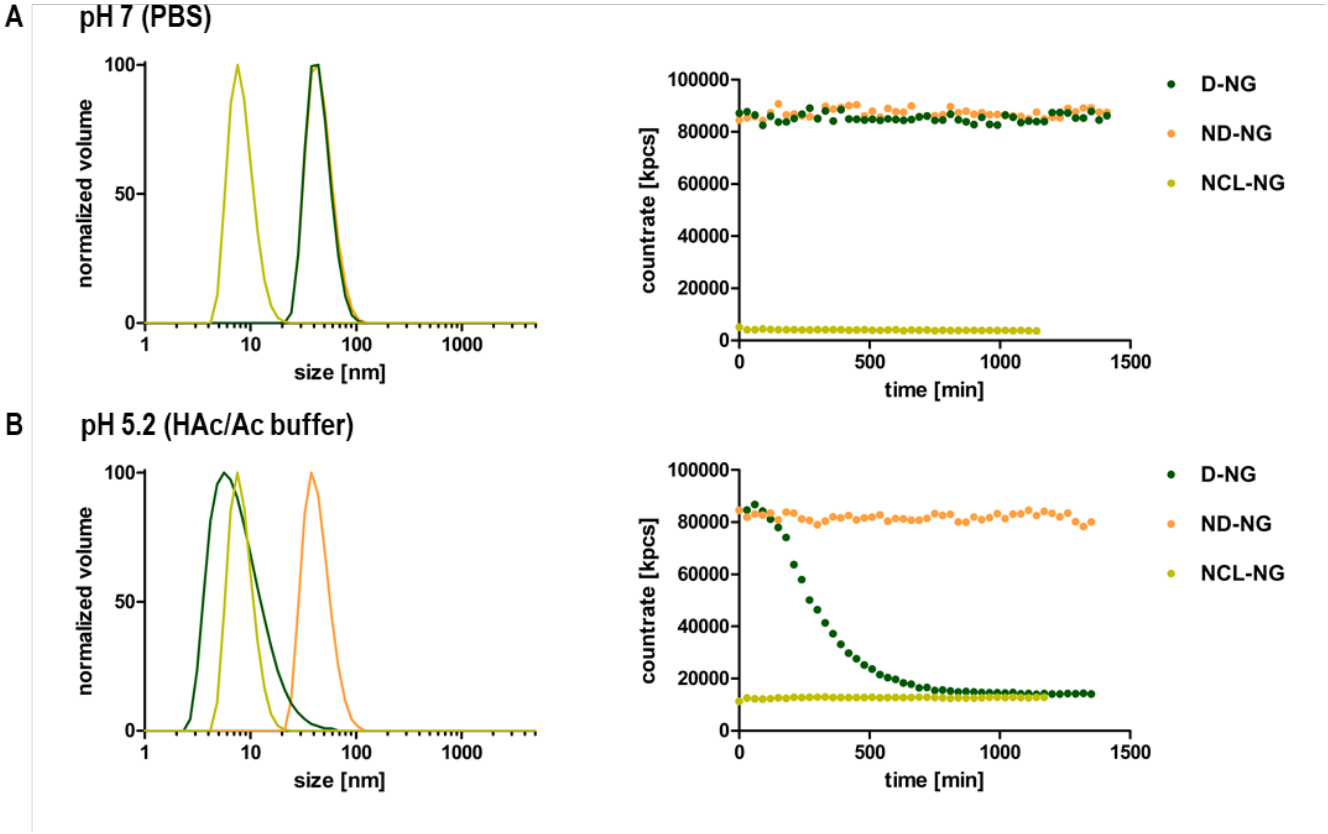

Figure S 54: DLS study of D-NG, ND-NG and NCL-NG (A) at neutral pH in PBS compared to (B) mildly acidic pH in HAc/Ac buffer. DLS count rate over time (left) and size distribution (right).

5. *In Vitro* Experiments

5.1 Cell culturing

RAW-Blue macrophages were cultured in Dulbecco's modified Eagle's medium (DMEM) supplemented with 10% fetal bovine serum, 1% penicillin/ streptomycin, 2 mM L-glutamine, 1 mM sodium pyruvate, and 0.01% zeocin at 37 °C with 5% CO_2 saturation.

5.2 Cell uptake experiment in RAW Blue-macrophages using confocal fluorescence microscopy

RAW-Blue macrophages were seeded on Willco-Dish glass bottom dishes (250 000 cells in 950 µL of culture medium) and incubated overnight. Next, cells were pulsed with 50 µL of a 2 mg/mL tetramethylrhodamine cadaverine-labeled nanogels (D-NG or ND-NG) or polymer solution (NCL-NG) in PBS (yielding a total nanogel/polymer concentration of 100 µg/mL) followed by incubation for 4 h and 24 h. Afterwards, culture medium was aspirated, and cells were washed two times with PBS. Next, 500 µL of 4% paraformaldehyde was added and allowed to fixate for 30 min at 37 °C. A staining solution was prepared by adding cholera toxin B (CTB)- AF488 (10 µL of a 1 mg/mL stock in PBS) and Hoechst 33258 (20 µL of a 1 mg/mL stock in PBS) to a PBS buffer containing 1% of BSA (2 mL). After aspiration and washing, 500 µL of this staining solution was added to the fixed cells and incubated for 30 min at 37 °C. Finally, cells were washed and stored in 1 mL PBS containing 1% of BSA. Confocal microscopy images were recorded by DMI6000 microscope purchased from Leica (Wetzlar, Germany) with a 1.40 NA 63x oil immersion objective, coupled to an Andor DSD2 scanner system. Images were processed by ImageJ software package.

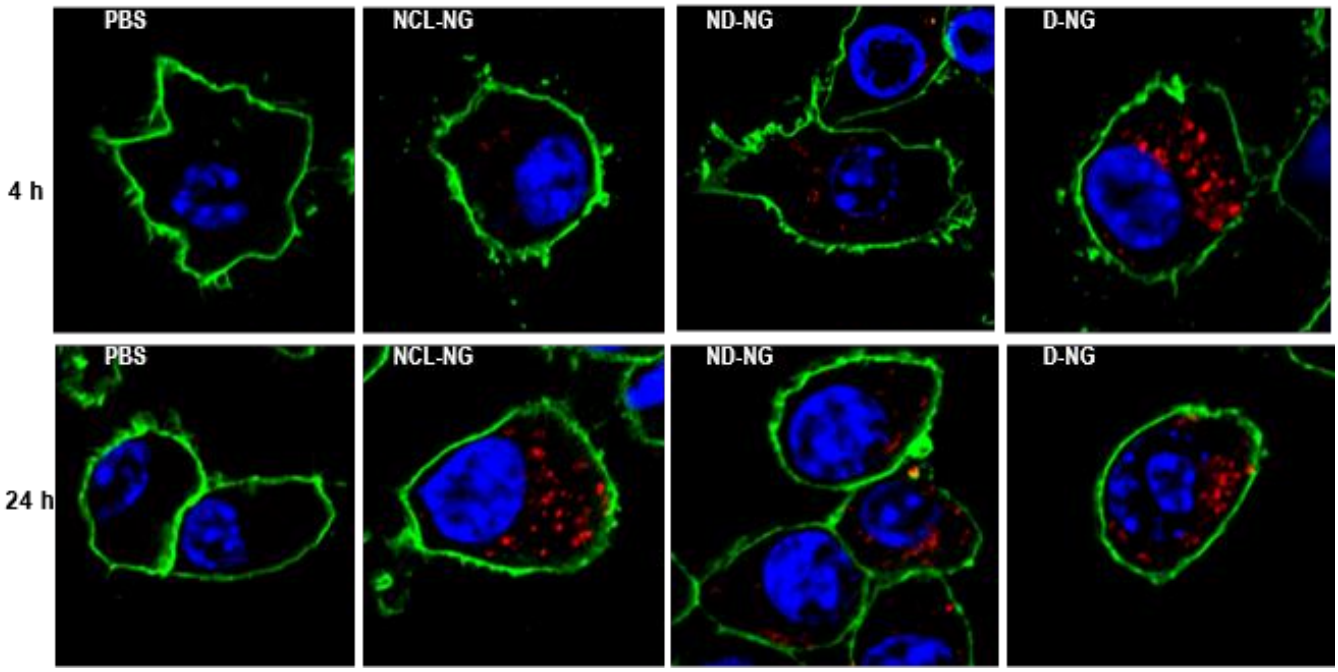

Figure S 55: Confocal microscopy images of RAW Blue macrophages incubated with PBS (control), NCL-NG, ND-NG, or D-NG at 100 µg/mL for 24 h (blue: nuclei stained with Hoechst 33258; green: cell membrane stained with cholera toxin B (CTB)- AF488; red: nanogel samples labeled with tetramethylrhodamine (TMR)).

5.3 Flow cytometry (FACS)

RAW-Blue macrophages were seeded into 24-well titer plates (250 000 cells per well in 950 µL of culture medium) and incubated overnight to allow cell sedimentation and subsequent adhesion to the bottom of the wells. Next, cells were incubated with 50 µL of tetramethylrhodamine-labeled nanogel (D-NG and ND-NG) or polymer solution (NCL-NG) in PBS (yielding a total nanogel/polymer concentration of 10 µg/mL, 50 µg/mL or 100 µg/mL). All samples were run in triplicate (n = 3) and the experiment was conducted for 24 h at 37°C. Cell culture medium was then aspirated, and cells were washed with 1 mL of PBS and incubated with 250 µL of Cell dissociation buffer (15 min, 37°C). The cell suspensions were then diluted with 750 µL of cell culture medium, transferred into Eppendorf tubes and centrifuged immediately (350*g*, 10 min, 5°C). Finally, the supernatant was aspirated, and the cell pellets were suspended in 250 µL of PBS. They were kept on ice to maintain cell integrity prior to flow cytometric analysis performed on a BD Accuri C6 (BD Biosciences). The data was processed by FlowJo software.

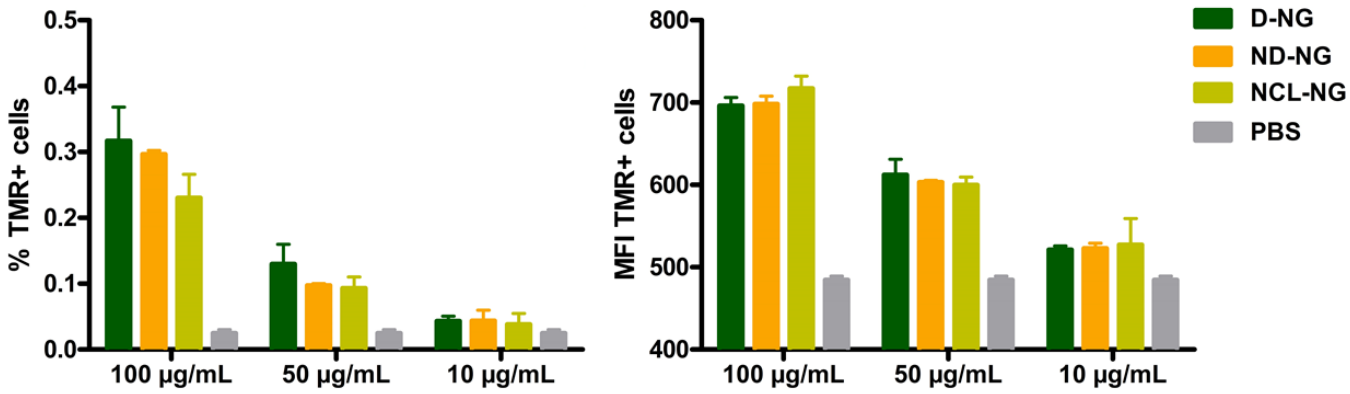

Figure S 56: Flow cytometry analysis revealing percentage of cells positive for tetramethylrhodamine (%TMR+ cells) and mean cellular fluorescence intensity (MFI) of RAW Blue macrophages incubated with tetramethylrhodamine-labeled D-NG, ND-NG, NCL-NG at 100, 50, and 10 µg/mL or PBS as control for 24 h.

5.4 Cellular metabolic activity of RAW-Blue macrophages using MTT assay

Cellular metabolic activity as indicator of cell viability, proliferation and cytotoxicity was determined after incubation of RAW-Blue Macrophages with IMDQ-loaded nanogels using a colorimetric MTT assay. Each well containing RAW-Blue macrophages was treated with IMDQ-loaded or empty nanogels at given concentrations. After 24 h 25 µL of 3-(4,5-dimethylthiazol-2-yl)-2,5-diphenyltetrazolium bromide (MTT, 2 mg/mL in PBS) was added, respectively, before the macrophages were incubated at 37 °C for 1.5 h. To dissolve the formed formazan crystals, 100 µL of 10% SDS (m/v)/0.01 M HCl was added to each well followed by incubation at 37 °C overnight. Cellular metabolic activity was determined in relation to positive (PBS blank, 100% activity) and negative (10% DMSO, 0% activity) control samples based on absorbance measurements at 570 nm. Experiments were performed in quadruplicate (n = 4).

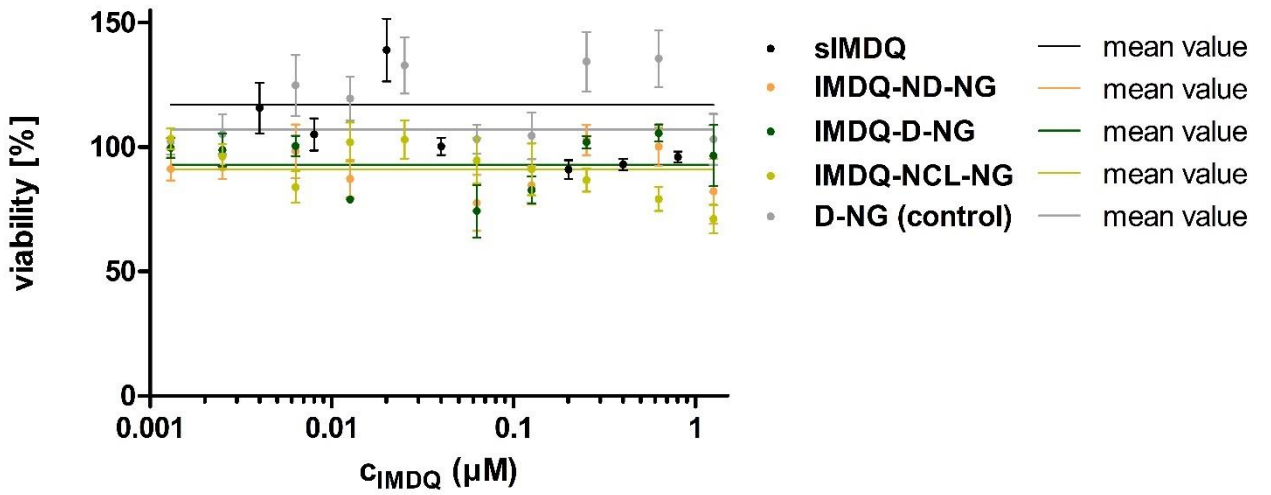

Figure S 57: MTT Assay indicating cell viability of RAW-Blue macrophages treated with sIMDQ, IMDQ-D-NG, IMDQ-ND-NG, IMDQ-NCL-NG and D-NG (control) (n = 4).

5.5 RAW-Blue macrophage TLR reporter assay

To compare the immune-modulatory properties of prepared IMDQ-loaded nanogels with the free drug (sIMDQ) *in vitro* TLR receptor stimulation was analyzed by RAW-Blue Macrophage reporter assay. Therefore, NF-κB/AP-1 activation following TLR receptor stimulation was detected by secreted embryonic alkaline phosphatase (SEAP) as proposed by the manufacturer InvivoGen. RAW-Blue cells were seeded into 96-well plates (90,0000 cells/well in 180 µL culture medium) and allowed to adhere overnight. The next day, 20 µL of IMDQ-loaded nanogel or control samples (sIMDQ, empty NG) was added to each well at given final concentrations. After 24 h or 48 h incubation at 37 °C, 50 µL supernatant of each well was collected and transferred into another 96-well plate. Subsequently, levels of SEAP were quantified by QUANTI-Blue Assay. After addition of 150 µL QUANTI-Blue solution, samples were incubated at 37 °C for 2 h. Detection of optical density at 620 nm with a plate reader determined SEAP levels. An increase in optical density relative to the negative control (PBS treated) declared TLR receptor stimulation. All experiments were performed in quadruplicate (n=4).

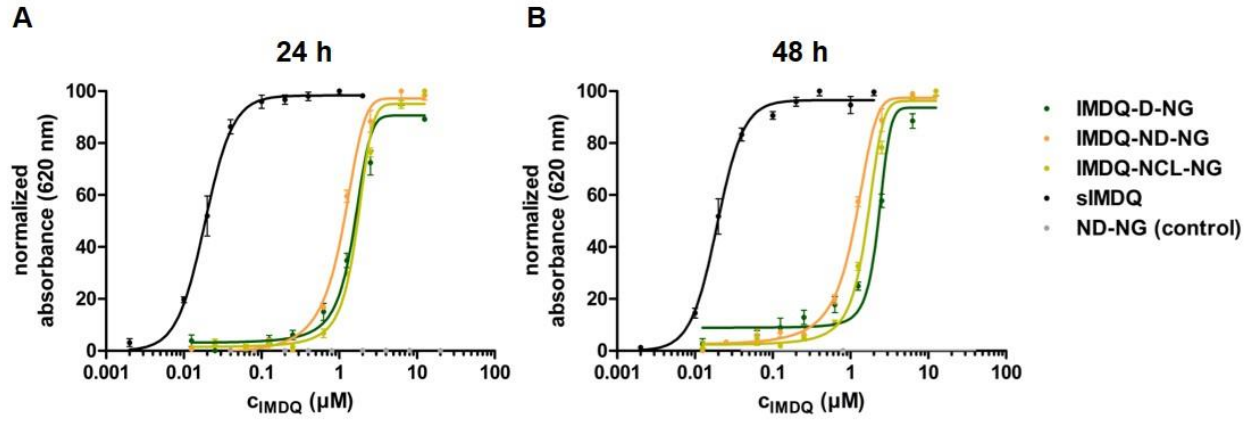

Figure S 58: RAW-Blue Assay indicating TLR stimulation of RAW-Blue macrophages incubated (A) for 24 h or (B) for 48 h with sIMDQ, IMDQ-D-NG, IMDQ-ND-NG, IMDQ-NCL-NG and ND-NG (control) (n = 4).

6. *In Vivo* Experiments

6.1 Biodistribution imaging of 800RS-labeled nanogels

The conducted animal study followed an approval by the local ethics committee on animal care (number 23 177-07/G 17-1-030, Government of Rhineland Palatinate, Germany). 8–10 week-old female BALB/c mice (body weight ~20–25 g) were obtained from Charles River (Sulzfeld, Germany) and kept according to the guidelines of the institute and the local government (12 h light-dark cycles at 25 °C and 40–60% humidity with humane care, access to regular chow and water ad libitum). To investigate the biodistribution of the nanogels 100 µL of 800RS-labeled nanogels (2 mg/mL in PBS) were injected intravenously into Balb/c mice (n = 3, two mice treated with PBS served as control). Prior to injection mice were anesthetized with isoflurane gas and treated *via* tail vein injection with the nanogels. After 24 h, mice were again anesthetized with isoflurane gas and transferred into an IVIS (*in vivo* imaging spectrum) system (Caliper Life Sciences, Hopkinton, MA, USA) for *in vivo* NIR fluorescence imaging. Picture integration time of the fluorescence source was set to 4 s. Recording parameters were set for excitation at 745 nm and emission at 800 nm to visualize the near infrared dye RS800 labeled nanogels. Afterwards, mice were sacrificed, and organs were harvested and put again into the imaging chamber for *ex vivo* signal quantification using Live Image software from PerkinElmer (Waltham, MA, USA). Organs were carefully circumscribed by region-of-interests (ROIs), and then their fluorescence was quantified as the average of area-normalized radiant efficiency.

6.2 Bioactivity imaging of IMDQ-loaded nanogels

To study the immune-stimulating effect of IMDQ-loaded nanogels, heterozygous BALB/c IFN-β (IFN-$\beta^{+/\Delta\beta\text{-luc}}$) reporter mice in the range of 7−9 weeks were housed in individual ventilated cages and given ad libitum access to food and water. The mice were subjected to intravenous injection of 5 µg IMDQ (soluble or bound to nanogel in 100 µL of PBS) *via* tail vein injection (n = 3, a mouse treated with PBS served as control). For subsequent *in vivo* bioactivity imaging, mice were injected subcutaneously with 200 µL D-luciferin (15 mg/mL, Gold Biotechnology, USA) at the given time points (0, 4, 24, and 48 h post injection), and *in vivo* luminescence imaging was recorded 12 min later using the IVIS Lumina II imaging system from PerkinElmer, (Waltham, MA, USA). Photon flux was analyzed by Living Image 4.4 software from Caliper life sciences (Hopkinton, MA, USA).

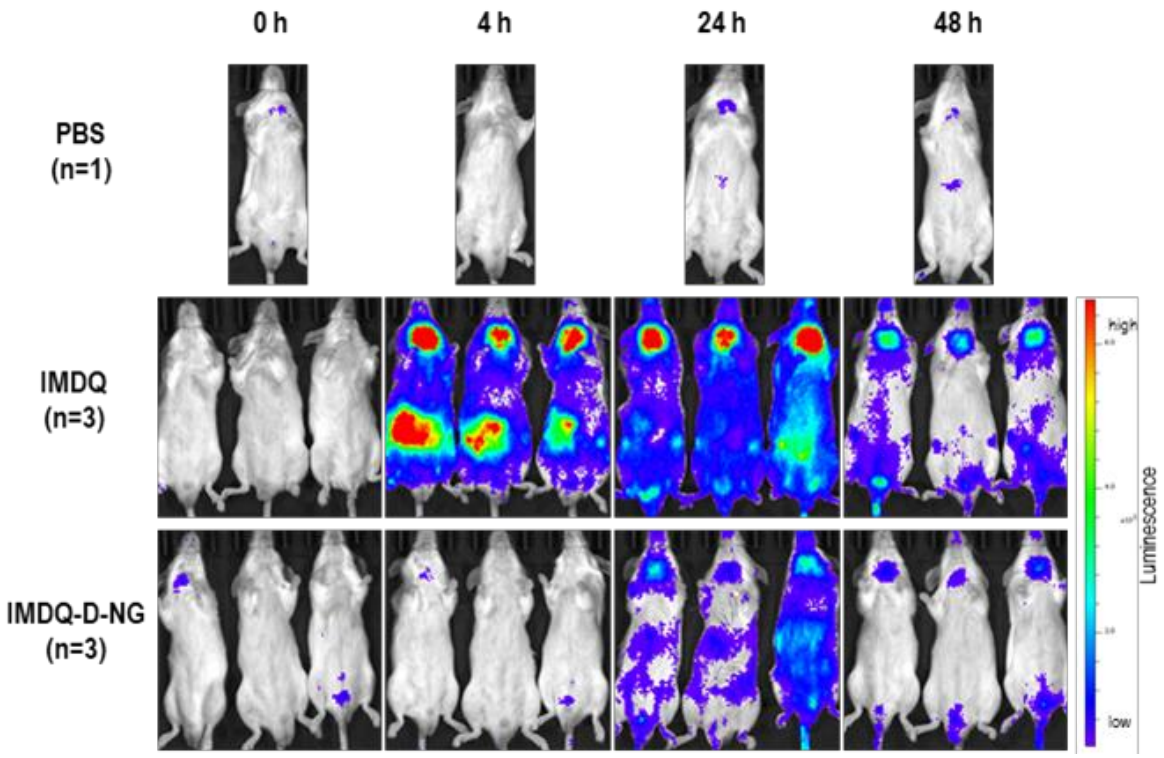

Figure S 59: In vivo bioactivity of soluble and nanogel bound IMDQ (IMDQ and IMDQ-D-NG) after intravenous. injection into heterozygous BALB/c IFN-β (IFN-β$^{+/\Delta\beta\text{-luc}}$) reporter mice (n = 3).

6.3 Flow cytometry analysis of splenic innate immune activation

Heterozygous BALB/c IFN-β (IFN-β$^{+/\Delta\beta\text{-luc}}$) reporter mice were intravenously injected with 5 µg IMDQ (soluble or bound to nanogel in 100 µL of PBS, n = 3) were sacrificed after 48 h and spleens where isolated for flow cytometry analysis. A single cell suspension was prepared form the dissected organ for analysis by flow cytometry. Isolated splenocytes were collected in ice cold PBS, smashed through 70 µm cell strainers, washed with PBS and stained for 30min at 4°C with a live-dead stain and the following primary labeled monoclonal antibodies: CD3e, CD11c, CD11b, CD19, CD69, CD80, CD86, F4-80, Ly-6G, and MHC-II. 123count ebeads were added to determine cellularity prior to acquiring them on by flow cytometry (BD FACS Aria). Analyses were done using the FlowJo software package according to the following gating procedure.

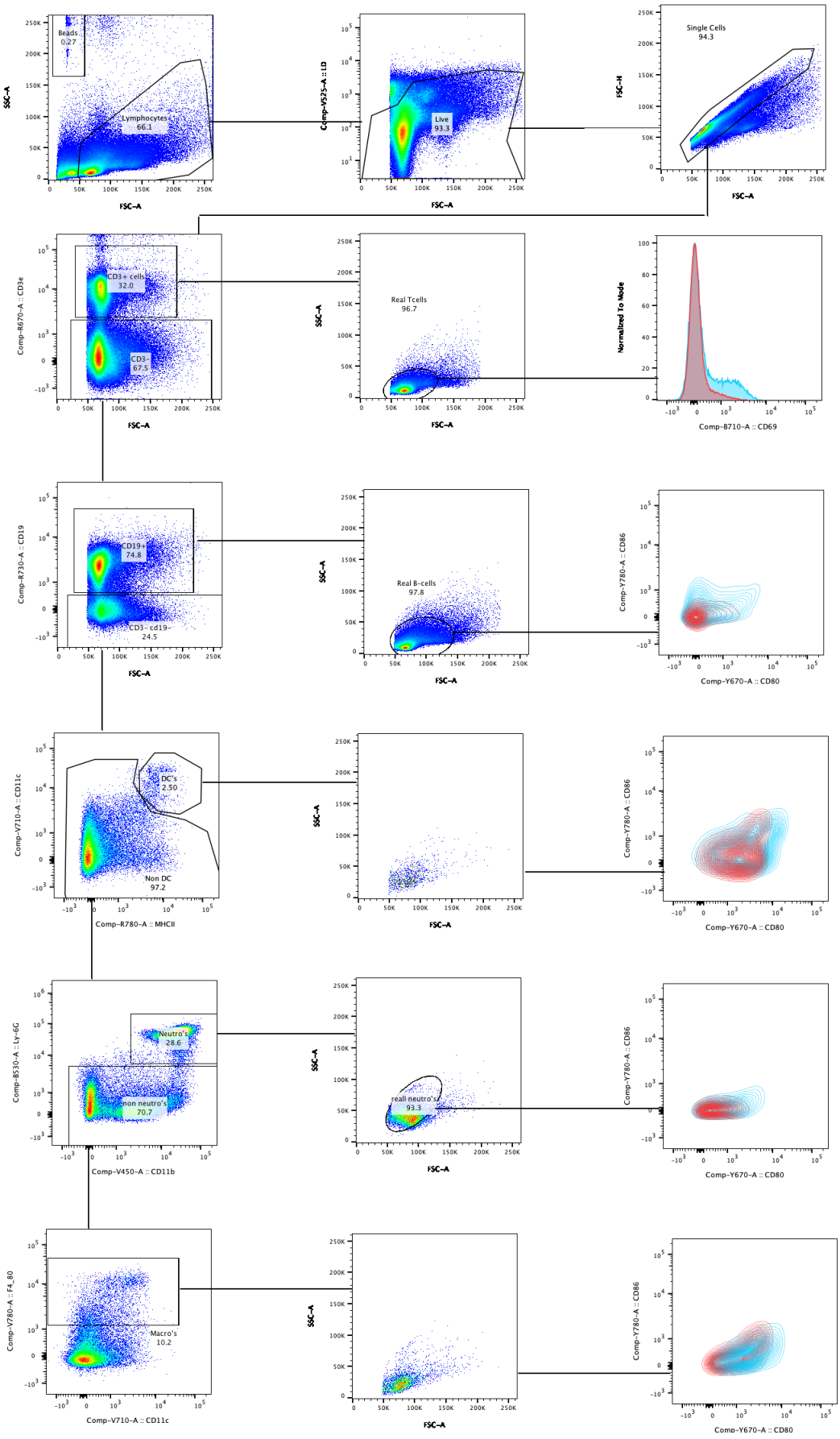

Figure S 60: Gating procedure for flow cytometry analysis of splenic innate immune activation.

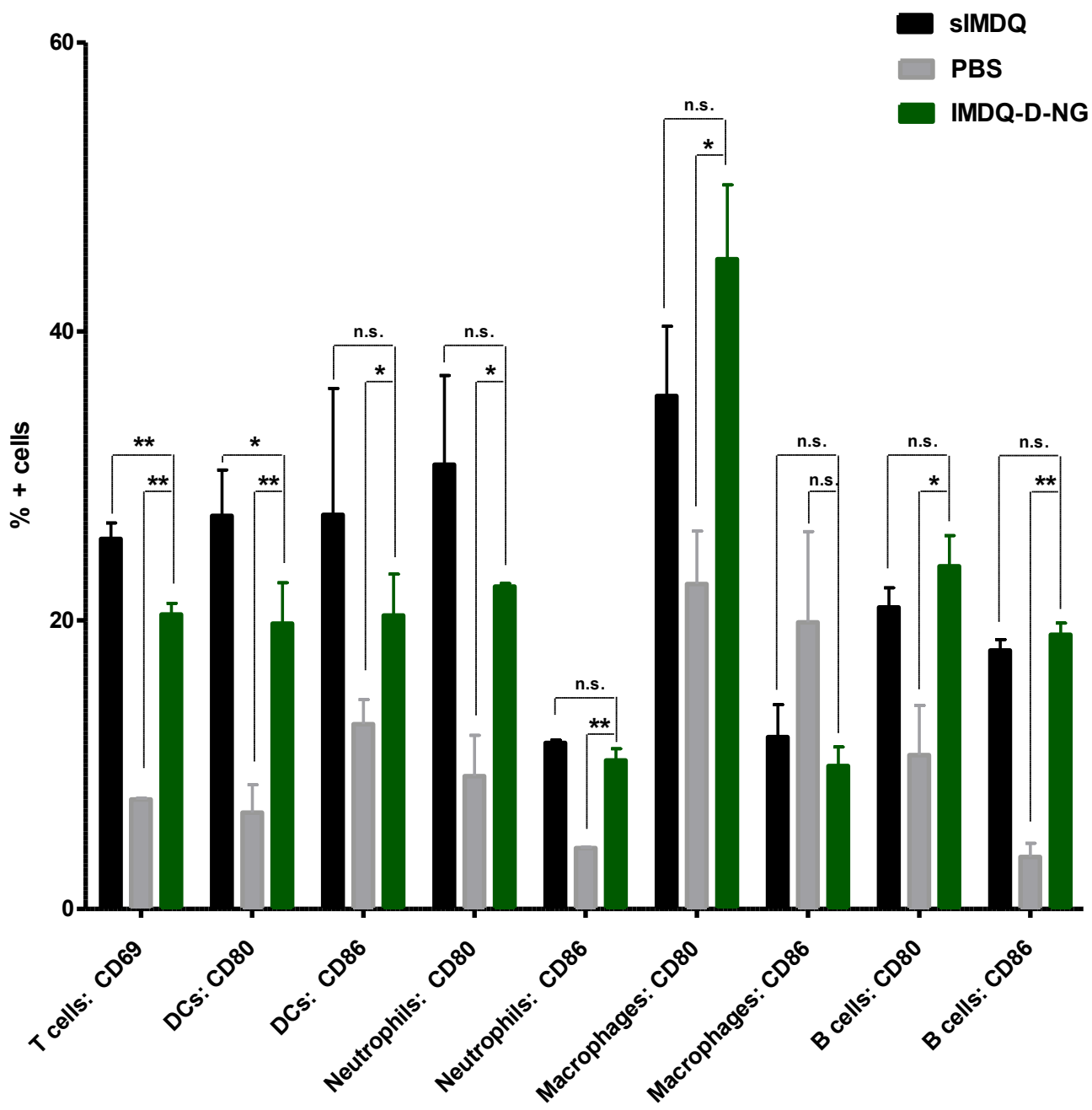

Figure S 61: Percentage of immune activation marker positive cells in the respective immune cell subpopulation (CD69 for T cells and CD80/CD86 for DCs, neutrophils, macrophages, and B cells) according to the gating procedure above.

6.4 Acute toxicity studies

To investigate acute *in vivo* toxicity BALB/c mice were intravenously injected with 5 µg of soluble or nanogel bound IMDQ (n = 4, 100 µL of sIMDQ (0.05 mg/mL in PBS) or IMDQ-D-NG (2 mg/mL in PBS), PBS served as control). After 4 or 24 h, mice were sacrificed and blood was retrieved by heart puncture to determine the serum contents for aspartate aminotransferase (AST), alanine aminotransferase (ALT), glutamate hydrogenase (GLDH), lipase (LIP), and blood urea by nitrogen content (BUN). The parameters were measured by the central laboratory of the University Medical Center of Mainz. The remaining sera were diluted 1:4 and stored at -20°C. Cytokine concentrations for TNF-α, IFN-γ and IL-6 were determined by cytometric bead assay (CBA; BD Biosciences, San Jose, CA) as recommended by the manufacturer. For that purpose, bead populations with distinct fluorescence intensities were conjugated with cytokine-specific capture antibodies. Recombinant cytokines were used to prepare standard dilutions. Samples were mixed with capture beads, subsequently incubated with PE-conjugated detection antibodies for 1 h (at room temperature in the dark), and subjected to flow cytometric analysis. Results were analyzed using FCAP Array Analysis Software v.1.0.1 (BD Biosciences).

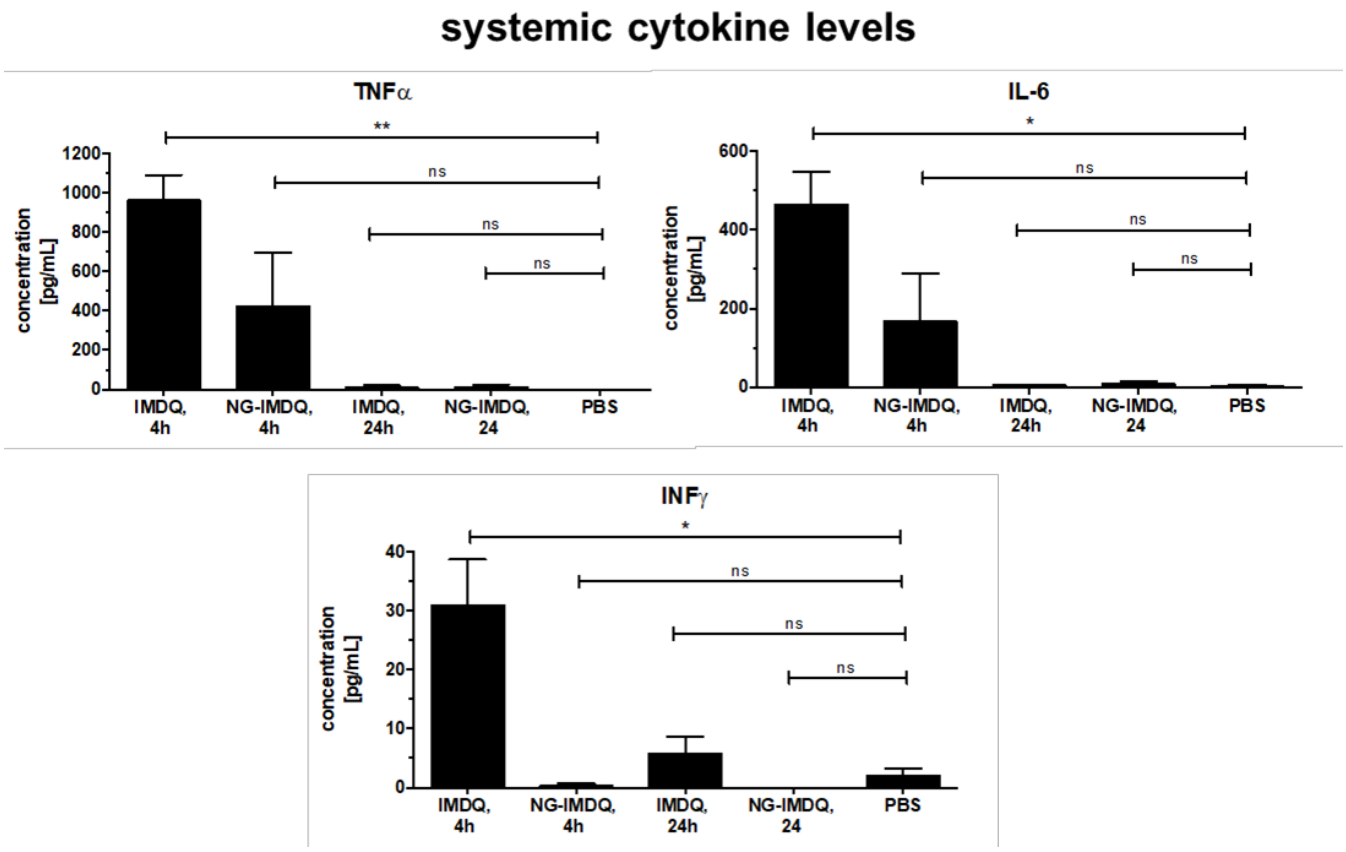

Figure S 62: Serum cytokine levels of mice treated with 5 µg soluble or nanogel bound IMDQ (n = 4).

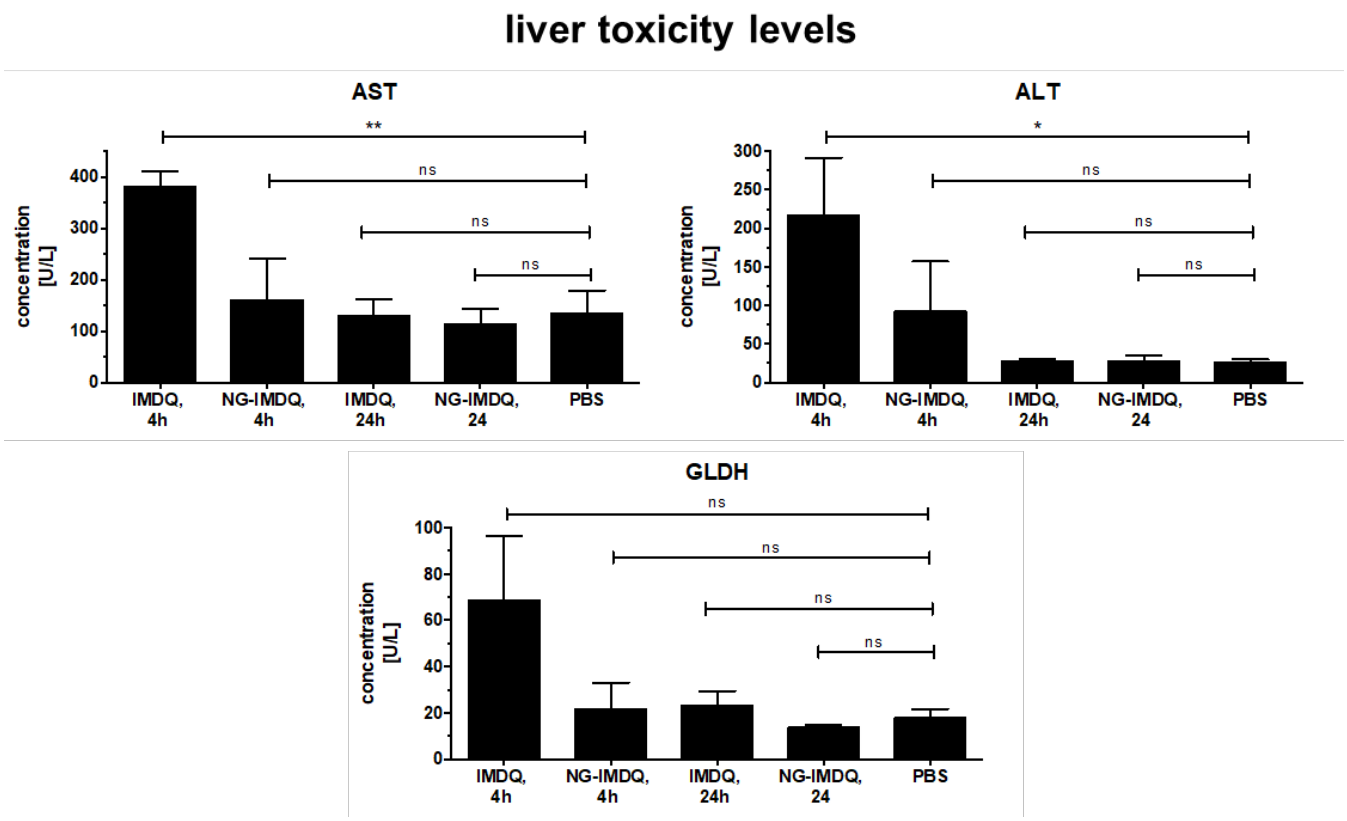

Figure S 63: Liver enzyme serum activities of mice treated with 5 µg soluble or nanogel bound IMDQ (n = 4).

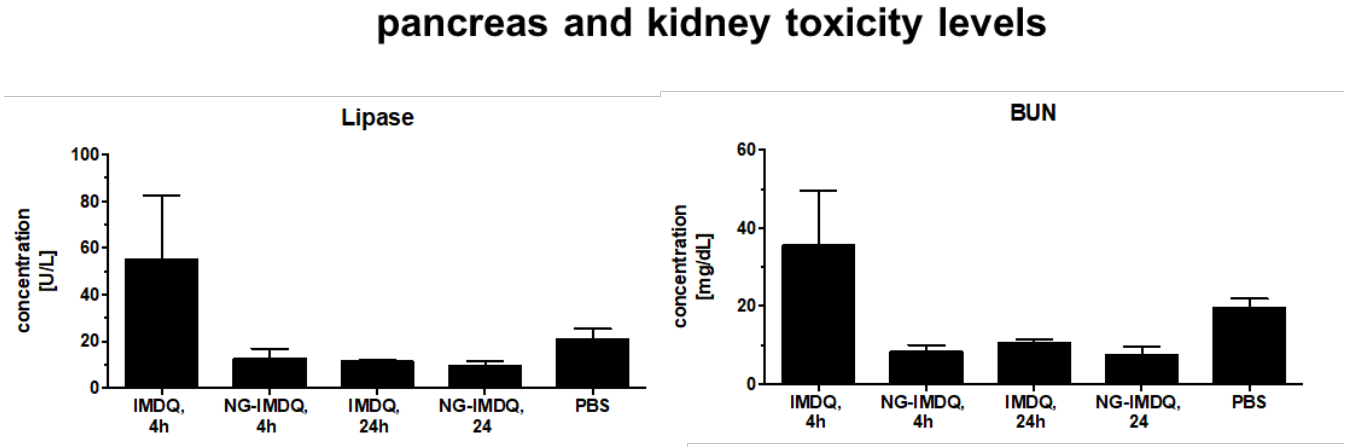

Figure S 64: Pancreas lipase serum activity and kidney toxicity related blood urea nitrogen (BUN) concentration of mice treated with 5 µg soluble or nanogel bound IMDQ (n = 4).

7. Statistical analysis

Data are shown as mean values + standard deviation. To calculate statistical significance of the mean values, unpaired Student's t-test with Welch's correction was performed using Graph Pad Prism 8 software (*: $p \leq 0.05$; **: $p \leq 0.01$; ***: $p \leq 0.001$).

10.4. Publication 4

"Density of conjugated antibody determines the extent of Fc receptor dependent capture of NP by liver sinusoidal endothelial cells"

This study has been published in ACS Nano (ACS Publications). As a co-author, I was mainly responsible for the biological evaluation of polysarcosine-based peptobrushes (PBs) in several *in vitro* and *in vivo* experiments, including uptake and activation tests of the peptobrushes in different immune cell populations, followed by biodistribution and ex vivo imaging on organ level. In this work, we asked whether the number of cell-targeting antibodies per NP determined the extent of NP accumulation in the liver. We also addressed the mechanisms by which antibody-coated NPs were retained in this organ. For this, we used polysarcosine-based peptobrushes (PBs) conjugated with defined numbers (2, 6, and 12) of antibodies specific for the DC surface receptor DEC205. We assessed the time-dependent biodistribution of PB–antibody conjugates by *in vivo* imaging and flow cytometry. We observed that the extent of liver accumulation of PB-antibody conjugates strongly correlated with the number of attached antibodies. PB–antibody conjugates were selectively captured in the liver *via* Fc receptors (FcR) on liver sinusoidal endothelial cells (LSECs), since systemic administration of FcR-blocking agents or the use of $F(ab')_2$ fragments of the DEC205 antibody for PB conjugation prevented liver accumulation. Our study revealed a novel role for LSECs in capturing antibody-coated NPs in the liver. Low antibody numbers on NPs and $F(ab')_2$ fragments were key for specific targeting of secondary lymphoid organs, minimizing undesired liver accumulation.

DOI: 10.1021/acsnano.1c05713
Published in: *ACS Nano.* **2021**, 15, 9, 15191–15209
Reprinted with permission from [Cinja Kappel, Christine Seidl, **Carolina Medina-Montano**, Meike Schinnerer, Irina Alberg, Christian Leps, Julian Sohl, Ann-Kathrin Hartmann, Michael Fichter, Michael Kuske, Jenny Schunke, Gabor Kuhn, Ingrid Tubbe, David Paßlick, Dominika Hobernik, Rebekka Bent, Katharina Haas, Evelyn Montermann, Kerstin Walzer, Mustafa Diken, Manfred Schmidt, Rudolf Zentel, Lutz Nuhn, Hansjörg Schild, Stefan Tenzer, Volker Mailänder, Matthias Barz, Matthias Bros, and Stephan Grabbe. *ACS Nano* **2021** *15* (9), 15191-1520]. Copyright [2023] American Chemical Society.

ACSNANO

www.acsnano.org

ARTICLE

Density of Conjugated Antibody Determines the Extent of Fc Receptor Dependent Capture of Nanoparticles by Liver Sinusoidal Endothelial Cells

Cinja Kappel, Christine Seidl, Carolina Medina-Montano, Meike Schinnerer, Irina Alberg, Christian Leps, Julian Sohl, Ann-Kathrin Hartmann, Michael Fichter, Michael Kuske, Jenny Schunke, Gabor Kuhn, Ingrid Tubbe, David Paßlick, Dominika Hobernik, Rebekka Bent, Katharina Haas, Evelyn Montermann, Kerstin Walzer, Mustafa Diken, Manfred Schmidt, Rudolf Zentel, Lutz Nuhn, Hansjörg Schild, Stefan Tenzer, Volker Mailänder, Matthias Barz,* Matthias Bros,* and Stephan Grabbe*

Cite This: https://doi.org/10.1021/acsnano.1c05713

Read Online

ACCESS | Metrics & More | Article Recommendations | Supporting Information

Downloaded via UNIV MAINZ on August 26, 2021 at 11:38:38 (UTC).
See https://pubs.acs.org/sharingguidelines for options on how to legitimately share published articles.

ABSTRACT: Despite considerable progress in the design of multifunctionalized nanoparticles (NPs) that selectively target specific cell types, their systemic application often results in unwanted liver accumulation. The exact mechanisms for this general observation are still unclear. Here we asked whether the number of cell-targeting antibodies per NP determines the extent of NP liver accumulation and also addressed the mechanisms by which antibody-coated NPs are retained in the liver. We used polysarcosine-based peptobrushes (PBs), which in an unmodified form remain in the circulation for >24 h due to the absence of a protein corona formation and low unspecific cell binding, and conjugated them with specific average numbers (2, 6, and 12) of antibodies specific for the dendritic cell (DC) surface receptor, DEC205. We assessed the time-dependent biodistribution of PB−antibody conjugates by *in vivo* imaging and flow cytometry. We observed that PB−antibody conjugates were trapped in the liver and that the extent of liver accumulation strongly increased with the number of attached antibodies. PB−antibody conjugates were selectively captured in the liver *via* Fc receptors (FcR) on liver sinusoidal endothelial cells, since systemic administration of FcR-blocking agents or the use of $F(ab')_2$ fragments prevented liver accumulation. Cumulatively, our study demonstrates that liver endothelial cells play a yet scarcely acknowledged role in liver entrapment of antibody-coated NPs and that low antibody numbers on NPs and the use of $F(ab')_2$ antibody fragments are both sufficient for cell type-specific targeting of secondary lymphoid organs and necessary to minimize unwanted liver accumulation.

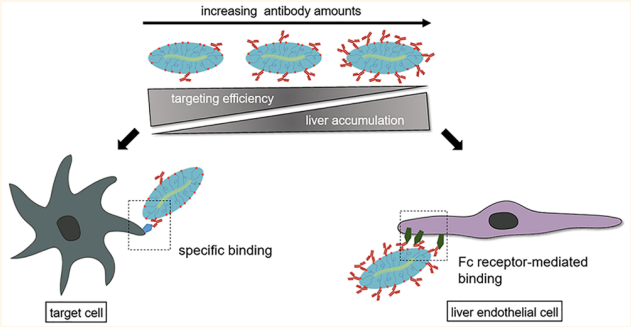

KEYWORDS: *nanoparticle, antibody, targeting, biodistribution, liver accumulation, liver endothelial cells, polypept(o)ides*

INTRODUCTION

During the last 40 years, nanoparticles (NPs) have evolved as carrier systems for tissue- and cell type-directed drug delivery to reduce adverse effects of active pharmaceutical ingredients.[1] However, the efficacy at which systemically applied NPs deliver drugs to specific cell types *in vivo* is still far from optimal.[2] The first generation of NPs developed for tumor targeting, *e.g.*, Doxil, exploited passive accumulation within solid tumors by the enhanced permeability and retention (EPR) effect.[3] More recently, NP-mediated targeting of immune cells in order to induce immunity against tumors[4] or pathogens[5] has attracted increasing interest,[6] since immune cells within blood or lymphoid organs are more easily

Received: July 6, 2021
Accepted: August 3, 2021

ACS Publications

© XXXX The Authors. Published by American Chemical Society

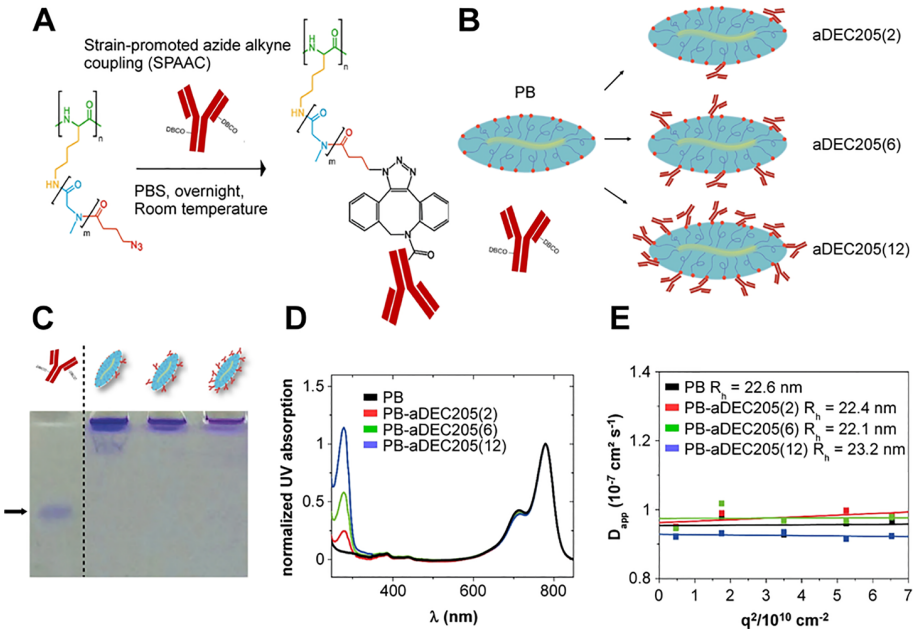

Figure 1. Synthesis and characterization of PB−antibody conjugates: (A) Scheme of strain-promoted azide−alkyne cycloaddition (SPAAC) reaction employed for antibody conjugation; (B) schematic illustration of PB−aDEC205 antibody conjugates; (C) SDS-PAGE electrophoresis to control for contaminating free Ab within the PB conjugates (lane 1: nonconjugated aDEC205 antibody (band indicated by arrow), lanes 2−4 PB−aDEC205 antibody conjugates); (D) UV−vis analysis of the effectivity of antibody conjugation; (E) multiangle DLS analysis of PB−aDEC205 antibody conjugates.

accessible by systemically applied NPs.[7] Myeloid cells, such as macrophages (Mphs) and dendritic cells (DCs), that are specialized to recognize nanosized pathogens[8] were shown to internalize synthetic NPs spontaneously and after complement- or immunoglobulin-mediated opsonisation.[9,10] Mphs degrade and internalize material more efficiently than DCs, whereas DCs potently process pathogen-derived antigens and present them to T cells as a necessary step to induce antigen-specific T cell responses for induction of immunity or tolerance.[11] Therefore, the design of NPs that actively target DCs to minimize unwanted binding/uptake by Mphs and other cell types with endocytic and phagocytic capacity is in the focus of research.[12]

Antibodies are the most widely used tools to selectively target NPs to certain cell types such as DCs. The attachment of several antibodies per NP increases the overall avidity, which may result in enhanced NP binding and uptake, suggesting that an increase in valency of targeting moieties may be a desirable goal of NP design.[13] However, it was also reported that lowered avidity can increase selectivity of cell-targeting NPs.[4] Commonly applied antibody conjugation strategies result in a nonoriented attachment of the antibody to the NP, where the constant Fc (fragment crystallizable) part may be exposed and can facilitate unwanted binding to Fc receptors (FcRs) that are widely expressed in the body.[15] Thus, novel strategies to minimize capture of NPs by nontarget cells are needed to improve target cell selectivity requires a more detailed understanding of underlying effects.[16] To assess cell-specific targeting, NPs that exert minimal unspecific binding and thus elongated plasma circulation times of 24 h and seem beneficial,[10] which continues to be a significant methodological problem. Moreover, it has been a synthetic challenge to generate NPs with a defined (average) antibody number[17] in a reproducible and scalable manner.[18] Thus, comparative studies on the biodistribution of antibody-decorated NPs so far mainly focused either on NP accumulation in distinct organs[19] or on target cell type-specific binding.[20]

Therefore, our study aimed to delineate the role of antibody number on stealth-like NPs for their biodistribution at organ and single-cell levels, the specificity of cell type targeting, and the mechanisms by which nontargeted cell types may compete for NP engagement. To this end, we employed polysarcosine-based cylindrical polymer brushes[21] with a circulation half-life of >24 h, due to the stealth-like nature of polysarcosine[22] that results in very low interaction with plasma proteins and cells *in vivo*.[23,24] NPs were conjugated with distinct average numbers of antibodies, namely, 2, 6, and 12, targeting the surface receptor DEC205 (CD205), a type I cell surface protein predominantly expressed by DCs.[25] Using these antibody-coated peptobrushes, we analyzed their biodistribution by *in vivo* and *ex vivo* imaging and flow cytometry of liver, spleen, and lymph node (LN) cells, generating detailed insight on organ and cellular distributions of NPs in relation to the number of antibodies attached to their surface.

RESULTS AND DISCUSSION

Polysarcosine-Based Peptobrushes Can Be Precisely Functionalized with Defined Numbers of Antibodies. For synthesis of the polysarcosine-based cylindrical brush polymers, termed peptobrushes (PBs),[26] the backbone $pLys_{250}$ was used as a macroinitiator for the controlled living ring-opening polymerization of sarcosine *N*-carboxy anhydride yielding polysarcosine side chains (Figure 1A). End group functionalization was performed by azido-butyric acid pentafluorophenylester to obtain a quantitative azide functionality allowing antibody conjugation by azide−alkyne coupling. The polysarcosine side chains provide a high biocompatibility and enzymatic and oxidative biodegradability of the PBs.[27]

https://doi.org/10.1021/acsnano.1c05713
ACS Nano XXXX, XXX, XXX−XXX

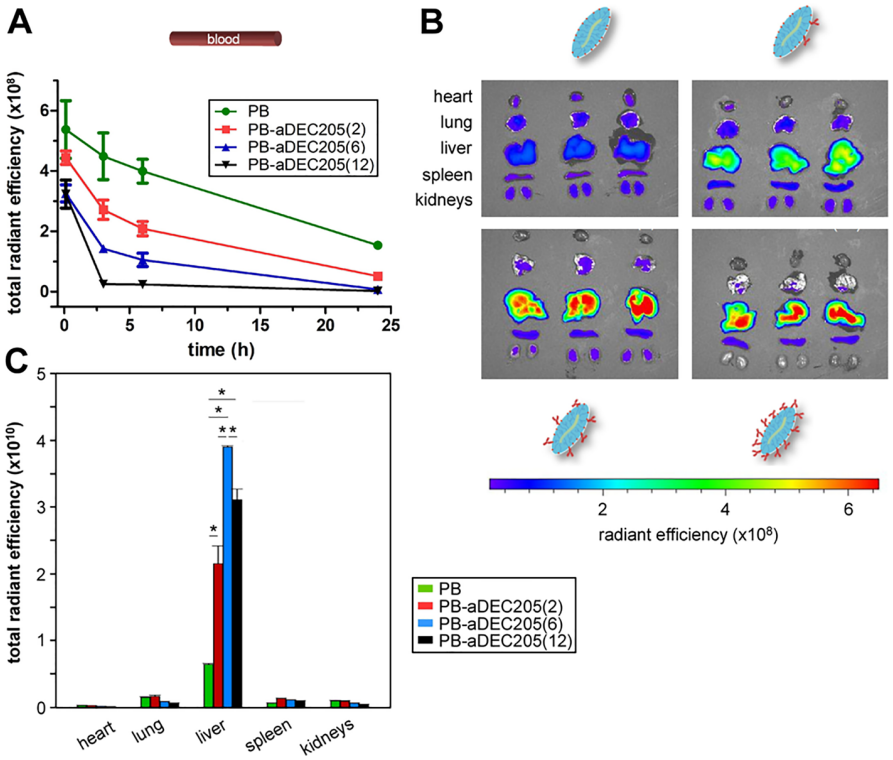

Figure 2. The extent of liver accumulation of systemically applied PB−antibody conjugates correlates with antibody density: (A−C) CW800-labeled PBs were systemically injected into mice. (A) Blood was retrieved at the time points indicated, and contents of PBs were quantified by measurement of fluorescence intensities. Data indicate the mean ± SEM of 3 samples per group and time point. (B) Fluorescence imaging of organs retrieved from mice treated with the various PBs at 24 hpi. (C) Quantification of organ-specific CW800 fluorescence (see B). Data denote the mean ± SEM of 6−8 samples per group (compiled from 2 to 3 experiments; one-way ANOVA, significance: *$p < 0.05$).

Furthermore, PBs of different sizes were shown to display long circulation half-lives of up to 7 days in zebrafish larvae.[28]

CD8α^+ conventional type 1 DCs (cDC1) are characterized by expression of the C-type lectin receptor DEC205 (CD205) and are capable of cross-presenting exogenous antigens *via* MHC-I to CD8$^+$ T cells.[29] We and others have previously shown that antigen targeted to DEC205 by specific antibodies results in endocytic uptake by DCs and efficient antigen presentation.[20,25] Therefore, to address DCs as a suitable target cell type for nanovaccines, we used an anti-DEC205 antibody (aDEC205) for conjugation with PBs. aDEC205 was modified with a DBCO linker to allow for chemoselective bioconjugation to azide groups on the peptobrush by strain-promoted azide−alkyne cycloaddition (SPAAC), a well-established protocol for the attachment of antibodies to nanoparticles.[30] The antibody retained its binding affinity toward DCs whenever fewer than three DBCO molecules on average were bound to the antibody. The conjugation to the brush, however, results in a more or less random manner since the reactive ester reacts with the primary amine of lysines within the antibody. As a consequence of this nondirective antibody conjugation to the NP surface, some of the NP-bound antibodies likely have an outward orientation of their Fc region, which may enable FcR-mediated binding. Since antibody conjugation is performed according to established protocols at physiological temperature and pH, the structural integrity of the antibody is maintained. Moreover, purely by stoichiometry a distinct average number of antibodies, namely, 2, 6, and 12, can be conjugated to PBs (Figure 1B). SDS-PAGE electrophoresis revealed complete conjugation of introduced antibodies (Figure 1C). UV−vis spectroscopy confirmed conjugation of the desired numbers of antibodies per PB (Figure 1D). Multiangle dynamic light scattering (DLS) analysis demonstrated similar sizes of all PB−antibody conjugates (Figure 1E). For detection of the PBs in subsequent analysis the near-infrared dye CW800 was conjugated by SPAAC.

The Antibody Number of PB Correlates with Their Accumulation in the Liver and Inversely Correlates with Their Blood Circulation Time. We used PB−antibody conjugates with the three different antibody numbers to investigate the impact of increasing antibody density per PB on their pharmacokinetics and biodistribution after intravenous injection. For this, *in vivo* imaging was combined with *ex vivo* analysis of blood and internal organs. As expected, PB without antibody displayed the longest half-life in blood (Figure 2A). All PB−antibody conjugates exhibited reduced blood circulation times, which inversely correlated with the number of attached antibodies. This effect was most pronounced in the case of PB conjugated with the highest number of antibodies (PB−aDEC205[12]). In accordance with the stealth-like properties, polysarcosine PB polymers without conjugated antibodies were scarcely detectable in any of the monitored internal organs at 24 h postinjection (hpi) (Figure 2B,C). In contrast, all PB−antibody conjugates could be found in the liver. The extent of liver deposition was lowest in the case of PB conjugated with two antibodies (PB−aDEC205[2]), whereas PB with intermediate (PB−aDEC205[6]) and high (PB−aDEC205[12]) antibody numbers per brush accumulated at higher extents (almost 2-fold for PB−aDEC205[12]).

https://doi.org/10.1021/acsnano.1c05713
ACS Nano XXXX, XXX, XXX−XXX

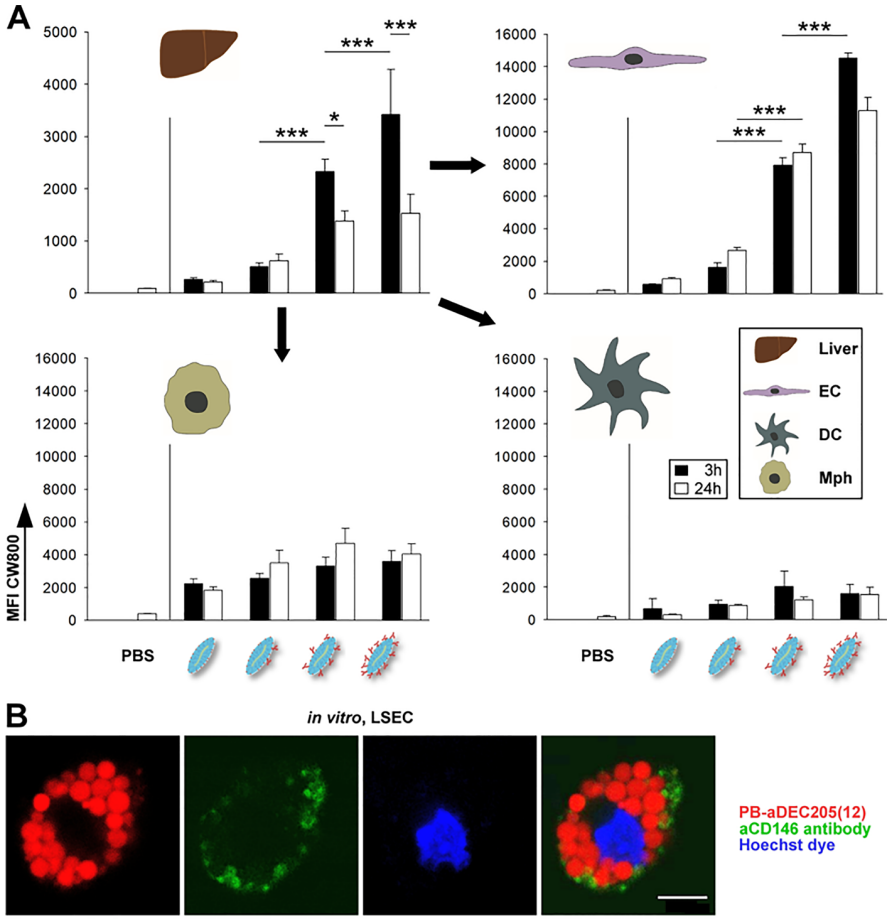

Figure 3. In the liver PB−antibody conjugates engage predominantly endothelial cells, in correlation with PB antibody number: (A) Flow cytometric analyses of liver non-parenchymal cell (NPC) populations at various time points after systemic application of different PB conjugates (black bars: 3 hpi, white bars: 24 hpi). Liver NPCs of mice differentially treated with CW800-labeled PBs were prepared and incubated with antibodies to differentiate liver endothelial cells (ECs: $CD45^-CD31^+$), macrophages (Mphs: $CD45^+F4/80^+$), and dendritic cells (DCs: $CD45^+CD11c^+$). Upper left panel: total liver NPCs, upper right panel: liver endothelial cells, lower left panel: liver Mphs, lower right panel: liver DCs. Data denote the CW800 mean fluorescence intensities (MFI) of either NPC population (mean ± SEM, $n = 6-8$ obtained from 2 to 3 experiments; one-way ANOVA, $*p < 0.05$, $***p < 0.001$). (B) Confocal laser scanning microscopy image of a liver endothelial cell incubated with PB−aDEC205(12) conjugate for 1 h *in vitro*. Cells were incubated with anti-CD146 antibodies to identify liver sinusoidal endothelial cells (LSECs: $CD45^-CD31^+CD146^+$) and Hoechst dye for nuclear staining. Scale bar: 10 μm.

A similar biodistribution pattern was observed also at 3 hpi (see Figure 4C, upper panel) and in Figure 4D.

To elucidate which cell populations within the liver engaged the various PBs, liver cell suspensions were subjected to flow cytometric analysis. Here we focused on non-parenchymal cell (NPC) types previously shown to interact with different types of NPs.[31,32] In accordance with the imaging results, we observed that the mean fluorescence intensity (MFI) of total liver NPCs increased in correlation with PB antibody density at 3 hpi as well as 24 hpi (Figure 3A, upper left panel).

Further analysis of distinct liver NPC populations revealed that PBs with intermediate/high antibody numbers were largely associated with liver endothelial cells (ECs) (Figure 3A, upper right panel). Again, the extent of EC engagement correlated with the number of antibodies per PB. On the contrary, the number of antibodies per PB had no major effect on engagement by $F4/80^+$ liver Mphs, which may be largely attributed to Kupffer cells that constitute >80% of liver Mphs,[33,34] and DCs, as measured by MFI, which correlates to the number of NPs per cell (Figure 3A) in the applied concentration range. In agreement, at 3 hpi the numbers of PB-positive liver NPCs and ECs correlated with the number of antibodies per PB, in contrast to Mphs and DCs (see Supp Figure 1).

Within the liver EC population, $CD146^+$ liver sinusoidal endothelial cells (LSECs) have been reported to engulf NPs.[19] Therefore, we assessed whether antibody-coated PBs were indeed internalized by these cells. As depicted in Figure 3B, PB−aDEC205(12) were readily internalized *in vitro* by $CD146^+$ LSECs after co-incubation for 1 h and accumulated in discrete intracellular vesicle-like structures.

Altogether, these findings indicate that PBs with low antibody numbers per PB exhibit only limited undesired liver accumulation, whereas an intermediate antibody density was sufficient to confer massive deposition of PB-based NPs in the liver. Surprisingly, liver ECs exerted a stronger PB−antibody conjugate binding capacity than Mphs (and DCs), in terms of both numbers of PB-engulfing cells and the number of PBs engaged per cell (MFI).

Liver ECs Engage PB−Antibody Conjugates *via* Fcγ Receptors. LSECs have been demonstrated to play an important immunological role by internalizing immune

https://doi.org/10.1021/acsnano.1c05713
ACS Nano XXXX, XXX, XXX−XXX

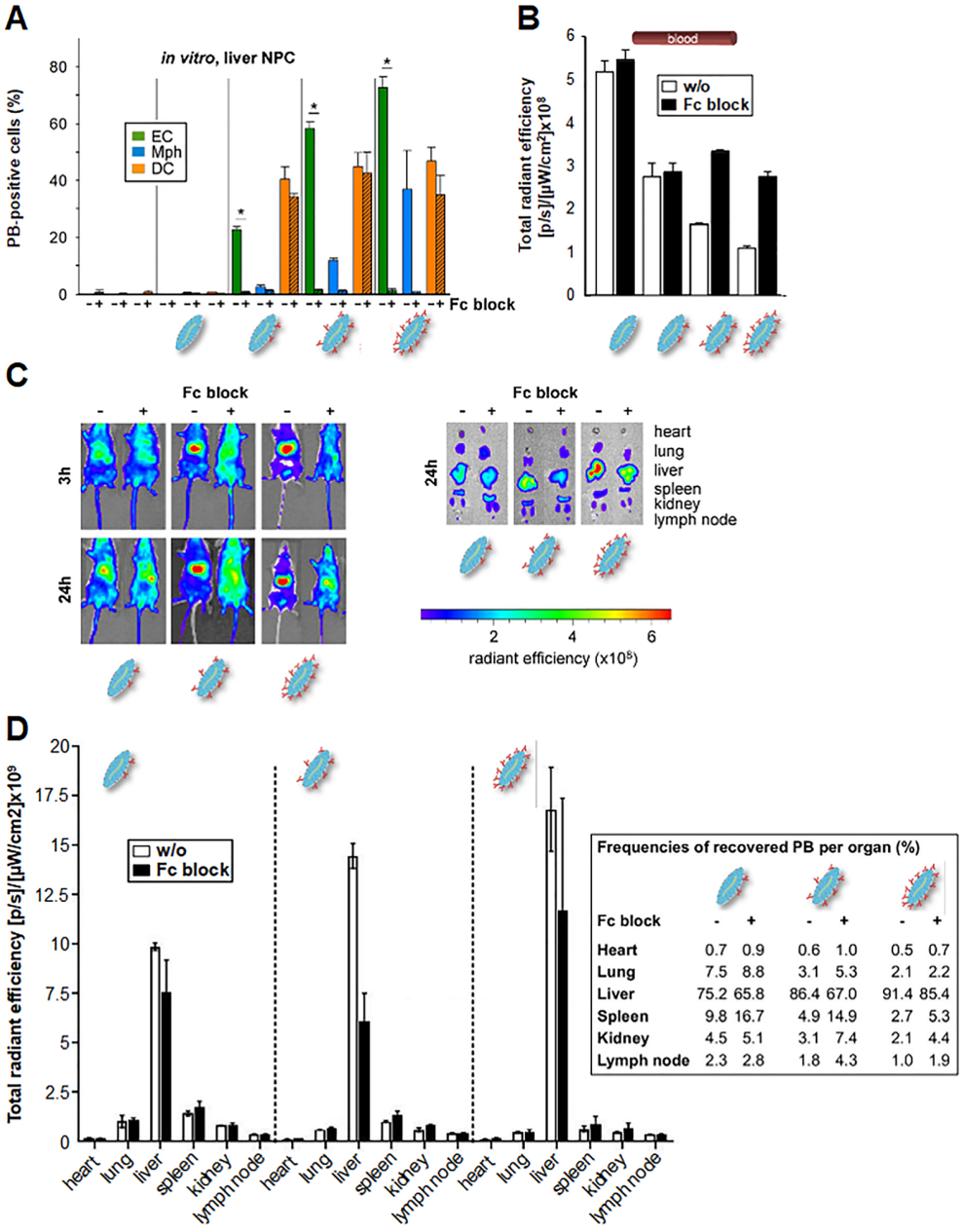

Figure 4. Systemic blockade of Fc receptors reduces liver accumulation of PB−antibody conjugates with intermediate and high antibody density: (A) Isolated liver NPCs (liver endothelial cells (ECs: $CD45^{-}CD31^{+}$), macrophages (Mphs: $CD45^{+}F4/80^{+}$), and dendritic cells (DCs: $CD45^{+}CD11c^{+}$)) were preincubated with an FcγRII/III-blocking antibody (Fc block), followed by incubation with PB conjugates for 1 h. Data denote the frequencies of PB-positive cells of the different NPC populations as assessed by flow cytometry (see legend of Figure 3A) and represent the mean ± SEM ($n = 3$; one-way ANOVA, $*p < 0.001$). (B−D) Mice were pretreated with Fc block, followed by systemic application of PB conjugates. (B) Blood was retrieved 6 hpi, and contents of PBs derived from mice left untreated (w/o) or after pretreatment with Fc block were quantified (mean ± SD, $n = 2$ per group). (C) Fluorescence imaging of mice at 3 and 24 hpi (left panel) and of organs retrieved 24 hpi (right panel). (D) Quantification of organ-specific fluorescence at 24 hpi (see C, right panel). Data denote the mean ± SD of 2 samples per group (one-way ANOVA, significance: $*p < 0.001$). Data in the table depict the relative percentage of recovered fluorescence per organ (fluorescence of all organs combined = 100%).

complexes *via* different types of surface receptors including the Fcγ receptor IIb (FcγRIIb),[35] which is not expressed by other hepatic EC populations and is largely confined to immune cells.[36] Since aDEC205 antibodies were conjugated to PBs in a more or less random manner, the Fc part of a fraction of these may be accessible for binding. We tested the potential role of the Fc/FcγRIIb interaction for the observed binding and uptake of PB−antibody conjugates by liver ECs in blocking studies. To this end, isolated primary liver NPCs were preincubated with anti-FcγRIIb/FcγRIII-specific antibodies known to block Fc-mediated binding and subsequently incubated with the different PB conjugates. PB without antibody showed no cellular interaction at the applied concentration (10^{12} particles per mL on 10^{6} cells). As observed before, the frequencies of ECs and Mphs that engaged PB−antibody conjugates correlated with increasing

https://doi.org/10.1021/acsnano.1c05713
ACS Nano XXXX, XXX, XXX−XXX

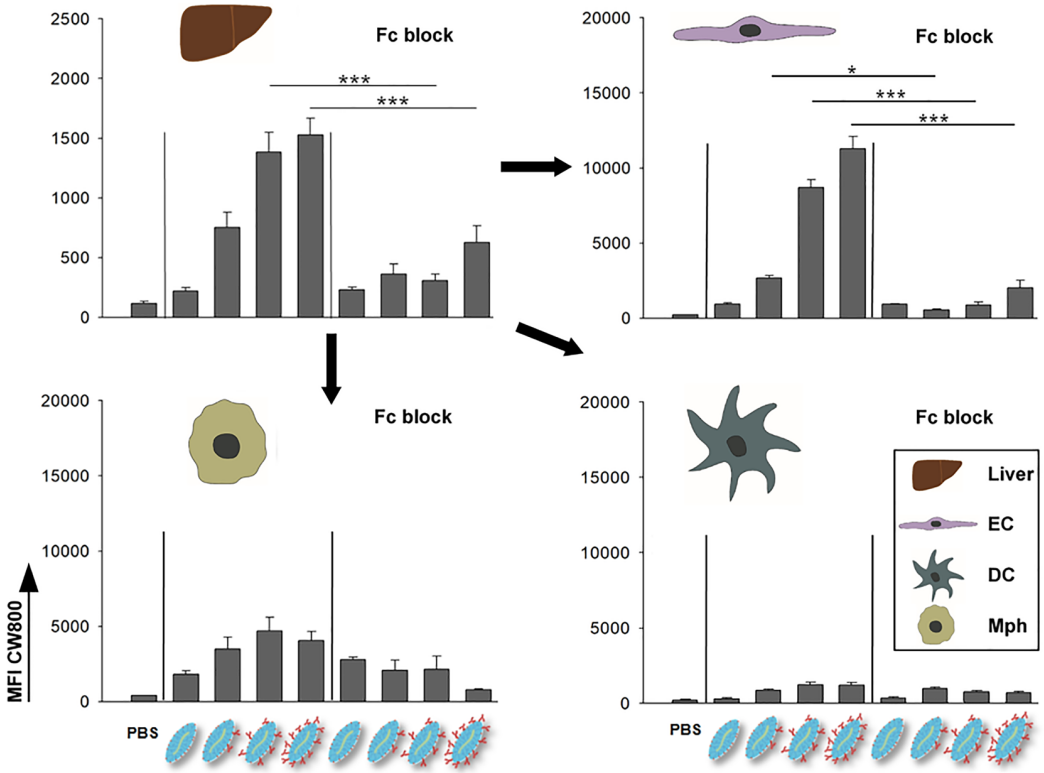

Figure 5. Systemic blockade of Fc receptors diminishes binding of PB−antibody conjugates to liver ECs. Mice were sequentially injected with Fc block and PB conjugates as described in the legend of Figure 4. Liver NPCs were prepared 24 hpi, and binding of CW800-labeled PB formulations (MFI) to either NPC population (liver endothelial cells (ECs: $CD45^{-}CD31^{+}$), macrophages (Mphs: $CD45^{+}F4/80^{+}$), and dendritic cells (DCs: $CD45^{+}CD11c^{+}$)) was assessed by flow cytometry (see legend of Figure 3A). Upper left panel: total liver NPCs, upper right panel: liver ECs, lower left panel: liver Mphs, lower right panel: liver DCs. Data denote the mean ± SEM (n = 6−8 obtained from 2 to 3 experiments; one-way ANOVA, $*p < 0.05$, $***p < 0.001$).

antibody numbers (Figure 4A). Again, each PB−antibody conjugate was associated with a higher fraction of liver ECs than Mphs. In contrast, liver DCs engaged with all PB−antibody conjugates at a comparable extent. Interestingly, *in vitro* blockade of Fc receptors using a commercially available CD16/CD32 (FcγRIIb/FcγRIII)-specific antibody,[37] for which the blocking efficiency was assessed beforehand (see Supp Figure 2), almost completely abrogated the binding of subsequently applied PB−antibody conjugates to ECs and Mphs, whereas their binding to DCs remained unaltered, suggesting that liver DCs mostly bound the NPs *via* specific interactions of the aDEC205 antibodies with their target, DEC205, whereas liver ECs and Mphs bound PBs *via* surface Fcγ receptors. This observation also indicates that within the liver EC population LSECs are largely responsible for binding of PB−antibody conjugates, since they are the only liver EC population that expresses FcγRIIb/FcγRIII.

To confirm the role of FcR-mediated accumulation of antibody-decorated PBs in the liver, we blocked FcR interactions by injection of 50 μg of CD16/CD32 (FcγRIIb/FcγRIII)-blocking antibodies, based on the results of a pre-experiment (see Supp Figure 3), prior to systemic application of PB conjugates *in vivo*. While FcR blockade had no effect on the amount of circulating PBs without antibody and in PB−aDEC205(2), significantly more PB−aDEC205(6) (2-fold) and PB−aDEC205(12) conjugates circulated in the blood at 6 hpi (up to 2.5-fold, Figure 4B). In agreement, FcR blockade had no effect on liver deposition of the PB conjugates with no and low antibody content, but drastically reduced liver accumulation of PB−antibody conjugates with intermediate and high antibody contents at 3 (Figure 4C, left panel) and 24 hpi (Figure 4C, right panel, D), resulting in a more uniform distribution of PB−aDEC205(6) and PB−aDEC205(12) within the animal (Figure 4C). We also calculated the relative fluorescence recovered from each organ. Here, it became apparent that PB accumulation in lymphatic organs (spleen, LN) inversely correlated with the number of attached antibodies. In contrast to the *in vitro* situation (Figure 4A), *in vivo* administration of Fc-blocking antibodies only partially reduced the dominant PB accumulation in the liver, but still improved accumulation of PBs in the spleen and LNs significantly, again—in line with our expectations—inversely correlating with the number of attached antibodies per PB [PB−aDEC205(2) > PB−aDEC205(6) > PB−aDEC205(12)].

Flow cytometric *ex vivo* analysis confirmed the almost abrogated binding of PB with intermediate or high antibody numbers to liver NPCs after FcR blockade (Figure 5, left upper panel, Supp Figure 4, left upper panel, Supp Figure 5A). Fc blockade strongly reduced binding of all PB−antibody conjugates to ECs at all time points investigated (Figure 5 and Supp Figure 4, Supp Figure 5B), whereas binding of PB−antibody conjugates to Mphs was significantly reduced only at 3 hpi (Supp Figure 4), but not at 24 hpi (Figure 5, Supp Figure 6), and binding of PBs to liver DCs was largely unaffected by Fc receptor blockade (Figure 5, Supp Figure 4, Supp Figure 6).

https://doi.org/10.1021/acsnano.1c05713
ACS Nano XXXX, XXX, XXX−XXX

Taken together, these *in vivo* results confirm that LSECs are responsible for the retention of antibody-coated NPs in the liver *via* FcR-mediated binding of the antibodies' Fc part.

PB−Antibody Conjugates with Low, but Not with Intermediate or High Numbers of DC-Targeting Antibodies Are Enriched in Secondary Lymphoid Organs. An important prerequisite of NP-based immunotherapeutic approaches that target antigen-presenting cells is that the NPs reach secondary lymphoid organs, especially LNs and the spleen.[6] Therefore, we next assessed to what extent intravenously injected PBs that were functionalized with different amounts of aDEC205 antibodies were detectable in the spleen and LNs on a single-cell level in a time-dependent manner.

As also shown before (see Figure 2C), more PB−antibody conjugates were trapped in the liver when functionalized with 6 or 12 antibodies per NP (PB−aDEC205[6], PB−aDEC205[12]) than with 2 antibodies per NP (PB−aDEC205[2]) (Figure 6, left panel). In general, the frequencies of PB-positive NPCs were lower at 24 hpi *versus* 3 hpi, suggesting that antibody-coated NPs are only temporarily retained in the liver. In the spleen, 0.1−0.5% of *ex vivo* isolated whole spleen cells were PB-positive for either PB−antibody conjugate applied. Similar to liver NPCs, the frequency of PB-positive spleen cells decreased over time. Only few LN cells (<0.4%) engaged either PB−antibody conjugate when assessed at 3 hpi, whereas a significant percentage of LN cells (4%) had acquired PBs at 24 hpi when these had been functionalized with low amounts of antibodies (PB−aDEC205(2)). Importantly, LN accumulation of PBs decreased dramatically with increasing amounts of antibody per PB (Figure 6, right panel). Taken together, these observations suggest that in liver and spleen a fraction of PB−antibody conjugates is engaged by cells in a transient manner and that only PBs coated with 2 antibodies per NP, but not those with 6 and 12 antibodies per NP, accumulate in their target cells later on.

PBs with a Higher Antibody Number Display a More Pronounced Protein Corona, and Its Constituents May Engage Various Cellular Receptors. Since PB−antibody conjugates may transiently interact with cells *via* additional mechanisms besides Fc/FcR, we questioned the potential role of the protein corona in this regard. So far, many types of NPs have been shown to be coated by a protein corona, which may affect their cellular binding.[10] Alberg and co-workers have recently reported that PB polymers that were similar to those used in this study showed a very low adsorption of plasma components (less than 1 protein per NP),[24] which is in accordance with their long blood circulation half-life. We asked whether antibody-conjugated PBs would cause the formation of a more pronounced protein corona or the binding of specific proteins such as complement factors, and thereby increase the probability of (transient) PB binding to cellular receptors, *e.g.*, FcγRIIb/FcγRIII, additionally affecting their overall biodistribution. To this end, naked PBs or PBs conjugated with a high number of aDEC205 antibodies were incubated with plasma, and protein−PB complexes were separated by asymmetrical flow field-flow fractionation (AF4) as recently described.[24] The PB−antibody conjugate displayed an unaltered AF4 retention time, indicating that the amount of adsorbed proteins is low and thus does not affect their size (Supp Figure 7A) nor cause any aggregation. This was additionally confirmed by DLS measurements (Supp Figure 7B) in blood plasma. The highly sensitive silver staining of the SDS-PAGE electrophoresis identified, however, some binding

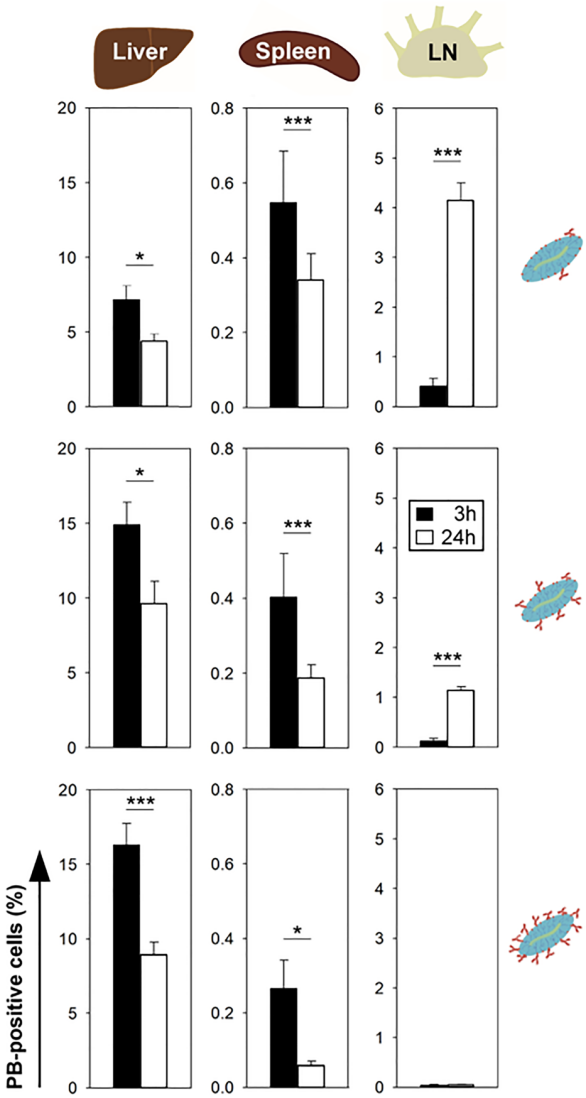

Figure 6. Liver accumulation of PB−antibody conjugates after systemic application decreases over time, paralleled by increased levels in lymph nodes in the case of low/intermediate PB antibody density. Mice were intravenously injected with PB formulations as described in the legend of Figure 2. After 3 hpi (black bars) and 24 hpi (white bars), liver, spleen, and LNs were retrieved. The frequencies of PB-positive cells of a given cell type within the relevant cell suspensions (liver NPC, total spleen, and LN cells) were assessed by flow cytometry. Data denote the mean ± SEM (n = 6−8, obtained from 2 to 3 experiments; one-way ANOVA, *p < 0.05, ***p < 0.001).

of proteins (60−80 kDa, 160−260 kDa) to the PB−aDEC205 conjugates (Supp Figure 7C).

Using mass spectroscopy, we were able to identify a total of 30 different proteins on naked PBs and 50 different proteins on aDEC205-conjugated PBs, although total amounts were very small in all cases. Among these, only seven proteins were identical (Figure 7A,B). Compared to naked PBs, significantly more protein bound to the surface of anti-DEC205-coated PBs (Figure 7B,C). In the protein corona of aDEC205-coated PBs, several genuine factors of the (classical) complement pathway and a number of immunoglobulins (Igs) were specifically enriched (Figure 7C, Supplemental Table 1). In this regard it is interesting to note that the constant regions of several Igs are

https://doi.org/10.1021/acsnano.1c05713
ACS Nano XXXX, XXX, XXX−XXX

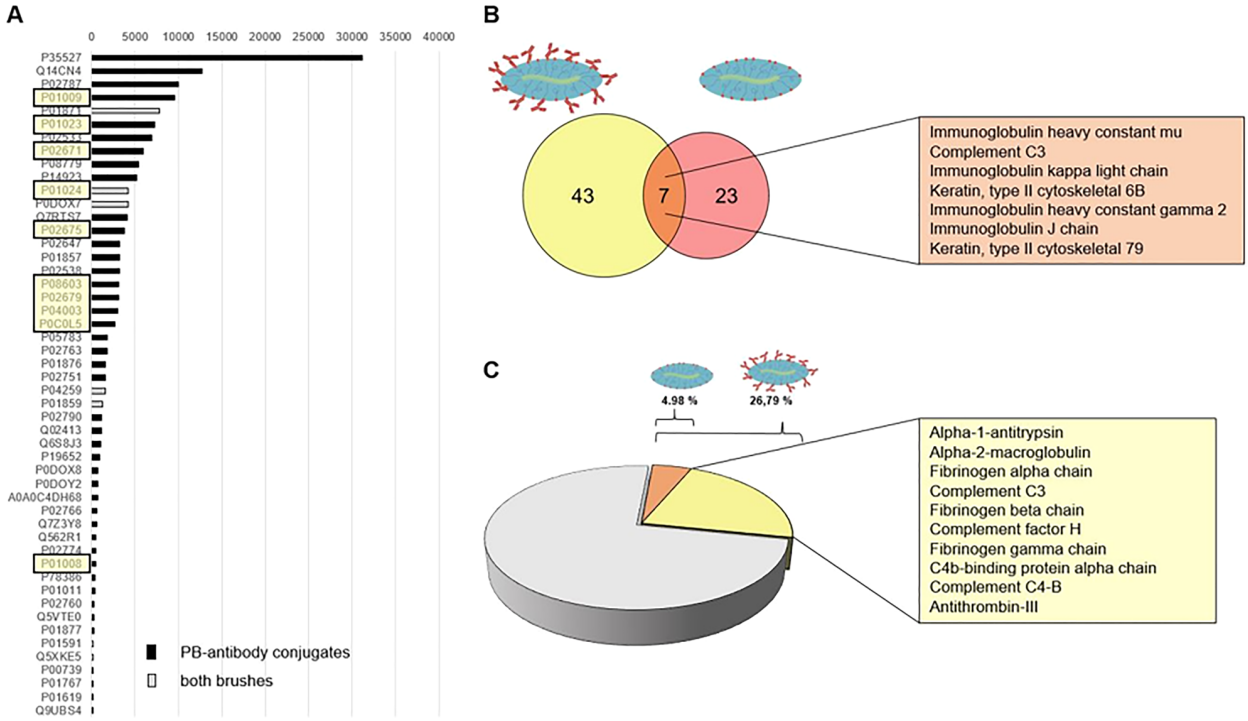

Figure 7. Antibody-induced protein corona formation: (A) Significantly enriched proteins associated with PB−antibody conjugate; (B) Venn diagram for enriched proteins in both controls on NPs. The overlap area shows the number of proteins significantly enriched on both NPs and (C) significantly enriched proteins related to the complement pathway and coagulation system in percentage of all identified proteins associated with the nanoparticle.

known to trigger the classical complement pathway.[38] Moreover, the protein corona of antibody-conjugated PBs also contained several factors that belong to the coagulation system, and four of these were shown to inhibit activation of the classical complement pathway.[39] We conclude that functionalization of PBs with high numbers of antibodies results in the formation of a distinct protein corona, which may contribute to the observed off-target accumulation and does not depend on specific Fc or Fab recognition. Since several corona proteins are known to engage with cellular receptors such as complement, immunoglobulin, and scavenger receptors, this provides an initial molecular explanation for further interactions of antibody-coated NPs with nontarget cells, including Fc receptors, complement, and coagulation factors, *in vitro* and *in vivo*.

The Effectiveness of DC Targeting Inversely Correlates with Antibody Number on the PB. We showed that in the liver the extent of accumulation of PBs correlated directly with the number of attached antibodies (see Figures 3, 4, and 5). In a complementary manner, the frequencies of PB-positive spleen (Figure 8) and LN cells (Supp Figure 8, upper panel) and even more obviously their overall MFI (LNs: Supp Figure 8, lower panel, spleen cells: Supp Figure 9) inversely correlated with the average antibody number per PB as assessed at 24 hpi. FcR blockade exerted no significant increase in frequencies of PB-positive cells or their MFI in either organ, indicating that PBs primarily bound to cells in lymphatic organs *via* specific interactions of the aDEC205 antibody with its cellular target DEC205. *In vitro* studies using bone-marrow-derived DCs confirmed that PB antibody conjugates engaged DCs to a comparable extent irrespective of their antibody density (Supp Figure 10). Blockade of Fc receptors had no major effect on binding of either PB formulation to DCs.

In the spleen, DEC205$^+$ DCs coexpress CD8a.[25] Thus, within the total DC population, CD8a$^+$ but not CD8a$^-$ DCs were specifically addressed by aDEC205-coated PBs (Figure 8). Notably, in both the spleen and LNs the extent of DC binding inversely correlated with the number of attached antibodies, presumably due to quantitative accumulation of PBs with intermediate/high antibody numbers as a first pass effect in the liver. Notably, more than 8% of the CD8a$^+$ DCs, compared to less than 1% of CD8a$^-$ DCs, in the spleen took up detectable numbers of PBs coated with an average of two aDEC205 antibodies, thus proving the high efficacy and selectivity of the DC targeting with antibody decorated NPs presented in this work.

In order to estimate the maximal number of antibody-conjugated PBs that engaged a DC, bone-marrow-derived DCs were incubated *in vitro* overnight with a high number of PB−aDEC205 antibodies labeled with AF647 or were left untreated. As assessed by flow cytometric analysis the whole cell population displayed a shift toward increased AF647 intensities (not shown), which indicated that all cells engaged PB antibody conjugates to varying extents. Concomitant analysis of serially diluted cell lysates and of PB−aDEC205(12) particles suggested that, on average, each DC had engaged about 50 000 PB−antibody conjugates when incubated with saturating NP doses (Supp Figure 11).

PB Conjugated with F(ab′)$_2$ Antibody Fragments No Longer Accumulate in the Liver, but Are Not Further Enriched in Secondary Lymphoid Organs. In order to corroborate our findings on the role of the Fc part of the attached antibodies for unwanted liver accumulation, we

https://doi.org/10.1021/acsnano.1c05713
ACS Nano XXXX, XXX, XXX−XXX

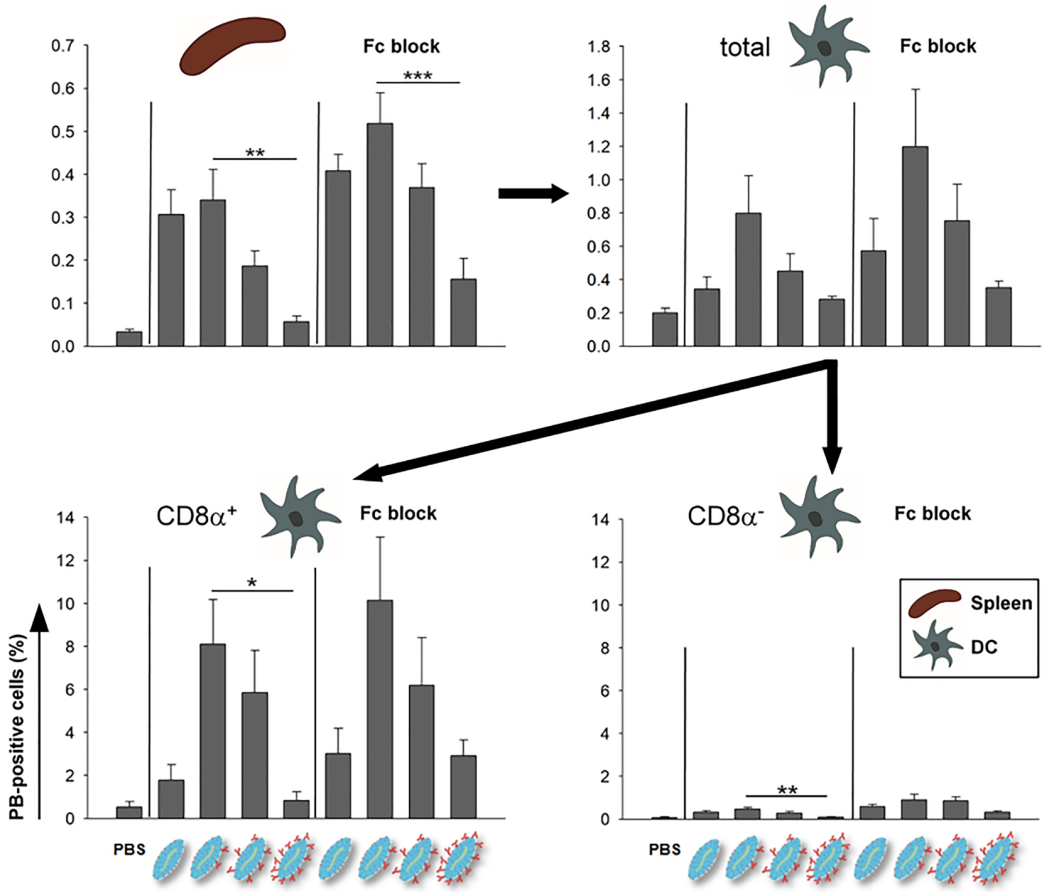

Figure 8. Systemically applied PB−antibody conjugates address splenic DCs most efficiently when equipped with low antibody numbers. Mice were treated with Fc block before i.v. injection of PB nanoparticles as described in the legend of Figure 4. Spleens were retrieved at 24 hpi, and frequencies of PB-positive spleen cells, total DCs ($CD11c^+$), and the $CD8a^+$ *versus* $CD8a^-$ DC populations within the splenic leukocyte population were delineated by flow cytometry. (A, B) Data denote the mean ± SEM (n = 6−8, obtained from 2 to 3 experiments; one-way ANOVA, *p < 0.05, **p < 0.01, ***p < 0.001).

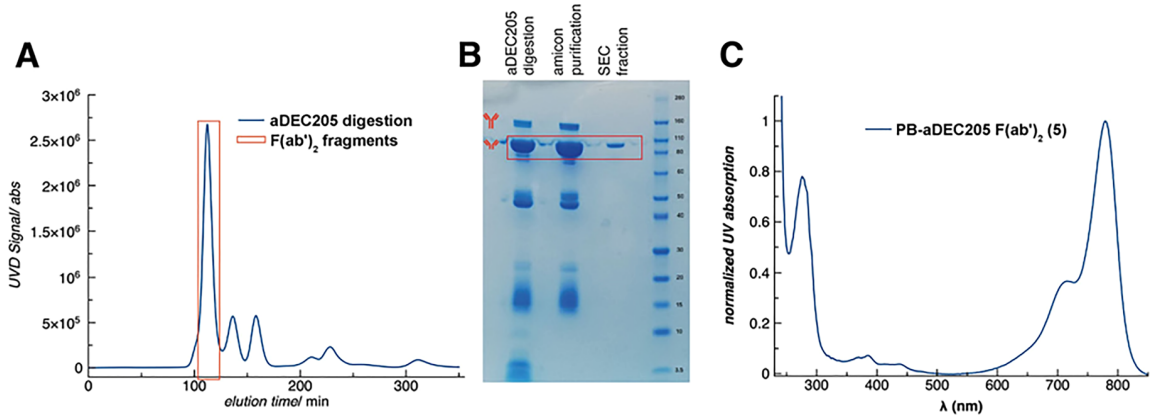

Figure 9. Synthesis and characterization of PB−$F(ab')_2$ antibody conjugates: (A) SEC elugram of aDEC205 digestion; (B) SDS PAGE of digestion and purified aDEC205 $F(ab')_2$ fragments of (1) digestion solution aDEC205, (2) digestion solution purified with Amicon spin filtration, (3) isolated $F(ab')_2$ fragments *via* SEC; (C) UV−vis analysis of the effectivity of PB−antibody conjugation.

conducted further biodistribution studies. We analyzed the biodistribution of PBs functionalized with an isotype control antibody bearing the same Fc part as the aDEC205 antibody, but lacking its specificity, and PBs conjugated with aDEC205 antibody lacking the Fc part (aDEC205-$F(ab')_2$), generated by enzymatic cleavage. We generated PBs with an intermediate number of antibodies per PB, which had resulted in pronounced Fc-mediated liver accumulation.

The aDEC205 antibody derived $F(ab')_2$ fragments were generated based on established protocols[40] (Supp Figure 12). aDEC205-derived $(Fab')_2$ fragments generated under optimized conditions were characterized by SEC elugrams (Figure 9A) and with SDS-PAGE (Figure 9B). The DBCO

https://doi.org/10.1021/acsnano.1c05713
ACS Nano XXXX, XXX, XXX−XXX

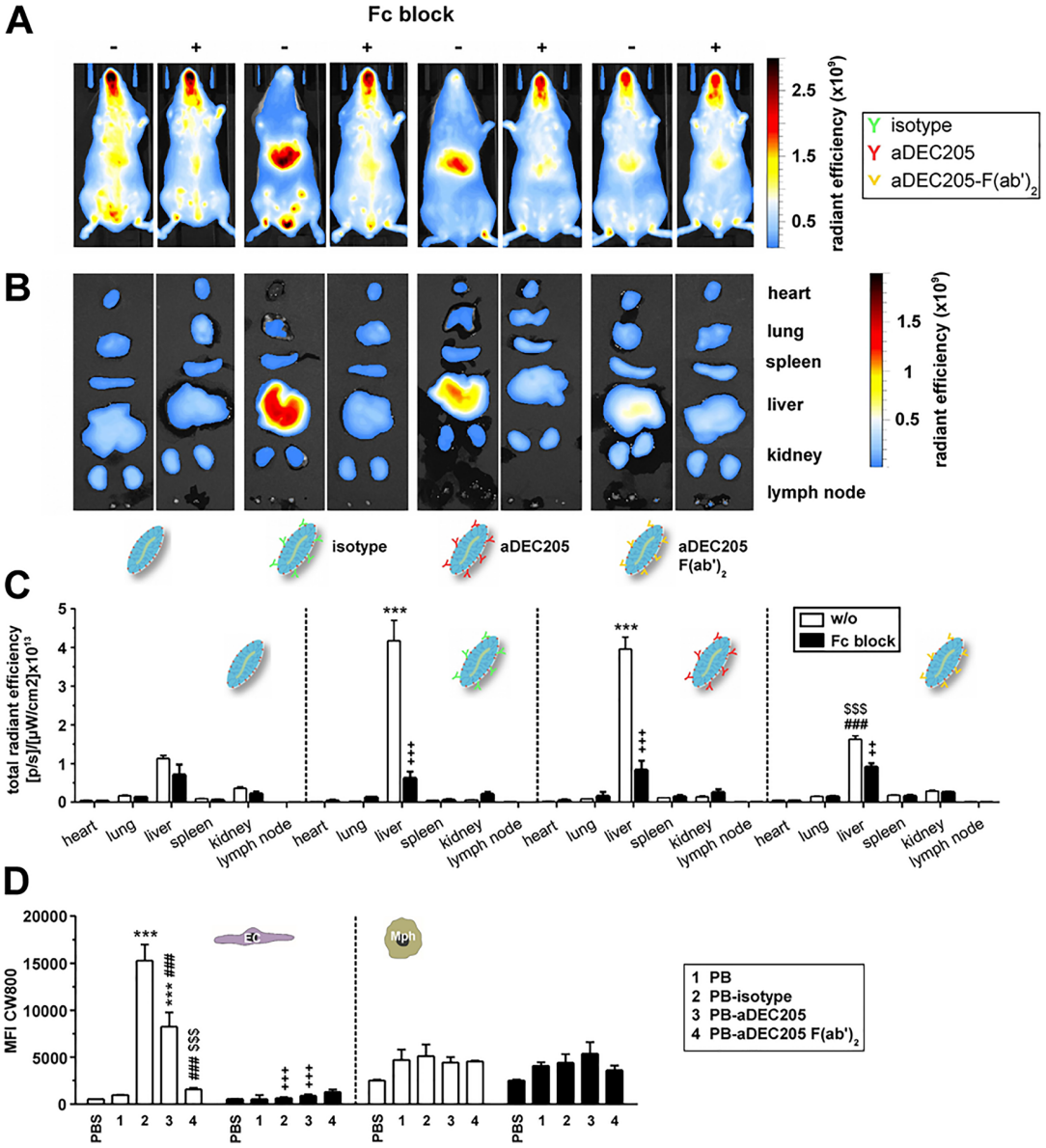

Figure 10. PBs conjugated with aDEC205 F(ab′)$_2$ antibody fragments do not accumulate in the liver. Mice were treated in parallel with PBs conjugated with full-length anti-DEC205 antibodies and derived F(ab′)$_2$ antibody fragments. PBs conjugated with a related full-length isotype control antibody and nonconjugated PBs served as controls. In parallel assays, mice were treated with Fc receptor blocking antibodies prior to administration of PB formulations. Distribution of PB formulations was assessed 3 hpi. (A) Fluorescence imaging of mice and (B) of retrieved organs. (A, B) Graphs are representative of 3 mice/group. (C) Quantification of organ-specific CW800 fluorescence (see B). (D) Binding of CW800-labeled PB formulations (MFI) to either liver NPC population (liver endothelial cells (ECs: CD45$^-$CD31$^+$) and macrophages (Mphs: CD45$^+$F4/80$^+$)) was assessed by flow cytometry (see legend of Figure 3A). (C, D) Data denote the mean ± SEM (n = 3; one-way ANOVA; **versus* nonconjugated PB, $^+$*versus* w/o Fc block of related formulation, $^\#$*versus* isotype control antibody-conjugated PB, $^\$$*versus* aDEC205-conjugated PB ($^+p < 0.05$, $^{***,+++,\#\#\#,\$\$\$}p < 0.001$).

modification and conjugation was performed as described before. An average number of five aDEC205 F(ab′)$_2$ fragments per PB was conjugated as confirmed by UV−vis spectroscopy (Figure 9C).

Since already with six antibodies binding to DCs reached its maximum in terms of % positive cells and MFI, we decided to compare PBs conjugated with the aDEC205 antibody, the related isotype control antibody (6 antibodies each per PB), and an aDEC205-derived F(ab′)$_2$ fragment (5 antibodies per PB) and nonconjugated PBs and applied them systemically to mice. In parallel settings, mice were pretreated with FcR-blocking antibodies. PBs conjugated with either the isotype control antibody or the full-length aDEC205 antibody predominantly accumulated in the liver as assessed 3 hpi (Figure 10A−C). In contrast, PBs conjugated with aDEC205-F(ab′)$_2$ showed significantly lower enrichment in the liver than PBs conjugated with full-length antibodies (isotype or aDEC205) and were comparable to nonfunctionalized PBs. As expected, pretreatment of mice with Fc receptor blocking antibodies resulted in strongly attenuated liver accumulation of the two PBs conjugated with either full-length antibody but only slightly reduced liver accumulation of PBs conjugated with aDEC205-F(ab′)$_2$. In the liver, PBs functionalized with either full-length antibody (isotype, aDEC205) predominantly

https://doi.org/10.1021/acsnano.1c05713
ACS Nano XXXX, XXX, XXX−XXX

engaged ECs (Figure 10D), whereas PBs conjugated with aDEC205-F(ab′)$_2$ displayed no major binding. Liver Mphs engaged all PBs to some extent, irrespective of a conjugated antibody. Blockade of FcR prior to injection of PB formulations strongly reduced binding of each full antibody−PB conjugate to liver ECs, whereas no effect was observed for liver Mphs.

These results confirm that at a higher antibody number per PB the antibodies' Fc part strongly contributes to liver accumulation of systemically applied PBs, predominantly mediated by liver endothelial cells. However, also PBs conjugated with aDEC205-F(ab′)$_2$ displayed some liver accumulation in F4/80$^+$ liver Mphs (Figure 10, Supp Figure 13), which may be attributed to Kupffer cells,[33] which constitute the vast majority of liver Mphs.[34] Despite lower liver accumulation of PB−aDEC205-F(ab′)$_2$ as compared to PBs conjugated with aDEC205 full antibody (see Figure 10 A−C), we observed only a slightly enhanced targeting efficacy to DCs in the spleen or LNs. In line with this finding, the overall frequencies of PB-positive CD8a$^+$ DCs (Supp Figure 13C) were not higher than the ones achieved using PBs conjugated with a low number (2) of aDEC205 antibodies (see Figure 8), which may be attributed to a reduced stability of F(ab′)$_2$ fragments compared to full antibodies.

In summary, PBs with a low antibody number are superior to those with intermediate/high numbers of antibody or intermediate numbers of F(ab′)$_2$ fragments for targeting of DCs in secondary lymphoid organs, since antibody-coated PBs with >2 antibodies per PB are trapped by LSECs in the liver in a FcR-mediated fashion, depleting PBs from circulation and thus preventing them from reaching their target cells. Interestingly, PBs with an average of 2 aDEC205 antibodies per NP effectively target DCs in secondary lymphoid organs, reaching a total of 10% positive CD8α^+ DCs in the spleen and around 5% in LNs.

Liver entrapment is a common outcome of systemic NP application,[32] both for nonfunctionalized NPs[41] and for NPs that are surface-functionalized with antibodies.[42] Our study aimed to delineate the number of antibodies per NP as a determinant for undesirable liver accumulation *versus* the desired antibody-mediated target cell specificity in secondary lymphoid organs. For this, we employed PBs that are characterized by minimal cellular interactions and subsequently long plasma circulation half-life and allow fine-tunable attachment of antibodies at lysine residues in an adjustable and well-reproducible manner. We chose a very common method of antibody attachment that utilizes the strain-promoted azide−alkyne coupling reactions between a DBCO-modified antibody and azide-containing polypept(o)-ide-based molecular polymer brushes based on a polylysine backbone (DP = 250) and polysarcosine side chains (DP = 100). The binding affinity of the modified DEC205 antibody was not affected by this ligation type,[43] and the Fc domain remains—most likely—accessible. The robust synthetic approach chosen in this study[41−43] enabled us to adjust the average antibody number per particle, an important prerequisite for comparative analysis. The polymer brushes used for the synthesis of different PB−antibody conjugates as well as the number of near-infrared (NIR) dyes used for *in vivo* and *ex vivo* tracking were identical for all the different systems, enabling an unbiased comparative analysis. The various PBs were conjugated with the NIR dye CW800 since such dyes were shown to confer deep tissue penetration at low background.[44] This enables *in vivo* tracking of NPs and thereby also *ex vivo* quantification of NP accumulation in tissues. In addition, NIR dyes, including the CW800, are also detectable by flow cytometry,[45] which allows assessment of cell type-specific NP binding and uptake.[46]

We show that PBs conjugated with an average of only two antibodies on one hand displayed only moderate liver accumulation and, on the other hand, efficiently addressed DCs in secondary lymphatic organs. In contrast, PBs conjugated with higher numbers of antibody (6, 12) predominantly accumulated in the liver. We demonstrate that liver ECs contribute at much higher extent to liver entrapment of antibody-coated PB nanoparticles than F4/80$^+$ liver Mphs. We also demonstrate that LSECs—and to a much lesser extent also liver Mphs —bind the Fc part of PB-conjugated aDEC205 antibodies *via* FcR expressed on the surface of these cells. FcR blockade *in vitro* on isolated liver NPCs almost completely abolished binding of PB−antibody conjugates to LSECs and Mphs. Likewise, FcR blockade *in vivo* also potently reduced liver entrapment of subsequently applied PB−antibody conjugates.

So far, in most studies the liver-resident Mph population (mainly Kupffer cells) has been described as the main NP binding cell population in the liver.[47] In contrast, the contribution of LSECs in this regard is just becoming elucidated.[48] This cell population internalizes PB−antibody conjugates most likely *via* FcγRIIB since LSECs express only this FcR and since LSECs were reported to facilitate uptake of IgG immune complexes *via* FcγRIIB.[35] Similar to Mphs, LSECs are also equipped with various pattern recognition receptors, *e.g.*, of the C-type lectin family such as the mannose receptor[49] and L-SIGN[50] as well as different scavenger receptors.[51,52] Consequently, ECs compete with Mphs for NP uptake, as also indicated by zebrafish embryo studies published by Hayashi and co-workers.[53] These sets of surface receptors enable efficient binding and uptake of a vast array of exogenous material *via* endocytosis, including viruses such as HIV-1[54] whose size is on the same order of magnitude as that of PB-antibody conjugates (see Figure 1E). Therefore, LSECs may considerably contribute to the frequently observed liver entrapment of different types of NPs coated with antibodies[55] or carbohydrates,[56] since besides FcR-mediated mechanisms, liver accumulation can also result from recognition of NP surface structures by pattern recognition receptors such as mannose[57] and scavenger receptors.[53,58] Thus, surface functionalization of nanovaccines should account for immunoglobulin, carbohydrate, and scavenger receptors expressed at high density by LSECs and liver Mphs.[57,58] The adequate form of stealth providing polymers can further contribute to a long blood circulation by preventing NP uptake by liver ECs or other immune cells.[59] Notably, Sivaram and colleagues demonstrated in studies on the organ and cell level that there might be a "sweet spot" for the optimal balance between targeting and stealth effects.[60] Furthermore, it is well established that cellular interactions and *in vivo* biodistribution of NPs may be affected by a protein corona consisting of adsorbed serum constituents,[10] as exemplified here for PBs with a high density of full-length antibody (see Figure 7).

The protein corona of antibody-functionalized PBs is composed of Igs, components of the (classical) complement pathway, and the coagulation system (Supplementary Table 1), known to interact with the complement pathway.[39] In contrast, nonfunctionalized PBs bound very few serum proteins on their

https://doi.org/10.1021/acsnano.1c05713
ACS Nano XXXX, XXX, XXX−XXX

surface, which may well be one reason for the long plasma half-life of naked PBs (Figure 2). The composition of the protein corona of antibody-conjugated PBs suggests that these NPs are recognized by natural antibodies,[61] which may trigger activation of the classical complement pathway,[62] negatively controlled by several factors of the coagulation system.[39] These findings suggest that the protein corona formed around PBs with high antibody density may further aggravate binding to FcR-expressing cells within the liver *via* the exposed Fc part of conjugated aDEC205 antibodies and adsorbed natural antibodies. In addition, these and other corona proteins on antibody-coated NPs may bind to additional cell surface receptors expressed by other cell types throughout the body, which may be one reason that we observed no increase in target cell binding of PBs after FcR blockade *in vivo* (Figure 8).

We also observed that numbers of PB−antibody conjugates that were trapped in the liver or spleen decreased over time (Figure 6), whereas a time-dependent decrease in PB−antibody conjugate deposition was not observed for isolated splenic DCs (data not shown). In parallel, PB−antibody conjugates with low, but not with high antibody density accumulated in LNs over time. We speculate that this may be due to redistribution of PB particles from the liver to the LNs, where $CD205^+$ cDC1 target cells are relatively abundant, or because of much slower transport of macromolecules within the lymphatic system compared to blood.[63] In contrast, PB−aDEC205(12) disappeared from the liver and spleen over time without accumulating in LNs, which suggests that high-avidity PB−aDEC205(12) antibody conjugates may subsequently bind other cell types throughout the body, potentially *via* protein corona induced interactions as outlined above, thus preventing their time-dependent redistribution toward their target cells.

In order to avoid FcR binding and liver accumulation, natural or engineered antibody fragments devoid of the Fc region, such as Fab fragments and single-chain Fv fragments[64] as well as other epitope-binding moieties such as affibodies[65] or aptamers,[66] may provide another pathway to circumvent liver accumulation of targeted NPs.[64] In accordance, we show that PBs conjugated with five $F(ab')_2$ fragments of aDEC205 displayed much lower liver accumulation as compared to PBs conjugated with the same number of isotype control antibody and aDEC205 full-length antibody, respectively.

However, full antibodies do not need expensive engineering, and several of them are commercially available in GMP grade, thus facilitating clinical translation. Furthermore, the Fc part may play an additional functional role as exemplified for agonistic CD40 antibodies, which require the Fc part to trigger target cell stimulation.[67] FcR-mediated effects may be circumvented by using peptides that specifically bind to the Fc region of antibodies, as demonstrated by Kedmi and coworkers for the modification of liposomes.[68] Moreover, Mailänder and co-workers have recently shown that polystyrene NPs preadsorbed with an anti-CD63 antibody retained receptor-specific targeting *ex vivo*.[69] Most importantly, since we demonstrate here that an average of two antibodies per NP is both sufficient for target cell engagement and necessary to avoid nonspecific accumulation in other organs such as the liver, careful control of the number of antibodies per NP may be generally advisable to enhance target cell specificity of antibody-coated NPs.

As mentioned above we are not aware of other comparative studies that identified the number or density of full-length antibodies on long circulating synthetic NPs as a determinant of unspecific liver accumulation *versus* cell type-specific targeting. However, effects of the number/density of receptor-targeting peptides per NP on their biodistribution have been addressed in several studies. For example, NP derivatives decorated with a prostate-specific membrane antigen binding aptamer for tumor cell targeting accumulated preferably in the liver in correlation with aptamer density, but not in the spleen. The underlying mechanism, however, was not assessed. In another study, liposomal formulations decorated with various densities of CD38 and CD138 receptor binding peptides, respectively, for engagement of myeloma cells showed a density-dependent increase (CD38) or decrease (CD138) in tumor cell binding as compared to nontargeting liposomes.[70] Accumulation of these formulations in other organs, including the liver, was not affected by the density of either peptide. Similarly, for nanohydrogels, which accumulated predominantly in the liver and spleen, conjugation with "high" amounts of epidermal growth factor receptor-binding peptides elevated tumor targeting, but had no effect on their predominant accumulation in the liver and spleen.[71] Concerning the targeting behavior of NPs decorated with various numbers of full-length antibodies, Zern and co-workers reported that a moderate number of ICAM-1-specific antibodies per NP achieved a better targeting specificity of inflamed vasculature expressing ICAM-1 than NPs decorated with high antibody numbers.[14,17] In aggregate, these studies underscore that NPs conjugated with receptor-binding peptides may accumulate in the liver as well and that the density of targeting units plays a role in this regard. So far, several strategies, including PEGylation and decoration with proteins such as CD47 serving as a "don't-eat-me" signal, have been developed to minimize unspecific NP uptake by liver NPCs.[10] For example, Samuelsson and co-workers demonstrated that PEGylation of liposomes strongly reduced their uptake by Kupffer cells in the liver as well as spleen accumulation and thereby significantly elevated their concentration in the blood.[47] Similarly, Zhou and coworkers reported that PEGylated PLGA-based NPs equipped with a second PEG layer minimized binding to Kupffer cells as well as LSECs.[59] It remains, however, an open question whether this approach can be combined with active targeting and improve NP accumulation at their target cells. In addition, the combination of various ligands may induce secondary effects, *e.g.*, protein corona formation. As an alternative strategy, we could show that modification of the size and zeta potential of mRNA-containing lipoplexes determined their accumulation in the liver or spleen as well as efficient targeting and transfection of splenic DCs without the necessity of a DC-targeting structure on the NP surface.[72]

CONCLUSIONS

The aim of this study was to investigate to what extent the decoration of NPs with targeting antibodies can induce off-target accumulation, *e.g.*, in the liver, upon intravenous application of NPs. To demonstrate this, we generated polysarcosine-based polymer brushes with distinct average antibody numbers ranging from a "low" (2 molecules), to "intermediate" (6 molecules) and a "high" amount (12 molecules). These conjugates were similar in size and free of unbound antibodies. We were able to show that an average of two antibodies per NP are sufficient to reach an acceptable percentage of target cells in lymphoid organs while bypassing

https://doi.org/10.1021/acsnano.1c05713
ACS Nano XXXX, XXX, XXX−XXX

the liver. PBs decorated with more than two antibodies accumulate rapidly in the liver due to recognition by FcRs or complement receptors as demonstrated by *in vivo* studies and *ex vivo* analysis of the nanoparticle-associated protein corona. We demonstrate that liver accumulation of antibody-coated NPs is mostly due to binding of PB conjugates to FcRs expressed on LSECs. Most importantly, capture of antibody-coated NPs by LSECs can be greatly reduced if antibody numbers per NP are kept low or if $F(ab')_2$ antibody fragments are used, thus preventing liver accumulation while retaining effective target-specific binding to DEC205 on DCs in secondary lymphatic organs. Since LSECs are potent inducers of antigen-specific tolerance, nanovaccines intended to induce immunity should minimize uptake by LSECs and other FcR-expressing cells in order to prevent tolerance induction, which underlines the importance of controlling antibody numbers on synthetic nanoparticle-based vaccines. Due to their enhanced circulation half-life, minimal entrapment in the liver, and effective binding to their target cells, PBs with an average of two full aDEC205 antibodies as well as $F(ab)_2$ fragments thereof seem to be a suitable platform for the development of DC-targeting nanovaccines for systemic applications.

MATERIALS AND METHODS

Peptobrush Synthesis. *Synthesis of Sarcosine N-Carboxyanhydride (NCA).* Synthesis of sarcosine NCA was performed as described with some modifications.[21,27,73] First, 20.52 g (230.2 mmol) of sarcosine (dried under vacuum for 1 h) was weighed into a three-neck, round-bottom flask. Then, 300 mL of absolute THF (tetrahydrofuran) was added under a nitrogen flow, and 184 mmol of diphosgene were added using a syringe. This solution was mildly refluxed for 3 h. The outlet was connected to two gas washing bottles containing an aqueous NaOH solution to neutralize phosgene, and dry nitrogen was led through the solution for 3 h. The obtained brownish oil was dried under reduced pressure (1×10^{-3} mbar for 2 h). The obtained amorphous solid crude product was redissolved in 40 mL of THF and was precipitated using 300 mL of dry hexane. The solution was stored overnight in a −20 °C freezer. On the next day, the precipitated product was filtered under a dry nitrogen atmosphere and dried sequentially for 60−90 min using dry nitrogen and for 2 h under high vacuum in a sublimation apparatus. Then, the product was sublimated (85 °C, 1×10^{-3} mbar) and was collected from the sublimation apparatus in a glovebox on the same day. The purified product (156 mmol, 68% yield, constituting colorless crystallites with a melting point of 102−104 °C (lit:[78] 102−105 °C)) was stored in a Schlenk tube at −80 °C and was handled in a glovebox at all times.

^{1}H NMR (300 MHz, $CDCl_3$): δ [ppm] = 4.22 (2 H, s, $-CH_2-CO-$), 2.86 (3 H, s, $-CH_3$).

Synthesis of Azidobutyric Acid Pentafluorphenylester. γ-Azidobutyric acid (7.74 mmol) was dissolved in predried THF, and triethylamine (15.0 mmol, 2 equiv) was added. The solution was stirred at room temperature (RT) for 30 min. Then, two volumes of pentafluorophenol trifluoroacetate (15.0 mmol) were added dropwise. The reaction mixture was stirred overnight at RT. Completion of the reaction was evaluated with TLC (thin-layer chromatography). THF was distilled, and the remaining solid was first dissolved in dichloromethane and then was extracted three times with water. The organic phase was dried with $MgSO_4$, and DCM (dichloromethane) was distilled off the product. The product was purified by column chromatography.

^{1}H NMR (400 MHz, $CDCl_3$): δ [ppm] = 3.46 (2 H, t, $-CH_2-CH_2-\mathbf{CH_2}-N_3$), 2.80 (2 H, t, $-\mathbf{CH_2}-CH_2-CH_2-N_3$), 2.05 (2 H, m, $-CH_2-\mathbf{CH_2}-CH_2-N_3$). ^{19}F NMR (400 MHz, $CDCl_3$): δ [ppm] = −153.95 (2F, d, *o*-CF), −158.90 (1F, t, *p*-CF), −163.32 (2F, t, *m*-CF).

PB Synthesis. The synthesis was performed as described with some modifications.[26] The following stock solutions were prepared directly prior to use under a dry nitrogen atmosphere: 228 mg mL^{-1} DIPEA (diisopropylethylamine) in 3.7 mL of DMF (dimethylformamide), 7.83 g sarcosine NCA in 40 mL of DMF, and 218 mg of azidobutyric acid pentafluorphenylester in 2 mL of DMF. The following operations were performed under a steady flow of dry nitrogen. A 0.80 mL (351 μmol) amount of DIPEA−DMF was added *via* syringe to a Schlenk tube containing 71 mg (292 μmol) of poly(L-lysine trifluoroacetate) (DP = 258) dissolved in 2 mL of DMF solution. After 1 h stirring, 16.8 mL (29 mmol) of sarcosine NCA in DMF was added. The solution was stirred at RT and kept at a constant pressure of 1.25 bar of dry nitrogen *via* a Schlenk line to prevent impurities from entering the reaction vessel while allowing CO_2 to escape. When the reaction was finished (completion of the reaction was confirmed by IR spectroscopy by the disappearance of the NCA peaks), 0.95 mL of azidobutyric acid pentafluorphenylester in DMF (1.2-fold excess based on the amine groups) was added, and the reaction mixture was stirred for 2 days at 40 °C. The final azide-functionalized polymer brush was precipitated in ether and centrifuged (4500 rpm at 4 °C for 15 min). After discarding the liquid fraction, fresh ether was added and the polymer was resuspended using a sonic bath. The suspension was centrifuged again, and the procedure was repeated. The polymer was dissolved in Milli-Q water and purified using Amicon Ultra centrifugal filters (50 kDa, 4000*g*, 4 × 20 min). After lyophilization, a colorless product was obtained. Yield: 63%.

Dye Labeling of PBs. The dyes AlexaFluor647-DBCO and 800CW-DBCO were conjugated to the PBs *via* SPAAC. In a typical experiment, the PB was dissolved in DPBS (Dulbecco's phosphate-buffered saline) (c_{PB} = 50 g·L^{-1}) and the dye was dissolved in DMSO (c_{Dye} = 5 mM). As the reaction is quantitative, 1 equiv of the desired amount of dyes per brush was added. After incubation overnight at RT under light exclusion, the reaction mixture was purified by Amicon Ultra centrifugal filter devices to remove unbound dye (15 mL, 50 kDa, 4000*g*, 10 times). The resulting solution was concentrated with Amicon Ultra centrifugal filter devices (50 kDa, 4000*g*) and filtered through sterile 0.22 μm Millex-GS filters. R_h was measured by DLS and FCS (fluorescence correlation spectroscopy). FCS was also used to prove the absence of unconjugated dye and to determine the number of dyes per brush. To evaluate quenching effects, emission spectra of the free dye and the dye-labeled PBs were recorded, using solutions of the same optical density. If quenching effects were detected, the number of dyes determined by FCS were corrected by the extent of quenching.

Synthesis of DBCO-Functionalized aDEC205. In a typical experiment, 2 equiv of DBCO-PEG_4-NHS-ester (dissolved in DMSO [dimethyl sulfoxide], c = 10 g·L^{-1}) was added to the antibodies. aDEC205 and ratIgG2a were used as received (dissolved in DPBS, $c_{aDEC205}$ = 4−7 g/L). After incubation overnight at RT, the reaction mixture was purified by Amicon Ultra centrifugal filter devices (15 mL, 10 kDa, 4000*g*, 10 times) to remove unbound DBCO-PEG_4-NHS-ester and NHS. Afterward, preparative size-exclusion chromatography was performed using a Sepharose 4 FF XK 16/70 column (flow 0.5 mL·min^{-1}) to remove aggregates (aDEC205-DBCO fraction, 80−110 mL). The resulting solution was concentrated with Amicon Ultra centrifugal filter devices (10 kDa, 4000*g*) and filtered through sterile 0.22 μm Millex-GS filters. $R_{h,antibody\text{-}DBCO}$ = 5−6 nm. The antibody concentrations as well as the number of DBCO per bioactive component were determined by UV−vis spectroscopy as described in the literature.

Synthesis of Dye-Labeled PLys250. PLys258 (20 mg, 320 nmol) was dissolved in 2 mL of DPBS, and AlexaFluor647-NHS ester (2.5 equiv, 1 mg, 800 nmol) dissolved in DMSO (160 μL) was added. The reaction mixture was incubated overnight under light exclusion at RT. The reaction product was purified using Amicon Ultra centrifugal filter devices (15 mL, 10 kDa, 4000*g*, 20 times). R_h(FCS) = 7.6 nm. Each molecule contained two dye residues as determined by FCS. FCS analysis demonstrated that the solution contained 15% free dye, taken into account for calculations of the dye concentrations. The pLys concentration was determined by dividing the dye concentration of the conjugated dye by 2.

https://doi.org/10.1021/acsnano.1c05713
ACS Nano XXXX, XXX, XXX−XXX

Synthesis of Dye-Labeled aDEC205. In a typical experiment, 2 equiv of AlexaFluor647-NHS ester (dissolved in DMSO, c = 5 mM) was added to the antibodies, respectively. aDEC205 antibody (clone NLDC145) was used as received (dissolved in DPBS, $c_{\alpha DEC205}$ = 4−7 g/L). After incubation overnight at RT, the reaction mixture was purified using Amicon Ultra centrifugal filter devices (15 mL, 10 kDa, 4000*g*, 10 times) to remove unbound AlexaFluor647-NHS ester and NHS. The resulting solution was filtered sequentially through Anotop 20 nm filters and sterile 0.22 μm Millex-GS filters. $R_{h,antibody\text{-}FD}$ = 5−6 nm. FCS shows that there is still 15−20% free dye in the solution. The antibody concentration is calculated from the UV−vis spectrum using the specific antibody absorption at 280 nm.

Synthesis of PB Conjugates with aDEC205, ratIgG2a, and aDEC205 F(ab')$_2$ Fragments. aDEC205-derived F(ab')$_2$ fragments were generated according to established protocols with modifications.[74] A 36.3 mg amount of aDEC205 (0.24 μM) was transferred into 0.2 M sodium acetate buffer using Amicon Ultra centrifugal filter devices (15 mL, 10 kDa, 4000*g*, 5 times). Pepsin was dissolved in the same buffer, getting a concentration of 10 mg/mL. After several small-scale pilot digestions with final w/w ratios of pepsin to antibody from 1:1 to 1:1000, the large-scale digestion was performed with a final w/w ratio of pepsin to antibody of 1:4 at 37 °C and 550 rpm. After incubation the pH was adjusted to 7.8 with 2 M Trizma base to stop the reaction. Digestion progress was determined *via* SDS-PAGE (sodium dodecyl sulfate polyacrylamide gel electrophoresis). To isolate the F(ab)$_2$ fragments a size-exclusion chromatography was performed using a HiPrep 16/60 Sephacryl S-500 HR column (sterile DPBS, flow 0.5 mL·min^{-1}). The fractions 105−125 min were concentrated with Amicon Ultra centrifugal filter devices (15 mL, 10 kDa, 4000*g*) and filtered through sterile 0.22 μm Millex-GV filters. The purified F(ab)$_2$ fragment was DBCO modified as described before.

Antibody conjugates comprising 2, 6, 10, and 12 aDEC205 antibodies per PB and an intermediate number of rat IgG2a and F(ab)$_2$ fragments, respectively, were synthesized. The amount of the DBCO-modified antibody that was added to the brush depends on the number of DBCO (N_{DBCO}) per component; 1/(0.34N_{DBCO}) equiv of the DBCO-modified component (dissolved in DPBS, $c_{antibody\text{-}DBCO}$ = 5−15 g·L^{-1}) was added to the dye-labeled brush dissolved in DPBS (c_{PB} = 1 × 10^{-5} to 1 × 10^{-6} M). The reaction mixture was incubated overnight at RT. To remove bridged brushes and unconjugated antibodies, PB conjugates were purified *via* preparative SEC using a Sepharose 4 FF XK 16/70 column (flow 0.5 mL·min^{-1}). The fraction from 55 to 75 mL was collected, concentrated using Amicon Ultra centrifugal filter devices (50 kDa, 4000*g*), and filtered through sterile 0.22 μm Millex-GS filters. Each conjugate was analyzed by DLS, FCS, UV−vis spectroscopy, and SDS-PAGE.

Biological Materials and Assays. *Animals.* Female C57/Bl6 (*in vitro* studies) and BALB/c (*in vivo* studies) mice were purchased from Envigo.

Antibodies. CD45-FITC (Invitrogen), CD31-PE (eBioscience), CD146-APC (Biolegend), CD11c-APC (eBioscience), F4/80-eFluor450 (Invitrogen), CD19-AF488 (eBioscience), CD8a-PE (BD Pharmingen), aCD16/CD32 (clone 2.4G2), and *in vivo* ready anti-mouse CD16/CD32 and isotype control (TONBO Bioscience) were obtained.

Isolation of Liver NPCs. Liver NPCs of female C57/Bl6 and BALB/c mice were isolated by an organ perfusion method including collagenase digestion as previously described.[70] In short, mice were anesthetized with a ketamine/rompun mixture, and the abdominal cavity was opened. By cannulating the *vena portae*, 20 mL of HBSS (Hank's balanced salt solution) (ThermoFisher Scientific) containing collagenase A (Sigma-Aldrich) and DNase I (Sigma-Aldrich) flushed the liver after the aorta had been cut. The liver, largely devoid of erythrocytes or other loosely bound cells, was then dissected into pieces and incubated for 15 min at 37 °C in a 50 mL tube containing the perfusion enzyme solution. After incubation the liver was put through a 70 μm nylon cell strainer and the enzymatic reaction was stopped with medium (DMEM (Dulbecco's modified Eagle medium)/F-12 GlutaMAX, ThermoFisher Scientific). To remove hepatocytes, the cell suspension was centrifuged at 300*g* for 15 min. The remaining cells in the suspension were further purified by 30% Histodenz−HBSS gradient centrifugation as specified before.[75] The obtained liver NPCs were then either cultured in medium (DMEM/F-12, GlutaMAX, ThermoFisher Scientific) (described in the following section) or subjected to antibody staining for subsequent flow cytometry analysis. For *ex vivo* studies the liver dissociation kit from Milteny was used following the instructions.

In Vitro NP Incubation. After isolation, NPCs were seeded into a nontreated 12-well plate in a volume of 1 mL and 1 million cells per well. NPCs were treated with different brush−antibody conjugates at 37 °C for 1 h. For this 10^{12} particles were used. Following incubation, NPCs were rinsed on ice and transferred to flow cytometry tubes for staining.

Flow Cytometry. Single-cell suspensions of respective organs were obtained after mechanical digestion and filtering using a 70 μm nylon cell strainer. Livers were digested previously using the liver dissociation kit (Milteny). After lysis of erythrocytes (liver, spleen), cells were incubated with receptor-specific antibodies for FACS analysis. For this, cells were washed (2% FCS in DPBS), and FcRs were blocked with aCD16/CD32 (2.4G2 clone) for 10 min. Afterward, liver NPCs were incubated with receptor-specific antibodies (CD45-FITC, CD31-PE, CD11c-APC, and F4/80-eFluor450) for 20 min at 4 °C. Within the CD45$^+$ liver NPC fraction, DCs (CD11c$^+$), ECs (CD31$^+$), and Mphs (F4/80$^+$) were identified according to the expression of their corresponding lineage marker. Spleen and LN cells were incubated with anti-CD11c-APC to detect DCs and in the case of spleen cells in addition with anti-CD8a-PE to differentiate CD8a$^+$ and CD8a$^-$ DC subpopulations. All antibodies were obtained from Thermo Scientific. Cells were fixed with 0.7% PFA and subjected to flow cytometry (Attune NxT flow cytometer, Thermo Scientific). Results were evaluated with Attune NxT flow cytometer software.

cLSM (Confocal Laser Scanning Microscopy). Liver NPCs were incubated with 10^{12} particles for 1 h at 37 °C as described above. After washing the cells with PBS, Hoechst dye (2 μM) was added and samples were incubated at RT for 30 min to stain the nucleus. To flag LSECs, samples were incubated with a CD146-specific antibody (APC-labeled) for 20 min at 4 °C. Cells were washed twice with DPBS, and images were taken using a TCS SP5 confocal microscope at the Institute of Molecular Biology, Mainz.

Biodistribution and Blood Circulation. The PB−antibody conjugates (0.5−1.8 mg, equimolar amounts of PBs) and FcR blocking antibody (anti-CD16/CD32;[37] 50 μg) were injected i.v. into BALB/c mice. Particle injection followed 3 h after injection of the blocking antibody. The animals were imaged at the indicated time points using the IVIS Spectrum Imaging System (PerkinElmer) with the excitation/emission filter set of 745/800 nm. Blood was retrieved retroorbitally and also imaged to measure fluorescence intensities. Background fluorescence (PBS group) was subtracted. To estimate the starting concentration of PBs in the blood (t = 0), each 50 μL of blood, which corresponds to about 1:30 of the total blood volume of a mouse of the age used in this study by us, of two different mice was mixed with a 1:30 ratio of the respective PB formulations applied *in vivo*, and fluorescence levels were measured (PBs: 7664 ± 0.3098, PB−aDEC205[2]: 5784 ± 1399, PB−aDEC205[6]: 6752 ± 2167, PB−aDEC205[12]: 6624 ± 1090). Mice were sacrificed at the indicated time points, and organs (liver, heart, lungs, spleen, and inguinal as well as popliteal LNs) were dissected and imaged as above. Fluorescence intensities are presented as total radiant efficiency ([p/s]/[μW/cm^2]).

Separation by Asymmetrical Flow Field-Flow Fractionation (AF4). The AF4 measurements were performed using an installation from the ConSenxuS GmbH. The setup was composed of a constaMETRICR 3200 main pump and a Spectra Series UV150 detector from Thermos Separation, a Dark V3 LS detector from ConSenxuS GmbH, a Pharmacia P-3500 injection pump, an LV-F flow controller from Horiba ATEC, a Waters in-line degasser-AF, and a separation channel with a 190 μm spacer and a regenerated cellulose membrane with a molecular weight cutoff of 10 kDa. The UV

https://doi.org/10.1021/acsnano.1c05713
ACS Nano XXXX, XXX, XXX−XXX

absorption of PBs was detected at 220 nm. For all measurements, phosphate-buffered saline (151.7×10^{-3} m) was used as solvent; it also contained sodium azide in a concentration of 0.2×10^{-3} m. The main flow was 1 mL min^{-1} higher than the cross-flow for each measurement. The cross-flow is illustrated in the AF4 elugram (see Supp Figure 5). Every measurement was carried out at least three times from three independent incubation experiments. PB fractions were collected from 13.3 to 18.3 min. To increase the concentration of the collected fractions from the AF4 after the separation process, they were filtrated with Amikon Ultra centrifugal filters from Merck Millipore with a regenerated cellulose membrane and a molecular weight cutoff of 3 kDa. Plasma and particle controls were performed as described.[24]

SDS-PAGE. SDS-PAGE experiments were performed following the general protocol of Laemmli. The polyacrylamide gels were composed of a 12% separation gel (with 8% stacking gel), and the electrophoresis was carried out for 45 min at 200 V with a Mini-PROTEAN Tetra Vertical electrophoresis chamber from BIO-RAD. A 7.5 μL amount of each sample was incubated with 2.5 μL of loading buffer (NuPAGE LDS sample buffer, Invitrogen) for 5 min at 95 °C. Novex Sharp pre-stained protein standard from Invitrogen was loaded on each gel as a protein ladder for comparison. The proteins in the gels were visualized using silver staining.

Dynamic Light Scattering. For DLS experiments the collected fractions from the AF4 were prepared in a dust-free flow-box. They were filtered with syringe filters from PALL Life Science with a diameter of 13 mm and a GHP membrane (0.2 μm pores) into dust-free cylindrical scattering cells (Suprasil, 20 mm diameter). The measurements were performed with a Uniphase He/Ne laser (632.8 nm, 22 mW), an ALV-SP125 goniometer, an ALV/High QE APD-Avalanche photodiode, an ALV5000/E/PCI correlator, and a Lauda RC-6 thermostat unit. All angular-dependent measurements were carried out in 20° steps between 30° and 150°. Data analysis was performed according to the procedure described by Rausch and co-workers.[76]

Protein Digestion. Lyophilized protein corona proteins were digested according to the SP3 ("single-pot solid-phase-enhanced sample preparation") protocol.[77] After solubilization in SDS-Lysis buffer (1% SDS, 1× complete Protease Inhibitor Cocktail-EDTA, 50 mM HEPES, pH 8,5), proteins were reduced by adding 5 μL of 200 mM dithiothreitol (DTT) per 100 μL of lysate (45 °C, 30 min). Free cysteines were subsequently alkylated by adding 10 μL of 100 mM iodoacetamide (IAA) per 100 μL of lysate (RT, 30 min, in the dark). Subsequently, the remaining IAA was quenched by adding 10 μL of 200 mM DTT per 100 μL of lysate. Magnetic carboxylate-modified particle beads (SpeedBeads, Sigma) were used for protein clean-up, and acetonitrile (ACN), in a final concentration of 70%, was added to the samples to induce the binding of the proteins to the beads by hydrophilic interactions (RT, 18 min). By incubating the bead–protein mixture on a magnetic stand for 2 min, the sample was bound to the magnet and the supernatant was removed, followed by two washing steps with 70% ethanol (EtOH), addition of 180 μL of ACN, incubation for 15 s, and removal of the solvent. Finally, 5 μL of digestion buffer (50 mM ammonium bicarbonate, 1:25 w/w trypsin:protein ratio) was added to the air-dried bead–protein mixtures and incubated overnight at 37 °C. To purify peptides after digestion, ACN was added to a final concentration of 95%. After another washing step (see Sielaff *et al.*, 2017, for detailed information) the beads were resuspended in 10 μL of 2% DMSO (in water), put into an ultrasonic bath for 1 min, and then shortly centrifuged. A 10 μL portion of the resulting supernatant was mixed with 5 μL of 100 fmol/μL Enolase digest (Waters, Eschborn, Germany) and acidified with 5 μL of 1% formic acid (FA).

Liquid Chromatography–Mass Spectroscopy (LC-MS). LC analysis of tryptic peptides was performed on a NanoAQUITY UPLC system (Waters Corporation, Milford, MA, USA) equipped with 75 μM × 250 mm HSS-T3 C18 column (Waters Corporation). Mobile phase A was 0.1% (v/v) FA and 3% (v/v) DMSO in water. Mobile phase B was 0.1% (v/v) FA and 3% (v/v) DMSO in ACN. Peptides were separated running a gradient from 5% to 60% (v/v) mobile phase B at a flow rate of 300 nL/min over 60 min. The column was heated to 55 °C. MS analysis of eluting peptides was performed by data-independent acquisition in MS^E. In brief, precursor ion information was collected in low-energy MS mode at a constant collision energy of 4 eV. Fragment ion information was obtained in the elevated energy scan applying drift-time-specific collision energies. The spectral acquisition time in each mode was 0.6 s with a 0.05 s interscan delay, resulting in an overall cycle time of 1.3 s for the acquisition of one cycle of low and elevated energy data. [Glu1]-fibrinopeptide was used as lock mass at 100 fmol/μL and sampled every 30 s into the mass spectrometer *via* the reference sprayer of the NanoLockSpray source. All samples were analyzed in three technical replicates.

Data Processing and Label-Free Quantification. MS^E data processing and database search were performed using ProteinLynx Global Server (PLGS, ver. 3.0.2, Waters Corporation). The resulting proteins were searched in the UniProt human proteome database (UniProtKB release 2017_05, 20,201 entries)[78] supplemented with a list of common contaminants. The database search was specified by trypsin as enzyme for digestion, and peptides with up to two missed cleavages were included. Furthermore, carbamidomethyl cysteine was set as fixed modification and oxidized methionine as variable modification. False discovery rate assessment for peptide and protein identification was done using the target-decoy strategy by searching a reverse database and was set to 0.01 for database search in PLGS. Retention time alignment, exact mass retention time, normalization, and filtering was performed in ISOQuant ver.1.8.[79] By using TOP3 quantification,[80] absolute in-sample amounts of proteins were calculated. Statistical analysis was done in Perseus,[81] by performing two-tailed, paired tests and subsequent Benjamini–Hochberg correction.[82] Q-values < 0.05 were considered significant.

ASSOCIATED CONTENT

Supporting Information

The Supporting Information is available free of charge at https://pubs.acs.org/doi/10.1021/acsnano.1c05713.

Binding of PB derivatives to liver cell populations, effects of FcR blockade on binding to liver cell populations, LN and spleen DC populations (PDF)

AUTHOR INFORMATION

Corresponding Authors

Matthias Bros − *Department of Dermatology, University Medical Center of the Johannes Gutenberg University Mainz, 55131 Mainz, Germany*; Email: mbros@uni-mainz.de

Stephan Grabbe − *Department of Dermatology, University Medical Center of the Johannes Gutenberg University Mainz, 55131 Mainz, Germany*; Email: stephan.grabbe@unimedizin-mainz.de

Matthias Barz − *Leiden Academic Center for Drug Research (LACDR), Leiden University, 2333 CC Leiden, The Netherlands; Department of Chemistry, Johannes Gutenberg University, 55099 Mainz, Germany; Department of Dermatology, University Medical Center of the Johannes Gutenberg University Mainz, 55131 Mainz, Germany*; orcid.org/0000-0002-1749-9034; Email: mbarz@lacdr.leidenuniv.nl

Authors

Cinja Kappel − *Department of Dermatology, University Medical Center of the Johannes Gutenberg University Mainz, 55131 Mainz, Germany*; orcid.org/0000-0002-9122-0601

Christine Seidl − *Department of Chemistry, Johannes Gutenberg University, 55099 Mainz, Germany; Leiden*

https://doi.org/10.1021/acsnano.1c05713
ACS Nano XXXX, XXX, XXX−XXX

Academic Center for Drug Research (LACDR), Leiden University, 2333 CC Leiden, The Netherlands
Carolina Medina-Montano − *Department of Dermatology, University Medical Center of the Johannes Gutenberg University Mainz, 55131 Mainz, Germany*
Meike Schinnerer − *Department of Chemistry, Johannes Gutenberg University, 55099 Mainz, Germany*
Irina Alberg − *Department of Chemistry, Johannes Gutenberg University, 55099 Mainz, Germany*
Christian Leps − *Institute for Immunology, University Medical Center of the Johannes Gutenberg University Mainz, 55131 Mainz, Germany*
Julian Sohl − *Institute for Immunology, University Medical Center of the Johannes Gutenberg University Mainz, 55131 Mainz, Germany*
Ann-Kathrin Hartmann − *Institute for Immunology, University Medical Center of the Johannes Gutenberg University Mainz, 55131 Mainz, Germany*
Michael Fichter − *Department of Dermatology, University Medical Center of the Johannes Gutenberg University Mainz, 55131 Mainz, Germany*
Michael Kuske − *Department of Dermatology, University Medical Center of the Johannes Gutenberg University Mainz, 55131 Mainz, Germany*
Jenny Schunke − *Department of Dermatology, University Medical Center of the Johannes Gutenberg University Mainz, 55131 Mainz, Germany*
Gabor Kuhn − *Department of Dermatology, University Medical Center of the Johannes Gutenberg University Mainz, 55131 Mainz, Germany*
Ingrid Tubbe − *Department of Dermatology, University Medical Center of the Johannes Gutenberg University Mainz, 55131 Mainz, Germany*
David Paßlick − *Department of Dermatology, University Medical Center of the Johannes Gutenberg University Mainz, 55131 Mainz, Germany*
Dominika Hobernik − *Department of Dermatology, University Medical Center of the Johannes Gutenberg University Mainz, 55131 Mainz, Germany*
Rebekka Bent − *Department of Dermatology, University Medical Center of the Johannes Gutenberg University Mainz, 55131 Mainz, Germany*
Katharina Haas − *Department of Dermatology, University Medical Center of the Johannes Gutenberg University Mainz, 55131 Mainz, Germany*
Evelyn Montermann − *Department of Dermatology, University Medical Center of the Johannes Gutenberg University Mainz, 55131 Mainz, Germany*
Kerstin Walzer − *TRON−Translational Oncology at the University Medical Center of the Johannes Gutenberg University GmbH, 55131 Mainz, Germany*
Mustafa Diken − *TRON−Translational Oncology at the University Medical Center of the Johannes Gutenberg University GmbH, 55131 Mainz, Germany; Biontech AG, 55131 Mainz, Germany*
Manfred Schmidt − *Institute for Physical Chemistry, Johannes Gutenberg University, 55099 Mainz, Germany*
Rudolf Zentel − *Department of Chemistry, Johannes Gutenberg University, 55099 Mainz, Germany;* orcid.org/0000-0001-9206-6047
Lutz Nuhn − *Max Planck Institute for Polymer Research, 55128 Mainz, Germany;* orcid.org/0000-0003-0761-1106
Hansjörg Schild − *Institute for Immunology, University Medical Center of the Johannes Gutenberg University Mainz, 55131 Mainz, Germany*
Stefan Tenzer − *Institute for Immunology, University Medical Center of the Johannes Gutenberg University Mainz, 55131 Mainz, Germany;* orcid.org/0000-0003-3034-0017
Volker Mailänder − *Department of Dermatology, University Medical Center of the Johannes Gutenberg University Mainz, 55131 Mainz, Germany;* orcid.org/0000-0001-6583-8136

Complete contact information is available at: https://pubs.acs.org/10.1021/acsnano.1c05713

Author Contributions

C. Kappel and C. Medina-Montano performed the *in vitro* and *in vivo* studies. C. Seidl and M. Schinnerer synthesized and characterized the polymer brushes and corresponding conjugates, etc. M. Fichter, M. Kuske, J. Schunke, G. Kuhn, I. Tubbe, D. Paßlick, D. Hobernik, R. Bent, K. Haas, E. Montermann, J. Sohl, and A.-K. Hartmann assisted during or performed the *in vivo* studies. M. Diken and K. Walzer conducted the biodistribution studies. C. Leps and I. Alberg conducted and Stefan Tenzer supervised the mass spectroscopy studies on protein corona formation. V. Mailänder contributed to the planning of the *in vivo* studies and the discussion of the results. M. Schmidt, R. Zentel, L. Nuhn, and H. Schild contributed to evaluation of data and contributed to the discussion of results. The project was designed and supervised by M. Barz, M. Bros, and S. Grabbe.

Notes

The authors declare no competing financial interest.

ACKNOWLEDGMENTS

This work was funded by the Deutsche Forschungsgemeinschaft (DFG, German Research Foundation) SFB-Geschäftszeichen SFB 1066/3 2021 213555243; TP B4, TP A6, Q6. We would like to thank S. Gehring and co-workers for their support, as well as the Institute of Molecular Biology (IMB, Mainz Germany). We also thank C. Rosenauer (Morsbach lab, Max Planck Institute for Polymer Research, Mainz, Germany) for performing DLS measurements.

REFERENCES

(1) Kulshrestha, S.; Khan, A. U. Nanomedicine for Anticancer and Antimicrobial Treatment: An Overview. *IET Nanobiotechnol.* **2018**, *12* (8), 1009−1017.
(2) Ajorlou, E.; Khosroushahi, A. Y. Trends on Polymer- and Lipid-Based Nanostructures for Parenteral Drug Delivery to Tumors. *Cancer Chemother. Pharmacol.* **2017**, *79* (2), 251−265.
(3) Maeda, H.; Nakamura, H.; Fang, J. The EPR Effect for Macromolecular Drug Delivery to Solid Tumors: Improvement of Tumor Uptake, Lowering of Systemic Toxicity, and Distinct Tumor Imaging *in Vivo*. *Adv. Drug Delivery Rev.* **2013**, *65* (1), 71−9.
(4) Huang, P.; Wang, X.; Liang, X.; Yang, J.; Zhang, C.; Kong, D.; Wang, W. Nano-, Micro-, and Macroscale Drug Delivery Systems for Cancer Immunotherapy. *Acta Biomater.* **2019**, *85*, 1−26.
(5) Kelly, H. G.; Kent, S. J.; Wheatley, A. K. Immunological Basis for Enhanced Immunity of Nanoparticle Vaccines. *Expert Rev. Vaccines* **2019**, *18* (3), 269−280.
(6) Grabbe, S.; Landfester, K.; Schuppan, D.; Barz, M.; Zentel, R. Nanoparticles and the Immune System: Challenges and Opportunities. *Nanomedicine (London, U. K.)* **2016**, *11* (20), 2621−2624.
(7) Lee, G.; Han, S.; Inocencio, I.; Cao, E.; Hong, J.; Phillips, A. R. J.; Windsor, J. A.; Porter, C. J. H.; Trevaskis, N. L. Lymphatic Uptake

of Liposomes after Intraperitoneal Administration Primarily Occurs *via* the Diaphragmatic Lymphatics and Is Dependent on Liposome Surface Properties. *Mol. Pharmaceutics* **2019**, *16* (12), 4987−4999.
(8) Germic, N.; Frangez, Z.; Yousefi, S.; Simon, H. U. Regulation of the Innate Immune System by Autophagy: Monocytes, Macrophages, Dendritic Cells and Antigen Presentation. *Cell Death Differ.* **2019**, *26* (4), 715−727.
(9) Shen, L.; Tenzer, S.; Storck, W.; Hobernik, D.; Raker, V. K.; Fischer, K.; Decker, S.; Dzionek, A.; Krauthauser, S.; Diken, M.; Nikolaev, A.; Maxeiner, J.; Schuster, P.; Kappel, C.; Verschoor, A.; Schild, H.; Grabbe, S.; Bros, M. Protein Corona-Mediated Targeting of Nanocarriers to B Cells Allows Redirection of Allergic Immune Responses. *J. Allergy Clin. Immunol.* **2018**, *142* (5), 1558−1570.
(10) Bros, M.; Nuhn, L.; Simon, J.; Moll, L.; Mailander, V.; Landfester, K.; Grabbe, S. The Protein Corona as a Confounding Variable of Nanoparticle-Mediated Targeted Vaccine Delivery. *Front. Immunol.* **2018**, *9*, 1760.
(11) Hey, Y. Y.; O'Neill, H. C. Murine Spleen Contains a Diversity of Myeloid and Dendritic Cells Distinct in Antigen Presenting Function. *Journal of Cellular and Molecular Medicine* **2012**, *16* (11), 2611−9.
(12) Tran, T. H.; Tran, T. T. P.; Nguyen, H. T.; Phung, C. D.; Jeong, J. H.; Stenzel, M. H.; Jin, S. G.; Yong, C. S.; Truong, D. H.; Kim, J. O. Nanoparticles for Dendritic Cell-Based Immunotherapy. *Int. J. Pharm.* **2018**, *542* (1−2), 253−265.
(13) Tjandra, K. C.; Thordarson, P. Multivalency in Drug Delivery-When Is It Too Much of a Good Thing? *Bioconjugate Chem.* **2019**, *30* (3), 503−514.
(14) Zern, B. J.; Chacko, A. M.; Liu, J.; Greineder, C. F.; Blankemeyer, E. R.; Radhakrishnan, R.; Muzykantov, V. Reduction of Nanoparticle Avidity Enhances the Selectivity of Vascular Targeting and PET Detection of Pulmonary Inflammation. *ACS Nano* **2013**, *7* (3), 2461−9.
(15) Sondermann, P.; Szymkowski, D. E. Harnessing Fc Receptor Biology in the Design of Therapeutic Antibodies. *Curr. Opin. Immunol.* **2016**, *40*, 78−87.
(16) Alkilany, A. M.; Zhu, L.; Weller, H.; Mews, A.; Parak, W. J.; Barz, M.; Feliu, N. Ligand Density on Nanoparticles: A Parameter with Critical Impact on Nanomedicine. *Adv. Drug Delivery Rev.* **2019**, *143*, 22−36.
(17) Faria, M.; Bjornmalm, M.; Thurecht, K. J.; Kent, S. J.; Parton, R. G.; Kavallaris, M.; Johnston, A. P. R.; Gooding, J. J.; Corrie, S. R.; Boyd, B. J.; Thordarson, P.; Whittaker, A. K.; Stevens, M. M.; Prestidge, C. A.; Porter, C. J. H.; Parak, W. J.; Davis, T. P.; Crampin, E. J.; Caruso, F. Minimum Information Reporting in Bio-Nano Experimental Literature. *Nat. Nanotechnol.* **2018**, *13* (9), 777−785.
(18) Buhler, J.; Gietzen, S.; Reuter, A.; Kappel, C.; Fischer, K.; Decker, S.; Schaffel, D.; Koynov, K.; Bros, M.; Tubbe, I.; Grabbe, S.; Schmidt, M. Selective Uptake of Cylindrical Poly(2-Oxazoline) Brush-AntiDEC205 Antibody-OVA Antigen Conjugates into DEC-Positive Dendritic Cells and Subsequent T-Cell Activation. *Chem. - Eur. J.* **2014**, *20* (39), 12405−10.
(19) Bargheer, D.; Giemsa, A.; Freund, B.; Heine, M.; Waurisch, C.; Stachowski, G. M.; Hickey, S. G.; Eychmuller, A.; Heeren, J.; Nielsen, P. The Distribution and Degradation of Radiolabeled Superparamagnetic Iron Oxide Nanoparticles and Quantum Dots in Mice. *Beilstein J. Nanotechnol.* **2015**, *6*, 111−123.
(20) Shen, L.; Krauthauser, S.; Fischer, K.; Hobernik, D.; Abassi, Y.; Dzionek, A.; Nikolaev, A.; Voltz, N.; Diken, M.; Krummen, M.; Montermann, E.; Tubbe, I.; Lorenz, S.; Strand, D.; Schild, H.; Grabbe, S.; Bros, M. Vaccination with Trifunctional Nanoparticles that Address CD8(+) Dendritic Cells Inhibits Growth of Established Melanoma. *Nanomedicine (London, U. K.)* **2016**, *11* (20), 2647−2662.
(21) Birke, A.; Huesmann, D.; Kelsch, A.; Weilbacher, M.; Xie, J.; Bros, M.; Bopp, T.; Becker, C.; Landfester, K.; Barz, M. Polypeptoid-Block-Polypeptide Copolymers: Synthesis, Characterization, and Application of Amphiphilic Block Copolypept(o)ides in Drug Formulations and Miniemulsion Techniques. *Biomacromolecules* **2014**, *15* (2), 548−57.
(22) Birke, A.; Ling, J.; Barz, M. Polysarcosine-Containing Copolymers: Synthesis, Characterization, Self-Assembly, and Applications. *Prog. Polym. Sci.* **2018**, *81*, 163−208.
(23) Fenaroli, F.; Repnik, U.; Xu, Y.; Johann, K.; Van Herck, S.; Dey, P.; Skjeldal, F. M.; Frei, D. M.; Bagherifam, S.; Kocere, A.; Haag, R.; De Geest, B. G.; Barz, M.; Russell, D. G.; Griffiths, G. Enhanced Permeability and Retention-Like Extravasation of Nanoparticles from the Vasculature into Tuberculosis Granulomas in Zebrafish and Mouse Models. *ACS Nano* **2018**, *12* (8), 8646−8661.
(24) Alberg, I.; Kramer, S.; Schinnerer, M.; Hu, Q.; Seidl, C.; Leps, C.; Drude, N.; Mockel, D.; Rijcken, C.; Lammers, T.; Diken, M.; Maskos, M.; Morsbach, S.; Landfester, K.; Tenzer, S.; Barz, M.; Zentel, R. Polymeric Nanoparticles with Neglectable Protein Corona. *Small* **2020**, *16* (18), No. e1907574.
(25) Bonifaz, L. C.; Bonnyay, D. P.; Charalambous, A.; Darguste, D. I.; Fujii, S.; Soares, H.; Brimnes, M. K.; Moltedo, B.; Moran, T. M.; Steinman, R. M. *In vivo* Targeting of Antigens to Maturing Dendritic Cells *via* The DEC-205 Receptor Improves T Cell Vaccination. *J. Exp. Med.* **2004**, *199* (6), 815−24.
(26) Hörtz, C.; Birke, A.; Kaps, L.; Decker, S.; Wächtersbach, E.; Fischer, K.; Schuppan, D.; Barz, M.; Schmidt, M. Cylindrical Brush Polymers with Polysarcosine Side Chains: A Novel Biocompatible Carrier for Biomedical Applications. *Macromolecules* **2015**, *48* (7), 2074−2086.
(27) Ulbricht, J.; Jordan, R.; Luxenhofer, R. On the Biodegradability of Polyethylene Glycol, Polypeptoids and Poly(2-Oxazoline)s. *Biomaterials* **2014**, *35* (17), 4848−61.
(28) Dal, N. K.; Kocere, A.; Wohlmann, J.; Van Herck, S.; Bauer, T. A.; Resseguier, J.; Bagherifam, S.; Hyldmo, H.; Barz, M.; De Geest, B. G.; Fenaroli, F. Zebrafish Embryos Allow Prediction of Nanoparticle Circulation Times in Mice and Facilitate Quantification of Nanoparticle-Cell Interactions. *Small* **2020**, *16* (5), No. e1906719.
(29) Shortman, K.; Heath, W. R. The CD8+ Dendritic Cell Subset. *Immunol. Rev.* **2010**, *234* (1), 18−31.
(30) Yi, G.; Son, J.; Yoo, J.; Park, C.; Koo, H. Application of Click Chemistry in Nanoparticle Modification and Its Targeted Delivery. *Biomaterials Research* **2018**, *22*, 13.
(31) Sadauskas, E.; Wallin, H.; Stoltenberg, M.; Vogel, U.; Doering, P.; Larsen, A.; Danscher, G. Kupffer Cells Are Central in the Removal of Nanoparticles from the Organism. *Part. Fibre Toxicol.* **2007**, *4*, 10.
(32) Zhang, Y. N.; Poon, W.; Tavares, A. J.; McGilvray, I. D.; Chan, W. C. W. Nanoparticle-Liver Interactions: Cellular Uptake and Hepatobiliary Elimination. *J. Controlled Release* **2016**, *240*, 332−348.
(33) Scott, C. L.; Zheng, F.; De Baetselier, P.; Martens, L.; Saeys, Y.; De Prijck, S.; Lippens, S.; Abels, C.; Schoonooghe, S.; Raes, G.; Devoogdt, N.; Lambrecht, B. N.; Beschin, A.; Guilliams, M. Bone Marrow-Derived Monocytes Give Rise to Self-Renewing and Fully Differentiated Kupffer Cells. *Nat. Commun.* **2016**, *7*, 10321.
(34) Jenne, C. N.; Kubes, P. Immune Surveillance by the Liver. *Nat. Immunol.* **2013**, *14* (10), 996−1006.
(35) Ganesan, L. P.; Kim, J.; Wu, Y.; Mohanty, S.; Phillips, G. S.; Birmingham, D. J.; Robinson, J. M.; Anderson, C. L. FcgammaRIIb on Liver Sinusoidal Endothelium Clears Small Immune Complexes. *J. Immunol.* **2012**, *189* (10), 4981−8.
(36) Anania, J. C.; Chenoweth, A. M.; Wines, B. D.; Hogarth, P. M. The Human FcgammaRII (CD32) Family of Leukocyte FcR in Health and Disease. *Front. Immunol.* **2019**, *10*, 464.
(37) Kurlander, R. J.; Ellison, D. M.; Hall, J. The Blockade of Fc Receptor-Mediated Clearance of Immune Complexes *in Vivo* by a Monoclonal Antibody (2.4G2) Directed against Fc Receptors on Murine Leukocytes. *J. Immunol.* **1984**, *133* (2), 855−862.
(38) Vidarsson, G.; Dekkers, G.; Rispens, T. IgG Subclasses and Allotypes: From Structure to Effector Functions. *Front. Immunol.* **2014**, *5*, 520.
(39) Dzik, S. Complement and Coagulation: Cross Talk through Time. *Transfusion Medicine Reviews* **2019**, *33* (4), 199−206.
(40) Andrew, S. M.; Titus, J. A., Fragmentation of Immunoglobulin G. *Curr. Protoc Cell Biol.* 2003, Chapter 16, Unit 16.4.

https://doi.org/10.1021/acsnano.1c05713
ACS Nano XXXX, XXX, XXX−XXX

(41) De Jong, W. H.; Hagens, W. I.; Krystek, P.; Burger, M. C.; Sips, A. J.; Geertsma, R. E. Particle Size-Dependent Organ Distribution of Gold Nanoparticles after Intravenous Administration. *Biomaterials* **2008**, *29* (12), 1912−9.
(42) Chattopadhyay, N.; Fonge, H.; Cai, Z.; Scollard, D.; Lechtman, E.; Done, S. J.; Pignol, J. P.; Reilly, R. M. Role of Antibody-Mediated Tumor Targeting and Route of Administration in Nanoparticle Tumor Accumulation *in Vivo*. *Mol. Pharmaceutics* **2012**, *9* (8), 2168−79.
(43) Jain, N.; Smith, S. W.; Ghone, S.; Tomczuk, B. Current ADC Linker Chemistry. *Pharm. Res.* **2015**, *32* (11), 3526−40.
(44) Yang, Y.; Mu, J.; Xing, B. Photoactivated Drug Delivery and Bioimaging. *Wiley Interdisciplinary Reviews. Nanomedicine and Nanobiotechnology* **2017**, *9* (2), 1−19.
(45) Nessler, I.; Cilliers, C.; Thurber, G. M. Practical Guide for Quantification of *in Vivo* Degradation Rates for Therapeutic Proteins with Single-Cell Resolution Using Fluorescence Ratio Imaging. *Pharmaceutics* **2020**, *12* (2), 1−13.
(46) Yu, S. S. Evaluating Nanoparticle Binding to Blood Compartment Immune Cells in High-Throughput with Flow Cytometry. *Methods Mol. Biol. (N. Y., NY, U. S.)* **2017**, *1570*, 139−153.
(47) Samuelsson, E.; Shen, H.; Blanco, E.; Ferrari, M.; Wolfram, J. Contribution of Kupffer Cells to Liposome Accumulation in the Liver. *Colloids Surf., B* **2017**, *158*, 356−362.
(48) Park, J. K.; Utsumi, T.; Seo, Y. E.; Deng, Y.; Satoh, A.; Saltzman, W. M.; Iwakiri, Y. Cellular Distribution of Injected PLGA-Nanoparticles in the Liver. *Nanomedicine* **2016**, *12* (5), 1365−74.
(49) Malovic, I.; Sorensen, K. K.; Elvevold, K. H.; Nedredal, G. I.; Paulsen, S.; Erofeev, A. V.; Smedsrod, B. H.; McCourt, P. A. The Mannose Receptor on Murine Liver Sinusoidal Endothelial Cells Is the Main Denatured Collagen Clearance Receptor. *Hepatology (Hoboken, NJ, U. S.)* **2007**, *45* (6), 1454−61.
(50) Seckert, C. K.; Renzaho, A.; Tervo, H. M.; Krause, C.; Deegen, P.; Kuhnapfel, B.; Reddehase, M. J.; Grzimek, N. K. Liver Sinusoidal Endothelial Cells Are a Site of Murine Cytomegalovirus Latency and Reactivation. *J. Virol.* **2009**, *83* (17), 8869−84.
(51) Oie, C. I.; Appa, R. S.; Hilden, I.; Petersen, H. H.; Gruhler, A.; Smedsrod, B.; Hansen, J. B. Rat Liver Sinusoidal Endothelial Cells (LSECs) Express Functional Low Density Lipoprotein Receptor-Related Protein-1 (LRP-1). *J. Hepatol.* **2011**, *55* (6), 1346−52.
(52) Ganesan, L. P.; Mates, J. M.; Cheplowitz, A. M.; Avila, C. L.; Zimmerer, J. M.; Yao, Z.; Maiseyeu, A.; Rajaram, M. V.; Robinson, J. M.; Anderson, C. L. Scavenger Receptor B1, the HDL Receptor, Is Expressed Abundantly in Liver Sinusoidal Endothelial Cells. *Sci. Rep.* **2016**, *6*, 20646.
(53) Hayashi, Y.; Takamiya, M.; Jensen, P. B.; Ojea-Jiménez, I.; Claude, H.; Antony, C.; Kjaer-Sorensen, K.; Grabher, C.; Boesen, T.; Gilliland, D.; Oxvig, C.; Strähle, U.; Weiss, C. Differential Nanoparticle Sequestration by Macrophages and Scavenger Endothelial Cells Visualized *in Vivo* in Real-Time and at Ultrastructural Resolution. *ACS Nano* **2020**, *14* (2), 1665−1681.
(54) Mates, J. M.; Yao, Z.; Cheplowitz, A. M.; Suer, O.; Phillips, G. S.; Kwiek, J. J.; Rajaram, M. V.; Kim, J.; Robinson, J. M.; Ganesan, L. P.; Anderson, C. L. Mouse Liver Sinusoidal Endothelium Eliminates HIV-Like Particles from Blood at a Rate of 100 Million per Minute by a Second-Order Kinetic Process. *Front. Immunol.* **2017**, *8*, 35.
(55) Cheng, W. W.; Allen, T. M. Targeted Delivery of Anti-CD19 Liposomal Doxorubicin in B-cell Lymphoma: A Comparison of Whole Monoclonal Antibody, Fab' Fragments and Single Chain Fv. *J. Controlled Release* **2008**, *126* (1), 50−8.
(56) Chaubey, P.; Mishra, B. Mannose-Conjugated Chitosan Nanoparticles Loaded with Rifampicin for the Treatment of Visceral Leishmaniasis. *Carbohydr. Polym.* **2014**, *101*, 1101−8.
(57) Higuchi, Y.; Nishikawa, M.; Kawakami, S.; Yamashita, F.; Hashida, M. Uptake Characteristics of Mannosylated and Fucosylated Bovine Serum Albumin in Primary Cultured Rat Sinusoidal Endothelial Cells and Kupffer Cells. *Int. J. Pharm.* **2004**, *287* (1−2), 147−54.
(58) Armengol, C.; Bartoli, R.; Sanjurjo, L.; Serra, I.; Amezaga, N.; Sala, M.; Sarrias, M. R. Role of Scavenger Receptors in the Pathophysiology of Chronic Liver Diseases. *Crit. Rev. Immunol.* **2013**, *33* (1), 57−96.
(59) Zhou, H.; Fan, Z.; Li, P. Y.; Deng, J.; Arhontoulis, D. C.; Li, C. Y.; Bowne, W. B.; Cheng, H. Dense and Dynamic Polyethylene Glycol Shells Cloak Nanoparticles from Uptake by Liver Endothelial Cells for Long Blood Circulation. *ACS Nano* **2018**, *12* (10), 10130−10141.
(60) Sivaram, A. J.; Wardiana, A.; Alcantara, S.; Sonderegger, S. E.; Fletcher, N. L.; Houston, Z. H.; Howard, C. B.; Mahler, S. M.; Alexander, C.; Kent, S. J.; Bell, C. A.; Thurecht, K. J. Controlling the Biological Fate of Micellar Nanoparticles: Balancing Stealth and Targeting. *ACS Nano* **2020**, *14* (10), 13739−13753.
(61) Kohler, H. Natural Antibodies: Next Steps Toward Translational Investigation. *Methods Mol. Biol. (N. Y., NY, U. S.)* **2017**, *1643*, 1−3.
(62) Thurman, J. M.; Panzer, S. E.; Le Quintrec, M. The Role of Complement in Antibody Mediated Transplant Rejection. *Mol. Immunol.* **2019**, *112*, 240−246.
(63) Trevaskis, N. L.; Kaminskas, L. M.; Porter, C. J. From Sewer to Saviour - Targeting the Lymphatic System to Promote Drug Exposure and Activity. *Nat. Rev. Drug Discovery* **2015**, *14* (11), 781−803.
(64) Richards, D. A.; Maruani, A.; Chudasama, V. Antibody Fragments as Nanoparticle Targeting Ligands: A Step in the Right Direction. *Chemical Science* **2017**, *8* (1), 63−77.
(65) Leenheer, D.; Ten Dijke, P.; Hipolito, C. J. A Current Perspective on Applications of Macrocyclic-Peptide-Based High-Affinity Ligands. *Biopolymers* **2016**, *106* (6), 889−900.
(66) Hu, P. P. Recent Advances in Aptamers Targeting Immune System. *Inflammation* **2017**, *40* (1), 295−302.
(67) White, A. L.; Chan, H. T.; Roghanian, A.; French, R. R.; Mockridge, C. I.; Tutt, A. L.; Dixon, S. V.; Ajona, D.; Verbeek, J. S.; Al-Shamkhani, A.; Cragg, M. S.; Beers, S. A.; Glennie, M. J. Interaction with FcgammaRIIB is Critical for the Agonistic Activity of Anti-CD40 Monoclonal Antibody. *J. Immunol.* **2011**, *187* (4), 1754−63.
(68) Kedmi, R.; Veiga, N.; Ramishetti, S.; Goldsmith, M.; Rosenblum, D.; Dammes, N.; Hazan-Halevy, I.; Nahary, L.; Leviatan-Ben-Arye, S.; Harlev, M.; Behlke, M.; Benhar, I.; Lieberman, J.; Peer, D. A Modular Platform for Targeted RNAi Therapeutics. *Nat. Nanotechnol.* **2018**, *13* (3), 214−219.
(69) Tonigold, M.; Simon, J.; Estupinan, D.; Kokkinopoulou, M.; Reinholz, J.; Kintzel, U.; Kaltbeitzel, A.; Renz, P.; Domogalla, M. P.; Steinbrink, K.; Lieberwirth, I.; Crespy, D.; Landfester, K.; Mailander, V. Pre-Adsorption of Antibodies Anables Targeting of Nanocarriers Despite a Biomolecular Corona. *Nat. Nanotechnol.* **2018**, *13* (9), 862−869.
(70) Omstead, D. T.; Mejia, F.; Sjoerdsma, J.; Kim, B.; Shin, J.; Khan, S.; Wu, J.; Kiziltepe, T.; Littlepage, L. E.; Bilgicer, B. *In Vivo* Evaluation of CD38 and CD138 as Targets for Nanoparticle-Based Drug Delivery in Multiple Myeloma. *J. Hematol. Oncol.* **2020**, *13* (1), 145.
(71) Reuter, K. G.; Perry, J. L.; Kim, D.; Luft, J. C.; Liu, R.; DeSimone, J. M. Targeted PRINT Hydrogels: The Role of Nanoparticle Size and Ligand Density on Cell Association, Biodistribution, and Tumor Accumulation. *Nano Lett.* **2015**, *15* (10), 6371−8.
(72) Kranz, L. M.; Diken, M.; Haas, H.; Kreiter, S.; Loquai, C.; Reuter, K. C.; Meng, M.; Fritz, D.; Vascotto, F.; Hefesha, H.; Grunwitz, C.; Vormehr, M.; Hüsemann, Y.; Selmi, A.; Kuhn, A. N.; Buck, J.; Derhovanessian, E.; Rae, R.; Attig, S.; Diekmann, J.; et al. Systemic RNA Delivery to Dendritic Cells Exploits Antiviral Defence for Cancer Immunotherapy. *Nature* **2016**, *534* (7607), 396−401.
(73) Fetsch, C.; Grossmann, A.; Holz, L.; Nawroth, J. F.; Luxenhofer, R. Polypeptoids from *N*-Substituted Glycine *N*-Carboxyanhydrides: Hydrophilic, Hydrophobic, and Amphiphilic Polymers with Poisson Distribution. *Macromolecules* **2011**, *44* (17), 6746−6758.

https://doi.org/10.1021/acsnano.1c05713
ACS Nano XXXX, XXX, XXX−XXX

(74) Gauci, P. J. *Pepsin Digestion of Antibodies to Produce Functional Antigen-Binding Fragments (Fab): A Scientific Fantasy ?/ Penelope J. Gauci and Malcolm R. Alderton*; DSTO Aeronautical and Maritime Research Laboratory: Melbourne, Vic, 2001.
(75) Fichter, M.; Baier, G.; Dedters, M.; Pretsch, L.; Pietrzak-Nguyen, A.; Landfester, K.; Gehring, S. Nanocapsules Generated Out of a Polymeric Dexamethasone Shell Suppress the Inflammatory Response of Liver Macrophages. *Nanomedicine* **2013**, *9* (8), 1223−34.
(76) Rausch, K.; Reuter, A.; Fischer, K.; Schmidt, M. Evaluation of Nanoparticle Aggregation in Human Blood Serum. *Biomacromolecules* **2010**, *11* (11), 2836−9.
(77) Sielaff, M.; Kuharev, J.; Bohn, T.; Hahlbrock, J.; Bopp, T.; Tenzer, S.; Distler, U. Evaluation of FASP, SP3, and iST Protocols for Proteomic Sample Preparation in the Low Microgram Range. *J. Proteome Res.* **2017**, *16* (11), 4060−4072.
(78) UniProt: A Worldwide Wub of Protein Knowledge. *Nucleic Acids Res.* **2019**, *47* (D1), D506−d515.
(79) Distler, U.; Kuharev, J.; Navarro, P.; Tenzer, S. Label-free Quantification in Ion Mobility-Enhanced Data-independent Acquisition Proteomics. *Nat. Protoc.* **2016**, *11* (4), 795−812.
(80) Silva, J. C.; Gorenstein, M. V.; Li, G. Z.; Vissers, J. P.; Geromanos, S. J. Absolute Quantification of Proteins by LCMSE: A Virtue of Parallel MS Acquisition. *Molecular & Cellular Proteomics: MCP* **2006**, *5* (1), 144−56.
(81) Tyanova, S.; Cox, J. Perseus: A Bioinformatics Platform for Integrative Analysis of Proteomics Data in Cancer Research. *Methods Mol. Biol. (N. Y., NY, U. S.)* **2018**, *1711*, 133−148.
(82) Benjamini, Y.; Drai, D.; Elmer, G.; Kafkafi, N.; Golani, I. Controlling the False Discovery Rate in Behavior Genetics Research. *Behav. Brain Res.* **2001**, *125* (1−2), 279−84.

https://doi.org/10.1021/acsnano.1c05713
ACS Nano XXXX, XXX, XXX−XXX

Supplemental Information

Density of Conjugated Antibody Determines the Extent of Fc Receptor Dependent Capture of Nanoparticles by Liver Sinusoidal Endothelial Cells

Cinja Kappel[†], Christine Seidl[&,¶], Carolina Medina-Montano[†], Meike Schinnerer[&], Irina Alberg[&], Christian Leps[§], Julian Sohl[§], Ann-Kathrin Hartmann[§], Michael Fichter[†], Michael Kuske[†], Jenny Schunke[†], Gabor Kuhn[†], Ingrid Tubbe[†], David Paßlick[†], Dominika Hobernik[†], Rebekka Bent[†], Katharina Haas[†], Evelyn Montermann[†], Kerstin Walzer[#], Mustafa Diken[#§], Manfred Schmidt ‡, Rudolf Zentel[&], Lutz Nuhn[+], Hansjörg Schild[§], Stefan Tenzer[§], Volker Mailänder[†], Matthias Barz[&,¶,†,], Matthias Bros[†,*], Stephan Grabbe[†,*]*

† Department of Dermatology, University Medical Center of the Johannes Gutenberg University Mainz, Langenbeckstraße 1, 55131 Mainz, Germany

& Department of Chemistry, Johannes Gutenberg University, Duesbergweg 10-14, 55099 Mainz, Germany

¶ Leiden Academic Center for Drug Research (LACDR), Leiden University, Einsteinweg 55, 2333 CC Leiden, The Netherlands

§ Institute for Immunology, University Medical Center of the Johannes Gutenberg University Mainz, Langenbeckstraße 1, 55131 Mainz, Germany

‡ Institute for Physical Chemistry, Johannes Gutenberg University, Welder Weg 11, 55099 Mainz, Germany

TRON–Translational Oncology at the University Medical Center of the Johannes Gutenberg University GmbH, Freiligrathstr. 12, 55131 Mainz, Germany

+ Max Planck Institute for Polymer Research, Ackermannweg 10, 55128 Mainz, Germany

$ Biontech AG, An der Goldgrube 12, 55131, Mainz, Germany

Supporting Information

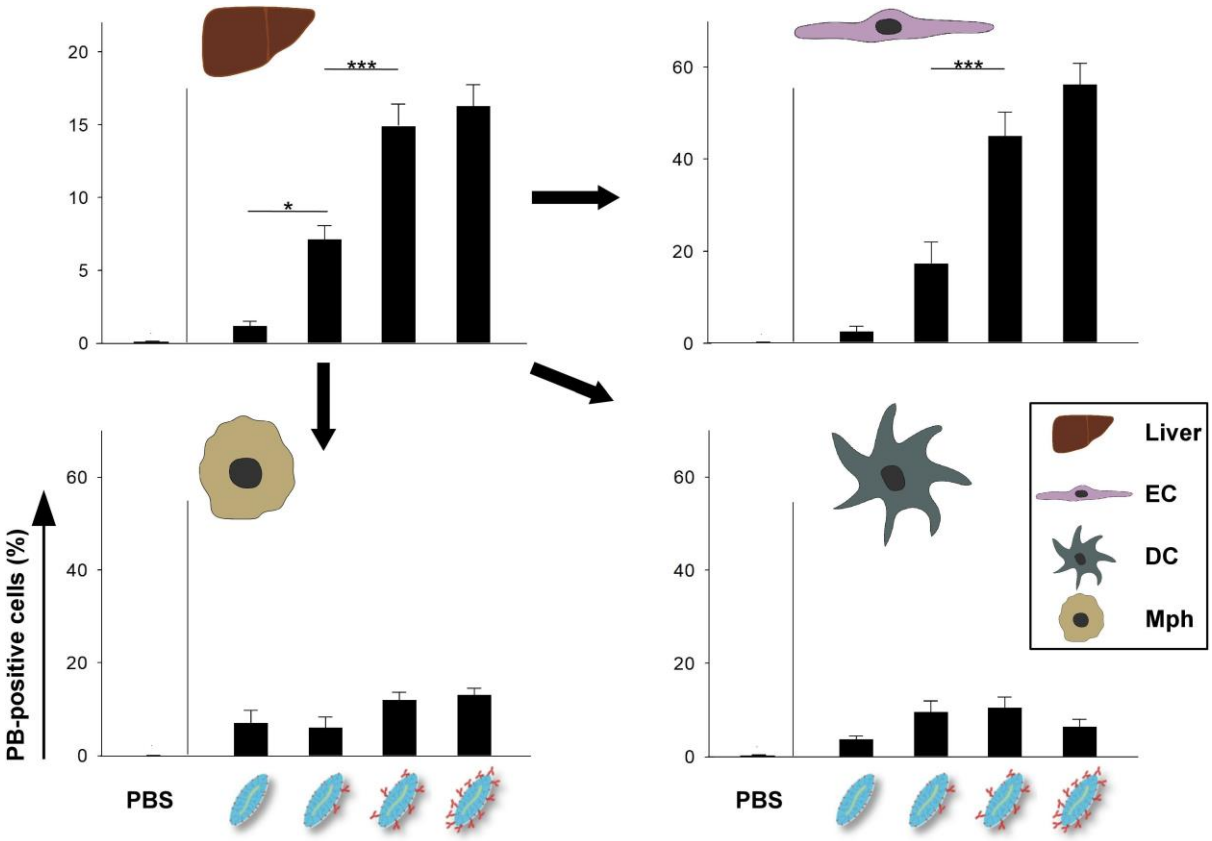

Supp Figure 1. Liver endothelial cells strongly bind PB formulations with intermediate/high antibody density. Flow cytometric analyses of liver NPC populations at 3 hpi after systemic application of different PB formulations. Liver NPCs derived from mice differentially treated with CW800-labeleld PB formulations were incubated with cell type-identifying antibodies to differentiate ECs, Mphs and DCs (liver endothelial cells (EC: $CD45^-CD31^+$), macrophages (Mph: $CD45^+F4/80^+$), and dendritic cells (DC: $CD45^+CD11c^+$)). Data denote the frequencies of PB-positive cells of the according NPC population (mean±SEM, n=6-8 obtained from 2-3 experiments; one way ANOVA, *$p<0.05$, ***$p<0.001$).

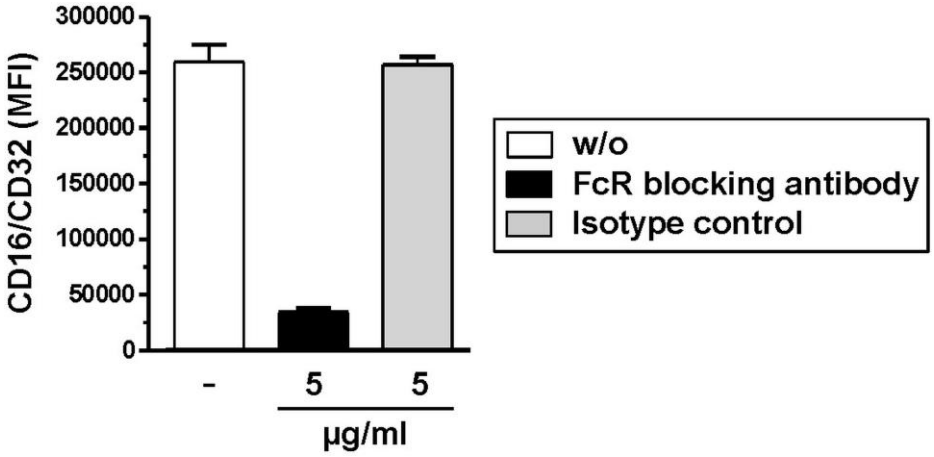

Supp Figure 2. Efficacy of FcR-blocking antibody on liver NPCs. Isolated liver NPC (10^6/ml, 1 ml) were incubated with FcR (CD16/CD32)-blocking or isotype control antibody (each 5 µg/ml), followed by detection of CD16/CD32 expression using a FITC-labeled anti-CD16/CD32 antibody (same antibody clone as used for blocking). Data denote the mean fluorescence intensity (MFI)±SD of 2 experiments.

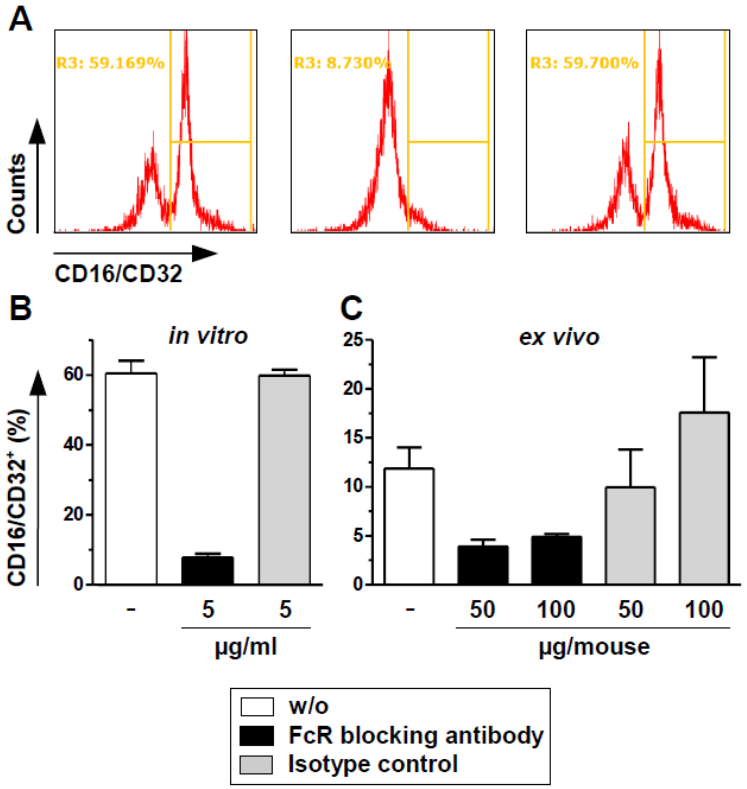

Supp Figure 3. Assessment of antibody-mediated FcR blockade *in vitro* and *in vivo*. Flow cytometry analyses of (A,B) isolated spleen cells (10^6/ml, 1 ml) after 1 hour incubation with FcR-blocking or isotype control antibody (each 5 µg/ml), followed by detection of CD16/CD32 expression using a FITC-labeled anti-CD16/CD32 antibody. (A) FACS plots are representative

of 2 independent experiments. (B) Quantification of FcR blockade efficiency. Data denote the mean±SD of 2 experiments. (C) Quantification of FcR blockade efficiency *ex vivo* using liver NPCs retrieved 3h after *in vivo* application of FcR-blocking and isotype control antibody (each 50µg and 100 µg per mouse). Spleen cells were assayed for detectability of CD16/CD32 by flow cytometry. Data denote the mean±SD of 2 experiments.

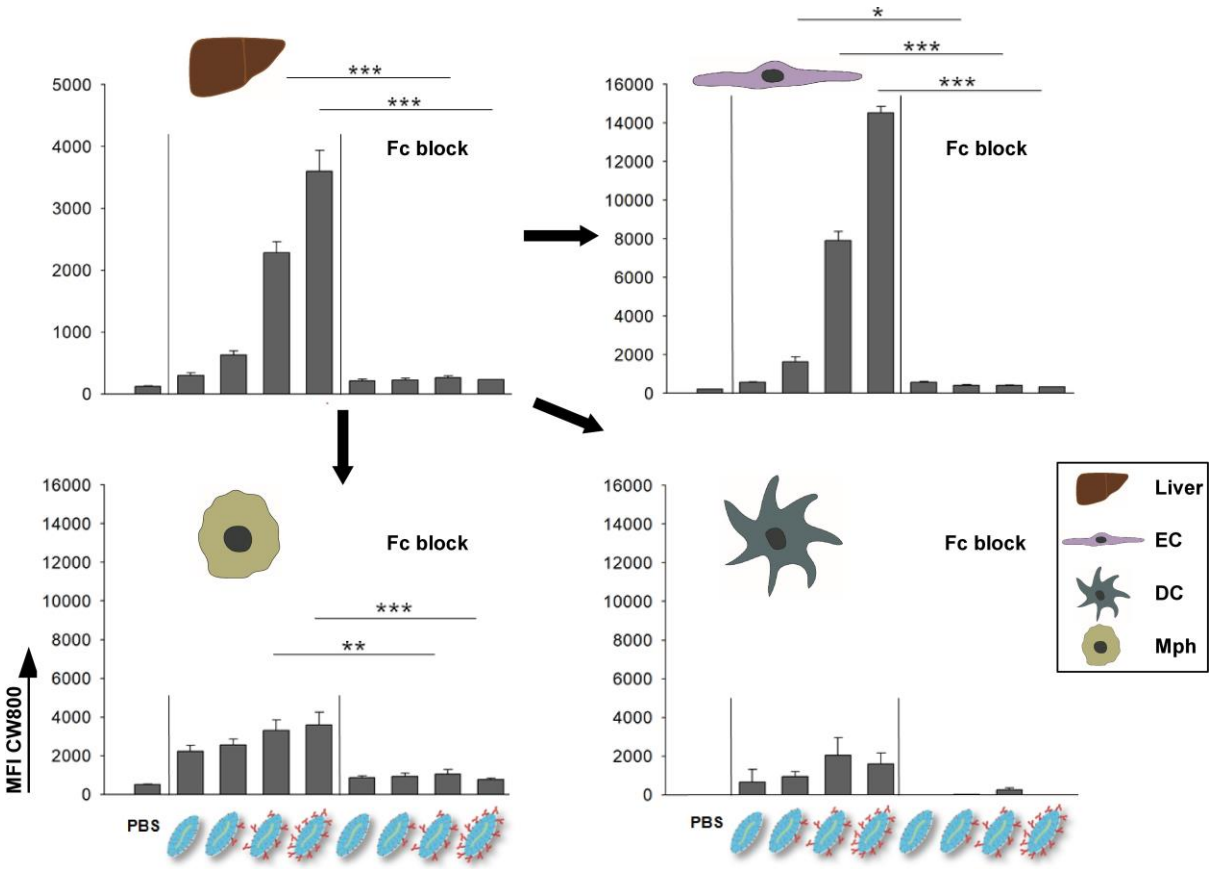

Supp Figure 4. Blockade of Fc receptors attenuates binding of PB-antibody conjugates to liver EC and Mph. Mice were consecutively injected with FcR-blocking antibody and PB formulations as described in the legend of Figure 4. Liver NPCs were prepared 3 hpi, and the MFI of CW800 of either NPC population (liver endothelial cells (EC: $CD45^{-}CD31^{+}$), macrophages (Mph: $CD45^{+}F4/80^{+}$)), and dendritic cells (DC: $CD45^{+}CD11c^{+}$) was monitored by flow cytometry. Data denote the mean ±SEM (n=6-8 obtained from 2-3 experiments; one way ANOVA, *p<0.05, **p<0.01, ***p<0.001).

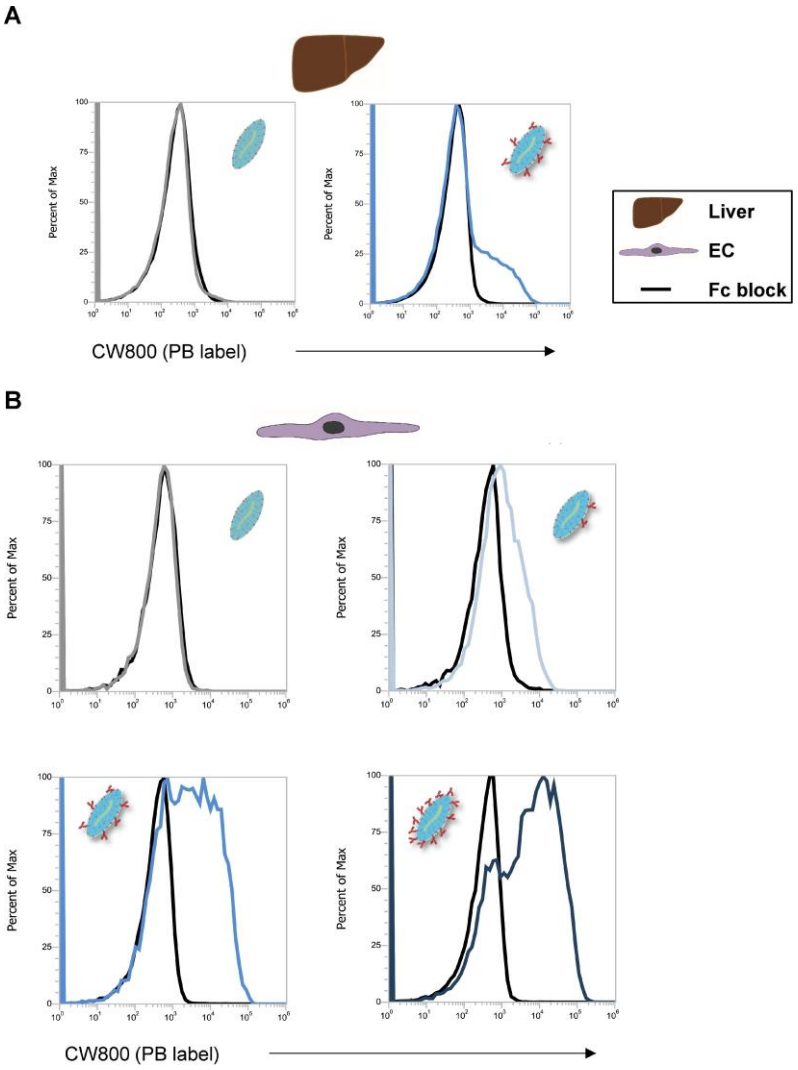

Supp Figure 5. FcR blockade reduces binding of antibody coated PBs by liver cells. Mice were left untreated or were treated with Fc block, CW800-labeled PB formulations were applied, followed by isolation of liver NPCs as described (liver endothelial cells (EC: $CD45^-$ $CD31^+$)). Histograms show CW800 intensities of (A) total NPCs and (B) ECs derived from mice treated with the indicated PB formulations (blue lines). In case of FcR blockade (Fc block; black line) total liver NPCs and liver ECs show attenuated binding of PB-antibody conjugates.

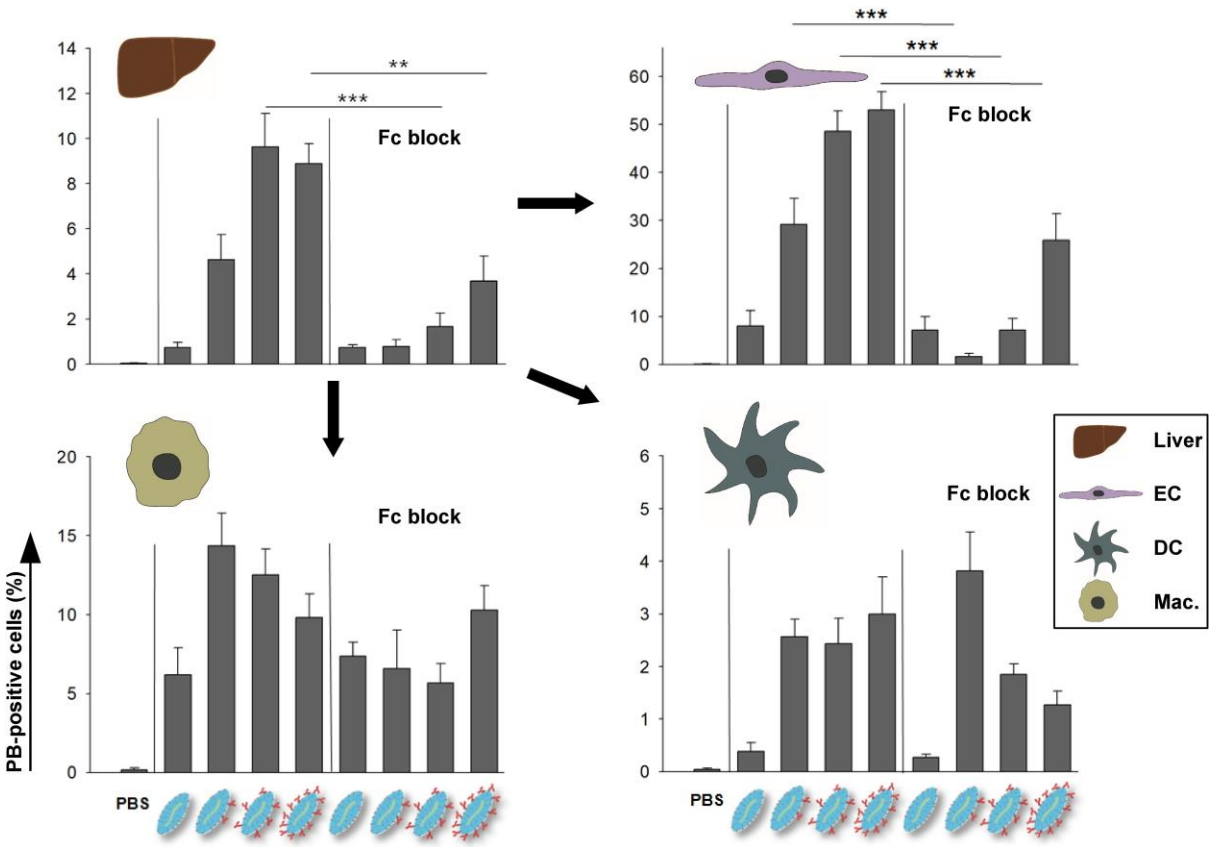

Supp Figure 6. Blockade of Fc receptors attenuates binding of PB-antibody conjugates to liver ECs also after 24 hpi. Mice were consecutively injected with FcR-blocking antibody and PB formulations as described in the legend of Figure 4. Liver NPCs were prepared 24 hpi of PB formulations, and the frequencies of CW800-positive cells of either NPC population (liver endothelial cells (EC: $CD45^{-}CD31^{+}$), macrophages (Mph: $CD45^{+}F4/80^{+}$)) was analyzed by flow cytometry. Data denote the mean ±SEM (n=6-8 obtained from 2-3 experiments; one way ANOVA, **p<0.01, ***p<0.001).

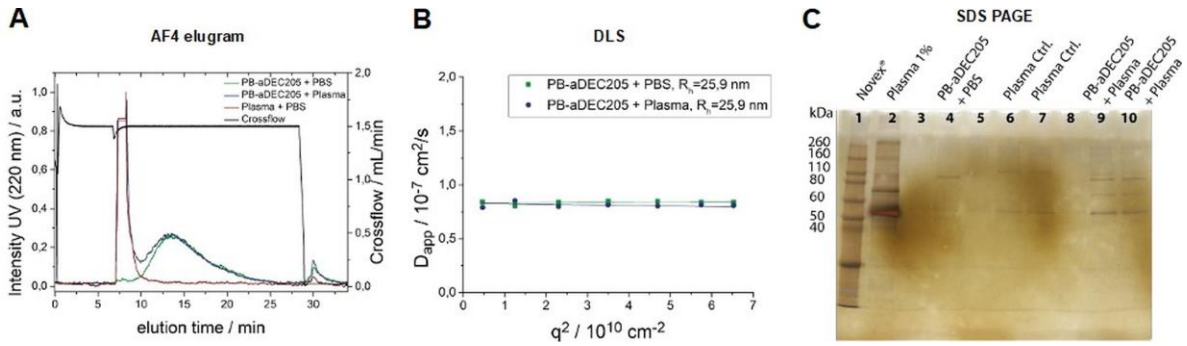

Supp Figure 7. Assessment of the protein corona of PB-aDEC205. A) Asymmetrical flow field-flow fractionation (AF4) elugram of PB-aDEC205 (green), plasma (red), and in plasma incubated PB-aDEC205 (blue). The AF4 elugram shows that there is no size increase or aggregate formation due to nanoparticle–protein-interactions. B) Apparent diffusion coefficient *versus* scattering vector of in PBS (green) and in plasma (blue) incubated PB-aDEC205 after isolation with AF4. The hydrodynamic radius did not increase due to possible protein adsorption. Also, the diffusion coefficient is identical at seven different scattering angles (30°, 50°, 70°, 90°, 110°, 130°, 150°) indicating a narrow size distribution of PB-aDEC205. C) Silver stained gel of isolated fractions of PB-aDEC205 after AF4 purification. 1) Novex® Sharp Pre-Stained Protein Standard, 2) Human Blood Plasma 1%, 3) Empty, 4) PB-aDEC205 + PBS, 5) Empty, 6 & 7) Plasma and PBS in elution area of PB-aDEC205 (Plasma Control), 8) Empty, 9 & 10) PB-aDEC205 + Plasma. Some data obtained for non-functionalized PB have been published recently by Alberg and co-workers.[1]

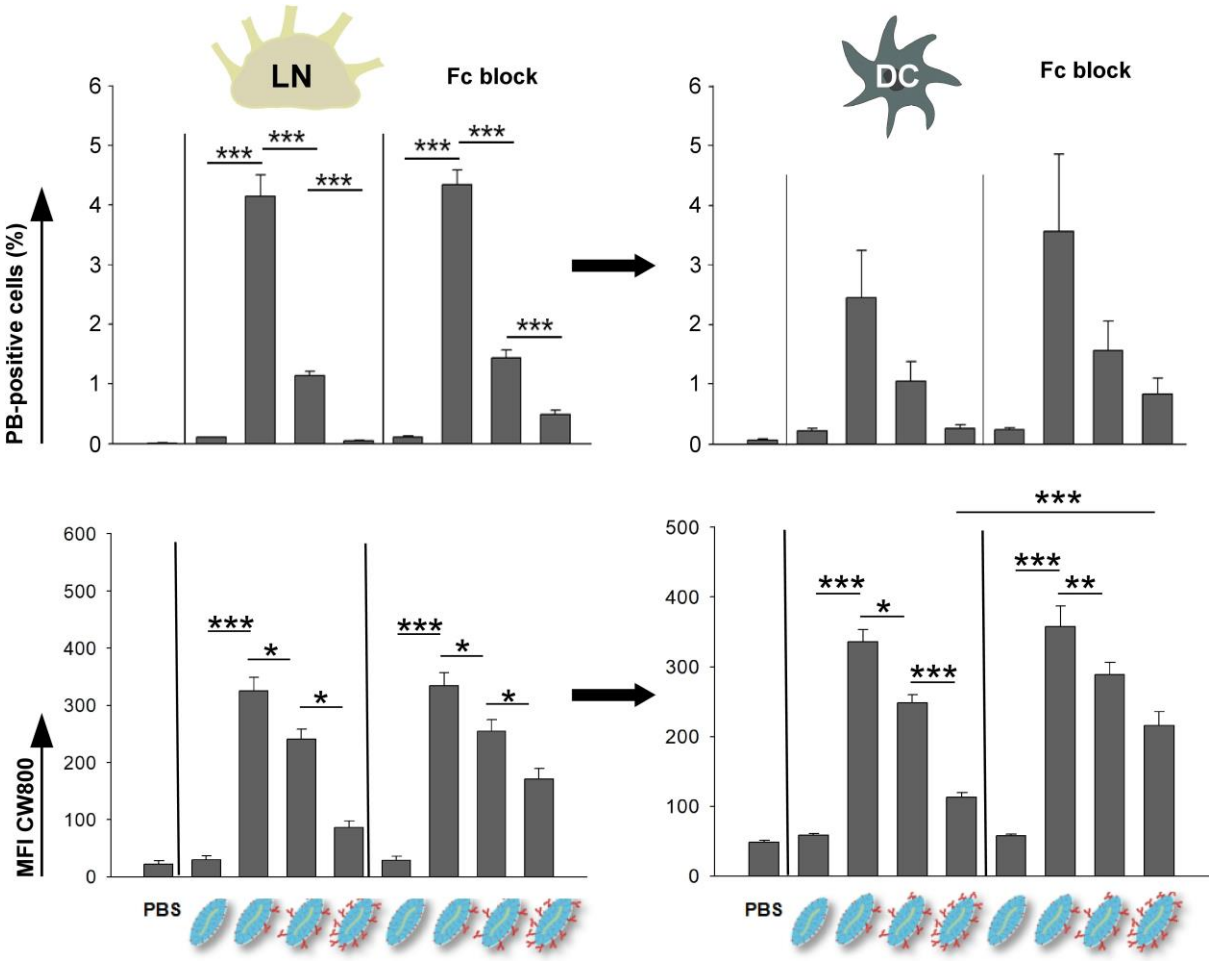

Supp Figure 8. **Antibody density on PB determines the targeting efficacy of DC in peripheral LN, irrespective of FcR blockade.** Mice were treated with Fc block and PB formulations as described in the legend of Figure 4. After 24 hpi LNs were retrieved, and frequencies of PB-positive LN cells and $CD11c^+$ DCs (upper panel) as well as corresponding CW800 intensities (MFI) (lower panel) were monitored by flow cytometry. Data denote the mean ±SEM (n=6-8 obtained from 2-3 experiments; one way ANOVA, *p<0.05, **p<0.01, ***p<0.001).

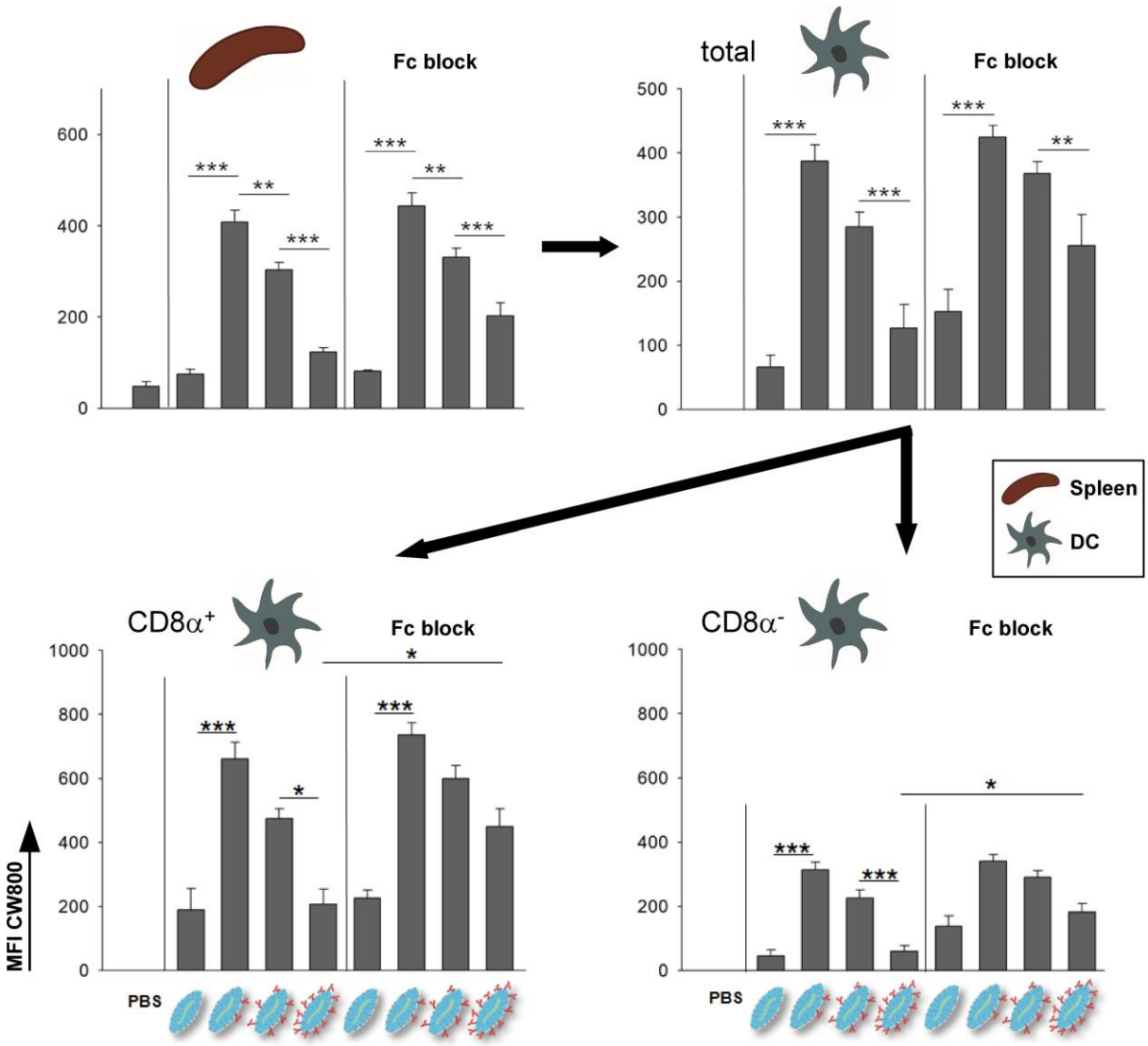

Supp Figure 9. **Antibody density on PB determines the targeting efficacy of splenic CD8a$^+$ DC, irrespective of FcR blockade.** Mice were treated with Fc block and PB formulations as described in the legend of Figure 4. After 24 hpi the spleen was retrieved, and CW800 intensities (MFI) of total spleen cells, total DCs (CD11c$^+$) and DC subpopulations was assessed by flow cytometry. Data denote the mean ±SEM (n=6-8 obtained from 2-3 experiments; one way ANOVA, *p<0.05, **p<0.01, ***p<0.001).

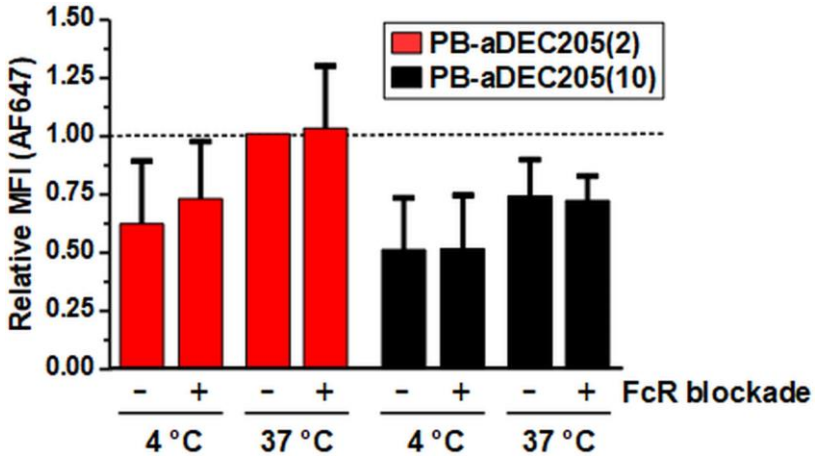

Supp Figure 10. **FcR blockade has no effect on the binding of PB aDEC205 antibody conjugates to DC.** Bone marrow-derived (BM)DCs were kept in parallel at 4°C and at 37 °C to dissect temperature-independent binding from temperature-dependent uptake of PB formulations. BMDCs were either preincubated with Fc receptor blocking CD16/CD32-specific antibody (10 µg/ml) or were left untreated. After 1 h, PB-aDEC205 conjugates labeled with AF647 (each 10^{12} particles) were applied, and samples were incubated for another 1 h. Graphs show the mean fluorescence intensity (AF647) of $CD11c^+$ BMDCs, normalized in each experiment to the level obtained for cells incubated with PB-aDEC205(2) at 37 °C. Data denote the mean±SD of 2-6 independent experiments each.

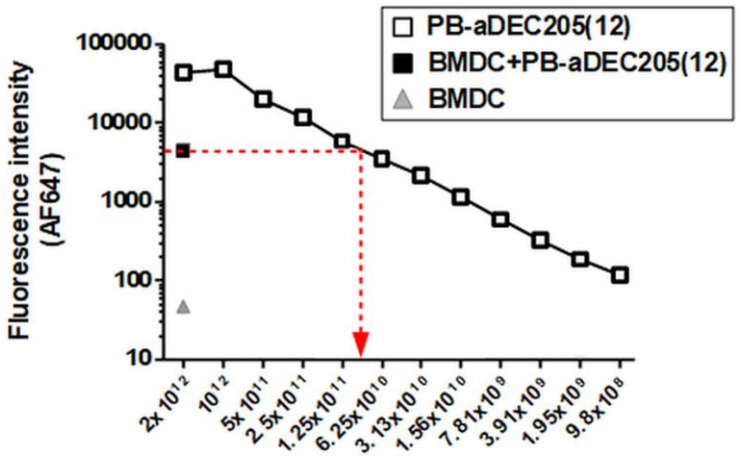

Supp. Figure 11. **Quantitation of PB-aDEC205 uptake by DC *in vitro*.** In parallel assays BMDCs were incubated overnight with $2x10^{12}$ AF647 labelled PB-aDEC205(12) particles or were left untreated. On the next day, particle uptake was confirmed by flow cytometry using an aliquot of cells (not shown), and cells were lysed for detection of fluorescence intensities using a fluorescence plate reader. PB-aDEC205(12) particles were serially diluted in lysis buffer in a 96 well plate and recorded in a plate reader, to generate a reference curve. Likewise, the fluorescence intensities of a serial dilution of lysed BMDCs ($3.9x10^5$) were determined. By dividing the measured fluorescence intensity by the cell number counted prior to fluorescence measurements, on an average approximately 50,000 PB-aDEC205(12) particles were taken up per cell. The graph denotes AF647 fluorescence intensities. Background fluorescence of lysis buffer was below 10 relative fluorescence units (not shown). The graph is representative of 3 independent experiments.

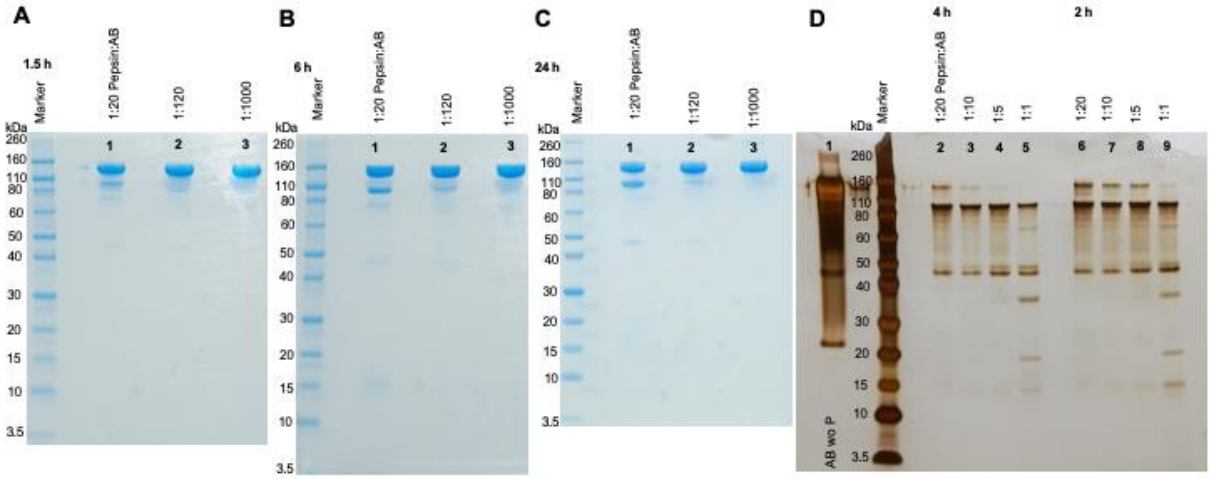

Supp. Figure 12. Characterization of F(ab')$_2$ fragments derived from aDEC205 antibodies. Digests of aDEC205 antibody at various pepsin to antibody (AB) ratios and incubation periods to optimize F(ab')$_2$ fragment generation. A) Coomassie stained gel of 90 min digests of aDEC205 antibody. 1) Pepsin:AB 1:20, 2) Pepsin:AB 1:120, 3) Pepsin:AB 1:1000, B) Coomassie stained gel of digestions of aDEC205 antibody (6 h digeston). 1) Pepsin:AB 1:20, 2) Pepsin:AB 1:120, 3) Pepsin:AB 1:1000, C) Coomassie stained gel of aDEC205 digests after 24 h. 1) Pepsin:AB 1:20, 2) Pepsin:AB 1:120, 3) Pepsin:AB 1:1000, D) Silver stained gel of aDEC205 digestafter various durations of incubation (2 h, 4 h). 1) aDEC205 without pepsin, 2) Pepsin:AB 1:20 4h, 3) Pepsin:AB 1:10 4h, 4) Pepsin:AB 1:5 4h, 5) Pepsin:AB 1:5 4h, 6) Pepsin:AB 1:20 2h, 7) Pepsin:AB 1:10 2h, 8) Pepsin:AB 1:5 2h, 9) Pepsin:AB 1:5 2h.

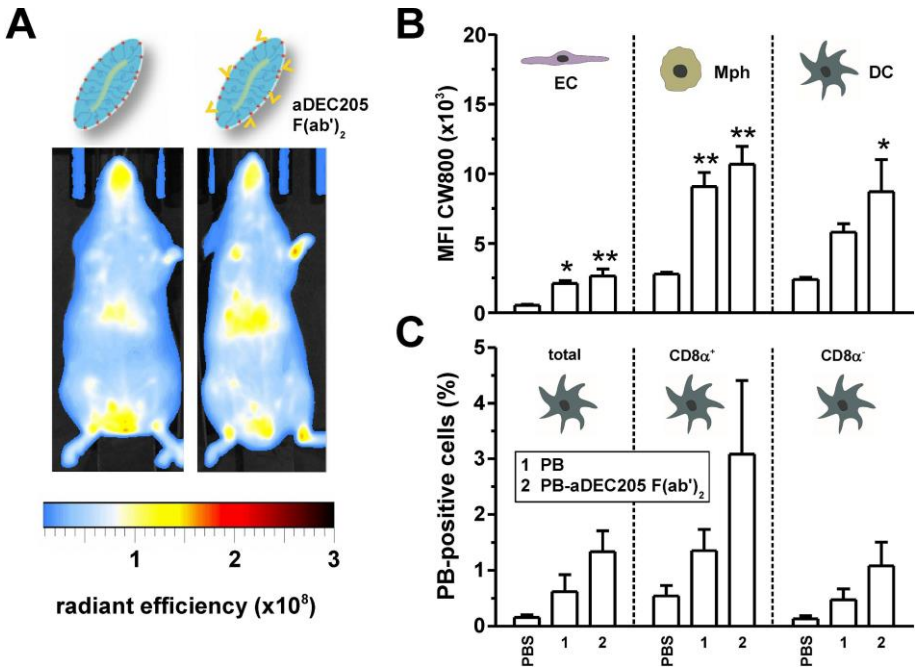

Supp. Figure 13. Efficacy of target cell engagement by peptobrushes coated with aDEC205 F(ab´)2 fragments. Mice were treated in parallel with anti-DEC205 F(ab')$_2$ conjugated PBs and with non-conjugated PBs. Distribution of PB formulations was assessed 24 hpi. A) PBs conjugated with aDEC205 F(ab')$_2$ antibody show a similar biodistribution as non-conjugated PBs, as assessed by *in vivo* fluorescence imaging. B,C) Binding of CW800-labeled PB formulations to liver NPC populations (MFI) (B) or to splenic DCs and the CD8a$^+$ *versus* CD8a$^-$ DC populations (% PB-positive cells) (C) was assessed by flow cytometry. Data denote the mean±SEM (n= 3). D) One way ANOVA; *versus PBS (*p<0.05, **p<0.01).

Supplemental Table 1. **Biological function of plasma proteins[1] identified as specifically enriched in the protein corona of PB-**

Protein	**Gene name**	**Function(s)**				
		Antibody response	**Complement system**	**Coagulation system**	**Iron metabolism**	**Other**
P02787	Serotransferrin				transports iron	
P01009	Alpha-1-antitrypsin (Serpina1)			serine protease inhibitor		
P01023	Alpha-2-macroglobulin (A2M)		negative regulator	proteinase inhibitor		
P02671	Fibrinogen alpha chain (FGA)		inhibitor (classical pathway)	blood clotting		
P02675	Fibrinogen beta chain (FGB)		inhibitor (classical pathway	blood clotting		
P02647	Apolipoprotein A-I (APOA1)					lipoprotein metabolism
P01857	Immunoglobulin heavy constant gamma 1 (IGHG1)	Ig subdomain	activator (classical pathway)			
P08603	Complement factor H (CFH)		inhibitor (all pathways)			
P02679	Fibrinogen gamma chain (FGG)		inhibitor (classical pathway)	blood clotting		
P04003	C4b-binding protein alpha chain (C4BPA)		inhibitor classical pathway			
P02763	Alpha-1-acid glycoprotein 1 (ORM1)					binds/transports various proteins

Protein	Gene name	Function(s)				
		Antibody response	**Complement system**	**Coagulation system**	**Iron metabolism**	**Other**
P0C0L5	Complement C4-B (C4B)		activator (classical/lectin pathways)			
P01876	Immunoglobulin heavy constant alpha 1 (IGHA1)	Ig subdomain	activator (classical pathway)			
P02751	Fibronectin (FN1)		binds C1q (classical pathway)	negative regulator of thrombosis		
P02790	Hemopexin (HPX)				transports heme	
Q6S8J3	POTE ankyrin domain family member E (POTEE)					binds (glyco)proteins
P19652	Alpha-1-acid glycoprotein 2 (ORM2)					binds/transports various proteins
P0DOX8	Immunoglobulin lambda-1 light chain	Ig subdomain				
P0DOY2	Immunoglobulin lambda constant 2 (IGLC2)	Ig subdomain	activator (classical pathway)			
A0A0C4DH68	Immunoglobulin kappa variable 2-24 (IGKV2-24)	Ig subdomain				
P02766	Transthyretin (TTR)					transports thyroxine
P02774	Vitamin D-binding protein (GC)					transports vitamin D
P01008	Antithrombin-III (SERPINC1)			inhibits coagulation factors		
P01011	Alpha-1-antichymotrypsin (SERPINA3)					Lipid metabolism/ inhibits endopeptidases

Protein	Gene name	Function(s)				
		Antibody response	**Complement system**	**Coagulation system**	**Iron metabolism**	**Other**
P02760	Protein AMBP (AMBP)				heme degradation	
P01877	Immunoglobulin heavy constant alpha 2 (IGHA2)	Ig subdomain	activator (classical pathway)			
P00739	Haptoglobin-related protein (HPR)				transports hemoglobin	
		Antibody response	**Complement system**	**Coagulation system**	**Iron metabolism**	**Other**
P01767	Immunoglobulin heavy variable 3-53 (IGHV3-53)	Ig subdomain				
P01619	Immunoglobulin kappa variable 3-20 (IGKV3-20)	Ig subdomain	activator (classical pathway)			

1: Biological functions were retrieved from UniProt database (www.uniprot.org).

MATERIALS AND METHODS

Incubation of PB formulations with human blood plasma

Human blood plasma was provided by the Blood Transfusion Unit of the University Medical Center Mainz. It was pooled of six healthy donors and stabilized with EDTA. PB (15 mg mL^{-1}) were incubated with EDTA-stabilized, pure and undiluted plasma 2:1 (v:v) at 37 °C for 1 h.

Separation by asymmetrical flow field-flow fractionation (AF4)

The AF4 measurements were performed using an installation from the ConSenxuS GmbH. The setup was composed of a constaMETRICR 3200 main pump and a Spectra Series UV150 detector from Thermos Separation, a Dark V3 LS Detector from ConSenxuS GmbH, a Pharmacia P-3500 injection pump, a LV-F flow controller from HORIBA ATEC, a Waters In-Line Degasser-AF, and a separation channel with a 190 μm spacer and a reg. cellulose membrane with a molecular weight cutoff of 10 kDa. The UV absorption of PB was detected at 220 nm. For all measurements, phosphate buffered saline (151.7×10^{-3} m) was used as solvent, it also contained sodium azide in a concentration of 0.2×10^{-3} m. The main flow was 1 mL min−1 higher than the crossflow for each measurement. The crossflow is illustrated in the AF4 elugram. Every measurement was carried out at least three times from three independent incubation experiments. PB fractions were collected from 13.3 to 18.3 min. To increase the concentration of the collected fractions from the AF4 after the separation process, they were filtrated with Amikon Ultra Centrifugal Filters from Merck Millipore with a regenerated cellulose membrane and a molecular weight cut off of 3 kDa. Plasma and particle controls were performed as described.[1]

SDS PAGE

SDS-PAGE experiments were performed following the general protocol of Laemmli. The polyacrylamide gels were composed of a 12%-separation gel (with 8% stacking gel) and the electrophoresis was carried out for 45 min at 200 V with a Mini-PROTEAN Tetra Vertical electrophoresis-chamber from BIO-RAD. 7.5 μL of each sample was incubated with 2.5 μL loading buffer (NuPAGE LDS Sample Buffer, Invitrogen) for 5 min at 95 °C. Novex® Sharp Pre-Stained Protein Standard from INVITROGEN was loaded on each gel as a protein ladder for comparison. The proteins in the gels were visualized using a silver staining.

DLS

For dynamic light scattering (DLS) experiments the collected fractions from the AF4 were prepared in a dustfree flowbox. They were filtered with syringe filters from PALL Life Science with a diameter of 13 mm and a GHP membrane (0.2 µm pores) into dust free cylindrical scattering cells (Suprasil, 20 mm diameter). The measurements were performed with a Uniphase He/Ne Laser (632.8 nm, 22 mW), an ALV-SP125 Goniometer, an ALV/High QE APD-Avalanche photodiode, an ALV5000/E/PCI-correlator and a Lauda RC-6 thermostat unit. All angular dependent measurements were carried out in 20° steps between 30° and 150°. Data analysis was performed according to the procedure described by Rausch and co-workers.[2]

Protein Digestion

Lyophilized protein corona proteins were digested according to the SP3 ("Single-Pot Solid-Phase-Enhanced Sample Preparation") protocol.[3] After solubilization in SDS-Lysis buffer (1% SDS, 1x complete Protease Inhibitor Cocktail-EDTA, 50 mM HEPES, pH 8,5), proteins were reduced by adding 5 µl of 200 mM Dithiothreitol (DTT) per 100 µl lysate (45 °C, 30 min). Free cysteins were subsequently alkylated by adding 10 µl 100 mM Iodoacetamide (IAA) per 100 µl lysate (Room temperature, 30 min, in the dark). Subsequently, remaining IAA was quenched by adding 10 µl 200 mM DTT per 100 µl lysate. Magnetic carboxylate modified particles Beads (SpeedBeads, Sigma) were used for Protein Clean-up and Acetonitrile (ACN), in a final concentration of 70%, was added to the samples to induce the binding of the proteins to the beads by hydrophilic interactions (room temperature, 18 min). By incubating the bead-protein mixture on a magnetic stand for 2 min, the sample was bound to the magnet and the supernatant was removed, followed by two washing-steps with 70% ethanol (EtOH), addition of 180 µl ACN, incubation for 15 s and removal of the solvent. Finally, 5 µl digest buffer (50 mM ammonium bicarbonate, 1:25 w/w trypsin:protein ratio) were added to the air-dried bead-protein mixtures and incubated over night at 37 °C. To purify peptides after digestion, ACN was added to a final concentration of 95%. After another washing step (s. Sielaff *et al.*, 2017 for detailed information) the beads were resuspended in 10 µl 2% DMSO (in water), put into an ultrasonic bath for 1 min and then shortly centrifuged. 10 µl of the resulting supernatant was mixed with 5 µl 100 fmol/µl Enolase digest (Waters, Eschborn, Germany) and acidified with 5 µl 1% formic acid (FA).

LC-MS Analysis

Liquid chromatography (LC) of tryptic peptides was performed on a NanoAQUITY UPLC system (Waters Corporation, Milford, MA) equipped with 75 µM x 250 mm HSS-T3 C18 column (Waters corporation). Mobile phase A was 0.1% (v/v) formic acid (FA) and 3% (v/v) dimethyl sulfoxide (DMSO) in water. Mobile phase B was 0.1% (v/v) FA and 3% (v/v) DMSO in acetonitrile (ACN). Peptides were separated running a gradient from 5 to 60% (v/v) mobile phase B at a flow rate of 300 nL/ min over 60 min. The column was heated to 55 °C. MS analysis of eluting peptides was performed by data-independent acquisition (DIA) in MS^E. In brief, precursor ion information was collected in low-energy MS mode at a constant collision energy of 4 eV. Fragment ion information was obtained in the elevated energy scan applying drift-time specific collision energies. The spectral acquisition time in each mode was 0.6 s with a 0.05 s-interscan delay resulting in an overall cycle time of 1.3 s for the acquisition of one cycle of low and elevated energy data. [Glu1]-fibrinopeptide was used as lock mass at 100 fmol/µL and sampled every 30 s into the mass spectrometer *via* the reference sprayer of the NanoLockSpray source. All samples were analyzed in three technical replicates.

Data Processing and Label-Free Quantification

MS^E data processing and database search was performed using ProteinLynx Global Server (PLGS, ver. 3.0.2, Waters Corporation). The resulting proteins were searched in the UniProt Human proteome database (UniProtKB release 2017_05, 20,201 entries)[4] supplemented with a list of common contaminants. The database search was specified by trypsin as enzyme for digestion and peptides with up to two missed cleavages were included. Furthermore, carbamidomethyl cysteine was set as fixed modification and oxidized methionine as variable modification. False discovery rate (FDR) assessment for peptide and protein identification was done using the target-decoy strategy by searching a reverse database and was set to 0.01 for database search in PLGS. Retention time alignment, exact mass retention time (EMRT), as well as normalization and filtering was performed in ISOQuant ver.1.8.[5] By using TOP3 quantification,[6] absolute in-sample amounts of proteins were calculated. Statistical analysis was done in Perseus,[7] by performing two-tailed, paired -tests and subsequent Benjamini-Hochberg correction.[8] Q-values < 0.05 were considered as significant.

BMDC culture

Bone marrow (BM) cells were isolated from femurs and tibiae of C57BL/6 mice, and were resuspended in IMDM medium containing 5% FBS, 2 mM L-glutamine, 100 IU/ml penicillin, 100 µg/ml streptomycin and 50 µM β-Mercaptoethanol (all reagents from Sigma-Aldrich, Deisenhofen, Germany), and supplemented with 10 ng/ml recombinant murine GM-CSF (R&D Systems, Wiesbaden, Germany). BM cells were seeded in 12 well suspension cell culture cluster plates ($2x10^5$/ml).On days 3 and 6 culture media was replenished. On day 7-8 the volume of BMDC cultures was adjusted to 1ml/well and cells were subjected to experimental treatment.

Flow cytometry

BMDC incubated with PB formulations as indicated for 1 h were harvested and transferred to FACS tubes. Samples were incubated with a rat anti-mouse CD16/CD32 antibody (15 min, 4 °C) to prevent Fc-mediated binding of subsequently applied antibody. BMDC were incubated with a BV421-conjugated anti-CD11c antibody (20 min, 4°C) (Thermo Fisher, Waltham, MA). Afterwards, samples were fixed (4 % paraformaldehyde, 2mM EDTA) and analysed in an Attune NxT flow cytometer (Thermo Fisher) equipped with Attune Nxt Software v3.1.1.

Fluorescence measurements

BMDC left untreated or incubated overnight with PB-aDEC205(12) (1 ml) were lysed in Passive Lysis Buffer (PLB; Promega, Madison, WI). Cell lysates and PB-aDEC205(12) were serially diluted in PLB in a black 96 well plate with clear bottom (each 100 µl). AF647 fluorescence intensitites were recorded (Excitation: 638 nm, bandwith 10nm; Emission: 677 nm, bandwith: 10 nm; integration time 40 µs) in a microplate reader (Spark; Tecan, Männedorf, Switzerland).

References

1. Alberg, I.; Kramer, S.; Schinnerer, M.; Hu, Q.; Seidl, C.; Leps, C.; Drude, N.; Mockel, D.; Rijcken, C.; Lammers, T.; Diken, M.; Maskos, M.; Morsbach, S.; Landfester, K.; Tenzer, S.; Barz, M.; Zentel, R., Polymeric Nanoparticles with Neglectable Protein Corona. *Small (Weinheim an der Bergstrasse, Germany)* **2020**, e1907574.
2. Rausch, K.; Reuter, A.; Fischer, K.; Schmidt, M., Evaluation of Nanoparticle Aggregation in Human Blood Serum. *Biomacromolecules* **2010,** *11* (11), 2836-9.

3. Sielaff, M.; Kuharev, J.; Bohn, T.; Hahlbrock, J.; Bopp, T.; Tenzer, S.; Distler, U., Evaluation of FASP, SP3, and iST Protocols for Proteomic Sample Preparation in the Low Microgram Range. *Journal of Proteome Research* **2017,** *16* (11), 4060-4072.
4. UniProt: A Worldwide Hub of Protein Knowledge. *Nucleic Acids Research* **2019,** *47* (D1), D506-d515.
5. Distler, U.; Kuharev, J.; Navarro, P.; Tenzer, S., Label-Free Quantification in Ion Mobility-Enhanced Data-Independent Acquisition Proteomics. *Nature Protocols* **2016,** *11* (4), 795-812.
6. Silva, J. C.; Gorenstein, M. V.; Li, G. Z.; Vissers, J. P.; Geromanos, S. J., Absolute Quantification of Proteins by LCMSE: A Virtue of Parallel MS Acquisition. *Molecular & Cellular Proteomics : MCP* **2006,** *5* (1), 144-56.
7. Tyanova, S.; Cox, J., Perseus: A Bioinformatics Platform for Integrative Analysis of Proteomics Data in Cancer Research. *Methods in Molecular Biology (Clifton, N.J.)* **2018,** *1711*, 133-148.
8. Benjamini, Y.; Drai, D.; Elmer, G.; Kafkafi, N.; Golani, I., Controlling the False Discovery Rate in Behavior Genetics Research. *Behavioural Brain Research* **2001,** *125* (1-2), 279-84.

10.5. Publication 5.

"Systemically administered TLR7/8 agonist and antigen-conjugated nanogels govern immune responses against tumors"

This study has been published in ACS Nano. As a co-author, I focused mainly on the biological evaluation of Imidazoquinoline (IMDQ)-loaded nanogels in several *in vitro* and *in vivo* experiments, including uptake and maturation tests of the IMDQ-loaded nanogels in several immune cell populations, followed by biodistribution and *ex vivo* Imaging. In this work, we introduced a pH-responsive nanogel platform as a two-component antitumor vaccine that considered to be safe for intravenous application and aimed to elicit robust immune responses *in vitro* and *in vivo*. The underlying chemical design allowed for straightforward covalent attachment of a model antigen (ovalbumin) and an immune adjuvant (Imidazoquinoline-type TLR7/8 agonist) onto the same nanocarrier system. In addition to inducing antigen-specific T and B cell responses that outperformed mixtures of individual components, our two-component nanovaccine in prophylactic and therapeutic studies led to an antigen-specific growth reduction of different tumors expressing ovalbumin intracellularly or on their surface. Regarding the versatile opportunities for functionalization, our nanogels may be promising platforms for the development of highly customized and potent nanovaccines.

DOI: 10.1021/acsnano.1c10709

Published in: *ACS Nano.* **2022**, 16, 3, 4426–4443

Reprinted with permission from [Judith Stickdorn, Lara Stein, Danielle Arnold-Schild, Jennifer Hahlbrock, **Carolina Medina-Montano**, Joschka Bartneck, Tanja Zieß, Evelyn Montermann, Cinja Kappel, Dominika Hobernik, Maximilian Haist, Hajime Yurugi, Marco Raabe, Andreas Best, Krishnaraj Rajalingam, Markus P. Radsak, Sunil A. David, Kaloian Koynov, Matthias Bros, Stephan Grabbe, Hansjörg Schild, and Lutz Nuhn. *ACS Nano* **2022** *16* (3), 4426-4443]. Copyright [2023] American Chemical Society.

ACSNANO

www.acsnano.org

ARTICLE

Systemically Administered TLR7/8 Agonist and Antigen-Conjugated Nanogels Govern Immune Responses against Tumors

Judith Stickdorn,[‡] Lara Stein,[‡] Danielle Arnold-Schild, Jennifer Hahlbrock, Carolina Medina-Montano, Joschka Bartneck, Tanja Ziß, Evelyn Montermann, Cinja Kappel, Dominika Hobernik, Maximilian Haist, Hajime Yurugi, Marco Raabe, Andreas Best, Krishnaraj Rajalingam, Markus P. Radsak, Sunil A. David, Kaloian Koynov, Matthias Bros, Stephan Grabbe,* Hansjörg Schild,* and Lutz Nuhn*

Cite This: https://doi.org/10.1021/acsnano.1c10709

Read Online

ACCESS | Metrics & More | Article Recommendations | Supporting Information

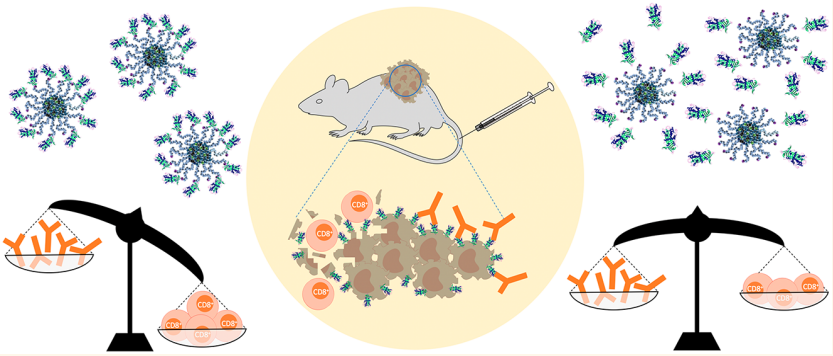

ABSTRACT: **The generation of specific humoral and cellular immune responses plays a pivotal role in the development of effective vaccines against tumors. Especially the presence of antigen-specific, cytotoxic T cells influences the outcome of therapeutic cancer vaccinations. Different strategies, ranging from delivering antigen-encoding mRNAs to peptides or full antigens, are accessible but often suffer from insufficient immunogenicity and require immune-boosting adjuvants as well as carrier platforms to ensure stability and adequate retention. Here, we introduce a pH-responsive nanogel platform as a two-component antitumor vaccine that is safe for intravenous application and elicits robust immune responses *in vitro* and *in vivo*. The underlying chemical design allows for straightforward covalent attachment of a model antigen (ovalbumin) and an immune adjuvant (imidazoquinoline-type TLR7/8 agonist) onto the same nanocarrier system. In addition to eliciting antigen-specific T and B cell responses that outperform mixtures of individual components, our two-component nanovaccine leads in prophylactic and therapeutic studies to an antigen-specific growth reduction of different tumors expressing ovalbumin intracellularly or on their surface. Regarding the versatile opportunities for functionalization, our nanogels are promising for the development of highly customized and potent nanovaccines.**

KEYWORDS: *nanogel, vaccine, immunotherapy, block copolymer, TLR agonist, polymer protein conjugate*

Endeavors in cancer immunotherapy seek to exploit the inherent capacity of immune cells to recognize and neutralize tumor cells. The individual background of each tumor as well as the diversity of each patients' immune status necessitates the development of personalized antitumor vaccines.[1] Research accomplishments of the last decades unveiled the role of immune evasion and checkpoint inhibition in tumorigenesis and drew attention to various immune cells as crucial targets in cancer immunotherapy.[2] To elicit a robust and persistent immune response, vaccines need to trigger an interlude of innate and adaptive immune events both cellularly

Received: December 2, 2021
Accepted: January 27, 2022

Downloaded via UNIV MAINZ on February 2, 2022 at 09:45:49 (UTC).
See https://pubs.acs.org/sharingguidelines for options on how to legitimately share published articles.

ACS Publications

© XXXX The Authors. Published by American Chemical Society

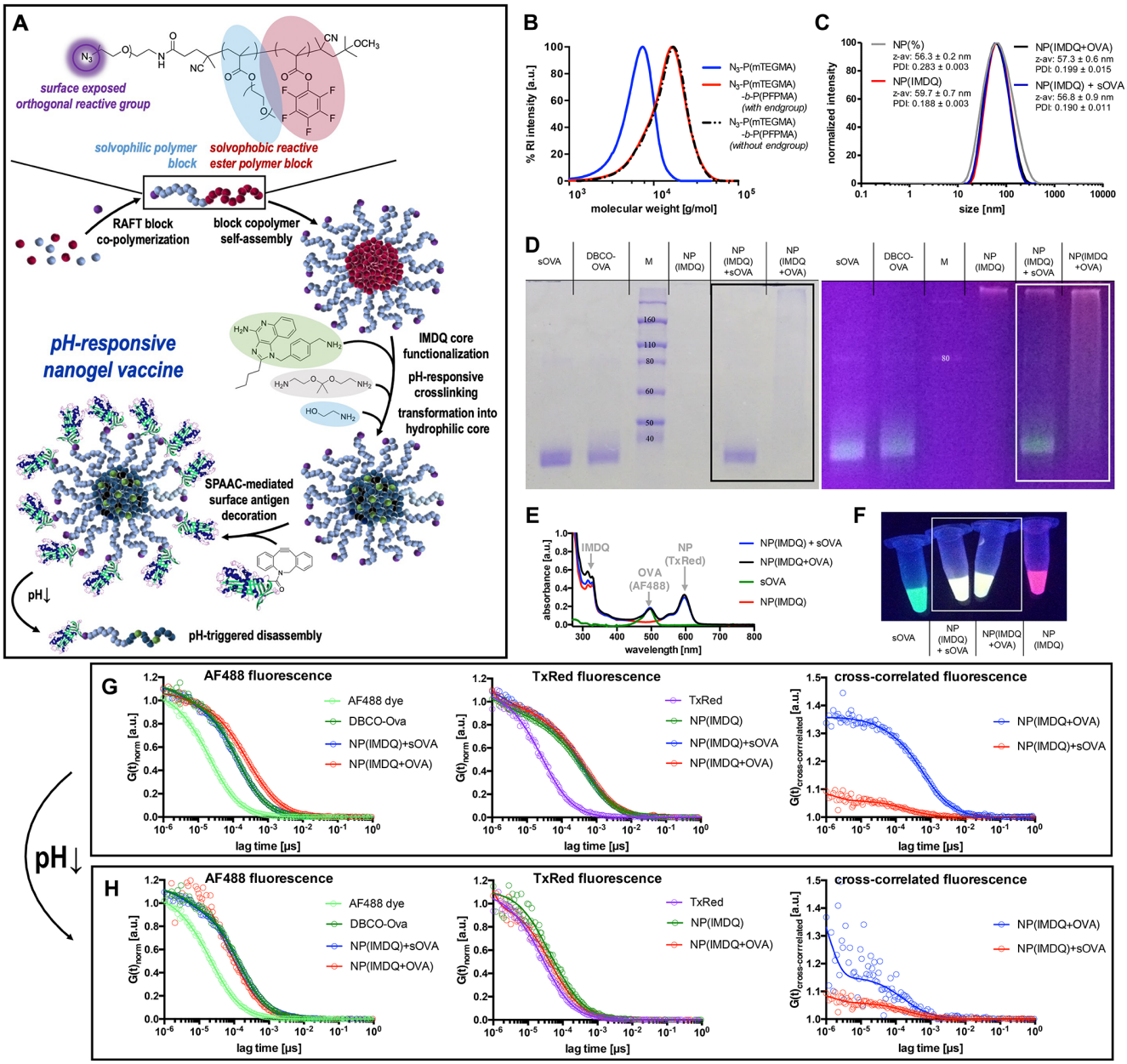

Figure 1. Characterization of TLR7/8-agonist- and protein conjugated nanogels for precise co-delivery of adjuvant and antigen during i.v. antitumor vaccination. (A) Synthetic design concept based on double reactive precursor block copolymers that self-assemble into block copolymer micelles with amine-reactive cores and a SPAAC-reactive corona. *Via* aminolysis of the pentafluorophenyl esters, the cores are covalently functionalized with the TLR 7/8 agonist IMDQ and Texas Red cadaverine and then sequentially cross-linked and transformed into pH-responsive nanogels. The corona is modified *via* click ligation of the surface-exposed azides to DBCO-modified (and Alexa Fluor 488-labeled) OVA as model antigen. (B) SEC chromatography of the RAFT-derived reactive homo and block copolymer (before and after removal of the dithiobenzoate end group). (C) DLS intensity size distribution plots of the resulting nanogels (with and without covalent IMDQ loading), mixed or covalently modified with OVA. (D) SDS-PAGE of modified OVA (labeled with Alexa Fluor 488) mixed or covalently conjugated to IMDQ-loaded nanogels (labeled with Texas Red) (left, Coomassie staining; right, UV excitation of the fluorescent dyes (red, Texas Red-labeled nanogel; green, Alex Fluor 488-labeled OVA). (E) UV−vis spectrum of the fluorescently labeled samples and (F) corresponding image of the samples upon excitation by a UV lamp. (G) FCS correlograms derived from Alexa Fluor 488 and Texas Red fluorescence, as well as their cross-correlated correlogram indicating successful OVA conjugation to the nanogel. (H) FCS correlograms and corresponding cross-correlated correlogram upon exposure to endosomal acidic pH conditions indicating successful particle degradation.

and humorally.[3] While the positive contributions of humoral antitumor responses and the function of B cells are currently still discussed,[4] the effective priming of cytotoxic $CD8^+$ T cells against tumor-specific antigens through MHC class I-restricted presentation of antigenic peptides on dendritic cells (DCs), so-called cross-priming,[5] is of particular importance since the existence of $CD8^+$ T cells in the tumor microenvironment can be correlated to improved tumor outcome and patient survival.[6−9] Recent attempts succeeded by applying antigen encoding mRNAs,[10−12] however, depending on efficient translation and potent presentation through antigen-presenting cells (APCs).[13,14] Alternatively, peptide- or protein-based

https://doi.org/10.1021/acsnano.1c10709
ACS Nano XXXX, XXX, XXX−XXX

anticancer vaccine strategies have been explored even longer.[15,16] Unfortunately, they mostly suffer from insufficient immune activation with risk of tolerance[17,18] and tumor relapse.[19] Consequently, the development of improved carrier systems and the investigation of potent immune modulators such as Toll-like receptor (TLR) agonists as new vaccine adjuvants are addressed to boost vaccination outcome.[20,21]

Small-molecule imidazoquinoline-based TLR7/8 agonists are promising adjuvant candidates efficiently activating a broad spectrum of APCs, including different types of DCs.[22] Moreover, they have been demonstrated to trigger high levels of cytokines like TNF-α, INF-γ, IL-6, IL-12, and type I interferon, resulting in Th1-mediated immune responses[23] and cytotoxic T cells that act against intracellular pathogens or cancer cells.[24] Nevertheless, clinical use of those small-molecule adjuvants is hampered based on their pharmacokinetic profile causing severe systemic inflammation.[25−27] Covalent conjugation of TLR7/8 agonists to polymer scaffolds, however, has been shown to amend their safety profile and hinder fast clearance.[28]

The delivery of not only small-molecule adjuvants but also antigenic components including proteins or peptides provides several advantages when combined with polymer-based platforms.[29] In addition to prolonged circulation and improved pharmacokinetics, nanoparticular systems benefit from accumulation in lymphatic organs and uptake in immune cells based on their morphological and compositional similarities to pathogens.[28,30,31] If designed properly, they enable co-delivery of adjuvant and antigen to the same DC or other APCs and, thus, foster essential priming of $CD8^+$ T cells.[32,33] Carrier designs range from peptide- or lipid- to synthetic polymer-based systems including self-assembling micelles as well as core-cross-linked structures, which either physically encapsulate or covalently bind the desired cargo.[34−38] Incorporation of pH-responsive units that trigger disintegration after endosomal uptake seem to enhance antigen presentation and improve priming of $CD8^+$ T cells,[35] in addition to prevent undesired long-term accumulation.[39] Several studies emphasize that not only co-delivery of adjuvant and antigen to APCs plays a pivotal role in the effectiveness of a vaccine, but also the application of the nanocarrier itself already benefits its efficacy when compared to co-administration of the mixed components without a nanocarrier.[34,36,40]

One straightforward method to obtain amphiphilic, self-assembling polymers for nanocarrier syntheses is the reversible addition−fragmentation chain transfer (RAFT)-polymerization.[41] RAFT procedures allow the adjustable fabrication of copolymers regarding posterior nanoparticle size and tolerate the introduction of a great variety of functionalities.[42] While a tailored design of applied chain-transfer agents (CTAs) enables corona modifications, the introduction of reactive monomers allows core-functionalization in post-polymerization reactions.[43−47] We have combined RAFT-derived hetero-telechelic block copolymers with a post-polymerization modification approach[46] to generate core-cross-linked nanogels[48] and recently demonstrated that covalent nanogel conjugation with the TLR7/8 agonist 1-(4-(aminomethyl)-benzyl)-2-butyl-1*H*-imidazo[4,5-*c*]quinolin-4-amine (IMDQ) leads to localized immune activation after subcutaneous (s.c.) injection with safe antiviral and antitumor immune responses.[30,45,49]

In this study, we report on the evolution of this pH-responsive nanogel platform toward a multi-component antitumor vaccine that is even safe for intravenous (i.v.) administration and facilitates co-delivery of TLR7/8 agonist IMDQ and ovalbumin (OVA) as model antigen for improved generation of $CD8^+$ T cells *in vitro*. While the nanogel platform itself is immunologically silent, the nanoparticular co-delivery of IMDQ and OVA induces robust immune responses *in vitro* that outperform soluble mixtures of components. Prophylactic and therapeutic immunization against OVA-expressing tumors revealed the efficacy and specificity of this multi-component vaccine *in vivo*. Based on its chemical design, the herein described nanogel platform allows versatile adjustments regarding the introduced small molecules and attached antigens without morphological changes of the carrier and, therefore, might be an interesting candidate even for personalized anticancer immunotherapies.

RESULTS AND DISCUSSION

Core and Surface Modification of pH-Degradable Nanogel Platform for Dual Delivery of TLR7/8 Agonist and OVA Antigen. To realize quantifiable co-delivery of antigen and immune stimulant *via* a precise nanoscale carrier, we applied a tunable nanogel platform based on amphiphilic reactive precursor block copolymers that enable both core and corona functionalization *via* post-polymerization modifications. Through covalent conjugations, these nanogels ensure co-delivery of the attached TLR7/8 agonist and OVA as model protein antigen to immune cells both *in vitro* and *in vivo* (Figure 1A).

The underlying block copolymer is accessible through RAFT block copolymerization of methoxy tri(ethylene glycol) methacrylate (mTEGMA) and pentafluorophenyl methacrylate (PFPMA).[47,50] While the hydrophilic P(mTEGMA) block provides micellar stability and shielding properties, the solvophobic P(PFPMA)-block drives self-assembly to micelles in polar-aprotic solvents like DMSO and facilitates posterior core functionalization of the nanosized precursors by aminolysis of the reactive esters.[51] When applying the azide-functionalized chain-transfer agent 1-azido-16-cyano-13-oxo-3,6,9-trioxa-12-azaheptadecan-16-yl benzodithioate (azide-CTA) during the RAFT polymerization process,[50] click-reactive functionalities are installed on the surface of the resulting nanogels allowing for orthogonal surface-modifications through strain-promoted azide−alkyne cycloaddition (SPAAC)[52] with dibenzyl cyclooctyne (DBCO)-modified counterparts (Figure 1A).

RAFT block copolymerization of mTEGMA and PFPMA using the low-temperature initiator 2,2′-azobis(4-methoxy-2,4-dimethylvaleronitrile (AMDVN) afforded monodisperse block copolymers with a moderate PDI of 1.3 and a number-average molecular weight of around 12 kDa after removal of the dithiobenzoate end groups (Figure 1B; for detailed characterization of $P(mTEGMA)_{25}$ and block copolymer $P(mTEGMA)_{25}$-*b*-$P(PFPMA)_{34}$ compare Figures S1−S10). Formation of reactive precursor micelles after block copolymer self-assembly in DMSO was assessed by dynamic light scattering (DLS) (Figure S12). Subsequent covalent attachment of IMDQ as well as fluorescent labeling with Texas Red dye was achieved through aminolysis of the reactive esters inside the core (Figure 1A). Integrity of the P(mTEGMA) segment during aminolysis of PFP esters was confirmed by ^{1}H NMR measurements (Figure S10) in addition to a detailed characterization of the sequential aminolysis of PFP esters by ^{19}F NMR monitoring (Figure S9). Further core-cross-linking

https://doi.org/10.1021/acsnano.1c10709
ACS Nano XXXX, XXX, XXX−XXX

with the acid-sensitive cross-linker 2,2-bis(aminoethoxy)-propane and conversion of the remaining PFP esters into fully hydrophilic moieties by 2-aminoethanol yielded the hydrophilic, pH-labile IMDQ-loaded nanogels that could be purified by dialysis and stored as dry powder after lyophilization. The introduction of the ketal-based cross-linker locks in the nanogels' morphology and size but at the same time assures disassembly of nanogels into single polymer chains after endosomal uptake.[53] Particle formation of IMDQ-loaded nanogels as well as their degradation behavior upon an acidic stimulus and long-term stability under physiological conditions were analyzed by DLS and FCS (Figures S13–S15). IMDQ-loading of redispersed nanogels was quantified *via* UV–vis spectroscopy as 9.5 wt% (Figure S11).

In a subsequent experiment, we verified the accessibility of the RAFT CTA-derived, surface-exposed azide groups for SPAAC conjugation. For this purpose, IMDQ-loaded nanogels were incubated with cyclooctyne-modified Oregon Green dye. UV–vis measurements after removal of unbound dye confirmed covalent attachment of the Oregon Green dye and, hence, preserved accessibility of azide-groups for covalent conjugation (Figure S16; a negative control sample of unmodified Oregon Green showed almost complete dye removal). Based on these results, we proceeded with the generation of the envisaged two-component antitumor vaccine composed of IMDQ-nanogels and surface attached model antigen.

Especially for i.v. administration, adjuvants and antigens should be combined into the same carrier system to guarantee co-delivery to the same immune cell subpopulations.[54] Prior to conjugation of the model antigen OVA to the nanogels, the protein's lysine-derived amino side chains were exploited through NHS ester chemistry for modification with a SPAAC-reactive DBCO-PEG_4 linker and an Alexa Fluor 488 label for monitoring (note that OVA is equipped with 20 potential lysine modification sites, and on average one Alexa Fluor 488 and five DBCO-PEG_4 linkers were attached according to UV–vis spectroscopy; Figure S17). DBCO modification did not alter the integrity or stability of the protein (Figure S18), and it was also well accessible for azide-terminated polymers for conjugation reactions (Figure S19). Interestingly, although one of the modification sites is localized in the $CD8^+$ T cell epitope region (compare Supporting Information), DBCO modification did not alter the protein's antigenicity (Figure S20).

Consequently, covalent conjugation of OVA to the azide-surface exposed nanogels could be performed by simply mixing both components dissolved in PBS, resulting in a protein to azide molar ratio of 1:20. Note that mixing the individually labeled compounds (Texas Red-labeled nanogel and the Alexa Fluor 488-labeled proteins) provided a yellow fluorescent sample (Figure 1E,F and Figure S21) from which successful conjugation could be validated macroscopically by sodium dodecyl sulfate–polyacrylamide gel electrophoresis (SDS-PAGE) (Figure 1D). Soluble ovalbumin (sOVA) as well as DBCO-modified ovalbumin (DBCO-OVA) showed distinct bands after UV excitation as well as after Coomassie staining. The disappearance of unbound DBCO-OVA after SPAAC reaction (NP(IMDQ+OVA)) indicated complete conjugation of DBCO-OVA to azide nanogels NP(IMDQ), while the mixture of sOVA and NP(IMDQ) did not lead to any ligation of sOVA (Figure 1D). In-depth characterization of various protein to azide molar ratios revealed no cross-linking between particles and confirmed the necessity of the excess azide (Figure S24). Further conjugate characterization by DLS revealed monodisperse nanogel formation with sizes around 58 nm that were independent of IMDQ and OVA loading (Figure 1C). Zeta potential measurements revealed a slight decrease in surface charge after conjugation of ovalbumin from −4 to −9.5 mV (Figure S23). Moreover, OVA-bearing particles still showed an acidic degradation profile upon exposure to endosomal pH (Figure S22).

In agreement with the gel electrophoresis experiment, subsequent fluorescence correlation spectroscopy (FCS) measurements[55] were performed to affirm covalent conjugation of IMDQ-loaded nanogels and DBCO-OVA on a molecular level (Figure 1G). The selection of fluorescent dyes allowed to monitor independently from each other the autocorrelation of the Texas Red-labeled NP(IMDQ) as well as the Alexa Fluor 488-labeled OVA (Figure 1E and Figure S18). Based on this setup, we found for the Alexa Fluor 488-derived OVA autocorrelation a quantitative shift to higher lag times which corresponds to larger species after SPAAC reaction, demonstrating covalent association of OVA to the nanogels (Figure 1G). This shift was independent from IMDQ-loading (compare to FCS measurement of nanogels without IMDQ, Figure S25). *Via* Texas Red-derived nanogel autocorrelation, also a slight increase in size was found (Figure 1G and Figure S26), indicating successful OVA conjugation. In addition, simultaneous analysis of both channels *via* fluorescent cross-correlation spectroscopy (FCCS) revealed an exclusive cross-correlation for NP(IMDQ+OVA) in comparison to the mixture of NP(IMDQ) and sOVA, thus manifesting dual-loading of nanogels also on a molecular level (Figure 1G and Figure S27). Upon acidification, the previously observed cross-correlation dropped and almost disappeared (Figure 1H), reflecting the pH-responsiveness of the nanogels and their disintegration into many non-cross-correlating single polymer chains, as observed also by the Texas Red-derived autocorrelation of NP(IMDQ) before (Figure 1H). Similar results were found again for empty nanogels without IMDQ NP(−) and are summarized in the Supporting Information (Figures S25–S27). Moreover, detailed calculation of the hydrodynamic radii derived from the resulting autocorrelation functions confirmed both conjugation of DBCO-modified OVA to the nanogel as well as degradation of IMDQ-loaded nanogels upon acidification (compare Tables S1 and S2 in the Supporting Information). Summarizing, the underlying chemical design allows for a well-defined and also reproducible fabrication process (compare Figure S28) toward precise co-delivery of immune stimulant and immunogenic part within one nanogel carrier system that is pre-defined in morphology and guarantees control over the co-delivery of each vaccine component.

IMDQ-Loaded, OVA-Decorated Nanogels Enable Co-delivery and Lead to Activation and Maturation of Immune Cells through TLR7/8-Dependent Signaling. After successful conjugation of IMDQ and OVA to the pH-responsive nanogels, we wanted to evaluate the system's co-delivering capacity and initiation of immune responses by its interaction with immune cells. While it has already been demonstrated that IMDQ-loaded nanogels outperform IMDQ-loaded polymer chains regarding TLR activation *in vivo*,[45] we first sought to investigate the influence of OVA co-administration, either covalently attached to the nanogel surface or solely admixed, on a TLR reporter cell line (Figure 2). Engineered RAW-Blue macrophages allow for a broad

https://doi.org/10.1021/acsnano.1c10709
ACS Nano XXXX, XXX, XXX–XXX

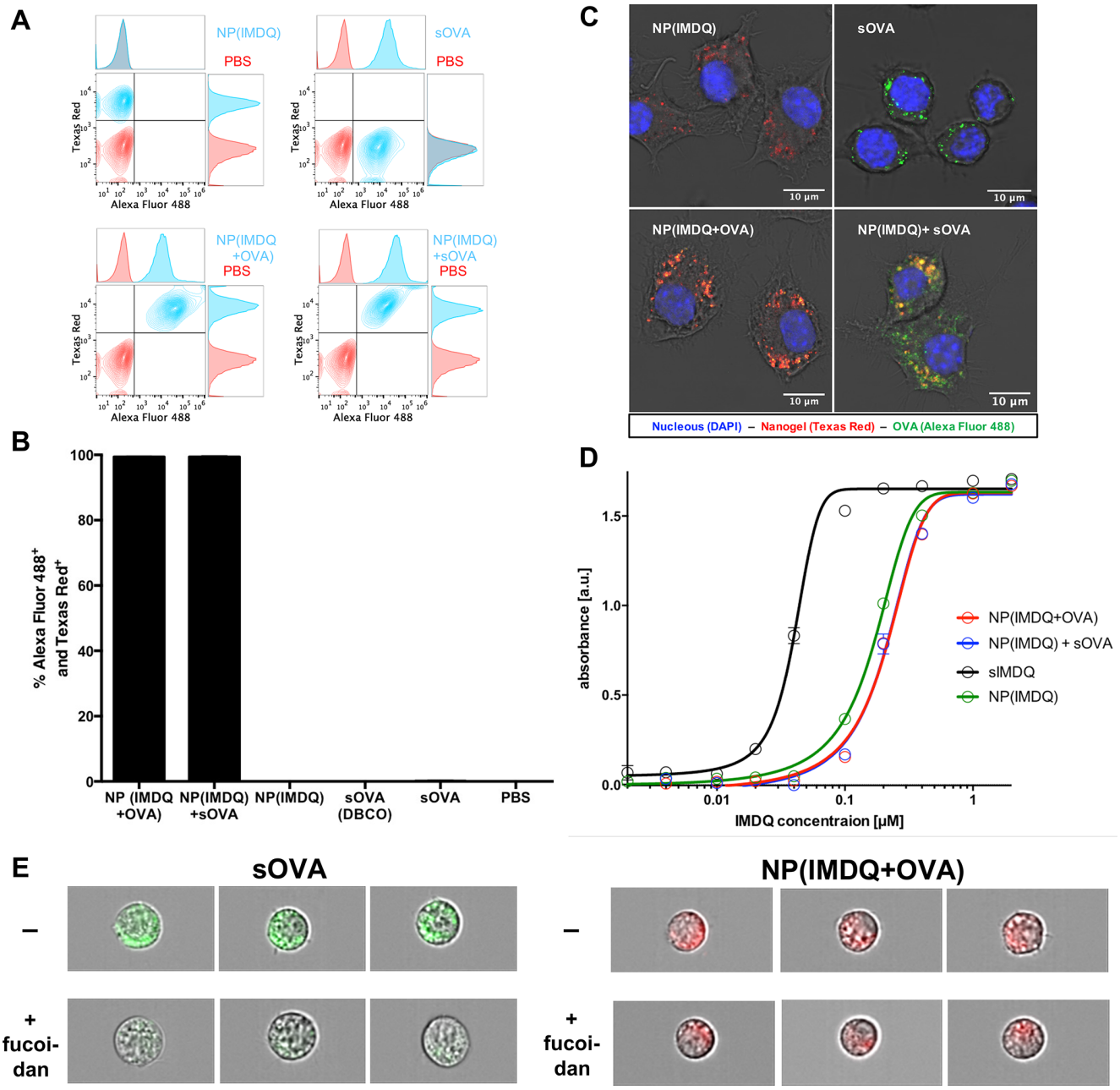

Figure 2. Nanogel-mediated co-delivery and immune cell stimulation by TLR7/8-agonist IMDQ and model protein antigen OVA in an immune reporter cell line. (A) Flow cytometric plots, (B) corresponding percentage of particle and antigen positive RAW-Blue macrophages, and (C) fluorescent confocal microscopy images after incubation with the respective nanogel conjugates and single compounds. (D) TLR agonistic activity measured by NF-kB activation *via* the RAW-Blue reporter assay. (E) Fluorescence imaging of DCs that have internalized soluble OVA (green) (left) or NP(IMDQ+OVA) nanogels. In the presence of the scavenger receptor inhibitor fucoidan (300 μg/mL) the uptake of sOVA is inhibited, but the nanogel sample is still internalized (for quantification, compare Figures S45 and S46).

screening of TLR activity and were, therefore, selected. *Via* MTT assay, no influence on the cells' viability was found in the relevant concentration range (Figure S29). By flow cytometry and fluorescent confocal microscopy experiments, RAW macrophages could be characterized to concomitantly internalize nanogels and co-delivered OVA. For that purpose, cells were incubated for 16 h with nanogel and OVA samples. We found that both nanogels and OVA were taken up independently from each other (Figure 2A and Figure S31). Interestingly, both co-delivery of covalently attached or co-administered soluble sOVA provided almost 100% Alexa Fluor 488 and Texas Red positive cells (Figure 2B). Additionally, by confocal microscopy both nanogel and OVA-derived fluorescence could be found internalized by cells (Figure 2C and Figure S32). While for the mixture of NP(IMDQ) and sOVA separate and co-localized fluorescent signals could be found for each species inside the cells, only the NP(IMDQ+OVA) sample with covalently attached OVA provided co-localization of both components inside same compartments. This could also be further confirmed on other antigen-presenting cell

https://doi.org/10.1021/acsnano.1c10709
ACS Nano XXXX, XXX, XXX–XXX

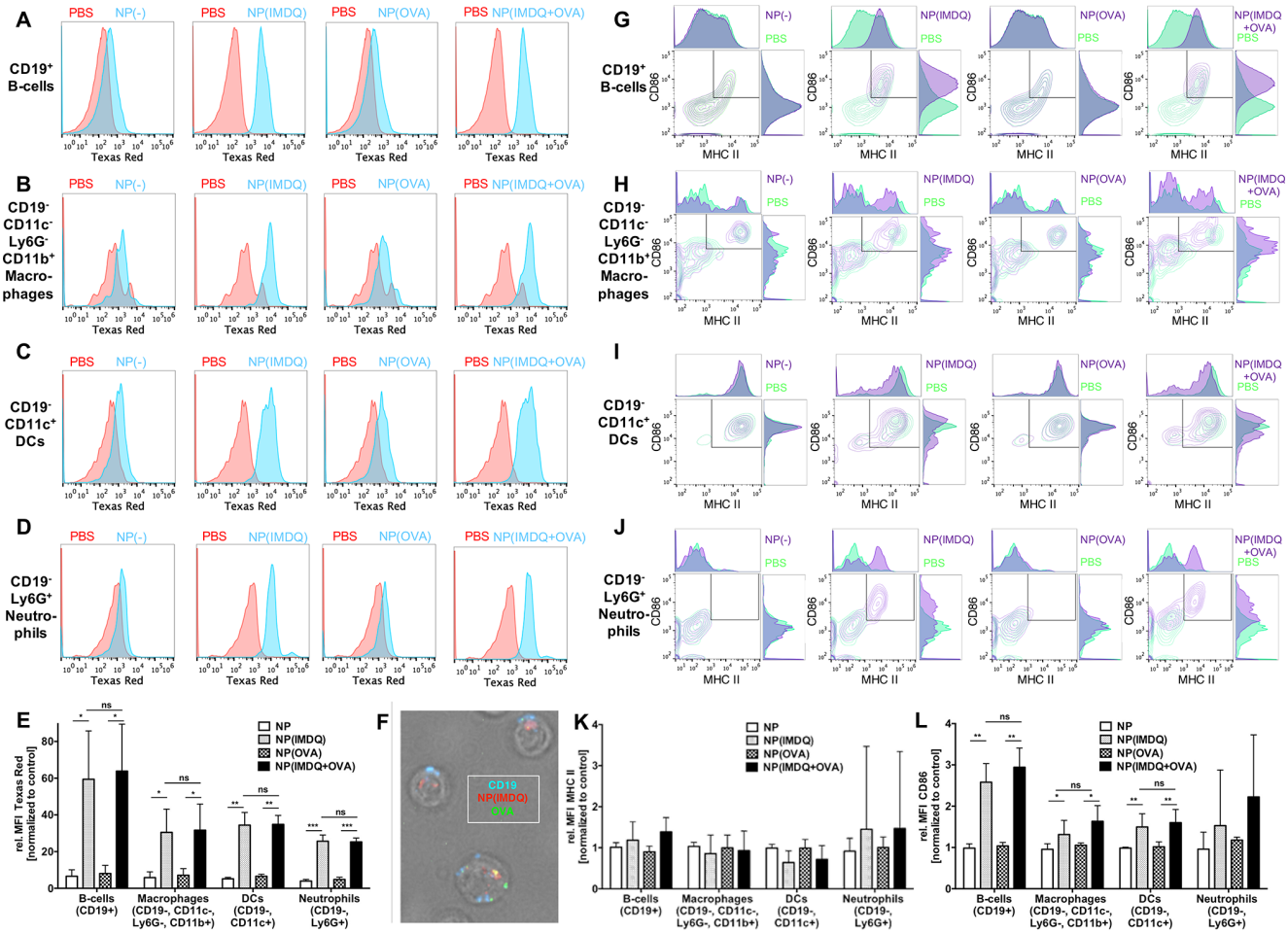

Figure 3. Nanogel-mediated co-delivery and immune cell stimulation by TLR7/8-agonist IMDQ and model protein antigen OVA in primary heterogeneous immune cells. Flow cytometric histograms of particle uptake in B cells (A), macrophages (B), DCs (C), and neutrophils (D) obtained from incubating spleen cells *ex vivo* with the respective nanogel conjugates. (E) Summary of particle-derived relative mean fluorescence intensity (MFI, normalized to PBS as control) of respective immune cells. (F) Fluorescent microscopy image of spleen cells identified as B cells (by CD19 expression, blue) which have internalized both NP(IMDQ) (red) and OVA (green) after incubation of total spleen cells *ex vivo* with NP(IMDQ+OVA). Flow cytometric plots of maturation status by CD86 and MHC-II expression of B cells (G), macrophages (H), DCs (I), and neutrophils (J) after incubating spleen cells with the respective nanogel conjugates. Summary of (K) MHC-II- and (L) CD86-derived relative mean fluorescence intensity (MFI, normalized to PBS as control). Due to immune cell preparation, CD86 serves as appropriate maturation marker for the respective immune cells after incubation with respective nanogel conjugates.

lines, *e.g.*, on DC2.4 (compare Figure S33). By flow cytometric analysis applying the ImageStream technology, overlays of OVA-derived fluorescence with bright field imaging confirmed again an intracellular localization of the antigen both in its soluble or particle-bound version (Figure S44). We additionally compared the uptake of sOVA (Alexa Fluor 488-labeled) with the NP(IMDQ+OVA) nanogel conjugate (Cy5-labeled) in the presence of fucoidan, a potent scavenger receptor inhibitor.[56] In Figure 2E (as well as in Figure S45) scavenger receptor inhibition caused a reduction of internalization for the sOVA, while for the nanogel sample NP(IMDQ+OVA) particles could still get internalized independent from the scavenger receptor (Figure S46). Note that scavenger receptors are usually associated with phagocytosis of bacterial pathogens and other extracellular antigens.[57] They further afford an intracellular processing leading to more MHC-II antigen presentation than MHC-I presentation. This would favor $CD4^+$ T cell responses at the expense of cytotoxic $CD8^+$ T cell immune responses.[58] Circumventing this intracellular processing by using the nanogel-bound version seems to be more attractive in order to enhance cross-presentation and generate a higher amount of antigen-specific $CD8^+$ T cells (see Figure 4). These observations underline again that the dual functionalized carriers guarantee successful co-delivery of both antigen and adjuvant into the same immune cell simultaneously.

Moreover, the co-delivered IMDQ is able to stimulate TLR receptor for an effective maturation of the APCs that are required for the induction of cellular and humoral immune responses. This could be monitored by RAW-Blue macrophages *via* secretion of the embryonic alkaline phosphatase (SEAP) in the cell culture supernatant caused by the NF-kB signaling. Compared to non-conjugated IMDQ, nanoparticular conjugated agonist led to a slightly reduced but still highly potent TLR activation in the sub-micromolar regime (Figure 2D). Similarly, OVA-decorated IMDQ nanogels also induced significant TLR activation comparable to IMDQ-loaded nanogels without OVA loading. Hence, OVA loading did not interfere with the TLR agonist−receptor interaction.

https://doi.org/10.1021/acsnano.1c10709
ACS Nano XXXX, XXX, XXX−XXX

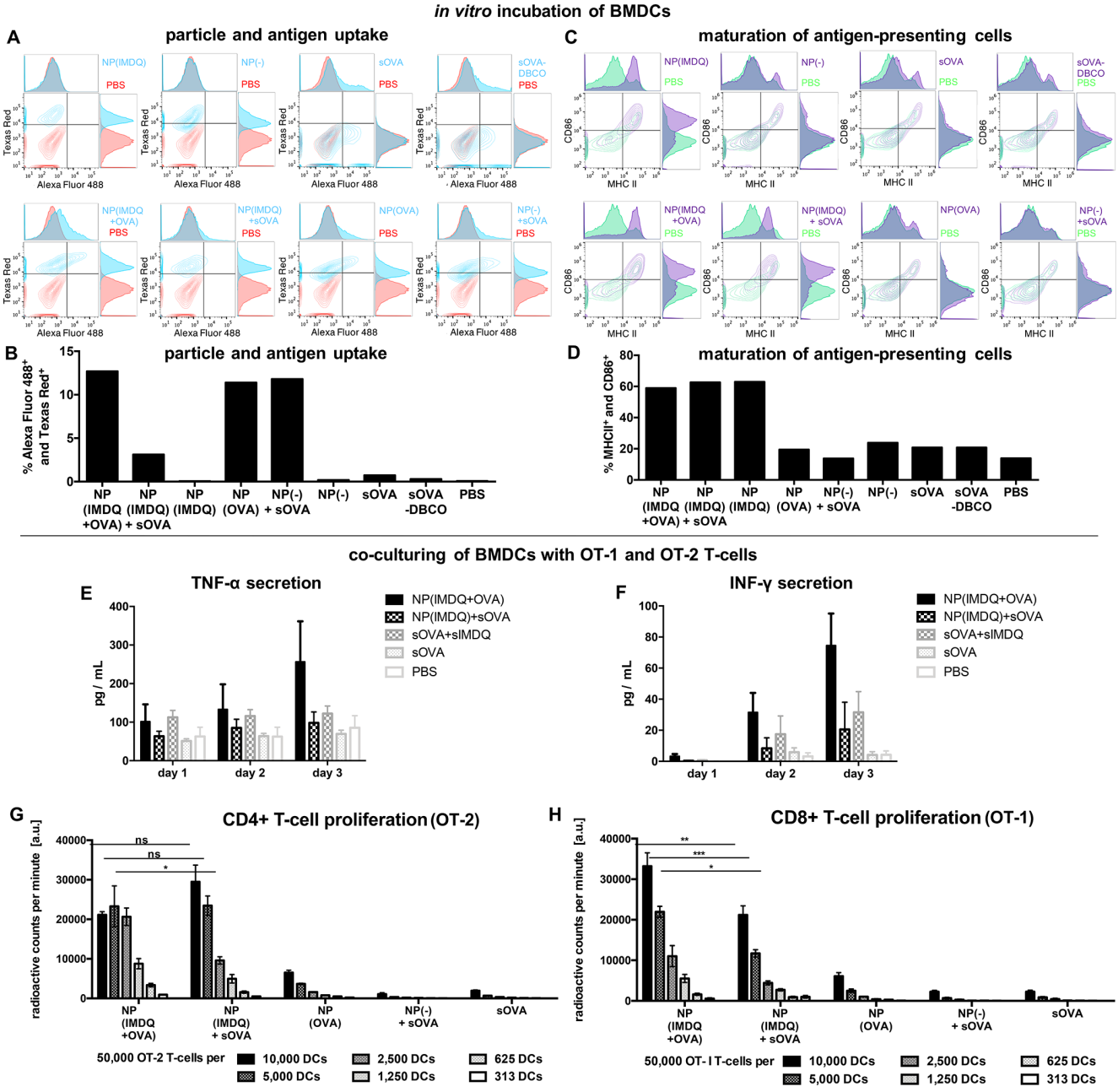

Figure 4. Nanogel-mediated co-delivery of antigen and adjuvant triggers maturation of primary dendritic cells and T cell proliferation *in vitro*. (A) Flow cytometric histogram and (B) percentage of both particle and antigen positive BMDCs after incubation with the respective nanogel conjugates and single compounds. (C) Flow cytometric histogram and (D) percentage of CD86 and MHC-II positive BMDCs after incubation with the respective nanogel conjugates. After co-culturing of nanogel-pulsed BMDCs with OVA-specific T cells secreted cytokines tumor necrosis factor TNF-α (E) and interferon INF-γ (F) were determined from the cell culture supernatant. OVA-specific T cell proliferation was determined at different ratio BMDC to T cell ratios with (G) OT-2 T cells for $CD4^+$ T cell proliferation and (H) OT-1 T cells for $CD8^+$ T cell proliferation. For the latter, covalently attached OVA seems to favor the secretion of pro-inflammatory cytokines and the induction of a $CD8^+$ T cell immune response pathway.

To assess the interaction of the nanogels with immune cells that are more relevant for successful *in vivo* immunization, we next performed similar studies using primary APCs *in vitro*. For that purpose, we selected murine splenocytes as heterogeneous primary immune cell population and incubated them with our nanogel samples (Figure 3), followed by flow cytometric analysis to identify each immune cell population (Figure S34). As visualized by the histogram plots in Figure 3A–D, a boosted nanogel uptake could generally be found when they were loaded with IMDQ in comparison to "empty" nanogels, independently from their additional OVA payload. A more in-depth evaluation of the involved immune cell subsets revealed that this is especially the case for B cells ($CD19^+$), but also macrophages ($CD19^-$, $CD11c^-$, $CD11b^+$, $Ly6G^-$), DCs ($CD11c^+$), and neutrophils ($Ly6G^+$) seem to follow this trend (Figure 3E). Interestingly, a pre-incubation of the nanogel samples with mouse serum prior to addition to spleen cells did not affect this uptake behavior (Figure S35). Besides,

https://doi.org/10.1021/acsnano.1c10709
ACS Nano XXXX, XXX, XXX–XXX

also by fluorescent microscopy a preferential interaction with B cells could be observed, as both Texas Red-derived nanogel fluorescence and Alexa Fluor 488-derived OVA fluorescence were generally associated with $CD19^+$ B cells (Figure 3F and Figure S38). In fact, similar preferential association to B cells has also been found for IMDQ-loaded nanogels *in vivo* after s.c. injection and subsequent analysis of the draining lymph nodes before.[30]

We then also looked at maturation markers in the corresponding immune cell subpopulations by staining them for the expression of the co-stimulatory molecules CD86 and MHC-II, typical maturation markers for successful antigen presentation (Figure 3G–J). Particle-delivered IMDQ triggered the expression levels especially of CD86 in almost all analyzed APCs. MHC-II expression alone was already at relatively high basal levels in the negative control samples due to the applied splenic isolation conditions (Figure S37) and, thus, showed only a minor trend toward IMDQ-mediated maturation (Figure 3K). However, CD86 expression is much more sensitive and was exclusively stimulated by the nanogel-bound IMDQ in almost all immune cell populations (Figure 3L and Figure S36). Interestingly, B cells increased again most strikingly their maturation status. Taken into account their vigorous uptake of IMDQ- and OVA-loaded nanogels, these observations make them promising candidates for successful antigen presenting after i.v. applications, as nanogel pre-incubation with serum did also not alter this behavior either (Figures S36 and S37).

Two-Component Nanogel Platform Favors $CD8^+$ over $CD4^+$ T Cell Proliferation *In Vitro*. To further elucidate the downstream immune responses triggered by co-delivering antigen and adjuvant through our pH-degradable nanogel platform *in vitro*, we selected bone marrow-derived primary dendritic cells (BMDCs) and incubated them again for 16 h with the nanogel system (Figure 4). The previously observed simultaneous uptake of IMDQ-nanogels and OVA could again be confirmed. Interestingly, flow cytometry analysis revealed that for nanoparticle conjugated IMDQ the percentage of double positive cells (both particle/Texas Red and antigen/Alexa Fluor 488) was increased when OVA was covalently attached to the nanogels' surface. The amount of internalized sOVA is reduced when cells were already stimulated by NP(IMDQ) (Figure 4A,B and Figure S40). This is in agreement with other studies where maturation of APCs has been shown to reduce additional particle uptake capacities[59] and, thus, underlines the necessity of antigen and adjuvant co-delivery.

The cells' maturation profile could again be identified during flow cytometry analysis (Figure S41; for BMDCs, MHC-II expression is now also more reliable). Only for BMDCs pulsed with IMDQ-containing samples, both MHC-II and CD86 maturation markers were upregulated concurrently, while nanogels without TLR7/8 agonist did not trigger BMDC maturation independent of co-administration of OVA, demonstrating again that the nanogel system itself is immunogenically silent (Figure 4C,D).

Moreover, the BMDC maturation approach allowed us to further characterize *in vitro* antigen-specific $CD4^+$ and $CD8^+$ T cell immune responses, an assumed pre-requisite for successful induction of tumor immunity. Therefore, after stimulation with our IMDQ- and OVA-loaded nanogels overnight, BMDCs were then co-cultivated with dilutions of OVA-specific T cell receptor transgenic OT-1 and OT-2 T cells, isolated from the spleen of OT-1 or OT-2 mice, corresponding to the induction of OVA-specific $CD4^+$ (OT-2) and $CD8^+$ (OT-1) T cells. On the following days, cell culture supernatants were quantified for pro-inflammatory cytokines that support Th1-biased immune responses, and interestingly the nanogel conjugate of NP-(IMDQ+OVA) yielded highest secretion of tumor necrosis factor TNF-α and interferon INF-γ (Figure 4E,F). The T cell proliferation triggered by BMDC maturation and corresponding antigen presentation (either the $CD4^+$ epitope for OT-2 or the $CD8^+$ epitope for OT-1) could be measured radioactively *via* incorporation of ^{3}H-thymidine (Figures S42 and S43). Interestingly, the enhanced co-delivery and stimulation of our two-component nanogel vaccine had again a significant impact on the co-applied T cells. Only the combination of OVA with IMDQ-containing samples led to an increased proliferation of OT-1 and OT-2 cells, emphasizing the importance of co-administering antigen and adjuvant (Figure 4G,H).

Furthermore, covalent attachment of OVA to IMDQ-nanogels led to a significantly increased proliferation of OVA-specific OT-1/$CD8^+$ T cells compared to the mixture of sOVA and NP(IMDQ) (Figure 4H). For OT-2 cells ($CD4^+$ T cells), however, similar elevated proliferation levels were found for the covalent two-component system as well as the non-covalent mixture (Figure 4G). Consequently, our covalent NP(IMDQ+OVA) construct seems to boost OT-1/$CD8^+$ T cell proliferation significantly, probably by the increase in TNF-α and INF-γ secretion. This is in accordance with several previous reports demonstrating that a carrier-mediated co-delivery of OVA favors cross-presentation and the induction of $CD8^+$-governed immune responses.[60−62] Hence, under the applied *in vitro* settings our covalent nanogel platform which co-delivers antigen and adjuvant seems to amend the immune response in favor of $CD8^+$ T cell generation.

Two-Component Nanogel Platform Can Be Safely Applied Intravenously and Generates OVA-Specific Humoral and Cellular Immune Responses. Based on these promising *in vitro* results, we pursued *in vivo* applications for our nanovaccine. It is known that small-molecule TLR agonists are prone to cause systemic immune responses followed by systemic inflammation leading to severe side effects.[27] Conjugation of TLR7/8 agonists to polymeric carriers, however, has been shown to confine the subsequent immune response to draining lymph nodes after s.c. injection.[28,30] Interestingly, latest findings by Lynn and co-workers indicate that i.v. injection improves vaccine efficacy compared to s.c. immunization. Especially in case of a physical linkage between antigen and adjuvant affording nanosized particles, $CD8^+$ T cell responses were significantly higher after i.v. administration.[34] However, when applying carrier-bound TLR7/8 agonists into the bloodstream, their influence on hematologic toxicities should be monitored carefully in reflection to other reported systemic type I IFN responses.[63]

In this context, we injected our IMDQ-loaded nanogels i.v. into mice and first analyzed their biodistribution. For that purpose, we used Cy5-labeled nanogels and injected them with and without covalently attached ovalbumin (NP(IMDQ+OVA) and NP(IMDQ)+sOVA) into the tail vein of mice (for each sample an adjuvant dose corresponding to 10 μg of IMDQ was used according to our previous local immunization experiments[30,45]—additionally, an antigen dose corresponding to 30 μg of OVA was used, as at this ratio all antigen can quantitatively be conjugated to the nanogel, compare Figure S23). A mixture of soluble IMDQ and OVA (sIMDQ+sOVA)

https://doi.org/10.1021/acsnano.1c10709
ACS Nano XXXX, XXX, XXX−XXX

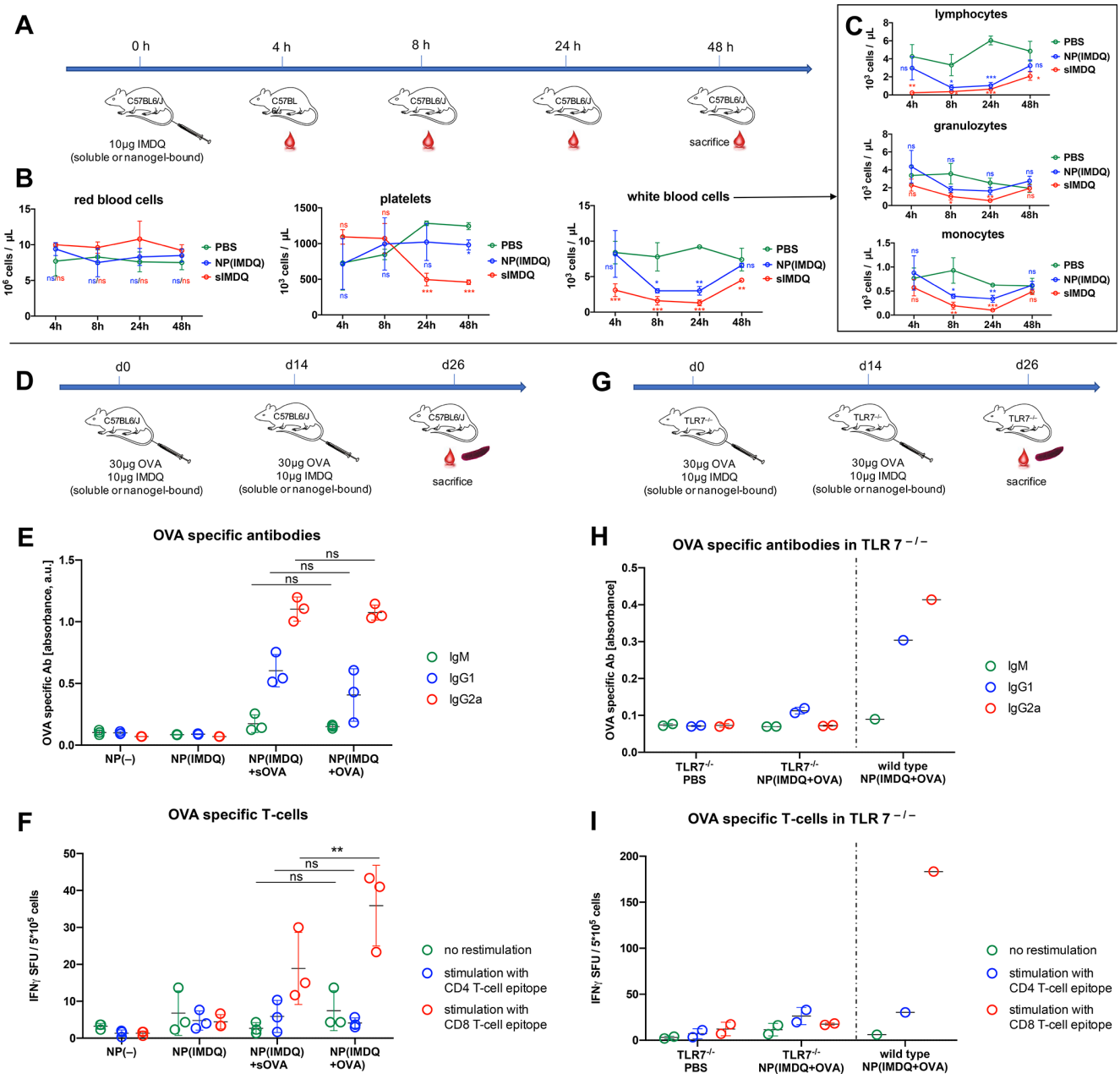

Figure 5. IMDQ- and OVA-loaded nanogel can be administered i.v. safely and generate OVA-specific humoral and superior cellular immune responses. (A) Schedule for analyzing hematologic toxicities of soluble or nanogel-bound TLR7/8 agonist IMDQ after single i.v. injection. (B) Corresponding blood cell results and (C) their differentiated white blood cells. (D) Immunization schedule for IMDQ- and OVA-loaded nanogel in wild-type mice and (E) the corresponding OVA specific antibodies determined by ELISA of the blood serum, as well as (F) the corresponding T cells determined by ELISpot of the isolated spleen cells. (G) Analogous immunization schedule for IMDQ- and OVA-loaded nanogel in TLR7$^{-/-}$ mice. (H) No OVA-specific antibodies could be found by ELISA in the blood serum as well as (I) no corresponding T cells could be determined by ELISpot of the isolated spleen cells, in contrast to a wild-type mouse serving as control during these experiments.

served as control. Cy5-labeling allowed us to monitor particle organ distribution after dissection using an IVIS imaging system (Figure S48). The majority of the particles were either found in the liver, a typical non-specific sink for systemically administered nanocarriers, and in the kidneys, probably due to the pH-induced particle degradation and unfolding into single polymer chains that can be cleared renally. Nonetheless, a significant amount could still be detected in the spleen as relevant lymphatic organ to induce antigen-specific immune responses.

We therefore conducted flow cytometry analyses of liver and spleen-derived single cell suspensions (Figures S54–S57) and observed an uptake of particles with and without OVA into various antigen-presenting immune cell subpopulations. Interestingly, co-delivery of IMDQ-functionalized particle (Cy5-labeled) with antigen (Alexa Fluor 488-labeled OVA) worked best for the covalent conjugate in most of these immune cells (Figures S55B and S57B). In analogy to the previous *ex vivo* incubation experiments on isolated spleen cells, we also analyzed maturation markers in the correspond-

https://doi.org/10.1021/acsnano.1c10709
ACS Nano XXXX, XXX, XXX−XXX

ing immune cell subpopulations by staining them for co-stimulatory factors CD86 and MHC-II. Interestingly, none of these markers could be stimulated inside the liver, in line with its immunosuppressive microenvironment (Figure S55C,D). However, in the spleen, all IMDQ-containing NP increased the expression levels of CD86 in B cells, DCs, neutrophils ,and macrophages (MHC-II expression alone was again already at relatively high basal levels in the PBS control due to the applied splenic isolation conditions, Figure S57C,D). However, CD86 expression seems again to be more sensitive, as it was also exclusively most stimulated by the nanogel-bound IMDQ in almost all of these immune cell populations in the spleen (Figure S57C).

To further prove that nanogel-bound IMDQ on OVA-loaded nanogels has the potential to induce promising immune responses, we also checked for the cytokine profile of those mice 24 h after i.v. injection and found highest levels of the pro-inflammatory cytokines TNF-α and INF-γ for the dual-loaded nanogel NP(IMDQ+OVA) (Figure S51). These results are in accordance with the cytokine data of the *in vitro*-stimulated BMDCs (compare Figure 4E,F) and confirm that the nanogel-mediated co-delivery of both antigen and immune stimulant provides a good basis for successful immunizations. For additional insights into the innate immune response, we analyzed a larger panel of TLR7/8-driven cytokines also 4 h after the nanogel injection. Again, the nanovaccine led to elevated levels of most analyzed cytokines 24 h after i.v. injection. However, administration of sIMDQ+sOVA resulted in a rapid production of cytokines early after the injection (4 h), illustrating an undesired cytokine storm caused by sIMDQ when applied without a carrier system (Figure S52).

We further aimed to evaluate this toxicity after i.v. injection. Prompted by the strong accumulation of the nanogels in the liver (compare Figures S48 and S55), we looked at the liver enzyme parameters in the blood but could not observe any differences between different samples both after 4 and 24 h (Figures S49 and S50). Moreover, histopathological analyses by hematoxylin−eosin staining of liver, spleen, kidney, heart, and lung tissue showed no histological anomalies after i.v. injection of the nanovaccine (Figure S53).

However, a major impact especially for the i.v. administration of the soluble IMDQ could be detected on the composition of cells in the blood (Figure 5A−C). Earlier experiments revealed that, when bound to nanogels, the negative influence on the blood cell profile can be prevented and the immune response remains localized to draining lymph nodes after s.c. injection.[30,49] To provide an overview of IMDQ's impact after i.v. injection over time, mice were treated again with 100 μL of samples containing 10 μg equivalents of IMDQ, and blood samples were taken after 4, 8, 24, and 48 h for analysis of their red and white blood cell content as well as for the amount of platelets (Figure 5A). Systemic injection of TLR agonists resulting in uncontrolled release of type I interferons has been linked to strongly reduced numbers of platelets and white blood cells in the blood.[63]

While the number of red blood cells was not affected during all our studies (Figure 5B), the massive drop of platelets could be reconfirmed for the sIMDQ after 24 h, while the nanogel-bound TLR7/8 agonist had no effect, also after 48 h (Figure 5B). We relate this unfavorable site effect of the sIMDQ to the earlier detected massive cytokine expression when applied without a carrier system (Figure S52). Interestingly, such immunization-related severe thrombocytopenia is also associated as side effect of currently administered viral vector-based SARS-CoV-2 vaccines causing sinus vein thrombosis[64] and should therefore be circumvented already at an early stage of vaccine development.

Compared to sIMDQ, mice treated with nanogel-bound IMDQ (NP(IMDQ)) displaced no drop in platelets and only a reduced drop in lymphocytes that recovered more after 48 h effectively (Figure 5B). Specifically, white blood cell analyses revealed that the levels of lymphocytes, granulocytes and monocytes were also less affected by the nanogel-bound IMDQ than by sIMDQ and recovered to values of PBS-treated mice (Figure 5C). Moreover, empty nanogels or IMDQ-loaded nanogels decorated with OVA antigen never affected all hematologic parameters as much as sIMDQ after i.v. administration (Figure S47). Altogether, these findings highlight the enhanced safety profile of nanogel-bound IMDQ even after injection into the bloodstream, avoiding adverse systemic immune responses but instead providing more access to circulating immune cells for improved vaccination performance.

Proven effective and safe for i.v. injection, we used our two-component nanogels for immunizing naïve wild-type mice. On day 0 they were immunized i.v. with different nanogel samples, namely empty nanogels NP(−), IMDQ-loaded nanogels NP(IMDQ), two-component nanogels NP(IMDQ+OVA), and IMDQ nanogels mixed with sOVA (NP(IMDQ)+sOVA), followed by a boost immunization on day 14 (Figure 5D). On day 26 mice were sacrificed to analyze the generation of OVA-specific antibodies in the blood serum by ELISA (Figure 5E) and OVA-specific T cells in the spleen by ELISpot analysis (Figure 5F). As expected, only mice immunized with samples containing OVA and IMDQ showed secretion of OVA-specific antibodies. Both formulations, two-component vaccine and soluble mixture, led to increased secretion of IgG-type antibodies, especially the IgG2a subtype, which indicates a Th1-biased immune response. Here, covalent attachment of OVA did not have any drastic influence on the humoral response (Figure 5E). On the cellular level, however, spleen analysis of mice immunized with NP(IMDQ+OVA) revealed a significantly increased number of OVA-specific $CD8^+$ T cells compared to NP(IMDQ)+sOVA (Figure 5F). This observation is in accordance with our previous *in vitro* results (Figure 4G) indicating that OVA-bound IMDQ-nanogels mediate enhanced cross-presentation and favor a $CD8^+$ T cell response also *in vivo*.

Additionally, immunization experiments were repeated in $TLR7^{-/-}$ mice (Figure 5G) and revealed no priming of specific B cell (Figure 5H) and T cell (Figure 5I) immune responses. This clearly demonstrates that the nanogel-mediated Th1-biased humoral and cellular immune responses are mediated by TLR7 receptor stimulation triggered through nanogel-conjugated IMDQ.

Based on these results, we analyzed the effects of i.v. vaccination compared to s.c. vaccination on humoral and cellular responses, as similar systems have already been shown suitable for s.c. injection by us and others.[30,34] Hence, mice were injected twice with our nanovaccine. Again blood serum and spleen cells were tested for OVA-specific antibodies and T cells. This time, MHC-tetramer staining revealed $CD8^+$ T cells in blood after prime and boost immunization with our nanovaccine (Figure S58) but no significant differences between s.c. and i.v. administration. Similarly, recent data from Baharom *et al.* shows that i.v. vaccination does not trigger

https://doi.org/10.1021/acsnano.1c10709
ACS Nano XXXX, XXX, XXX−XXX

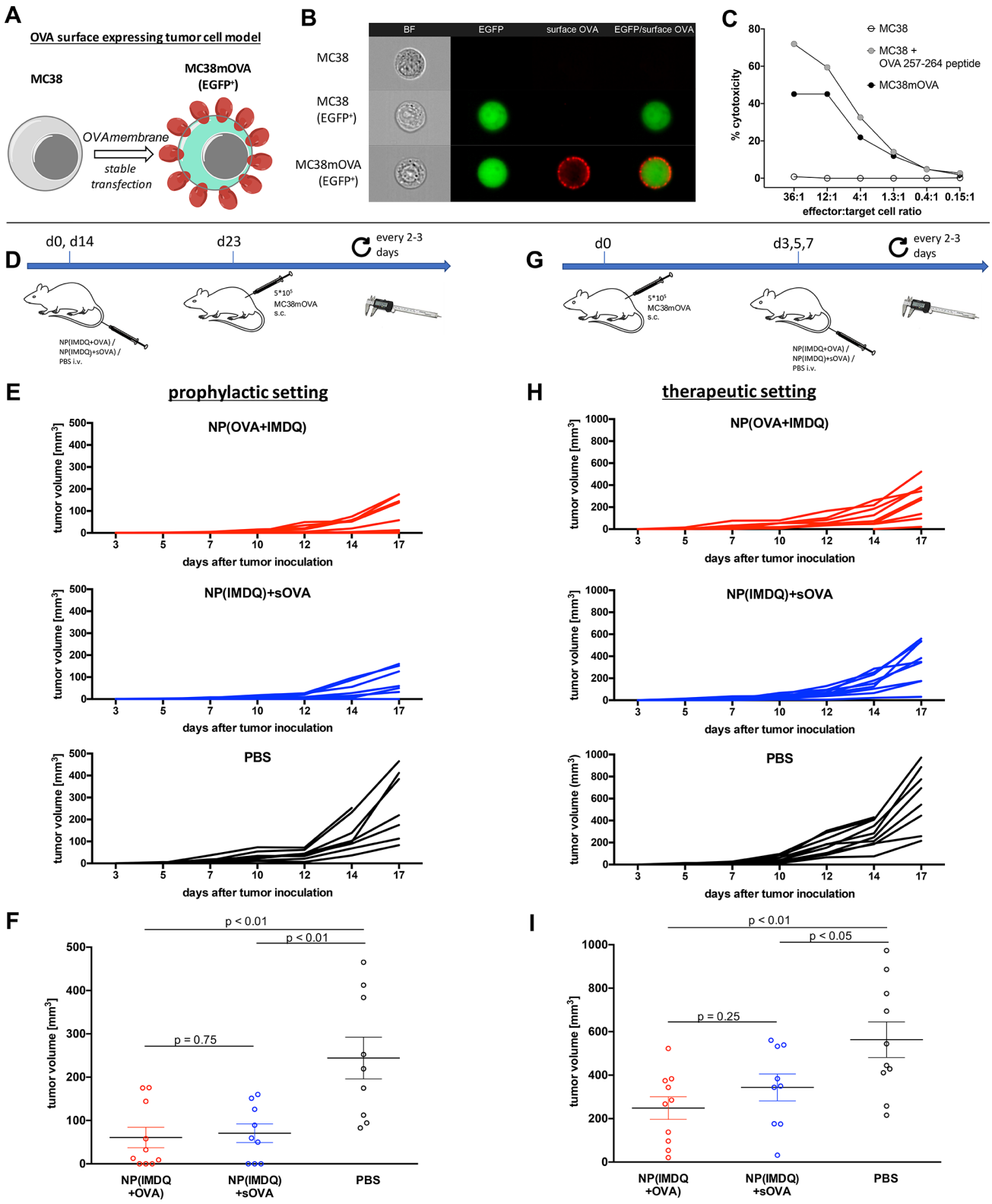

Figure 6. IMDQ- and OVA-loaded nanogels provide both prophylactic and therapeutic immunity toward a surface neoantigen-expressing tumor model. (A) MC38 cancer cells were genetically engineered to stably express OVA on their surface. (B) ImageStream analysis of wild-type MC38 cells (top), MC38 cells expressing only EGFP (middle) and MC38mOVA (EGFP$^+$, bottom) stained for surface OVA by OVA-specific antibodies. Image panels (left to right) show brightfield (BF, magnification 40×), EGFP expression (green), surface OVA expression (Alexa Fluor 647, red), and overlay image (EGFP/surface OVA). (C) CD8$^+$ T cell-mediated killing of MC38mOVA and control target cells (MC38 and peptide-pulsed MC38 (1 μM, 45 min at 37 °C)) after incubation with OT-I T cells at the indicated ratios (specific target lysis was calculated as described in the Supporting Information). (D) Prophylactic immunization schedule and challenge with MC38mOVA tumor cells. (E) Results of the individual tumors after prophylactic immunization with the corresponding nanogel samples or PBS (n = 10).

https://doi.org/10.1021/acsnano.1c10709
ACS Nano XXXX, XXX, XXX−XXX

Figure 6. continued

(F) End point tumor volume showing reduced tumor growth for NP(IMDQ+OVA)- and NP(IMDQ)+sOVA-immunized mice compared to PBS group; however, no significant difference between NP(IMDQ+OVA) and NP(IMDQ)+sOVA could be found. (G) Therapeutic schedule for the treatment of mice challenged with MC38mOVA tumor cells (n = 10). (H) Results of the individual tumors after therapeutic treatment with the corresponding nanogel samples or PBS. (I) End point tumor volume showing reduced tumor growth for NP(IMDQ+OVA) and NP(IMDQ)+sOVA-treated mice compared to PBS group. A more significant difference between NP(IMDQ+OVA) and NP(IMDQ)+sOVA could be found compared to the prophylactic treatment.

higher numbers of antigen-specific T cells compared to s.c. vaccination but creates subtypes of $CD8^+$ T cells with superior antitumor capacity.[65] In our study, i.v. administration of NP(IMDQ+OVA) significantly outperformed s.c. injection in the generation of OVA-specific IgG2a antibodies (Figure S59A). Furthermore, investigating the INF-γ secretion of OVA-specific T cells *via* ELISpot, we found an improved performance of the i.v. immunization for both $CD4^+$ and $CD8^+$ T cells (Figure S59B).

In addition, mice body weight was monitored over time during these immunization studies. Note that NP(IMDQ+OVA) conjugate was well tolerated for i.v. and s.c. injection routes. However, the administration of sIMDQ as adjuvant led to a rapid drop in body weight and confirmed the necessity of covalent IMDQ-attachment once more (Figure S60) and its impact on generation of OVA-specific T cells (Figure S61).

Summarizing, our IMDQ nanogels could be demonstrated as safe for i.v. immunization and elicit robust humoral and cellular immune responses. Furthermore, our results are indicating that covalent attachment of OVA benefits the formation of OVA-specific cytotoxic $CD8^+$ T cells both *in vitro* and *in vivo*.

Prophylactic Immunization with Two-Component Nanovaccine Reduces Tumor Growth and Leads to Enhanced Tumor Protection during Therapeutic Vaccination. The presence and the activation of antigen-specific cytotoxic T cells in the tumor microenvironment is often correlated with improved tumor regression and therapy output.[66] Referring to superior generation of OVA-specific $CD8^+$ T cells after immunization with our two-component nanogels, we next asked whether this observation might be displayed by enhanced tumor regression *in vivo*, too. For that purpose, we first aimed to implement an OVA-dependent tumor model system that is accessible to both humoral and cellular immune responses (the classical B16-OVA model, for instance, has some limitations: its cytosolic OVA expression does not provide access for antibody-mediated immune responses[67] and its downregulated MHC-I expression allows only reduced CD8 epitope presentation[68]). We therefore first selected the MC38 colon cancer cell line and established an OVA antigen model for our studies (Figure 6).

Cancer immunotherapy seeks to enable immunization against tumor-specific antigens either as overexpressing antigens or as neoantigens. In contrast to patient-specific neoepitopes usually found intracellularly, we hypothesize that cancer-specific cell surface expressed neoantigens display better suited targets since they are accessible for both cellular as well as humoral immune responses. Hence, the MC38 tumor model was genetically engineered to stably express membrane-bound OVA and, thereby, allows the elimination by OVA-specific cellular as well as humoral immune responses (Figure 6A). OVA surface expression could be verified by ImageStream analysis, clearly showing OVA-dependent fluorescence at the cell surface after incubation with OVA-specific antibodies (non-transfected or EGFP transfected control cells could not be stained by OVA-specific antibodies on their surface) (Figure 6B). These data suggest that these tumor cells can be detected by humoral immune responses. Furthermore, OVA-expressing MC38 cells were also recognized and eliminated by OVA-specific $CD8^+$ T cells obtained from OT-1 mice. When co-incubated for 4 h with OT-1 T cells, OVA-surface-expressing MC38 cells (MC38mOVA) were killed in a T cell dose-dependent way, in analogy to wild-type MC38 cells externally loaded with MHC-I binding CD8 T cell epitope OVA 257-264 peptide. Non-treated MC38 cells lacking OVA expression were not lysed at all (Figure 6C). Consequently, these experiments confirm that also cellular immune responses are capable of recognizing and responding to our tumor model in an antigen-specific fashion. Summarizing, our OVA-expressing MC38 tumor cell model was considered to be suitable for analyzing tumor-specific humoral and cellular immune responses triggered by our two-component nanovaccine.

Subsequently, the OVA membrane-expressing MC38 cell line was applied to wild-type mice. We first assessed prophylactic tumor protection *in vivo* by immunization two times (on day 0 and day 14) with either NP(IMDQ+OVA) conjugate or the mixture NP(IMDQ)+sOVA (Figure 6D). On day 23 mice were then subcutaneously inoculated with membranous-expressing OVA MC38 cells and tumor growth was analyzed each 2−3 days. While tumors rapidly grew in the non-immunized control group (PBS) from day 12 after inoculation, prophylactic immunization against OVA with both nanogel samples resulted in significantly reduced tumor growth (Figure 6E). However, no significant differences in tumor protection based on the nature of OVA delivery, covalently attached or administered, could be observed by comparing final tumor volumes (Figure 6F). In accordance with our previous *in vivo* findings that both NP(IMDQ+OVA) conjugate or the mixture NP(IMDQ)+sOVA were able to induce similar humoral immune responses (Figure 5E), we hypothesize that these mechanisms might primarily be responsible here to inhibit growth of the surface antigen-expressing tumor cells under prophylactic conditions.

Alternatively, we further assessed the influence of NP(IMDQ+OVA) on tumor regression under therapeutic conditions. For that purpose, mice were first inoculated s.c. with OVA MC38 cells on day 0, and on day 3 palpable tumors could be detected at a volume below 5 mm^3. Next, i.v. immunization with NP(IMDQ+OVA) or NP(IMDQ)+sOVA was performed on days 3, 5, and 7 (Figure 6G). Again, analysis of tumor growth showed that both formulations could trigger significant tumor regression (Figure 6H). Interestingly, treatment with NP(IMDQ+OVA) seemed to have a slightly improved effect on controlling final tumor volumes than the mixture of NP(IMDQ)+sOVA (Figure 6I). This is in line with our previous finding that covalent attachment of OVA guarantees more efficient co-delivery of OVA and IMDQ

https://doi.org/10.1021/acsnano.1c10709
ACS Nano XXXX, XXX, XXX−XXX

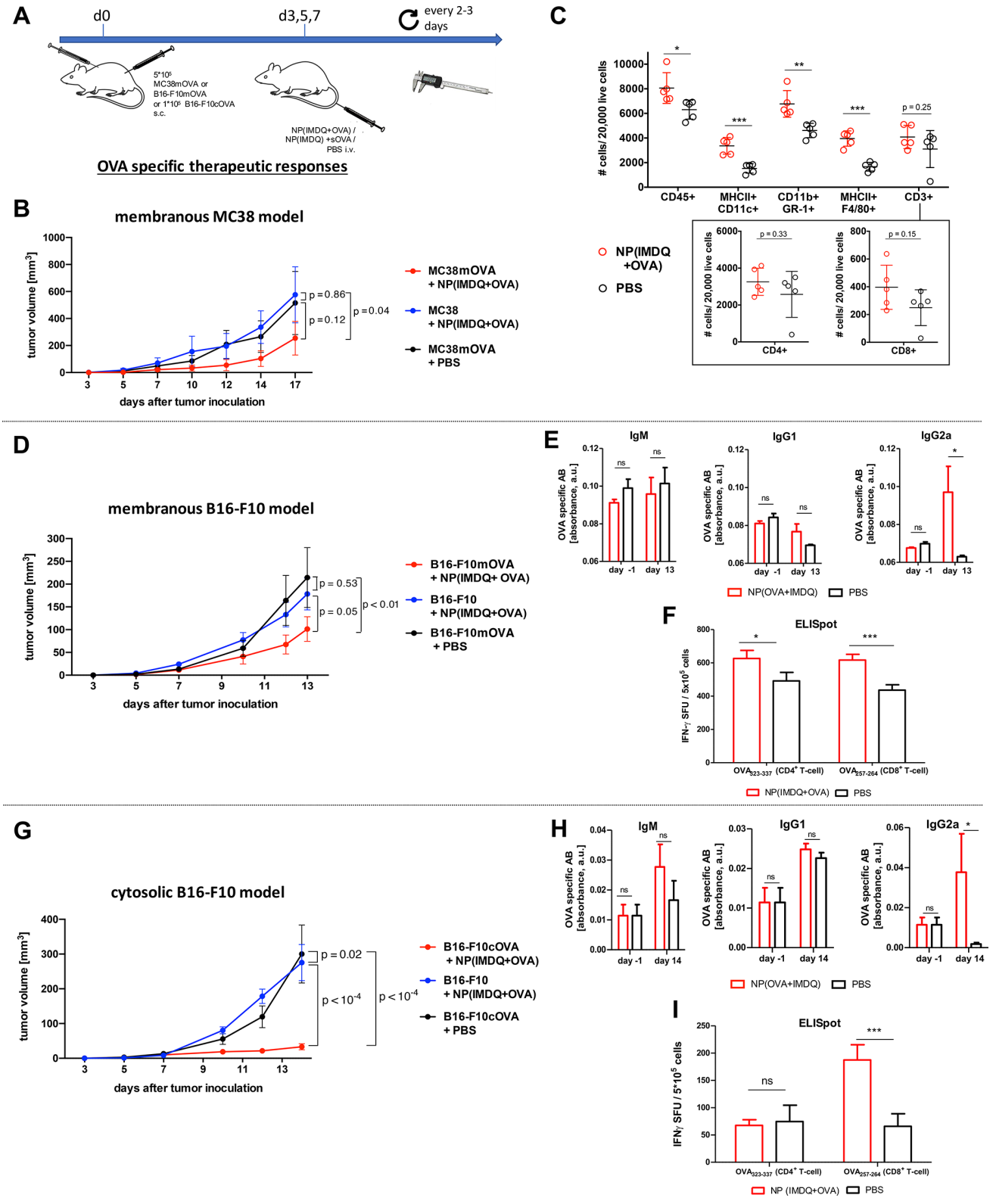

Figure 7. IMDQ- and OVA-loaded nanogels provide antigen-specific tumor immunity by induction of Th-1-biased immune responses with respect to increasing levels of antigen-specific IgG2a titers, increasing numbers of antigen-specific $CD8^+$ and $CD4^+$ T cells and increasing numbers of tumor-infiltrating immune cells. (A) Therapeutic schedule for the treatment of mice challenged with both MC38mOVA and wild-type MC38, B16-F10mOVA and wild-type B16-F10, or B16-F10cOVA and wild-type B16-F10 tumor cells. (B) Results of the MC38mOVA or MC38 tumor sizes after treatment either with NP(IMDQ+OVA) or PBS (n = 10). (C) Flow cytometric analysis of single-cell tumor suspensions derived from MC38mOVA tumors treated with NP(IMDQ+OVA) or PBS. (D) Results of B16-F10mOVA or B16-F10 tumor sizes after treatment with NP(IMDQ+OVA) or PBS (n = 9−11). (E) ELISA analysis of blood serum samples taken on day −1 (so before tumor inoculation and treatment with the nanogel) and day 13 after tumor inoculation from B16-F10mOVA-bearing mice treated

https://doi.org/10.1021/acsnano.1c10709
ACS Nano XXXX, XXX, XXX−XXX

Figure 7. continued

with NP(IMDQ+OVA) or PBS. (F) ELISpot analysis of the isolated spleen cells taken on day 13 after tumor inoculation from B16-F10mOVA-bearing mice treated with NP(IMDQ+OVA) or PBS. (G) Results of B16-F10cOVA or B16-F10 tumor sizes after treatment with NP(IMDQ+OVA) or PBS (n = 10). (H) ELISA analysis of blood serum samples taken on day −1 and day 14 after tumor inoculation from B16-F10cOVA-bearing mice treated with NP(IMDQ+OVA) or PBS. (I) ELISpot analysis of the isolated spleen cells taken on day 14 after tumor inoculation from B16-F10cOVA-bearing mice treated with NP(IMDQ+OVA) or PBS.

followed by rapid immune cell stimulation, cross-presentation, and induction of OVA-dependent $CD8^+$ cells (Figure 5F).

OVA- and IMDQ-Loaded Two-Component Nanovaccine Governs Antigen-Specific Tumor Growth by Increasing the Number of Infiltrating Immune Cells into the Tumor Microenvironment. In a subsequent experiment, we wanted to confirm these observations and investigated whether the observed antitumor effects fully rely on OVA-specific immune responses. For that purpose, mice were inoculated on one flank with MC38mOVA cells and on the other flank with wild-type MC38 cells not expressing OVA. On days 3, 5, and 7, mice were then treated with NP(IMDQ+OVA) or PBS as control (Figure 7A). Whereas nanovaccine treatment induced again an immune response that recognized the OVA-expressing MC38 tumors selectively and caused reduced tumor growth, the MC38 tumors did not respond to the immunization and grew comparable to the MC38mOVA tumors of PBS-treated mice (Figure 7B).

Moreover, we looked at the immune status by determining the number of infiltrating immune cells in the MC38mOVA tumor micromilieu after treatment with NP(IMDQ+OVA) (Figure 7C and Figures S63 and S64). We generally observed a significant increase in the number of immune cells ($CD45^+$) compared to PBS-treated tumors, most notably in number of infiltrating myeloid cell populations, as reflected by an increase in numbers of MHC-II^+ $CD11c^+$ dendritic cells, $CD11b^+$ Gr-1^+ neutrophils, and MHC-II+$F4/80^+$ macrophages, all considered as antitumoral. Beyond that, also a slight increase in $CD3^+$ T cells was observed. When analyzing this population more carefully, we confirmed that the number of infiltrating $CD8^+$ T cells, but not of $CD4^+$ T cells, increased within the tumors after treatment with NP(IMDQ+OVA), reflecting the proposed enhanced cellular antitumoral immune response induced by NP(IMDQ+OVA).

Based on these results, we further applied the same experimental conditions using the commonly used B16-F10 tumor model but also engineered the cell line with a membrane expressing OVA in analogy to the MC38 model. Although the B16-F10 cell line is known to have down-regulated MHC-I expression and, thus, only reduced CD8 epitope presentation,[68] we observed again similar results for this B16-F10mOVA model as for the MC38mOVA model. Therapeutic treatment with our two-component vaccine led to an antigen-specific reduction of the transplanted B16-F10mOVA tumor, while the wild-type B16-F10 tumors were not affected in the same way as the untreated B16-F10mOVA tumors (Figure 7D). These results confirm that our IMDQ- and OVA-loaded nanogel fully guarantees selective antigen-specific antitumor responses in mice after i.v. administration, independent from the tumor source.

To shine further light on the immunologic mechanism behind these findings, we performed ELISA analysis of blood serum samples taken from of B16-F10mOVA-bearing mice before tumor inoculation (day −1) and after nanogel treatment (day 13 after tumor inoculation). Again, they revealed a significant increase especially of IgG2a antibodies after treatment with NP(IMDQ+OVA) (Figure 7E), indicating a Th1-biased immune response in analogy to the previous immunization experiments (Figure 5D). This was further proven by cytokine analysis of those blood samples revealing a significant induction of the pro-inflammatory cytokines TNF-α and INF-γ (Figure S62), as already demonstrated after nanogel treatment *in vitro* (Figure 4E,F) and *in vivo* (Figure S51). This finally resulted in an increase of the number of OVA-specific $CD4^+$ and $CD8^+$ T cells in the spleen determined by ELISpot analysis (Figure 7F), which are again in accordance with our immunization studies (Figure 5F).

Indicating that the antigen-specific generation of antibodies plays a crucial role in the rejection of tumors that present OVA on the cell surface, we decided to investigate the impact of humoral and cellular immune responses in a mice model lacking antibody production. Hence, antibody-deficient mice, referred to as IgMi mice,[69] were challenged with MC38mOVA tumors but in contrast to wild-type mice no tumor reduction was observable. Further analysis of spleen cells revealed that IgMi mice, besides lacking antibodies, also show reduced generation of antigen-specific $CD8^+$ T cells compared to wild-type mice (Figure S65). Hence, we propose that failed tumor rejection in IgMi mice cannot exclusively be attributed to antibody deficiency and might also depend on reduced generation of T cells. This makes it difficult to draw clear conclusions regarding the impact of antibodies and T cells on tumor control.

Therefore, we modified our tumor model by generating B16-F10 cells expressing OVA exclusively in the cytosol (B16-F10cOVA). Interestingly, we were also able to observe antigen-specific and robust reduction of tumors in this model, while control wild-type B16-F10 tumors were not affected (Figure 7G). Subsequent analysis of antibody secretion and OVA-specific T cell generation revealed again increased secretion of OVA-specific IgG2a antibodies and more importantly a rise in OVA-specific $CD8^+$ T cells (Figure 7H,I), giving evidence that the induction of cellular immune responses is primarily essential for the antitumor effect induced by our nanovaccine. These properties might therefore also become relevant when addressing currently investigated clinical settings of cancer-specific neoepitopes.

Altogether these results confirm that the i.v.-administered, co-delivering two-component nanovaccine NP(IMDQ+OVA) induces robust antigen-specific humoral and cellular immune responses *in vitro* and *in vivo* that install enhanced antitumor efficacy, after both prophylactic and therapeutic immunization.

CONCLUSION

Therapeutic vaccination against tumor-associated antigens is of great interest regarding the variety of tumor types and individual immune condition for each patient. Vaccines need to elicit antigen-specific stable humoral and cellular immune responses to ensure immunogenicity and avoid tolerance. Here, we reported on a RAFT-based nanogel system that

https://doi.org/10.1021/acsnano.1c10709
ACS Nano XXXX, XXX, XXX−XXX

chemically allows covalent attachment of antigens and core functionalization with small molecules in a straightforward way, resulting in a two-component nanovaccine that is safe for i.v. immunization and allows physical co-delivery of antigen and adjuvant. We showed that covalent attachment of OVA to our IMDQ-loaded nanogels elicits robust humoral and cellular immune responses and, in addition, benefits the generation of antigen-specific $CD8^+$ T cells both *in vitro* and *in vivo*. These observations are in accordance with studies by other groups that emphasize the importance of incorporation of immune adjuvant and antigen into the same carrier system.[34−36] The development of well-defined OVA-dependent MC38 and B16-F10 tumors facilitated tumor studies with membrane-bound OVA, mimicking the expression of tumor-associated neo-antigens in clinical relevant tumors that are responsive toward both humoral and cellular immune responses as well as studying the exclusive impact of cellular immunity on cytosolically expressed OVA.

Our nanogels elicited OVA-dependent antitumor responses in both prophylactic and therapeutic approaches. The demand for personalized cancer vaccines promotes the need for customizable vaccine platforms. Regarding the chemical design of our nanogel platform, easy modifications toward co-delivery of other immune-interfering drugs and antigens or peptides are possible, since both components only need to exhibit either amino functionalities due to the reactive ester approach for core conjugation or DBCO modification for ligation to the particle surface. As well, multi-targeting by combination with immune checkpoint inhibitors or different antigens on one nanogel is conceivable. Based on the selected RAFT polymerization conditions and core-cross-linking of polymeric micelles, the size and morphology of our nanovaccines are pre-defined before functionalization; hence, the nanoparticulate formulation is fully independent of the immunologically relevant payload. Their pharmacokinetic profile will exclusively rely on the performance of the immunogenically silent carrier. In addition, the results of this study conclude that the pH-degradable nanogel system further facilitates a safe i.v. administration of highly immune stimulating imidazoquino-line-type TLR7/8 adjuvants in combination with co-delivered cancer-associated antigens and, thus, provides—in contrast to currently investigated antigen-free adjuvant treatments of tumors—opportunities to install cancer-specific immunity.

Overall, our nanogel approach can be considered as a highly versatile immunocarrier platform that is able to trigger antitumor capacities and might be interesting for the development of highly customized nanovaccines, not only for clinically more relevant tumors but also against other pandemic viral diseases.

MATERIALS AND METHODS

Detailed information on instrumentations, materials, cells and mice, as well as experimental procedures can be found in the Supporting Information.

ASSOCIATED CONTENT

Supporting Information

The Supporting Information is available free of charge at https://pubs.acs.org/doi/10.1021/acsnano.1c10709.

Instrumentation, materials, cells and mice, experimental procedures, and data, including Figures S1−S65 (PDF)

AUTHOR INFORMATION

Corresponding Authors

Stephan Grabbe − *Department of Dermatology, University Medical Center of Johannes Gutenberg-University Mainz, 55131 Mainz, Germany*; Email: stephan.grabbe@unimedizin-mainz.de

Hansjörg Schild − *Institute of Immunology, University Medical Center of Johannes Gutenberg-University Mainz, 55131 Mainz, Germany*; Email: schild@uni-mainz.de

Lutz Nuhn − *Max Planck Institute for Polymer Research, 55128 Mainz, Germany*; orcid.org/0000-0003-0761-1106; Email: lutz.nuhn@mpip-mainz.mpg.de

Authors

Judith Stickdorn − *Max Planck Institute for Polymer Research, 55128 Mainz, Germany*

Lara Stein − *Institute of Immunology, University Medical Center of Johannes Gutenberg-University Mainz, 55131 Mainz, Germany*

Danielle Arnold-Schild − *Institute of Immunology, University Medical Center of Johannes Gutenberg-University Mainz, 55131 Mainz, Germany*

Jennifer Hahlbrock − *Institute of Immunology, University Medical Center of Johannes Gutenberg-University Mainz, 55131 Mainz, Germany*

Carolina Medina-Montano − *Department of Dermatology, University Medical Center of Johannes Gutenberg-University Mainz, 55131 Mainz, Germany*

Joschka Bartneck − *IIIrd Department of Medicine - Hematology, Oncology, Pneumology, University Medical Center of the Johannes Gutenberg-University Mainz, 55131 Mainz, Germany*

Tanja Ziß − *Institute of Immunology, University Medical Center of Johannes Gutenberg-University Mainz, 55131 Mainz, Germany*

Evelyn Montermann − *Department of Dermatology, University Medical Center of Johannes Gutenberg-University Mainz, 55131 Mainz, Germany*

Cinja Kappel − *Department of Dermatology, University Medical Center of Johannes Gutenberg-University Mainz, 55131 Mainz, Germany*; orcid.org/0000-0002-9122-0601

Dominika Hobernik − *Department of Dermatology, University Medical Center of Johannes Gutenberg-University Mainz, 55131 Mainz, Germany*

Maximilian Haist − *Department of Dermatology, University Medical Center of Johannes Gutenberg-University Mainz, 55131 Mainz, Germany*

Hajime Yurugi − *Cell Biology Unit, University Medical Center of Johannes Gutenberg-University Mainz, 55131 Mainz, Germany*

Marco Raabe − *Max Planck Institute for Polymer Research, 55128 Mainz, Germany*; orcid.org/0000-0002-3677-6615

Andreas Best − *Max Planck Institute for Polymer Research, 55128 Mainz, Germany*

Krishnaraj Rajalingam − *Cell Biology Unit, University Medical Center of Johannes Gutenberg-University Mainz, 55131 Mainz, Germany*

Markus P. Radsak − *IIIrd Department of Medicine - Hematology, Oncology, Pneumology, University Medical Center of the Johannes Gutenberg-University Mainz, 55131 Mainz, Germany*

https://doi.org/10.1021/acsnano.1c10709
ACS Nano XXXX, XXX, XXX−XXX

Sunil A. David − *ViroVax, LLC, Lawrence 66047-1620 Kansas, United States;* orcid.org/0000-0003-1655-4641
Kaloian Koynov − *Max Planck Institute for Polymer Research, 55128 Mainz, Germany;* orcid.org/0000-0002-4062-8834
Matthias Bros − *Department of Dermatology, University Medical Center of Johannes Gutenberg-University Mainz, 55131 Mainz, Germany*

Complete contact information is available at: https://pubs.acs.org/10.1021/acsnano.1c10709

Author Contributions

‡J.S. and L.S. contributed equally.

Funding

Open access funded by Max Planck Society.

Notes

The authors declare no competing financial interest.

ACKNOWLEDGMENTS

The authors gratefully acknowledge support through the DFG SFB 1066 Project B04. Moreover, L.N. would like to thank the DFG Emmy-Noether program, the Liebig Program of the Fonds der Chemischen Industrie (FCI), and the Max Buchner Research Foundation for their generous support. The authors thank Claudia Braun from the Histology Core Facility of the Research Center for Immunotherapy of the Johannes Gutenberg University Mainz for the preparation of tissue sections and H&E staining.

REFERENCES

(1) Sahin, U.; Türeci, Ö. Personalized Vaccines for Cancer Immunotherapy. *Science* **2018**, *359* (6382), 1355−1360.
(2) Parish, C. R. Cancer Immunotherapy: The Past, the Present and the Future. *Immunol. Cell Biol.* **2003**, *81* (2), 106−113.
(3) Guy, B. The Perfect Mix: Recent Progress in Adjuvant Research. *Nat. Rev. Microbiol.* **2007**, *5* (7), 396−397.
(4) Sharonov, G. V.; Serebrovskaya, E. O.; Yuzhakova, D. V.; Britanova, O. V.; Chudakov, D. M. B Cells, Plasma Cells and Antibody Repertoires in the Tumour Microenvironment. *Nat. Rev. Immunol.* **2020**, *20* (5), 294−307.
(5) Sánchez-Paulete, A. R.; Teijeira, A.; Cueto, F. J.; Garasa, S.; Pérez-Gracia, J. L.; Sánchez-Arráez, A.; Sancho, D.; Melero, I. Antigen Cross-Presentation and T cell Cross-Priming in Cancer Immunology and Immunotherapy. *Ann. Oncol.* **2017**, *28* (5), xii44−xii55.
(6) Sato, E.; Olson, S. H.; Ahn, J.; Bundy, B.; Nishikawa, H.; Qian, F.; Jungbluth, A. A.; Frosina, D.; Gnjatic, S.; Ambrosone, C.; et al. Intraepithelial CD8+ Tumor-Infiltrating Lymphocytes and a High CD8+/Regulatory T Cell Ratio Are Associated with Favorable Prognosis in Ovarian Cancer. *Proc. Natl. Acad. Sci. U. S. A.* **2005**, *102* (51), 18538−18543.
(7) Mahmoud, S. M. A.; Paish, E. C.; Powe, D. G.; Macmillan, R. D.; Grainge, M. J.; Lee, A. H. S.; Ellis, I. O.; Green, A. R. Tumor-Infiltrating CD8+ Lymphocytes Predict Clinical Outcome in Breast Cancer. *J. Clin. Oncol.* **2011**, *29* (15), 1949−1955.
(8) Naito, Y.; Saito, K.; Shiiba, K.; Ohuchi, A.; Saigenji, K.; Nagura, H.; Ohtani, H. CD8+ T Cells Infiltrated within Cancer Cell Nests as a Prognostic Factor in Human Colorectal Cancer. *Cancer Res.* **1998**, *58* (16), 3491−3494.
(9) Nakano, O.; Naito, Y.; Nagura, H.; Ohtani, H.; Nakano, O.; Sato, M.; Suzuki, K.; Orikasa, S.; Aizawa, M.; Suzuki, Y.; et al. Proliferative Activity of Intratumoral CD8+ T-Lymphocytes as a Prognostic Factor in Human Renal Cell Carcinoma: Clinicopathologic Demonstration of Antitumor Immunity. *Cancer Res.* **2001**, *61* (13), 5132−5136.
(10) Verbeke, R.; Lentacker, I.; De Smedt, S. C.; Dewitte, H. Three Decades of Messenger RNA Vaccine Development. *Nano Today* **2019**, *28*, 100766.
(11) Sahin, U.; Derhovanessian, E.; Miller, M.; Kloke, B. P.; Simon, P.; Löwer, M.; Bukur, V.; Tadmor, A. D.; Luxemburger, U.; Schrörs, B.; et al. Personalized RNA Mutanome Vaccines Mobilize Poly-Specific Therapeutic Immunity against Cancer. *Nature* **2017**, *547* (7662), 222−226.
(12) Grabbe, S.; Haas, H.; Diken, M.; Kranz, L. M.; Langguth, P.; Sahin, U. Translating Nanoparticulate-Personalized Cancer Vaccines into Clinical Applications: Case Study with RNA-Lipoplexes for the Treatment of Melanoma. *Nanomedicine* **2016**, *11* (20), 2723−2734.
(13) Pardi, N.; Hogan, M. J.; Porter, F. W.; Weissman, D. MRNA Vaccines — a New Era in Vaccinology. *Nat. Rev. Drug Discovery* **2018**, *17* (4), 261−279.
(14) Karikó, K.; Muramatsu, H.; Welsh, F. A.; Ludwig, J.; Kato, H.; Akira, S.; Weissman, D. Incorporation of Pseudouridine Into mRNA Yields Superior Nonimmunogenic Vector With Increased Translational Capacity and Biological Stability. *Mol. Ther.* **2008**, *16* (11), 1833−1840.
(15) Purcell, A. W.; McCluskey, J.; Rossjohn, J. More than One Reason to Rethink the Use of Peptides in Vaccine Design. *Nat. Rev. Drug Discovery* **2007**, *6* (5), 404−414.
(16) Hollingsworth, R. E.; Jansen, K. Turning the Corner on Therapeutic Cancer Vaccines. *npj Vaccines* **2019**, *4* (1), 7.
(17) Toes, R. E. M.; Offringa, R.; Blom, R. J. J.; Melief, C. J. M.; Kast, W. M. Peptide Vaccination Can Lead to Enhanced Tumor Growth through Specific T cell Tolerance Induction. *Proc. Natl. Acad. Sci. U. S. A.* **1996**, *93* (15), 7855−7860.
(18) Hailemichael, Y.; Dai, Z.; Jaffarzad, N.; Ye, Y.; Medina, M. A.; Huang, X.-F.; Dorta-Estremera, S. M.; Greeley, N. R.; Nitti, G.; Peng, W.; et al. Persistent Antigen at Vaccination Sites Induces Tumor-Specific CD8+ T Cell Sequestration, Dysfunction and Deletion. *Nat. Med.* **2013**, *19* (4), 465−472.
(19) Li, W.; Joshi, M. D.; Singhania, S.; Ramsey, K. H.; Murthy, A. K. Peptide Vaccine: Progress and Challenges. *Vaccines (Basel)* **2014**, *2* (3), 515−536.
(20) Gnjatic, S.; Sawhney, N.; Bhardwaj, N. TLR Agonists: Are They Good Adjuvants? *Cancer J.* **2010**, *16* (4), 382−391.
(21) Foged, C. Subunit Vaccines of the Future: The Need for Safe, Customized and Optimized Particulate Delivery Systems. *Ther. Delivery* **2011**, *2* (8), 1057−1077.
(22) Beesu, M.; Salyer, A. C. D.; Brush, M. J. H.; Trautman, K. L.; Hill, J. K.; David, S. A. Identification of High-Potency Human TLR8 and Dual TLR7/TLR8 Agonists in Pyrimidine-2,4-Diamines. *J. Med. Chem.* **2017**, *60* (5), 2084−2098.
(23) Dowling, D. J. Recent Advances in the Discovery and Delivery of TLR7/8 Agonists as Vaccine Adjuvants. *ImmunoHorizons* **2018**, *2* (6), 185−197.
(24) Zitvogel, L.; Galluzzi, L.; Kepp, O.; Smyth, M. J.; Kroemer, G. Type I Interferons in Anticancer Immunity. *Nat. Rev. Immunol.* **2015**, *15* (7), 405−414.
(25) Harrison, L. I.; Astry, C.; Kumar, S.; Yunis, C. Pharmacokinetics of 852A, an Imidazoquinoline Toll-like Receptor 7-Specific Agonist, Following Intravenous, Subcutaneous, and Oral Administrations in Humans. *J. Clin. Pharmacol.* **2007**, *47* (8), 962−969.
(26) Weigel, B. J.; Cooley, S.; DeFor, T.; Weisdorf, D. J.; Panoskaltsis-Mortari, A.; Chen, W.; Blazar, B. R.; Miller, J. S. Prolonged Subcutaneous Administration of 852A, a Novel Systemic Toll-like Receptor 7 Agonist, to Activate Innate Immune Responses in Patients with Advanced Hematologic Malignancies. *Am. J. Hematol.* **2012**, *87* (10), 953−956.
(27) Engel, A. L.; Holt, G. E.; Lu, H. The Pharmacokinetics of Toll-like Receptor Agonists and the Impact on the Immune System. *Expert Rev. Clin. Pharmacol.* **2011**, *4* (2), 275−289.
(28) Lynn, G. M.; Laga, R.; Darrah, P. A.; Ishizuka, A. S.; Balaci, A. J.; Dulcey, A. E.; Pechar, M.; Pola, R.; Gerner, M. Y.; Yamamoto, A.; et al. In Vivo Characterization of the Physicochemical Properties of

Polymer-Linked TLR Agonists That Enhance Vaccine Immunogenicity. *Nat. Biotechnol.* **2015**, *33* (11), 1201−1210.
(29) Lybaert, L.; Vermaelen, K.; De Geest, B. G.; Nuhn, L. Immunoengineering through Cancer Vaccines − A Personalized and Multi-Step Vaccine Approach towards Precise Cancer Immunity. *J. Controlled Release* **2018**, *289* (May), 125−145.
(30) Nuhn, L.; Vanparijs, N.; De Beuckelaer, A.; Lybaert, L.; Verstraete, G.; Deswarte, K.; Lienenklaus, S.; Shukla, N. M.; Salyer, A. C. D.; Lambrecht, B. N.; et al. PH-Degradable Imidazoquinoline-Ligated Nanogels for Lymph Node-Focused Immune Activation. *Proc. Natl. Acad. Sci. U. S. A.* **2016**, *113* (29), 8098−8103.
(31) Lepeltier, E.; Nuhn, L.; Lehr, C.-M.; Zentel, R. Not Just for Tumor Targeting: Unmet Medical Needs and Opportunities for Nanomedice. *Nanomedicine (Lond).* **2015**, *10* (20), 3147−3166.
(32) Wilson, J. T.; Keller, S.; Manganiello, M. J.; Cheng, C.; Lee, C.; Opara, C.; Convertine, A.; Stayton, P. S. pH-Responsive Nanoparticle Vaccines for Dual-Delivery of Antigens and Immunostimulatory Oligonucleotides. *ACS Nano* **2013**, *7* (5), 3912−3925.
(33) Schlosser, E.; Mueller, M.; Fischer, S.; Basta, S.; Busch, D. H.; Gander, B.; Groettrup, M. TLR Ligands and Antigen Need to Be Coencapsulated into the Same Biodegradable Microsphere for the Generation of Potent Cytotoxic T Lymphocyte Responses. *Vaccine* **2008**, *26*, 1626−1637.
(34) Lynn, G. M.; Sedlik, C.; Baharom, F.; Zhu, Y.; Ramirez-Valdez, R. A.; Coble, V. L.; Tobin, K.; Nichols, S. R.; Itzkowitz, Y.; Zaidi, N.; et al. Peptide−TLR-7/8a Conjugate Vaccines Chemically Programmed for Nanoparticle Self-Assembly Enhance CD8 T cell Immunity to Tumor Antigens. *Nat. Biotechnol.* **2020**, *38* (3), 320−332.
(35) Knight, F. C.; Gilchuk, P.; Kumar, A.; Becker, K. W.; Sevimli, S.; Jacobson, M. E.; Suryadevara, N.; Wang-Bishop, L.; Boyd, K. L.; Crowe, J. E.; et al. Mucosal Immunization with a PH-Responsive Nanoparticle Vaccine Induces Protective CD8+ Lung-Resident Memory T Cells. *ACS Nano* **2019**, *13* (10), 10939−10960.
(36) Wilson, D. S.; Hirosue, S.; Raczy, M. M.; Bonilla-Ramirez, L.; Jeanbart, L.; Wang, R.; Kwissa, M.; Franetich, J. F.; Broggi, M. A. S.; Diaceri, G.; et al. Antigens Reversibly Conjugated to a Polymeric Glyco-Adjuvant Induce Protective Humoral and Cellular Immunity. *Nat. Mater.* **2019**, *18* (2), 175−185.
(37) Traini, G.; Ruiz-de-Angulo, A.; Blanco-Canosa, J. B.; Zamacola Bascarán, K.; Molinaro, A.; Silipo, A.; Escors, D.; Mareque-Rivas, J. C. Cancer Immunotherapy of TLR4 Agonist−Antigen Constructs Enhanced with Pathogen-Mimicking Magnetite Nanoparticles and Checkpoint Blockade of PD-L1. *Small* **2019**, *15* (4), 1803993.
(38) Moon, J. J.; Suh, H.; Bershteyn, A.; Stephan, M. T.; Liu, H.; Huang, B.; Sohail, M.; Luo, S.; Ho Um, S.; Khant, H.; et al. Interbilayer-Crosslinked Multilamellar Vesicles as Synthetic Vaccines for Potent Humoral and Cellular Immune Responses. *Nat. Mater.* **2011**, *10* (3), 243−251.
(39) Sharifi, S.; Behzadi, S.; Laurent, S.; Laird Forrest, M.; Stroeve, P.; Mahmoudi, M. Toxicity of Nanomaterials. *Chem. Soc. Rev.* **2012**, *41* (6), 2323−2343.
(40) Conniot, J.; Scomparin, A.; Peres, C.; Yeini, E.; Pozzi, S.; Matos, A. I.; Kleiner, R.; Moura, L. I. F.; Zupančič, E.; Viana, A. S.; et al. Immunization with Mannosylated Nanovaccines and Inhibition of the Immune-Suppressing Microenvironment Sensitizes Melanoma to Immune Checkpoint Modulators. *Nat. Nanotechnol.* **2019**, *14* (9), 891−901.
(41) Moad, G.; Rizzardo, E.; Thang, S. H. RAFT Polymerization and Some of Its Applications. *Chem. - An Asian J.* **2013**, *8* (8), 1634−1644.
(42) York, A.; Kirkland, S.; McCormick, C. Advances in the Synthesis of Amphiphilic Block Copolymers via RAFT Polymerization: Stimuli-Responsive Drug and Gene Delivery. *Adv. Drug Delivery Rev.* **2008**, *60* (9), 1018−1036.
(43) York, A. W.; Huang, F.; McCormick, C. L. Rational Design of Targeted Cancer Therapeutics through the Multiconjugation of Folate and Cleavable SiRNA to RAFT-Synthesized (HPMA-s-APMA) Copolymers. *Biomacromolecules* **2010**, *11* (2), 505−514.
(44) Vanparijs, N.; Nuhn, L.; Paluck, S. J.; Kokkinopoulou, M.; Lieberwirth, I.; Maynard, H. D.; De Geest, B. G. Core/Shell Protein-Reactive Nanogels via a Combination of RAFT Polymerization and Vinyl Sulfone Postmodification. *Nanomedicine* **2016**, *11* (20), 2631−2645.
(45) Nuhn, L.; Van Hoecke, L.; Deswarte, K.; Schepens, B.; Li, Y.; Lambrecht, B. N.; De Koker, S.; David, S. A.; Saelens, X.; De Geest, B. G. Potent Anti-Viral Vaccine Adjuvant Based on PH-Degradable Nanogels with Covalently Linked Small Molecule Imidazoquinoline TLR7/8 Agonist. *Biomaterials* **2018**, *178*, 643−651.
(46) Das, A.; Theato, P. Activated Ester Containing Polymers: Opportunities and Challenges for the Design of Functional Macromolecules. *Chem. Rev.* **2016**, *116* (3), 1434−1495.
(47) Nuhn, L.; Bolli, E.; Massa, S.; Vandenberghe, I.; Movahedi, K.; Devreese, B.; Van Ginderachter, J. A.; De Geest, B. G. Targeting Protumoral Tumor-Associated Macrophages with Nanobody-Functionalized Nanogels through Strain Promoted Azide Alkyne Cycloaddition Ligation. *Bioconjugate Chem.* **2018**, *29* (7), 2394−2405.
(48) Stickdorn, J.; Nuhn, L. Reactive-Ester Derived Polymer Nanogels for Cancer Immunotherapy. *Eur. Polym. J.* **2020**, *124*, 109481.
(49) Nuhn, L.; De Koker, S.; Van Lint, S.; Zhong, Z.; Catani, J. P.; Combes, F.; Deswarte, K.; Li, Y.; Lambrecht, B. N.; Lienenklaus, S.; et al. Nanoparticle-Conjugate TLR7/8 Agonist Localized Immunotherapy Provokes Safe Antitumoral Responses. *Adv. Mater.* **2018**, *30* (45), 1803397.
(50) Nuhn, L.; Kaps, L.; Diken, M.; Schuppan, D.; Zentel, R. Reductive Decationizable Block Copolymers for Stimuli-Responsive MRNA Delivery. *Macromol. Rapid Commun.* **2016**, *37* (11), 924−933.
(51) Nuhn, L.; Hirsch, M.; Krieg, B.; Koynov, K.; Fischer, K.; Schmidt, M.; Helm, M.; Zentel, R. Cationic Nanohydrogel Particles as Potential siRNA Carriers for Cellular Delivery. *ACS Nano* **2012**, *6* (3), 2198−2214.
(52) Agard, N. J.; Prescher, J. A.; Bertozzi, C. R. A Strain-Promoted [3 + 2] Azide-Alkyne Cycloaddition for Covalent Modification of Biomolecules in Living Systems. *J. Am. Chem. Soc.* **2004**, *126* (46), 15046−15047.
(53) Nuhn, L.; Van Herck, S.; Best, A.; Deswarte, K.; Kokkinopoulou, M.; Lieberwirth, I.; Koynov, K.; Lambrecht, B. N.; De Geest, B. G. FRET Monitoring of Intracellular Ketal Hydrolysis in Synthetic Nanoparticles. *Angew. Chemie Int. Ed.* **2018**, *57* (33), 10760−10764.
(54) Deres, K.; Schild, H.; Wiesmüller, K.-H.; Jung, G.; Rammensee, H.-G. In Vivo Priming of Virus-Specific Cytotoxic T Lymphocytes with Synthetic Lipopeptide Vaccine. *Nature* **1989**, *342* (6249), 561−564.
(55) Koynov, K.; Butt, H. Current Opinion in Colloid & Interface Science Fluorescence Correlation Spectroscopy in Colloid and Interface Science. *Curr. Opin. Colloid Interface Sci.* **2012**, *17* (6), 377−387.
(56) Bermudez, L. E.; Parker, A.; Goodman, J. R. Growth within Macrophages Increases the Efficiency of Mycobacterium Avium in Invading Other Macrophages by a Complement Receptor-Independent Pathway. *Infect. Immun.* **1997**, *65* (5), 1916−1925.
(57) Peiser, L.; Gough, P. J.; Kodama, T.; Gordon, S. Macrophage Class A Scavenger Receptor-Mediated Phagocytosis of Escherichia Coli: Role of Cell Heterogeneity, Microbial Strain, and Culture Conditions in Vitro. *Infect. Immun.* **2000**, *68* (4), 1953−1963.
(58) Wang, X. Y.; Facciponte, J.; Chen, X.; Subjeck, J. R.; Repasky, E. A. Scavenger Receptor-A Negatively Regulates Antitumor Immunity. *Cancer Res.* **2007**, *67* (10), 4996−5002.
(59) Diken, M.; Kreiter, S.; Selmi, A.; Britten, C. M.; Huber, C.; Türeci, Ö.; Sahin, U. Selective Uptake of Naked Vaccine RNA by Dendritic Cells Is Driven by Macropinocytosis and Abrogated upon DC Maturation. *Gene Ther.* **2011**, *18* (7), 702−708.
(60) Shen, H.; Ackerman, A. L.; Cody, V.; Giodini, A.; Hinson, E. R.; Cresswell, P.; Edelson, R. L.; Saltzman, W. M.; Hanlon, D. J. Enhanced and Prolonged Cross-Presentation Following Endosomal

https://doi.org/10.1021/acsnano.1c10709
ACS Nano XXXX, XXX, XXX−XXX

Escape of Exogenous Antigens Encapsulated in Biodegradable Nanoparticles. *Immunology* **2006**, *117* (1), 78−88.
(61) Hirosue, S.; Kourtis, I. C.; van der Vlies, A. J.; Hubbell, J. A.; Swartz, M. A. Antigen Delivery to Dendritic Cells by Poly(Propylene Sulfide) Nanoparticles with Disulfide Conjugated Peptides: Cross-Presentation and T Cell Activation. *Vaccine* **2010**, *28* (50), 7897−7906.
(62) De Koker, S.; De Geest, B. G.; Singh, S. K.; De Rycke, R.; Naessens, T.; Van Kooyk, Y.; Demeester, J.; De Smedt, S. C.; Grooten, J. Polyelectrolyte Microcapsules as Antigen Delivery Vehicles to Dendritic Cells: Uptake, Processing, and Cross-Presentation of Encapsulated Antigens. *Angew. Chemie - Int. Ed.* **2009**, *48* (45), 8485−8489.
(63) Cauwels, A.; Van Lint, S.; Paul, F.; Garcin, G.; De Koker, S.; Van Parys, A.; Wueest, T.; Gerlo, S.; Van der Heyden, J.; Bordat, Y.; et al. Delivering Type I Interferon to Dendritic Cells Empowers Tumor Eradication and Immune Combination Treatments. *Cancer Res.* **2018**, *78* (2), 463−474.
(64) Greinacher, A.; Thiele, T.; Warkentin, T. E.; Weisser, K.; Kyrle, P. A.; Eichinger, S. Thrombotic Thrombocytopenia after ChAdOx1 NCov-19 Vaccination. *N. Engl. J. Med.* **2021**, *384* (22), 2092−2101.
(65) Baharom, F.; Ramirez-Valdez, R. A.; Tobin, K. K. S.; Yamane, H.; Dutertre, C. A.; Khalilnezhad, A.; Reynoso, G. V.; Coble, V. L.; Lynn, G. M.; Mulè, M. P.; et al. Intravenous Nanoparticle Vaccination Generates Stem-like TCF1+ Neoantigen-Specific CD8+ T Cells. *Nat. Immunol.* **2021**, *22* (1), 41−52.
(66) Fridman, W. H.; Pages, F.; Sautès-Fridman, C.; Galon, J. The Immune Contexture in Human Tumours: Impact on Clinical Outcome. *Nat. Rev. Cancer* **2012**, *12* (4), 298−306.
(67) Brown, D. M.; Fisher, T. L.; Wei, C.; Frelinger, J. G.; Lord, E. M. Tumours Can Act as Adjuvants for Humoral Immunity. *Immunology* **2001**, *102* (4), 486−497.
(68) Seliger, B.; Wollscheid, U.; Momburg, F.; Blankenstein, T.; Huber, C. Characterization of the Major Histocompatibility Complex Class I Deficiencies in B16 Melanoma Cells. *Cancer Res.* **2001**, *61* (3), 1095−1099.
(69) Waisman, A.; Croxford, A. L.; Demircik, F. New Tools to Study the Role of B Cells in Cytomegalovirus Infections. *Med. Microbiol. Immunol.* **2008**, *197* (2), 145−149.

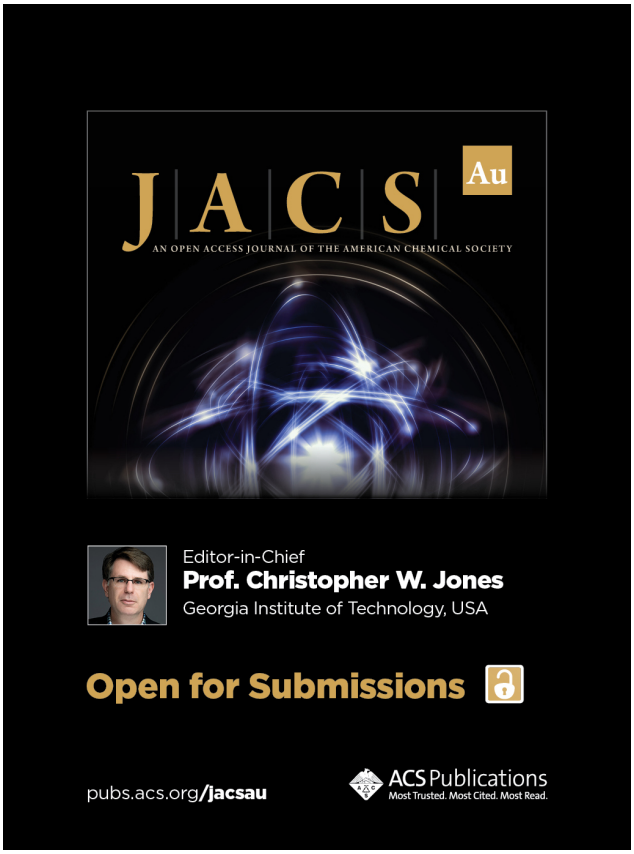

https://doi.org/10.1021/acsnano.1c10709
ACS Nano XXXX, XXX, XXX−XXX

Systemically Administered TLR7/8-Agonist and Antigen Conjugated Nanogels Govern Immune Responses against Tumors

- Supporting Information -

Judith Stickdorn,[1,‡] Lara Stein,[2,‡] Danielle Arnold-Schild,[2] Jennifer Hahlbrock,[2] Carolina Medina-Montano,[3] Joschka Bartneck,[4] Tanja Zieß,[2] Evelyn Montermann,[3] Cinja Kappel,[3] Dominika Hobernik,[3] Maximilian Haist,[3] Hajime Yurugi,[5] Marco Raabe,[1] Andreas Best,[1] Krishnaraj Rajalingam,[5] Markus P. Radsak,[4] Sunil A. David,[6] Kaloian Koynov,[1] Matthias Bros,[3] Stephan Grabbe,[3,*] Hansjörg Schild,[2,*] Lutz Nuhn[1,*]

‡: equally contributed.
[1]: Max Planck Institute for Polymer Research, Ackermannweg 10, 55128 Mainz, Germany – email: lutz.nuhn@mpip-mainz.mpg.de.
[2]: Institute of Immunology, University Medical Center of Johannes Gutenberg-University Mainz, Langenbeckstraße 1, 55131 Mainz, Germany – email: schild@uni-mainz.de.
[3]: Department of Dermatology, University Medical Center of Johannes Gutenberg-University Mainz, Langenbeckstraße 1, 55131 Mainz, Germany – email: stephan.grabbe@unimedizin-mainz.de.
[4]: III[rd] Department of Medicine - Hematology, Oncology, Pneumology, University Medical Center of the Johannes Gutenberg-University Mainz, Langenbeckstraße 1, 55131 Mainz, Germany
[5]: Cell Biology Unit, University Medical Center of Johannes Gutenberg-University Mainz, Langenbeckstraße 1, 55131 Mainz, Germany
[6]: ViroVax, LLC, 2029 Becker Drive Suite 100E, Lawrence 66047-1620, Kansas, United States.
* corresponding authors (lutz.nuhn@mpip-mainz.mpg.de, schild@uni-mainz.de, stephan.grabbe@unimedizin-mainz.de).

Instrumentation

All ^{1}H- and ^{19}F-NMR spectra were recorded on a Bruker 400 MHz FT NMR spectrometer. Chemical shifts (δ) are provided in ppm relative to TMS. Samples were prepared in $CDCl_3$ and their signals referenced to residual nondeuterated signals of the solvent. UV-Vis spectra were recorded with a Jasco V-630 spectrophotometer with a JASCO ETC-717 peltier thermostatted cell holder. Spectra were recorded at 20 °C using a water thermostat (A. Knüss Optronic V50). For analytical size exclusion chromatography (SEC) with THF as eluent, columns packed with MZ-Gel SDplus 102 Å and MZ-Gel SDplus 106 Å obtained from MZ-Analysentechnik were used. Polymers were detected at a wavelength of 254 nm with a UV-detector (JASCO UV-1575) and a RI-detector (JASCO RI-1530). Molecular weights were determined with a polystyrene calibration obtained from PSS Polymer Standard Services GmbH and toluene as internal standard. Dynamic light scattering (DLS) measurements were carried out using a ZetaSizer Nano ZS instrument (Malvern Instruments Ltd., Worcestershire, UK) equipped with a He-Ne laser. Measurements were performed at a temperature of 25 °C and a detection angle of 173°. Micro BCA Protein Assay, RAW-Blue TLR reporter assay and MTT assay were performed with a Spark 20M Multimode Microplate Reader from Tecan. SDS-PAGE was performed with a Mini-PROTEAN Tetra Cell from Bio-Rad. Gel imaging was conducted with a smart phone camera.
Fluorescence cross-correlation spectroscopy (FCCS) experiments were performed on a commercial setup (LSM 880, Carl Zeiss, Jena, Germany).
Flow cytometric analyses were done with an Attune NxT flow cytometer (Thermo Fisher).

Materials, Cells and Mice

Unless otherwise stated, solvents and chemicals were obtained from Sigma Aldrich and Acros Organics. Dioxane and THF were dried over sodium, DCM over calcium hydride, and freshly distilled prior to use. Millipore water was prepared using a MILLI-Q® Reference A+ System. DBCO-PEG_4-NHS ester was purchased from Jena Bioscience, Alexa Fluor-TFP ester from Thermo Fisher and EndoFit™ Ovalbumin from InvivoGen. AMDVN (V-70) was obtained from Wako Chemical and the TLR 7/8 agonist 1-(4-(aminomethyl) benzyl)-2-butyl-1H-imidazo[4,5-c]quinolin-4- amine (IMDQ) could be provided following an earlier report.[1] Dialysis was performed using Spectra/Por 3 membranes obtained from Spectrum Labs with a molecular weight cutoff 1000 g mol−1.

Dulbecco's PBS, cell culture medium and supplements were purchased from Thermo Fisher Scientific. The RAW-Blue reporter cell line and QUANTI-Blue were obtained from InvivoGen.

RAW-Blue macrophages purchased from InvivoGen were cultured in DMEM-GlutaMAX™ medium supplemented with 10% fetal bovine serum (FBS), 1% penicillin/streptomycin, 0.01% zeocin and 0.02% normocin at 37°C with 5% CO_2 saturation.

DC2.4 cells, kindly provided by V. Mailänder (Department of Dermatology, University Medical Center, Johannes Gutenberg-University Mainz) were maintained in IMDM (Thermo Fisher Scientific) supplemented with 5 % FBS, 2 mM L-Glutamine, 200 mg/mL penicillin and 200 U/mL streptomycin.

MC38 colon adenocarcinoma cells were kindly provided by H.-C. Probst (Institute for Immunology, University Medical Center, Johannes Gutenberg-University Mainz) and B16-F10 melanoma cells were purchased from ATCC (USA). Stable cell lines expressing membrane-bound OVA (MC38mOVA, B16-F10mOVA) were produced by electroporation using expression plasmids (pIRES2-EGFP (Clontech) for MC38 and pcDNA3.1+P2A-eGFP (Genscript Biotech) for B16-F10) containing cDNA encoding full-length OVA protein linked to the transmembrane region of $H2\text{-}D^b$, which was generously provided by T. Tedder (Department of Immunology, Duke University School of Medicine, North Carolina). To obtain stable B16-F10 cells expressing cytosolic OVA (B16-F10cOVA), B16-F10 cells were electroporated using the pcDNA3.1+P2A-eGFP vector containing cDNA encoding full-length OVA. Cells expressing EGFP were selected by three rounds of screening using a FACS Aria (BD Biosciences) at the Core Facility of the Research Center for Immunotherapy (University Medical Center, Johannes Gutenberg-University Mainz. Cells were maintained in DMEM high glucose supplemented with 10 % FBS, 2 mM L-Glutamine, 200 mg/mL penicillin, 200 U/mL streptomycin and 1 mM sodium pyruvate. To maintain EGFP and OVA expressions, transfected cell cultures contained G418 (400 µg/mL for MC38mOVA, 1000 µg/mL for B16-F10mOVA and B16-F10cOVA).

BALB/c mice were obtained from the Translational Animal Research Center (TARC) of the Johannes Gutenberg-University Mainz). C57BL/6J mice were purchased from Envigo or bred inhouse. Mice carrying heterozygous *lox*P-flanked alleles for TLR7 were obtained from the European Mouse Mutant Archive (EMMA) at the Helmholtz Center Munich and were intercrossed with a CreDeleter mouse provided by Ari Waismain (Institute for Molecular Medicine, University Medical Center Mainz) to obtain mice deficient in TLR7 (*TLR7*$^{-/-}$). IgMi mice were also kindly provided by Ari Waisman. OT-I transgenic mice were provided by R. Holtappels-Geginat (Institute of Virology, University Medical Center, Johannes Gutenberg-University Mainz). For *in vivo* experiments, mice were 8-12 weeks old and experiments were performed in a blinded fashion. All mice were housed at the animal facility of the Johannes Gutenberg-University Mainz. Animal experiments were performed following institutional guidelines and with permission of the State Rhineland Palatinate.

Bone marrow cells were isolated from femurs and tibiae of C57BL/6 mice and resuspended in IMDM-based culture medium supplemented with 5% FBS, 2 mM L-glutamine, 100 IU/mL penicillin, 100 µg/mL streptomycin and 50 µM β-mercaptoethanol (Sigma-Aldrich, Deisenhofen, Germany) and with 10 ng/mL recombinant murine GM-CSF (R&D Systems, Wiesbaden, Germany).

OT-I splenocytes were cultured in RPMI 1640 (Thermo Fisher Scientific) supplemented with 10 % FCS, 2 mM L-Glutamine, 200 mg/mL penicillin, 200 U/mL streptomycin, 50 µM β-mercaptoethanol, in the presence of IL-2 (supernatant of XL-63 cells used at a dilution of 1:250, kindly provided by H.-C. Probst (Institute for Immunology, University Medical Center, Johannes Gutenberg-University Mainz)) and $OVA_{257-264}$ peptide (1 µg/mL) for 5 to 7 days.

Experimental

Synthesis of chain transfer agent (CTA)
pentafluorophenyl 4-cyano-4((phenylcarbonothioyl)thio)pentanoate

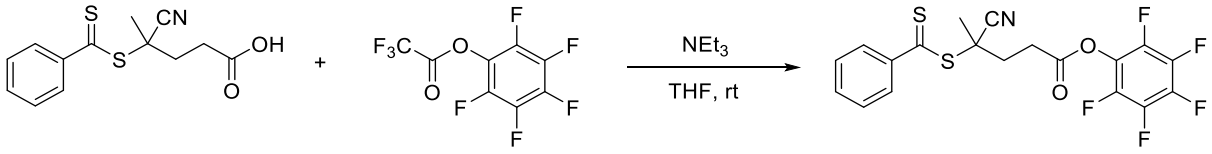

Corresponding to earlier studies[2], 4-cyano-4-((phenylcarbonothioyl)thio)pentanoic acid (2.75 g, 9.9 mmol) was dissolved under Ar-atmosphere in 90 mL anhydrous THF in a predried round bottom flask. Then, triethylamine (4.9 mL, 35.5 mmol) was added dropwise, followed by the dropwise addition of pentafluorophenyl 2,2,2-trifluoroacetate (4.4 mL, 25.6 mmol). After stirring at room temperature for 4 h the reaction mixture was supplemented with 100 mL DCM and washed two times with water. The organic layers were dried over Na_2SO_4 and concentrated in vacuum. The crude product was purified by silica column chromatography (DCM) and yielded pentafluorophenyl 4-cyano-4((phenylcarbonothioyl)thio)pentanoate as a pink solid after concentration under vacuum (3.18 g, 72%).
^{1}H-NMR ($CDCl_3$, 400 MHz): δ [ppm] = 7.93 (d, J = 8,0 Hz, 2H, ortho-Ar*H*), 7.59 (t, J = 8 Hz, 1H, p-Ar*H*), 7.42 (t, J = 8 Hz, 2H, m-Ar*H*), 3.14–3.00 (m, 2H, -COO-CH_2-, 2.81–2.73 (m, 1H, -COO-CH_2-CH_2-), 2.60–2.52 (m, 1H, -COO-CH_2-CH_2-), 1.99 (s, 3H, -CH_3).

^{19}F-NMR ($CDCl_3$, 282 MHz): δ [ppm] = -153.64 (d, 2F, o-Ar*F*), -158.38 (t, 1F, p-Ar*F*), -162.99 (t, 2F, m-Ar*F*).

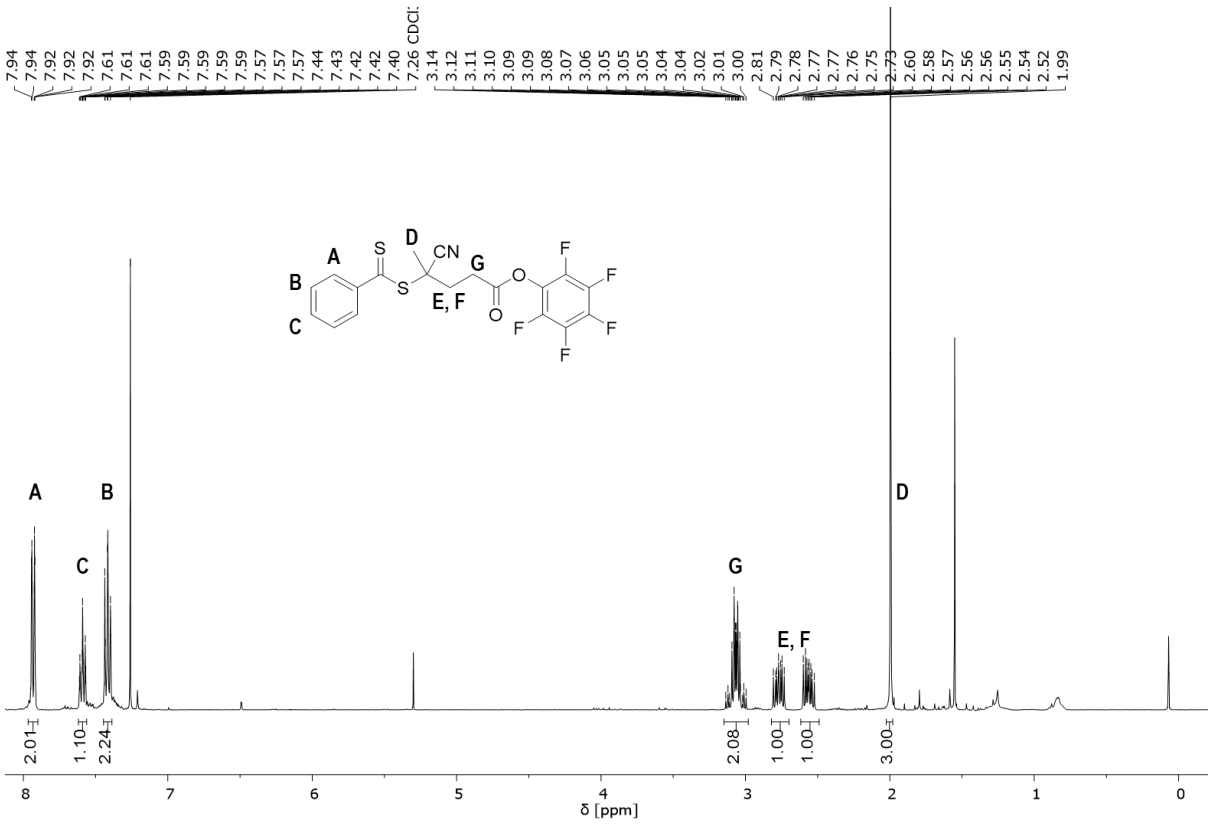

Figure S1: ^{1}H-NMR (400 MHz, $CDCl_3$) of pentafluorophenyl 4-cyano-4((phenylcarbonothioyl)thio)pentanoate.

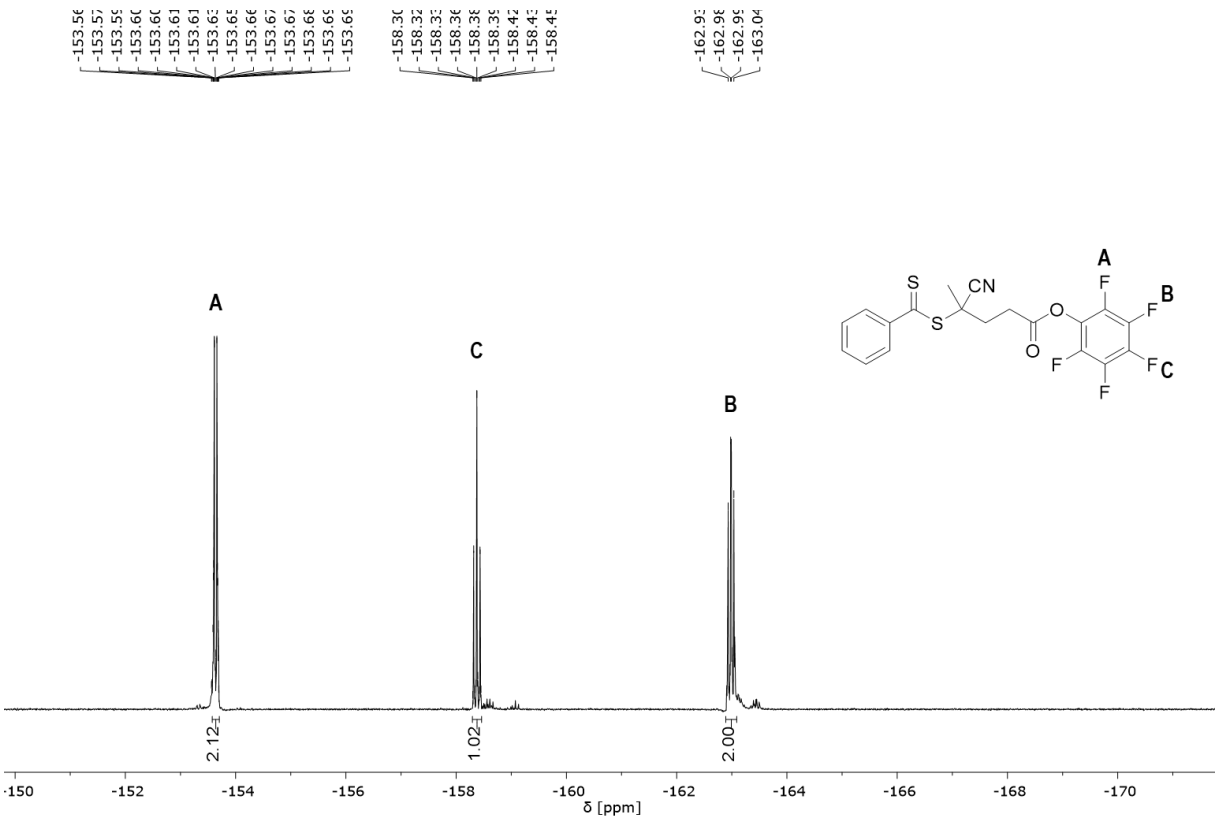

Figure S2: ^{19}F-NMR (282 MHz, $CDCl_3$) of pentafluorophenyl 4-cyano-4((phenylcarbonothioyl)thio)pentanoate.

Synthesis of azide-CTA 1-azido-16-cyano-13-oxo-3,6,9-trioxa-12-azaheptadecan-16-yl benzodithioate

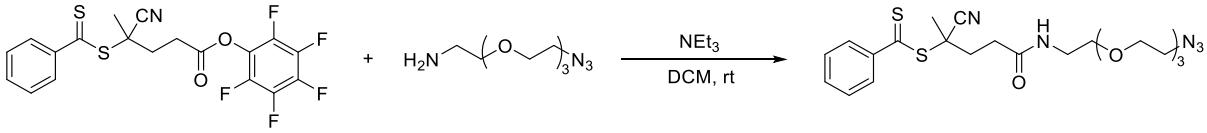

In analogy to earlier reports,[3] pentafluorophenyl 4-cyano-4((phenylcarbonothioyl)thio)pentanoate (1.2 g, 2.69 mmol) was dissolved in 15 mL anhydrous DCM under Ar-atmosphere in a predried flask. 11-Azido-3,6,9-trioxaundecan-1-amine (0.21 mL, 1.08 mmol) and triethylamine (0.45 mL, 3.23 mmol) were dissolved in 5 mL anhydrous DCM and added dropwise to the dissolved CTA. The reaction mixture was stirred in the dark for 17 h at room temperature. Reaction monitoring by TLC showed complete conversion of amine. The crude mixture was concentrated and purified by silica column chromatography (ethyl acetate : MeOH = 20:1) yielding 1-azido-16-cyano-13-oxo-3,6,9-trioxa-12-azaheptadecan-16-yl benzodithioate as a pink, viscous oil (quant.).

^{1}H-NMR ($CDCl_3$, 400 MHz): δ [ppm] = 7.90 (d, J = 8.0 Hz, 2H, o-Ar*H*), 7.56 (t, J = 8.0 Hz, 1H, p-Ar*H*), 7.39 (t, J = 8.0 Hz, 2H, m-Ar*H*), 6.32 (t, J = 4.0 Hz, 1H, -CON*H*), 3.68–3.66 (m, 8H, -O-CH_2-CH_2-O- CH_2-CH_2-O), 3.64–3.63 (m, 2H, -O-CH_2-CH$_2$-N$_3$), 3.57 (t, J = 4.0 Hz, 2H, -CONH-CH$_2$-CH_2-O-), 3.47 (q, J = 4.0 Hz, 2H, -CONH-CH_2-), 3.38 (t, J = 4.0 Hz, 2H, -CH_2-N$_3$), 2.67–2.60 (m, 1H, -CH*H*-CH$_2$-CONH-), 2.58–2.51 (m, 2H, -CH_2-CONH-), 2.45–2.38 (m, 1H, -C*H*H-CH$_2$-CONH-), 1.94 (s, 3H, -CH_3).

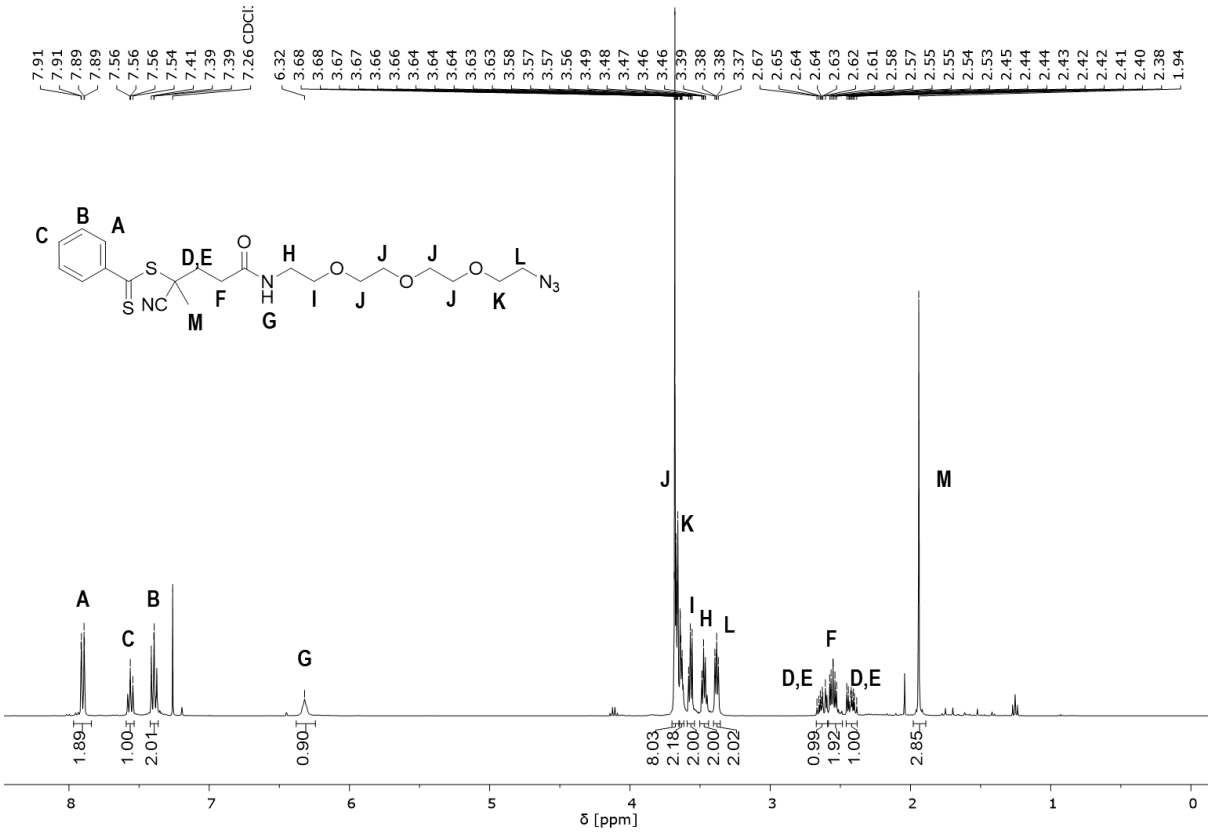

Figure S3: ^{1}H-NMR (400 MHz, $CDCl_3$) of azide-CTA 1-azido-16-cyano-13-oxo-3,6,9-trioxa-12-azaheptadecan-16-yl benzodithioate.

Synthesis of amphiphilic block copolymer P(mTEGMA)-b-P(PFPMA) by RAFT block copolymerization

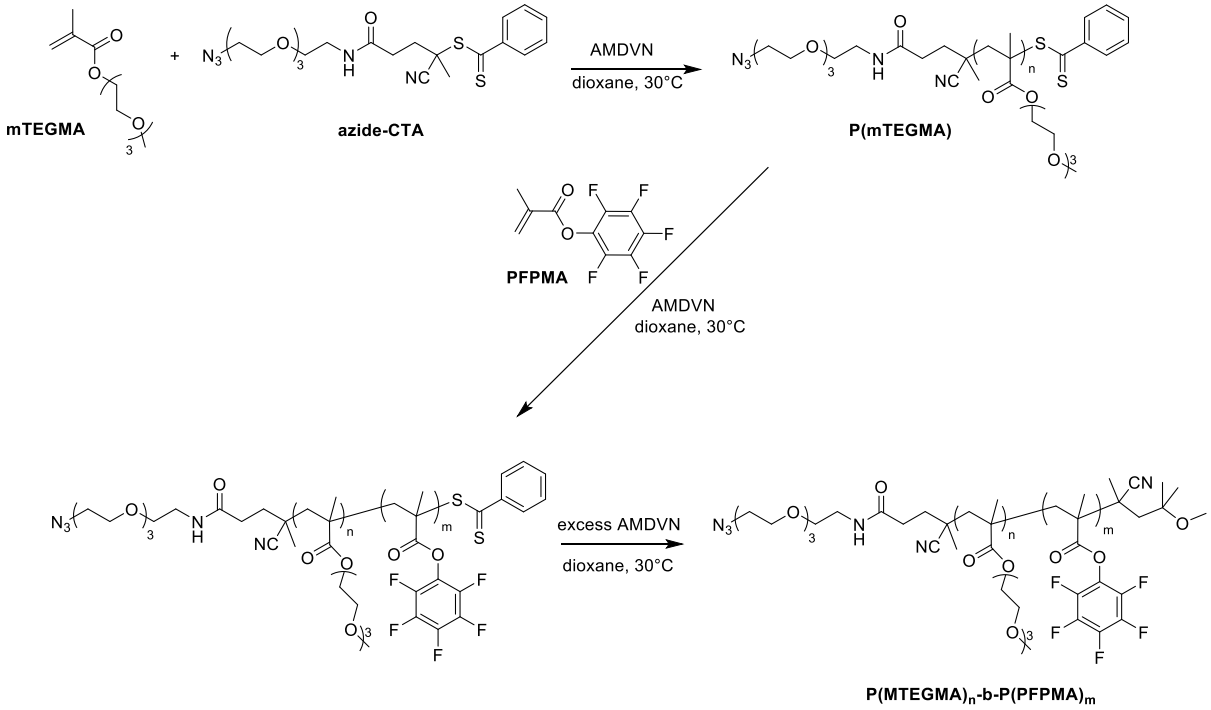

Synthesis of poly(tri(ethylene glycol)methyl ether methacrylate) P(mTEGMA)

P(mTEGMA) was synthesized via RAFT polymerization as reported previously.[4] 1-azido-16-cyano-13-oxo-3,6,9-trioxa-12-azaheptadecan-16-yl benzodithioate (azide-CTA) (92.5 mg, 0.192 mmol) and tri(ethyleneglycol)methyl ether methacrylate/mTEGMA (896 mg, 3.857 mmol) were loaded into a Schlenk tube and dissolved in 2 mL anhydrous 1,4-dioxane. Low temperature initiator 2,2′-azobis(4-methoxy-2,4-dimethylvaleronitrile) (AMDVN) (5.95 mg, 0.019 mmol) was added. After performing three freeze pump thaw cycles the reaction mixture was stirred at 30°C for 16 h. Analysis of a reaction aliquot by ^{1}H-NMR revealed a monomer conversion of 74%. The polymer was then isolated by precipitation in hexane followed by centrifugation. After re-dissolving the polymer in 2 mL dioxane the precipitation procedure was repeated two more times. Drying under vacuum overnight afforded P(mTEGMA) as a red oil (592 mg, 78%). End group analysis based on ^{1}H-NMR showed a chain length χ_n of 25 for P(mTEGMA).

^{1}H-NMR ($CDCl_3$, 400 MHz): δ [ppm] = 4.08 (br, 2H, -COO-CH_2), 3.64 (br, 8H, -COO-CH$_2$-CH_2-O-CH_2-CH_2-O-CH_2-), 3.55 (br, 2H, -CH_2-O-CH$_3$), 3.38 (br, 3H, -O-CH_3), 2.12–1.67 (br, 2H, -CH_2- polymer main chain), 1.38–0.64 (br, 3H, -CH_3 polymer main chain).

SEC (THF, PS-Std.): M_n = 5050 g/mol , M_w = 6160 g/mol , PDI = 1.22.

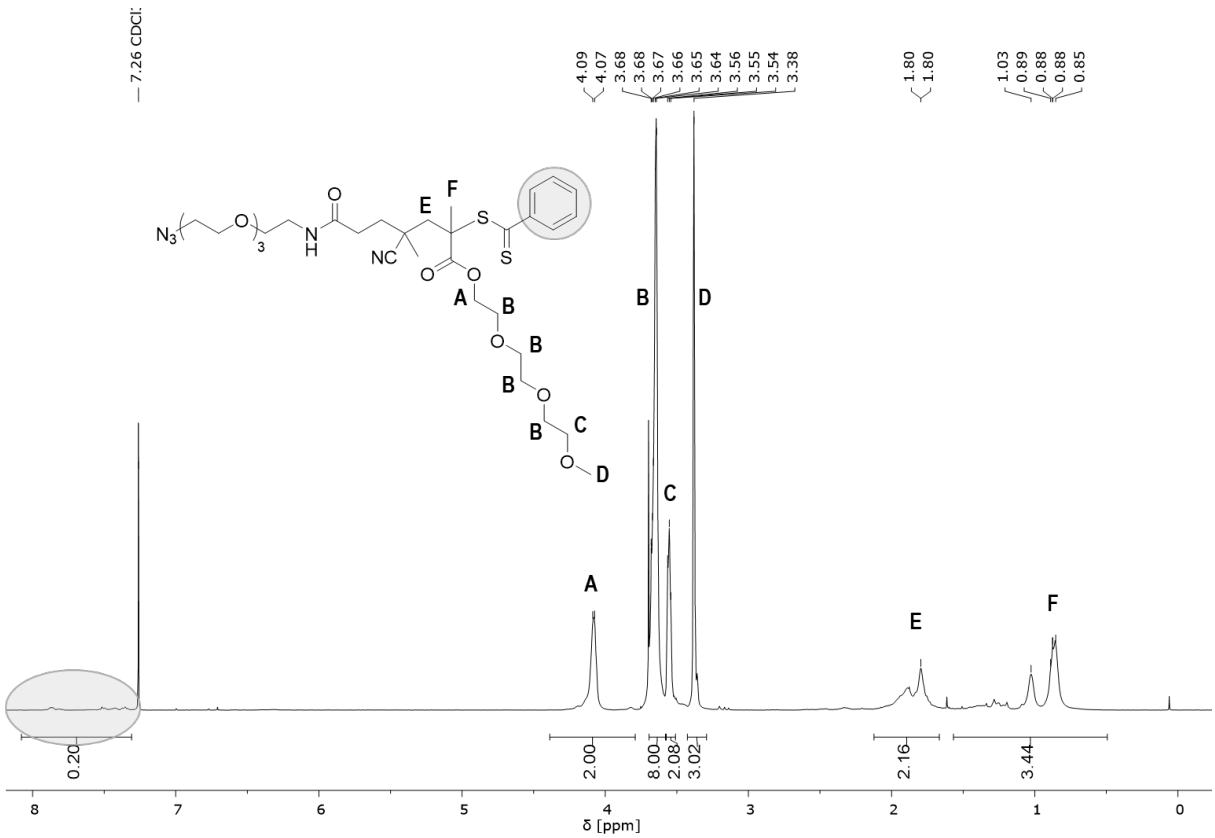

Figure S4: [1]H-NMR (400 MHz, $CDCl_3$) of P(mTEGMA).

Synthesis of poly(tri(ethylene glycol)methyl ether methacrylate)–block–poly(pentafluorophenyl methacrylate) P(mTEGMA)-b-P(PFPMA)

Corresponding to earlier reports[4], P(mTEGMA) as macro-CTA (578 mg, 0.113 mmol) and pentafluorophenyl methacrylate (PFPMA) (1280 mg, 5.1 mmol) were dissolved in 2 mL anhydrous dioxane in a Schlenk tube with a stirring bar. After addition of AMDVN (3.4 mg, 0.01 mmol) three freeze pump thaw cycles were performed. The degassed reaction mixture was then stirred for 40 h at 30°C. Analysis by ^{1}H-NMR and ^{19}F-NMR of a reaction aliquot in $CDCl_3$ revealed a PFPMA-conversion around 50%. The polymer was purified by repeated precipitation in hexane and centrifugation (3 times). Drying overnight under vacuum afforded P(mTEGMA)-*b*-P(PFPMA) as a red powder (1.3 g, quant.).

Removal of dithiobenzoate end groups of P(mTEGMA)-b-P(PFPMA)

Removal of dithiobenzoate end groups of previously synthesized P(mTEGMA)-*b*-(PFPMA) was achieved by treating the polymer with an excess of the initiator AMDVN. Therefore, P(mTEGMA)-*b*-P(PFPMA) (1.33 g, 87.9 µmol) was dissolved in 2 mL anhydrous dioxane in a Schlenk tube with a stir bar. After addition of AMDVN (813 mg, 264 µmol) the reaction mixture was stirred overnight under nitrogen atmosphere at 30°C. Successful removal of dithiobenzoate end groups was observed by a loss of red color of the reaction mixture and was confirmed by UV-Vis spectroscopy. The colorless polymer was purified by precipitation in hexane followed by centrifugation. The precipitation process was repeated two times after re-dissolving the polymer in 2 mL dioxane. Vacuum drying afforded P(mTEGMA)-*b*-P(PFPMA) as a colorless powder (946 mg). Copolymer composition was analyzed based on ^{1}H-NMR spectra of P(mTEGMA)-*b*-P(PFPMA) by normalization to the methoxy group of P(mTEGMA)

followed by a comparison of signals of polymer main chains of P(mTEGMA) and P(PFPMA) blocks. Referring to a block copolymer composition of P(mTEGMA) : P(PFPMA) = 1 : 1.36 a chain length χ_n of 34 was found for P(PFPMA).

^{1}H-NMR ($CDCl_3$, 400 MHz): δ [ppm] = 4.08 (br, 2H, -COO-CH_2), 3.65 (br, 8H, -COO-CH$_2$-CH_2-O-CH_2-CH_2-O-CH_2-), 3.56 (br, 2H, -CH_2-O-CH$_3$), 3.38 (br, 3H, -O-CH_3), 2.71–2.00 (br, 2H, -CH$_2$- PFPMA polymer main chain), 1.90–1.67 (br, 2H, -CH_2- mTEGMA polymer main chain), 1.64–1.23 (br, 3H, -CH_3 PFPMA polymer main chain), 1.16–0.62 (br, 3H, -CH_3 mTEGMA polymer main chain).

^{19}F-NMR ($CDCl_3$, 282 MHz): δ [ppm] = -150.90–153.36 (br, 2F, o-Ar*F*), -158.09 (br, 1F, p-Ar*F*), -163.27 (br, 2F, m-Ar*F*).

SEC (THF, PS-Std.): M_n = 12050 g/mol, M_w =15950 g/mol, PDI = 1.33.

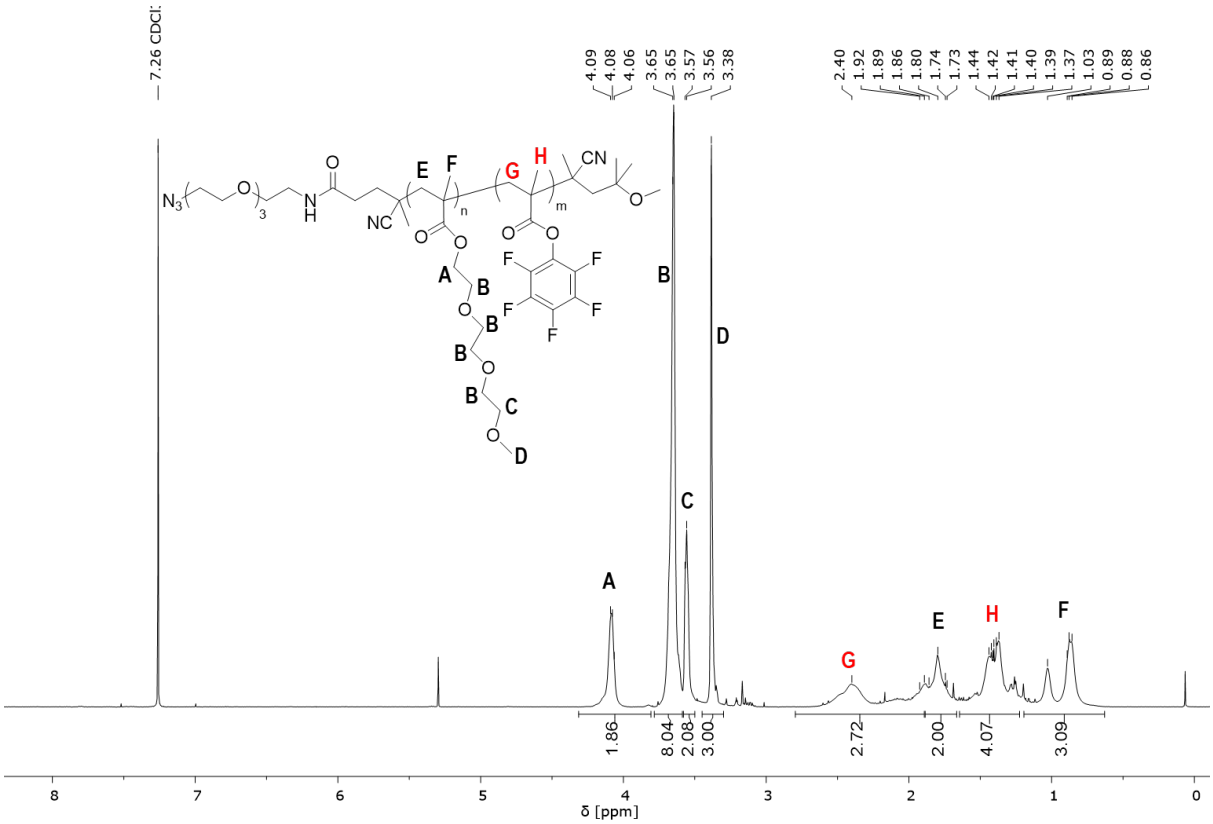

Figure S5: ^{1}H-NMR ($CDCl_3$, 400 MHz) of P(mTEGMA)-b-P(PFPMA) after RAFT end group removal.

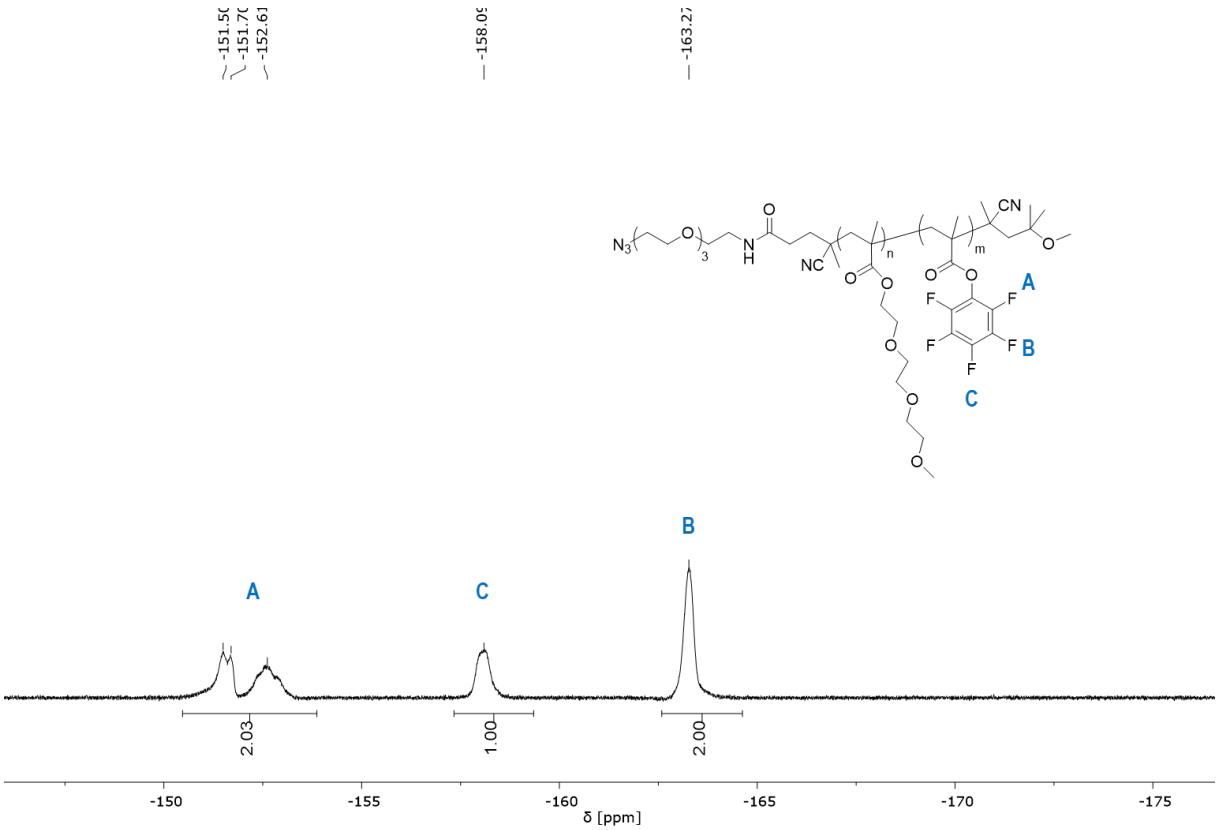

Figure S6: ^{19}F-NMR ($CDCl_3$, 282 MHz) of P(mTEGMA)-b-P(PFPMA) after RAFT end group removal.

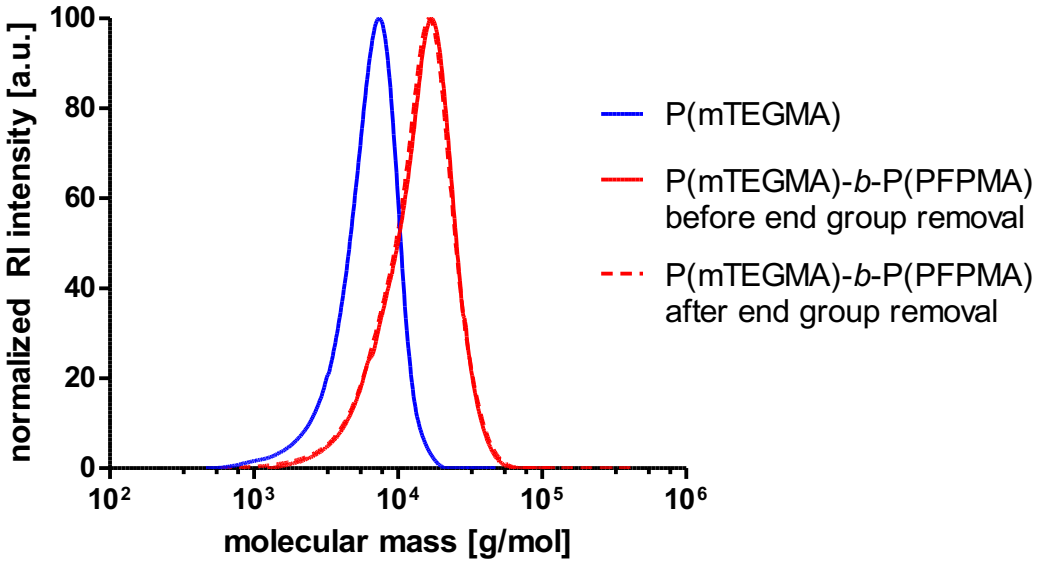

Figure S7: SEC trace (THF. PS-Std.) of P(mTEGMA) and P(mTEGMA)-b-P(PFPMA) before and after RAFT end group removal.

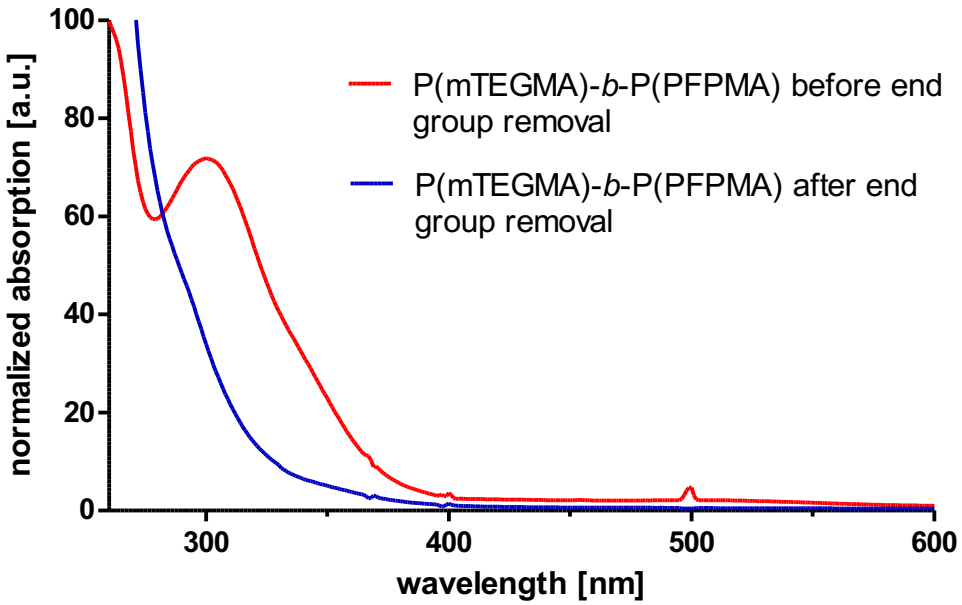

Figure S8: UV-Vis spectra of P(mTEGMA)-b-P(PFPMA) in dioxane before and after removal of RAFT end groups.

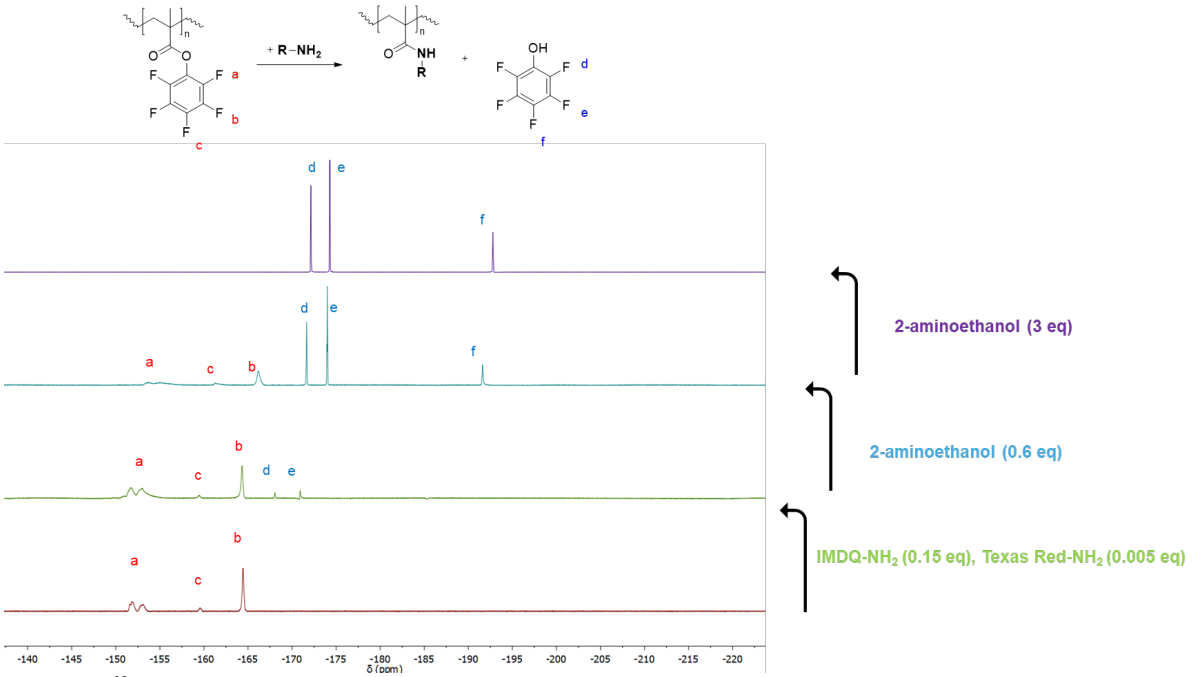

Figure S9: ^{19}F-NMR (THF-d8, 471 MHz) of subsequential aminolysis of PFP esters of P(mTEGMA)-b-P(PFPMA) by TLR7/8 agonist IMDQ and fluorescent dye followed by hydrophilization with 2-aminoethanol.

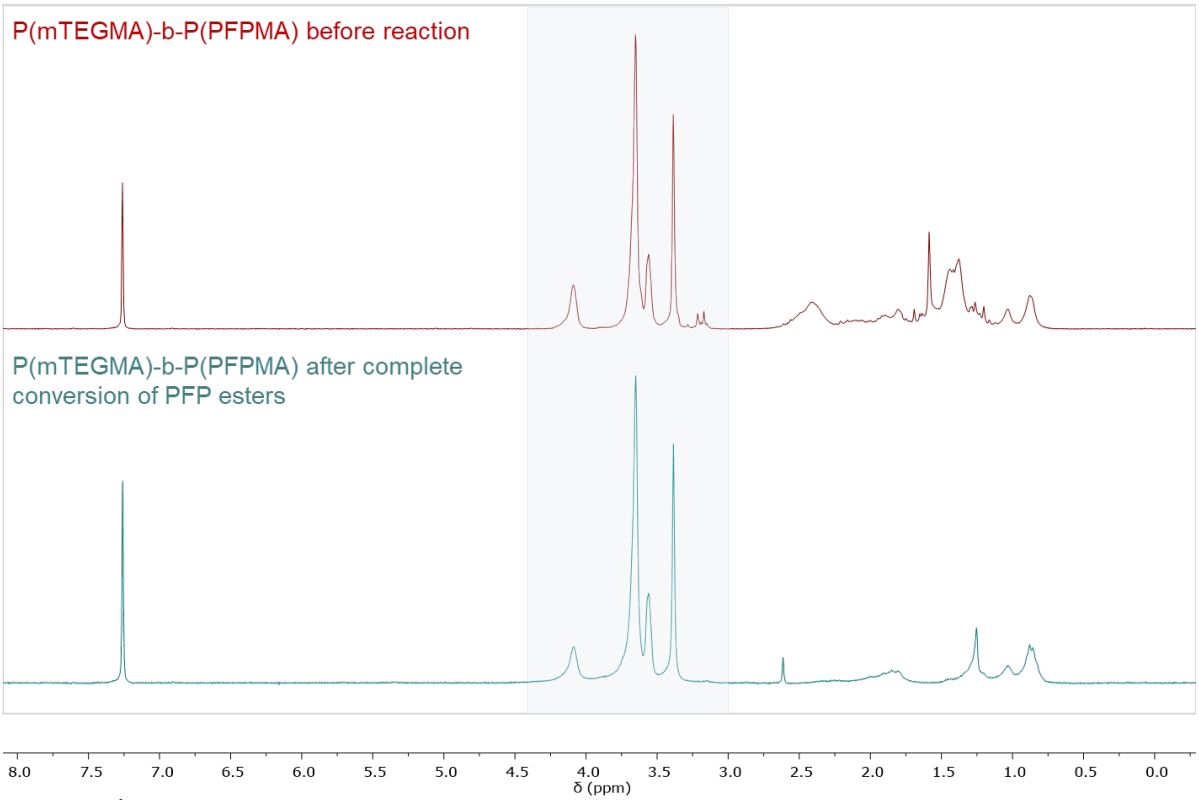

Figure S10: [1]H-NMR (CDCl3, 300 MHz) of P(mTEGMA)-b-P(PFPMA) before and after conversion of PFP esters with IMDQ and 2-ethanolamine. Ester bonds of the P(mTEGMA) segment show no reactivity towards added amines during aminolysis of PFP esters,

Nanogel synthesis

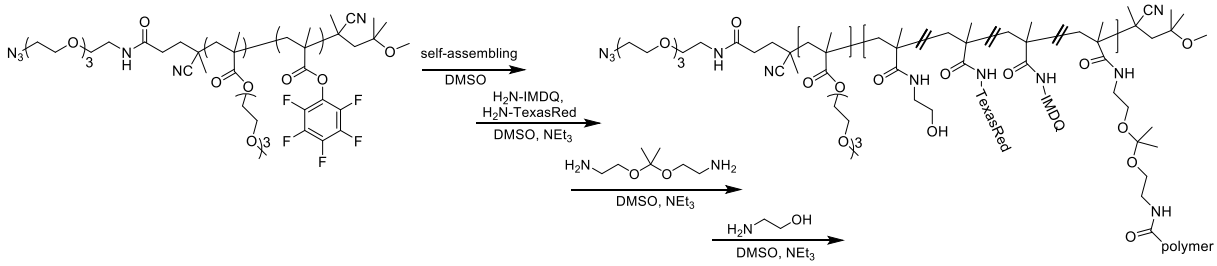

Two different types of acid-degradable, fluorescently labeled nanogels (IMDQ-loaded or without IMDQ/control) were prepared based on a modified procedure from earlier reports.[5] The reactive precursor polymer P(mTEGMA)-*b*-P(PFPMA) was dispersed at 10 mg/mL in anhydrous DMSO under nitrogen atmosphere followed by sonication for 1h. Formation of polymeric micelles was verified by DLS measurements and micellar dispersions were further used for the nanogel synthesis.

For each nanogel type a micellar dispersion of P(mTEGMA)-*b*-P(PFPMA) (10 mL, 230 µmol reactive ester) was transferred into a Schlenk tube equipped with a stir bar. For fluorescent labeling, Cy5 cadaverine or Texas Red cadaverine (2.5 mg/mL, 317 µL, 1.15 µmol) was added under nitrogen atmosphere. In case of covalent loading with the immune modulator IMDQ, IMDQ (10 mg/mL, 1490 µL, 34.5 µmol) was added. After the addition of triethylamine (48 µL, 345 µmol) the reaction mixture was stirred under nitrogen atmosphere at 40°C for 48 h. To achieve pH-degradable crosslinking, 2,2-bis(aminoethoxy)propane (10.1 µL, 68.9 µmol) and triethylamine (96 µL, 689 µmol) were added and the reaction mixture was stirred under nitrogen atmosphere at 50°C for 24 h. To obtain fully hydrophilic nanogels the reaction mixture was quenched with 2-aminoethanol (41.6 µL, 689 µmol) and triethylamine (96 µL, 689 µmol) and stirred for a half day at 50°C. Then, nanogel preparations were transferred into dialysis membranes (MWCO 3.5 kDa) and dialyzed against water supplemented with 0.1 % (v/v) ammonia for three days. Lyophilization afforded nanogels as voluminous solids (77 mg, 91%). Lyophilized nanogels were re-dispersed in water supplemented with 0.1% (v/v) ammonia or PBS at given concentrations followed by sonication for 1 h under ice cooling prior to application in described experiments. IMDQ-loading was determined based on a calibration curve and adjusted equations from literature and revealed a drug-loading of 9.4 wt%.[5]

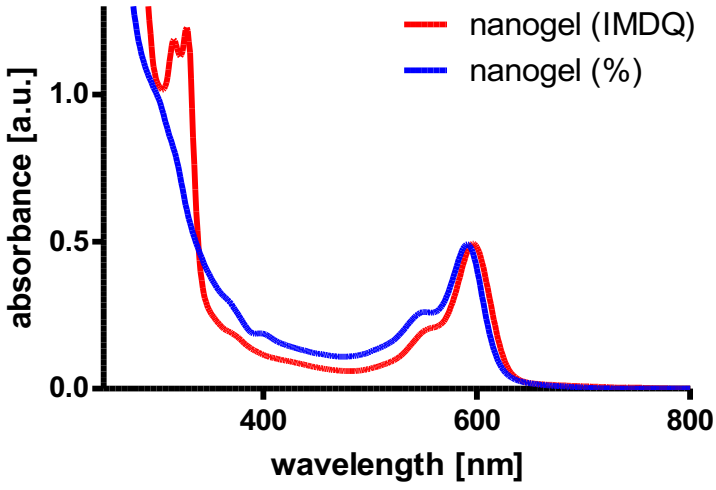

Figure S11: UV-Vis spectra of re-dispersed nanogel samples at 1 mg/mLfor determination of IMDQ-loading.

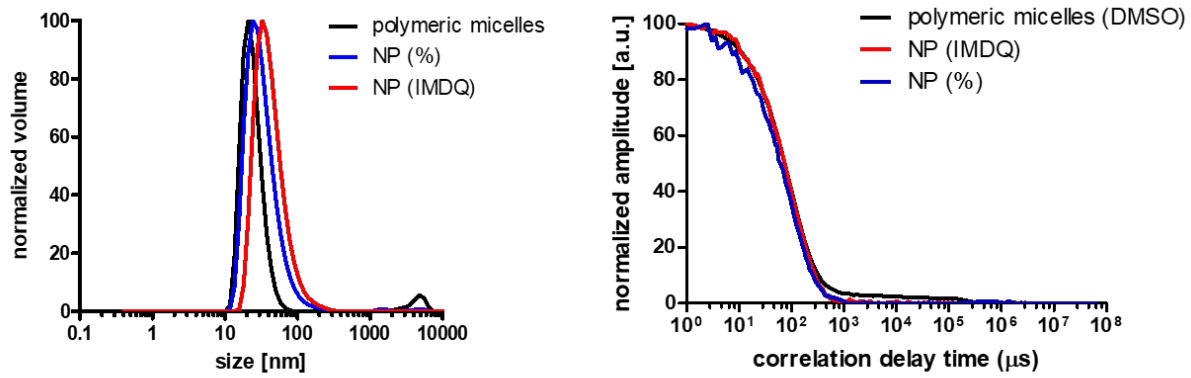

0.5 mg/mL	z-average [nm]	PDI
polymeric micelle	32.5 ± 0.2	0.25 ± 0.05
nanogel (%)	58.1 ± 1.9	0.38 ± 0.05
nanogel (IMDQ)	67.4 ± 2.0	0.23 ± 0.03

Figure S12: DLS results of polymeric micelles in DMSO (10 mg/mL) and resulting hydrophilic nanogels with or without (%) IMDQ at 0.5 mg/mL PBS.

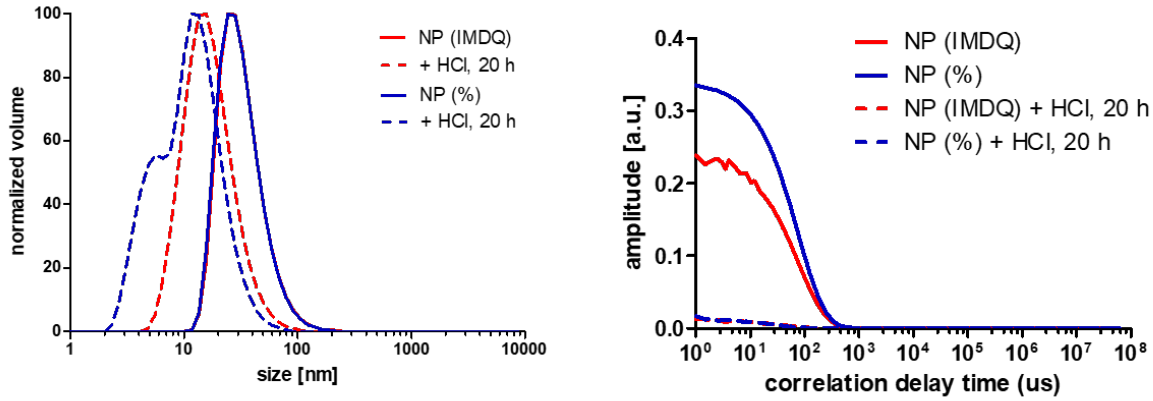

	z-average [nm]	PDI	volume mean [nm]
NP (%)	51.7 ± 1.3	0.209 ± 0.003	34.1 ± 1.0
+ HCl, 20 h	24.0 ± 1.8	0.312 ± 0.110	10.1 ± 7.1
NP (IMDQ)	53.8 ± 0.7	0.216 ± 0.008	34.6 ± 1.4
+ HCl, 20 h	33.0 ± 1.5	0.218 ± 0.056	18.5 ± 3.7

Figure S13: DLS study of nanogel degradation under acidic conditions at 1 mg/mL. 10 v% 1M HCl was added to each nanogel solution.

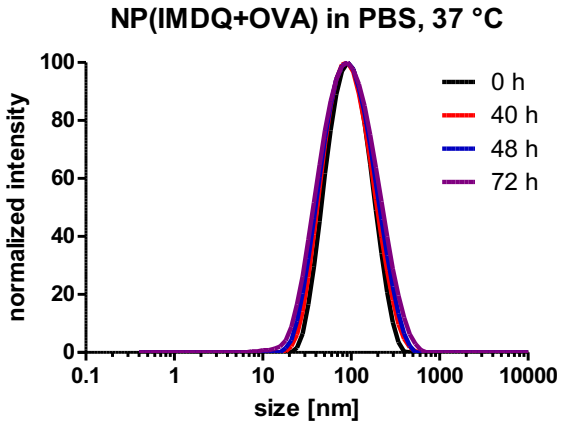

Figure S14: DLS study of nanogel stability under physiological conditions at 37°C. Nanogels are stable for at least 72 h.

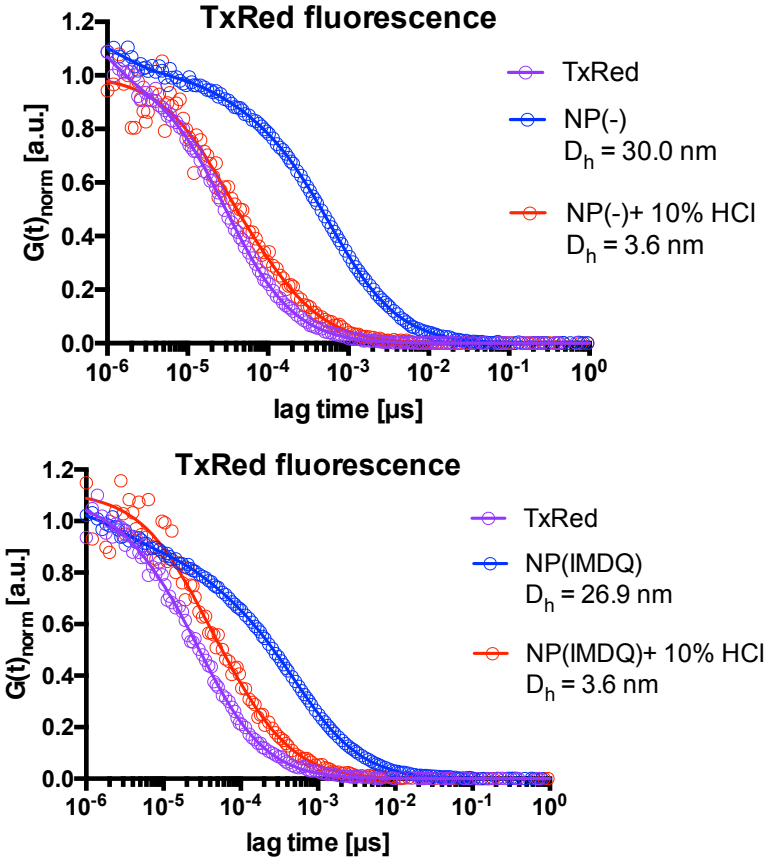

Figure S15: FCS study of empty and IMDQ-loaded nanogel degradation under acidic conditions at 2.4 µg/mL. in PBS alone or supplemented with 10 v% 1M HCl to each nanogel solution.

To ensure azide-accessibility nanogels were applied in a SPAAC reaction with a cyclooctyne-modified dye prior to antigen conjugation. To this regard, cyclooctyne tetra(ethylene oxide)-*N*-hydroxysuccinimidyl-ester (NHS ester) (10 mg/mL, 5.7 µL, 128.8 nmol), derived from earlier reports,[3] was added to Oregon Green cadaverine (2.5 mg/mL, 25.1 µL, 128.8 nmol) together with triethylamine (0.25 µL) and shaken overnight at room temperature (as control, an Oregon Green cadaverine solution was prepared at same concentration in DMSO with triethylamine, but without addition of cyclooctyne tetra(ethylene oxide)-NHS ester). To both samples (cyclooctyne-modified Oregon Green and non-modified Oregon Green) a solution of nanogel (2 mg/mL PBS, 250 µL) was then added and the reaction mixture was incubated overnight at room temperature. Repetitive centrifugal filtration with water supplemented with 0.1% (v/v) ammonia was used to purify SPAAC-conjugates from free Oregon Green dye. Successful conjugation could be monitored by UV-Vis spectroscopy.

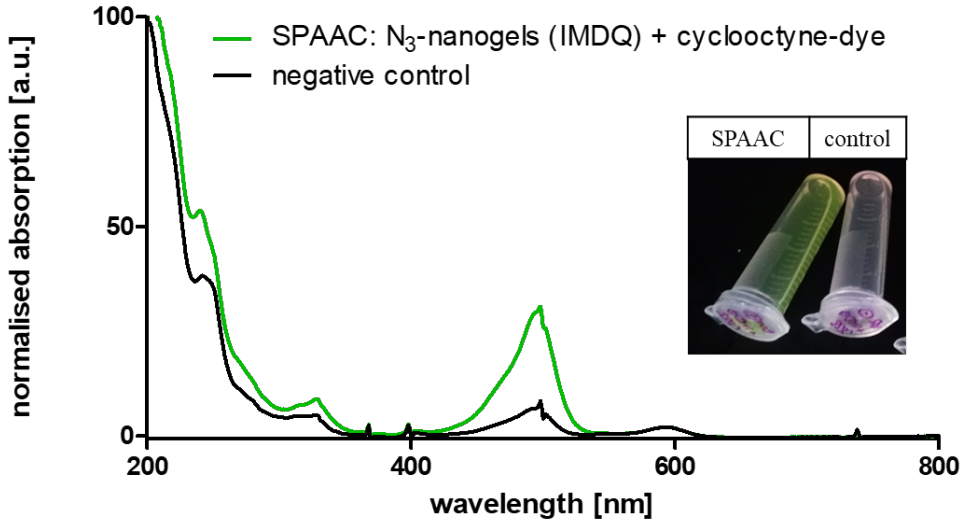

Figure S16: UV-Vis spectra and photograph of SPAAC reaction between IMDQ-loaded nanogels and cycloocytane-modified Oregon Green dye after several steps of centrifugal filtration.

Fluorescent labeling and modification of model-antigen ovalbumin with DBCO-PEG$_4$-linker for SPAAC reaction

The sequence of ovalbumin can be found on PDB (https://www.rcsb.org/pdb/explore/remediatedSequence.do?structureId=1OVA):

Ac-
GSIGAASMEFCFDVFKELKVHHANENIFYCPIAIMSALAMVYLGAKDSTRTQINKVV
RFD
KLPGFGDS^{phos}IEAQCGTSVNVHSSLRDILNQITKPNDVYSFSLASRLYAEERYPILPEY
LQCVKELYRGGLEPINFQTAADQARELINSWVESQTNGIIRNVLQPSSVDSQTAMVL
VNAIVFKGLWEKAFKDEDTQAMPFRVTEQESKPVQMMYQIGLFRVASMASEKMKI
LELPFASGTMSMLVLLPDEVSGLEQLE[*SIINFEKL*]$^{MHC\ I\ epitope}$TEWTSSNVMEERKIKV
YLPRMKMEEKYN^{N_acetylglucosamine}LTSVLMAMGITDVFSSSANLSGISSAESLK[*ISQAVH
AAHAEINEAGR*]$^{MHC\ II\ epitope}$EVVG*S*^{phos}AEAGVDAASVSEEFRADHPFLFCIKHIATNAVLF
FGRCVSP.

Amon the 386 amino acids affording a molecular weight of 42.8 kDa there are 20 lysine residues as potential modification sites for NHS-ester derived amidations. Only one potential modification site is located in the MHC-I sequence (*SIINFEKL*) but none can be found inside the MHC-II sequence (*ISQAVHAAHAEINEAGR).*

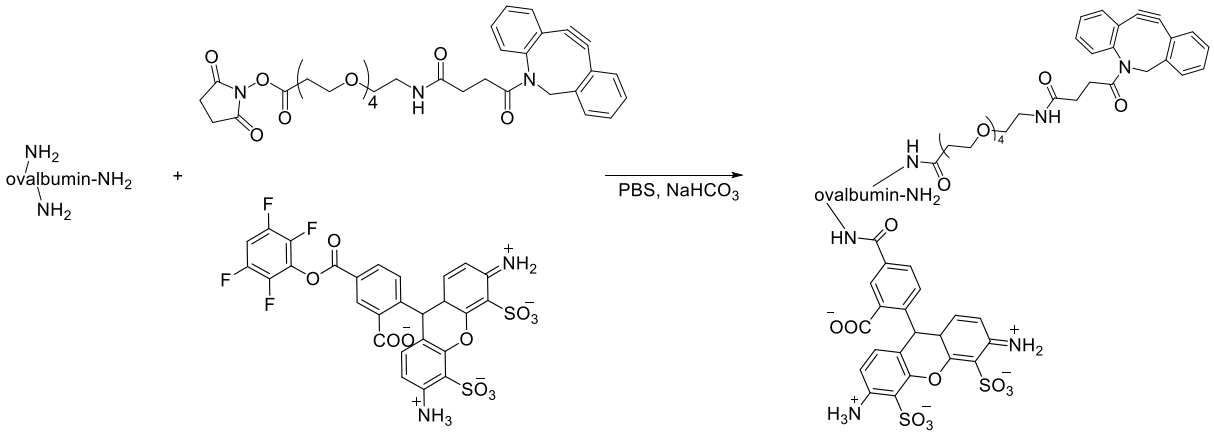

Fluorescent labeling with Alexa Fluor 488 and the introduction of a SPAAC-reactive DBCO-PEG$_4$-linker was performed simultaneously at the amino-containing side chains of ovalbumin. To a solution of ovalbumin in sterile, endotoxin-free water (2 mg/mL, 500 µL, 23.4 nmol) supplemented with bicarbonate buffer (1 M, 50 µL, pH 8.3) Alexa Fluor 488-tetrafluorophenyl ester (2 mg/mL DMSO, 35 µL, 79 nmol) was added. In case of desired DBCO-modification dibenzylcylooctyne-PEG$_4$-NHS ester (10 mg/mL DMSO, 11.4 µL, 175 nmol) was added, too. The reaction mixture was vigorously stirred in the dark at room temperature for 4 h and the purified by size-exclusion chromatography under sterile conditions (eluent: sterile PBS). Protein concentration was determined using Micro BCA Protein Assay (Thermo Fisher) with a standard curve generated from ovalbumin samples of known concentrations.

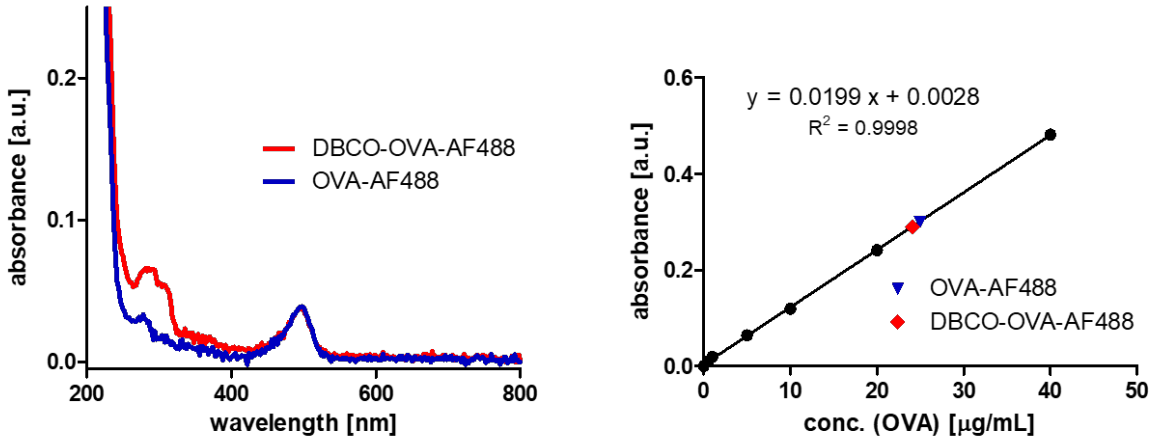

Figure S17: UV-Vis spectra and calibration curve for determination of protein concentration of fluorescently labeled ovalbumin with and without additional introduction of a SPAAC-reactive DBCO-linker.

The degree of labeling (DL) can be estimated by the absorbance maxima at 496 nm and 280 nm (the extinction coefficients of Alexa Fluor 488 (AF488) and DBCO-PEG$_4$-linker (DBCO) are provided by the supplier):

For OVA-AF488 DL_{AF488} can be estimated by $\frac{A_{496nm}}{A_{280nm}} = \frac{DL_{AF488} \cdot \varepsilon_{AF488\ at\ 496\ nm}}{DL_{AF488} \cdot \varepsilon_{AF488\ at\ 280\ nm} + \varepsilon_{OVA\ at\ 280\ nm}}$

$$=> DL_{AF488} = \frac{\frac{A_{496nm}}{A_{280nm}} \cdot \varepsilon_{OVA\ at\ 280\ nm}}{\varepsilon_{AF488\ at\ 496\ nm} - \frac{A_{496nm}}{A_{280nm}} \cdot \varepsilon_{AF488\ at\ 280\ nm}} = \frac{\frac{0.04}{0.03} \cdot 30590}{71000 - \frac{0.04}{0.03} \cdot 7800} \approx 1$$

For DBCO-OVA-AF488 DL_{DBCO} can be estimated assuming the same $DL_{AF488} \approx 1$ by

$$\frac{A_{496nm}}{A_{280nm}} = \frac{DL_{AF488} \cdot \varepsilon_{AF488\ at\ 496\ nm}}{DL_{AF488} \cdot \varepsilon_{AF488\ at\ 280\ nm} + DL_{DBCO} \cdot \varepsilon_{DBCO\ at\ 280\ nm} + \varepsilon_{OVA\ at\ 280\ nm}}$$

$$=> DL_{DBCO} = \frac{\frac{A_{280nm}}{A_{496nm}} \cdot DL_{AF488} \cdot \varepsilon_{AF488\ at\ 496\ nm} - DL_{AF488} \cdot \varepsilon_{AF488\ at\ 280\ nm} - \varepsilon_{OVA\ at\ 280\ nm}}{\varepsilon_{DBCO\ at\ 280\ nm}}$$

$$= \frac{\frac{0.06}{0.04} \cdot 1 \cdot 71000 - 1 \cdot 7800 - 30590}{13100} \approx 5$$

By FCS (see description below) only a slight increase in size was observed between DBCO-OVA-AF488 and OVA-AF488 confirming successful ligation of the SPAAC-reactive DBCO-PEG$_4$-linker, yet, this did not interfere with protein integrity or stability as no aggregates were found in PBS.

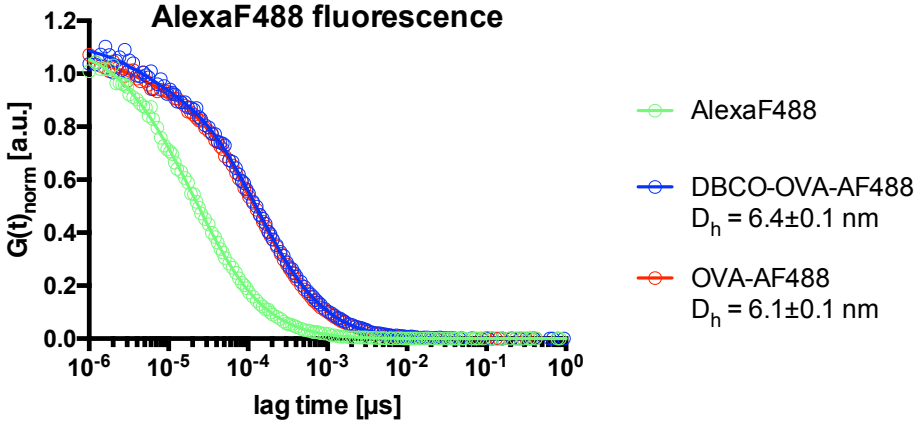

Figure S18: FCS correlogram of AF488 and SPAAC-reactive DBCO-linker modified ovalbumin.

SDS-PAGE was used to further verify OVA-DBCO modification (see description below). Samples were prepared by mixing 4.5µl of a the 0.5 µg/µg modified OVA samples (OVA-AF488 or DBCO-OVA-AF488) with 6.5 µl of a 10 µg/µl 5kDA N_3-PEG-OH sample in PBS (corresponding controls were prepared at similar concentrations) and incubated overnight at room temperature. Samples were then treated with 4x reducing Laemmli sample buffer before loading.

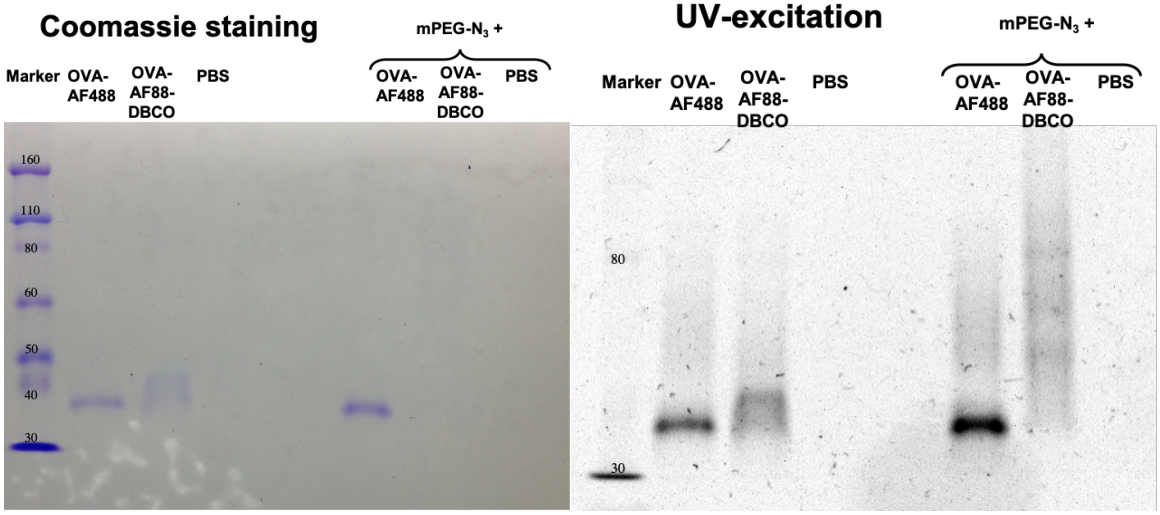

Figure S19: SDS-PAGE of AF488 and SPAAC-reactive DBCO-linker modified ovalbumin alone and incubated with azide-terminated mPEG-N_3 (5kDA). By both Coomassie staining and UV-excitation to visualize AF488-labeling successful DBCO-protein modification could be found via SPAAC-selective PEGylation.

T-cell proliferation was further applied to assure antigen bioactivity after ovalbumin-modification with AF488 and DBCO linker. For that purpose, BMDCs were incubated with OVA-AF488 and OVA-AF488-DBCO and TLR7/8 agonist IMDQ at 1µg/mL, harvested on the next day and then serially diluted and incubated with either $CD8^+$ T cells from OT-I mice or $CD4^+$ T cells from OT-II mice as indicated (see description below). No difference between the two samples was obtained.

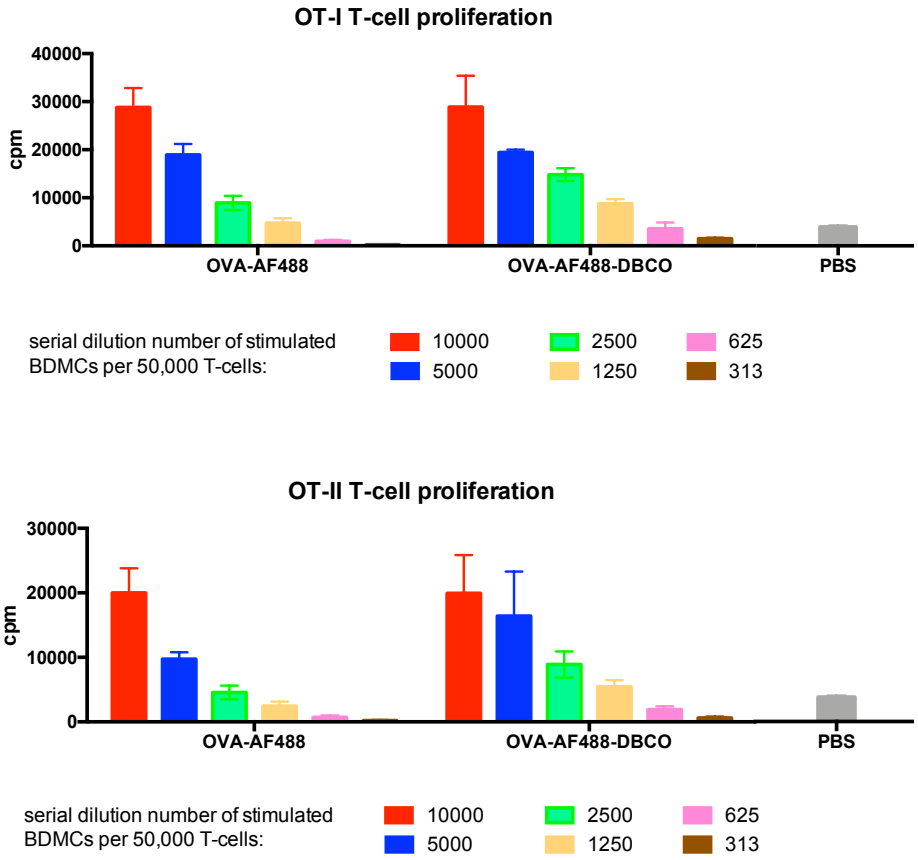

Figure S20: $CD8^+$ and $CD4^+$ specific T-cell proliferation derived from OT-I and OT-II T cells incubated with serial dilutions of BMDCs pulsed with OVA-AF488 and OVA-AF488-DBCO.

Surface decoration of azide-exposing nanogels by SPAAC reaction

For detailed *in vitro* and *in vivo* studies different nanogel formulations were prepared for each experiment freshly at final concentrations of 0.3 mg/mL ovalbumin and 0.1 mg/mL IMDQ. To covalently attach the antigen onto the nanogel surface, lyophilized nanogels (+/- IMDQ, 5 mg/mL) were dispersed in water supplemented with 0.1% (v/v) ammonia and sonicated for 1 h. Then, the nanogel solution (5 mg/mL, 38 µL, 15.2 nmol azide) was added to DBCO-modified ovalbumin (0.8 mg/mL, 37.5 µL, 0.7 nmol) and the mixture was filled up to 100 µL with sterile PBS to adjust concentrations. The mixture was incubated at 4°C for 48 h. To obtain a simple mixture of antigen and nanogel for comparative studies, nanogels and fluorescent labeled ovalbumin without DBCO-modification were mixed and incubated. Based on this procedure several sample compositions were prepared regarding different combinations of covalent or admixed IMDQ- and antigen-addition. After incubation samples were analyzed by SDS-PAGE, UV-Vis and fluorescence spectroscopy, DLS and Zeta-potential measurements.

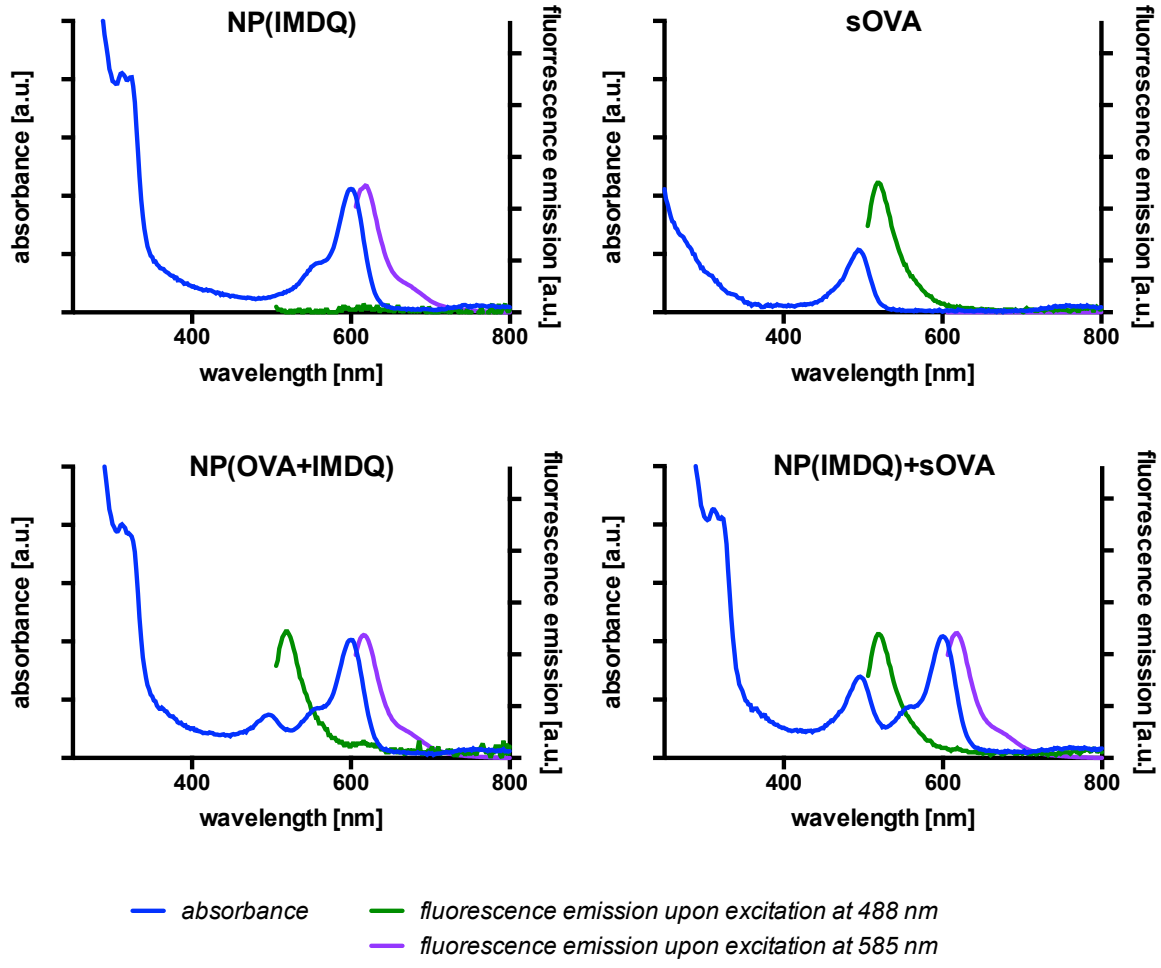

Figure S21: UV-Vis and fluorescence spectra of IMDQ-loaded nanogels, sOVA and both components either separate or covalently attached at 0.4 mg/mL of equivalent nanogel concentration. Note that the fluorescent dyes can be addressed individually from each other.

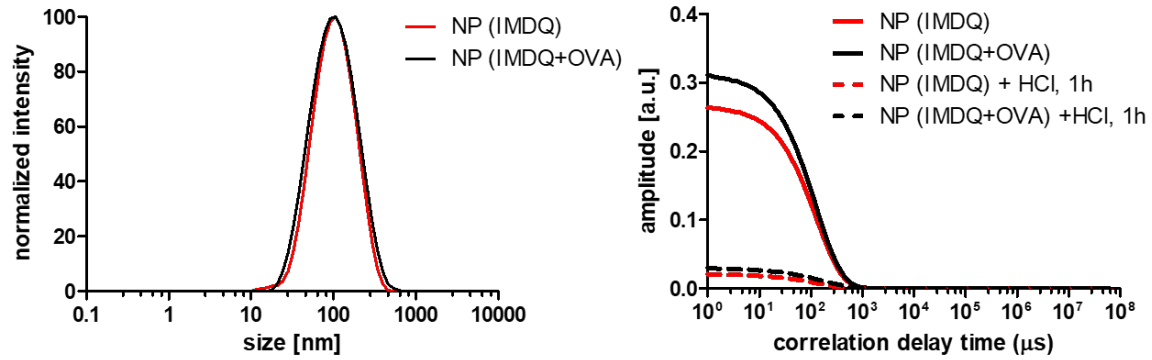

Figure S22: DLS characterization of IMDQ-loaded nanogels with or without covalently attached ovalbumin. After addition of 3 v% 1M HCl correlation strongly decreases due to nanogel degradation into single polymer chains.

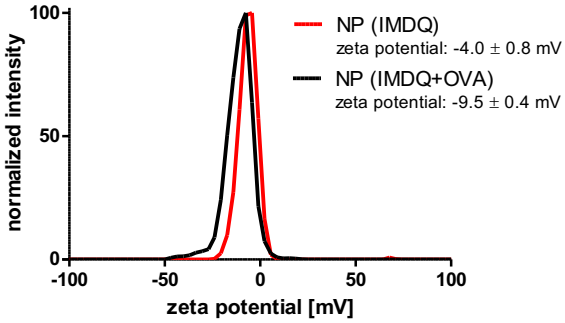

Figure S23: Zeta potential measurements of IMDQ-loaded nanogels with or without covalently attached ovalbumin. Measurements were performed at 0.25 mg/mL in 1 mM KCl.

SDS-PAGE

Reaction monitoring of SPAAC conjugation was performed by SDS-PAGE. SDS-PAGE was performed with 15% polyacrylamide separation gel and 5% polyacrylamide loading gel using the Mini-PROTEAN Tetra Cell from Bio-Rad. Samples were prepared by mixing the corresponding volume of 3 µg protein with 4x reducing Laemmli sample buffer before loading. For molecular weight comparisons Novex™ Sharp Pre-Stained Protein Standard was used. Gel electrophoresis was performed for 55 min at 160 mV. Gel image were obtained after excitation with a UV lamp and after staining with Coomassie Blue with smart phone camera.

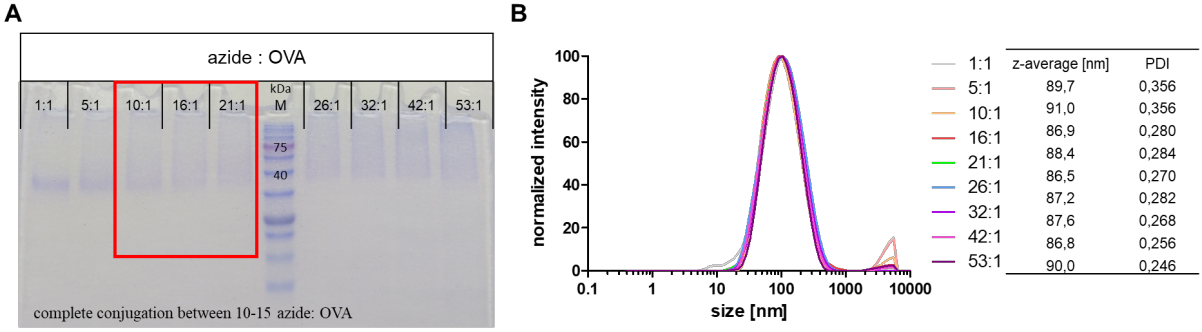

Figure S24: Influence of azide-protein ratio on SPAAC reaction and nanogel size. (A) SDS-PAGE analysis of conjugation of DBCO-ovalbumin to azide-nanogels. (B) DLS intensity size distribution of resulting nanogels. Increasing excess of azide-nanogels does not lead to size changes.

FCS measurements

For FCS measurements nanogels were purified from unbound Texas Red dye prior to conjugate preparation. Hence, 10 mg of each nanogel type (+/- IDMQ) were dissolved in 2 mL of a mixture (1:1) of methanol and water supplemented with 0.1% (v/v) ammonia and sonicated for 1 h. Unbound, free dye was removed by spin-filtration (MWCO 100000 g/mol) of nanogels with the water-methanol mixture. The procedure was repeated until complete disappearance of Texas Red dye-derived absorbance maximum (588 nm) monitored by UV-Vis measurements. Samples were lyophilized and used for preparation of following formulations: NP(IMDQ), NP(IMDQ+OVA), NP(IMDQ) + sOVA. Nanogels were re-dispersed in water supplemented with 0.1% (v/v) ammonia and sonicated for 1 h. Preparation of the different nanogel-ovalbumin compositions was performed as already described. All samples were incubated for two days at 4°C. To investigate degradation behavior hydrochloric acid (3% (v/v), 1 M) was added to one part of each sample. Usually for each FCS measurements 1µL of each sample was diluted with 500 µL PBS in an eight-well polystyrene, chambered cover glass (Laboratory-Tek, Nalge Nunc International). For excitation of the Alexa 488 and TxRed labeled species an argon ion laser (488 nm) and a He/Ne-laser (543 nm) were used simultaneously. The excitation light was focused into the sample by a high numerical aperture water immersion objective (C-Apochromat 40x/1.2 W, Carl Zeiss, Jena, Germany). The fluorescence was collected with the same objective and after passing through a confocal pinhole, directed to a spectral detection unit (Quasar, Carl Zeiss). In this unit emission was spectrally separated by a grating element on a 32-channel array of GaAsP detectors operating in a single photon counting mode. The emission of Alexa 488 was detected in the spectral range 500- 517 nm and that of TxRed in the range 624-696 nm. These arrangements resulted in the formation of two overlapping confocal observation volumes V_b and V_r that superimpose to a common observation volume V_{br}. The sizes of the observation volumes were obtained by performing calibration experiments using Alexa 488 and TxRed as reference dyes with known diffusion coefficients. For each solution, a series of twenty measurements with a total duration of 3 min were performed. The obtained experimental auto- and cross-correlation curves were fitted with the theoretical model function for an ensemble of either 1 or 2 types of freely diffusing fluorescence species for $G(\tau) = 1 + \left[1 + \frac{f_T}{1 - f_T} \cdot e^{-\tau/\tau_T}\right] \cdot \frac{1}{N} \sum_{i=1}^{m} \frac{f_i}{\left[1 + \frac{\tau}{\tau_{D,i}}\right] \cdot \sqrt{1 + \frac{\tau}{S^2 \cdot \tau_{D,i}}}}$ (with m = 1 or 2).[6] The fits yielded the diffusion times of the fluorescent species from which the respective diffusion coefficients were evaluated by $\tau_{D,i} = \frac{\omega^2}{4D_i}$. Finally, the hydrodynamic radii were calculated (assuming spherical particles) by using the Stokes-Einstein relation $R_{h,i} = \frac{k_B T}{6 \cdot \pi \cdot \eta \cdot D_i}$.

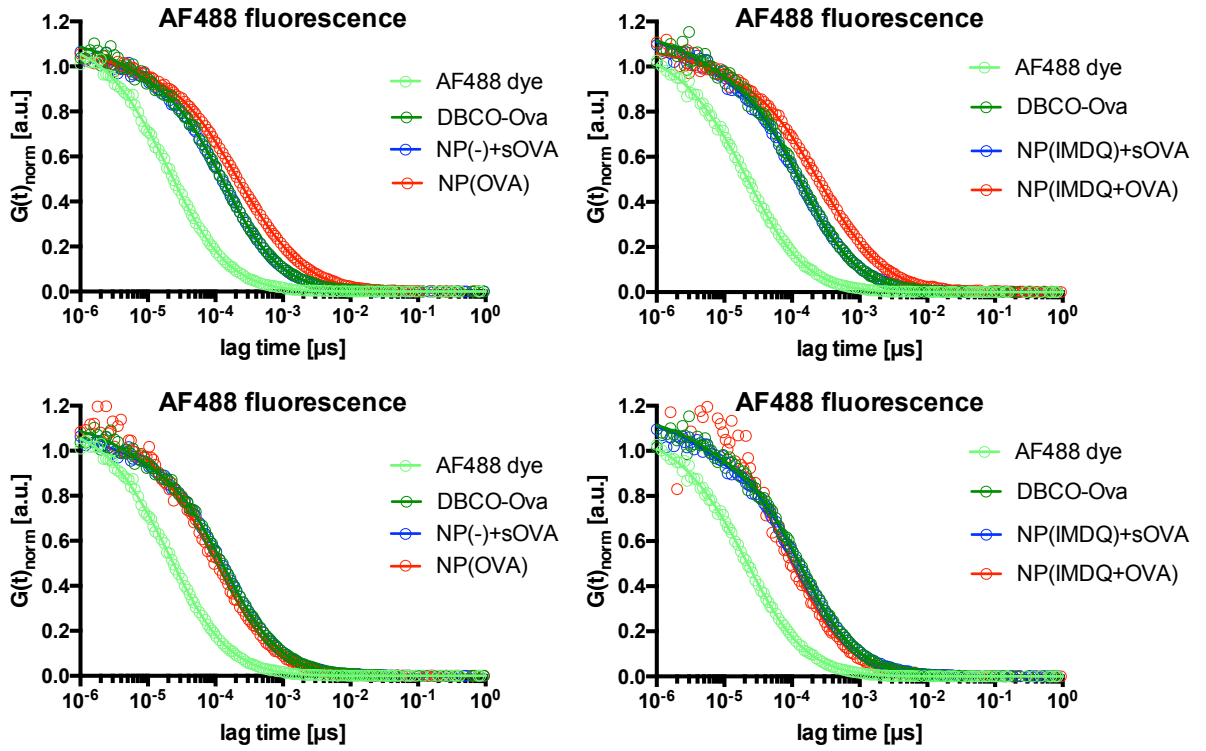

Figure S25: Alexa Fluor 488-based FCS autocorrelation derived from the fluorescently labeled ovalbumin mixed or covalently conjugated to either empty nanogels (left) or IMDQ-loaded nanogels (right) before (top row) or after (bottom row) acidification with 3vol% 1M HCl. Note that the larger correlation times for NP(OVA) and NP(IMDQ+OVA) corresponding to ovalbumin conjugated to nanogels disappear upon acid-triggered particle degradation.

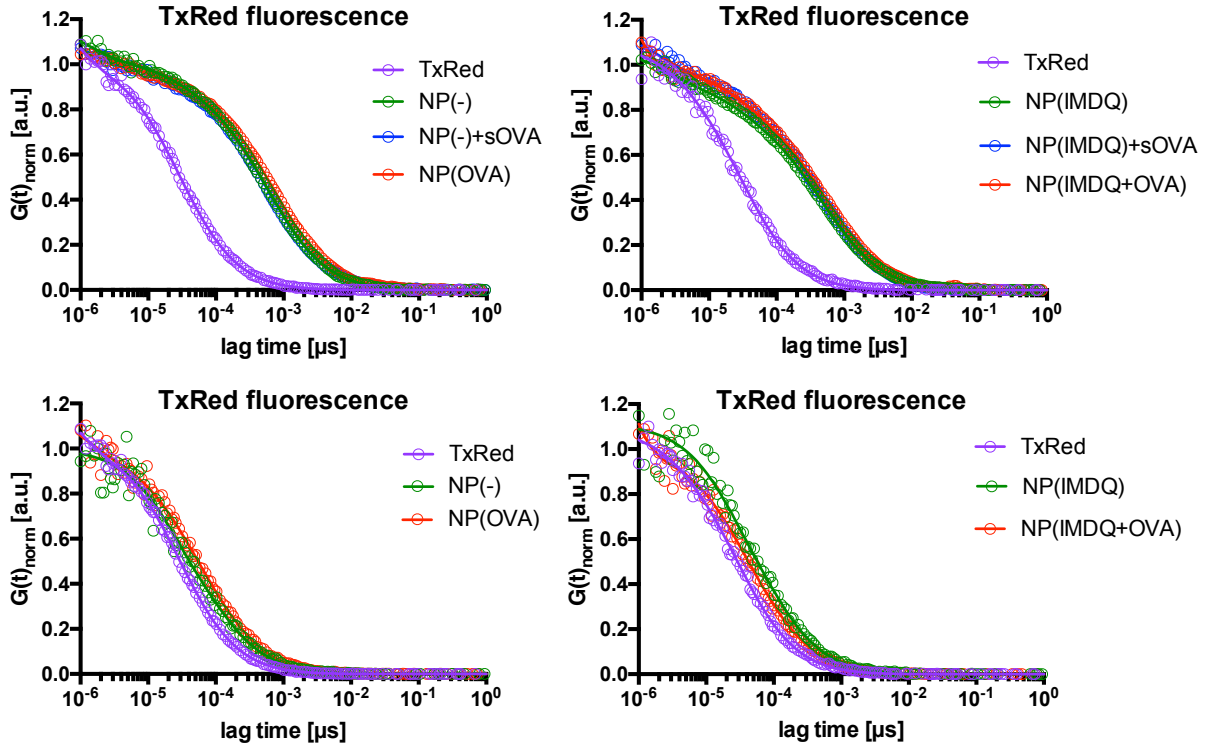

Figure S26: Texas Red-based FCS autocorrelation derived from the fluorescently labeled empty (left) or IMDQ-loaded nanogels (right) mixed or covalently conjugated with ovalbumin before (top row) or after (bottom row) acidification with 3vol% 1M HCl. Note that the larger correlation times for NP(-), NP(IMDQ), NP(OVA) and NP(OVQ+IMDQ) corresponding to intact nanogels disappear upon acid-triggered particle degradation.

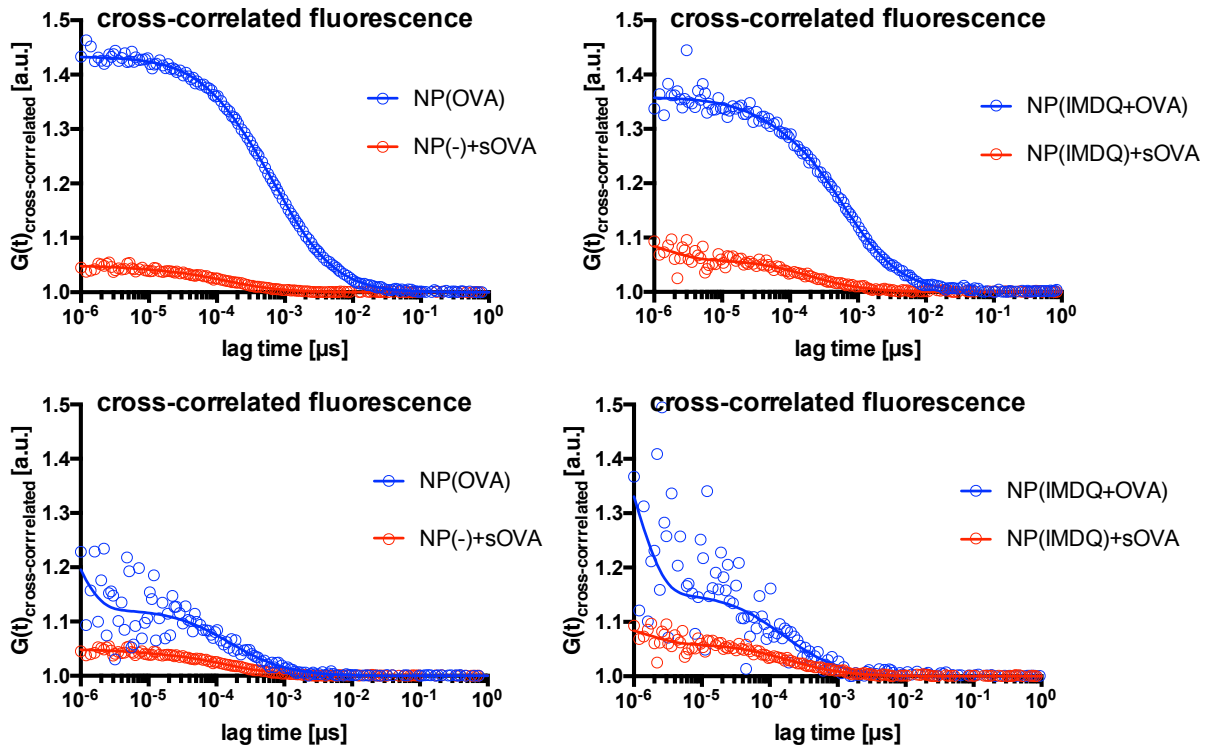

Figure S27: Alexa Fluor 488 and Texas Red derived fluorescent cross-correlation of empty (left) or IMDQ-loaded nanogels (right) mixed or covalently conjugated with ovalbumin before (top row) or after (bottom row) acidification with 3vol% 1M HCl. Note that the cross-correlations for NP(OVA) and NP(IMDQ+OVA) corresponding to ovalbumin conjugated to the nanogel disappear upon acid-triggered particle degradation.

Table S1: Results of Alexa Fluor 488-based FCS measurements derived from the fluorescently labeled ovalbumin mixed or covalently conjugated to either empty or IMDQ-loaded nanogels.

Hydrodynamic diameter determined by Alexa Fluor 488 derived FCS *(correlation times and % from one- or two-component fitting)*				
Alexa Fluor 488	1.1 nm τ_1 = 23.1 µs (100%)			
OVA	6.1 nm τ_1 = 125.6 µs (100%)			
OVA-DBCO	6.4 nm τ_1 = 130.5 µs (100%)			
NP(-)+sOVA	6.2 nm τ_1 = 127.9 µs (100%, unbound OVA)		**NP(IMDQ)+sOVA**	6.3 nm τ_1 = 130.4 µs (100%, unbound OVA)
NP(OVA)	32.7 nm τ_1 = 671.2 µs (34%) τ_2 = 130.5 µs (66%, free OVA)		**NP(IMDQ+OVA)**	29.9 nm τ_1 = 620.0 µs (43%) τ_2 = 130.5 µs (57%, free OVA)
NP(OVA) acidified	5.3 nm τ_1 = 107.7 µs (100%)		**NP(IMDQ+OVA) acidified**	4.9 nm τ_1 = 102.3 µs (100%)

Table S2: Results Texas Red-based FCS measurements derived from the fluorescently labeled empty or IMDQ-loaded nanogels mixed or covalently conjugated with ovalbumin.

Hydrodynamic diameter determined by Texas Red derived FCS *(correlation times and % from one- or two-component fitting)*				
Texas Red cadaverine	1.4 nm τ_1 = 29.5 µs (100%)			
NP(-)	30.0 nm τ_1 = 614.3 µs (84%) τ_2 = 29.5 µs (16%, free dye)		**NP (IMDQ)**	26.8 nm τ_1 = 558.4 µs (75%) τ_2 = 29.5 µs (25%, free dye)
NP(-) acidified	3.6 nm τ_1 = 74.8 µs (99%) τ_2 = 29.5 µs (<1%, free dye)		**NP(IMDQ) acidified**	3.6 nm τ_1 = 74.3 µs (99%) τ_2 = 29.5 µs (<1%, free dye)
NP(-)+sOVA	30.4 nm τ_1 = 623.8 µs (85%) τ_2 = 29.5 µs (15%, free dye)		**NP(IMDQ)+sOVA**	25.2 nm τ_1 = 519.7 µs (77%) τ_2 = 29.5 µs (23%, free dye)
NP(OVA)	36.7 nm τ_1 = 752.5 µs (87%) τ_2 = 29.5 µs (13%, free dye)		**NP(IMDQ+OVA)**	29.1 nm τ_1 = 605.0 µs (75%) τ_2 = 29.5 µs (25%, free dye)
NP(OVA) acidified	5.4 nm τ_1 = 110.6 µs (50%) τ_2 = 29.5 µs (50%, free dye)		**NP(IMDQ+OVA) acidified**	4.9 nm τ_1 = 101.2 µs (32%) τ_2 = 29.5 µs (%, free dye

Reproducibility of nanogel fabrication

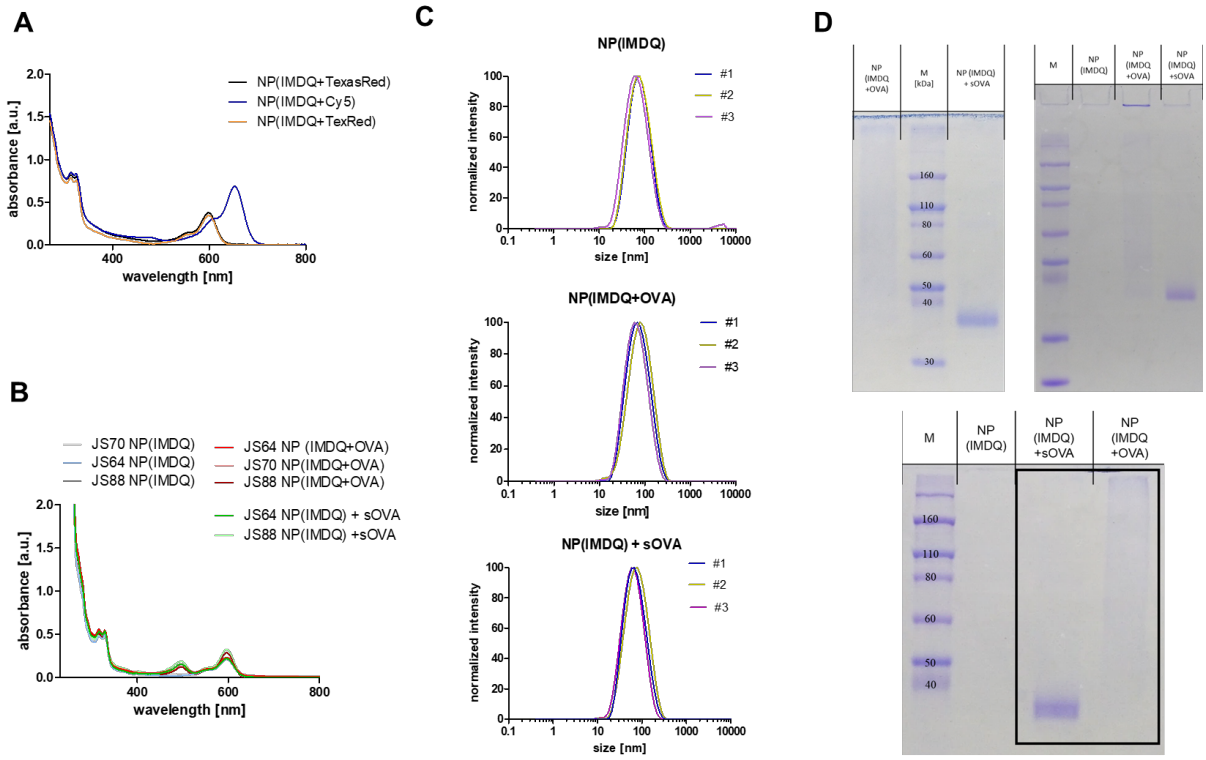

Figure S28: Representative data of various nanogel preparations demonstrating a reproducible fabrication process. (A) UV-Vis spectra of 3 batches of IMDQ-loaded nanogels showing similar drug-loading and dye-labeling (TexasRed). (B) UV-Vis spectra of nanogel samples with or without addition of ovalbumin used for in vitro an in vivo experiments. Same concentrations of IMDQ and OVA are observable. (C) DLS intensity size distribution plots of three nanogel preparations showing similar sizes between the preparations independent of samples type. (D) SDS-PAGE analyses of three different SPAAC conjugations of azide-nanogels and ovalbumin revealing complete conjugation of protein to the carrier system.

RAW-Blue macrophage TLR reporter assay

IMDQ-triggered TLR receptor stimulation followed by NF-kB/AP-1 activation (detectable by secretion of embryonic alkaline phosphatase) was performed on RAW-Blue macrophages as proposed by the manufacturer (InvivoGen) and in analogy to earlier reports.[7,8] Into a 96-well plate RAW-Blue cells were seeded at 90000 cells/well in 180 µL cell culture medium. After cell adhesion overnight each well was incubated with 20 µL of IMDQ-containing samples at given concentrations for 16 h. Then, 50 µL of the supernatant of each well was transferred into a new 96-well plate and tested for secreted embryonic alkaline phosphatase using the QUANTI-Blue assay (InvivoGen). 150 µL QUANTI-Blue solution was added to each well and samples were incubated at 37°C for 30 min. Levels of secreted embryonic alkaline phosphatase were determined by measuring optical density at 620 nm with a microplate reader. Increased TLR activity was determined by an increase in optical density relative to a negative control treated with PBS. IMDQ served as positive control and experiments were performed in quadruplicate (n = 4).

RAW-Blue macrophage cell viability by MTT assay

25 µL of 3-(4,5-dimethylthiazol-2-yl)-2,5-diphenyltetrazolium bromide (MTT, 2 mg/mL PBS) was added to each well containing RAW-Blue macrophages which were treated with IMDQ-samples at given concentrations. After incubation at 37°C for 1 h, 100 µL of 10% SDS (m/v)/0.01 M HCl were added to each well to dissolve formed formazan crystals followed by incubation overnight at 37°C. Cell viability was determined in relation to positive (PBS blank, 100% viability) and negative (10% DMSO, 0% viability) control samples based on absorbance measurements at 570 nm. Experiments were performed in quadruplicate (n = 4).

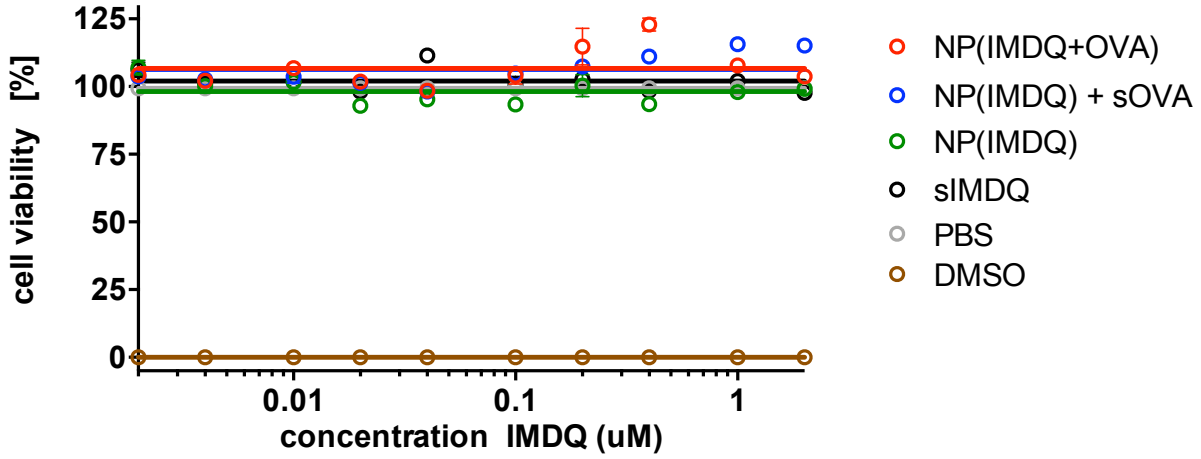

Figure S29: In vitro evaluation of IMDQ-loaded nanogels in comparison to soluble TLR agonist. Nanogels show no negative effect on cell viability.

Flow cytometry of RAW-Blue macrophages

RAW-Blue macrophages were seeded into 24-well plates in a density of 250000 cells/well in 980 µL cell culture medium and incubated overnight to allow cell adhesion. To each well 20 µL nanogel sample (resulting in a nanogel concentration of 40 µg/mL) was added and cells were incubated at 37°C. After 16 h of incubation, cell culture medium was aspirated and cells were washed with 1 mL PBS followed by an incubation with 500 µL Cell Dissociation Buffer for 20 min. Then, cells were detached and cell suspensions were transferred into Eppendorf tubes and centrifuged immediately (300 g, 10 min, 5°C). The supernatant was aspirated and cell pellets were re-suspended in 500 µL PBS and put on ice. All samples were run in triplicate (n = 3). Flow cytometric analysis was performed on an Attune NxT flow cytometer (Thermo Fisher) and the resulting data processed by FlowJo software following the displayed gating strategy.

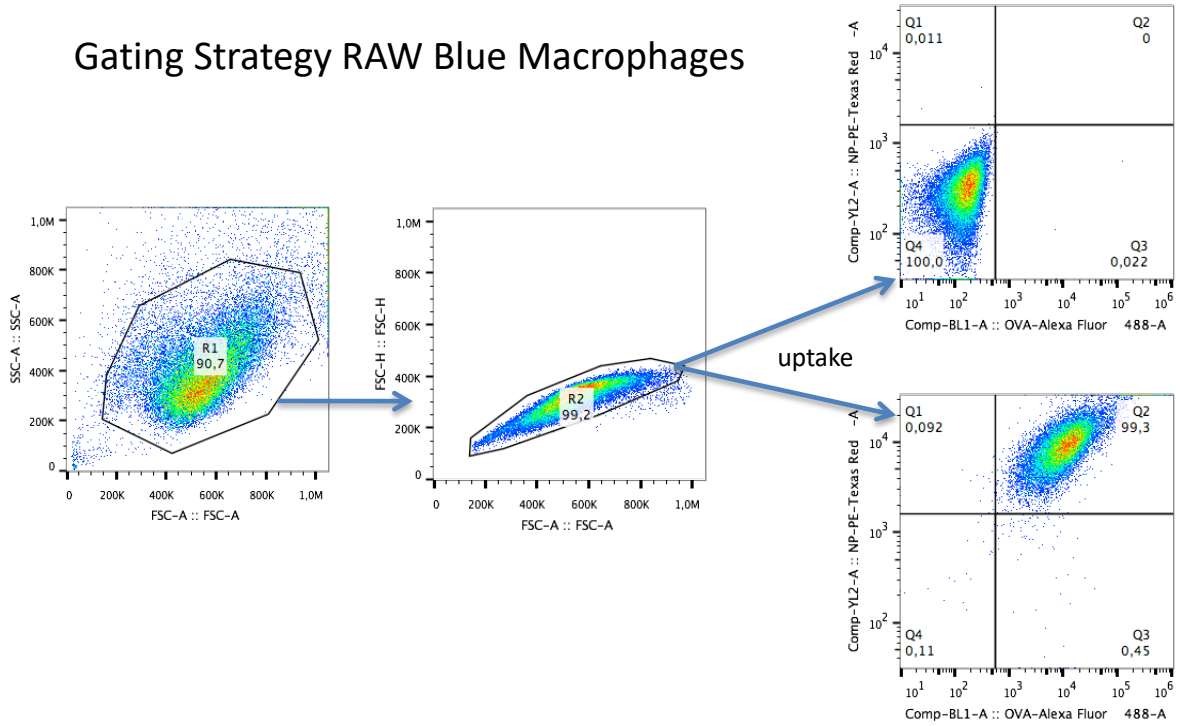

Figure S30: Gating strategy for flow cytometry analysis of the uptake of different IMDQ-nanogel formulations and ovalbumin by RAW-Blue macrophages of (n = 3).

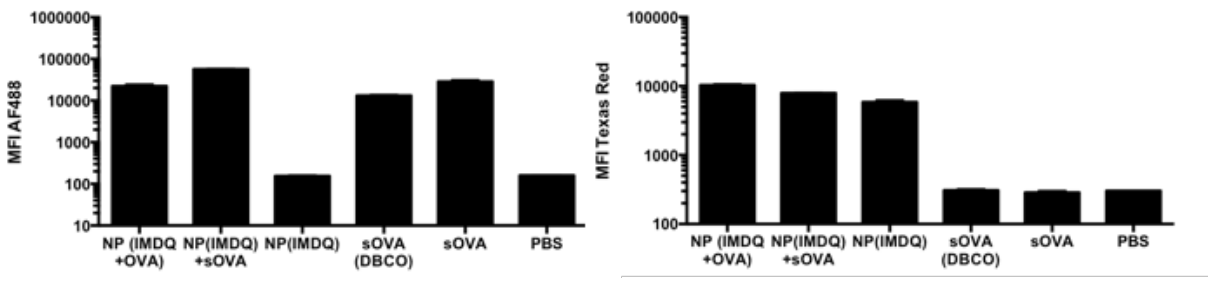

Figure S31: Results of mean fluorescence intensity (MFI) from the flow cytometry analysis of the uptake different IMDQ-nanogel formulations and ovalbumin by RAW-Blue macrophages (n = 3).

Confocal fluorescence microscopy of RAW-Blue macrophages and DC2.4

RAW-Blue macrophages (50,000 cells/well, suspended in 0.18 mL of the culture medium) were seeded into Ibidi µ-slide eight-well confocal microscopy chambers and left to adhere overnight. Afterwards, cells were incubated with 20 µL nanogel sample with soluble or covalently attached OVA sample (yielding a total nanogel concentration of 40 µg/mL) for 16 h. Then, culture medium was aspirated and cells were washed three times with PBS. Next, 200 µL of 4% paraformaldehyde was added and allowed to fixate for 15 min at 37 °C. Subsequently, cells were washed again three times with PBS and their nuclei were stained with 200 µL of 4′,6-diamidino-2-phenylindole (DAPI) (50 µg/mL in PBS) for 15 min at 37 °C. Finally, cells were washed three times with PBS and stored under an aqueous mounting medium. Fluorescence confocal laser scanning microscopy images were recorded on a Leica SP5 confocal microscope system with a 63× immersion objective. All images were finally processed by the ImageJ software package.

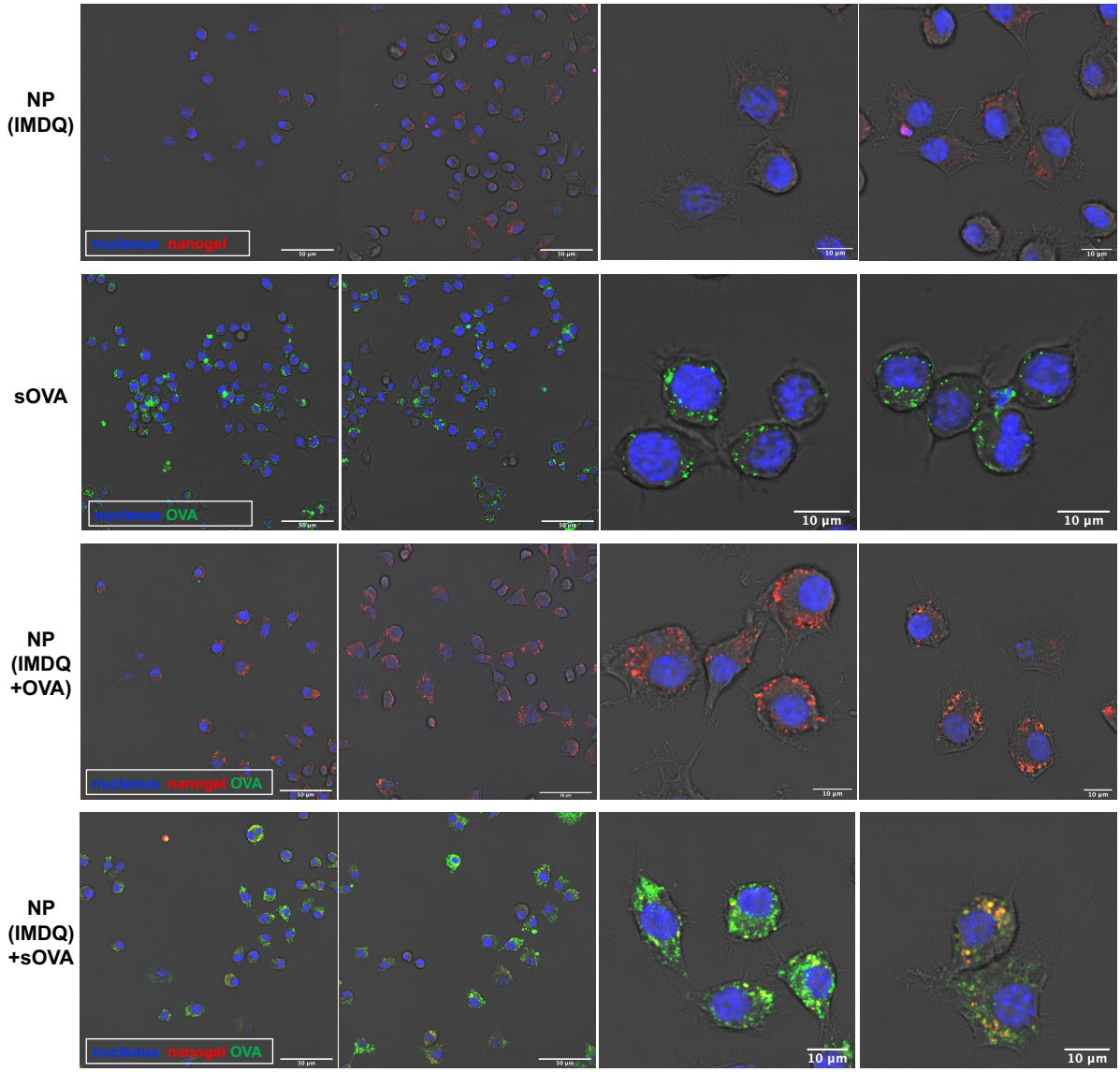

Figure S32: Fluorescence confocal microscopy image of RAW Blue macrophages incubated with IMDQ- and OVA-loaded nanogels NP(IMDQ+OVA) as well as their corresponding controls NP(IMDQ), sOVA and .NP(IMDQ)+sOVA. Nanogels could be identified by their Texas Reed label (red), while OVA could be visualized by the Alexa Fluor 488 label (green).

Under similar conditions DC2.4 dendritic cells were also incubated with soluble or covalently attached OVA samples and imaged by confocal microscopy. Again, a strong co-localization was found for OVA covalently bound to the nanogel carrier.

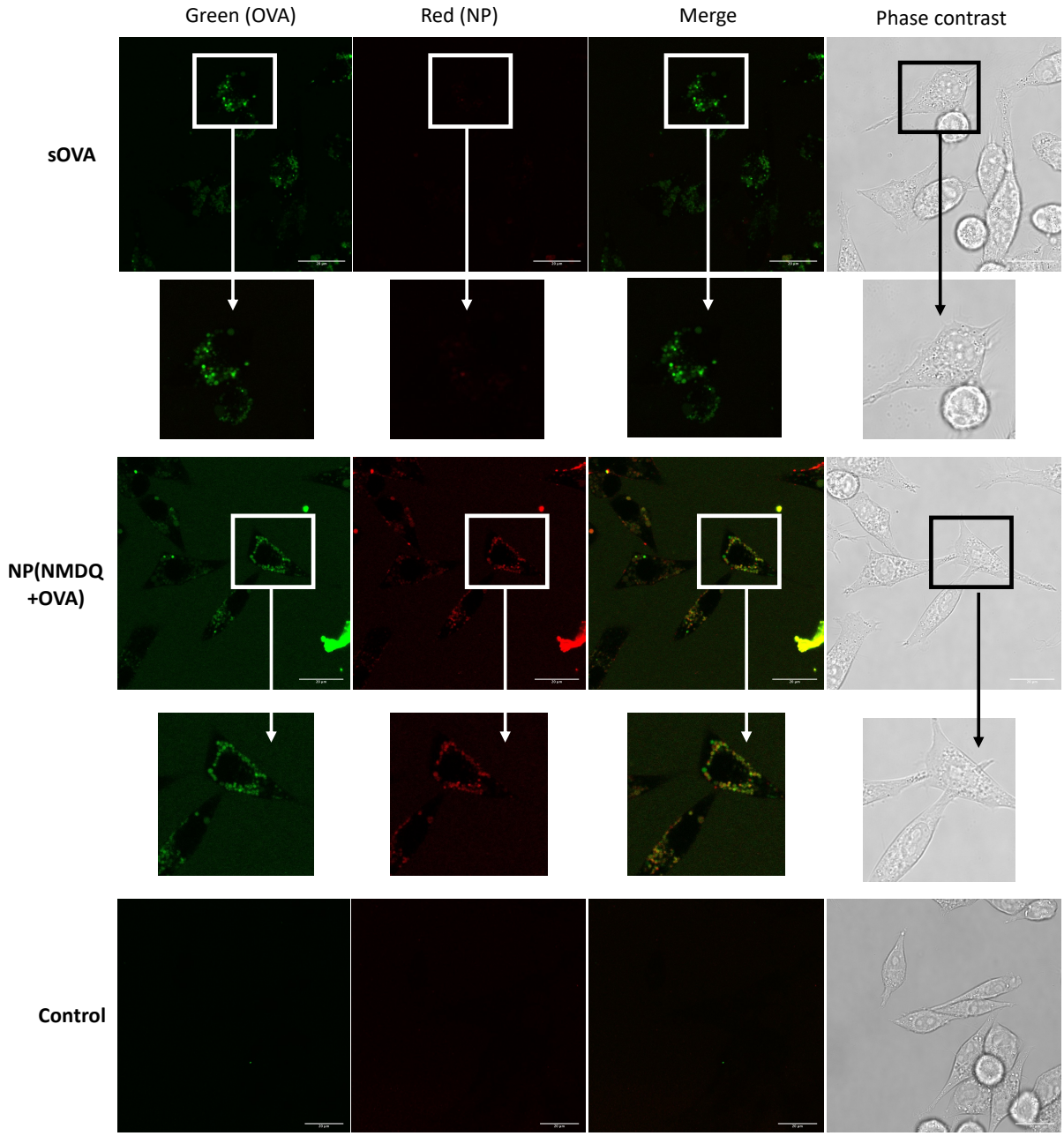

Figure S33: Fluorescence confocal microscopy image of DC2.4 dendritic cells incubated with sOVA and IMDQ- and OVA-loaded nanogels NP(IMDQ+OVA). Nanogels could be identified by their Texas Red label (red), while OVA could be visualized by the Alexa Fluor 488 label (green).

In vitro read-out in spleen cells

Spleen cells were derived from C57BL/6 mice, and erythrocytes were lysed using a hypotonic lysis buffer (155 mM NH_4Cl, 10 mM $KHCO_3$, 100 μM EDTA, pH 7.4). Spleen cells were resuspended in IMDM-based culture medium ($4x10^6$/mL). Aliquots were transferred into sterile FACS tubes (each 500 µl). The various NP formulations (1 µg/mL) were applied either directly or after preincubation with the same volume of native mouse serum (30 min, 37 °C) to exclude the influence of a potentially formed protein corona. On the next day, samples were washed, and subjected to flow cytometric analysis.

Flow cytometry of spleen cells

Again, in order to prevent unspecific binding of subsequently added antibodies, samples were incubated first with a rat anti-mouse CD16/CD32 (Fc-block) antibody (15 min, 4 °C). Next, spleen cells were incubated for 20 min at 4 °C with specific antibodies for CD11b (SB600), CD11c (PE-Cy7), CD19 (SB702), Ly6G (PE), MHC-II(APC) and CD86 (FITC – note that its labeling was way much stronger that the weak fluorescence derived from the AF488-labeled OVA, e.g. no difference between NP(IMDQ) and NP(IMDQ+OVA)). All antibodies were obtained from BioLegend (San Diego, CA) or Thermo Fisher (Waltham, MA). After antibody incubation, samples were incubated with fixable viability dye (FVD) eFl450 (Thermo Fisher) to exclude dead cells. Samples left untreated, incubated with only a NP formulation or with a single antibody only served as controls. Washed samples were fixed and subjected to flow cytometric analysis employing an Attune NxT flow cytometer (Thermo Fisher). The resulting data were processed by FlowJo software following the displayed gating strategy. All samples were run in biological triplicate (n = 3) and referenced to the negative control sample (PBS group).

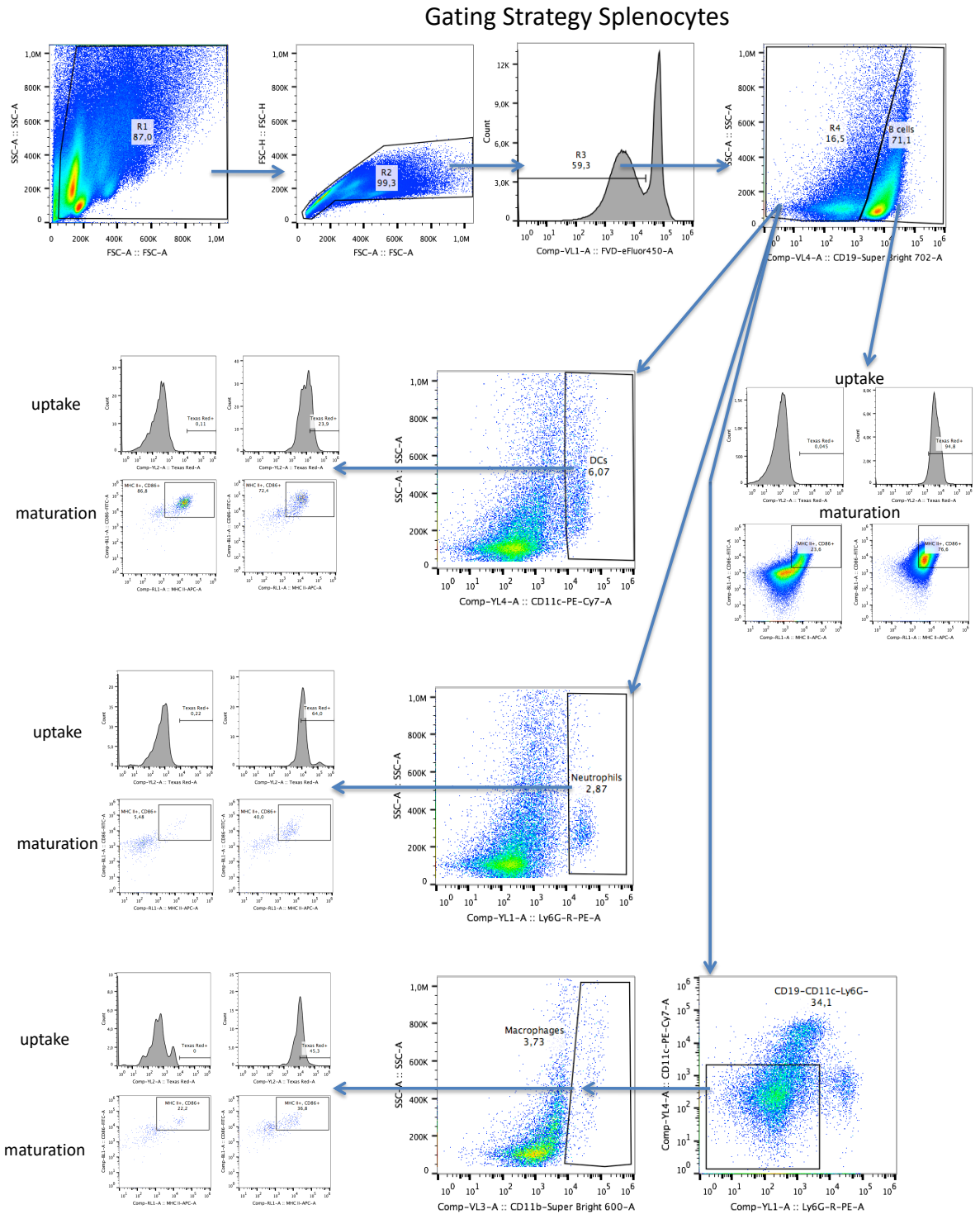

Figure S34: Gating strategy for flow cytometry analysis of spleen cells incubated with IMDQ/OVA nanogel formulations with respect to particle uptake and immune cell maturation.

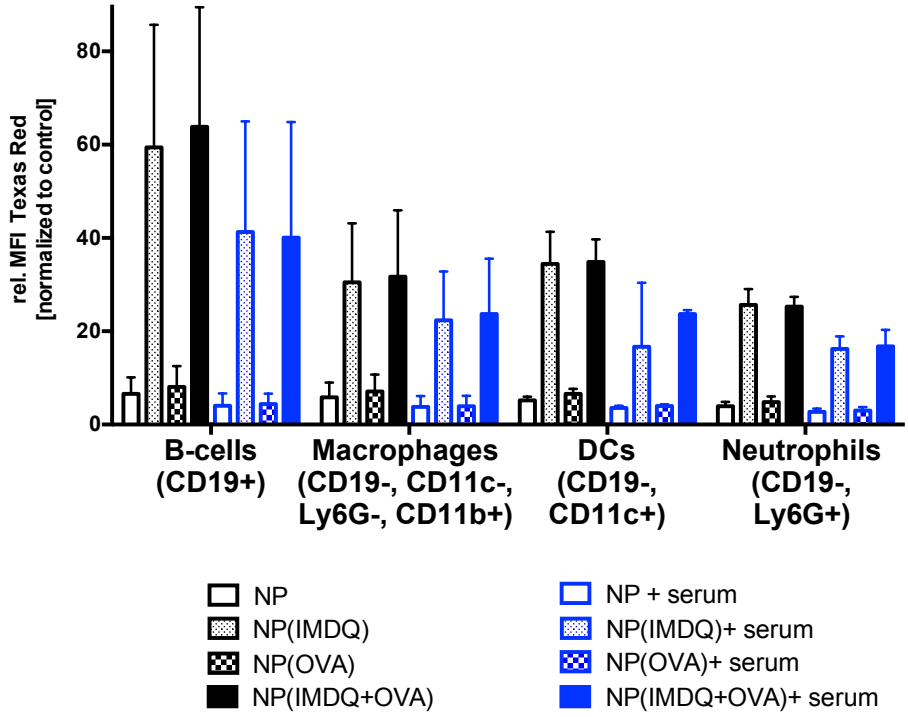

Figure S35: Results of relative mean fluorescence intensity (MFI – in relation to cells treated with PBS9 from the flow cytometry analysis of splenocytes incubated with covalent IMDQ and OVA nanogel formulations. Note that a pre-incubation of nanogels with mouse serum (blue) did not affect the uptake of the nanogels into the different immune cell populations.

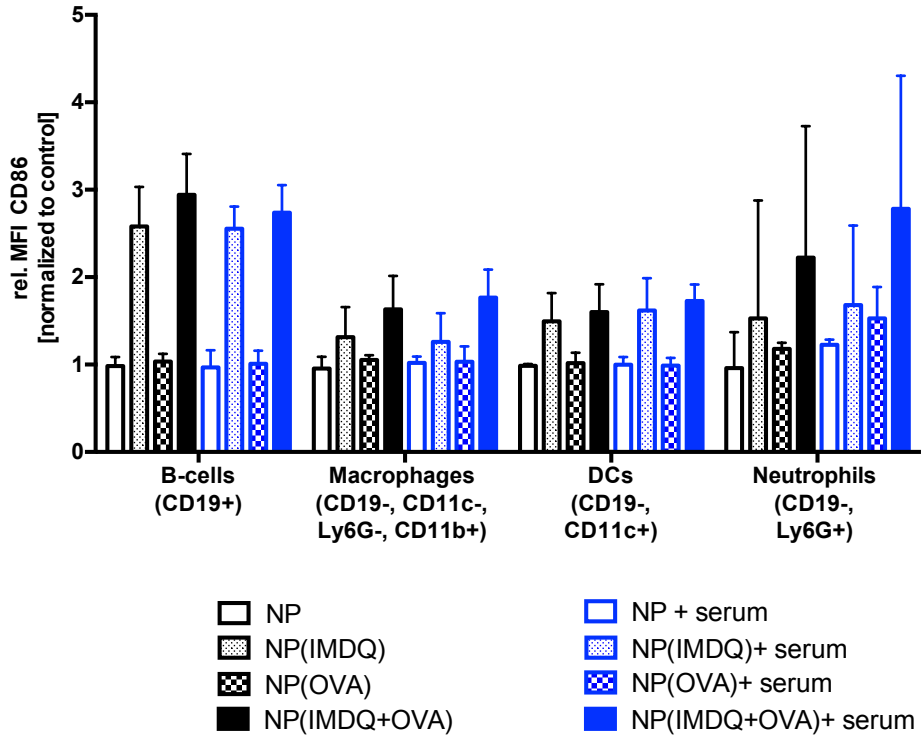

Figure S36: Results of relative mean fluorescence intensity (MFI – in relation to cells treated with PBS) from the flow cytometry analysis of splenocytes incubated with covalent IMDQ and OVA nanogel formulations. Note that a pre-incubation of nanogels with mouse serum did not affect the maturation status (MFI of CD86 expression) of the different immune cell populations after x vivo treatment with nanogels.

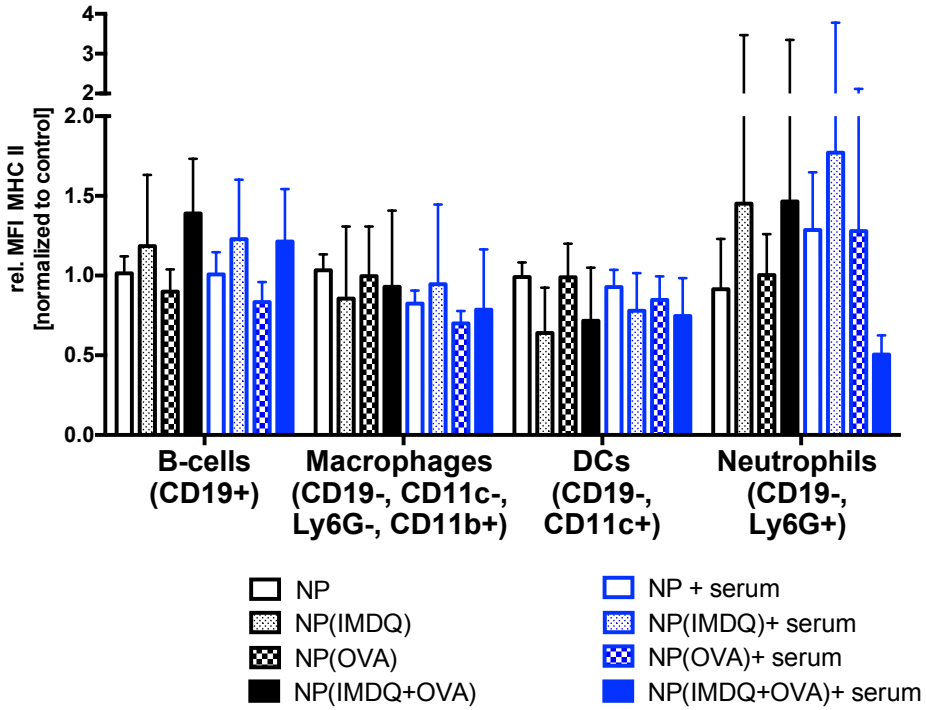

Figure S37: Results of relative mean fluorescence intensity (MFI – in relation to cells treated with PBS) from the flow cytometry analysis of splenocytes incubated with covalent IMDQ and OVA nanogel formulations. Note that the basal expression levels of MHC-II were already quite high and a pre-incubation of nanogels with mouse serum did not alter the maturation status either (MFI of MHC-II expression).

Microscopy analysis of spleen cells

For interaction analyses, a wildtype mouse was sacrificed and the splenocytes were isolated. $1x10^6$ splenocytes were seeded into a well of a 6-well plate and glass bottom dishes (MatTek Corporation, Ashland, United States) and were either treated with 100 µl of NP(IMDQ+OVA) or left untreated. After 4 hours of incubation at 37 °C, the cells were harvested, washed and then stained with CD19-Biotin followed by a secondary staining against CD19-Biotin with Streptavidin-Pacific Blue (obtained from BioLegend (San Diego, CA) and Thermo Fisher (Waltham, MA)), both for 1 hour at room temperature in PBS/1 % FCS. At least, the cells were covered with PBS and analysed on a fluorescence microscope (Axiovert 200 M, Carl Zeiss, Jena), kindly supported by R. Stauber (Department of Otolaryngology, Head and Neck Surgery, University Medical Center Mainz). Brightness and contrast of the images were adapted using the Canvas™ software (ACD Systems, Seattle, United States).

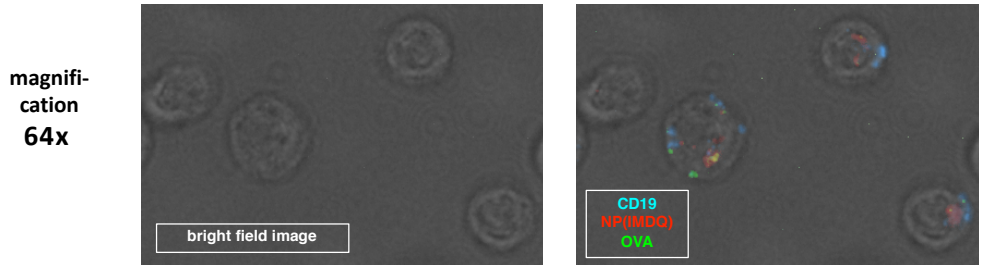

Figure S38: Fluorescence microscopy image of splenocytes incubated with IMDQ- and OVA-loaded nanogels NP(IMDQ+OVA). Nanogels could be identified by their Texas Reed label (red), while OVA could be visualized by the Alexa Fluor 488 label (green). Moreover, B-cells could be identified by antibody staining against CD19.

In vitro read-out in bone marrow-derived dendritic cells (BMDCs)

Bone marrow cells were seeded in 12 well suspension cell culture cluster plates (each $2x10^5$/mL). Culture media was replenished on days 2 and 6. On day 7-8 the different NP formulations were applied (1 µg/mL). On the following day, samples were harvested and subjected to flow cytometric analysis or employed as stimulators in T cell proliferation assays.

Flow cytometry of BMDCs

In order to prevent unspecific binding of subsequently added antibodies, samples were first incubated with a rat anti-mouse CD16/CD32 (Fc-block) antibody (15 min, 4 °C). Specific antibodies for CD11c (conjugated with PE-CY7), MHC-II (APC) and CD86 (eFl450) were applied for 20 min at 4 °C. All antibodies were obtained from BioLegend (San Diego, CA) or Thermo Fisher (Waltham, MA). Samples left untreated, incubated with only a NP formulation or with a single antibody only served as controls. Washed samples were fixed and subjected to flow cytometric analysis employing an Attune NxT flow cytometer (Thermo Fisher) The resulting data were processed by FlowJo software following the displayed gating strategy.

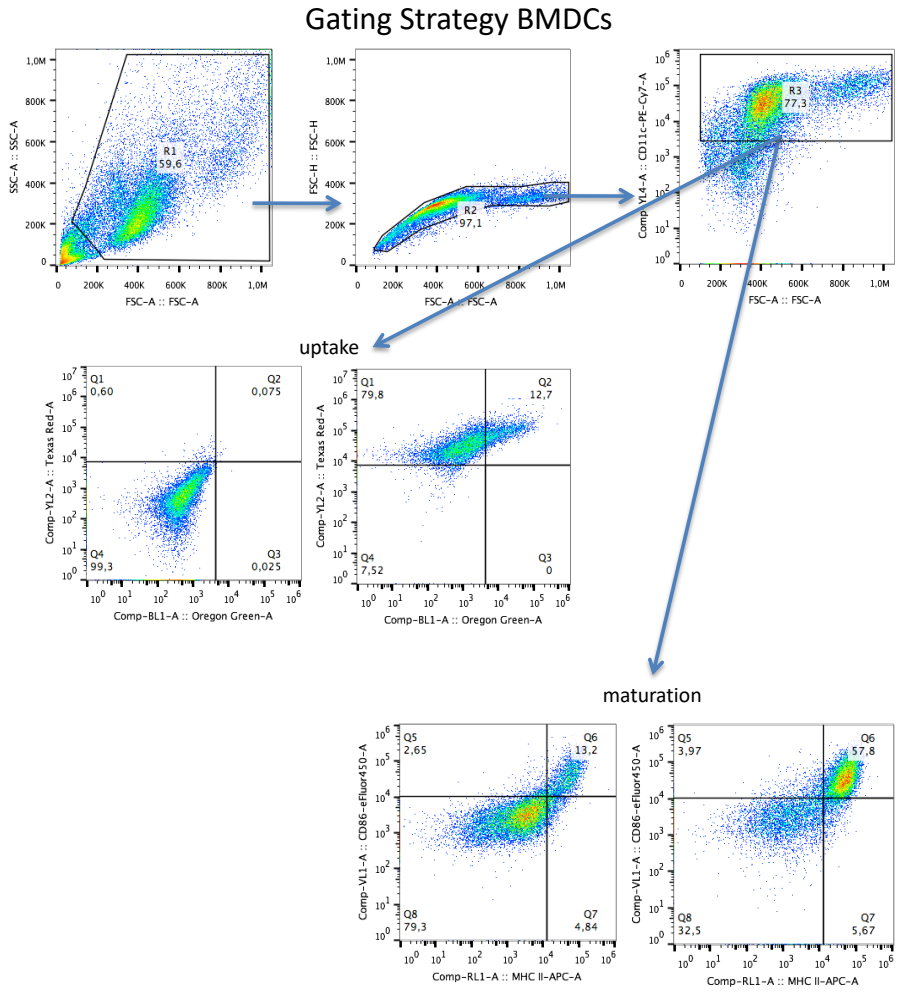

Figure S39: Gating strategy for flow cytometry analysis of uptake of different IMDQ-nanogel formulations and immune cell maturation by BMDCs.

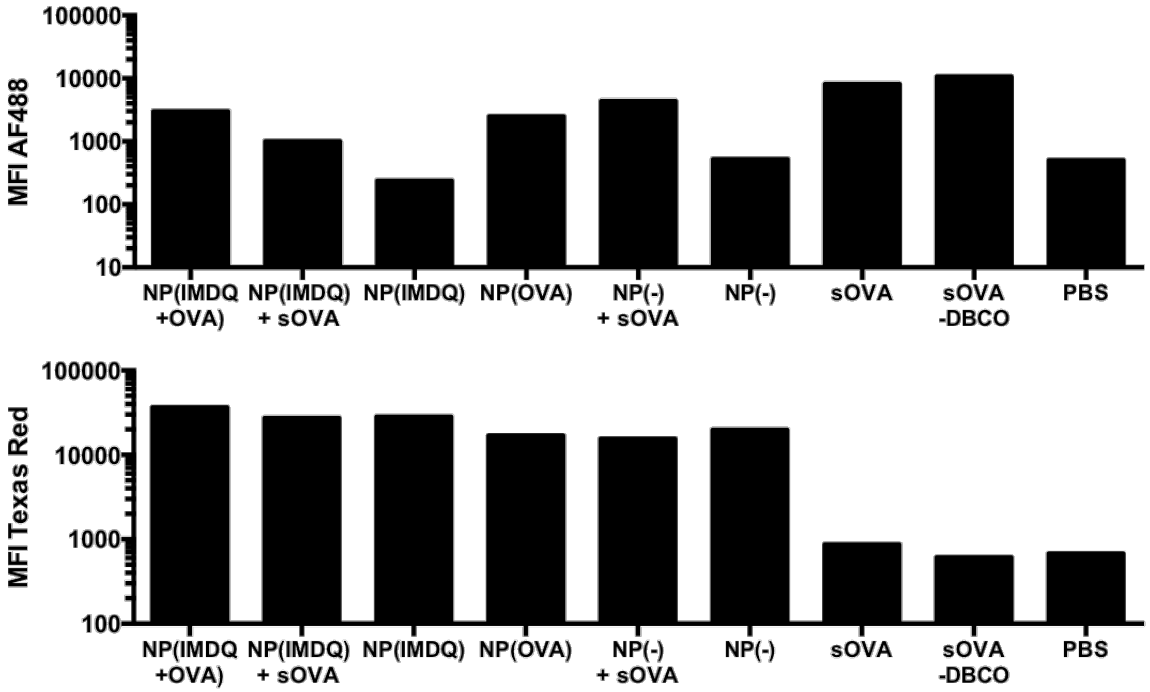

Figure S40: Results of mean fluorescence intensity (MFI) from the flow cytometry analysis of the uptake different IMDQ-nanogel formulations and ovalbumin by BMDCs.

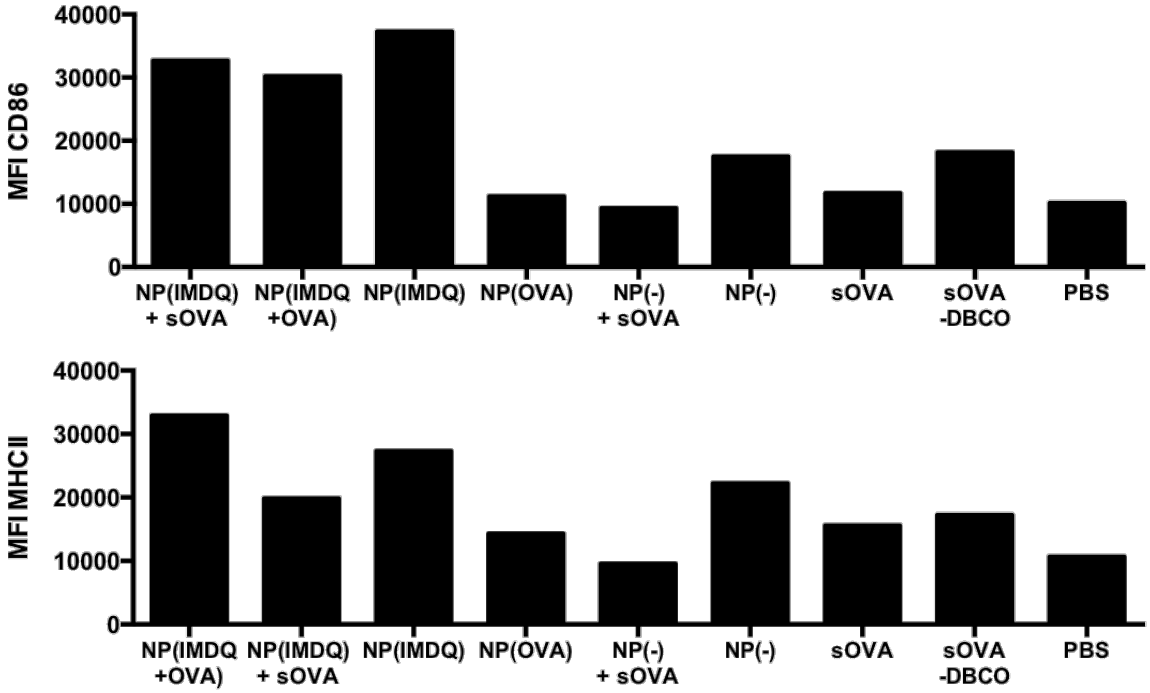

Figure S41: Results of mean fluorescence intensity (MFI) from the flow cytometry analysis of the maturation of BMDCs by different IMDQ-nanogel formulations and ovalbumin.

T-cell proliferation and cytokine assay

Differentially pretreated BMDCs were harvested and reseeded in triplicates into 96-well plates (10^5/mL; 100 µl/well) and were serially diluted. OVA peptide-specific splenic $CD8^+$ T cells from OT-I mice (https://www.ncbi.nlm.nih.gov/pubmed/10762410) and $CD4^+$ T cells from OT-II mice (https://www.ncbi.nlm.nih.gov/pubmed/9553774) were isolated by negative immunomagnetic enrichment (Miltenyi, Bergisch-Gladbach, Germany). Isolated T cells ($5x10^5$/mL; each 100 µl) were added to diluted BMDC. Aliquots of cell culture supernatants were taken on day 1, 2 and 3 and stored at -20 ºC. Then they were analyzed by a cytometric bead array according to the manufacturer (BD, Cytometric Bead Array Soluble Protein Flex Set – beads were measured with a Attune NxT flow cytometer, Thermo Fisher). On day 3, 3H-thymidine (0.5 µCi/well) was added for the last 16-18 h of coculture. Afterwards, cells were harvested onto glass fiber filters, and retained radioactivity was quantified in a microplate scintillation counter (1450 MicroBeta Trilux; Perkin Elmer, Waltham, MA). All samples were run in triplicate (n = 3).

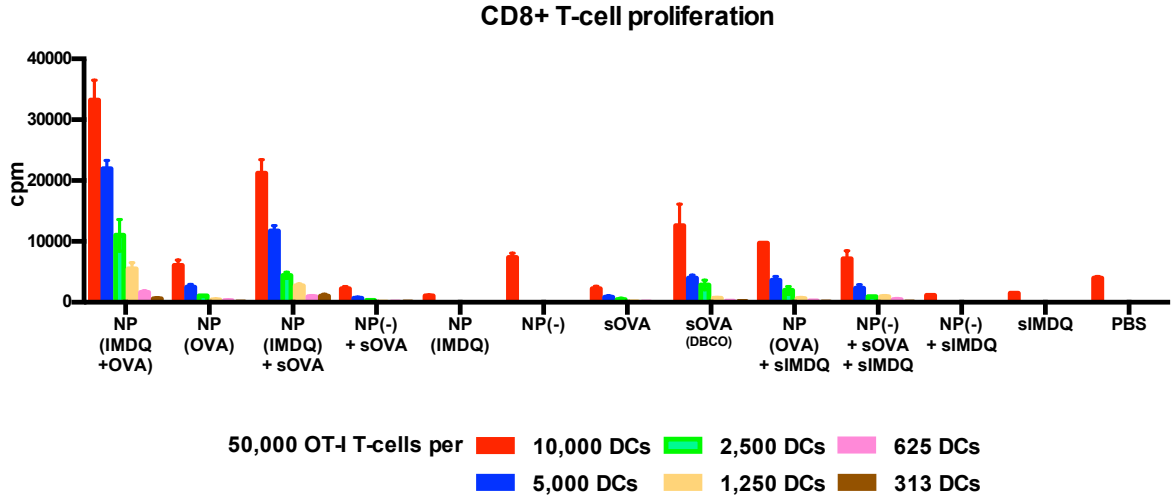

Figure S42: $CD8^+$ specific T-cell proliferation derived from OT-I T cells incubated with serial dilutions of BMDCs pulsed with nanogel samples loaded with IMDQ and/ or OVA as well as respective control samples of nanogels with soluble compounds.

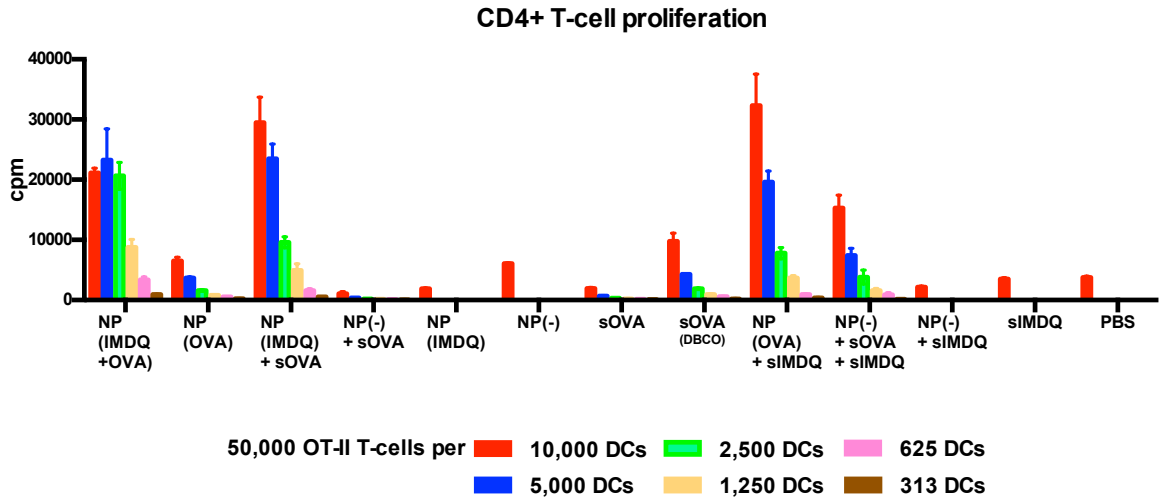

Figure S43: $CD4^+$ specific T-cell proliferation derived from OT-II T cells incubated with serial dilutions of BMDCs pulsed with nanogel samples loaded with IMDQ and/ or OVA as well as respective control samples of nanogels with soluble compounds.

Internalization and inhibition of NP(IMDQ+OVA-FITC) and sOVA by dendritic cells

For internalization experiments, 1 x 10^6 DC2.4 cells were incubated with NP(IMDQ+OVA) at a dilution of 1:150 in the presence of 2 % mouse serum for 30 min at 37°C after 1h starvation in serum-free X-VIVO medium. For inhibition experiments, 300 µg/mL Fucoidan (Sigma) was added. Analysis of the internalized NP by DC2.4 cells was performed using an Amnis ImageStream Mk II flow cytometer (Luminex) at the Core Facility of the Research Center for Immunotherapy (University Medical Center, Johannes Gutenberg-University Mainz). Data were evaluated using the IDEAS software (Luminex). Dead cells were gated out using DAPI (Thermo Fisher Scientific) at a dilution of 1:10,000.

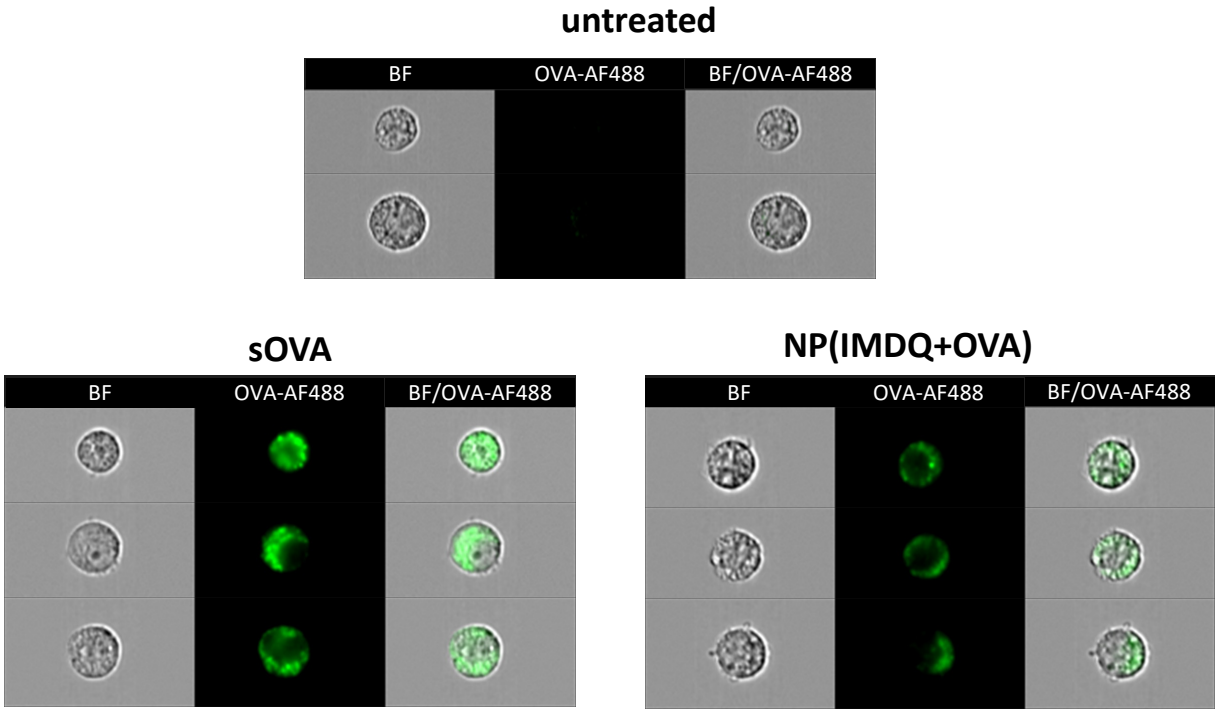

Figure S44: Results of imaging flow cytometry of DCs incubated with sOVA and OVA-conjugated IMDQ-nanogel formulations. ImageStream recorded images of bright field (BF), Alexa Fluor 488 derived OVA fluorescence and overlay of untreated DC2.4 or incubated with sOVA and NP(OVA+IMDQ) (magnification 40x).

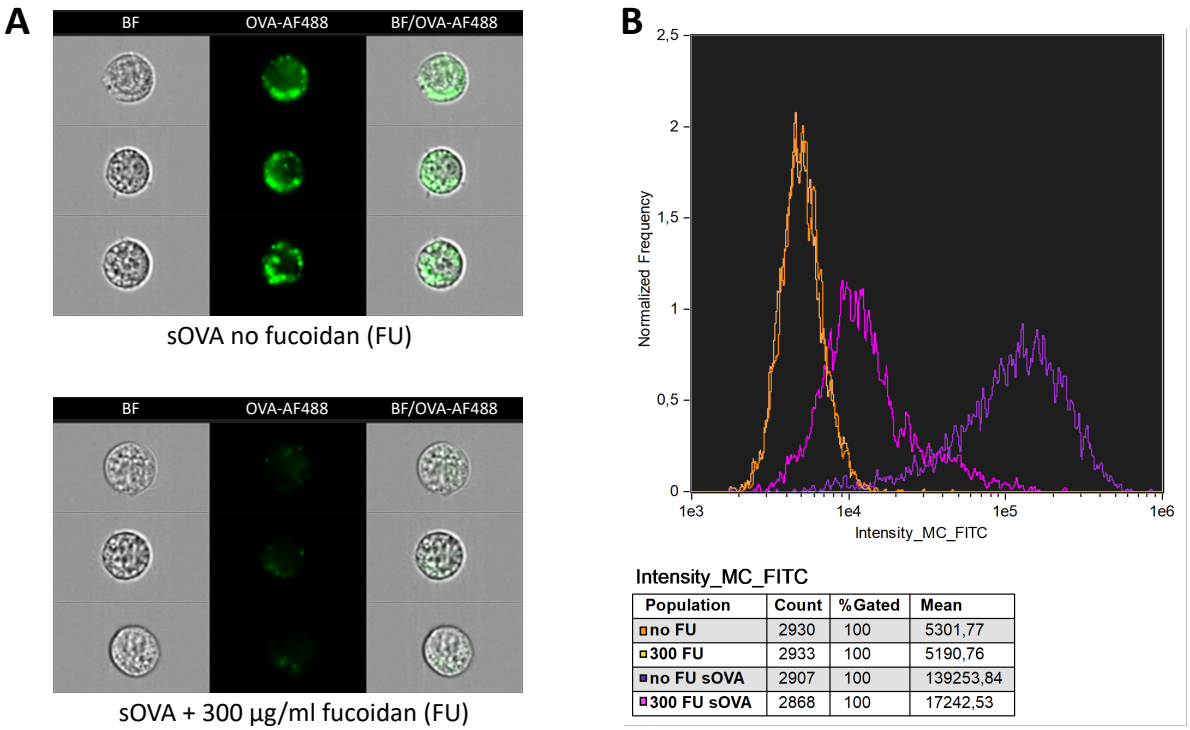

Figure S45: Results of imaging flow cytometry of DCs incubated with sOVA with and without 300 µg/mL fucoidan (FU). (A) ImageStream recorded images of bright field (BF), Alexa Fluor 488 derived OVA fluorescence and overlay (magnification 40x). (B) Derived histogram for the samples with and without 300 µg/mL fucoidan (FU).

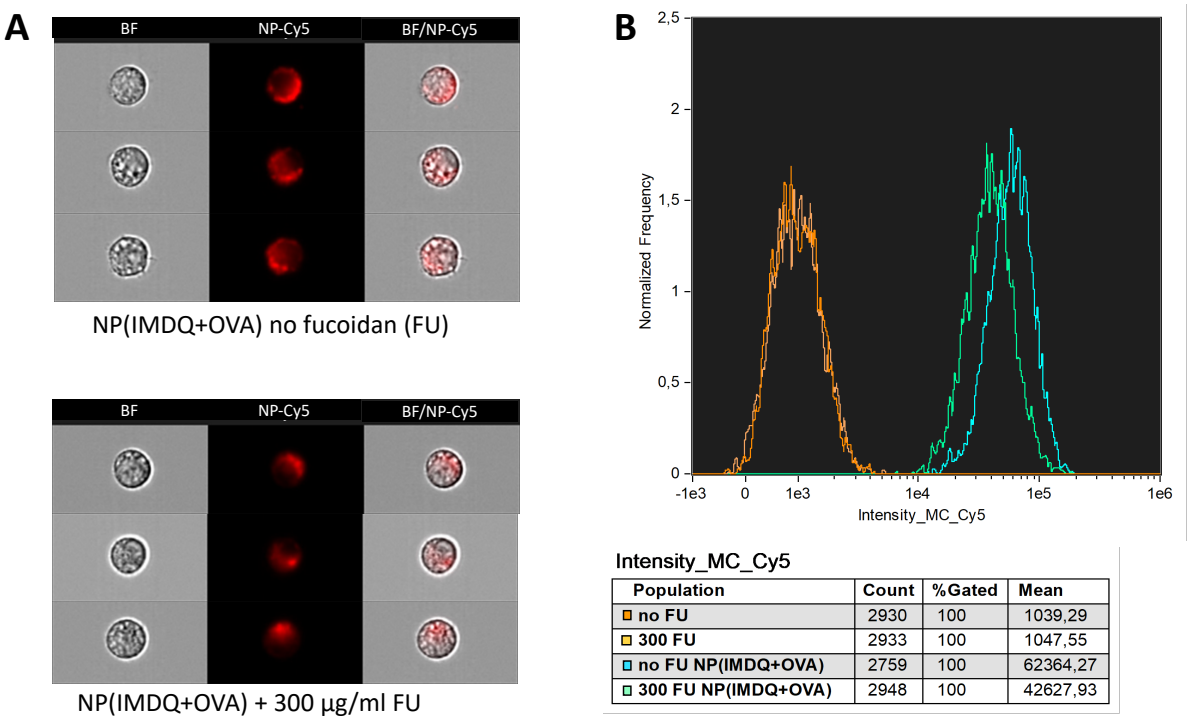

Figure S46: Results of imaging flow cytometry of DCs incubated with NP(IMDQ+OVA) with and without 300 µg/mL fucoidan (FU). (A) ImageStream recorded images of bright field (BF), Cy5 derived NP fluorescence and overlay (magnification 40x). (B) Derived histogram for the samples with and without 300 µg/mL fucoidan (FU).

In vivo toxicity assay

To analyse the *in vivo* tolerance of the used nanoparticles, we immunized the mice intravenously (i.v.) with 100 µl of nanoparticles or soluble TLR agonist (corresponding to 10 µg of IMDQ, or 30 µg OVA) and took blood samples at 4, 8 and 24 h. After 48 h mice were sacrificed and blood was taken again. At each time point blood samples were analyzed on a scil Vet^{abc} Animal Blood Counter for parameters like numbers of white and red blood cells and platelets as indicators for homological toxicities (n=3).

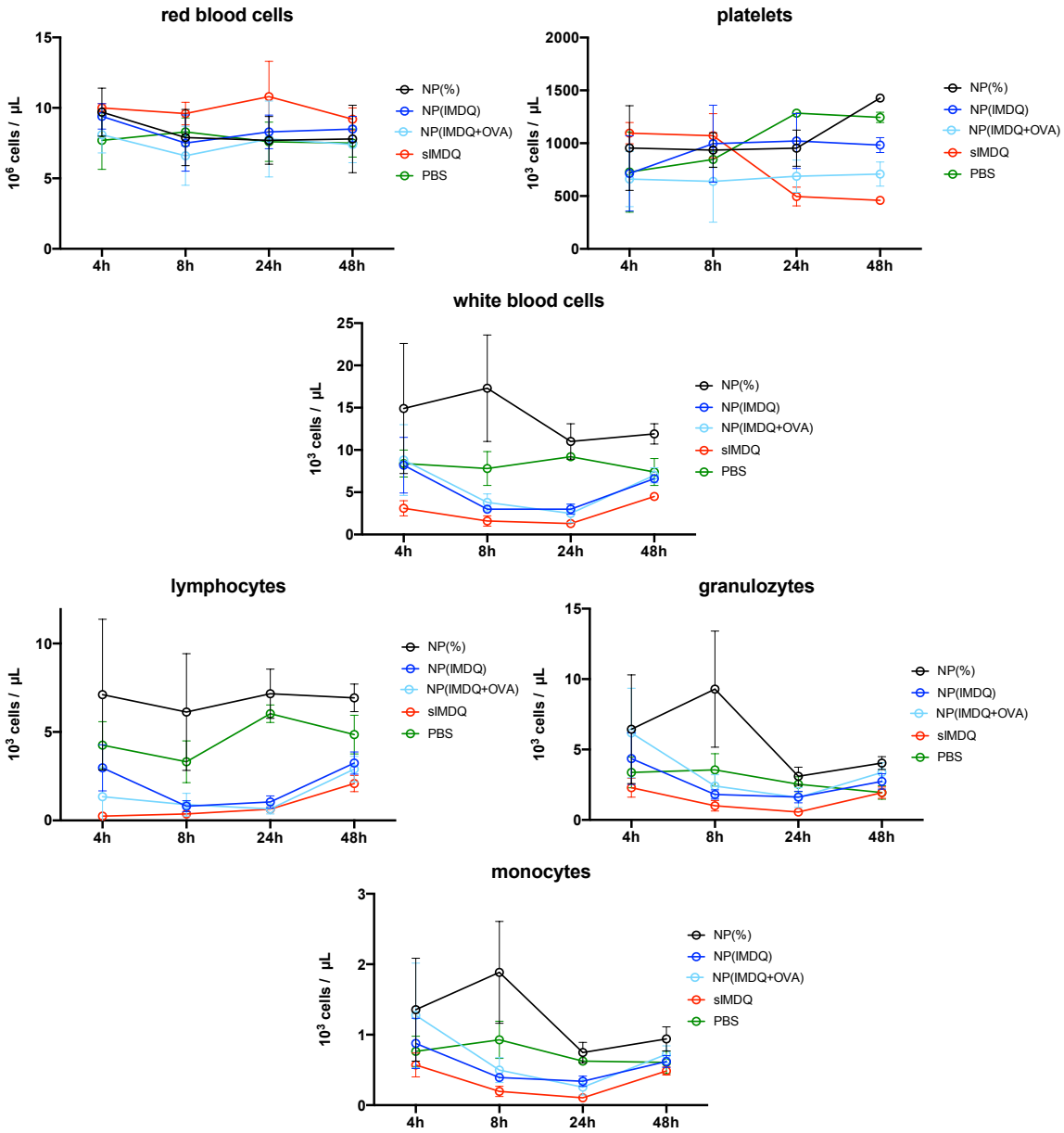

Figure S47: Hematologic toxicity analysis of empty nanogels, IMDQ-loaded nanogels, IMDQ- and OVA-loaded nanogels versus soluble IMDQ after single i.v. injection. While no effect was found on red blood cells, platelets are significantly most reduced sIMDQ. Same is found for white blood cells including lymphocytes, granulocytes and monocytes.

Biodistribution of IMDQ-loaded nanogels (IVIS + FACS)

To analyse the *in vivo* biodistribution of the used nanoparticles, BALB/c mice were injected intravenously via the tail vain with 100 µl of Cy5 labeled nanoparticles conjugated or mixed with OVA (NP(IMDQ+OVA) or NP(IMDQ)+sOVA) as well as a mixture of soluble TLR agonist with sOVA in PBS (n=3). For each sample a dose corresponding to 10 µg of IMDQ or 30 µg OVA was used. After 24 h, blood was taken from these mice by heart punction and analyzed for cytokine production as well as liver parameters with respect to liver related toxicities. Afterwards, organs were dissected and imaged by an IVIS Spectrum Imaging CT system (excitation/emission: 633/647nm; Caliper Life Sciences, Waltham, MA) in order to localize the distribution of the Cy5-labeled nanogels. Regions of interest (ROI) were drawn and mean fluorescence signal was measured within these ROIs for semi-quantitative analysis of the biodistribution (fluorescence intensities are presented as total radiant efficiency ([p/s]/[µW/cm^2]; attention should be drawn to the fact that quantification of Cy5 signal is restricted and can only be used for indicative comparison). From liver and spleen, single cell suspensions were prepared following standard protocols (liver non-parenchymal cells (NPC) were obtained by enzymatic/mechanical digestion (Liver Dissociation Kit; Miltenyi Biotec, Bergisch-Gladbach, Germany); spleen cell suspensions were generated by mechanical dissociation of the according organs).

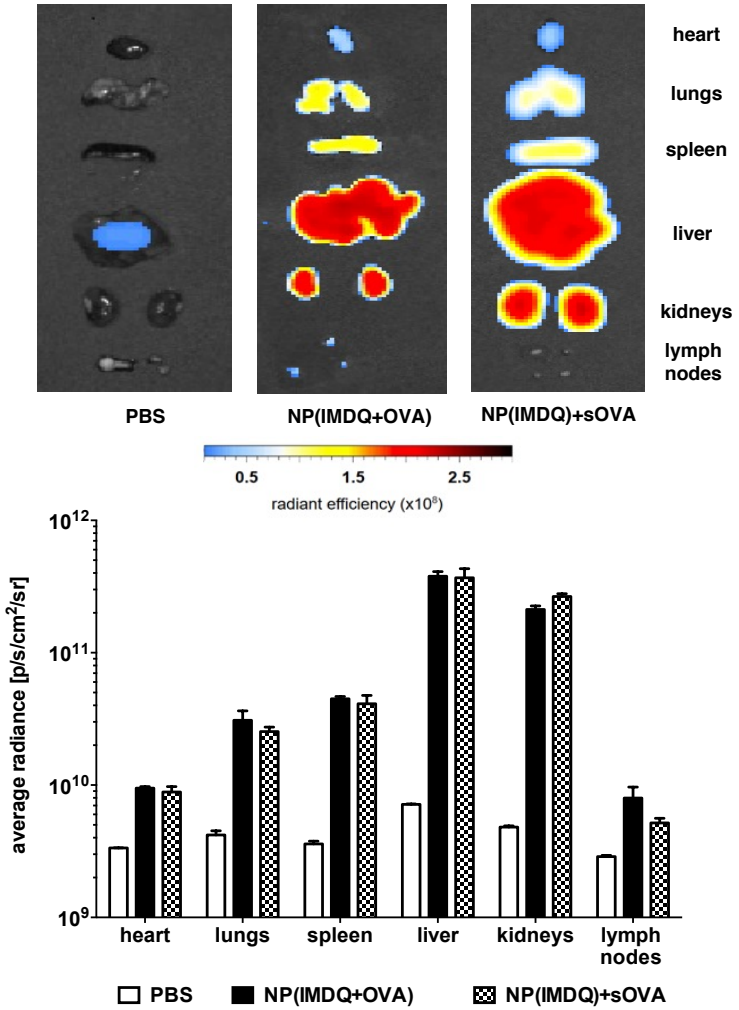

Figure S48: Biodistribution of IMDQ-loaded nanogels after i.v. injection. (A) Evaluation of organ-specific accumulation of IMDQ-loaded Cy5-labeled nanogels 24 h after i.v. injection. (B) Quantification of organ-specific accumulation of Cy5-labeled nanogels.

Liver enzyme activity

Blood that was retrieved by heart puncture was used for determining the serum contents for aspartate aminotransferase (AST), alanine aminotransferase (ALT), alkaline phosphatase (ALP), L-lactate dehydrogenase (LDH) and blood urea by nitrogen content (BUN). The parameters were measured by the central laboratory of the University Medical Center of Mainz.

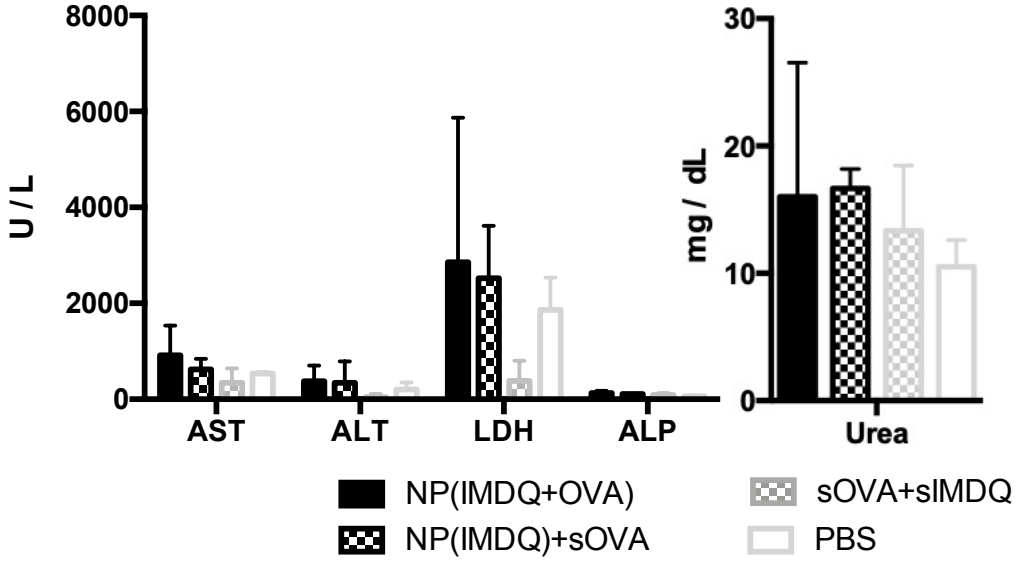

Figure S49: Liver toxicity parameters of IMDQ-loaded nanogels from blood 24h after i.v. injection. Note that the large variation of LDH activity is related to some hemolytic blood samples.

For additional insights into the immediate immune response, experiments were repeated and blood samples were collected 4 h and 24 h after i.v. injection of NP(IMDQ+OVA) or sIMDQ+sOVA. Again, liver enzyme parameter swere measured by the central laboratory of the University Medical Center of Mainz.

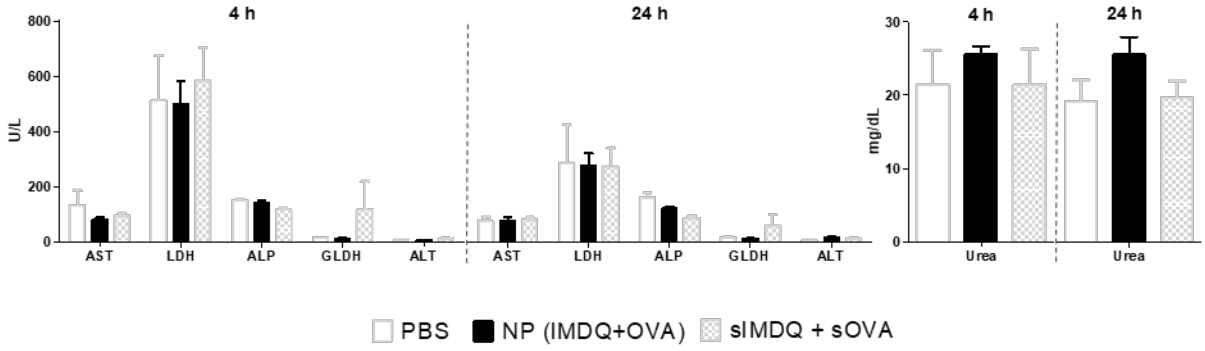

Figure S50: Liver toxicity parameters of IMDQ-loaded nanogels from blood 4 h and 24h after i.v. injection.

Cytokine analysis by cytometric bead array

Cytokine concentrations were determined by cytometric bead array (CBA; BD Biosciences, San Jose, CA) as recommended by the manufacturer. For this, bead populations with distinct fluorescence intensities were conjugated with cytokine-specific capture antibodies. Recombinant cytokines were used to prepare standard dilutions. Samples were mixed with capture beads, subsequently incubated with PE-conjugated detection antibodies for 1 h (all at room temperature in the dark) and subjected to flow cytometric analysis. Results were analyzed using FCAP Array Analysis Software v.1.0.1 (BD Biosciences).

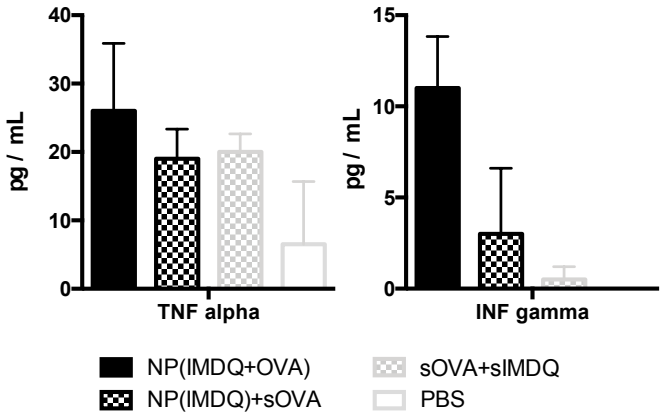

Figure S51: Cytokine parameters of IMDQ-loaded nanogels from blood 24h after i.v. injection.

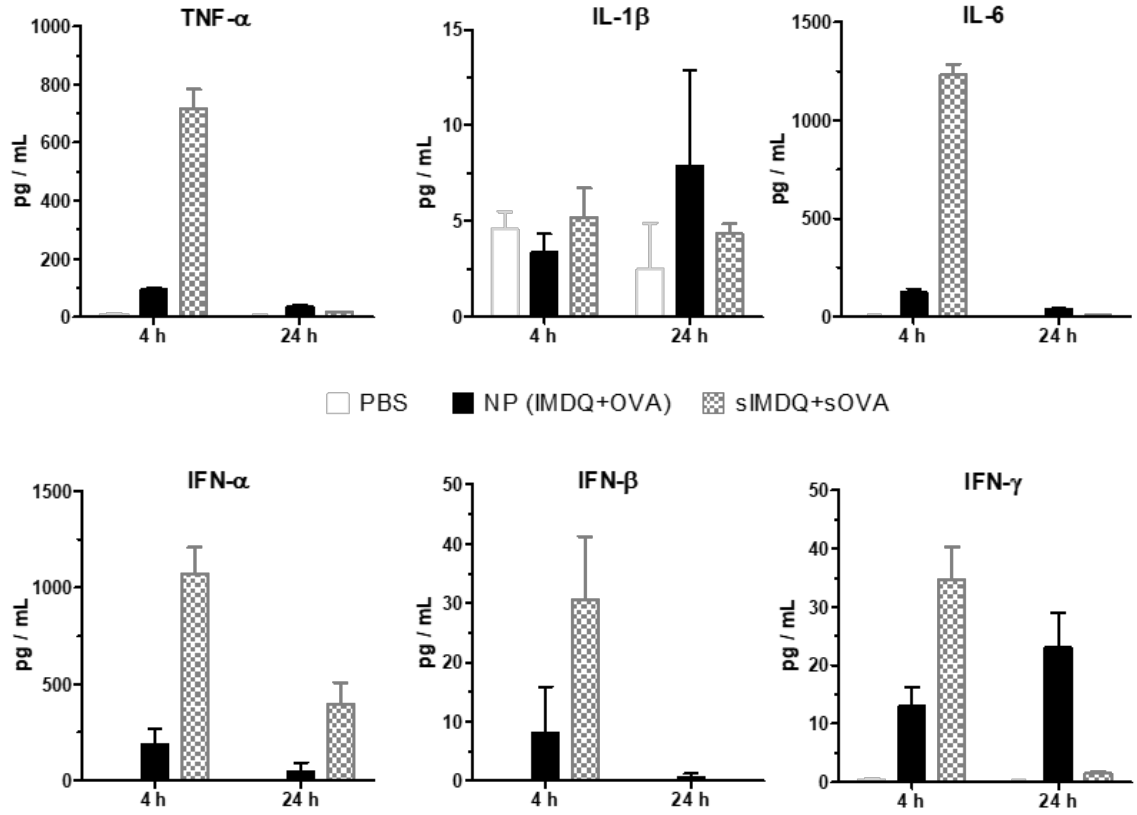

Figure S52: Cytokine parameters of IMDQ-loaded nanogels from blood 4 h and 24 h after i.v. injection measured by CBA.

Histopathological analysis by HE staining

Mice were injected with 100 ul either NP(IMDQ+OVA) or sIMDQ+sOVA, each containing 10 µg IMDQ and 30 µg OVA, i.v. in the tail vain. For histopathological analysis inner organs of mice (namely: heart, lungs, liver, spleen and kidneys) were retrieved after 24 h, paraffin-embedded blocks were prepared, and derived tissue sections (3 µm) were stained with haematoxylin & eosin (H&E) to assess inflammatory responses and tissue injury. To this end, H&E-stained tissue sections were examined by microscopy in a blinded fashion by an independent pathologist using a scoring system that quantifies the degree of tissue inflammation or tissue injury (0–3). In general, three randomly selected areas on each slide were analyzed with an Axioscope 5 equipped with a Axiocam 208 (Zeiss, Jena, Germany).

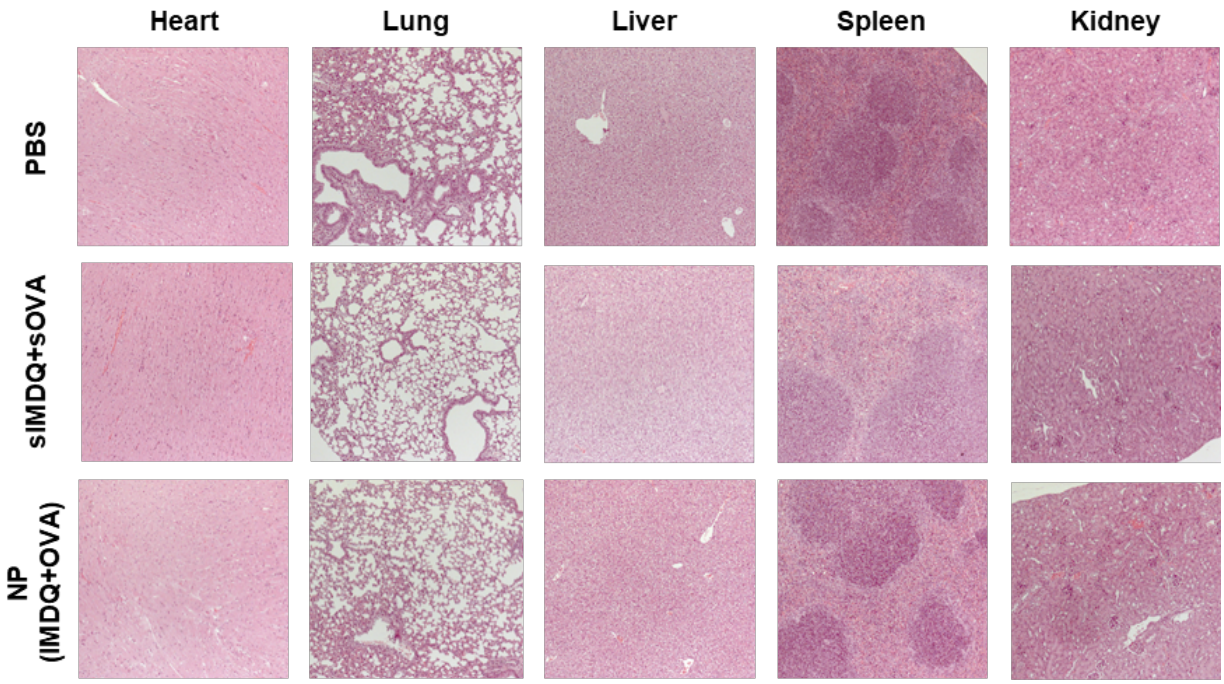

Figure S53: Histological analysis of various tissues by HE staining after iv injection of IMDQ- and OVA-containing formulations. No histological anomalies were observable for both samples.

Flow cytometry of liver and spleen cells

Liver and spleen single cell suspensions were incubated first with a rat anti-mouse CD16/CD32 (Fc-block) antibody (15 min, 4 °C) and washed with 2% FBS in PBS.
For analyzing liver non-parenchymal cells (NPC), they were further incubated for 20 min at 4 °C with antibodies specific for CD45 (BV711), CD32b (PE), CD11c (PE-Cy7), MHC-II (eFluor610, CD86 (eFluor450) and F4/80 (eFluor506).
For analyzing spleen cells, they were further incubated for 20 min at 4 °C with specific antibodies for CD3 (eFluor5069, CD19 (Super Bright 702), CD11b (Super Bright 600), CD11c (Brilliant Violet 421), MHC-II (PE), CD86 (PE-Cy7), Ly6G (eFluor610) and F4/80 (eFluor506).
All antibodies were obtained Thermo Fisher (Waltham, MA). After antibody incubation, samples were incubated with fixable viability dye (FVD) APC-eFluor780 (Thermo Fisher) to exclude dead cells. Washed samples were fixed with 0.7% PFA and subjected to flow cytometric analysis employing an Attune NxT flow cytometer (Thermo Fisher). The resulting data were processed by FlowJo software following the displayed gating strategy.

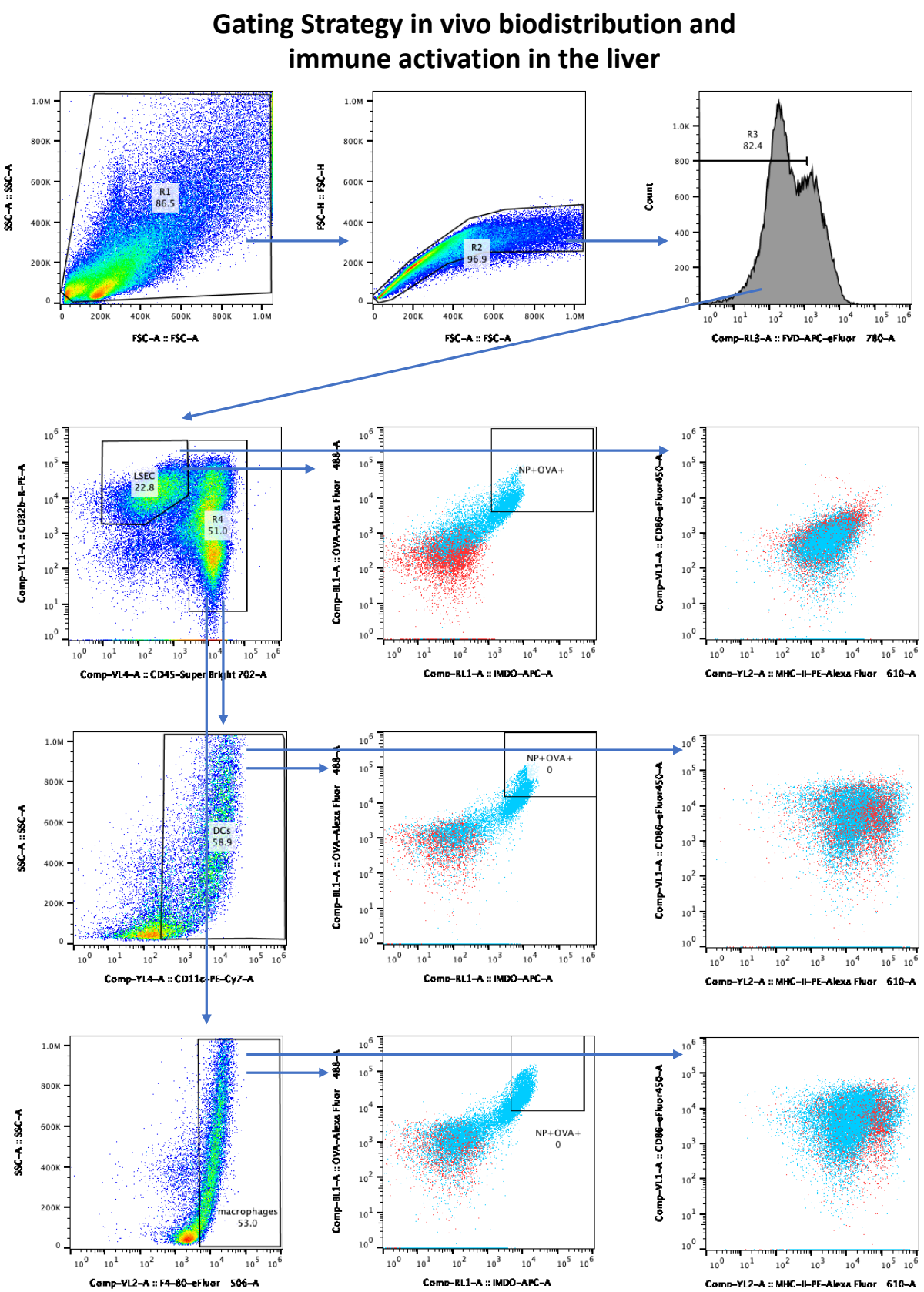

Figure S54: Gating strategy for flow cytometry analysis of liver single cell suspensions after 24 h treatment with NP(IMDQ+OVA), NP(IMDQ)+sOVA, sOVA+sIMDQ or PBS (n = 3).

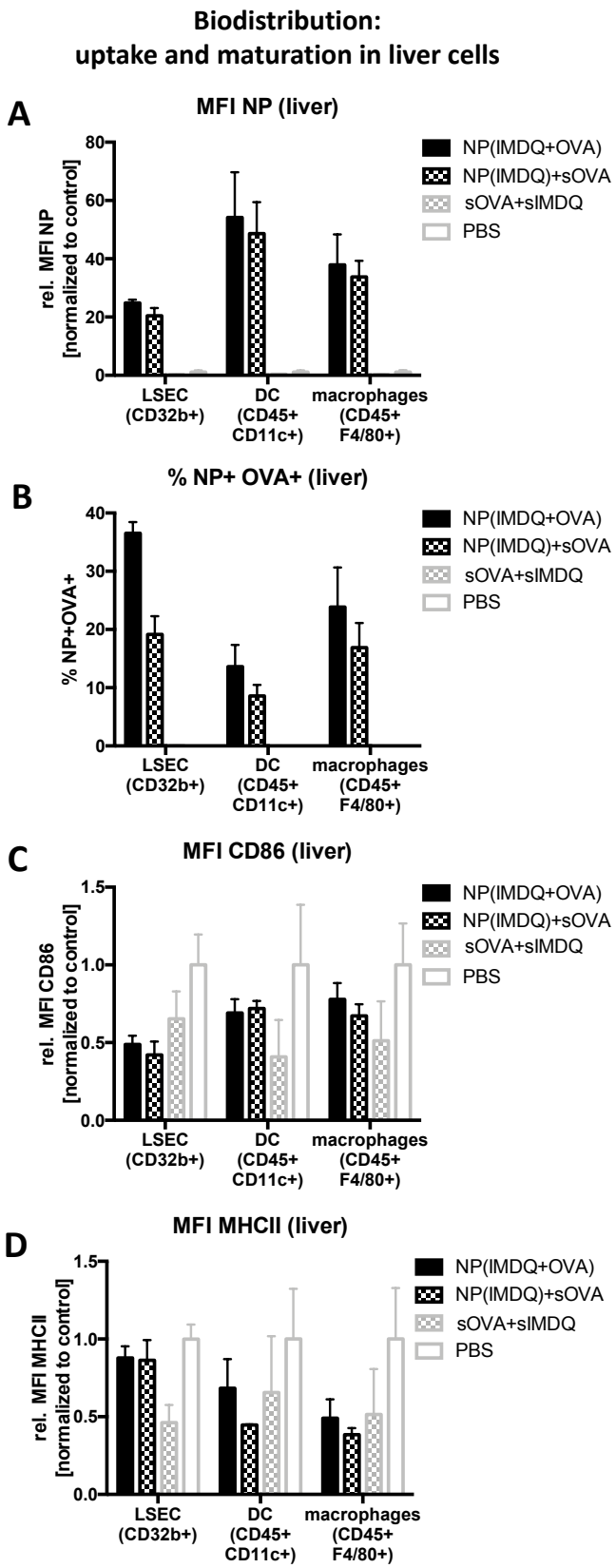

Figure S55: Results of particle uptake (A, relative MFI of Cy5-labeled nanogels in the corresponding liver associated immune cells and liver sinusoidal endothelial cells LSEC in relation to PBS treated cells), antigen co-delivery (B, Cy5-NP$^+$ and AF488-OVA$^+$), as well as relative mean fluorescence intensity (MFI) values of the maturation markers CD86 (C) and MHC-II (D) in relation to PBS treated mice. Note that particles can be found mostly in DCs and macrophages as antigen-presenting cells. A co-delivery of the antigen OVA works best for the covalent conjugate NP(IMDQ+OVA). However, none of the maturation markers CD86 and MHC-II can be upregulated compared to the PBS control, probably because of the immunosuppressive microenvironment in the liver.

Gating Strategy in vivo biodistribution and immune activation in the spleen

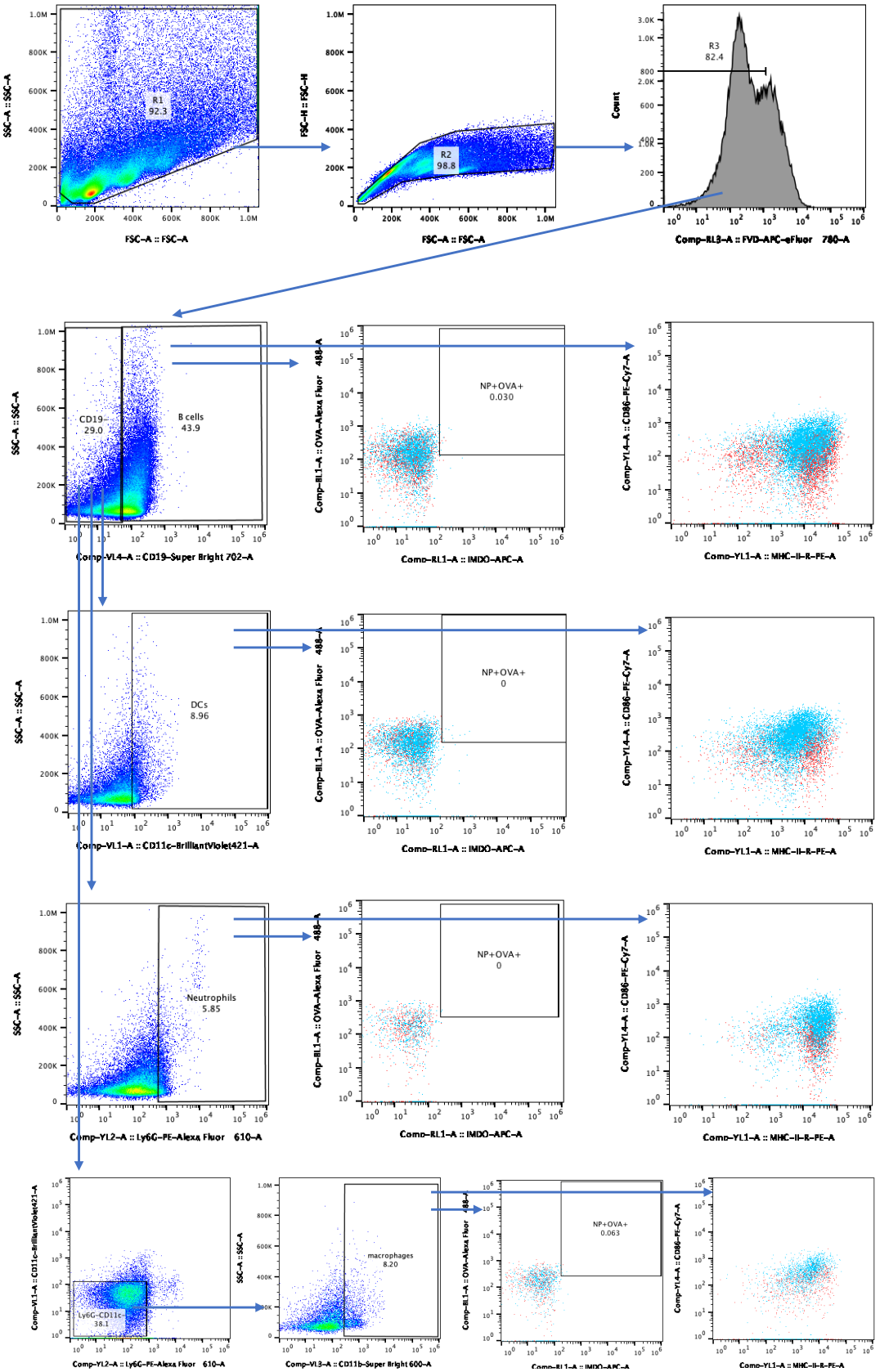

Figure S56: Gating strategy for flow cytometry analysis of spleen single cell suspensions after 24 h treatment with NP(IMDQ+OVA), NP(IMDQ)+sOVA, sOVA+sIMDQ or PBS (n = 3).

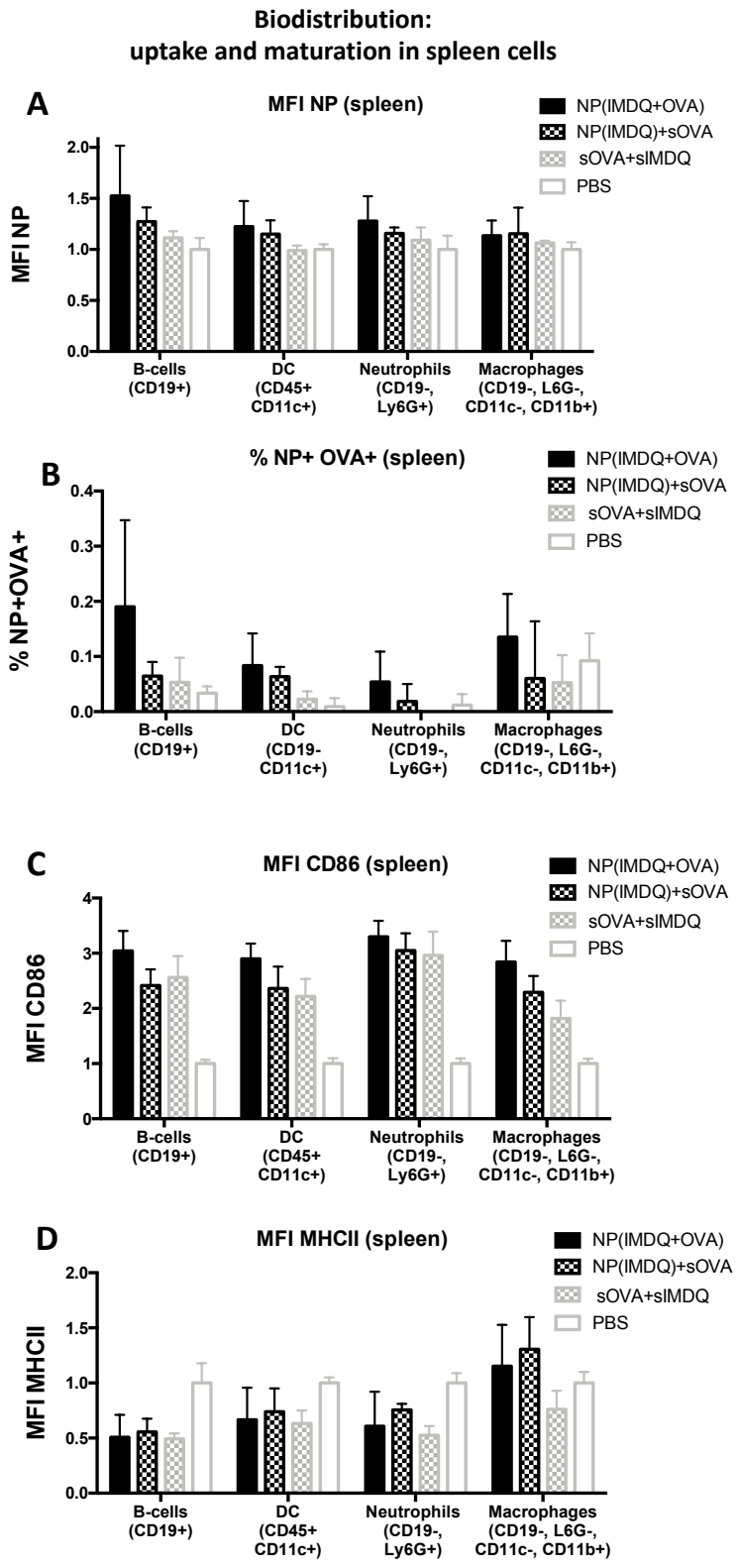

Figure S57: Results of particle uptake (A, relative MFI of Cy5-labeled nanogels in the corresponding antigen-presenting immune cells (APCs) in the spleen in relation to PBS treated cells), antigen co-delivery (B, Cy5-NP$^+$ and AF488-OVA$^+$), as well as relative mean fluorescence intensity (MFI) values of the maturation markers CD86 (C) and MHC-II (D) in relation to PBS treated mice. Note that in analogy to the ex vivo experiments with splenocytes (Fig. S33 – S37) particles can be found mostly B-cells. A co-delivery of the antigen OVA works best for the covalent conjugate NP(IMDQ+OVA) into all spleen-associated APCs. Moreover, particle-bound IMDQ yields also the highest expression levels of the maturation maker CD86 – only the relative MFI values for MHC-II are again not very reliable, which is in accordance with Fig. S36 for the ex vivo experiments and may be related to the relatively high basal levels in the PBS control samples due to the applied splenic isolation conditions.

Immunization experiments

For immunization, 100 µl of nanoparticles (120 µg of nanoparticle, 10 µg IMDQ and 30 µg OVA respectively) were injected i.v. into the tail vein of the mice (n=3 for wild type mice and n=2 for *TLR7*$^{-/-}$ mice). 14 days later, the immunization was repeated the same way ("boost"). Mice were sacrificed on day 26 to analyse antibody titres in the blood and cytotoxic T cells in the spleen. The respective control groups received 100 µl PBS or unfunctionalized nanoparticles (NP(%)).

For a comparison of administration routes, nanoparticles were injected either s.c. or i.v. into the tail vein of mice as described before. Again, antibody titres were determined from blood by ELISA and T cells in the spleen by ELISpot analysis. In addition, body weight of mice was recorded each 3-4 days.

ELISA analysis

ELISA analyses were performed using sera from immunized mice before and after immunization with different kinds of nanoparticles. In brief, 96-well plates were coated with 25 mg/mL OVA at 4 °C over night. After blocking the 96-well plate, the serum was added 1:100 in the first well and titrated serially 1:2 over the plate. After 1 hour of incubation at 37 °C, detection of OVA-specific antibody production was performed using anti-IgG1-HRP, anti-IgG2a-HRP and anti-IgM-HRP antibodies (all received from Abcam, Cambridge, United Kingdom), which were incubated for 30 min at 37 °C. After washing the plate, 5 mg/mL ABTS was added and after 10 – 15 min of incubation at room temperature, the absorbance was measured at 410 nm. As a positive control, an anti-OVA-HRP antibody (Sigma Aldrich, St. Louis, Missouri, United States) was used.

ELISpot analysis

96-well plates (MultiScreenHTS IP, 0.45 mm, Merck Millipore, Darmstadt, Germany) were coated with 10 µg/mL of anti-IFNγ antibody (clone AN18, Mabtech, Nacka Strand, Sweden) at 4 °C over night. After blocking the plate, splenocytes were plated. Therefore, mice were sacrificed and the spleen was removed. After isolating the splenocytes by using a cell strainer and lysis of erythrocytes, cells were counted and plated at $5x10^5$ per well. They were restimulated with either 1 µM $OVA_{257-264}$, 1 µM $OVA_{323-337}$ or left untreated and incubated at 37 °C for 20 hours. After washing the plate, 2 mg/mL of a biotinylated anti-IFNγ antibody (clone R4-6A2, Mabtech) was added and incubated for 2 hours at 37 °C. Afterwards Vectastain ABC Kit (Vector Laboratories, Burlingame, USA) / AEC (Sigma-Aldrich, Taufkirchen, Germany)-Complex was added according to manufacturer 's constructions. After spots were visible plates were washed with water and dried overnight. Spot counting was performed on an AID iSpot ELISpot Reader (AID AutoimmunDiagnostika, Straßberg, Germany).

Tetramer and antibody staining

Peripheral blood samples were collected and incubated with the following antibodies: BV421conjugated anti-CD8, APC-conjugated anti-CD44 and FITC-conjugated anti-CD62L (all from eBioscience) after hypotonic lysis. H-$2K^b$-$OVA_{257-264}$-specific T cells were detected by H2-K^b tetramers containing $OVA_{257-264}$ peptides as described.[9] The samples were analyzed by flow cytometry.

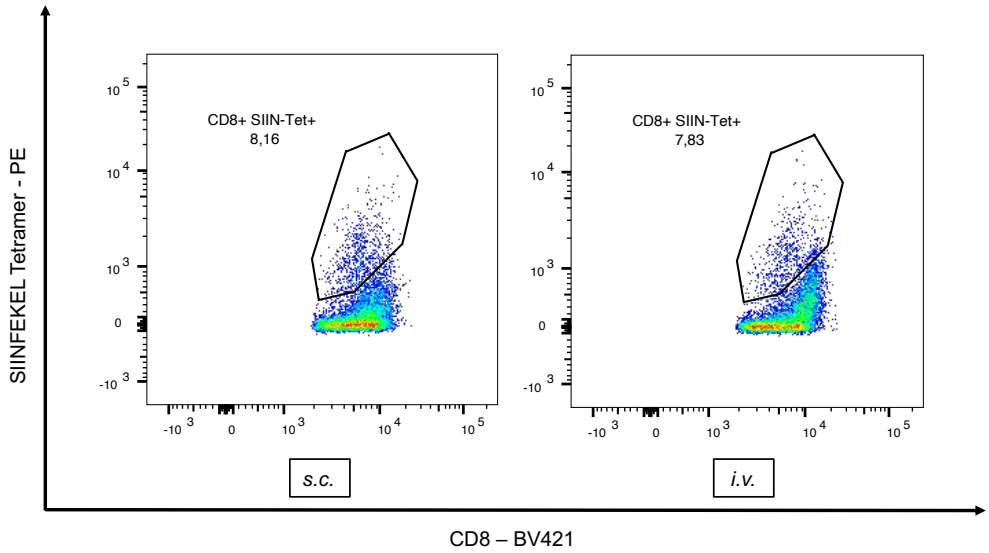

Figure S58: FACS Plots from flow cytometry gated for OVA-specific CD8⁺ T cells in blood after s.c. and i.v. injection of NP(IMDQ+OVA) determined by tetramer staining.

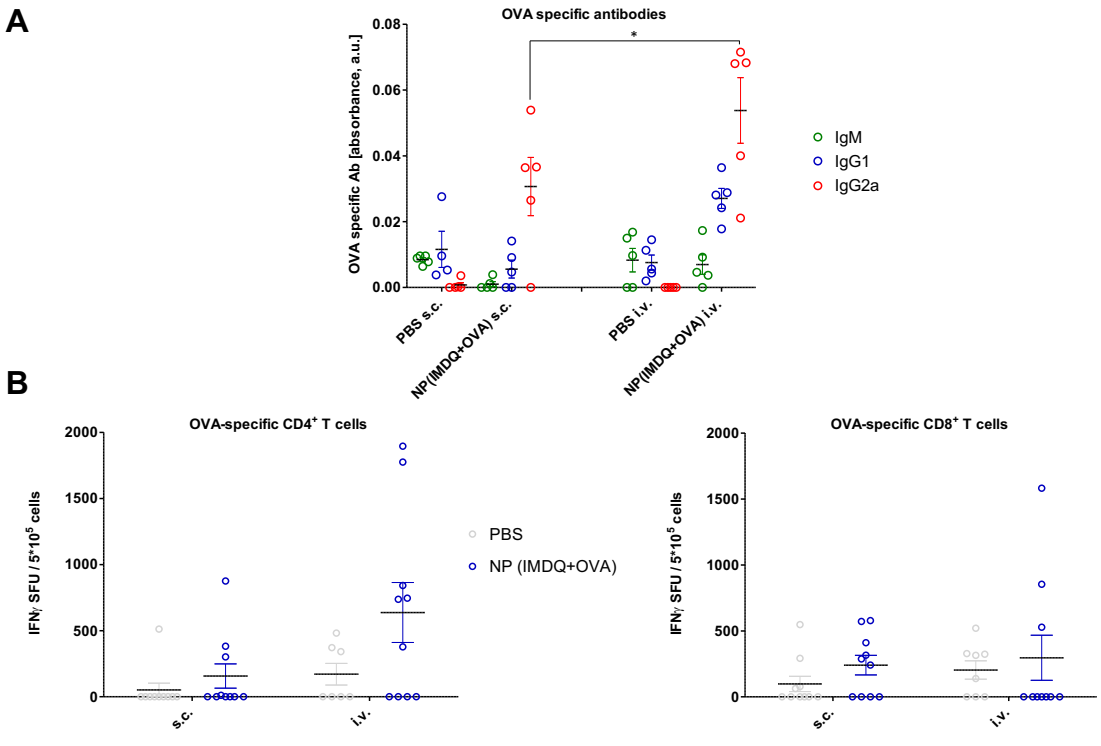

Figure S59: Humoral and cellular immune responses after s.c. and i.v. administration of NP(IMDQ+OVA). A) OVA specific antibodies determined by ELISA of the blood serum, (B) corresponding T cells determined by ELISpot of the isolated spleen cells of mice.

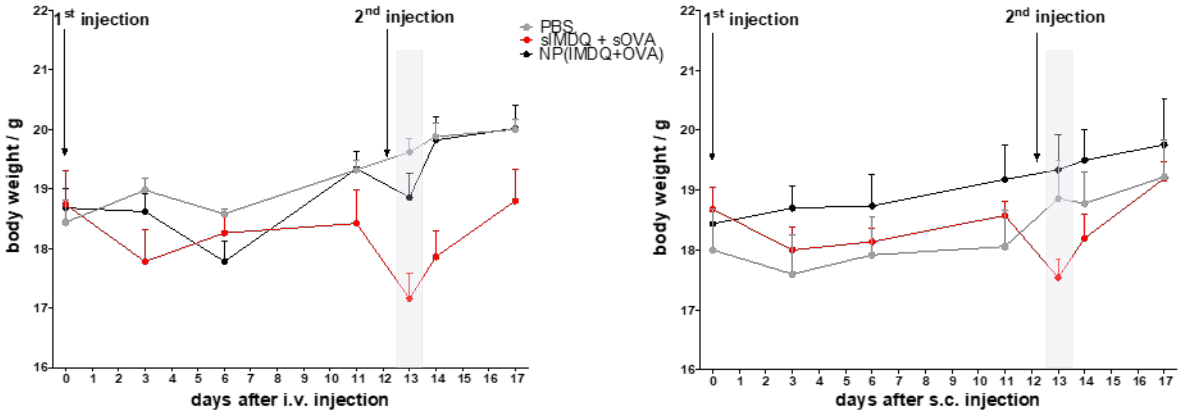

Figure S60: Body weight of wild type mice after i.v. (left) or s.c. (right) administration of IMDQ-containing formulations. Independent of the application route sIMDQ+sOVA lead to a drop in body weight after the boost injection and slower recovery.

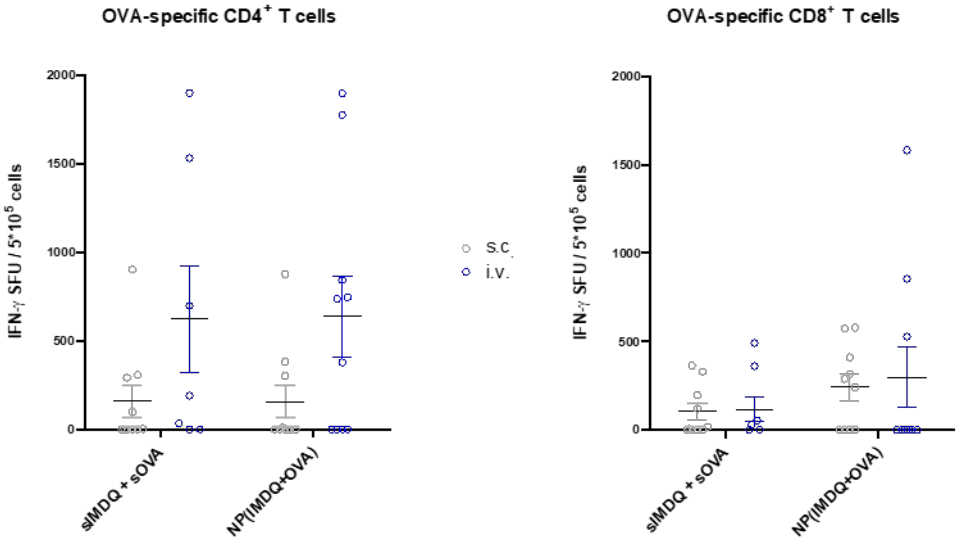

Figure S61: ELISpot analysis of on day 25 isolated spleen cells after i.v. or s.c. injection of sIMDQ+sOVA or NP(IMDQ+OVA).

Surface and cytosolic OVA expressing tumor cell line

To maintain EGFP and OVA expressions, transfected cells were cultured in media containing G418 (400 µg/mL for MC38mOVA, 1000 µg/mL for B16-F10mOVA and B16-F10cOVA).
For surface OVA staining, MC38 cells, MC38 mock-transfected cells expressing only EGFP or MC38mOVA were incubated for 20 min at 4°C with a rabbit polyclonal antibody against OVA (dilution 1:300), which was kindly provided by H.-C. Probst (Institute for Immunology, University Medical Center, Johannes Gutenberg-University Mainz) and K. Schäkel (Department of Dermatology, University Hospital Heidelberg). After secondary antibody staining using a goat anti-rabbit IgG (H+L) conjugated to Alexa Fluor 647 (Thermo Fisher Scientific, dilution 1:500), data were acquired on an Amnis ImageStream Mk II flow cytometer (Luminex) at the Core Facility of the Research Center for Immunotherapy (University Medical Center, Johannes Gutenberg-University Mainz) and analysed using the IDEAS software (Luminex). Dead cells were gated out using DAPI (Thermo Fisher Scientific, dilution 1:10,000).

For recognizing and eliminating OVA-expressing cells by T cells, OT-I transgenic mice were used to generate $CD8^+$ T cells that respond to peptide 257-264 of OVA. Cytotoxicity activity was measured using the CytoTox96 Non-Radioactive Cytotoxicity Assay kit (Promega) and by following the manufacturer´s instructions. In brief, target cells were incubated with varying numbers of effector cells for 4 h, and supernatants were then analysed for lactate dehydrogenase release. The results are expressed as percent specific lysis, calculated as (Experimental release – Spontaneous release)/(Total release – Spontaneous release) x 100%.

In vivo tumor experiments

In therapeutic tumor experiments, 8-12 weeks old mice were subcutaneously (s.c.) inoculated either with $5x10^5$ MC38mOVA cells, B16-F10mOVA cells or $1x10^5$ B16-F10cOVA in 100 µl PBS into the right flank. In each experiment the same number of corresponding parental tumor cells were inoculated as control. On day 3, 5 and 7 after tumor inoculation, 100 µl of nanoparticles or PBS were i.v. injected into the tail vein of the mice. Tumor growth was observed over a time period of 17-19 days. Tumor size was measured every 2-3 days using a caliber and tumor volume was calculated by the formula $width^2$ x length x 0,5. Mice were sacrificed when the tumor volume reached more than $600mm^3$ or when there was external necrosis.
In a prophylactic tumor model, the mice first received 100 µl of nanoparticles i.v. into the tail vein on day 0 and day 14 and the tumor cells were inoculated on day 23. From now on, the experimental procedure was the same as described for the therapeutic tumor models.

ELISA, ELISpot and cytokine analysis of tumor bearing mice

ELISA and cytokine analysis of the B16-F10 in vivo tumor experiments were performed with blood sera from mice on day -1 (so before tumor inoculation and treatment with the nanogel) and day 13 after tumor inoculation. For ELISA, same protocols were followed as described above, while for cytokine analysis they were determined by cytometric bead assay according to the manufacturer (BD, Cytometric Bead Array Soluble Protein Flex Set). Diluted samples (1:4) were measured with a Attune NxT flow cytometer (Thermo Fisher) and analyzed after filtering with the FCAP FCS filter v.1.0.4.@2005-2008, soft flow with the FCAP Array software v.1.0.1.@2006, soft flow. For ELISpot analysis, splenocytes were isolated from the mice on day 13 after tumor inoculation and analyzed by the protocols described above.

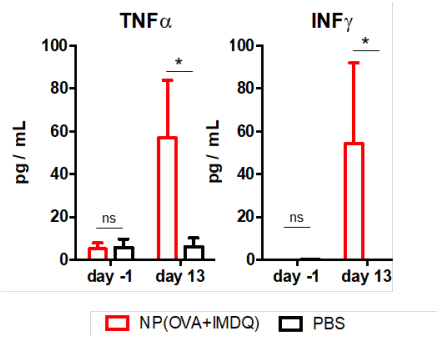

Figure S62: Cytokine analysis of blood serum samples taken on day -1 and day 13 after tumor inoculation from B16-F10mOVA bearing mice treated with NP(IMDQ+OVA) or PBS.

Flow cytometry of tumor cells

From MC38mOVA tumors treated with PBS or NP(IMDQ+OVA), cell suspensions were prepared following standard protocols, then transferred into sterile FACS tubes and incubated first with a rat anti-mouse CD16/CD32 (Fc-block) antibody (15 min, 4 °C). For analyzing myeloid cells, they were further incubated for 20 min at 4 °C with antibodies specific for CD45 (BV421), CD11c (PE-Cy7), CD11b (PE), MHC-II (BV510), Gr-1 (AF488) and F4/80 (APC-A). For T-cell analysis, they were incubated with antibodies specific for CD45 (BV421), TCR

(PE-Cy5), CD4 (BV711) or CD8 (BV510). All antibodies were obtained from BioLegend (San Diego, CA) or Thermo Fisher (Waltham, MA). After antibody incubation, samples were incubated with fixable viability dye (FVD) APC-Cy7 (Thermo Fisher) to exclude dead cells. Washed samples were fixed and subjected to flow cytometric analysis employing an Attune NxT flow cytometer (Thermo Fisher). The resulting data were processed by FACSDiva V6.0 software following the displayed gating strategy. All samples were run at n = 6.

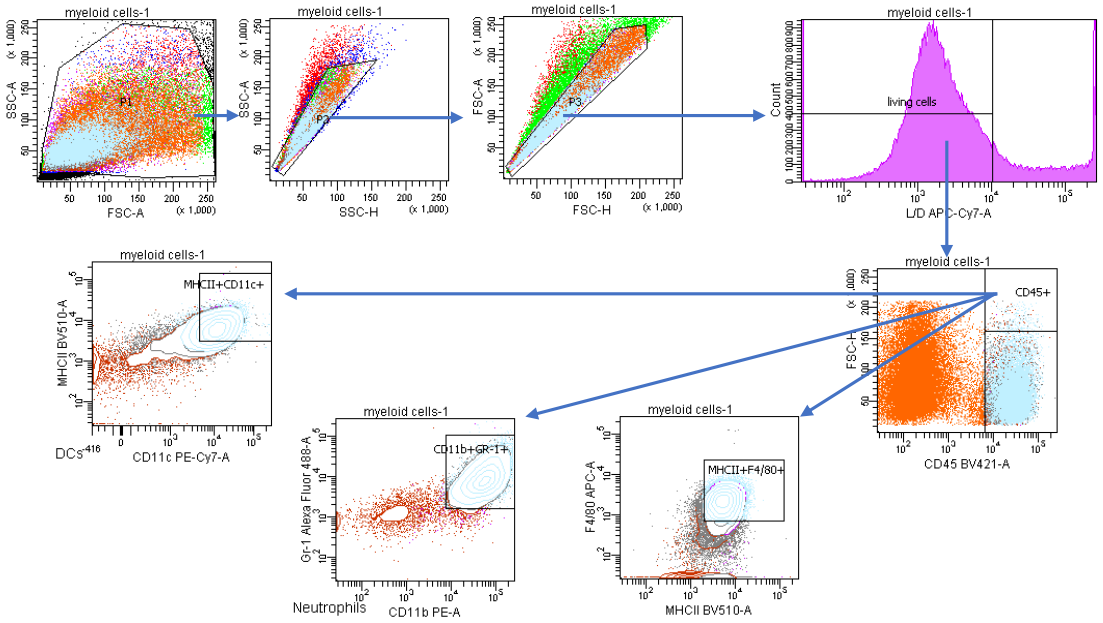

Figure S63: Gating strategy for flow cytometry analysis of myeloid cells from tumor single cell suspensions after treatment with NP(IMDQ+OVA) or PBS (n = 6).

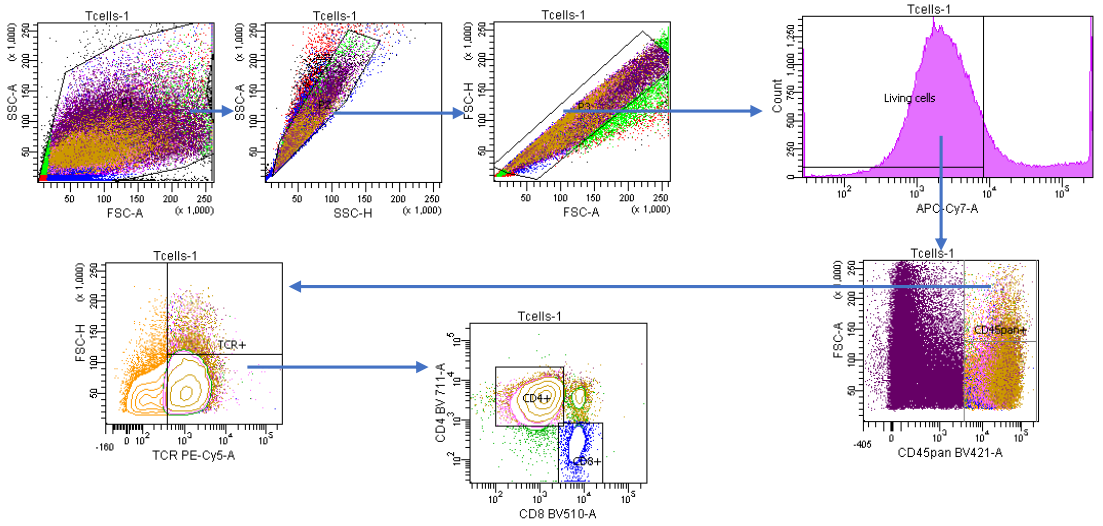

Figure S64: Gating strategy for flow cytometry analysis of T cells from tumor single cell suspensions after treatment with NP(IMDQ+OVA) or PBS (n = 6).

IgMi mice tumor experiments

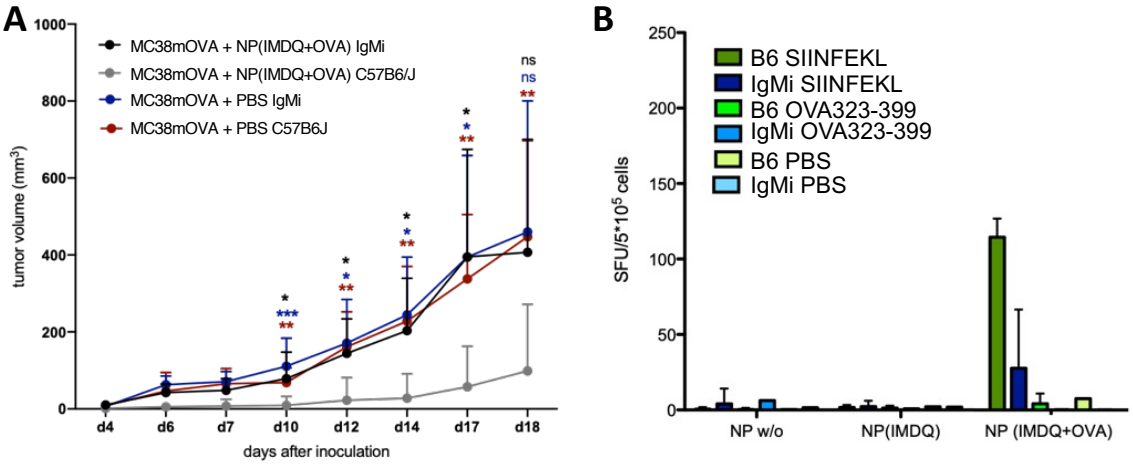

*Figure S65: Nanogel NP(IMDQ+OVA) vaccination in IgMi and wild type B6 (C57BL/6J) mice. (**A**) Mice were also challenged with MC38mOVA tumors but only in the wild type B6-mice a significant reduction in tumor growth was observed. (**B**) ELISpot analysis of spleens of IgMi and wild type B6 mice immunized with NP(IMDQ+OVA), NP(IMDQ) and PBS. A strong induction of OVA-specific $CD8^+$ T cells was found in the in the wild type B6-mice, while in the IgMi group this number was already reduced. This further explains the low antigen-specific antitumor response in this mouse model challenged with MC38mOVA.*

Statistical analyses

Data are shown as mean values + standard deviation unless otherwise specified in the figure legend. To calculate statistical significance of the mean values student's t-test with Welch's correction was performed. For the tumor as well as mice experiments and the corresponding measurements (ELISA, ELISpot) the 2-way-ANOVA test was used. All statistical analyses were done using the graph pad prism 8 software. In all figures * = $P \leq 0.05$; ** = $P \leq 0.01$; *** = $P \leq 0.001$ or otherwise mentioned.

References

(1) Shukla, N. M.; Malladi, S. S.; Mutz, C. A.; Balakrishna, R.; David, S. A. Structure−Activity Relationships in Human Toll-Like Receptor 7-Active Imidazoquinoline Analogues. *J. Med. Chem.* **2010**, *53* (11), 4450–4465.

(2) Leber, N.; Kaps, L.; Yang, A.; Aslam, M.; Giardino, M.; Klefenz, A.; Choteschovsky, N.; Rosigkeit, S.; Mostafa, A.; Nuhn, L.; et al. α-Mannosyl-Functionalized Cationic Nanohydrogel Particles for Targeted Gene Knockdown in Immunosuppressive Macrophages. *Macromol. Biosci.* **2019**, *1900162*, 1–12.

(3) Nuhn, L.; Kaps, L.; Diken, M.; Schuppan, D.; Zentel, R. Reductive Decationizable Block Copolymers for Stimuli-Responsive MRNA Delivery. *Macromol. Rapid Commun.* **2016**, *37* (11), 924–933.

(4) Nuhn, L.; Bolli, E.; Massa, S.; Vandenberghe, I.; Movahedi, K.; Devreese, B.; Van Ginderachter, J. A.; De Geest, B. G. Targeting Protumoral Tumor-Associated Macrophages with Nanobody-Functionalized Nanogels through Strain Promoted Azide Alkyne Cycloaddition Ligation. *Bioconjug. Chem.* **2018**, *29* (7), 2394–2405.

(5) Nuhn, L.; Vanparijs, N.; De Beuckelaer, A.; Lybaert, L.; Verstraete, G.; Deswarte, K.; Lienenklaus, S.; Shukla, N. M.; Salyer, A. C. D.; Lambrecht, B. N.; et al. PH-Degradable Imidazoquinoline-Ligated Nanogels for Lymph Node-Focused Immune Activation. *Proc. Natl. Acad. Sci.* **2016**, *113* (29), 8098–8103.

(6) Rigler, R.; Elson, E. S. *Fluorescence Correlation Spectroscopy - Theory and Applications*; Springer: Heidelberg, 2001.

(7) Nuhn, L.; De Koker, S.; Van Lint, S.; Zhong, Z.; Catani, J. P.; Combes, F.; Deswarte, K.; Li, Y.; Lambrecht, B. N.; Lienenklaus, S.; et al. Nanoparticle-Conjugate TLR7/8 Agonist Localized Immunotherapy Provokes Safe Antitumoral Responses. *Adv. Mater.* **2018**, *30* (45), 1803397.

(8) Nuhn, L.; Van Hoecke, L.; Deswarte, K.; Schepens, B.; Li, Y.; Lambrecht, B. N.; De Koker, S.; David, S. A.; Saelens, X.; De Geest, B. G. Potent Anti-Viral Vaccine Adjuvant Based on PH-Degradable Nanogels with Covalently Linked Small Molecule Imidazoquinoline TLR7/8 Agonist. *Biomaterials* **2018**, *178*, 643–651.

(9) Bialojan, A.; Sohl, J.; Rausch, J.; Aranda Lopez, P.; Denny, M.; Langguth, P.; Hartmann, A.; Yagita, H.; Probst, H. C.; Schild, H.; et al. Transcutaneous Immunization with CD40 Ligation Boosts Cytotoxic T Lymphocyte Mediated Antitumor Immunity Independent of CD4 Helper Cells in Mice. *Eur. J. Immunol.* **2019**, *49* (11), 2083–2094.

10.6. Publication 6

"End group dye-labeled polycarbonate block copolymers for micellar (immuno-) drug delivery"

The following chapter has been published in Macromolecular Rapid Communications. My colleague Dr. Czysch designed an end group dye-labeled polycarbonate block polymer, resulting in dispersed ~25 nm-sized micelles that can simultaneously encapsulate multiple hydrophobic (immuno-) drugs. We used such end group dye-labeled polycarbonate block copolymers because they displayed ideal features to permit targeted delivery of hydrophobic drugs to key immune cells for vaccination and cancer immunotherapy.

The covalently attached fluorescent dye can be used to monitor both stability under biologically relevant conditions and cellular uptake, including incubation with blood plasma and blood circulation time kinetic studys in zebrafish embryos. By encapsulation of the Toll-like receptor 7/8 (TLR7/8) agonist CL075, immune stimulatory polymeric micelles are generated that were internalized by several antigen-presenting dendritic cells (APCs) and promote their maturation. As the second author I conducted *in vitro* studies on macrophages regarding immunostimulation/activation and particle uptake.

DOI: 10.1002/marc.202200095

Published in: *Macromolecular Rapid Communications,* **2022**, 43, 12

Reprinted with permission under creative commons attribution 4.0 (CC BY-NC) from C. Czysch, **C. Medina-Montano**, N. K. Dal, T. Dinh, Y. Fröder, P. Winterwerber, K. Maxeiner, H. Räder, D. Schuppan, H. Schild, M. Bros, B. Biersack, F. Feranoli, S. Grabbe, L. Nuhn, Macromol. Rapid Commun. **2022**, 43, 2200095.

Check for updates

RESEARCH ARTICLE

Macromolecular Rapid Communications
www.mrc-journal.de

End Group Dye-Labeled Polycarbonate Block Copolymers for Micellar (Immuno-)Drug Delivery

*Christian Czysch, Carolina Medina-Montano, Nils-Jørgen Knudsen Dal, Thi Dinh, Yannick Fröder, Pia Winterwerber, Konrad Maxeiner, Hans-Joachim Räder, Detlef Schuppan, Hansjörg Schild, Matthias Bros, Bernhard Biersack, Federico Feranoli, Stephan Grabbe, and Lutz Nuhn**

Defined conjugation of functional molecules to block copolymer end groups is a powerful strategy to enhance the scope of micellar carriers for drug delivery. In this study, an approach to access well-defined polycarbonate-based block copolymers by labeling their end groups with single fluorescent dye molecules is established. Following controlled polymerization conditions, the block copolymers' primary hydroxy end group can be converted into activated pentafluorophenyl ester carbonates and subsequently aminolyzed with fluorescent dyes that are equipped with primary amines. During a solvent-evaporation process, the resulting end group dye-labeled block copolymers self-assemble into narrowly dispersed ~25 nm-sized micelles and simultaneously encapsulate hydrophobic (immuno-)drugs. The covalently attached fluorescent tracer can be used to monitor both uptake into cells and stability under biologically relevant conditions, including incubation with blood plasma or during blood circulation in zebrafish embryos. By encapsulation of the toll-like receptor 7/8 (TLR7/8) agonist CL075, immune stimulatory polymeric micelles are generated that get internalized by various antigen-presenting dendritic cells and promote their maturation. Generally, such end group dye-labeled polycarbonate block copolymers display ideal features to permit targeted delivery of hydrophobic drugs to key immune cells for vaccination and cancer immunotherapy.

1. Introduction

Several recently discovered pharmaceutically active compounds target highly promising cellular receptors or pathways, but have poor aqueous solubility for efficient in vivo application. To increase those drugs' bioavailability, nanometer-sized polymer particles can assist as carriers which both solubilize the compounds in water and enhance their delivery to desired site-of-actions while avoiding off-target effects.[1–5]

Especially in immunotherapy, such nanocarriers are crucial to focus the delivery of immunomodulatory drugs to restricted sites and thereby avoid unwanted toxicities through systemic immunostimulation.[6,7] Most notably, the body's immune response can be activated by addressing the innate immune system through pattern recognition receptors (PRRs). Among them, the toll-like receptors (TLRs) can effectively be stimulated by poly(I:C) (TLR3), lipopolysaccharide (LPS;TLR4), imidazoquinolines

C. Czysch, T. Dinh, Y. Fröder, P. Winterwerber, K. Maxeiner, H.-J. Räder, L. Nuhn
Max Planck Institute for Polymer Research Mainz
Ackermannweg 10, 55128 Mainz, Germany
E-mail: lutz.nuhn@mpip-mainz.mpg.de

C. Medina-Montano, M. Bros, S. Grabbe
Department of Dermatology
University Medical Center Mainz
Langenbeckstraße 1, 555131 Mainz, Germany

N.-J. K. Dal, F. Feranoli
Department of Bioscience
University of Oslo
Blindernveien 31, Oslo 0371, Norway

D. Schuppan
Institute of Translational Immunology
University Medical Center Mainz
Obere Zahlbacherstraße 63, 55131 Mainz, Germany

D. Schuppan
Division of Gastroenterology, Beth Israel Deaconess Medical Center
Harvard Medical School Boston
330 Brookline Ave, Boston, MA 02215, USA

H. Schild
Institute for Immunology
University Medical Center Mainz
Langenbeckstraße 1, 55131 Mainz, Germany

B. Biersack
Organic Chemistry Laboratory
University of Bayreuth
Universitätsstraße 30, 95447 Bayreuth, Germany

The ORCID identification number(s) for the author(s) of this article can be found under https://doi.org/10.1002/marc.202200095

© 2022 The Authors. Macromolecular Rapid Communications published by Wiley-VCH GmbH. This is an open access article under the terms of the Creative Commons Attribution-NonCommercial License, which permits use, distribution and reproduction in any medium, provided the original work is properly cited and is not used for commercial purposes.

DOI: 10.1002/marc.202200095

(TLR7/8), or CpG-oligonucleotides (TLR9).[8,9] These receptors are residing, for instance, on dendritic cells that orchestrate efficient immune responses through antigen presentation.[10,11] TLR agonists are therefore suitable adjuvants for vaccination purposes (e.g., the TLR7/8 imidazoquinoline agonist IMDG is currently successfully applied by Bharat Biotech in their Covid-19 vaccine Covaxin (BBV152)).[12–14] Additionally, academia-driven research has confirmed the applicability of TLR stimulation for the treatment of cancer.[15,16] By administering TLR agonists via nano-sized drug carriers, they can more precisely be maneuvered to lymph nodes, the tumor microenvironment, or other sites of the immune system and thereby dampen undesired off-target effects.[17,18] The hydrophobic TLR7/8 agonist 2-propylthiazolo[4,5-*c*]quinolin-4-amine (CL075)[19,20] is highly attractive for such purposes. It provides only low aqueous solubility, but nano-sized micellar carriers have been demonstrated to encapsulate CL075 or similar TLR7/8 agonists into their hydrophobic cores.[21–23]

Among different types of polymeric materials for micellar drug delivery, aliphatic carbonates have lately been discussed as attractive alternatives.[24] Due to their hydrolytic biodegradability and biocompatibility, these features strongly suggest their translatability into clinical applications.[25–27] The carbonate motif has already been employed for degradable systems carrying carbonate moieties in the side chain[28,29] and, more significantly, as backbone in aliphatic polycarbonates.[30–32] Using amphiphilic polycarbonate block copolymers, nanoparticular systems can be self-assembled and applied for various therapeutic applications.[33–35] However, these materials often lack the possibility to covalently introduce additional functionalities, such as dyes for precise carrier monitoring during delivery.

We herein present an elegant way to design such materials by employing the active ester chemistry for controlled polymer end group functionalization.[36] This approach requires the synthesis of polymers with highly defined end groups followed by a quantitative activation and conjugation of the cargo, as lately demonstrated by us for RAFT polymerization-derived end groups.[37] In the current study, we apply this approach for the first time to polycarbonate-based block copolymers obtained by organocatalytic ring-opening polymerization. The primary hydroxy end group could be converted into a pentafluorophenyl carbonate and subsequently derivatized with primary amine bearing fluorescent dyes. This enabled us to efficiently track micelles derived from these block copolymers in the blood stream and during cell uptake. We additionally quantified efficient drug encapsulation, including the TLR7/8 thiazoloquinoline agonist CL075, which confirmed its immune stimulatory potential on various types of primary dendritic cells. Altogether, these features promote the applicability of end group dye-labeled polycarbonate block copolymers for micellar (immuno-)drug delivery.

2. Results and Discussion

To provide access to such highly defined polymeric carrier systems, it is crucial to control block copolymer length and assure desired end groups. Especially for ring-opening polymerization reactions, it is necessary to use highly pure starting materials. The herein presented polycarbonate-based micelles were self-assembled from end group functionalized $mPEG_{113}$-*b*-poly(MTC-OBn)$_{15}$ block copolymers. For a well-defined synthesis of these polymers, the highly pure 5-methyl-5-benzyloxycarbonyl-1,3-dioxan-2-one (MTC-OBn) monomer[38] was used (as shown by X-ray diffraction of the recrystallized monomers, **Figure 1**A and characterization data in Figures S1–S3, Supporting Information). All starting materials had to be dried by azeotropic distillation with benzene prior to polymerization under inert atmosphere. During polymerization, side reactions such as backbiting and homopolymerization had to be avoided to yield end group defined polymers. Therefore, ring-opening polymerizations were conducted at decreased temperatures of −20 °C using the organocatalyst 1,8-diazabicyclo[5.4.0]undec-7-ene (DBU). Polymerization conditions were first tested by homopolymerization of MTC-OBn, and detailed product analyses including MALDI-ToF mass spectrometry confirmed the integrity of end group defined homopolymers (compare Figure S4, Supporting Information).

The optimized reaction conditions were then successfully applied for block copolymerization, initiated from a $mPEG_{113}$-OH macroinitiator. After precipitation in diethyl ether, block copolymers with an increase of molecular weight comparted to $mPEG_{113}$ and narrow dispersities of 1.05 were yielded (Figure 1B). Further analyses such as DOSY-NMR (Figure 1C) and MALDI-ToF mass spectrometry demonstrated again the high definition of the $mPEG_{113}$-*b*-poly(MTC-OBn)$_{15}$ block copolymer product (Figures S5 and S9, Supporting Information).

Prior to block copolymer self-assembly into micelles, we aimed to label the carrier material with a fluorescent dye to track the material in a biological system. For circulation in the blood stream we selected the fluorescent dye Alexa Fluor 647 (AF647), while for cellular uptake experiments we chose tetramethyl rhodamine (TMR). For covalent conjugation to the $mPEG_{113}$-*b*-poly(MTC-OBn)$_{15}$ block copolymers, the primary hydroxy end groups were activated by reaction with bis(pentafluorophenyl)carbonate to form a highly reactive pentafluorophenyl carbonate (2) (**Figure 2**A). This reaction sequence allows the defined synthesis of single labeled polymers with almost unaltered molecular integrity, as verified by size exclusion chromatography (SEC; Figure 2B, full spectra Figure S8, Supporting Information). Successful labeling was further demonstrated by SEC using UV–vis detection at dye specific wavelengths. Compared to the non-labeled starting material, both AF647- and TMR-labeled block polymers provided absorptions at the respective wavelengths 647 (for AF647) and 549 nm (for TMR) (Figure 2B), which was also proven by recording the whole UV–vis spectra of the purified polymers (Figure 2C). Moreover, MALDI-ToF mass spectrometry and NMR spectroscopy further confirmed the high specificity of the active ester approach and the covalent conjugation of one single dye molecule to the block copolymer (compare Figures S6–S9, Supporting Information).

For the preparation of drug-loaded polymeric micelles, we next opted for the solvent-evaporation method due to its high encapsulation efficiency and high reproducibility.[39] Non-encapsulated drug outside of the micellar core usually precipitates during this process and can easily be filtered off by standard sterile filtration

L. Nuhn
Chair of Macromolecular Chemistry, Faculty of Chemistry and Pharmacy
Julius Maximilian University Würzburg
Röntgenring 11, 97070 Würzburg, Germany

 © 2022 The Authors. Macromolecular Rapid Communications published by Wiley-VCH GmbH

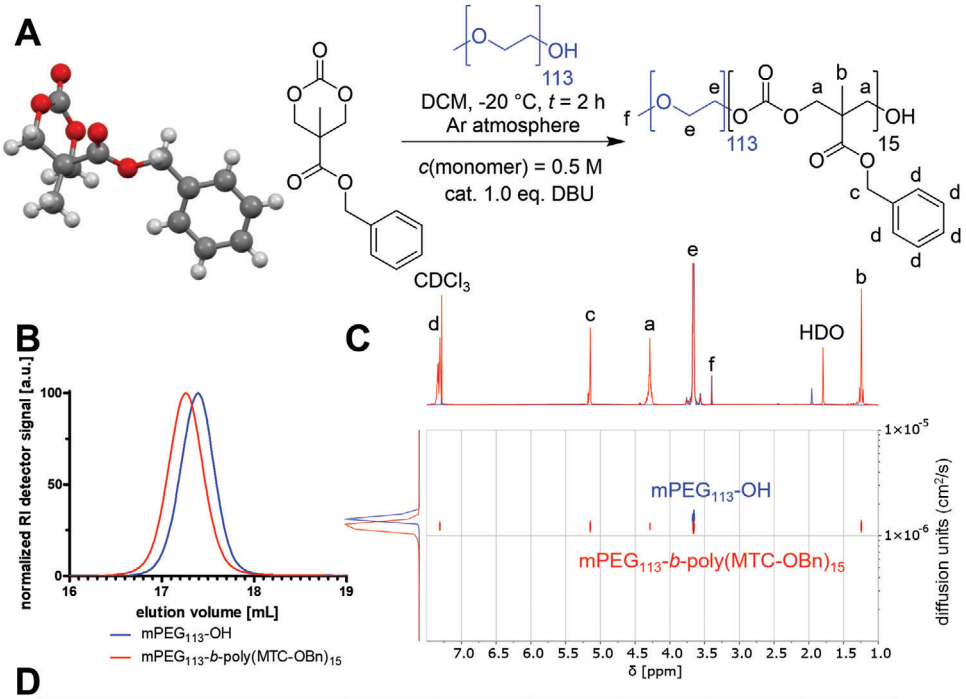

	χ_n^{targ}	conv. [%][a]	M_n^{theo} [g/mol][a]	M_n^{prod} [g/mol][a]	M_n^{prod} [g/mol][b]	$Đ$ [b]
$mPEG_{113}$-*b*-poly(MTC-OBn)$_{15}$	15	97.8	8670	8750	35200	1.05

Figure 1. Synthesis and characterization of polycarbonate block copolymer functionalized $mPEG_{113}$-b-poly(MTC-OBn)$_{15}$. A) Crystal structure of 6-ring carbonate monomer 5-methyl-5-benzyloxycarbonyl-1,3-dioxan-2-one (MTC-OBn) and ring-opening polymerization of MTC-OBn initiated from $mPEG_{113}$ using the organocatalyst 1,8-diazabicyclo[5.4.0]undec-7-ene (DBU). B) Size exclusion chromatogram[b] (SEC, refractive index, RI) of $mPEG_{113}$-b-poly(MTC-OBn)$_{15}$ block copolymer compared to the $mPEG_{113}$ macroinitiator. Block copolymers show a shift toward higher molecular weight (lower elution volume) but a similar narrow distribution ($Đ = 1.05$). C) ^{1}H DOSY-NMR of block copolymers (red) provide a higher diffusion coefficient and additional signals for the polycarbonate block compared to $mPEG_{113}$ (blue). D) Characterization summary of $mPEG_{113}$-b-poly(MTC-OBn)$_{15}$. [[a]Determined by ^{1}H NMR analysis. [b]Determined by HFIP (hexafluoroisopropanol) size exclusion chromatography, calibrated with PMMA standards.]

processes. The feasibility of this approach was first demonstrated by encapsulating the hydrophobic compound 3,3'-((3,4-difluorophenyl)methylene)bis(1*H*-indole) (DIM-DF, **Figure 3**A). The anticancer drug DIM-DF was chosen as a model drug[40] due to its high log(*P*) value of 4.5 and its straightforward quantification by ^{19}F NMR. Formulations of DIM-DF were prepared by dropping a polymer–drug mixture in acetone of 10:1 polymer to drug (weight-to-weight ratio, 9.09 wt% drug) into water. During the evaporation of the volatile acetone, micelles were formed by spontaneous self-assembly. Simultaneously the hydrophobic drug molecule is encapsulated inside the core. Polymeric micelles with uniform monomodal sizes were yielded and characterized by dynamic light scattering (DLS; Figure 3D, *z*-average hydrodynamic diameter of 26.0 nm, PDI = 0.09). We assume that the strong π–π interaction of the benzyl ester side chains inside the micelle favor the encapsulation of hydrophobic compounds that are rich in aromatic groups, too.[41,42] This feature might also stabilize the block copolymer micelles when adsorbed and dried on flat surfaces, as atomic force microscopy (AFM) images still confirmed the presence of spherical-shaped nanoparticles (compare Figure S10, Supporting Information). Interestingly, precise quantification of the drug load was achieved by analyzing freeze-dried material by ^{19}F NMR spectroscopy and comparing the value to a DIM-DF standard calibration (Figure 3B). Via this method a drug load of 8.97 wt% was determined. Compared to the targeted drug load of 9.09 wt%, this solvent-evaporation process yielded a high encapsulation efficiency of 98.6% (Figure 3E and Figure S12, Supporting Information for calculations as well as additional UV–vis spectra in Figure S11, Supporting Information).

While for biological testing of DIM-DF-loaded micelles the AF647-labeled block copolymers were used, the encapsulation of the hydrophobic immunodrug CL075 could in analogy be performed using the TMR-labeled block copolymers. Due to the partial solubility of CL075 at the slightly acidic pH, which occurs in Millipore water, the CL075-loaded micelles were prepared in PBS at pH 7.4. Similar to the preparation of DIM-DF-loaded micelles, we checked for a precise quantification method for CL075 encapsulation after micelle formulation. Interestingly, CL075 provides a typical absorbance at 350 nm, which could be compared to a calibration of the drug itself (Figure 3C). This afforded a drug load of 1.78 wt% (at an aimed drug load 1.96 wt%) and confirmed again the high encapsulation efficiency of 90.6% for this formulation method (Figure 3E and Figure S13, Supporting Information for calculations).

© 2022 The Authors. Macromolecular Rapid Communications published by Wiley-VCH GmbH

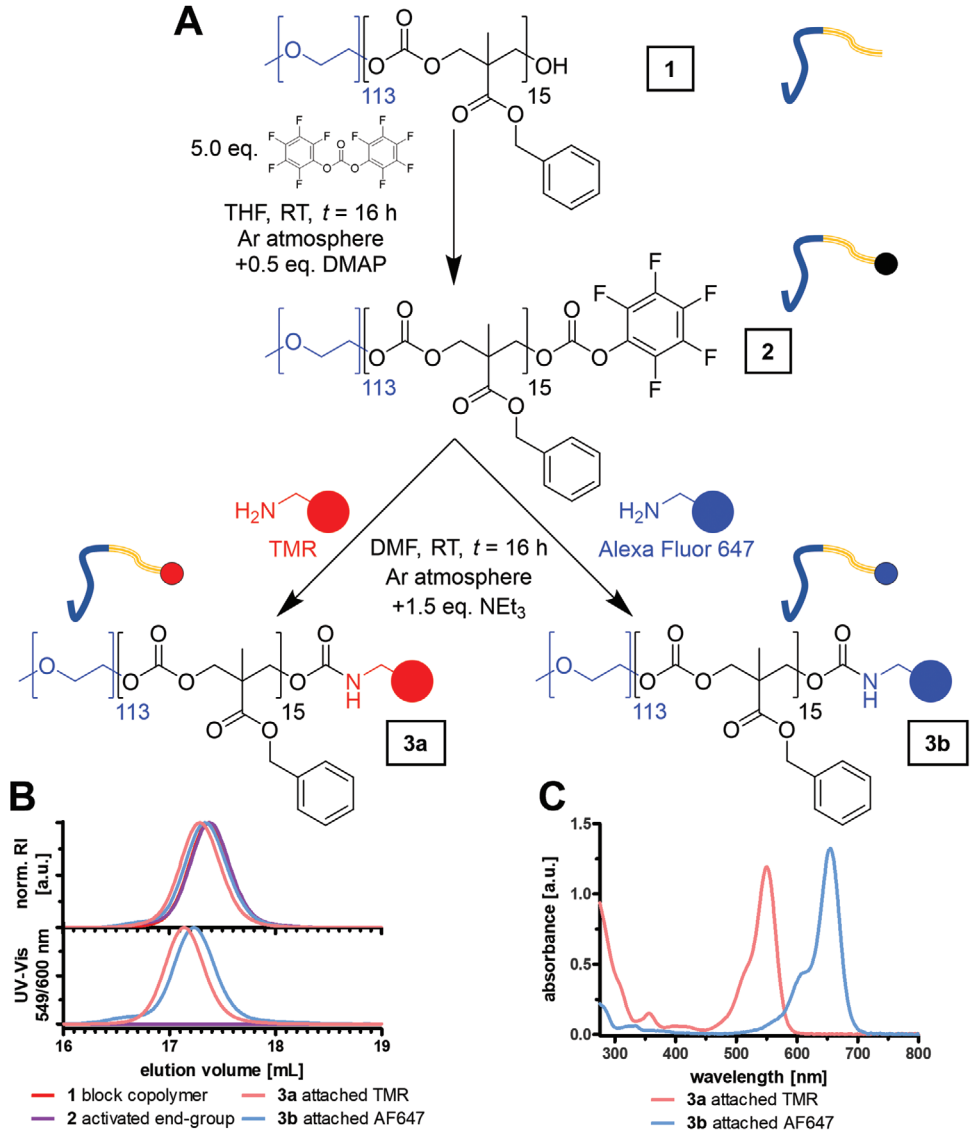

Figure 2. Synthesis of end group functionalized polycarbonate block copolymers. A) Through reactive ester carbonate activation the block copolymer 2 is subsequently aminolyzed with primary amine functionalized dye molecules yielding block copolymer 3a (with tetramethyl rhodamine [TMR]) and 3b (with Alexa Fluor 647 (AF647)). B) HFIP SEC elugram of the respective block copolymers showing highly defined end group functionalized block copolymers, both by normalized (norm.) RI traces (top) and additional absorption traces at dye specific wavelengths (bottom, UV traces at 549 nm for TMR detection and 600 nm for AF647). C) Corresponding UV–vis absorbance spectra of the block copolymers 3a and 3b.

With these drug-loaded micelles, formulated from well-defined dye-labeled block copolymers, their performance was tested in a biological context. Aiming for the application as an anticancer drug carrier with prolonged blood circulation to accumulate in tumorous tissue (e.g., via the enhanced permeability and retention (EPR) effect[43]), it was initially investigated if the particles remain stable under physiologically relevant protein-rich conditions. Therefore, particles were incubated with human blood serum for 1 h at 37 °C followed by a multi-angle DLS analysis established by Rausch et al. (**Figure 4**A).[44] For $mPEG_{113}$-*b*-poly(MTC-OBn)$_{15}$ micelles no significant differences were found between recorded and predicted autocorrelation curves at multiple angles indicating that the micelles do not aggregate upon protein incubation but remain stable. Identical results were obtained for the DIM-DF drug-loaded micelles, too (see Figure S14, Supporting Information).

Encouraged by these promising results, the circulation of the micelles in the blood stream of zebrafish embryos was recorded. The AF647-labeled polymeric micelles provide ideal fluorescent properties to track them within the blood vessels of the transparent zebrafish embryos (Figure 4B1). Fortunately, polymeric micelles were found circulating in the zebrafish embryos over 72 h after injection in the posterior cardinal vein (Figure 4B2). After an initial drop, about 50% of the injected particles were found in the blood stream after 4 h and around 30% after 24 h. Interestingly, this amount remained stable for the following 2 days. After 72 h, still ≈30% of both DIM-DF-loaded and empty micelles were found circulating

 © 2022 The Authors. Macromolecular Rapid Communications published by Wiley-VCH GmbH

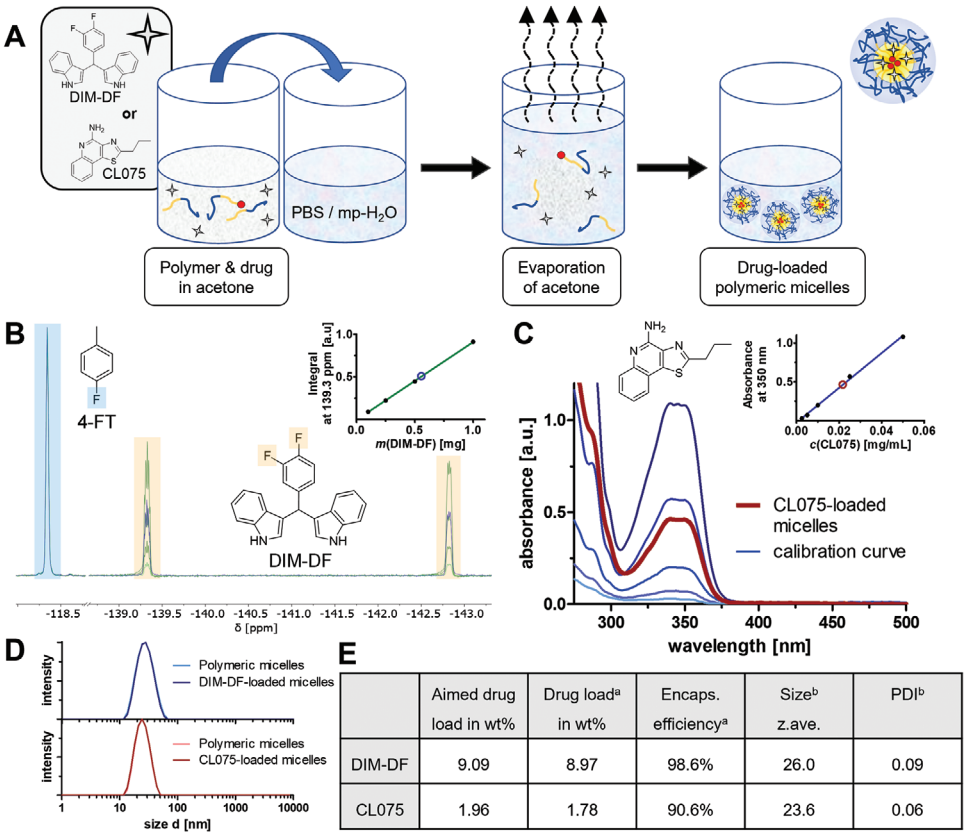

E

	Aimed drug load in wt%	Drug load[a] in wt%	Encaps. efficiency[a]	Size[b] z.ave.	PDI[b]
DIM-DF	9.09	8.97	98.6%	26.0	0.09
CL075	1.96	1.78	90.6%	23.6	0.06

Figure 3. Fabrication and characterization of drug-loaded polymeric micelles prepared by solvent-evaporation of end group functionalized polycarbonate block copolymers. A) Self-assembly process of micelles by solvent evaporation. The polymer/drug solution is dropped into aqueous media at a volumetric 1:1 ratio of acetone and water. During evaporation of the volatile acetone, the drug-loaded micelles are formed. Micelles were either loaded with DIM-DF, a hydrophobic anticancer drug, or the immunostimulatory TLR7/8 agonist CL075. B) Determination of DIM-DF drug load by ^{19}F-NMR using a DIM-DF calibration curve ($y = 0.9108\ mg^{-1} \cdot x - 0.0027$). Solvent was spiked with 4-fluorotoluene as reference compound for spectrum intensity normalization. Freeze-dried DIM-DF-loaded micelles (dissolved in DMSO-d_6) were measured to calculate the drug load. C) Determination of CL075 drug load by a UV–vis calibration curve ($y = 22.445\ mL \cdot mg^{-1} \cdot x - 0.0276$). All measurements were recorded in a volumetric 1:1:2 mixture of water:PBS:THF. Drug-loaded micelles were diluted similarly using a water/THF mixture and measured. D) Particle sizes recorded by DLS showing narrow monomodal distributions of both DIM-DF-loaded micelles (top) and CL075-loaded micelles (bottom). E) Characterization summary of DIM-DF and CL075-loaded end group functionalized polycarbonate block copolymer micelles. [[a]Determined by ^{19}F NMR (DIM-DF)/UV–vis (CL075). [b]Determined by DLS.]

in the blood stream and, thus, provide similar circulation properties as reported for other effective long-circulating particles.[45–48]

Beyond micelles' stability, we were also interested in their potential hydrolytic degradability rendered by the polycarbonate backbone. For that purpose, particle samples were measured by DLS at different time points. In PBS, the micelles remained stable even after several months (Figure S15, Supporting Information) supporting their favorable long shelf life. Alkaline conditions, however, immediately triggered their gradual disintegration (Figure 4C1). Upon addition of 10 vol% 1 M NaOH (pH 13), particles rearranged and immediately formed large aggregates with sizes larger than 100 nm. We followed this aggregation process and observed a slow disintegration over a time span of ≈2 days with decreasing particle sizes and drastically declining particle count rates (Figure 4C1). Finally, complete degradation occurred with sizes below 5 nm. At lower pH conditions (pH 9.2) a slower degradation was observed (Figures S15 and S16, Supporting Information—degradation half-life $t_{1/2}$ = 17.8 h at pH 9.2 compared to $t_{1/2}$ = 9.3 h at pH 13).

Mass spectrometric analysis (Figure 4C2) of the degradation products could be performed with the TMR-labeled block copolymers after incubation in ammonium bicarbonate buffer (10 μM, pH 8, see Figure S17, Supporting Information for full ESI-MS spectrum). Interestingly, besides multiple charged species of the remaining mPEG$_{113}$-OH macroinitiator, the expected degradation product of the TMR end group could be found as carbamate motif attached to one single repeating unit of decarboxylated monomer MTC-OBn (M = 764.34 g mol^{-1}, recorded as m/z = 765.34 [M + H]$^+$). The appearance of this degradation product once again proves the successful attachment of the dye and, most notably, the degradability of poly(MTC-OBn) through the polycarbonate motif. Interestingly, under the applied conditions hydrolysis did not occur at the benzyl ester side chain, but at the more labile carbonate groups.[49] These degradation experiments exemplify the general hydrolytic degradation potential of polycarbonates (under base catalyzed conditions, potentially also mediated by degrading enzymes, as reported earlier for polycarbonate bulk materials).[24,50] However, they also disclose their limited relevance at physiological pH

© 2022 The Authors. Macromolecular Rapid Communications published by Wiley-VCH GmbH

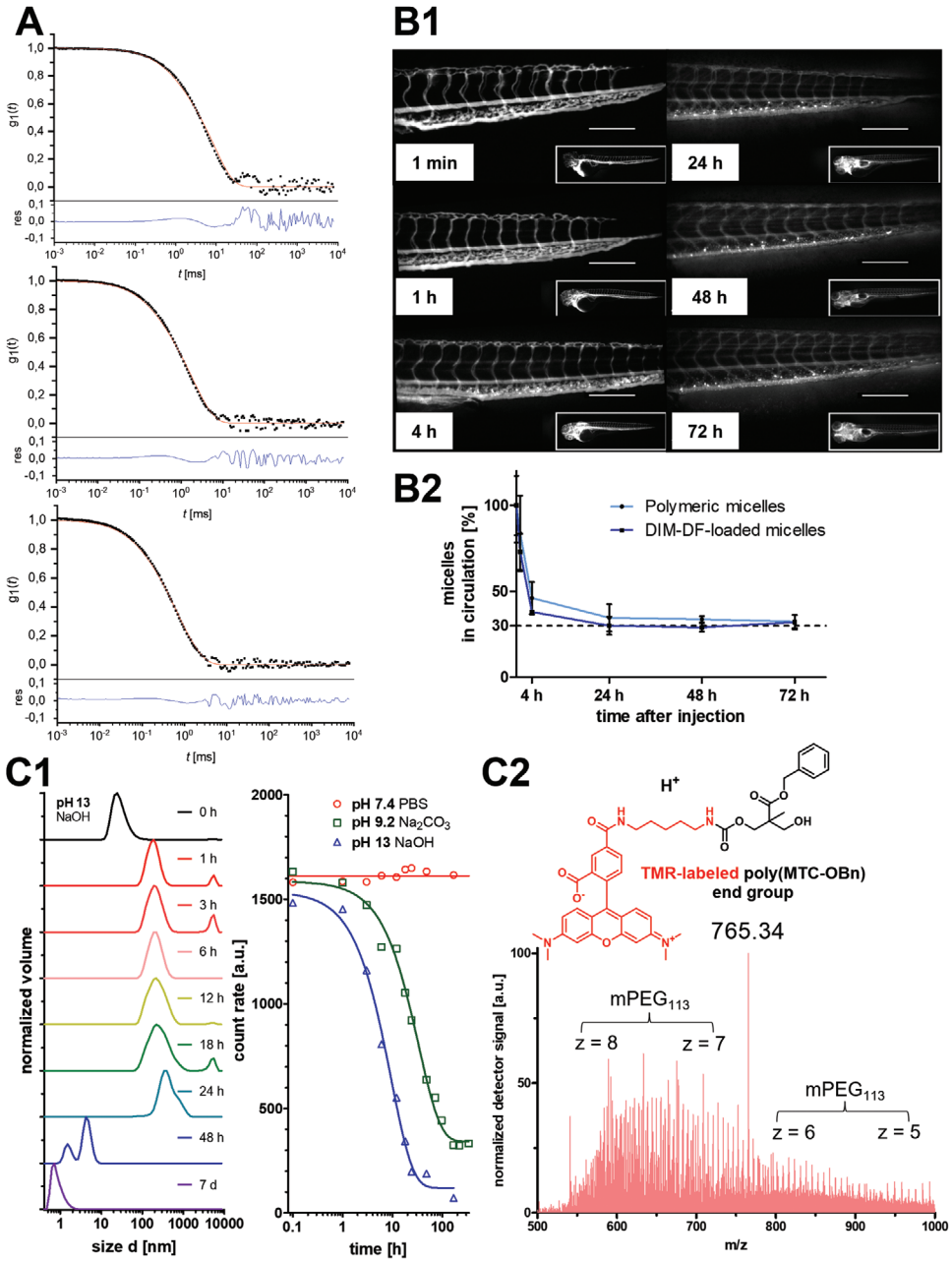

Figure 4. Evaluation of dye end group functionalized polycarbonate block copolymer micelles in biological media and their hydrolytic degradation potential. A) Blood plasma incubation studies by multi-angle DLS of $mPEG_{113}$-b-poly(MTC-OBn)$_{15}$ micelles. After incubation for 1 h in human blood plasma, their autocorrelation curves were recorded at different angles (30°, 60°, and 90°, from top to bottom—black dots) and compared to the sum of autocorrelation curves obtained from individual measurements of plasma and micelles (red curve). B) Blood circulation of AF647-labeled micelles in zebrafish embryos investigated by fluorescence intensity at multiple time points over 72 h (B1). Even after 72 h, ≈30% of the micelles could still be found circulating in the blood stream (B2). C) Hydrolytic degradation behavior of polycarbonate micelles. C1) Micelles fully disintegrated after addition of 10 vol% 1 M NaOH, as indicated by DLS analysis of size changes (first aggregation to larger particles, followed by total disintegration—left) and declining particle count rates within the first 48 h (right, blue curve). Incubation at pH 9.2 (green curve) triggers analogous degradation within ≈4 days. At pH 7.4 in PBS (red line) particles count rates as well as sizes remain stable (compare also Figures S15 and S16, Supporting Information). C2) Mass spectrometric analysis of the degradation products from hydrolyzed TMR-labeled polymeric micelles (note that an incubation with ammonium bicarbonate buffer [10 µm, pH 8] was necessary for ESI-MS in the presence of volatile salts). Interestingly, besides multiple charged species of the remaining mPEG-OH macroinitiator ($z = 5$, 6, 7, and 8), the TMR-labeled end group was also found as carbamate attached to the decarboxylated MTC-OBn monomer.

© 2022 The Authors. Macromolecular Rapid Communications published by Wiley-VCH GmbH

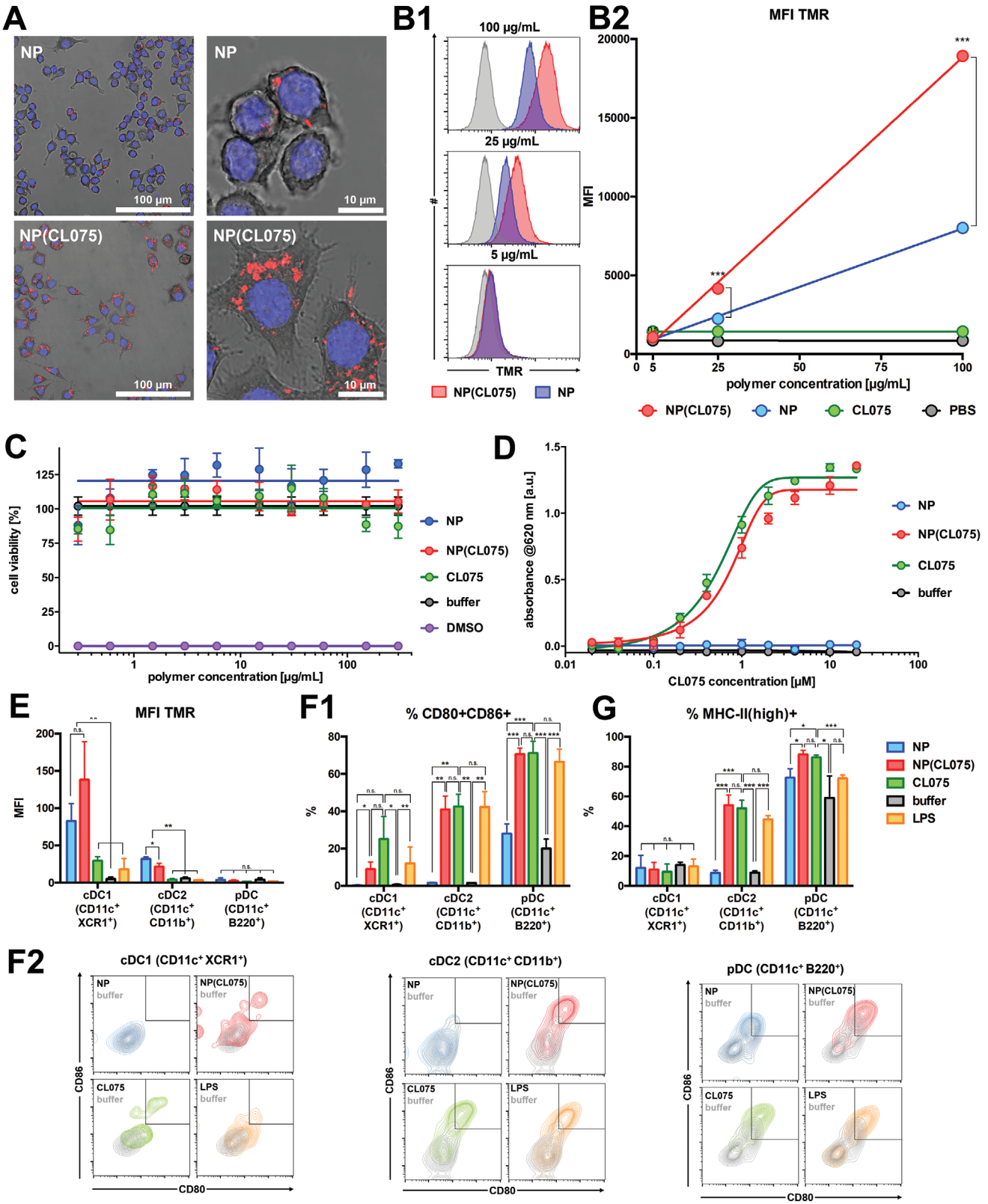

Figure 5. Biological evaluation of TMR end-group-labeled block copolymer micelles loaded with the immune stimulatory TLR7/8 agonist CL075. A) Confocal microscopy of RAW Blue macrophages incubated with 100 µg mL^{-1} empty (NP) and CL075-loaded NP(CL075) micelles derived from TMR end-group-labeled polycarbonate block copolymers (red: polymer—blue: nuclei stained with DAPI). B) Flow cytometry of RAW Blue macrophages incubated with increasing doses of empty (NP) and CL075-loaded NP(CL075) micelles determined by B1) histogram and B2) mean fluorescence intensity (MFI)

© 2022 The Authors. Macromolecular Rapid Communications published by Wiley-VCH GmbH

values at which $mPEG_{113}$-*b*-poly(MTC-OBn)$_{15}$ so far did not hydrolyze. Possibly, water exclusion within the hydrophobic polycarbonate core enhances hydrolytic stability, thereby requiring increased pH values (or degrading enzymes) for facilitating biodegradation.

The CL075 immunodrug-loaded block copolymer micelles were finally checked for their pharmacologic activity. TMR-labeled micelles were used and first checked in vitro for their cellular uptake behavior on RAW macrophages. For that purpose, cells were incubated overnight with and without CL075-loaded micelles and then analyzed by confocal microscopy (**Figure 5**A and Figures S20–S22, Supporting Information). Compared to empty micelles (NP), the drug-loaded micelles (NP(CL075)) revealed a much stronger internalization and accumulation in intracellular vesicular compartments. They also affected cell morphology (Figure 5A) which correlated with the TLR7/8 receptor stimulation of the CL075 payload (compare Figures S20–S22, Supporting Information).

This cell uptake was further quantified by flow cytometry (Figure 5B and Figure S19, Supporting Information). A linear dose dependency of particle internalization was found, and the significantly enhanced uptake of NP(CL075) was confirmed (Figure 5B). Interestingly, no influence on cell viability was observed over a broad range of polymer concentrations up to 300 μg mL^{-1} (Figure 5C—note also that CL075 drug loading or the free drug itself did not affect the cell viability at the applied dose regime).

The Raw macrophages used for these experiments are genetically modified to provide a reporter function upon TLR7/8 receptor stimulation (RAW Blue macrophages). Upon subsequent activation of their NF-κB pathway, these cells secrete alkaline phosphatase, which can easily be quantified spectrophotometrically from the cell culture supernatant by a Quanti Blue assay. A broad range of TLR7/8 agonist CL075 concentrations formulated in the block copolymer micelles was screened and compared to empty micelles (Figure 5D). While the empty micelles NP did not affect the TLR stimulation, a sub-μM activation was found for drug-loaded micelles NP(CL075), which was identical to the drug alone applied from a DMSO stock solution. Note that if the drug was diluted in PBS from an aqueous stock solution (prepared by the solvent-evaporation process without block copolymers), its activity was tenfold lower (Figure S18, Supporting Information). Considering the limited applicability of DMSO formulation for in vivo purposes (according to the toxicity of DMSO demonstrated in Figure 5C), the end group functionalized polycarbonate block copolymer micelles provide ideal features for encapsulation and release of CL075. Micellar delivery may further improve the biodistribution during in vivo applications and focus its delivery ideally to draining lymph nodes or other lymphoid organs, as demonstrated for other TLR7/8 agonist nanoparticle formulations by us and others before.[6,18,51–54]

Finally, to evaluate the immune stimulation potency of the CL075-loaded micelles, we investigated their effect on dendritic cells (DC) derived from murine bone marrow (BMDC). Generally, DC are considered as the most effective antigen-presenting cells and therefore are of major importance to get stimulated for vaccination or cancer immunotherapy purposes. Upon cultivation for 1 week in Fms-related tyrosine kinase 3 receptor (FLT3) ligand supplemented media, bone marrow cells differentiate into different subtypes of DC characterized by their specific surface markers (compare Figure S23, Supporting Information). Among them, conventional (myeloid) DC type 1, cDC1, is identified as $CD11c^+$ $XCR1^+$ and considered to preferentially trigger prime type 1 immune responses (cytotoxic T cell responses against viral infections or cancer).[11] Additionally, conventional (myeloid) DC type 2, cDC2, provides a $CD11c^+$ $CD11b^+$ surface expression and is known to induce type 2 immune responses (against parasites or bacteria),[55] while plasmacytoid dendritic cells, pDC, identified as $CD11c^+$ $B220^+$, are renowned for their high type 1 interferon secretion and pronounced antigen-presentation capacity.[56,57]

After incubation of FLT3 ligand differentiated BMDCs for 24 h with empty and CL075-loaded micelles (and soluble CL075 and the TLR4 agonist LPS as control, both from a DMSO stock solution), we characterized micelle uptake by the DC subpopulations and their activation marker expression profile using flow cytometry. TMR fluorescence detection served to quantify micelle uptake into the three different DC subpopulations. Interestingly, the highest micelle uptake was observed for cDC1, followed by cDC2, but scarcely any uptake in pDC (Figure 5E and Figure S24, Supporting Information). Micelle uptake in cDC1 is desired in order to initiate cytotoxic T cell responses that are most favorable for cancer immunotherapy. A slightly higher (but not significant) uptake was found for the CL075-loaded NP(CL075) compared to empty micelles NP in cDC1, while for cDC2 the empty micelles seemed to get internalized more effectively (Figure 5E and Figure S24, Supporting information).

We also analyzed the maturation state for all three DC subtypes by quantifying the surface expression of the co-stimulatory molecules CD80 and CD86 as markers for dendritic cell maturation for antigen presentation (Figure 5F1,F2 and Figure S25, Supporting Information). For all three DC subpopulations (cDC1, cDC2, and pDC), the drug-loaded micelles NP(CL075) induced significantly upregulated expression of both co-stimulatory maturation markers CD80 and CD86, while the empty micelles NP remained immunologically silent (like the buffer control). Similar maturation levels could be obtained for the two positive controls, CL075 and LPS, demonstrating the safe delivery and efficient CL075 release from the end group block copolymer micelles.

Finally, we also checked for the surface expression of the antigen-presenting major histocompatibility class II (MHCII complex) in all three DC subtypes (Figure 5G and Figure S23, bottom, Supporting Information). While the expression and stimulation were—as expected—rather low in cDC1 (they rather favor

analyses ($n = 3$, $^{***}p < 0.001$). C) Cell viability determined by MTT assay ($n = 4$). D) TLR7/8 receptor stimulation by Raw Blue assay ($n = 4$). E) Cell uptake into FLT3 ligand differentiated BMDC subpopulations analyzed by flow cytometry ($n = 4$, $^{*}p < 0.05$, $^{**}p < 0.01$, $^{***}p < 0.005$). F) CD80 and CD86 expression of FLT3 ligand differentiated BMDC subpopulations analyzed by F1) flow cytometry and F2) their corresponding histograms ($n = 4$, $^{*}p < 0.05$, $^{**}p < 0.01$, $^{***}p < 0.001$). G) MHCII-high expression of FLT3 ligand-derived BMDC subpopulations analyzed by flow cytometry ($n = 4$, $^{*}p < 0.05$, $^{**}p < 0.01$, $^{***}p < 0.001$).

© 2022 The Authors. Macromolecular Rapid Communications published by Wiley-VCH GmbH

antigen presentation via MHCI), a significant increase of cells that highly express MHCII was observed in cDC2 after incubation with NP(CL075), similar to a stimulation with CL075 alone or LPS. Consequently, micelle-guided CL075 delivery can in principle also boost type 2 immune responses. For pDCs that already provide quite a high MHCII expression profile, NP(CL075) could also enhance their expression a bit further and, thus, may also enhance type 1 immune responses. Altogether, these findings underline that our TLR7/8 agonist-loaded micelles confer a safe and effective maturation and antigen-presentation capacity for various types of DC which are capable of eliciting a broad spectrum of type I and type II immune responses. These observations make our micelles highly attractive for instance as adjuvants during vaccination or cancer immunotherapy.

3. Conclusion

We could demonstrate the successful synthesis and application of single dye end group modified polycarbonate block copolymers and their resulting (immuno-)drug-loaded micelles. Highly controlled ring-opening polymerizations yielded alcohol end-group-defined block copolymers that could be activated as reactive pentafluorophenyl ester carbonates. To the best of our knowledge, the approach of installing single reactive end groups onto aliphatic polycarbonates has not been reported before. It allows us to access single dye-labeled polymer chains by aminolysis with various primary amine functionalized dyes. Via a subsequent solvent-evaporation method, these end group dye-labeled block copolymers could reproducibly be self-assembled into defined polymeric micelles of sizes around ≈25 nm and narrow PDI below 0.1. By including hydrophobic drugs during the self-assembly process, micellar formulations with high drug loads of 8.87 wt% for the anticancer drug DIM-DF and 1.74 wt% for the immunodrug CL075 were achieved with high encapsulation efficiencies above 87%. These micelles were shown to not only solubilize the cargo but to nicely envelop the drug, avoid protein aggregation in human blood plasma and promote prolonged circulation in the blood stream of zebrafish embryos. Hydrolytic disintegration of the micelles was only possible under alkaline conditions revealing expected end group degradation products. Biological evaluation of the immune-drug CL075-loaded micelles demonstrated uptake into key antigen-presenting cells as well as sufficient TLR7/8 activation both in an in vitro reporter cell line and in different subpopulations of bone marrow delivered primary dendritic cells. Overall, these experiments demonstrate that end group modified polycarbonate block copolymers seem highly suitable for the tracking of the encapsulation and delivery of various hydrophobic (immuno-)drugs and, thus, for paving the way of these drugs toward vaccination or cancer (immuno-)therapy.

Supporting Information

Supporting Information is available from the Wiley Online Library or from the author.

Acknowledgements

This work was gratefully supported by the DFG through the Emmy Noether program (to L.N.) and the CRC/SFB 1066 (to L.N., S.G., M.B., H.S., and D.S.). Dieter Schollmeyer is acknowledged for X-Ray Diffraction Analysis, Jutta Schnee and Stephan Türk for MALDI-ToF measurements, Christine Rosenauer for multi-angle DLS measurements, and Manfred Wagner for NMR measurements.

Open access funding enabled and organized by Projekt DEAL.

Conflict of Interest

The authors declare no conflict of interest.

Data Availability Statement

The data that support the findings of this study are available in the supplementary material of this article.

Keywords

aliphatic polycarbonates, block copolymers, immunodrug delivery, micelles, self-assembly

Received: February 2, 2022
Published online:

[1] M. Talelli, M. Barz, C. J. F. Rijcken, F. Kiessling, W. E. Hennink, T. Lammers, *Nano Today* **2015**, *10*, 93.
[2] R. Duncan, R. Gaspar, *Mol. Pharmaceutics* **2011**, *8*, 2101.
[3] Z. Ahmad, A. Shah, M. Siddiq, H.-B. Kraatz, *RSC Adv.* **2014**, *4*, 17028.
[4] H. Cabral, K. Kataoka, *J. Controlled Release* **2014**, *190*, 465.
[5] Y. Mai, A. Eisenberg, *Chem. Soc. Rev.* **2012**, *41*, 5969.
[6] L. Nuhn, N. Vanparijs, A. De Beuckelaer, L. Lybaert, G. Verstraete, K. Deswarte, S. Lienenklaus, N. M. Shukla, A. C. D. Salyer, B. N. Lambrecht, J. Grooten, S. A. David, S. De Koker, B. G. De Geest, *Proc. Natl. Acad. Sci. U. S. A.* **2016**, *113*, 8098.
[7] J. Shi, P. W. Kantoff, R. Wooster, O. C. Farokhzad, *Nat. Rev. Cancer* **2017**, *17*, 20.
[8] M. Saeed, J. Gao, Y. Shi, T. Lammers, H. Yu, *Theranostics* **2019**, *9*, 7981.
[9] S. Kaczanowska, A. M. Joseph, E. Davila, *J. Leukoc. Biol.* **2013**, *93*, 847.
[10] K. Palucka, J. Banchereau, *Nat. Rev. Cancer* **2012**, *12*, 265.
[11] M. Merad, P. Sathe, J. Helft, J. Miller, A. Mortha, *Annu. Rev. Immunol.* **2013**, *31*, 563.
[12] R. Ella, K. M. Vadrevu, H. Jogdand, S. Prasad, S. Reddy, V. Sarangi, B. Ganneru, G. Sapkal, P. Yadav, P. Abraham, S. Panda, N. Gupta, P. Reddy, S. Verma, S. Kumar Rai, C. Singh, S. V. Redkar, C. S. Gillurkar, J. S. Kushwaha, S. Mohapatra, V. Rao, R. Guleria, K. Ella, B. Bhargava, *Lancet Infect. Dis.* **2021**, *21*, 637.
[13] R. Ella, S. Reddy, H. Jogdand, V. Sarangi, B. Ganneru, S. Prasad, D. Das, D. Raju, U. Praturi, G. Sapkal, P. Yadav, P. Reddy, S. Verma, C. Singh, S. V. Redkar, C. S. Gillurkar, J. S. Kushwaha, S. Mohapatra, A. Bhate, S. Rai, S. Panda, P. Abraham, N. Gupta, K. Ella, B. Bhargava, K. M. Vadrevu, *Lancet Infect. Dis.* **2021**, *21*, 950.
[14] R. Ella, S. Reddy, W. Blackwelder, V. Potdar, P. Yadav, V. Sarangi, V. K. Aileni, S. Kanungo, S. Rai, P. Reddy, S. Verma, C. Singh, S. Redkar, S. Mohapatra, A. Pandey, P. Ranganadin, R. Gumashta, M. Multani, S. Mohammad, P. Bhatt, L. Kumari, G. Sapkal, N. Gupta, P. Abraham, S. Panda, S. Prasad, B. Bhargava, K. Ella, K. M. Vadrevu, P. Aggarwal, et al., *Lancet* **2021**, *398*, 2173.
[15] Y. Mi, C. T. Hagan, B. G. Vincent, A. Z. Wang, *Adv. Sci.* **2019**, *6*, 1801847.

 © 2022 The Authors. Macromolecular Rapid Communications published by Wiley-VCH GmbH

[16] J. Stickdorn, L. Stein, D. Arnold-Schild, J. Hahlbrock, C. Medina-Montano, J. Bartneck, T. Ziss, E. Montermann, C. Kappel, D. Hobernik, M. Haist, H. Yurugi, M. Raabe, A. Best, K. Rajalingam, M. Radsak, S. David, K. Koynov, M. Bros, S. Grabbe, H. Schild, L. Nuhn, *ACS Nano* **2022**, *16*, 4426.
[17] A. Huppertsberg, L. Kaps, Z. Zhong, S. Schmitt, J. Stickdorn, K. Deswarte, F. Combes, C. Czysch, J. De Vrieze, S. Kasmi, N. Choteschovsky, A. Klefenz, C. Medina-Montano, P. Winterwerber, C. Chen, M. Bros, S. Lienenklaus, N. N. Sanders, K. Koynov, D. Schuppan, B. N. Lambrecht, S. A. David, B. G. De Geest, L. Nuhn, *J. Am. Chem. Soc.* **2021**, *143*, 9872.
[18] L. Nuhn, S. De Koker, S. Van Lint, Z. Zhong, J. P. Catani, F. Combes, K. Deswarte, Y. Li, B. N. Lambrecht, S. Lienenklaus, N. N. Sanders, S. A. David, J. Tavernier, B. G. De Geest, *Adv. Mater.* **2018**, *30*, 1803397.
[19] S. Spranger, M. Javorovic, M. Bürdek, S. Wilde, B. Mosetter, S. Tippmer, I. Bigalke, C. Geiger, D J. Schendel, B. Frankenberger, *J. Immunol.* **2010**, *185*, 738.
[20] K. B. Gorden, K. S. Gorski, S. J. Gibson, R. M. Kedl, W. C. Kieper, X. Qiu, M. A. Tomai, S. S. Alkan, J. P. Vasilakos, *J. Immunol.* **2005**, *174*, 1259.
[21] N. Vanparijs, R. De Coen, D. Laplace, B. Louage, S. Maji, L. Lybaert, R. Hoogenboom, B. G. De Geest, *Chem. Commun.* **2015**, *51*, 13972.
[22] D. J. Dowling, E. A. Scott, A. Scheid, I. Bergelson, S. Joshi, C. Pietrasanta, S. Brightman, G. Sanchez-Schmitz, S. D. Van Haren, J. Ninković, D. Kats, C. Guiducci, A. De Titta, D. K. Bonner, S. Hirosue, M. A. Swartz, J. A. Hubbell, O. Levy, *J. Allergy Clin. Immunol.* **2017**, *140*, 1339.
[23] L. Bixenmann, J. Stickdorn, L. Nuhn, *Polym. Chem.* **2020**, *11*, 2441.
[24] K. Fukushima, *Biomater. Sci.* **2015**, *4*, 9.
[25] Y. Dai, X. Zhang, *Polym. Chem.* **2017**, *8*, 7429.
[26] B. Amsden, *Macromol. Biosci.* **2021**, *21*, 2100085.
[27] G. Becker, F. R. Wurm, *Chem. Soc. Rev.* **2018**, *47*, 7739.
[28] S. Kasmi, B. Louage, L. Nuhn, G. Verstraete, S. Van Herck, M. J. Van Steenbergen, C. Vervaet, W. E. Hennink, B. G. De Geest, *Polym. Chem.* **2017**, *8*, 6544.
[29] S. Kasmi, B. Louage, L. Nuhn, A. Van Driessche, J. Van Deun, I. Karalic, M. Risseeuw, S. Van Calenbergh, R. Hoogenboom, R. De Rycke, O. De Wever, W. E. Hennink, B. G. De Geest, *Biomacromolecules* **2016**, *17*, 119.
[30] S. Mohajeri, F. Chen, M. De Prinse, T. Phung, J. Burke-Kleinman, D. H. Maurice, B. G. Amsden, *Mol. Pharmaceutics* **2020**, *17*, 1363.
[31] R. P. Brannigan, A. P. Dove, *Biomater. Sci.* **2017**, *5*, 9.
[32] X. Wang, J. Wilhelm, W. Li, S. Li, Z. Wang, G. Huang, J. Wang, H. Tang, S. Khorsandi, Z. Sun, B. Evers, J. Gao, *Nat. Commun.* **2020**, *11*, 5828.
[33] W. Lu, F. Li, R. I. Mahato, *J. Pharm. Sci.* **2011**, *100*, 2418.
[34] F. Li, M. Danquah, R. I. Mahato, *Biomacromolecules* **2010**, *11*, 2610.
[35] X. Ke, D. J. Coady, C. Yang, A. C. Engler, J. L. Hedrick, Y. Y. Yang, *Polym. Chem.* **2014**, *5*, 2621.
[36] A. Das, P. Theato, *Chem. Rev.* **2016**, *116*, 1434.
[37] M. Scherger, H. J. Räder, L. Nuhn, *Macromol. Rapid Commun.* **2021**, *42*, 2000752.
[38] H. Guan, Z. Xie, Z. Tang, X. Xu, X. Chen, X. Jing, *Polymer* **2005**, *46*, 2817.
[39] B. Hassannia, B. Wiernicki, I. Ingold, F. Qu, S. Van Herck, Y. Y. Tyurina, H. Bayır, B. A. Abhari, J. P. F. Angeli, S. M. Choi, E. Meul, K. Heyninck, K. Declerck, C. S. Chirumamilla, M. Lahtela-Kakkonen, G. Van Camp, D. V. Krysko, P. G. Ekert, S. Fulda, B. G. De Geest, M. Conrad, V. E. Kagan, W. V. Berghe, P. Vandenabeele, T. V. Berghe, *J. Clin. Invest.* **2018**, *128*, 3341.
[40] A. Ahmad, P. Dandawate, S. Schruefer, S. Padhye, F. H. Sarkar, R. Schobert, B. Biersack, *Chem. Biodivers.* **2019**, *16*, e1900028.
[41] Y. Shi, R. Van Der Meel, B. Theek, E. O. Blenke, E. H. E. Pieters, M. H. A. M. Fens, J. Ehling, R. M. Schiffelers, G. Storm, C. F. Van Nostrum, T. Lammers, W. E. Hennink, *ACS Nano* **2015**, *9*, 3740.
[42] Y. Shi, M. J. Van Steenbergen, E. A. Teunissen, L. Novo, S. Gradmann, M. Baldus, C. F. Van Nostrum, W. E. Hennink, *Biomacromolecules* **2013**, *14*, 1826.
[43] H. Maeda, *J. Pers. Med.* **2021**, *11*, 229.
[44] K. Rausch, A. Reuter, K. Fischer, M. Schmidt, *Biomacromolecules* **2010**, *11*, 2836.
[45] L. Evensen, P. L. Johansen, G. Koster, K. Zhu, L. Herfindal, M. Speth, F. Fenaroli, J. Hildahl, S. Bagherifam, C. Tulotta, L. Prasmickaite, G. M. Mælandsmo, E. Snaar-Jagalska, G. Griffiths, *Nanoscale* **2016**, *8*, 862.
[46] F. Fenaroli, U. Repnik, Y. Xu, K. Johann, S. Van Herck, P. Dey, F. M. Skjeldal, D. M. Frei, S. Bagherifam, A. Kocere, R. Haag, B. G. De Geest, M. Barz, D. G. Russell, G. Griffiths, *ACS Nano* **2018**, *12*, 8646.
[47] S. Sieber, P. Grossen, J. Bussmann, F. Campbell, A. Kros, D. Witzigmann, J. Huwyler, *Adv. Drug Delivery Rev.* **2019**, *151-152*, 152.
[48] N.-J. K. Dal, A. Kocere, J. Wohlmann, S. Van Herck, T. A. Bauer, J. Resseguier, S. Bagherifam, H. Hyldmo, M. Barz, B. G. De Geest, F. Fenaroli, *Small* **2020**, *16*, 1906719.
[49] J. H. Jung, M. Ree, H. Kim, *Catal. Today* **2006**, *115*, 283.
[50] Z. Zhang, R. Kuijer, S. K. Bulstra, D. W. Grijpma, J. Feijen, *Biomaterials* **2006**, *27*, 1741.
[51] J. Kockelmann, J. Stickdorn, S. Kasmi, J. De Vrieze, M. Pieszka, D. Y. W. Ng, S. A. David, B. G. De Geest, L. Nuhn, *Biomacromolecules* **2020**, *21*, 2246.
[52] S. Van Herck, K. Deswarte, L. Nuhn, Z. Zhong, J. P. P. Catani, Y. Li, N. N. Sanders, S. Lienenklaus, S. De Koker, B. N. Lambrecht, S. A. David, B. G. De Geest, *J. Am. Chem. Soc.* **2018**, *140*, 14300.
[53] B. Wang, S. Van Herck, Y. Chen, X. Bai, Z. Zhong, K. Deswarte, B. N. Lambrecht, N. N. Sanders, S. Lienenklaus, H. W. Scheeren, S. A. David, F. Kiessling, T. Lammers, B. G. De Geest, Y. Shi, *J. Am. Chem. Soc.* **2020**, *142*, 12133.
[54] G. M. Lynn, R. Laga, P. A. Darrah, A. S. Ishizuka, A. J. Balaci, A. E. Dulcey, M. Pechar, R. Pola, M. Y. Gerner, A. Yamamoto, C. R. Buechler, K. M. Quinn, M. G. Smelkinson, O. Vanek, R. Cawood, T. Hills, O. Vasalatiy, K. Kastenmüller, J. R. Francica, L. Stutts, J. K. Tom, K. Ah Ryu, A. P. Esser-Kahn, T. Etrych, K. D. Fisher, L. W. Seymour, R. A. Seder, *Nat. Biotechnol.* **2015**, *33*, 1201.
[55] V. Durai, K. M. Murphy, *Immunity* **2016**, *45*, 719.
[56] F. Fallarino, C. Orabona, C. Vacca, R. Bianchi, S. Gizzi, C. Asselin-Paturel, M. C. Fioretti, G. Trinchieri, U. Grohmann, P. Puccetti, *Int. Immunol.* **2005**, *17*, 1429.
[57] S. Wirtz, C. Becker, M. C. Fantini, E. E. Nieuwenhuis, I. Tubbe, P. R. Galle, H.-J. Schild, M. Birkenbach, R. S. Blumberg, M. F. Neurath, *J. Immunol.* **2005**, *174*, 2814.

 © 2022 The Authors. Macromolecular Rapid Communications published by Wiley-VCH GmbH

Macromolecular Rapid Communications

Supporting Information

for *Macromol. Rapid Commun.*, DOI 10.1002/marc.202200095

End Group Dye-Labeled Polycarbonate Block Copolymers for Micellar (Immuno-)Drug Delivery

*Christian Czysch, Carolina Medina-Montano, Nils-Jørgen Knudsen Dal, Thi Dinh, Yannick Fröder, Pia Winterwerber, Konrad Maxeiner, Hans-Joachim Räder, Detlef Schuppan, Hansjörg Schild, Matthias Bros, Bernhard Biersack, Federico Feranoli, Stephan Grabbe and Lutz Nuhn**

End group dye-labeled polycarbonate block copolymers for micellar (immuno-)drug delivery

– Supporting Information –

Christian Czysch,[1] Carolina Medina-Montano,[2] Nils-Jørgen Knudsen Dal,[3] Thi Dinh,[1] Yannick Fröder,[1] Pia Winterwerber,[1] Konrad Maxeiner,[1] Hans-Joachim Räder,[1] Detlef Schuppan,[4,5] Hansjörg Schild,[6] Matthias Bros,[2] Bernhard Biersack,[7] Federico Feranoli,[3] Stephan Grabbe,[2] Lutz Nuhn[1,8,]*

1: Max Planck Institute for Polymer Research Mainz, Germany
2: Department of Dermatology, University Medical Center Mainz, Germany
3: Department of Bioscience, University of Oslo, Norway
4: Institute of Translational Immunology, University Medical Center Mainz, Germany
5: Division of Gastroenterology, Beth Israel Deaconess Medical Center, Harvard Medical School Boston, United States
6: Institute of Immunology, University Medical Center Mainz, Germany
7: Organic Chemistry Laboratory, University of Bayreuth, Germany
8: Chair of Macromolecular Chemistry, Faculty of Chemistry and Pharmacy, Julius Maximilian University Würzburg, Germany

** corresponding author (e-mail: lutz.nuhn@mpip-mainz.mpg.de).*

Materials and Methods

Materials

Solvents and reagents were purchased and used without further purification unless described. 2-Propylthiazolo[4,5-c]quinolin-4-amine (CL075), 2,2-bis(hydroxymethyl)propionic acid (Bis-MPA), triethylamine, benzyl bromide, ethyl chloroformate, tetrahydrofuran (dry), methylene chloride (dry) and DMF (dry) were purchased from Sigma Aldrich. 3,3'-((3,4-difluorophenyl)methylene)bis(1*H*-indole) was synthesized by Bernhard Biersack (University of Bayreuth, Germany).[1]
Bis(pentafluorophenyl)-carbonate and hexafluoroisopropanol (HFIP) were purchased from Fluorochem Ltd., Alexa Fluor 647 cadaverine was purchased from ThermoFisher Scientific and 5-(and-6-)-((N-(5-aminopentyl)amino)carbonyl)tetramethylrhodamine cadaverine (5(6)-TMR cadaverine) was purchased from Biotium. Poly(ethylene glycol) methyl ether ($mPEG_{113}$) was purchased from Rapp Polymere (Tübingen).
Millipore (mp) water was prepared using a MILLI-Q R Reference A+ System. Water was used at a resistivity of 18.2 MΩ·cm and total organic carbon of <5 ppm.

NMR spectroscopy

^{1}H, ^{19}F and DOSY NMR spectra were recorded on a Bruker Avance 300 MHz, a Bruker Avance 500 MHz spectrometer and a Bruker Avance III 700 MHz spectrometer. Diffusion ordered spectroscopy (DOSY) were conducted at room temperature and processed by Bayesian DOSY transformation (minimum: $1.00 \cdot 10^{-10}$, maximum: $1.00 \cdot 10^{-4}$, resolution factor: 1.00, repetition factor: 1, points in dimension: 128). Samples were prepared using deuterated solvents obtained from Sigma-Aldrich. Spectra were analyzed using MestReNova 14.2.0 by Mestrelab Research.

Size Exclusion Chromatography

Analytical size exclusion chromatography (SEC) was carried out at 40 °C on a SECcurity2instrument purchased from PSS, Mainz. HFIP with 3 g/L potassium trifluoroacetate was used as an eluent and the flow rate was set at 0.8 mL/min. The column material was composed of modified silica gel (PFG columns, particle size: 7 µm, porosity: 100 Å+ 1000 Å), purchased from PSS Polymer Standards Service GmbH, Mainz, Germany. For polymer detection a UV detector at a wavelength of λ = 254 nm and a RI detector were employed (or alternative UV detection at wavelength as

mentioned). Furthermore, the system was equipped with a SECcurity2isocratic pump, a degasser, an auto sampler, and a column thermostat.
Molecular weights were determined by using a calibration with PMMA (PSS Polymer Standards Services GmbH). Evaluation of the elution diagram was conducted with PSS WinGPC from PSS Polymer Standard Service GmbH.

Dynamic Light Scattering

Dynamic light scattering measurements were performed using a Malvern Z Nano instrument equipped with a He-Ne-Laser (λ = 632.8 nm) using ZetaSizer Software 7.12. Measurements were performed in triplicates at 25°C or 37°C and a detection angle of 173°. For measurements of AF647-labeled samples, the DLS setup was modified using a bandpass filter (center wavelength of 633 nm with a bandwidth of 10 nm) to avoid detection of AF647 fluorescence at the scattering detector.
For multi-angle light scattering, an alternative set up was used and scattering measurements recorded at angles of 30°-135° using a He-Ne-Laser as the incident beam (compare section “plasma aggregation studies”).

Atomic Force Microscopy

For atomic force microscopy imaging, polymeric micelles were diluted to 50 µg/mL in mp-water, drop-casted (5 µL) on a mica substrate (circular, 15 mm) and dried over-night in a dust-free environment.
AFM imaging measurements were performed using a Bruker Dimension FastScan Bio® atomic force microscope in Peak Force mode. Samples were scanned with scan rates of 0.994 – 1.41 Hz and AFM probes with a nominal spring constant of 0.25 N/m (FastScan-D, Bruker) were employed. Data was processed using NanoScope Analysis 1.8.

Ultraviolet-Vis Spectroscopy and Fluorescence Spectroscopy

UV-vis spectra were recorded using a Thermo Scientific™ NanoDrop™ 2000c spectrophotometer with Brand UV micro cuvettes for aqueous solutions or a Hellma Quartz Cuvette for solutions containing THF.
For fluorescence spectroscopy and absorbance read-out of RAW-blue and MTT assays, a Spark 20M Multimode Microplate Reader from TecanTrading AG (Mannedorf, Switzerland) was used.

Mass Spectrometry

MALDI measurements were carried out on a rapifleX^{TM} MALDI-TOF/TOF mass spectrometer from Bruker Daltonik GmbH (Bremen, Germany). The instrument was equipped with a scanning smartbeam 10 kHz Nd:YAG laser at a wavelength of 355 nm and a 10 bit 5 GHz digitizer. The acceleration voltage was set to 20 kV and the mass spectra were recorded in positive ion mode. Calibration was done by polymer standards of polyethylene glycol (from PSS Polymer Standards Services GmbH).

Syntheses

Synthesis of 2,2-bis(hydroxymethyl)propionic acid benzyl ester

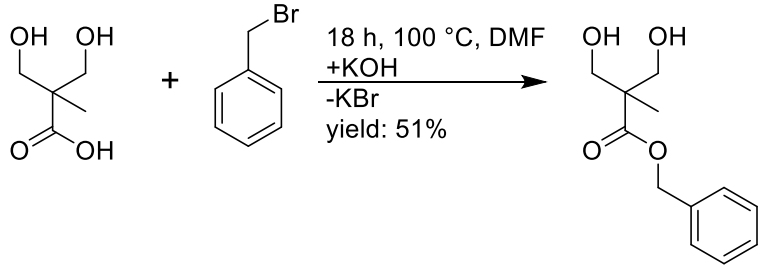

The synthesis of 2,2-bis(hydroxymethyl)propionic acid benzyl ester was adapted from literature and modified.[2] 45.0 g 2,2-bis(hydroxymethyl)propionic acid (333.5 mmol, 1.0 eq), 21.5 g potassium hydroxide (333.5 mmol, 1.0 eq) and 250 mL of absolute DMF were heated under nitrogen atmosphere at 100 °C in a three neck bottom flask until a homogenous solution was formed. Then 47.9 mL benzyl bromide (69.0 g, 403.5 mmol, 1.2 eq) was slowly added via a dropping funnel to the reaction mixture, which was stirred overnight at 100 °C. During the addition of the benzyl bromide, a colorless solid was formed. The solution was allowed to cool to room temperature and the solvent was removed under vacuum. Ethyl acetate (300 mL), hexane (300 mL) and water (200 mL) were added to the residue. The resulting organic layer of the solvent mixture was retained, washed with water, dried over $MgSO_4$ and evaporated. The crude product was recrystallized from toluene to give pure 2,2-bis(hydroxymethyl)propionic acid benzyl ester (38.0 g, 51%).

^{1}H NMR (300 MHz, DMSO-d_6) δ [ppm] = 7.38–7.27 (5H, m, **a**), 5.08 (2H, s, **b**), 4.70 (2H, t, **c+c'**), 3.54 (2H, dd, **d**), 3.45 (2H, dd, **d'**), 1.08 (3H, s, **e**).

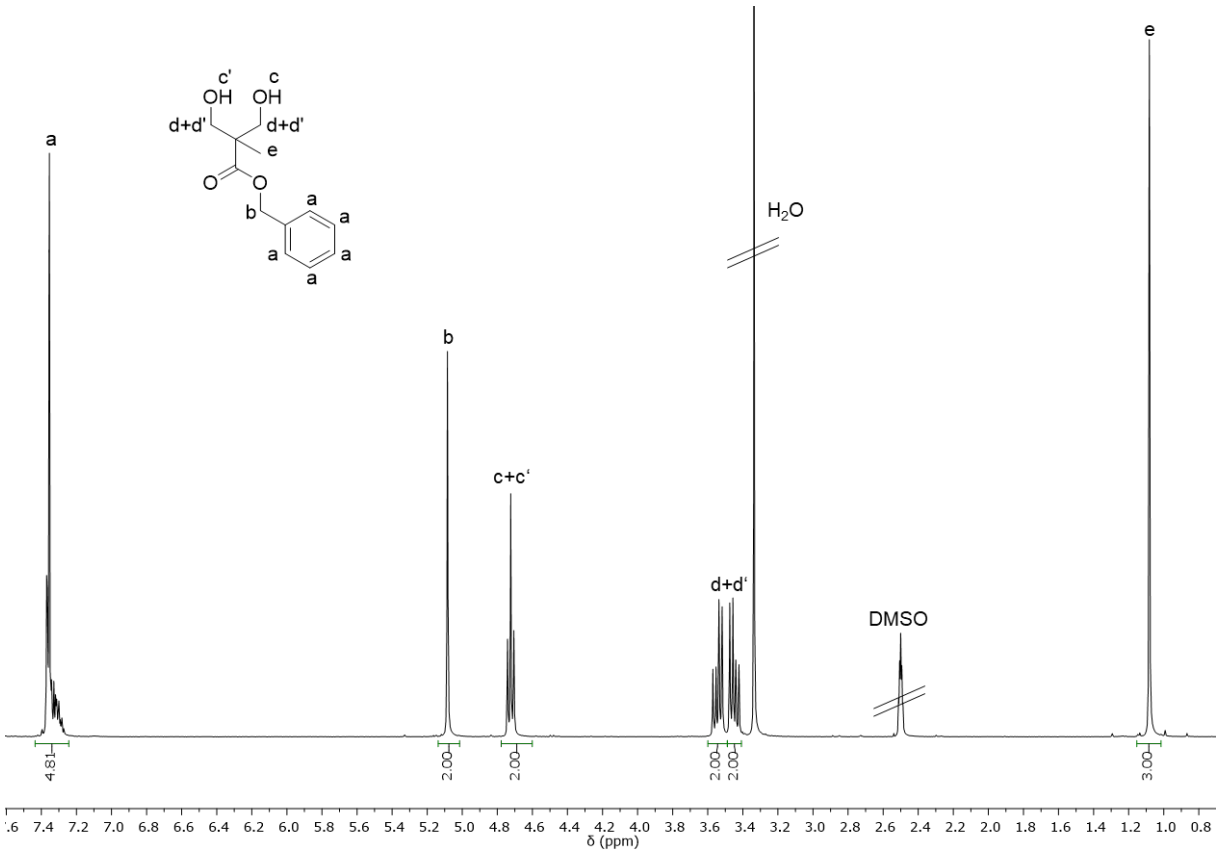

Figure S1: ^{1}H NMR spectrum (300 MHz) of 2,2-bis(hydroxymethyl)propionic acid benzyl ester in DMSO-*d*$_6$.

Synthesis of 5-methyl-5-benzyloxycarbonyl-1,3-dioxan-2-one

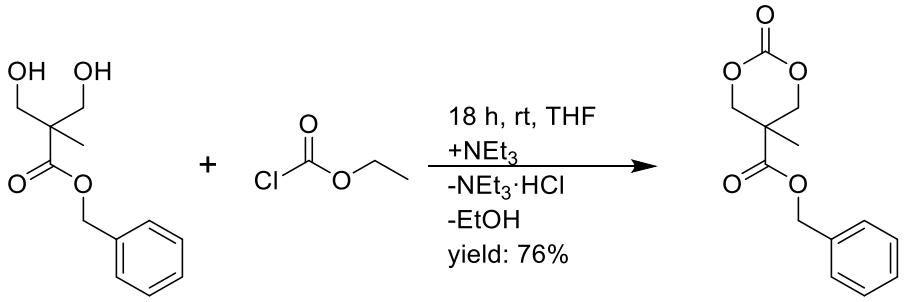

The synthesis of 5-methyl-5-benzyloxycarbonyl-1,3-dioxane-2-one was adapted from literature and modified.[3] In a three neck round bottom flask 20.0 g 2,2-bis(hydroxymethyl)propionic acid benzyl ester (89.2 mmol, 1 eq) and 56.92 g ethyl chloroformate (524.5 mmol, 6.0 eq) were dissolved in 500 mL dry THF and cooled to 0 °C. 72.8 mL triethylamine (56.1 g, 553.9 mmol) was slowly added via a dropping funnel, which resulted in the formation of colorless triethylamine hydrochloride. To achieve full conversion the mixture was stirred overnight at room temperature. The following day the precipitated salt (triethylamine hydrochloride) was filtered off and the filtrate was concentrated under reduced pressure.

5-Methyl-5-benzyloxycarbonyl-1,3-dioxane-2-one (17.0 g, 76%) was obtained as colorless crystals after being three times recrystallized from ethyl acetate.

^{1}H NMR (300 MHz, $CDCl_3$) δ [ppm] = 7.40–7.31 (5H, m, **a**), 5.22 (2H, s, **b**), 4.70 (2H, d, **c**), 4.20 (2H, d, **c'**), 1.33 (3H, s, **d**).

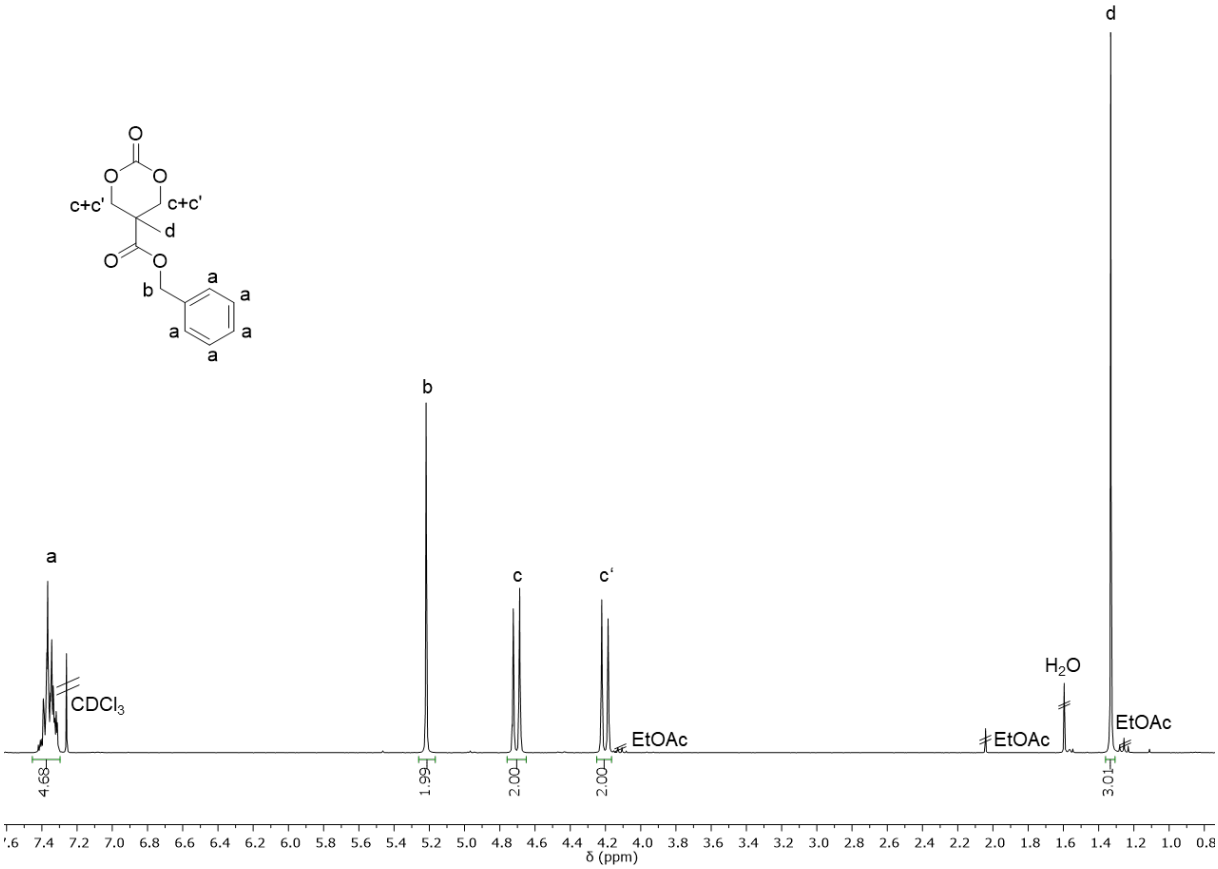

Figure S2: ^{1}H NMR spectrum (300 MHz) of 5-methyl-5-benzyloxycarbonyl-1,3-dioxane-2-one (MTC-OBn) in $CDCl_3$.

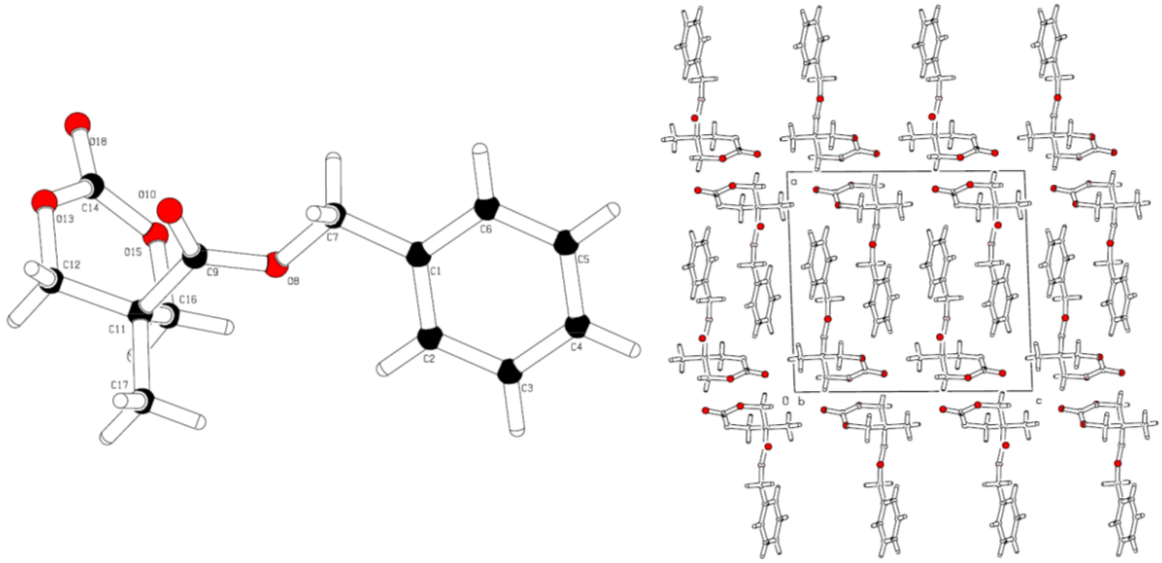

Figure S3: X-ray diffraction results of MTC-OBn. Single molecule of MTC-OBn (left), crystal lattice of MTC-OBn (right).

Polymer synthesis of $mPEG_{113}$-*b*-poly(MTC-OBn) and pyrene butanol-poly(MTC-OBn)

The synthesis of $mPEG_{113}$-*b*-poly(MTC-OBn) was adapted from literature and modified.[4] 0.1502 g MTC-OBn (0.600 mmol, 15 eq) was weighed into a 10 mL Schlenk-flask and dissolved in ~2 mL benzene. 0.200 g $mPEG_{113}$ (0.040 mol, 1 eq.) was dissolved in ~2 mL benzene. Both compounds were freed from residual water by azeotropic removal of benzene and water overnight *in vacuo*. On the following day, the flasks were purged with nitrogen and freshly dried dichloromethane (calcium hydride) was added *via* syringe. $mPEG_{113}$ was dissolved dry dichloromethane and transferred to the flask containing MTC-OBn. Dichloromethane was added to reach a final volume of 1.20 mL corresponding to a 0.5 M concentration of MTC-OBn. The reaction mixture was cooled to -20°C using a cryostat. For the initiation of the polymerization 5.97 µL 1,8-diazabicyclo[5.4.0]undec-7-ene (DBU, 6.09 mg, 0.040 mmol, 1.0 eq) was added to this mixture in a nitrogen countercurrent. After a reaction time of 2 h at -20°C conversion was determined by ^{1}H NMR (97.8% conversion) and the polymer was precipitated by addition into a large excess of cold diethyl ether (-20°C), centrifuged (4500 rpm, 10 min, 4 °C) and decanted. Subsequently, the pellet was dissolved in ~2 mL of dichloromethane and precipitated by dropwise addition to diethyl ether. The procedure was repeated once. After drying in vacuo overnight $mPEG_{113}$-*b*-poly(MTC-OBn) was obtained as a colorless solid (0.284 mg, 81.8% yield). To demonstrate the highly controlled manner of this polymerization technique, the homopolymer pyrene butanol-poly$(MTC\text{-}OBn)_{20}$ was prepared. Polymerization was initiated from pyrene butanol (8.2 mg, 0.030 mmol, 1.0 eq.; MTC-OBn 0.1502 g, 0.600 mmol, 20 eq; DBU, 4.6 mg, 0.030 mmol, 1.0 eq), the product was three times precipitated in *n*-hexane, dried *in vacuo* and analyzed in an analogous manner as described above (see Figure S4).

^{1}H NMR (700 MHz, $CDCl_3$) δ [ppm] = 7.39–7.27 (5H, m, **d**), 5.12 (2H, s, **c**), 4.27 (4H, s, **a**), 3.63 (4H, s, **e**), 3.36 (3H, s, **f**), 1.22 (3H, s, **b**).

HFIP SEC $mPEG_{113}$-*b*-poly$(MTC\text{-}OBn)_{15}$ M_n = 35210 g/mol, M_w = 37050 g/mol $Đ$ = 1.05 (RI detector).

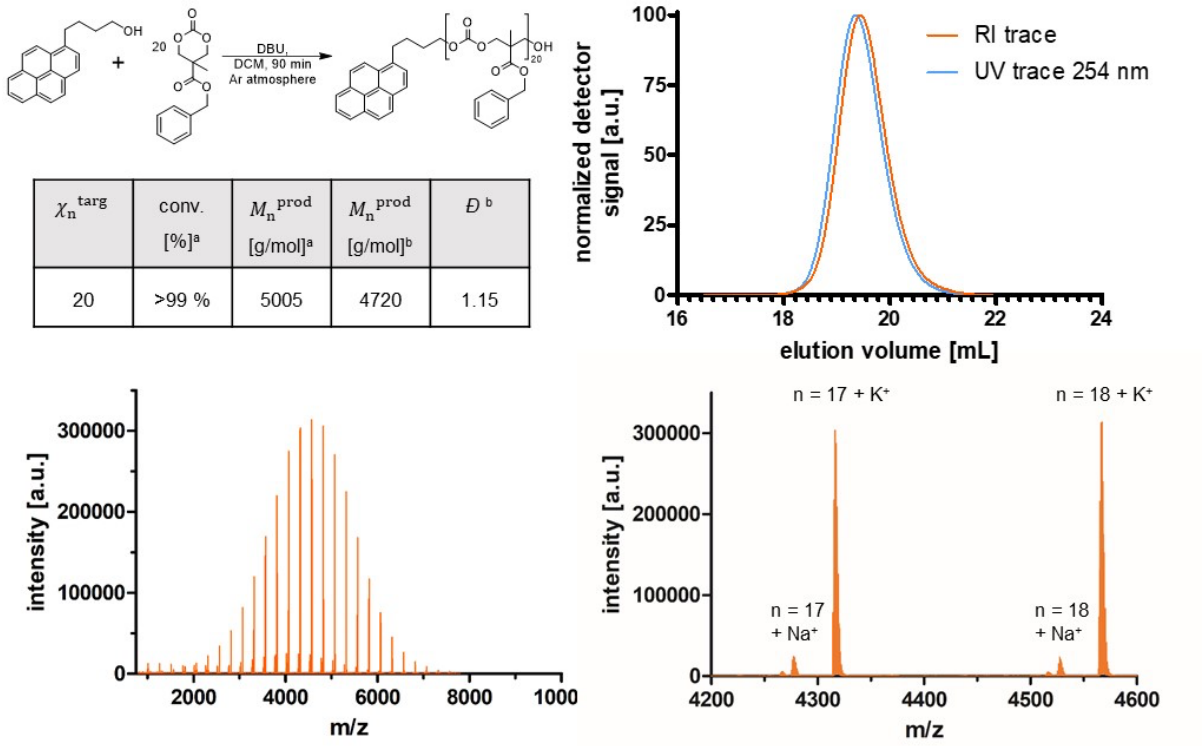

χ_n^{targ}	conv. [%][a]	M_n^{prod} [g/mol][a]	M_n^{prod} [g/mol][b]	$Đ$ [b]
20	>99 %	5005	4720	1.15

Figure S4: Pyrene butanol-MTC-OBn$_{20}$ homopolymer synthesis and characterization. Reaction was initiated by pyrene butanol in DCM at -20°C using DBU as a ROP catalyst aiming for a DP of 20. Table with a summary of the acquired data: Aimed number of repeating units χ_n^{targ}, conversion (conv.), molar mass of the product M_n^{prod} as determined by [a]NMR and [b]HFIP SEC (RI trace). HFIP SEC trace (top right) showing a narrow distribution. MALDI-ToF (bottom) demonstrating the defined architecture with the desired end groups.

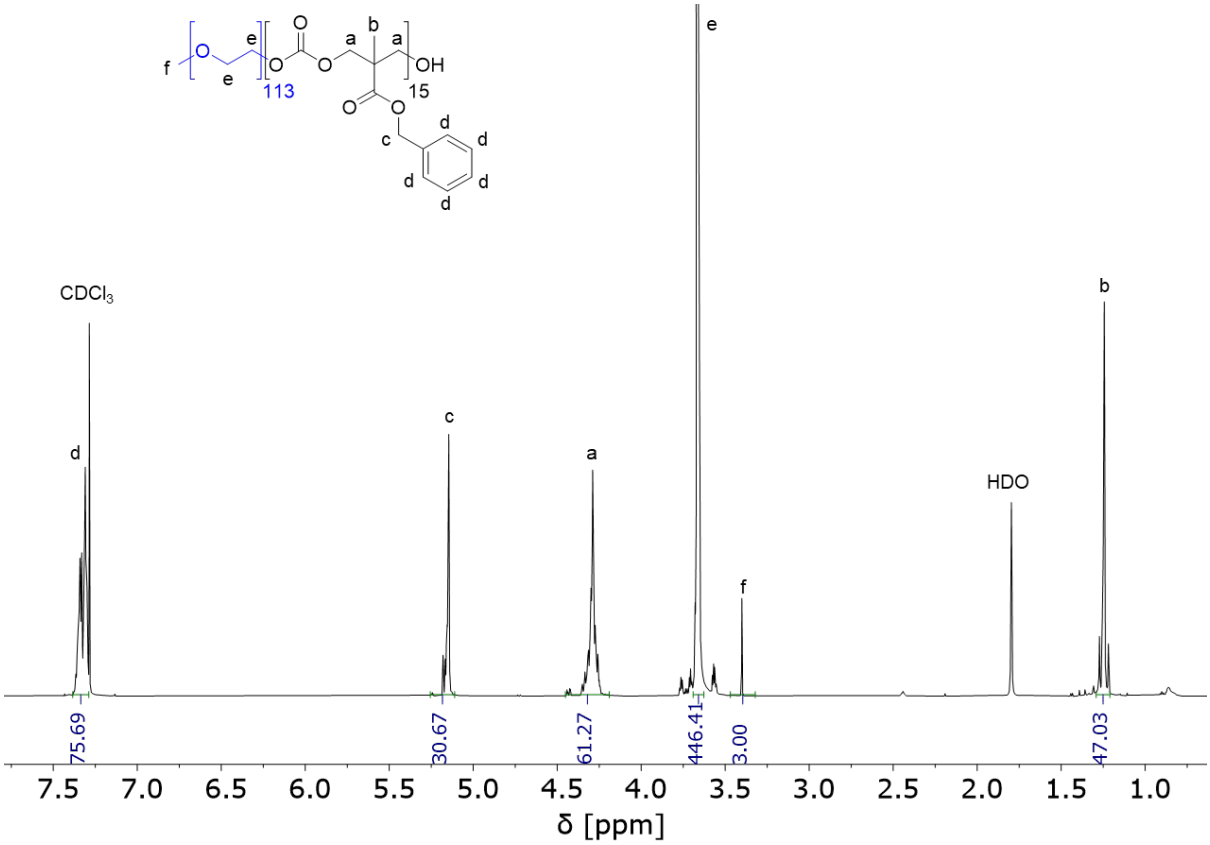

Figure S5: ^{1}H NMR spectrum (700 MHz) of mPEG$_{113}$-*b*-poly(MTC-OBn)$_{15}$ in $CDCl_3$.

End group functionalization of mPEG$_{113}$-*b*-poly(MTC-OBn)$_{15}$

In a 10 mL Schlenk tube a mixture of 14.8 mg bis(pentafluorophenyl) carbonate (0.0376 mmol, 5.8 eq.) and the catalyst DMAP (0.42 mg, 0.0035 mol, 0.5 eq.) was dissolved in 1.0 mL dry THF. In another tube 60.0 mg mPEG$_{113}$-*b*-poly(MTC-OBn)$_{15}$ (0.0069 mmol, 1 eq.) was dried by azeotropic distillation with benzene over-night and then dissolved in 0.8 mL dry THF and slowly added under stirring to the mixture of bis(pentafluorophenyl) carbonate and DMAP. The reaction was stirred under inert atmosphere at room temperature for 16 h when full conversion was observed by ^{19}F NMR. After precipitation in 50 mL diethyl ether (-20°C) and drying in vacuo overnight the end group activated mPEG$_{113}$-*b*-poly(MTC-OBn)$_{15}$-OCO-OPFP was obtained as a colorless solid.

^{1}H NMR (700 MHz, $CDCl_3$) δ [ppm] = 7.39–7.27 (72H, m, **d**), 5.17 (2H, s, **c'**), 5.12 (28H, s, **c**), 4.49 (2H, s, **a'**),4.27 (60H, s, **a**), 3.63 (461H, s, **e**), 3.36 (3H, s, **f**), 1.30 (3H, s, **b'**), 1.22 (43H, s, **b**).

^{19}F NMR (700 MHz, $CDCl_3$) δ [ppm] = -153.0 (2F, d, **a**), -157.1 (1F, t, **c**), -161.7 (2F, t, **b**).

HFIP SEC M_n = 28330 g/mol, M_w = 29570 g/mol $Đ$ = 1.04 (RI detector).

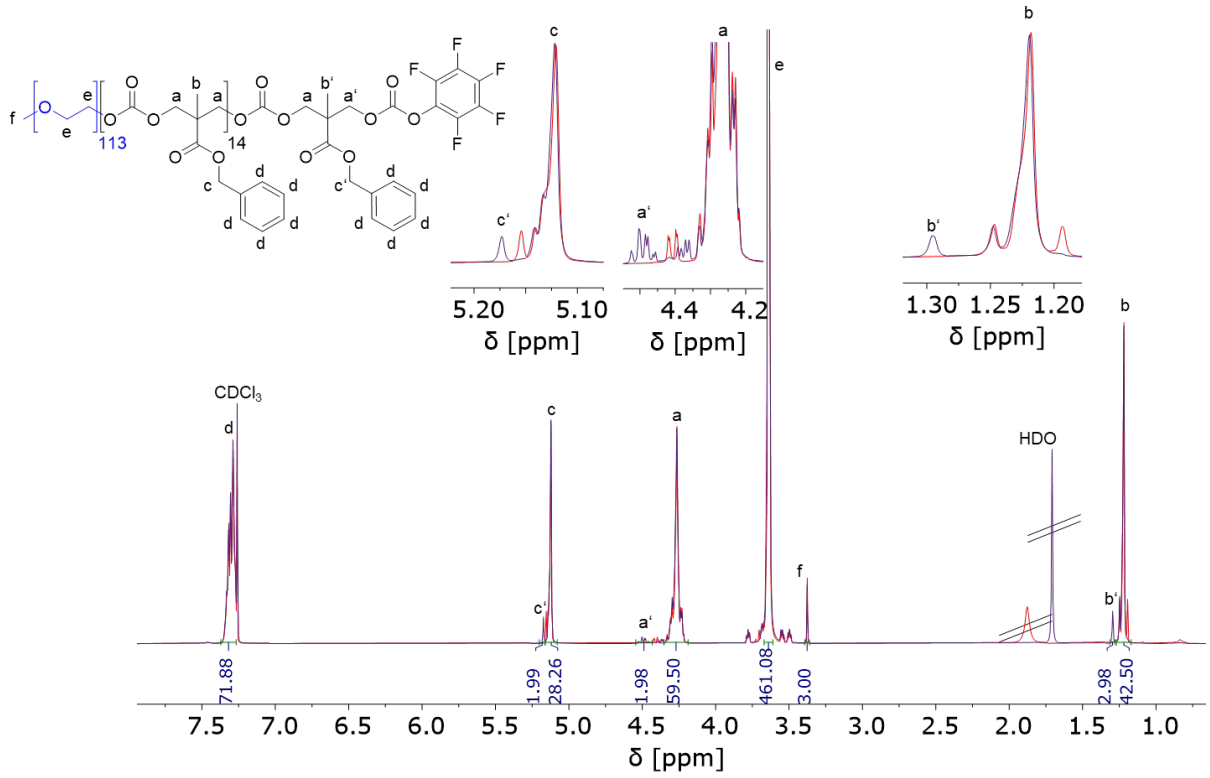

Figure S6: ^{1}H-NMR spectrum of end group activated mPEG$_{113}$-*b*-poly(MTC-OBn)$_{15}$-OCO-OPFP (purple line with integrals) and mPEG$_{113}$-*b*-poly(MTC-OBn)$_{15}$ (red line). After end group functionalization respective signals shift downfield (signal c from 5.15 ppm to 5.20 c', signal a from 4.30 to 4.50 ppm a' and signal b from 1.25 to b' 1.32). Integral values of end group signals (a', b', c') prove full conversion of end group activation, forming the activated carbonate ester.

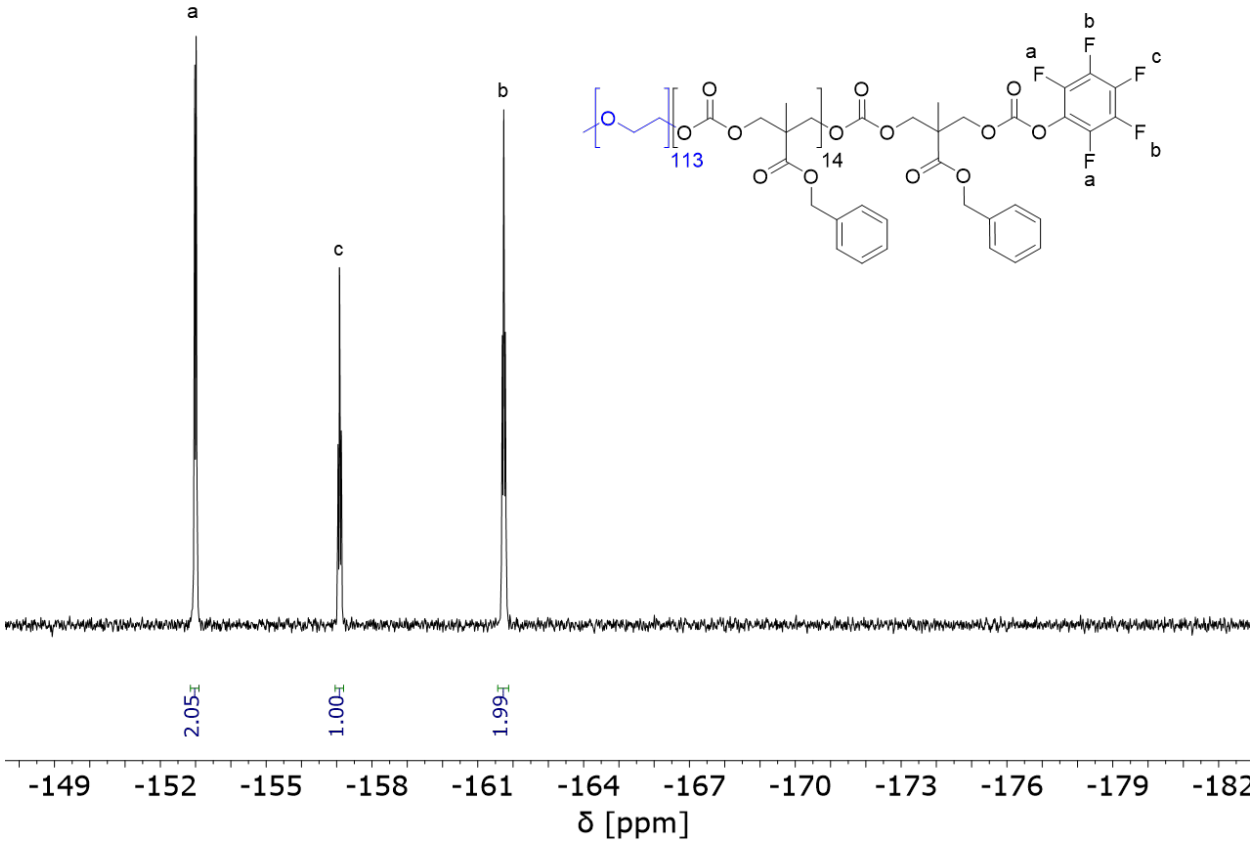

Figure S7: ^{19}F NMR spectrum of mPEG$_{113}$-*b*-poly(MTC-OBn)$_{15}$-OCO-OPFP.

Covalent attachment of dyes to polymer end groups of activated $mPEG_{113}$-*b*-poly(MTC-OBn)$_{15}$-OCO-OPFP

In a 10 mL Schlenk tube end group activated polymer $mPEG_{113}$-*b*-poly(MTC-OBn)$_{15}$-OCO-OPFP (10 mg, 55.6 µmol, 1.0 eq.) was dissolved in 0.5 mL dry DMF under inert atmosphere and triethyl amine was added from a stock solution (8.44 µmol, 1.5 eq.). Then tetramethylrhodamine cadaverine was added from a stock solution in DMSO (286 µg, 55.6 µmol, 1.0 eq.) and the mixture was stirred at room temperature for 16 h. Reaction was quenched by dropwise addition of the mixture to 3 mL of hydrochloric acid (pH 1) to avoid hydrolysis of the polycarbonate backbone that would occur at alkaline pH. The DMF/hydrochloric acid mixture was transferred to a dialysis tube with a 1 MWCO cut-off and dialyzed with frequent exchange of pH 4 mp-water (adjusted with hydrochloric acid) for 3 days.

Finally, the solution was filtered using a 0.22 µM syringe filter (hydrophilic PTFE) and freeze-dried. Dye-labeled polymer chains were analyzed by HFIP SEC by recording UV-Vis traces at 549 nm (TMR) and 600 nm (AF647). SEC both confirmed the absence of free dye and showed the narrow distribution of the products.

For the conjugation of Alexa Fluor 647, the scale of the reaction was halved: $mPEG_{113}$-*b*-poly(MTC-OBn)$_{15}$-OCO-OPFP (5 mg, 27.8 µmol, 1.0 eq.), Alexa Fluor 647-Cadaverine (279 µg, 27.8 µmol, 1.0 eq.), triethylamine (4.22 µmol, 1.5 eq.) in 0.25 mL DMF. After dialysis, minor amounts of free dye were found by RP-TLC. For the removal of free dye, spin filtration was conducted using a 100 kDa spin filter (RC, Amicon Ultra 4, Merck Millipore) after 3 filtration processes free dye was quantitatively removed from the polymeric solution.

HFIP SEC of dye-labeled $mPEG_{113}$-*b*-poly(MTC-OBn)$_{15}$

TMR-labeled: M_n = 30690 g/mol, M_w = 31700 g/mol $Đ$ = 1.03 (RI detector).

AF647-labeled: M_n = 32560 g/mol, M_w = 35320 g/mol $Đ$ = 1.08 (RI detector).

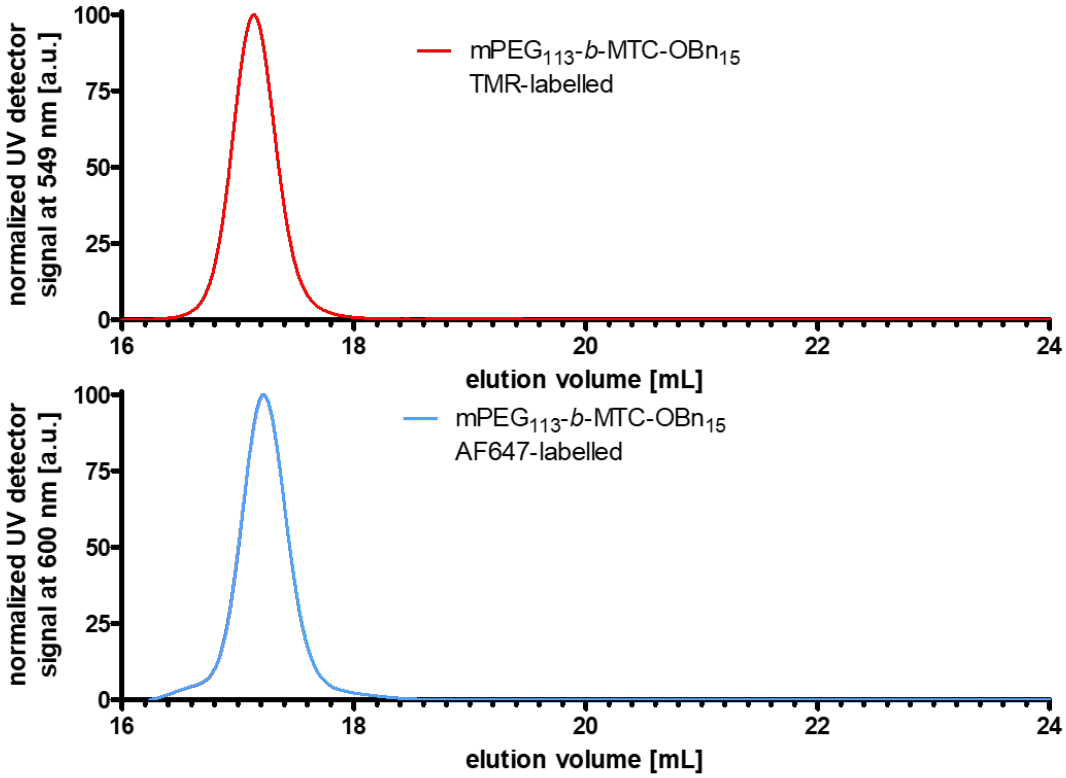

Figure S8: Full HFIP SEC elugram of dye-labeled block copolymers at 549/600 nm. TMR-labeled mPEG$_{113}$-*b*-poly(MTC-OBn)$_{15}$ (red) and AF647-labeled mPEG$_{113}$-*b*-poly(MTC-OBn)$_{15}$ (blue), both show no additional absorbance at higher elution volumes (correlating to lower molecular mass), thus SEC confirms the absence of unconjugated dyes.

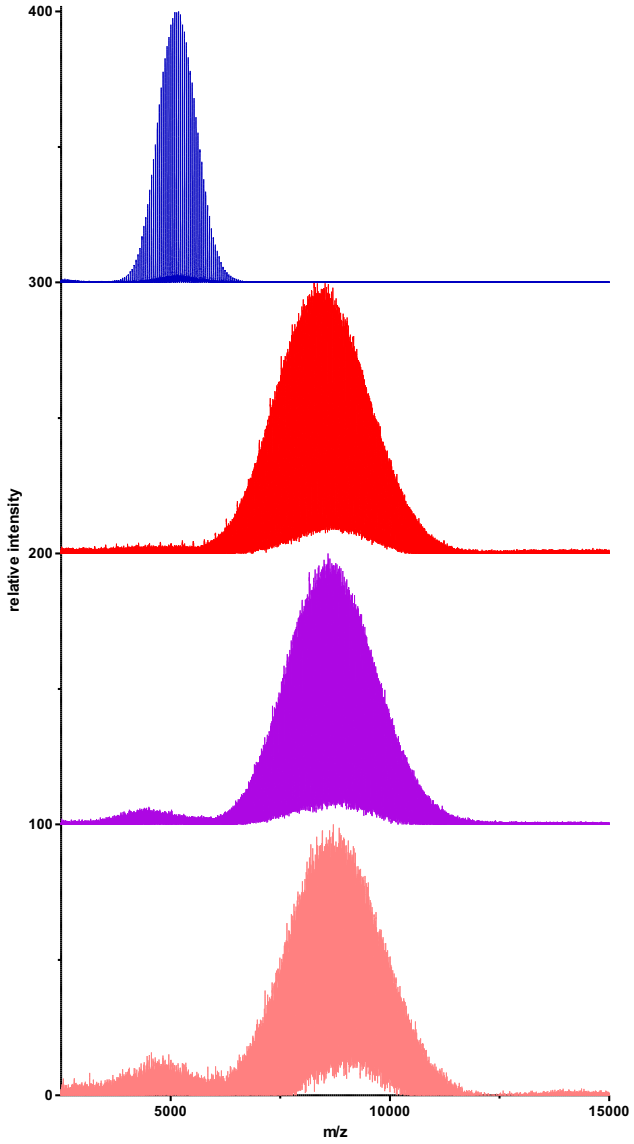

Figure S9: Mass spectrometric analysis (by MALDI-ToF) of end-group labeled polymers. Mass spectra of block copolymers by MALDI-ToF show the defined structure of the synthesized block copolymers: $mPEG_{113}$ (blue), $mPEG_{113}$-*b*-poly(MTC-OBn)$_{15}$ (red), $mPEG_{113}$-*b*-poly(MTC-OBn)$_{15}$-OCO-OPFP (purple) and TMR-labeled $mPEG_{113}$-*b*-poly(MTC-OBn)$_{15}$ (pink).

Assembly and drug-loading of dye-labeled polymeric micelles by solvent-evaporation

For the assembly of micelles, the polymers were dissolved in acetone at 5 mg/mL, which is a volatile, non-toxic solvent. For dye-labeled micelles a 1:4 ratio of labeled to non-labeled material was used (total amount of polymer 5 mg for CL075-loading and 10 mg for DIM-DF-loading). Then the desired amount of drug was added from a stock solution of the drug (DIM-DF or CL075) in acetone. This mixture was added dropwise to mp-water (in case of DIM-DF encapsulation) or PBS (in case of CL075 encapsulation). Samples were placed in a sterile fume hood over-night to evaporate the acetone. For quantitative removal of acetone samples were vaporized until only ~90% of the initially added water/PBS was left in the vessel (determined by weighing the water/PBS vessel before the polymeric acetone solution was added). The missing amount of water was subsequently added to the sample, thereby adjusting the concentration to the intended value of 5 mg/mL. Additionally, drug-free polymeric micelles as well as dye-free polymeric micelles with drugs were prepared. The solubility enhancing effect of the polymer was confirmed by dropping pure drug solution (in acetone) into mp-water (for DIM-DF) or PBS (for CL075). In both cases a precipitate was formed that could be filtered off using syringe filter with a pore size of 0.22 µm (membrane material: hydrophilized PTFE). Please note, that CL075 is slightly soluble in mp-water and insoluble in PBS at pH 7.4.

Samples were characterized by DLS and AFM.

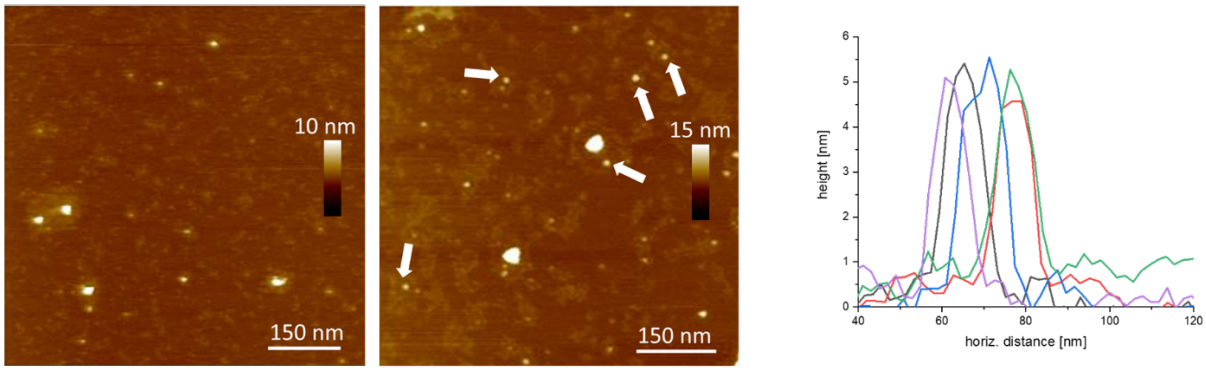

Figure S10: AFM images of dropcasted micelles measured in the dry state. Micelles were found as small spherical particles with heights of 5-6 nm (see heights profile of selected particles, right graph). Imaging in the dry state results in a minor formation of aggregates (larger bright spots).

For the encapsulation of DIM-DF, AF647-labeled material was employed, whereas TMR-labeled material was used for CL075 encapsulation. The selection of the dye reflects the application with AF647 for the tracking of DIM-DF loaded micelles within

zebrafish embryos and TMR, which matches the flow cytometry analysis panel that was used for cell tests.

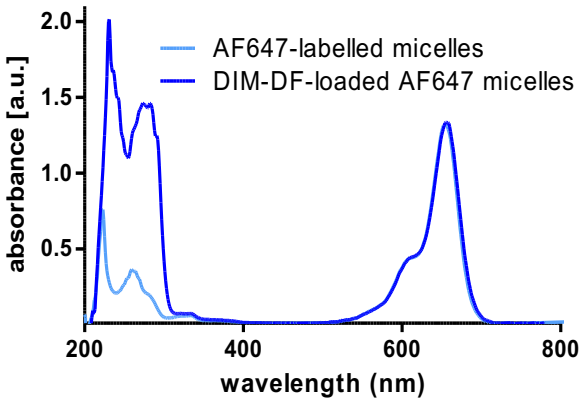

Figure S11: Additional UV-Vis spectrum of AF647-labeled micelles (light blue) and DIM-DF-loaded AF647-labeled micelles (dark blue) at a concentration of 0.5 mg/mL in mp-water. Both samples show strong AF647 absorption at ~655 nm. DIM-DF gave an additional absorption at 273 nm.

Determination of DIM-DF drug load by ^{19}F NMR

For the determination of drug load, DIM-DF-loaded polymeric micelles (2 mL of a 5 mg/mL polymer solution containing ~0.5 mg DIM-DF) were freeze-dried to yield ~10.5 mg of dried material. For NMR analysis, 6.266 mg was weighed in using a microbalance and dissolved in 500 µL deuterated DMSO, which was spiked with 4-fluorotoluene (4-FT) as a reference compound. In an analogous manner, different amounts of DIM-DF (reaching from 0.1 to 1.0 mg) were dissolved using the 4-FT spiked DMSO solvent. Samples were then analyzed by ^{19}F NMR spectroscopy. The relative integral values of the micellar DIM-DF compared to the 4-FT integral were used to calculate the DIM-DF content according to the DIM-DF calibration curve (calibration curve for the signal at 139.3 ppm).

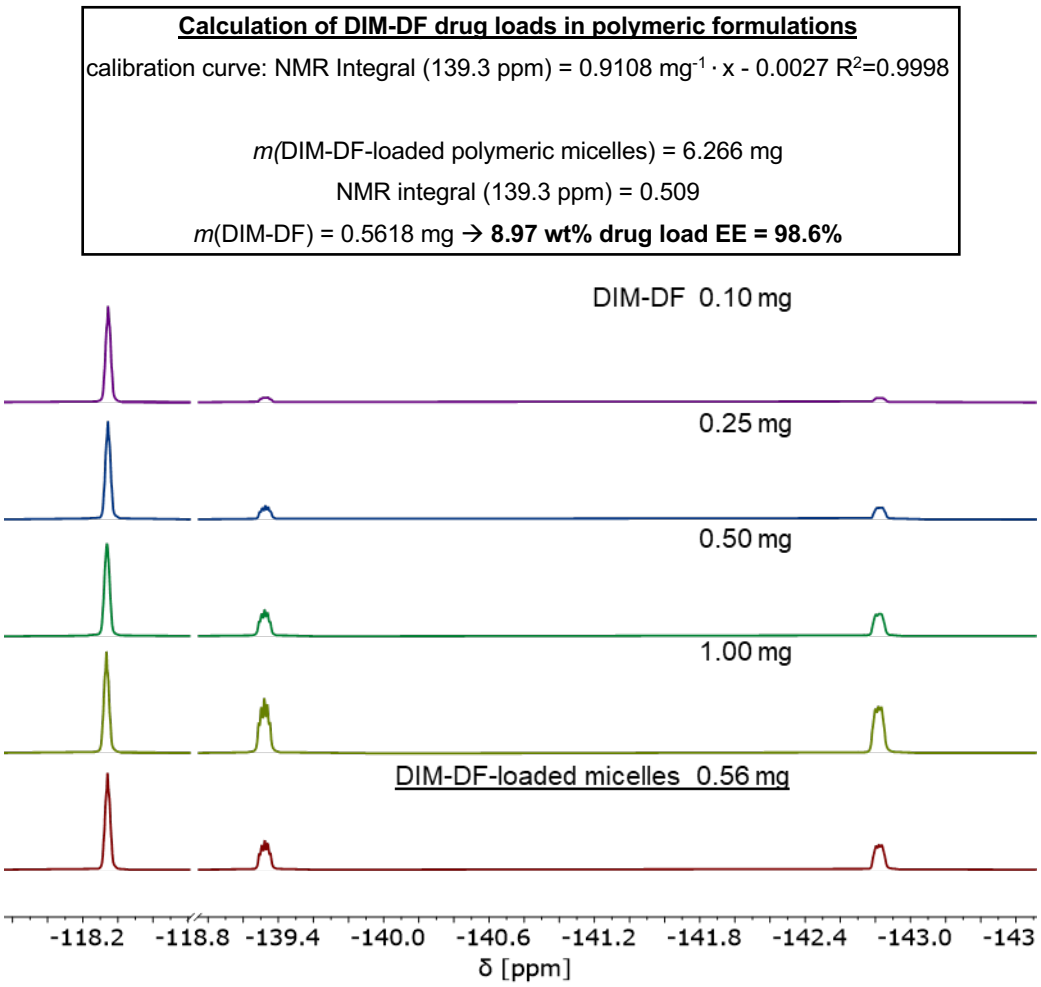

Figure S12: Calculation of DIM-DF drug load by ^{19}F calibration curve and respective NMR spectra of DIM-DF as well as DIM-DF-loaded micelles with a drug load of 8.97 wt% (aimed value 9.09 wt%) and an encapsulation efficiency of 98.6%. All samples were dissolved in DMSO-d_6 that was spiked with 4-fluorotoluene for spectra normalization.

Determination of drug-loads for CL075 micelles

For CL075 determination, a UV-Vis standard curve was created (ranging from 0.0025 mg/mL to 0.050 mg/mL). The compound was therefore dissolved in THF and mixed with the same amount of a 1:1 mp-water/PBS mixture. Thereby, it was possible to analyze the polymeric CL075 by dilution in water, followed by addition of THF, using the exact same solvent mixture for calibration and sample analysis. This circumvents the problem of the solvent-dependency of CL075 absorption and gives more accurate results.

All micellar samples were filtered using a 0.22 µm syringe filter (hydrophilic PTFE) to remove excess of CL075 drug.

Calculation of CL075 drug loads in polymeric formulations

calibration curve: absorbance(350 nm) = 22.445 mL/mg ·x-0.0276 R^2=0.998

*c(*polymeric micelles) = 1.25 mg/mL in 1:1:2 mp-water:PBS:THF

absorbance(350 nm of **CL075-loaded micelles**) = 0.460

c(CL075 at 5 mg/mL particle conc.) = 0.0869 mg/mL → **1.70 wt% drug load EE = 87.1%**

absorbance(350 nm of **CL075-loaded TMR-labeled micelles**) = 0.610

absorbance(350 nm of TMR-labeled micelles) = 0.130

absorbance(350 due to CL075) = 0.610 - 0.130 = 0.480

c(CL075 at 5 mg/mL particle conc.) = 0.0905 mg/mL → **1.78 wt% drug load EE = 90.6%**

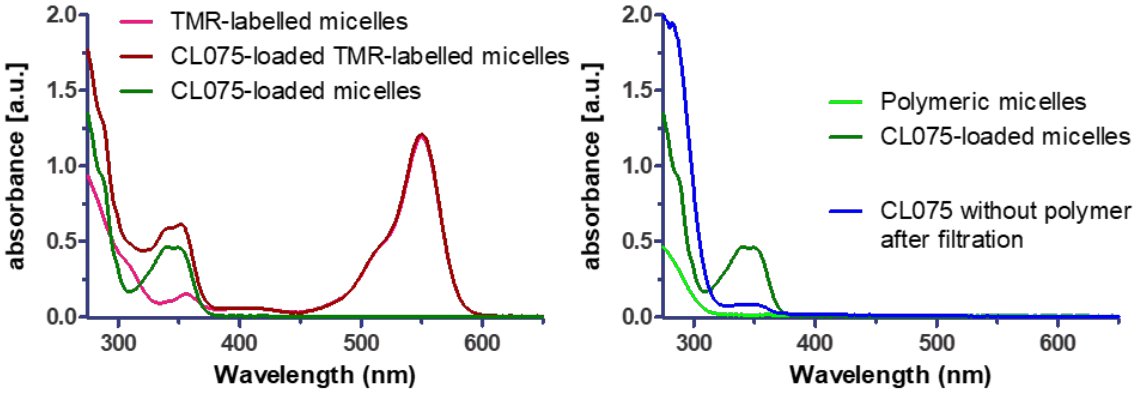

Figure S13: Calculation of CL075 drug load and respective UV-vis spectra of TMR-labeled and CL075-loaded micelles at a concentration of 1.25 mg/mL polymer in a 1:1:2 PBS, mp-water and THF (abs.) mixture. For calculating the CL075 content of CL075-loaded TMR-labeled micelles (left spectra, dark red line), TMR absorption at 350 nm was subtracted by the value obtained for non-loaded TMR-labeled micelles (left spectra, pink line). Moreover, it was shown that a CL075 sample (right spectra, blue line) which was prepared without polymer according to the solvent-evaporation method shows drastically reduced absorbance at 350 nm after filtration. This indicates that sample filtration that was conducted routinely for all polymer samples, indeed removes excess insoluble drug efficiently from the polymeric drug formulations.

Plasma aggregation studies

For multi-angle dynamic light scattering (DLS) experiments of plasma incubated block copolymer micelles with or without encapsulated CL075, all samples were prepared in a dust free flow box. Citrate stabilized human plasma was filtered through GS membrane syringe filters (0.2 µm pore size, PALL Life Science) and micelle samples at 5 mg/mL in PBS through LCR membrane syringe filters (0.45 µm pore size, PALL Life Science). Samples were mixed at a volume ratio of 80% plasma and 20 % micelle PBS solution into dust free cylindrical scattering cuvettes and incubated at 37 °C for 1 h. Subsequent DLS measurements were performed with a Uniphase He/Ne Laser (632.8 nm, 22 mW), an ALV-SP125 Goniometer, an ALV/High QE APD-Avalanche photodiode, an ALV5000/E/PCI-correlator and a Lauda RC-6 thermostat unit. The angular dependent measurements were performed between 30° and 150° in 30° steps. Data analysis was performed according to the procedure described by Rausch and co-workers.[5]

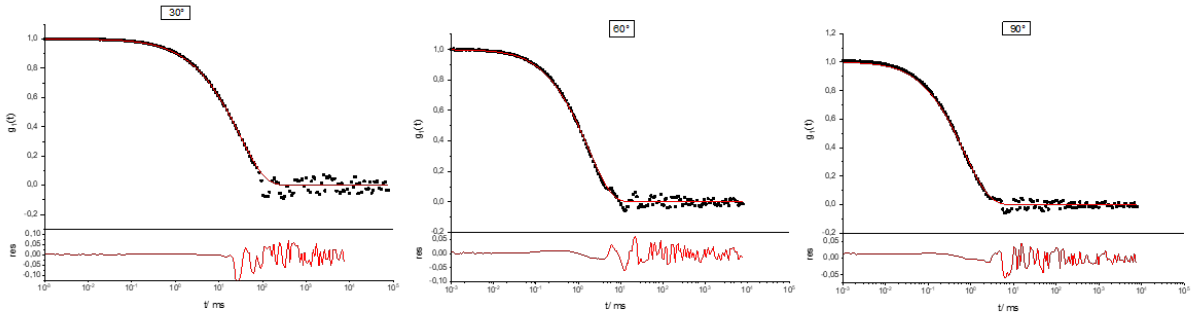

Figure S14: Blood plasma incubation studies by multi-angle DLS of DIM-DF-loaded $mPEG_{113}$-*b*-poly(MTC-OBn)$_{15}$ micelles. Blood plasma incubation shows identical results for DIM-DF-loaded micelles as presented for non-loaded micelles shown in Figure 4.

Circulation of AF647-labeled micelles in zebrafish embryos

For studying the blood circulation properties of the AF647-labeled micelles loaded with or without DIM-DF, zebrafish embryos were kept in Petri dishes containing zebrafish egg water supplemented with 0.003% phenythiourea (PTU) (Sigma-Aldrich). The Petri dishes were maintained in an incubator at a stable temperature of 28.5 °C. All experiments were performed in accordance with the ethical standards and legislation for animal research in Norway.

To evaluate the micelle blood circulation, a protocol recently introduced by Dal et al. was applied.[6,7] For that purpose, borosilicate needles for injections were prepared using a pipet puller (P-97, Sutter Instrument) and installed on a micromanipulator (Narishige MN-153) that was connected to an Eppendorf FemtoJet express pump. Before the injections, all zebrafish embryos were anaesthetized in a tricaine bath (Finquel; 0.02% in zebrafish egg water) and placed on a plate containing an agarose gel (2% in water). Two-day old zebrafish embryos were injected in the posterior cardinal vein with 5 nL of the micelle solution. At defined time points (5 min, 1, 4, 24, 48 and 72 h; 5 zebrafish per time point), images were recorded for the whole zebrafish (30× magnification) and the caudal region (120× magnification) using a Leica DFC365FX stereo microscope with a 1.0× plan apo lens. The average fluorescence intensity of the artery region (AF, 30×), normalized by the average total fluorescence intensity of the zebrafish (TF, 120X), was used to determine the nanoparticle circulation in the blood flow. The average artery fluorescence at 5 min (AF-5 min) was considered as 100%, meaning that all nanoparticles were considered to be in circulation at this time point. The obtained values were subtracted by the background fluorescence analyzed in zebrafish injected with PBS (n = 5).

Particle Degradation Studies by DLS

For particle degradation studies by DLS, non-loaded micelles were diluted to 0.3 mg/mL with the respective buffers and incubated at 37°C.

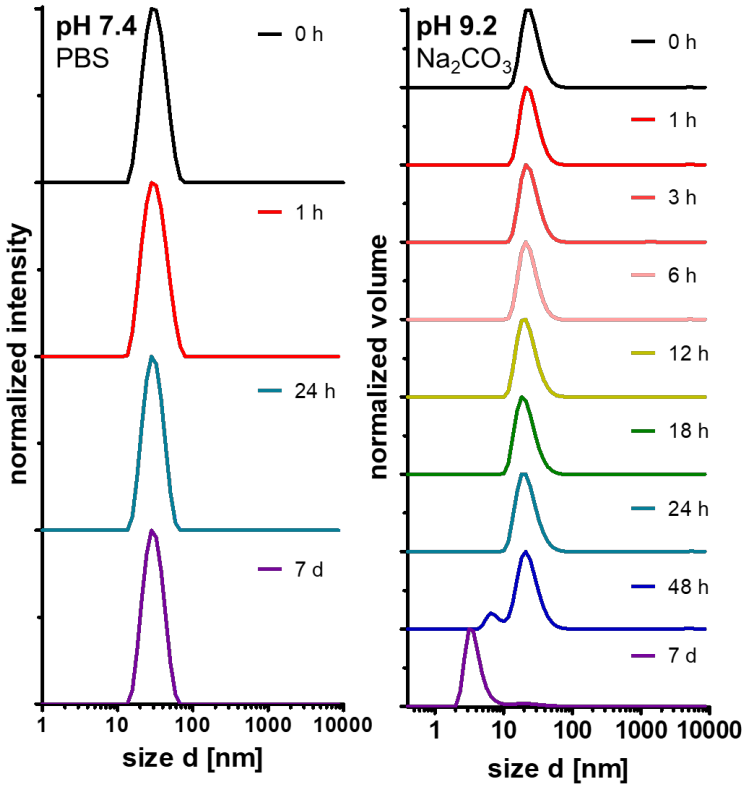

Figure S15: DLS distributions of polymeric micelles at pH 7.4 (PBS, left graph) and at pH 9.2 (Na_2CO_3, right graph) after 0 h (black), 1 h (red), 24 h (green) and 7 d (purple) incubation at 37°C at a concentration of 0.3 mg/mL. Particle sizes remain unchanged at pH 7.4 proving a high stability of $mPEG_{113}$-*b*-poly(MTC-OBn)$_{15}$ micelles (exemplary sizes: z.ave. = 29.13 nm, PDI = 0.09 at 0 h and z.ave. = 28.49 nm PDI = 0.07 after 7d). Alkaline conditions (pH 9.2) trigger degradation with gradually decreasing sizes towards sub-10 nm sizes after 7 d.

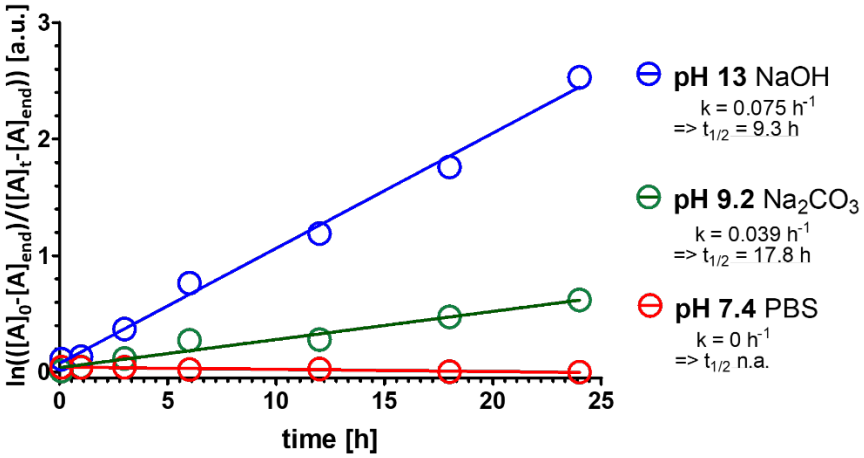

Figure S 16: Kinetic plot of particle count rates observed by DLS at pH 13 (NaOH), pH 9.2 (Na_2CO_3) and 7.4 (PBS, red). Data evaluation confirms an first-order decay degradation of polycarbonate micelles at pH 13 and pH 9.2 with half-lives ($t_{1/2}$) of 9.3 h and 17.8 h, respectively. At pH 7.4 no degradation was found.

Particle Degradation Studies by ESI-MS mass spectrometry

For recording mass spectrometry data of the degradation products, particles (1 mg/mL) were incubated in a 10 µM NH_4HCO_3 solution for 3 d. Samples were then diluted to 0.1 mg/mL with water and analyzed by a Waters SYNAPT G2-Si high definition Q-TOF mass spectrometer (Waters Corp., Manchester, UK) using electrospray ionization (ESI). The instrument was calibrated by clusters of sodium formate. Mass spectrometry data was analyzed using mMass.

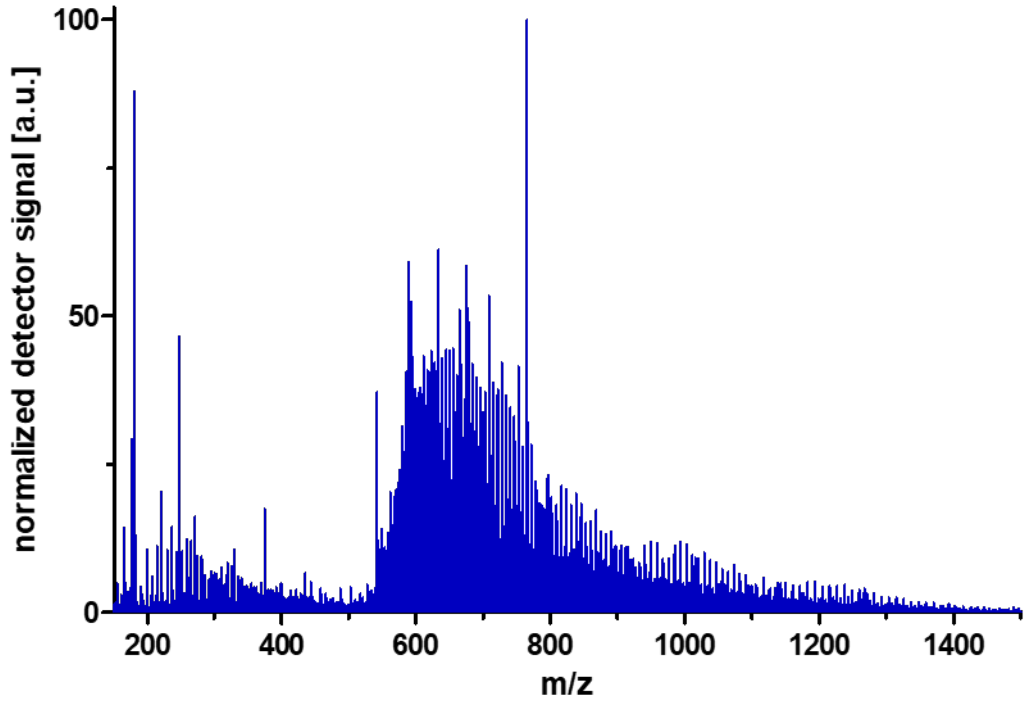

Figure S17: Mass spectrometry data of TMR-labeled polymeric micelles after degradation in 10 µM NH_4HCO_3 buffer by ESI-MS.

In vitro evaluation of polycarbonate nanogels

RAW-Blue macrophage TLR reporter assay (Quanti Blue Assay)

TLR reporter assay *via* downstream activation of AP-1/NF NF-κB and subsequent secretion of SEAP (secreted embryonic alkaline phosphatase) was conducted as recommended by InvivoGen. Cells were seeded into 96-well plates (90,000 cells/well in 180 µL culture medium) and incubated with 20 µL of the respective solutions at the given CL075 concentrations. After ~ 20 h of incubation, 50 µL of the supernatant was collected and probed by Quanti Blue Assay (InvivoGen) for the amount of SEAP. After incubation for 2 h at 37 °C wells were read-out for their absorbance at 620 nm using a plate reader. All experiments were performed in quadruplicates.

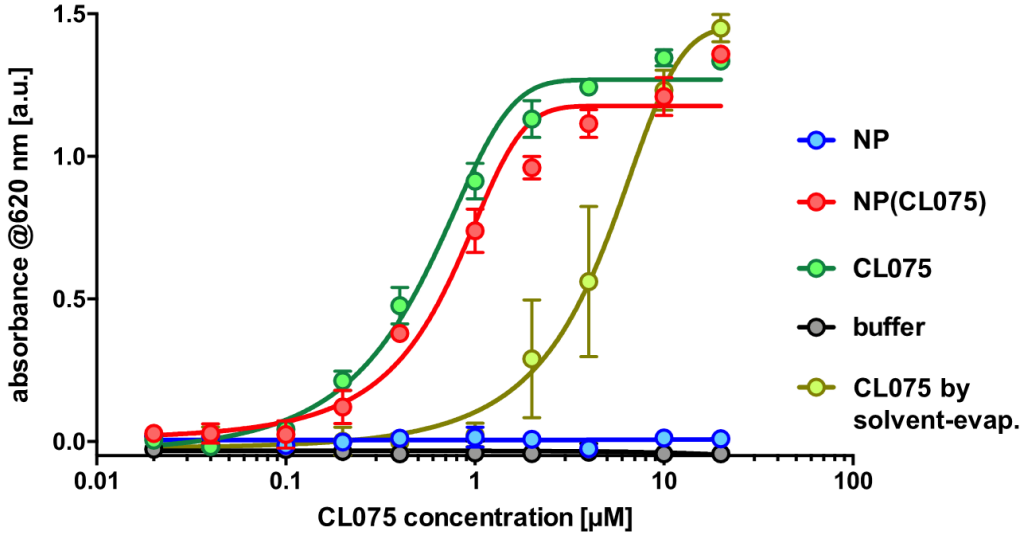

Figure S18: TLR 7/8 receptor stimulation by Raw Blue assay (n=4). Additionally, a sample of CL075 without polymer was prepared by solvent evaporation method (CL075 by solvent evaporation, yellow curve) resulting in precipitated drug. Without removal of precipitated drug by filtration, the sample was stepwise diluted in PBS and applied to the cells. Thereby, a decrease in activation compared to NP(CL075) was found, indicating that CL075 is effectively solubilized and delivered by micellar delivery (NP(CL075)) or has to be administered from DMSO solution directly into cell culture medium instead of PBS for stepwise dilution (green curve).

Determination of metabolic activity by MTT assay after micelle incubation on stimulated Raw Blue macrophages

For the analysis of the cells' metabolic activity as an indicator for toxicity and cell proliferation, stimulated cells were incubated with 30 µL of 2 mg/mL 3-(4,5-dimethylthiazol-2-yl)-2,5-diphenyltetrazolium bromide solution in PBS. After 3 h of incubation time, formazan crystals were dissolved by the addition of 100 µL of 10% m/v SDS/0.01 M HCl and incubated overnight at 37°C. Absorbance was measured at 590 nm using a plate reader. All experiments were performed in quadruplicates.

Determination of micellar uptake of TMR-labeled micelles by flow cytometry

For micelle uptake studies in Raw-Blue macrophages, cells were seeded in a 24-well plate (250,000 cells/well in 950 µL culture medium) and incubated with 50 µL of TMR-labeled polymeric micelles at the given concentrations. After 20 h of incubation time the medium was removed, cells were washed with 1 mL PBS and incubated with 250 µL of cell dissociation buffer for 30 min at 37 °C. Then 750 µL cell culture medium was added and the cells were centrifuged at 350 g for 10 min at 0 °C. The supernatants were removed, and the pellets were resuspended in 250 µL of PBS, to be analyzed on a BD Accuri C6 (BD Biosciences). Data was processed by FlowJo Software. All experiments were performed in triplicates.

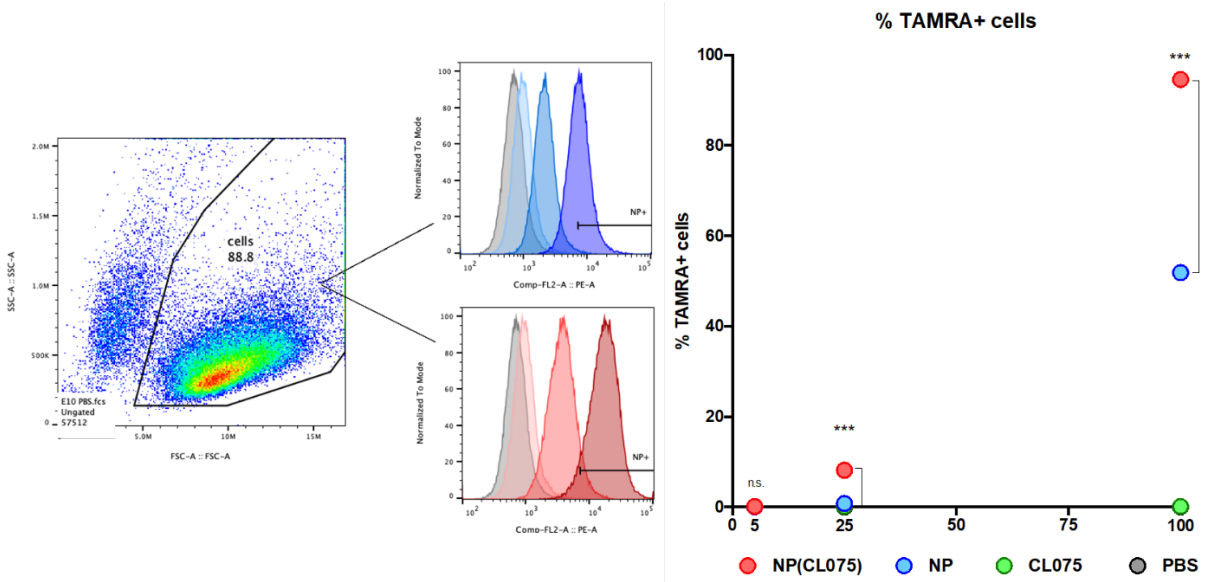

Figure S19: Gating strategy of flow cytometry of RAW Blue macrophages. Cells were incubated with increasing doses of empty (NP, top histogram) and CL075-loaded (NP(CL075), bottom histogram) TMR-labeled micelles. At the respective concentration of NP(CL075), NP, CL075 and PBS, a higher percentage of micelle positive cells for NP(CL075) compared to non-loaded NP were found.

Fluorescent confocal microscopy imaging

For fluorescent confocal laser scanning microscopy, RAW Blue macrophages (50,000 cells/well in 180 µL) were seeded in an eight-well polystyrene wells (Laboratory-Tek, Nalge Nunc International, Penfield, NY, USA). Respective amounts of TMR-labeled nanogels were added (20 µL solution) and incubated overnight. Then the medium was removed and the cells were washed with PBS three times. Cells were fixed applying 200 µL of a 4% paraformaldehyde solution for 30 minutes at 37°C. After washing with PBS three times, cell nuclei were stained using a 4′,6-diamidino-2-phenylindole (DAPI) solution (80 µg/mL in PBS) for 10 min at 37 °C. Finally, after washing with PBS three

times, the samples were stored in mounting media and analyzed on a Leica SP5 confocal microscope (Wetzlar, Germany) with a 63x oil immersion objective. Images were processed by ImageJ software package.

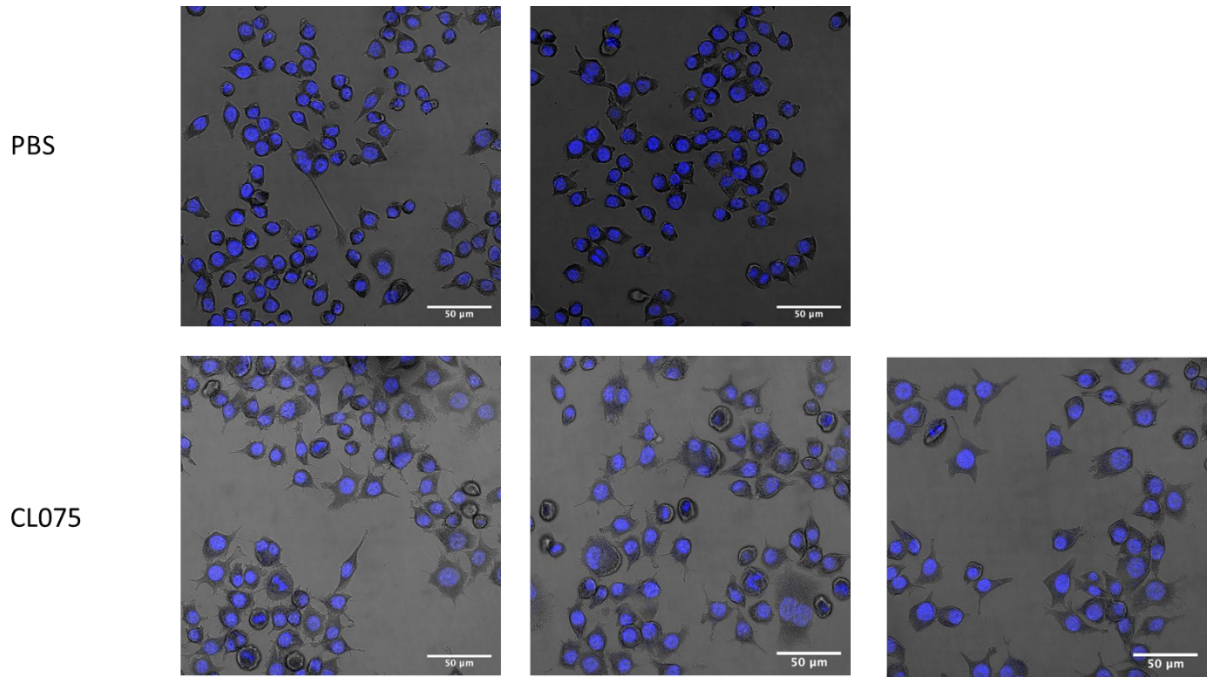

Figure S20: Additional confocal microscopy images of RAW macrophages incubated with PBS and CL075.

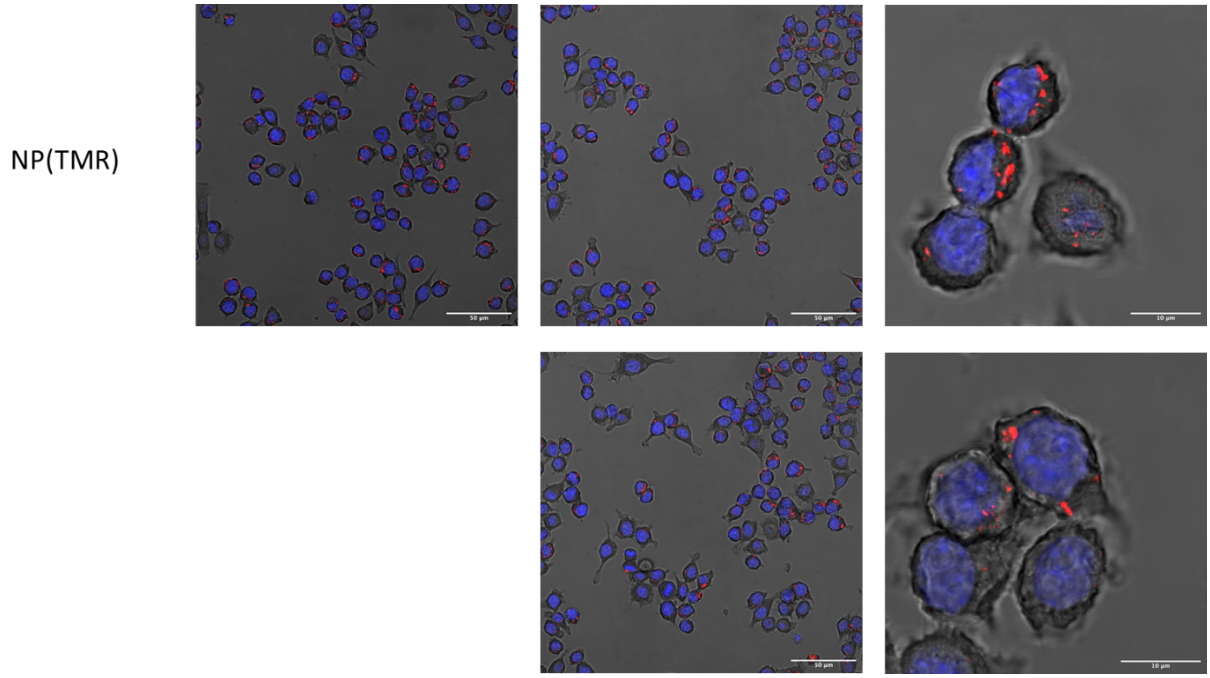

Figure S21: Additional confocal microscopy images of RAW macrophages incubated with TMR-labeled micelles (at 100 µg/mL).

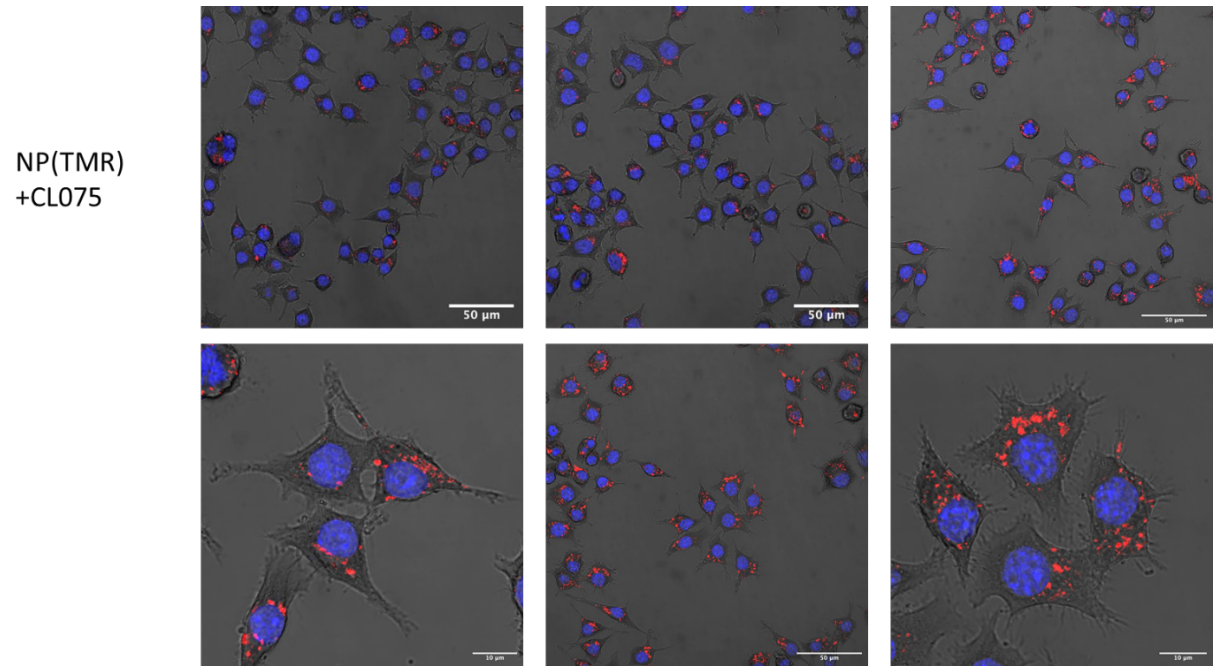

Figure S22: Additional confocal microscopy images of RAW macrophages incubated with CL075-loaded TMR-labeled micelles (at 100 µg/mL).

BMDCs-FLT3L (Bone marrow-derived dendritic cells – recombinant FMS-related tyrosine kinase 3 ligand)

Bone marrow cells were isolated from femurs and tibiae of C57BL/6 mice, and were resuspended in IMDM-based culture medium (see above), supplemented with 250 ng/ml FLT3 ligand (FLT3L) (BioLegend Way, San Diego, USA). Bone marrow cells were seeded in 12-well suspension cell culture cluster plates (each 10^6 cells/ml) and incubated for one week. Then, samples were treated with NP formulations as indicated. On the next day, samples were harvested, and subjected to flow cytometric analysis. All experiments were performed in quadruplicates.

Flow cytometry of BMDCs

In order to prevent unspecific binding of subsequently added antibodies, samples were incubated first with a rat anti-mouse CD16/CD32 blocking antibody (15 min, 4°C), followed by lineage and activation marker detecting antibodies (Table S1) for 20 min at 4°C. All antibodies were obtained from BioLegend (San Diego, CA, USA) or Thermo Fisher (Waltham, MA, USA).

Cell line	Antibody	Dye
BMDCs (GM-CSF)	CD11c	BV421
	CD80	PerCP-eFl710
	CD86	FITC
	MHC-II	PE-eFl610
	CD40	PE
BMDCs (FLT3L)	CD11c	PE-Cy7
	CD11b	SB600
	B220/CD45R	V500
	XCR1	AF647
	MHC-II	eFl450
	CD80	PerCP-eFl780
	CD86	FITC

Table S1: Antibodies used to characterize the different cell lines in BMDCs cultures

Samples left untreated, incubated with the according NP formulation alone or with either antibody alone served as controls. Fixable Viable Dye (FVDeFluor® 780, Carlsbad, CA, USA) was used to measure living cells. Washed samples were fixed and subjected to flow cytometric analysis employing an Attune NxT flow cytometer (Thermo Fisher). The resulting data were processed by FlowJo Software.

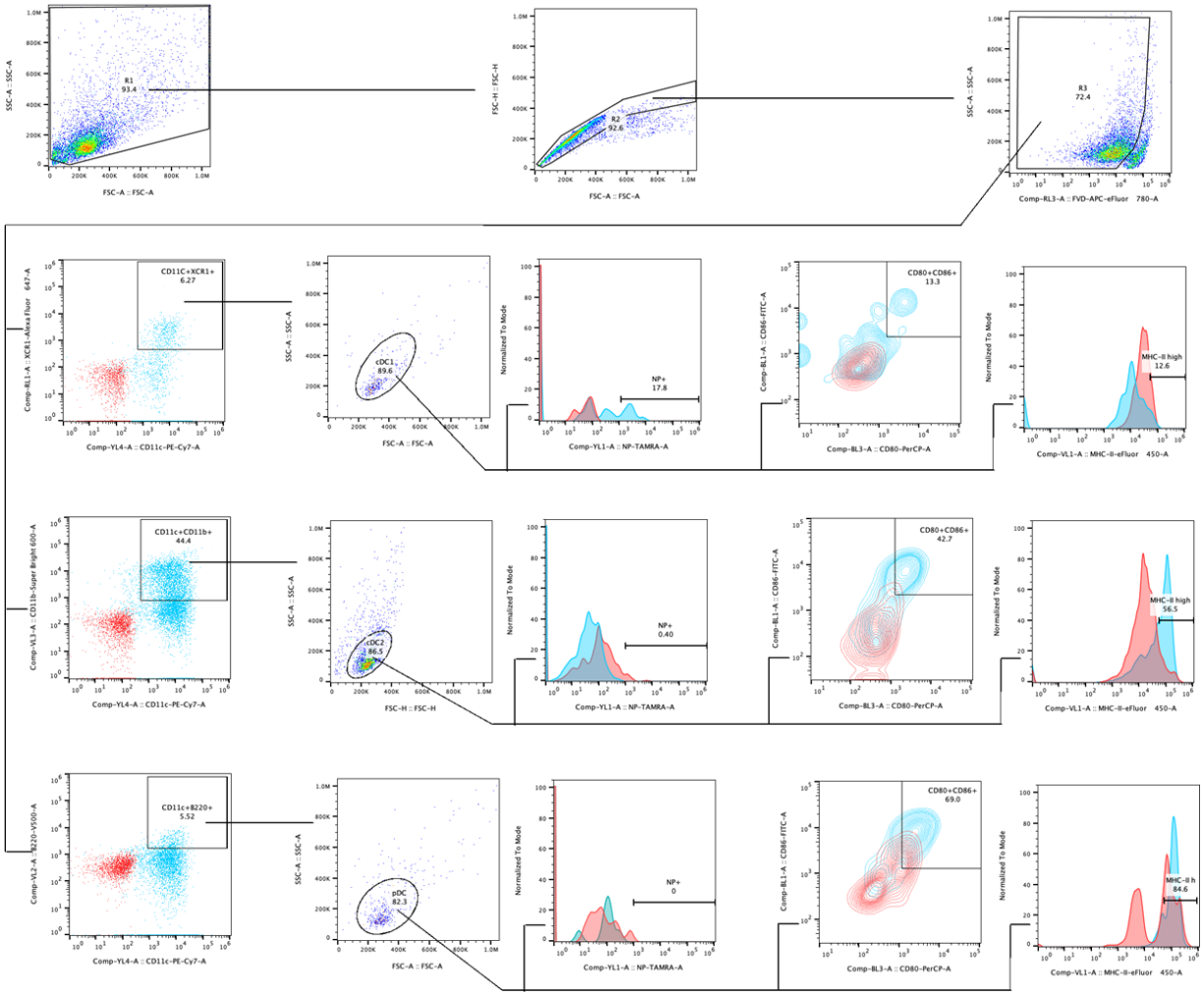

Figure S23: Gating strategy for gating of specific subpopulations in FLT3 BMDCs.

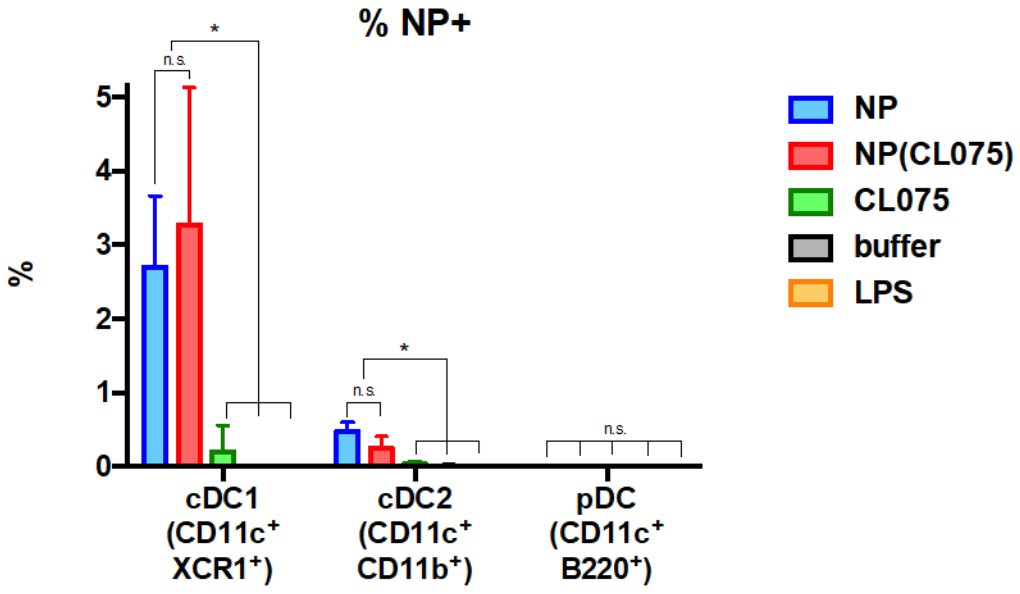

Figure S24: Fraction of TMR positive cells in cDC1, cDC2 and pDC subpopulations indicating the percentage uptake of TMR-labeled polymeric micelles (NP and NP(CL075).

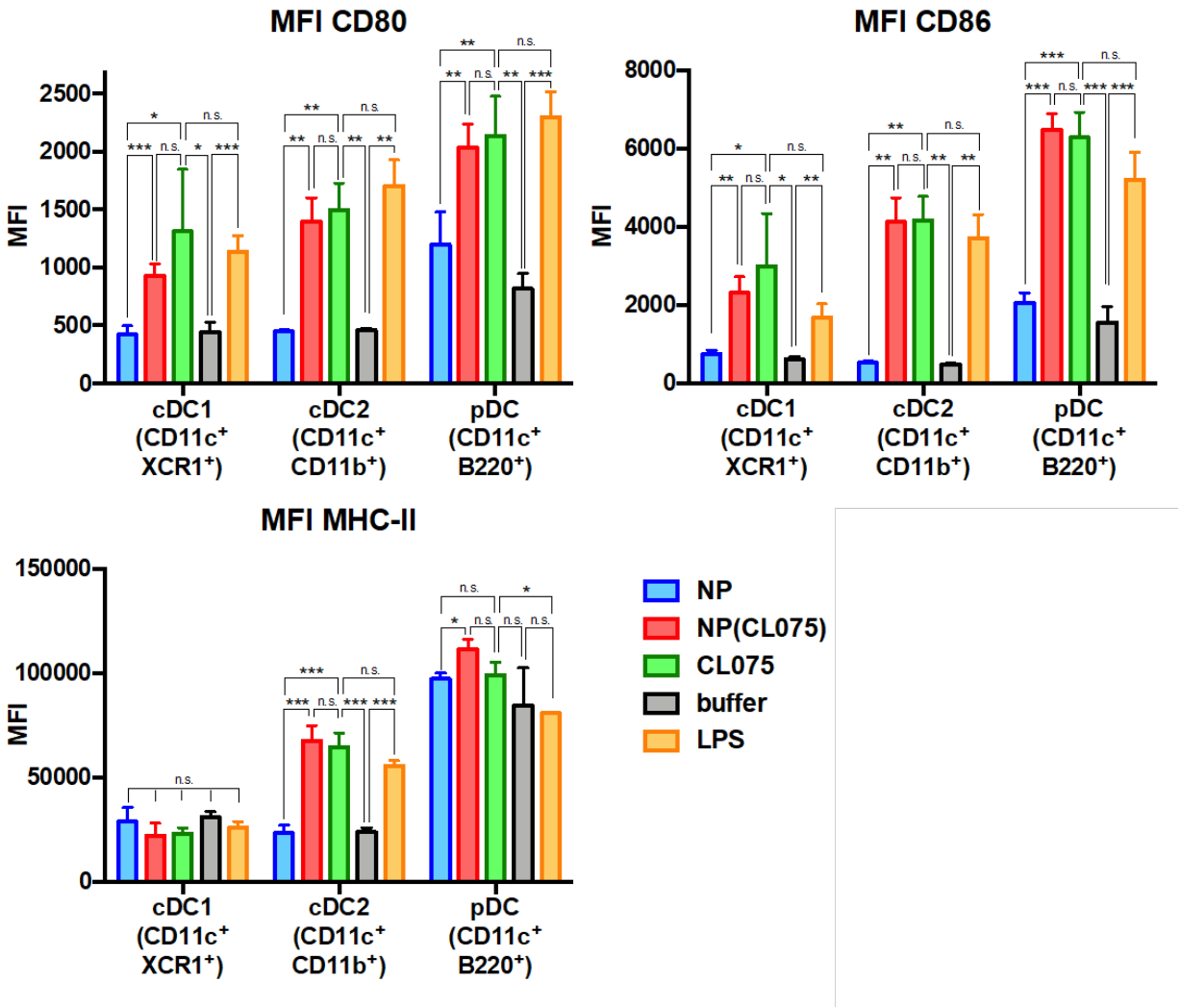

Figure S25: Expression of activation markers CD80, CD86 and MHC-II by mean fluorescence intensity (MFI) in cDC1s, cDC2s and pDCs after incubation with NP, NP(CL075, CL075, buffer and LPS (positive control). Results show comparable expression of activation markers for NP(CL075) to both CL075 and LPS.

Statistical analyses

Data are shown as mean values + standard deviation Statistical significances of the mean values were determined by unpaired Student's t-test with Welch's correction using Graph Pad Prism software (*: $p \leq 0.05$; **: $p \leq 0.01$; ***: $p \leq 0.001$).

Additional References

[1] A. Ahmad, P. Dandawate, S. Schruefer, S. Padhye, F. H. Sarkar, R. Schobert, B. Biersack, *Chemistry & Biodiversity* **2019**, *16*, e1900028.

[2] R. C. Pratt, F. Nederberg, R. M. Waymouth, J. L. Hedrick, *Chem. Commun.* **2008**, *2*, 114.

[3] T. F. Al-Azemi, K. S. Bisht, *Macromolecules* **1999**, *32*, 6536.

[4] W. Lu, F. Li, R. I. Mahato, *Journal of Pharmaceutical Sciences* **2011**, *100*, 2418.

[5] K. Rausch, A. Reuter, K. Fischer, M. Schmidt, *Biomacromolecules* **2010**, *11*, 2836.

[6] N.-J. K. Dal, A. Kocere, J. Wohlmann, S. Van Herck, T. A. Bauer, J. Resseguier, S. Bagherifam, H. Hyldmo, M. Barz, B. G. De Geest, F. Fenaroli, *Small* **2020**, *16*, 1906719.

[7] S. Siemer, T. A. Bauer, P. Scholz, C. Breder, F. Fenaroli, G. Harms, D. Dietrich, J. Dietrich, C. Rosenauer, M. Barz, S. Becker, S. Strieth, C. Reinhardt, T. Fauth, J. Hagemann, R. H. Stauber, *ACS Nano* **2021**, *15*, 18541.

10.7. Publication 7

"Enrichment methods for murine liver non-parenchymal cells differentially affect their immunophenotype and responsiveness towards stimulation"

The following chapter has been published in MDPI (International Journal of Molecular Sciences). As a shared first author, I conducted most *in vitro* biological experiments to establish and compare the discussed methods. In this work, we compared the suitability of two isolation methods for murine liver NPCs. Liver perfusion (LP) with collagenase/DNase that I applied via the portal vein led to efficient liver digestion, whereas the modified liver dissociation (LD) method combined mechanical dissociation of the retrieved organ with enzymatic degradation of the extracellular matrix. In both LP and LD, NPCs were enriched by subsequent gradient density centrifugation. Our results indicated that LP and LD were largely comparable with regards to the yield, purity, and composition of obtained liver NPCs. However, LD-enriched liver NPCs displayed a higher degree of activation after overnight cultivation, and accordingly were more responsive towards stimulation with Toll-like receptor ligands that are frequently used as adjuvants, e.g. in nano-vaccines. We concluded that LP was more suitable for obtaining liver NPCs for subsequent *in vitro* studies, whereas LD as the less laborious method was more convenient for parallel isolation of larger numbers of samples for *ex vivo* analysis.

DOI: 10.3390/ijms23126543

Published in: *International Journal of Molecular Sciences*. **2022** Jun 11;23(12):6543

Reprinted with permission under creative commons attribution 4.0 (CC BY-NC) from **Medina-Montano* C**, Cacicedo* ML, Svensson M, Limeres MJ, Zeyn Y, Chaves-Giraldo JE, Röhrig N, Grabbe S, Gehring S, Bros M. Enrichment Methods for Murine Liver Non-Parenchymal Cells Differentially Affect Their Immunophenotype and Responsiveness towards Stimulation. Int J Mol Sci. 2022 Jun 11;23(12):6543. doi: 10.3390/ijms23126543. PMID: 35742987; PMCID: PMC9223567.

***** Authors contributed equally

International Journal of
Molecular Sciences

MDPI

Communication

Enrichment Methods for Murine Liver Non-Parenchymal Cells Differentially Affect Their Immunophenotype and Responsiveness towards Stimulation

Carolina Medina-Montano [1,†], Maximiliano Luis Cacicedo [2,†], Malin Svensson [2], Maria Jose Limeres [2], Yanira Zeyn [1], Jean Emiro Chaves-Giraldo [1], Nadine Röhrig [1], Stephan Grabbe [1], Stephan Gehring [2,†] and Matthias Bros [1,*,†]

[1] Department of Dermatology, University Medical Center of the Johannes Gutenberg University Mainz, Langenbeckstraße 1, 55131 Mainz, Germany; gmedinam@uni-mainz.de (C.M.-M.); yanira.zeyn@uni-mainz.de (Y.Z.); jchavesg@students.uni-mainz.de (J.E.C.-G.); n.roehrig@uni-mainz.de (N.R.); stephan.grabbe@unimedizin-mainz.de (S.G.)
[2] Children's Hospital, University Medical Center of the Johannes Gutenberg University Mainz, Langenbeckstraße 1, 55131 Mainz, Germany; mcaciced@uni-mainz.de (M.L.C.); malin.svensson@uni-mainz.de (M.S.); mj.limeres@uni-mainz.de (M.J.L.); stephan.gehring@uni-mainz.de (S.G.)
* Correspondence: mbros@uni-mainz.de
† These authors contributed equally to this work.

Citation: Medina-Montano, C.; Cacicedo, M.L.; Svensson, M.; Limeres, M.J.; Zeyn, Y.; Chaves-Giraldo, J.E.; Röhrig, N.; Grabbe, S.; Gehring, S.; Bros, M. Enrichment Methods for Murine Liver Non-Parenchymal Cells Differentially Affect Their Immunophenotype and Responsiveness towards Stimulation. *Int. J. Mol. Sci.* **2022**, *23*, 6543. https://doi.org/10.3390/ijms23126543

Academic Editor: Jin-Kyu Park

Received: 20 May 2022
Accepted: 9 June 2022
Published: 11 June 2022

Publisher's Note: MDPI stays neutral with regard to jurisdictional claims in published maps and institutional affiliations.

Copyright: © 2022 by the authors. Licensee MDPI, Basel, Switzerland. This article is an open access article distributed under the terms and conditions of the Creative Commons Attribution (CC BY) license (https://creativecommons.org/licenses/by/4.0/).

Abstract: Hepatocytes comprise the majority of the liver and largely exert metabolic functions, whereas non-parenchymal cells (NPCs)—comprising Kupffer cells, dendritic cells and liver sinusoidal endothelial cells—control the immunological state within this organ. Here, we compared the suitability of two isolation methods for murine liver NPCs. Liver perfusion (LP) with collagenase/DNase I applied via the portal vein leads to efficient liver digestion, whereas the modified liver dissociation (LD) method combines mechanical dissociation of the retrieved organ with enzymatic degradation of the extracellular matrix. In cases of both LP and LD, NPCs were enriched by subsequent gradient density centrifugation. Our results indicate that LP and LD are largely comparable with regards to the yield, purity, and composition of liver NPCs. However, LD-enriched liver NPCs displayed a higher degree of activation after overnight cultivation, and accordingly were less responsive towards stimulation with toll-like receptor ligands that are frequently used as adjuvants, e.g., in nano-vaccines. We conclude that LP is more suitable for obtaining liver NPCs for subsequent in vitro studies, whereas LD as the less laborious method, is more convenient for parallel isolation of larger numbers of samples for ex vivo analysis.

Keywords: liver perfusion; liver dissociation; liver sinusoidal endothelial cells; Kupffer cells; dendritic cells; adjuvant; toll-like receptor ligand; liposome

1. Introduction

The liver is a central metabolic organ, but also plays an important immunological role, serving to maintain tolerance under homeostatic conditions [1–3]. The liver is comprised of hepatocytes, which make up approximately two thirds of its total cell population and exert largely metabolic functions, comprising the synthesis of numerous types of plasma proteins—for example, albumin [4], fatty acids [5], carbohydrates [6], and bile acid metabolism [7]—but are also pivotal for detoxification [8]. The heterogeneous group of non-parenchymal cells (NPCs) plays an important role in immune regulation [9]. Liver NPCs comprise liver sinusoidal endothelial cells (LSECs, approximately 50% of NPCs), Kupffer cells (KCs, 20%) that largely constitute the resident macrophage population, and dendritic cells (DCs, 25%). The minor fraction of liver NPCs is mainly composed of innate

immune cells comprising natural killer (NK) cells and NKT cells [10], biliary epithelial cells [7], and hepatic stellate cells (HSC) [11]. The latter are located in the perisinusoidal region between the sinoids and hepatocytes, and under steady state conditions remain in a quiescent state, but play an important role in the induction of liver diseases [12]. HSC are activated in response to liver damage and in this state constitute the main producers of extracellular matrix factors—thereby promoting liver fibrosis [13]. Furthermore, chronic inflammation of a fibrotic liver enhances the likeliness of hepatocellular carcinoma (HCC) development [14]. HCC in turn reprograms HSC to differentiate towards cancer-associated fibroblasts, which besides other cell types such as tumor-associated macrophages, shape the immune-evasive tumor microenvironment [15]. With regard to the major liver NPC fractions, KCs were recognized early on as promoting liver diseases [16] such as nonalcoholic fatty liver disease [17] and alcoholic hepatitis [18]. In general, KCs have been attributed protolerogenic functions [19,20]. Similar to KCs, liver DCs have been reported to exert protolerogenic functions under steady state conditions [21], but have also been reported to display a stimulated, proimmunogenic state at later stages of NAFLD and to contribute to liver fibrosis [22].

LSECs form the lining of hepatic sinusoids and are characterized by numerous pore-like structures, termed fenestrae, which allow the rapid transport of, e.g., lipoproteins from hepatocytes into the sinusoidal blood stream [23]. Furthermore, LSECs release vasodilatory mediators upon shear stress, and impaired generation of these factors has been implicated in non-alcoholic fatty liver disease [24]. Moreover, LSECs express numerous types of endocytic scavenger and C-type lectin receptors [25] as well as the Fcγ receptor IIb (CD32) [26], which enable the uptake of different types of pathogens [27,28] and immune complexes [26] and promote immune homeostasis by inducing regulatory T cells [29].

Altogether, liver NPCs on the one hand have the common property of maintaining antigen-specific T cell tolerance under homeostatic conditions [30,31], but on the other hand, may contribute to NAFLD and other liver diseases in cases of dysfunction [24,32,33]. Liver NPCs have also come into the focus of nanodrug-associated research as a large fraction of systemically applied nano-formulations accumulates in the liver [34–36]. Nanodrugs have the potential to co-deliver various agents in a tissue- and even cell type-specific manner, thereby reducing toxicity and other unwanted side effects associated with non-specific uptake of conventional therapeutics [37]. Therefore, both with regard to nanodrugs designed for the treatment of liver diseases [38] as well as nano-formulations developed to address other organs and cell types, it is highly important to address potential uptake by the liver.

In this regard, most studies have demonstrated endocytic uptake of nanodrugs by KCs [39–42]. Moreover, we and others have reported that DCs and LSECs may also significantly contribute in this regard [36]. The overall T cell tolerance-promoting function of liver NPCs may even be detrimental in cases of nano-vaccines developed to address antigen-presenting cells such as DCs in secondary lymphoid organs aimed at inducing tumor antigen-specific immune responses [9]. Therefore, it is of general interest to study in detail the interaction of liver NPCs with biologicals in vitro to test and eventually optimize their cell-targeting properties for subsequent in vivo studies. Along this line, ex vivo analysis of liver NPCs at the end of in vivo experiments enables the evaluation of in vivo cell type-targeting behavior and payload-dependent functional effects.

So far, liver perfusion (LP) is the standard method for NPC enrichment but requires laborious in situ pretreatment of the organ with collagenase and DNase I [43–46]. Hence, this approach limits the number of samples that can be processed. This issue may be especially important when liver NPCs need to be isolated from a number of animals after in vivo treatment for ex vivo analysis. Therefore, we compared the suitability of LP with ex vivo liver dissociation (LD) using a commercially available kit that allows for the parallel processing of numerous samples. We showed that both liver NPC enrichment procedures yielded similar results in terms of overall cell numbers, composition, and viability when

assessed directly after isolation. However, after overnight cultivation, NPCs enriched by LD displayed a higher state of activation and were less responsive towards stimulation with different toll-like receptor (TLR) ligands. Altogether, our results show that both methods are suitable for liver NPC isolation. LD proved less laborious than LP but might be more suitable in cases of direct ex vivo analysis of freshly isolated samples, whereas LP is the method of choice when liver NPCs are to be subjected to functional studies in vitro.

2. Results

2.1. LP and LD Yield Comparable Numbers of Enriched Viable NPCs

LP-mediated NPC enrichment starts with in situ perfusion of the liver via the portal vein with a collagenase/DNase I digestion mixture (Figure 1, left panel), whereas in cases of LD, only extra-corporal enzymatic tissue digestion of liver tissue is performed (Figure 1, right panel). Hence, LP is more demanding and laborious compared to LD. We modified the LD protocol by performing subsequent density centrifugation to enrich NPCs in the interphase (Figure 1, lower panel). This step is part of the LP method by default.

Both liver NPC enrichment methods resulted in similar outcomes in terms of total yield (Figure 2A), the frequency of enriched $CD45^+$ liver NPCs (50–60%; Figure 2B) and the composition of the NPC population with regard to $F4/80^+$ macrophages (MACs), $CD11c^+$ DCs, and $CD32b^+$ LSECs (Figure 2C). However, it is worth mentioning that after density centrifugation, cell suspensions obtained by LD contained more debris than observed when performing LP (not shown).

Next, we investigated the viability of enriched liver NPC populations. To this end, we employed FVD, which binds intracellular primary amines of dead cells [47]. In contrast to other live/dead markers, FVD-treated samples can be fixated, which, in contrast to DNA-intercalating agents (see below), allows flow cytometric analysis at later time points.

Unexpectedly, LP-enriched MACs displayed rather strong interactions with the FVD, which suggested that their viability was about 42% only as compared to about 80% in the case of LD-enriched MACs (Figure 2D, left panel). After overnight incubation, MACs interacted with the FVD to a high extent, irrespective of the liver NPC enrichment method—suggesting viability rates below 40%. On the contrary, incubation of liver NPCs both directly after isolation as well as after overnight cultivation with Sytox, which intercalates the genomic DNA of dead cells [48], in general delineated >75% of MACs as viable. Freshly isolated DCs (Figure 2D, middle panel) and LSECs (Figure 2D, right panel) displayed similar FVD/Sytox binding patterns, showing moderately lower viability when enriched by LP and incubated with FVD, whereas no difference in viability was apparent in the case of Sytox incubation. These method-dependent differences were less obvious after overnight incubation, suggesting largely comparable viability rates determined by either viability dye. Similar results were obtained when using FVD conjugated with a distinct fluorochrome, and 7-AAD instead of Sytox (not shown).

Taken together, these observations suggest that LP-mediated enrichment of liver NPCs resulted in stronger interactions with the FVD than after LD enrichment (MACs > DCs, LSECs).

The unexpected finding of enhanced engagement of the FVD by MACs prompted us to perform a comparative viability analysis of spleen cells after isolation as well as after overnight incubation using FVD and Sytox in parallel (Figure S2). None of the freshly isolated splenic immune cell types showed stronger engagement of the FVD than of Sytox. However, after overnight culture B cells, MACs and PMNs displayed a lower viability rate when using FVD for assessment as compared to Sytox. Comparable findings were made when using FVD with a distinct fluorochrome and 7-AAD instead of Sytox (not shown).

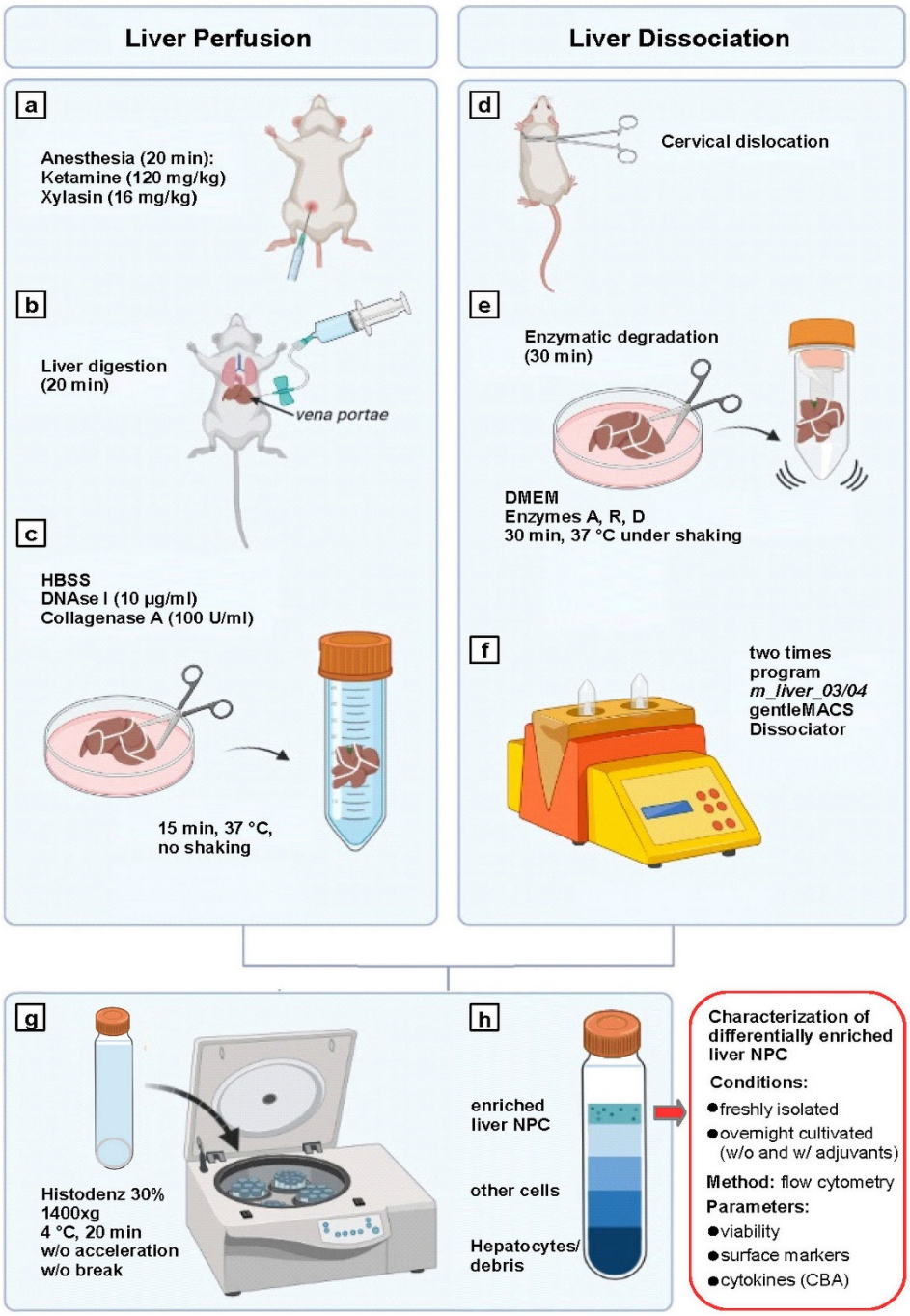

Figure 1. Schematic overview of liver non-parenchymal cell (NPC) enrichment by liver perfusion (LP) and liver dissociation (LD) and subsequent experimental readout. Left panel: LP mice were (**a**) anesthetized with ketamine/Xylazine, (**b**) the vena portae was cannulated and collagenase A/DNase I-containing PBS was infused for in situ tissue digestion. (**c**) The liver was retrieved, cut into pieces and further digested with collagenase A/DNase I. Liver tissue pieces were mashed to obtain a single cell suspension (not shown). Right panel: LD mice were (**d**) killed by cervical dislocation, and (**e**) the retrieved liver was cut into pieces and digested in an enzyme cocktail of proprietary composition (Miltenyi Biotec), (**f**) followed by mechanical dissociation using a gentleMACS (Miltenyi Biotec). Lower left panel: Liver cell suspensions generated by either method were (**g**) subjected to Histodenz density gradient centrifugation, (**h**) resulting in enrichment of liver NPCs in the interphase that was subjected to subsequent experiments. Lower right panel: differentially enriched liver NPCs were characterized in a freshly isolated state and after overnight incubation w/o and in the presence of adjuvants with regard to viability, surface marker expression, and cytokine contents by flow cytometry. (created with BioRender.com; accessed on 1 June2022).

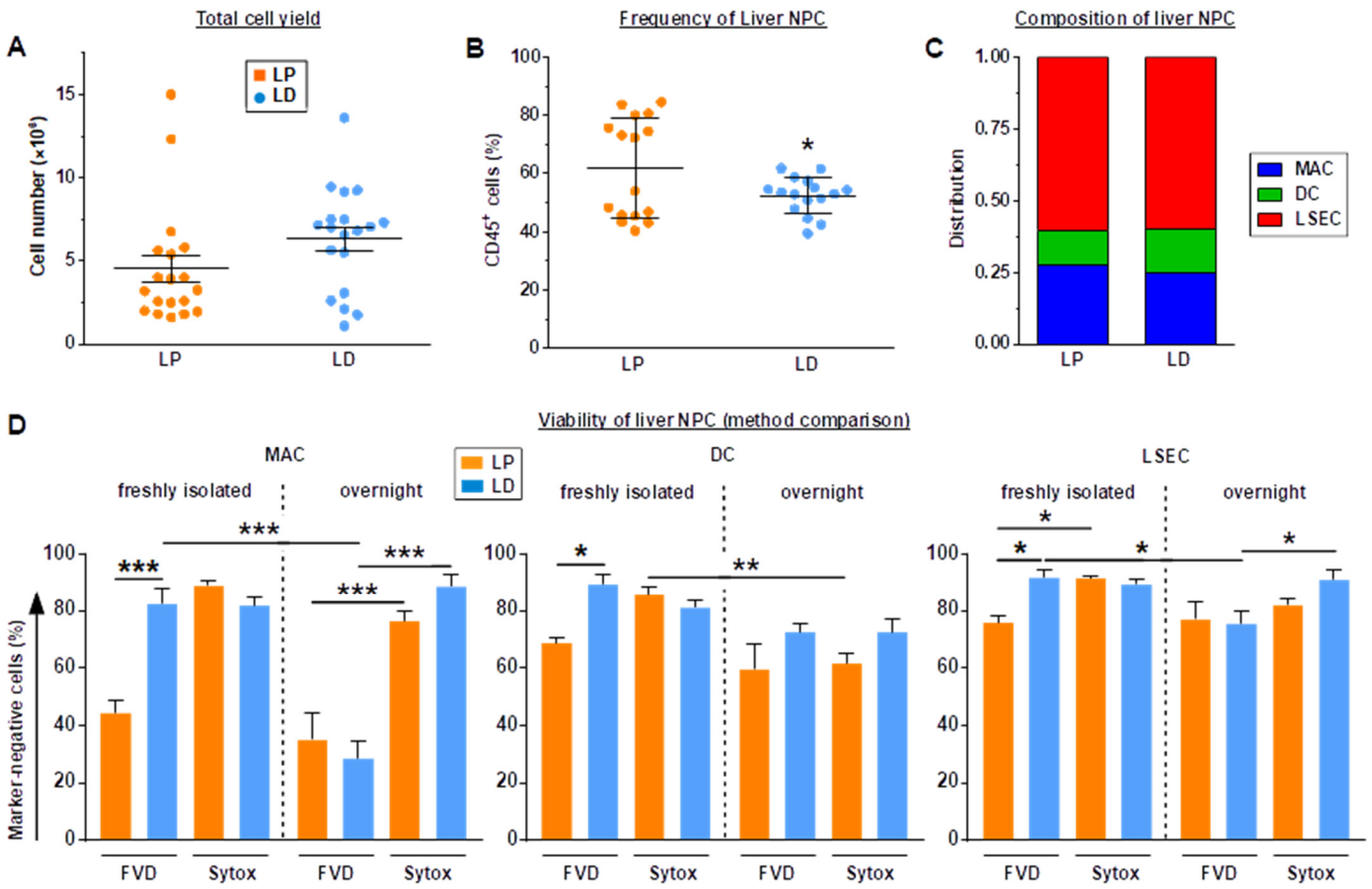

Figure 2. LP and LD yield comparable numbers and composition of liver NPCs, but LD-enriched cells appear dead when using FVD. (**A**) Total cell yield obtained after density centrifugation (mean ± SEM, each $n = 19$). (**B**) Frequencies of CD45⁺ cells within the enriched NPC suspensions were assessed by flow cytometry (mean ± SEM, each $n = 19$). (**C**) Composition of liver NPCs (CD11c⁺ DCs, F4/80⁺ MACs, CD32b⁺ LSECs) within the CD45⁺ cell population (mean, each $n = 19$; the gating strategy is shown in Figure S1). Statistically significant differences versus (**B**) *LP (*t*-test) and (**D**) * between groups (two-way ANOVA/Tukey test) are indicated. * $p < 0.05$, ** $p < 0.01$, *** $p < 0.001$.

Due to the cardinal advantage of FVD over Sytox/7-AAD to fixate samples after treatment, enabling flow cytometric measurements at later time points, we also tested whether Annexin V—which detects phosphatidyl serin on the surface of early/late apoptotic cells [49] and allows for sample fixation as well—could be used instead of FVD. However, a considerable proportion of LD-enriched liver NPCs engaged Annexin V to a similar extent as that observed for FVD (Figure S3).

Altogether, these observations suggest that DNA-intercalating agents (Sytox, 7-AAD) are more reliable for the viability analysis of liver NPCs.

2.2. Liver NPCs Enriched by LD Express Costimulatory Receptors at Higher Levels and Are Partially Refractory towards Stimulation

Our findings on the differential binding of liver NPCs to FVD viability dyes suggested that both liver NPC enrichment procedures may also affect their overall state of activation. Overnight-cultivated liver NPC populations displayed no method-associated differences in expression of the antigen-presenting receptor MHCII (Figure 3, Ctrl groups). In contrast, MACs, DCs and LSECs expressed the costimulatory receptors CD80 and CD86 to a higher extent when enriched by LD as compared to LP.

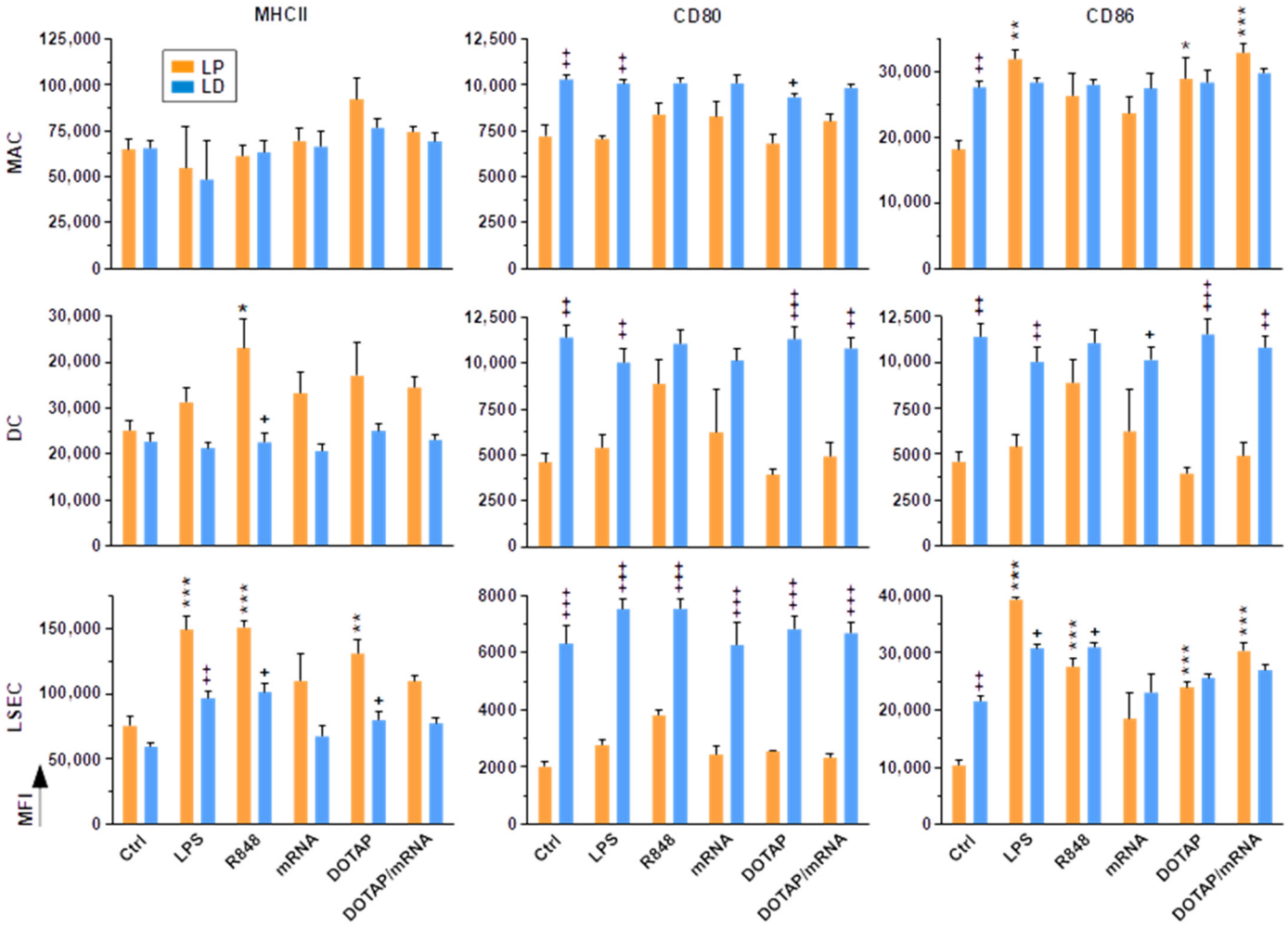

Figure 3. LD-enriched liver NPCs are pre-activated, as deduced from elevated activation marker expression. Liver NPCs enriched by LP and LD were seeded into wells of 96 well plates (10^5/100µL) and stimulated overnight with the agents indicated or left untreated. The man fluorescence intensity (MFI) of surface markers was assessed by flow cytometry (mean ± SEM, $n = 4$). Statistically significant differences versus *according Ctrl and versus $^{+}$LP are indicated (one way ANOVA, Tukey test). $^{*,+}$ $p < 0.05$, $^{**,++}$ $p < 0.01$, $^{***,+++}$ $p < 0.001$.

To assess the suitability of LP- and LD-derived liver NPCs for in vitro testing of adjuvants, e.g., as a component of nano-vaccines, we applied several TLR ligands—including the TLR4 ligand LPS, the TLR7/8 agonist R848, native mRNA (TLR3 agonist), the well-established liposomal carrier DOTAP, and DOTAP/mRNA complexes. MHCII expression of MACs enriched by either of the methods displayed was not altered by either stimulus. Similar observations were made for the co-stimulator CD80. In contrast, CD86 expression was upregulated in the case of LP-enriched MACs in response to either stimulus, whereas LD-derived MACs remained unresponsive in this regard. LP-enriched DCs upregulated MHCII and showed similar tendencies regarding both co-stimulators in response to stimulation, whereas DCs pre-activated due to enrichment by LD were refractory.

LP-enriched LSECs showed increased MHCII expression in response to LPS, R848 and DOTAP, but LD-enriched LSECs displayed only very moderately elevated levels. Similar to MACs and DCs, LD-derived LSECs in general scarcely upregulated either co-stimulator in response to stimulation. In contrast, LP-derived LSECs showed somewhat increased CD80 expression when stimulated with R848 and significant upregulation of CD86 upon application of most stimuli.

In line with the partially activated state of LD-enriched liver NPC populations after overnight cultivation, the respective cell culture supernatants contained higher concentrations of TNF-α, IL-6, and IL-10 than in the case of LP-derived NPCs (Figure 4). Type I (IFN-α, -β) and type II (IFN-γ) interferons were scarcely detectable under basal conditions. Most cytokines, except for IFN-α, were upregulated to the highest extent by stimulation with R848 and to a similar extent ,in an enrichment method-independent manner. Only IL-10 showed markedly higher absolute levels in the case of LD-enriched NPCs than those observed for LP-derived NPCs. Stimulation with LPS also increased cytokine concentrations—again except for IFN-α—albeit to a lower extent than that induced by R848. Again, for some cytokines (TNF-α, IL-6, IL-10), levels were somewhat higher in the case of LD-derived NPCs. Only in the case of IFN-γ did LP-derived NPCs produce more cytokine than that observed for LD-enriched NPCs. mRNA and DOTAP, when applied separately, exerted no stimulatory effect on the production of either cytokine—except for IFN-γ, which was markedly upregulated in the case of LP-enriched NPCs treated with mRNA. DOTAP/mRNA complexes, however, specifically increased type I IFN concentrations—again, interestingly, to a higher extent in the case of LP- than LD-derived liver NPCs.

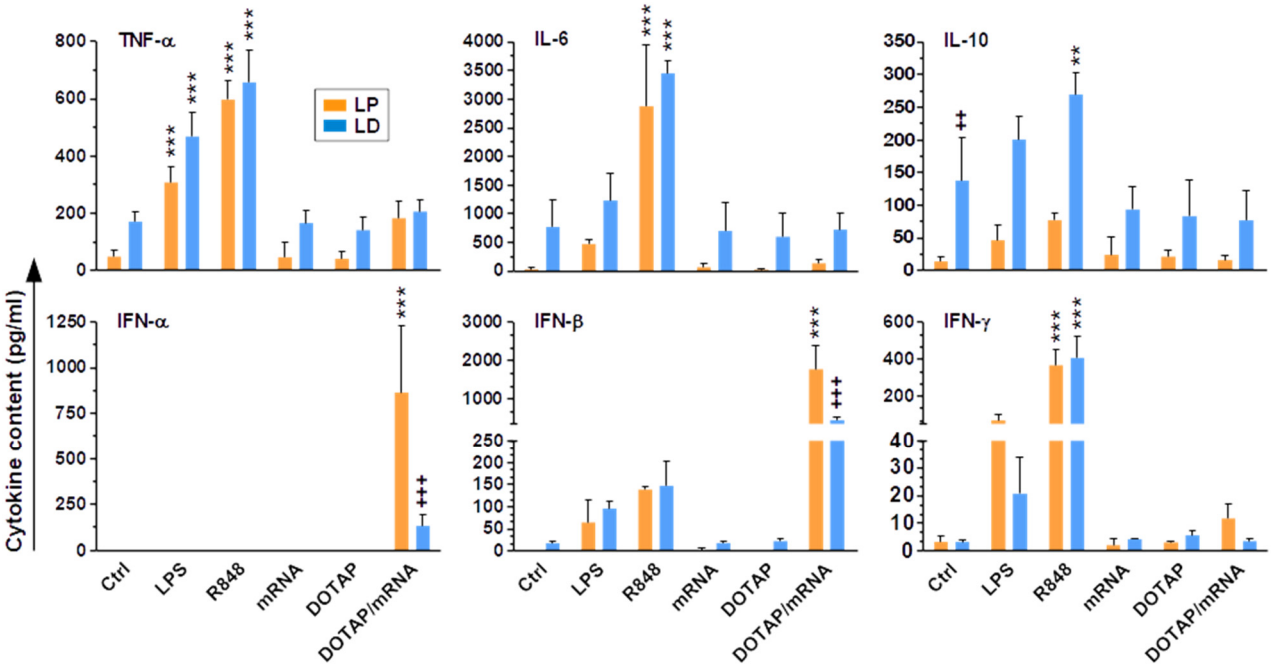

Figure 4. Liver NPCs generate cytokines in an adjuvant-specific manner and depending on the enrichment method used. Supernatants of differentially stimulated liver NPCs (see Figure 3) were assayed for cytokine contents in culture supernatants (mean ± SEM, n = 3). Statistically significant differences versus * according Ctrl and versus $^{+}$LP are indicated (one way ANOVA, Tukey test). **, $^{++}$ $p < 0.01$, ***, $^{+++}$ $p < 0.001$.

Altogether, these results suggest that LD results in the partial activation of enriched liver NPCs, which in the case of surface activation markers prevented stimulation-dependent upregulation. In agreement, LD-enriched liver NPCs showed higher basal levels of some cytokines, but in contrast to inducing non-responsiveness on the level of surface markers, were capable of upregulating cytokine production in response to stimulation.

3. Discussion

The immunological role of liver NPCs, and the frequent observation that nanodrugs intended to address other cell types are frequently enriched in this organ, underline the importance of studying the interactions of liver NPC populations with nanodrugs and the functional consequences thereof. Furthermore, liver NPCs have also been recognized as

an interesting target population for nanodrug-mediated approaches aimed at exploiting their intrinsic protolerogenic potential to inhibit unwanted immune reactions, as in the case of allergies [50]. Moreover, in the case of anti-tumor nano-vaccination approaches, it may be an important issue to overcome their tolerance-promoting properties by applying suitable adjuvants, as assessed in this study [9].

Therefore, the suitability of liver NPC isolation methods is an important issue. In this regard, LP has been well established over the last decades, and numerous modifications have been tested—as summarized in Table 1. However, LP requires time-consuming in situ treatment of the liver, which may limit the number of samples that can be processed, e.g., for ex vivo analysis after in vivo treatments—as for example in the case of biodistribution studies of nano-carriers [36]. Therefore, we compared LP with LD as an alternative approach in this study.

Table 1. Protocols for liver NPC enrichment.

Liver Digestion	Access to the Liver	Species	NPC Yield (×10⁶)	Gradient Centrifugation	Viability (%) [1]	Reference
Perfusion (aeration apparatus)	vp	r	-	-	-	[51]
0.05% Collagenase/0.10% hyaluronidase	vp	r	-	-	-	[52]
Pronase (*Streptomyces griseus*)	vp	r	2–15	yes	-	[53]
Pronase (*Streptomyces griseus*)	-	r	14/gr	-	-	[54]
Collagenase	-	r	0.5–0.6/gr	Percoll	-	[55]
Pronase/DNAse/Collagenase	vp	r	26 (LSEC), 13 (KC)	Stractan	90	[56]
Collagenase	vp	m	9	Metrizamide	-	[57]
Collagenase/DNAse	vp	m	-	Histodenz	-	[43]
Collagenase/DNAse	vp	m	-	Histodenz	-	[44]
Collagenase IV/Pronase	vp	m	-	Percoll	97	[9]
Collagenase IV (*C. histolyticum*)	ex vivo	h	KC: 1.8, LSEC: 4.3/gr	yes	-	[58]
EGTA/collagenase P	ex vivo	h	1.9 (KC), 0.27 (LSEC)/gr		>90	[59]
According to [53]	vp	m	-	yes	-	[60]
Collagenase II	ex vivo	m	5/gr tissue	-	-	[61]
Collagenase I	vp	r	KC: 3–5, LSEC: 18–20	Percoll	-	[62]
EGTA/collagenase P (two-step)	ex vivo	h	-	Yes	-	[63]
Collagenase/DNAse	vp	m	3.33	Histodenz	-	[36]

h: human, KC: Kupffer cell; LSEC: liver sinusoid endothelial cell; m: murin, vp: vena portae. [1] numbers given when viability was assessed in the study.

We show that both enrichment methods yielded overall comparable results in terms of yield of $CD45^+$ liver NPCs [9], displaying similar compositions of NPC populations with regard to DCs, MACs, and LSECs. Surprisingly, however, we observed that LD-enriched liver NPCs, and MACs especially, showed unspecific interactions with the FVD, and thereby would be considered dead. Similar findings were also made for the other liver NPCs populations. Furthermore, both LP- and LD-enriched MACs displayed low viability after overnight cultivation when using FVD. In contrast, DNA-intercalating agents (Sytox, 7-AAD) identified only <25% of MACs as dead, even after overnight incubation. Besides this, splenic MACs and PMN were also characterized by stronger interaction with FVD than DNA-intercalating dyes after overnight cultivation. Therefore, these findings suggest that endocytically active cell types in a viable state are prone to internalize FVD,

which favors the use of DNA-binding agents for delineating viability. It is unclear as of yet which receptors may play a role in this regard.

However, LD enrichment also resulted in partial activation of the assessed liver NPC types, which may compromise the outcome of in vitro studies aimed, e.g., at assessing the stimulatory activity of agents—as exemplified in this study for several TLR ligands. In this regard, the responsiveness of LD-dependently pre-activated liver NPCs on the level of surface markers was strongly impaired. LD-enriched NPCs generated easily detectable amounts of TNF-α, IL-6, and IL-10—even in the absence of stimulatory agents—but the difference towards LP-derived NPCs was most apparent in the case of IL-10. This potent anti-inflammatory cytokine has been implicated as an effector molecule upregulated in response to different types of stress [64] and has been shown to contribute in an essential manner to the overall pro-tolerogenic role of liver NPCs [65]. KCs have been reported to express IL-10 receptor at high levels, resulting in sustained activation of the transcription factor signal transducer and activator of transcription (STAT)3 [66]. STAT3 in turn is a major driver of IL-10 expression, thereby establishing a positive feedback loop for this cytokine [67]. However, LD-derived liver NPCs were still largely responsive towards stimulation on the cytokine level. Here, we observed that R848, and to lesser extent LPS, was a potent stimulator of TNF-α, IL-6, IL-10, and IFN-γ production—as previously shown by us and others [68]. In addition, we also demonstrated that complexed mRNA yielded considerable induction of type I IFN, as has also been described for antigen-presenting cells in secondary lymphoid organs upon transfection with mRNA-delivering liposomes [69–73].

Our results show that LP-derived liver NPCs can be used to study, e.g., the stimulatory effects of adjuvant-loaded nanodrugs in terms of surface activation marker expression and cytokine production. With regards to the latter, it will also be interesting to assess cytokine production on the single cell level by intracellular cytokine detection [74]. In the case of fluorescence-labeled nano-carriers, it will also be possible to study their liver NPC type-specific engagement—especially in the case of nanodrugs decorated with, e.g., C-type lectin receptor-targeting moieties such as carbohydrates [75]. Finally, in the case of nano-vaccines that co-deliver an antigen, subsequent cocultures of accordingly pretreated liver NPCs with antigen-specific T cells will show whether adjuvant-mediated NPC activation is able to overcome their intrinsic protolerogenic properties and result in efficient activation of antigen-specific T cells, e.g., to induce profound anti-tumor T cell responses [76].

Altogether, we conclude that LP is more reliable than LD for obtaining liver NPCs for subsequent in vitro studies. However, LP represents a laborious technique and well-trained operators are needed (Table 2). Therefore, LD is the method of choice in the case liver NPCs that need to be derived from a larger number of in vivo-treated animals for subsequent ex vivo analysis. In this case, the potential of LD to process a larger number of samples in parallel enables the completion of NPC isolation within a shorter period of time as compared to the rather continuous mode of handling in the case of LP. Additionally, our finding that LD partially activates NPCs in the course of subsequent overnight culture is not of primary concern when samples are to be analyzed directly after NPC isolation.

Table 2. Advantages and disadvantages of using LP or LD for NPC enrichment.

Aspect		LP	LD
Total yield		+++	+++
Purity ($CD45^+$)		62%	52%
NPC viability [1]	MAC	89% [2], 76% [3]	82%, 89%
	DC	86%, 62%	81%, 72%
	LSEC	92%, 82%	90%, 91%
NPC activation state		o/+	+++

NPC responsiveness towards stimulation	++	o/+
Preparation time	4–5 h	2–3 h
Costs	+	+++

[1] given for Sytox; [2] freshly isolated; [3] after overnight culture. O, unaltered; +, low; ++, intermediate, +++, high.

4. Materials and Methods

4.1. Animals

C57BL/6 mice were bred and housed in the Translational Animal Research Center (TARC) of the Johannes Gutenberg-University Mainz under specific pathogen-free conditions on a standard diet, according to the guidelines of the regional animal care committee. The guide for the care and use of laboratory animals [77] as well as the 3R principles in laboratory animal experiments [78] were followed. Mice were sacrificed at an age of between 12–16 weeks for organ retrieval according to § 4(3) TierSchG.

4.2. Spleen Cells

Spleens were mashed using a sterile syringe plunger on a PBS pre-soaked 40 μm cell strainer (EASYstrainer™; Sarstedt, Nümbrecht, Germany). Mashed spleen tissue was washed through the strainer using 10 mL of PBS/2 mM EDTA buffer, and cells were pelleted by centrifugation (1200 rpm, 10 min, 4 °C).

4.3. Enrichment of Liver NPCs

Mice NPCs were enriched by liver perfusion (LP) and liver dissociation (LD). For LP, mice were anesthetized with a Ketamine/Xylazine mixture (Ketamine 120 mg/Kg; Xylasin 16 mg/kg) and the abdominal cavity was opened (see Figure 1, left panel). The vena portae was cannulated and flushed with 20 mL of HBSS (Hank's Balanced Salt Solution; ThermoFisher, Waltham, MA, USA) containing 100 U/mL of collagenase A (Sigma-Aldrich, St. Louis, MO, USA) and 10 μg/mL of DNase I (Sigma-Aldrich, St. Louis, MO, USA). Then, the liver was retrieved, cut into pieces, and incubated for 15 min at 37 °C in a 50 mL tube with PBS containing 100 U/mL of collagenase A and 10 μg/mL of DNase I. Afterwards, the liver tissue was mashed through a 70 μm nylon cell strainer and medium (DMEM (Dulbecco's Modified Eagle Medium)/F-12 GlutaMAX™, ThermoFisher Scientific) was applied. The cell suspension was subjected to density centrifugation using 30% Histodenz-HBSS (both from Sigma-Aldrich, St. Louis, MO, USA) gradient centrifugation as described [45] (see Figure 1, lower panel).

For LD-mediated NPC enrichment, mice were killed by cervical dislocation and the liver was retrieved (see Figure 1, right panel). An enzyme-dependent dissociation mixture of proprietary composition (Liver dissociation kit; Miltenyi Biotec, Bergisch-Gladbach, Germany) was preincubated for 15 min in C tubes (Miltenyi Biotec). Then, liver tissues were cut in little pieces and transferred into prepared C tubes. The latter were placed into a gentleMACS Dissociator and the tissue was minced (two times program m_liver _03). Afterwards, the cell suspension was incubated for 30 min at 37 °C under continuous shaking, followed by another round of gentleMACS-mediated disintegration (two times program m_liver_04). The samples were cleared using a Cell Strainer (100μm; Sarstedt) and the liver NPCs were enriched by density centrifugation (see above).

4.4. Stimulation of Liver NPCs

Liver NPCs were seeded into wells of 96-well plates (10^5/100 μL) and were treated overnight with LPS, (100 ng/m; Kenilworth, NJ, USA), R848 (1 μg/m, Ínvivogen, San Diego, CA, USA), ovalbumine-encoding mRNA (1 μg/mL; Tri-Link, San Diego, CA, USA), DOTAP (6,4 μL/mL; Roth, Weiden, Germany), and DOTAP/mRNA complexes, which

were formed by mixing both components at the mentioned amounts as recommended by the manufacturer (Roth).

4.5. Flow Cytometry

Single cell suspensions were washed (2% FCS in PBS), and Fc receptors were blocked with aCD16/CD32 (clone 2.4G2 clone; Biolegend, San Diego, CA, USA) for 10 min. Afterwards, cells were incubated with receptor-specific antibodies (Table S1) obtained from ThermoFisher (Waltham, MA) or BD Biosciences (Franklin Lakes, NJ, USA) for 20 min at 4 °C. Afterwards, cell viability was assessed by using fixable viability dye (FVD)-450 and -780, 7AAD, Sytox AADvanced (all from ThermoFisher) and Annexin V-AF647 (Biolegend), as recommended by the manufacturer. Samples were subjected to flow cytometry using a Attune NxT Flow Cytometer (Thermo Scientific) and an LSRII (BD Biosciences), and analyzed with Attune NxT ((ThermoScientific and FlowJo software, respectively (BD Biosciences)). The gating strategies for liver NPCs (see Figure S1) and splenic leukocytes (see Figure S2a) are depicted in the supplementals.

4.6. Cytokines

Supernatants of cell cultures were retrieved and stored at −20 °C for subsequent analysis. TNF-α, IFN-γ, IL-6, IL-1ß, and IL-10 were quantified using a Cytometric Bead Assay (CBA; BD Biosciences) as recommended by the manufacturer. Results were analyzed using FCAP Array Analysis Software v.1.0.1 (BD Biosciences). IFN-α and IFN-β were measured using Legendplex reagents as recommended and data were analyzed using Qognit Legendplex Analysis Software (both from Biolegend).

4.7. Data Analysis

Data were analyzed using GraphPad PRISM v5 and v9 software (GraphPad Software Inc., San Diego, CA, USA). Data are given as mean ± SEM for the indicated number of independent experiments. Statistical differences were determined by unpaired Student's *t*-tests when comparing two groups, one way ANOVA followed by post-hoc Tukey`s test when comparing multiple groups monitored at a given time point, and two-way ANOVA/Tukey tests when comparing multiple groups assessed at different time points—assuming significant differences at $p < 0.05$ in either case.

Supplementary Materials: The following supporting information can be downloaded at: https://www.mdpi.com/article/10.3390/ijms23126542/s1.

Author Contributions: Conceptualization, C.M.-M., M.L.C. and M.B.; methodology, C.M.-M. and M.L.C.; software, C.M.-M., M.L.C., M.S., M.J.L., Y.Z., J.E.C.-G. and N.R.; validation, C.M.-M., M.L.C., M.S., M.J.L., Y.Z., J.E.C.-G., N.R. and M.B.; formal analysis, C.M.-M., M.L.C., M.S., M.J.L., Y.Z., J.E.C.-G. and N.R.; investigation, C.M.-M., M.L.C., M.S., M.J.L., Y.Z., J.E.C.-G. and N.R.; resources, C.M.-M., M.L.C., M.S., M.J.L., Y.Z., J.E.C.-G. and N.R.; data curation, C.M.-M., M.L.C., Y.Z. and M.B.; writing—original draft preparation, C.M.-M., M.L.C. and M.B.; writing—review and editing, C.M.-M., M.L.C., S.G. (Stephan Grabbe), S.G. (Stephan Gehring) and M.B.; visualization, C.M.-M., M.L.C., Y.Z. and M.B.; supervision, M.L.C., S.G. (Stephan Gehring) and M.B.; project administration, S.G. (Stephan Grabbe), S.G. (Stephan Gehring) and M.B.; funding acquisition, S.G. (Stephan Grabbe), S.G. (Stephan Gehring) and M.B. All authors have read and agreed to the published version of the manuscript.

Funding: This research was funded by Deutsche Forschungsgemeinschaft (SFB1066), grant numbers B4 (S.G. (Stephan Grabbe)) and B15 (S.G. (Stephan Gehring), M.B. (Matthias Bros)).

Institutional Review Board Statement: Mice were sacrificed for organ retrieval according to § 4(3) TierSchG.

Informed Consent Statement: Not applicable.

Data Availability Statement: Not applicable.

Acknowledgments: We thank the Research Center for Immunotherapy (FZI; University Medical Center, Mainz, Germany) for their continuous support.

Conflicts of Interest: The authors declare no conflict of interest.

References

1. Parker, G.A.; Picut, C.A. Liver immunobiology. *Toxicol. Pathol.* **2005**, *33*, 52–62. https://doi.org/10.1080/01926230590522365.
2. Gao, B.; Jeong, W.I.; Tian, Z. Liver: An organ with predominant innate immunity. *Hepatology* **2008**, *47*, 729–736. https://doi.org/10.1002/hep.22034.
3. Doherty, D.G. Immunity, tolerance and autoimmunity in the liver: A comprehensive review. *J. Autoimmun.* **2016**, *66*, 60–75. https://doi.org/10.1016/j.jaut.2015.08.020.
4. Kuscuoglu, D.; Janciauskiene, S.; Hamesch, K.; Haybaeck, J.; Trautwein, C.; Strnad, P. Liver - master and servant of serum proteome. *J. Hepatol.* **2018**, *69*, 512–524. https://doi.org/10.1016/j.jhep.2018.04.018.
5. Oteng, A.B.; Kersten, S. Mechanisms of Action of trans Fatty Acids. *Adv. Nutr.* **2020**, *11*, 697–708. https://doi.org/10.1093/advances/nmz125.
6. Vázquez-Borrego, M.C.; Del Rio-Moreno, M.; Kineman, R.D. Towards Understanding the Direct and Indirect Actions of Growth Hormone in Controlling Hepatocyte Carbohydrate and Lipid Metabolism. *Cells* **2021**, *10*, 2532. https://doi.org/10.3390/cells10102532.
7. Chiang, J.Y.L.; Ferrell, J.M. Bile Acid Metabolism in Liver Pathobiology. *Gene Expr.* **2018**, *18*, 71–87. https://doi.org/10.3727/105221618x15156018385515.
8. Andrade, R.J.; Chalasani, N.; Björnsson, E.S.; Suzuki, A.; Kullak-Ublick, G.A.; Watkins, P.B.; Devarbhavi, H.; Merz, M.; Lucena, M.I.; Kaplowitz, N.; et al. Drug-induced liver injury. *Nat. Rev. Dis. Primers* **2019**, *5*, 58. https://doi.org/10.1038/s41572-019-0105-0.
9. Cacicedo, M.L.; Medina-Montano, C.; Kaps, L.; Kappel, C.; Gehring, S.; Bros, M. Role of Liver-Mediated Tolerance in Nanoparticle-Based Tumor Therapy. *Cells* **2020**, *9*, 1985. https://doi.org/10.3390/cells9091985.
10. Racanelli, V.; Rehermann, B. The liver as an immunological organ. *Hepatology* **2006**, *43*, S54–S62. https://doi.org/10.1002/hep.21060.
11. Khomich, O.; Ivanov, A.V.; Bartosch, B. Metabolic Hallmarks of Hepatic Stellate Cells in Liver Fibrosis. *Cells* **2019**, *9*, 24. https://doi.org/10.3390/cells9010024.
12. Luo, N.; Li, J.; Wei, Y.; Lu, J.; Dong, R. Hepatic Stellate Cell: A Double-Edged Sword in the Liver. *Physiol. Res.* **2021**, *70*, 821–829. https://doi.org/10.33549/physiolres.934755.
13. Higashi, T.; Friedman, S.L.; Hoshida, Y. Hepatic stellate cells as key target in liver fibrosis. *Adv. Drug Deliv. Rev.* **2017**, *121*, 27–42. https://doi.org/10.1016/j.addr.2017.05.007.
14. Baglieri, J.; Brenner, D.A.; Kisseleva, T. The Role of Fibrosis and Liver-Associated Fibroblasts in the Pathogenesis of Hepatocellular Carcinoma. *Int. J. Mol. Sci.* **2019**, *20*, 1723. https://doi.org/10.3390/ijms20071723.
15. Matsuda, M.; Seki, E. Hepatic Stellate Cell-Macrophage Crosstalk in Liver Fibrosis and Carcinogenesis. *Semin. Liver Dis.* **2020**, *40*, 307–320. https://doi.org/10.1055/s-0040-1708876.
16. Kolios, G.; Valatas, V.; Kouroumalis, E. Role of Kupffer cells in the pathogenesis of liver disease. *World J. Gastroenterol.* **2006**, *12*, 7413–7420. https://doi.org/10.3748/wjg.v12.i46.7413.
17. Kazankov, K.; Jørgensen, S.M.D.; Thomsen, K.L.; Møller, H.J.; Vilstrup, H.; George, J.; Schuppan, D.; Grønbæk, H. The role of macrophages in nonalcoholic fatty liver disease and nonalcoholic steatohepatitis. *Nat. Rev. Gastroenterol. Hepatol.* **2019**, *16*, 145–159. https://doi.org/10.1038/s41575-018-0082-x.
18. Hosseini, N.; Shor, J.; Szabo, G. Alcoholic Hepatitis: A Review. *Alcohol Alcohol.* **2019**, *54*, 408–416. https://doi.org/10.1093/alcalc/agz036.
19. Yuan, F.; Zhang, W.; Mu, D.; Gong, J. Kupffer cells in immune activation and tolerance toward HBV/HCV infection. *Adv. Clin. Exp. Med.* **2017**, *26*, 739–745. https://doi.org/10.17219/acem/62759.
20. Zhang, W.; Cao, D.; Wang, M.; Wu, Y.; Gong, J.; Li, J.; Liu, Y. XBP1s repression regulates Kupffer cell polarization leading to immune suppressive effects protecting liver allograft in rats. *Int. Immunopharmacol.* **2021**, *91*, 107294. https://doi.org/10.1016/j.intimp.2020.107294.
21. Lau, A.H.; Thomson, A.W. Dendritic cells and immune regulation in the liver. *Gut* **2003**, *52*, 307–314. https://doi.org/10.1136/gut.52.2.307.
22. Almeda-Valdes, P.; Aguilar Olivos, N.E.; Barranco-Fragoso, B.; Uribe, M.; Méndez-Sánchez, N. The Role of Dendritic Cells in Fibrosis Progression in Nonalcoholic Fatty Liver Disease. *Biomed. Res. Int.* **2015**, *2015*, 768071. https://doi.org/10.1155/2015/768071.
23. Szafranska, K.; Kruse, L.D.; Holte, C.F.; McCourt, P.; Zapotoczny, B. The wHole Story About Fenestrations in LSEC. *Front. Physiol.* **2021**, *12*, 735573. https://doi.org/10.3389/fphys.2021.735573.
24. Hammoutene, A.; Rautou, P.E. Role of liver sinusoidal endothelial cells in non-alcoholic fatty liver disease. *J. Hepatol.* **2019**, *70*, 1278–1291. https://doi.org/10.1016/j.jhep.2019.02.012.
25. Bhandari, S.; Larsen, A.K.; McCourt, P.; Smedsrød, B.; Sørensen, K.K. The Scavenger Function of Liver Sinusoidal Endothelial Cells in Health and Disease. *Front. Physiol.* **2021**, *12*, 757469. https://doi.org/10.3389/fphys.2021.757469.

26. Ganesan, L.P.; Kim, J.; Wu, Y.; Mohanty, S.; Phillips, G.S.; Birmingham, D.J.; Robinson, J.M.; Anderson, C.L. FcγRIIb on liver sinusoidal endothelium clears small immune complexes. *J. Immunol.* **2012**, *189*, 4981–4988. https://doi.org/10.4049/jimmunol.1202017.
27. Mates, J.M.; Yao, Z.; Cheplowitz, A.M.; Suer, O.; Phillips, G.S.; Kwiek, J.J.; Rajaram, M.V.; Kim, J.; Robinson, J.M.; Ganesan, L.P.; et al. Mouse Liver Sinusoidal Endothelium Eliminates HIV-Like Particles from Blood at a Rate of 100 Million per Minute by a Second-Order Kinetic Process. *Front. Immunol.* **2017**, *8*, 35. https://doi.org/10.3389/fimmu.2017.00035.
28. Øie, C.I.; Wolfson, D.L.; Yasunori, T.; Dumitriu, G.; Sørensen, K.K.; McCourt, P.A.; Ahluwalia, B.S.; Smedsrød, B. Liver sinusoidal endothelial cells contribute to the uptake and degradation of entero bacterial viruses. *Sci. Rep.* **2020**, *10*, 898. https://doi.org/10.1038/s41598-020-57652-0.
29. Shetty, S.; Lalor, P.F.; Adams, D.H. Liver sinusoidal endothelial cells - gatekeepers of hepatic immunity. *Nat. Rev. Gastroenterol. Hepatol.* **2018**, *15*, 555–567. https://doi.org/10.1038/s41575-018-0020-y.
30. Mehrfeld, C.; Zenner, S.; Kornek, M.; Lukacs-Kornek, V. The Contribution of Non-Professional Antigen-Presenting Cells to Immunity and Tolerance in the Liver. *Front. Immunol.* **2018**, *9*, 635. https://doi.org/10.3389/fimmu.2018.00635.
31. Zheng, M.; Tian, Z. Liver-Mediated Adaptive Immune Tolerance. *Front. Immunol.* **2019**, *10*, 2525. https://doi.org/10.3389/fimmu.2019.02525.
32. Deczkowska, A.; David, E.; Ramadori, P.; Pfister, D.; Safran, M.; Li, B.; Giladi, A.; Jaitin, D.A.; Barboy, O.; Cohen, M.; et al. XCR1(+) type 1 conventional dendritic cells drive liver pathology in non-alcoholic steatohepatitis. *Nat. Med.* **2021**, *27*, 1043–1054. https://doi.org/10.1038/s41591-021-01344-3.
33. Sellau, J.; Puengel, T.; Hoenow, S.; Groneberg, M.; Tacke, F.; Lotter, H. Monocyte dysregulation: Consequences for hepatic infections. *Semin. Immunopathol.* **2021**, *43*, 493–506. https://doi.org/10.1007/s00281-021-00852-1.
34. Din, F.U.; Aman, W.; Ullah, I.; Qureshi, O.S.; Mustapha, O.; Shafique, S.; Zeb, A. Effective use of nanocarriers as drug delivery systems for the treatment of selected tumors. *Int. J. Nanomed.* **2017**, *12*, 7291–7309. https://doi.org/10.2147/IJN.S146315.
35. Su, S.; Kang, P.M. Recent Advances in Nanocarrier-Assisted Therapeutics Delivery Systems. *Pharmaceutics* **2020**, *12*, 837. https://doi.org/10.3390/pharmaceutics12090837.
36. Kappel, C.; Seidl, C.; Medina-Montano, C.; Schinnerer, M.; Alberg, I.; Leps, C.; Sohl, J.; Hartmann, A.K.; Fichter, M.; Kuske, M.; et al. Density of Conjugated Antibody Determines the Extent of Fc Receptor Dependent Capture of Nanoparticles by Liver Sinusoidal Endothelial Cells. *ACS Nano* **2021**, *15*, 15191–15209. https://doi.org/10.1021/acsnano.1c05713, doi:10.1021/acsnano.1c05713.
37. Mitchell, M.J.; Billingsley, M.M.; Haley, R.M.; Wechsler, M.E.; Peppas, N.A.; Langer, R. Engineering precision nanoparticles for drug delivery. *Nat. Rev. Drug Discov.* **2021**, *20*, 101–124. https://doi.org/10.1038/s41573-020-0090-8.
38. Driscoll, J.; Wehrkamp, C.; Ota, Y.; Thomas, J.N.; Yan, I.K.; Patel, T. Biological Nanotherapeutics for Liver Disease. *Hepatology* **2021**, *74*, 2863–2875. https://doi.org/10.1002/hep.31847.
39. Kadiu, I.; Nowacek, A.; McMillan, J.; Gendelman, H.E. Macrophage endocytic trafficking of antiretroviral nanoparticles. *Nanomedicine (Lond)* **2011**, *6*, 975–994. https://doi.org/10.2217/nnm.11.27.
40. Xu, S.; Olenyuk, B.Z.; Okamoto, C.T.; Hamm-Alvarez, S.F. Targeting receptor-mediated endocytotic pathways with nanoparticles: Rationale and advances. *Adv. Drug Deliv. Rev.* **2013**, *65*, 121–138. https://doi.org/10.1016/j.addr.2012.09.041.
41. Rennick, J.J.; Johnston, A.P.R.; Parton, R.G. Key principles and methods for studying the endocytosis of biological and nanoparticle therapeutics. *Nat. Nanotechnol.* **2021**, *16*, 266–276. https://doi.org/10.1038/s41565-021-00858-8.
42. Sousa de Almeida, M.; Susnik, E.; Drasler, B.; Taladriz-Blanco, P.; Petri-Fink, A.; Rothen-Rutishauser, B. Understanding nanoparticle endocytosis to improve targeting strategies in nanomedicine. *Chem. Soc. Rev.* **2021**, *50*, 5397–5434. https://doi.org/10.1039/d0cs01127d.
43. Gregory, S.H.; Cousens, L.P.; van Rooijen, N.; Dopp, E.A.; Carlos, T.M.; Wing, E.J. Complementary adhesion molecules promote neutrophil-Kupffer cell interaction and the elimination of bacteria taken up by the liver. *J. Immunol.* **2002**, *168*, 308–315. https://doi.org/10.4049/jimmunol.168.1.308.
44. Gehring, S.; Dickson, E.M.; San Martin, M.E.; van Rooijen, N.; Papa, E.F.; Harty, M.W.; Tracy, T.F., Jr.; Gregory, S.H. Kupffer cells abrogate cholestatic liver injury in mice. *Gastroenterology* **2006**, *130*, 810–822. https://doi.org/10.1053/j.gastro.2005.11.015.
45. Fichter, M.; Baier, G.; Dedters, M.; Pretsch, L.; Pietrzak-Nguyen, A.; Landfester, K.; Gehring, S. Nanocapsules generated out of a polymeric dexamethasone shell suppress the inflammatory response of liver macrophages. *Nanomedicine* **2013**, *9*, 1223–1234. https://doi.org/10.1016/j.nano.2013.05.005.
46. Vaughan, A.M. (Ed.) *Malaria Vaccines*; Humana Press: Totowa, NJ, USA; Springer: New York, NY, USA, 2015; p. 305. https://doi.org/10.1007/978-1-4939-2815-6.
47. Perfetto, S.P.; Chattopadhyay, P.K.; Lamoreaux, L.; Nguyen, R.; Ambrozak, D.; Koup, R.A.; Roederer, M. Amine reactive dyes: An effective tool to discriminate live and dead cells in polychromatic flow cytometry. *J. Immunol. Methods* **2006**, *313*, 199–208. https://doi.org/10.1016/j.jim.2006.04.007.
48. Poot, M.; Gibson, L.L.; Singer, V.L. Detection of apoptosis in live cells by MitoTracker red CMXRos and SYTO dye flow cytometry. *Cytometry* **1997**, *27*, 358–364.
49. Koopman, G.; Reutelingsperger, C.P.; Kuijten, G.A.; Keehnen, R.M.; Pals, S.T.; van Oers, M.H. Annexin V for flow cytometric detection of phosphatidylserine expression on B cells undergoing apoptosis. *Blood* **1994**, *84*, 1415–1420.

50. Liu, Q.; Wang, X.; Liu, X.; Liao, Y.P.; Chang, C.H.; Mei, K.C.; Jiang, J.; Tseng, S.; Gochman, G.; Huang, M.; et al. Antigen- and Epitope-Delivering Nanoparticles Targeting Liver Induce Comparable Immunotolerance in Allergic Airway Disease and Anaphylaxis as Nanoparticle-Delivering Pharmaceuticals. *ACS Nano* **2021**, *15*, 1608–1626. https://doi.org/10.1021/acsnano.0c09206.
51. Miller, L.L.; Bly, C.G.; Watson, M.L.; Bale, W.F. The dominant role of the liver in plasma protein synthesis; a direct study of the isolated perfused rat liver with the aid of lysine-epsilon-C14. *J. Exp. Med.* **1951**, *94*, 431–453. https://doi.org/10.1084/jem.94.5.431.
52. Berry, M.N.; Friend, D.S. High-yield preparation of isolated rat liver parenchymal cells: A biochemical and fine structural study. *J. Cell Biol.* **1969**, *43*, 506–520. https://doi.org/10.1083/jcb.43.3.506.
53. Seglen, P.O. Preparation of isolated rat liver cells. *Methods Cell Biol.* **1976**, *13*, 29–83. https://doi.org/10.1016/s0091-679x(08)61797-5.
54. Knook, D.L.; Barkway, C.; Sleyster, E.C. Lysosomal enzyme content of Kupffer and endothelial liver cells isolated from germfree and clean conventional rats. *Infect. Immun.* **1981**, *33*, 620–622. https://doi.org/10.1128/iai.33.2.620-622.1981.
55. Smedsrod, B.; Pertoft, H. Preparation of pure hepatocytes and reticuloendothelial cells in high yield from a single rat liver by means of Percoll centrifugation and selective adherence. *J. Leukoc. Biol.* **1985**, *38*, 213–230. https://doi.org/10.1002/jlb.38.2.213.
56. Friedman, S.L.; Roll, F.J. Isolation and culture of hepatic lipocytes, Kupffer cells, and sinusoidal endothelial cells by density gradient centrifugation with Stractan. *Anal. Biochem.* **1987**, *161*, 207–218. https://doi.org/10.1016/0003-2697(87)90673-7.
57. Deleve, L.D. Dacarbazine toxicity in murine liver cells: A model of hepatic endothelial injury and glutathione defense. *J. Pharmacol. Exp. Ther.* **1994**, *268*, 1261–1270.
58. Werner, M.; Driftmann, S.; Kleinehr, K.; Kaiser, G.M.; Mathe, Z.; Treckmann, J.W.; Paul, A.; Skibbe, K.; Timm, J.; Canbay, A.; et al. All-In-One: Advanced preparation of Human Parenchymal and Non-Parenchymal Liver Cells. *PLoS ONE* **2015**, *10*, e0138655. https://doi.org/10.1371/journal.pone.0138655.
59. Pfeiffer, E.; Kegel, V.; Zeilinger, K.; Hengstler, J.G.; Nussler, A.K.; Seehofer, D.; Damm, G. Featured Article: Isolation, characterization, and cultivation of human hepatocytes and non-parenchymal liver cells. *Exp. Biol. Med. (Maywood)* **2015**, *240*, 645–656. https://doi.org/10.1177/1535370214558025.
60. Mohar, I.; Brempelis, K.J.; Murray, S.A.; Ebrahimkhani, M.R.; Crispe, I.N. Isolation of Non-parenchymal Cells from the Mouse Liver. *Methods Mol. Biol.* **2015**, *1325*, 3–17. https://doi.org/10.1007/978-1-4939-2815-6_1.
61. Chou, C.H.; Lai, S.L.; Ho, C.M.; Lin, W.H.; Chen, C.N.; Lee, P.H.; Peng, F.C.; Kuo, S.H.; Wu, S.Y.; Lai, H.S. Lysophosphatidic acid alters the expression profiles of angiogenic factors, cytokines, and chemokines in mouse liver sinusoidal endothelial cells. *PLoS ONE* **2015**, *10*, e0122060. https://doi.org/10.1371/journal.pone.0122060.
62. Bale, S.S.; Geerts, S.; Jindal, R.; Yarmush, M.L. Isolation and co-culture of rat parenchymal and non-parenchymal liver cells to evaluate cellular interactions and response. *Sci. Rep.* **2016**, *6*, 25329. https://doi.org/10.1038/srep25329.
63. Kegel, V.; Deharde, D.; Pfeiffer, E.; Zeilinger, K.; Seehofer, D.; Damm, G. Protocol for Isolation of Primary Human Hepatocytes and Corresponding Major Populations of Non-parenchymal Liver Cells. *J. Vis. Exp.* **2016**, *109*, e53069. https://doi.org/10.3791/53069.
64. Hu, D.; Wan, L.; Chen, M.; Caudle, Y.; LeSage, G.; Li, Q.; Yin, D. Essential role of IL-10/STAT3 in chronic stress-induced immune suppression. *Brain Behav. Immun.* **2014**, *36*, 118–127. https://doi.org/10.1016/j.bbi.2013.10.016.
65. Moris, D.; Lu, L.; Qian, S. Mechanisms of liver-induced tolerance. *Curr. Opin. Organ. Transplant.* **2017**, *22*, 71–78. https://doi.org/10.1097/mot.0000000000000380.
66. Wang, H.; Lafdil, F.; Kong, X.; Gao, B. Signal transducer and activator of transcription 3 in liver diseases: A novel therapeutic target. *Int. J. Biol. Sci.* **2011**, *7*, 536–550. https://doi.org/10.7150/ijbs.7.536.
67. Bharadwaj, U.; Kasembeli, M.M.; Robinson, P.; Tweardy, D.J. Targeting Janus Kinases and Signal Transducer and Activator of Transcription 3 to Treat Inflammation, Fibrosis, and Cancer: Rationale, Progress, and Caution. *Pharmacol. Rev.* **2020**, *72*, 486–526. https://doi.org/10.1124/pr.119.018440.
68. Adzavon, Y.M.; Zhao, P.; Lv, B.; Liu, M.; Zhang, X.; Xie, F.; Yang, L.; Shang, L.; Zhang, M.; Li, Q.; et al. TLR7 and TLR8 agonist resiquimod (R848) differently regulates MIF expression in cells and organs. *Cytokine* **2017**, *97*, 156–166. https://doi.org/10.1016/j.cyto.2017.06.006.
69. Pollard, C.; Rejman, J.; De Haes, W.; Verrier, B.; Van Gulck, E.; Naessens, T.; De Smedt, S.; Bogaert, P.; Grooten, J.; Vanham, G.; et al. Type I IFN counteracts the induction of antigen-specific immune responses by lipid-based delivery of mRNA vaccines. *Mol. Ther.* **2013**, *21*, 251–259. https://doi.org/10.1038/mt.2012.202.
70. Broos, K.; Van der Jeught, K.; Puttemans, J.; Goyvaerts, C.; Heirman, C.; Dewitte, H.; Verbeke, R.; Lentacker, I.; Thielemans, K.; Breckpot, K. Particle-mediated Intravenous Delivery of Antigen mRNA Results in Strong Antigen-specific T-cell Responses Despite the Induction of Type I Interferon. *Mol. Ther. Nucleic Acids* **2016**, *5*, e326. https://doi.org/10.1038/mtna.2016.38.
71. De Beuckelaer, A.; Pollard, C.; Van Lint, S.; Roose, K.; Van Hoecke, L.; Naessens, T.; Udhayakumar, V.K.; Smet, M.; Sanders, N.; Lienenklaus, S.; et al. Type I Interferons Interfere with the Capacity of mRNA Lipoplex Vaccines to Elicit Cytolytic T Cell Responses. *Mol. Ther.* **2016**, *24*, 2012–2020. https://doi.org/10.1038/mt.2016.161.
72. Kranz, L.M.; Diken, M.; Haas, H.; Kreiter, S.; Loquai, C.; Reuter, K.C.; Meng, M.; Fritz, D.; Vascotto, F.; Hefesha, H.; et al. Systemic RNA delivery to dendritic cells exploits antiviral defence for cancer immunotherapy. *Nature* **2016**, *534*, 396–401. https://doi.org/10.1038/nature18300.
73. Van Hoecke, L.; Roose, K.; Ballegeer, M.; Zhong, Z.; Sanders, N.N.; De Koker, S.; Saelens, X.; Van Lint, S. The Opposing Effect of Type I IFN on the T Cell Response by Non-modified mRNA-Lipoplex Vaccines Is Determined by the Route of Administration. *Mol. Ther. Nucleic Acids* **2020**, *22*, 373–381. https://doi.org/10.1016/j.omtn.2020.09.004.

74. Fichter, M.; Piradashvili, K.; Pietrzak-Nguyen, A.; Pretsch, L.; Kuhn, G.; Strand, S.; Knuf, M.; Zepp, F.; Wurm, F.R.; Mailänder, V.; et al. Polymeric hepatitis C virus non-structural protein 5A nanocapsules induce intrahepatic antigen-specific immune responses. *Biomaterials* **2016**, *108*, 1–12. https://doi.org/10.1016/j.biomaterials.2016.08.046.
75. Wagener, K.; Bros, M.; Krumb, M.; Langhanki, J.; Pektor, S.; Worm, M.; Schinnerer, M.; Montermann, E.; Miederer, M.; Frey, H.; et al. Targeting of Immune Cells with Trimannosylated Liposomes. *Adv. Ther.* **2020**, *3*, 1900185. https://doi.org/10.1002/adtp.201900185.
76. Paßlick, D.; Piradashvili, K.; Bamberger, D.; Li, M.; Jiang, S.; Strand, D.; Wich, P.R.; Landfester, K.; Bros, M.; Grabbe, S.; et al. Delivering all in one: Antigen-nanocapsule loaded with dual adjuvant yields superadditive effects by DC-directed T cell stimulation. *J. Control. Release* **2018**, *289*, 23–34. https://doi.org/10.1016/j.jconrel.2018.09.008.
77. Albus, U. Guide for the Care and Use of Laboratory Animals (8th edn). *Lab. Anim.* **2012**, *46*, 267–268. https://doi.org/10.1258/la.2012.150312.
78. Lee, K.H.; Lee, D.W.; Kang, B.C. The 'R' principles in laboratory animal experiments. *Lab. Anim. Res.* **2020**, *36*, 45. https://doi.org/10.1186/s42826-020-00078-6.

International Journal of
Molecular Sciences

MDPI

Supplementals

Enrichment Methods for Murine Liver Non-Parenchymal Cells Differentially Affect Their Immunophenotype and Responsiveness towards Stimulation

Carolina Medina-Montano [1,†], Maximiliano Luis Cacicedo [2,†], Malin Svensson [2], Maria Jose Limeres [2], Yanira Zeyn [1], Jean Emiro Chaves-Giraldo [1], Nadine Röhrig [1], Stephan Grabbe [1], Stephan Gehring [2,†] and Matthias Bros [1,*,†]

[1] Department of Dermatology, University Medical Center of the Johannes Gutenberg University Mainz, Langenbeckstraße 1, 55131 Mainz, Germany; gmedinam@uni-mainz.de (C.M.-M.); yanira.zeyn@uni-mainz.de (Y.Z.); jchavesg@students.uni-mainz.de (J.E.C.-G.); n.roehrig@uni-mainz.de (N.R.); stephan.grabbe@unimedizin-mainz.de (S.G.)
[2] Children's Hospital, University Medical Center of the Johannes Gutenberg University Mainz, Langenbeckstraße 1, 55131 Mainz, Germany; mcaciced@uni-mainz.de (M.L.C.); malin.svensson@uni-mainz.de (M.S.); mj.limeres@uni-mainz.de (M.J.L.); stephan.gehring@uni-mainz.de (S.G.)
* Correspondence: mbros@uni-mainz.de
† These authors contributed equally to this work.

Citation: Medina-Montano, C.; Cacicedo, M.L.; Svensson, M.; Limeres, M.J.; Zeyn, Y.; Chaves-Giraldo, J.E.; Röhrig, N.; Grabbe, S.; Gehring, S.; Bros, M. Enrichment Methods for Murine Liver Non-Parenchymal Cells Differentially Affect Their Immunophenotype and Responsiveness towards Stimulation. *Int. J. Mol. Sci.* **2022**, *23*, 6543. https://doi.org/10.3390/ijms23126543

Academic Editor: Jin-Kyu Park

Received: 20 May 2022
Accepted: 9 June 2022
Published: 11 June 2022

Publisher's Note: MDPI stays neutral with regard to jurisdictional claims in published maps and institutional affiliations.

Copyright: © 2022 by the authors. Licensee MDPI, Basel, Switzerland. This article is an open access article distributed under the terms and conditions of the Creative Commons Attribution (CC BY) license (https://creativecommons.org/licenses/by/4.0/).

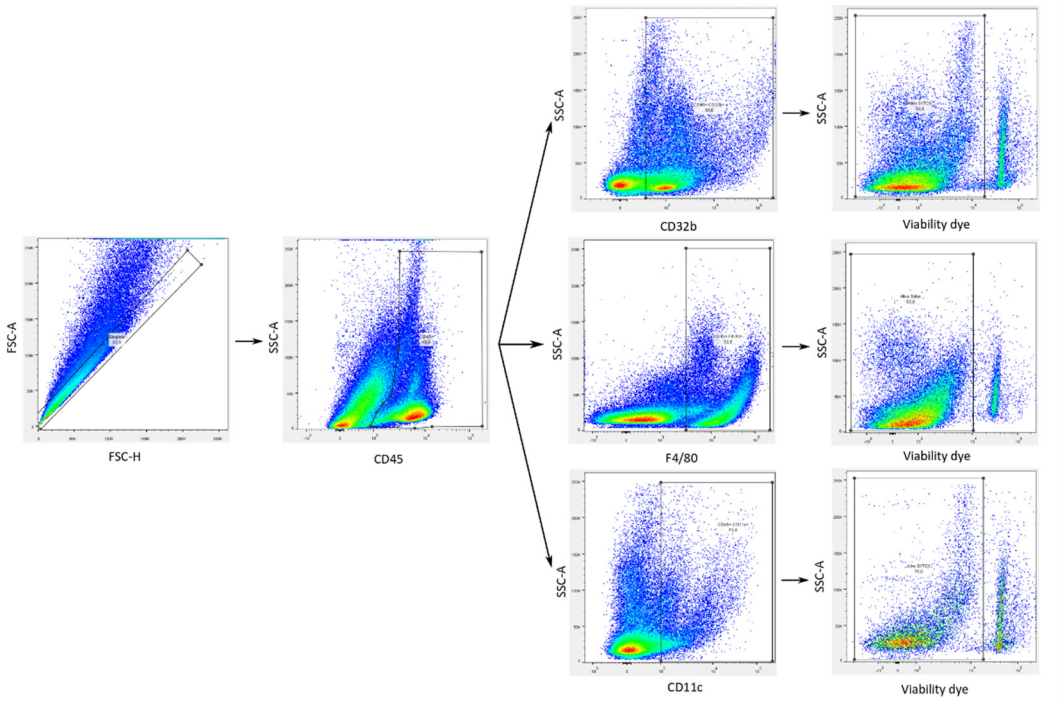

Figure S1. Gating strategy of liver NPC. After gating out debris and cell aggregates, CD45+ liver NPC were further identified by expression of CD32b (liver sinusoidal endothelial cells), F4/80 (macrophages) and CD11c (dendritic cells). Then, for each NPC population the frequency of viability dye negative cells was delineated (LSRII flow cytometer; analysed with FlowJo software).

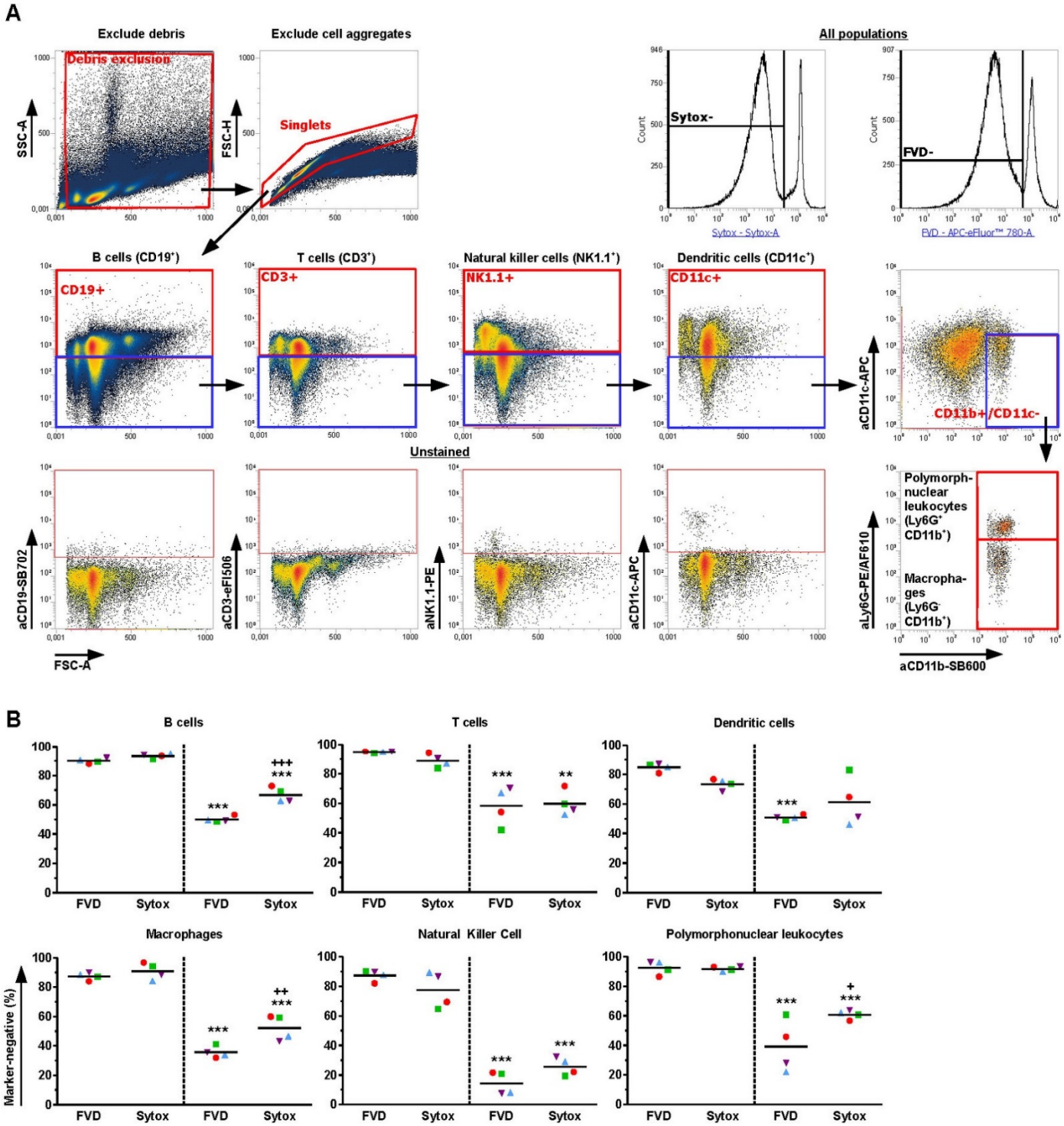

Figure S2. After overnight cultivation some splenic leukocyte populations engage FVD at higher extent than Sytox. Freshly isolated and overnight cultivated spleen cells were incubated in parallel with cell lineage-denoting antibodies, and live/dead cell-discriminating agents (FVD, Sytox). Then, samples were subjected to flow cytometric analysis. (**A**) Gating strategy. After gating out debris and cell aggregates, leukocyte populations were identified by lineage marker expression. Then, for each cell population, the frequencies of FVD and Sytox were delineated (Attune NxT Flow Cytometer; analysed with Attune NxT software). (**B**) Graphs denote the frequencies of FVD- and Sytox-negative (viable) cells (mean±SEM, n=4). Statistical significant differences versus *FVD and versus $^{+}$freshly isolated are indicated (one way ANOVA, Tukey test). $^{+}p<0.05$, $^{++}p<0.01$, $^{***,+++}p<0.001$.

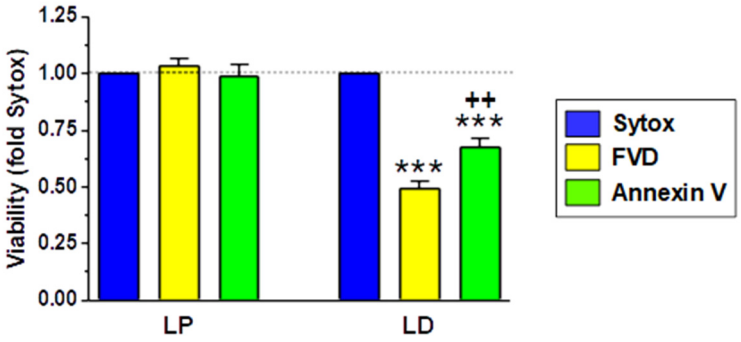

Figure S3. LD-derived liver NPC cultivated overnight engage AnnexinV at higher extent. Binding of LP- and LD-enriched CD45$^+$ liver NPCs after overnight cultivation to various live/dead-discriminating agents was assessed by flow cytometric analysis. Graph denote the frequencies of CD45$^+$ cells negative for Sytox-, FVD- and Annexin V (mean±SEM, n=3), normalized to values for Sytox in each experiment. Statistical significant differences versus *FVD and versus $^+$freshly isolated are indicated (one way ANOVA, Tukey test). $^{++}$p<0.01, ***p<0.001.

Table S1. Antibodies for flow cytometry

Target	**Clone**	**Fluorochrome**
Liver NPC		
CD11c	N418	PE-Cy7
CD32b	AT130-2	PE
CD45	30-F11	BV711
F4/80	BM8	eFl450
Spleen cells		
CD3	145-2C11	eFl506
CD11b	M1/70	SB600
CD11c	N418	APC
CD19	1D3	SB702
NK1.1	PK136	PE
Ly6G	1A8-Ly6g	PE-eFl610

10.8. Publication 8

"Transient lymph node immune activation by hydrolysable polycarbonate nanogels"

This chapter has been published in Advanced Functional Materials. As a second author, I was responsible for performing several *in vitro* biological experiments regarding the uptake and activation of different immune cells using IMDQ-polycarbonate nanogels.

In this work, we used an Imidazoquinoline-type TLR7/8 agonist that was covalently conjugated to polycarbonate nanogels. Polycarbonate nanogels were developed as degradable micellar NP for transient activation of lymph node immune cells. These properties limited the lifetime of the NPs, but their payload could still be successfully leveraged for immunological studies *in vitro* on primary immune cells as well as *in vivo*. For the latter, a control of immune cell activation in the draining lymph node was observed after subcutaneous injection. Overall, these features render polycarbonate nanogels a promising delivery system for transient activation of the immune system in lymph nodes and may consequently become very attractive for further development toward vaccination or cancer immunotherapy. Due to the intrinsic biodegradability and the high degree of control during the manufacturing process, these polycarbonate-based nanogels may be of great importance for clinical translation.

DOI: 10.1002/adfm.202203490

Published in: *Advanced Functional Materials*. **2022**, 32, 35

Reprinted with permission under creative commons attribution 4.0 (CC BY-NC) from C. Czysch, **C. Medina-Montano**, Z. Zhong, A. Fuchs, J. Stickdorn, P. Winterwerber, S. Schmitt, K. Deswarte, M. Raabe, M. Scherger, F. Combes, J. De Vrieze, S. Kasmi, N. N. Sandners, S. Lienenklaus, K. Koynov, H.-J. Räder, B. N. Lambrecht, S. A. David, M. Bros, H. Schild, S. Grabbe, B. G. De Geest, L. Nuhn, Adv. Funct. Mater. **2022**, 2203490.

Particles I

Access the latest eBook →

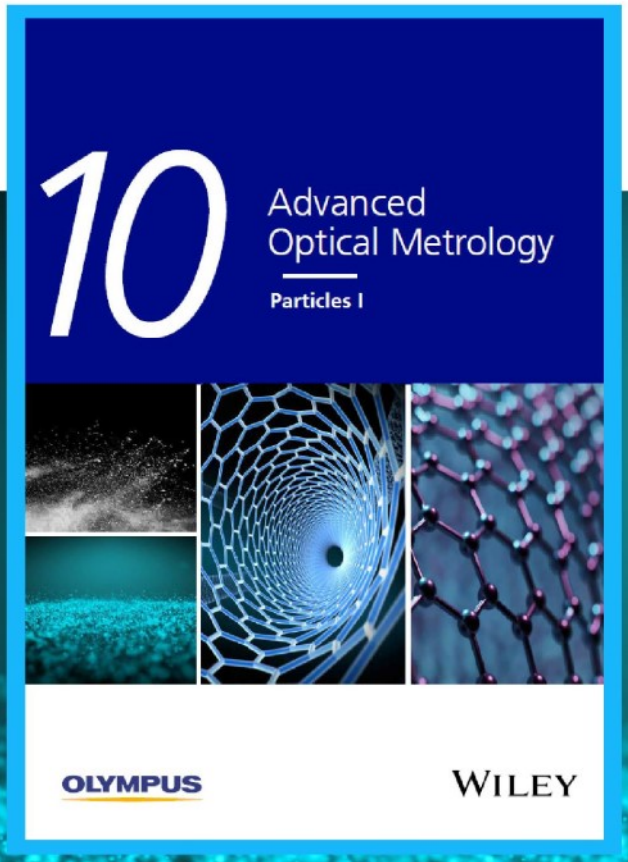

Particles: Unique Properties, Uncountable Applications

Read the latest eBook and better your knowledge with highlights from the recent studies on the design and characterization of micro- and nanoparticles for different application areas.

Access Now

This eBook is sponsored by

OLYMPUS

WILEY

ADVANCED FUNCTIONAL MATERIALS
www.afm-journal.de

Transient Lymph Node Immune Activation by Hydrolysable Polycarbonate Nanogels

*Christian Czysch, Carolina Medina-Montano, Zifu Zhong, Alexander Fuchs, Judith Stickdorn, Pia Winterwerber, Sascha Schmitt, Kim Deswarte, Marco Raabe, Maximilian Scherger, Francis Combes, Jana De Vrieze, Sabah Kasmi, Niek N. Sandners, Stefan Lienenklaus, Kaloian Koynov, Hans-Joachim Räder, Bart N. Lambrecht, Sunil A. David, Matthias Bros, Hansjörg Schild, Stephan Grabbe, Bruno G. De Geest, and Lutz Nuhn**

The development of controlled biodegradable materials is of fundamental importance in immunodrug delivery to spatiotemporally controlled immune stimulation but avoid systemic inflammatory side effects. Based on this, polycarbonate nanogels are developed as degradable micellar carriers for transient immunoactivation of lymph nodes. An imidazoquinoline-type TLR7/8 agonist is covalently conjugated via reactive ester chemistry to these nanocarriers. The nanogels not only provide access to complete disintegration by the hydrolysable polymer backbone, but also demonstrate a gradual disintegration within several days at physiological conditions (PBS, pH 6.4–7.4, 37 °C). These intrinsic properties limit the lifetime of the carriers but their payload can still be successfully leveraged for immunological studies in vitro on primary immune cells as well as in vitro. For the latter, a spatiotemporal control of immune cell activation in the draining lymph node is found after subcutaneous injection. Overall, these features render polycarbonate nanogels a promising delivery system for transient activation of the immune system in lymph nodes and may consequently become very attractive for further development toward vaccination or cancer immunotherapy. Due to the intrinsic biodegradability combined with the high chemical control during the manufacturing process, these polycarbonate-based nanogels may also be of great importance for clinical translation.

1. Introduction

Targeted immunotherapy offers the opportunity to leverage the specificity and power of the immune system to treat pathologies like viral infections[1] or tumors[2] effectively. For immune engineering, dendritic cells are one of the major interests due to their role as "nature's adjuvant."[3] Dendritic cells are antigen-presenting cells, which orchestrate immunity and activate T cells to execute, e.g., their antitumor effect.[4] One strategy of engineering DCs is to trigger their activation via pattern recognition receptors (PRRs) using small molecular agonists.[5,6] However, preclinical data and clinical trials show the limitation of these compounds.[7,8] Because of unfavorable pharmacokinetic properties, local applications lead to a systemic distribution of PRR agonists such as poly(I:C) (TLR3), imidazoquinolines (TLR7/8), or CpG (TLR9).[9–13] Consequently, immune stimulation and pro-inflammatory cascades are triggered off-target resulting in

C. Czysch, A. Fuchs, J. Stickdorn, P. Winterwerber, S. Schmitt, M. Raabe, M. Scherger, K. Koynov, H.-J. Räder, L. Nuhn
Max Planck Institute for Polymer Research
55128 Mainz, Germany
E-mail: lutz.nuhn@mpip-mainz.mpg.de

C. Medina-Montano, M. Bros, S. Grabbe
Department of Dermatology
University Medical Center of Johannes Gutenberg-University Mainz
55131 Mainz, Germany

The ORCID identification number(s) for the author(s) of this article can be found under https://doi.org/10.1002/adfm.202203490.

© 2022 The Authors. Advanced Functional Materials published by Wiley-VCH GmbH. This is an open access article under the terms of the Creative Commons Attribution-NonCommercial License, which permits use, distribution and reproduction in any medium, provided the original work is properly cited and is not used for commercial purposes.

DOI: 10.1002/adfm.202203490

Z. Zhong, J. De Vrieze, S. Kasmi, B. G. De Geest
Department of Pharmaceutics and Cancer Research Institute Ghent (CRIG)
Ghent University
9000 Ghent, Belgium

K. Deswarte, B. N. Lambrecht
Department of Internal Medicine and Pediatrics
VIB Center for Inflammation Research
Ghent University
9052 Ghent, Belgium

F. Combes, N. N. Sandners
Laboratory of Gene Therapy
Department of Nutrition
Genetics and Ethology
Ghent University
9820 Merelbeke, Belgium

S. Lienenklaus
Institute for Laboratory Animal Science and Institute of Immunology
Hannover Medical School
30625 Hannover, Germany

severe immune-related toxicities.[14–18] The therapeutic window of these compounds can strongly be enhanced by directing the immune activation to the site of interest or by covalent coupling to solid matrices. The latter approach was lately chosen in the successful development of the TLR7/8 adjuvanted COVID-19 vaccine Covaxin (BBV152), immobilizing an imidazoquinoline derivative to an alum matrix.[19–21] For altering the biodistribution toward the desired target, nanoparticles are especially suitable to serve as carrier systems.[9,10,22,23] Recently, the delivery to immune system sites such as lymph nodes and spleen has shown its potential for successfully engineering the body's immune response.[24–27] For this purpose, various polymeric systems such as poly(meth)acrylates and polynorbonenes have been employed.[23,26,28]

Nonetheless, after successful delivery, a problem remains: Polymeric particles often lack suitable degradability and their clearance from the body is limited.[29] The need for novel degradable materials has stimulated the development of stimuli-responsive materials. These materials are designed by the incorporation of pH or redox-degradable moieties, thus, allowing for disintegration and drug release at the target site.[30–32] However, this approach withholds the fact that a large fraction of particles does not reach the desired target.[33,34] Due to the then lacking external stimulus, these particles remain intact and accumulate in undesired places such as the liver, the lungs, the kidneys, or the spleen.[35] To enhance chemical translatability, materials with a broader range of degradability and an intrinsically limited lifetime are needed to prevent long-term toxicities.[36,37] These criteria could, for instance, be met by nanocarrier systems that gradually hydrolyze in aqueous environment.

Notable examples of hydrolysable architectures are aliphatic polyesters and aliphatic polycarbonates.[36,38–41] Unfortunately, as polyesters degrade, they acidify the surrounding media, which can lead to local tissue irritation and toxicity, limiting their applicability.[42–44] In contrast to that, aliphatic polycarbonates are more promising due to their favorable degradation products. In their case, degradation results in diols and the weak acid carbon dioxide which is unlikely to cause acidification and similar adverse effects.[36,45] Especially, the archetypal poly(trimethylene carbonate) (PTMC) was explored in this regard as a biodegradable and biocompatible implant material.[46–48] However, PTMC is lacking chemical moieties to introduce functionalities. To broaden the scope of applications, a range of functional polycarbonates were designed and investigated as degradable materials for bioapplications and nanomedicine.[39,49–52] Yet, for most of these structures, degradability was not investigated and just claimed by referring to the degradability of the archetypal, non-functionalized PTMC omitting further analysis to support the hypothesis. So far, it has been shown that polycarbonate degradability can be improved by increasing hydrophilicity.[53–55] The underlying rationale is to increase penetration of water into the structure that should allow for accelerated hydrolysis of the susceptible carbonate moieties. However, not all reported hydrophilic and water-soluble polycarbonates are readily degraded at physiological conditions and further investigations need to provide new insights.[56,57]

We opted for a polymeric carrier system based on aliphatic polycarbonates leveraging their degradability and biocompatibility. In contrast to previous nanogels derived from self-assembling poly(meth)acrylates/-amide or polynorbornene block copolymer micelles, polycarbonates provide unique access to backbone degradability, thus, should prevent long-term toxicological effects that could arise from accumulating materials after therapy.[22,26,58]

Conventional block copolymer micelles that are stabilized by physical (hydrophobic) interactions have limited stability and can disintegrate upon high dilution after injection into the bloodstream.[59] Core-cross-linked systems such as the nanogels of this study circumvent this problem by covalent linkages, strongly avoiding premature block copolymer disassembly.[59–61] Moreover, covalent cross-linking renders the introduction of additional functionalities as well as polarity variation from hydrophobic to hydrophilic inside the core, which is also crucial to enhance degradability. Efficient post-polymerization modification strategies with orthogonal conditions have to be applied to ensure controlled manufacturing. Therefore, we utilized the monomer 5-methyl-5-pentafluorophenyloxycarbonyl-1,3-dioxan-2-one (MTC-PFP) previously described by Hedrick et al. and polymerized it under strong cationic conditions by ring-opening polymerization (ROP), leaving the side-chain untouched and available for post-modification.[57,62,63] By highly increasing the achievable polycarbonate block length, we were able to assemble PEG-based amphiphilic block copolymers into poly(MTC-PFP) micelles and applied them as precursors to generate fully hydrophilic interlinked nanogels. Post-polymerization modification at the active ester side chain[64,65] was employed to conjugate functional primary amines such as fluorescent dyes or the immunostimulatory TLR7/8 agonist IMDQ, while applying non-nucleophilic tertiary amines as catalysts. We here extend this nanogel concept for the first time to polycarbonates and demonstrate that increasing hydrophilicity in polycarbonates indeed allows a gradual degradation at physiological conditions (PBS, pH 6.4–7.4, 37 °C). Investigating the degradation process and its products, the favorable properties of polycarbonate nanogels are shown, bridging toward the biological application as versatile immune-activating carrier systems. The biocompatible properties of the carrier, before as well as after disintegration, were confirmed. Covalent conjugation of the immune-stimulating TLR7/8 agonist IMDQ triggered a localized activation of antigen-presenting cell. As assessed in vitro, the degradation products were even of reduced activity than the intact nanogels, thus, featuring a transient immune stimulation behavior. Moreover, the intact nanogels could well

B. N. Lambrecht
Department of Pulmonary Medicine
Erasmus University Medical Center
3015 Rotterdam, The Netherlands
S. A. David
ViroVax, LLC
Lawrence, KS 66047, USA
H. Schild
Institute of Immunology
University Medical Center of Johannes Gutenberg-University Mainz
55131 Mainz, Germany
L. Nuhn
Macromolecular Chemistry
Department of Chemistry and Pharmacy
Julius Maximilian University Würzburg
97074 Würzburg, Germany

© 2022 The Authors. Advanced Functional Materials published by Wiley-VCH GmbH

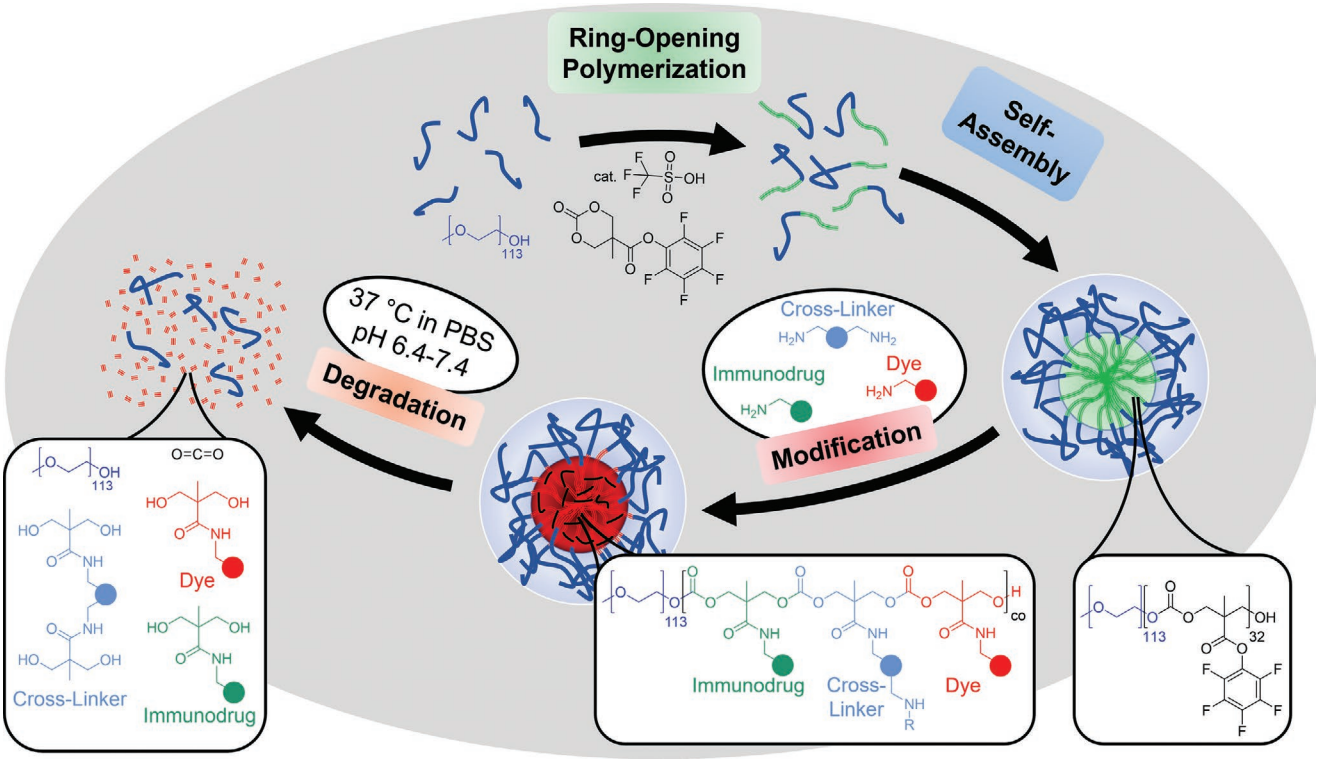

Figure 1. Fabrication of physiologically degradable polycarbonate nanogels. At first, side-chain reactive precursor polymers are produced by ring-opening polymerization. By self-assembly in a block selective solvent, uniform micelles are formed. Upon chemical modification, drug, dye, and cross-linking units are introduced, yielding fully hydrophilic nanogels. Those gels are hydrolytically degradable at body temperature in PBS (pH 6.4–7.4) showing both a pH- and a temperature-dependent degradation behavior.

drain to the lymph nodes and initiate a spatially controlled maturation of antigen-presenting cells while avoiding systemic off-target immune overstimulation. Altogether, the hydrolysable polycarbonate nanogel platform (**Figure 1**) provides beneficial features to improve the pharmacokinetics of immune-stimulatory drugs and guarantees their transient delivery into antigen-presenting cells in draining lymph nodes.

2. Results and Discussion

2.1. Synthesis of mPEG-Polycarbonate Block Copolymers

5-Methyl-5-pentafluorophenyloxycarbonyl-1,3-dioxan-2-one (MTC-PFP) can be conveniently synthesized in a one-step reaction starting from 2,2-bis(hydroxymethyl)propionic acid (Bis-MPA) by cyclization of the six-membered carbonate and esterification of the carboxylate group (**Figure 2**A; Figures S1–S3, Supporting Information).[66] For subsequent polymerization of MTC-PFP, we realized that it has to be of exceptional purity to achieve high block lengths and control over the polymerization. Since residual diols or other nucleophilic impurities would act as unwanted initiators, the product was recrystallized two times from a hexane/ethyl acetate mixture yielding colorless needles. Exceptional quality was confirmed by X-ray diffraction analysis that also gained insights into the molecular conformation (Figure 2A; Figure S1, Supporting Information). From the crystallographic data, it can be seen that the methyl side group and the pentafluorophenyl ring system are in proximity which potentially contributes to the high ring-opening polymerization reactivity by steric repulsion. In-depth analysis of the monomer by 2D NMR further demonstrated the high purity of the compound (Figures S2 and S3, Supporting Information).

In view of the requirements for bioapplications, polycarbonates were generated using an organocatalyst system.[67] By these means, the use of conventional metal-based catalysts should be avoided, as such potentially toxic compounds would hamper both safe application and regulatory acceptance of the material.[68] To this end, the amphiphilic block copolymers $mPEG_{113}$-*b*-poly(MTC-PFP) were synthesized by cationic ring-opening polymerization using trifluoromethanesulfonic acid (Figure 2A). High selectivity of this organocatalyst for the ring-opening reaction over side chain reaction has already been reported by Hedrick et al. using $mPEG_{113}$-OH as macroinitiator.[63,67] However, previously only short block lengths were achieved for block copolymers.[63] We observed that these block lengths are insufficient for the self-assembly of polymeric micelles and that the respective polymers remain molecularly soluble (Figure S9, Supporting Information). Yet, to employ these polymers as a platform for polymer analogous reactions within the resulting micelle cores, the polymerization technique had to be optimized toward increasing the polycarbonate block length. Using higher dilutions of the monomer at 0.5 M combined with a low catalyst loading, thoroughly drying all starting materials by azeotropic distillation, and applying water-free conditions in a nitrogen-purged glove box, polymers of a block length of ≈32 units were

© 2022 The Authors. Advanced Functional Materials published by Wiley-VCH GmbH

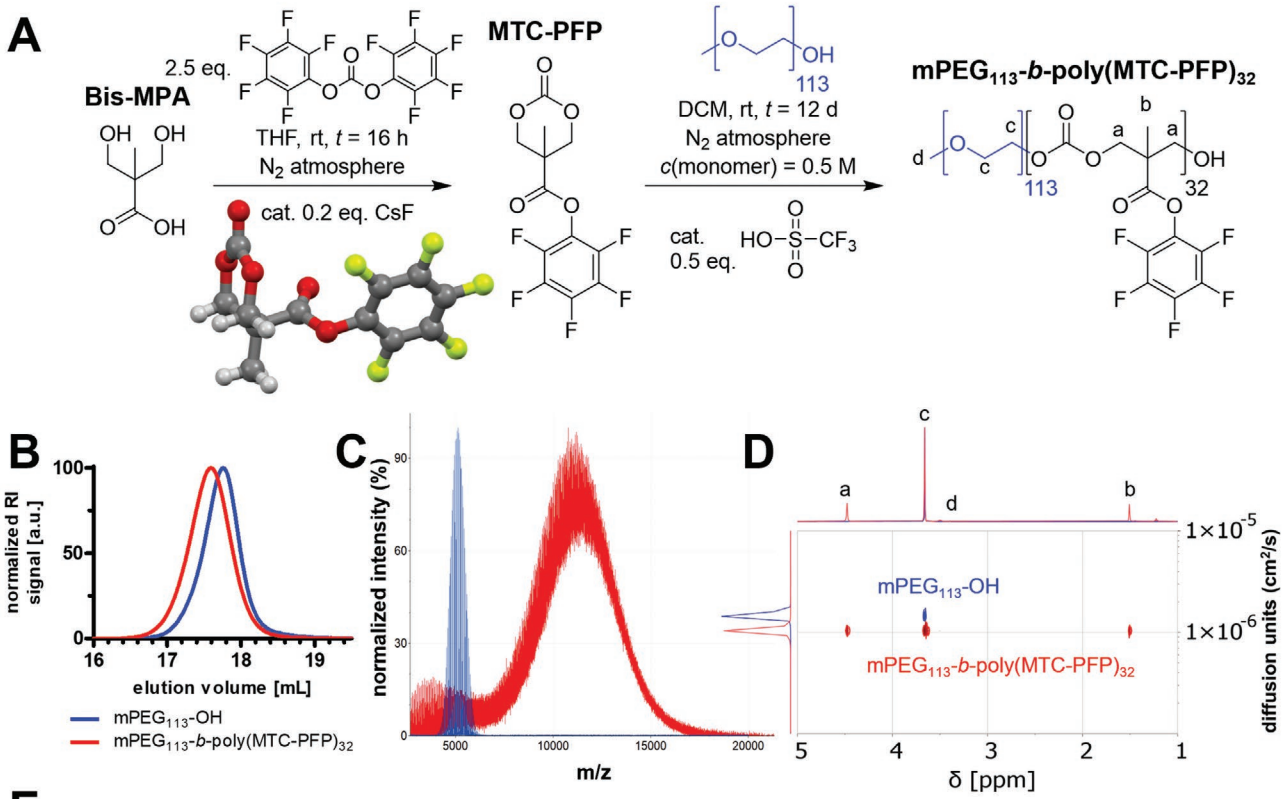

E

	χ_n^{targ}	conv. [%][a]	M_n^{theo} [g/mol][a]	M_n^{prod} [g/mol][a]	M_n^{prod} [g/mol][b]	$Đ$ [b]
$mPEG_{113}$-*b*-poly(MTC-PFP)$_{32}$	40	81.7	15700	15400	41700	1.16

Figure 2. Synthesis and characterization of polycarbonate-based reactive precursor polymers. A) Reaction scheme of monomer and block copolymer synthesis. 5-Methyl-5-pentafluorophenyloxycarbonyl-1,3-dioxan-2-one one (MTC-PFP) was yielded from the reaction of 2,2-bis(hydroxymethyl)propionic acid with bis(pentafluorophenyl)carbonate by simultaneous carbonate cyclization and side group esterification reaction. The X-ray diffraction analysis derived crystal structure of the MTC-PFP monomer is provided as well (further information can be found in Figure S1, Supporting Information). Polymerization was afterward initiated from polyethylene glycol using trifluoromethanesulfonic acid as organocatalyst. B) Size exclusion chromatography (SEC) elugram of $mPEG_{113}$-b-poly(MTC-PFP)$_{32}$ (red) and $mPEG_{113}$-OH (blue) showing successful block copolymer formation by a shift toward higher mass (lower retention time) and a monomodal distribution ($Đ = 1.16$). C) Mass spectrometric analysis of $mPEG_{113}$-OH (blue) and $mPEG_{113}$-b-poly(MTC-PFP)$_{32}$ (red). The block copolymer shifts toward higher molecular mass and contains no polycarbonate or $mPEG_{113}$-OH homopolymers. D) Diffusion Ordered Spectroscopy (DOSY) NMR of $mPEG_{113}$-OH macroinitiator (blue) and $mPEG_{113}$-b-poly(MTC-PFP)$_{32}$ block copolymer (red). For the latter, all signals appear at a larger diffusion coefficient indicating the purity of the block copolymer. E) Summary of the analytical results for $mPEG_{113}$-b-poly(MTC-PFP)$_{32}$. [a]Determined by ^{1}H NMR analysis; [b]Determined by SEC with HFIP (hexafluoroisopropanol) as eluent and calibration with PMMA standards.

yielded (Figure 2A,E; Figure S4–S8, Supporting Information). For polymer purification, the reaction mixtures were precipitated into ice-cold diethyl ether, decanted, and dried in vacuo. Successful grafting of the polycarbonate block to the polyethylene glycol macroinitiator was confirmed by size exclusion chromatography (SEC). The elugram (Figure 2B) shows a monomodal size distribution and a shift toward higher molecular mass, relative to the polyethylene glycol macroinitiator ($Đ = 1.16$). This finding was further supported by ^{1}H diffusion ordered NMR spectroscopy (^{1}H DOSY NMR) (Figure 2D) showing only one single diffusing species with polycarbonate and polyethylene glycol signals at higher diffusion units compared to the $mPEG_{113}$-OH macroinitiator. Moreover, mass spectrometry nicely demonstrated successful grafting of the carbonate block as well as the absence of homopolymers (Figure 2C—for detailed analysis compare Figures S5 and S6, Supporting Information).

2.2. Fabrication of Immunostimulatory Polycarbonate Nanogels

After successfully establishing a procedure for obtaining suitable polycarbonate block lengths, the polymers' self-assembly behavior was investigated (**Figure 3**A). Ethanol was selected as organic solvent in which PEG is fairly soluble, but the poly(MTC-PFP) block remains insoluble. Supported by ultrasonication the block copolymers were redispersed

© 2022 The Authors. Advanced Functional Materials published by Wiley-VCH GmbH

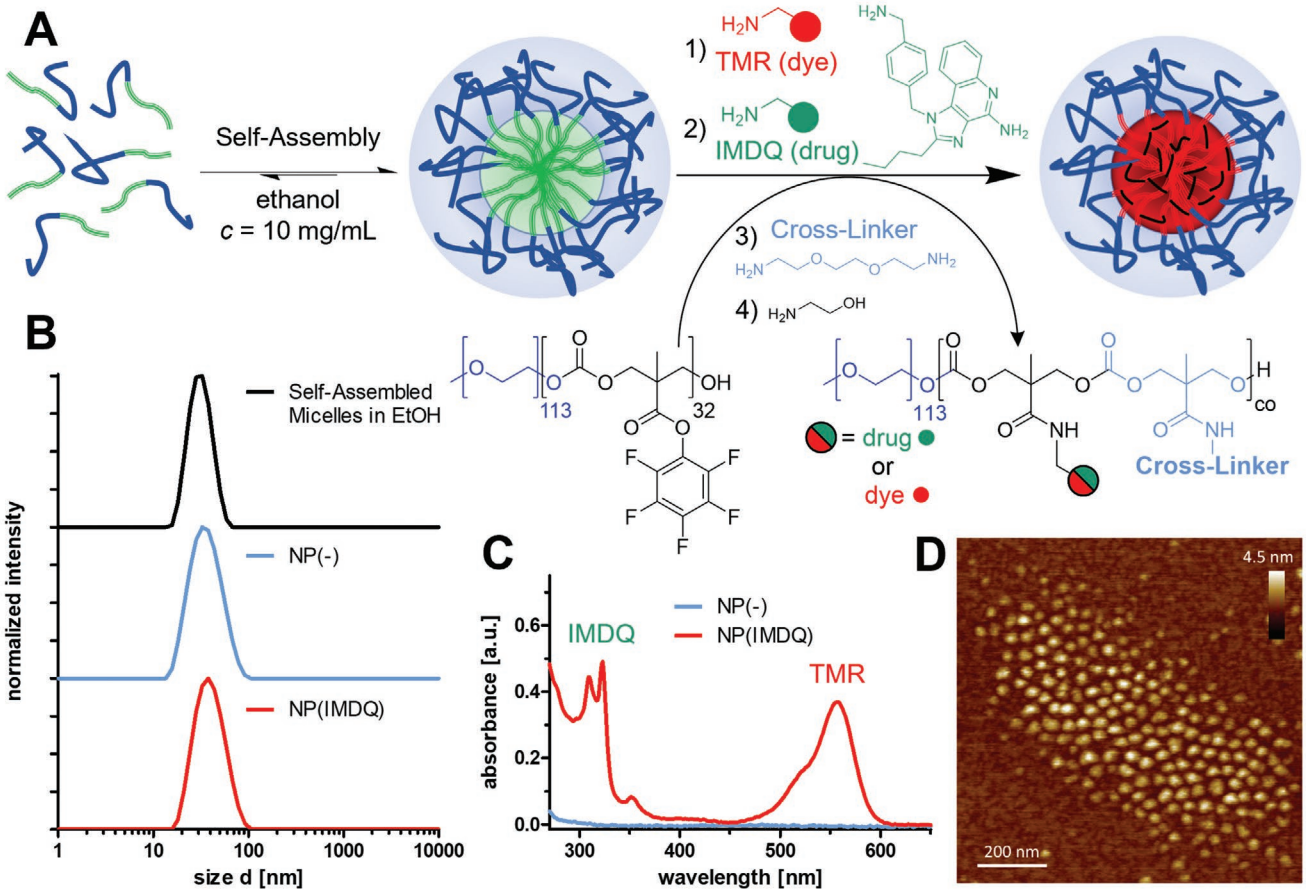

Figure 3. Fabrication of immunodrug-loaded polycarbonate nanogels. A) Reaction scheme for the synthesis of the polycarbonate nanogels. Self-assembly of $mPEG_{113}$-b-poly(MTC-PFP)$_{32}$ block copolymer could be achieved in the PEG block selective solvent ethanol supported by ultra-sonification, followed by the chemical modification of these precursor micelles into nanogels. Simultaneous core functionalization was obtained by aminolysis with amine-containing fluorescent dyes (TMR) and immune stimulatory drugs (IMDQ) prior to cross-linking with a hydrophilic bis-amine. Finally, an excess of ethanolamine was added to quench the remaining pentafluorophenyl esters. B) DLS analysis of the self-assembled precursor micelles and of the resulting core-cross-linked nanogels. Both show comparable hydrodynamic diameters (29.9, 32.4, and 36.2 nm for precursor micelles, nanogels and drug-loaded nanogels) and monomodal size distributions (PDI = 0.06, 0.06, and 0.14 for precursor micelles, nanogels and drug-loaded nanogels). C) UV–vis absorbance spectra of non-loaded (blue) versus drug- and dye-loaded nanogels (red). Covalent dye and drug conjugation results in additional absorption maxima at 550 (TMR absorption) and 321 nm (IMDQ absorption) from which the drug-load was determined (compare Figure S14, Supporting Information). D) AFM image of core-cross-linked nanogels dried on flat mica surfaces showing uniform particles with flattened heights of ≈2 nm and similar diameters of ≈33 nm (compare Figures S12 and S13, Supporting Information).

in that solution and then characterized by dynamic light scattering (DLS). When polymers with short polycarbonate block lengths were utilized, polymer chains remained in the solution and did not self-assembly into micelles (Figure S9, Supporting Information). Monodisperse micellar particles were only gained for larger poly(MTC-PFP) blocks, e.g., with $mPEG_{113}$-*b*-poly(MTC-PFP)$_{32}$ in ethanol as analyzed by DLS in Figure 3B. These polymeric micelles were then functionalized using primary amines. They can react with the activated pentafluorophenyl esters and form stabile amide bonds. By these means, cargo molecules such as fluorescent tracer molecules (e.g., tetramethyl rhodamine cadaverine (TMR)) or immunostimulatory drugs (e.g., the TLR 7/8 agonist IMDQ) were covalently attached to the polymeric chains (Figure 3A). We followed previously reported protocols for covalent cargo molecule conjugation to self-assembled pentafluorophenyl ester block copolymers,[22,23] and subsequently core-crosslinked the remaining activated esters inside the particles using the hydrophilic bisamine 1,8-diamino-3,6-dioxaoctane. Finally, to ensure that no residual perfluorinated active esters were present in the product, the thereby obtained nanogels were quenched by addition of excess ethanolamine affording fully hydrophilic cores. The reaction conversion was analyzed by ^{19}F NMR which is an ideal technique for this purpose due to low detection limit of ^{19}F and high specificity[69] (compare Figure S11, Supporting Information). Indeed, it was confirmed that these conjugation reactions proceeded to quantitative conversions even within several minutes. For particle functionalization a reaction time of 30 min was chosen to ensure complete conversion in the dense polymeric network. Subsequently, the reaction mixtures were added to 1 M hydrochloric acid to avoid an alkaline pH, which would trigger carbonate hydrolysis and

© 2022 The Authors. Advanced Functional Materials published by Wiley-VCH GmbH

loss of yield during the following dialyses steps. Side products, unreacted amines, and salts were removed by frequent exchange of water (pH 4). Afterward, the solutions were lyophilized to obtain nanogels as a voluminous powder that allowed long-term storage in the dried state.

Due to the highly hydrophilic properties, the lyophilized material could quickly be redissolved in water to provide fresh batches of nanogel solution. Notably, nanogel particles were obtained with comparable size to the initially self-assembled polymeric micelles in ethanol even after redispersion: Particle sizing by dynamic light scattering (DLS, Figure 3B) gave monodisperse particles with hydrodynamic diameters of 32.4 nm and a narrow dispersities (PDI = 0.06), while their respective precursor micelles provided sizes of 29.9 nm and PDI = 0.06 in ethanol (covalent IMDQ drug loading only marginally increased the size of the nanogels 36.2 nm at a PDI = 0.14, compare Figure S10, Supporting Information—for additional multi-angle DLS, compare Figure S20, Supporting Information). The fully converted nanogels yielded a neutral zeta-potential (Figure S12, Supporting Information), while atomic force microscopy (AFM) images of nanogels deposited on flat mica surfaces visualized their homogenous spherical shapes (Figure 3D), and thus confirmed the successful covalent cross-linking of the self-assembled block copolymers (statistical analysis of the recorded AFM images confirmed the remarkably narrow particle size distribution—compare Figures S12 and S13, Supporting Information). To precisely quantify fluorescent dye loading and—more importantly for therapeutical applications—the immunodrug loading, these covalently immobilized functional groups could be quantified by UV–vis absorbance measurements (Figure 3C). For IMDQ, a calibration curve was applied using the specific UV absorption of the drug compound ≈321 nm yielding an IMDQ-load of ≈6.5 wt.% (compare Figure S14, Supporting Information).

2.3. Behavior of Polycarbonate Nanogels at Physiological Conditions

Aliphatic polycarbonates are a class of materials that are reported to be hydrolytically degradable, however, detailed identification of the degradation products is often overlooked. Moreover, degradation kinetics providing important information on the degradation conditions and the related timescales are missing. Yet, they are relevant to apply the material for instance in vivo. Especially for fine-tuned applications like nanocarrier-guided immunotherapies, it is of major importance to not only trigger immune responses but also to terminate the activation in order to avoid severe over-activation followed by auto-immunity.[14,15] In view of drug safety regulation and translatability of polymeric drug delivery systems, long-term accumulation of the polymeric material and respective degradation products have to be avoided.[70,71]

With this in mind, we investigated the hydrolytic degradation profile of the hydrophilic nanogels (**Figure 4**A) using several complementary techniques, including dynamic light scattering (DLS), fluorescence correlation spectroscopy (FCS), NMR spectroscopy, and mass spectrometry. According to the IUPAC definition, materials are described as "hydro-degradable" if they disintegrate upon action of water.[72] Since hydrolytic degradation strongly depends on the pH, we first investigated its influence on the hydrolysis of polycarbonate nanogels. Hence, nanogels were redispersed and diluted to respective pH values followed by incubation at 37 °C for several days (Figure 4B, for respective size distributions, compare Figure S16, Supporting Information). They were measured frequently by DLS to gain information about the size and the scattering count rate (the latter can be seen as a proximation for the particle concentration). It was observed that nanogels remained exclusively stable over a period of several weeks at non-physiological acidic pH of 4.0 or 5.5 (Figure 4B1). This would allow nanogel storage at such pH values in aqueous media. In stark contrast, rapid degradation was observed in alkaline media at pH 9.0 by immediate decreasing sizes and count rates (a half-life of ≈3 h was estimated—compare Figure S17, Supporting Information). Most notably, the sample incubated in PBS of pH 7.4 at 37 °C showed also gradual particle disintegration with a scattering count rate half-life of ≈24 h (Figure 4B1—compare Figure S17, Supporting Information). This half-life time is still sufficient to ensure sample stability for a reasonable period for in vitro or in vivo applications at 37 °C. The behavior of particles to remain stable before decaying is an important feature for avoiding long-term toxicological effects as well as for timed immune stimulation. Additionally, we also observed a gradual but slower decay at physiological acidic pH values of 6.4 and 6.8 (with half-life of 66 and 30 h, respectively, Figure 4B1; Figure S17, Supporting Information) that can be found in lymph nodes[73] and tumor sites.[74,75] Thus, even at those locations a clearance of nanogels by hydrolytic disintegration can still occur. Interestingly, polycarbonate nanogels also show a temperature-dependent degradation profile as demonstrated by prolonged stability at 4 °C even after several weeks (Figure 4B2, compare Figure S18, Supporting Information for half-life times). Consequently, polycarbonate nanogel degradation does not only depend on pH but can also be controlled at physiological conditions by temperature. This further provides an ideal storage possibility in solution at 4 °C but excludes possible long-term accumulation effects upon application within a biological system at 37 °C.

Additionally, degradation was analyzed by fluorescence correlation spectroscopy (FCS), which is a method to provide size information of fluorescently labeled material (Figure 4C). Thereby, the small molecular fluorescence dye TMR, which was covalently immobilized inside the nanogels, was tracked. Its degradative release was observed over time and served as a model for the release of covalently attached drug molecules. The dye-labeled nanogels were incubated in PBS at 37 °C and the related autocorrelation functions were recorded at several time points (Figure 4C1). In the beginning, most of the dye molecules were attached to the particles providing an average hydrodynamic diameter of 32.8 nm, in analogy to the previous DLS measurements. Over time, an increasing amount of released fluorescent dye was detected (Figure 4C3), while the size of the nanogel also gradually decreased (Figure 4C2). From the release kinetics of the fluorescent dye, a half-life of ≈54 h could be determined that is in a similar regime as obtained previously (we assume that the slightly larger half-life is probably due to some dye entrapment inside the degrading nanogel—compare Figure S19, Supporting Information). Approximately after 3 days, most of the dye was released that assures sufficient time for delivery of

© 2022 The Authors. Advanced Functional Materials published by Wiley-VCH GmbH

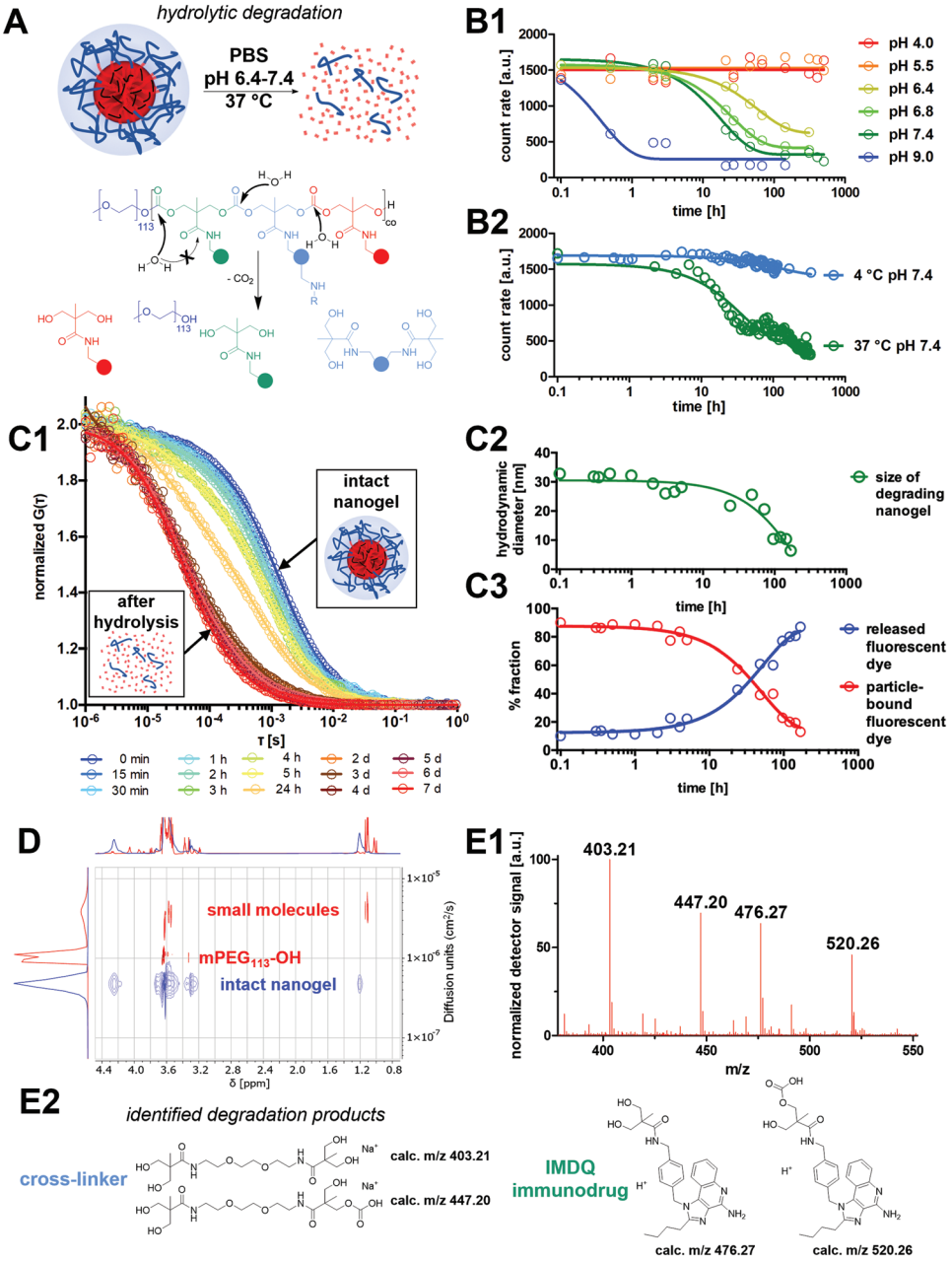

Figure 4. Gradual degradation of polycarbonate nanogels under physiological conditions. A) Hydrolytic cleavage of the polycarbonate nanogels with the expected degradation products: hydrophilic diols, carbon dioxide, and polyethylene glycol. B) pH (1) and temperature (2) dependent degradation monitored by DLS. Under degradation triggering conditions particle sizes and scattering count rates drop. C) FCS degradation kinetics of TMR-labeled nanogels in PBS (37 °C) monitored by the corresponding autocorrelation functions (1) followed by the fit-derived remaining hydrodynamic nanogel diameter (2) and the fractions (3) of particle-bound and released fluorescent dye. D) Release of small molecules and $mPEG_{113}$-OH (red) from the nanogel's network (blue) investigated by ^1H DOSY NMR measurements (PBS, pH 7.4). E1) Recorded ESI-MS spectrum after nanogel degradation. E2) Identified degradation products according to the recorded ESI-MS spectrum confirming respective diol product formation.

the carrier system during bioapplications. Degradation of polycarbonate nanogels yields small-molecular weight dye molecules, which distinguishes the polycarbonate-based systems from earlier nanogel systems where degradability was introduced by pH-degradable crosslinkers. The pH-triggered particle unfolding results in single soluble polymer chains that are still covalently equipped with the fluorescent dye or drug.[76–78] For the polycarbonate nanogels introduced in this study, hydrolytic degradation affects the polymeric backbone yielding small molecular weight hydrolysis products (that are assumed to have easier access to metabolic recovery or renal clearance). To study the hydrolysis products in more detail, we next applied NMR spectroscopy and mass spectrometry to identify the molecular structures formed during nanogel degradation.

© 2022 The Authors. Advanced Functional Materials published by Wiley-VCH GmbH

Drastic size changes and generation of small degradation products were observed in liquid ^{1}H DOSY NMR. Nanogels were diluted in deuterated water and detectable as a single slow diffusing, high molecular weight species (Figure 4D). Upon addition of PBS and incubation at 37 °C for a prolonged time, novel low molecular species were released from the high molecular nanogel (compare Figure S22, Supporting Information). Ultimately, the polymeric particles' signal shifted toward higher diffusion coefficients, and signals of the polycarbonate backbone vanished. This strongly indicates the degradation of polycarbonate backbone, which is contrasted by the stability of polyethylene glycol that was still found as polymeric species by ^{1}H DOSY NMR. In conclusion, it was shown that small molecular species were released from nanogel networks during degradation at the relevant physiological conditions. High-Resolution Magic Angle Spinning (HRMAS) ^{1}H NMR measurements were performed to get further insights into the processes that occur within the densely interlinked nanogel core (compare Figure S23, Supporting Information—note that conventional ^{1}H NMR was less reliable for quantification purposes). Upon addition of PBS and incubation at 37 °C for prolonged time, degradation of the polycarbonate backbone was observed, as can be seen by the slow decline of signals of the methyl sidechain as well as the methylene groups of the backbone. Most significantly, the amide bonds remained untouched which nicely shows the higher stability of these linkages compared to the susceptible carbonate backbone: During degradation amide signal integral remained unchanged, indicating that no reactions are taking place at the side chain (Figure S23, Supporting Information). Kinetic evaluation of the degradation process by HRMAS revealed comparable half-life degradation values to FCS and DLS in PBS (Figure S24, Supporting Information) and thus implied that indeed the molecular process of polycarbonate backbone disintegration triggers the particle disassembly.

Finally, mass spectrometry was employed to ultimately identify the small molecular degradation products, as highlighted in Figure 4A. First, electrospray ionization mass spectrometry (ESI-MS) was applied to aqueous solutions of nanogels incubated for several days at 37 °C in a 1:100 water/triethylamine solution (to ensure full degradation in the presence of volatile salts/molecules that are tolerable for ESI-MS measurements). Indeed, analysis of the recorded spectra confirmed the diolic derivates of the cross-linker (m/z = 403.21) as well as the drug compound (m/z = 476.27) as main species (Figure 4E1,E2; Figure S25, Supporting Information). Thereby, it was not only confirmed that the carbonate backbone is more susceptible than the amide side chains, but also additional side reactions that could have occurred during nanogel synthesis could be excluded (e.g., PFP hydrolysis or transesterification with ethanol, as none of the afforded by-products could be found either). In addition, matrix-assisted laser desorption/ionization (MALDI) MS spectra were recorded to analyze the molecular architecture of the residual polymeric degradation products after incubation in PBS at 37 °C for 2 weeks. While the initial precursor block copolymers provided a molecular weight of ≈15 kDa (Figure 2D), the nanogels after degradation provided again polymeric material with a mass of ≈5 kDa, which exactly matched with the mass of the initially used polyethylene glycol homopolymer (compare Figure S26, Supporting Information). Again, it could be confirmed that a full degradation of polycarbonate nanogels under physiological conditions leads to hydrophilic diols and renally clearable polyethylene glycol,[79] making it an ideal degradable carrier system for biological application. The intrinsically limited lifetime of polycarbonate nanogels at physiological conditions can prevent long-term toxicity but provides a high temporal control over immunotherapeutic stimulation.

Prior to further in vitro and in vivo investigations, we were also interested in the behavior of the intact nanogel exposed to complex biological media. Therefore, particle stability in physiological relevant protein-rich conditions was investigated by incubation in human blood plasma for 1 h at 37 °C, followed by a multi-angle light scattering analysis to test for potential polymer-protein-aggregates (Figure S21, Supporting Information). By this well-established method,[80] no significant differences of recorded and predicted autocorrelation curves were found, indicating that the nanogels with or without IMDQ do not aggregate upon protein incubation but remain stable.

2.4. In Vitro Performance of Immunostimulatory Nanogels

In-depth characterization of the covalently functionalized polycarbonate nanogels as well as their favorable transient degradation profile suggested their suitability for further developments toward biological application. Initial in vitro tests focused on the cellular toxicological profile of the polycarbonate nanogels and confirmed their high biocompatible properties. Cell viability of empty and drug-loaded nanogels NP(-) and NP(IMDQ) was not impaired across a broad range of concentrations up to >0.5 mg mL^{-1} on macrophages (Raw Blue cell line) (**Figure 5**A). Next, nanogel uptake was investigated by incubation of macrophages with fluorescent dye-labeled nanogels (compare Figure S15, Supporting Information for the nanogels' fluorescence emission properties). Flow cytometry showed a concentration-dependent particle uptake (Figure 5B as well as Figures S27 and S28, Supporting Information). Interestingly, compared to empty nanogels NP(-), the uptake of the IMDQ-loaded particles NP(IMDQ) was significantly higher (Figure 5B; Figure S28, Supporting Information). Similar results were obtained by confocal microscopy confirming the internalization, especially of the drug-loaded particles (Figure 5C; Figures S29 and S30, Supporting Information). This preferential uptake could probably be triggered by the immunostimulatory effect of the nanogels' payload.

To investigate IMDQ-mediated TLR7/8 receptor stimulation, the reporter function of macrophages (Raw Blue cell line) was applied. These cells have been genetically engineered to express alkaline phosphatase in response to NF-κB activation. Secreted alkaline phosphatase can subsequently be quantified spectrophotometrically in the cell culture supernatant by the Quanti Blue assay. By screening a broad range of concentrations, the NF-κB inducing activity of the highly potent soluble IMDQ (sIMDQ) increased from lower to higher nanomolar range when conjugated to the nanogel, while the empty nanogel induced no NF-κB activity and, thus, remained immunologically silent (Figure 5D). We also studied the degraded

© 2022 The Authors. Advanced Functional Materials published by Wiley-VCH GmbH

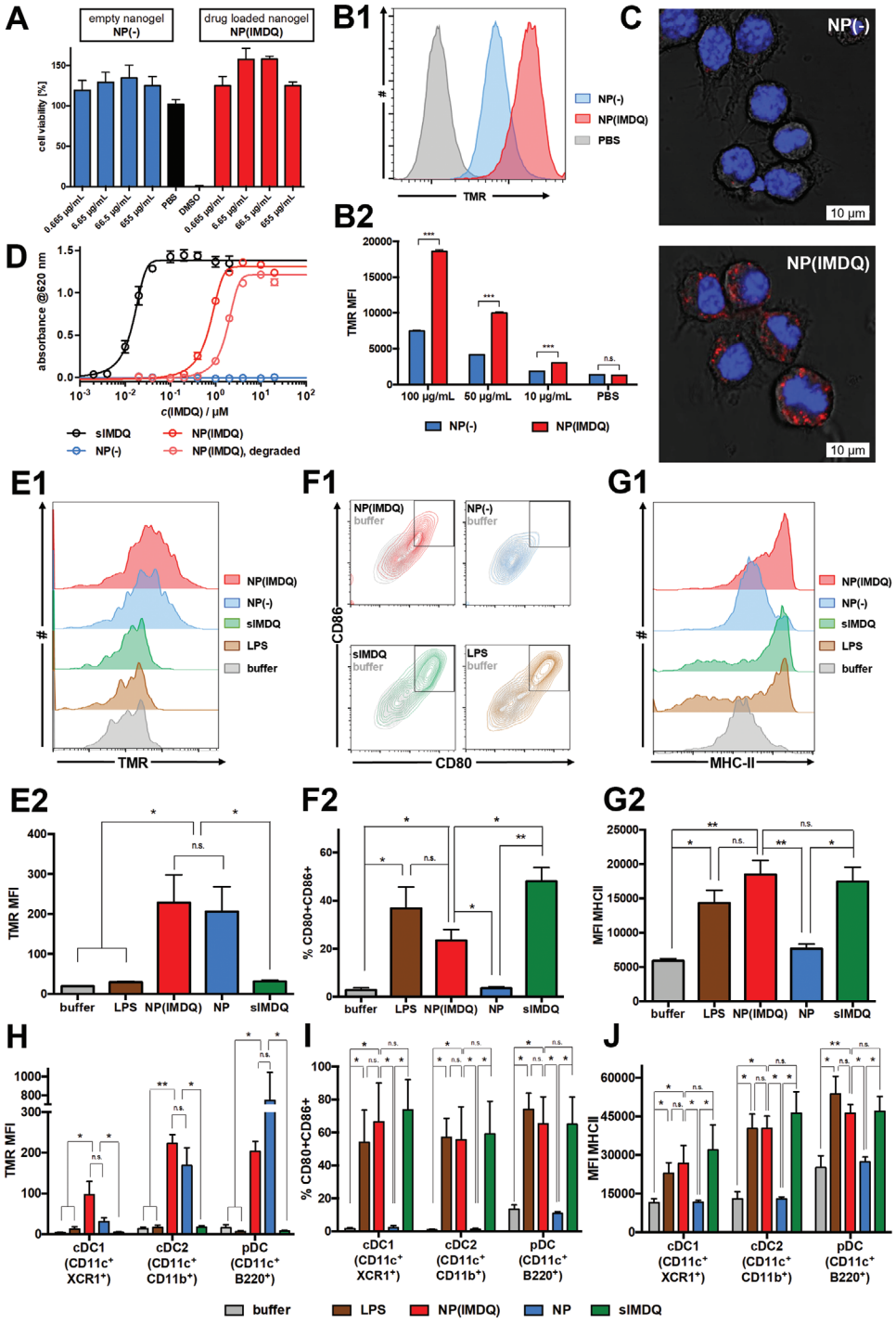

Figure 5. In vitro evaluation of immunodrug-loaded polycarbonate nanogels. A) Cell viability testing by MTT-Assay indicates high compatibility over a broad concentration range in Raw Blue Macrophages ($n = 4$). B) Cell uptake of TMR-labeled nanogels in Raw Blue macrophages quantified by flow cytometry histogram (1) or mean fluorescence intensity (MFI) (2) analysis ($n = 3$). C) Cell internalization could be confirmed by confocal microscopy of RAW Blue macrophages incubated with TMR-labeled nanogels (red) and nuclei stained with DAPI (blue). D) TLR7/8 activation of RAW Blue macrophages quantified by Quanti Blue assay of cell culture supernatant ($n = 4$). E) Cell uptake of TMR-labeled nanogels in GM-CSF derived BMDCs analyzed by flow cytometry histogram (1) or mean fluorescence intensities (MFI) (2) (n = 4). F) CD80 and CD86 expression of GM-CSF derived BMDCs analyzed by flow cytometry histogram (1) or mean fluorescence intensities (MFI) (2) ($n = 4$). G) MHCII expression of GM-CSF derived BMDCs analyzed by flow cytometry histogram (1) or mean fluorescence intensities (MFI) (2) ($n = 4$). H) Cell uptake of TMR-labeled nanogels in Flt3 ligand derived BMDC subpopulations analyzed by flow cytometry MFI ($n = 3$). I) CD80 and CD86 expression of Flt3 ligand derived BMDC subpopulations analyzed by flow cytometry MFI ($n = 3$). J) MHCII expression of Flt3 ligand derived BMDC subpopulations analyzed by flow cytometry MFI ($n = 3$; $^{*}p \leq 0.05$; $^{**}p \leq 0.01$; n.s.: not significant).

© 2022 The Authors. Advanced Functional Materials published by Wiley-VCH GmbH

NP(IMDQ) after complete nanogel hydrolysis and found a further reduced immune stimulatory activity with a shift into the micromolar regime. Similar effects have been reported by us for polynorbornene-derived nanogels covalently functionalized with IMDQ.[28] Upon pH-triggered nanogel unfolding, a reduction of the TLR7/8 receptor activation was found there, too, and thus suggested a suitable clinical safety profile for both systems: Their degradation products not only circumvent non-favorable nanoparticle accumulation in the body, but also provide less active IMDQ species. Only the intact nanogel carriers seems to support sufficient IMDQ's receptor stimulation (probably by enforced endosomal internalization), while unwanted systemic immune activation is reduced after particle disintegration.

To further evaluate the immunostimulatory profile of the intact polycarbonate nanogels loaded with IMDQ, we investigated their behavior on primary dendritic cells differentiated from murine bone marrow. Upon differentiation in the presence of GM-CSF supplemented media, inflammatory bone-marrow-derived dendritic cells (BMDCs) were obtained and incubated overnight with empty and IMDQ-loaded nanogels, as well as soluble IMDQ and the TLR4 agonist LPS as a control (Figure 5E–G). By flow cytometric analysis (Figure S31, Supporting Information), binding of both particles NP(-) and NP(IMDQ) was observed (Figure 5E). However, a difference in terms of binding or uptake between the two particle species could not be found (compared to the macrophage cell line in Figure 5B,C).

We also checked for the immunostimulatory phenotype on these BMDCs and determined the surface expression of the costimulatory molecules CD80 and CD86 as relevant markers for dendritic cell maturation (Figure 5F). While the empty nanogels NP(-) again exerted no stimulatory effect (like the buffer control), the covalently attached IMDQ inside the nanogels NP(IMDQ) triggered simultaneous upregulation of both maturation markers, as observed for sIMDQ and LPS. Likewise, the antigen presenting receptor MHCII was strongly upregulated in response to treatment with NP(IMDQ), at similar extent as evoked by sIMDQ and LPS (Figure 5G). Altogether, these observations underline the particles' immune stimulatory potential on primary immune cells.

Murine bone marrow cells can also be used to differentiate into different dendritic cell subpopulations by applying Flt3 ligand supplemented media. By this means, conventional (myeoloid) dendritic cells cDC1 ($CD11c^+$ $XCR1^+$) and cDC2 ($CD11c^+$ $CD11b^+$) as well as plasmacytoid dendritic cells pDC ($CD11c^+$ $B220^+$) are obtained (compare Figure S32, Supporting Information). cDC1 cells are considered to preferentially induce type 1 immune responses yielding cytotoxic T cells that kill infected and malignant cells.[81] cDC2 preferably induces type 2 immune responses that are directed against parasites and bacteria.[82] pDCs are renowned for their high type 1 interferon secretion and pronounced antigen presentation capacity, especially in the context of viral infections.[83,84] Similar to inflammatory BMDC induced by GM-CSF, Flt3 ligand differentiated BMDC, comprising a mixture of cDC1/2 and pDC, were again incubated for 24 h with empty and IMDQ-loaded nanogels, as well as soluble IMDQ and LPS as control and afterward analyzed by flow cytometry (Figure S32, Supporting Information). Nanogel uptake could be monitored by TMR fluorescence in those different subtypes. Again, no significant difference between NP(–) and NP(IMDQ) was observed in all dendritic cell populations, although particle uptake seemed to be slightly higher in cDC1 for IMDQ-loaded nanogels than empty nanogels, while the reverse observation could be made in pDC (Figure 5H; Figure S33, Supporting Information). We also checked the maturation status of all three dendritic cell subtypes. In agreement with our previous observations on the GM-CSF induced BMDCs, the empty nanogel NP(-) behaved immunologically silent like the buffer control, whereas the nanogel-bound IMDQ samples NP(IMDQ) triggered simultaneous upregulation of both co-stimulatory maturation markers CD80 and CD86 in cDC1, cDC2, and pDC cells (Figure 5I; Figure S33, Supporting Information). Similar levels could also be obtained for sIMDQ and LPS. Moreover, in all three dendritic cell subtypes, the expression of MHCII was also further stimulated for differentially stimulated samples, including the treatment with NP(IMDQ) (Figure 5J; Figure S33, Supporting Information). These findings underline the pronounced nanogels' potential to retain the drugs' immune-stimulatory performance on various immune cells when covalently attached to the hydrolysable nanogel carrier.

2.5. In Vivo Performance of Immunostimulatory Nanogels for Lymph Node-Targeted Delivery

Following these promising in vitro results on cultured cell lines and primary immune cells, we were interested in the nanogels' in vivo applicability. In previous reports, we could demonstrate that various types of macromolecular carriers can spatiotemporally control the delivery of covalently attached IMDQ while omitting the drug's systemic inflammatory off-target effects.[22,26,85–89] Giving the fact that the empty nanogel NP(–) remained immunologically silent during the in vitro experiments, we therefore administered the IMDQ-nanogel NP(IMDQ) versus the soluble drug sIMDQ subcutaneously into the footpad of mice. We aimed for a focused delivery of the nanogels to the draining lymph nodes followed by a local activation of lymph node residing and infiltrating immune cells while excluding a systemic activation of immune system. A visualization of the immune cell activation can be performed in IFN-β luciferase reporter (IFN-$\beta^{+/\Delta\beta\text{-luc}}$) mice that provide local bioluminescence upon stimulation of IFN-β secretion.

We monitored the bioluminescence for 48 h (**Figure 6**A; Figure S34, Supporting Information) and indeed observed a local activation upon NP(IMDQ) footpad injection in the draining popliteal lymph node while injection of the soluble drug sIMDQ led to distribution all over the body and caused severe systemic inflammations that prolonged for 24 h and then gradually decreased after 48 h. For the nanogels, however, beyond some luciferase liver background signal that was also found before injection ($t = 0$ h) (Figure 6A) or in the buffer control (Figure S34, Supporting Information), a pronounced signal was found only in the local lymph node, especially at 4 h. It also gradually decayed over time, which goes along well with hydrolytic degradation profile of the hydrolysable polycarbonate nanogels (compare Figure 4) affording less immunostimulatory by-products (compare Figure 5D).

© 2022 The Authors. Advanced Functional Materials published by Wiley-VCH GmbH

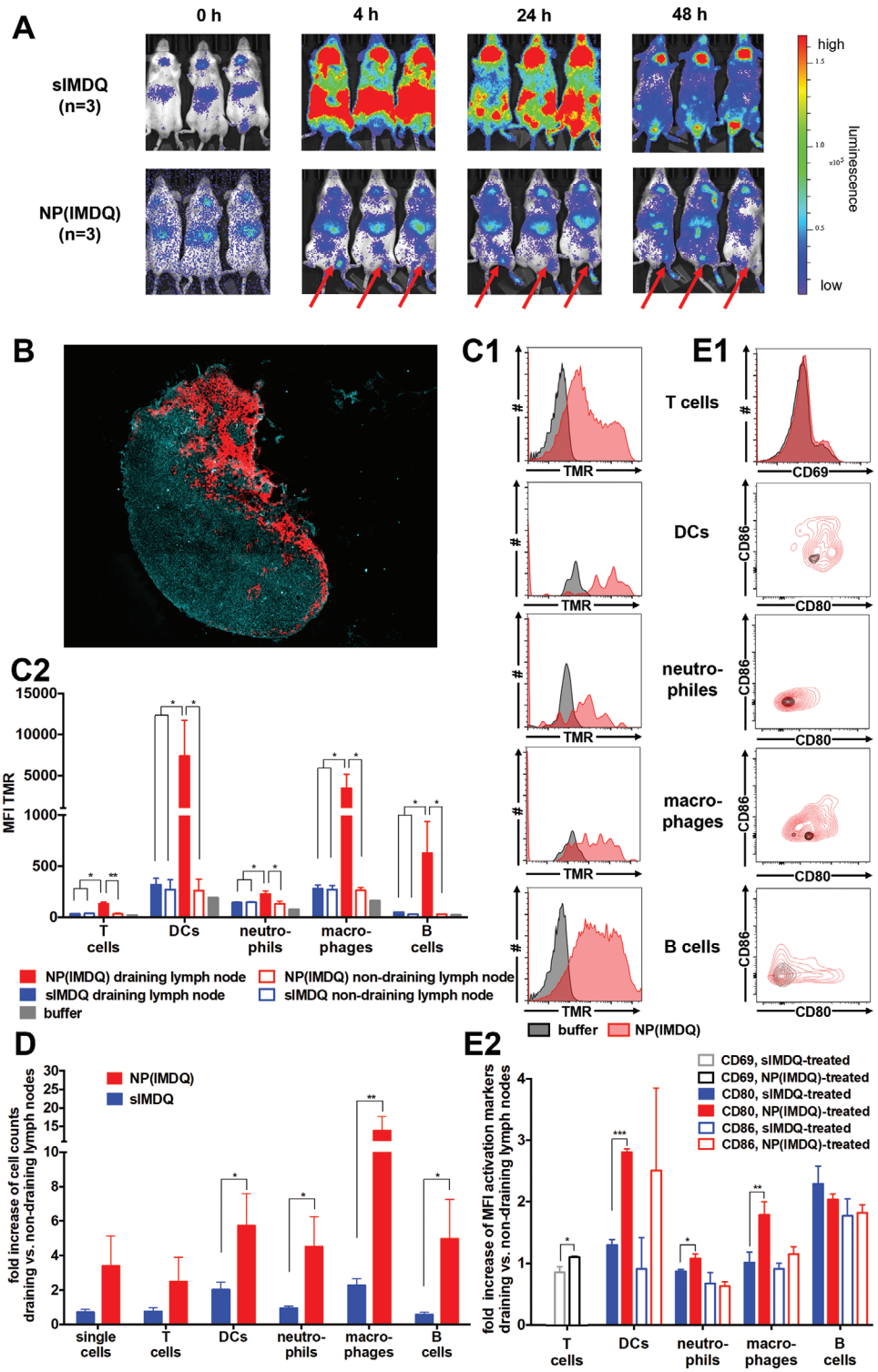

Figure 6. NP(IMDQ)-mediated local activation of draining lymph nodes by subcutaneous footpad injection. A) Visualization of immune activation in IFN-β luciferase reporter (IFN-$\beta^{+/\Delta\beta\text{-luc}}$) mice. In contrast to the small molecule sIMDQ, the immunodrug-loaded nanogels NP(IMDQ) provides a lymph node-focused immune cell activation ($n = 3$). B) Confocal imaging of a draining lymph node tissue section with nanogels (red) arriving in the subcapsular sinus and then spreading over to the medulla. C) Flow cytometric analysis of TMR-labeled NP(IMDQ) uptake in different types of immune cells residing in draining and non-draining lymph nodes, as analyzed by flow cytometry histogram (1) or mean fluorescence intensities (MFI) (2) ($n = 3$). D) Increase of cells of draining versus non-draining lymph nodes by flow cytometric cell count analysis ($n = 3$). E) Additional flow cytometric analysis of maturation marker expression (CD80 and CD86, or CD69 for T cells, respectively) determined by flow cytometry histogram (1) or by mean MFI fold increase (2) of immune cells for draining versus non-draining lymph nodes ($n = 3$; ($^{*}p \leq 0.05$; $^{**}p \leq 0.01$; $^{***}p \leq 0.001$; n.s.: not significant).

© 2022 The Authors. Advanced Functional Materials published by Wiley-VCH GmbH

Both popliteal lymph nodes, the one drained by the lymph of injection site (draining lymph node), as well as the one of the opposite leg (as non-draining lymph node), were isolated and analyzed for nanogel uptake as well as for stimulation of the residing immune cells. Tissue sections were imaged by confocal microscopy and revealed an accumulation of the TMR-labeled nanogels only in the draining lymph node. The particles seemed to have arrived from the subcapsular sinus and then spread over the medulla (Figure 6B) in analogy to previously reported macromolecular carrier systems.[22,87,88,90]

Additionally, single cell suspensions were prepared from the isolated lymph nodes and analyzed by flow cytometry to identify various types of immune cells (compare Figure S35, Supporting Information). Looking at the TMR-derived fluorescence in each immune cell population, an uptake of dye-labeled nanogels NP(IMDQ) could only be found in the draining and not in the non-draining popliteal lymph node. For the draining lymph node, all immune cells (T cells, dendritic cells (DCs), neutrophiles, macrophages, and B cells) provided TMR-derived fluorescence (Figure 6C; Figure S36, Supporting Information). Interestingly, the internalization in B cells as well as macrophages and especially dendritic cells, which are considered to be most effective for antigen presentation, was most pronounced (Figure 6C2).

We then also looked at the immune stimulatory behavior of the delivered TLR7/8 agonist and first compared the number of cells per lymph node for NP(IMDQ) and sIMDQ treated mice (to each lymph node single cell suspension a defined number of beads was added and referenced during flow cytometry—compare Figure S37, Supporting Information). As the massive systemic immune activation caused an alteration of immune cells for sIMDQ in both lymph nodes (compare Figure S37, Supporting Information), we therefore examined the increase of immune cells for the draining compared with the non-draining lymph node, and we observed that the nanogel locally elevated the number of all immune cells, most significantly the number of neutrophiles, B cells, dendritic cells and especially macrophages (Figure 6D). The latter could probably increase due to an additional infiltration of circulating monocytes from the bloodstream that recognize the exclusive stimulation of the draining lymph node by the nanogel-delivered TLR7/8 agonist.

We next checked for the costimulatory maturation surface markers CD80 and CD86 on these immune cell populations (and CD69 as maturation marker on T cells, respectively). In all cases, their expression levels were increased when sIMDQ or NP(IMDQ) was administered compared to the buffer control (Figure 6E1; Figure S38, Supporting Information). However, only for the NP(IMDQ) sample a difference between draining compared to non-draining lymph node was found. We therefore compared again the increase in maturation markers for the draining versus the nondraining lymph node and confirmed once more that only the IMDQ-loaded nanogel locally maturates these immune cells, most significantly neutrophils, macrophages, and especially dendritic cells (Figure 6E2). These observations reiterate that the biodegradable polycarbonate nanogels deliver the TLR7/8 agonist to the draining lymph node and provide a locally well-defined activation of immune cells while omitting systemic inflammatory off-target effects. Such properties are ideal for instance for vaccination or cancer immunotherapeutic purposes, as demonstrated before for similar but less degradable nanogel carriers.[23,81] All in vivo experiments had been approved by the Ethical Committee of the Faculty of Veterinary Medicine and the Faculty of Bioscience Engineering of Ghent University (No. EC2018/92).

3. Conclusion

In conclusion, we reported on a degradable polycarbonate-based nanogel platform that allows the covalent attachment of highly potent TLR7/8 immunodrugs for transient immune activation. For this purpose, we expanded the concept of using reactive precursor block copolymers for the synthesis of core-crosslinked nanogels to hydrolysable polycarbonate-based polymers. Notably, evaluation of polycarbonate nanogel's degradation behavior by various methods revealed a gradual disintegration within several days at physiological conditions (PBS, pH 6.4–7.4, 37 °C). Moreover, the nanogels' disintegration strongly depends on pH and temperature and they are therefore equipped with an intrinsically limited lifetime once they are applied in biological systems. The desired interplay of the chemical structure and biological outcome was validated by the high tolerability of the degraded material and a decreased immune activation upon degradation. The conjugated imidazoquinoline-based TLR7/8 agonists IMDQ retained their bioactivity in vitro on primary immune cells as well as in vivo. For the latter, a spatiotemporal control of immune cell activation only in the draining lymph node after subcutaneous injection could be verified. Altogether, these features make polycarbonate nanogels a promising carrier system for transient lymph node immune activation applications and, thus, also highly attractive for further development toward vaccination or cancer immunotherapeutic purposes. Due to their intrinsic biodegradability while still providing high chemical control during the fabrication process, these carriers might be highly relevant for improved clinical translational perspectives.

Supporting Information

Supporting Information is available from the Wiley Online Library or from the author.

Acknowledgements

The authors thank Dieter Schollmeyer for X-ray diffraction analysis, Jutta Schnee and Stephan Türk for MALDI measurements, Christine Rosenauer for multi-angle DLS measurements, and Manfred Wagner for NMR measurements. Moreover, the authors kindly acknowledge financial support by the DFG through the Emmy Noether program (to L.N.) as well as the SFB 1066 projects B03, B04, Q02 and Q04 (to L.N., S.G., H.S., M.B., and K.K.). C.C. and L.N. would also like to thank Tanja Weil for providing access to excellent laboratory facilities.

Open access funding enabled and organized by Projekt DEAL.

Conflict of Interest

The authors declare no conflict of interest.

© 2022 The Authors. Advanced Functional Materials published by Wiley-VCH GmbH

Data Availability Statement

The data that support the findings of this study are available in the supplementary material of this article.

Keywords

biodegradable, immunodrug delivery, lymph nodes, nanogels, polycarbonates

Received: March 27, 2022
Revised: June 2, 2022
Published online:

[1] T. Ye, Z. Zhong, A. García-Sastre, M. Schotsaert, B. G. De Geest, *Angew. Chem., Int. Ed.* **2020**, *59*, 18885.
[2] U. Sahin, Ö. Türeci, *Science* **2018**, *359*, 1355.
[3] S. Gallucci, M. Lolkema, P. Matzinger, *Nat. Med. (N. Y., NY, U. S.)* **1999**, *5*, 1249.
[4] K. Palucka, J. Banchereau, *Nat. Rev. Cancer* **2012**, *12*, 265.
[5] T. A. Yap, E. E. Parkes, W. Peng, J. T. Moyers, M. A. Curran, H. A. Tawbi, *Cancer Discovery* **2021**, *11*, 1368.
[6] H. Cabral, H. Kinoh, K. Kataoka, *Acc. Chem. Res.* **2020**, *53*, 2765.
[7] A. Marabelle, L. Tselikas, T. de Baere, R. Houot, *Ann. Oncol.* **2017**, *28*, xii33.
[8] S. Champiat, L. Tselikas, S. Farhane, T. Raoult, M. Texier, E. Lanoy, C. Massard, C. Robert, S. Ammari, T. de Baere, A. Marabelle, *Clin. Cancer Res.* **2021**, *27*, 665.
[9] G. M. Lynn, R. Laga, P. A. Darrah, A. S. Ishizuka, A. J. Balaci, A. E. Dulcey, M. Pechar, R. Pola, M. Y. Gerner, A. Yamamoto, C. R. Buechler, K. M. Quinn, M. G. Smelkinson, O. Vanek, R. Cawood, T. Hills, O. Vasalatiy, K. Kastenmüller, J. R. Francica, L. Stutts, J. K. Tom, K. A. Ryu, A. P. Esser-Kahn, T. Etrych, K. D. Fisher, L. W. Seymour, R. A. Seder, *Nat. Biotechnol.* **2015**, *33*, 1201.
[10] M. C. Hanson, M. P. Crespo, W. Abraham, K. D. Moynihan, G. L. Szeto, S. H. Chen, M. B. Melo, S. Mueller, D. J. Irvine, *J. Clin. Invest.* **2015**, *125*, 2532.
[11] M. Saeed, J. Gao, Y. Shi, T. Lammers, H. Yu, *Theranostics* **2019**, *9*, 7981.
[12] X. Zhu, F. Nishimura, K. Sasaki, M. Fujita, J. E. Dusak, J. Eguchi, W. Fellows-Mayle, W. J. Storkus, P. R. Walker, A. M. Salazar, H. Okada, *J. Transl. Med.* **2007**, *5*, 10.
[13] L. Hammerich, T. U. Marron, R. Upadhyay, J. Svensson-Arvelund, M. Dhainaut, S. Hussein, Y. Zhan, D. Ostrowski, M. Yellin, H. Marsh, A. M. Salazar, A. H. Rahman, B. D. Brown, M. Merad, J. D. Brody, *Nat. Med.* **2019**, *25*, 814.
[14] G. Frega, Q. Wu, J. L.e Naour, E. Vacchelli, L. Galluzzi, G. Kroemer, O. Kepp, *Oncoimmunology* **2020**, *9*, 1796002.
[15] L. I. Harrison, C. Astry, S. Kumar, C. Yunis, *J. Clin. Pharmacol.* **2007**, *47*, 962.
[16] P. Savage, V. Horton, J. Moore, M. Owens, P. Witt, M. E. Gore, *Br. J. Cancer* **1996**, *74*, 1482.
[17] P. J. Pockros, D. Guyader, H. Patton, M. J. Tong, T. Wright, J. G. McHutchison, T. C. Meng, *J. Hepatol.* **2007**, *47*, 174.
[18] S. Hamm, S. Rath, S. Michel, R. Baumgartner, *J. Immunotoxicol.* **2009**, *6*, 257.
[19] R. Ella, S. Reddy, W. Blackwelder, V. Potdar, P. Yadav, V. Sarangi, V. K. Aileni, S. Kanungo, S. Rai, P. Reddy, S. Verma, C. Singh, S. Redkar, S. Mohapatra, A. Pandey, P. Ranganadin, R. Gumashta, M. Multani, S. Mohammad, P. Bhatt, L. Kumari, G. Sapkal, N. Gupta, P. Abraham, S. Panda, S. Prasad, B. Bhargava, K. Ella, K. M. Vadrevu, P. Aggarwal, et al, *Lancet* **2021**, *398*, 2173.
[20] R. Ella, K. M. Vadrevu, H. Jogdand, S. Prasad, S. Reddy, V. Sarangi, B. Ganneru, G. Sapkal, P. Yadav, P. Abraham, S. Panda, N. Gupta, P. Reddy, S. Verma, S. Kumar Rai, C. Singh, S. V. Redkar, C. S. Gillurkar, J. S. Kushwaha, S. Mohapatra, V. Rao, R. Guleria, K. Ella, B. Bhargava, *Lancet Infect. Dis.* **2021**, *21*, 637.
[21] R. Ella, S. Reddy, H. Jogdand, V. Sarangi, B. Ganneru, S. Prasad, D. Das, D. Raju, U. Praturi, G. Sapkal, P. Yadav, P. Reddy, S. Verma, C. Singh, S. V. Redkar, C. S. Gillurkar, J. S. Kushwaha, S. Mohapatra, A. Bhate, S. Rai, S. Panda, P. Abraham, N. Gupta, K. Ella, B. Bhargava, K. M. Vadrevu, *Lancet Infect. Dis.* **2021**, *21*, 950.
[22] L. Nuhn, N. Vanparijs, A. De Beuckelaer, L. Lybaert, G. Verstraete, K. Deswarte, S. Lienenklaus, N. M. Shukla, A. C. D. Salyer, B. N. Lambrecht, J. Grooten, S. A. David, S. De Koker, B. G. De Geest, *Proc. Natl. Acad. Sci. USA* **2016**, *113*, 8098.
[23] L. Nuhn, S. De Koker, S. Van Lint, Z. Zhong, J. P. Catani, F. Combes, K. Deswarte, Y. Li, B. N. Lambrecht, S. Lienenklaus, N. N. Sanders, S. A. David, J. Tavernier, B. G. De Geest, *Adv. Mater.* **2018**, *30*, 1803397.
[24] A. Schudel, D. M. Francis, S. N. Thomas, *Nat. Rev. Mater.* **2019**, *4*, 415.
[25] H. Cabral, J. Makino, Y. Matsumoto, P. Mi, H. Wu, T. Nomoto, K. Toh, N. Yamada, Y. Higuchi, S. Konishi, M. R. Kano, H. Nishihara, Y. Miura, N. Nishiyama, K. Kataoka, *ACS Nano* **2015**, *9*, 4957.
[26] A. Huppertsberg, L. Kaps, Z. Zhong, S. Schmitt, J. Stickdorn, K. Deswarte, F. Combes, C. Czysch, J. De Vrieze, S. Kasmi, N. Choteschovsky, A. Klefenz, C. Medina-Montano, P. Winterwerber, C. Chen, M. Bros, S. Lienenklaus, N. N. Sanders, K. Koynov, D. Schuppan, B. N. Lambrecht, S. A. David, B. G. De Geest, L. Nuhn, *J. Am. Chem. Soc.* **2021**, *143*, 9872.
[27] Y. Chen, S. De Koker, B. G. De Geest, *Acc. Chem. Res.* **2020**, *53*, 2055.
[28] J. Kockelmann, J. Stickdorn, S. Kasmi, J. De Vrieze, M. Pieszka, D. Y. W. Ng, S. A. David, B. G. De Geest, L. Nuhn, *Biomacromolecules* **2020**, *21*, 2246.
[29] R. Duncan, R. Gaspar, *Mol. Pharmaceutics* **2011**, *8*, 2101.
[30] Q. Jin, Y. Deng, X. Chen, J. Ji, *ACS Nano* **2019**, *13*, 954.
[31] P. Schattling, F. D. Jochum, P. Theato, *Polym. Chem.* **2014**, *5*, 25.
[32] M. Wei, Y. Gao, X. Li, M. J. Serpe, *Polym. Chem.* **2017**, *8*, 127.
[33] S. Wilhelm, A. J. Tavares, Q. Dai, S. Ohta, J. Audet, H. F. Dvorak, W. C. W. Chan, *Nat. Rev. Mater.* **2016**, *1*, 16014.
[34] T. Lammers, F. Kiessling, M. Ashford, W. Hennink, D. Crommelin, G. Strom, *Nat. Rev. Mater.* **2016**, *1*, 16069.
[35] S. C. Baetke, T. Lammers, F. Kiessling, *Br. J. Radiol.* **2015**, *88*, 20150207.
[36] B. Amsden, *Macromol. Biosci.* **2021**, *21*, 210085.
[37] Y. Lu, A. A. Aimetti, R. Langer, Z. Gu, *Nat. Rev. Mater.* **2017**, *2*, 16075.
[38] P. Mainil-Varlet, R. Curtis, S. Gogolewski, *J. Biomed. Mater. Res.* **1997**, *36*, 360.
[39] F. Chen, R. Qi, L. D. Huyer, B. G. Amsden, *Polym. Degrad. Stab.* **2018**, *158*, 83.
[40] G. Becker, F. R. Wurm, *Chem. Soc. Rev.* **2018**, *47*, 7739.
[41] J. H. Jung, M. Ree, H. Kim, *Catal. Today* **2006**, *115*, 283.
[42] S. J. Yoon, S. H. Kim, H. J. Ha, Y. K. Ko, J. W. So, M. S. Kim, Y. Il Yang, G. Khang, J. M. Rhee, H. B. Lee, *Tissue Eng., Part A* **2008**, *14*, 539.
[43] E. Lih, C. H. Kum, W. Park, S. Y. Chun, Y. Cho, Y. K. Joung, K.-S. Park, Y. J. Hong, D. J. Ahn, B.-S. Kim, T. G. Kwon, M. H. Jeong, J. A. Hubbell, D. K. Han, *ACS Nano* **2018**, *12*, 6917.
[44] K. Fu, D. W. Pack, A. M. Klibanov, R. Langer, *Pharm. Res.* **2000**, *17*, 100.
[45] S. Tempelaar, L. Mespouille, O. Coulembier, P. Dubois, A. P. Dove, *Chem. Soc. Rev.* **2013**, *42*, 1312.

© 2022 The Authors. Advanced Functional Materials published by Wiley-VCH GmbH

[46] Z. Zhang, R. Kuijer, S. K. Bulstra, D. W. Grijpma, J. Feijen, *Biomaterials* **2006**, *27*, 1741.
[47] M. Acemoglu, *Int. J. Pharm.* **2004**, *277*, 133.
[48] J. Xu, E. Feng, J. Song, *J. Appl. Polym. Sci.* **2014**, *131*, 39822.
[49] S. Mohajeri, F. Chen, M. de Prinse, T. Phung, J. Burke-Kleinman, D. H. Maurice, B. G. Amsden, *Mol. Pharmaceutics* **2020**, *17*, 1363.
[50] X.-L. Wang, R.-X. Zhuo, L.-J. Liu, F. He, G. Liu, *J. Polym. Sci., Part A: Polym. Chem.* **2002**, *40*, 70.
[51] J. Liu, W. Liu, I. Weitzhandler, J. Bhattacharyya, X. Li, J. Wang, Y. Qi, S. Bhattacharjee, A. Chilkoti, *Angew. Chem., Int. Ed.* **2015**, *54*, 1002.
[52] C. Czysch, C. Medina-Montano, N.-J. K. Dal, T. Dinh, X. Li, Y. Fröder, P. Winterwerber, K. Maxeiner, H.-J. Räder, D. Schuppan, H. Schild, M. Bros, B. Biersack, F. Feranoli, S. Grabbe, L. Nuhn, *Macromol. Rapid. Commun.* **2022**, *43*, 2200095.
[53] H. Ajiro, Y. Takahashi, M. Akashi, *Macromolecules* **2012**, *45*, 2668.
[54] H.-F. Wang, X.-H. Luo, C.-W. Liu, J. Feng, X.-Z. Zhang, R.-X. Zhuo, *Acta Biomater.* **2012**, *8*, 589.
[55] X. Wang, J. Wilhelm, W. Li, S. Li, Z. Wang, G. Huang, J. Wang, H. Tang, S. Khorsandi, Z. Sun, B. Evers, J. Gao, *Nat. Commun.* **2020**, *11*, 5828.
[56] S. Cho, G. S. Heo, S. Khan, A. M. Gonzalez, M. Elsabahy, K. L. Wooley, *Macromolecules* **2015**, *48*, 8797.
[57] A. C. Engler, X. Ke, S. Gao, J. M. W. Chan, D. J. Coady, R. J. Ono, R. Lubbers, A. Nelson, Y. Y. Yang, J. L. Hedrick, *Macromolecules* **2015**, *48*, 1673.
[58] J. Kockelmann, J. Stickdorn, S. Kasmi, J. De Vrieze, M. Pieszka, D. Y. W. Ng, S. A. David, B. G. De Geest, L. Nuhn, *Biomacromolecules* **2020**, *21*, 2246.
[59] M. Talelli, M. Barz, C. J. F. Rijcken, F. Kiessling, W. E. Hennink, T. Lammers, *Nano Today* **2015**, *10*, 93.
[60] A. E. Ekkelenkamp, M. R. Elzes, J. F. J. Engbersen, J. M. J. Paulusse, *J. Mater. Chem. B* **2018**, *6*, 210.
[61] J. K. Oh, R. Drumright, D. J. Siegwart, K. Matyjaszewski, *Prog. Polym. Sci.* **2008**, *33*, 448.
[62] D. P. Sanders, D. J. Coady, M. Yasumoto, M. Fujiwara, H. Sardon, J. L. Hedrick, *Polym. Chem.* **2014**, *5*, 327.
[63] A. C. Engler, J. M. W. Chan, D. J. Coady, J. M. O'Brien, H. Sardon, A. Nelson, D. P. Sanders, Y. Y. Yang, J. L. Hedrick, *Macromolecules* **2013**, *46*, 1283.
[64] M. Eberhardt, R. Mruk, R. Zentel, P. Théato, *Eur. Polym. J.* **2005**, *41*, 1569.
[65] A. Das, P. Theato, *Chem. Rev.* **2016**, *116*, 1434.
[66] D. P. Sanders, K. Fukushima, D. J. Coady, A. Nelson, M. Fujiwara, M. Yasumoto, J. L. Hedrick, *J. Am. Chem. Soc.* **2010**, *132*, 14724.
[67] D. J. Coady, H. W. Horn, G. O. Jones, H. Sardon, A. C. Engler, R. M. Waymouth, J. E. Rice, Y. Y. Yang, J. L. Hedrick, *ACS Macro Lett.* **2013**, *2*, 306.
[68] L. Mespouille, O. Coulembier, M. Kawalec, A. P. Dove, P. Dubois, *Prog. Polym. Sci.* **2014**, *39*, 1144.
[69] P. W. A. Howe, *Prog. Nucl. Magn. Reson. Spectrosc.* **2020**, *118–119*, 1.
[70] A. M. Nyström, B. Fadeel, *J. Controlled Release* **2012**, *161*, 403.
[71] J. Paradise, *AMA J. Ethics* **2019**, *21*, 347.
[72] M. Vert, Y. Doi, K.-H. Hellwich, M. Hess, P. Hodge, P. Kubisa, M. Rinaudo, F. Schué, *Pure Appl. Chem.* **2012**, *84*, 377.
[73] H. Wu, V. Estrella, M. Beatty, D. Abrahams, A. El-Kenawi, S. Russell, A. Ibrahim-Hashim, D. L. Longo, Y. K. Reshetnyak, A. Moshnikova, O. A. Andreev, K. Luddy, M. Damaghi, K. Kodumudi, S. R. Pillai, P. Enriquez-Navas, S. Pilon-Thomas, P. Swietach, R. J. Gillies, *Nat. Commun.* **2020**, *11*, 4113.
[74] E. Boedtkjer, S. F. Pedersen, *Annu. Rev. Physiol.* **2020**, *82*, 103.
[75] C.-H. Chang, J. Qiu, D. O'Sullivan, M. D. Buck, T. Noguchi, J. D. Curtis, Q. Chen, M. Gindin, M. M. Gubin, G. J. W. van der Windt, E. Tonc, R. D. Schreiber, E. J. Pearce, E. L. Pearce, *Cell* **2015**, *162*, 1229.
[76] L. Nuhn, S. Van Herck, A. Best, K. Deswarte, M. Kokkinopoulou, I. Lieberwirth, K. Koynov, B. N. Lambrecht, B. G. De Geest, *Angew. Chem., Int. Ed.* **2018**, *57*, 10760.
[77] N. Leber, L. Kaps, M. Aslam, J. Schupp, A. Brose, D. Schäffel, K. Fischer, M. Diken, D. Strand, K. Koynov, A. Tuettenberg, L. Nuhn, R. Zentel, D. Schuppan, *J. Controlled Release* **2017**, *248*, 10.
[78] L. Nuhn, L. Braun, I. Overhoff, A. Kelsch, D. Schaeffel, K. Koynov, R. Zentel, *Macromol. Rapid Commun.* **2014**, *35*, 2057.
[79] A. Baumann, D. Tuerck, S. Prabhu, L. Dickmann, J. Sims, *Drug Discov. Today* **2014**, *19*, 1623.
[80] K. Rausch, A. Reuter, K. Fischer, M. Schmidt, *Biomacromolecules* **2010**, *11*, 2836.
[81] L. Nuhn, L. Van Hoecke, K. Deswarte, B. Schepens, Y. Li, B. N. Lambrecht, S. De Koker, S. A. David, X. Saelens, B. G. De Geest, *Biomaterials* **2018**, *178*, 643.
[82] V. Durai, K. M. Murphy, *Immunity* **2016**, *45*, 719.
[83] S. Wirtz, C. Becker, M. C. Fantini, E. E. Nieuwenhuis, I. Tubbe, P. R. Galle, H.-J. Schild, M. Birkenbach, R. S. Blumberg, M. F. Neurath, *J. Immunol.* **2005**, *174*, 2814.
[84] F. Fallarino, C. Orabona, C. Vacca, R. Bianchi, S. Gizzi, C. Asselin-Paturel, M. C. Fioretti, G. Trinchieri, U. Grohmann, P. Puccetti, *Int. Immunol.* **2005**, *17*, 1429.
[85] S. Jangra, J. De Vrieze, A. Choi, R. Rathnasinghe, G. Laghlali, A. Uvyn, S. Van Herck, L. Nuhn, K. Deswarte, Z. Zhong, N. N. Sanders, S. Lienenklaus, S. A. David, S. Strohmeier, F. Amanat, F. Krammer, H. Hammad, B. N. Lambrecht, L. Coughlan, A. García-Sastre, B. G. De Geest, M. Schotsaert, *Angew. Chem., Int. Ed. Engl.* **2021**, *60*, 9467.
[86] H. Li, S. Van Herck, Y. Liu, Y. Hao, X. Ding, L. Nuhn, Z. Zhong, F. Combes, N. N. Sanders, S. Lienenklaus, S. D. Koker, S. A. David, Y. Wang, B. G. De Geest, Z. Zhang, *ACS Biomater. Sci. Eng.* **2020**, *6*, 4993.
[87] S. Van Herck, K. Deswarte, L. Nuhn, Z. Zhong, J. P. Portela Catani, Y. Li, N. N. Sanders, S. Lienenklaus, S. De Koker, B. N. Lambrecht, S. A. David, B. G. De Geest, *J. Am. Chem. Soc.* **2018**, *140*, 14300.
[88] J. De Vrieze, B. Louage, K. Deswarte, Z. Zhong, R. De Coen, S. Van Herck, L. Nuhn, C. K. Frich, A. N. Zelikin, S. Lienenklaus, N. N. Sanders, B. N. Lambrecht, S. A. David, B. G. De Geest, *Angew. Chem., Int. Ed.* **2019**, *58*, 15390.
[89] J. Stickdorn, L. Stein, D. Arnold-Schild, J. Hahlbrock, C. Medina-Montano, J. Bartneck, T. Ziß, E. Montermann, C. Kappel, D. Hobernik, M. Haist, H. Yurugi, M. Raabe, A. Best, K. Rajalingam, M. P. Radsak, S. A. David, K. Koynov, M. Bros, S. Grabbe, H. Schild, L. Nuhn, *ACS Nano* **2022**, *16*, 4426.
[90] J. De Vrieze, A. P. Baptista, L. Nuhn, S. Van Herck, K. Deswarte, H. Yu, B. N. Lambrecht, B. G. De Geest, *Adv. Ther.* **2021**, *4*, 2100079.

© 2022 The Authors. Advanced Functional Materials published by Wiley-VCH GmbH

ADVANCED FUNCTIONAL MATERIALS

Supporting Information

for *Adv. Funct. Mater.,* DOI: 10.1002/adfm.202203490

Transient Lymph Node Immune Activation by Hydrolysable Polycarbonate Nanogels

*Christian Czysch, Carolina Medina-Montano, Zifu Zhong, Alexander Fuchs, Judith Stickdorn, Pia Winterwerber, Sascha Schmitt, Kim Deswarte, Marco Raabe, Maximilian Scherger, Francis Combes, Jana De Vrieze, Sabah Kasmi, Niek N. Sandners, Stefan Lienenklaus, Kaloian Koynov, Hans-Joachim Räder, Bart N. Lambrecht, Sunil A. David, Matthias Bros, Hansjörg Schild, Stephan Grabbe, Bruno G. De Geest, and Lutz Nuhn**

Transient Lymph Node Immune Activation by Hydrolysable Polycarbonate Nanogels

– Supporting Information –

Christian Czysch,[1] Carolina Medina-Montano,[2] Zifu Zhong,[3] Alexander Fuchs,[1] Judith Stickdorn,[1] Pia Winterwerber,[1] Sascha Schmitt,[1] Kim Deswarte,[4] Marco Raabe,[1] Maximilian Scherger,[1] Francis Combes,[5] Jana De Vrieze,[3] Sabah Kasmi,[3] Niek N. Sandners,[5] Stefan Lienenklaus,[6] Kaloian Koynov,[1] Hans-Joachim Räder,[1] Bart N. Lambrecht,[4,7] Sunil A. David,[8] Matthias Bros,[2] Hansjörg Schild,[9] Stephan Grabbe,[2] Bruno G. De Geest,[3] Lutz Nuhn[1,10,]*

1: Max Planck Institute for Polymer Research, 55128 Mainz, Germany;
2: Department of Dermatology, University Medical Center of Johannes Gutenberg-University Mainz, 55131 Mainz, Germany;
3: Department of Pharmaceutics and Cancer Research Institute Ghent (CRIG), Ghent University, Ghent 9000, Belgium;
4: Department of Internal Medicine and Pediatrics, Ghent University, VIB Center for Inflammation Research, Ghent 9052, Belgium;
5: Laboratory of Gene Therapy, Department of Nutrition, Genetics and Ethology, Ghent University, Merelbeke 9820, Belgium;
6: Institute for Laboratory Animal Science and Institute of Immunology, Hannover Medical School, 30625 Hannover, Germany;
7: Department of Pulmonary Medicine, Erasmus University Medical Center, Rotterdam 3015, Netherlands;
8: ViroVax, LLC, Lawrence, Kansas 66047, United States;
9: Institute of Immunology, University Medical Center of Johannes Gutenberg-University Mainz, 55131 Mainz, Germany.
10: Chair of Macromolecular Chemistry, Department of Chemistry and Pharmacy, Julius Maximilian University Würzburg, 97074 Würzburg.

*: contact orcid.org/0000-0003-0761-1106; phone: +49 (0) 6131-379-311; email: lutz.nuhn@mpip-mainz.mpg.de.

Materials and Methods

Solvents and reagents were purchased and used without further purification. 2,2-Bis(hydroxymethyl)propionic acid (Bis-MPA), triethylamine, cesium fluoride, Poly (ethylene glycol) methyl ether ($mPEG_{113}$), trifluoromethanesulfonic acid, tetrahydrofuran (dry), methylene chloride (dry), ethanol amine, 3,6-Dioxa-1,8-diaminooctane and Phosphate-Buffered Saline (PBS) tablets were purchased from Sigma Aldrich. Immunodrug 1-(4-(aminomethyl)-benzyl)-2-butyl-1H-imidazo[4,5-*c*]quinolin-4-amine (IMDQ) was synthesized by Sunil A. David.
Bis-(Pentafluorophenyl)-carbonate and hexafluoro isopropanol (HFIP) were purchased from Fluorochem Ltd. and 5(6)-TMR Cadaverine was purchased from Biotium.
Millipore water was prepared using a MILLI-Q R Reference A+ System. Water was used at a resistivity of 18.2 MΩ·cm and total organic carbon of <5 ppm.

Instrumentation

NMR spectroscopy

^{1}H, ^{13}C, ^{19}F, 2D and DOSY NMR spectra were recorded on a Bruker Avance 500 MHz spectrometer and a Bruker Avance III 700 MHz spectrometer. High-resolution magic angle spinning (HRMAS) was conducted using a 4 mm Bruker rotor kit (12 µL sample volume) at a Bruker Avance III 700 MHz spectrometer. Samples were prepared using deuterated solvents obtained from Sigma-Aldrich. Spectra were analyzed using MestReNova 14.2.0 by Mestrelab Research.

Size Exclusion Chromatography

Analytical size exclusion chromatography (SEC) was carried out at 40 °C on a SECcurity2instrument purchased from PSS, Mainz. HFIP with 3 g/L potassium trifluoroacetate was used as an eluent and the flow rate was set at 0.8 mL/min. The column material was composed of modified silica gel (PFG columns, particle size: 7 µm, porosity: 100 Å+ 1000 Å), purchased from PSS Polymer Standards Service GmbH. For polymer detection a UV detector at a wavelength of λ = 230 nm and a RI detector were employed. Furthermore, the system was equipped with a SECcurity2isocratic pump, a degasser, an auto sampler and a column thermostat.

Molecular weights were determined by using a calibration with PMMA (PSS Polymer Standards Services GmbH). Evaluation of the elution diagram was conducted with PSS WinGPC from PSS Polymer Standard Service GmbH.

Dynamic Light Scattering

Dynamic light scattering measurements were performed using a Malvern Z Nano instrument equipped with a He-Ne-Laser (λ = 632.8 nm) using ZetaSizer Software 7.12. Measurements were performed in triplicates at 4 °C, 25 °C or 37 °C and a detection angle of 173°. For multi-angle light scattering an alternative machine was used measuring at angles of 30° using a He-Ne-Laser as the incident beam.

Atomic Force Microscopy

For atomic force microscopy imaging, nanogels were diluted to 50 mg/L, drop casted (5 µL) onto a freshly cleaved mica substrate (circular, 15 mm). AFM imaging measurements were performed using a Bruker Dimension FastScan Bio®atomic force microscope in Peak Force mode. Samples were scanned with scan rates of 0.994 – 1.41 Hz and AFM probes with a nominal spring constant of 0.25 N/m (FastScan-D, Bruker) were employed. Data was processed using NanoScope Analysis 1.8.

Ultraviolet-Vis Spectroscopy and Fluorescence Spectroscopy

UV-Vis spectra were recorded using a Thermo Scientific™ NanoDrop™ 2000c spectrophotometer using Brand UV micro cuvettes.
For Fluorescence Spectroscopy and read-out of RAW-blue and MTT assays a Spark 20M Multimode Microplate Reader from TecanTrading AG (Mannedorf, Switzerland) was used.

Fluorescence Correlation Spectroscopy

FCS measurements were performed using a commercial LSM880 setup (Carl Zeiss, Jena, Germany) equipped with a C-Apochromat 40x/1.2 W water immersion objective. For excitation of Tetramethyl Rhodamine a helium-neon laser (633 nm) was used. The fluorescence light was collected with the same objective and after passing a pinhole directed to a spectral detection unit (Quasar, Carl Zeiss). There the fluorescence light is separated spectrally by a grating element on a 32-channel array of GaAsP detectors operating in a single photon counting mode. The fluorescent signal in the range of 650-

700 nm was detected. All measurements were performed in eight-well polystyrene-chambered cover glass (Laboratory-Tek, Nalge Nunc International). The obtained FCS autocorrelation curves were fitted with the theoretical model function for an ensemble of either one or two types of freely diffusing fluorescence species. The fits yielded the diffusion coefficients (D) of the studied species. Finally, the hydrodynamic radii (R_H) were calculated using the Stokes-Einstein relation: $R_{\mathrm{H}} = \frac{\kappa_B T}{6\pi\eta D}$, where κ_b the Boltzmann constant, *T* is the temperature, and *η* is the viscosity of the solvent.

Mass Spectrometry

Matrix Assisted Laser Desorption Ionization-Time of Flight Mass Spectrometry (MALDI-ToF) measurements were carried out on a rapifleX™ MALDI-TOF/TOF mass spectrometer from Bruker Daltonik GmbH, Fahrenheitstraße 4, 28359 Bremen. The instrument is equipped with a scanning smartbeam 10 kHz Nd:YAG laser at a wavelength of 355 nm and a 10 bit 5 GHz digitizer. The acceleration voltage was set to 20 kV and the mass spectra were recorded in positive ion mode. Calibration was done by polymer standards of polyethylene glycol.

Mass spectrometry by electrospray ionization (ESI-MS) were performed on a SYNAPT G2-Si high-definition Q-TOF mass spectrometer (Waters Corp., Manchester, UK). The instrument was calibrated by clusters of sodium formate. Mass spectrometry data were analyzed using mMass.

Syntheses

Synthesis of 5-methyl-5-pentafluorophenyloxycarbonyl-1,3-dioxan-2-one

5-methyl-5-pentafluorophenyloxycarbonyl-1,3-dioxan-2-one (MTC-PFP) was obtained by cyclization of 2,2-Bis(hydroxymethyl)propionic acid (Bis-MPA) using Bis-(pentafluorophenyl)-carbonate as reported in the literature.[1] The crude product was recrystallized two times from a 1:1 mixture of ethyl acetate with hexane to yield colorless crystals that were analyzed by NMR and X-ray diffraction.

^{1}H NMR (300 MHz, $CDCl_3$, 25 °C) δ = 4.85 (d, ^{2}J(H,H)*)* = 11 Hz, 2H; *CH_2*), 4.35 (d, ^{2}J(H,H), 2 H; *CH_2)* = 11 Hz, 2H), 1.56 (s, 3H, *CH_3*).
^{19}F NMR (376 MHz, $CDCl_3$) δ [ppm] = -153.71 – -154.23 (d, ^{3}J(F,F) = 22 Hz, 2 F; *m*-F), -157.13 (dd, ^{3}J(F,F) = 22 Hz, 1 F; *p*-F), -162.26 (dd, ^{3}J(F,F) = 22 Hz, 2 F; *o*-F).

Crystallographic data: CCDC 2178256. Data can be accessed from the Cambridge Crystallographic Data Centre. https://www.ccdc.cam.ac.uk/structures/

Synthesis of methyl-poly(ethyleneglycol)-*b*-poly(5-methyl-5-pentafluorophenyloxy-carbonyl-1,3-dioxan-2-one) ($mPEG_{113}$-*b*-poly(MTC-PFP)

$mPEG_{113}$-*b*-poly(MTC-PFP) was synthesized by an adapted literature protocol.[2] 0.7828 g MTC-PFP (2.4 mmol, 40 eq) was weighed into a 10 mL Schlenk-flask and ~2 mL of dry benzene was added. 0.300 g $mPEG_{113}$ (0.060 mol, 1 eq.) was dissolved in ~2 mL benzene. Both compounds were freed from residual water by azeotropic removal of benzene and water overnight *in vacuo*. On the following day, the flasks were introduced into a glove box (nitrogen atmosphere) and dry dichloromethane was added *via* syringe. $mPEG_{113}$ was dissolved in dichloromethane and transferred to the flask containing MTC-PFP. Dichloromethane was added to reach a final volume of 4.80 mL corresponding to a 0.5 M concentration of MTC-PFP. For the initiation of the polymerization 5.27 µL trifluoromethanesulfonic acid (9.0 mg, 0.06 mmol, 1.0 eq) was added to this mixture. After a reaction time of ~12 d at room temperature conversion was determined by ^{1}H NMR (81.6% conversion) and ^{19}F NMR (81.3% conversion) and the polymer was precipitated into a large excess of ice-cold diethyl ether (-20 °C), centrifuged (4500 rpm, 10 min, 4 °C) and decanted. Subsequently, the pellet was dissolved in ~1 mL of dichloromethane and precipitated into diethyl ether. The

procedure was repeated one more time. After drying *in vacuo* overnight mPEG$_{113}$-*b*-poly(MTC-PFP)$_{32}$ was obtained as a colorless solid. The product was analyzed by NMR, HFIP-SEC and MALDI.

^{1}H NMR (300 MHz, $CDCl_3$, 25 °C) δ = 4.46 (s, 4 H; *CH$_2$* MTC-PFP), 3.63 (s, 4 H; O*CH$_2$CH$_2$* PEG), 3.36 (s, 3 H; *CH$_3$*O PEG), 1.49 (s, 3 H; *CH$_3$* MTC-PFP).
^{19}F NMR (282 MHz, $CDCl_3$, 25 °C) δ = -154.29 (d, ^3J(F,F) = 22 Hz, 2 F; *m*-F), -158.27 (t, ^3J(F,F) = 22 Hz, 1 F; *p*-F), -163.26 (t, ^3J(F,F) = 22 Hz, 2 F; *o*-F).

Preparation of Core-Cross-linked Polymeric Micelles Based on mPEG-*b*-poly(MTC-PFP)

Polymeric micelles were formed by ultra-sonification of 80.0 mg mPEG$_{113}$-*b*-poly(MTC-PFP)$_{32}$ at 30 °C in 8 mL ethanol (with a water content of ~1 wt%) to form a clear 10 mg/mL solution. Analysis by DLS confirmed the size and monomodal distribution of the prepared polymeric micelles. Thereafter, the solution was aliquoted into four vials each containing 2 mL of the solution (20 mg, 1.307 µmol containing 41.3 µmol PFP ester units 32 per polymer chain). Following reagents were added to the vials:

I 0.5 Eq. 3,6-Dioxa-1,8-diaminooctane **3.01 µL** (3.06 mg, 20.6 µmol) and 1.05 Eq. Triethylamine **6.01 µL** (4.39 mg, 43.4 µmol)
II TMR Cadaverine **16.6 µL** (10 mg/mL in EtOH, 0.166 mg, 0.32 µmol), 0.5 Eq. 3,6-Dioxa-1,8-diaminooctane **3.01 µL** (3.06 mg, 20.6 µmol) and 1.05 Eq. Triethylamine **6.01 µL** (4.39 mg, 43.4 µmol)
III IMDQ·2 HCl **216.6 µL** (10 mg/mL in EtOH, 2.165 mg, 6.02 µmol), 1.30 Eq. Triethylamine **7.44 µL** (5.43 mg, 53.7 µmol) and 0.427 Eq. 3,6-Dioxa-1,8-diaminooctane **2.57 µL** (2.61 mg, 17.6 µmol)
IV TMR Cadaverine **16.6 µL** (10 mg/mL in EtOH, 0.166 mg, 0.32 µmol) and 1.30 Eq. Triethylamine **7.44 µL** (5.43 mg, 53.7 µmol), IMDQ·2 HCl **216.6 µL** (10 mg/mL in EtOH, 2.165 mg, 6.02 µmol) and 0.427 Eq. 3,6-Dioxa-1,8-diaminooctane **2.57 µL** (2.61 mg, 17.6 µmol)
and stirred at rt for 25 min (total reaction time).

At the end of reaction time conversion was determined by ^{19}F NMR. Residual PFP esters were quenched by reaction with ethanolamine (3.03 mg, 18.24 mmol, 1 eq) and

conversion was checked once again by ^{19}F NMR. Reaction mixtures were quenched by addition of 8 mL 1M hydrochloric acid and dialyzed (1 kDa MWCO) over-night against hydrochloric acid of pH 4 to replace the solvent as well as to remove reaction reagents and byproducts such as triethylamine salts. Subsequently, the solutions (~ 17 mL each) were analyzed by DLS and freeze-dried for 48 h to yield colorless/red powders (~16 mg each) which were resuspended by short ultra-sonification in the desired media (pH 4 water for DLS, UV-Vis experiments and biological testing, DMSO-d_6 for NMR etc.).

Particle Degradation Studies

For DLS degradation studies, freeze-dried material (non-labeled) was redispersed at 10 mg/mL in Millipore water. To test the stability at different pH values this solution was diluted to 1 mg/mL using the respective buffer/media (pH 4 diluted hydrochloric acid, pH 6.4, 6.8 and 7.4 Phosphate Buffered Saline, pH 9 sodium carbonate buffer). The solutions were incubated at 37 °C on a thermo shaker and analyzed at different time points by DLS.

For long-term stability tests in PBS, particles were diluted as described above and incubated in the DLS instrument at 4 °C/37 °C. Measurements were automatically recorded every 2 hours.

Tracking the release of conjugated dye molecules, covalently dye-labeled nanogels (tetramethyl rhodamine cadaverine) were used at a concentration of 0.01 mg/mL in PBS (pH 7.4) and analyzed by FCS at different time points.

Degradation was also investigated by ^{1}H-NMR. Therefore, nanogels were redispersed at a concentration of 5 mg/mL in D_2O. Successful particle redispersion was tested by DLS. Particles were analyzed by DOSY-NMR and degradation was induced by addition of 10x PBS in D_2O to adjust pH to 7.4 at a 1x PBS buffer strength. Samples were incubated at RT for several days and measured at different time points.

For High-Resolution Magic Angle Spinning-NMR (HRMAS) 1 mg of particle was dispersed in 20 µL of 9:1 H_2O/D_2O and transferred to a 4 mm zirconium oxide rotor (12 µL volume). The sample was spun at 5000 Hz and analyzed by one-dimensional NMR measurements. The sample was incubated at 37 °C (310 K) and measured at different time points.

For mass spectrometric analysis by MALDI-ToF, particle solutions (1 mg/mL) were incubated in PBS at pH 7.4 for 3 weeks and complete degradation was confirmed by DLS. MALDI-ToF measurements were conducted using α-Cyano-4-hydroxycinnamic acid (CHCA) as matrix. For electrospray ionization (ESI) mass spectrometry, particles (1 mg/mL) were incubated in a 1:100 mixture of trimethylamine in water for ~16 h. Samples were then diluted to 0.1 mg/mL with water and measured with a waters SYNAPT G2-Si high-definition Q-TOF mass spectrometer (Waters Corp., Manchester, UK) using electrospray ionization.

***In vitro* experiments**

RAW-Blue macrophage TLR reporter assay (Quanti Blue Assay)

TLR reporter assay *via* downstream activation of AP-1/NF NF-κB and subsequent secretion of SEAP (secreted embryonic alkaline phosphatase) was conducted as recommended by InvivoGen. Cells were seeded into 96-well plates (90000 cells/well in 180 µL culture medium) and incubated with 20 µL of the respective solutions at the given IMDQ concentrations. After ~ 20 h of incubation 50 µL of the supernatant was collected and probed by Quanti Blue Assay (InvivoGen) for the amount of SEAP. After incubation for 2 h at 37 °C wells were read-out for their absorbance at 620 nm using a plate reader. All experiments were performed in quadruplicates.

Determination of metabolic activity by MTT assay on stimulated Raw Blue macrophages

To analyze the metabolic activity of the cell as an indicator of toxicity and cell proliferation, stimulated cells were incubated with 30 µL of 2 mg/mL 3-(4,5-dimethylthiazol-2-yl)-2,5-diphenyltetrazolium bromide solution in PBS. After 3 h of incubation time, formazan crystals were dissolved by the addition of 100 µL of 10% m/v SDS/0.01 M HCl and incubated overnight at 37 °C. Absorbance was measured at 590 nm using a plate reader. All experiments were performed in quadruplicates.

Determination of nanogel uptake by flow cytometry

To determine nanogel uptake in Raw-Blue macrophages cells were seeded in a 24 well plate (250000 cells/well in 950 µL culture medium) and incubated with TMR-labeled nanogels at the given concentrations. After ~20 h of incubation time the medium was removed, the cells were washed with 1 mL of PBS and incubated with 250 µL of cell dissociation buffer for 30 min at 37 °C. Then 750 µL of cell culture medium was added and the cells were centrifuged at 350 g for 10 min at 0 °C to yield a cell pellet. The supernatants were removed and the pellets were resuspended in 250 µL of PBS, to be analyzed on a BD Accuri C6 (BD Biosciences). Data was processed by FlowJo Software.

Confocal microscopy

For microscopy, cells (50000 cells/well in 180 µL) were seeded in an eight-well polystyrene-chambered coverglass (Laboratory-Tek, Nalge Nunc International, Penfield, NY, USA). Respective amounts of TMR-labeled nanogels were added (20 µL solution) and incubated overnight. Then the medium was removed and the cells were washed with PBS three times. Cells were fixated applying 200 µL of a 4% paraformaldehyde solution for 30 minutes at 37 °C. Cell nuclei were stained using a 4′,6-diamidino-2-phenylindole (DAPI) solution (80 µg/mL in PBS) for 10 min at 37 °C. Finally, the samples were analyzed on a Leica SP5 confocal microscope (Wetzlar, Germany) with a 63x oil immersion objective. Images were processed by ImageJ software package.

BMDCs (Bone marrow-derived dendritic cells)

Bone marrow cells were isolated from femurs and tibiae of C57BL/6 mice, and were resuspended in IMDM-based culture medium (5% FBS, 2 mM L-glutamine, 100 IU/ml penicillin, 100 µg/ml streptomycin and 50 µM β-mercaptoethanol; all from Sigma-Aldrich, Deisenhofen, Germany), supplemented either with 10 ng/ml recombinant murine GM-CSF (R&D Systems, Wiesbaden, Germany) to obtain inflammatory BMDCs or with 250 ng FT3L (BioLegend Way, San Diego, USA) to yield a mixture of plasmacytoid pDC, and conventional cDC type 1 and 2, respectively. To this end, bone marrow cells were seeded in 12 well suspension cell culture cluster plates (GM-CSF: $2x10^5$/mL – FT3L: 10^6/mL). In case of GM-CSF cultured cells, the cell culture media had to be replenished on days 3 and 6. On days 7-8, the different NP formulations were applied to the differentiated cells as indicated. On the next day, samples were harvested and were subjected to flow cytometric analysis.

Flow cytometry of BMDCs

Samples were preincubated with Fcγ receptor (CD16/CD32) blocking antibody (rat-anti-mouse, clone 2G4) to prevent non-specific binding of other antibodies (15 min, 4 °C). Then lineage and activation marker detecting antibodies (Table 1) were applied for 20 min at 4 °C. All antibodies were purchased from BioLegend (San Diego, CA, USA) or Thermo Fisher (Waltham, MA, USA).

Cell line	Antibody	Clone	Dye
BMDCs (GM-CSF)	CD11c	N418	BV421
	CD80	16-10A1	PerCP-eFl710
	CD86	GL1	FITC
	MHC-II	2G9	PE-eFl610
	CD40	1C10	PE
BMDCs (FLT3L)	CD11c	N418	PE-Cy7
	CD11b	M1/70	SB600
	B220/CD45R	RA3-6B2	V500
	XCR1	ZET	AF647
	MHC-II	2G9	eFl450
	CD80	16-10A1	PerCP-eFl780
	CD86	GL1	FITC

Table S1: Antibodies used to characterize the activation state of the various BMDC populations.

Samples left untreated, incubated with the NP formulation alone or with single antibody served as controls. Fixable Viable Dye (FVD-eFluor® 780, Thermo, CA, USA) was used to discriminate live/dead cells. Fixed samples were analyzed on a Attune NxT flow cytometer (Thermo Fisher) and the obtained data processed using the Attune NxT Flow cytometer software (Thermo Fisher) and FlowJo Software.

***In vivo* experiments**

All in vivo experiments had been approved by the Ethical Committee of the Faculty of Veterinary Medicine and the Faculty of Bioscience Engineering of Ghent University (No. EC2018/92).

Bioactivity imaging of IMDQ-loaded nanogels

Heterozygous BALB/c IFN-β (IFN-$\beta^{+/\Delta\beta\text{- luc}}$) reporter mice in the range of 7−9 weeks were housed in individual ventilated cages and given ad libitum access to food and water. 20 µL of the nanogel NP(IMDQ) or soluble IMDQ were injected subcutaneously in the footpad at an equivalent dose of 10 µg IMDQ (n = 3, a mouse treated with PBS served as control). For subsequent in vivo bioactivity imaging, mice were injected subcutaneously with 200 µL D-luciferin (15 mg/ mL, Gold Biotechnology, USA) at the

given time points (0, 4, 24, and 48 h post injection), and in vivo luminescence imaging was recorded 12 min later using the IVIS Lumina II imaging system from PerkinElmer, (Waltham, MA, USA). Photon flux was analyzed by Living Image 4.4 software from Caliper life sciences (Hopkinton, MA, USA).

Analysis of lymphocyte targeting and activation

Heterozygous BALB/c IFN-β (IFN-$\beta^{+/\Delta\beta\text{-luc}}$) reporter mice were subcutaneously injected in the footpad with 10 µg IMDQ (soluble or bound to nanogel in 20 µL of PBS, n = 4) and sacrificed after 48 h. Popliteal lymph nodes were isolated for flow cytometry and confocal microscopy imaging analysis. A single cell suspension was prepared form three of the dissected lymph nodes for analysis by flow cytometry. The isolated lymph nodes were collected in ice cold PBS, smashed through 70 µm cell strainers, washed with PBS and stained for 30min at 4 °C with a live-dead stain and the following primary labeled monoclonal antibodies: CD3e, CD11c, CD11b, CD19, CD69, CD80, CD86, F4-80, Ly-6G, and MHC-II. 123count ebeads were added to determine cellularity prior to acquiring them on by flow cytometry (BD FACS Aria). Analyses were done using the FlowJo software package according to the gating procedure of Figure S32.

For confocal imaging of the popliteal lymph nodes, an exemplary sample was frozen in OCT cryomedium (Sakura, 4583) and frozen sections (8-µm) were cut by cryostat. These sections where fixed for 4 min in PFA 2% (v/v), and washed with PBS. Images were acquired on a Zeiss LSM710 confocal microscope equipped with 488-nm, 561-nm and 633-nm lasers and with a tunable two-photon laser. Confocal imaging was done using a Leica DMI6000B microscope (10x 0.70 NA objective) coupled to an AndorDSD2 confocal scanner and a Zyla5.5 CMOS camera. Image processing was done using the ImageJ software package.

Statistical Analysis

All data are shown as mean values ± standard deviation (mean ± SD). Samples sizes (n) were mentioned for each data set. To calculate statistical significance of the mean values, unpaired Student's t-test with Welch's correction was performed using Graph Pad Prism 8 software (*: $p \leq 0.05$; **: $p \leq 0.01$; ***: $p \leq 0.001$).

Additional Characterization Data

Monomer Synthesis

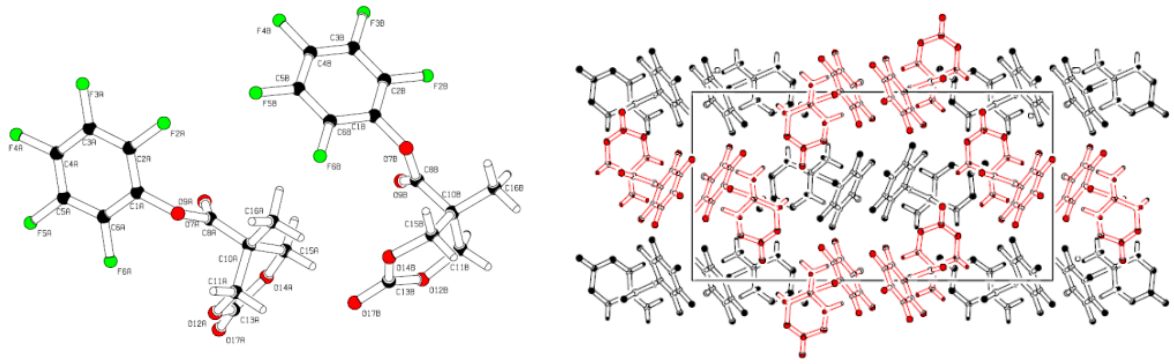

Figure S1: Structure and arrangement of the MTC-PFP monomer within the primitive cell in the crystal lattice. Monomer molecules crystallize in a P $2_1/c$ space group. The crystal structure is available at the Cambridge Crystallographic Data Centre (https://www.ccdc.cam.ac.uk/structures/) under deposition number 2178256.

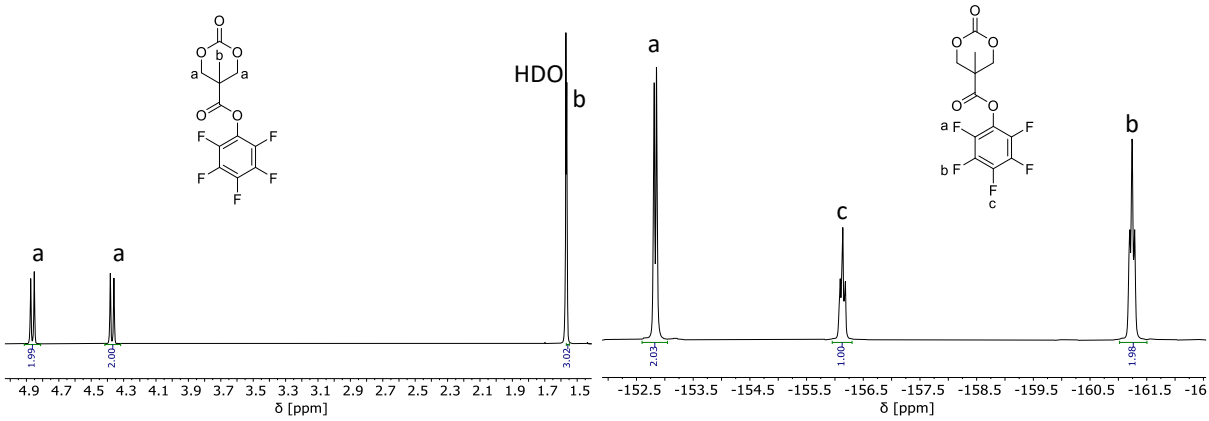

Figure S2: ^{1}H-NMR and ^{19}F-NMR of MTC-PFP with assignments.

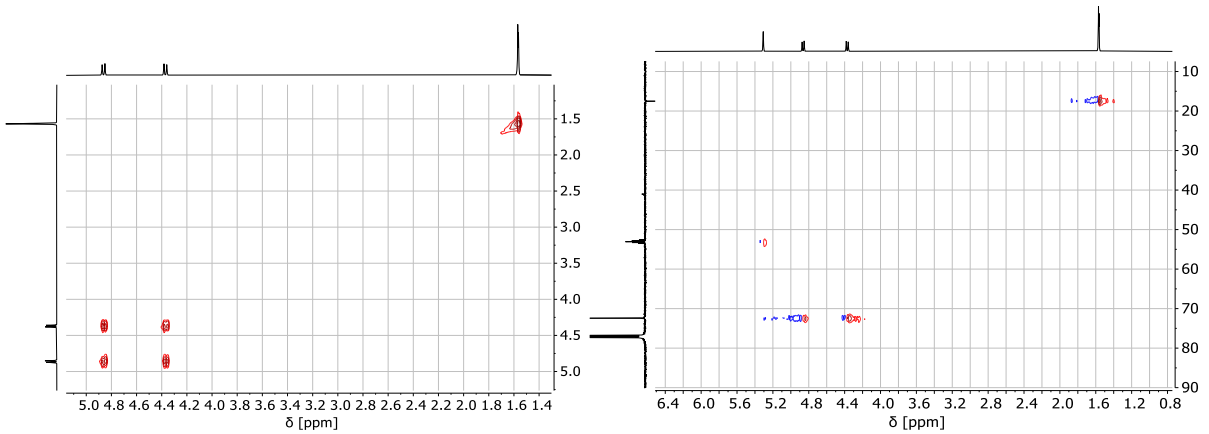

Figure S3: 2D-NMR of MTC-PFP. ^{1}H-^{1}H-COSY (left) and ^{1}H-^{13}C HSQC.

Polymerization

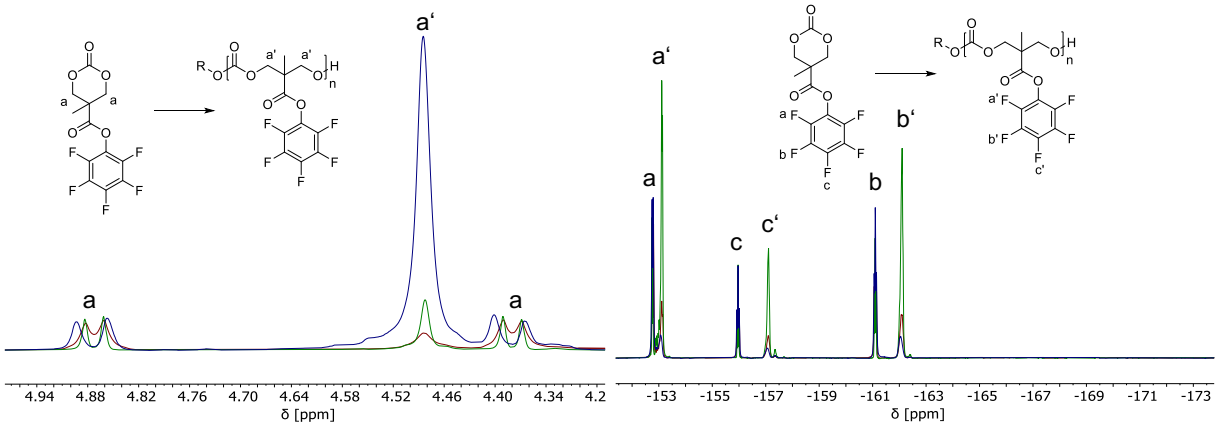

Figure S4: Monomer conversion of MTC-PFP by ^{1}H (left) and ^{19}F (right) NMR monitoring during polymerization onto $mPEG_{113}$ recorded at three timepoints (*t* = 3 d, 6 d, 11 d).

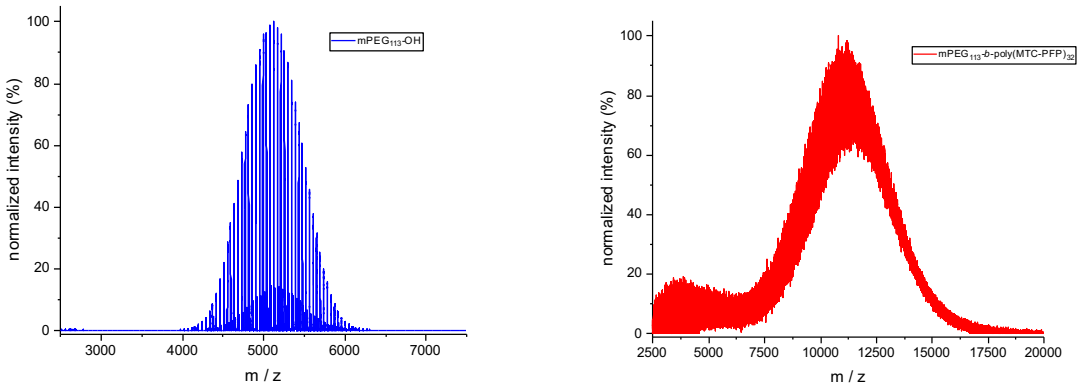

Figure S5: Mass spectrometric data (MALDI-ToF) of $mPEG_{113}$ (left, blue) and $mPEG_{113}$-*b*-poly(MTC-PFP)$_{32}$ (right, red) using 2-[(2E)-3-(4-tert-butylphenyl)-2-methylprop-2-enylidene]malononitrile (DCTB) as matrix.

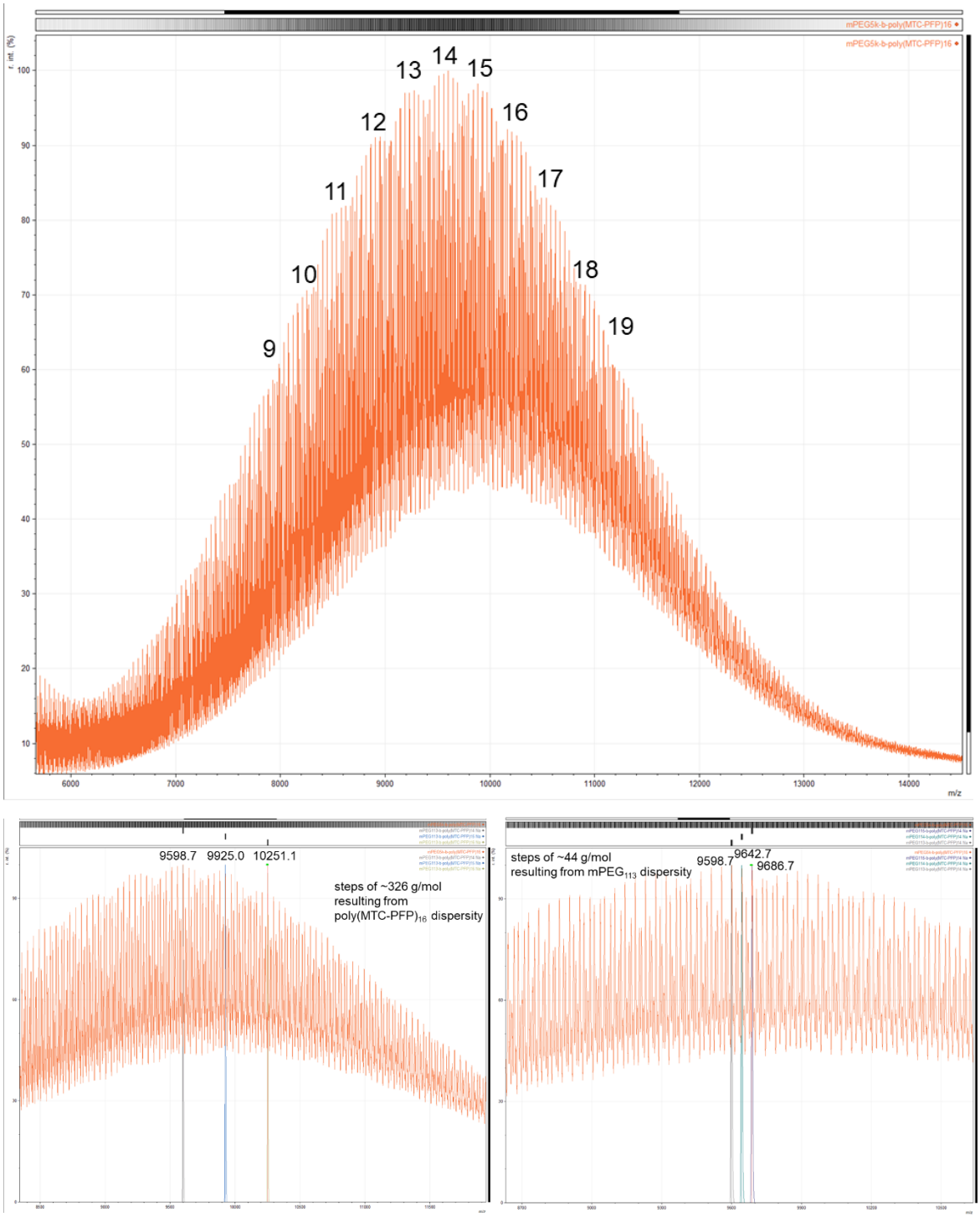

Figure S6: MALDI-ToF of $mPEG_{113}$-*b*-$poly(MTC\text{-}PFP)_{16}$. Spectra of block copolymer (top) showing overlapping mass distributions of mPEG polymers with 9-19 repeating units of the poly(MTC-PFP) block. Individual peaks within these distributions can be attributed by simulating peaks of different block length regarding the poly(MTC-PFP) block with degree of polymerization (DP) of 14-16 (bottom left, graph) showing m/z shifts of ~326 which correspond to the molar mass of the MTC-PFP repeating unit. Analogously, mPEG block with DP of 113-115 were attributed showing m/z shifts of ~44 corresponding to the molar mass of one ethylene glycol repeating unit. Polymers were detected as Na^+ ionized form in reflector mode using 2-[(2E)-3-(4-tert-butylphenyl)-2-methylprop-2-enylidene]malononitrile (DCTB) as matrix.

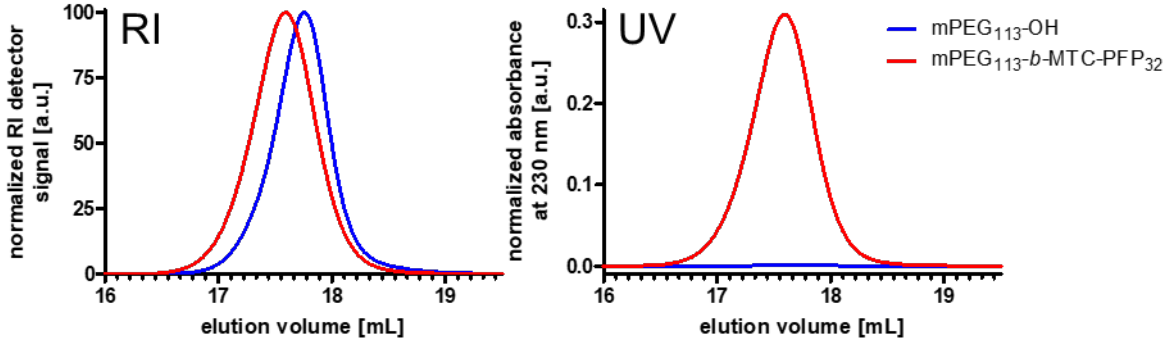

Figure S7: SEC traces of $mPEG_{113}$ (blue) and $mPEG_{113}$-*b*-poly(MTC-PFP)$_{32}$ (red) detected by refractive index detector (left) and UV (right) at 230 nm. Refractive index (RI, left graph) traces: For $mPEG_{113}$ a molar mass of M_n = 34300 g/mol with a $Đ$ = 1.15 was found relative to the PMMA standard and for $mPEG_{113}$-*b*-poly(MTC-PFP)$_{32}$ a molar mass of M_n = 41700 g/mol with a $Đ$ = 1.16 was determined. Using UV-Vis detection a M_n = 42200 g/mol with a $Đ$ = 1.15 was found. Notably, UV-Vis traces show additional absorbance for $mPEG_{113}$-*b*-poly(MTC-PFP)$_{32}$ at 230 nm due to the poly(MTC-PFP) block while $mPEG_{113}$ alone shows no absorbance at that wavelength, indicating the successful synthesis of the block copolymer.

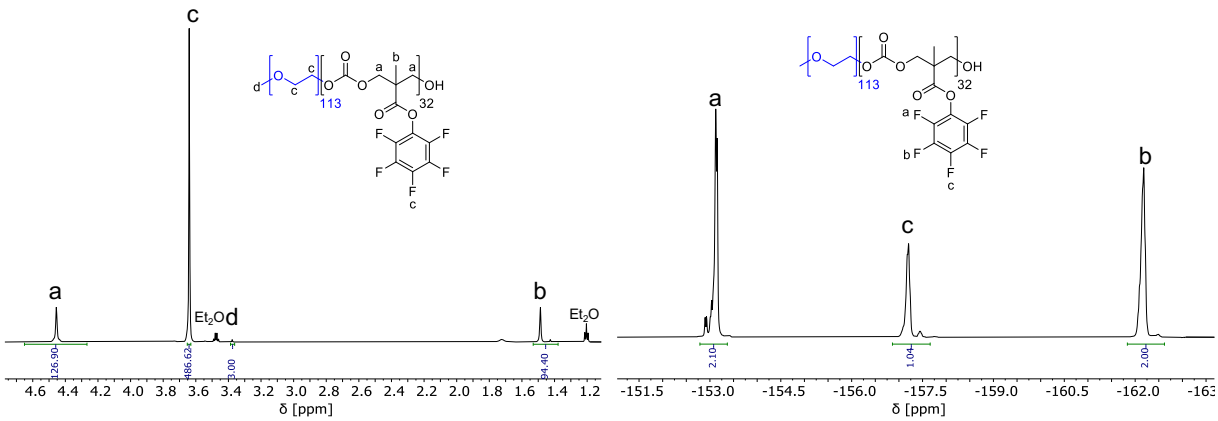

Figure S8: ^{1}H and ^{19}F NMR spectra of the purified block copolymer $mPEG_{113}$-*b*-poly(MTC-PFP)$_{32}$ with assignments.

Nanogel Synthesis

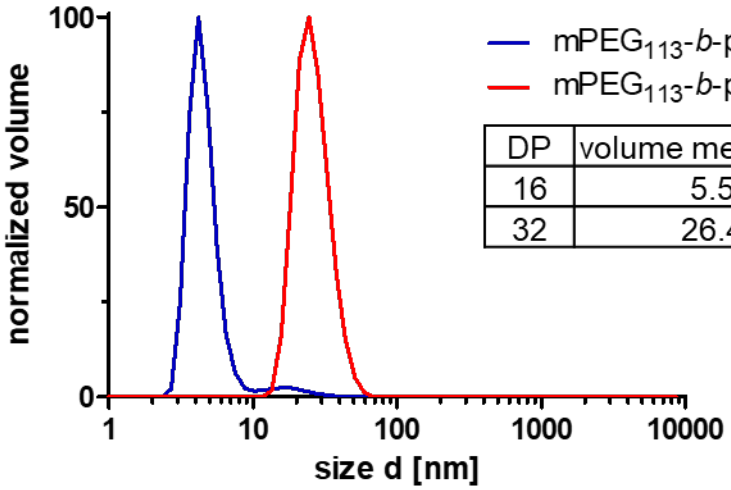

DP	volume mean [nm]	PDI	derived count rate
16	5.5	0.20	944
32	26.4	0.05	9395

Figure S9: DLS volume-weighted size distributions of block copolymers in ethanol at different polycarbonate block lengths. Block copolymers with short polycarbonate block length (degree of polymerization, DP = 16) are fully soluble in ethanol and do not form micelles (size by volume mean = 5.5 nm with low derived count rates of 944 counts) whereas micelles are formed from polymers with longer polycarbonate block lengths (DP=32, size by volume mean = 26.4 nm, 9395 counts). Both increasing sizes as well as count rates prove aggregation of micellar particles for mPEG$_{113}$-*b*-poly(MTC-PFP)$_{32}$ and indicate the requirement of sufficient polycarbonate block lengths for successful nanogel fabrication.

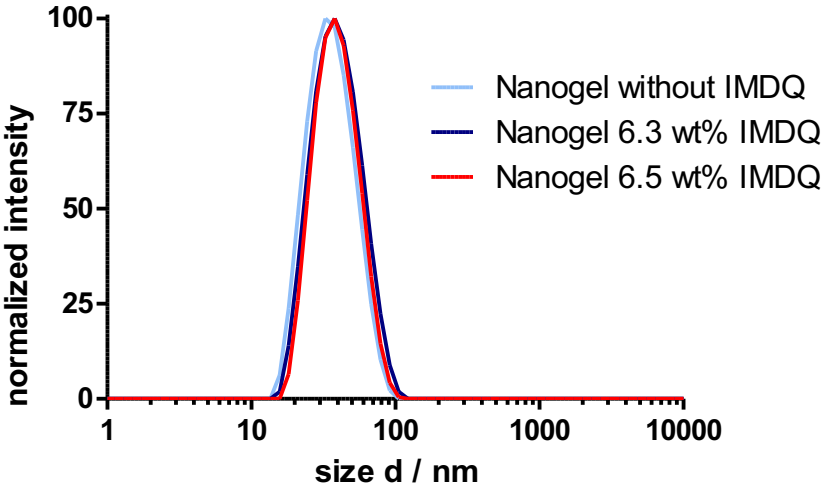

Figure S10: DLS intensity-weighted size distributions of nanogels in mp-water without IMDQ (z.ave. = 33.2 nm, PDI 0.13) and two individual batches loaded with 6.3 wt% (z.ave. = 36.8 nm, PDI 0.14) and 6.5 wt% (z.ave. = 36.8 nm, PDI 0.13) IMDQ confirming that IMDQ-loading has no influence on the particle sizes and distributions and that particle synthesis reproducibly yields drug-loaded nanogels similar size and loading.

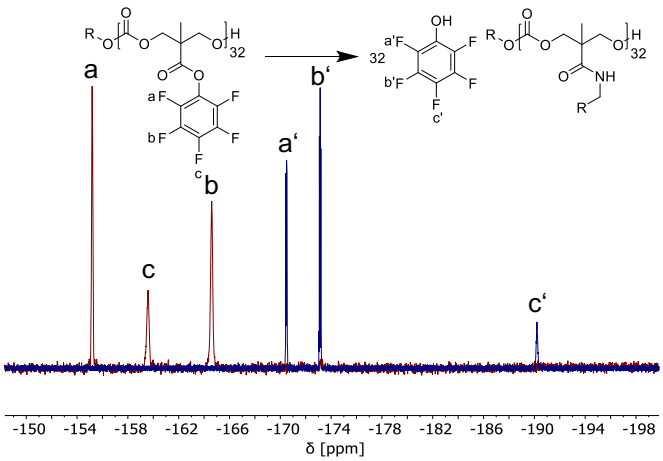

Figure S11: ^{19}F NMR spectrum to determine the conversion of the amidation during nanogel synthesis. Bound PFP-ester is converted to free pentafluorophenol detecting the quantitative conversion of the active ester sidechain in the reaction mixture. After purification by dialysis and lyophilization pentafluorophenol was quantitatively removed.

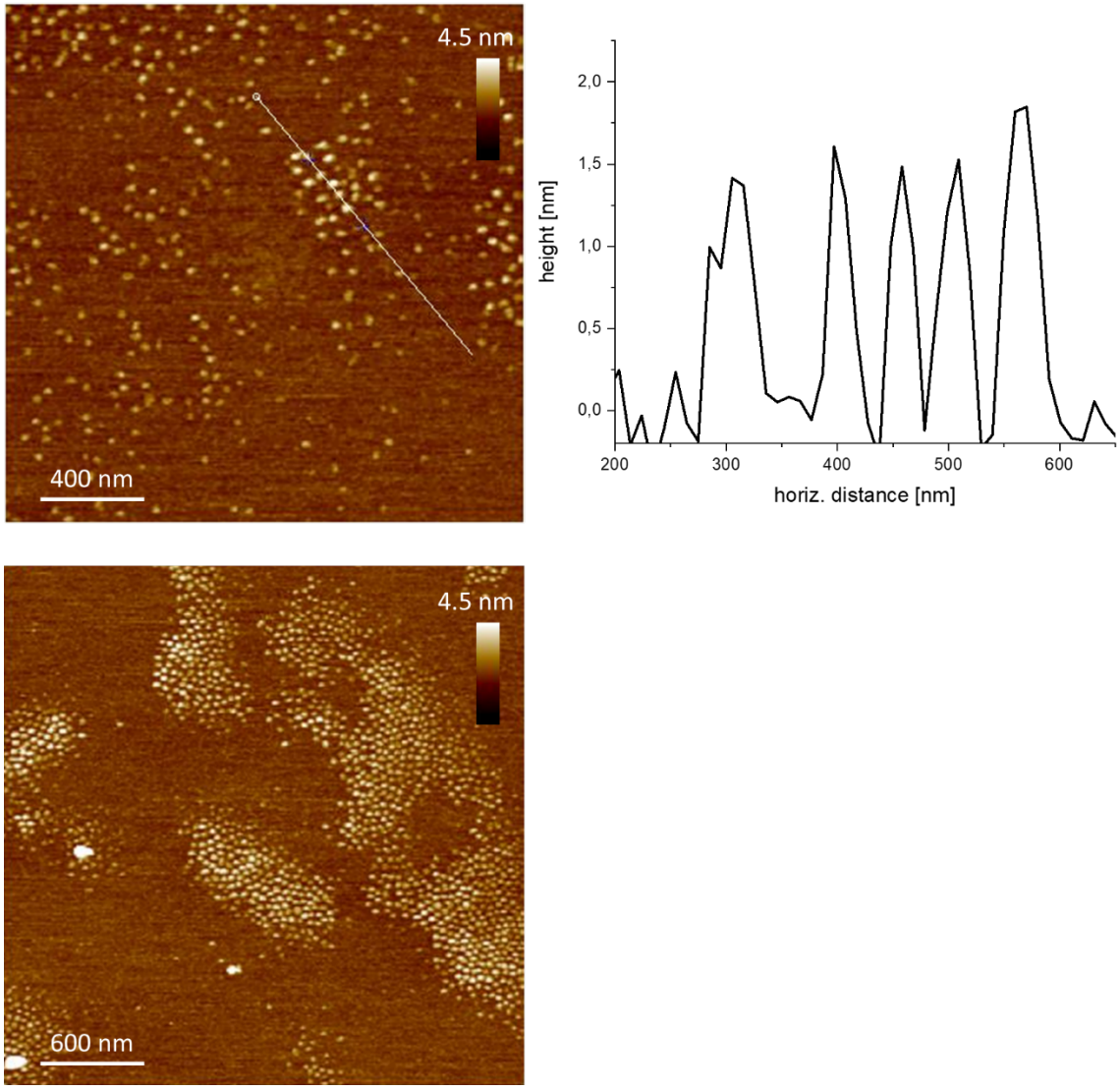

Figure S12: Additional AFM images of core-cross-linked nanogels with height profile showing heights of ~2 nm.

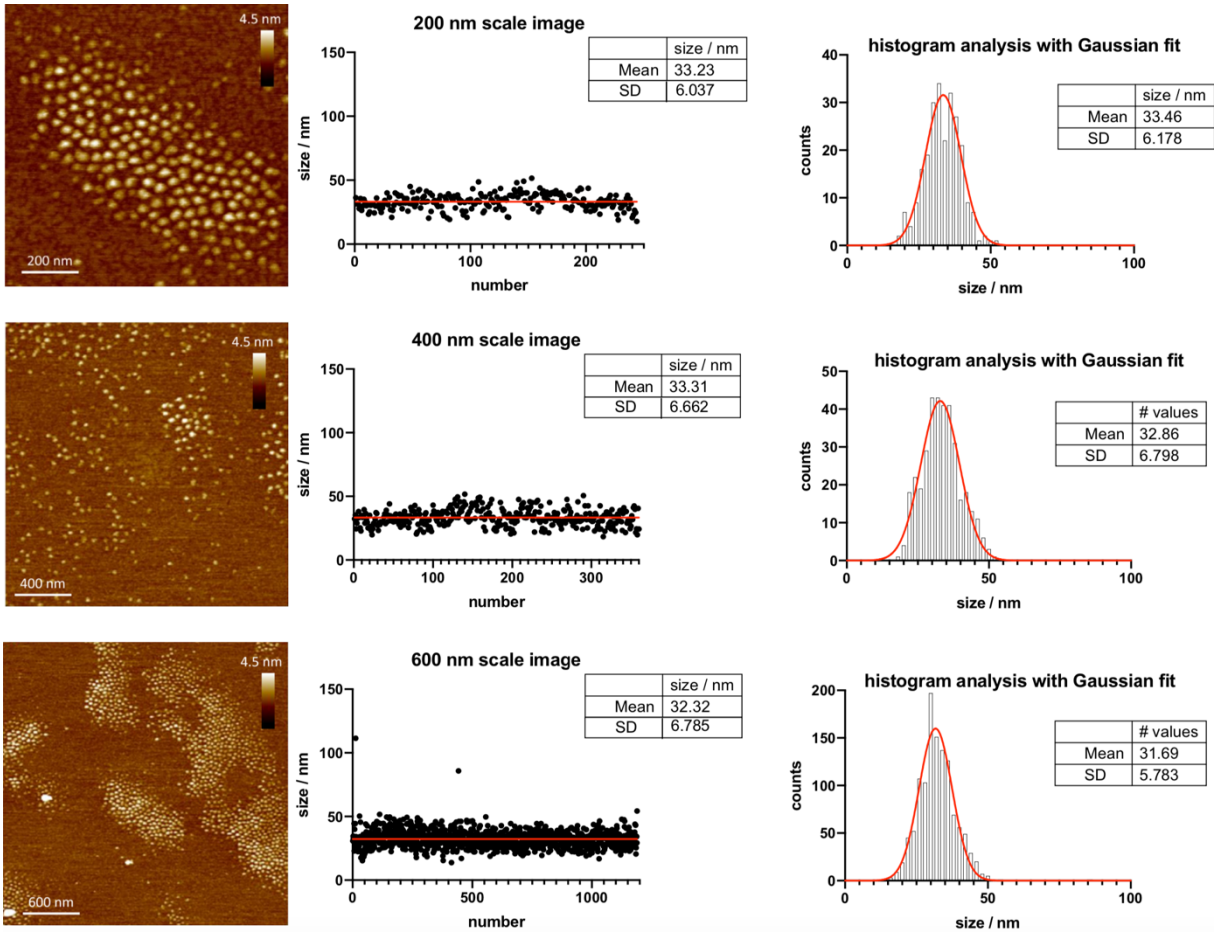

Figure S13: Detailed analysis of different AFM images (from Figure 3+S12, left) regarding the diameter of the nanogels. Diameters from individually particles were counted and mean average and standard deviation calculated (middle). Corresponding histograms with Gaussian fits for particle size distributions and respective mean and standard derivation values were obtained (right). Remarkably, mean sizes of 31-33 nm and standard derivations of 5-7 nm were found underlining the narrow size distributions that were found by AFM in analogy to the DLS measurements of the swollen nanogels in aqueous environment (compare e.g. Figure S10).

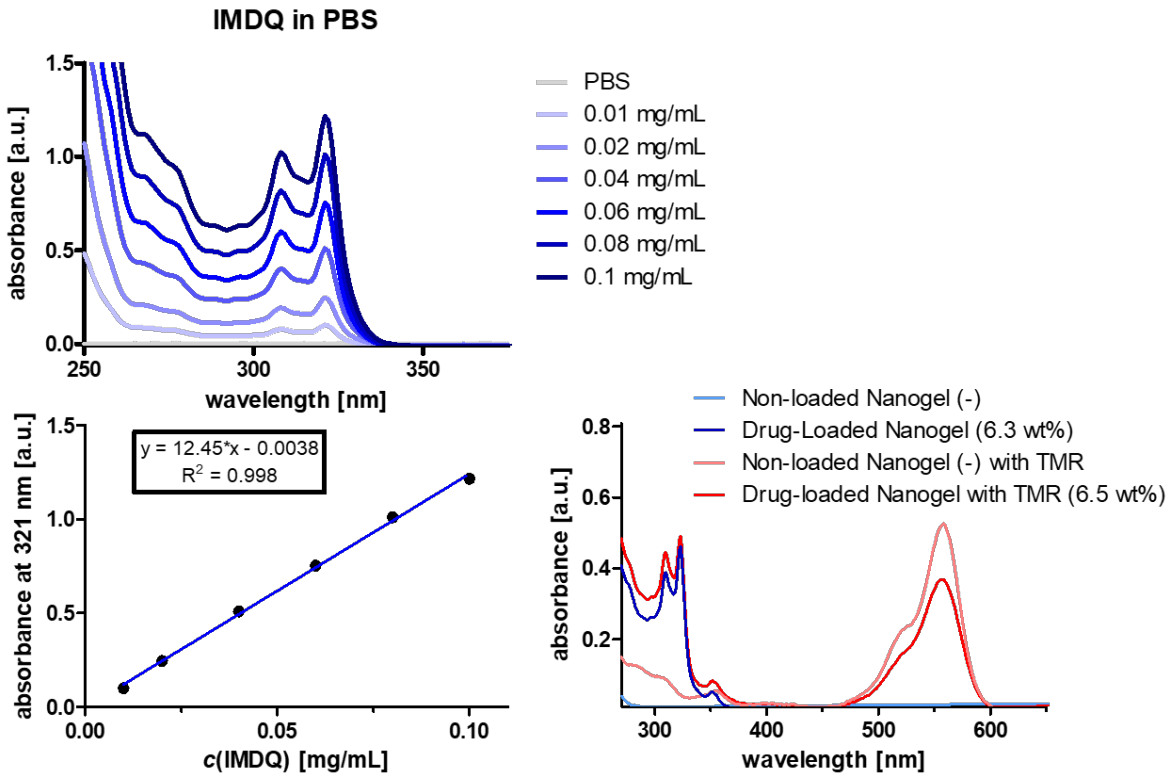

Figure S14: UV-Vis calibration at 321 nm of the immunodrug IMDQ in PBS for determination of the drug-load in core-cross-linked nanogels. Drug-load was found to be 6.3 wt% for drug-loaded nanogels and 6.5 wt% for TMR-conjugated drug-loaded nanogels which were later used in the biological studies.

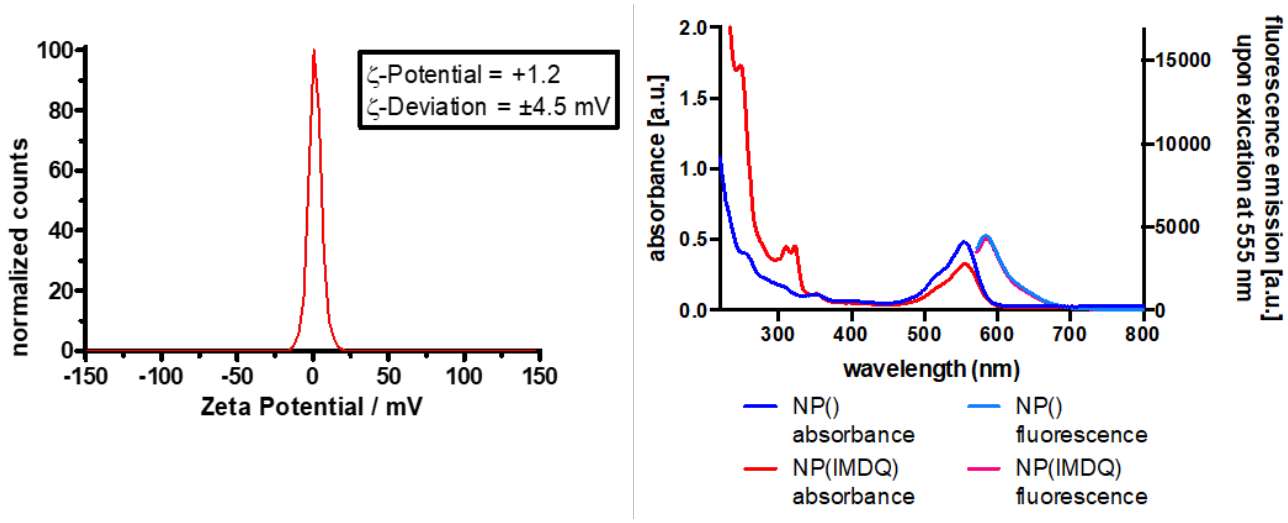

Figure S15: Zeta potential curve of nanogel (left) show a neutral zeta potential which shows the defined synthesis of nanogels without formation of positive or negative species. Absorption and fluorescence emission spectra (right) shows that loaded (red) and non-loaded nanogels (blue) have identical fluorescence intensity.

DLS Degradation Studies

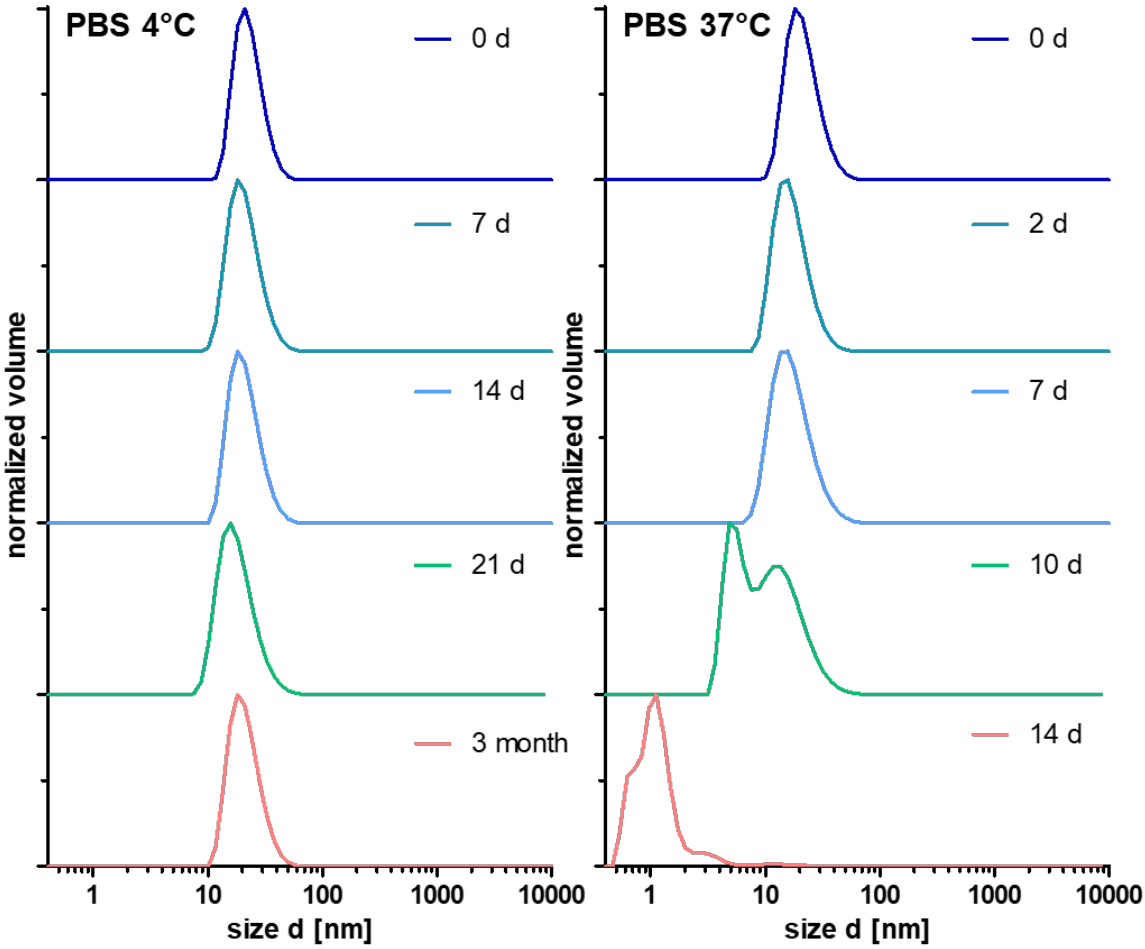

Figure S16: Size of nanogels during incubation in PBS (pH 7.4) at 4 °C (left) and 37 °C (right) during different time points as investigated by DLS volume distribution analysis. Particles remain stable at 4 °C over a period of more than 3 month and are degraded at 37 °C with steady decline in size. Thereby it was shown that at 37 °C not only particle concentration is decreasing as investigated by dropping derived count rates but also that the nanogels disintegrate as shown by decreasing particle sizes over-time.

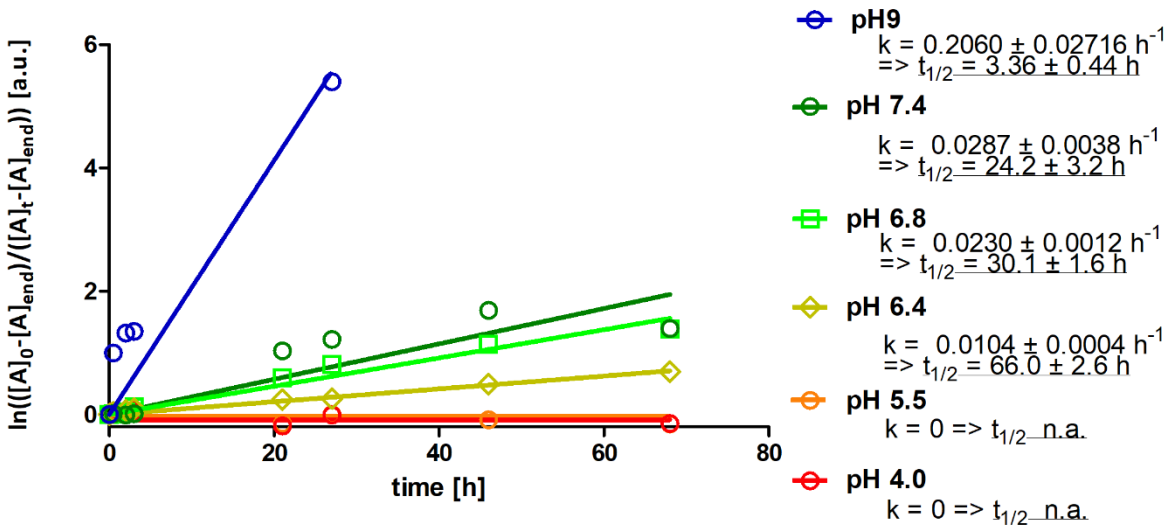

Figure S17: Logarithmic plots of nanogel degradation in different media at pH 4.0, 5.5, 6.4, 6.8, 7.4 and 9.0 to determine first-order kinetic decay of nanogels with the respective rate constants investigated by DLS ([A]: recorded scattering intensity). Nanogels are stable at 4.0 and 5.5 and decay with a half-life of ~66 h in PBS at pH 6.4, ~30 h at pH 6.8 and ~24 h at pH 7.4. In alkaline media of pH 9.0 the decay progresses even faster with half-life of ~3 h.

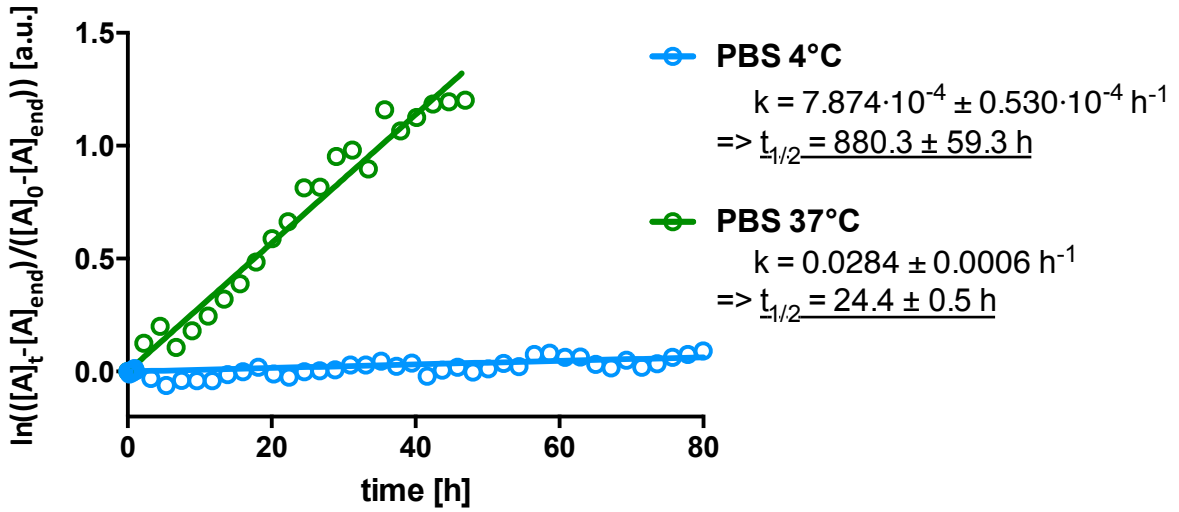

Figure S18: Temperature-dependence of nanogel behavior in PBS at pH 7.4 investigated by DLS ([A]: recorded scattering intensity). Logarithmic plots of the decay at 4 °C (blue) and 37 °C (green) in PBS with the respective rate constants assuming first order-kinetics. Compared to rapid decay at 37 °C with a half-life time of 24 h, high stability was found for 4 °C with a half-life time of ~880 h.

FCS Degradation Studies

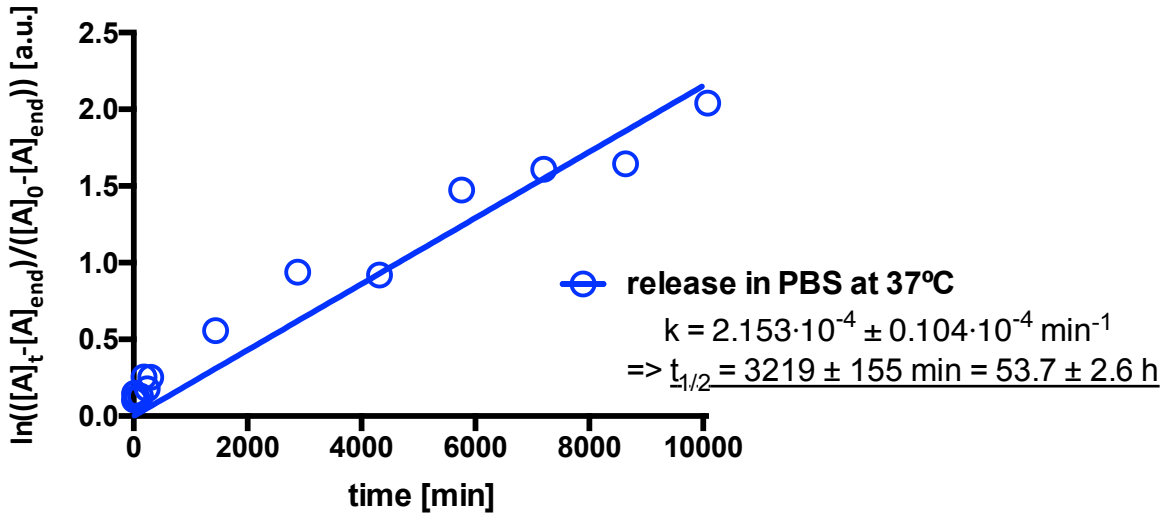

Figure S19: Release of covalently attached tetramethyl rhodamine (TMR-dye) from the nanogel core in PBS (pH 7.4) at 37 °C investigated by FCS ([A]: fraction of recorded intact particle). TMR is a traceable model compound to determine small molecular release.

Multi-angle DLS Characterization in PBS and DLS in Human Blood Plasma

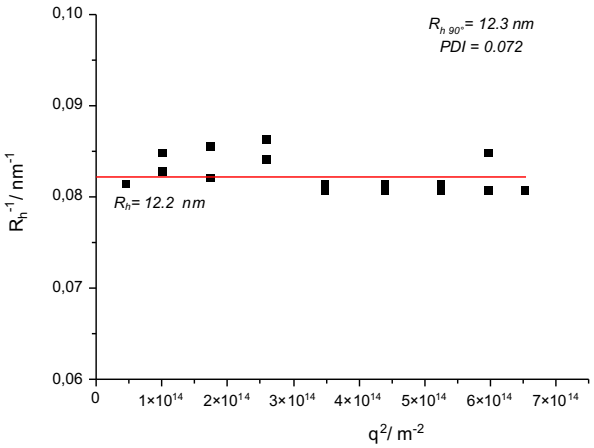

Figure S20: Multiangle DLS measurement of polycarbonate nanogel. Nanogels have a radius of 12.3 nm (diameter of 24.6 nm) and a narrow monomodal PDI of 0.072. Data matches prior analysis with DLS at 173° (by Malvern ZetaSizer).

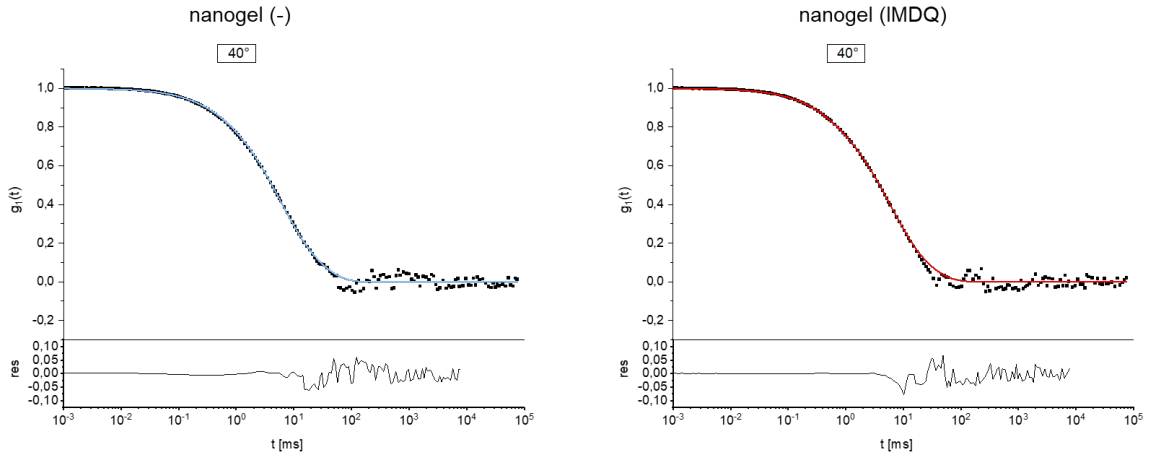

Figure S21: Plasma aggregation studies of non-loaded polycarbonate nanogels (left graph) and IMDQ-loaded nanogels (right graph) by DLS measurements at 40° scattering angle. The particles were incubated for 1 h at 37 °C with human blood plasma at pH 7.4. Then multiangle DLS measurements were performed. Fitting of the curve shows that no aggregation occurs upon incubation of both non-loaded (left) and IMDQ-loaded (right) polycarbonate nanogels with plasma proteins (bottom part of the graphs). Therefore, it was concluded that drug-loading with IMDQ does not alter the performance of the nanogels in complex biological environments.

NMR Degradation Studies

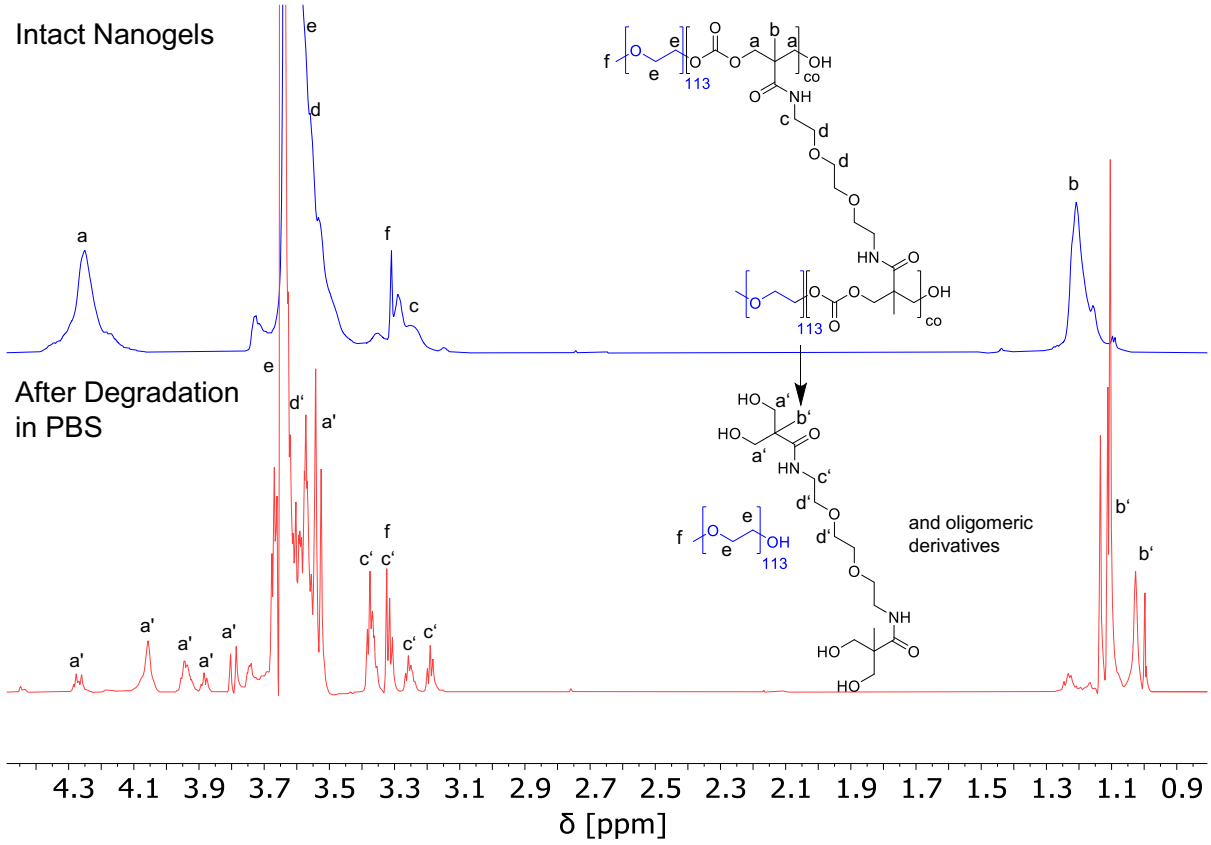

Figure S22: Conventional ^{1}H NMR spectrum of nanogels before (upper part) and after degradation (bottom part) in PBS at room temperature. Peaks of the polycarbonate backbone (a) shift towards higher field (a') during the formation of oligomeric degradation products. Moreover, the methyl side-group signal (b) shifts to (b') and novel sharp signals emerge (c', d') from broader signals (c, d). Occurrence of multiple signals and rising signal complexity indicates formation of diverse small molecular products from single and broader polymeric signals. Overall, additional signals arise due to the inability of conventional ^{1}H-NMR to visualize protons in a densely interlinked nanoparticular core.

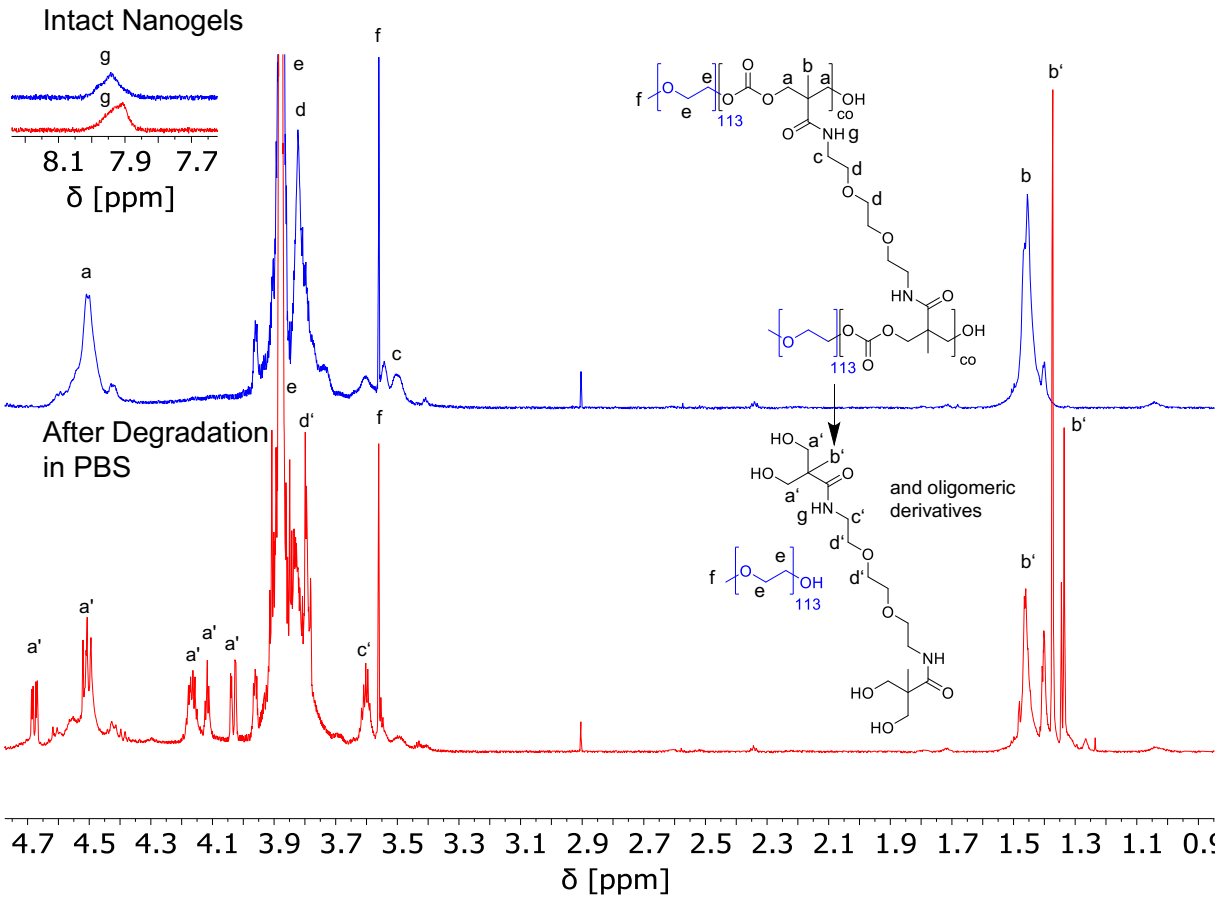

Figure S23: High-Resolution Magic Angle Spinning (HRMAS) ^{1}H NMR measurement of core-cross-linked nanogels before (top) and after degradation (bottom). Compared to conventional ^{1}H NMR the signal g of the amid proton was additionally detectable and polycarbonate as well as linker protons were quantifiable to larger extents whereas, conventional ^{1}H NMR only allows incomplete quantification.

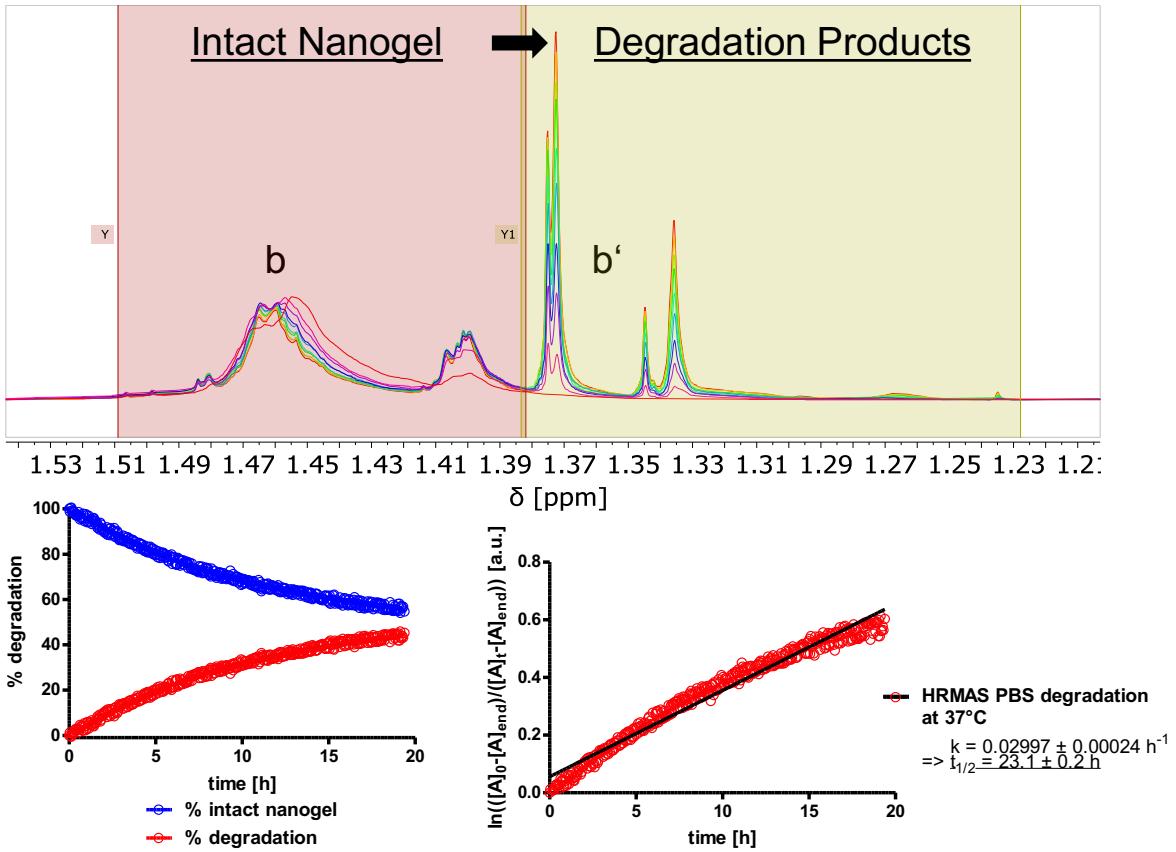

Figure S24: Kinetic degradation of nanogels in PBS at 37 °C investigated by HRMAS ^{1}H NMR measurements. Upon polycarbonate degradation, smaller fragments are formed and thereby signals of the methyl side chains of the polymer b shift towards smaller values of released molecules (b'). Integral of signal b was attributed to intact nanogels whereas b' was attributed to the degradation products and plotted against the degradation time (A: fraction of intact particle). Assuming first order kinetics a nanogel half-life of ~23 h was found which is comparable with half-lives found in previous analysis in FCS and DLS.

Mass Spectrometry Degradation Studies

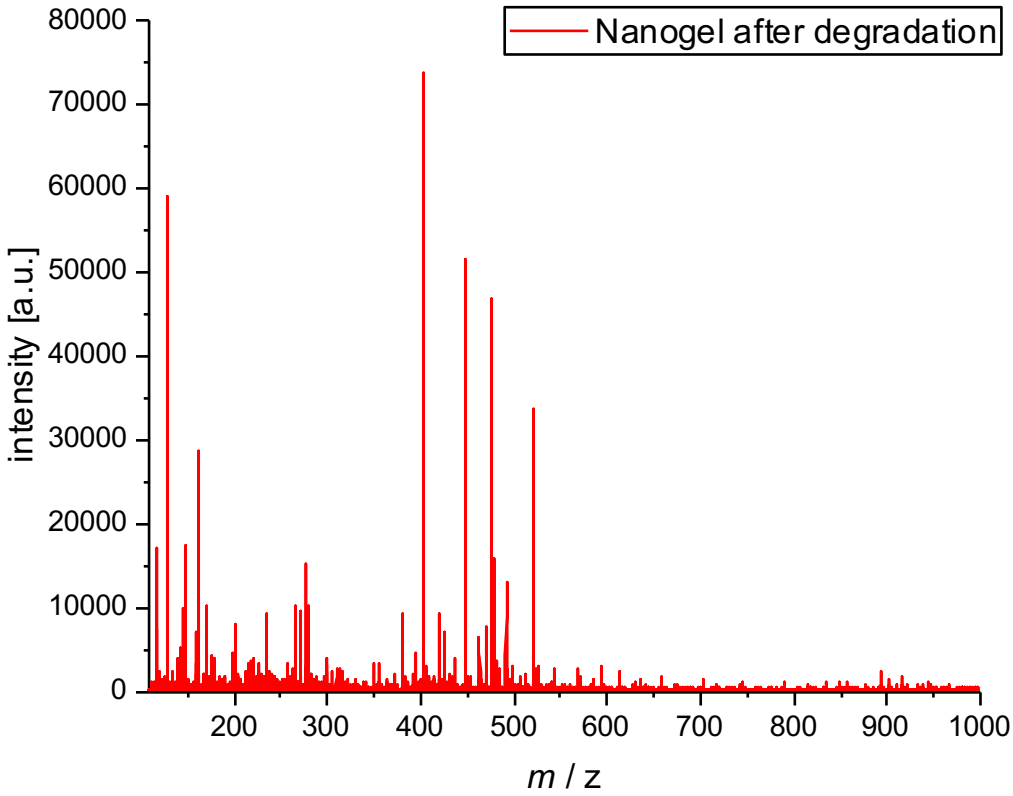

Figure S25: Mass spectrometric analysis (ESI-MS) of the degradation products from drug-loaded nanogels (without TMR-labeling). The assigned products for the degradation of drug and cross-linker were found in the range of 400 to 500 m/z, as indicated in Figure 4E.

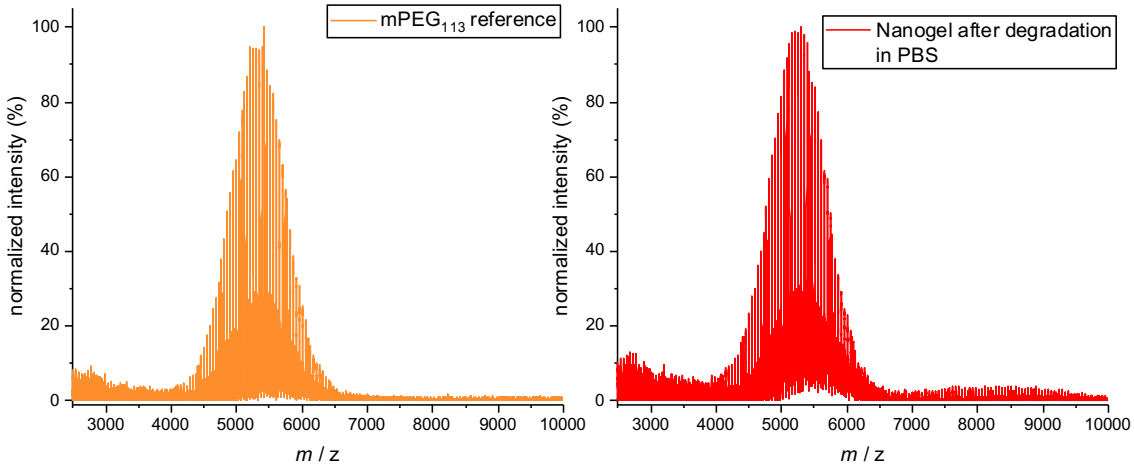

Figure S26: Mass spectrometric analysis (MALDI-ToF) of nanogel after degradation (red) in PBS. $mPEG_{113}$ was measured as a reference (orange). After degradation of the nanogels only $mPEG_{113}$ was found, showing the complete degradability of the polycarbonate blocks. Thereby it was proven that only hydrophilic molecules are yielded after degradation that should be clearable *via* the kidney.

In vitro Experiments

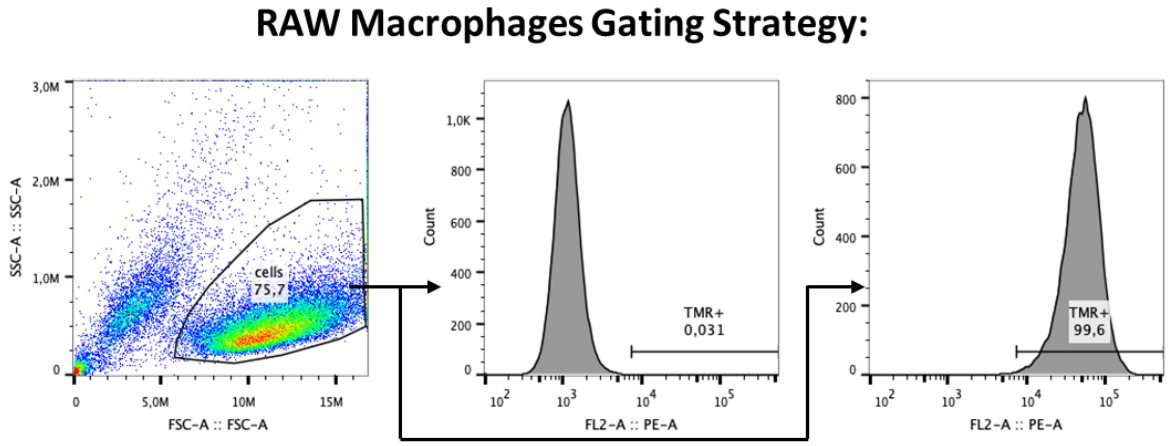

Figure S27: Gating Strategy for uptake experiments by FACS analysis of TMR-labeled nanogels in RAW Macrophages. The population of living cells was preselected by scattering detectors (left). Living cells incubated with PBS (middle) show negligible TMR+ counts above the gate value for TMR fluorescence. Incubation of macrophages with NP(IMDQ) nanogels at 100 µg/mL (right) results in 99.6% of TMR positive cells, confirming the strong uptake of these particles.

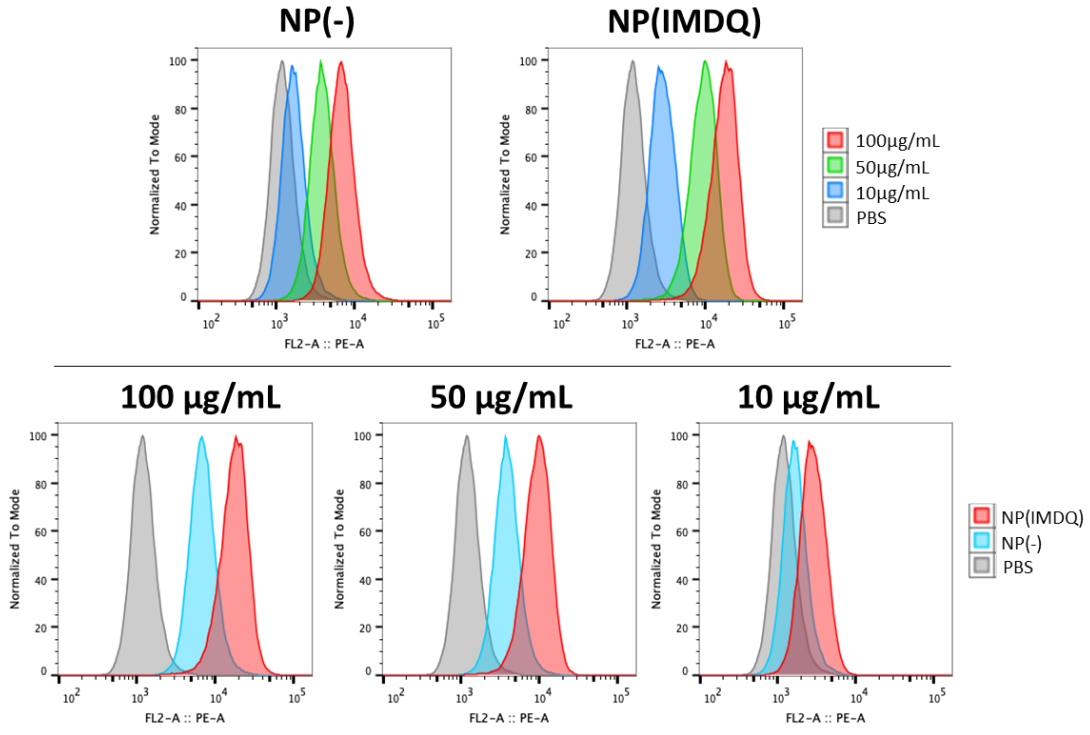

Figure S28: FACS uptake analysis in Raw Blue macrophages for TMR-labeled NP(-) and NP(IMDQ) nanogels at different concentrations. For NP(-) and NP(IMDQ) a concentration dependent increase of +TMR cells was found (top part). At same concentrations NP(IMDQ) shows higher uptake compared to NP(-).

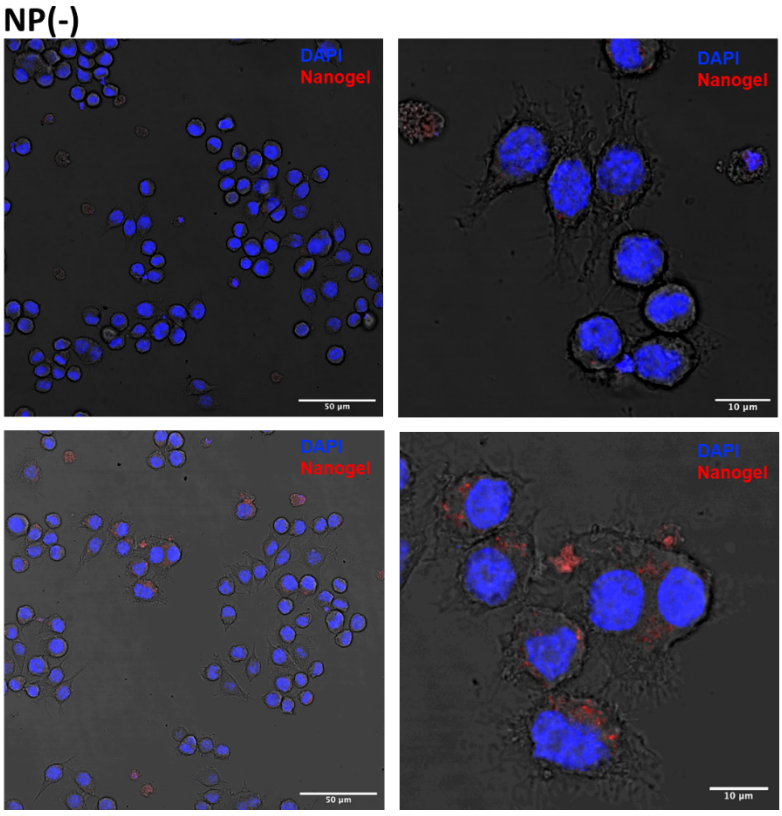

Figure S29: Additional confocal microscopy images of Raw Blue macrophages incubated with NP(-) nanogels (100 µg/mL). Nuclei were stained with DAPI dye and TMR-fluorescence is shown in red.

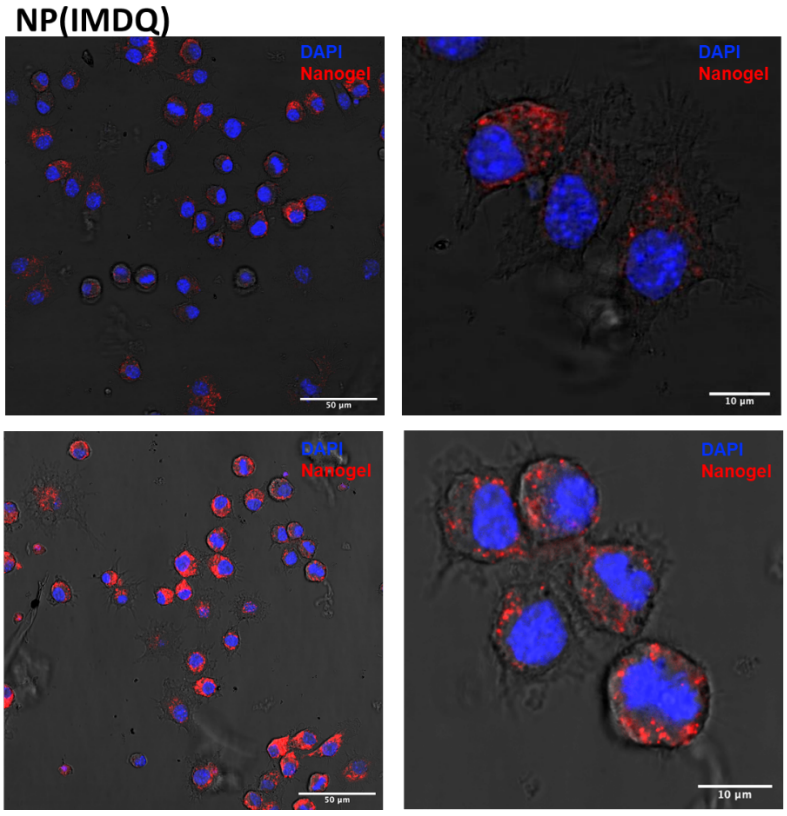

Figure S30: Additional confocal microscopy images of Raw Blue macrophages incubated with NP(IMDQ) nanogels (100 µg/mL). Nuclei were stained with DAPI dye and TMR-fluorescence is shown in red. The increased uptake for NP(IMDQ) was also found by confocal images as can be seen by larger amounts of red TMR fluorescence.

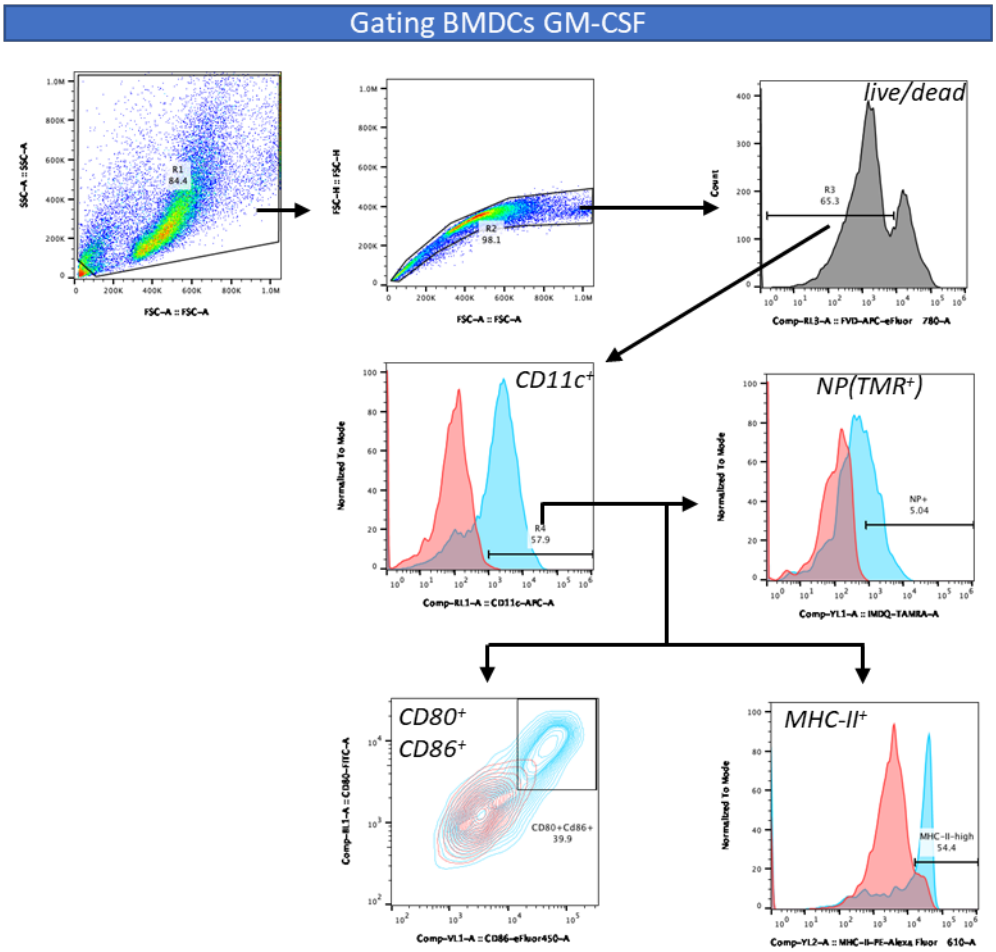

Figure S31: Gating strategy for GM-CSF BMDCs for determination of CDc11^{+} dendritic cells. Their uptake of nanogels was determined by TMR^{+}, while their maturation was characterized by the expression of CD80^{+}CD86^{+} and MHC-II^{+}.

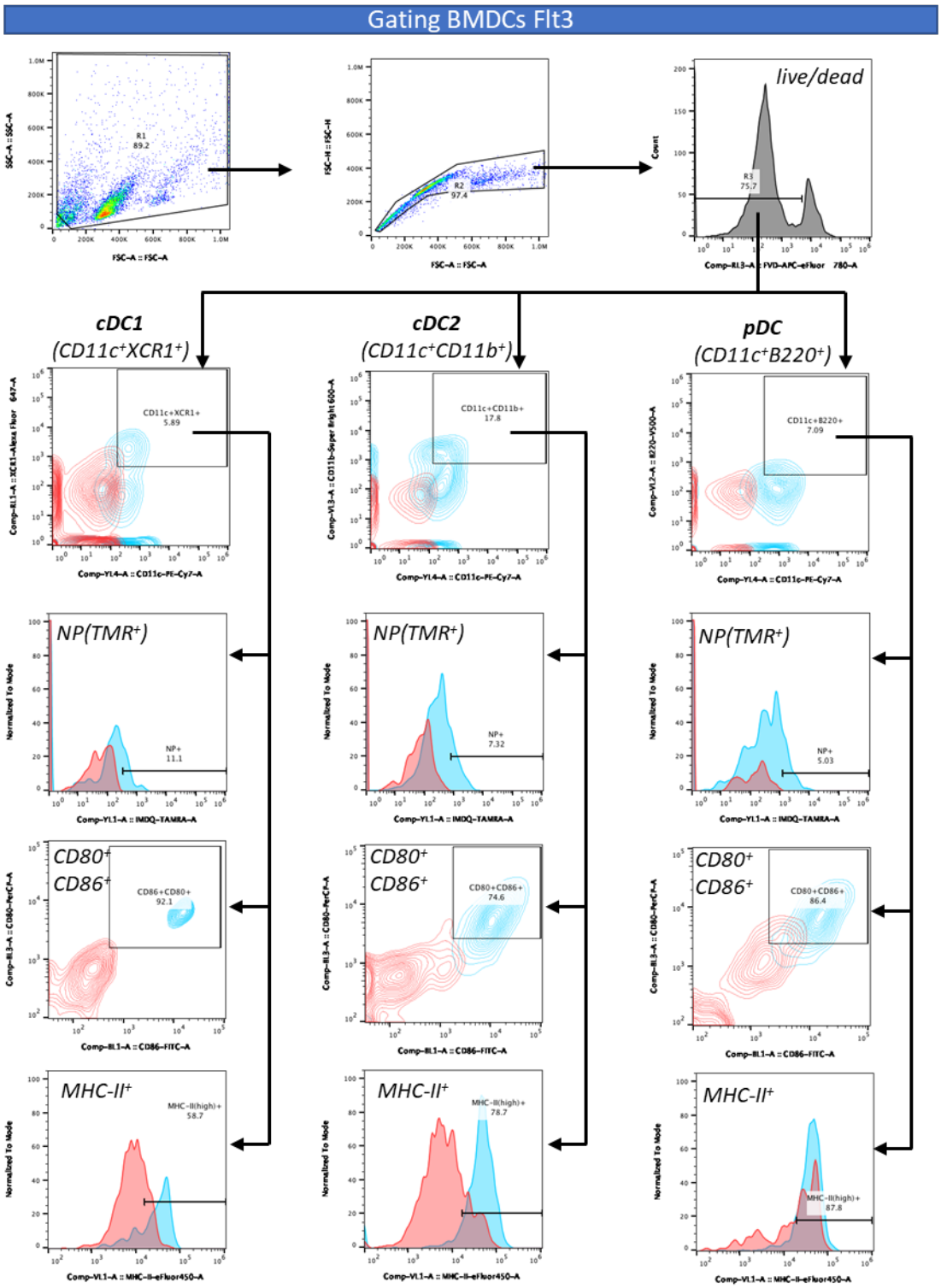

Figure S32: Gating strategy for Flt3 BMDCs for cDC1 as $CD11c^+XCR1^+$, cDC2 as $CD11c^+CD11b^+$, and pDCs as $CD11c^+B220^+$. Their uptake of nanogels was determined by TMR^+, while their maturation was characterized by the expression of $CD80^+CD86^+$ and MHC-II^+.

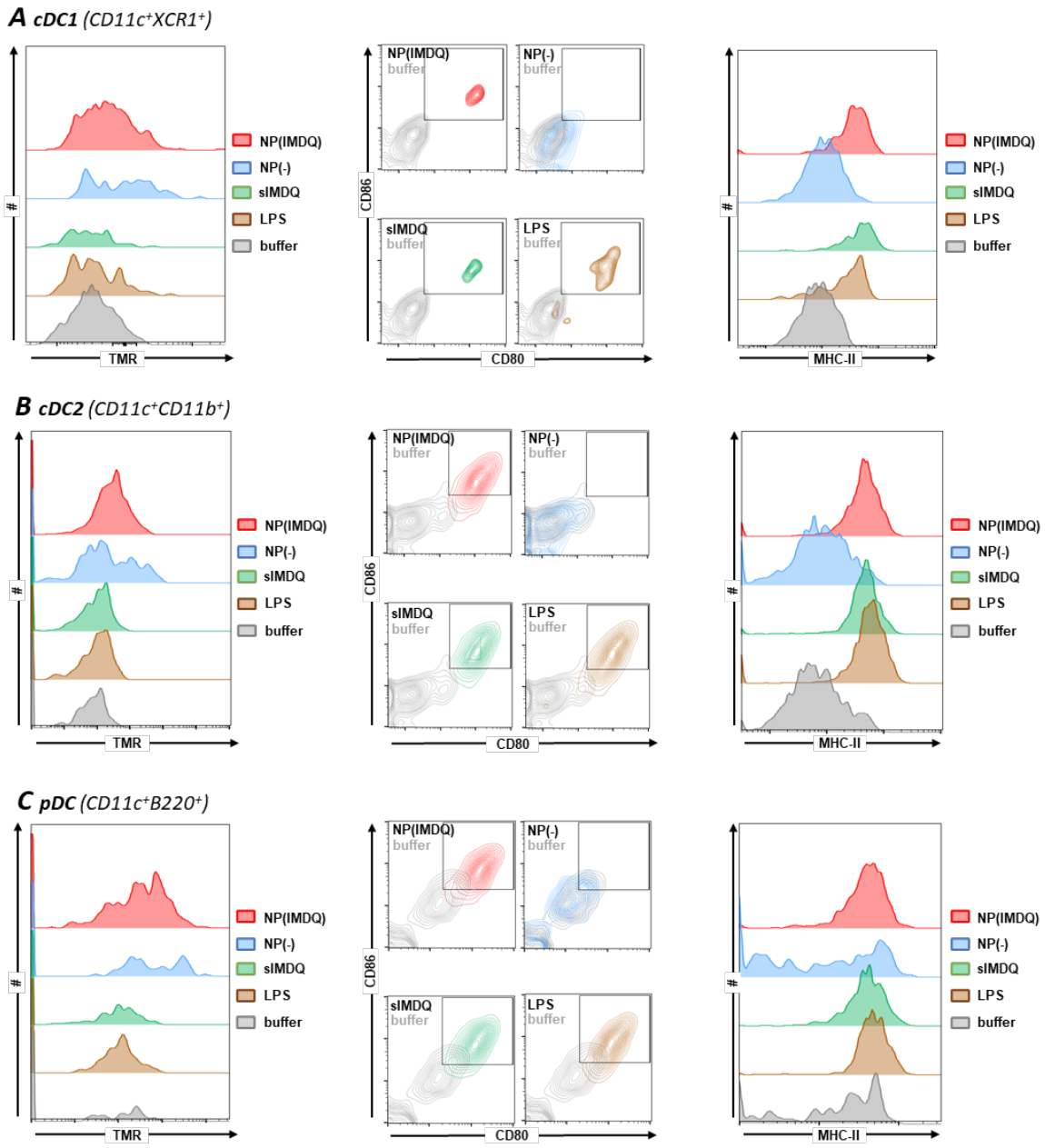

Figure S33: FACS analysis of cDC1 (A), cDC2 (B) and pDC (C) of Flt3 BMDCs regarding the uptake of the TMR-labeled nanogel (left) and the activation of the maturation markers CD80 and CD86 (middle) as well as MHC-II (right).

In vivo Experiments

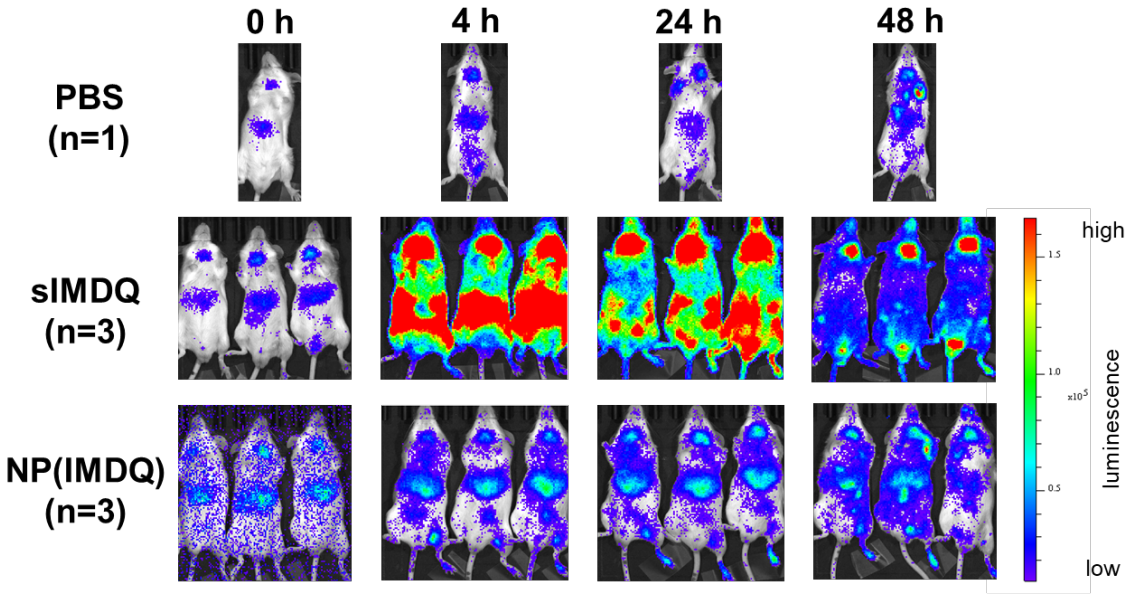

Figure S34: NP(IMDQ)-mediated local activation of draining lymph nodes by subcutaneous footpad injection. Additional images of immune activation in IFN-β luciferase reporter (IFN-$\beta^{+/\Delta\beta\text{-luc}}$) mice at 0 h, 4 h, 24 h and 48 h for PBS control, sIMDQ and NP(IMDQ). In contrast to the small molecule sIMDQ, the immunodrug-loaded nanogels NP(IMDQ) provides a lymph node-focused immune cell activation.

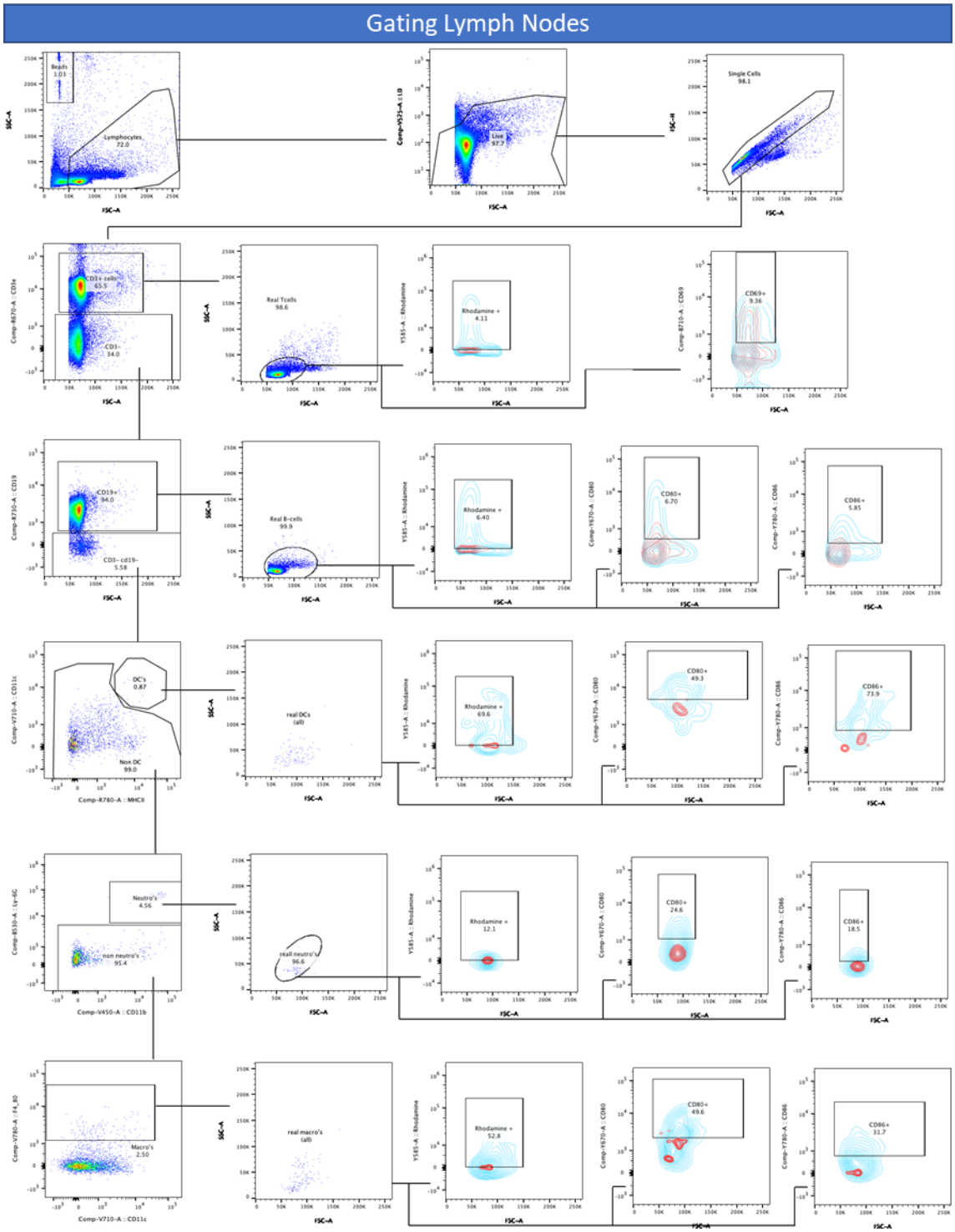

Figure S35: Gating strategy for FACS analysis of dissected lymph nodes after subcutaneous footpad injection of NP(IMDQ)-mediated local activation of draining lymph nodes. T-cells were characterized as $CD3^+$, B-cells as $CD3^-CD19^+$, DCs as $CD3^-CD19^-CD11c^+$, neutrophils as $CD3^-CD19^-CD11c^-Ly6G^+CD11b^+$, and macrophages as $CD3^-CD19^-CD11c^-Ly6G^-F4/80^+$. Their uptake of nanogels was determined by TMR(Rhodamine)$^+$, while their maturation was characterized by the expression of $CD80^+$ and $CD86^+$ (or $CD69^+$ for T-cells).

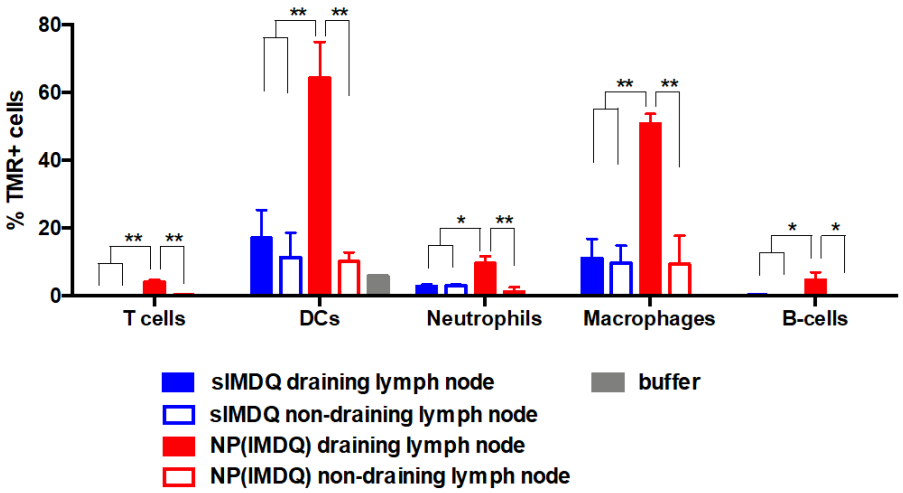

Figure S36: FACS analysis of TMR-labeled NP(IMDQ) uptake in different types of immune cell populations residing in draining and non-draining lymph nodes, as analyzed by fraction of TMR^+ cells (n = 3) (*: $p \leq 0.05$; **: $p \leq 0.01$).

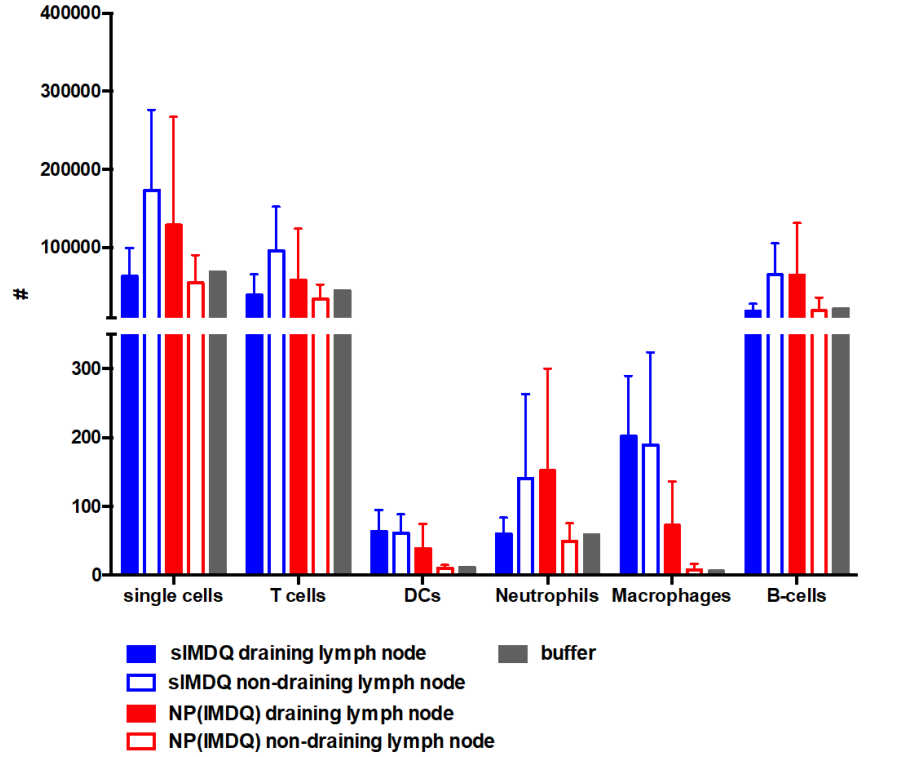

Figure S37: Absolute cell counts of immune cell populations in draining versus non-draining lymph nodes after treatment with sIMDQ or NP(IMDQ).

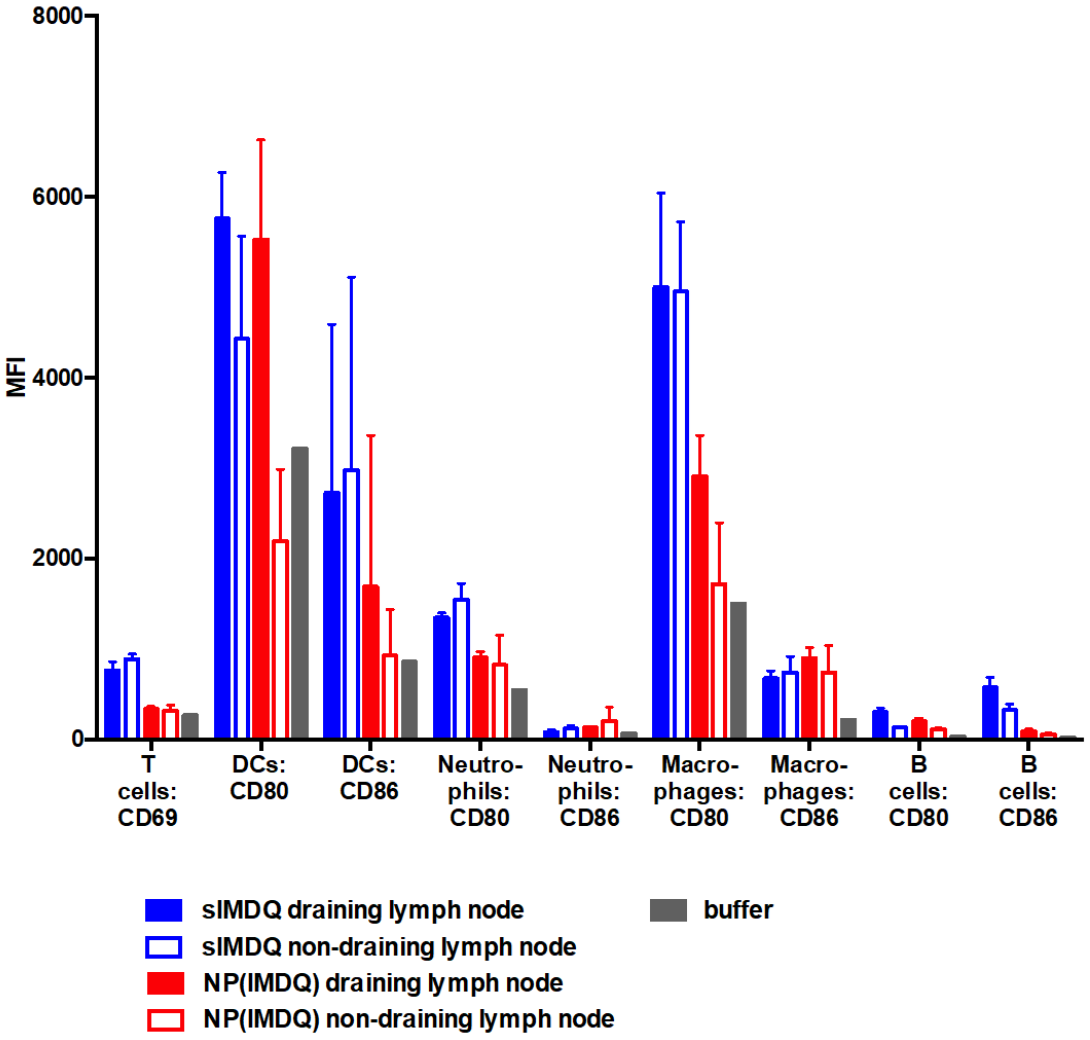

Figure S38: Mean fluorescence intensities in different cell populations with respective activation markers in draining versus non-draining lymph nodes after treatment with sIMDQ and NP(IMDQ).

Additional References

[1] D. P. Sanders, K. Fukushima, D. J. Coady, A. Nelson, M. Fujiwara, M. Yasumoto, J. L. Hedrick, *J. Am. Chem. Soc.* **2010**, *132*, 14724.

[2] A. C. Engler, J. M. W. Chan, D. J. Coady, J. M. O'Brien, H. Sardon, A. Nelson, D. P. Sanders, Y. Y. Yang, J. L. Hedrick, *Macromolecules* **2013**, *46*, 1283.

10.9. Publication 9

"Nanostructured lipid carriers loaded with dexamethasone (DXM) prevent inflammatory responses in primary non-parenchymal liver cells"

This study has been published in MDPI (Pharmaceutics). As a shared-first author, I was responsible for the performance of several *in vitro* biological experiments testing DXM-loaded lipid NPs on liver non-parenchymal cells.

In this work, my collaborators from La Universidad de la Plata in Argentina designed nanostructured lipid carriers for efficient encapsulation and intracellular release of DXM. This nano-formulation proved to be stable over time, did not interact *in vitro* with plasma opsonins, and was well tolerated by primary liver NPCs. Released DXM preserved its pharmacological activity as evidenced by inducing robust anti-inflammatory responses in NPCs. Taken together, nanostructured lipid carriers may constitute a reliable platform for the delivery of DXM to treat pathologies associated with chronic liver inflammation.

DOI: 10.3390/pharmaceutics14081611

Published in: *Pharmaceutics.* **2022** Aug 2;14(8):1611

Reprinted with permission under creative commons attribution 4.0 (CC BY-NC) from **Medina-Montano* C**, Rivero Berti I*, Gambaro RC, Limeres MJ, Svensson M, Padula G, Chain CY, Cisneros JS, Castro GR, Grabbe S, Bros M, Gehring S, Islan GA, Cacicedo ML. Nanostructured Lipid Carriers Loaded with Dexamethasone Prevent Inflammatory Responses in Primary Non-Parenchymal Liver Cells. Pharmaceutics. 2022 Aug 2;14(8):1611. doi: 10.3390/pharmaceutics14081611. PMID: 36015237; PMCID: PMC9413549.

***** Authors contributed equally

pharmaceutics

MDPI

Article

Nanostructured Lipid Carriers Loaded with Dexamethasone Prevent Inflammatory Responses in Primary Non-Parenchymal Liver Cells

Carolina Medina-Montano [1,†], Ignacio Rivero Berti [2,†], Rocío C. Gambaro [3], María José Limeres [4], Malin Svensson [4], Gisel Padula [3], Cecilia Y. Chain [5], José Sebastián Cisneros [5], Guillermo R. Castro [6], Stephan Grabbe [1], Matthias Bros [1], Stephan Gehring [4], German A. Islan [2,*] and Maximiliano L. Cacicedo [4,*]

1 Department of Dermatology, University Medical Center of the Johannes Gutenberg University Mainz, Langenbeckstraße 1, 55131 Mainz, Germany; gmedinam@students.uni-mainz.de (C.M.-M.); stephan.grabbe@unimedizin-maiz.de (S.G.); mbros@uni-mainz.de (M.B.)
2 Laboratorio de Nanobiomateriales, Centro de Investigación y Desarrollo en Fermentaciones Industriales (CINDEFI), Departamento de Química, Facultad de Ciencias Exactas, Universidad Nacional de La Plata (UNLP)-CONICET (CCT La Plata), Calle 47 y 115, La Plata B1900, Argentina; iriveroberti@gmail.com
3 Instituto de Genética Veterinaria (IGEVET, UNLP-CONICET La Plata), Facultad de Ciencias Veterinarias, Universidad Nacional de La Plata (UNLP), La Plata B1900, Argentina; rociogambaro@gmail.com (R.C.G.); gpadula@igevet.gob.ar (G.P.)
4 Children's Hospital, University Medical Center of the Johannes-Gutenberg University Mainz, Langenbeckstr. 1, 55131 Mainz, Germany; mj.limeres@uni-mainz.de (M.J.L.); malin.svensson@uni-mainz.de (M.S.); stephan.gehring@uni-mainz.de (S.G.)
5 Instituto de Investigaciones Fisicoquímicas Teóricas y Aplicadas (CONICET-UNLP), La Plata B1900, Argentina; yamil@inifta.unlp.edu.ar (C.Y.C.); josesebastiancisneros@biol.unlp.edu.ar (J.S.C.)
6 Max Planck Laboratory for Structural Biology, Chemistry and Molecular Biophysics of Rosario (MPLbioR, UNR-MPIbpC), Partner Laboratory of the Max Planck Institute for Biophysical Chemistry (MPIbpC, MPG), Centro de Estudios Interdisciplinarios (CEI), Universidad Nacional de Rosario, Maipú 1065, Rosario S2000, Argentina; grcastro@gmail.com
* Correspondence: mcaciced@uni-mainz.de (M.L.C.); germanislan@biol.unlp.edu.ar (G.A.I.)
† These authors contributed equally to this work.

check for updates

Citation: Medina-Montano, C.; Rivero Berti, I.; Gambaro, R.C.; Limeres, M.J.; Svensson, M.; Padula, G.; Chain, C.Y.; Cisneros, J.S.; Castro, G.R.; Grabbe, S.; et al. Nanostructured Lipid Carriers Loaded with Dexamethasone Prevent Inflammatory Responses in Primary Non-Parenchymal Liver Cells. *Pharmaceutics* **2022**, *14*, 1611. https://doi.org/10.3390/pharmaceutics14081611

Academic Editor: Sophia G. Antimisiaris

Received: 1 July 2022
Accepted: 29 July 2022
Published: 2 August 2022

Publisher's Note: MDPI stays neutral with regard to jurisdictional claims in published maps and institutional affiliations.

Copyright: © 2022 by the authors. Licensee MDPI, Basel, Switzerland. This article is an open access article distributed under the terms and conditions of the Creative Commons Attribution (CC BY) license (https://creativecommons.org/licenses/by/4.0/).

Abstract: Liver inflammation represents a major clinical problem in a wide range of pathologies. Among the strategies to prevent liver failure, dexamethasone (DXM) has been widely used to suppress inflammatory responses. The use of nanocarriers for encapsulation and sustained release of glucocorticoids to liver cells could provide a solution to prevent severe side effects associated with systemic delivery as the conventional treatment regime. Here we describe a nanostructured lipid carrier developed to efficiently encapsulate and release DXM. This nano-formulation proved to be stable over time, did not interact in vitro with plasma opsonins, and was well tolerated by primary non-parenchymal liver cells (NPCs). Released DXM preserved its pharmacological activity, as evidenced by inducing robust anti-inflammatory responses in NPCs. Taken together, nanostructured lipid carriers may constitute a reliable platform for the delivery of DXM to treat pathologies associated with chronic liver inflammation.

Keywords: glucocorticoids; lipid nanoparticles; liver inflammation; liver immunology; autoimmune hepatitis; dexamethasone; drug-controlled release

1. Introduction

Chronic liver inflammation is a characteristic of pathologies, such as chronic viral hepatitis and autoimmune hepatitis [1,2]. In these patients, persistent inflammation has been described as the main cause of hepatic fibrosis and cirrhosis [3]. Potential approaches to inhibit the fibrotic process mainly include strategies to suppress inflammation, by reducing viral load and downregulating liver NPC-driven immune response [4]. During

recent decades, synthetic glucocorticoids have been widely used for the treatment of liver diseases. Although dexamethasone (DXM) possesses remarkable anti-inflammatory action, its use also leads to severe adverse effects, mainly due to immunosuppression [5]. Moreover, administration of synthetic glucocorticoids, such as DXM, to pediatric patients has been associated with severe adverse effects, like gastrointestinal perforation and decreased growth [6,7]. Multiple nanomedicine-related strategies have been studied to counteract these side effects associated with systemic delivery of soluble DXM. One of the main advantages of such approaches is the frequent observation that nanoparticles (NPs), after systemic administration, usually accumulate in the liver [8]. Furthermore, it is well established that NPs within the liver most often engage with liver non-parenchymal cells (NPCs), comprising mainly macrophages like Kupffer cells (KCs) and liver sinusoidal endothelial cells (LSECs) [9]. Both cell types are well recognized as protagonists in the modulation of liver inflammation [10,11]. For years we and others have evaluated strategies to load NPs with DXM aiming to decrease liver inflammation, while avoiding systemic adverse effects [12–16]. Nevertheless, no DXM-loaded NP has been successfully transferred to the clinic so far [17]. The most common difficulties associated with encapsulation of relatively small molecules like DXM are low encapsulation efficiency, poor formulation stability and unsuccessful drug release kinetics [18,19].

In this context, solid lipid nanoparticles (SLNs) have been described as stable and well-tolerated NPs for drug delivery [20]. The development of SLNs introduced advantages over other lipid-based nano-carriers, such as the avoidance of non-aqueous solvents during the synthesis process and the easy access to upscaling processes [21]. Despite these beneficial characteristics, low drug loading efficiency and poor stability over time limited the application of SLNs as drug carriers [22]. To overcome such limitations, a second generation of lipid nanoparticles, called nanostructured lipid carriers (NLCs) was developed [23,24]. Notably, during the synthesis process, the incorporation of a liquid lipid generates an amorphous zone inside the crystalline matrix of the lipid nanoparticle. In this regard, creating a less ordered solid lipid matrix leads to a higher drug loading efficiency. Drug molecules self-arrange in the spaces between fatty acid chains and in the amorphous areas of the liquid lipid, forming drug clusters [22]. We have recently demonstrated the flexibility and reliability of an NLC platform, by reporting on the suitability of multiple NLC-based formulations for the delivery of different types of drugs [25–33].

It is worth mentioning that DXM is generally considered to be a hydrophobic drug [34,35]. Thus, the hydrophobic nature of NLCs could potentially provide a notable environment for DXM delivery. In the study presented here, a novel NLC formulation has been developed for the encapsulation and sustained release of DXM (NLCs-DXM). By changing the liquid lipid ratio within the formulation, we obtained candidates with different DXM encapsulation efficiencies and physicochemical characteristics. The top candidate showed high DXM loading, persistent stability over time, and sustained DXM release, as well as negligible interaction with plasma proteins that could diminish the in vivo circulation time. We further observed no hemotoxic effects of these NLCs-DXM in human blood. Moreover, functional effects of NLCs-DXM were evaluated in primary cultures of murine NPCs. NLCs were internalized by NPCs in a dose-dependent manner. DXM released from NLCs showed pharmacological activity, as evidenced by decreasing levels of inflammatory cytokines (IL-6 and TNF-α) in LPS-stimulated NPCs. As another indication of anti-inflammatory effects, both soluble DXM and NLCs-DXM decreased levels of the conventional activation marker CD86 in stimulated LSECs and DCs. Finally, delayed release of biologically active DXM from NLCs was confirmed in time kinetics studies using a NF-κB reporter cell line. Taken together, these findings suggest that NLCs could provide a reliable platform for the delivery of DXM to the liver. This approach would be beneficial for improving the treatment of pathologies associated with chronic liver inflammation.

2. Materials and Methods

2.1. Materials

Myristyl myristate (Crodamol™, MM) and the oil (Crodamol™ GTCC-LQ) were donated by Croda (Buenos Aires, Argentina). Poloxamer 188 (Pluronic® F68) and Dexamethasone (DXM) were purchased from Sigma-Aldrich (Buenos Aires, Argentina). All other reagents (buffers, solvents) were of analytical grade.

2.2. Preparation of DXM Loaded Nanostructured Lipid Carriers (NLC)

DXM-loaded NLCs were prepared by the hot-homogenization and ultra-sonication method, based on previous protocols from our laboratory [28,29]. Briefly, 400 mg of MM lipid (2.0% *w*/*v*, weight/volume; melting point 36–40 °C) was melted at 60–70 °C in a water bath, followed by the addition of 10 mg of DXM. Different amounts of liquid oil ranging from 0–100 µL were added to the lipidic phase to produce the different NLC formulations (F1–F4). After ten minutes, a pre-warmed aqueous solution (20 mL) containing 3.0% *w*/*v* poloxamer 188 was added to the melted lipid phase. Then, the mixture was sonicated in an ultrasonic processor at 80% amplitude for 30 min (130 W, Cole-Parmer, Vernon Hills, IL, USA; 6 mm titanium tip). The dispersion was cooled first at room temperature, and then stored at 4 °C.

2.3. Analytical Detection of DXM

The analytical determination of DXM in the range of 0–50 µg/mL was performed by UV-Vis spectrophotometry in a microplate reader (TECAN Infinite 200 PRO, Crailsheim, Germany) at λ_{max} = 242 nm.

2.4. Determination of Encapsulation Efficiency (EE) and Drug Loading (DL)

After NLCs were prepared, 500 µL of the formulation was transferred to an ultrafiltration centrifugal device (MWCO 3000, Microcon, Millipore, MA, USA) and centrifuged at 10,000× *g* and 25 °C for 10 min in a microcentrifuge (Eppendorf MiniSpin, Hamburg, Germany). The DXM concentration in the filtered solution was determined by UV-Vis spectrophotometry (microplate reader TECAN Infinite 200 PRO, Männedorf, Switzerland). The EE and DL were calculated as follows:

$$\text{EE } (\%) = \frac{(Q_0 - (C_r \times V)) \times 100}{Q_0} \quad (1)$$

$$\text{DL} = \frac{\text{Mass of encapsulated DXM } (\mu g)}{\text{Mass of MM lipid matrix } (mg)} \quad (2)$$

Q_0 (initial mass of DXM); C_r (DXM concentration measured in the filtered solution); V (final volume of the formulation).

2.5. Particle Size, Zeta Potential (Z pot), and Polydispersity Index (PDI)

The mean diameter, size distribution (PDI), and zeta potential (Z pot) of the NLC formulations were determined in a Nano ZS Zetasizer (Malvern Instruments Corp., Malvern, UK) in polystyrene cuvettes with a path length of 10 mm at 25 °C and in capillary cells with a path length of 10 mm, using Milli-Q water. All measurements were carried out in triplicate.

The stability of the formulations was followed up by testing particle size, Z pot, and NLC drug content (EE) for up to 12 months.

2.6. Transmission Electron Microscopy (TEM)

The formulations were diluted with Milli-Q water (1:10), and a drop of the dispersion was spread onto a 400-mesh collodion-coated Cu grid (Merck KGaA, Darmstadt, Germany). Phospho-tungstic acid was added to enhance contrast. Images were observed in a Jeol-1200 EX II-TEM microscope (Jeol, MA, USA).

2.7. In Vitro Release of DXM

The various NLC formulations were placed into dialysis devices (1 mL; Spectra-Por® Float-A-Lyzer® G2, MWCO $\frac{1}{4}$ 100 kDa), followed by incubation in a Falcon tube with 30 mL of 10 mM phosphate buffer saline (PBS) at pH 7.4 and 37 °C. Additionally, a DXM solution with equivalent concentration as formulations was prepared to estimate the diffusive effect through the dialysis device. The release assays were performed in an orbital shaker (DLAB-HM100 Pro) at 100 rpm. Samples of 300 µL were retrieved and scanned with an UV-Vis spectrophotometer (TECAN-infinite M200 Pro) at intervals of 1, 2, 3, 4, 5, 6, and 24 h to determine concentrations of released DXM. The fitting curve tool of SigmaPlot 10.0 Notebook program (Systat Software Inc., San José, CA, USA) was used to fit the experimental data according to four release-mechanism models from the fit library.

2.8. Hemotoxicity Studies

Heparinized venous blood was obtained from healthy donors after written informed consent. It was centrifuged at 2500× *g* for 10 min. The plasma was discarded, and the erythrocyte concentrate was washed 3 times with PBS. Erythrocytes were diluted 1:4 in PBS. A volume of 2.0 mL was incubated with different concentrations of NLC formulations at 37 °C for 1, 24, and 72 h. After incubation, the mixture was centrifuged at 2500× *g* for 5 min and the precipitate was discarded. The percentage of lysed erythrocytes was determined by quantification of released hemoglobin at λ = 540 nm. The 100% hemolysis value was established by treatment of erythrocytes with 1%Triton X-100 for 1 h, and the negative control by incubation of erythrocytes with PBS.

2.9. In Vitro Interaction with Plasma Proteins

In order to investigate the biomolecular interactions that may occur between NLCs-DXM and plasma proteins, surface plasmon resonance (SPR) measurements were performed. In the present work, immunoglobin (IgG) and fibrinogen were tested as examples of opsonins (shown to diminish circulation time) [36] and human serum albumin (HSA) as a disopsonin (reported to enhance circulation time) [37].

Protein was immobilized by physical adsorption [38] by injecting protein solutions into a SPR Navi® 210A (BioNavis, Tampere, Finland) instrument operated at 22 °C and with λ= 785 nm. Samples of HSA, IgG and fibrinogen (each 100 µg/mL) in 10 mM sodium acetate (pH 4.4) were injected (10 µL/min, 20 min) through flow cell 1 over the sensor chip in each three different individual experiments. Control surfaces were obtained by injection of buffer solution w/o protein (flow cell 2). The SPR response ($\Delta\theta_{SPR}$) was measured as the difference between the θ_{SPR} value after protein injection and the θ_{SPR} value of the baseline (before injection).

Interactions of immobilized protein with NLCs were studied by injecting a ten-fold dilution of NLCs-DXM in PBS (pH 7.4) using the SPR setup (10 µL/min, 10 min) as described above, followed by a regeneration step using 1% Triton X100 (100 µL/min, 1 min). The SPR response assigned to biomolecular interaction corresponded to the plateau of $\Delta\theta_{SPR}$ in the period between the end of the NLCs-DXM injection and the start of the regeneration step (around 720 s of each cycle).

2.10. Isolation of Liver Non-Parenchymal Cells (NPCs)

NPCs were isolated from livers of female C57BL/6J mice as previously reported [16,39]. Collected NPCs were centrifuged at 300× *g* and resuspended in ice-cold Histodenz solution (30%). Another centrifugation step at 1500× *g* at 4 °C for 20 min was performed. NPCs were collected at the HBSS/Histodenz interface using a Pasteur pipette and resuspended in RPMI 1640 medium containing 10% FCS, 1% penicillin/streptomycin, 1 mM L-glutamine, 1% essential and non-essential amino acids, 50 µM 2-mercaptoethanol (all media, buffers, and reagents from ThermoFisher Scientific, Waltham, MA, USA).

2.11. Flow Cytometry

After cell isolation, NPCs were incubated with receptor-specific antibodies for flow cytometry analysis. Cells were washed (2% FCS in PBS), and Fc receptors were blocked with a CD16/CD32-specific antibody (clone 2.4G2) for 10 min. Afterwards, NPCs were incubated with cell lineage-specific antibodies (CD45-BV711, CD32b-PE, CD11c-PE-Cy7, F4/80-eFluor450) for 20 min at 4 °C. Next, cells were washed (2% FCS in PBS) and live/dead markers (FVD-780, 7AAD) were added. Cells were washed again and subjected to flow cytometry (Attune NxT Flow Cytometer, Thermo Scientific, Waltham, MA, USA). Results were analyzed with Attune NxT Flow Cytometer Software.

2.12. Cytometric Bead Array

NPC culture supernatants were collected and stored at −20 °C. To measure TNF-α, IFN-γ, IL-6, IL-1ß, and IL-10, Cytometric Bead Assays were performed, as recommended by the manufacturer (BD Biosciences, CA, USA). Recombinant cytokines were used to prepare standard dilutions. Samples were mixed with capture beads and subsequently incubated with PE-conjugated detection antibodies for 1h (all at room temperature in the dark) and measured by flow cytometry. Results were analyzed using FCAP Array Analysis Software v.1.0.1 (BD Biosciences).

2.13. Detection of Nuclear Factor 'Kappa-Light-Chain-Enhancer' of Activated B-Cells (NF-κB) in a Raw-Blue™ Reporter Cell Line

The macrophage reporter subline RAW-Blue™ (InvivoGen, San Diego, CA, USA) was used to determine NF-κB activity. RAW-Blue™ cells express secreted embryonic alkaline phosphatase (SEAP) which is inducible by active NF-κB. Raw-Blue™ cells were incubated with 1000 µg/mL of DXM and equimolar amounts of NLC-encapsulated DXM as indicated and stimulated with LPS applied 45 min later. Supernatants (20 µL) were collected 6h and 24h after LPS stimulation. All samples were treated in parallel with Quanti Blue solution (180 µL; InvivoGen) serving as SEAP substrate according to the vendor. Finally, NF-kB activity was determined as substrate turnover by colorimetric analysis in a spectrophotometer (EMax® Pus Microplate Reader; Molecular Devises, San José, CA, USA) at 620–655 nm.

2.14. Statistical Analysis

Statistical analyses were performed with Prism software (Graphpad Software, San Diego, CA, USA) performing one- and two-way ANOVA as indicated. Data are presented as the means ± SEM. p-values < 0.05 were considered significant.

3. Results

3.1. Preparation and Characterization of DXM-Loaded NLCs

NLCs matrices combining different amounts of solid lipid with liquid oil were prepared by the ultra-sonication method [25]. The solid lipid matrix was mainly composed of MM. MM was selected as the main building block of the NLC structure, due to its low melting point (of around 40 °C), which is suitable to preserve the integrity of the encapsulated drugs and to prepare stable emulsions. MM acts as a co-emulsifier by thickening the emulsions, due to the combination of fatty alcohol and fatty acids that prevent instability caused by temperature variations. Moreover, MM is a natural product extracted from plants and has been reported to be non-toxic [25]. The addition of an inert oil (GTCC-LQ) to the NLCs' matrices aimed to modify the crystalline structure of the SLNs, without affecting their biological properties. This hypothesis was supported by previous reports from our group demonstrating that combinations of MM/GTCC-LQ oil resulted in the formation of non-toxic NLCs [28]. In the current study, stable NLC formulations were obtained by incorporating different amounts of the liquid oil into the synthesis mixture. NLCs were further characterized by the determination of EE and other physicochemical parameters, as described in Table 1. The F1 formulation, formally SLNs because of the absence of oil,

showed an EE of 86% with a mean size around 152 nm, low PDI, and negative surface charge. The addition of 25 µL of oil to the lipid phase, generated NLCs (F2) with an increased EE of 98%, a mean diameter of 145 nm, and a Z pot 5.0 mV less negative than the measured for F1. In the cases of F3 and F4, increasing the amount of oil added to the MM lipid did not significantly affect the physicochemical properties of these NLCs in comparison with F2. In all cases, drug loading ranged from 21 to 25 µg of DXM per mg of MM lipid. The PDI values of all prepared formulations were below 0.3.

Table 1. Characteristics of NLC formulations.

Sample	*Composition*			*EE* [a] **(%)**	*DL* [b]	*Mean Diameter* **(nm)**	*PDI*	*Z Pot* [c] **(mV)**
	MM (mg)	**DXM (mg)**	**Oil (µL)**					
F1	400	10	0	86.4 ± 3.0	21.6	152.2 ± 2.8	0.24 ± 0.01	−15.9 ± 1.0
F2	400	10	25	97.7 ± 3.1 *	24.4	144.9 + 1.0 *	0.22 ± 0.01	−10.4 ± 0.8
F3	400	10	50	94.3 ± 2.9 *	23.6	142.1 + 1.9 *	0.20 ± 0.01	−9.1 ± 0.4
F4	400	10	100	94.2 ± 3.0 *	23.6	145.0 + 0.8 *	0.20 ± 0.01	−9.3 ± 1.4

The results express the mean ± SD (n = 3). [a] Encapsulation efficiency. [b] Drug loading expressed as µg of DXM/mg of MM lipid. [c] Zeta potential, * $p < 0.05$ in comparison with F1 (SLNs-DXM).

The morphology of the different formulations was determined by TEM (Figure 1). Clear spherical NPs presented with a narrow PDI. In correlation with the results of previous studies presented above, the addition of liquid oil to the lipid matrix did not affect NLC morphology. In all images, the presence of small micelles of Poloxamer 188 could be visualized. No aggregates or precipitates of NLCs were observed, suggesting stability of the formulations.

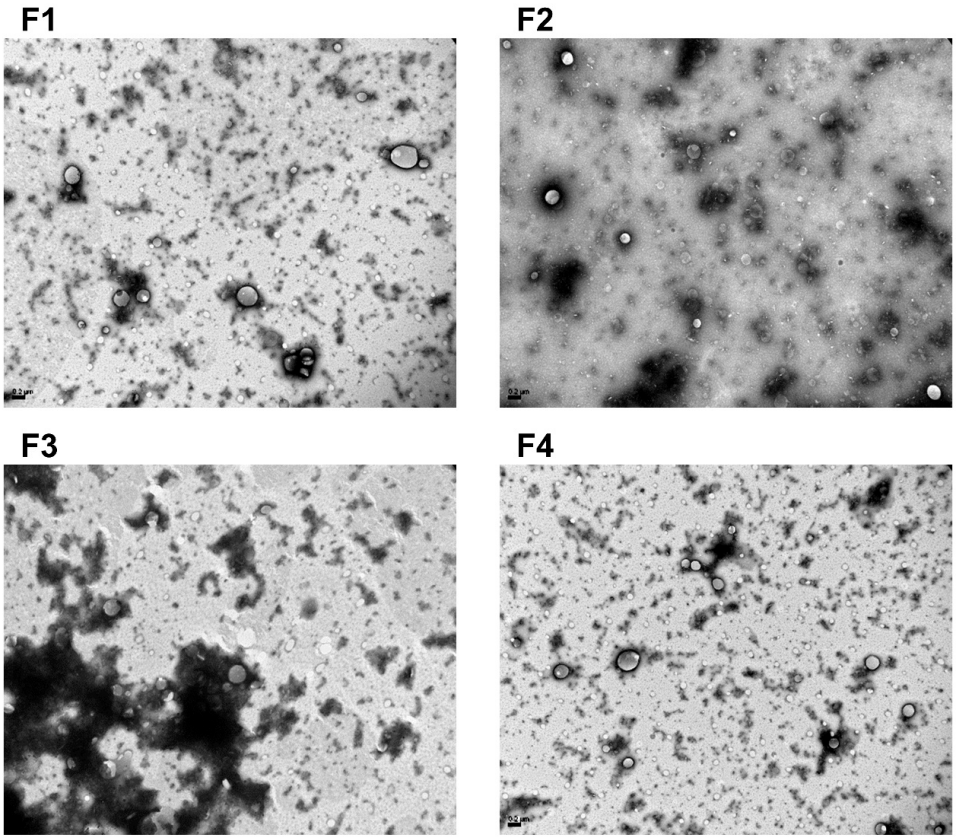

Figure 1. TEM images of NLCs (F1 to F4 formulations). The freshly prepared formulations (20 mg MM lipid/mL) were diluted with Milli-Q water (1:10) and the contrast was enhanced with phospho-tungstic acid. All images were taken at 30,000× (scale bar = 200 nm).

3.2. DXM Release from NLCs

DXM release by NLC formulations was determined to study drug kinetic mechanisms (Figure 2). All formulations showed a typical bi-phasic release profile, with a burst release during the first 3 h followed by a sustained release at a lower rate. Additionally, all formulations showed a longer release profile compared to the soluble DXM control. An increase in the content of liquid oil in the matrix resulted in a slower release of DXM. Thus, 74.0% (F1), 67.1% (F2), 57.4% (F3), 48.3% (F4) of DXM was released in the course of a 24 h incubation, respectively. In particular, F4 released less than 40% of the drug within 12 h. Formulation-specific DXM release kinetics were fitted with different established models to delineate drug release mechanisms: First Order, Higuchi, Korsmeyer-Peppas, and Hixon and Crowell (Table S1). The release model that fitted best to the experimental data was selected according to the calculations of the coefficient of determination (R^2). The release of DMX from all tested formulations matched with the Korsmeyer-Peppas model (Figures S1–S4) [40]. The *n*-value is indicative of the mechanisms involved in drug release from the matrix. The adjustments resulted in the determination of release exponents ("n") lower than 0.5 for the various NLC formulations. The experimental data values (dots)according to Korsmeyer-Peppas fitting curves (lines) are depicted in Figure 2.

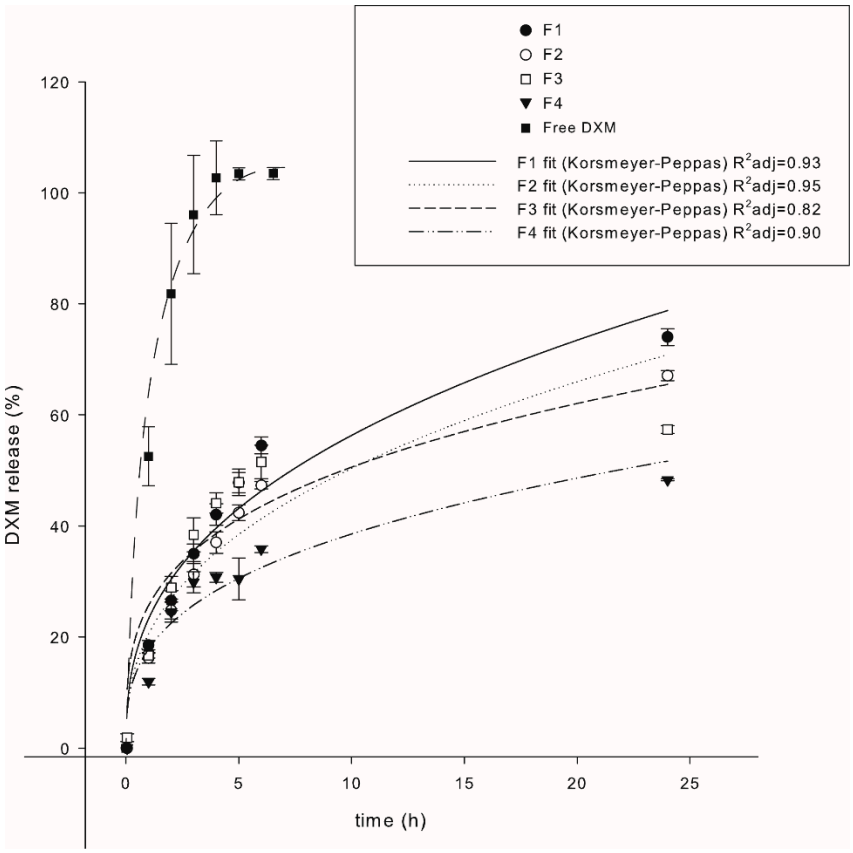

Figure 2. DXM release inversely correlates with oil content of the NLC matrix. Time-dependent DXM release from the different NLC formulations in 10 mM PBS pH 7.4 and 37 °C, (n = 3).

3.3. Stability after Storage

Based on the results of the comprehensive analyses of the different NLC formulations, F4 was selected as the top candidate for further evaluations (from now on called NLCs-DXM). This NLC-DXM formulation was stable for at least 1 year when stored at 4 °C. No significant changes in size distribution and PDI were observed (Figure 3, upper panel). The Z pot values of freshly prepared NLCs and 1 year-stored NLCs were -9.3 ± 1.4 mV and -12.0 ± 0.4 mV, respectively, suggesting no significant changes ($p \geq 0.05$). Furthermore,

no significant differences were noted regarding the NLC drug content (EE) measured every 3 months for a total of 1 year (Figure 3, lower panel).

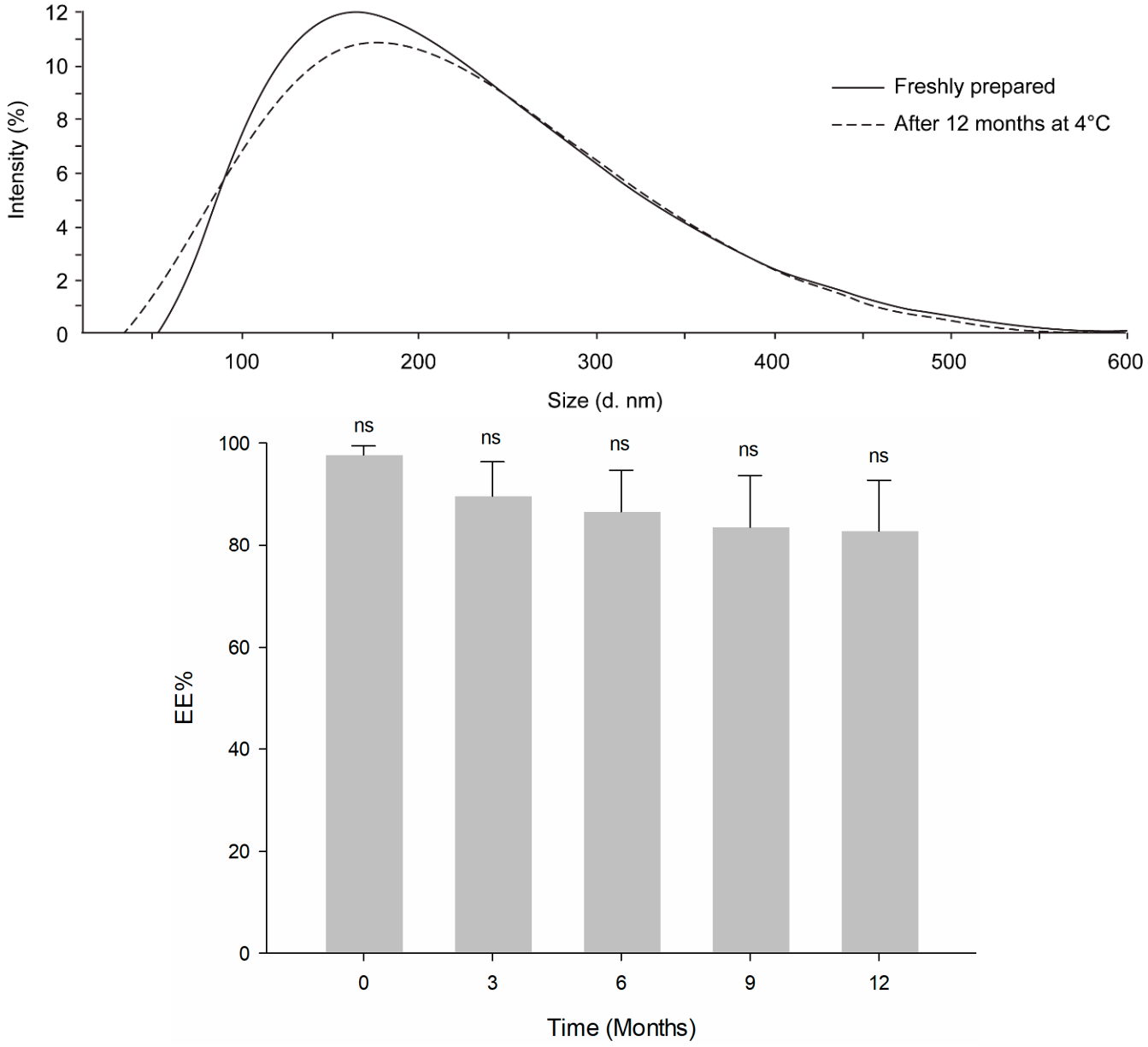

Figure 3. NLC formulations are stable over time. Stability of NLCs-DXM formulation after 12 months stored at 4 °C. **Upper panel**: size distribution- Original sample: Mean diameter: 145.0 ± 0.8 nm; PDI: 0.20 ± 0.01; older formulation: size: 150.8 ± 2.5 nm; PDI: 0.24 ± 0.02; **lower panel**: evolution of the EE measured every 3 months, (n = 3); no significant difference (ns) (Two-way ANOVA, Dunnett's multiple comparisons test).

3.4. Hemotoxicity Studies

Next, the hemocompatibility of NLC formulations was assayed (Figure 4). Different concentrations in the range from 20.0 to 1000.0 µg MM lipid/mL were tested. Negligible hemotoxic effects (<0.4%) were observed when applying both NLCs and NLCs-DXM formulations (1 h) to erythrocytes at the highest NLC concentration tested (1.0 mg/mL). After 24 h incubation, a low degree of hemolysis was observed with values below 1.1%. After 72 h incubation at the highest NLC concentration, about 1.5% of erythrocytes were lysed by either NLC formulation.

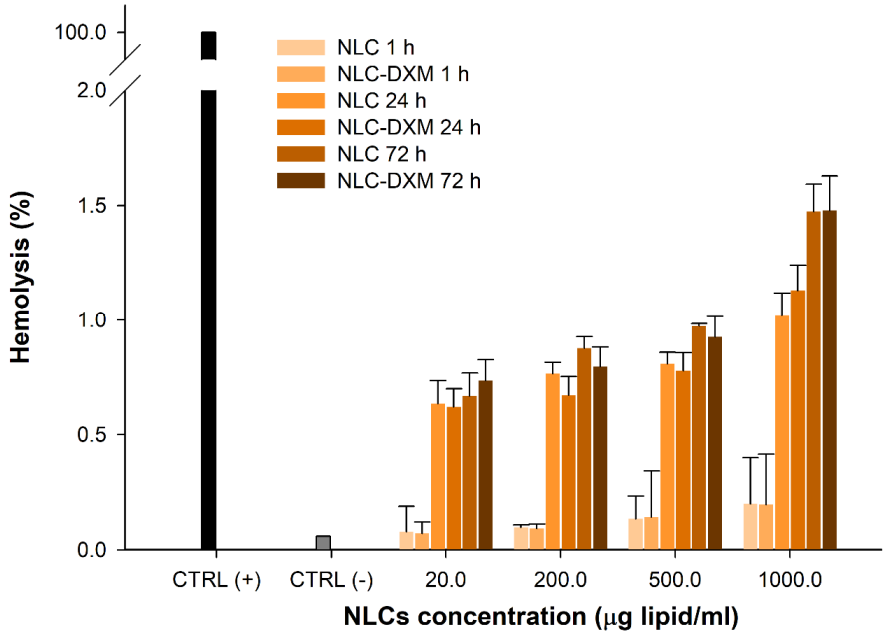

Figure 4. At high concentrations NLCs induce only minimal hemotoxicity. Hemotoxicity of empty and DXM loaded NLCs at different concentrations after 1, 24 and 72 h incubation. Controls: (−) untreated; (+) 1% Triton X-100-lysed erythrocytes, (n = 3).

3.5. Interactions of DXM-Loaded NLCs with Serum Proteins

The interaction of NLCs-DXM with three different plasma proteins commonly found in the protein corona of NPs was studied by SPR experiments. In this regard, potential interactions with HSA, IgG and fibrinogen were tested. Net changes in θ_{SPR} were observed after the injection of the protein solutions onto the SPR chip, verifying the physical adsorption of HSA, IgG and fibrinogen ($\Delta\Theta_{SPR}$ of 0.25, 0.23 and 0.43 degrees, respectively).

SPR sensor-grams obtained after the injection of NLCs-DXM onto protein-modified chips or control surfaces are shown in Figure 5. They verified a minimal $\Delta\theta_{SPR}$ (0–0.005) in the case of bare gold or opsonin-covered sensor surface [24]. NLC-DXM, immobilized had $\Delta\theta_{SPR}$ (~0.035), and evident in vitro interaction was revealed.

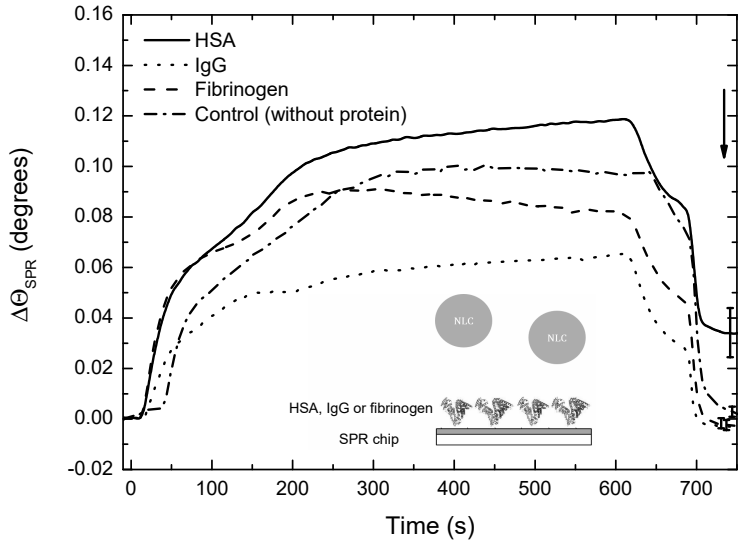

Figure 5. HSA, but no opsonin interacts with NLCs. SPR studies to determine interactions of DXM-NLCs with serum protein having HSA, IgG and fibrinogen. All sensor-grams are presented as mean ± SEM of 3 independent experiments. The arrow indicates the final time of the experiment, when interactions were analyzed.

3.6. NLCs Binding to Liver NPC Populations

The biological activity of NLC formulations was tested using primary murine NPCs as potential target cells for DXM delivery. NPCs were incubated for 24 h with NLCs at different concentrations ranging from 0 to 200 µg of solid MM lipid/mL of culture media. Viability assessment showed no apparent cytotoxic effects of NLCs on NPCs after incubation (Figure 6). Furthermore, NLC uptake was evaluated using NLCs labeled with DiD dye. Flow cytometry results demonstrated a dose-dependent uptake of NLCs by NPCs, up to 20% in case of the highest dose applied.

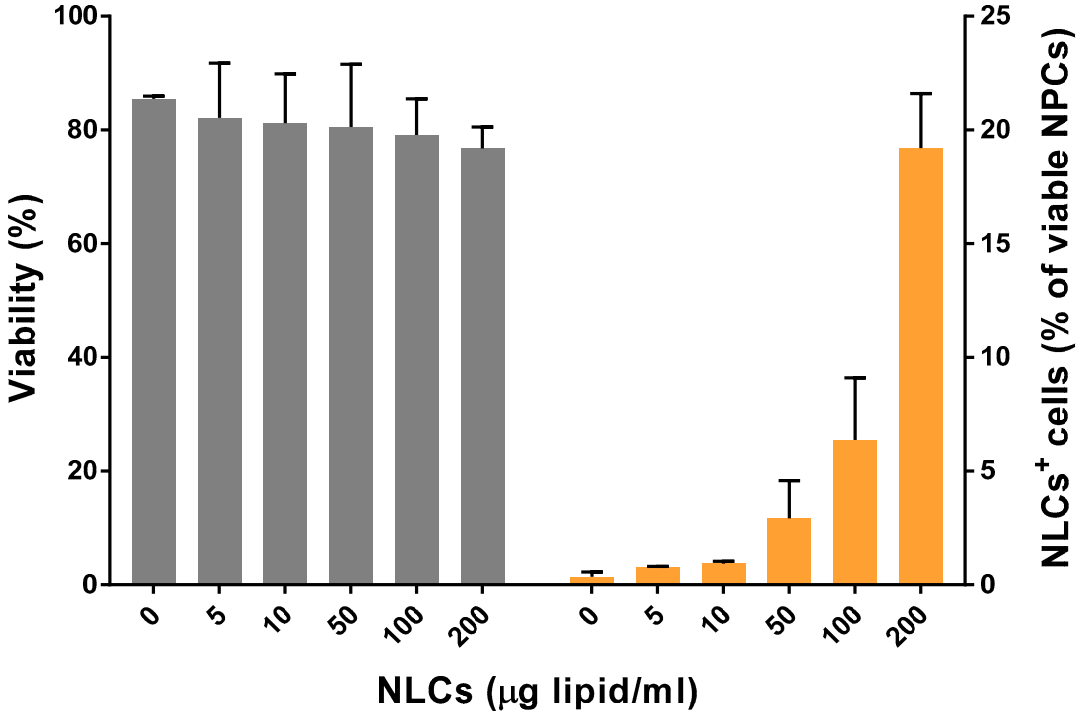

Figure 6. NLCs are internalized by NPC in a dose-dependent manner and are devoid of cytotoxic activity. NPCs were incubated for 24 h with NLCs at concentrations between 0 and 200 µg/mL to evaluate potential cytotoxic effects (left *y*-axis). In the same concentration range, DiD-labeled NLCs were used to study cellular uptake (right *y*-axis). NLCs concentrations are expressed as µg of MM (solid lipid) per mL. Data are the means ± SEM obtained in 3 independent experiments.

3.7. DXM Functionality Is Not Affected by Encapsulation into NLCs

Due to the high DXM loading capacity of NLCs, only the concentration range between 5 and 50 µg of solid MM lipid/mL of culture media was tested further. Freshly isolated NPCs were incubated with equimolar amounts of DXM in its soluble and particulate (NLCs-DXM) forms, and empty NLCs (same dose as for NLCs-DXM). LPS was applied 45 min later to trigger pro-inflammatory responses. After 24 h incubation, supernatants were retrieved for cytokine measurements. The results showed that soluble DXM at all concentrations tested reduced pro-inflammatory cytokine levels, as compared to the positive control (LPS only) (Figure 7). Notably, NLCs-DXM induced a similar response as soluble DXM. Interestingly, empty NLCs also affected cytokine secretion in comparison with the control in several cases. Whereas IL-1β levels were not altered upon preincubation of liver NPC with NLCs prior to LPS stimulation, a significant decrease in TNF-α production was observed at the highest NLC concentration. A similar tendency was noted in the case of IL-6. In contrast, NLCs at low and intermediate concentrations further increased LPS-induced IFN-γ production.

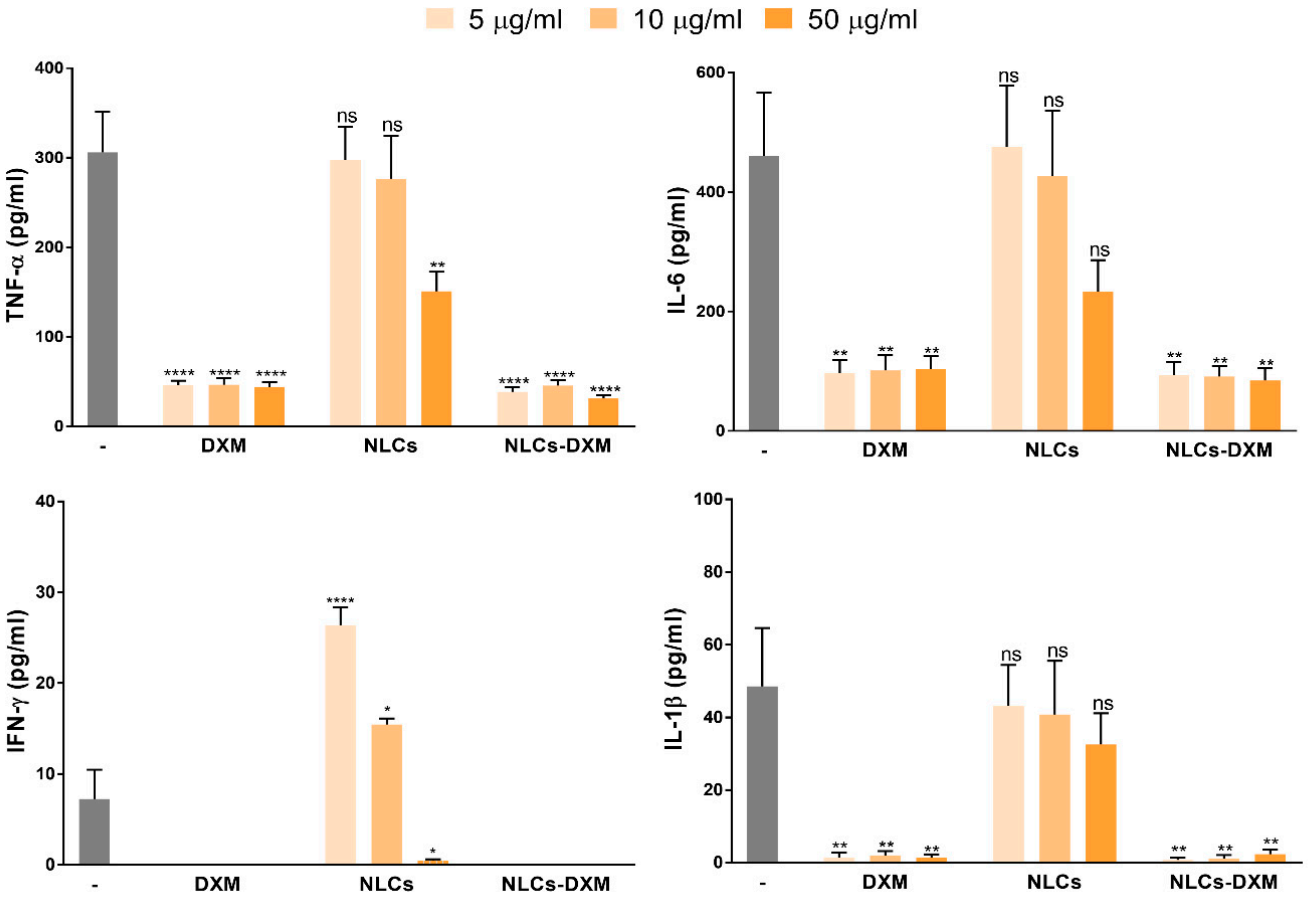

Figure 7. NLC-derived DXM prevents LPS-induced NPC activation. TNF-α, IL-6, IFN-γ and IL-1β levels of DXM-treated of NPCs cultures were monitored. NPCs were incubated with NLC formulations (5, 10 and 50 μg/mL), followed by LPS (100 ng/mL) application. On the next day, supernatants were subjected to cytokine analysis. Data denote the means ± SEM obtained in 3 independent experiments. Significantly different from control (LPS only): no significant difference (ns); * $p < 0.05$; ** $p < 0.01$; **** $p < 0.0001$ (Two-way ANOVA, Dunnett's multiple comparisons test).

3.8. NLCs Induce Anti-Inflammatory Effects Evidenced by the Reduced Activation State of NPCs Subpopulations

The cellular activation state was further evaluated for each of the NPC subpopulations. As expected, LPS treatment induced an up-regulation of the co-stimulatory marker CD86 by either NPC population. However, when NPCs were pre-treated with soluble DXM the frequency of $CD86^+$ cells reduced. This decrease in cellular activation confirmed the anti-inflammatory effects of DXM for each of the NPC populations studied. Moreover, very similar effects were observed in the case of treatment with NLCs-DXM (Figure 8). Empty NLCs also prevented the LPS-induced upregulation of CD86 by either liver NPC population, but only in the case of the highest dose. However, in KCs only the highest concentration of DXM in soluble or particulate form significantly attenuated LPS-induced CD86 upregulation. In contrast, LSECs and DCs displayed total inhibition of LPS-induced CD86 upregulation when treated with DXM in soluble or particulate form, in either case even at the lowest dose (5 μg/mL) applied.

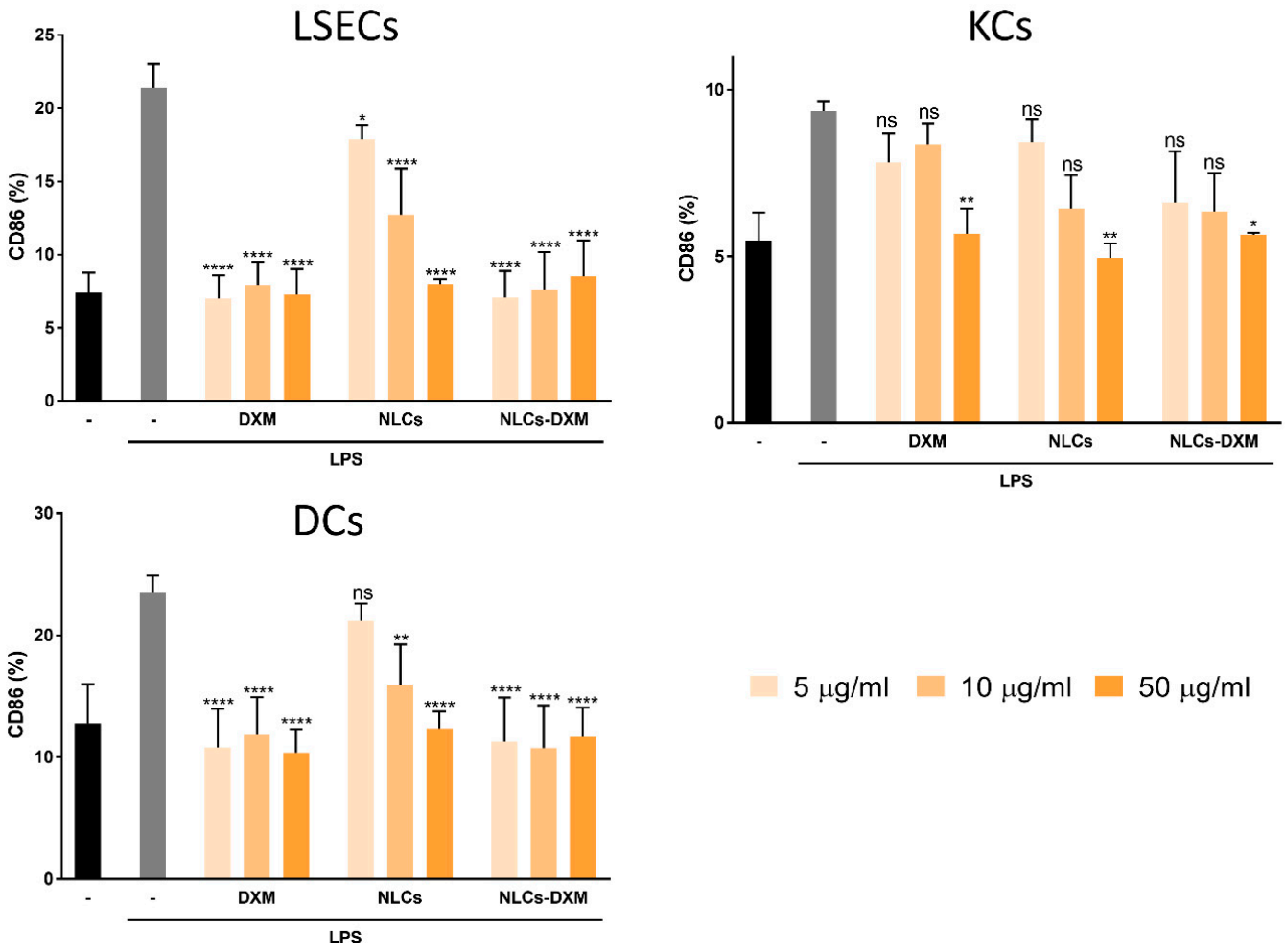

Figure 8. DXM released from NLCs counteracts induction of CD86 by LPS. NPC cultures were treated with soluble DXM, empty NLCs and DXM-loaded NLCs at three different concentrations (5, 10 and 50 µg/mL). LPS (100 ng/mL) was applied 45 min later. On the next day, NPC populations were phenotypically characterized: LSECs ($CD45^+$ $CD32b^+$), KCs ($CD45^+$ $F4/80^+$) and DCs ($CD45^+$ $CD11c^+$). The activation state of each cell type was studied by CD86 marker assessment. The gating strategy has been described [39]. Data represents the mean ± SEM obtained in 3 independent experiments. Significantly different from positive control (LPS only): no significant difference (ns); * $p < 0.05$; ** $p < 0.01$; **** $p < 0.0001$ (one-way ANOVA, Dunnett's multiple comparisons test).

3.9. Delayed Release of DXM from NLCs Affects LPS-Induced NF-kB Activity in a Time-Dependent Manner

To elucidate whether DXM was released in a sustained manner from NLCs a reporter cell line carrying a reporter construct with a NF-κB-inducible promotor was pre-incubated for 45 min with DXM or NLCs-DXM prior to LPS treatment and NF-kB activity was monitored after the indicated period of time. DXM treatment partially inhibited LPS induction of NF-κB when assessed 6 h later (Figure 9). In the case of NLCs-DXM treatment NF-κB activity by LPS was fully inhibited only at 24 h after the onset of incubation, similar to DXM-treated cells. This finding confirmed a slow release of DXM from NLC.

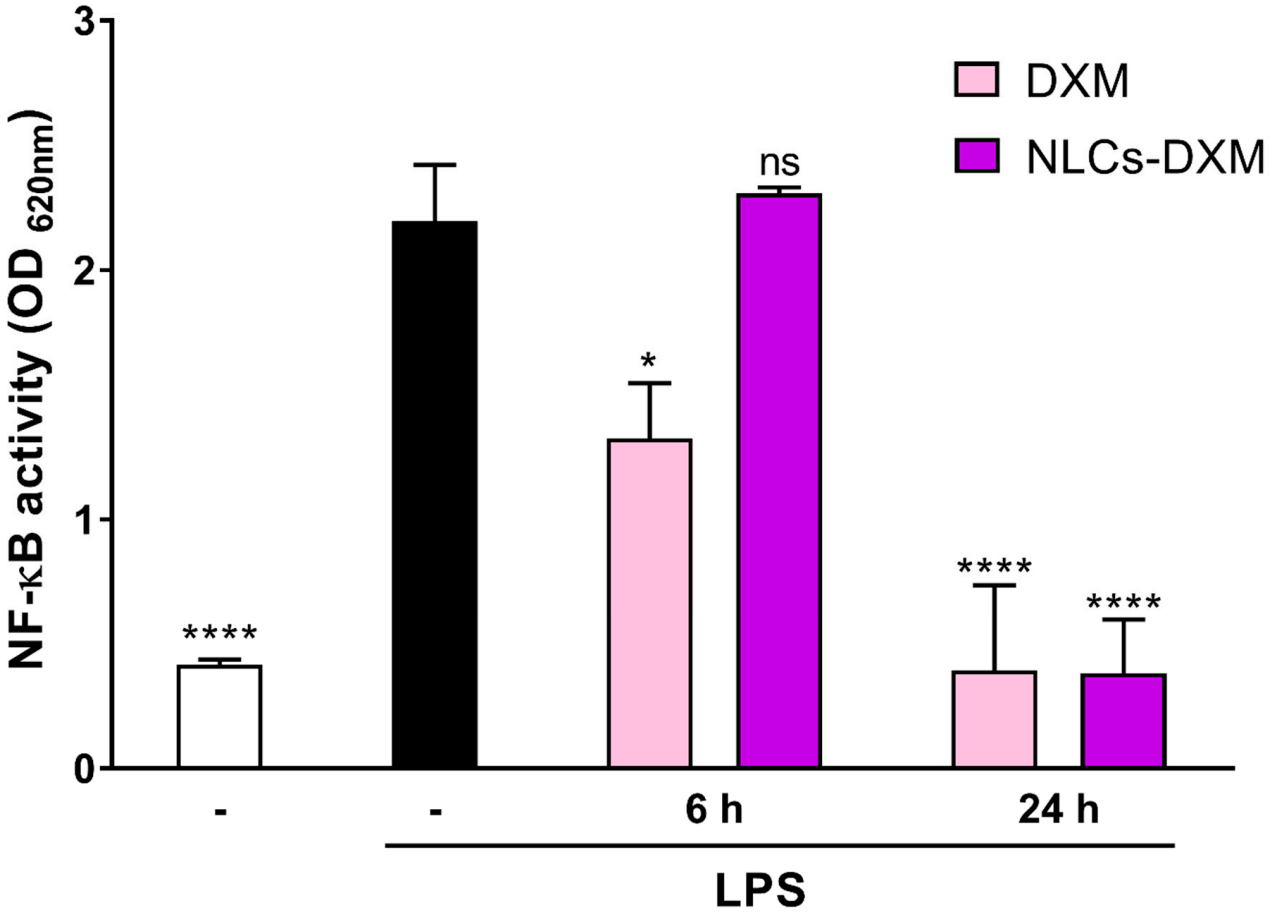

Figure 9. NLCs-DXM inhibit LPS stimulation due to delayed release of the drug. RAW-Blue™ cells, derived from RAW 264.7 macrophages and containing SEAP reporter construct inducible by NF-κβ, were pre-treated with DXM or NLCs-DXM (each 1000 μg/mL). Next, LPS was added to the culture media to induce NF-κβ activation. DXM-mediated inhibition of this response by both treatment options was measured by NF-κβ-dependent, SEAP activation. Data represent the means ± SEM obtained in 3 independent experiments. Significant differences versus LPS^+ untreated cells are indicated: no significant difference (ns); * $p < 0.05$; **** $p < 0.0001$ (Two-way ANOVA, Dunnett's multiple comparisons test).

4. Discussion

The incorporation of liquid oils into solid lipid matrices is an important step toward the formation of NLCs [21]. Previous work from our group has provided evidence that the combination of MM/GTCC-LQ oil resulted in the formation of non-toxic NLCs. Based on this previous study, we aimed to use NLCs for DXM delivery. Formulation F1 represented conventional SLNs without the addition of oil, which is necessary to produce the nanostructure of the matrix [22]. Incorporation of 1/16 ratio (vol./lipid weight) of oil into the lipid generated NLCs (F2) with a somewhat smaller diameter and less negative zeta potential than F1, suggesting a modification of the structure of the lipidic matrix due to the presence of the liquid oil [28]. The same tendencies were observed for formulations with higher oil content (F3, F4), but without significant differences in comparison to F2 ($p > 0.05$). The PDI of the formulations was very low, which suits biological applications [41]. Additionally, TEM results showed a narrow size distribution of the spherical NLCs in accordance with previous work from our laboratory that reported the stability of such colloidal systems [25].

Drug release kinetics from delivery devices constitute a critical point regarding the necessity to obtain desirable concentrations of that drug in a therapeutic range over a longer period of time [40]. In the case of DXM, the major challenge was to improve patient compliance by decreasing the dosing frequency to reduce side effects, but without

losing therapeutic effectiveness. All comparatively assessed NLC formulations showed a typical bi-phasic release profile, with a burst release in the first hours followed by a sustained release afterwards. Different reports have described the same behavior for drugs encapsulated into SLNs/NLCs [31,42]. The fitting of experimental data with the different release model mechanisms demonstrated that the formulations F1 to F4 adjusted best to Korsmeyer-Peppas [40]. This semi-empirical model was originally developed to describe the release of drugs from polymeric matrices; however, it has also been used for other types of matrices as well [43]. In particular, the exponential parameter of the model "n" is useful to study the mechanism which determines the release behavior. For "n" < 0.5 the mechanism is considered to be diffusion following Fick's law, while for higher "n" other mechanisms, such as matrix swelling, were found to be relevant [44]. For all formulations tested in this work, the release exponent "n" was found to be <0.5. This finding is consistent with the fact that NLC lipid matrices do not undergo swelling like polymeric matrices [45]. Several factors, like drug-lipid specific interactions, drug location inside nanoparticle and nanoparticle structure, were reported to govern the release of drugs from NLC systems. Mainly because of this, either extension or reduction in release intervals have been reported when modifying NLC structure with liquid oils [46]. As stated before, the inclusion of an oil in the lipid matrix prevents crystallization and the consequent expulsion of the drug from the nanoparticle. However, other mechanisms could explain the profiles observed in the release kinetics from the different formulations. The increase in the proportion of liquid oil could be generating "pockets" inside the NLC, moving the DXM away from the interface and delaying its release [46]. In this context, the slow and controlled release of DXM from formulation F4 was a very interesting result, since it may allow controlling DXM release for a prolonged period of time. This constitutes an important progress in controlling the release of DXM from NPs in comparison to previous studies. For instance, Xiang et al. showed that the extent of DXM released from SLNs was around 75% after 12 h [47]. In the work from Wang et al. a 40% release was obtained after 12 h [48], while Xu et al. reported a 70% release within 12 h [49], both using NLCs matrices. Altogether, formulations developed for DXM delivery have showed undesirable release profiles so far, since a considerable amount of the cargo was released rapidly after administration. The main characteristic of an according formulation should be a steady low-level release to prevent concentration-associated side effects.

Based on size distribution, EE and DXM release kinetics, formulation F4 was selected for further experiments. Remarkably, good stability of F4-derived NLCs-DXM was observed even after 12-month storage, which constitutes a great advance considering the need to ensure a reliable half-life of nanodrugs. Moreover, particle size distribution and zeta potential remained unaltered, which suggested no changes in crystallinity of the lipids during storage, conceivably attributed to the presence of the liquid oil into the matrix [50]. The low Z potential values observed in the formulation were due to stabilization with a non-ionic surfactant (Poloxamer 188). The steric groups of the surfactant stabilized the formulation by avoiding the agglomeration of nanoparticles in suspension [51,52]. Kovacevik et al., reported that the inclusion of a non-ionic surfactant in the formulation of NPs contributes to the stability of the formulation, even in NPs with ZP that does not reach the critical −30 mV [53]. Shah et al., referred to the physical stability of nanoparticles depending on many other factors that contribute to producing stable formulations. In this regard, NLCs in suspension with a non-ionic surfactant showed stability despite the lower zeta potential (and less electrostatic stabilization), but with great steric stabilization [54].

Nanodrugs frequently interact with serum factors which may selectively adsorb to the surface of the nano-carrier and, thereby, control its cellular interaction [55]. Therefore, it is necessary to study potential interactions that NLCs may establish with biomolecules and cells [56]. In the case of intravenous administration, NLCs-DXM may contact erythrocytes. In fact, some types of NPs have been reported to exert inflammatory responses and hemolysis [57]. According to ISO/TR 7406, biomaterials that induce a critical hemolytic ratio < 5% are considered safe for human applications [58]. Our results demonstrated

that NLCs-DXM did not cause hemolysis exceeding this level, even after 72 h exposition, suggesting the absence of potential hemotoxic side effects. Another parameter to study was the protein corona of the nano-carrier, which can mask its chemical identity and affect its biodistribution [59]. SPR experiments verified that the in vitro biomolecular interaction between NLCs-DXM and the opsonins IgG or fibrinogen was negligible, whereas NLCs-DXM readily engaged HSA, which may enhance the in vivo circulation time of the NP.

Most likely, after entering systemic circulation, NLCs-DXM will end up in the liver, which constitutes an intended target organ for the delivery of DXM. Among the wide range of DXM applications, the treatment of liver inflammation with this anti-inflammatory agent has been reported in detail [60,61]. Therefore, we studied the functional effects of NLC formulations using liver NPCs. This heterogeneous cell population confers most immune-related responses within the liver [9]. NPCs have the capacity to react towards exogenous stimuli, such as antigenic compounds or danger signals like LPS. The latter, mediated by TLR4 binding, induces proinflammatory responses [62]. In this study, NPCs were pre-treated with DXM to induce an anti-inflammatory state, followed by LPS application. Notably, NPC viability was not affected after 24 h incubation with NLCs. Besides this, NLCs uptake by NPCs proved to be successful within the concentration range tested. This might be mainly associated with the particular endocytic phenotype of the different NPC cell types [9]. Furthermore, the reduction of proinflammatory cytokine levels in the case of DXM and NLCs-DXM treatment proved that DXM released from the NLCs preserved its pharmacological activity. Remarkably, empty NLCs at the concentration of 50 µg/mL also partially inhibited cytokine secretion. These findings prompted us to perform more detailed analyses of the effects generated by NLCs on the NPC subpopulations. Thus, LSECs, KCs, and DCs were separately characterized phenotypically. As expected, NPCs reacted to LPS treatment by upregulating CD86 expression in all analyzed NPC types. Most importantly, NLCs-DXM applied before LPS prevented an increase in the frequencies of $CD86^+$ cells, similarly to soluble DXM. Surprisingly, the highest tested concentration of empty NLCs also inhibited CD86 upregulation to a similar extent, as observed for DXM treatment. These results confirmed that NLCs could potentially have some intrinsic inhibitory effects on liver NPC population. In a similar way, other lipid-based nanocarriers were reported to have intrinsic anti-inflammatory effects, due to macrophage engagement generating an inhibition on proinflammatory cytokine secretion, both in vitro and in vivo [63,64]. Furthermore, NPs of other natures, such as gold NPs, quantum dots, silica NPs and food-derived NPs, were found to affect DC maturation showing inhibition of activation marker upregulation after LPS challenge [65–68]. Further experiments will be necessary to study, in more detail, the potential effects associated with NLC engagement by NPCs.

Finally, the question of whether NLCs-DXM released DXM in a sustained way also under cell culture conditions was addressed by using the RAW-Blue™ NF-κβ reporter cell line. Our results showed that, contrary to the inhibition of LPS-induced NF-κβ activity by soluble DXM assessed 6h after DXM/LPS application, treatment with NLCs-DXM had no effect after short time incubation. At the 24 h time point, however, NLCs-DXM inhibited NF-kB activity to a comparable extent as directly applied DXM, which might be a consequence of almost complete DXM release.

In summary, the following conclusions can be drawn: (1) NLCs composed of MM and GTCC-LQ oil show superior EE, stability and DXM release kinetics; (2) NLCs are well tolerated by human erythrocytes; (3) NLCs show negligible in vitro interaction with plasma opsonins; (4) Liver NPCs are capable of internalizing NLCs in a dose-dependent manner; (5) DXM released from NLCs preserves its anti-inflammatory activity.

Taken together, these findings provide evidence that the NLC platform introduced in this study has the potential to serve as a well-tolerated nano-carrier for the delivery and sustained release of bioactive DXM to the liver, potentially reducing systemic side effects otherwise associated with systemic DXM application in the treatment of liver inflammation.

Supplementary Materials: The following supporting information can be downloaded at: https://www.mdpi.com/article/10.3390/pharmaceutics14081611/s1, Table S1: Calculations of the coefficient of determination (R^2) for DXM release. Figures S1–S4: DXM release fitting curves with the Korsmeyer-Peppas model from all tested formulations.

Author Contributions: Conceptualization, M.L.C., G.A.I., S.G. (Stephan Gehring) and M.B.; methodology, C.M.-M., I.R.B., R.C.G., M.J.L., M.S., C.Y.C., J.S.C., G.A.I. and M.L.C.; validation, G.A.I., M.L.C., M.B., C.M.-M., I.R.B., R.C.G., M.J.L., M.S., C.Y.C. and J.S.C.; formal analysis, C.M.-M., I.R.B., R.C.G., M.J.L., C.Y.C., J.S.C., G.A.I. and M.L.C.; resources, G.P., G.R.C., S.G. (Stephan Gehring), S.G. (Stephan Grabbe), M.B., G.A.I. and M.L.C.; writing—original draft preparation, G.A.I. and M.L.C.; writing—review and editing, S.G. (Stephan Gehring), M.B., G.A.I. and M.L.C.; supervision, G.A.I. and M.L.C.; project administration, G.A.I., M.L.C., S.G. (Stephan Gehring) and M.B.; funding acquisition, G.P., G.R.C., S.G. (Stephan Gehring), S.G. (Stephan Grabbe), M.B., G.A.I. and M.L.C. All authors have read and agreed to the published version of the manuscript.

Funding: This work was partially supported by UNLP (X041, X815, X861), CONICET (PIP 0034, PIP 0671), and ANPCyT (PICT 2016-1574, PICT 2017-2251, PICT 2016-4597; PICT 2017-0359). Also, this research was funded by Deutsche Forschungsgemeinschaft (SFB1066), grant numbers B4 (S.G. (Stephan Grabbe)) and B15 (S.G. (Stephan Gehring), M.B.).

Institutional Review Board Statement: For blood samples, the study was conducted according to the guidelines of the Declaration of Helsinki and approved by the Advisory Committee on Bioethics of National University of La Plata (File Nr. 0100-015036/17-000; date: 20/08/2017), Argentina. For mouse-derived samples, mice were sacrificed for organ retrieval according to § 4(3) TierSchG, Germany.

Informed Consent Statement: Informed consent was obtained from all subjects involved in the study.

Data Availability Statement: The data that support the findings of this study are available from the corresponding authors, M.L.C. and G.A.I., upon request.

Acknowledgments: We appreciate the donations from Croda.

Conflicts of Interest: The authors declare no conflict of interest.

References

1. Mieli-Vergani, G.; Vergani, D.; Czaja, A.J.; Manns, M.P.; Krawitt, E.L.; Vierling, J.M.; Lohse, A.W.; Montano-Loza, A.J. Autoimmune Hepatitis. *Nat. Rev. Dis. Primers* **2018**, *4*, 18017. [CrossRef] [PubMed]
2. Wang, C.C.; Cheng, P.N.; Kao, J.H. Systematic Review: Chronic Viral Hepatitis and Metabolic Derangement. *Aliment. Pharmacol. Ther.* **2020**, *51*, 216–230. [CrossRef] [PubMed]
3. Czaja, A.J.; Carpenter, H.A. Progressive Fibrosis during Corticosteroid Therapy of Autoimmune Hepatitis. *Hepatology* **2004**, *39*, 1631–1638. [CrossRef] [PubMed]
4. Czaja, A.J. Hepatic Inflammation and Progressive Liver Fibrosis in Chronic Liver Disease. *World J. Gastroenterol.* **2014**, *20*, 2515–2532. [CrossRef]
5. FakhriRavari, A.; Jin, S.; Kachouei, F.H.; Le, D.; Lopez, M. Systemic Corticosteroids for Management of COVID-19: Saving Lives or Causing Harm? *Int. J. Immunopathol. Pharmacol.* **2021**, *35*, 20587384211063976. [CrossRef]
6. Stark, A.; Carlo, W.; Tyson, J.; Papile, A.; Wright, L.; Shankaran, S.; Donovan, E.; Oh, W.; Bauer, C.; Saha, S.; et al. Adverse Effects of Early Dexamethasone Treatment in Extremely-Low-Birth-Weight Infants. *N. Engl. J. Med.* **2001**, *344*, 95–101. [CrossRef]
7. Doyle, L.W.; Ehrenkranz, R.A.; Halliday, H.L. Dexamethasone Treatment in the First Week of Life for Preventing Bronchopulmonary Dysplasia in Preterm Infants: A Systematic Review. *Neonatology* **2010**, *98*, 217–224. [CrossRef]
8. Zhang, Y.N.; Poon, W.; Tavares, A.J.; McGilvray, I.D.; Chan, W.C.W. Nanoparticle-Liver Interactions: Cellular Uptake and Hepatobiliary Elimination. *J. Control. Release* **2016**, *240*, 332–348. [CrossRef]
9. Cacicedo, M.L.; Medina-Montano, C.; Kaps, L.; Kappel, C.; Gehring, S.; Bros, M. Role of Liver-Mediated Tolerance in Nanoparticle-Based Tumor Therapy. *Cells* **2020**, *9*, 1985. [CrossRef] [PubMed]
10. Koyama, Y.; Brenner, D.A.; Koyama, Y.; Brenner, D.A. Liver Inflammation and Fibrosis Find the Latest Version: Liver Inflammation and Fibrosis. *J. Clin. Investig.* **2017**, *127*, 55–64. [CrossRef]
11. Poisson, J.; Lemoinne, S.; Boulanger, C.; Durand, F.; Moreau, R.; Valla, D.; Rautou, P.E. Liver Sinusoidal Endothelial Cells: Physiology and Role in Liver Diseases. *J. Hepatol.* **2017**, *66*, 212–227. [CrossRef] [PubMed]
12. Li, M.; Jiang, S.; Haller, A.; Wirsching, S.; Fichter, M.; Simon, J.; Wagner, M.; Mailänder, V.; Gehring, S.; Crespy, D.; et al. Encapsulation of Polyprodrugs Enables an Efficient and Controlled Release of Dexamethasone. *Nanoscale Horiz.* **2021**, *6*, 791–800. [CrossRef]

13. Bartneck, M.; Scheyda, K.M.; Warzecha, K.T.; Rizzo, L.Y.; Hittatiya, K.; Luedde, T.; Storm, G.; Trautwein, C.; Lammers, T.; Tacke, F. Fluorescent Cell-Traceable Dexamethasone-Loaded Liposomes for the Treatment of Inflammatory Liver Diseases. *Biomaterials* **2015**, *37*, 367–382. [CrossRef] [PubMed]
14. Bartneck, M.; Peters, F.M.; Warzecha, K.T.; Bienert, M.; van Bloois, L.; Trautwein, C.; Lammers, T.; Tacke, F. Liposomal Encapsulation of Dexamethasone Modulates Cytotoxicity, Inflammatory Cytokine Response, and Migratory Properties of Primary Human Macrophages. *Nanomed. Nanotechnol. Biol. Med.* **2014**, *10*, 1209–1220. [CrossRef] [PubMed]
15. Jiang, S.; Prozeller, D.; Pereira, J.; Simon, J.; Han, S.; Wirsching, S.; Fichter, M.; Mottola, M.; Lieberwirth, I.; Morsbach, S.; et al. Controlling Protein Interactions in Blood for Effective Liver Immunosuppressive Therapy by Silica Nanocapsules. *Nanoscale* **2020**, *12*, 2626–2637. [CrossRef]
16. Fichter, M.; Baier, G.; Dedters, M.; Pretsch, L.; Pietrzak-Nguyen, A.; Landfester, K.; Gehring, S. Nanocapsules Generated out of a Polymeric Dexamethasone Shell Suppress the Inflammatory Response of Liver Macrophages. *Nanomed. Nanotechnol. Biol. Med.* **2013**, *9*, 1223–1234. [CrossRef]
17. Lammers, T.; Sofias, A.M.; van der Meel, R.; Schiffelers, R.; Storm, G.; Tacke, F.; Koschmieder, S.; Brümmendorf, T.H.; Kiessling, F.; Metselaar, J.M. Dexamethasone Nanomedicines for COVID-19. *Nat. Nanotechnol.* **2020**, *15*, 622–624. [CrossRef]
18. Simón-Vázquez, R.; Tsapis, N.; Lorscheider, M.; Rodríguez, A.; Calleja, P.; Mousnier, L.; de Miguel Villegas, E.; González-Fernández, Á.; Fattal, E. Improving Dexamethasone Drug Loading and Efficacy in Treating Arthritis through a Lipophilic Prodrug Entrapped into PLGA-PEG Nanoparticles. *Drug Deliv. Transl. Res.* **2022**, *12*, 1270–1284. [CrossRef]
19. Wang, H.; Zhou, Y.; Sun, Q.; Zhou, C.; Hu, S.; Lenahan, C.; Xu, W.; Deng, Y.; Li, G.; Tao, S. Update on Nanoparticle-Based Drug Delivery System for Anti-Inflammatory Treatment. *Front. Bioeng. Biotechnol.* **2021**, *9*, 630352. [CrossRef]
20. Mirchandani, Y.; Patravale, V.B.; Brijesh, S. Solid Lipid Nanoparticles for Hydrophilic Drugs. *J. Control. Release* **2021**, *335*, 457–464. [CrossRef]
21. Haider, M.; Abdin, S.M.; Kamal, L.; Orive, G. Nanostructured Lipid Carriers for Delivery of Chemotherapeutics: A Review. *Pharmaceutics* **2020**, *12*, 288. [CrossRef]
22. Pardeike, J.; Hommoss, A.; Müller, R.H. Lipid Nanoparticles (SLN, NLC) in Cosmetic and Pharmaceutical Dermal Products. *Int. J. Pharm.* **2009**, *366*, 170–184. [CrossRef] [PubMed]
23. Duan, Y.; Dhar, A.; Patel, C.; Khimani, M.; Neogi, S.; Sharma, P.; Siva Kumar, N.; Vekariya, R.L. A Brief Review on Solid Lipid Nanoparticles: Part and Parcel of Contemporary Drug Delivery Systems. *RSC Adv.* **2020**, *10*, 26777–26791. [CrossRef] [PubMed]
24. Mishra, V.; Bansal, K.K.; Verma, A.; Yadav, N.; Thakur, S.; Sudhakar, K.; Rosenholm, J.M. Solid Lipid Nanoparticles: Emerging Colloidal Nano Drug Delivery Systems. *Pharmaceutics* **2018**, *10*, 191. [CrossRef] [PubMed]
25. Rodenak-Kladniew, B.; Noacco, N.; Pérez de Berti, I.; Stewart, S.J.; Cabrera, A.F.; Alvarez, V.A.; García de Bravo, M.; Durán, N.; Castro, G.R.; Islan, G.A. Design of Magnetic Hybrid Nanostructured Lipid Carriers Containing 1,8-Cineole as Delivery Systems for Anticancer Drugs: Physicochemical and Cytotoxic Studies. *Colloids Surf. B Biointerfaces* **2021**, *202*, 111710. [CrossRef]
26. Scioli Montoto, S.; Muraca, G.; di Ianni, M.; Couyoupetrou, M.; Pesce, G.; Islan, G.A.; Chain, C.Y.; Vela, M.E.; Ruiz, M.E.; Talevi, A.; et al. Preparation, Physicochemical and Biopharmaceutical Characterization of Oxcarbazepine-Loaded Nanostructured Lipid Carriers as Potential Antiepileptic Devices. *J. Drug Deliv. Sci. Technol.* **2021**, *63*, 102470. [CrossRef]
27. Muraca, G.S.; Soler-Arango, J.; Castro, G.R.; Islan, G.A.; Brelles-Mariño, G. Improving Ciprofloxacin Antimicrobial Activity through Lipid Nanoencapsulation or Non-Thermal Plasma on Pseudomonas Aeruginosa Biofilms. *J. Drug Deliv. Sci. Technol.* **2021**, *64*, 102644. [CrossRef]
28. Rodenak-Kladniew, B.; Scioli Montoto, S.; Sbaraglini, M.L.; di Ianni, M.; Ruiz, M.E.; Talevi, A.; Alvarez, V.A.; Durán, N.; Castro, G.R.; Islan, G.A. Hybrid Ofloxacin/Eugenol Co-Loaded Solid Lipid Nanoparticles with Enhanced and Targetable Antimicrobial Properties. *Int. J. Pharm.* **2019**, *569*, 118575. [CrossRef]
29. Islan, G.A.; Gonçalves, L.M.D.; Marto, J.; Duarte, A.; Alvarez, V.A.; Castro, G.R.; Almeida, A.J. Effect of α-Tocopherol on the Physicochemical, Antioxidant and Antibacterial Properties of Levofloxacin Loaded Hybrid Lipid Nanocarriers. *New J. Chem.* **2021**, *45*, 1029–1042. [CrossRef]
30. Rodenak-Kladniew, B.; Islan, G.A.; de Bravo, M.G.; Durán, N.; Castro, G.R. Design, Characterization and in Vitro Evaluation of Linalool-Loaded Solid Lipid Nanoparticles as Potent Tool in Cancer Therapy. *Colloids Surf. B Biointerfaces* **2017**, *154*, 123–132. [CrossRef]
31. Islan, G.A.; Tornello, P.C.; Abraham, G.A.; Duran, N.; Castro, G.R. Smart Lipid Nanoparticles Containing Levofloxacin and DNase for Lung Delivery. Design and Characterization. *Colloids Surf. B Biointerfaces* **2016**, *143*, 168–176. [CrossRef] [PubMed]
32. Cacicedo, M.L.; Ruiz, M.C.; Scioli-Montoto, S.; Ruiz, M.E.; Fernández, M.A.; Torres-Sanchez, R.M.; Baran, E.J.; Castro, G.R.; León, I.E. Lipid Nanoparticles-Metvan: Revealing a Novel Way to Deliver a Vanadium Compound to Bone Cancer Cells. *New J. Chem.* **2019**, *43*, 17726–17734. [CrossRef]
33. Scioli Montoto, S.; Sbaraglini, M.L.; Talevi, A.; Couyoupetrou, M.; di Ianni, M.; Pesce, G.O.; Alvarez, V.A.; Bruno-Blanch, L.E.; Castro, G.R.; Ruiz, M.E.; et al. Carbamazepine-Loaded Solid Lipid Nanoparticles and Nanostructured Lipid Carriers: Physicochemical Characterization and in Vitro/in Vivo Evaluation. *Colloids Surf. B Biointerfaces* **2018**, *167*, 73–81. [CrossRef] [PubMed]
34. Salgarella, A.R.; Zahoranová, A.; Šrámková, P.; Majerčíková, M.; Pavlova, E.; Luxenhofer, R.; Kronek, J.; Lacík, I.; Ricotti, L. Investigation of Drug Release Modulation from Poly(2-Oxazoline) Micelles through Ultrasound. *Sci. Rep.* **2018**, *8*, 9893. [CrossRef] [PubMed]

35. Thote, A.J.; Chappell, J.T.; Gupta, R.B.; Kumar, R. Reduction in the Initial-Burst Release by Surface Crosslinking of PLGA Microparticles Containing Hydrophilic or Hydrophobic Drugs. *Drug Dev. Ind. Pharm.* **2005**, *31*, 43–57. [CrossRef]
36. Abbina, S.; Takeuchi, L.E.; Anilkumar, P.; Yu, K.; Rogalski, J.C.; Shenoi, R.A.; Constantinescu, I.; Kizhakkedathu, J.N. Blood Circulation of Soft Nanomaterials Is Governed by Dynamic Remodeling of Protein Opsonins at Nano-Biointerface. *Nat. Commun.* **2020**, *11*, 3048. [CrossRef]
37. Rampado, R.; Crotti, S.; Caliceti, P.; Pucciarelli, S.; Agostini, M. Recent Advances in Understanding the Protein Corona of Nanoparticles and in the Formulation of "Stealthy" Nanomaterials. *Front. Bioeng. Biotechnol.* **2020**, *8*, 166. [CrossRef] [PubMed]
38. Hermanson, G. *Bioconjugate Techniques*, 3rd ed.; Elsevier: Amsterdam, The Netherlands, 2013.
39. Medina-Montano, C.; Cacicedo, M.L.; Svensson, M.; Limeres, M.J.; Zeyn, Y.; Chaves-Giraldo, J.E.; Röhrig, N.; Grabbe, S.; Gehring, S.; Bros, M. Enrichment Methods for Murine Liver Non-Parenchymal Cells Differentially Affect Their Immunophenotype and Responsiveness towards Stimulation. *Int. J. Mol. Sci.* **2022**, *23*, 6543. [CrossRef]
40. Mansour, H.M.; Sohn, M.J.; Al-Ghananeem, A.; DeLuca, P.P. Materials for Pharmaceutical Dosage Forms: Molecular Pharmaceutics and Controlled Release Drug Delivery Aspects. *Int. J. Mol. Sci.* **2010**, *11*, 3298–3322. [CrossRef] [PubMed]
41. Murdock, R.C.; Braydich-Stolle, L.; Schrand, A.M.; Schlager, J.J.; Hussain, S.M. Characterization of Nanomaterial Dispersion in Solution Prior to in Vitro Exposure Using Dynamic Light Scattering Technique. *Toxicol. Sci.* **2008**, *101*, 239–253. [CrossRef] [PubMed]
42. Cacicedo, M.L.; Islan, G.A.; León, I.E.; Álvarez, V.A.; Chourpa, I.; Allard-Vannier, E.; García-Aranda, N.; Díaz-Riascos, Z.V.; Fernández, Y.; Schwartz, S.; et al. Bacterial Cellulose Hydrogel Loaded with Lipid Nanoparticles for Localized Cancer Treatment. *Colloids Surf. B Biointerfaces* **2018**, *170*, 596–608. [CrossRef] [PubMed]
43. Bruschi, M.L. Mathematical Models of Drug Release. In *Strategies to Modify the Drug Release from Pharmaceutical Systems*; Elsevier: Amsterdam, The Netherlands, 2015; pp. 63–86.
44. Permanadewi, I.; Kumoro, A.C.; Wardhani, D.H.; Aryanti, N. Modelling of Controlled Drug Release in Gastrointestinal Tract Simulation. In *Journal of Physics: Conference Series*; Institute of Physics Publishing: Bristol, UK, 2019; Volume 1295.
45. Kamaly, N.; Yameen, B.; Wu, J.; Farokhzad, O.C. Degradable Controlled-Release Polymers and Polymeric Nanoparticles: Mechanisms of Controlling Drug Release. *Chem. Rev.* **2016**, *116*, 2602–2663. [CrossRef] [PubMed]
46. Gordillo-Galeano, A.; Mora-Huertas, C.E. Solid Lipid Nanoparticles and Nanostructured Lipid Carriers: A Review Emphasizing on Particle Structure and Drug Release. *Eur. J. Pharm. Biopharm.* **2018**, *133*, 285–308. [CrossRef]
47. Xiang, Q.Y.; Wang, M.T.; Chen, F.; Gong, T.; Jian, Y.L.; Zhang, Z.R.; Huang, Y. Lung-Targeting Delivery of Dexamethasone Acetate Loaded Solid Lipid Nanoparticles. *Arch. Pharm. Res.* **2007**, *30*, 519–525. [CrossRef]
48. Wang, M.T.; Jin, Y.; Yang, Y.X.; Zhao, C.Y.; Yang, H.Y.; Xu, X.F.; Qin, X.; Wang, Z.D.; Zhang, Z.R.; Jian, Y.L.; et al. In Vivo Biodistribution, Anti-Inflammatory, and Hepatoprotective Effects of Liver Targeting Dexamethasone Acetate Loaded Nanostructured Lipid Carrier System. *Int. J. Nanomed.* **2010**, *5*, 487–497. [CrossRef]
49. Xu, X.; Zhao, C.; Yang, H.; Jian, Y.; Zhang, Z.; Huang, Y. Anti-Inflammatory Activity of Injectable Dexamethasone Acetate-Loaded Nanostructured Lipid Carriers. *Drug Deliv.* **2011**, *18*, 485–492. [CrossRef]
50. Doktorovova, S.; Souto, E.B. Nanostructured Lipid Carrier-Based Hydrogel Formulations for Drug Delivery: A Comprehensive Review. *Expert Opin. Drug Deliv.* **2009**, *6*, 165–176. [CrossRef] [PubMed]
51. Lourenco, C.; Teixeira, M.; Simoes, S.; Gaspar, R. Steric Stabilization of Nanoparticles: Size and Surface Properties. *Int. J. Pharm.* **1996**, *138*, 1–12. [CrossRef]
52. Santander-Ortega, M.J.; Jódar-Reyes, A.B.; Csaba, N.; Bastos-González, D.; Ortega-Vinuesa, J.L. Colloidal Stability of Pluronic F68-Coated PLGA Nanoparticles: A Variety of Stabilisation Mechanisms. *J. Colloid Interface Sci.* **2006**, *302*, 522–529. [CrossRef]
53. Kovacevic, A.; Savic, S.; Vuleta, G.; Müller, R.H.; Keck, C.M. Polyhydroxy Surfactants for the Formulation of Lipid Nanoparticles (SLN and NLC): Effects on Size, Physical Stability and Particle Matrix Structure. *Int. J. Pharm.* **2011**, *406*, 163–172. [CrossRef]
54. Shah, R.; Eldridge, D.; Palombo, E.; Harding, I. Optimisation and Stability Assessment of Solid Lipid Nanoparticles Using Particle Size and Zeta Potential. *J. Phys. Sci.* **2014**, *25*, 59–75.
55. Richtering, W.; Alberg, I.; Zentel, R. Nanoparticles in the Biological Context: Surface Morphology and Protein Corona Formation. *Small* **2020**, *16*, 2002162. [CrossRef]
56. de la Harpe, K.; Kondiah, P.; Choonara, Y.; Marimuthu, T.; du Toit, L.; Pillay, V. The Hemocompatibility of Nanoparticles: A Review of Cell–Nanoparticle Interactions and Hemostasis. *Cells* **2019**, *8*, 1209. [CrossRef] [PubMed]
57. Mekkawy, I.A.; Mahmoud, U.M.; Hana, M.N.; Sayed, A.E.D.H. Cytotoxic and Hemotoxic Effects of Silver Nanoparticles on the African Catfish, Clarias Gariepinus (Burchell, 1822). *Ecotoxicol. Environ. Saf.* **2019**, *171*, 638–646. [CrossRef] [PubMed]
58. Chinnaiyan, S.K.; Karthikeyan, D.; Gadela, V.R. Development and Characterization of Metformin Loaded Pectin Nanoparticles for T2 Diabetes Mellitus. *Pharm. Nanotechnol.* **2018**, *6*, 253–263. [CrossRef] [PubMed]
59. Chain, C.Y.; Daza Millone, M.A.; Cisneros, J.S.; Ramirez, E.A.; Vela, M.E. Surface Plasmon Resonance as a Characterization Tool for Lipid Nanoparticles Used in Drug Delivery. *Front. Chem.* **2021**, *8*, 605307. [CrossRef]
60. Rahim, M.N.; Liberal, R.; Miquel, R.; Heaton, N.D.; Heneghan, M.A. Acute Severe Autoimmune Hepatitis: Corticosteroids or Liver Transplantation? *Liver Transpl.* **2019**, *25*, 946–959. [CrossRef] [PubMed]
61. Melgert, B.N.; Olinga, P.; van der Laan, J.M.S.; Weert, B.; Cho, J.; Schuppan, D.; Groothuis, G.M.M.; Meijer, D.K.F.; Poelstra, K. Targeting Dexamethasone to Kupffer Cells: Effects on Liver Inflammation and Fibrosis in Rats. *Hepatology* **2001**, *34*, 719–728. [CrossRef]

62. Bale, S.S.; Geerts, S.; Jindal, R.; Yarmush, M.L. Isolation and Co-Culture of Rat Parenchymal and Non-Parenchymal Liver Cells to Evaluate Cellular Interactions and Response. *Sci. Rep.* **2016**, *6*, 25329. [CrossRef] [PubMed]
63. Molinaro, R.; Pastò, A.; Corbo, C.; Taraballi, F.; Giordano, F.; Martinez, J.O.; Zhao, P.; Wang, X.; Zinger, A.; Boada, C.; et al. Macrophage-Derived Nanovesicles Exert Intrinsic Anti-Inflammatory Properties and Prolong Survival in Sepsis through a Direct Interaction with Macrophages. *Nanoscale* **2019**, *11*, 13576–13586. [CrossRef] [PubMed]
64. Corbo, C.; Cromer, W.E.; Molinaro, R.; Toledano Furman, N.E.; Hartman, K.A.; de Rosa, E.; Boada, C.; Wang, X.; Zawieja, D.C.; Agostini, M.; et al. Engineered Biomimetic Nanovesicles Show Intrinsic Anti-Inflammatory Properties for the Treatment of Inflammatory Bowel Diseases. *Nanoscale* **2017**, *9*, 14581–14591. [CrossRef] [PubMed]
65. Deng, Z.; Rong, Y.; Teng, Y.; Mu, J.; Zhuang, X.; Tseng, M.; Samykutty, A.; Zhang, L.; Yan, J.; Miller, D.; et al. Broccoli-Derived Nanoparticle Inhibits Mouse Colitis by Activating Dendritic Cell AMP-Activated Protein Kinase. *Mol. Ther.* **2017**, *25*, 1641–1654. [CrossRef] [PubMed]
66. Zhang, L.W.; Bäumer, W.; Monteiro-Riviere, N.A. Cellular Uptake Mechanisms and Toxicity of Quantum Dots in Dendritic Cells. *Nanomedicine* **2011**, *6*, 777–791. [CrossRef] [PubMed]
67. Tomić, S.; Dokić, J.; Vasilijić, S.; Ogrinc, N.; Rudolf, R.; Pelicon, P.; Vučević, D.; Milosavljević, P.; Janković, S.; Anžel, I.; et al. Size-Dependent Effects of Gold Nanoparticles Uptake on Maturation and Antitumor Functions of Human Dendritic Cells in Vitro. *PLoS ONE* **2014**, *9*, e96584. [CrossRef] [PubMed]
68. Vallhov, H.; Gabrielsson, S.; Strømme, M.; Scheynius, A.; Garcia-Bennett, A.E. Mesoporous Silica Particles Induce Size Dependent Effects on Human Dendritic Cells. *Nano Lett.* **2007**, *7*, 3576–3582. [CrossRef]

Article

Nanostructured Lipid Carriers Loaded with Dexamethasone Prevent Inflammatory Responses in Primary Non-Parenchymal Liver Cells

Carolina Medina-Montano & Ignacio Rivero Berti et al.

Supplementary Material

Table S1. DXM release kinetics of the different formulations were fitted with different models used for the description of drug release mechanisms (First Order, Higuchi, Korsmeyer-Peppas, and Hixon and Crowell). The release model that best fitted to the experimental data was selected according to the calculations of the coefficient of determination (R^2).

Model Name	Equation	F1	F2	F3	F4
First Order model	$\log Q_t = log\ Q_0 + \frac{k_i t}{2.303}$	0.85	0.75	0.37	0.14
Higuchi model	$Q_t = K_H\sqrt{t}$	0.88	0.90	0.58	0.76
Korsmeyer-Peppas	$\frac{Q_t}{Q_0} = K_k t^n$	0.93	0.95	0.82	0.90
Hixon and Crowell	$\sqrt[3]{Q_0} - \sqrt[3]{Q_t} = K_s t$	0.79	0.61	0.22	0.08

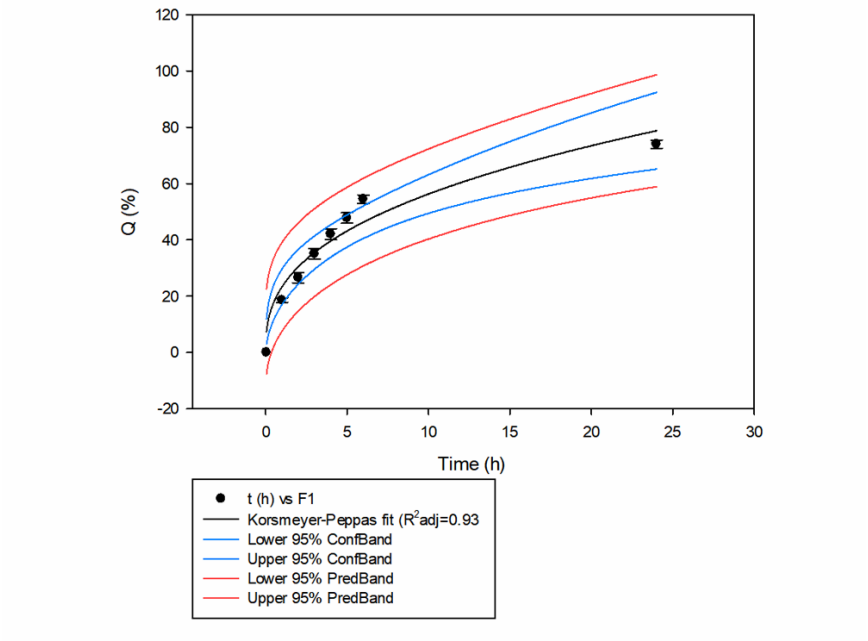

Figure S1. DXM release profile from F1. Continuous black line represents Korsmeyer-Peppas model fit. Blue lines correspond to upper and lower 95% confidence intervals and red lines upper and lower 95% prediction intervals.

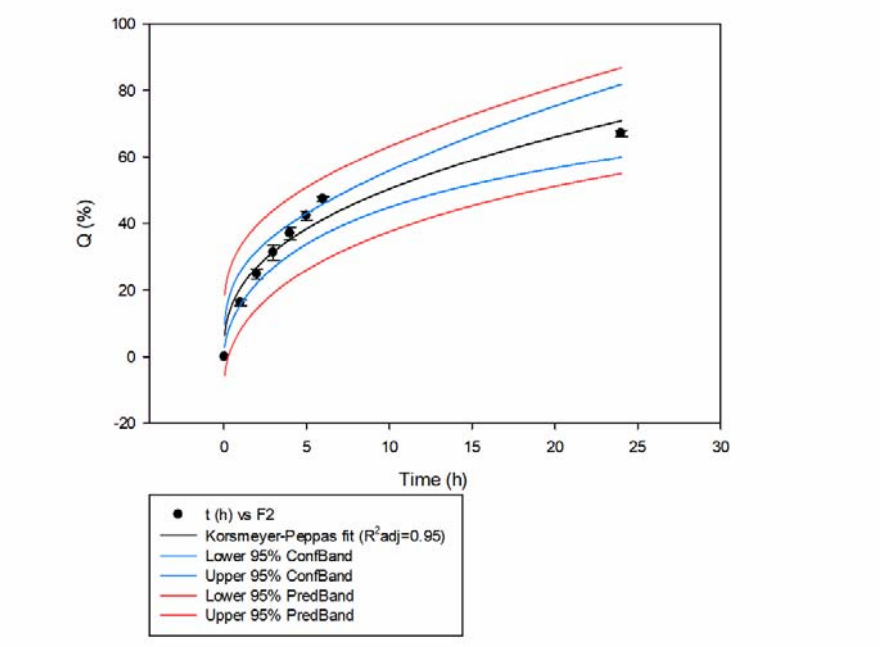

Figure S2. DXM release profile from F2. Continuous black line represents Korsmeyer-Peppas model fit. Blue lines correspond to upper and lower 95% confidence intervals and red lines upper and lower 95% prediction intervals.

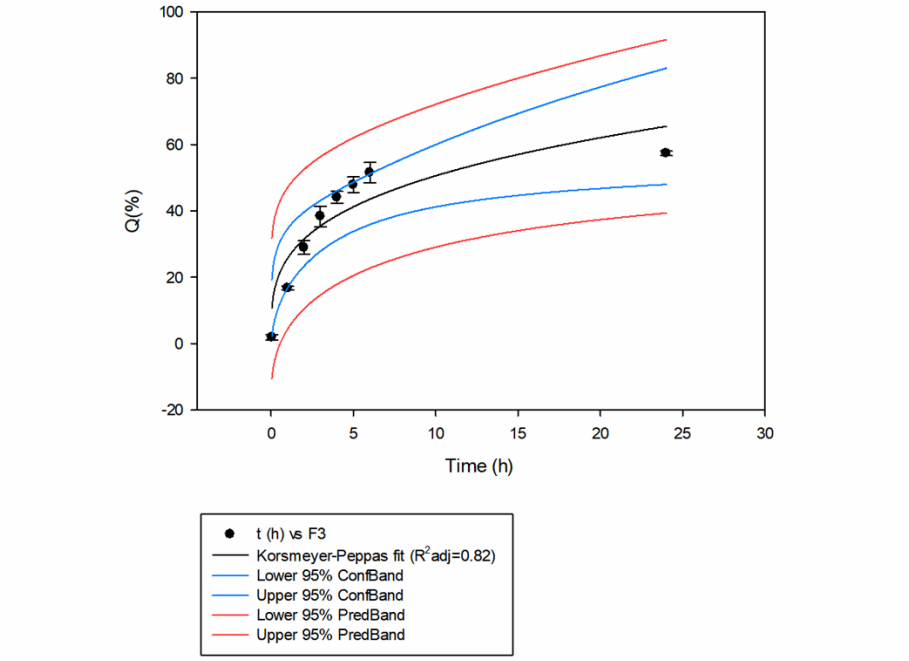

Figure S3. DXM release profile from F3. Continuous black line represents Korsmeyer-Peppas model fit. Blue lines correspond to upper and lower 95% confidence intervals and red lines upper and lower 95% prediction intervals.

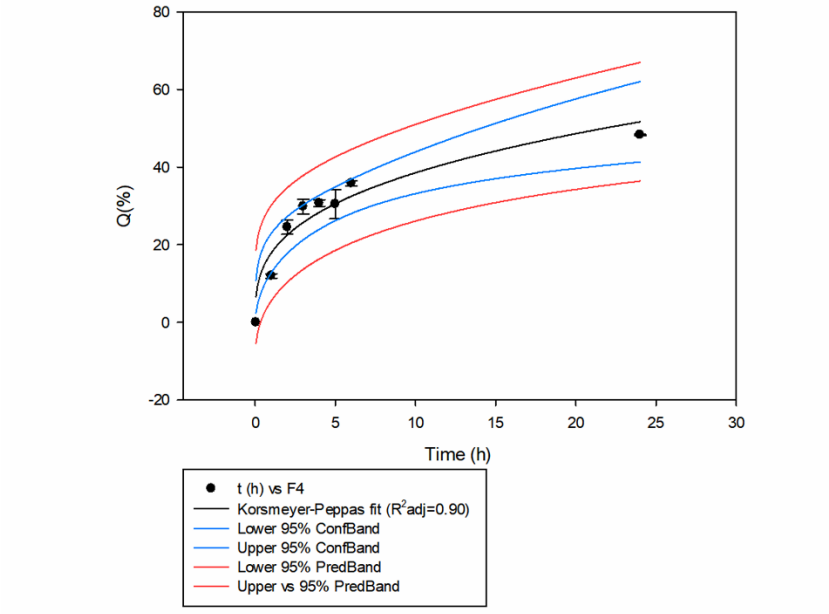

Figure S4. DXM release profile from F4. Continuous black line represents Korsmeyer-Peppas model fit. Blue lines correspond to upper and lower 95% confidence intervals and red lines upper and lower 95% prediction intervals.

10.10. Publication 10

"Peptide-decorated degradable polycarbonate nanogels for eliciting antigen-specific immune responses"

This study has been published in MDPI (International Journal of Molecular Sciences). My focus as a co-author was on conducting biological *in vitro* experiments to assess the efficacy and immunostimulatory properties of the developed biodegradable polycarbonate nanogels. By combining the potential of Imidazoquinoline-based Toll-like receptor 7/8 agonists and peptide antigens, our study represents a significant step towards achieving robust antigen-specific immune responses. Through meticulous evaluation, we confirmed the ability of nanogels to stimulate mature primary antigen-presenting cells, paving the way for potent CD4+-T cell priming-a crucial aspect in the landscape of cancer immunotherapy. The success of our in vitro experiments underscores the potential of this multifaceted approach for future applications in the field.

DOI: 10.3390/ijms242015417

Published in: *International Journal of Molecular Sciences*. **2023**, 24(20), 15417

Reprinted with permission under creative commons attribution 4.0 (CC BY-NC) from Stickdorn, J.; Czysch, C.; **Medina-Montano, C**.; Stein, L.; Xu, L.; Scherger, M.; Schild, H.; Grabbe, S.; Nuhn, L. Peptide-Decorated Degradable Polycarbonate Nanogels for Eliciting Antigen-Specific Immune Responses. Int. J. Mol. Sci. 2023, 24, 15417. https://doi.org/10.3390/ijms242015417.

International Journal of
Molecular Sciences

MDPI

Article

Peptide-Decorated Degradable Polycarbonate Nanogels for Eliciting Antigen-Specific Immune Responses

Judith Stickdorn [1,†], Christian Czysch [1,†], Carolina Medina-Montano [2], Lara Stein [3], Lujuan Xu [1,4], Maximilian Scherger [1], Hansjörg Schild [3], Stephan Grabbe [2] and Lutz Nuhn [1,5,*]

1 Max Planck Institute for Polymer Research, 55128 Mainz, Germany
2 Department of Dermatology, University Medical Center, Johannes Gutenberg-University Mainz, 55131 Mainz, Germany
3 Institute of Immunology, University Medical Center, Johannes Gutenberg-University Mainz, 55131 Mainz, Germany
4 Zhejiang Cancer Hospital, The Key Laboratory of Zhejiang Province for Aptamers and Theranostics, Hangzhou Institute of Medicine (HIM), Chinese Academy of Sciences, Hangzhou 310022, China
5 Chair of Macromolecular Chemistry, Institute of Functional Materials and Biofabrication, Department of Chemistry and Pharmacy, Julius-Maximilians-Universität Würzburg, 97074 Würzburg, Germany
* Correspondence: lutz.nuhn@uni-wuerzburg.de
† These authors contributed equally to this work.

Abstract: For successful therapeutic interventions in cancer immunotherapy, strong antigen-specific immune responses are required. To this end, immunostimulating cues must be combined with antigens to simultaneously arrive at antigen-presenting cells and initiate cellular immune responses. Recently, imidazoquinolines have shown their vast potential as small molecular Toll-like receptor 7/8 (TLR7/8) agonists for immunostimulation when delivered by nanocarriers. At the same time, peptide antigens are promising antigen candidates but require combination with immune-stimulating adjuvants to boost their immunogenicity and exploit their full potential. Consequently, we herein present biodegradable polycarbonate nanogels as versatile delivery system for adjuvants within the particles' core as well as for peptide antigens by surface decoration. For that purpose, orthogonally addressable multifunctional polycarbonate block copolymers were synthesized, enabling adjuvant conjugation through reactive ester chemistry and peptide decoration by strain-promoted alkyne-azide cycloaddition (SPAAC). In preparation for SPAAC, $CD4^+$-specific peptide sequences of the model protein antigen ovalbumin were equipped with DBCO-moieties by site-selective modification at their *N*-terminal cysteine. With their azide groups exposed on their surface, the adjuvant-loaded nanogels were then efficiently decorated with DBCO-functional $CD4^+$-peptides by SPAAC. In vitro evaluation of the adjuvant-loaded peptide-decorated gels then confirmed their strong immunostimulating properties as well as their high biocompatibility. Despite their covalent conjugation, the $CD4^+$-peptide-decorated nanogels led to maturation of primary antigen-presenting cells and the downstream priming of $CD4^+$-T cells. Subsequently, the peptide-decorated nanogels loaded with TLR7/8 agonist were successfully processed by antigen-presenting cells, enabling potent immune responses for future application in antigen-specific cancer immunotherapy.

Keywords: aliphatic polycarbonate; post-polymerization modification; peptide antigen; polymer peptide conjugate; nanovaccine

check for updates

Citation: Stickdorn, J.; Czysch, C.; Medina-Montano, C.; Stein, L.; Xu, L.; Scherger, M.; Schild, H.; Grabbe, S.; Nuhn, L. Peptide-Decorated Degradable Polycarbonate Nanogels for Eliciting Antigen-Specific Immune Responses. *Int. J. Mol. Sci.* **2023**, *24*, 15417. https://doi.org/10.3390/ijms242015417

Academic Editor: Keng-Shiang Huang

Received: 30 September 2023
Revised: 8 October 2023
Accepted: 19 October 2023
Published: 21 October 2023

Copyright: © 2023 by the authors. Licensee MDPI, Basel, Switzerland. This article is an open access article distributed under the terms and conditions of the Creative Commons Attribution (CC BY) license (https://creativecommons.org/licenses/by/4.0/).

1. Introduction

The development of vaccines revolutionized the world's response towards infectious diseases throughout the most recent centuries and is estimated to prevent millions of deaths yearly [1,2]. During the last decades, the scope of possible antigenic moieties that induce an adaptive immune response expanded from inactivated or attenuated pathogens to proteins in subunit vaccines [2]. In recent years, accelerated by the COVID-19 pandemic,

even smaller immunogenic cargos such as peptides [3] and mRNAs [4] showed their vast potential for mass application in vaccines [5]. Being readily adaptable, peptide and mRNA-based vaccines can be employed against fast mutating viruses or highly heterogeneous cancer types based on their presently well-established and automated synthesis of distinct epitope sequences [6].

Proteins and peptides generally exhibit reduced immunogenicity compared to attenuated pathogens [7]. Thus, towards an effective therapeutic treatment with these subunit vaccines, not only the proper selection of the antigen but also a precise co-delivery with immune cell-stimulating adjuvants is of importance [8]. In this regard, Toll-like receptor (TLR) agonists that evoke a strong innate and adaptive immune stimulation can be employed. These agonists include nucleic acid adjuvants [9,10] (poly(I:C)-TLR3 and CpG-TLR9) as well as small molecular agonists such as imidazoquinolines (TLR7/8) [11–13]. These agonists bind to the TLRs expressed on endosomal membranes of antigen-presenting cells (APCs), e.g., dendritic cells (DCs), leading to their maturation and the upregulation of MHC-I and II expression besides co-stimulatory signaling and the release of pro-inflammatory cytokines that lead to the downstream activation of other immune cells [14]. Based on their capacity to present exogenous antigens to T cells, the activation and maturation of APCs like dendritic cells is a prerequisite for eliciting potent immune reactions [15,16]. This process, called cross-presentation, leads to the induction of antigen-specific cytotoxic $CD8^+$ T cells that are presumed crucial in eliminating malignant tumor cells [17]. Apart from $CD8^+$ cell epitopes, peptide-based vaccines must also contain epitopes of $CD4^+$ T cells to ensure the generation of antigen-specific T helper cells. The resulting interaction of those T helper cells with antigen-specific $CD8^+$ T cells is necessary to provoke an effective cellular immunity [14].

Beyond cheaper and faster production when compared to full proteins, peptide antigens also allow sequence-selective tuning for specific (e.g., mutated) epitopes. Especially in targeting patient-specific tumor neoantigens, peptide antigens can be tailored to an individual's neoantigen repertoire [6,18]. Due to their fully synthetic character, they also improve drug safety by diminishing risks of contaminations from pathogens and toxins [19]. Yet, the absence of inherent immunogenicity has to be taken into account prior to administration. It allows for an improved control over respective downstream immune responses. Depending on the co-administration of potent adjuvants of choice a precise activation of desired immune responses can be achieved and fine-tuned [20].

However, when adjuvants and peptide antigens are applied as such, they distribute systemically and the adjuvants in particular can trigger severe off-target toxicities [21–25]. Nanoparticular delivery allows for a more localized immunostimulation focused to sites of the immune system (e.g., lymph nodes and spleen) [26–28]. Thus, nanoparticles can improve the drug's therapeutic window and safety [29]. In addition to that, nanoparticles can mimic pathogens by presenting multiple antigens on their surface. Therefore, they enable multivalency effects which have been shown to elicit stronger immune responses than the single presentation of antigens and thus ameliorate immunotherapeutic interventions [30–32].

For the safe application of nanoparticulate vaccines, it is of great importance that the polymeric materials used are biocompatible [33]. In this regard, aliphatic polycarbonates are a promising material class, even offering a degradable polymer backbone that permits disintegration after therapy [34–36]. Polycarbonate's degradation results in weak acid carbon dioxide and hydrophilic diols, which generally do not exert adverse effects but can get excreted from the body via renal clearance [37]. Moreover, a plethora of functional polycarbonates is readily accessible by polymerizing monomers with various ester or ether side chains [36,38,39]. Most relevant for the generation of functional materials, 5-methyl-5-pentafluorophenyloxycarbonyl-1,3-dioxan-2-one (MTC-PFP), a monomer with a reactive ester side chain, was polymerized via cationic ring-opening polymerization (ROP) [40,41]. After polymerization, these active ester side chains allow for the tuning of material properties via post-polymerization modification with amines [42,43]. Similar to

other polymeric architectures that were successfully applied to generate nanocarriers for immunostimulation by the post-polymerization modification approach [44–46], reactive ester polycarbonates are suitable materials in this regard [47]. Recently established polycarbonate carriers were not only shown to be readily modifiable, but are also hydrolytically degradable in physiological media, enabling spatio-temporal control over immunostimulation via degradation [48]. Moreover, they allow for the attachment of multiple functionalities for immunodrug delivery such as small molecular adjuvants, dyes, or cross-linkers for enhanced stability. However, for further development towards vaccination, immunostimulatory nanocarriers must be combined with antigens to elicit strong antigen-specific immune responses [28,49–51].

For that purpose, we expanded the strategy of polycarbonate nanogels derived from MTC-PFP by orthogonally addressable azide click groups at the surface of the nanogels, which allow for a covalent conjugation of DBCO-modified peptide antigens via strain-promoted alkyne-azide cycloaddition (SPAAC). Both the antigen- and adjuvant-loaded biodegradable nanogels can effectively co-deliver both entities to antigen-presenting cells for eliciting antigen-specific immune responses, thus serving as promising customizable nanovaccines (Figure 1).

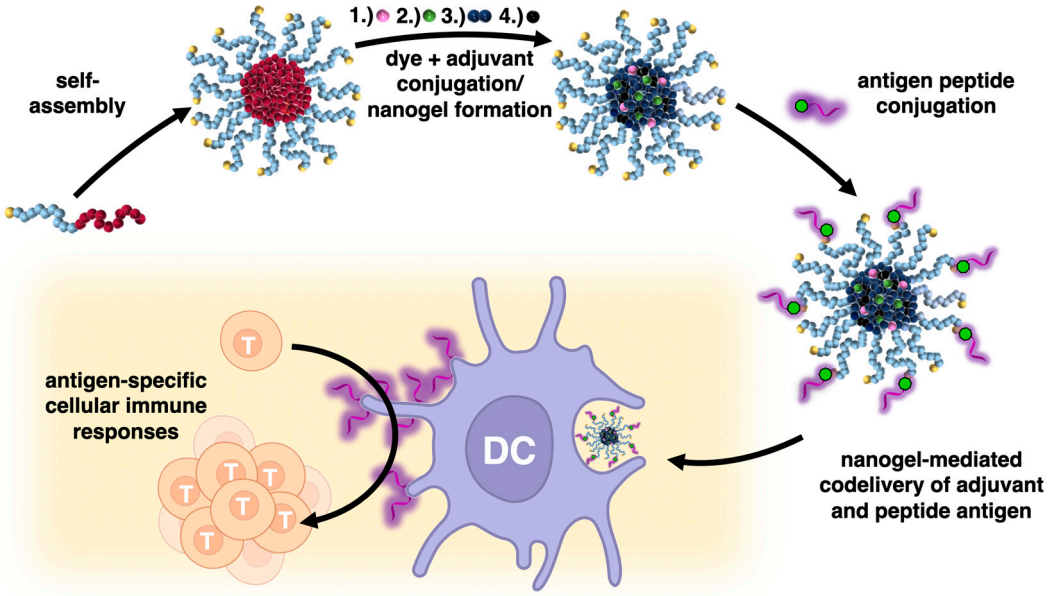

Figure 1. The strategy of covalent co-delivery of small molecular imidazoquinoline-based TLR 7/8 agonists with peptide antigens via polycarbonate block copolymer-derived nanogels. Core-functionalization through sequential reactive ester chemistry conversion is combined with biorthogonal strain-promoted alkyne-azide cycloaddition (SPAAC) click chemistry on the surface of the nanogel to generate both adjuvant- and antigen-loaded biodegradable nanogels that efficiently co-deliver both entities to antigen-presenting dendritic cells and trigger an antigen-specific T-cell proliferation.

2. Results and Discussion

We opted for the polycarbonate nanogel platform with the aim of combining them with peptide antigens via functionalization of the particular surface. For that purpose, polymers containing reactive moieties were synthesized and subsequently assembled to form functionalizable nanocarriers. Extending the nanogel platform for covalent attachments to the nanoparticular surface, we opted for azide-functional block copolymers that enable functionalization through orthogonally addressable click chemistry. Such block copolymers can be synthesized using functional macroinitiators with a clickable end group such as α-azido-ω-hydroxy-terminated polyethylene glycol (azide-PEG_{113}-OH). Polymerizing a second polymer block from this macroinitiator should enable the self-assembly to form polymeric micelles and subsequently convert them into nanogels via post-polymerization

modification. Therefore, the six-membered active ester monomer MTC-PFP was polymerized by cationic ROP initiated from azide-PEG$_{113}$-OH (Figure 2A). Ensuring ideal reaction conditions for a controlled polymerization, reagents were thoroughly dried beforehand, and the reaction was conducted in a nitrogen-purged glove box. By these means, narrowly distributed block copolymers were obtained as analyzed using size exclusion chromatography (Figure 2B, $Đ$ = 1.18 and Figure S1). Further characterization data acquired with NMR spectroscopy and mass spectrometry confirmed the controlled synthesis of the block copolymer azide-PEG$_{113}$-*b*-poly(MTC-PFP)$_{28}$ (Figures S2–S4).

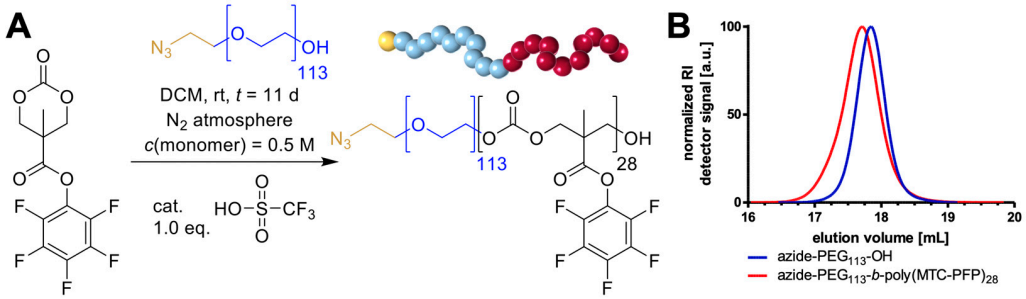

Figure 2. Polycarbonate block copolymer synthesis via organocatalyzed ring-opening polymerization (ROP) of 5 methyl-5-pentafluorophenyloxycarbonyl-1,3-dioxan-2-one (MTC-PFP) initiated by azide functionalized polyethylene glycol (azide-PEG$_{113}$-OH). (**A**) Cationic ROP of MTC-PFP catalyzed by trifluoromethanesulfonic acid (TFMSA) affording azide-PEG$_{113}$-*b*-poly(MTC-PFP)$_{28}$ block copolymers. (**B**) Size exclusion chromatography (SEC) elugram recorded by a refractive index (RI) detector of azide-PEG$_{113}$-OH (blue, $Đ$ = 1.10) and azide-PEG$_{113}$-*b*-poly(MTC-PFP)$_{28}$ (red, $Đ$ = 1.18), showing narrowly distributed homo and block copolymers.

These active ester precursor polymers were then employed in the fabrication of azide-functional nanogels (Figure 3). First, polymers were assembled into micelles (Figure 3(B1), top) to form narrowly distributed nanoparticles (z-ave. = 23.6 nm; PDI = 0.20). These assemblies were then functionalized in a post-polymerization modification approach. Therefore, amine functional molecules were covalently attached to the nanogels by amidation reactions. Starting with the attachment of amine functional tetramethylrhodamine (TMR) cadaverine and TLR7/8 agonist IMDQ, small molecular cargos were loaded that later act as sensors within biological systems and boost strong immune responses, respectively. The micelles were core-crosslinked with the hydrophilic bisamine 1,8-diamino-3,6-dioxaoctane, forming fully hydrophilic nanogels. Ensuring the complete removal of the remaining reactive ester sidechains within the nanogels, an excess of ethanolamine was added. By altering the attached amines, both drug-loaded and non-drug-loaded nanogels were prepared. Byproducts such as pentafluorophenol as well as other non-bound drugs or dyes were then removed by dialysis. The resulting nanogels were again analyzed by DLS (Figure 3(B1)) and showed sizes of 25.3 nm (z-ave. and PDI of 0.15) for IMDQ-loaded nanogels (azide-NP(IMDQ), blue line) and of 26.4 nm (z-ave. and PDI of 0.08, red line) for non-loaded nanogels (azide-NP(-)). Note that both nanogels provided similar sizes as their initially self-assembled micelles. Additionally, the nanogels revealed a gradual disintegration behavior at physiological conditions (PBS, pH 7.4, 37 °C) over a timespan of several days, forming small molecular degradation products (Figure S5). These properties underline the polycarbonate-based hydrolytic degradation feature favorable for biodegradation and transient immunodrug delivery purposes [48]. Additionally, covalent IMDQ drug-load was determined via UV–Vis measurement (Figure 3(B2)), and applying an external IMDQ calibration curve afforded a drug-load of 4.6 wt% (Figure S6).

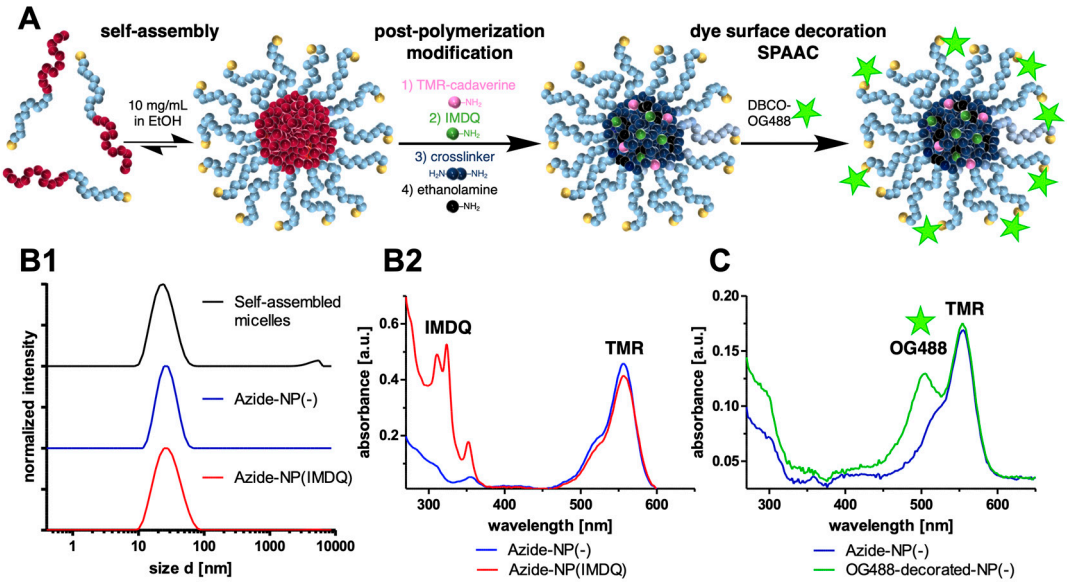

Figure 3. Preparation of azide-functional polycarbonate nanogels from azide-PEG_{113}-b-poly(MTC-$PFP)_{28}$ by post-polymerization modification and their surface-modification by strain-promoted alkyne-azide cycloaddition (SPAAC). (**A**) Nanogel fabrication via self-assembly of reactive precursor polymers in ethanol, forming azide-functional polymeric micelles. Post-polymerization modification by attachment of amine-functional molecules such as tetramethylrhodamine (TMR) cadaverine fluorescent dye, TLR7/8 agonist IMDQ and hydrophilic crosslinker 1,8-diamino-3,6-dioxaoctane. By these means, drug-loaded nanogels (azide-NP(IMDQ)) and non-drug-loaded nanogels (azide-NP(-)) were prepared. Surface functionalization of the azide-functional nanogels and the accessibility of the azide moieties on the surface was then demonstrated by attaching the DBCO-modified fluorescent dye Oregon Green 488 (OG488—green star). (**B**) Characterization data of azide-functional nanogels. (**B1**) Dynamic light scattering (DLS) measurements confirming the uniform size of nanogels (azide-NP(-), blue) and IMDQ-loaded nanogels (azide-NP(IMDQ), red), comparable to the initially self-assembled micelles (black). (**B2**) UV–Vis spectra of the nanogels showing both the TMR absorption at ~550 nm and the IMDQ absorption for azide-NP(IMDQ) at ~321 nm. (**C**) UV–Vis spectra of the surface functionalization of azide-NP(-) with DBCO-modified fluorescent dye OG488. After SPAAC and thorough removal of excess dye, the additional absorbance of OG488 at ~488 nm demonstrated successful surface modification to yield OG488-decorated-NP(-) (green). A control sample of azide-NP(-) treated with OG488 cadaverine showed no conjugation to the nanogel and quantitative removal during spin-filtration workup (blue line).

For the following preparation of peptide-decorated nanogels using the anticipated click approach, it had to be ensured that the nanocarriers' azide-groups were accessible and still able to react with their alkyne counterparts during SPAAC. In this regard, the attachment of a DBCO-modified fluorescent dye (OG488) to the surface of the carriers was attempted. After work-up by excessive spin filtration for the removal of potentially unreacted dye, an additional UV-absorption at 488 nm was found (Figure 3C, green line). Contrarily, the control reaction where an OG488 cadaverine dye was used instead showed that the dye was not conjugated to the nanogels and quantitively removed during spin-filtration workup (Figure 3C, blue line and Figure S7). Therefore, it was proven that azide-groups are indeed accessible for click reaction, enabling the efficient surface decoration of nanogels.

Proven reactive towards DBCO-displaying molecules, we proceeded with the conjugation of antigenic peptides to the azide-functional nanogels. An antigenic peptide sequence was selected based on the $CD4^+$ T cell epitope of the model protein ovalbumin (OVA) [52], which is widely used to evaluate vaccine delivery systems for cancer immunotherapy [50,53,54]. We previously demonstrated that the attachment of the full protein to the surface of IMDQ-loaded methacrylate-based nanogels is able to trigger

profound cellular and humoral immune responses [50]. Here, we wanted to expand the strategy towards the application of antigenic peptide sequences that can specifically initiate $CD4^+$-T cell responses exclusively. To ensure the co-delivery of peptides and adjuvants into the same immune cell populations and an improved immune response, both compounds should be combined into the same nanocarrier [53,55–57].

For this purpose, the selected peptide sequence had to be modified with a DBCO-functionality for the subsequent SPAAC conjugation to nanogels. Hence, we exploited the *N*-terminal cysteine for a site-selective modification with DBCO-PEG_{12}-maleimide (Figure 4A). For monitoring the delivery process of the peptide by the nanogel to the antigen-presenting cells, we used a peptide sequence that was further equipped with covalently attached 5-carboxyfluorescein (5-FAM) at its *N*-terminus (5-FAM-CSSAESLKISQAVH-AAHAEINEAGR). Successful DBCO-modification was determined by LC-MS (Figure 4(B1,B2) and showed nearly complete conversion by a quantitative shift in the HPLC trace compared to the unmodified peptide (Figure 4(B1)). In addition, expected molecular weights of DBCO-modified peptide conjugates were found by ESI-MS, while traces of unmodified peptide residues remained elusive (Figure 4(B2), Figures S8 and S9). Based on these results, the DBCO-modified $CD4^+$ peptide was directly used without further purification for the SPAAC conjugation to the azide-nanogels.

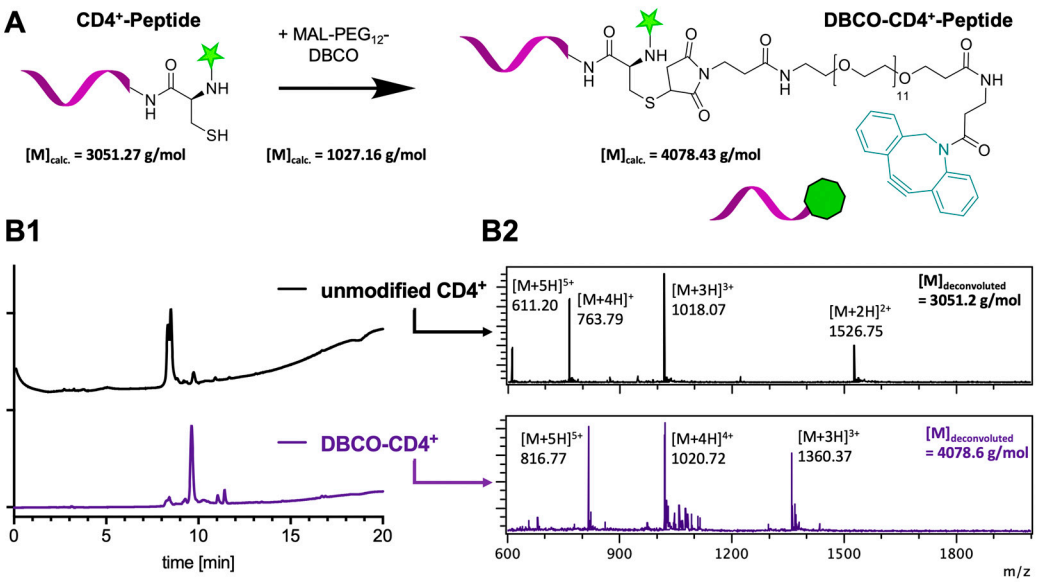

Figure 4. Ovalbumin-derived $CD4^+$-peptide antigen modification. (**A**) Reaction of the peptide's *N*-terminal cysteine thiol moieties with maleimide-functional DBCO (MAL-PEG_{12}-DBCO) by Michael-addition. For fluorescence tracing, the peptides are covalently equipped with 5-carboxyfluorescein (5-FAM) dye (green star) at their *N*-terminus. (**B**) Characterization results by LCMS. (**B1**) HPLC trace of DBCO-conjugated $CD4^+$-peptide antigen detected by UV–Vis at 254 nm in comparison to unmodified $CD4^+$-peptide before Michael-addition of MAL-PEG_{12}-DBCO. (**B2**) ESI-MS data of the respective ionized species for unmodified and DBCO-conjugated $CD4^+$-peptide antigen. After deconvolution an increase in molecular weight of 1027.4 g/mol was found for the modified $CD4^+$-peptide antigen which corresponds to the molecular weight of MAL-PEG_{12}-DBCO.

Consequently, the covalent attachment of peptides to nanogels was pursued by mixing the DBCO-modified $CD4^+$-peptide antigens with the IMDQ-loaded azide-functional nanocarrier in water (supplemented with hydrochloric acid at pH 4 to avoid premature hydrolytic nanogel degradation) (Figure 5A). SPAAC conjugation was performed in a molar ratio of 1:9 (DBCO to azide) and analyzed by sodium dodecyl sulfate–polyacrylamide gel electrophoresis (SDS-PAGE). Fluorescent labeling of both peptide (5-FAM) and nanogel (TMR) allowed for a direct optical visualization of successful conjugation on the polyacrylamide gel upon illumination (Figure 5C for UV–Vis absorbance spectra). For the

conjugation of the modified CD4$^+$-peptide antigen, the band of the free DBCO-modified CD4$^+$-peptide disappeared after incubation of the peptides with nanogels (Figure 5D). In the case of mixing the non-DBCO modified soluble CD4$^+$-peptide with the nanogel, no change in band intensity was observable for the free peptide. Furthermore, the successful conjugation of the CD4$^+$-peptide was confirmed by a yellowish trace in the sample well and at the intersection between stacking and separating gel, where the nanogel NP(IMDQ) or the control sample (NP(IMDQ)+sol. CD4$^+$) provided a red-orange color(Figure 5D).

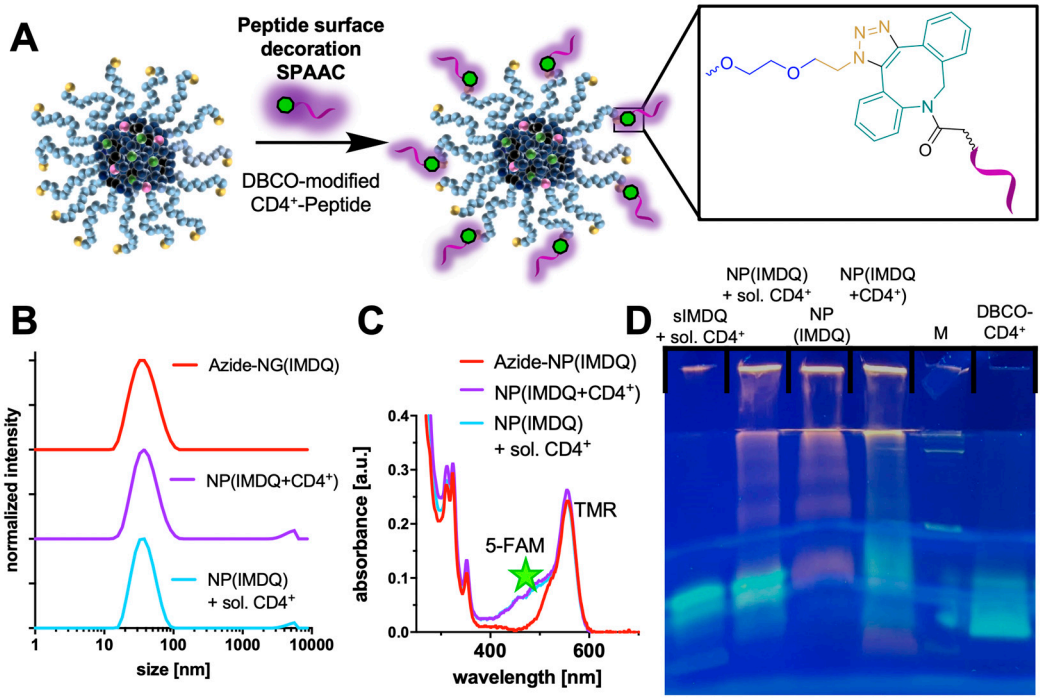

Figure 5. Surface decoration of adjuvant-loaded polycarbonate nanogels. (**A**) Conjugation of CD4$^+$-peptide antigens to the nanogel surface by SPAAC. Magnification of the triazol product (right) that covalently links the peptides to the nanogel surface. (**B**) DLS measurements of azide-NP(IMDQ) and NP(IMDQ+CD4$^+$) after SPAAC and control (NP(IMDQ) + sol. CD4$^+$). (**C**) UV–Vis measurements of NPs showing additional UV absorption at 488 nm of 5-FAM after addition of the CD4$^+$-peptide solution. (**D**) SDS-PAGE proving the covalent attachment of DBCO-CD4$^+$ to the nanogel surface (NP(IMDQ+CD4$^+$).

During subsequent characterization of the nanogel formulations by DLS measurements, uniform sizes without major differences between the samples were recorded (Figure 5B). IMDQ-loaded nanogels showed sizes of 34.5 nm (z. ave. size and PDI of 0.15) and CD4$^+$-peptide antigen-decorated nanogels of 38.7 nm nm (z. ave. size and PDI of 0.23). The mixture of IMDQ-loaded nanogels and soluble CD4$^+$-peptide antigens exhibited a size of 36.3 nm (z. ave. size and PDI of 0.18). Hence, attachment of the small peptides into the nanogel corona did not alter the nanogels' dimensions significantly. Additionally, atomic force microscopy (AFM) images confirmed the spherical shape of the peptide-decorated nanogels (Figure S10). Further characterization was performed by UV–Vis measurements and confirmed similar IMDQ-loading as well as dye-functionalization for soluble or conjugated CD4$^+$-peptide antigens to nanogels for subsequent in vitro analyses (Figure 5C).

Having established the fabrication of adjuvant-loaded nanogels with a peptide-decorated surface, we next evaluated the biological behavior of the carrier system. To this end, first in vitro tests were conducted on RAW Blue macrophages to evaluate the nanogels' immunostimulation and biocompatibility [58]. These experiments confirmed that IMDQ-loaded nanogels are able to effectively stimulate macrophages at concentrations in the

µM range (Figure S11). Moreover, they do not exert negative effects on cell viability as investigated by MTT assays (for particle concentrations of up to 0.061 mg/mL).

Next, the co-delivery potential of peptide-decorated particles was investigated on this cell line by confocal microscopy images according to the dual labeling of nanogel (TMR) and antigen peptide (5-FAM). As shown in Figure 6, nanogels are generally well internalized by the RAW macrophage cells and provide a signal in the TMR-channel. However, detection of 5-FAM fluorescence related to the $CD4^+$-peptide antigen can only be observed when it is covalently attached to the nanogel. Non-conjugated $CD4^+$-peptide alone or mixed with the nanogel cannot become internalized by the cells. Only after SPAAC-mediated covalent conjugation to the nanogel surface can a co-localization of the 5-FAM fluorescence of the $CD4^+$-peptide with TMR fluorescence of the nanogels be found (Figures 6 and S12).

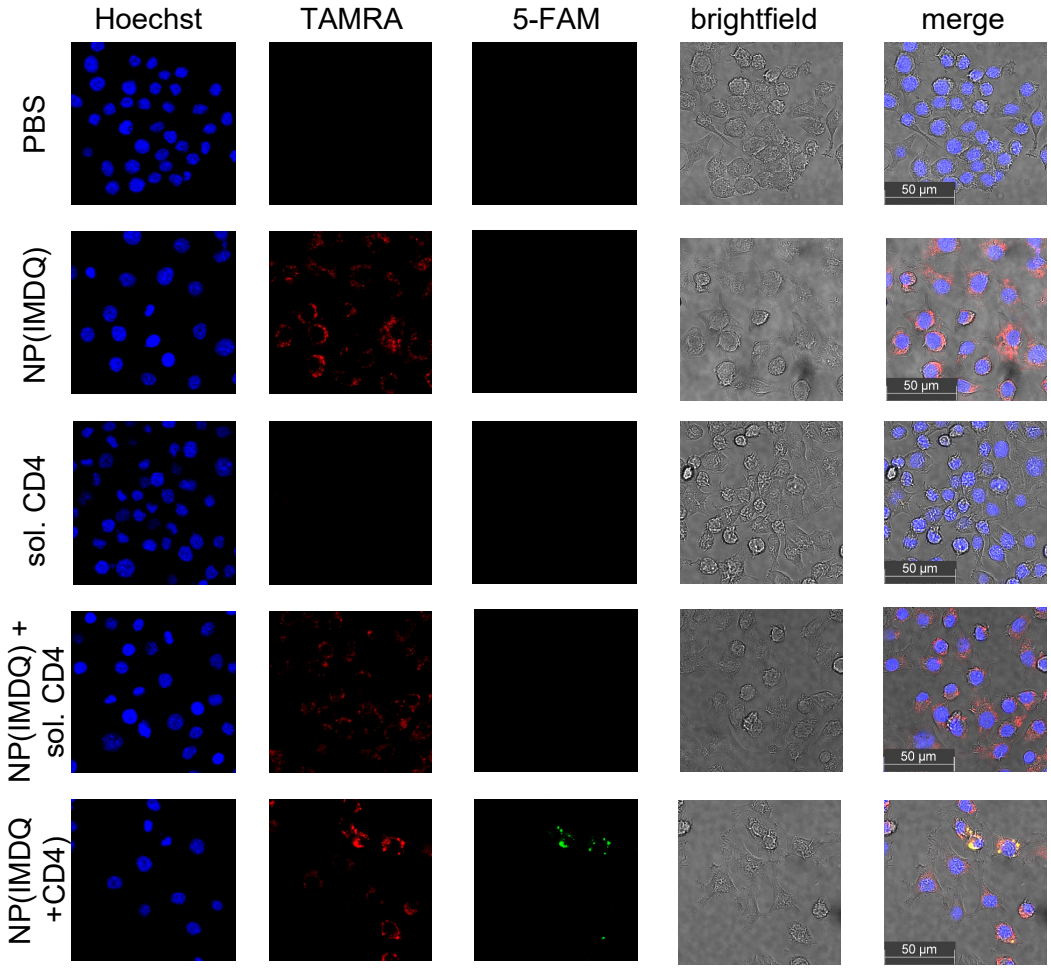

Figure 6. Confocal microscopy on RAW macrophages showing the internalization of nanogels by TMR fluorescence (red) and synchronously the co-uptake of $CD4^+$-peptides by 5-FAM fluorescence (green) only when covalently attached to the nanogel. Nuclei were stained with Hoechst dye (blue) and bright-field images (grey) were used for visualizing cellular morphologies.

Since antigens need to be processed and presented by antigen-presenting cells (APCs) for the subsequent activation and priming of T cells, further experiments were performed on primary antigen-presenting cells (APCs). Incubation of bone marrow-derived dendritic cells (BMDCs) with peptide-decorated nanogels followed by flow cytometric quantification provided similar uptake behavior as observed before on RAW Blue macrophages (Figure 6). While samples containing nanogels provided signals in the TMR channel (Figure 7(A1)), superior signals for the FAM-labeled $CD4^+$-peptide antigens were preferentially found when they were covalently attached to the nanogel surface as NP(IMDQ+$CD4^+$) (Figure 7(A2)).

These observations confirm again the successful co-delivery properties for polycarbonate nanogels for promoting the cellular internalization of peptide-based antigens after covalent conjugation to the nanogel surface.

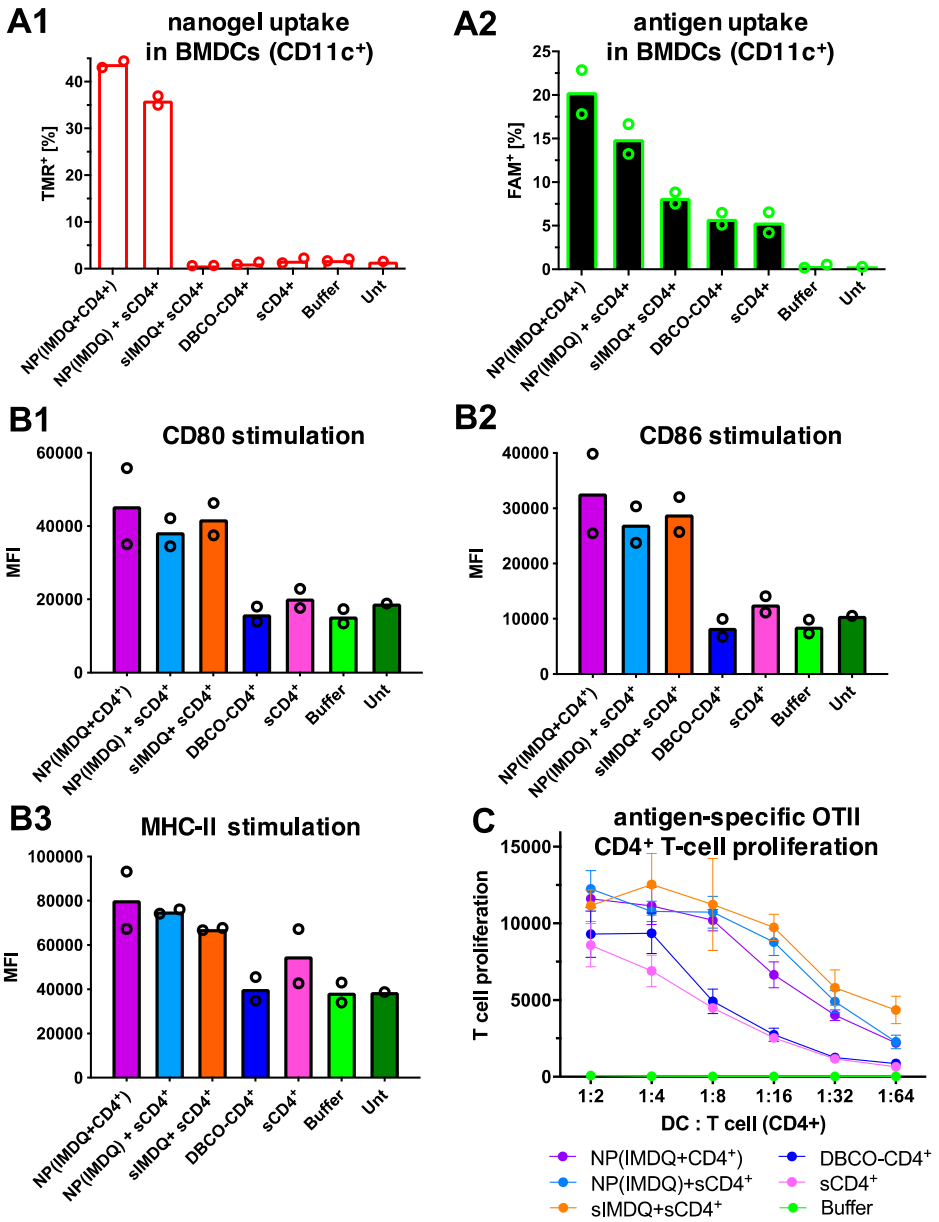

Figure 7. In vitro immune stimulatory evaluation of CD4+-peptide antigen-decorated nanogels NP(IMDQ+CD4+) on bone marrow-derived dendritic cells (BMDCs) as two biological replicates. (**A**) Uptake of CD4+-peptide antigen-decorated nanogels into BMDCs determined by flow cytometry. (**A1**) Nanogel uptake by TMR fluorescence. (**A2**) CD4+-peptide antigen uptake by FAM fluorescence. (**B**) The maturation of BMDCs determined by flow cytometry. An upregulation of maturation markers can be found for those cells that were treated with samples containing the TLR7/8 agonist IMDQ (**B1**) Stimulation of maturation marker CD-80. (**B2**) Stimulation of maturation marker CD-86. (**B3**) Stimulation of maturation marker MHC-II. (**C**) Dendritic cells incubated with adjuvant and CD4+-peptide antigen-containing samples efficiently stimulate CD4+-peptide antigen-specific T cells. In a co-culture model experiment of BMDCs with OTII cells, a strong proliferation of the CD4+-peptide antigen-specific T cells was found even at a low DC:T cell ratio. Similar antigen-specific proliferations were found when both components (IMDQ adjuvant and CD4+-peptide antigen) were covalently ligated and co-delivered by the polycarbonate nanogels.

More significantly, the antigen- and adjuvant-loaded nanogels subsequently stimulate the BMDCs and efficiently promote their maturation. For those BMDC samples, the expression of the typical maturation markers CD80 (Figure 7(B1)), CD86 (Figure 7(B2)), and MHC-II (Figure 7(B3)) were upregulated when they were exposed to soluble or nanogel-bound IMDQ. Since maturated DCs are a prerequisite for downstream activation of other immune cells, these results motivated us to further investigate the effective peptide antigen presentation on APCs (Figure 7C). Based on this, the downstream activation of antigen-specific $CD4^+$ T cells can be monitored via co-culturing and proliferation. To these means, OVA-specific OT-2 cells, corresponding to OVA-specific $CD4^+$ T cells, were co-cultured with maturated BMDCs, and T cell proliferation was then analyzed via incorporation of radioactive ^{3}H-thymidine. Interestingly, these antigen-specific $CD4^+$ T cells became exclusively stimulated and proliferated most effectively when both adjuvant and peptides were presented on the same particle or co-administered (Figure 7C). Neither the covalent conjugation of the peptide antigen nor the small molecule TLR7/8 adjuvant to the nanogel impacted their biological activity. These experiments therefore exemplify the unique immunostimulation properties of the adjuvant-loaded peptide-decorated nanogels and their ability to elicit antigen-specific immune responses.

3. Materials and Methods

3.1. Materials

Solvents and reagents were purchased from commercial suppliers and used without further purification unless otherwise mentioned. Trifluoromethanesulfonic acid, benzene (dry), methylene chloride (dry), diethyl ether, dimethyl sulfoxide (DMSO), acetonitrile (ACN, HPLC grade), ethanol amine, 3,6-dioxa-1,8-diaminooctane, DBCO-PEG_{12}-maleimide and phosphate-buffered saline (PBS) tablets were purchased from Sigma-Aldrich. Azido poly (ethylene glycol) methyl ether (azide-PEG_{113}-OH) was purchased from Rapp Polymere, 5(6)-tetramethyl rhodamine (TMR) cadaverine was purchased from Biotium, and the peptide sequence was obtained from GenScript. 1-(4-(aminomethyl)-benzyl)-2-butyl-1H-imidazo[4,5-*c*]quinolin-4-amine (IMDQ) was synthesized as reported here [59–61] and 5-methyl-5-pentafluorophenyloxycarbonyl-1,3-dioxan-2-one (MTC-PFP) was synthesized as reported here [48]. Millipore water was prepared using a MILLI-Q R Reference A+ system at a resistivity of 18.2 MΩ·cm and total organic carbon of <5 ppm. Dialysis was performed using Spectra/Por® 7 dialysis membranes with a molecular weight cutoff of 1000 g mol^{-1}, and Amicon spin filters were used with a molecular weight cut-off (MWCO) of 10,000 g mol^{-1} obtained from Merck Millipore.

3.2. Instrumentation

^{1}H and ^{19}F NMR spectra were recorded on a Bruker Avance 400 MHz spectrometer (Bruker, Billerica, MA, USA). Samples were prepared using deuterated solvents obtained from Sigma-Aldrich (St. Louis, MO, USA), and the resulting spectra were analyzed using MestReNova 14.2.0 by Mestrelab Research.

Analytical size exclusion chromatography (SEC) was carried out on a SECcurity^2-instrument from PSS Polymer Standards Service GmbH with 1,1,1,3,3,3-hexafluoroisopropanol (HFIP) as eluent, containing 3 g/L potassium trifluoroacetate. The system was equipped with a SECcurity^{2}isocratic pump, a degasser, an auto sampler, and a column thermostat. The flow rate was set at 0.8 mL/min, and the column was equilibrated at 40 °C. The column material was composed of modified silica gel (PFG columns, particle size: 7 µm, porosity: 100 Å + 1000 Å) from PSS. For polymer detection, a UV detector at a wavelength of λ = 230 nm and a RI detector were employed. Furthermore, molecular weights were determined via calibration with PMMA (PSS). Evaluation of the elution diagram was conducted with PSS WinGPC softwareUniChrom 8.4.

Dynamic light scattering measurements were performed on a Malvern Z Nano instrument containing a He-Ne-Laser (λ = 632.8 nm). Measurements were performed in triplicates at a detection angle of 173°. For sample analysis, ZetaSizer Software 7.12 was applied.

For atomic force microscopy imaging, nanogels were diluted to 50 mg/L, drop-casted (5 µL) onto a freshly cleaved mica substrate (circular, 15 mm). AFM imaging measurements were performed using a Bruker Dimension FastScan Bio®atomic force microscope in Peak Force mode. Samples were scanned with scan rates of 0.994–1.41 Hz, and AFM probes with a nominal spring constant of 0.25 N/m (FastScan-D, Bruker) were employed. Data was processed using NanoScope Analysis 1.8.

UV–Vis spectra were recorded on a Thermo Scientific™ NanoDrop™ 2000c spectrophotometer using Brand UV micro cuvettes.

Fluorescence spectroscopy measurements as well as multi-well UV–Vis absorbance spectra for RAW-blue and MTT assays were conducted on a Spark 20M Multimode Microplate Reader from TecanTrading (TECAN plate reader, Tecan, Männedorf, Switzerland).

Matrix-assisted laser desorption ionization time of flight mass spectrometry (MALDI-ToF) measurements were carried out on a rapifleXTM MALDI-TOF/TOF mass spectrometer from Bruker Daltonik GmbH. The instrument is equipped with a scanning smartbeam 10 kHz Nd:YAG laser at a wavelength of 355 nm and a 10 bit 5 GHz digitizer. The acceleration voltage was set to 20 kV, and the mass spectra were recorded in positive ion mode. Calibration was done with polyethylene glycol standards from PSS. Mass spectrometry data were analyzed using mMass.

High performance liquid chromatography coupled with mass spectrometry (LCMS) measurements were performed on a Shimadzu LCMS2020 with a Kinetex 2.6 µm EVO C18 100 Å LC 50 ×2.1 mm column, an electrospray ionization source, and an SPD-20A UV–Vis detector. Millipore water and ACN supplemented with 0.1% formic acid were used as eluents for all the measurements, with gradients running from 5% ACN/95% water to 100% ACN at 16 min, followed by 5% ACN/95% water for a 20 min equilibration prior to the next measurements. Data were processed with LabSolutions provided by Shimadzu.

Sodium dodecyl sulfate polyacrylamide gel electrophoresis (SDS-PAGE) was performed with 15% polyacrylamide separation gels and 5% polyacrylamide loading gels using the Mini-PROTEAN Tetra Cell from Bio-Rad. Samples were prepared by mixing the corresponding volume of 3 µg peptide with 4× reducing Laemmli sample buffer before loading. For molecular weight comparisons, the NovexTM Sharp Pre-Stained Protein Standard was used. Gel electrophoresis was performed for 55 min at 160 mV. Gel images were obtained after excitation with a UV lamp.

3.3. Block Copolymer Synthesis of Azide-PEG$_{113}$-b-Poly(MTC-PFP)

The synthesis of azide-PEG$_{113}$-*b*-poly(MTC-PFP) was conducted following a preparation modified from previous block copolymer synthesis for mPEG$_{113}$-*b*-poly(MTC-PFP) [41,48].

An amount of 0.200 g (0.040 mmol, 1.0 eq.) of azido functional polyethylene glycol (azide-PEG$_{113}$-OH) and 0.522 g (1.600 mmol, 40.0 eq.) MTC-PFP were dried via azeotropic distillation using 3 mL benzene under reduced pressure in two separate Schlenk tubes. After being transferred into a nitrogen purged glovebox, 1.6 mL of dry DCM was added to each tube. The solubilized azide-PEG$_{113}$-OH was then added to MTC-PFP (final monomer concentration of 0.5 m). For the initiation of cationic ROP, 3.52 µL (0.006 g, 0.040 mmol, 1.0 eq.) trifluoromethanesulfonic acid (TFMSA) was pipetted to the polymerization mixture and stirred for 11 d at room temperature. Monomer conversion was checked regularly by NMR measurements, and the reaction was terminated at a conversion of 86.8% via precipitation into cold diethyl ether. Centrifugation (4500 rpm, 10 min, 4 °C) then yielded the block copolymer as a colorless solid. After two additional precipitation steps in an analogous manner, the polymer was dried under reduced pressure (0.402 g, 62% yield by mass when using the conversion of 86.8%).

Hexafluoroisopropanol (HFIP) SEC calibrated by a PMMA standard:

$$\text{Azide-PEG}_{113}\text{-OH: } M_n = 3.07 \cdot 10^4 \text{ g/mol } M_w = 3.37 \cdot 10^4 \text{ g/mol, } Đ = 1.10$$

Azide-PEG_{113}-*b*-poly(MTC-PFP)$_{28}$: $M_N = 3.60 \cdot 10^4$ g/mol $M_w = 4.24 \cdot 10^4$ g/mol, $Đ = 1.18$

^{1}H NMR (300 MHz, $CDCl_3$, 25 °C) δ = 4.45 (s, 4 H; CH_2 MTC-PFP), 3.64 (s, 4 H; OCH_2CH_2 PEG), 1.49 (s, 3 H; CH_3 MTC-PFP).

^{19}F NMR (282 MHz, $CDCl_3$, 25 °C) δ = −153.1 (2 F; *m*-F), −157.1 (1 F; *p*-F), −162.1 (2 F; *o*-F).

3.4. Adjuvant-Loaded Azide-Functional Nanogels

For nanogel preparation with TMR or IMDQ, azide-PEG_{113}-*b*-poly(MTC-PFP)$_{28}$ block copolymers were dispersed at 10 mg/mL in ethanol (2% water content by volume) via ultrasonication (20 min at ~35 °C). The size of the micellar assembly was then determined by DLS, showing narrowly distributed particles with z-average sizes of 23.6 nm and a PDI of 0.20. An amount of 1 mL of the particle solution was then transferred to each glass vial. The vessels were equipped with a stir bar and placed on a magnetic stirring plate to ensure thorough mixing during particle functionalization. Amine reactants were added consecutively, and each was allowed to react for 4 min for dye attachment, 10 min IMDQ attachment, and 10 min for core-crosslinking.

Azide-NP(-): TMR Cadaverine 17.2 µL (5 mg/mL in EtOH, 0.086 mg, 0.17 µmol), 0.5 eq. 3,6-dioxa-1,8-diaminooctane 1.44 µL (1.44 mg, 23.7 µmol), and 1.05 eq. Triethylamine 2.87 µL (2.09 mg, 20.7 µmol).

Azide-NP(IMDQ): TMR Cadaverine 17.2 µL (5 mg/mL in EtOH, 0.086 mg, 0.17 µmol), IMDQ 58.0 µL (10 mg/mL in EtOH, 0.58 mg, 1.61 µmol), 1.30 eq. Triethylamine 3.55 µL (2.59 mg, 25.6 µmol), and 0.459 eq. 3,6-dioxa-1,8-diaminooctane 1.32 µL (1.34 mg, 9.05 µmol).

Finally, 1.44 µL of ethanolamine (1.44 mg, 23.7 µmol, 1.2 eq.) was added to each reaction in order to quench any remaining PFP-esters and stirred for further 10 min.

To terminate both reactions, they were added to 4 mL of hydrochloric acid (c = 1 mol/L). The byproducts were removed via dialysis in a tube with a 1 kDa cutoff against 1 L of diluted hydrochloric acid (pH = 4) for about ~24 h. The dialysis medium was exchanged frequently. The nanogels were finally obtained as a red solution and filtered using a 0.2 µm syringe filter.

An aliquot was freeze-dried to determine the nanogel content of the solution (6.6 mg of azide-NP(-), and 4.8 mg of azide-NP(IMDQ) were obtained from 10 mg of the precursor block copolymer).

3.5. SPAAC of Azide-Functional Nanogels with DBCO-Modified Oregon Green 488

Dibenzocycloazaoctyne (DBCO)-modified Oregon Green 488 was prepared by a previously described preparation method [50]. To test the accessibility and reactivity of the azide-groups on the nanogels' surface, 670 µL nanogel solution in pH 4 HCl (0.5 mg, c = 0.75 mg/mL, 11.079 g/mol per azide group, 45.1 nmol, 1.0 eq.) was mixed with 29.8 µL of DBCO-modified Oregon Green 488 (0.0745 mg, c = 2.5 mg/mL in DMSO, 812.85 g/mol per DBCO group, 91.7 nmol, 2.0 eq.). As a control, a second mixture was prepared using azide nanogels mixed with Oregon Green 488 cadaverine. Lacking DBCO moieties, this dye would not react with the azide-functional nanogels and would be fully removed during work-up. After 4 days of incubation, excess Orgon Green 488 (OG488) dye was removed using spin filters with a molecular weight cut-off (MWCO) of 10,000 and centrifugation at 4000× *g*. Samples were washed repeatedly until the filtrate did not show any detectable UV–Vis absorption. Finally, particle solutions were filled up to 100 µL, and all samples were analyzed again via UV–Vis on a TECAN plate reader.

3.6. DBCO-Peptide Modification by Site-Selective Modification of Cysteine

The peptide sequences based on the $CD4^+$ (MHC-II) class epitope of ovalbumin (OVA) [52] CSSAESLKISQAVHAAHAEINEAGR was selected and purchased with *N*-terminal fluorescent labeling of 5-FAM-Ahx (5-Carboxyfluorescein) and a *N*-terminal cysteine for further modification. An amount of 150 µg of $CD4^+$ epitope peptide (47.4 nmol, 1.0 eq.) was dissolved at 1 mg/mL in a 1:1 mixture of acetonitrile and phosphate buffer

(pH 7.4). DBCO-PEG_{12}-maleimide (40 mg/mL in DMSO, 1.0 µL, 37.9 nmol, 0.8 eq.) was added, and the mixture was incubated overnight at room temperature. After analysis by LCMS and HPLC showing complete peptide modification, the mixture was directly used for SPAAC conjugation with the azide-nanogels.

LCMS: DBCO-PEG_{12}-$CD4^+$ peptide: m/z found: 1020.7 $[M+4H]^{4+}$, m/z calculated: 1021.1 $[M+4H]^{4+}$.

3.7. SPAAC of DBCO-Modified Peptides and Azide-Functional Nanogels

For the generation of $CD4^+$ epitope-decorated nanogels, azide-functional nanogels were concentrated to 5 mg/mL in dissolved hydrochloric acid (pH 4) using a vacuum concentrator. Then, 60 µL of the nanogel solution (5 mg/mL, 27 nmol azide, 9.0 eq.) was added to a 9.6 µL DBCO-modified $CD4^+$ epitope (1.28 mg/mL, 3 nmol, 1.0 eq.), and the mixture was filled to a total volume of 100 µL with sterile water/hydrochloric acid (pH 4). Similar to that, mixtures of nanogels and non-conjugating soluble peptides were prepared with an unmodified $CD4^+$ epitope (1 mg/mL, 9.5 µL, 3 nmol). All formulations were incubated at 4 °C for 48 h before analysis by SDS-PAGE, UV–Vis, and DLS measurements.

3.8. IMDQ-Loaded Azide-Functionalized Nanogel TLR Activity on RAW-Blue Macrophage Reporter Cell Line

RAW Blue macrophages can be used as TLR reporter assay because of their downstream activation of AP-1/NF NF-κB and subsequent secretion of SEAP (secreted embryonic alkaline phosphatase). They were purchased from InvivoGen, and the TLR report assay was conducted as recommended by the supplier. Cells were seeded into 96-well plates (90,000 cells/well in 180 µL culture medium) and incubated with 20 µL of the serial dilutions of equivalent IMDQ concentrations. After ~20 h of incubation, 50 µL of the supernatant was collected, added to 150 µL of Quanti Blue solution (InvivoGen, San Diego, CA, USA), and analyzed for the secretion of SEAP. After incubation for 2 h at 37 °C, the wells were read out for their absorbance at 620 nm using a plate reader. All experiments were performed in quadruplicate.

3.9. Influence of the IMDQ-Loaded Azide-Functionalized Nanogels on the Metabolic Activity of the Stimulated Raw Blue Macrophages by MTT Assay

To simultaneously analyze the metabolic activity of the cell as an indicator of toxicity and cell proliferation, the previously stimulated cells were incubated with 30 µL of 2 mg/mL 3-(4,5-dimethylthiazol-2-yl)-2,5-diphenyltetrazolium bromide solution in PBS. After 3 h of incubation, the formed formazan crystals were dissolved by the addition of 100 µL of 10% m/v SDS/0.01 M HCl and incubated overnight at 37 °C. Absorbance was measured at 590 nm using a plate reader. All experiments were performed in quadruplicate.

3.10. Confocal Microscopy Studies of Raw Blue Macrophages Stimulated with IMDQ-Loaded and Peptide-Decorated Nanogels

Raw Blue macrophage cells (50,000 cells/well in 180 µL) were seeded in an eight-well polystyrene-chambered cover glass (Laboratory-Tek, Nalge Nunc International, Penfield, NY, USA). Respective amounts of TMR-labeled nanogels and FAM-labeled CD4+ peptides (as covalent conjugates, alone or as mixtures) were added (20 µL solution) and incubated overnight. The medium was removed, and the cells were washed with PBS three times. The cells were fixed with 200 µL of a 4% paraformaldehyde solution for 30 min at 37 °C. Afterwards, the cells were washed again with PBS three times, and the cell nuclei were stained using a 4′,6-diamidino-2-phenylindole (DAPI) solution (80 µg/mL in PBS) for 10 min at 37 °C. Finally, the samples were again carefully washed using PBS three times and subsequently analyzed on a Leica SP5 confocal microscope with a 63× oil immersion objective. Images were processed by the ImageJ software package (version 1.53o).

3.11. Bone Marrow-Derived Dendritic Cells (BMDCs) Culture

Bone marrow cells isolated from the femurs and tibiae of C57BL/6 mic were seeded in 12-well suspension cell culture plates (each 10^5/mL) and incubated in an IMDM-based culture medium (5% FBS, 2 mM L-glutamine, 100 IU/mL penicillin, 100 µg/mL streptomycin and 50 µM β-mercaptoethanol; all from Sigma-Aldrich) supplemented with 10 ng/mL recombinant murine GM-CSF (R & D Systems) to obtain inflammatory BMDCs. Culture media was changed on days 2 and 6. On day 7/8, different nanoformulations were applied (1.5 µg/mL). On the following day, the samples were harvested and subjected to flow cytometric analysis or employed as stimulators in T cell proliferation assays.

3.12. Flow Cytometry

BMDC were harvested and transferred to FACS tubes. In order to prevent unspecific Fc-mediated binding, samples were incubated with a rat anti-mouse CD16/CD32 antibody for 10 min at 4 °C. Afterwards, BMDC were incubated with specific antibodies for DC lineage (CD11c) and activation (MHCII, CD80, CD86) markers for 20 min at 4 °C. All antibodies were obtained from BioLegend or Thermo Fisher (Waltham, MA, USA) (Table S1). Samples left untreated, incubated with a nanoformulation only, or with a single antibody served as controls. Then, the samples were washed and fixed (4% paraformaldehyde, 2 mM EDTA) and analyzed in an Attune NxT flow cytometer equipped with Attune Nxt Software v3.1.1 (both from Thermo Fisher). Data were evaluated following the gating strategy of Figure S13.

3.13. T-Cell Proliferation

Differentially treated BMDCs were harvested and reseeded in triplicates into 96-well plates (10^5/mL; 100 µL/well) by serial dilution. OVA peptide-specific splenic $CD4^+$ T cells from OT-II mice (https://www.ncbi.nlm.nih.gov/pubmed/9553774, accessed on 1 September 2023) were isolated via negative immunomagnetic enrichment (Miltenyi) and added as $5{\cdot}10^5$/mL per 100 µL to each diluted BMDC. After one day of co-culturing, ^{3}H-thymidine (0.5 µCi/well) was added for another 16–18 h of co-culture. Afterwards, cells were harvested onto glass fiber filters, and retained radioactivity was quantified in a microplate Scintillation counter (1450 MicroBeta Trilux; Perkin Elmer, Waltham, MA, USA). All samples were run in triplicate.

4. Conclusions

In this study, we introduced the synthesis and application of peptide-decorated polycarbonate nanogels. Starting from the controlled ROP for the synthesis of multifunctional block copolymers, polymeric micelles were assembled. Exploiting the post-polymerization modification of azide-PEG_{113}-*b*-poly(MTC-$PFP)_{28}$ at the reactive ester side chain, small molecular TLR7/8 agonists and core-crosslinkers were incorporated into these nanogels. Subsequently, the azide-moieties were shown to be presented on the surface of the nanogels and to be accessible for SPAAC via covalent conjugation of a DBCO-functional dye. Towards vaccination with peptide antigens, a $CD4^+$-T-cell-specific peptide sequence of ovalbumin as a model antigen was functionalized with DBCO moieties via site-specific conjugation to its *N*-terminal cysteine. The peptide was then successfully attached to the surface of the nanocarrier to form peptide-decorated nanogels. Following in vitro studies confirmed the nanogels' ability to effectively deliver the peptide into immune cells. Adjuvant-loading was shown to result in strong immunostimulation. Finally, the interplay of the adjuvant and peptides was demonstrated by presentation of the $CD4^+$-peptide on dendritic cells, resulting in a sequence-specific and adjuvant-boosted $CD4^+$ T cell proliferation.

Consequently, azide-functional polycarbonate nanogels can be considered attractive carrier systems for both core-functionalization with small molecular cargoes and simultaneous surface decoration with peptide antigens. Our findings strongly motivate us to characterize the particles' vaccination performance in further in vivo studies in order to address and optimize adjuvant and peptide antigen-specific immune responses. Further

development of these multifunctional nanogels presented herein may pave the way for alternative peptide nanogel vaccines, especially relevant for therapeutic interventions in cancer immunotherapy.

Supplementary Materials: The following supporting information can be downloaded at: https://www.mdpi.com/article/10.3390/ijms242015417/s1.

Author Contributions: Conceptualization, H.S., S.G. and L.N.; methodology, L.S., L.X. and M.S.; experiments, J.S., C.C. and C.M.-M.; writing, review and editing, C.C., J.S. and L.N. All authors have read and agreed to the published version of the manuscript.

Funding: This research was funded by DFG, grant numbers 417278389 (Emmy Noether to L.N.) and 213555243 (CRC 1066 to L.N., S.G. and H.S.); by the Max Buchner Research Foundation, grant number 3807 (to L.N.); and by the National Science Foundation of China, grant number 22304181 (to L.X.).

Institutional Review Board Statement: Ethical review and approval were waived for this study due to exclusive use of isolated mouse cells derived from mice sacrificed for organ retrieval according to § 4(3) TierSchG.

Informed Consent Statement: Not applicable.

Data Availability Statement: All data can be found in the manuscript or Supporting Information and can be further provided by the authors.

Acknowledgments: The authors would like to thank the DFG for funding by the Emmy Noether program to L.N. (project number: 417278389) and the CRC1066 projects to L.N., S.G., and H.S (project number: 213555243). Furthermore, L.N. is grateful to the Max Buchner Research Foundation for their generous support (project number: 3807), and L.X. acknowledges support from the National Science Foundation of China (project number: 22304181). Moreover, technical support by Hans Joachim Räder, Stephan Türk, and Jutta Schnee for MALDI-ToF measurements, as well as Pia Winterwerber for AFM images is gratefully acknowledged by all co-authors.

Conflicts of Interest: The authors declare no conflict of interest.

References

1. Delany, I.; Rappuoli, R.; De Gregorio, E. Vaccines for the 21st century. *EMBO Mol. Med.* **2014**, *6*, 708–720. [CrossRef]
2. Iwasaki, A.; Omer, S.B. Why and how vaccines work. *Cell* **2020**, *183*, 290–295. [CrossRef] [PubMed]
3. Heitmann, J.S.; Bilich, T.; Tandler, C.; Nelde, A.; Maringer, Y.; Marconato, M.; Reusch, J.; Jäger, S.; Denk, M.; Richter, M.; et al. A COVID-19 peptide vaccine for the induction of SARS-CoV-2 T cell immunity. *Nature* **2022**, *601*, 617–622. [CrossRef] [PubMed]
4. Polack, F.P.; Thomas, S.J.; Kitchin, N.; Absalon, J.; Gurtman, A.; Lockhart, S.; Perez, J.L.; Marc, G.P.; Moreira, E.D.; Zerbini, C.; et al. Safety and efficacy of the BNT162b2 mRNA Covid-19 vaccine. *N. Engl. J. Med.* **2020**, *383*, 2603–2615. [CrossRef] [PubMed]
5. Shin, M.D.; Shukla, S.; Chung, Y.H.; Beiss, V.; Chan, S.K.; Ortega-Rivera, O.A.; Wirth, D.M.; Chen, A.; Sack, M.; Pokorski, J.K.; et al. COVID-19 vaccine development and a potential nanomaterial path forward. *Nat. Nanotechnol.* **2020**, *15*, 646–655. [CrossRef] [PubMed]
6. Sahin, U.; Türeci, Ö. Personalized vaccines for cancer immunotherapy. *Science* **2018**, *359*, 1355–1360. [CrossRef]
7. Malonis, R.J.; Lai, J.R.; Vergnolle, O. Peptide-based vaccines: Current progress and future challenges. *Chem. Rev.* **2020**, *120*, 3210–3229. [CrossRef]
8. Purcell, A.W.; McCluskey, J.; Rossjohn, J. More than one reason to rethink the use of peptides in vaccine design. *Nat. Rev. Drug Discov.* **2007**, *6*, 404–414. [CrossRef]
9. Matsumoto, M.; Seya, T. TLR3: Interferon induction by double-stranded RNA including poly (I:C). *Adv. Drug Deliv. Rev.* **2008**, *60*, 805–812. [CrossRef]
10. Latz, E.; Schoenemeyer, A.; Visintin, A.; Fitzgerald, K.A.; Monks, B.G.; Knetter, C.F.; Lien, E.; Nilsen, N.J.; Espevik, T.; Golenbock, D.T. TLR9 signals after translocating from the ER to CpG DNA in the lysosome. *Nat. Immunol.* **2004**, *5*, 190–198. [CrossRef]
11. Shukla, N.M.; Malladi, S.S.; Mutz, C.A.; Balakrishna, R.; David, S.A. Structure−activity relationships in human Toll-like receptor 7-active imidazoquinoline analogues. *J. Med. Chem.* **2010**, *53*, 4450–4456. [CrossRef]
12. Bhagchandani, S.; Johnson, J.A.; Irvine, D.J. Evolution of Toll-like receptor 7/8 agonist therapeutics and their delivery approaches: From antiviral formulations to vaccine adjuvants. *Adv. Drug Deliv. Rev.* **2021**, *175*, 113803. [CrossRef]
13. Federico, S.; Pozzetti, L.; Papa, A.; Carullo, G.; Gemma, S.; Butini, S.; Campiani, G.; Relitti, N. Modulation of the innate immune response by targeting toll-like receptors: A perspective on their agonists and antagonists. *J. Med. Chem.* **2020**, *63*, 13466–13513. [CrossRef] [PubMed]

14. Stephens, A.J.; Burgess-Brown, N.A.; Jiang, S. Beyond just peptide antigens: The complex world of peptide-based cancer vaccines. *Front. Immunol.* **2021**, *12*, 696791. [CrossRef] [PubMed]
15. Palucka, K.; Banchereau, J. Cancer immunotherapy via dendritic cells. *Nat. Rev. Cancer* **2012**, *12*, 265–277. [CrossRef] [PubMed]
16. Merad, M.; Sathe, P.; Helft, J.; Miller, J.; Mortha, A. The dendritic cell lineage: Ontogeny and function of dendritic cells and their subsets in the steady state and the inflamed setting. *Annu. Rev. Immunol.* **2013**, *31*, 563–604. [CrossRef]
17. Farhood, B.; Najafi, M.; Mortezaee, K. CD^{8+} cytotoxic T lymphocytes in cancer immunotherapy: A review. *J. Cell. Physiol.* **2019**, *234*, 8509–8521. [CrossRef]
18. Desrichard, A.; Snyder, A.; Chan, T.A. Cancer neoantigens and applications for immunotherapy. *Clin. Cancer Res.* **2016**, *22*, 807–812. [CrossRef]
19. Li, W.; Joshi, M.D.; Singhania, S.; Ramsey, K.H.; Murthy, A.K. Peptide vaccine: Progress and challenges. *Vaccines* **2014**, *2*, 515–536. [CrossRef]
20. Khong, H.; Overwijk, W.W. Adjuvants for peptide-based cancer vaccines. *J. Immunother. Cancer* **2016**, *4*, 56. [CrossRef]
21. Lynn, G.M.; Laga, R.; Darrah, P.A.; Ishizuka, A.S.; Balaci, A.J.; Dulcey, A.E.; Pechar, M.; Pola, R.; Gerner, M.Y.; Yamamoto, A.; et al. In vivo characterization of the physicochemical properties of polymer-linked TLR agonists that enhance vaccine immunogenicity. *Nat. Biotechnol.* **2015**, *33*, 1201–1210. [CrossRef] [PubMed]
22. Hanson, M.C.; Crespo, M.P.; Abraham, W.; Moynihan, K.D.; Szeto, G.L.; Chen, S.H.; Melo, M.B.; Mueller, S.; Irvine, D.J. Nanoparticulate STING agonists are potent lymph node–targeted vaccine adjuvants. *J. Clin. Investig.* **2015**, *125*, 2532–2546. [CrossRef] [PubMed]
23. Saeed, M.; Gao, J.; Shi, Y.; Lammers, T.; Yu, H. Engineering nanoparticles to reprogram the tumor immune microenvironment for improved cancer immunotherapy. *Theranostics* **2019**, *9*, 7981–8000. [CrossRef]
24. Zhu, X.; Nishimura, F.; Sasaki, K.; Fujita, M.; Dusak, J.E.; Eguchi, J.; Fellows-Mayle, W.; Storkus, W.J.; Walker, P.R.; Salazar, A.M.; et al. Toll like receptor-3 ligand poly-ICLC promotes the efficacy of peripheral vaccinations with tumor antigen-derived peptide epitopes in murine CNS tumor models. *J. Transl. Med.* **2007**, *5*, 10. [CrossRef]
25. Hammerich, L.; Marron, T.U.; Upadhyay, R.; Svensson-Arvelund, J.; Dhainaut, M.; Hussein, S.; Zhan, Y.; Ostrowski, D.; Yellin, M.; Marsh, H.; et al. Systemic clinical tumor regressions and potentiation of PD1 blockade with in situ vaccination. *Nat. Med.* **2019**, *25*, 814–824. [CrossRef]
26. Nuhn, L.; De Koker, S.; Van Lint, S.; Zhong, Z.; Catani, J.P.; Combes, F.; Deswarte, K.; Li, Y.; Lambrecht, B.N.; Lienenklaus, S.; et al. Nanoparticle-Conjugate TLR7/8 Agonist Localized Immunotherapy Provokes Safe Antitumoral Responses. *Adv. Mater.* **2018**, *30*, 1803397. [CrossRef]
27. Zhang, Y.; Li, N.; Suh, H.; Irvine, D.J. Nanoparticle anchoring targets immune agonists to tumors enabling anti-cancer immunity without systemic toxicity. *Nat. Commun.* **2018**, *9*, 6. [CrossRef] [PubMed]
28. Irvine, D.J.; Dane, E.L. Enhancing cancer immunotherapy with nanomedicine. *Nat. Rev. Immunol.* **2020**, *20*, 321–344. [CrossRef]
29. Goldberg, M.S. Improving cancer immunotherapy through nanotechnology. *Nat. Rev. Cancer* **2019**, *19*, 587–602. [CrossRef]
30. O'Neill, C.L.; Shrimali, P.C.; Clapacs, Z.P.; Files, M.A.; Rudra, J.S. Peptide-based supramolecular vaccine systems. *Acta Biomater.* **2021**, *133*, 153–167. [CrossRef]
31. Zacco, E.; Anish, C.; Martin, C.E.; Berlepsch, H.V.; Brandenburg, E.; Seeberger, P.H.; Koksch, B. A self-assembling peptide scaffold for the multivalent presentation of antigens. *Biomacromolecules* **2015**, *16*, 2188–2197. [CrossRef] [PubMed]
32. Bachmann, M.F.; Jennings, G.T. Vaccine delivery: A matter of size, geometry, kinetics and molecular patterns. *Nat. Rev. Immunol.* **2010**, *10*, 787–796. [CrossRef] [PubMed]
33. Sun, Q.; Barz, M.; De Geest, B.G.; Diken, M.; Hennink, W.E.; Kiessling, F.; Lammers, T.; Shi, Y. Nanomedicine and macroscale materials in immuno-oncology. *Chem. Soc. Rev.* **2019**, *48*, 351–381. [CrossRef] [PubMed]
34. Yu, W.; Maynard, E.; Chiaradia, V.; Arno, M.C.; Dove, A.P. Aliphatic polycarbonates from cyclic carbonate monomers and their application as biomaterials. *Chem. Rev.* **2021**, *121*, 10865–10907. [CrossRef]
35. Brannigan, R.P.; Dove, A.P. Synthesis, properties and biomedical applications of hydrolytically degradable materials based on aliphatic polyesters and polycarbonates. *Biomater. Sci.* **2017**, *5*, 9–21. [CrossRef]
36. Becker, G.; Wurm, F.R. Functional biodegradable polymers via ring-opening polymerization of monomers without protective groups. *Chem. Soc. Rev.* **2018**, *47*, 7739–7782. [CrossRef]
37. Amsden, B. In vivo degradation mechanisms of aliphatic polycarbonates and functionalized aliphatic polycarbonates. *Macromol. Biosci.* **2021**, *21*, 2100085. [CrossRef]
38. Pratt, R.C.; Nederberg, F.; Waymouth, R.M.; Hedrick, J.L. Tagging alcohols with cyclic carbonate: A versatile equivalent of (meth) acrylate for ring-opening polymerization. *Chem. Commun.* **2008**, *2*, 114–116. [CrossRef]
39. Czysch, C.; Ding, T.; Fröder, Y.; Bixenmann, L.; Komforth, P.; Balint, A.; Räder, H.-J.; Naumann, S.; Nuhn, L. Nontoxic N-Heterocyclic Olefin Catalyst Systems for Well-Defined Polymerization of Biocompatible Aliphatic Polycarbonates. *ACS Polym. Au* **2022**, *2*, 371–379. [CrossRef]

40. Sanders, D.P.; Fukushima, K.; Coady, D.J.; Nelson, A.; Fujiwara, M.; Yasumoto, M.; Hedrick, J.L. A simple and efficient synthesis of functionalized cyclic carbonate monomers using a versatile pentafluorophenyl ester intermediate. *J. Am. Chem. Soc.* **2010**, *132*, 14724–14726. [CrossRef]
41. Engler, A.C.; Chan, J.M.W.; Coady, D.J.; O'Brien, J.M.; Sardon, H.; Nelson, A.; Sanders, D.P.; Yang, Y.Y.; Hedrick, J.L. Accessing new materials through polymerization and modification of a polycarbonate with a pendant activated ester. *Macromolecules* **2013**, *46*, 1283–1290. [CrossRef]
42. Engler, A.C.; Ke, X.; Gao, S.; Chan, J.M.W.; Coady, D.J.; Ono, R.J.; Lubbers, R.; Nelson, A.; Yang, Y.Y.; Hedrick, J.L. Hydrophilic polycarbonates: Promising degradable alternatives to poly (ethylene glycol)-based stealth materials. *Macromolecules* **2015**, *48*, 1673–1678. [CrossRef]
43. Chan, J.M.W.; Sardon, H.; Engler, A.C.; García, J.M.; Hedrick, J.L. Tetra-n-butylammonium fluoride as an efficient transesterification catalyst for functionalizing cyclic carbonates and aliphatic polycarbonates. *ACS Macro Lett.* **2013**, *2*, 860–864. [CrossRef] [PubMed]
44. Kockelmann, J.; Stickdorn, J.; Kasmi, S.; De Vrieze, J.; Pieszka, M.; Ng, D.Y.W.; David, S.A.; De Geest, B.G.; Nuhn, L. Control over Imidazoquinoline Immune Stimulation by pH-Degradable Poly(norbornene) Nanogels. *Biomacromolecules* **2020**, *21*, 2246–2257. [CrossRef] [PubMed]
45. Nuhn, L.; Hartmann, S.; Palitzsch, B.; Gerlitzki, B.; Schmitt, E.; Zentel, R.; Kunz, H. Water-soluble polymers coupled with glycopeptide antigens and T-cell epitopes as potential antitumor vaccines. *Angew. Chemie Int. Ed.* **2013**, *52*, 10652–10656. [CrossRef]
46. De Vrieze, J.; Van Herck, S.; Nuhn, L.; De Geest, B.G. Design of pH-Degradable Polymer-Lipid Amphiphiles Using a Ketal-Functionalized RAFT Chain Transfer Agent. *Macromol. Rapid Commun.* **2020**, *41*, 2000034. [CrossRef] [PubMed]
47. Czysch, C.; Medina-Montano, C.; Dal, N.K.; Dinh, T.; Fröder, Y.; Winterwerber, P.; Maxeiner, K.; Räder, H.; Schuppan, D.; Schild, H.; et al. End Group Dye-Labeled Polycarbonate Block Copolymers for Micellar (Immuno-) Drug Delivery. *Macromol. Rapid Commun.* **2022**, *43*, 2200095. [CrossRef]
48. Czysch, C.; Medina-Montano, C.; Zhong, Z.; Fuchs, A.; Stickdorn, J.; Winterwerber, P.; Schmitt, S.; Deswarte, K.; Raabe, M.; Scherger, M.; et al. Transient Lymph Node Immune Activation by Hydrolysable Polycarbonate Nanogels. *Adv. Funct. Mater.* **2022**, *32*, 2203490. [CrossRef]
49. Nuhn, L.; Vanparijs, N.; De Beuckelaer, A.; Lybaert, L.; Verstraete, G.; Deswarte, K.; Lienenklaus, S.; Shukla, N.M.; Salyer, A.C.D.; Lambrecht, B.N.; et al. pH-degradable imidazoquinoline-ligated nanogels for lymph node-focused immune activation. *Proc. Natl. Acad. Sci. USA* **2016**, *113*, 8098–8103. [CrossRef]
50. Stickdorn, J.; Stein, L.; Arnold-Schild, D.; Hahlbrock, J.; Medina-Montano, C.; Bartneck, J.; Ziß, T.; Montermann, E.; Kappel, C.; Hobernik, D.; et al. Systemically administered TLR7/8 agonist and antigen-conjugated nanogels govern immune responses against tumors. *ACS Nano* **2022**, *16*, 4426–4443. [CrossRef]
51. Irvine, D.J.; Swartz, M.A.; Szeto, G.L. Engineering synthetic vaccines using cues from natural immunity. *Nat. Mater.* **2013**, *12*, 978–990. [CrossRef] [PubMed]
52. Hirosue, S.; Kourtis, I.C.; van der Vlies, A.J.; Hubbell, J.A.; Swartz, M.A. Antigen delivery to dendritic cells by poly (propylene sulfide) nanoparticles with disulfide conjugated peptides: Cross-presentation and T cell activation. *Vaccine* **2010**, *28*, 7897–7906. [CrossRef] [PubMed]
53. Lynn, G.M.; Sedlik, C.; Baharom, F.; Zhu, Y.; Ramirez-Valdez, R.A.; Coble, V.L.; Tobin, K.; Nichols, S.R.; Itzkowitz, Y.; Zaidi, N.; et al. Peptide–TLR-7/8a conjugate vaccines chemically programmed for nanoparticle self-assembly enhance CD8 T-cell immunity to tumor antigens. *Nat. Biotechnol.* **2020**, *38*, 320–332. [CrossRef] [PubMed]
54. Wilson, D.S.; Hirosue, S.; Raczy, M.M.; Bonilla-Ramirez, L.; Jeanbart, L.; Wang, R.; Kwissa, M.; Franetich, J.F.; Broggi, M.A.S.; Diaceri, G.; et al. Antigens reversibly conjugated to a polymeric glyco-adjuvant induce protective humoral and cellular immunity. *Nat. Mater.* **2019**, *18*, 175–185. [CrossRef]
55. Zom, G.G.; Khan, S.; Britten, C.M.; Sommandas, V.; Camps, M.G.M.; Loof, N.M.; Budden, C.F.; Meeuwenoord, N.J.; Filippov, D.V.; van der Marel, G.A.; et al. Efficient induction of antitumor immunity by synthetic toll-like receptor ligand–peptide conjugates. *Cancer Immunol. Res.* **2014**, *2*, 756–764. [CrossRef]
56. Meng, J.; Zhang, P.; Chen, Q.; Wang, Z.; Gu, Y.; Ma, J.; Li, W.; Yang, C.; Qiao, Y.; Hou, Y.; et al. Two-Pronged Intracellular Co-Delivery of Antigen and Adjuvant for Synergistic Cancer Immunotherapy. *Adv. Mater.* **2022**, *34*, 2202168. [CrossRef]
57. Silva, J.M.; Zupancic, E.; Vandermeulen, G.; Oliveira, V.G.; Salgado, A.; Videira, M.; Gaspar, M.; Graca, L.; Préat, V.; Florindo, H.F. In vivo delivery of peptides and Toll-like receptor ligands by mannose-functionalized polymeric nanoparticles induces prophylactic and therapeutic anti-tumor immune responses in a melanoma model. *J. Control. Release* **2015**, *198*, 91–103. [CrossRef]
58. Nuhn, L.; Van Hoecke, L.; Deswarte, K.; Schepens, B.; Li, Y.; Lambrecht, B.N.; De Koker, S.; David, S.A.; Saelens, X.; De Geest, B.G. Potent anti-viral vaccine adjuvant based on pH-degradable nanogels with covalently linked small molecule imidazoquinoline TLR7/8 agonist. *Biomaterials* **2018**, *178*, 643–651. [CrossRef]
59. Bolli, E.; Scherger, M.; Arnouk, S.M.; Antunes, A.R.P.; Straßburger, D.; Urschbach, M.; Stickdorn, J.; De Vlaminck, K.; Movahedi, K.; Räder, H.-J.; et al. Targeted repolarization of tumor-associated macrophages via imidazoquinoline-linked nanobodies. *Adv. Sci.* **2021**, *8*, 2004574. [CrossRef]

60. Scherger, M.; Pilger, Y.A.; Stickdorn, J.; Komforth, P.; Schmitt, S.; Koynov, K.; Räder, H.-J.; Nuhn, L. Efficient Self-Immolative RAFT End Group Modification for Macromolecular Immunodrug Delivery. *Biomacromolecules* **2023**, *24*, 2380–2391. [CrossRef]
61. Scherger, M.; Pilger, Y.A.; Stickdorn, J.; Komforth, P.; Schmitt, S.; Arnouk, S.M.; Lebegge, E.; Koynov, K.; Räder, H.-J.; Van Ginderachter, J.A.; et al. Self-Immolative Nanobody-Cysteine Residue Modification for Controlled Immunodrug Delivery. *Adv. Ther.* **2023**, 202300076. [CrossRef]

Disclaimer/Publisher's Note: The statements, opinions and data contained in all publications are solely those of the individual author(s) and contributor(s) and not of MDPI and/or the editor(s). MDPI and/or the editor(s) disclaim responsibility for any injury to people or property resulting from any ideas, methods, instructions or products referred to in the content.

International Journal of
Molecular Sciences

MDPI

Supplementals

Peptide-decorated Degradable Polycarbonate Nanogels for Eliciting Antigen-Specific Immune Responses

Judith Stickdorn [1,†], Christian Czysch [1,†], Carolina Medina-Montano [2], Lara Stein[3], Lujuan Xu [1,4], Maximilian Scherger [1], Hansjörg Schild [3], Stephan Grabbe [2] and Lutz Nuhn [1,5,*]

1 Max Planck Institute for Polymer Research, 55128 Mainz, Germany
2 Department of Dermatology, University Medical Center of the Johannes Gutenberg-University Mainz, 55131 Mainz, Germany
3 Institute of Immunology, University Medical Center of the Johannes Gutenberg-University Mainz, 55131 Mainz, Germany
4 Zhejiang Cancer Hospital, The Key Laboratory of Zhejiang Province for Aptamers and Theranostics, Hangzhou Institute of Medicine (HIM), Chinese Academy of Sciences, 310022 Hangzhou, China
5 Chair for Macromolecular Chemistry, Institute of Functional Materials and Biofabrication, Department of Chemistry and Pharmacy, Julius-Maximilians-Universität Würzburg, 97074 Würzburg

† These authors contributed equally to this work.
* Correspondence: lutz.nuhn@uni-wuerzburg.de.

Citation: To be added by editorial staff during production.

Academic Editor: Firstname Lastname

Received: date
Revised: date
Accepted: date
Published: date

Copyright: © 2023 by the authors. Submitted for possible open access publication under the terms and conditions of the Creative Commons Attribution (CC BY) license (https://creativecommons.org/licenses/by/4.0/).

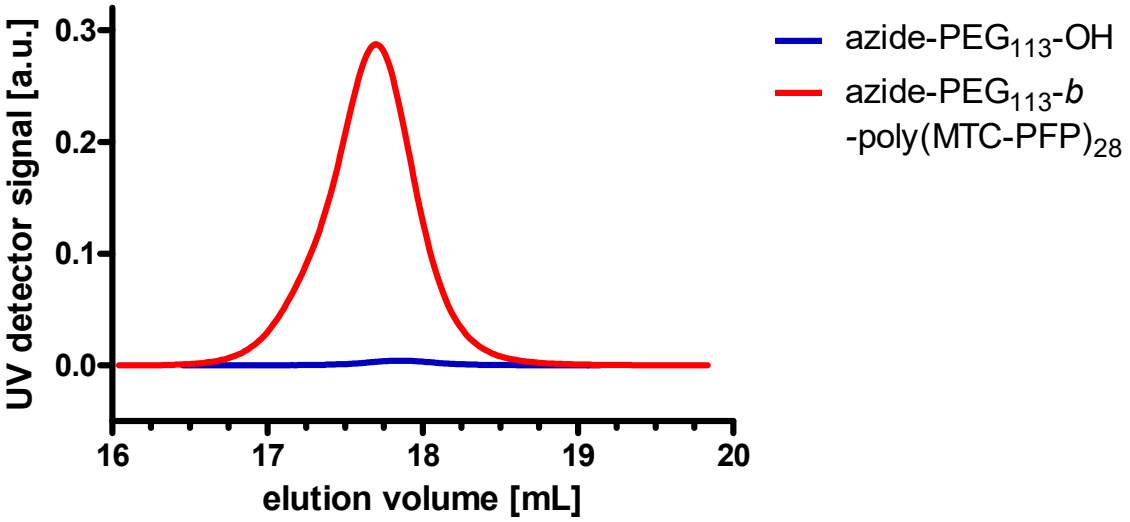

Figure S1. Size exclusion chromatography (SEC) elugram recorded by UV-Vis detector at 230 nm (UV) of azide-PEG$_{113}$-OH (blue) and azide-PEG$_{113}$-*b*-poly(MTC-PFP)$_{28}$ (red, $Đ$ = 1.17) showing narrowly distributed monomodal polymers and a drastic increase of UV absorbance by polymerization of the poly(MTC-PFP) block. This indicates the synthesis of block copolymers without homopolymer impurities.

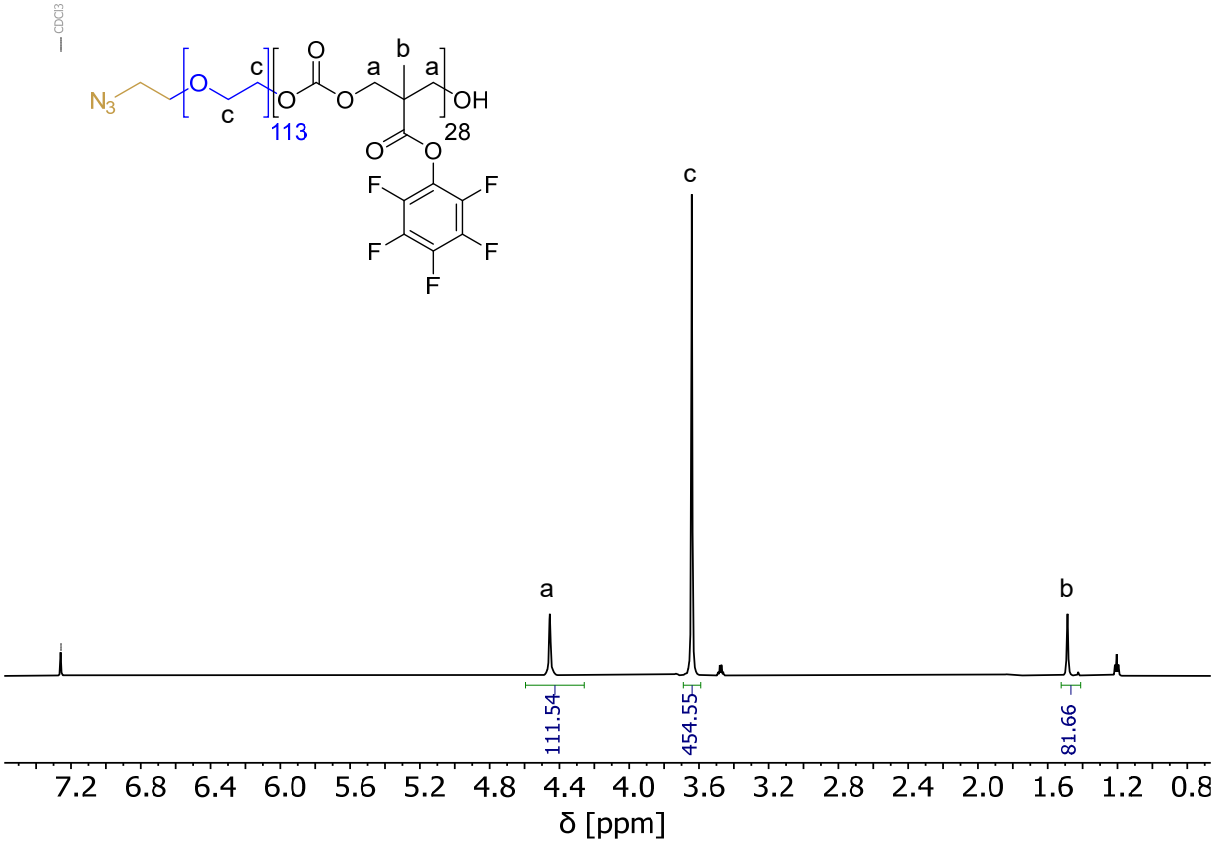

Figure S2. ^{1}H NMR spectrum of the purified block copolymer azide-PEG$_{113}$-*b*-poly(MTC-PFP)$_{28}$ dissolved in $CDCl_3$ with assignments.

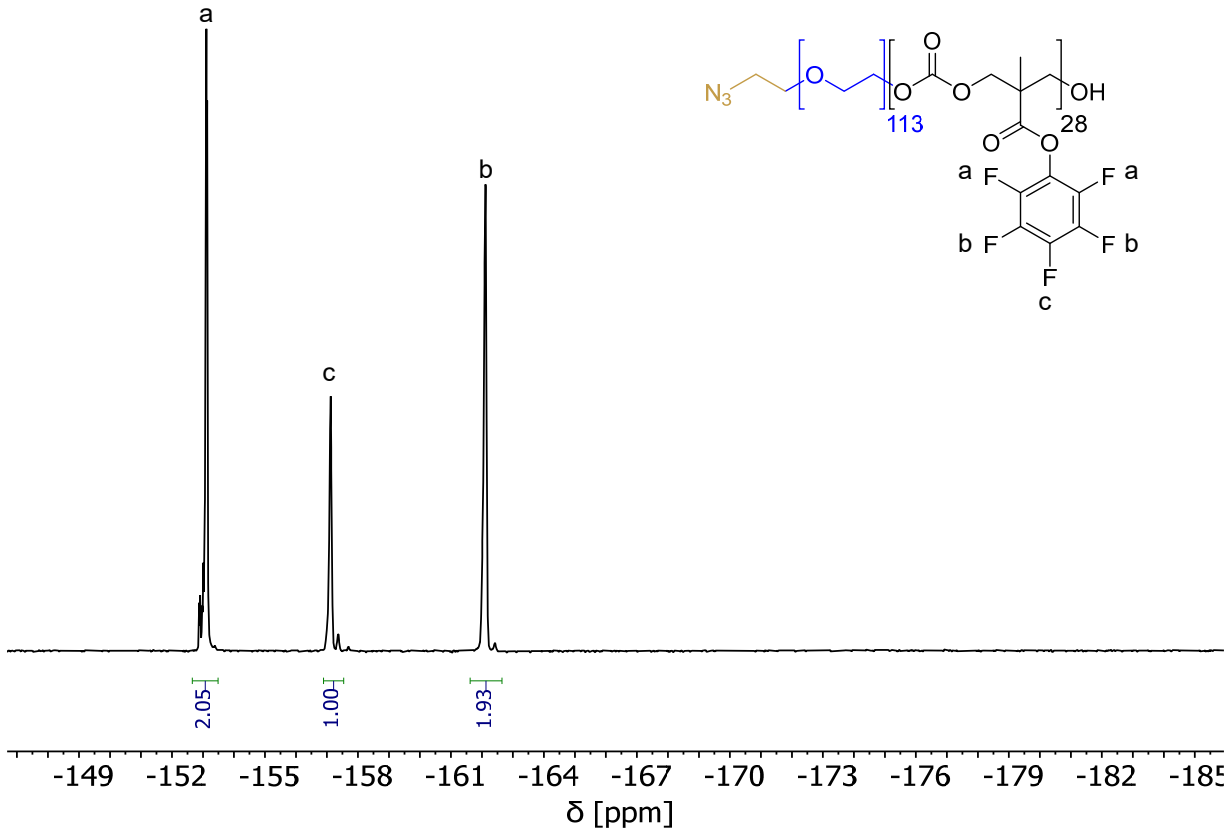

Figure S3. ^{19}F NMR spectrum of the purified block copolymer azide-PEG$_{113}$-*b*-poly(MTC-PFP)$_{28}$ dissolved in $CDCl_3$ with assignments.

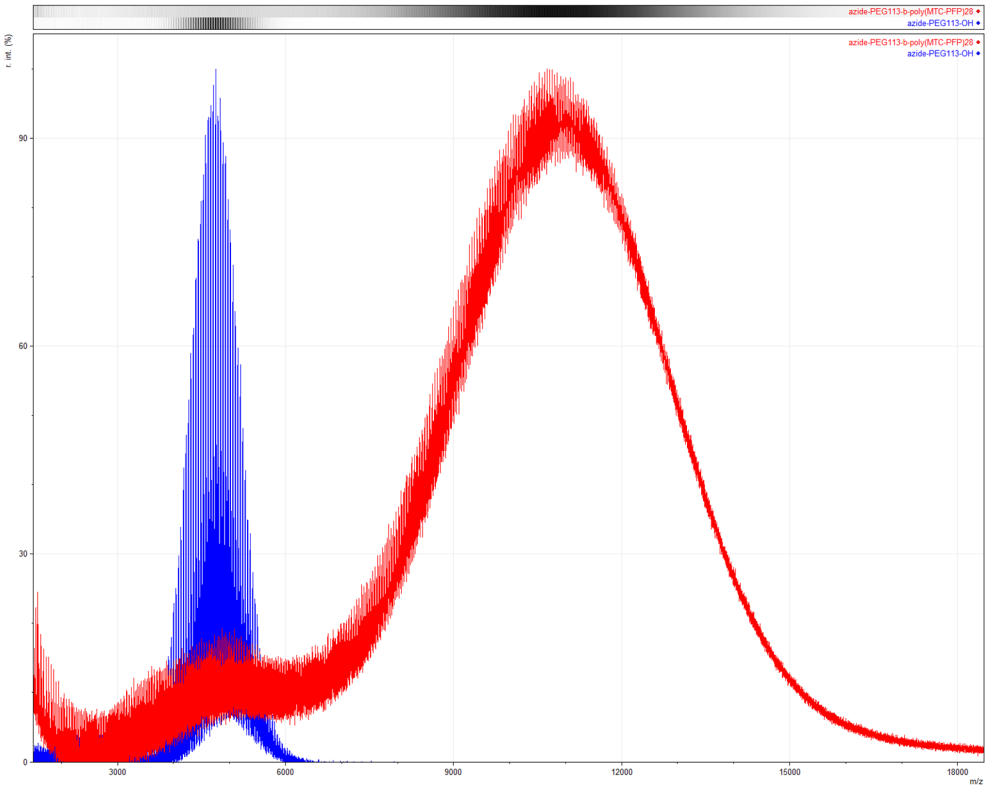

Figure S4. Mass spectrometric data (MALDI-ToF) of azide-PEG$_{113}$-OH (blue) and azide-PEG$_{113}$-*b*-poly(MTC-PFP)$_{28}$ (red) recorded in linear mode using 2-[(2E)-3-(4-tert-butylphenyl)-2-methylprop-2-enylidene]malononitrile (DCTB) as matrix.

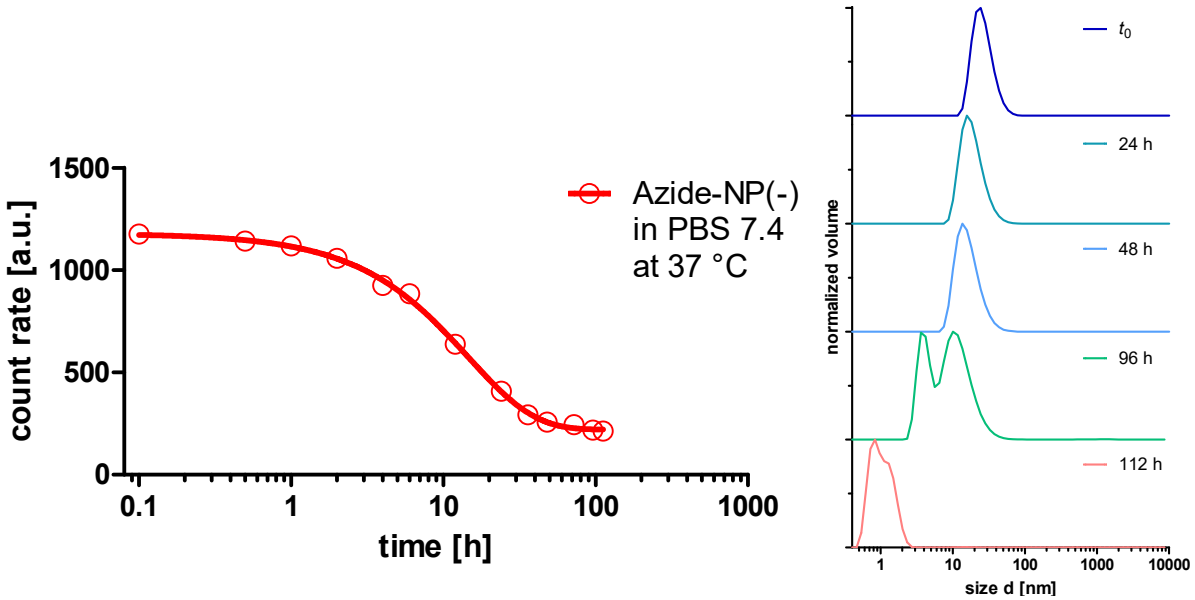

Figure S5. Degradation of azide-NP(-) in PBS (pH 7.4) at 37 °C over time investigated by DLS measurements. Dropping count rates indicate the disintegration of the particles (left graph, estimated half-life times 12-24 h). In addition to that particle sizes decrease from volume means of 27 nm at the t = 0 h to 18 nm after 48 h, finally reaching sizes below 5 nm after 112 h (right graph).

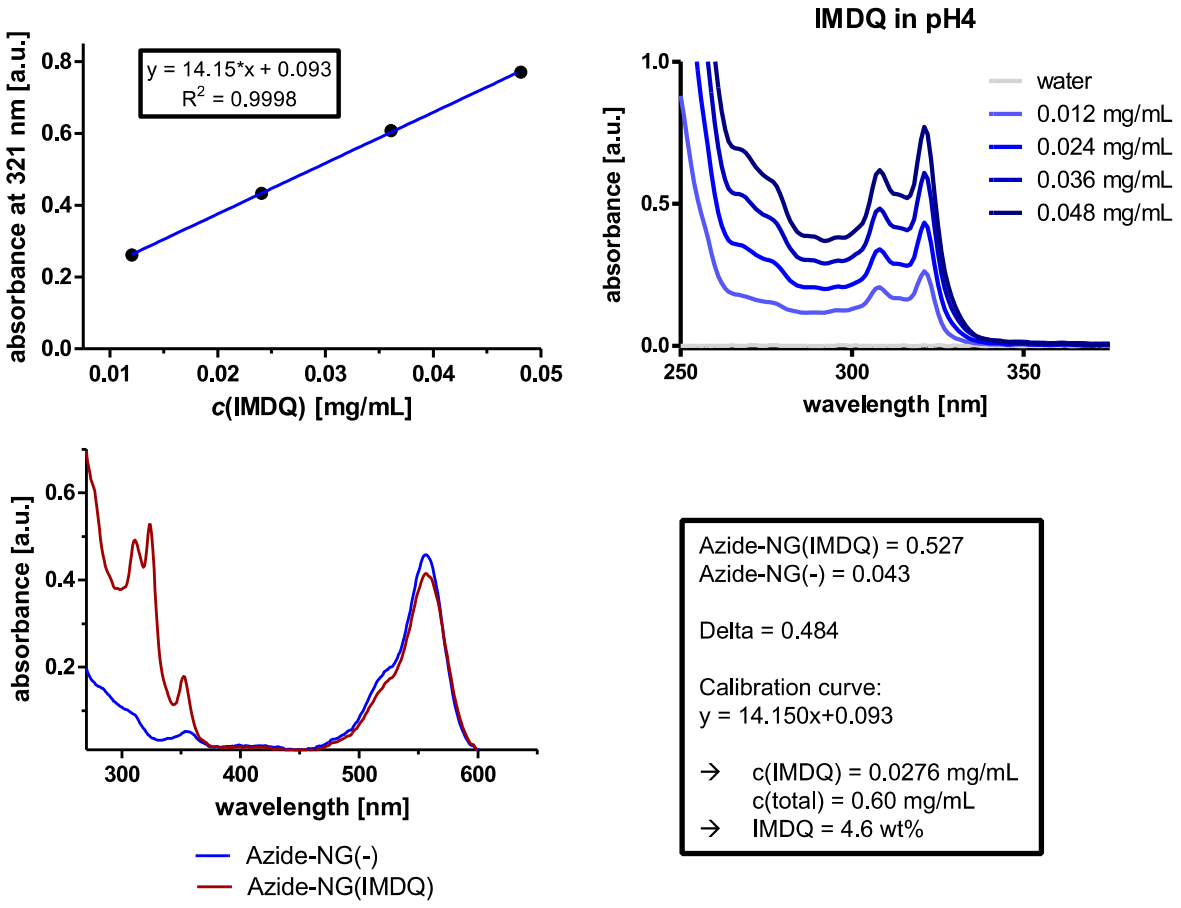

Figure S6. UV-Vis calibration of the immunodrug IMDQ in water supplemented with hydrochloric acid (pH 4) for determination of the drug-load in azide-functional nanogels by IMDQ's UV-absorbance at 321 nm. Azide-NP(IMDQ) provides an IMDQ-drug-load of 4.6 wt%. UV-Vis absorbance spectra of IMDQ in water at pH4 (right graph).

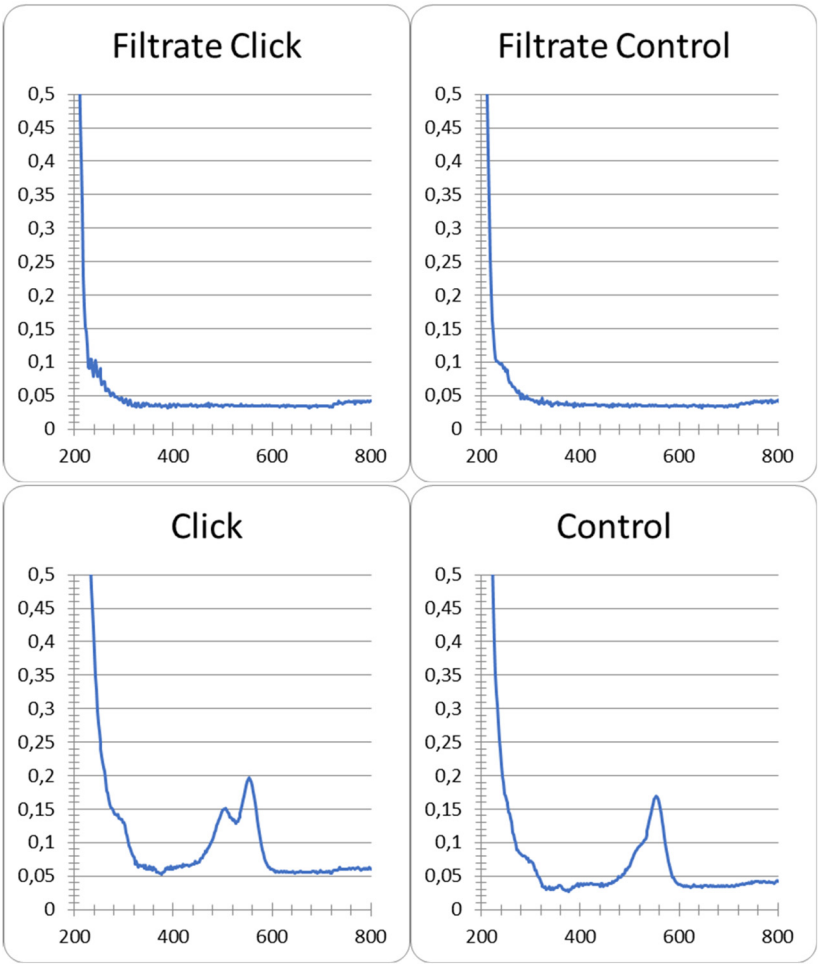

Figure S7. Additional UV-Vis spectra of the attachment of DBCO-OG488 to TMR-labeled azide-NP(-) (left spectra) and control experiment (right) of a non-SPAAC-reactive dye OG488-cadaverine to TMR-labeled azide-NP(-). Top spectra prove that after thorough spin-filtration no free (OG488) dye is present in the filtrate of both SPAAC sample and control sample, suggesting that nanogel samples were successfully purified from excess dye. The bottom spectra after SPAAC (left) shows an additional dye-absorbance of OG488 at ~488 nm. In contrast to that, no additional absorbance is found in the control sample.

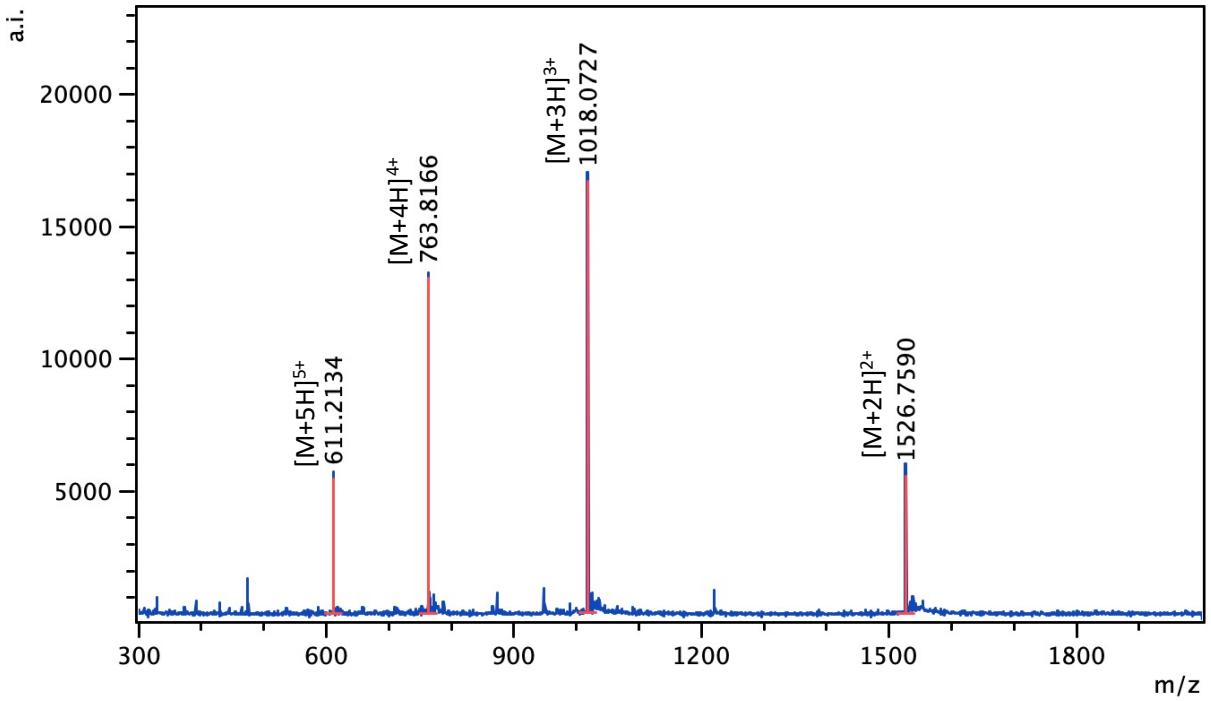

Figure S8. Mass spectrometric data of elution volume from 0-10 mL recorded by LC-MS of unmodified $CD4^+$ epitope ionized by electro spray ionization (ESI). Peaks are assigned in the spectra and correspond to the peptide product exclusively.

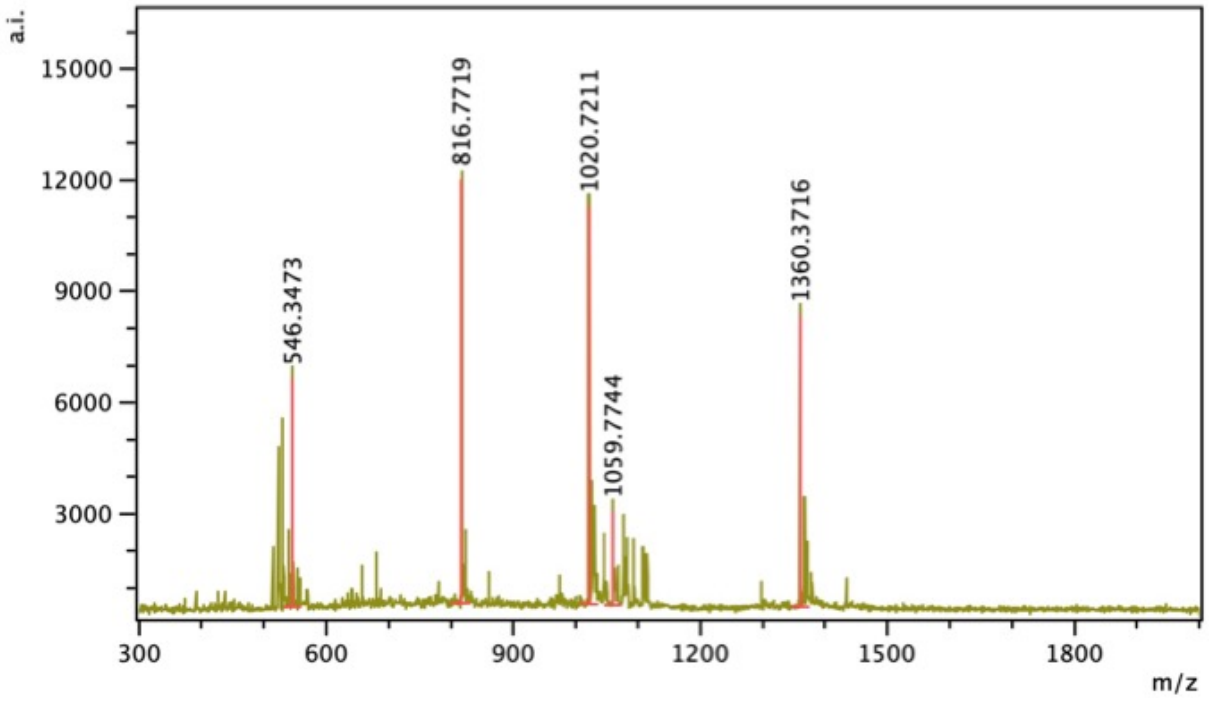

Figure S9. Mass spectrometric data of elution volume from 0-10 mL recorded by LC-MS of DBCO-modified $CD4^+$ epitope ionized by electro spray ionization (ESI). Peaks are assigned in the spectra and correspond to the peptide product with multiple counter ions and some hydrolyzed NHS-ester DBCO-PEG_{12}-maleimide linker.

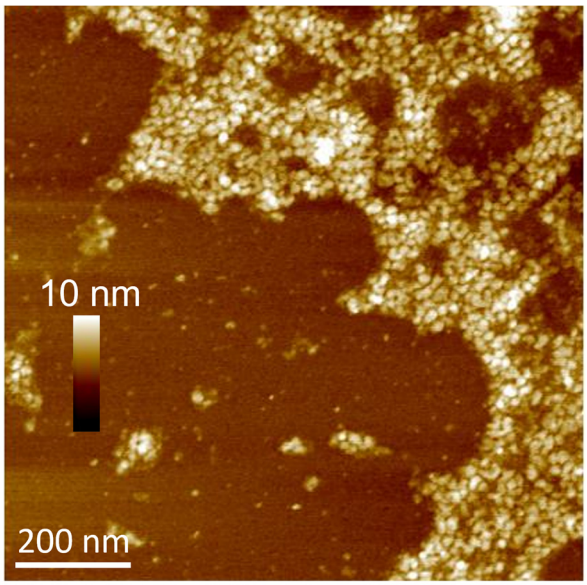

Figure S10. Atomic force microscope (AFM) image of peptide antigen decorated NP(IMDQ) showing spherical particles with heights of 5-10 nm. For sample preparation 5 µL of a 0.05 g/L particle solution in Millipore water was applied to the mica substrate (circular, 15 mm) and allowed to dry overnight.

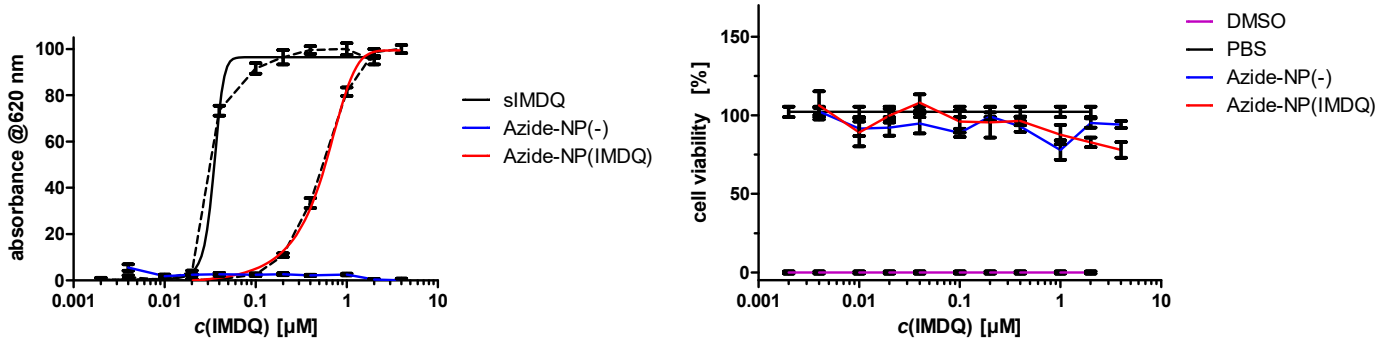

Figure S11. *In vitro* evaluation of azide-NP(-) and azide-NP(IMDQ) on RAW Blue macrophages. Adjuvant-loaded azide-NP(IMDQ) show potent immunostimulation in the range of 1 µM, whereas azide-NP(-) do not exert immunostimulating effects as determined by QuantiBlue Assay (left graph). MTT assay for cell viability confirms the high biocompatibility of azide-functional nanogels showing similar cell viability to PBS control with concentrations of IMDQ-load ranging 0.004 µM-4 µM (corresponding to particle concentrations of 0.061 µg/mL-0.061 mg/mL).

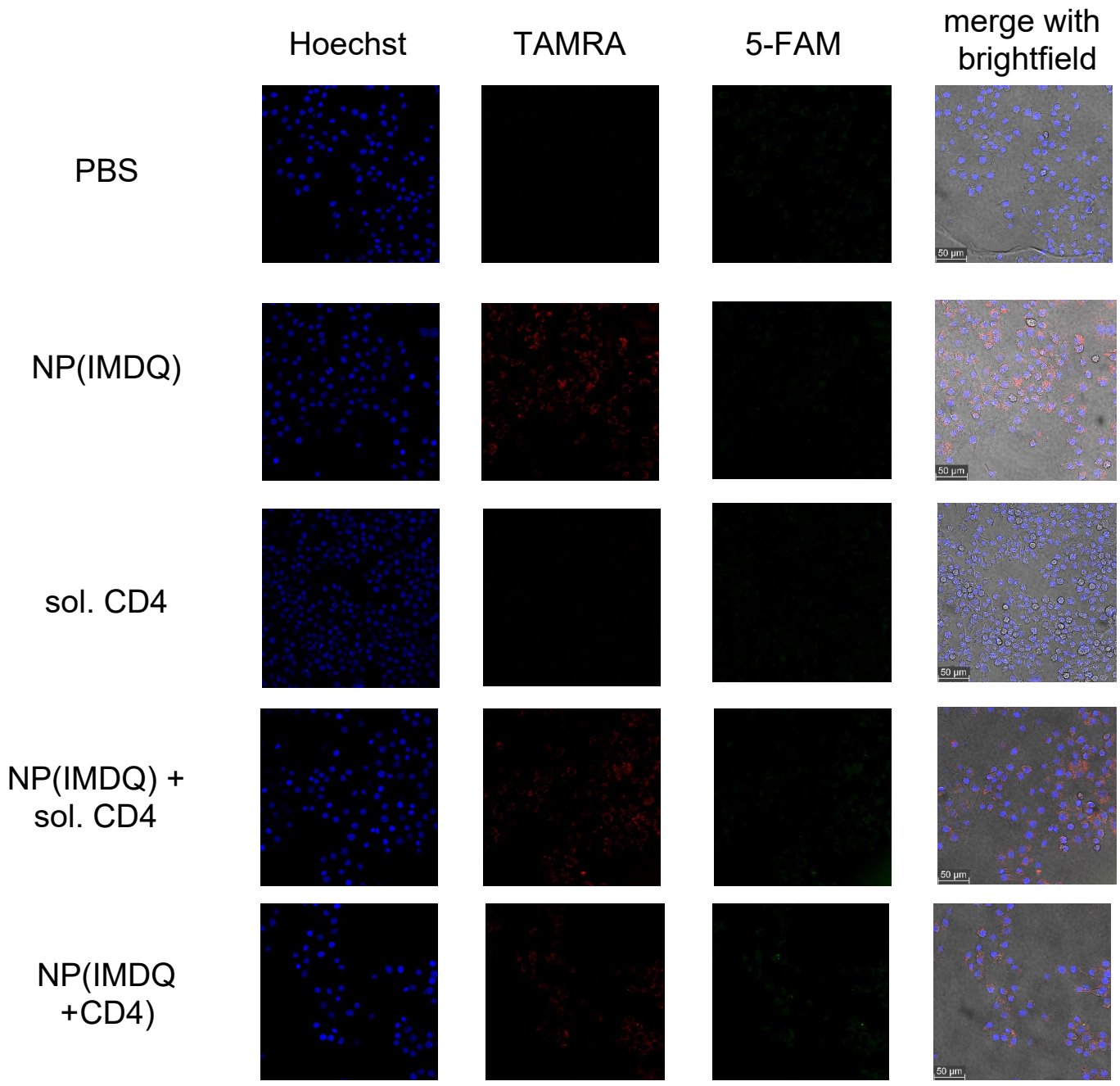

Figure S12. Additional confocal microscopy images of RAW Blue macrophages showing the internalization of nanogels by TMR fluorescence (red) and synchronously the co-uptake of $CD4^+$-peptides by 5-FAM fluorescence (green) when covalently attached to the nanogel. Nuclei were stained with Hoechst dye (blue) and a bright-field images (grey) were used for visualizing cellular morphologies.

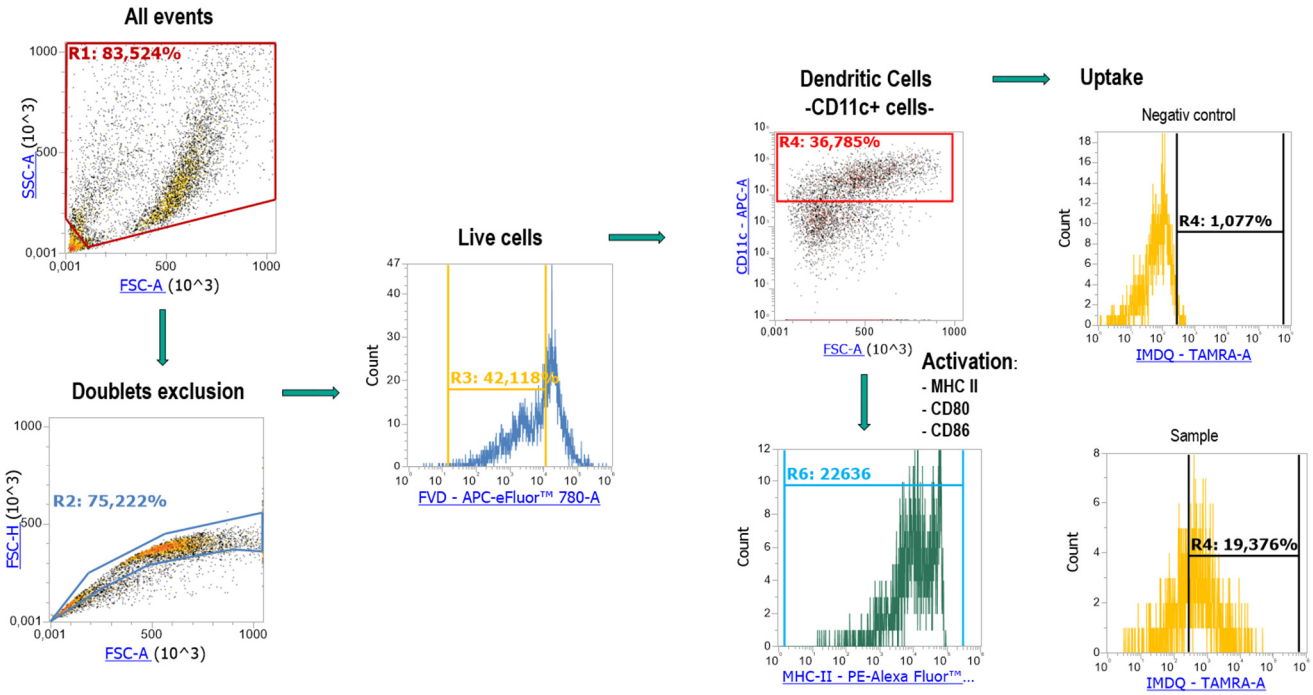

Figure S13. Gating strategy using in BMDCs (GM-CSF) to characterize dendritic cells, nanogel uptake and their activation after treatment with the different nanoparticles.

Table S1. Specific antibodies used for flow cytometry.

	Antibody	**Dye**
Lineage	CD11c	APC
Activation Markers	MHC-II	PE-eFl610
	CD86	eFl450
	CD80	PerCP-eFl780
Live/Dead	FVD780	eFl780

10.11. Publication 11 (submitted)

“A molecular vaccine platform based on cylindrical bottle brush polymers: adjusting size, shape and surface functionality for efficient tumor immunotherapy”

Meike Schinnerer, Cinja Kappel, Natascha Luther, Jennifer Schulze, Christine Seidl, **Carolina Medina-Montano**, Sandra Decker, Kaloian Koynov, Kerstin Reuter, Mustafa Diken, Romina Forst, Benjamin Weber, Karl Fischer, Matthias Bros, Christian Becker, Stephan Grabbe, Manfred Schmidt and Matthias Barz

The following work will be submitted to a peer-reviewed journal after biological evaluations have been completed. As a co-author, I´ve been responsible for the conduction and evaluation of *in vitro and in vivo* biological experiments concerning T cell proliferation using peptobrushes functionalized with a model antigen (OVA), an immune activator (CpG) and a targeting antibody (aDEC205).

This work reports on the synthesis of differentially sized and shaped cylindrical brush polymers as nanovaccines. My colleagues, Dr. Schinnerer and Ms Seidl designed the cylindrical brush polymers consisting of a polylysine backbone and polysarcosine side chains (peptobrushes). Different physico-chemical properties as size, shape and surface functionality can be well controlled. I tested peptobrushes that contained a model antigen (OVA), an immune activator (CpG) and a targeting antibody (aDEC205) in *in vitro* and *in vivo* experiments. These peptobrushes were well tolerated by immune cells, showed no aggregation in blood serum and showed extended circulation in the blood stream of mice after intravenous injection independent of their size and shape. Interestingly, the vaccine with the rod-like shape led to the most potent T cell proliferation response *in vitro* (OTI model) and was able to provide a protection from tumor growth in mice after subcutaneous vaccination. These findings underline the meaning of NP architecture to maximize immunity.

A Molecular Vaccine Platform based on Cylindrical Bottle Brush Polymers: Adjusting Size, Shape and Surface Functionality for Efficient Tumor Immunotherapy

Christine Seidl,[1,2,3‡] *Meike Schinnerer,*[1,2,6,‡,†] *Cinja Kappel,*[3] *Natascha Luther,*[3] *Fatehmeh Shahneh,*[3] ***Carolina Medina Montano****,*[3] *Jennifer Schulze,*[4] *Sandra Decker,*[2] *Kaloian Koynov,*[4] *Kerstin Reuter,*[5] *Mustafa Diken,*[5,6] *Federico Fenaroli,*[7] *Romina Forst,*[2] *Benjamin Weber,*[2,6] *Karl Fischer,*[2] *Lixin Liu,*[8] *Yongming Chen,*[8,9] *Matthias Bros,*[3] *Stefan Grabbe,*[3] *Christian Becker,*[3,10,†,*] *Manfred Schmidt*[2] *and Matthias Barz*[1,2,3*]

1 Division of Biotherapeutics, Leiden Academic Center for Drug Research (LACDR), Leiden University, Einsteinweg 55, 2333 CC Leiden, the Netherlands

2 Department of Chemistry, Johannes Gutenberg University, Duesbergweg 10-14, D-55099 Mainz, Germany

3 Department of Dermatology, University Medical Center of the Johannes Gutenberg, University Mainz, Langenbeckstrasse 1, D-55131 Mainz, Germany

4 Max Planck Institute for Polymer Research, Ackermannweg 10, D-55128 Mainz, Germany

5 Biopharmaceutical New Technologies (BioNTech) Corporation, An der Goldgrube 12, D-55131 Mainz, Germany.

6 TRON–Translational Oncology at the University Medical Center of the Johannes Gutenberg-

University GmbH, Freiligrathstr. 12, D-55131 Mainz, Germany.

7 Department of Biosciences, University of Oslo, Blindernveien 31, NO-0371 Oslo, Norway.

8 School of Materials Science and Engineering, Key Laboratory for Polymeric Composite and Functional Materials of Ministry of Education, Sun Yat-sen University, Guangzhou 510275, China

9 State Key Laboratory of Oncology in Southern China, Sun Yat-sen University Cancer Center, Guangzhou 510060, China

10 Department of Dermatology, University Hospital Münster, von Esmarch-Strasse 58, D-48149 Münster, Germany.

‡These authors contributed equally to this work.

† Present address differs from that at which the work was done.

ABSTRACT.

Nanoparticulate vaccines outperform conventional and subunit vaccines in terms of stability and control of functionality, making them particularly suitable for effective immune activation. Here, we report the development and testing of cylindrical amino acid-based brush polymer vaccines of defined size, shape, and surface functionality and demonstrate their efficacy as tumor vaccines. Cylindrical brush polymers composed of a polylysine backbone and polysarcosine side chains (peptobrushes) with molecular weights ranging from $2.2 \cdot 10^5$ to $10.4 \cdot 10^5$ g·mol^{-1}, dispersity indices less than 1.2, and hydrodynamic radii of 11 to 21 nm were ignored by cells, did not interact with blood serum components, and showed very long circulation times in zebrafish larvae and mice ($t_{1/2}$ > 24h). By stepwise conjugation, these peptobrushes were decorated with defined amounts of ovalbumin (OVA), immune activator (CpG) and antibody against the dendritic cell surface molecule DEC205. Subcutaneously applied triple conjugated peptobrushes elicited antigen-specific protective tumor immunity and were therapeutically effective in mice with previously established B16 OVA melanomas. The reported results highlight the enormous potential of cylindrical brush polymers for unique tailoring and as molecular vaccine for cancer immunotherapy.

KEYWORDS. Polypeptoids, polypeptides, brush polymers, vaccination, dendritic cells

INTRODUCTION

Vaccines represent the most cost-effective means of preventing or treating disease as recently experienced with the COVID-19 pandemic. The overall discussion showed a new generation of nanoparticle-based vaccines should have the potential to be particularly safe and effective due to its modular structure and versatile adaptability of size, shape, charge, adjuvant effect and cell specificity. In recent years nanovaccines emerged to being suitable to not only be protective but also therapeutic, as required for the treatment of chronic infections and tumors.

Over the past decade it became clear that not only size, rigidity and surface chemistry have a determining effect on the biological behaviour of nanomaterials, but that shape is equally important. For further insides and more detailed explanation we refer to recent reviews.[1–3] Several studies showed that anisotropic nanoparticles excel their spherical counterfeit in circulation time, targeting avidity and unspecific in vivo clearance leading to possible superior immune responses.[4–6] Due to the strongly interdependent characteristics of size, geometry and surface chemistry it is crucial to be precise in synthesis and characterization to exclude cross influences.

We have developed a platform technology based on cylindrical brush polymers that, for the first time, allows the size, shape and surface functionality to be independently adjusted and to combine a specific number of antigens, adjuvants and targeting moieties in the particles.

After its discovery in 1994[7] cylindrical brush polymers (sometimes called "bottlebrushes") have received considerable attention because any flexible backbone can be forced into an extended cylindrical conformation due to the repulsive interaction of the densely grafted side chains. In particular, due to the high graft density, the chain length ratio of main and side chains, and thus the length (backbone) and width (side chain) of the final polymeric nanoparticle, can be determined.[8] Hence, a variety of cylindrical brush

polymers (CPBs) have been synthesized by "grafting through",[9–14] "grafting from",[15–20] and "grafting onto"[21–24] techniques with different combinations of main and side chain monomers.

We have reported the synthesis of CPBs with polysarcosine (pSar) side chains using poly(N-(6-aminohexyl)methacrylamide) (PAHMA) and poly(L-lysine) (pLys) macroinitiators.[8] Both macroinitiators exhibited high weight-average molecular weights (Mw) of 3.7 (PAHMA) and $5.8 \cdot 10^5$ $g \cdot mol^{-1}$ (pLys) and quite high dispersity indices of about 1.7 due to the broad molar mass distribution of the macroinitiators used. Since main chain and side chain length of the cylindrical brushes can be controlled independently, their size and shape (aspect ratio) can be varied continuously from spherical (main chain < side chain length) to ellipsoidal (main chain > side chain length) to rod- or worm-shaped brushes (main chain >> side chain length). Müllner and coworkers have shown that an increase in aspect ratio leads to increased plasma clearance and increased deposition in MPS organs, reducing the blood half-life from 29.3 h to 20.4 h.[25] However, the majority of shape dependent behaviour studies were performed with particles at the end of the nanometer scale.[26,27] Experiments with particles at smaller scales give contradictory results which lead to further needed investigations.[28]

In addition to morphology and previous mentioned parameters, the particle material is a main factor influencing the biological properties of nanoparticles. Besides established materials for nanomedicines,[29] polymers of polypeptides and polypeptoids have gained increasing attention in recent years.[30–37]

To eliminate interdependent influences, effects of particle material and further contribute to insights for nanoparticles at smaller size ranges we synthesized "all polypept(o)ide" CPBs (cylindrical peptobrushes) composed exclusively of polypept(o)ides[30,38] with more defined morphology in terms of narrow main chain length distribution below 50 nm in diameter. This precise morphology was combined with high end group integrity for controlled conjugation of the antigen ovalbumin (OVA), adjuvant CpG

oligodeoxynucleotide (CpG), and the antibody anti-DEC205 by strain-promoted azide-alkyne coupling (SPAAC). This click-chemistry approach allows the average number of individual components to be adjusted on cylindrical polymer brushes. This enables the formulation of a nanoparticle vaccine platform in which the size, shape, and number of antigens, adjuvants, and targeting moieties can be optimized to induce antigen-specific immunity.

RESULTS AND DISCUSSION

Synthesis and Characterization of Peptobrushes

Cylindrical brushes with polylysine backbone and polysarcosine side chains (peptobrushes) were synthesized by nucleophilic ring opening polymerization using narrowly distributed polylysines as macroinitiators (see scheme 1). The pLys had a degree of polymerization (DP) and dispersity of $P_{n,1}$ = 102, Đ = 1.07 and $P_{n,2}$ = 258, Đ = 1.09. Dynamic light scattering experiments at a concentration of 1 $g \cdot L^{-1}$ in 0.1 M NaBr revealed hydrodynamic radii $R_{h,1}$ = 3.9 nm and $R_{h,2}$ = 7 nm. At full conversion the pSar side chain lengths were calculated to $P_{n,theo}$ = 50 and 100 for $pLys_1$ and $P_{n,theo}$ = 100 for $PLys_2$. After full monomer conversion was observed secondary amine end groups were quenched with azido butyric acid pentafluorophenyl ester introducing terminal azide functionalities for subsequent selective conjugation of biologically active substrates.

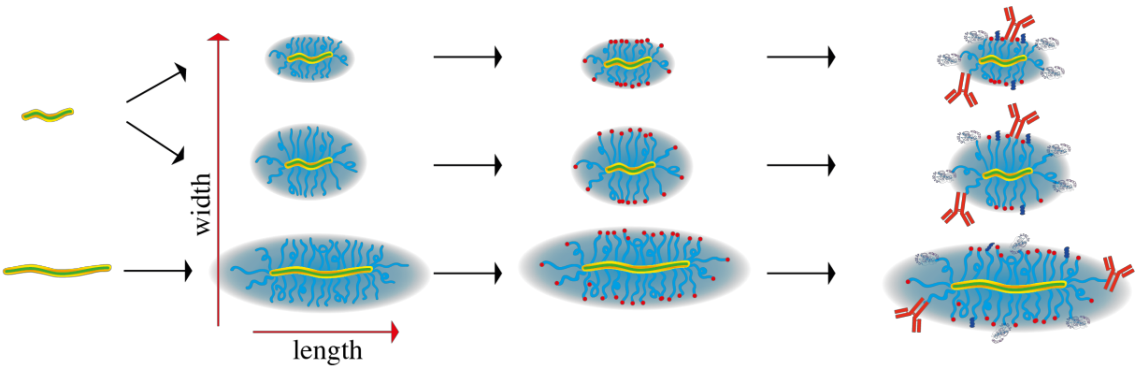

Control of length and width by degree of polymerization of main and side chain

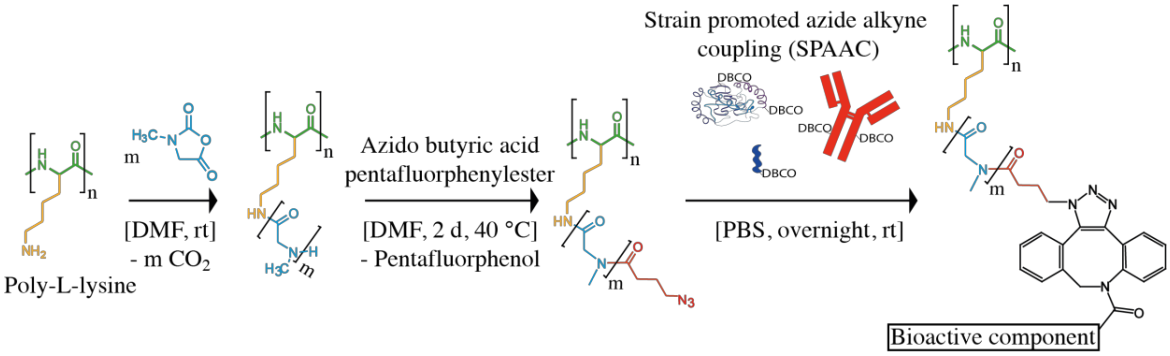

Scheme 1. Sequential synthesis of peptobrush based molecular vaccines: Adjustment of CPBs properties by degree of polymerization of main and side chain and adjustment of antigen, adjuvant and antibody loading. Synthesis of CPBs by sequential ring opening polymerization of α-amino acid *N*-carboxyanhydrides, end group modification for strain promoted azide-alkyne coupling (SPAAC).

Size exclusion chromatography revealed that all CPBs display a narrow monomodal molecular weight distribution with dispersity indices (Đ) of around 1.2 (see Fig. 1a). The GPC plots, however, display a slight high molecular weight tailing, that relates to the macroinitiator pLys itself (see Fig. S1). Dispersity index values of all brushes can be considered low for such large molecules and underline the well-controlled synthesis.

Therefore, static light scattering was performed to determine the molar mass of the brushes and to derive the average pSar side chain length. A typical Zimm-plot for **PB3** is shown in Fig. 1c and the results are summarized in Tab. 1 displaying the average molecular weights of $2.2 \cdot 10^5$ g/mol for **PB1** (Fig. S2), $4.2 \cdot 10^5$ g/mol for **PB2** (Fig. S3) and $10.4 \cdot 10^5$ g/mol for **PB3** (Fig. 1c).

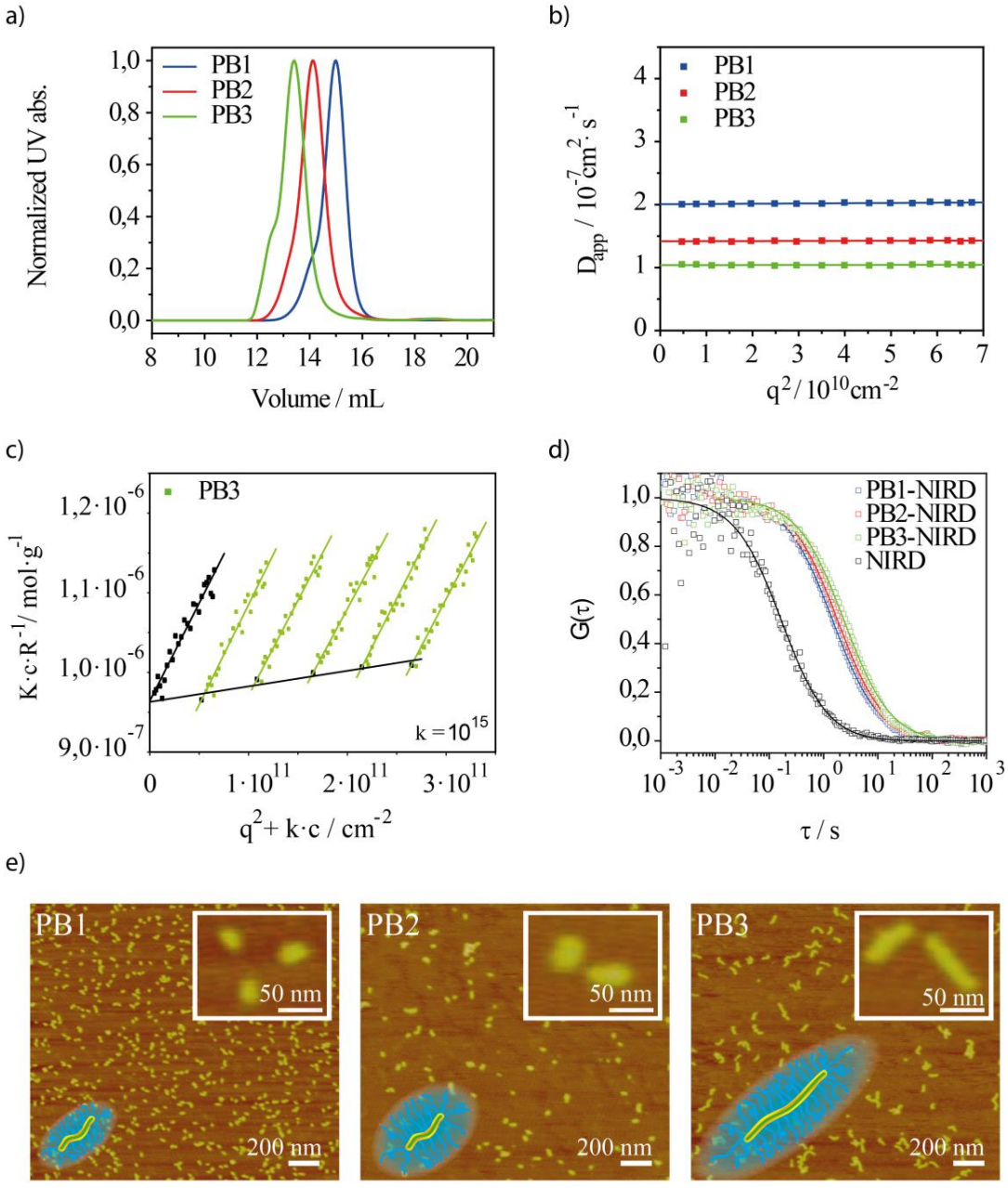

Figure 1. Characterization of peptobrushes **PB1**, **PB2** and **PB3**: a) GPC in HFIP (c(potassium trifluoroacetate) = 3 g·L^{-1}), b) multi angle dynamic lightscattering (DLS) in DPBS (c = 1 g·L^{-1}), c) Zimm-Plot for **PB3** in DPBS d) Near Infrared Fluorescence correlation spectroscopy (NIR-FCS) of near infrared dye (NIRD) and NIRD-labeled peptobrushes in DPBS (c = 2·10^{-8} M), e) Atomic force microscopy (AFM) of peptobrushes on mica in dry state.

Besides the analysis of molecular weight distribution GPC was also used to determine the enzymatic degradability of peptobrushes. Therefore, we used the enzymes derived from *Streptomyces griseus* and incubated the CPBs in its presence at 37°C for up to 2 weeks. The GPC plots reveal that brushes are degraded over the time frame of weeks (see Fig S4). Since the degradation by the applied peptidase is restricted to the pLys backbone, degradation yields the pSar side chains. The side chains can be analyzed applying an established pSar calibration.[39] The obtained side chain lengths are 25 for PB1, 108 for PB2 and 96 for PB3. Comparing the obtained side chain lengths after enzymatic degradation with the average side chain lengths calculated from SLS leads to grafting densities of 94 % for PB1, 43 % for PB2 and 44 % for PB3. The reason for the variation in the grafting density is currently not understood. According to literature[39] the corresponding R_h to a polymerization degree of 108 of pSar is 2.3 nm. Therefore, the remaining pSar segments are well below the renal excretion limit and thus can ensure rapid elimination upon enzymatic degradation.[40]

Table 1. Characterization of Peptobrushes PB1, PB2, PB3.

PB	$\langle \frac{1}{R_h} \rangle_z^{-1}$ / nm [a]	M_w / g·mol^{-1} [b]	R_g / nm [c]	$Đ_{HFIP}$ [d]	Average side chain length [e),f]	ζ. / mV [g]	Aspect ratio [h]
PB1	11	2.2E5	10	1.2	24 / 25	-6 ± 4	1.5
PB2	15	4.2E5	15	1.2	47 / 108	-4 ± 3	1.5
PB3	21	10.4E5	23	1.3	42 / 96	-3 ± 5	4.0

a) determined by dynamic light scattering in DPBS

b,c) determined by static light scattering in DPBS

d) determined by size exclusion chromatography in hexafluoroisopropanol

e) determined by static light scattering in DPBS (estimating 100% grafting density)

f) determined by size exclusion chromatography in hexafluoroisopropanol after enzymatic degradation

g) determined by zeta potential measurements in 10 mM NaCl

h) determined by atomic force microscopy on mica substrates (measured particles to determine the aspect ratio for PB1: 177, for PB2: 97, for PB3: 109).

Dynamic light scattering (DLS) experiments were performed at a concentration of 1 $g \cdot L^{-1}$ in DPBS buffer and yielded hydrodynamic radii R_h = 11 nm for **PB1**, R_h = 15 nm for **PB2** and R_h = 21 nm for **PB3**. We could not detect any angle dependency of the scattering vector q^2 (see Figure 1b) as expected for narrowly distributed polymer brushes in this size regime. The hydrodynamic radii were confirmed by fluorescence correlation spectroscopy (FCS) after subsequent labeling of polymers with Carboxyrhodamin110 employing strain promoted azide alkyne coupling (Fig. S5). The autocorrelation functions of NIR-dye labeled brushes showed no free dye (Fig. 1d). Removal of free dye is crucial since remaining dye can lead to interferences in detection of the labeled particle in biodistribution experiments by adding false positive intensity, changing the outcome of the experiment. Finally, the morphology of peptobrushes was visualized by atomic force microscopy (AFM) on mica substrates. The brushes were spin cast from aqueous solution and analyzed in dry state. As displayed in Figure 1e for **PB1** ellipsoidal structures with an average length of 29 nm and a width of 20 nm were observed representative of an average aspect ratio of 1.5. For **PB2** we found an average length of 46 nm and a width of 30 nm representing a comparable average aspect ratio of 1.5 and ellipsoidal structure. AFM experiments of **PB3** visualize worm-like nanoparticles with an average length of 79 nm, a width of 20 nm and thus an aspect ratio of 4. It should be noted that the AFM dimensions discussed above should be treated with caution, because the brushes are adsorbed and dried on Mica resulting in deformed, i.e. flattened, structures. It is also likely, that upon drying the brushes do collapse and or partially fold back resulting in thicker and shorter chains. Therefore, we have attempted to analyze the solution dimensions of the brushes given in Tab. 1 by two models (for details see SI). In the prolate ellipsoid model[41] the brushes are treated as rigid

structures with semi-axis a and b. Application of the wormlike chain model[42–44] accounting for some flexibility in terms of the Kuhn statistical segment length (l_k = 80 nm) yielded similar values (Tab. 2).

Table 2. Results of Solution Dimensions of Peptobrushes PB1, PB2, PB3.

	Prolate Ellipsoid Model[41]			Wormlike Chain Model[42–44]		
PB	L = 2*a/ nm	d = 2*b / nm	Aspect ratio a/b	L = 2*a/ nm	d = 2*b / nm	Aspect ratio a/b
PB1	40	14	2.8	38	13.5	2.8
PB2	64	16.5	3.9	60	16.5	3.6
PB3	100	19	5.3	100	19	5.3

Within experimental error the results from the ellipsoidal and wormlike chain model agree. In both models the small polydispersity of the brushes was neglected, since no significant influence is to be expected. Obviously, the introduction of main chain flexibilty does hardly change the fit results as expected for $L/l_k < 1.5$.[45] The results clearly demonstrate that the AFM results do not reflect the brush dimensions in solution.

Our findings show that both, length and width, of brushes can be controlled by the degree of polymerization of macroinitiator and side chains yielding bottlebrush polymers with low dispersity (Đ).

Ex vivo Evaluation of Plain Peptobrushes

Before any *in vivo* application, cytotoxicity and aggregation in serum was analyzed *ex vivo*. Cytotoxic effects of the polymer brushes were assessed with DC-like DC2.4 cells and fibroblast-like HEK293ZT cells (Fig. S6). The different types of polymer brushes showed no significant cell toxicity in the MTT assay over a wide concentration range (0.05 to 5 mg/mL) surpassing *in vivo* concentrations.

In addition to material-related cytotoxicity, *in vivo* toxicity may occur through aggregation of polymeric nanoparticles induced by serum proteins or high ionic strength.[46] To ensure that the peptobrushes do not form aggregates in blood serum (human), they were analyzed by DLS in serum, a method introduced and described in detail by Rausch *et al.*.[47] Firstly, the intensity-time correlation function of polymer and serum are measured separately. Secondly, a mixture of polymer and serum is measured. If there are no aggregates formed, the autocorrelation function of the mixture can be well described by a force fit which is the sum of the correlation functions of each of the components. The formation of larger aggregates would require an additional exponential term to describe the autocorrelation function of the mixture. After mixing the NIRD-labelled peptobrushes **PB1**, **PB2** and **PB3** with human serum, the autocorrelation function of the mixture was well described by the force fit (Figure 2). This indicates that all three peptobrushes do not form aggregates in the presence of 90 % human serum.

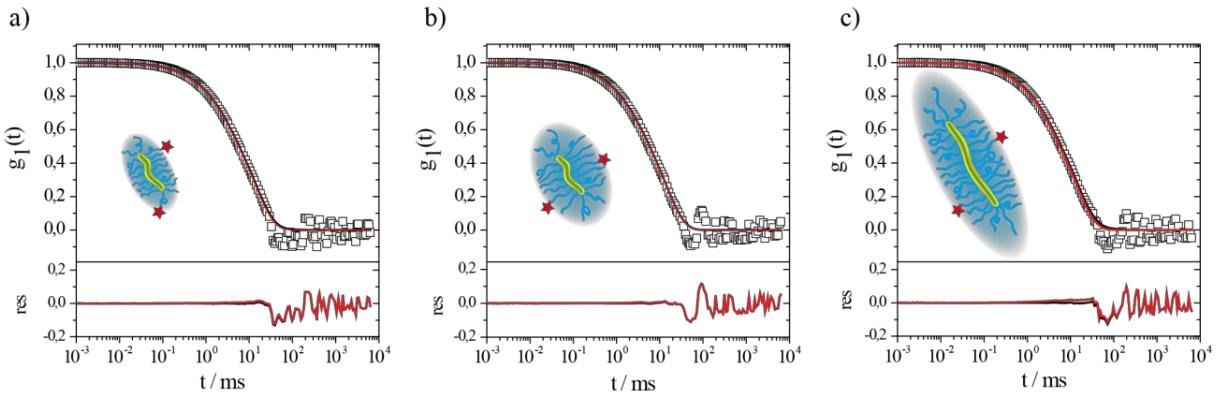

Figure 2. Characterization of NIR-Dye labeled peptobrushes **PB1**, **PB2** and **PB3** in 90 % human serum by DLS at 30°. Autocorrelation functions $g_1(t)$ recorded from PB1-NIRD, PB2-NIRD and PB3-NIRD in 90 % human serum (□ squares). Red line: Force fit. Black line: Fit with a variable component. a) PB1-NIRD, c_{PB1} = 0.2 g·L^{-1}. b) PB2-NIRD, c_{PB2} = 0.4 g·L^{-1}. c) PB3-NIRD c_{PB3} = 0.8 g·L^{-1}.

In vivo Evaluation of Peptobrushes

Having ensured that peptobrushes PB1-PB3 do not induce cytotoxicity at relevant doses, do not aggregate or cause aggregation of serum proteins, we determined their biodistribution and stability first in zebrafish larvae and after promising results in mice. To this end, all peptobrushes were marked with 800CW, a NIR dye that allows to track the CPBs in both animal models. Having ensured that fluorescence intensity scales linearly with particle concentration in the range of applied concentration (Fig. S7), circulation times were determined by fluorescence microscopy at different time points over the course of 7 days in zebrafish larvae (Figure 3b and c). Linear polylysine chains as control aggregated already 5 minutes after intravenous injection so that no particles remained in the blood stream (Figure 3a and Video X). In contrast, PB1-PB3 peptobrushes still circulated a considerable amount (31 %, 28 % and 26% for **PB1**, **PB2** and **PB3**) 7 days after injection (Figure 3c and Video xyz). Peptobrushes are thus the longest circulating nanoparticles in zebrafish larvae, outperforming PEGylated liposomes.[53]

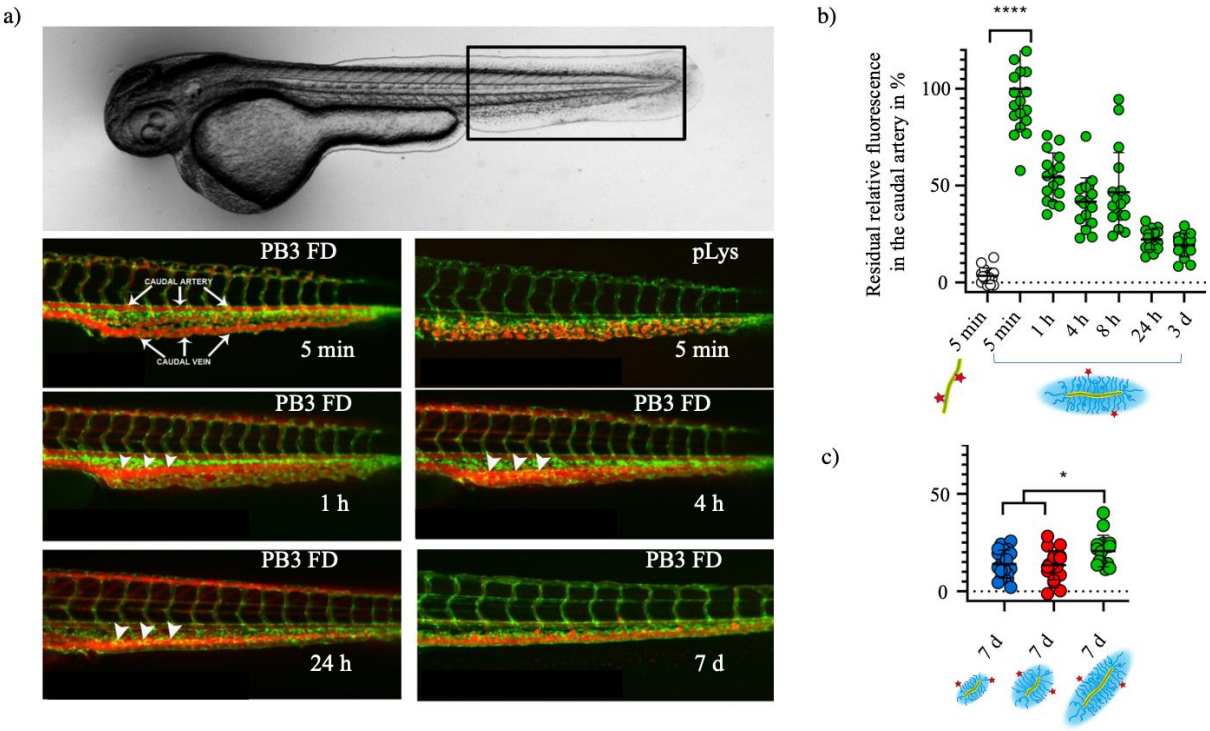

Figure 3. Stability of peptobrushes in zebrafish larvae. a) *In vivo* imaging of zebrafish larvae. b) Fluorescence intensity in zebrafish larvae at indicated time points, c) Fluorescence intensity zebrafish larvae of PB1-PB3 at 7 days.

We did not observe morphology-associated differences in circulation residence time for PB1 and PB2. However, compared to the smaller peptobrushes PB3 has a slightly higher circulation time, indicating that the **in vivo** stability of CBPs slightly depends on their size or shape. These results are not substantiated by PK studies of the peptobrushes in BALB/c mice (Fig. 4), where no significant difference in circulation times was observed. In mice, PB1 and PB3 CBPs circulated without specific accumulation in liver, lung, or kidney upon systemic application (Fig. 4a, b). However, PB2 showed slightly increased liver accumulation without reasonable explanation. After 24 h, approximately 70% of the injected particles were still present in the bloodstream. Here, PB1, PB2, and PB3 had half-lives well above 2 days without significant differences (see Fig. 4c). Particle-associated fluorescence was detectable in blood even 9 days (endpoint of PK study) after application using fluorescence imaging.

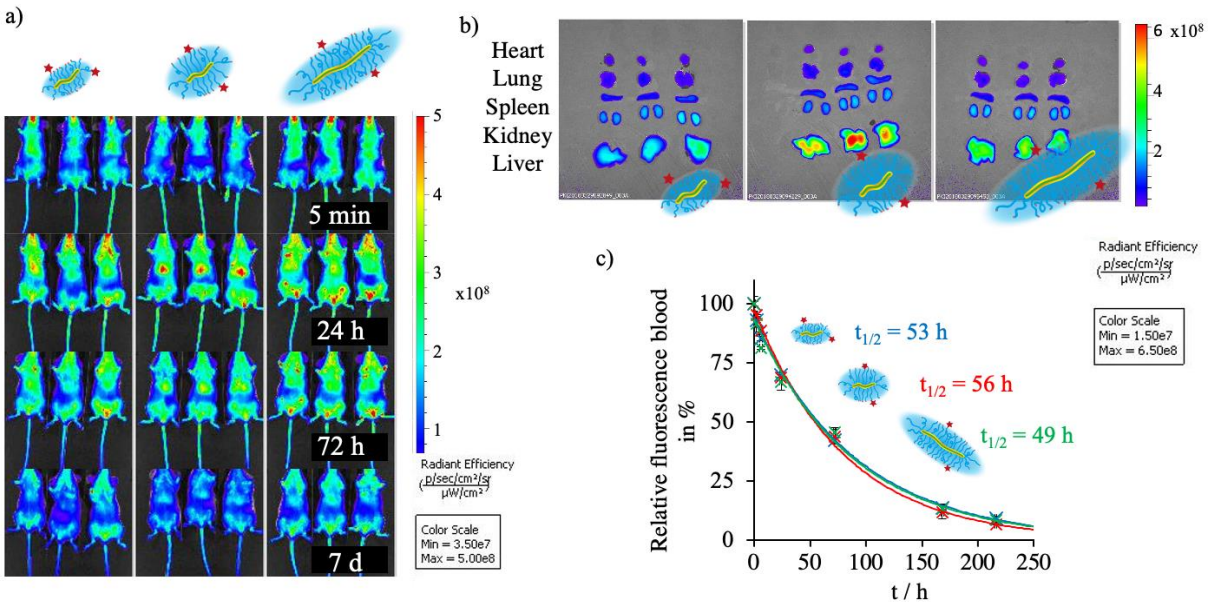

Figure 4. Stability of peptobrushes in mice. a) *In vivo* imaging of mice, b) Imaging of mouse organs taken 9 days after injection of the particles, c) Fluorescence intensity in the blood of mice at specified times. Intensities at 5 min set as 100%. The solid curve is a single exponential fit.

In summary, the morphological variants of peptobrushes studied show high stability and very little interaction with tissues in *vivo*. In this regard, the circulation times of peptobrushes are even among the longest reported,[48,49] which may be due to the fact that peptobrushes do not increase their hydrodynamic radius in whole blood.[50]

Because of this property, our peptobrushes appeared to represent an excellent basis for vaccines that are intended to interact with the immune system exclusively via additionally conjugated moieties. Due to the similar behaviour and same aspect ratios of PB1 and PB2 we choose to only investigate PB1 and PB3 for comparison.

Synthesis and Characterization of Peptobrush Conjugates

The high surface-to-volume ratio of worm-shaped peptobrushes is of interest for the synthesis of molecular vaccines, as increased aspect ratios and reduced surface curvatures are expected to improve the presentation of ligands, e.g., antibodies or immune activators.[51–53] To test the efficacy of peptobrushes as cancer vaccines in the B16-OVA melamoma model, we chose ovalbumin as the model antigen, CpG-ODN as the adjuvant, and an antibody against the surface molecule of dendritic cells, DEC205 as the targeting ligand.

In the B16-OVA model, ovalbumin represents a tumor-specific antigen.[54–56] We used the complete molecule here, because it was shown that antigen presentation is prolonged and an additional humoral immune response is induced in comparison to using short peptide sequences.[57,58] Immunostimulatory CpG-rich oligonucleotides (CpG-ODN) bind to endosomal and lysosomal TLR9 and induce DC-mediated Th1/Tc1 polarization for antitumor response.[59,60] To prevent rapid degradation by nucleases, the CpG-ODN was provided with a phosphorothioate backbone. In addition, antibodies against the C-type multilectin DEC-205 (anti-DEC205) were targeted to improve vaccination efficacy by targeting brushes

into dendritic cells.[60–62] Since the end groups on our polymer brushes bear azide groups, strain promoted azide alkyne coupling (SPAAC) was chosen to conjugate the different biomolecules to the CPBs.[63,64] Therefore, anti-DEC205 and OVA were modified with DBCO-PEG$_4$-NHS ester following the protocol established by S. Gietzen and Bühler *et al.*.[65,66] The purification procedure to achieve aggregate free DBCO-modified components however was changed from spin filtration to SEC resulting in significantly improved yields (70 - 90 % compared to 20 - 30 %).[66] The first purification step consisted of centrifugation with 10 kDa Amicon centrifugal filters to remove unbound DBCO-PEG$_4$-NHS ester and NHS. Afterwards, SEC was used to purify the DBCO-modified components from larger aggregates. The average number of DBCO per anti-DEC205 or OVA (N_{DBCO}) was determined as demonstrated in the SI. An anti-DEC205 mAb containing an average of 1.5 DBCO does not affect binding efficiency to dendritic cells (Figure S9a). In line with these results, the DBCO modification does also not change ovalbumin antigenicity in comparison to unmodified OVA (Figure S9b). Commercially available CpG1826 oligodeoxynucleotides with a DBCO modification at the 3' end (CpG-DBCO) were included as immune-stimulating agents. CpG1826 ODN is optimized for activation of B cells and dendritic cells and Th1-like cytokine expression.[67] CpG-DBCO shows a activation of BMDCs comparable to native CpG (Figure S9c). Upon engraftment of DBCO-modified antibody, antigen and adjuvant, the peptobrush conjugates were prepared employing the standard SPAAC protocol (Scheme 1).[68] In the following section, the synthesis is described as an example for the triple conjugate **PB3 FD-OVA(7)-anti-DEC205(3)–CpG(6)**. The average number of bound components is indicated in brackets. A detailed description of the calculations of the average number of bioactive components per brush can be found in the SI**.** All conjugation reactions were performed at room temperature over 16h. Firstly, **PB3** is labeled with fluorescent dye AlexaFluor647-DBCO and purified by spin filtration. The hydrodynamic radius of **PB3 FD** determined by multiangle DLS and FCS is 23 nm. Moreover, FCS experiments ensure the absence of

free dye (Fig. 5a) in the sample. Furthermore, the average number of dyes per brush (N_{AF647}), which is important for further calculations, can be determined directly by FCS (see SI) and was set to be 5 for **PB1 FD** and 6 for **PB3 FD**.

To synthesize OVA- or anti-DEC205-brush-conjugates an excess of OVA-DBCO or anti-DEC205-DBCO needs to be used. The yield of bound OVA or anti-DEC205 per brush depends on the number of DBCO per component. In the range of 1 - 2 DBCO per component an excess of $1/(0.34*N_{DBCO})$ needs to be employed (Figure S11). For the described example, a 20-fold excess of OVA-DBCO (1.2 DBCO per OVA) was added to **PB3 FD**. The conjugates were purified by SEC and analyzed by DLS, FCS, UV-VIS and PAGE. The hydrodynamic radius of **PB3 FD-OVA(7)** determined by DLS and confirmed by FCS is 22 nm. As the number of DBCO per OVA or anti-DEC205 is a statistical value, it is also possible that two brushes bind to one bioactive component resulting in bridged brushes. Due to the separation via SEC those bridged brushes are removed (Figure S10). During this process a part of the high molecular weight fraction is removed leading to a slight decrease of R_h of **PB3 FD-OVA(7)** (R_h = 22 nm) compared to **PB3 FD** (R_h = 23 nm)**.** Besides, the fractionation results in a slightly lower average number of dyes per brush. As the number of dyes per brush is an important value for calculating concentrations, FCS is measured after every conjugation step. For **PB3 FD-OVA(7)** the final average number of dyes per brush is 6. The OVA concentration is calculated from the absorption at 280 nm (Fig. 5d). A detailed description of the calculations of the average number of bioactive components per brush can be found in the SI yielding to 7 OVA per brush for **PB3 FD-OVA(7)**. It should be noted that the calculations are only valid if there is no unbound OVA in the purified conjugates. The absence of free OVA was ensured by SDS-PAGE (Fig. 5b). The synthesis, purification and characterization of DEC-205-specific antibody-conjugates are similar to the described procedure of the OVA-conjugate. Using a 5-fold excess of DEC-205-specific antibody-DBCO with 1.6 DBCO per DEC-205-specific antibody yields to an average number of 3 anti-DEC205

per brush, determined by UV-VIS Spectroscopy (Fig. 5d). The absence of unbound anti-DEC205 is proven by SDS-PAGE (Fig. 5b). The hydrodynamic radius of **PB3 FD-OVA(7)-anti-DEC205(3)** measured by DLS and FCS is 22 nm.

The last step in the exemplified triple conjugate synthesis consists of the addition of CpG-DBCO. In contrast to OVA-DBCO and DEC-205-specific antibody-DBCO, exactly 1 DBCO is attached to the terminal side of CpG, which reduces steric constrains, and therefore the yield of the CpG coupling is found to be almost quantitative. To synthesize **PB3 FD-OVA(7)-anti-DEC205(3)–CpG(6)**, a 7 fold excess of CpG-DBCO was added to **PB3 FD-OVA(7)-anti-DEC205(3)**. As there is only 1 DBCO per CpG, no bridged brushes are formed and the conjugates can be purified by spin filtration with Amicon 50 kDa centrifugal filters only. The successful removal of CpG-DBCO can be shown by TBE-Urea PAGE (Fig. 5c) and the average number of CpG per brush can be calculated again from the UV-VIS Spectra (Fig. 5d). The hydrodynamic radius determined by DLS and FCS is 22 nm (Fig. 5e). Obviously, the addition of 6 CpG is once again not sufficient to alter the total brush dimension. The synthesis of all combinations of bioactive components conjugated to **PB3 FD** is described in the experimental section and proofs the reproducibility (table S1). To synthesize conjugates with the small brush **PB1**, the protocol can be adopted from the big brush. Due to the smaller size of **PB1** and to achieve an adequate separation between brush and antibody the purification requires the use of 2 columns in the SEC setup (Figure S14). Although the order of the conjugation steps does not influence the number of bioactive components per brush in the case of **PB3**, the order of the conjugation reactions needs to be changed for **PB1** to achieve the same number of bioactive components. The addition of CpG in a 7-fold excess to the conjugate **PB1 FD-OVA(7)-anti-DEC205(2)** only yields an average number of 2 CpG per brush. Because of these results, the CpG-DBCO was added first, followed by the addition of OVA-DBCO and anti-DEC205-DBCO. This reaction order leads to a triple conjugate with comparable amounts of bioactive components

to the big brush **PB1 FD-OVA(7) -anti-DEC205(3) –CpG(7).** The UV-VIS spectra and PAGE analysis of the precursors of **PB1 FD-OVA(7)-anti-DEC205(3) –CpG(7)** are shown in the SI (Figure S15), ensuring separation from unbound bioactive components. The hydrodynamic radius determined by DLS (Fig. 5e) as well as FCS is 17 nm.

Besides choosing the type of biomolecules and the most applicable conjugation chemistry, the adjustment of the right number of these moieties is also a key factor in efficient immune activation. In T cell proliferation assays, we determined a number of 7 ovalbumin antigens per brush as the optimal amount of antigen (Fig. S16). Titration of CpG either did not show sufficient activation at low levels of adjuvant (<6) or induced unspecific uptake of conjugates at high levels (>10). To achieve activation without unspecific uptake, the ideal average number of CpG per brush was set to 7 CpG per brush. A larger study by Kappel *et al.* was performed to identify the optimal amount of antibody per brush.[69] In this study, different amounts of antibody per brush and their *in vivo* biodistribution were compared. It was shown that larger amounts of antibodies taken up by sinusoidal endothelial cells of the liver lead to a strong off-target accumulation after i.v. injection. By blocking Fc receptors *in vivo*, it was possible to reduce liver uptake. By using $F(ab)_2$ fragments or by reducing the number of bound the antibody molecules to an average of 3 per brush, liver accumulation was greatly reduced. Interestingly, specific cellular uptake did not increase even *in vitro* when more than 3 antibodies per brush were conjugated. Based on these observations, we used PB1 and PB3 peptobrushes to prepare molecular vaccines containing an average of 3 anti-DEC205, 7 CpG oligonucleotides (CpG1826), and 7 antigens (ovalbumin) (see SI).

To ensure the synthesis of endotoxin-free conjugates, the use of a sterile SEC setup was necessary. For this purpose, a sterilization procedure was established that the SEC had to undergo repeatedly to ensure the pyrogen-free setup. The SEC column (Sepharose 4 FF XK 16/70) is equipped with a special material

that can withstand basic conditions up to 2 M NaOH. After every 3 days, the setup had to be purified with 1 M NaOH (3 column volumes), followed by 0.1 M NaOH (3 column volumes).

In summary, the developed synthetic pathway allows the preparation of endotoxin-free peptobrushes with precisely controlled amounts of covalently bound antibody (anti-DEC205), adjuvant (CpG), antigen (ovalbumin), and fluorescent dye (AlexaFluor647, CW800).

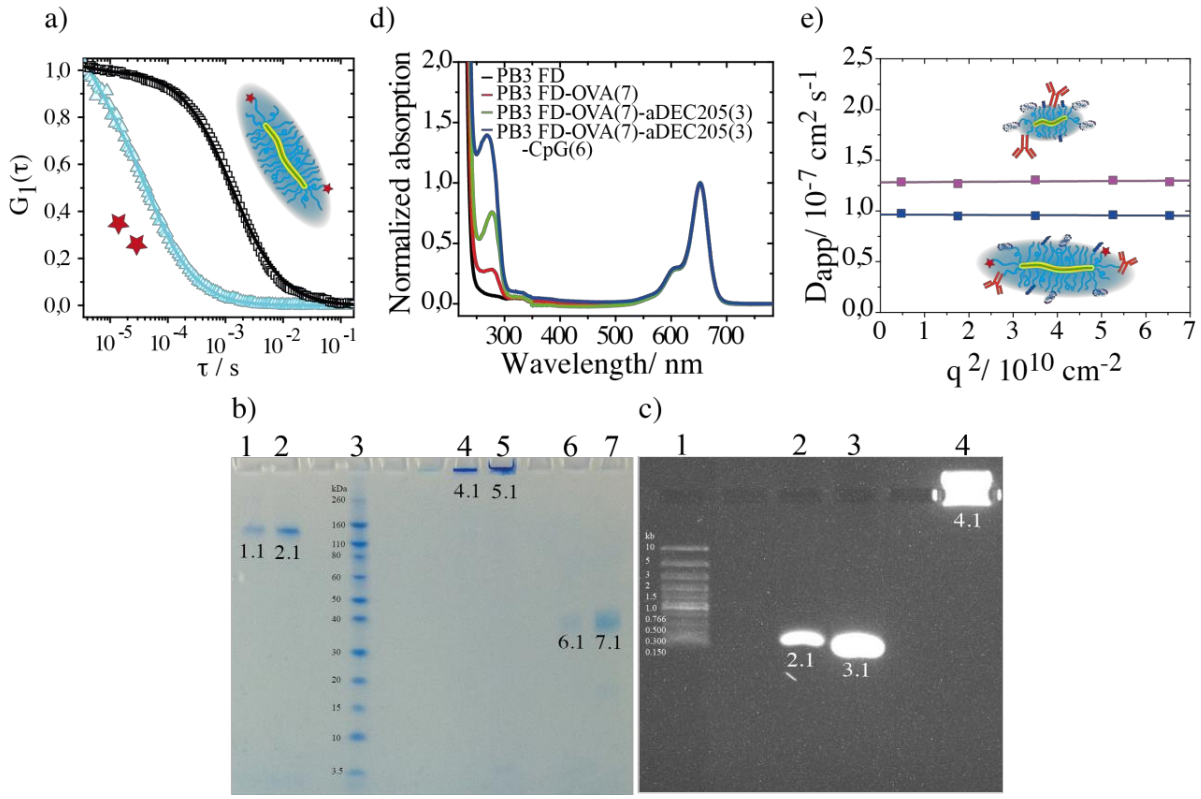

Figure 5. Characterization of peptobrush based triple conjugates. a) Fluorescence correlation spectroscopy (FCS) in DPBS buffer (c = $1 \cdot 10^{-8}$ M) of AF647-DBCO and **PB3 FD** confirms the labeling of **PB3**. b) UV-vis spectra of the triple conjugate and the triple conjugate precursors normalized to the absorption of the fluorescent dye. c) Multi angle dynamic lightscattering (DLS) in DPBS buffer of the triple conjugates of the small brush **PB1 FD-OVA(7)-anti-DEC205(3)–CpG(7)** and big brush **PB3 FD-OVA(7)-anti-DEC205(3)–CpG(6)**. d) SDS PAGE of the precursors **PB3 FD-anti-DEC205(3)** (4.1) **PB3 FD-OVA(7)-anti-DEC205(3)** (5.1) show no unbound OVA-DBCO (6.1 and 7.1) or anti-DEC205-DBCO (1.1 and 2.1). 1 = 0.1 µg anti-DEC205-DBCO, 1 = 0.3 µg anti-DEC205-DBCO, 6 = 0.1 µg OVA-DBCO, 7 = 0.3 µg OVA-DBCO 4 = **PB3 FD–anti-DEC205(3)** equal to 8 µg anti-DEC205, 5 = **PB3 FD–OVA(7)-anti-DEC205(3)** equal to 5 µg OVA and 8 µg anti-DEC205. e) TBE Urea gel electrophoresis of **PB3 FD-**

OVA(7)-anti-DEC205(3)–CpG(6) (4.1) shows no unbound CpG-DBCO (2.1 and 3.1). 2 = 25 ng CpG-DBCO, 3 = 50 ng CpG-DBCO, 4 = **PB3 FD-OVA(7)-anti-DEC205(3)–CpG(6)** equal to 1000 ng CpG.

Application of brush conjugates for vaccination: *in vitro* testing

Since the coupling of antibody, antigen, and immune activator affects the interaction with cells and tissues, the aggregation behavior and potential toxicity of the fully decorated CBPs were investigated. *In vivo*, the conjugates showed no detectable toxicity up to the maximum dose of 1 g/L studied. However, prior to *in vivo* application of the vaccines, DLS and FCS were used in serum to exclude aggregation in protein-rich body fluids. While DLS is a very sensitive technique to detect larger aggregates formed by the coexistence of nanoparticles and concentrated blood serum, FCS monitors changes in the hydrodynamic radius of individual nanoparticles.[47] A solution of the triple conjugate, e.g., PB3 FD-OVA(13)-aDEC-205(2)-CpG(6) in DPBS, was added to pooled human serum from 6 healthy donors, resulting in a final solution containing 90% human serum and only 10% PB3 FD-OVA(13)-aDEC-205(2)-CpG(6) solution in DPBS. DLS measurements showed no aggregate formation (see Fig. 6a).

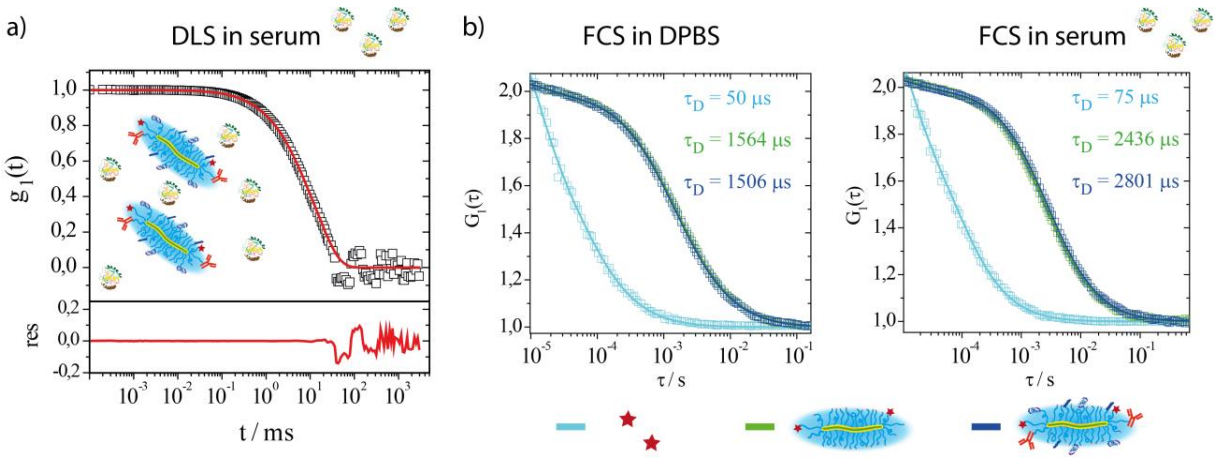

Figure 6. Evaluation of the interaction of triple conjugates with serum. a) Autocorrelation function $g_1(t)$ recorded from **PB3 FD –OVA(13)–anti-DEC205(2)–CpG(6)** in 90% human plasma ($c_{brush} = 2 \cdot 10^{-7}$ M). Scattering angle 30°. b) Autocorrelation functions of AlexaFluor647 (light blue) **PB3 FD** (green) and **PB3 FD –OVA(7)–anti-DEC205(2)–CpG(6)** (dark blue) in DPBS and 90 % human serum ($c_{FD} = 5 \cdot 10^{-8}$ M).

The diffusion time τ_D of particles in serum increases due to the increased viscosity of serum compared to buffer.[50] However, the fluorescent brightness should remain almost the same in the absence of particle aggregation. As shown in Fig. 6 b, τ_D of the dye AlexaFluor647 is 1.5 times higher, which is well in line with the factor 1.43 related to enhanced viscosity of serum reported in literature. τ_D of **PB3 FD** increases by a factor of 1.56 and the fluorescence brightness stays constant in the experimental error (27 kHz in DPBS and 31 kHz in serum). Those observations indicate no significant change in the R_h of **PB3 FD** in serum as well as no aggregation in the presence of 90 % serum. τ_D of the triple conjugate **PB3 FD – OVA(7)-anti-DEC205(2)-CpG(6)** increases from 1506 µs to 2801 µs which belongs to an increase from 21.8 nm to 24.5 nm. Since the fluorescence intensity remains almost constant (26 kHz in DPBS and 31 kHz in serum), we conclude that the increased R_h in serum is caused by a slight adsorption of individual serum proteins, which could be due to protein interactions with OVA and anti-DEC205 or electrostatic interactions with the CpG. Whether adsorption of serum proteins affects the interaction of conjugates with cells is not yet clear, but is part of current research projects. PB1 FD OVA(7)-anti-DEC205(2)-CpG(6) showed the same behavior in the experimental setup. The hydrodynamic radius increased in blood serum from 11.6 nm to 14.4 nm.

In summary, peptobrush triple conjugates did not induce serum protein aggregation and showed little size increase in serum, making them promising candidates for local or systemic vaccination. Next, we investigated the anti-DEC205 mediated targeting of molecular vaccines to dendritic cells. Uptake was determined via CLSM and showed efficient uptake of the anti-DEC205-PB3 conjugate, while no uptake was detectable for **PB3** and **PB3 FD-IsoType(2)** (Fig. 7).

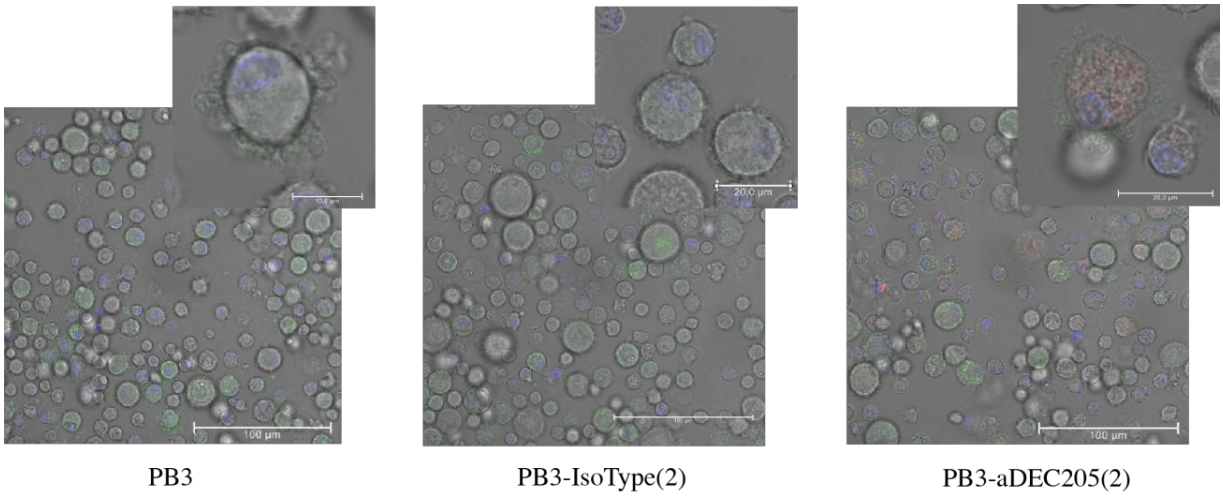

Figure 7. Evaluation of binding and uptake of peptobrush conjugates in BDMC. CLSM picture of **PB3-FD**, **PB3 FD –IsoType(2), PB3 FD –anti-DEC205(2)**. 1E12 particles per 5E5 cells, 1 h incubation at 37 °C. Blue = cell core (Hoechst 3342), green = DC, red = FD (equivalent with peptobrush).

Activation of OVA-specific CD4$^+$ and CD8$^+$ T cells *in vitro* and *in vivo*

Besides uptake the induction of an efficient response is essential for the desired immune response. As reported in literature[62], using nanoparticle formulations with simultaneously covalent attached adjuvant, antigen and antibody, only cells which have taken up the antigen will be activated. This approach will induce predominantly immunity instead of tolerance and reduces the required amount of adjuvant significant. As basis for testing the peptobrush conjugates *in vivo*, we wanted to ensure a potent immune response. Several combinations were tested in an OT-I and OT-II proliferation assay. Besides the molecular vaccines **PB1 FD OVA(7)-anti-DEC205(3)-CpG(7)** and **PB3 FD –OVA(7)-anti-DEC205(2)-CpG(6)** also an **anti-DEC205** and **CpG** mediated cell uptake could induce a T cell proliferation with the regarding OVA conjugates.

Transgenic OVA-specific (OT-I) CD8+ T cells were also activated by OVA conjugates (Fig. S17). Here, only the PB1 FD OVA(7)-anti-DEC205(3)-CpG(7) and PB3 FD-OVA(7)-anti-DEC205(2)-CpG(6) conjugate could induce strong cell proliferation. All other conjugates had similarly low levels. These

results indicate that the OVA conjugates are still in working order and can induce the desired immune response. To follow the fate of conjugated brushes *in vivo*, they were injected subcutaneously into mice and the fluorescence distribution in skin and immune system wasexamined 1 and 16 hours later (Fig. 8). Labeled OVA served as a control. One hour after injection, PB3 fluorescence was found almost exclusively in the skin around the injection site, both in $CD45^{neg}$ tissue cells and $CD45^{+}$ immune cells. In contrast, soluble OVA coupled fluorescence was also found in the draining lymph nodes at this time point. After 16 hours, the fluorescence of brushes was still detectable in the skin and started to reach the draining lymph nodes and spleen while the OVA fluorescence had already completely disappeared from the

organism (Fig. 8b). These results indicate that the brushes retain coupled OVA at the injection site.

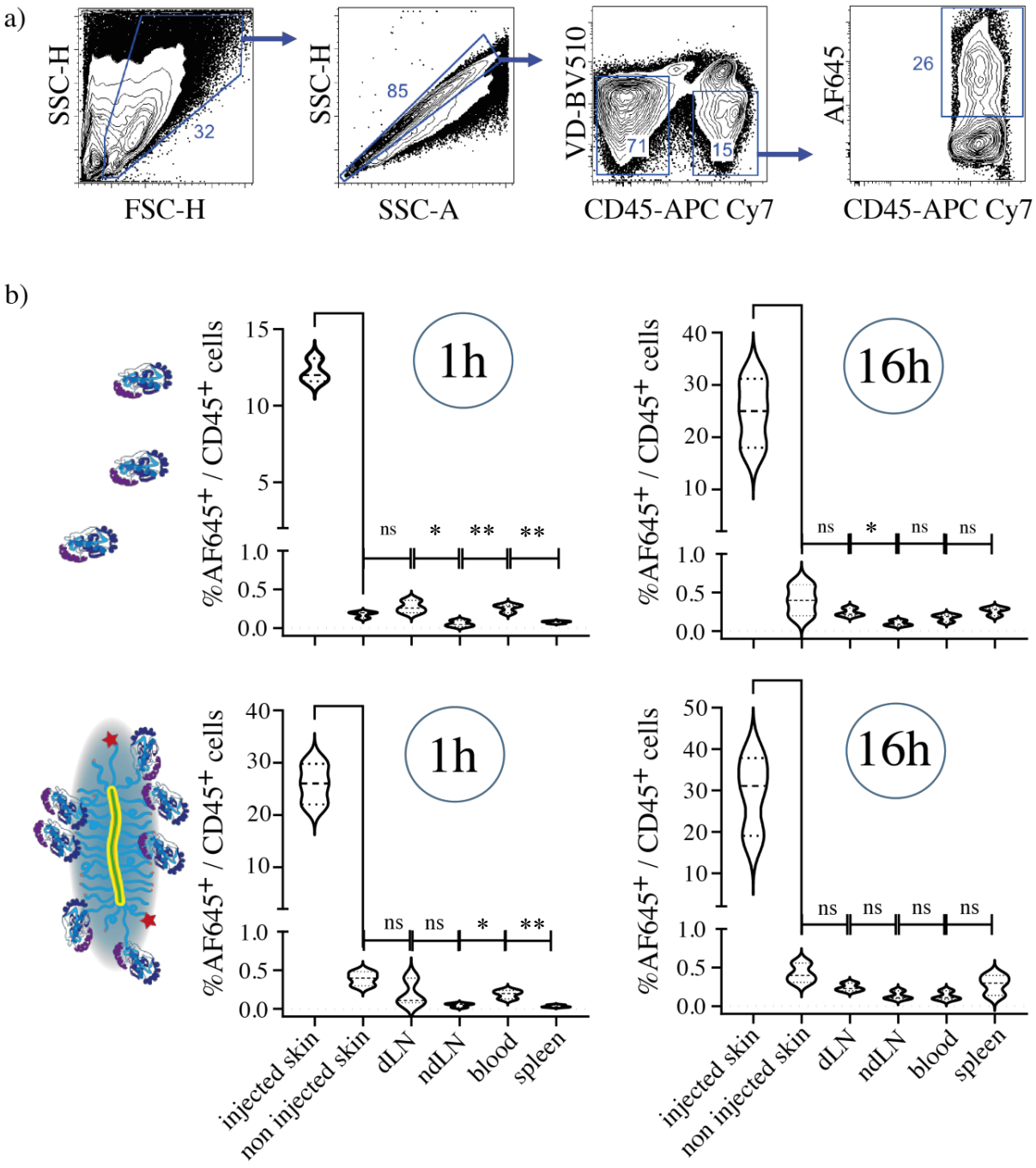

Figure 8. a) Selection scheme for single cell imaging. b) Binding distribution of **soluble OVA** and **PB3-FD-OVA(8)** in different organs after subcutaneous injection. Extraction of organs after 1 h and 16 h.

To analyze whether the observed differences in fluorescence handling are associated with differences in OVA presentation to T cells, we investigated when and where OVA-specific CD8+ and CD4+ T cells become activated after injection of OVA-coupled polymer brushes. Cell tracer-labelled OT-I and OT-II transgenic T cells were adoptively transferred into C57BL/6J mice and the recipients subsequently injected with equal amounts of OVA-coupled polymer brushes or soluble OVA (Fig. 9).

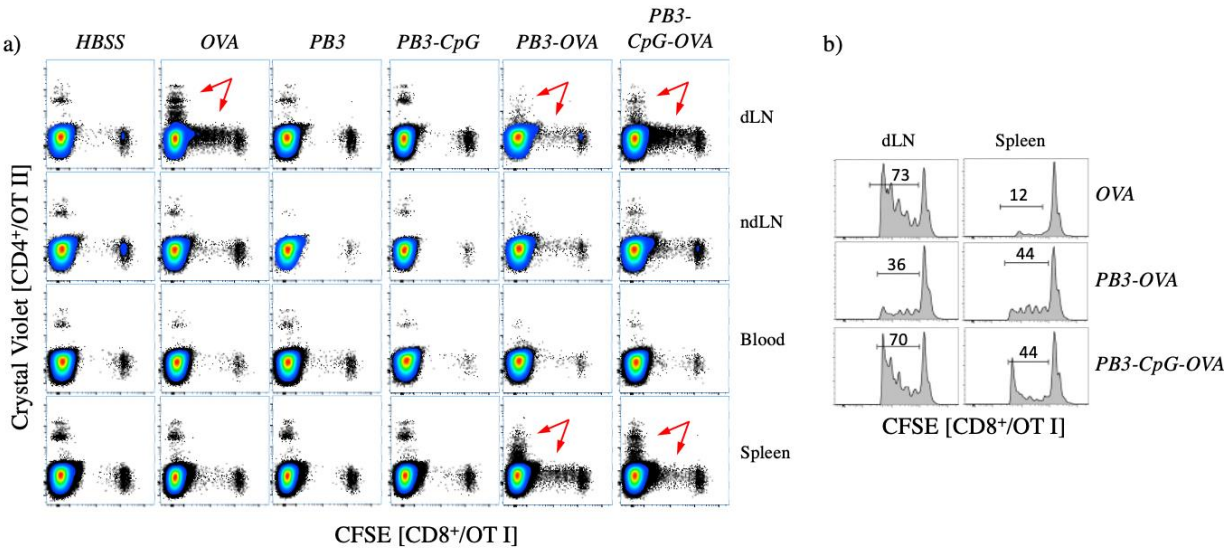

Figure 9. *In vivo* T cell proliferation after 5 days of buffer, soluble OVA and various PB3 conjugates (**PB3-FD, PB3-FD-CpG, PB3-FD-OVA, PB3-FD-OVA-CpG**) s.c. injection. a) Evaluation of OT-I (CD8+ T cells) and OT-II (CD4+ T cells) response after 5 days of injection with **buffer (HBBS), soluble OVA, PB3-FD, PB3-FD-CpG, PB3-FD-OVA, PB3-FD-OVA-CpG** b) Comparison of OT-I (CD8+ T cells) proliferation in draining lymphnodes and spleen induced by ovalbumin containing samples.

While soluble OVA could only trigger activation of OVA-specific T cells in skin-draining lymph nodes, OVA-specific T cells were released by OVA-coupled polymer brushes in both the skin-draining lymph nodes and in the spleen and even in lymph nodes whose skin sections were not injected. The injection of buffer and polymer brush without OVA showed no T-cell activation.

These observations show that, unlike the protein alone, decorated brushes trigger very efficient systemic T-cell activation. In contrast to previously produced *in vitro* OT-I results (data not shown), a proliferation for the OVA-coupled polymer brushes without the presence of CpG is also demonstrated here. With additionally bound CpG, however, the proliferation in the skin-draining lymph nodes was increased, which proves an adjuvant effect.

Protective and Therapeutic Tumor Vaccination

In order to test the effectiveness of the developed decorated brushes as cancer vaccines, we examined their protective and therapeutic effects in the B16-OVA model. To measure the protective effect, C57BL / 6J mice were immunized three times subcutaneously in one flank with differently conjugated PB1 and PB3 brushes and one week after the last immunization subcutaneously with B16-OVA melanoma cells on the other flank. While the OVA-decorated brushes already led to significantly reduced tumor growth, immunization with the OVA-CpG-anti-DEC205 decorated brushes induced full protection (Figure 10a). However, no differences between PB1 and PB3 brushes were detectable.

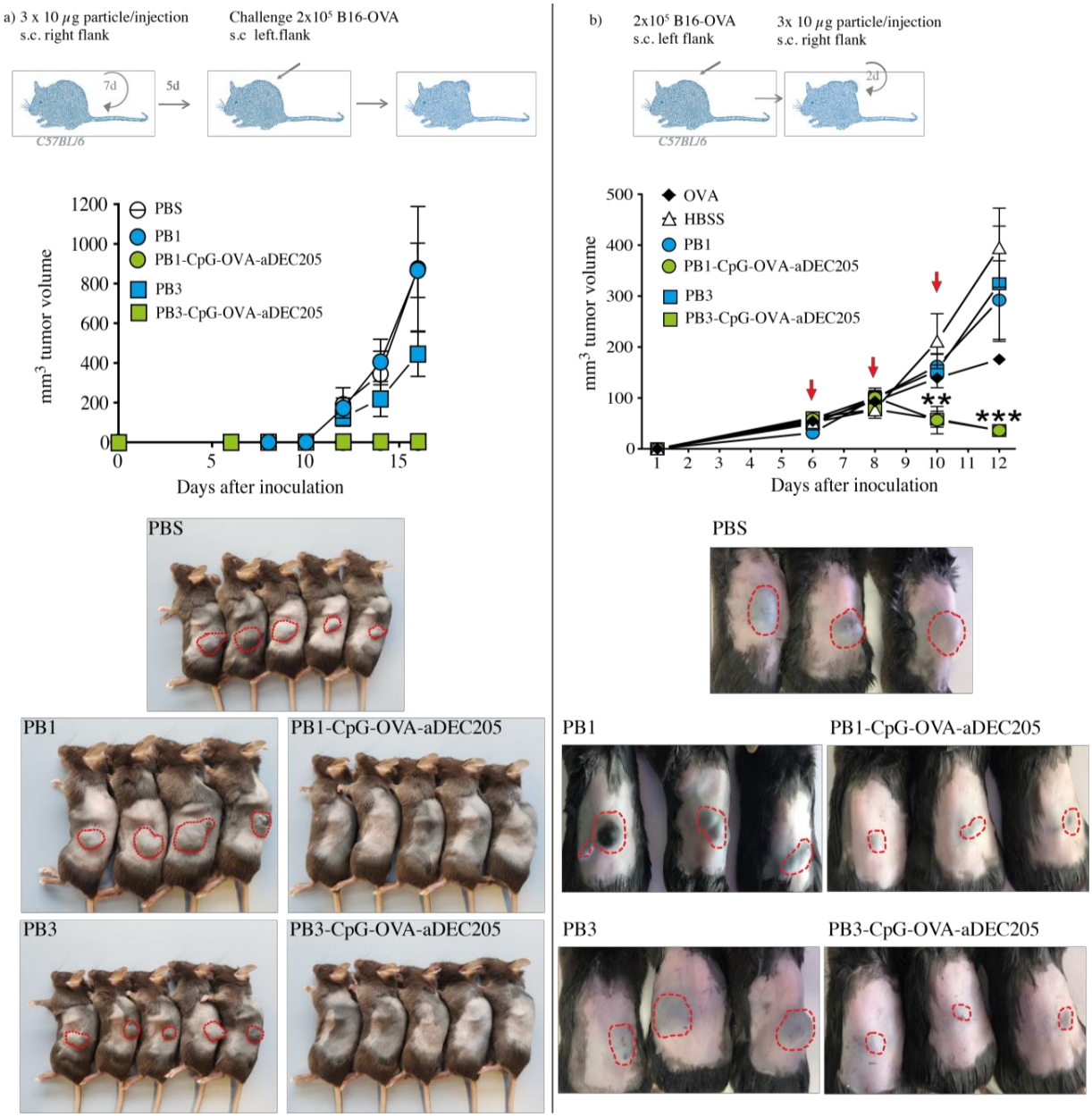

Figure 10. a) Evaluation of tumor growth after 18 days of protective immunization with **PBS, PB1/3-FD, PB1/3-FD-OVA-CpG**. b) Evaluation of tumor growth after therapeutic vaccination. Comparison of **PB1** and **PB3 OVA-anti-DEC205-CpG** conjugates with **soluble OVA** and **buffer (HBSS)** as control. Subcutaneous injection of formulations at day 6,8 and 10 after inoculation with B16-OVA melanoma cells.

In the therapeutic setting, the tumors were first implanted subcutaneously and allowed to grow to a volume of 50 mm³ before the molecular vaccine was applied. In both settings we applied doses of the molecular vaccine from 6 µg to 25 µg (relative to OVA). For this purpose, C57BL / 6J mice were first implanted subcutaneously with B16-OVA melanomas and, after growing to a volume of 50 mm³, the decorated brushes were injected contralaterally subcutaneously three times at an interval of two days. No significant difference in tumor growth rate was observed between the non-vaccinated control group and the mice that received polymer brushes without OVA and without CpG. Soluble OVA was able to reduce tumor growth by a factor of two. In contrast, the triple conjugated CPBs **PB1 FD OVA(8)-anti-DEC205(3)-CpG(8)** and **PB3 FD-OVA(9)-anti-DEC205(3)-CpG(6)** strongly inhibited tumor growth even triggered a decrease in tumor volume (Fig. 10b). Again, no differences were observed between the PB1 and PB3 conjugates. These observations show that the polypept(o)id-based CPB platform developed by us is ideally suited for the production of vaccines for tumor therapy.

CONCLUSIONS

In this work we have shown the synthesis of peptobrush-based vaccines. The synthesis of bottle brush polymers with lysine backbone and polysarcosine side chains allows to tailor the morphology of polypept(o)ide-based nanoparticles by the degree of polymerization of the backbone and side chains. It has been shown that the formed peptobrushes have molecular weights from 2.2-105 to 10.4-105 g/mol and dispersion indices of 1.2-1.3, underlining the well-controlled synthesis. In addition, peptobrushes are very well cell tolerant, have a low non-specific cell uptake and do not cause any detectable protein aggregates in full serum. In line with these results, a high stability and residence time in the blood of mice could be observed (half-life of 2 days). However, no size and morphology dependent behaviour was observed for blood circulation. Due to the observed stealth like nature of peptobrushes, we consider them an ideal platform for molecular vaccines in which the nanoparticle itself does not cause immune reaction

and thus allows for independent engineering immune responses. Therefore, we have selected these novel peptobrushes for further modification with antibodies for dendritic cell targeting (aDEC-205 specific antibodies), antigens (ovalbumin) and immune activators (CpG). The copper-free, strain-promoted azide-alkine coupling allows sequential chemoselectivity of all components on the bottle brush polymers and allows precise adjustment of the average number of each component. Remarkably, even the final conjugate does not induce protein aggregation in human serum, which motivated the research on local protective and therapeutic vaccination. Preliminary *in vitro* T cell proliferation showed that the CPB PB3 alone was able to induce efficient immune responses and indicate differences due to size and shape. After subcutaneous injection of OVA-coupled peptobrush, conjugates were found in draining lymph nodes and spleen, showing sufficient OT-I and OT-II T cell proliferation and thus indicating systemic T cell immunity. To review the influence of size and morphology on immune response and vaccination efficacy, local and therapeutic vaccination was done with PB1 and PB3 conjugates. Remarkably, both systems were able to inhibit tumor growth and induce tumor regression in the B16-melanoma model. Contradictory to several studies[25,70], no differences related to size or particle morphology have been observed in this study. Especially the similar study of Sun *et al.* showed a preferable AR and differences in biological behaviour.[6] However, looking at the size ranges it needs to mentioned that our systems are again smaller than their investigated particles. Our findings, nevertheless, clearly underline that CPBs are an excellent platform for the synthesis of tailored molecular vaccines. Nonetheless, to fully determine the influence of size and morphology for these CPBs further studies including systems with higher aspect ratios and different administration routes have to be performed.

EXPERIMENTAL SECTION

Materials

DMF was purchased from Acros (99.8%, Extra Dry over Molecular Sieve) dried over BaO and distilled *in vacuo* followed by excessive stirring *in vacuo* to remove traces of dimethylamine. THF and hexane were purchased from Sigma Aldrich and distilled from sodium. DIPEA was purchased from Sigma Aldrich, dried over NaOH and freshly distilled prior to use. Triethylamine was purchased from Carl Roth and distilled from potassium hydroxide.

Used as received: DEC-205-specific antibodies (DEC205/HB290, rat αmouse IgG2a), BioXCell; AlexaFluor647-DBCO, Invitrogen; AlexaFluor647-N_3, Invitrogen; AlexaFluor647-NHS Ester, Invitrogen; 4-azidobutyric acid, Chiralix; CpG-1826-DBCO, IBA; CW800-DBCO, LICOR; DBCO-PEG_4-5/6-Carboxyrhodamine 110, Jena Bioscience; DBCO-PEG_4-NHS Ester, Jena Bioscience; DMSO, Sigma Aldrich; DPBS (no calcium, no magnesium), Sigma Aldrich; poly(L-lysine trifluoroacetate) 100, Alamanda; poly(L-lysine trifluoroacetate) 250, Alamanda; EndoFit Ovalbumin, InvivoGen; Sarcosine, Sigma Aldrich; *Streptomyces griseus* Typ XIV, Sigma Aldrich.

Animals

C57BL/6, OT-I (C57BL/6-Tg(TcraTcrb)1100Mjb/J) and OT-II (B6.Cg-Tg(TcraTcrb)425Cbn/J) mice were bread in the central animal facility of the University Medical Center Mainz. All animal procedures were carried out in accordance with relevant laws (authorization G 17-1-069), current institutional guidelines and in accordance with the European Union normative for care and use of experimental animals.

Characterization

Static and Dynamic Light Scattering

The light scattering measurements were performed at 20 °C. All solutions were prepared in a dust free flow box and the cylindrical quartz cuvettes (Hellma, Mühlheim, Germany) were cleaned by dust free distilled acetone. Static light scattering (SLS) experiments were conducted by the following instrument: Apparatus 1 consists of an ALV SP86 goniometer, an ALV 3000 correlator, a Uniphase HeNe Laser (25 mW output power at λ = 632.8 nm wavelength) and an ALV/High QE APD avalanche diode fiber optic detection system. The scattered intensity was divided by a beam splitter (approximately 50:50), each portion of which was detected by a photomultiplier. The two signals were cross correlated in order to minimize non-random electronic noise. Dynamic light scattering measurements were performed with a HeNe Laser (25 mW output power at λ = 632.8 nm, 25 mW) and an ALV-CGS 8F SLS/DLS 5022F goniometer with eight simultaneously working ALV 7004 correlators and eight QEAPD avalanche photodiode detectors. PB1, PB2 and PB3 were filtered through 0.2 µm pore size Millex GHP filters (Millipore). PLys1 and Plys2 were filtered through 0.02 µm pore size Whatman Anotop filters and 0.2 µm pore size Pall GHP filters.

The static scattering intensities were analyzed according to Zimm in order to yield the weight average molar mass, M_w, the square root of z-average mean square radius of gyration, $R_g = \langle R_g^2 \rangle_z^{0.5}$, and the second viral coefficient A_2. The experimental uncertainties are estimated to be ±5% for M_w and R_g. The correlation functions of the particles showed a monomodal decay and were fitted using a sum of two exponentials. The z-average diffusion coefficient D_z was calculated by extrapolating D_{app} for q = 0. By formal application of Stokes law, the inverse z-average hydrodynamic radius is $R_h = \langle R_h^{-1} \rangle_z^{-1}$. The experimental uncertainties are estimated to ±2% for Rh. The experimental uncertainties are estimated to

±2% for Rh. For static light scattering, stock solutions of each sample were prepared. PB1, PB2 and PB3 were filtered through 0.2 µm pore size Pall GHP filters. The measurements were done in 20 mm diameter quartz cuvettes (Hellma). Further dilutions were made by subsequent addition of 0.2 µm pore size Pall GHP filtered solvent into the LS cuvette and the respective concentrations were obtained by weighing.

To investigate the aggregation behavior of PBs in human serum, serum pooled from 6 patients was used. The serum was obtained from the University Medical Center of the Johannes Gutenberg-University Mainz (Germany). The serum was filtered through a Millex GS 0.22 µm filter (Millipore). PBs and DPBS were filtered through 0.2 µm pore size Millex GHP filters (Millipore). The following mixtures have been prepared: serum:DPBS 9:1 and serum:PB 9:1 ($c_{PB4} = 3.4 \cdot 10^{-8}$ M). The cuvettes were incubated for 20 min at room temperature before measurement.

UV-VIS Spectroscopy

Measurements were done on a Carry 100 Bio UV-VIS Spectrometer (Varian, Inc). The spectra were analyzed with Cary Win UV Scan Application (V 02.00(25)).

Fluorescence Correlation Spectroscopy

The fluorescence correlation spectroscopy (FCS) experiments with AlexaFluor647 dye were performed using a commercial setup (Zeiss, Germany) consisting of the module ConfoCor 2 and an inverted microscope model Axiovert 200 with a Zeiss C-Apochromat 40 × /1.2 W water immersion objective. Dyes were excited by a HeNe laser (633 nm). Fluorescence light was filtered (LP650 long pass emission filter) and collected by an avalanche photodiode that enables single-photon counting. Eight-well polystyrene-chambered coverglass (Laboratory-Tek, Nalge Nunc International) was used as a sample cell. For each sample, a series of 10 measurements (10 s each) were performed. The experimental autocorrelation curves

were fitted with a single component, free 3D diffusion analytical model function to obtain the diffusion coefficient and consequently through the Stokes-Einstein equation the hydrodynamic radius of the fluorescent species. The confocal observation volume was calibrated using Alexa Fluor 647 as a reference dye with a known diffusion coefficient. The fluorescence correlation spectroscopy (FCS) experiments with 800CW dye were performed on a LSM880 confocal microscope (Zeiss, Germany) coupled to a FCS detection module (PicoQuant, Germany). In all experiments a Zeiss C-Apochromat 40 × /1.2 W water immersion objective was used. The studied fluorophores were excited either at 633 nm or 780 nm and the fluorescence light detected after filtering with respectively LP650 or LP800 long pass emission filters. Eight-well polystyrene-chambered coverglass (Laboratory-Tek, Nalge Nunc International) was used as a sample cell. For each sample, a series of 10 measurements (30 s each) were performed. The experimental autocorrelation curves were fitted with a single component, free 3D diffusion analytical model function to obtain the diffusion coefficient and consequently through the Stokes-Einstein equation the hydrodynamic radius of the fluorescent species.

Fluorescence Spectroscopy

Fluorescence spectra were recorded using Jasco FP-6500 (ETC-273) Spectrometer equipped with the software FP-6500 JASCO-SpectraManager, Spectrum Measurement. For NIR dye labeled samples two fluorometers were used. Fluorometer 1 is a LS55 fluorometer from Perkin Elmer. The spectra were analyzed with the BL Studio (Basic Fl). Fluorometer 2 is a Plate Reader Infinite^{TM} 200 PRO (Tecan Life Sciences). The spectra were analyzed with Tecan i-control (V 1.10.4.0).

Gel permeation Chromatography (HFIP-GPC)

Hexafluoroisopropanol (HFIP) gel permeation chromatography (GPC) was performed with HFIP containing 3 g/l potassium trifluoroacetate as eluent at 40°C and a flow rate of 0.8 mL min^{-1}. The columns

were packed with modified silica (PFG columns; particle size: 7 µm, porosity: 100 & 1000 Å). Polymers were detected with a refractive index detector (G 1362A RID, JASCO) and a UV/Vis Detector (UV-2075 Plus, JASCO). Molecular weights were calculated using a calibration performed with PMMA standards (Polymer Standards Services GmbH) and toluene as internal standard. Elution diagrams were analyzed using WinGPC UniChrome 8.00 (Build 994) software from Polymer Standards Services. All solutions were filtered through a 200 nm Filter.

Preparative Gel Permeation Chromatography

For purification of anti-DEC205-DBCO, OVA-DBCO or brush-conjugates preparative SEC was performed using a Sepharose 4 FF XK 16/70 column (GE Healthcare Life Sciences), a L-2310 LaChrom Elite (Hitachi) and a 2487 UV-detector (Waters). The UV-VIS absorption was measured at 220 nm. The spectra were analyzed with the software Chromatographica V1.0.26. DPBS buffer was used as an eluent and the flow rate was set to 0.5 $mL \cdot min^{-1}$. The column was cleaned every 7 days with 1 M NaOH over night at 0.5 $mL \cdot min^{-1}$, followed by 72 h with 0.1 M NaOH at 0.1 $mL \cdot min^{-1}$.

Infrared Spectroscopy

Attenuated total reflectance Fourier transformed infrared (ATR-FTIR) spectroscopy was performed on a FT/IR-4100 (JASCO) with an ATR sampling accessory (MIRacleTM, Pike Technologies). IR Spectra were analyzed using Spectra Manager 2.0 (JASCO).

Melting Point

The melting point of Sarcosine-NCA was determined using a METTLER FP62 (METTLER WAAGEN GMBH).

PAGE

The SDS PAGE was performed in a XCell Surelock Mini-Cell using precast NuPAGE Novex™ 4-12% Bis-Tris gels. The gels were run in a 1x NUPAGE™ SDS MES running buffer, usually at a constant voltage of 200 V for 35 min. The samples were diluted with 2.5 µl NuPAGE™ LDS sample buffer and Milli-Q water to a final volume of 10 µl. Novex™ Sharp Pre-Stained Protein Standard was chosen for molecular weight estimation. The gels were stained with SimplyBlue™ SafeStain following the standard protocol. To proof the absence of unbound CpG, TBE Urea PAGE was performed in a XCell Surelock Mini-Cell using precast denaturating Novex™ 15 % TBE-Urea gels. The gels were run in a 1x TBE running buffer, usually at a constant voltage of 180 V for 75 min. The samples were diluted with 5 µl TBE-Urea sample buffer and Milli-Q water to a final volume of 10 µl. The gels were stained with SYBR Green™ II following the standard protocol. Upon excitation at 365 nm, fluorescence was imaged with a conventional digital camera. All components were purchased from Invitrogen and used as received.

Zetasizer

Measurements of the zeta potential were performed in 10 mM NaCl at 1 $g \cdot L^{-1}$ with a Zetasizer Nano ZS (Malvern).

Atomic Force Microscopy

Measurements were performed with a Veeco MultiMode Scanning Probe Microscope and a Nanoscope IIIa Controller. All micrographs were taken in the Tapping mode. The samples were spin coated on mica. For measurements on the dried samples, Olympus OMCL-AC160-W2 cantilevers with a resonance frequency of 300 kHz (spring constant 42 N/m) were utilized. The length and width were analyzed with the software Pen.

^{1}H-NMR/^{19}F-NMR

300 MHz ^{1}H-NMR spectra were recorded on a Bruker AC 300. 400 MHz ^{1}H-NMR and ^{19}F-NMR measurements were performed on a Bruker Avance III HD 400. All spectra were recorded at room temperature and analyzed with MestReNova software.

Enzymatic degradation

The enzymatic degradation of the PBs was evaluated after the addition of the protease *Streptomyces griseus*. 2 mg protease (*Streptomyces griseus* Typ XIV, Sigma Aldrich) was dissolved in 1 mL protease buffer (10 mM Natriumacetate, 5 mM Calciumacetate, pH 7) and added to 20 mg PB dissolved in 1 mL protease buffer. The mixture was incubated at 37 °C. An aliquot was taken at the indicated timepoints (Fig. S4), lyophilized and analyzed by HFIP-GPC.

Endotoxin Assay

Pierce™ LAL Chromogenic Endotoxin Quantitation Kit (Thermo Fisher) was used following the standard protocol to determine the endotoxin values of the samples.

Biological Assays

MTT Assay

Cytotoxic effects of polymer brushes were evaluated by MTT assay (Promega, Heidelberg, Germany). For this, cells (each 5x10^{4}/ml) from the mouse DC-like cell line DC2.4 (5×104/ml) and the human embryonic kidney cell line (HEK293) were seeded in wells (100 µl) of 96-well cell culture-treated plates. On the next day, polymer brushes were applied to triplicates at different concentrations (50-5000 µg/ml)

to triplicates. Samples treated with DMSO at cytotoxic concentration (10%) served as a negative control, and samples treated with DPBS (10%) as a solvent control. On the next day, the metabolic activity of the cells was assayed by sequential addition of MTT substrate and of stop solution. Formazan product quantification was performed using an ELISA plate reader as recommended by the manufacturer. Data denote the mean±SEM of triplicates of one experiment, normalized to the solvent control. The graphs shown are representative of two independent experiments.

Generation of bone marrow-derived DC (BMDC)

Mouse (C57BL/6) bone marrow cells ($2x10^5$/ml) were seeded in 12 well plates (Greiner Bio-One, Frickenhausen, Germany) in culture medium consisting of IMDM media containing 2 mM L-glutamine, 100 U/ml penicillin, 100 µg/ml streptomycin (all from Sigma-Aldrich, Deisenhofen, Germany), and 50 µM ß-mercaptoethanol (Roth, Karlsruhe, Germany) supplemented with 5% FCS (Sigma-Aldrich) and 10 ng/ml recombinant murine GM-CSF (R&D Systems, Wiesbaden, Germany). Plates were cultured at 37 °C in a humified incubator (5% CO_2). On d3 of culture, 700 µl of media were added, and on d6 900 µl of culture media were replenished. For treatment of BMDC, on d7-8 the sample volume was adjusted to 1 ml, and agents were applied as indicated.

Flow cytometric analysis

Differentially pretreated BMDC (see above) were transferred to FACS tubes. All samples (BMDC, spleen cells) were washed with FACS buffer (PBS, 1 % FCS). Fc gamma receptors were blocked by incubation with an appropriate rat anti-mouse antibody (clone 2.4G2; room temperature, 10 min). Then, antibodies (each 0.5 µg/samples) were applied as indiacted (V500-labelled anti-CD3 [clone 145-2C11], FITC-anti-CD8a [53-6.7], BV421- or PE-Cy7-anti-CD11c [N418], PerCP/Cy5.5-anti-CD19 [1D3], PE-anti-CD68 [FA-11], FITC-anti-CD80 [16-10A1], eFluor450-, FITC- or PE-anti-CD86 [GL-1], eFluor450- of FITC-

anti-MHCII [M5/114.15.2]). Samples were incubated for 20 min at 4 °C. Samples left untreated, and incubated with one antibody only served as controls. All antibodies were purchased from BioLegend (San Diego, CA) or eBiosciences/ThermoFisher (Waltham, MA). After antibody incubation, samples were washed by centrifugation (see above), resuspended in PBS/0.7% paraformaldehyde, and fluorescence intensities were assessed employing an Attune Nxt flow cytometer (ThermoFisher). Data were analyzed using FlowJo software (FLOWJO, Ashland, OR).

Confocal laser scanning microscopy (CLSM)

Sample preparation furs CLSM. Cells were stained with … Samples were measured at the Institute of Molecular Biology (IMB, Mainz). The imaging of the cells was performed in ivbiTreat µ-slides (IBIDI, Germany) using a TCS SP5 confocal microscope (Leica).

In vivo fluorescence imaging in zebrafish larvae

We used zebrafish larvae with fluorescent vasculature, tg(fli1a:EGFP) which were kept in embryo water (Cosma et al 2006, Current protocols in microbiology) containing phenylthiourea (0.003% Aldrich) at a temperature of 28,5 °C. All experiments conducted were approved by the Norwegian food safety authority. Microinjections were performed in the posterior caudal vein of 2 day old zebrafish larvae. For this, solutions of peptobrushes were loaded in a borosilicate needle (GC100T-10, Harvard Instruments) previously made using a pipette puller (P-97 Sutter Instruments). The needles were in turn connected to a Eppendorf Femtojet express pump and micromanipulated using a Narishige MN-153 instrument. The injections were performed on previously sedated (Tricaine 0.02 % in embryo water) zebrafish larvae and placed on a dish containing hardened agarose (2% in milliQ water). In order to analyze the circulation of peptobrushes, zebrafish larvae were imaged after the injection at different times using a Leica

DFC365FX stereomicroscope with a 1.0X planapo lesn. For each embryo an image of the caudal region was taken at 120X while one of the whole fish was taken at 30X. For obtaining absolute values, the average fluorescence measured in three selected sites of the caudal artery (120X image) was normalized relative to the overall fluorescence of the zebrafish (30X image). These measurements were obtained using the program Fiji. The conversion of these absolute values into percentages was made by considering 0% the value associated to polylysine NP at 5 minutes while 100% was considered the value of peptobrushes 5 minutes post injection. Videos of Peptobrushes and Polylysine NP were made with a high speed Andor Dragonfly Spinning disc using a Nikon 60X 1.4 NA Lens.

In vivo fluorescence imaging in mice

In vivo fluorescence imaging of NIR dye 800CW-DBCO-labeled brushes (PB NIRD) was performed with the IVIS Spectrum Imaging system (Perkin Elmer). Briefly, mice were anesthetized with isoflurane prior to injection of the brush intravenously and were transferred to the light-tight chamber of the imaging system. 150 µL of PB NIRD in DPBS ($c_{NIR\text{-}Dye} = 1.5 \cdot 10^{-5}$ M) were injected per mouse. Whole body imaging was performed at indicated time points using the filter set at 745 nm for excitation and at 800 nm for emission with an integration time of 3 sec. *Ex vivo* imaging of the organs was performed using the same instrumental setting. Blood kinetics were determined by retrieval of blood at indicated time points upon brush injection followed by *ex vivo* imaging as described above.

In Vivo Tracking of Polymer Brushes

To investigate the uptake and distribution of the various polymer brushes after subcutaneous injection in mice, Alexa Fluor 647-labelled polymer brushes were injected into the skin of the right flank. Commercial Alexa Fluor 647-labelled OVA was used as a control. 1 or 16 hours after injection, the injected skin, non-

injected skin, skin-draining lymph nodes, blood and spleen were isolated and single cell suspensions analyzed by flow cytometry using additional markers to distinguish between tissue and immune cells as well as immune cell subtypes.

In Vivo Determination of T Cell Responses to OVA-coupled Polymer Brushes

Single cell suspensions of spleens of OT-I and OT-II mice were labelled with the fluorescent cell division dyes carboxyfluorescein succinimidyl ester (CFSE, 5µM) and cell trace violet (CTV, 5µM), respectively. C57BL/6J mice were intraperitoneally injected with each 2x106 labelled OT-I and OT-II cells (each 150µl), respectively. After 1 h, the recipient animals were injected subcutaneously on their right flank with either empty or functionalized peptobrushes, (each 150µl, respectively). Five days later the spleen, blood and skin-draining lymph nodes of injected and non-injected skin lymph nodes were analyzed by flow cytometry.

Protective vaccination

C57BL/6J mice were subcutaneously (s.c.) injected three times at one-week intervals on their right flank with polymer brushes. Hank's Balanced Salt Solution (HBSS)-injected and OVA-injected animals served as controls. The amount of OVA-bearing particles used per injection was equivalent to 10 µg OVA. One week after the last injection, the mice were subcutaneously injected with 2x105 B16OVA-F10 melanoma cells on the left flank and tumor growth was subsequently monitored for two weeks.

Therapeutic vaccination

To evaluate the therapeutic potential of OVA-coupled polymer brushes mice were inoculated with with B16-OVA melanoma cells and polymer brushes injected contralaterally to the tumor at days 6, 8 and 10 after inoculation. Control animals were injected with HBSS.

Statistical Evaluation

GraphPad Prism® 6, GraphPad Software, Inc., La Jolla, CA, USA was used for the statistical analysis of all data. Results are shown as mean ±SEM. The unpaired Student t test was applied to evaluate differences between 2 study groups. One-way ANOVA with post hoc Tukey multiple comparisons test was performed when comparing more than 2 groups. P values of ≤0.05 denote significant changes. *P<0.05, **P<0.01, ***P<0.001, ****P<0.0001

Synthesis

Synthesis of Sarcosine N-Carboxyanhydride

The synthesis of sarcosine NCA was adapted from literature and modified.[71] A total of 20.52 g (230.2 mmol) sarcosine, dried under vacuum for 1 h, was weighed into a pre-dried, three-neck, round-bottom flask. A total of 300 mL of abs. THF was added under a steady flow of nitrogen and 22.3 mL (184 mmol) of diphosgene were added slowly via syringe, and the nitrogen stream was reduced. The colorless suspension was mildly refluxed for 3 h, yielding a clear solution. Afterward, a steady flow of dry nitrogen was led through the solution for another 3 h while the outlet was connected to two gas washing bottles filled with aqueous NaOH solution to neutralize phosgene. The solvent was evaporated under reduced pressure, yielding a brownish oil as a crude reaction product. The oil was dried under reduced pressure ($1 \cdot 10^{-3}$ mbar for 2 h) to obtain an amorphous solid, free of phosgene and HCl, confirmed by testing against

silver nitrate solution. The crude product was redissolved in 40 mL of THF and precipitated with 300 mL of dry hexane. The solution was cooled to −18 °C overnight to complete precipitation. The solid was filtered under dry nitrogen atmosphere and dried in a stream of dry nitrogen for 60−90 min and afterwards under high vacuum for 2 h in the sublimation apparatus. The crude product was sublimated at 85 °C and $1 \cdot 10^{-3}$ mbar. The product was collected from the sublimation apparatus in a glovebox on the same day. The purified product (156 mmol, 68% yield, colorless crystallites; melting point: 102−104 °C (lit:[71] 102-105 °C) was stored in a Schlenk tube at −80 °C and only handled in a glovebox.

^{1}H NMR (300 MHz, $CDCl_3$): δ [ppm] = 4.22 (2 H, s, -CH_2-CO-), 2.86 (3 H, s, -CH_3).

Synthesis of Azido-butyricacid Pentafluorphenylester

1 g of γ-azido butyric acid (7.74 mmol) was dissolved in pre dried THF. After adding 2.15 mL triethylamine (15.0 mmol, 2 eq.) the solution was stirred for 30 min at room temperature. Two equivalents of pentafluorophenol trifluoro acetat (2.66 mL, 15.0 mmol) were added dropwise with a syringe and the reaction mixture was stirred over night at room temperature. Completion of the reaction was verified with thin layer chromatography (TLC). After THF was distilled, the remaining solid was taken up in dichloromethane and three times extracted with water. The organic phase was dried with $MgSO_4$ and DCM was distilled off the product. The product was purified by column chromatography.

^{1}H NMR (400 MHz, $CDCl_3$): δ [ppm] = 3.46 (2 H, t, -CH_2-CH_2-**CH_2**-N_3), 2.80 (2 H, t, -**CH_2**-CH_2-CH_2-N_3), 2.05 (2 H, m, -CH_2-**CH_2**-CH_2-N_3).

^{19}F NMR (400 MHz, $CDCl_3$): δ [ppm] = -153.95 (2F, d, *o*-CF), -158.90 (1F, t, *p*-CF), -163.32 (2F, t, *m*-CF).

Synthesis of Peptobrushes (PB1)

The following stock solutions were prepared directly before use and under dry nitrogen atmosphere: 228 mg DIPEA in 3.7 mL DMF, 7.83 g Sarcosine NCA in 40 mL DMF and 218 mg azido-butyricacid pentafluorphenylester in 2 mL DMF. The following operations are done under a steady flow of dry nitrogen. 0.44 mL (193 µmol) of DIPEA-DMF was added *via* syringe to a schlenk tube containing 39 mg (160 µmol) poly(L-lysine trifluoroacetate) (DP = 102) dissolved in 2 mL DMF solution. After 1 hour stirring, 4.6 mL (8 mmol) Sarcosine NCA in DMF was added. The solution was stirred at room temperature and kept at a constant pressure of 1.25 bar of dry nitrogen via the Schlenk line to prevent impurities from entering the reaction vessel while allowing CO_2 to escape. When the reaction was finished (completion of the reaction was confirmed by IR spectroscopy by the disappearance of the NCA peaks), 0.52 mL azido-butyricacid pentafluorphenylester in DMF (1.2-fold excess based on the amine groups) was added and the reaction mixture was stirred for 2 days at 40°C. The final azide functionalized polymer brush was precipitated in ether and centrifuged (4500 rpm at 4°C for 15 min). After discarding the liquid fraction, fresh ether was added and the polymer was resuspended using a sonic bath. The suspension was centrifuged again and the procedure was repeated. The polymer was dissolved in MilliQ water, centrifuged with Amicon Ultra Centrifugal Filters (50 kDa, 4000xg, 4x20 min). After lyophilization, a colorless product was obtained. Yield: 73%. The characterization of PB1 is described in the text and summarized in table 1.

Synthesis of Peptobrushes (PB2)

The synthesis of PB2 was carried out similar to PB1 using 0.45 mL DIPEA (198 µmol) dissolved in DMF, 40 mg (165 µmol) poly(L-lysine trifluoroacetate) (DP = 102), 9.5 mL (16 mmol) Sarcosine NCA in DMF

and 0.53 mL azido-butyricacid pentafluorphenylester in DMF. Yield: 59%. The characterization of PB2 is described in the text and summarized in table 1.

Synthesis of Peptobrushes (PB3)

The synthesis of PB3 was carried out similar to PB1 using 0.80 mL DIPEA (351 µmol) dissolved in DMF, 71 mg (292 µmol) poly(L-lysine trifluoroacetate) (DP = 258), 16.8 mL (29 mmol) Sarcosine NCA in DMF and 0.95 mL azido-butyricacid pentafluorphenylester in DMF. Yield: 63%. The characterization of PB3 is described in the text and summarized in table 1.

Dye labeling of Peptobrushes

The dyes DBCO-PEG4-5/6-Carboxyrhodamine 110, AlexaFluor647-DBCO and 800CW-DBCO were conjugated to the peptobrushes *via* SPAAC. In a typical experiment, PB was dissolved in DPBS (c_{PB} = 50 $g \cdot L^{-1}$) and the dye was dissolved in DMSO (c_{Dye} = 5 mM). As the reaction is quantitative, 1 equivalent of the desired amount of dyes per brush was added. After incubation over night at rt under light exclusion, the reaction mixture was purified by Amicon Ultra Centrifugal Filter Devices to remove unbound dye (15 mL, 50 kDa, 4000xg, 10 times). The resulting solution was concentrated with Amicon Ultra Centrifugal Filter Devices (50 kDa, 4000xg) and filtered through sterile 0.22 µm Millex-GS filters. R_h was measured by DLS and FCS. FCS was also used to proof the absence of unconjugated dye and to determine the number of dyes per brush. To evaluate quenching effects, emission spectra of the free dye and the dye labeled PB were recorded, using solutions of the same optical density. If quenching effects were detected, the number of dyes determined by FCS were corrected by the amount of quenching.

Synthesis of DBCO-functionalized OVA and DEC-205-specific antibodies

In a typical experiment, 2 eq. DBCO-PEG$_4$-NHS-Ester (dissolved in DMSO, c = 10 g·L^{-1}) were added to DEC-205-specific antibodies or OVA. anti-DEC205 was used as received (dissolved in buffer, $c_{anti-DEC205}$ = 4 - 7 g·L^{-1}) and OVA was dissolved in DPBS (c_{OVA} = 14 g·L^{-1}). After incubation over night at rt, the reaction mixture was purified by Amicon Ultra Centrifugal Filter Devices (15 mL, 10 kDa, 4000xg, 10 times) to remove unbound DBCO-PEG$_4$-NHS-Ester and NHS. Afterwards preparative SEC was performed using a Sepharose 4 FF XK 16/70 column (flow 0.5 ml·min^{-1}) to remove aggregates. OVA-DBCO (fraction 90 – 110 mL) and anti-DEC205-DBCO (fraction 80 – 110 mL) The resulting solution was concentrated with Amicon Ultra Centrifugal Filter Devices (10 kDa, 4000xg) and filtered through sterile 0.22 µm Millex-GS filters. Yield: 80 – 90 %. $R_{h,OVA-DBCO}$ = 3.3 nm. $R_{h,anti-DEC205}$ = 5.8 nm. The OVA and anti-DEC205 concentrations as well as the number of DBCO per bioactive component were determined by UV-VIS spectroscopy as described in the SI.

Synthesis of dye labeled PLys250

20 mg PLys258 (320 nmol) were dissolved in 2 mL DPBS. 1 mg AlexaFluor647-NHS Ester (2.5 eq., 800 nmol) dissolved in 160 µL DMSO was added and the reaction mixture was incubated over night at rt under light exclusion. Purification was done with Amicon Ultra Centrifugal Filter Devices (15 mL, 10 kDa, 4000xg, 20 times). R_h(FCS) = 7.6 nm. The number of dyes per molecule is 2.

Synthesis of PB conjugates with OVA and DEC-205-specific antibodies

The synthesis of OVA and anti-DEC205 Peptobrush conjugates is similar for both bioactive components. The amount of the DBCO-modified component that needs to be added depends on the number of DBCO per component (N_{DBCO} between 1 – 2, see Fig. S11). $1/(0.34 \cdot N_{DBCO})$ equivalents of the DBCO modified

component (dissolved in DPBS, $c_{OVA\text{-}DBCO/anti\text{-}DEC205\text{-}DBCO}$ = 5 –15 g·L^{-1}) were added to the dye labeled brush dissolved in DPBS (c_{PB} = 1·10^{-5} – 1·10^{-6} M). The reaction mixture was incubated over night at rt. To remove bridged brushes and unconjugated bioactive components, PB3-conjugates were purified *via* preparative SEC using a Sepharose 4 FF XK 16/70 column (flow 0.5 ml·min^{-1}). The fraction from 55 mL to 75 mL was collected. For PB1-conjugates, two columns were coupled. For PB1-OVA-conjugates 110 mL to 145 mL and for PB1-anti-DEC205-conjugates 100 mL to 130 mL were collected. The fractions were concentrated using Amicon Ultra Centrifugal Filter Devices (50 kDa, 4000xg) and filtered through sterile 0.22 µm Millex-GS filters. Each conjugate was analyzed by DLS, FCS, UV-VIS spectroscopy and SDS-PAGE as described in the discussion. The calculation of the average number of bioactive components per brush is described in the SI.

Synthesis of PB conjugates with CpG

1.1 equivalents of CpG-DBCO ($c_{CpG\text{-}DBCO}$ = 100 µmol·L^{-1}) were added to the dye labeled brush dissolved in DPBS (c_{PB} = 1·10^{-5} – 1·10^{-6} M). The reaction mixture was incubated over night at rt followed by purification with Amicon Ultra Centrifugal Filter Devices (15 mL, 50 kDa, 4000xg, 10 times) to remove unbound CpG-DBCO. After filtration through sterile 0.22 µm Millex-GS filters the conjugate was analyzed by DLS, FCS, UV-VIS spectroscopy and TBE Urea PAGE as described in the discussion. The calculation of the average number of CpG per brush is described in the SI.

ASSOCIATED CONTENT

Supporting Information.

The following files are available free of charge at .

SLS, DLS, SEC elugrams, FCS, MTT assay, UV-VIS spectra, determination calculation for bioconjugates, Table of tested conjugates, T cell proliferation assay.

AUTHOR INFORMATION

Corresponding Author

Matthias Barz - Division of Biotherapeutics, Leiden Academic Center for Drug Research (LACDR), Leiden University, Einsteinweg 55, 2333 CC Leiden, the Netherlands

Department of Dermatology, University Medical Center of the Johannes Gutenberg, University Mainz, Langenbeckstrasse 1, D-55131 Mainz, Germany

Department of Chemistry, Johannes Gutenberg University, Duesbergweg 10-14, D-55099 Mainz, Germany

Present Addresses

†If an author's address is different than the one given in the affiliation line, this information may be included here.

Author Contributions

The manuscript was written through contributions of all authors. All authors have given approval to the final version of the manuscript. ‡These authors contributed equally.

Funding Sources

Any funds used to support the research of the manuscript should be placed here (per journal style).

Notes

Any additional relevant notes should be placed here.

ACKNOWLEDGMENT

The authors acknowledge support of the DFG (SFB 1066). The authors would like to thank Dr. Hossam Hefesha for support with fluorescence measurements.

ABBREVIATIONS

OVA Ovalbumin, **anti-DEC205** DEC-205 specific antibody, **DC** dendritic cell, **CPB** cylindrical brush polymers, **pSar** polysarcosine, pLys poly(l-Lysine), **PAHMA** poly(N-(6-aminohexyl)methacrylamide), **PB** peptobrush, **SPAAC** strain promoted azide-alkyne coupling, **NIRD** near infrared dye, **NIR-FCS** near infrared fluorescence correlation spectroscopy, **DLS** dynamic light scattering, **GPC** gel permeation chromatography, **AFM** atomic force microscopy, **SEC** size exclusion chromatography, **SLS** static light scattering, **FCS** fluorescence correlation spectroscopy, **DBCO** Dibenzocyclooctyne.

REFERENCES

(Word Style “TF_References_Section”). References are placed at the end of the manuscript. Authors are responsible for the accuracy and completeness of all references. Examples of the recommended format for the various reference types can be found at http://pubs.acs.org/page/4authors/index.html. Detailed information on reference style can be found in *The ACS Style Guide,* available from Oxford Press.

(1) Dong, Z.; Liu, W.; Liu, K.; Lu, Y.; Wu, W.; Qi, J.; Chen, Z. Effects on Immunization of the Physicochemical Parameters of Particles as Vaccine Carriers. *Drug Discov. Today* **2021**, *26* (7), 1712–1720. https://doi.org/10.1016/j.drudis.2021.03.007.
(2) He, R.; Zang, J.; Zhao, Y.; Dong, H.; Li, Y. Nanotechnology-Based Approaches to Promote Lymph Node Targeted Delivery of Cancer Vaccines. *ACS Biomater. Sci. Eng.* **2022**, *8* (2), 406–423. https://doi.org/10.1021/acsbiomaterials.1c01274.
(3) Deng, J.; Wang, J.; Shi, J.; Li, H.; Lu, M.; Fan, Z.; Gu, Z.; Cheng, H. Tailoring the Physicochemical Properties of Nanomaterials for Immunomodulation. *Adv. Drug Deliv. Rev.* **2022**, *180*, 114039. https://doi.org/10.1016/j.addr.2021.114039.
(4) Kumar, S.; Anselmo, A. C.; Banerjee, A.; Zakrewsky, M.; Mitragotri, S. Shape and Size-Dependent Immune Response to Antigen-Carrying Nanoparticles. *J. Controlled Release* **2015**, *220*, 141–148. https://doi.org/10.1016/j.jconrel.2015.09.069.
(5) Li, H.; Liu, H.; Nie, T.; Chen, Y.; Wang, Z.; Huang, H.; Liu, L.; Chen, Y. Molecular Bottlebrush as a Unimolecular Vehicle with Tunable Shape for Photothermal Cancer Therapy. *Biomaterials* **2018**, *178*, 620–629. https://doi.org/10.1016/j.biomaterials.2018.03.032.
(6) Sun, Z.; Qiao, D.; Shi, Y.; Barz, M.; Liu, L.; Chen, Y. Precision Wormlike Nanoadjuvant Governs Potency of Vaccination. *Nano Lett.* **2021**, *21* (17), 7236–7243. https://doi.org/10.1021/acs.nanolett.1c02274.
(7) Wintermantel, M.; Schmidt, M.; Tsukahara, Y.; Kajiwara, K.; Kohjiya, S. Rodlike Combs. *Macromol. Rapid Commun.* **1994**, *15* (3), 279–284. https://doi.org/10.1002/marc.1994.030150315.
(8) Hörtz, C.; Birke, A.; Kaps, L.; Decker, S.; Wächtersbach, E.; Fischer, K.; Schuppan, D.; Barz, M.; Schmidt, M. Cylindrical Brush Polymers with Polysarcosine Side Chains: A Novel Biocompatible Carrier for Biomedical Applications. *Macromolecules* **2015**, *48* (7), 2074–2086. https://doi.org/10.1021/ma502497x.
(9) Vohidov, F.; Milling, L. E.; Chen, Q.; Zhang, W.; Bhagchandani, S.; Nguyen, H. V.-T.; Irvine, D. J.; Johnson, J. A. ABC Triblock Bottlebrush Copolymer-Based Injectable Hydrogels: Design, Synthesis, and Application to Expanding the Therapeutic Index of Cancer Immunochemotherapy. *Chem. Sci.* **2020**, *11* (23), 5974–5986. https://doi.org/10.1039/D0SC02611E.
(10) Alvaradejo, G. G.; Nguyen, H. V.-T.; Harvey, P.; Gallagher, N. M.; Le, D.; Ottaviani, M. F.; Jasanoff, A.; Delaittre, G.; Johnson, J. A. Polyoxazoline-Based Bottlebrush and Brush-Arm Star Polymers via ROMP: Syntheses and Applications as Organic Radical Contrast Agents. *ACS Macro Lett.* **2019**, *8* (4), 473–478. https://doi.org/10.1021/acsmacrolett.9b00016.
(11) Wintermantel, M.; Gerle, M.; Fischer, K.; Schmidt, M.; Wataoka, I.; Urakawa, H.; Kajiwara, K.; Tsukahara, Y. Molecular Bottlebrushes \textlesssup\textgreater†\textless/Sup\textgreater. *Macromolecules* **1996**, *29* (3), 978–983. https://doi.org/10.1021/ma950227s.
(12) Dziezok, P.; Fischer, K.; Schmidt, M.; Sheiko, S. S.; Möller, M. Cylindrical Molecular Brushes. *Angew. Chem. Int. Ed. Engl.* **1997**, *36* (24), 2812–2815. https://doi.org/10.1002/anie.199728121.
(13) Gerle, M.; Fischer, K.; Roos, S.; Müller, A. H. E.; Schmidt, M.; Sheiko, S. S.; Prokhorova, S.; Möller, M. Main Chain Conformation and Anomalous Elution Behavior of Cylindrical Brushes As Revealed by GPC/MALLS, Light Scattering, and SFM. *Macromolecules* **1999**, *32* (8), 2629–2637. https://doi.org/10.1021/ma9816463.
(14) Radzinski, S. C.; Foster, J. C.; Scannelli, S. J.; Weaver, J. R.; Arrington, K. J.; Matson, J. B. Tapered Bottlebrush Polymers: Cone-Shaped Nanostructures by Sequential Addition of

Macromonomers. *ACS Macro Lett.* **2017**, *6* (10), 1175–1179. https://doi.org/10.1021/acsmacrolett.7b00724.
(15) Fu, L.; Jafari, H.; Gießl, M.; Yerneni, S. S.; Sun, M.; Wang, Z.; Liu, T.; Kapil, K.; Cheng, B. C.; Yu, A.; Averick, S. E.; Matyjaszewski, K. Grafting Polymer Brushes by ATRP from Functionalized Poly(Ether Ether Ketone) Microparticles. *Polym. Adv. Technol.* **2021**, pat.5405. https://doi.org/10.1002/pat.5405.
(16) Olszewski, M.; Li, L.; Xie, G.; Keith, A.; Sheiko, S. S.; Matyjaszewski, K. Degradable Cellulose-based Polymer Brushes with Controlled Grafting Densities. *J. Polym. Sci. Part Polym. Chem.* **2019**, *57* (24), 2426–2435. https://doi.org/10.1002/pola.29481.
(17) Chen, Y.; Zhou, H.; Sun, Z.; Li, H.; Huang, H.; Liu, L.; Chen, Y. Shell of Amphiphilic Molecular Bottlebrush Matters as Unimolecular Micelle. *Polymer* **2018**, *149*, 316–324. https://doi.org/10.1016/j.polymer.2018.06.078.
(18) Beers, K. L.; Gaynor, S. G.; Matyjaszewski, K.; Sheiko, S. S.; Moeller, M. Synthesis of Densely Grafted Copolymers by Atom Transfer Radical Polymerization. *Macromolecules* **1998**, *31* (26), 9413–9415. https://doi.org/10.1021/ma981402i.
(19) Börner, H. G.; Beers, K.; Matyjaszewski, K.; Sheiko, S. S.; Möller, M. Synthesis of Molecular Brushes with Block Copolymer Side Chains Using Atom Transfer Radical Polymerization. *Macromolecules* **2001**, *34* (13), 4375–4383. https://doi.org/10.1021/ma010001r.
(20) Cheng, G.; Böker, A.; Zhang, M.; Krausch, G.; Müller, A. H. E. Amphiphilic Cylindrical Core-Shell Brushes via a "Grafting from" Process Using ATRP. *Macromolecules* **2001**, *34* (20), 6883–6888. https://doi.org/10.1021/ma0013962.
(21) Radzinski, S. C.; Foster, J. C.; Lewis, S. E.; French, E. V.; Matson, J. B. Factors Affecting Bottlebrush Polymer Synthesis by the Transfer-to Method Using Reversible Addition–Fragmentation Chain Transfer (RAFT) Polymerization. *Polym. Chem.* **2017**, *8* (10), 1636–1643. https://doi.org/10.1039/C6PY01982J.
(22) Dai, Y.; Hu, Z.; Wang, X.; Liu, X.; Li, Y.; Shi, Y.; Chen, Y. Synthesis of Fully Degradable Cationic Polymers with Various Topological Structures *via* Postpolymerization Modification by Using Thio-Bromo "Click" Reaction. *Polym. Chem.* **2021**, *12* (17), 2592–2597. https://doi.org/10.1039/D1PY00106J.
(23) Deffieux, A.; Schappacher, M. Synthesis and Characterization of Star and Comb Polystyrenes Using Isometric Poly(Chloroethyl Vinyl Ether) Oligomers as Reactive Backbone. *Macromolecules* **1999**, *32* (6), 1797–1802. https://doi.org/10.1021/ma981612v.
(24) Schappacher, M.; Deffieux, A. New Polymer Chain Architecture: Synthesis and Characterization of Star Polymers with Comb Polystyrene Branches. *Macromolecules* **2000**, *33* (20), 7371–7377. https://doi.org/10.1021/ma0001436.
(25) Müllner, M.; Dodds, S. J.; Nguyen, T. H.; Senyschyn, D.; Porter, C. J. H.; Boyd, B. J.; Caruso, F. Size and Rigidity of Cylindrical Polymer Brushes Dictate Long Circulating Properties in Vivo. *ACS Nano* **2015**, *9* (2), 1294–1304. https://doi.org/10.1021/nn505125f.
(26) Gratton, S. E. A.; Ropp, P. A.; Pohlhaus, P. D.; Luft, J. C.; Madden, V. J.; Napier, M. E.; DeSimone, J. M. The Effect of Particle Design on Cellular Internalization Pathways. *Proc. Natl. Acad. Sci.* **2008**, *105* (33), 11613–11618. https://doi.org/10.1073/pnas.0801763105.
(27) Geng, Y. A. N.; Dalhaimer, P.; Cai, S.; Tsai, R.; Minko, T.; Discher, D. E. Shape Effects of Filaments versus Spherical Particles in Flow and Drug Delivery. **2009**, *2* (4), 249–255. https://doi.org/10.1038/nnano.2007.70.Shape.

(28) Kinnear, C.; Moore, T. L.; Rodriguez-Lorenzo, L.; Rothen-Rutishauser, B.; Petri-Fink, A. Form Follows Function: Nanoparticle Shape and Its Implications for Nanomedicine. *Chem. Rev.* **2017**, *117* (17), 11476–11521. https://doi.org/10.1021/acs.chemrev.7b00194.
(29) Barz, M.; Luxenhofer, R.; Zentel, R.; Vicent, M. J. Overcoming the PEG-Addiction: Well-Defined Alternatives to PEG, from Structure–Property Relationships to Better Defined Therapeutics. *Polym. Chem.* **2011**, *2* (9), 1900–1918. https://doi.org/10.1039/C0PY00406E.
(30) Klinker, K.; Barz, M. Polypept(o)Ides: Hybrid Systems Based on Polypeptides and Polypeptoids. *Macromol. Rapid Commun.* **2015**, *36* (22), 1943–1957. https://doi.org/10.1002/marc.201500403.
(31) Huesmann, D.; Sevenich, A.; Weber, B.; Barz, M. A Head-to-Head Comparison of Poly(Sarcosine) and Poly(Ethylene Glycol) in Peptidic, Amphiphilic Block Copolymers. *Polym. U. K.* **2015**, *67*, 240–248. https://doi.org/10.1016/j.polymer.2015.04.070.
(32) Holm, R.; Klinker, K.; Weber, B.; Barz, M. Synthesis of Amphiphilic Block Copolypept (o) Ides by Bifunctional Initiators : Making PeptoMicelles Redox Sensitive. 2083–2091.
(33) Fokina, A.; Klinker, K.; Braun, L.; Jeong, B. G.; Bae, W. K.; Barz, M.; Zentel, R. Multidentate Polysarcosine-Based Ligands for Water-Soluble Quantum Dots. *Macromolecules* **2016**, *49* (10), 3663–3671. https://doi.org/10.1021/acs.macromol.6b00582.
(34) Heller, P.; Mohr, N.; Birke, A.; Weber, B.; Reske-Kunz, A.; Bros, M.; Barz, M. Directed Interactions of Block Copolypept(o) Ides with Mannose-Binding Receptors: Peptomicelles Targeted to Cells of the Innate Immune System. *Macromol. Biosci.* **2015**, *15* (1), 63–73. https://doi.org/10.1002/mabi.201400417.
(35) Heller, P.; Birke, A.; Huesmann, D.; Weber, B.; Fischer, K.; Reske-Kunz, A.; Bros, M.; Barz, M. Introducing PeptoPlexes: Polylysine-Block-Polysarcosine Based Polyplexes for Transfection of HEK 293T Cells. *Macromol. Biosci.* **2014**, *14* (10), 1380–1395. https://doi.org/10.1002/mabi.201400167.
(36) Makino, A.; Hara, E.; Hara, I.; Ozeki, E.; Kimura, S. Size Control of Core-Shell-Type Polymeric Micelle with a Nanometer Precision. *Langmuir* **2014**, *30* (2), 669–674. https://doi.org/10.1021/la404488n.
(37) Yamamoto, F.; Yamahara, R.; Makino, A.; Kurihara, K.; Tsukada, H.; Hara, E.; Hara, I.; Kizaka-Kondoh, S.; Ohkubo, Y.; Ozeki, E.; Kimura, S. Radiosynthesis and Initial Evaluation of 18F Labeled Nanocarrier Composed of Poly(L-Lactic Acid)-Block-Poly(Sarcosine) Amphiphilic Polydepsipeptide. *Nucl. Med. Biol.* **2013**, *40* (3), 387–394. https://doi.org/10.1016/j.nucmedbio.2012.12.008.
(38) Birke, A.; Huesmann, D.; Kelsch, A.; Weilbächer, M.; Xie, J.; Bros, M.; Bopp, T.; Becker, C.; Landfester, K.; Barz, M. Polypeptoid- \textlessi\textgreaterblock\textless/I\textgreater - Polypeptide Copolymers: Synthesis, Characterization, and Application of Amphiphilic Block Copolypept(o)Ides in Drug Formulations and Miniemulsion Techniques. *Biomacromolecules* **2014**, *15* (2), 548–557. https://doi.org/10.1021/bm401542z.
(39) Weber, B.; Birke, A.; Fischer, K.; Schmidt, M.; Barz, M. Solution Properties of Polysarcosine: Absolute and Relative Molar Mass Determinations. *Macromolecules* **2018**, *51* (7), 2653–2661. https://doi.org/10.1021/acs.macromol.8b00258.
(40) Ohlson, M.; Sörensson, J.; Haraldsson, B. A Gel-Membrane Model of Glomerular Charge and Size Selectivity in Series. *Am. J. Physiol.-Ren. Physiol.* **2001**, *280* (3), F396–F405. https://doi.org/10.1152/ajprenal.2001.280.3.F396.

(41) Perrin, F. Mouvement Brownien d'un Ellipsoide - I. Dispersion Diélectrique Pour Des Molécules Ellipsoidales. *J. Phys. Radium* **1934**, *5* (10), 497–511. https://doi.org/10.1051/jphysrad:01934005010049700.
(42) Kratky, O.; Porod, G. Röntgenuntersuchung Gelöster Fadenmoleküle. *Recl. Trav. Chim. Pays-Bas* **1949**, *68* (12), 1106–1122. https://doi.org/10.1002/recl.19490681203.
(43) Yamakawa, H.; Fujii, M. Translational Friction Coefficient of Wormlike Chains. *Macromolecules* **1973**, *6* (3), 407–415. https://doi.org/10.1021/ma60033a018.
(44) Benoit, H.; Doty, P. Light Scattering from Non-Gaussian Chains. *J. Phys. Chem.* **1953**, *57* (9), 958–963. https://doi.org/10.1021/j150510a025.
(45) Schmidt, M. Combined Integrated and Dynamic Light Scattering by Poly(7-Benzyl Glutamate) in a Helicogenic Solvent. **1984**, *17* (4), 8.
(46) Nel, A. E. Understanding Biophysicochemical Interactions at the Nano–Bio Interface. *Nat. Mater.* **2009**, *8*, 15.
(47) Rausch, K.; Reuter, A.; Fischer, K.; Schmidt, M. Evaluation of Nanoparticle Aggregation in Human Blood Serum. *Biomacromolecules* **2010**, *11* (11), 2836–2839. https://doi.org/10.1021/bm100971q.
(48) Abbina, S.; Takeuchi, L. E.; Anilkumar, P.; Yu, K.; Rogalski, J. C.; Shenoi, R. A.; Constantinescu, I.; Kizhakkedathu, J. N. Blood Circulation of Soft Nanomaterials Is Governed by Dynamic Remodeling of Protein Opsonins at Nano-Biointerface. *Nat. Commun.* **2020**, *11* (1), 3048. https://doi.org/10.1038/s41467-020-16772-x.
(49) Fam, S. Y.; Chee, C. F.; Yong, C. Y.; Ho, K. L.; Mariatulqabtiah, A. R.; Tan, W. S. Stealth Coating of Nanoparticles in Drug-Delivery Systems. *Nanomaterials* **2020**, *10* (4), 787. https://doi.org/10.3390/nano10040787.
(50) Negwer, I.; Best, A.; Schinnerer, M.; Schäfer, O.; Schmidt, M.; Mailänder, V.; Helm, M.; Barz, M.; Butt, H.-J.; Koynov, K. Monitoring Drug Nanocarriers in Human Blood by Near-Infrared Fluorescence Correlation Spectroscopy. *Nat. Methods* **2018**, *submitted*.
(51) Fasting, C.; Schalley, C. A.; Weber, M.; Seitz, O.; Hecht, S.; Koksch, B.; Dernedde, J.; Graf, C.; Knapp, E. W.; Haag, R. Multivalency as a Chemical Organization and Action Principle. *Angew. Chem. - Int. Ed.* **2012**, *51* (42), 10472–10498. https://doi.org/10.1002/anie.201201114.
(52) Bertozzi, C. R.; Kiessling, L. L. Chemical Glycobiology. *Science* **2001**, *291* (5512), 2357–2364.
(53) Kiessling, L. L.; Gestwicki, J. E.; Strong, L. E. Synthetic Multivalent Ligands as Probes of Signal Transduction. *Angew. Chem. - Int. Ed.* **2006**, *45* (15), 2348–2368. https://doi.org/10.1002/anie.200502794.
(54) Shen, L.; Krauthäuser, S.; Fischer, K.; Hobernik, D.; Abassi, Y.; Dzionek, A.; Nikolaev, A.; Voltz, N.; Diken, M.; Krummen, M.; Montermann, E.; Tubbe, I.; Lorenz, S.; Strand, D.; Schild, H.; Grabbe, S.; Bros, M. Vaccination with Trifunctional Nanoparticles That Address CD8(+) Dendritic Cells Inhibits Growth of Established Melanoma. *Nanomed.* **2016**, *11* (20), 2647–2662. https://doi.org/10.2217/nnm-2016-0174.
(55) Bühler, J.; Gietzen, S.; Reuter, A.; Kappel, C.; Fischer, K.; Decker, S.; Schäffel, D.; Koynov, K.; Bros, M.; Tubbe, I.; Grabbe, S.; Schmidt, M. Selective Uptake of Cylindrical Poly(2-Oxazoline) Brush-AntiDEC205 Antibody-OVA Antigen Conjugates into DEC-Positive Dendritic Cells and Subsequent T-Cell Activation. *Chem. - Eur. J.* **2014**, *20* (39), 12405–12410. https://doi.org/10.1002/chem.201403942.
(56) Fifis, T.; Mottram, P.; Bogdanoska, V.; Hanley, J.; Plebanski, M. Short Peptide Sequences Containing MHC Class I and/or Class II Epitopes Linked to Nano-Beads Induce Strong

Immunity and Inhibition of Growth of Antigen-Specific Tumour Challenge in Mice. *Vaccine* **2004**, *23* (2), 258–266. https://doi.org/10.1016/j.vaccine.2004.05.022.
(57) Bijker, M. S.; van den Eeden, S. J. F.; Franken, K. L.; Melief, C. J. M.; van der Burg, S. H.; Offringa, R. Superior Induction of Anti-Tumor CTL Immunity by Extended Peptide Vaccines Involves Prolonged, DC-Focused Antigen Presentation. *Eur. J. Immunol.* **2008**, *38* (4), 1033–1042. https://doi.org/10.1002/eji.200737995.
(58) Radford, K. J.; Caminschi, I. New Generation of Dendritic Cell Vaccines. *Hum. Vaccines Immunother.* **2013**, *9* (2), 259–264. https://doi.org/10.4161/hv.22487.
(59) Ballas, Z. K.; Krieg, A. M.; Warren, T.; Rasmussen, W.; Davis, H. L.; Waldschmidt, M.; Weiner, G. J. Divergent Therapeutic and Immunologic Effects of Oligodeoxynucleotides with Distinct CpG Motifs. *J. Immunol.* **2001**, *167* (9), 4878–4886. https://doi.org/10.4049/jimmunol.167.9.4878.
(60) Lahoud, M. H.; Ahmet, F.; Zhang, J.-G.; Meuter, S.; Polichen, A. N.; Kitsoulis, S.; Lee, C.-N.; O´Keeffe, M.; Sullivan, L. C.; Brooks, A. G.; Berry, R.; Rossjohn, J.; Mintern, J. D.; Vega-Ramos, J.; Villadangos, J. A.; Nicola, N. A.; Nussenzweig, M. C.; Stacey, K. J.; Shortman, K.; Heath, W. R.; Caminschi, I. DEC-205 Is a Cell Surface Receptor for CpG Oligonucleotides. *OncoImmunology* **2013**, *2* (3). https://doi.org/10.4161/onci.23128.
(61) Jiang, H.; Wang, Q.; Sun, X. Lymph Node Targeting Strategies to Improve Vaccination Efficacy. *J. Controlled Release* **2017**, *267*, 47–56. https://doi.org/10.1016/j.jconrel.2017.08.009.
(62) Wang, F.; Ullah, A.; Fan, X.; Xu, Z.; Zong, R.; Wang, X.; Chen, G. Delivery of Nanoparticle Antigens to Antigen-Presenting Cells: From Extracellular Specific Targeting to Intracellular Responsive Presentation. *J. Controlled Release* **2021**, *333*, 107–128. https://doi.org/10.1016/j.jconrel.2021.03.027.
(63) Hang, H. C.; Yu, C.; Kato, D. L.; Bertozzi, C. R. A Metabolic Labeling Approach toward Proteomic Analysis of Mucin-Type O-Linked Glycosylation. *Proc. Natl. Acad. Sci.* **2003**, *100* (25), 14846–14851. https://doi.org/10.1073/pnas.2335201100.
(64) Agard, N. J.; Baskin, J. M.; Prescher, J. A.; Lo, A.; Bertozzi, C. R. A Comparative Study of Bioorthogonal Reactions with Azides. *ACS Chem. Biol.* **2006**, *1* (10), 644–648.
(65) Bühler, J.; Gietzen, S.; Reuter, A.; Kappel, C.; Fischer, K.; Decker, S.; Schäffel, D.; Koynov, K.; Bros, M.; Tubbe, I.; Grabbe, S.; Schmidt, M. Selective Uptake of Cylindrical Poly(2-Oxazoline) Brush-AntiDEC205 Antibody-OVA Antigen Conjugates into DEC-Positive Dendritic Cells and Subsequent T-Cell Activation. *Chem. - Eur. J.* **2014**, *20* (39), 12405–12410. https://doi.org/10.1002/chem.201403942.
(66) Gietzen, S. Synthese Und Charakterisierung von Polymer-Wirkstoff-Antikörper Konjugaten Zur Anwendung in Der Krebsimmuntherapie, 2015.
(67) Weiner Rasmussen, G. J.; Davis, H. L.; Waldschmidt, M.; Ballas, Z. K.; Krieg, A. M.; Warren, T.; Rasmussen, W.; Weiner, G. J. CpG Motifs Distinct Effects of Oligodeoxynucleotides with Divergent Therapeutic and Immunologic Divergent Therapeutic and Immunologic Effects of Oligodeoxynucleotides with Distinct CpG Motifs. *J Immunol Ref. J. Immunol.* **2016**, *167*, 4878–4886. https://doi.org/10.4049/jimmunol.167.9.4878.
(68) Hermanson, G. T. *Bioconjugate Techniques*; Elsevier Acad. Press: Amsterdam, 2008.
(69) Kappel, C.; Seidl, C.; Medina-Montano, C.; Schinnerer, M.; Alberg, I.; Leps, C.; Sohl, J.; Hartmann, A.-K.; Fichter, M.; Kuske, M.; Schunke, J.; Kuhn, G.; Tubbe, I.; Paßlick, D.; Hobernik, D.; Bent, R.; Haas, K.; Montermann, E.; Walzer, K.; Diken, M.; Schmidt, M.; Zentel, R.; Nuhn, L.; Schild, H.; Tenzer, S.; Mailänder, V.; Barz, M.; Bros, M.; Grabbe, S. Density of Conjugated Antibody Determines the Extent of Fc Receptor Dependent Capture of Nanoparticles by

Liver Sinusoidal Endothelial Cells. *ACS Nano* **2021**, *15* (9), 15191–15209. https://doi.org/10.1021/acsnano.1c05713.
(70) Meyer, R. A.; Sunshine, J. C.; Perica, K.; Kosmides, A. K.; Aje, K.; Schneck, J. P.; Green, J. J. Biodegradable Nanoellipsoidal Artificial Antigen Presenting Cells for Antigen Specific T-Cell Activation. *Small* **2015**, *11* (13), 1519–1525. https://doi.org/10.1002/smll.201402369.
(71) Fetsch, C.; Grossmann, A.; Holz, L.; Nawroth, J. F.; Luxenhofer, R. Polypeptoids from N-Substituted Glycine n-Carboxyanhydrides: Hydrophilic, Hydrophobic, and Amphiphilic Polymers with Poisson Distribution. *Macromolecules* **2011**, *44* (17), 6746–6758. https://doi.org/10.1021/ma201015y.